98555

Property of NCAR Library
Boulder, Colorado

QC921.5
I55
1976

INTERNATIONAL CLOUD PHYSICS CONFERENCE

JULY 26-30, 1976
BOULDER, COLORADO, U.S.A.

SPONSORS

INTERNATIONAL COMMISSION ON CLOUD PHYSICS (ICCP) OF THE INTERNATIONAL ASSOCIATION OF METEOROLOGY AND ATMOSPHERIC PHYSICS (IAMAP);

AMERICAN METEOROLOGICAL SOCIETY;

AMERICAN GEOPHYSICAL UNION;

NATIONAL OCEANIC AND ATMOSPHERIC ADMINISTRATION;

AND

NATIONAL CENTER FOR ATMOSPHERIC RESEARCH (Supported by NSF).

NATIONAL CENTER FOR ATMOSPHERIC RESEARCH
LIBRARY
OCT 6 1976

The manuscripts reproduced in this collection of preprints are unrefereed papers presented at the International Conference on Cloud Physics; their appearance in this collection does not constitute formal publication.

Prepared by and available from:

AMERICAN METEOROLOGICAL SOCIETY
45 Beacon Street, Boston, Massachusetts, 02108, U.S.A.

FOREWORD

This book contains a selection of papers contributed to the International Cloud Physics Conference. An approximate total of 175 papers was received of which the International Program Committee accepted approximately 100 for oral presentation and 45 as reserve papers, while about 30 were rejected. The abstracts of all papers submitted have been included in the Second Circular to the conference.

The overwhelming response to the Call for Papers made it very difficult for the Program Committee to assign papers to the above categories, considering the physical limitations imposed by the available time. In the Call for Papers it was, therefore, mentioned that submissions related to nuclei and nucleation should be limited in view of the forthcoming International Conference on Nucleation in Galway, Ireland in 1977, therefore only a few key papers in this area were accepted. Furthermore, the guidelines for selection placed emphasis on measurements and observations. The reason is that the store of measurements describing fundamental cloud physics parameters, which are so important for model development and verification, has become nearly exhausted. Indeed, what is needed now is a new "renaissance" of basic research in cloud physics. Not only are the basic cloud processes still poorly understood, such as nucleation, formation of droplet spectra, growth habits of ice crystals, and development of precipitation particles, they are frequently related through complicated feedback mechanisms to the mesoscale of atmospheric motion in and around clouds which in themselves are poorly understood. It becomes ever clearer that processes in cloud physics are extremely complex, as if nature protects this part of her kingdom with special care.

An important session of this conference is being dedicated to the memory of the late Dr. A. Borovikov, who devoted most of his scientific career to investigating and understanding basic cloud physical processes. His work is a shining example of what is urgently needed in the future, namely a dedication to conduct intensively basic research.

We consider it significant that this conference occurs back-to-back with the Second WMO Scientific Conference on Weather Modification. There is probably no area of modern meteorological research, in which new data from basic research projects in cloud and precipitation physics is more urgently needed, than in weather modification.

May this book and the corresponding volume of the Weather Modification Conference supplement each other and contribute to mutually beneficial cross fertilization.

Helmut K. Weickmann, Chairman
International Program Committee
Ilja Mazin
Erno Meszaros
R. Guy Soulage
Roland List
Harold D. Orville
Choji Magono
Stanley C. Mossop
J. Doyne Sartor
Walter F. Hitschfeld

TABLE OF CONTENTS

*Manuscript not available. **Manuscript will appear in the back of the book; if received in time.

*Manuscript not available. **Manuscript will appear in the back of the book; if received in time.

*Manuscript not available.

Page

Page

Page

*Manuscript not available.

Page

AUTHOR INDEX

*Manuscript not available. **Manuscript will appear in the back of the book; if received in time.

*Manuscript not available. Manuscript will appear in the back of the book; if received in time.

*Manuscript not available. **Manuscript will appear in the back of the book; if received in time.

Special Invited Lecture

THE IMPACT OF NUMERICAL MODELING ON CLOUD PHYSICS RESEARCH

Harold D. Orville

Institute of Atmospheric Sciences
South Dakota School of Mines and Technology
Rapid City, South Dakota 57701

EXTENDED ABSTRACT

Numerical modeling and computers pervade almost every facet of cloud physics research. Modeling has been used to study many microphysical processes, such as: stochastic drop coalescence, improved condensation theory, collection efficiencies with and without atmospheric electrical influences, ice nucleation, ice crystal and hailstone growth; and many larger scale cloud processes, such as: the initiation and evolution of rainstorms and hailstorms, the interaction of cloud and precipitation processes with the cloud and environmental airflows, the interactions of the lower boundary layer with clouds, the influence of the mesoscale on storm development and vice versa, and the genesis of Great Lakes' snowstorms. Large computers have been a prime tool in these studies. Smaller minicomputers have been vital for the collection and processing of data.

Even with this omnipresence of modeling its impact has not been strong in every phase and application of cloud physics research. Most evident has been its positive impact in weather modification and air pollution studies. It has been least influential, yet potentially could be most significant for application to local forecasting -- the prediction of rain, hail, snow, strong winds, and lightning. Also its use in field projects has been spotty, some relying heavily on modeling, some not at all.

This paper will concentrate on examples where models have gone astray, where observations have gone astray, and where combinations of modeling and observations have led to solid, meaningful results. The list is still being compiled but will include model results of large supersaturations, unrealistic water contents, inappropriate precipitation distribution functions, incomplete turbulence formulations, and unsuitable model dimensionality; the observational list will include inconsistent water content measurements and radar reflectivity factor values, unrealistically large radar reflectivity factors, the interpretation of negatively buoyant updrafts, inconsistent atmospheric electricity parameters, hygroscopic seeding effects on strong updrafts, and past observations causing a bias towards small clouds; good examples of coordinated work will include the explanation of ice nuclei and hygroscopic seeding effects, the explanation of high radar reflectivity factors, the interpretation of updraft and particle distributions in severe storms, improved condensation equation work resulting from urban pollution measurements, and tropical cloud and hurricane modeling and observational work.

The ingredients for successful coordinated modeling and observational programs will be analyzed. Reasons to hope for more and better efforts are that:

1) Models have matured (although many improvements can be foreseen),

2) observations and instruments have improved,

3) dedicated talented personnel are engaged in the research; and

4) computing power has increased and will increase even more in the future.

A plea will be made to structure models and observations in a common framework whenever possible. I suggest that since most cloud models are based on conservation equations, so also might the experimentalists try to fit their observations into such a scheme. Examples will be given.

Finally, although modeling can be used to test almost any cloud physics hypothesis, whether it be the effects of air pollutants on cloud and precipitation processes, the effects of ice nuclei seeding on rain, hail, and snow, the effects of powdered cement on cloudy updrafts, or the stimulation of convection by carbon black dust, to name only a few, yet the studies should not be conducted in isolation or be used to replace <u>field experimentation, which is absolutely necessary to complete the research</u>. Indeed, an expanded effort in the field is needed to insure that numerical modeling will continue to have an impact on cloud physics research. Data to verify models are critically needed. Modeling done in isolation from the observations is a sterile exercise doomed to eventual failure. Coordinated modeling and good field experimentation will move cloud physics to the forefront in meteorological research, having unlimited impact on local forecasting, weather modification, air pollution studies, and the understanding of severe weather events.

1.1.1 CONCENTRATIONS OF AITKEN, CLOUD DROPLET CONDENSATION AND ICE NUCLEI OVER SELECTED OCEANIC AND CONTINENTAL SITES

Paul A. Allee

Atmospheric Physics and Chemistry Laboratory
National Oceanic and Atmospheric Administration
Boulder, Colorado

Robert I. Sax and Emil Delgado

National Hurricane and Experimental Meteorology Laboratory
National Oceanic and Atmospheric Administration
Coral Gables, Florida

1. INTRODUCTION

With the development of advanced design instrumentation during the last decade it has become feasible to measure concurrent values of the concentration of Aitken nuclei (AN), cloud droplet condensation nuclei (CCN) and ice nuclei (IN) in the atmosphere by aircraft. Availability of space and sufficient electric power of the National Oceanic and Atmospheric Administration (NOAA) DC-6 and C-130 research aircraft has afforded the opportunity for measuring at many different localities the particulate concentrations in the atmosphere important to cloud physics. The Aitken nucleus concentrations were measured at first with a Gardner Small Particle Detector, and more recently with a continuously sampling Environment One (E-1) Condensation Nuclei Monitor. Cloud droplet condensation nucleus concentrations were measured with a thermal diffusion chamber constructed by NOAA. The ice nucleus concentrations were measured with a National Center for Atmospheric Research (NCAR) designed acoustic ice nuclei counter, the same instrument having been used for IN concentration measurements on all projects. On some flights the characteristics of the particulates were analyzed with a nephelometer. Atmospheric particulate samples collected on membrane filters during some flights were analyzed for size distribution with a transmission electron microscope, and for size distribution and elemental constituents with an x-ray energy spectrometer equipped scanning electron microscope.

Background particulate concentrations of AN, CCN and IN, and the contribution of urban areas have been measured over the mountains of Colorado, New Mexico (Bodhaine and Allee, 1976), the Great Lakes region (Allee et al., 1970), the Atlantic Ocean during the BOMEX (Allee, 1974) and GATE projects, and over the south Florida peninsula.

2. THE GATE PROJECT 1974

The NOAA DC-6, based at Dakar, Senegal, measured the concentration of AN, CCN (at 1% supersaturation) and IN (at -20°C). Particulate samples were collected on a 0.45 µm pore size membrane filter. AN concentrations and membrane filter samples were also taken on the NOAA ship OCEANOGRAPHER located about 800 km southwest of Dakar.

Nucleus concentration and particulate samples were obtained on 28 flights, from June 30 through August 15, 1974. Most flights were from Dakar to within the GATE surface ship array centered at 23° 30'W and 8° 30'N, southwest of Dakar. A few flights were made to investigate the dust in the Saharan air outbreaks over the Atlantic Ocean and to the intertropical convergence zone near the equator south of Dakar.

Fig. 1 is a typical record of nucleus concentrations on a flight (242-1A) consisting of a two hour ferry flight from Dakar to the ship array area 800 km southwest of Dakar, execution of a five hour preplanned flight path at low level within the ship array area, and a two hour ferry flight return to Dakar. Ferry flight altitudes varied between 1000 and 7000 ft. Within 200 km of the African coast the AN concentration was occasionally near 1000 ml^{-1}, beyond that distance rarely more than a few hundred per milliliter. The CCN concentration was usually about one half the value of the AN concentration. Often the CCN concentration would be less than the 44 CCN ml^{-1} threshold of sensitivity of the thermal diffusion chamber. The IN concentration varied from concentration measurements of 100 IN l^{-1} to less than 0.1 l^{-1}. On Fig. 1 the IN concentration was about 20 l^{-1} near the African coast, decreasing to less than 1 IN l^{-1} over the ship array flight pattern, increasing again to over 20 IN l^{-1} near the African coast on the return ferry flight. On most flights to the ship array area the IN concentration varied between 1 and 10 IN l^{-1}, only occasionally showing increased IN concentration near the African coast as noted on Fig. 1.

One flight was made during an outbreak of Saharan dust over the Atlantic Ocean to determine the character and concentration of the dust particles. The flight path was from Dakar west-northwest 300 km to the Cape Verde Islands and vicinity. The results of this flight is shown on Fig. 2. The AN concentration in the thickest portion of the dust near Sal Island was 1700 AN ml^{-1}. The CCN concentration was mostly below the 44 CCN ml^{-1} threshold of sensitivity of the thermal diffusion chamber. The IN concentration reached the highest measured value of the GATE project. There were 3.5 hours of flight time with the -20°C active IN concentration of 20 l^{-1} or greater, 2 hours with 30 IN l^{-1} or greater, 1 hour with 50 IN l^{-1} or greater, and during three short time intervals the IN concentration was greater than 100 IN l^{-1}. Visibility during portions of the flight in the vicinity of Sal Island was restricted by dust to about 1.5 km.

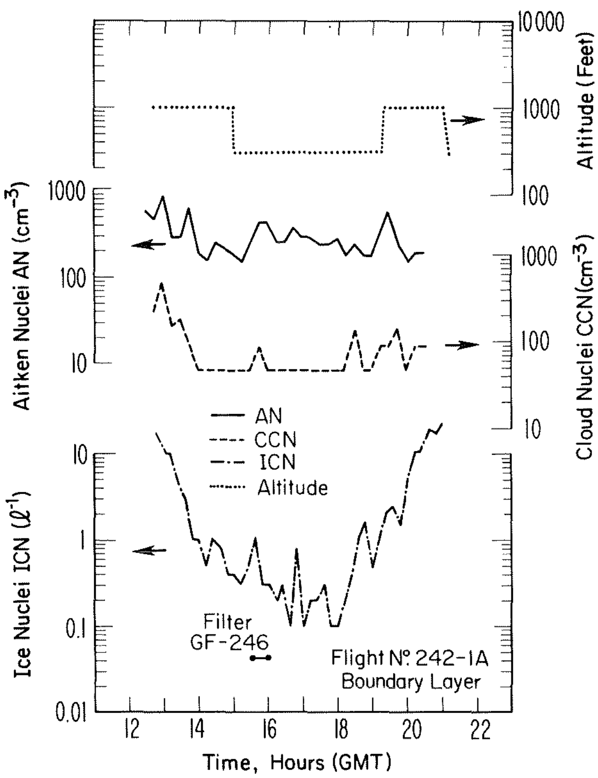

Fig. 1. AN, CCN, IN and altitude, Flight 242-1A August 30, 1974.

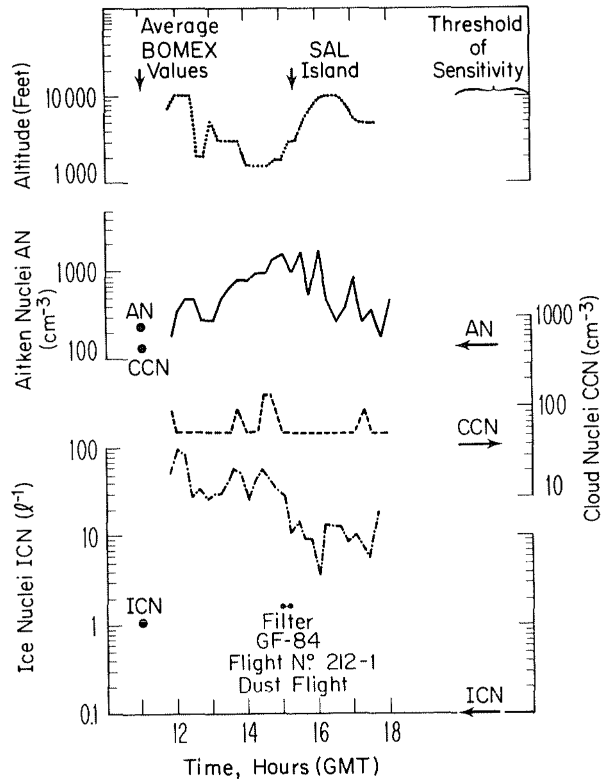

Fig. 2. AN, CCN, IN and altitude, Flight 212-1, July 31, 1974.

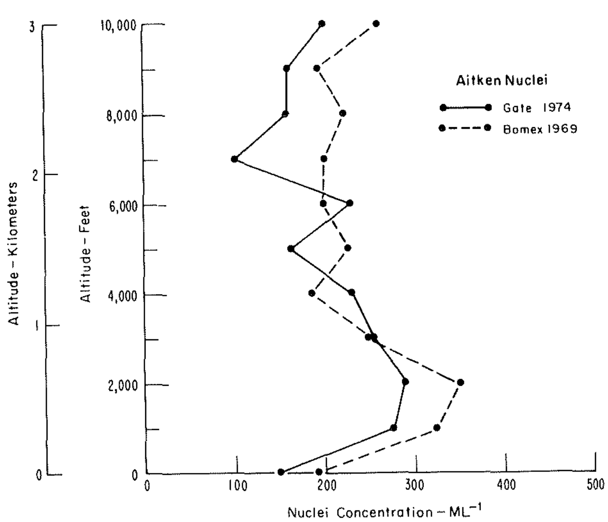

Fig. 3. Variation of average AN concentration with altitude.

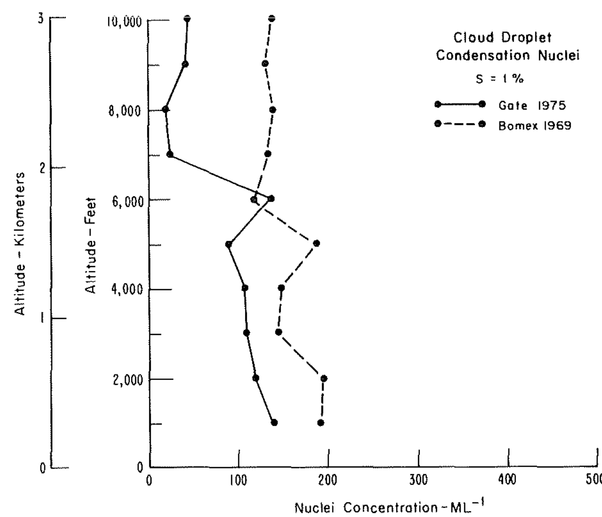

Fig. 4. Variation of average CCN concentration with altitude.

Fig. 3 shows the variation of the average AN concentration with altitude for all available data, excepting the dust flight, 212-1. The standard deviation for unclassified data of the GATE average AN concentrations at 7000 ft. altitude and below varied between 109 and 157. The variation of the average CCN concentration with altitude for all available data, excepting the dust flight, 212-1, is shown on Fig. 4. The standard deviation for unclassified data of the GATE average CCN concentrations at 6000 ft. altitude and below varied between 24 and 91.

Transmission electron microscope sizing of the dust particles captured on membrane filters GF84 and GF246 during the time noted on Figs. 4 and 3 is shown on Fig. 5. The particulate concentration measured during the collection period of filter GF84 was 2100 particles ml^{-1}, and for filter GF246 was 296 particles ml^{-1}. These values of particulate concentration are quite close to the values of AN concentrations, 1650 and 300

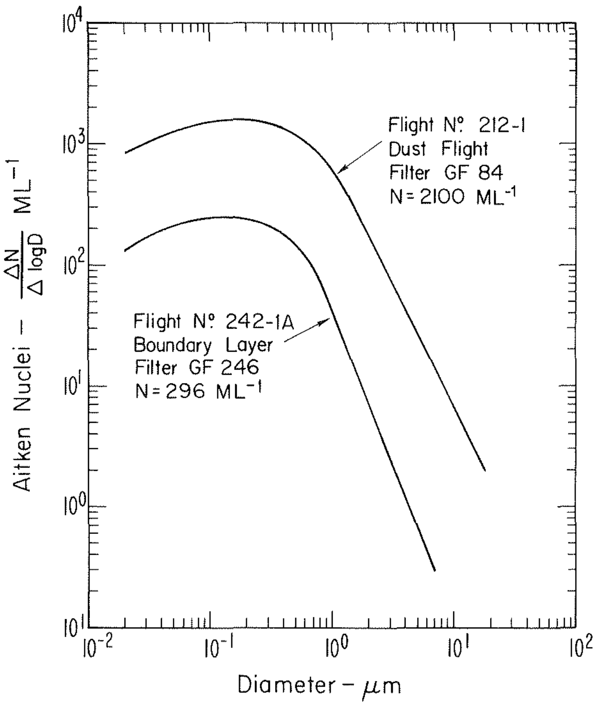

Fig. 5. Particulate size frequency $\Delta N/\Delta$ log D (ml^{-1}) versus diameter for Flights 242-1A and 212-1.

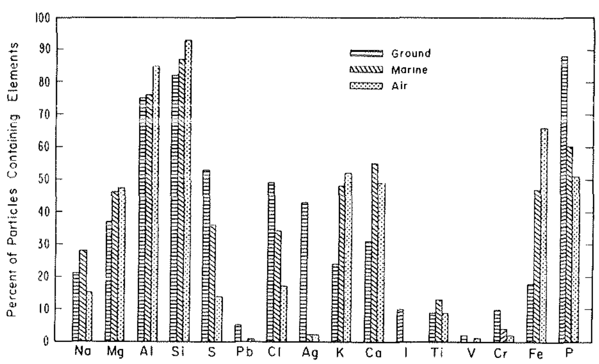

Fig. 6. Relative abundance (%) of particles according to elemental constituents.

respectively, measured with the Gardner counter, and indicates that there are few AN particles smaller than 0.02 μm diameter.

Elemental constituents of the particles captured on the membrane filters were analyzed with a scanning electron microscope. The results are shown in Fig. 6. The particles collected at ground level along the coast of Africa, the airborne filter samples and the maritime filter samples collected on the NOAA ship OCEANOGRAPHER are composed of essentially the same elements and appear to have their origin in the phosphorus rich clays of the Sahara desert. Particulate samples taken north and south of the intertropical convergence zone have essentially the same elemental constituents as the air samples shown in Fig. 6.

3. GATE PROJECT 1974, CONCLUSIONS

AN concentration measurements over the Atlantic Ocean southwest of Dakar are essentially the same as those measured during the BOMEX project in 1969, excepting during outbreaks of dust from the Sahara desert. The CCN concentration is low as it was during the BOMEX project, even within the outbreak of dust from the Sahara desert. Cloud droplets forming on these nuclei would result in relatively large cloud droplets. The warm rain mechanism would therefore work efficiently over the Atlantic Ocean and would result in rainout of clouds of low vertical development.

The IN concentration over the Atlantic Ocean during the BOMEX project averaged between 1 and 2 IN l^{-1} (Allee, 1974), and averaged in the same manner the IN concentration during the GATE project was between 3 and 9 IN l^{-1}. However, because of large variations of IN concentration due to Saharan dust outbreaks near the African continent it is best to consider the IN concentration for each individual flight. The higher IN concentration in the Saharan dust outbreaks indicates that at subfreezing temperature clouds should glaciate readily. That such is the case has been observed by Weickmann (1975).

4. THE 1975 FACE EXPERIMENT

As part of the 1975 Florida Area Cumulus Experiment (FACE) conducted by the Cumulus Group of NOAA's National Hurricane and Experimental Laboratory, the DC-6 aircraft was used to obtain aerosol data at 0.6 km, just below the cloud base level, during traverses across the south Florida peninsula at latitude 26°30'N. In addition to the previously described aerosol instrumentation the DC-6 carried a Barnes PRT-5 infrared sensor that was used to map the surface temperature profile along the flight track. Particulates were sampled with a membrane filter.

Fig. 7 locates the flight track relative to the south Florida peninsula. The flight track started at Point A (long. 79°30'W), ended at Point B (long.82°25'W). Points B, E, and F mark the east coastline, west mainland coastline and the Gulf coastline. The location of power plants in operation July, 1975 are also marked. All power plants burned oil except the Fort Myers plant that used gas and the complex south of Coral Gables (Turkey Point) that is partially nuclear fueled. With the exception of the very narrow urban strip along the east coast in the West Palm Beach area, and the developing urban area around Fort Myers, the flight track was over partly cultivated rural land. The eastern portion of the flight path was over a narrow area of urban development, a large fresh water reservoir, and an agriculture area consisting mostly of cane fields. The central area of the peninsula has grassy fresh water marshes with tree covered islands. The western portion was over sandy soil with pine trees, shrubs, small hardwood trees, some vegetable cultivation, some small swamps, the Fort Myers urban area at the mainland shore, and a few offshore islands. Surface elevation

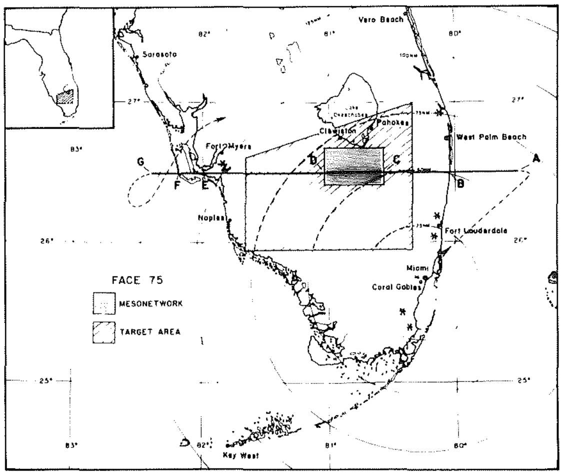

Fig. 7. Location of the cross-peninsula flight path in relation to the FACE target area. Asterisks (*) indicate location of FPL power plants.

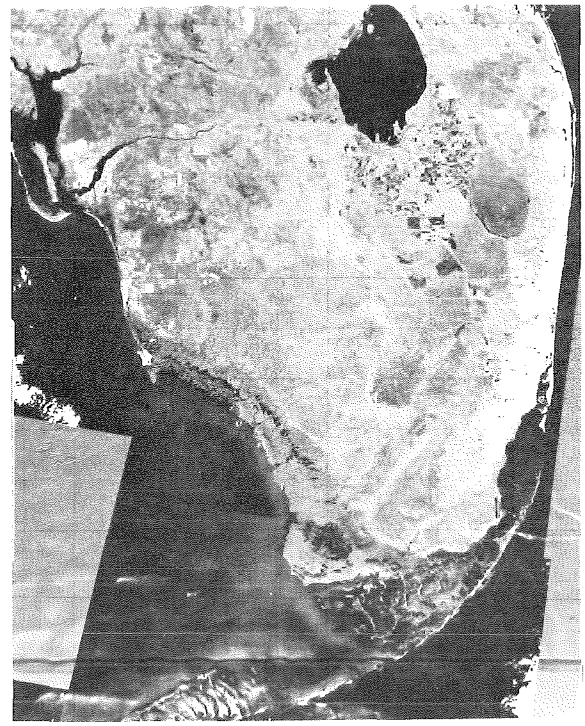

Fig. 8. ERTS multi-spectral infrared composite of the south Florida peninsula.

across the entire south Florida peninsula varies from sea level by no more than about 10 m.

Fig. 8, a mosiac photograph of the Earth Resources Technological Satellite (ERTS) multi-spectral infrared satellite information, clearly delineates the type of terrain underneath the flight track. The extent of urban development along the east coast of Florida and at Fort Myers on the west coast is apparent. South of Lake Okeechobee can be seen the rectangular fields of the sugar cane industry. Between the cane fields and the urban development along the east coast can be located a fresh water reservoir, completely overgrown with water hyacinth during July. The western half of the flight path are over sandy soil, swamps, and some agricultural areas.

5. FACE 1975 DISCUSSION

The objective of the FACE aerosol program was to determine the daily distribution and interrelationship of the various types of nuclei (AN, CCN and IN) within the boundary layer with the ultimate goal of correlating the aerosol spectra with the in-cloud microphysical data obtained at higher altitudes. Since the low-level cross-peninsula flight on each day was a stand-

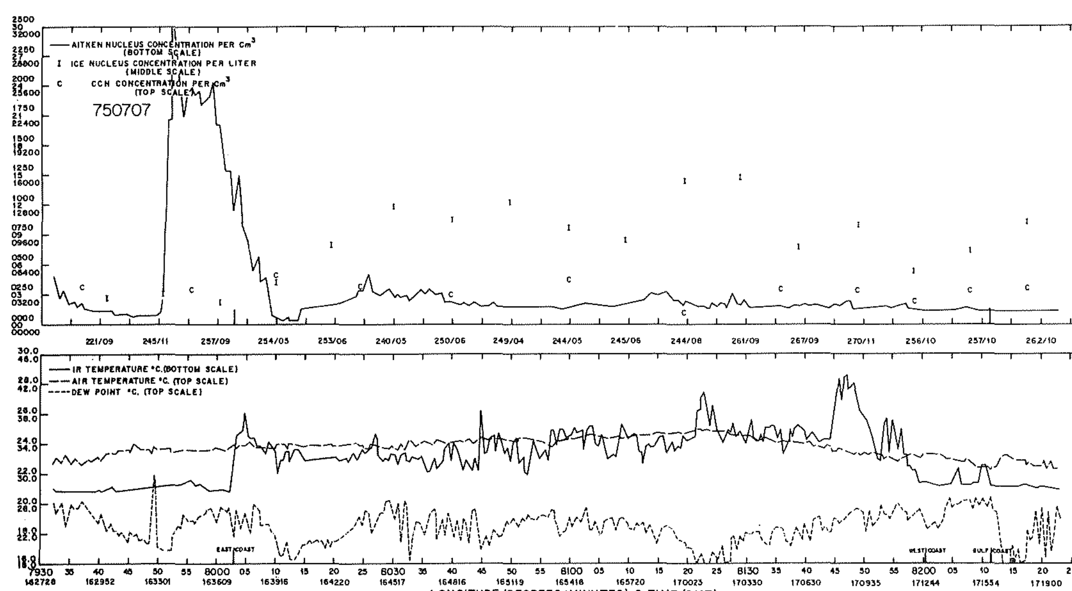

Fig. 9. Cross-peninsula aerosol profile for 7 July 1975.

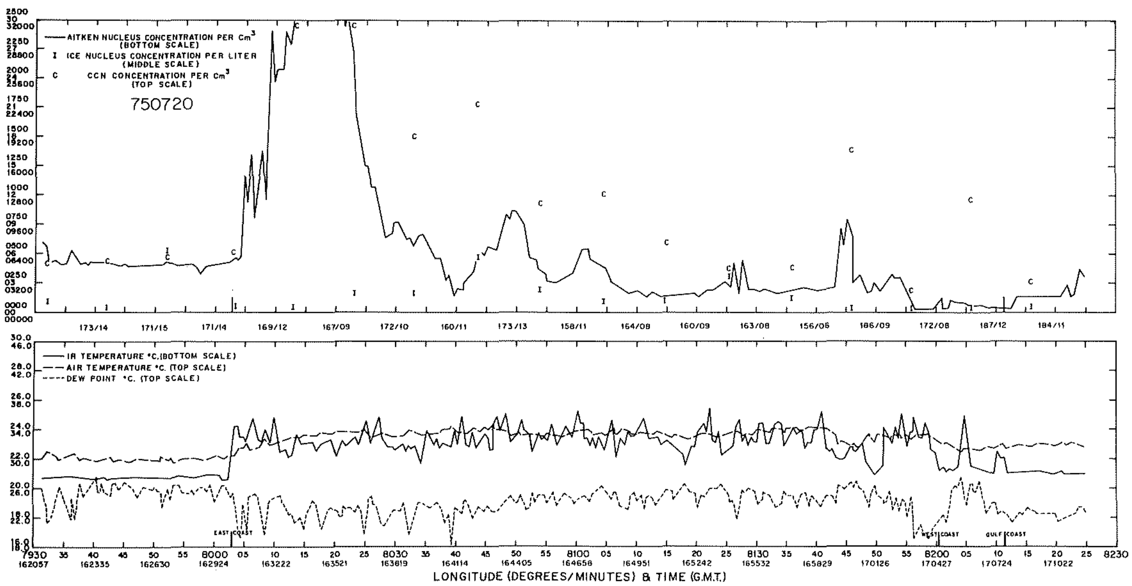

Fig. 10. Cross-peninsula profile for 20 July 1975.

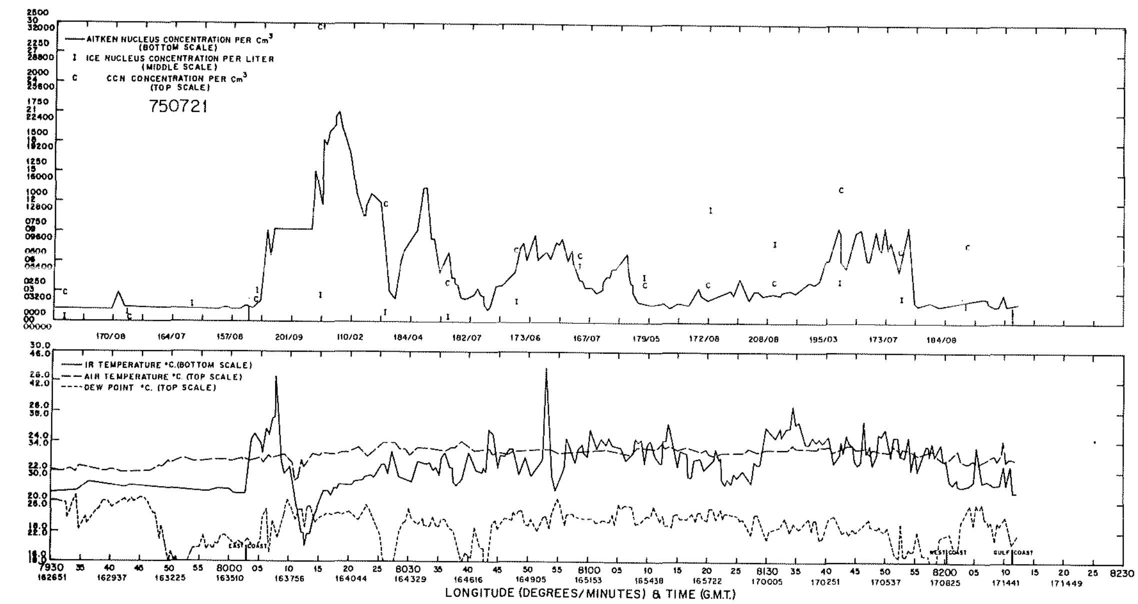

Fig. 11. Cross-peninsula aerosol profile for 21 July 1975.

dard pattern and time, the aerosol data could be normalized to a fixed longitudinal position.

Point values of CCN were obtained approximately every three minutes from the thermal diffusion chamber operated at 0.75% supersaturation. Pulses from the acoustic ice nucleus counter were summed over a three minute sampling period. The AN concentration was sampled every second, and a 10-second (approximately 1 km) centermean smoothing was applied to the data. A similar 10-second smoothing scheme was also applied to the infrared surface temperature, ambient air temperature, and ambient dew point data, all of which were sampled at a rate of once per second.

Figs. 9, 10 and 11 show the cross-peninsula profiles of aerosol and temperature information for 7, 20 and 21 July. These are examples that show in detail the type of data analyses used to interpret the aerosol distributions. The starting point at Point A varied by less than 15 minutes for these three examples. The aircraft-measured winds (shown between the aerosol and temperature plots) were westerly on the 7th and southeasterly on the 20th and 21st. The AN concentration was just to the west of the eastern coastline with southeasterly flow, and over and to the east of the eastern coastline with westerly flow. The downwind discontinuity (or "Aitken front") is extremely sharp on the 7th and 20th. The concentration of CCN is relatively high, though not uniformly so, across the peninsula on the 20th, and quite low (500 ml^{-1}) on the 7th. The concentration of IN active at $-20^{o}C$ is very high (5-10 l^{-1}) on the 7th, and low ($\simeq 1\ l^{-1}$ or

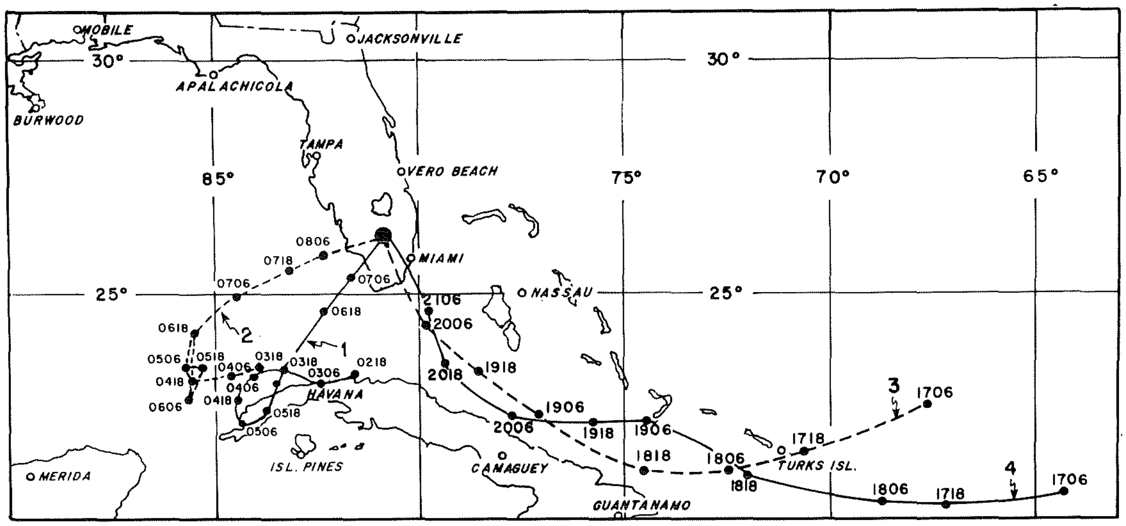

Fig. 12. Airmass trajectories (five-day) terminating at 1800 GMT on 7, 8, 20, and 21 July (curves #1, 2, 3 and 4, respectively).

less) on the 20th. The 21st contains a mixture of aerosol features, with relatively low AN peak concentration and moderate concentrations of CCN and IN. Aside from the east coast peak, the spatial variability of AN concentration across the peninsula was greatest on the 21st and least on the 7th. The variability in the IR surface temperature structure is pronounced on all three days, but certain peak values (e.g. the east coast shoreline)can be discerned. An IR positive anomaly occurs on several days (note the 7th and 21st) near longitude 80°50'W, a location which corresponds to a section of the cultivated sugar cane region.

Of the 13 low-level cross-peninsula traverses conducted during July, 10 took place on days characterized by primarily easterly or southerly component winds at flight level. A first analysis of data from all the flights has revealed the following general features of the aerosol distribution across the peninsula:

1. The concentration of CCN active at 0.75 supersaturation is highly variable from place to place and from day to day, with values ranging from 240 to 2500 ml^{-1}. There is a tendency for lower concentrations of CCN on days with westerly flow, particularly along that portion of the flight track west of longitude 80°15W. The CCN concentration is lower across the peninsula on those days with an easterly or southerly wind arriving onshore with speeds in excess of about 7 m sec^{-1}. However, the sample size is not large enough for good correlation.

2. The location of the east coast AN pulse is well correlated to the location of the initial IR anomaly on easterly and southerly flow days; the magnitudes of each, however, appear to be independent. The Gulf and west coast IR anomalies on westerly flow days produce almost no perturbation in the AN concentration profile.

3. The peak value of AN concentration on all days is well correlated with the urbanization of the east coast. The spatial structure of the AN profile is simplified on westerly flow days, the decay downwind off shore is sharper than the decay downwind over land on easterly flow days. This indicates a reinforcement of the AN concentration over the land. A secondary peak in the AN concentration occurs on most days in the vicinity of 80°50'W that relates well to the IR temperature anomaly generally found in that location.

4. The CCN concentration over the peninsula is clearly land-generated on most days. An exception to this is July 7, a day on which the CCN concentration is suppressed across the peninsula. There may be some relationship between CCN formation over the land and the presence of Saharan dust (as occurred on the 7th) that may be acting to decrease solar radiation reaching the surface.

5. The IN concentration active at -20°C is very high (>10 l^{-1}) on two days (e.g. Fig. 9), moderately high (5-10 l^{-1}) in places on several other days (e.g. Fig. 11) and uniformly low (<2 l^{-1}) on most days (e.g. Fig. 10). The highest daily IN concentrations were associated with three distinct outbreaks of Saharan dust (4-8 July, 21-23 July, and 28-29 July). The IN concentration over land was higher in such cases than the concentration upwind over the water.

6. Correlations using log and fourth-root transforms of the aerosol data indicate a high degree of direct association between CCN and AN concentrations on 8 of the 13 flight days, and a high inverse association on one other day (8 July). The four remaining cases showed no strong association between CCN and AN. Attempts were made to correlate IN concentration with either AN or CCN concentrations, but, with the exception of one day (18 July) that showed a significant inverse relationship for both; the variables were not found to be strongly associated with each other.

7. Differences in the aerosol distribution do not seem to be a strong function of the origin of the air mass five days earlier. The easterly and southerly flow days have similar 5-day trajectories originating generally between 17°30'N and 22°30'N latitude and 64°W to 72°W longitude. Two of the three westerly flow days had 5-day trajectories originating north of the western tip of Cuba, while the third day had its air mass originate in the Bahamas east of Florida. Fig. 12 shows the 5-day trajectories for the air mass situated over the FACE target area at 1800 GMT on 7 July (#1), 8 July (#2), 20 July (#3), and 21 July (#4). It can be seen that the trajectories for the 20th and 21st are not too dissimilar, yet the aerosol characteristics across the peninsula on those days are quite different (see Figs. 10 and 11). In fact, the aerosol characteristics over the water upwind of the land are also different, with considerably higher values of AN, CCN, and IN occurring on the 20th.

8. The differences in the aerosol profile between the 20th and 21st are difficult to explain on the basis of thermal stability. Both days were found to have a similar thermal structure to 700 mb, with a moderately stable layer near 900 mb and a nearly dry adiabatic lapse rate below about 920 mb. Special early-afternoon (1600 to 1800 GMT) radiosondes launched from the FACE mesonetwork (Fig. 7) provided the information for the analysis of thermal stability.

9. Electron microscopy analyses of the chemical composition of material collected by the membrane filters during the cross-peninsula traverses on several days is shown on Fig. 13. They indicate that the source of most of the particles was from the surface of some land mass. The presence of heavy metals would be indicative of the capability of the particles to act as ice nucleation centers in supercooled water. 80% of the particles on filter number 21 did not respond to x-ray spectrographic analysis, an indication that they were composed of organic compounds, and some of these could act as CCN and low temperature active IN. The large percentage of organic particulates is to be expected in view of the nature of the peat and mulch soil, swamps and vegetative character of the surface of the Florida peninsula.

6. FACE 1975 CONCLUSIONS

A study such as this raises as many or more questions than it answers. The origin of the CCN is a particularly important problem in relation to the FACE effort, as there is some evidence (Hallet et al., 1976) to suggest an association between droplet size spectra (a function of CCN concentration) and secondary ice crystal production in Florida cumuli clouds. It is evident from this study that the relationship of the aerosol characteristics to wind flow, stability, airmass trajectory, and/or IR thermal structure is not straightforward. On the other hand, there is a suggestion on a majority of days that the CCN concentration is related to the AN concentration, and, since the AN peaks seem to be associated with anthropogenic activity, it may be that man himself is responsible in some manner for the CCN distribution across the peninsula. It is not

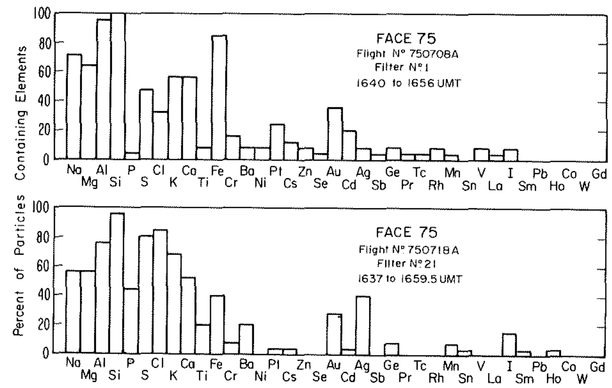

Fig. 13. Relative abundance (%) of particles according to elemental constituents.

unreasonable to assume that at least some of the CCN were formed from agglomeration of AN. There is also evidence from the study to suggest a relationship between outbreaks of Saharan dust and high IN activity (and possibly low CCN activity as well). The problem of resolving the correlation between aerosol (particularly AN pulses) concentration and IR temperature anomalies must await a more sophisticated analysis of the data set. It may well be that the variability in the AN concentration may be useful in predicting the onset of convection, since the aerosol field may respond to convergence patterns in the atmosphere before visible clouds are produced.

REFERENCES

Allee, P. A., 1974: Atmospheric particulate concentration measured over the Atlantic Ocean during the 1969 BOMEX experiment. Jour. de Rech. Atmos., VIII, 947-955.

Allee, P. A., T. B. Harris, Jr., and R. Proulx, 1970: Atmospheric constituents near Lake Erie. Proc. 13th Conf. Great Lakes Research. Internat. Assoc. Great Lakes Res., 779-789.

Bodhaine, B. A., and P. A. Allee, 1976: Background nuclei over northwestern New Mexico; San Luis Valley, Colorado; and Lake Michigan. To be published: NOAA-ERL Technical Report.

Hallett, J., D. Lamb, A. S. R. Murtry, and R. I. Sax, 1976: Aircraft measurements relating to secondary ice crystal production in Florida cumuli. Proc. International Cloud Physics Conference, 26-30 July 1976, Boulder, Colorado, USA. International Commission on Cloud Physics (ICCP) of the International Association of Meteorology and Atmospheric Physics (IAMAP), Americal Meteorological Society, American Geophysical Union, National Oceanic and Atmospheric Administration.

Weickmann, H. K., 1975: Observations on convective clouds over the tropical Atlantic. GATE Report No. 14., World Meteorological Organization, International Council of Scientific Unions.

CLOUD CONDENSATION NUCLEUS SIZE DISTRIBUTIONS AND THEIR EFFECTS ON CLOUD DROPLET SIZE DISTRIBUTIONS

Edward E. Hindman II
Michelson Laboratories
China Lake, California 93555

Peter V. Hobbs and Lawrence F. Radke
University of Washington
Seattle, Washington 98195

1. INTRODUCTION

Airborne measurements of the size distributions of aerosol particles and the supersaturation spectra of cloud condensation nuclei (CCN) were made beneath small, non-raining, warm, cumulus clouds in western and eastern Washington during May, July, and August, 1974. Shortly after the sub-cloud measurements were made, the size distributions of the droplets within the clouds were measured and meteorological sounding data were collected in the vicinity of the clouds. The aerosol particle and CCN measurements were used to derive the size distributions of the CCN. The CCN size distributions were used, along with the meteorological data, to calculate the droplet size distributions in clouds near cloud base using the theoretical warm cumulus model developed by Silverman and Glass (1973).

In this paper we present the effects on the cloud droplet size distributions (measured and calculated) caused by variations in the sub-cloud CCN size distributions.

2. MEASUREMENTS

The following airborne measurements were obtained using the array of particle sampling instrumentation described by Hobbs et al. (1976): (a) the size distributions of aerosol particles (0.004 to 100 μm diameter); (b) the concentrations of CCN active at 0.2, 0.5, 1.0 and 1.5% supersaturation; (c) the concentrations of particles ⩾ 1 μm diameter which acted as CCN and their elemental compositions (using techniques described by Hindman et al., 1976), (d) the size distributions of cloud droplets (5 to 70 μm diameter) near cloud base, and (e) free-air temperature, dew point and pressure in the sub-cloud layer (to refine National Weather Service soundings taken at Quillayute and Spokane, Washington, and soundings taken at the University of Washington, Seattle).

On May 28, 1974, measurements were made 16 km east of Seattle in western Washington and 28 km northeast of Wenatchee in eastern Washington. On July 12, August 12, and August 20, 1974, measurements were made in the plume of the paper mill located at Port Townsend in western Washington, in nearby air unaffected by the plume, and in warm clouds located in and out of the plume. Details of these measurements have been reported by Hindman (1975).

3. CLOUD CONDENSATION NUCLEUS SIZE DISTRIBUTIONS

An analysis of the aerosol particle and CCN measurements made in and out of the paper mill plume by Hindman et al. (1976) indicates that all of the particles 0.07 to 0.2 μm diameter acted as CCN and were composed of inorganic salts. A subsequent analysis of the aerosol particle and CCN measurements made east of Seattle and northeast of Wenatchee indicates that a majority of the particles 0.07 to 0.2 μm diameter acted as CCN. Therefore, the measured size distributions of aerosol particles (0.07 to 0.21 μm) were assumed to represent the size distributions of CCN with diameters 0.07 to 0.21 μm.

The concentrations of CCN with diameters ⩾ 1 μm and ⩾ 5 μm were determined by multiplying the measured concentrations of aerosol particles by the fraction of the particles which deliquesced. The fraction of particles with diameters ⩾ 1 μm which deliquesced was determined from the ratio of the number of the particles which contained primarily the chemical elements found in simple inorganic salts (e.g., sodium, potassium, calcium, chlorine, sulfur, etc.) to the total number of particles analyzed. The fraction of particles ⩾ 5 μm which deliquesced was determined from the ratio of the number of particles observed to deliquesce between 50 and 95% relative humidity to the total number of particles observed. The fractions of the particles in each size category which deliquesced are shown in Table 1.

Table 1.

Fractions of Particles Which Deliquesced

Location	Particle Diameter	
	⩾ 1 μm	⩾ 5 μm
In paper mill plume	0.61	0.63
Near paper mill plume	0.25	0.36
16 km east of Seattle, WA	0.40	0.52
28 km northeast Wenatchee, WA	0.0	0.04

The CCN size distributions over the interval 0.07 to 0.21 μm were extended to cover the interval 0.07 to 5 μm by including the concentrations of CCN with diameters ⩾ 1 μm and ⩾ 5 μm. The results then were extrapolated to 20 μm (an arbitrary upper size limit). A lower size limit had to be specified because the CCN size distribution used in the calculations had to be that of activated CCN. Therefore, the lower size limit was defined as the CCN size at which the total concentration of CCN greater than or equal to that size equaled the total concentration of droplets measured in the clouds.

The CCN size distributions which resulted from the measurements in the paper mill plume and in ambient air are given in Figure 1; the CCN size distributions measured 16 km east of Seattle in western Washington and 28 km northeast of Wenatchee in eastern Washington are given in Figure 2.

4. CLOUD DROPLET SIZE DISTRIBUTIONS

The cloud droplet size distributions measured from clouds located in the paper mill plume and in ambient air are shown in Figure 3. The measured concentrations of droplets with diameters $\geqslant 5$ μm (considered here to be total droplet concentrations) were essentially the same in the clouds located in and out of the paper mill plume. This result is supported by measurements which indicate that the paper mill plume does not increase the concentrations of small CCN ($0.7 \lesssim D < 0.2$ μm) above background concentrations (Hindman et al., 1976); these CCN form the bulk of the total concentration of cloud droplets. The measured concentrations of droplets with diameters $\geqslant 30$ μm were found to be higher, by a factor of four, in the clouds located in the plume than in clouds located in the ambient air, a result which confirms the droplet measurements made by Eagan et al. (1973) from clouds located in the plume of the same paper mill. These high concentrations of large droplets are consistent with the high concentrations of large CCN ($0.2 \leqslant D \leqslant 1$ μm) and giant CCN ($D > 1$ μm) measured in the plume of the paper mill (see Figure 1).

The droplet size distributions which were calculated from the CCN measurements made shortly before the droplet measurements are also shown in Figure 3. The calculated droplet size distributions should apply near cloud base. The calculated distributions contain liquid water contents comparable to the liquid water contents of the measured droplet size distributions. It can be seen from the results shown in Figure 3 that the calculated size distributions of the cloud droplets which form on the plume CCN are broader than the calculated size distributions of the cloud droplets which form on the ambient CCN, a result which agrees qualitatively with the measured droplet size distributions. Quantitative agreement between the calculations and measurements is indicated by the following observations: (a) the difference between the calculated concentrations of large drops ($D_p \geqslant 30$ μm) which formed on the plume CCN and ambient CCN is of the same order as the difference between the measured concentrations, (b) the mean droplet sizes calculated from the plume and ambient CCN size distributions agree with the mean droplet sizes from the droplet measurements, and (c) the difference between the dispersion coefficients (standard deviation/mean droplet size; indicates breadth of a distribution) of the calculated drop size distributions is the same order as the difference between the dispersion coefficients of the measured droplet size distributions.

The good agreement between the measured and calculated droplet size distributions indicates the following: (a) the CCN size distributions in

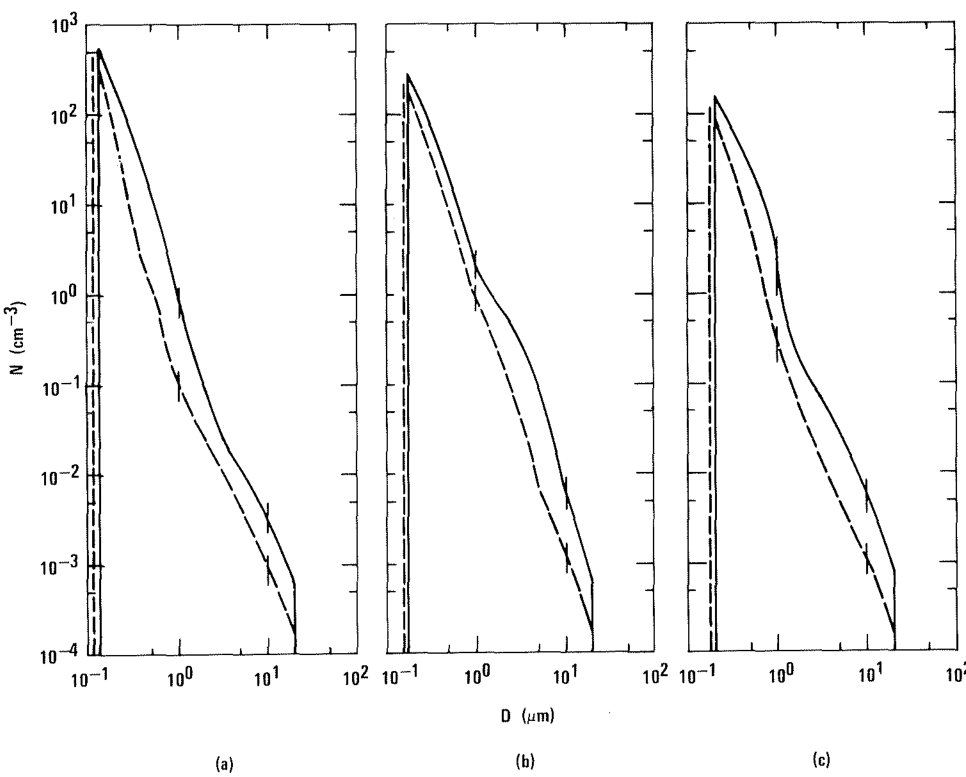

Fig. 1. Cloud condensation nucleus (CCN) size distributions in the plume of the paper mill (solid lines) and in nearby ambient air (dashed lines). The data were collected on (a) July 12, 1974, (b) August 12, 1974, and (c) August 20, 1974. N is the concentration of CCN with diameters greater than or equal to D.

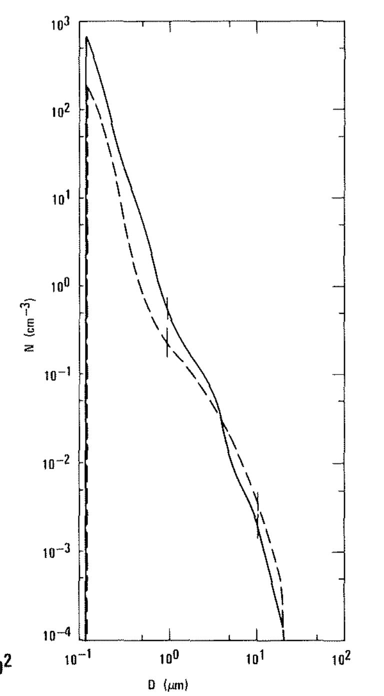

Fig. 2. Cloud condensation nucleus (CCN) size distributions in western Washington (solid line) and in eastern Washington (dashed line) on May 28, 1974. N is the concentration of CCN with diameters greater than or equal to D.

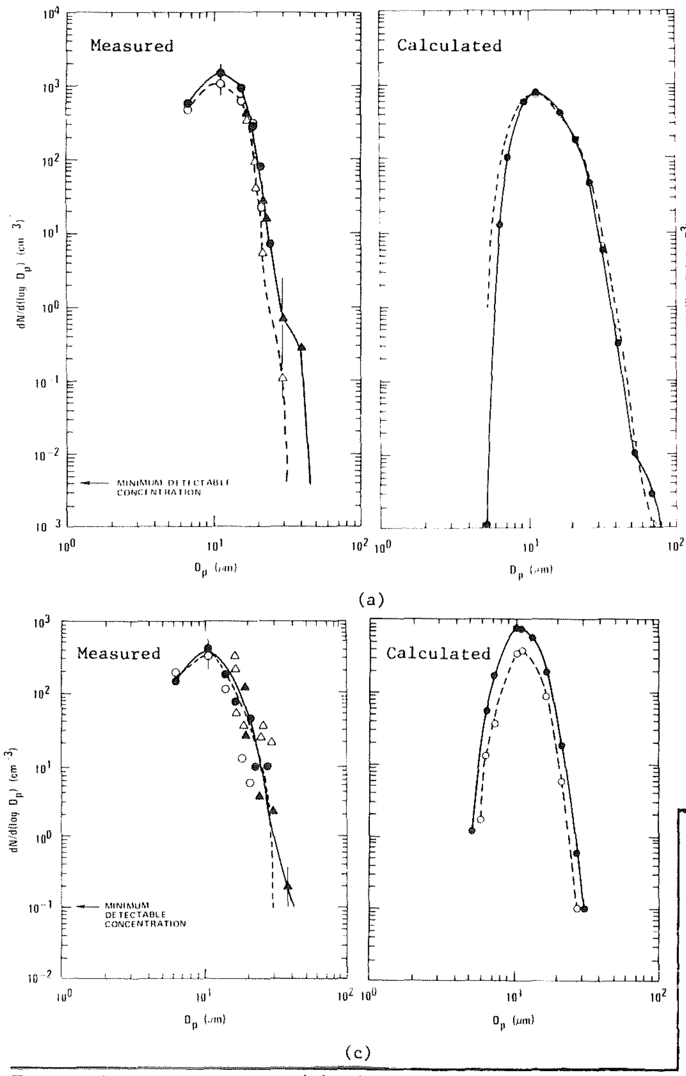

Fig. 3. Cloud droplet size distributions measured from clouds located in the plume of the paper mill (solid lines) and measured from clouds located in nearby ambient air unaffected by the plume (dashed lines). The circles are data from an axially scattering spectrometer probe; the triangles are data from a continuous particle sampler. Cloud droplet size distributions calculated from CCN data collected in the plume (solid lines) and from CCN data collected in nearby ambient air (dashed lines). The data were collected on (a) July 12, 1974, (b) August 12, 1974, and (c) August 20, 1974.

Figure 1 are accurate, (b) the large and giant CCN emitted by the paper mill cause the anomalously high concentrations of large droplets in clouds located downwind, and (c) that given two CCN size distributions with similar concentrations of small CCN, but with one distribution containing higher concentrations of large and giant CCN, the distribution with the higher concentrations of large and giant CCN will produce the broader cloud droplet size distribution.

The cloud droplet size distributions measured from clouds located in western and eastern Washington are shown in Figure 4. The measured concentrations of droplets with diameters $\geqslant$ 4 µm were higher in the clouds located in western Washington. However, no droplets greater than 20 µm were measured in the clouds in western Washington, while droplets greater than 30 µm diameter were measured in the clouds in eastern Washington. The total droplet concentrations were higher in the clouds in western Washington because more small CCN existed in western Washington (see Figure 2); this is possibly a reflection of the numerous industrial sources of CCN which have been identified by Hobbs et al. (1970).

The droplet size distributions calculated from the CCN measurements made shortly before the droplet measurements are also shown in Figure 4. The results of the calculations from the eastern Washington measurements indicate concentrations of droplets greater than 30 µm which are in reasonable agreement with the measured concentrations. The results of the calculations from the western Washington measurements do not contain droplets greater than 20 µm, a result which is consistent with the measurements.

The presence of large drops in the eastern Washington clouds, and their absence in the western Washington clouds, was not a result of the presence of giant CCN in eastern Washington and their absence in western Washington since their concentrations differed by only a factor of two (see Figure 2). Instead, it appears that the high concentrations of small CCN in western Washington caused the high total droplet concentrations which in turn increased the collodial stability of the clouds, thereby decreasing the production of

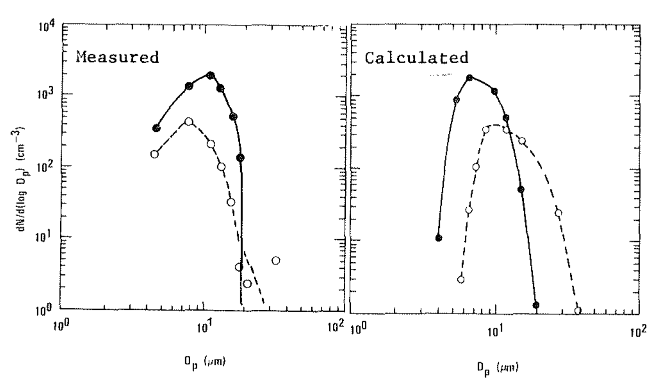

Fig. 4. Measured and calculated cloud droplet size distributions for May 28, 1974. The droplet size distributions for western and for eastern Washington are represented by the solid lines and the dashed lines, respectively.

large drops by the coalescence mechanism. Calculations by Hindman and Hobbs (1974), using the same theoretical warm cumulus model, have shown that droplet size distributions in small, non-raining, warm cumulus become narrower when the concentrations of small CCN are increased and the concentrations of large and giant CCN are held constant. High droplet concentrations are commonly observed with narrow droplet size distributions and vice versa as shown by the measurements of Squires (1956, 1958). Hindman and Hobbs also found that the breadth of droplet size distributions is unaffected when the concentrations of giant CCN are increased and the concentrations of small and large CCN are held constant. The measurements of Squires and Twomey (1958) and the calculations of Takahashi (1974) support this result.

It is concluded from the results of the calculations based on measurements in western and eastern Washington, and from the results of the calculations by Hindman and Hobbs (1974), that high concentrations of small CCN will produce narrow droplet size distributions in small, non-raining, warm cumulus regardless of the concentrations of large and giant CCN.

5. CONCLUSIONS

Cloud droplet size distributions have been calculated from CCN measurements made beneath small, non-raining, warm, cumulus clouds. The calculations are based on a theoretical model of warm cumulus clouds developed by Silverman and Glass (1973). The calculated drop size distributions agree with drop size distributions measured from the warm cumulus shortly after sub-cloud CCN measurements. Both the calculations and the measurements showed that high concentrations of large ($0.2 \leqslant D \leqslant 1$ μm) and giant ($D > 1$ μm) CCN lead to broad droplet size distributions only if low concentrations of small ($0.07 < D < 0.2$ μm) CCN are present If high concentrations of small CCN are present, the droplet size distributions will be narrow regardless of the concentrations of large and giant CCN.

Acknowledgements. The field portion of the study was executed at the University of Washington and was supported in part by grants from the National Science Foundation. One of us (E.E.H.) was supported at the University of Washington by a Fellowship from the Michelson Laboratories.

6. REFERENCES

Eagan, R.C., P.V. Hobbs, and L.F. Radke, 1974: Particle emissions from a large Kraft paper mill and their effects on the microstructure of warm clouds. J. Appl. Met., 13, 535-552.

Hindman, E.E., II and P.V. Hobbs, 1974: Modifications to the microstructure of warm clouds by cloud condensation nuclei from paper mills: A numerical study. Preprints - 4th Conf. Wea. Mod., AMS, Boston, 401-404.

Hindman, E.E., II, 1975: The nature of aerosol particles from a paper mill and their effects on clouds and precipitation. Ph.D. Dissertation, Department of Atmospheric Sciences, University of Washington, Seattle, 242 pp. (Available from University Microfilms, 300 N. Zeeb Rd., Ann Arbor, Michigan 48106.)

Hindman, E.E., II, P.V. Hobbs, and L.F. Radke, 1976: Airborne investigations of aerosol particles from a paper mill. J. Air. Poll. Cont. Assn., in press.

Hobbs, P.V., L.F. Radke, and S.E. Shumway, 1970: Cloud condensation nuclei from industrial sources and their apparent influence on precipitation in Washington State. J. Atmos. Sci., 27, 81-89.

Hobbs, P.V., L.F. Radke, and E.E. Hindman, II, 1976: An integrated airborne particle sampling facility and its preliminary use in aerosol studies. J. Aerosol Sci., in press.

Silverman, B.A., and M. Glass, 1973: A numerical simulation of warm cumulus clouds. Part I - Parameterized vs. non-parameterized microphysics. J. Atmos. Sci., 30, 1620-1637.

Squires, P., 1956: The microstructure of cumuli in maritime and continental air. Tellus, 8, 443-444.

Squires, P., 1958: The microsture and colloidal stability of warm clouds, Part I - The relation between structure and stability. Tellus, 10, 256-261.

Squires, P., and S. Twomey, 1958: Some observations related to the stability of warm cumuli. Tellus, 10, 272-275.

Takahashi, T., 1974: Effective cloud nuclei size range for the formation of raindrops in maritime warm clouds. Preprints - Conf. Cld. Phys., AMS, Boston, 205-210.

A SIMPLE NUMERICAL SIMULATION OF THE CONDENSATIONAL GROWTH OF CLOUD DROPLETS IN BACKGROUND AIR

K. Bónis, E. Koflanovits, A. Mészáros and E. Mészáros

Institute for Atmospheric Physics
Budapest, Hungary

1. INTRODUCTION

One of most important problems of the cloud physics is to explain and understand the condensational stage of the cloud formation. The size distribution and concentration of drops formed by condensation can control the further development of the clouds, that is these parameters can play an important part in the formation of atmospheric precipitation. It is also well documented that the initial cloud microstructure largely depends on the characteristics of active condensation nuclei and on the updraft velocity.

For this reason from the classical work of Howell/1949/ many calculations were made to simulate numerically the condensational growth of cloud droplets by using different spectra of sodium chloride and different rates of ascent. From these studies the works of Mordy /1959/ and of Mason and Chien /1962/ should be mentioned who took into account the effect of the particles settling velocity and that of the mixing of air parcel with its environment, respectively. Soviet workers /p.e. Sedunov, 1972/ as well as Warner /1969/ studied by model calculations the stochastic growth of cloud drops due to the atmospheric turbulence.

The aim of this lecture is not to refine the numerical model. It is rather proposed to apply the "classical" model by using new informations about the so-called tropospheric background aerosol. In this way the results will give some contributions to the understanding of the cloud formation in a large part of the troposphere.

2. THE MODEL

The model used in this study is essentially equivalent to that summarized by Fletcher /1962/. According to this model at a given temperature and pressure, by neglecting the so-called ventillation factor, the time /t/ variation of the radius /r/ of an individual solution droplet, the supersaturation /S defined as $p/p_\infty -1$, where p is the actual, p_∞ is the saturation vapor pressure/ and the liquid water content /w/ in the cloud can be described by the following equations:

$$\frac{dr}{dt}=\frac{G}{r}\left[\ln(S+1)-\frac{2\sigma v}{kTr}-g\ln(1-\nu x_s)\right] , \qquad (1)$$

$$\frac{dS}{dt}=Q_1\frac{dh}{dt}-Q_2\frac{dw}{dt} , \qquad (2)$$

$$\frac{dw}{dt}=\sum_r 4\pi r^2 N\frac{dr}{dt}\varrho_w , \qquad (3)$$

where G is a numerical factor depending on the droplet radius because of the function of the diffusion coefficient of water vapor and of the thermal conductivity of the air on the droplet radius /under our conditions:pressure 800 mb, temperature 273 K°, accomodation coefficient 0,7/:

$$G=\frac{4{,}90.10^{-6}r}{\dfrac{r}{0{,}138+7{,}30.10^{-7}\frac{1}{r}}+1{,}52.10^{-4}}$$

σ is the surface tension of the solution, v is the reciprocal value of the number of water molecules in the unit volume of the solution, k is the Boltzmann's constant, T is the absolute temperature, g is the rational osmotic coefficient of water, ν is the number of ions formed by the dissociation of one molecule of the solute, x_s is the concentration of solute molecules in the solution, Q_1 and Q_2 are also constant /in our case: $Q_1 = 5{,}85542.10^{-6}$ CGS; $Q_2 = 3{,}83725.10^{+5}$ CGS/, h is the height, N is the concentration of droplets with radius r and finally ϱ_w is the density of the liquid water.

It is to be noted that, for a given soluble material, g and σ could be determined from x_s /see: textbook on physical chemistry of solutions/, while v and x_s are the function of the mass /m/ of the dry nucleus and of the solution droplet radius /these relations can easily be deducted and are not exposed here/.

3. THE NUCLEUS SPECTRA

It was demonstrated by Junge's work /Junge, 1963/ that about the 80 % of the troposphere is filled with a rather uniform aerosol called tropospheric background aerosol. Our measurements, carried out in pure maritime atmosphere in the Southern Hemisphere during the summer 1971-1972 on the board of a Soviet research ship, have shown /Mészáros and Vissy, 1974/ that these background aerosol particles, neglecting the sea-salt component important only in the lower 2 km of oceanic atmosphere, are composed of sulfates, mainly ammonium sulfate. Briefly, the particles were captured on the surface of membrane filters and they were counted and sized for the size range of $0,03 \leq r \leq 60\ \mu m$ by optical and electron microscopy. The identification of ammonium sulfate was done by simple morphological analysis up to 0,25 μm. By converting the size distribution of particles to supersaturation spectra /Mészáros et al., 1975/ it was possible to demonstrate that these sulfate particles play an important role in the condensation processes.

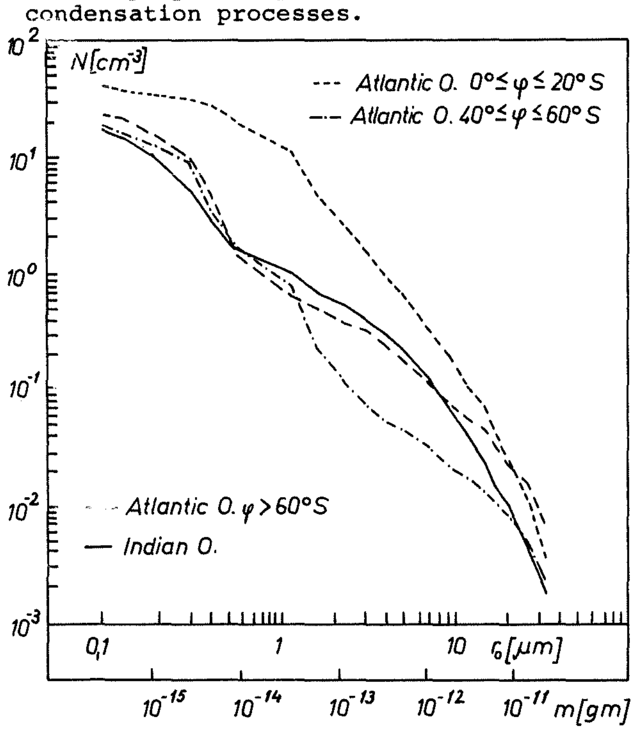

Fig. 1: Size distribution of ammonium sulfate particles as a function of their radius at 100 % R.H. /r_o/ under different geographical conditions. The dry mass of particles /m/ is also plotted. N gives the concentration of nuclei larger than r_o.

Fig. 1 gives the size distritution of ammonium sulfate particles with mass greater than $3,2.10^{-16}$ gm /about 0,045 μm dry radius/ as a function of the equilibrium droplet radius at a relative humidity of 100 %. These distributions were calculated from dry spectra measured under four different geographical conditions. It should be mentioned that the spectrum for tropical Atlentic Ocean /$10^o \leq \varphi \leq 20^o$ S/ was completed in the range of large and giant particles with the distribution of excess sulfate/not sea-salt/ measured by Gravenhorst /1975/ over tropical Atlantic in the Northern Hemisphere. In the case of the other three distributions in the range of $r > 0,3\ \mu m$ from the total number concentration that ot the sea-salt was substracted and the remaining distributions were taken as the spectra of ammonium sulfate nuclei. This was possible since no insoluble particles were found in this size range at these locations. Furthermore it was supposed that in individual mixed particles /mixture of ammonium sulfate and sea-salt/ the ratio of these two materials was the same as for the bulk concentration in the size interval considered.

These aerosol measurements were carried out near the sea level, though the calculations were made for an atmospheric level of 800 mb. Thus it is assumed, which seems to be rather probable, that the concentration of cloud nuclei does not varie with height in the lower layers of the atmosphere over the oceaans.

4. RESULTS AND DISCUSSION

The calculations were made with a Hewlett-Packard calculator /type: 9810 A/ by using the four spectra given in Fig. 1 /distributed in 20 size classes/ for the following constant vertical speeds: 12,5 , 25, 50 and 100 cm/sec in such a way that in t=0 S and w were also taken to be equal to zero. In the time t=0 the nuclei were in equilibrium with their environment of 100 % relative humidity. During the numerical intagration of equations dt was 0,01 sec up to 10 sec and further its value was increased to 0,1 sec. In all 16 calculations the final time was 100 sec.

Table I

Microstructure of clouds with life time of 100 sec formed on spectrum I in the case of different updrafts /U in $cm.sec^{-1}$/. S_m: maximum supersaturation in %, sw: spectrum width, r mean droplet radius /both in μm/, L.W.C.: liquid water content in g/m^3, N drop concentration is cm^{-3}.

U	S_m	sw	r	L.W.C.	N
100	0,97	9,1-34,8	9,4	o,143	40,7
50	0,59	6,8-34,3	7,4	0,071	40,7
25	0,38	5,0-34,0	6,0	0,o35	38,5
12,5	0,26	3,4-33,8	4,5	0,018	36,3

The results of the calculations for the nucleus distribution I are illustrated by the data in Table I. It can be seen that the calculated cloud microstructural characteristics seem to be reasonable. This means that, although measured cloud data for this area are missing, the agreement of the calculated values with the microstructure of Hawaiian orographic clouds and maritime cumuli as observed by Squires /see Fletcher, 1962/ is not bad. The only exception is the fact that calculated liquid water contents are smaller than those observed which can be explained in the following way. Our model calculations refer to heights of 12,5 - 100 m above the cloud base. It is a well known fact that at these levels the liquid water contents are generally small. To prove this, the calculations were repeated up to 1000 sec /125-1000 m above the cloud base/. The liquid water contents were in these cases about one order of magnitude greater /p.e.: 0,19 $g.m^{-3}$ for the updraft of 12,5 $cm.sec^{-1}$/ than those listed in the table. Furthermore the measurements of Squires reflect the effect of sea-salt particles excluded from our calculations. The number concentration of these nuclei is relatively small, but because of their giant size they can play a role in the formation of liquid water content. This opinion is supported by the fact that in the maritime clouds of Squires larger drops were found. However, the concentration of drops with radius greater than about 30 μm is in our case around 1 drop per liter which means that even without the giant sea-salt nuclei in the background clouds the coagulation is probably not excluded. It is to be also noted that in our calculations for updrafts of 50-100 cm/sec all nucleus groups were activated which means that the drop concentrations would be probably greater than about 40 cm^{-3} given in the table if smaller nuclei were taken into account. In other words this means that ammonium sulfate nuclei with dry radius smaller than 0,045 μm probably play a part in the cloud condensation under background conditions. This conclusion is of general validity since the same results were received even for the other three nucleus spectra. One can also seen from Table I, which is well known among cloud physicists, that greater updraft results in a narrower drop spectrum if only the condensation growth is taken into account.

Table II

Microstructure of clouds with life time of 100 sec formed over different geographical locations /see: Fig.1./ with an updraft of 12,5 $cm.sec^{-1}$. For heading letters see: Table I, H: Hungary.

Loc.	S_m	sw	r	L.W.C.	N
I	0,26	3,4-33,8	4,5	0,018	36,3
II	0,40	4,4-34,0	5,1	0,010	16,3
III	0,37	4,1-34,0	4,9	0,014	21,6
IV	0,41	4,5-34,0	5,1	0,010	15,6
H	0,09	1,1-33,6	2,5	0,038	270

The results for the four nucleus distributions, that is for different geographical locations, are shown in Table II for an updraft velocity of 12,5 cm/sec. In the table, for comparison, the results calculated by using average aerosol data measured in Hungary during summer-time with the same methods is also listed /labelled with H/. It can be seen that the larger continental aerosol concentration results, first of all, in a higher number of cloud drops, while the differences in liquid water content and supersaturation are not so important. The maximum size of drops is very similar in all cases, while the minimum and average drop sizes are inversely proportional to the nucleus concentration /in Hungary the concentration of ammonium sulfate nuclei with dry radius larger than 0,045 μm was about 1000 cm^{-3}/. Furthermore the data show that different characteristics of the microstructure of background clouds vary only within a factor of about two that is the characteristics of clouds do not change very much as a function of place /and probably time/. At a given place, however, the liquid water content and maximum supersaturation /see Table I/ obviously largely depend on the updraft velocity. It was previously stated /Mészáros and Vissy, 1974/ that the higher ammonium sulfate concentration over tropical Atlantic Ocean is a result partly of the advection of particle forming trace gases from Africa and partly of the favourable conditions for the photochemical and thermal chemical reactions of sulfur gases.

It should be mentioned that in our model clouds the maximum supersaturations were obtained between 30-80 sec as a function of the nucleus spectrum and updraft speed. The absolute maximum was 1,5 % received in the case of the fourth nucleus spectrum with an ascent of 100 cm/sec. The absolute minimum under background conditions was 0,26 % /see Table I./

For the chemical budget of background clouds the determination of the ammonium sulfate concentration in cloud water is also of interest. It is well known /Junge, 1963/ that the chemical composition of cloud water is a result of the interaction of different processes. From the results of our model calculations the concentration of ammonium sulfata due alone to the effect of condensation nuclei can be determined.

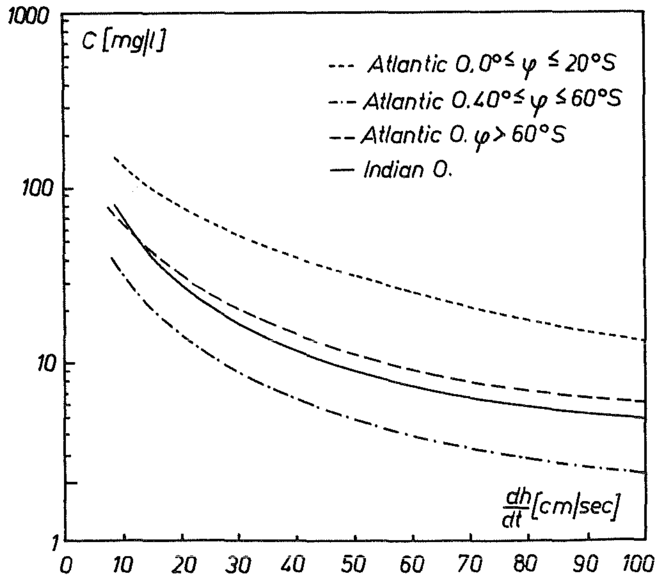

Fig.2: Ammonium sulfate concentration /C/ in cloud water as a function of updraft velocity and geographical locations. /see: Fig.1/ The values refer to a cloud life time of 100 sec.

Fig. 2. gives this concentration for a cloud life time of 100 sec in the case of different geographical locations as a function of the upraft velocity. As it was aspected higher updraft results in a smaller ammonium sulfate concentration in the cloud water because of the greater liquid water content. The highest values occur over the tropical Atlantic Ocean because of the reason mentioned above.

Finally it can be concluded that the results presented in this paper are of preliminary character. Much more measurements are needed under tropospheric background conditions to improve the reliability of input data and to give a possibility for the control of output results. The refinement ot the numerical model seems to be also desirable.

REFERENCES

Fletcher, N.H., 1962: The physics of rainclouds. University Press, Cambridge.

Gravenhorst, G., 1975: The sulphate component in aerosol samples over the North Atlantic. "Meteor" Forsch. Erg. B. 10. 22-31.

Howell, W.E., 1949: The growth of cloud drops in uniformly cooled air. J. Meteorol. 6, 134-149.

Junge, C.E., 1963: Air chemistry and radioactivity. Academic Press, New York and London.

Mason, B.J. and Chien, C.W., 1962: Cloud-droplet growth by condensation in cumulus. Quart J.Roy. Meteorol. Soc., 88, 136-142.

Mészáros, A. and Vissy, K., 1974: Concentration, size distribution and chemical nature of atmospheric aerosol particles in remote oceanic areas. J. Aerosol Sci., 5, 101-109.

Mészáros, E., Mészáros, A. and Vissy, K., 1975: Estimation of the size and nature of cloud nuclei from aerosol measurements carried out in pure maritime air. In "Proc. VIII Internat. Conf. on Nucleation", 431-436. Gidrometeoizdat, Moscow.

Mordy, W., 1959: Computations of the growth by condensation of cloud droplets. Tellus 11, 16-44.

Sedunov, Y. S., 1972: Physics of the formation of droplet phase in the atmosphere /in Russian/. Gidrometeoizdat, Moscow.

Warner, J., 1969: The microstructure of cumulus clouds, Part II. J. Atmosph. Sci., 26, 1272-1282.

1.2.5

THE EFFECT OF RETARDED NUCLEUS ACTIVITY ON THE EVOLUTION OF THE CLOUD DROPLET SIZE SPECTRUM

Josef Podzimek
Graduate Center for Cloud Physics Research
University of Missouri-Rolla
Rolla, Mo. 65401

1. INTRODUCTION

In spite of the promising results of the suppression of "evaporation-type fog" by covering the sea surface with a thin film of a surfactant (i.e. Bakhanova and Solyanek, 1968) the application of surfactants for the modification of cloud droplet size spectrum or for fog dispersion have not yet reached a state of final crystallization. The results of large-scale experiments with cloud or fog modification using surfactants are still inconclusive (Jiusto, 1964; Bigg et al., 1969; Kocmond et al., 1972). A number of laboratory studies have resulted in conflicting trends since the experiments by Hardy (1925) and Trapeznikov (1940) who studied the influence of the coverage of water bubbles by surfactants (i.e., oleic acid). Leonov and Prokhorov (1967) observed that the evaporation of 3 to 4 mm drops is considerably retarded when the drops are covered by surfactants, however Leonov et al., (1971) later found that a very low concentration of some surfactants increases the drop evaporation instead of suppressing it. The study of the evaporation rates of small freely falling water drops covered by various amount of surfactant by Duguin and Stampfer (1971), Hughes and Stampfer (1971) and by Sierawski (1973) led to the same conclusion.

One finds a large discrepancy between the laboratory experiments with the influence of surfactant coating on the water drop evaporation and the observed contamination of atmospheric air by surfactants. Despite the different opinions of how organic substances can be concentrated in the surface layer of the ocean and how they can be transported in the air (i.e., Wilson, 1959; Fogg, 1965; Menzel, 1966) we still have too little information on the amount and nature of surfactants in the air. Barger and Garrett (1970) found a low concentration of weak surface active material on the coast of the Oahn Island in the Hawaiian group. A larger amount was found in the north Atlantic (0.7μg of surface active material covering the area of 1 cm^2) by Scheiman and Jarvic (1963). However, the nature of these films which might cause the coating of active condensation nuclei is largely unknown. Garrett (1967) believes that they are composed mainly of fatty acids and alcohols and that hydrocarbons are the main constituent of the monolayers. Baier et al., (1974), on the other hand showed that they are composed mainly of glycoproteins and proteoglycans. Very little is known about what kind of material is bound on aerosol particles of a certain size. Blanchard (1968) found that the amount of organic material carried by sea salt particles is inversely proportional to particle size. During our field measurements on Padre Island (Texas) Russell and Stampfer (1976) measured the highest concentration of organic materials which can be converted from C_{14} to C_{20} methyl esters on particles smaller than about 0.7 μm with the C_{16} ester the most abundant.

The scarsity of reliable data led to the speculative nature of many of the published models on the possible role of surfactants in the formation of cloud droplet spectrum. Our one dimensional model (Saad, et al., 1976; Podzimek and Saad, 1975) represents no exception of this statement. It is based on Derjaguin's and Kurgin's (1969) assumption of the critical thickness of the in water insoluble surface active material. The other very important assumption is that all sizes of sodium chloride nuclei are coated evenly by the cetyl alcohol so that the thickness of the protective layer on all nuclei is originally the same. After a short description of the main results of this model a more general case of preferential coating of smaller particulates will be discussed.

2. EVENLY COATED NUCLEI

Because most of the results of the model dealing with evenly coated nuclei have been published (Podzimek and Saad, 1975) we would like to repeat only the most interesting features of the time change of the size distribution of sodium chloride solution drops.

The model is based on several equations describing:

a) The change of temperature with time

$$\frac{dT}{dt} = \frac{-L(dG_v/dt)-G_m Ug}{G_m C_{pm}+S_w G_w} \tag{1}$$

In Eq. 1, L is the latent heat liberated by condensation of water vapor; G_w, G_v, G_w, G_m are the mass of water vapor, liquid water and moist air; S_w is the specific heat of liquid water; C_{pm}, ρ_m and p_m are specific heat, density and pressure of moist air respectively.

b) The droplet growth equations

$$\frac{dr}{dt} = \frac{\rho_{sat}}{\rho_w}\frac{D_{eff^*}}{r}(S-S^*) \tag{2}$$

in which

$$\frac{1}{D_{eff}^{*}} = \frac{bL[1+(l_\alpha/r)]}{K} + \frac{[1+(l_\beta/r)]}{D} \qquad (3)$$

and

$$l_\alpha = (1-\frac{\alpha}{2})\frac{K}{\alpha p_m}\frac{\gamma-1}{\gamma+1}(\frac{8\pi}{R_aT})^{1/2} \qquad (4)$$

$$l_\beta = (1-\frac{\beta}{2})\frac{D}{\beta}(\frac{2\pi}{R_vT})^{1/2} \qquad (5)$$

$$S^{*} = \frac{r^{*}}{r} - \frac{3i}{4\pi}\frac{M_w}{M_n}\frac{m_o}{r^3} \qquad (6)$$

$$r^{*} = \frac{2\sigma}{\rho_w R_v T}. \qquad (7)$$

S_{sat} is the saturation vapor density at infinity [$\rho_{sat} = f(T)$]; ρ_w is the density of liquid water. S^* is the supersaturation over the droplet of the radius r; b is the linearized constant from the course $\rho_{sat}=f(T)$. $\gamma = cp/cv$; β is condensation coefficient for water vapor; accommodation coefficient $\alpha = 1$; i is van't Hoff's factor (i=2 for NaCl); M_w, M_n are molecular weights of water and salt, m_o is the mass of dissolved salt; σ is the surface tension and R_v is the gas constant of the water vapor.

c) The relationship between the liquid water content W and the size spectrum of drops. One assumes that the cloud elements do not leave the air parcel and that the droplet distribution function remains constant. Therefore

$$\frac{dW}{dt} = 4\pi\,\rho_w \sum_{j=1}^{n} N_j r_j^2 \frac{dr_j}{dt} \qquad (8)$$

and also

$$\frac{dG_v}{dt} = -\frac{dW}{dt} \qquad (9)$$

d) The supersaturation S change inside of the air parcel

$$\frac{dS}{dt} = \frac{(1+S)}{p_m}\frac{dp_m}{dt} - \frac{1}{\rho_{sat}}\frac{dW}{dt} - \frac{(1+S)}{R_vT^2}\frac{dT}{dt} \qquad (10)$$

e) The discontinuity in the protective capability of the layer of the surfactant (cetyl alcohol). For the layer thickness of $\delta \geq 0.976 \times 10^{-7}$ cm we assumed σ=43 dyn cm^{-1} and $\beta = 3.5 \times 10^{-5}$ and for $\delta < 0.976\text{x}10^{-7}$ cm that σ = 73 dyn cm^{-1} and $\beta = 3.6 \times 10^{-2}$ in accordance with Derjaguin and Kurgin (1969). The initial layer thickness on each drop was the same ($\delta_o = 0.98 \times 10^{-6}$ cm) and the mass of cetyl alcohol was supposed to be constant during the droplet growth [$d/dt(4\pi r^2\delta\rho_c) = 0$; ρ_c is the density of cetyl alcohol].

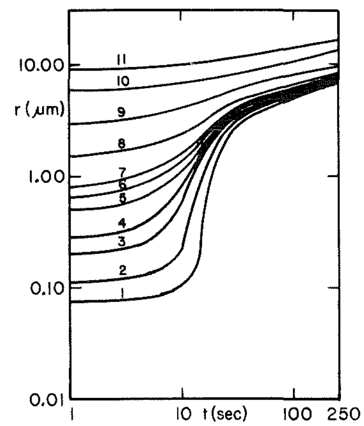

Fig. 1. Growth curves for uncontaminated nuclei at an updraft velocity of 100 cm s^{-1}.

If we assume a size spectrum of NaCl nuclei at the time t=0 then the growth of individual uncontaminated nuclei is described in Fig. 1 in which the size of drops is plotted as a function of time. The simulated updraft velocity was constant and equal to 100 cm sec^{-1}. In Fig. 2 the growth curves are plotted for nuclei covered by a protecting layer of cetyl alcohol of the original thickness δ_o = 0.98 x 10^{-6} cm. The most important feature of the contaminated nuclei is the fact

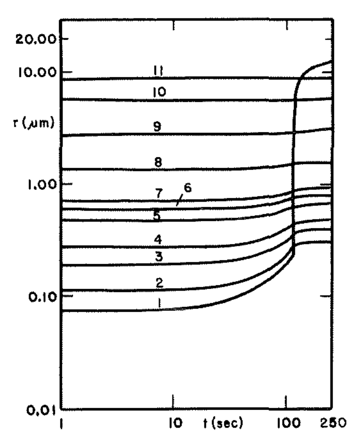

Fig. 2. Growth curves for nuclei covered by layer of cetyl alcohol at an updraft velocity of 100 cm s^{-1}.

that their growth is slowed down and suddenly, after the protective layer thickness of the smallest nuclei will reach the critical thickness of 0.976 x 10^{-7} cm, the smallest nuclei start to grow (after 100 sec). This growth is so intense that the supersaturation after reaching a value almost one order of magnitude higher than that of uncontaminated nuclei in the same time falls down to a value almost comparable with the uncontaminated nuclei (Fig. 3). The

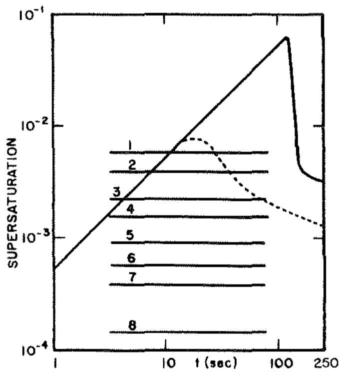

Fig. 3. Variation of the supersaturation with time during the process of water vapor condensation upon salt nuclei covered by cetyl alcohol layer (solid line). Expansion rate corresponds to an updraft velocity of 100 cm s^{-1}. Dashed curve shows the case of uncontaminated nuclei.

conclusion from this simple model experiment is the following: If one would be able to coat the smallest size of nuclei by insoluble surfactants the colloidal instability of the cloud would be supported. The smallest sizes of nuclei will come into the class of the largest drops which, however, are in mean smaller compared with the uncontaminated case and the size spectrum of contaminated drops is much broader. At the same time the high supersaturation will activate those nuclei which under normal conditions would remain inactive.

Partly coated nuclei or the coating of nuclei of the smallest size are interesting cases. The last case corresponds more to the observations made by Blanchard (1968) and by Russell and Stampfer (1976).

3. COATING OF THE SMALLEST NUCLEI

The model was quite similar to the previous one. However, the nuclei size distribution was different. There were 15 classes of nuclei starting with radii $r_o = 2.224\mathrm{x}10^{-5}$ cm. Further, it was assumed that only the three classes of smallest nuclei (up to r = 2.515 μm) were coated by cetyl alcohol. The conditions for the discontinuity in the protective capability of the cetyl alcohol layer were the same as in the previous case. However, the time of observation of the microstructural changes in the cloud was longer (up to 2,000 sec).

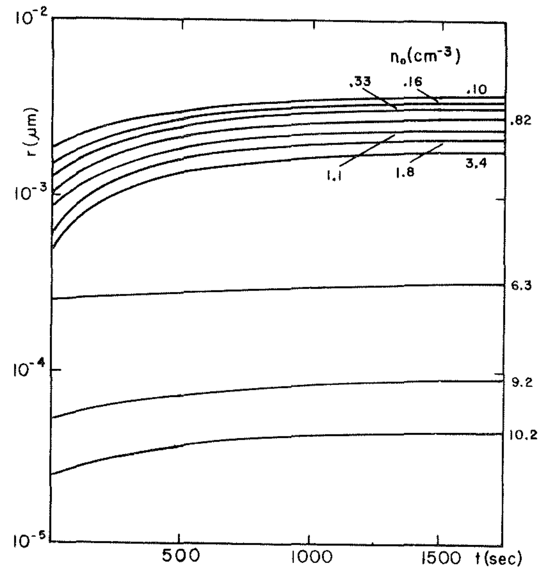

Fig. 4. Growth curves for larger salt nuclei the first three classes of which are covered by a protecting layer of cetyl alcohol. n_o is the initial concentration of nuclei.

In the case of a cloud, the elements of which did not reach the size corresponding to the critical thickness of the protecting layer (δ = 0.976 x 10^{-7} cm) one can observe the following features: coating of the three first classes of the size distribution of NaCl nuclei by 0.98 x 10^{-6} cm thick layer of cetyl alcohol contributes to the broadening of the size spectrum of cloud elements. There is a class (in the calculated case class No. 3) the nuclei of which almost remain unchanged during whole condensation process (Fig. 4). Correspondingly to this the thickness of the protecting layer for r_o = 2.515 x 10^{-4} cm changes only slightly (Fig. 5). There is a potential use of this result for stabilization of a fog with narrow size spectrum of elements. In comparison with the uncoated nuclei case the liquid water content and the supersaturation is a little higher for partly coated nuclei cloud.

The model of cloud droplet growth on partly coated nuclei with elements reaching such a size that the protective layer thickness was smaller than 0.976 x 10^{-7} cm behaved in a different way: At the moment when the surfactant layer thickness reached the critical value, the small nuclei suddenly started to grow reaching in several seconds the size of the elements corresponding to the largest size of nuclei. The size spectrum was broader in comparison with the case of uncoated nuclei, however, narrower than in the previous case. The final result was the increase in number of larger nuclei and the higher liquid water content of the cloud.

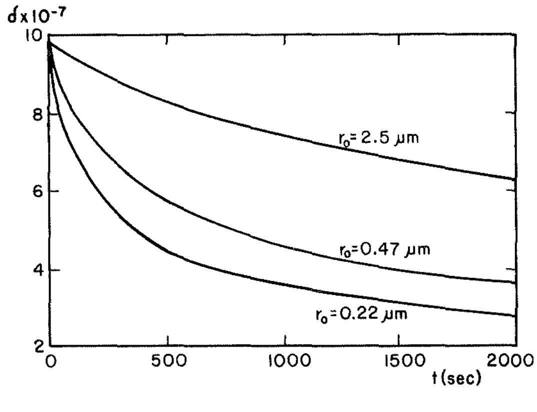

Fig. 5. Thickness of the protecting layer δ for the three different classes of nuclei covered by cetyl alcohol. r_o is the initial radius of a nucleus.

CONCLUSION

In this contribution, the consideration is restricted to an artificial model of a cloud forming on one sort of hygroscopic nuclei covered or not covered by cetyl alcohol. Moreover, it is based mainly on measurements and simple theoretical studies of one group of scientists (Derjaguin and his fellow workers). It does not appear, however, that this lack of realism will completely vitiate the usefulness of some of the obtained results: the coating of active nuclei will considerably influence the braodness of the size spectrum of cloud elements. Partly coated nuclei of a certain size can delay the intense condensation process, can influence the supersaturation and the liquid water content of the cloud or fog.

The difficulty of establishing a more realistic model stems from the inability to accurately measure the amount and nature of surfactants on individual cloud elements and particulates in nature. Also, one can expect that the more complex and accurate model of the surfactant layer, whatever its other virtues, will be based on the comparison with careful laboratory measurements which will certainly cover the mixed nature of nuclei and surfactants and the dependence of accommodation and condensation coefficients upon the size of elements.

ACKNOWLEDGEMENTS

The author is indebted to Dr. A. N. Saad and to Mr. Wood for their help in modelling the cloud formation and in programming the numerical solution of equations. This research was supported by the National Science Foundation, Grant GA-36041.

REFERENCES

Baier, R. E., D. W. Goupil, S. Perlmutter, and R. King, 1974: Dominant chemical composition of sea-surface films, natural slicks, and foams, J. Rech. Atmos., 8, 571.

Bakhanova, R. A., and E. G. Solyanek, 1968: On the application of the surface active agents to prevent water evaporation of fogs over the unfreezing water basins in winter season, Proc. Int. Conf. on Cloud Physics, Univ. of Toronto, Ont., p. 688.

Barger, W. R., and W. D. Garrett, 1970: Surface active organic material in the marine atmosphere, J. Geophys. Res., 75, 4561.

Bigg, E. K., J. L. Brownscombe, and W. J. Thompson, 1969: Fog modification with long - chain alcohols, J. Appl. Meteor. 8, 75.

Blanchard, D. C., 1968: Surface active organic material on airborne salt particles, Proc. Int. Conf. on Cloud Physics, Univ. of Toronto, 25.

Deryaguin, B. V., and Yu.S. Kurgin, 1969: Theory of passivation of the growth of water condensation nuclei by cetyl alkohol vapour, Proc. 7-th Int. Conf. Cond. and Ice Nuclei, Prague - Viena, Academia, Prague, p. 461.

Duguin, H. A., and J. F. Stampfer, Jr., 1971; The evaporation rates of small freely falling water drops, J. Atmos. Sci., 28, 1233.

Fogg, G. E., 1965: Algal Cultures and Phytoplankton Ecology, Univ. of Visconsin, Press, Madison, p. 126.

Garrett, W. D., 1967: The organic chemical composition of the ocean surface, Deep-Sea Res., 14, 221.

Hardy, W., 1925: Chemistry at interfaces, J. Chem. Soc., 127, 1223.

Hughes, R. B., and J. F. Stampfer, Jr., 1971: Enhanced evaporation of small, freely falling water drops due to surface contamination, Science, 140; 1244.

Jiusto, J. E., 1964: Investigation of warm fog properties and fog modification concepts, Rep. RM-1788 - P - 4, Cornell Aeronaut. Lab., Buffalo, New York.

Kocmond, W. C., W. D. Garrett, and E. J. Mack, Modification of laboratory fog with organic surface films, J. Geophys. Res., 77, 3221.

Leonov, L. F., and P. S. Prokhorov, 1967: Influence of surface active substances on the evaporation of fine water drops, Izv. Akad. Nauk SSSR, ser. Khim, 4, 735.

Leonov, L. F., P. S. Prokhorov, T. A. Efanova, and I. A. Zolotarev, 1971: Passivation of condensation nuclei by cetyl alcohol vapor, in Advaces in Aerosol Physics, vol. 2, Israel Program for Sci. Translations, Jerusalem, p. 12.

Menzel, D. W., 1966: Bubbling of sea water and the production of organic particles: A re-evaluation, Deep Sea Res., 13, 963.

Podzimek, J., and A. N. Saad, 1975: Retardation of condensation nuclei growth by surfactant, J. Geophys. Res., 80, 3386.

Russell, C. A., and J. F. Stampfer, Jr., 1976: The dependence on particle size of the organic content of marine aerosols, Abstracts of the 42nd Annual Meeting of the Missouri Academy of Sciences, Rolla, April 23 and 24.

Saad, A. N., J. Podzimek, and J. C. Carstens, 1976: Some remarks on the modeling of the early stage of cloud formation in a simulation chamber, J. Appl. Meteor., 15, 145.

Scheiman, M. A., and N. L. Jarvic, 1963: Film studies of surface active material collected in the North Atlantic, NRL Memo. Rep. 1440, U.S. Nav. Res. Lab., Washington, D.C.

Sierawski, D. A., 1973: A study of the ability of surface active materials to increase the evaporation rates of small, freely falling water drops, M.S. Thesis, Univ. of Missouri, Rolla.

Trapeznikov, A. A., 1940: Effect of monolayers of insoluble substances on the stability of bubbles, Zh. Fiz. Khim., 14, 821.

Wilson, A. T., 1959: Airborne nitrogeneous material and other plant nutrients, Nature, 184, 99.

1.2.6

MICROPHYSICAL COMPUTATIONS IN URBAN AND RURAL CLOUDS

by

Harry T. Ochs, III

and

Richard G. Semonin

Illinois State Water Survey
Urbana, Illinois 61801

1. INTRODUCTION

The METROMEX field project research results show the existence of a precipitation and severe weather anomaly in proximity to St. Louis (Huff and Changnon, 1972) which confirms one of the goals stated for the project (Changnon et al., 1971). In an effort to physically explain the occurrence of the anomaly, aircraft probed the clouds and measured the atmospheric conditions in the storm updraft areas seeking data on microphysical and mesoscale alterations related to urban conditions. These measurements included cloud condensation nuclei (CCN) cloud microphysical structure, and the three-dimensional sub-cloud thermodynamic structure. Fitzgerald and Spyers-Duran (1973) reported observations of fair-weather cumulus micro-structure in clouds upwind and downwind of the urban industrial areas that indicated a definite alteration toward greater droplet concentrations and more narrow distributions in the urban and downwind clouds. These observations led Braham (1974) and Semonin and Changnon (1974) to hypothesize the existence of giant nuclei to justify the early formation of radar echoes and the distinct change in the surface drop size spectra (Semonin and Changnon, 1974). Unfortunately, it is not possible to directly measure giant condensation nuclei with existing instrumentation, but their affect can be assessed through the use of numerical models. The observed droplet spectra in the downwind clouds are suggestive of a deterrent to precipitation formation since the coalescence process is inhibited by a narrow distribution, but the radar first echo statistics indicate an enhanced development of precipitation particles below the freezing level.

The availability of a sophisticated numerical model of cloud microphysics in the METROMEX program makes it possible to examine this apparent paradox and to offer suggestions for future work. The model was developed to utilize field observations of CCN as initial inputs to maintain the ability to assess the effects of real data on the evolution of droplet spectra. Thus, the purpose of the computations presented in this paper is to test hypotheses that might explain these seemingly inconsistent observations. Two sets of computations were performed. The first was designed to see if the inclusion of giant condensation nuclei would significantly affect the production of precipitation size drops by warm rain processes while the second set was designed to observe the effect of increased nuclei concentrations.

2. MODEL DESCRIPTION

The microphysical simulations presented, depict the evolution of a droplet spectra from an initial population of CCN. The effects of condensation (or evaporation), coalescence, and breakup are computed in a rising parcel of air. The ascent rate of the parcel is prescribed and there is no interaction between the thermodynamics and the vertical velocity.

At the onset of the computations a small parcel of air is lifted at a chosen rate. Changes in the parcel temperature, relative humidity, and density are computed as a result of the prescribed ascent and latent heat processes. There is no mixing of heat or moisture with the parcel's environment, and thus the ascent is assumed adiabatic. In addition, the sedimentation of the larger drops from the parcel and the fall of drops into the parcel from above are not considered. Thus the model is assumed to depict the development of a droplet population in the early stages of cumulus development before many drops are present with appreciable fall velocities in comparison to the assumed vertical ascent rate.

As the ascending parcel expands and cools, the relative humidity within the parcel increases and has the effect of supplying moisture for the condensation process. The droplets grow in a Eulerian framework in which the mass doubles every second category. Thus, the droplet radius of category, J, is

$$R(J) = R_o \exp\left(\frac{J-1}{J_o}\right) \tag{1}$$

where J_o is 6/ln2. An Eulerian framework is chosen so that the microphysical simulation would be compatible with a full cloud simulation at a later time.

The equation for the condensational growth of droplets in the chosen framework is given by Fukuta and Walter (1970). The equation is used under the assumption that the droplets are in thermal equilibrium with their environment. In addition, the density, osmotic coefficient and surface tension of the solution droplet are computed as functions of the ratio of solute to water masses. For the purpose of these computations, the condensation nuclei were assumed to be completely soluble and to be composed of sodium chloride.

The numerical algorithm used for condensational growth employs the Egan and Mahoney (1972) scheme for the advection of droplets in radius space. This scheme reduces numerical spreading by allowing droplets to grow a portion of a radius category by condensation in a given computational time step. The growth equation is used to calculate the equilibrium radius for droplets that have not been activated. The advection scheme can then be employed such that these smaller droplets are not allowed to grow beyond their equilibrium radius in any time step. For the purpose of this paper, an activated droplet is one that does not have an equilibrium radius or has exceeded the radius at the peak of its Köhler curve.

The calculations presented begin in subsaturated air at a relative humidity of 80%. The condensation nuclei are assumed be be completely soluble and in a saturated solution at this point. As the parcel is lifted, condensation is computed with a 0.1 second time step until saturation is exceeded. Subsequently, as droplets begin to exhibit large growth rates, the time step is reduced such that no droplet can grow further than half of its category width in a time step. In addition, the total population of droplets may not condense more liquid than would reduce the supersaturation by 5% in a single time step.

The collection process is treated in the manner of Berry and Reinhardt (1974). The gain and loss integrals are integrated every 4.0 seconds of simulation time. The kernel employed in these computations is derived from the linear collision efficiencies, Y_c, given by Hocking and Jonas (1970) for a collector drop less than 40 μm and from Shafrir and Neiburger (1963) for larger drops.

The nuclei mass is retained as a single-valued function of category size for both the condensation and collection processes. This is accomplished by assigning a category nuclei mass to the weighted average nuclei mass per droplet of the droplets arriving or remaining in that category after a time step. In the collection process a gain and loss integral for nuclei mass is computed simultaneously with the gain and loss integrals for the droplet number density distribution.

Drop breakup is treated in the presented computations although significant numbers of drops of sufficient size to allow the breakup processes to appreciable alter the distribution shape were not present at the time at which the radar reflectivity factor first reached sufficient magnitude to return detectable signals to METROMEX weather radars. Two schemes for large drop breakup were used simultaneously. The first was that developed by Srivastava (1971). This scheme treats the aerodynamic disintegrations of large drops. Brazier-Smith, et al., (1972, 1973) developed the second scheme in which drops undergoing off-center collisions separate if the rotational energy generated in the collision exceeds the binding energy due to surface tension. These methods have been tested by Young (1975) who states that the second scheme (collision breakup) is more important than the first in determining the final distribution shape.

3. INITIALIZATION OF MODEL

Data for the initialization of the CCN spectra were measured in the St. Louis area by other METROMEX participants (Fitzgerald and Spyers-Duran, 1973). Samples of air gathered during aircraft flights were analyzed in a diffusion cloud chamber immediately upon landing, but giant nuclei concentrations cannot be measured adequately by this technique. The inability of the experimental apparatus to detect concentrations of nuclei that are activated at very low supersaturations does not preclude the existence of these large particles in the St. Louis atmosphere.

The measured spectra are presented in the form

$$N = C\ s^{k} \tag{2}$$

where N is the total number of CCN activated at a supersaturation, s, and C and k are constants. The values of C and k were evaluated by varying s between 0.17% and 1.0% and applying a best-fit analysis to the resulting data.

To initialize the microphysical simulation, the nuclei mass per particle and the concentrations of particles in each category must be determined. After assuming a chemical makeup for the CCN (in this case, sodium chloride), Eq. 2 can be used differentially in conjunction with the growth equation to determine the number density distributions in terms of nuclei mass. The growth equation determines the activation supersaturation as a function of physical properties of the solution droplet. The nuclei material is then assumed to be in a saturated solution at a relative humidity of 80% and the solution droplet number density distribution for the categories determined by Eq. 1 can be evaluated.

The CCN distribution shown by curve A in Fig. 1 was used with the addition of giant nuclei in 5 steps as indicated by the tick

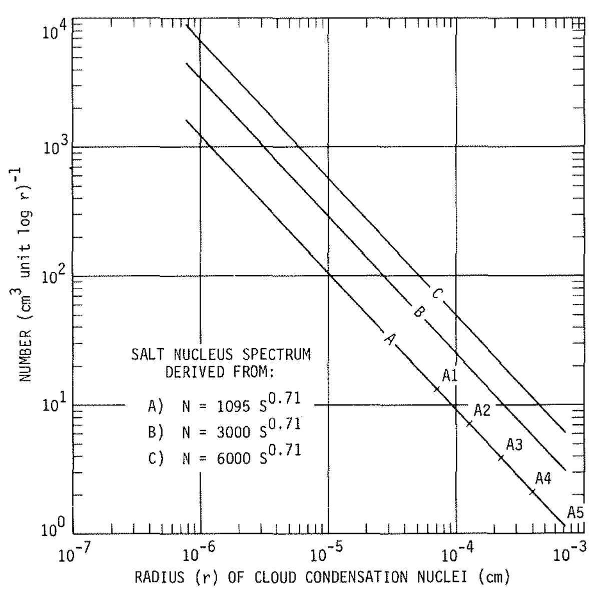

FIGURE 1.
Cloud condensation nuclei distributions.

marks. This procedure was followed to simulate the alteration of an upwind CCN distribution by the incorporation of locally produced giant nuclei. These alterations are described in more detail in Table 1 where the number concentration and largest nuclei mass are indicated for each of the five simulations. Also shown in Table 1 are the salient points of each simulation concerning the number of droplets activated, and the elapsed time to achieve 0 dbZ.

TABLE 1 Development of radar echo from CCN distribution A as shown in Fig. 1 with the addition of varying numbers of large nuclei.

	Largest CCN mass (grams)	*Number of initial particles*	*Cloud base droplets*	*Time from zero supersaturation to 0 dbZ (seconds)*	*Parcel temperature at 0 dbZ (°C)*
A1	3.29×10^{-12}	1594	992	1440	-5.9
A2	1.68×10^{-12}	1599	976	1241	-1.7
A3	1.05×10^{-10}	1602	958	984	3.5
A4	5.96×10^{-10}	1604	932	718	8.7
A5	3.37×10^{-9}	1604	897	473	12.9

The initial temperature and pressure at which all computations commenced was 25.3°C and 950 millibars. The mixing ratio for the parcel was about 17 gm kg^{-1}, and in all cases the parcel ascent rate was 4.0 m s^{-1}.

4. MODEL SENSITIVITY TO THE ADDITION OF GIANT NUCLEI

In order to test the sensitivity of the time to produce a minimum radar echo to the inclusion of giant condensation nuclei, it was necessary to extend the range of Eq. 2 to lower activation supersaturations than were used for field measurements. Since there are no observed data of giant nuclei for the St. Louis area Eq. 2 was assumed valid for all distributions. While there may be fewer or greater numbers of giant nuclei than those employed in these calculations, the object of this simulation is to assess the degree of their effect on precipitation development.

In each case, the rising parcels become slightly supersaturated, at which time a portion of the CCN become activated and form growing droplets. The remainder of the particles stay close to their equilibrium radius as the supersaturation slowly decreases due to the increased surface area of the activated droplets. The third column in Table 1 indicates the number of activated drops for each case. As more large nuclei are included in the parcel, fewer and fewer droplets are activated. In the last case there are 95 fewer cloud drops than in the first. Since the ascent rate is identical for each of the 5 computations, this general behavior is to be expected. The added condensation nuclei with their increased surface area condense the same amount of vapor as many smaller particles. The net effect, when larger nuclei are added, is to reduce the peak supersaturation achieved by the parcel, thus leading to a reduction in the total number of activated droplets.

Figure 2 depicts the evolution of the radar reflectivity factor as a function of time for the 5 cases. The computations indicate that the reflectivity factor grows rapidly to values which would return minimum detectable signals to METROMEX weather radars. At this time significant concentrations of drops with appreciable fall speeds develop, and the assumption of no sedimentation is no longer valid. Therefore, the calculations are only considered representative of the growth of droplets in a rising parcel in the updraft of a developing cumulus cloud to the time of first echo development.

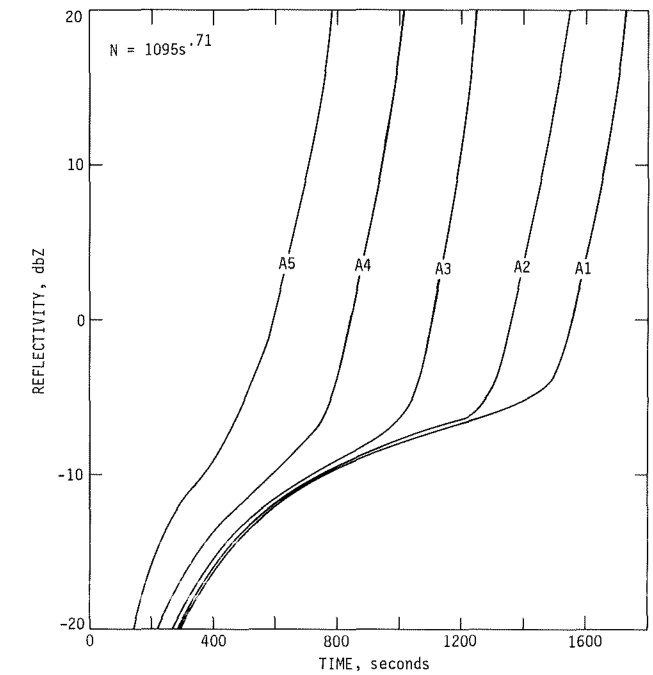

FIGURE 2.
Evolution of radar reflectivity for distributions A1 through A5 as shown in Figure 1.

Table 1 indicates the time for each parcel to achieve 0 dbZ and the parcel's temperature at this point. The computations clearly indicate that warm rain processes can play a significant role in the development of precipitation in the St. Louis area. With the chosen ascent rate, a radar echo easily develops before ice processes become important, especially if large condensation nuclei are present.

The most striking feature of Fig. 2 and the data in Table 1 is the great sensitivity of the time required for echo development to the presence of large particles in the initial distribution. All 5 initial distributions result in a narrow cloud droplet distribution above cloud base, however, adding giant nuclei to the CCN distribution increases the tail on the large radius end of the distribution. The net effect of the increased spread in the droplet distribution due to additional giant nuclei is to increase the opportunity of droplet pairs to undergo collision and coalescence resulting in the time differences for echo development in Fig. 2.

5. MODEL SENSITIVITY TO INCREASED CCN CONCENTRATIONS

The results presented in the previous section could be used to explain the observed differences in first echo bases in urban and rural clouds except for the fact that field measurements indicate significantly greater nuclei concentrations in and downwind of the St. Louis urban area compared to rural upwind areas. This section presents results of computations made for 2 additional distributions (curves B and C in Fig. 1) of varying concentration that contain nuclei over the same size range as in A5 of Fig. 1. Distribution A is a reasonable value for rural measurements. Distribution B is typical of CCN concentrations measured over and downwind of St. Louis, while C represents an extreme value of observed concentrations.

Distributions B and C contain increased numbers of nuclei in all size ranges. The presence of the greater number of nuclei in these distributions results in the delay of these parcels to reach saturation and reduces the peak supersaturation developed in each ascent. The supersaturations for the 3 distributions are plotted in Fig. 3. As Table 1 indicates, distribution A5 results in 897 cloud droplets above cloud base. Distribution B results in about 1490 cloud droplets and C produces approximately the same number of droplets as B.

The lower peak supersaturation for distribution B along with increased numbers of nuclei in all size ranges results in a broader cloud droplet spectra than resulted from distribution A5. For these reasons C results in the broadest distribution of the 3 cases. On the other hand, the droplet with the mean radius for A5 grows at the fastest rate of the 3 distributions. This is expected since there are fewer droplets in A5. The increase of the mean cloud droplet radius for distribution C proceeds slower than that of B. Since B and C have about the same numbers of droplets, the mean droplet of distribution C grows slower because of the presence of more large nuclei in C.

These 2 distribution characteristics affect the production of larger droplets by coalescence. A slowly increasing mean radius would retard the coalescence process while a greater spread would speed it up. The net result is shown in Fig. 4, which indicates that all 3 distributions result in minimum detectable radar echoes in about the same elapsed time.

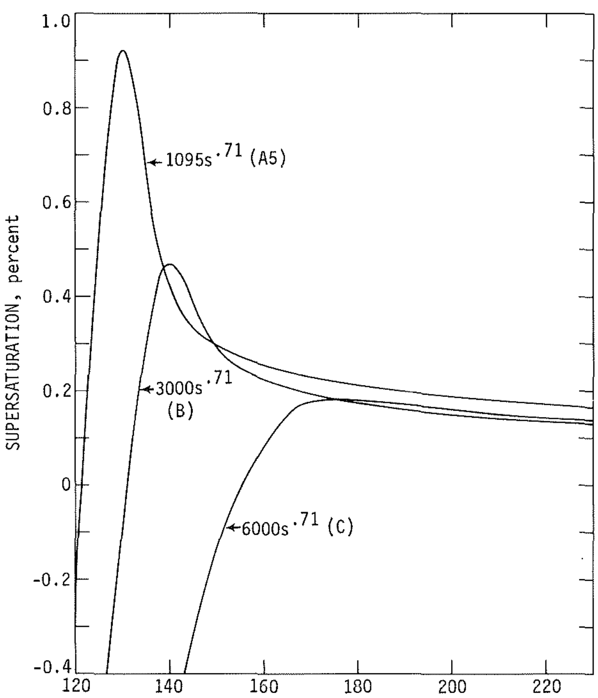

FIGURE 3.
Evolution of supersaturations for parcels containing distributions A5, B, and C.

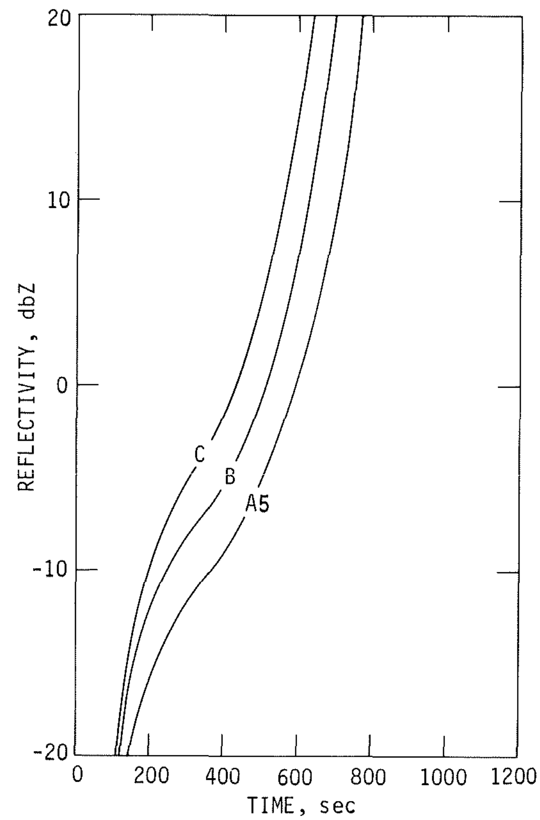

FIGURE 4.
Evolution of radar reflectivity for distributions A5, B, and C.

6. APPLICATION AND RESULTS

A two part objective constituted the impetus for pursuing the research presented here. A number of field observations gathered by METROMEX participants were seemingly in conflict. The results presented, offer a plausible explanation of how these field data can be viewed in a self-consistent manner.

METROMEX data and observations indicate that on the average, there are more CCN over and downwind of St. Louis than are present in upwind rural areas. This result has persisted for each year of the project in which these data have been gathered and analyzed.

Aircraft observations indicate that visual cloud bases average approximately 600 m higher over the urban area than over surrounding rural locations. On the other hand, radar observations indicate lower average first echo bases in city clouds. The difference in elevation of first echo bases between urban and rural clouds averages about 600 m.

The observations of CCN concentrations suggest that increased numbers of cloud droplets might impede the production of larger raindrops as a result of competition for available moisture and a narrowing of the droplet distribution. However, the radar first echo data and aircraft observations of cloud bases indicate a more efficient warm rain process in the urban clouds as compared to rural clouds. Assuming similar average updraft speeds in urban and rural clouds, first echoes develop more rapidly in rising parcels of urban clouds.

The results of these calculations indicate that giant nuclei may play a significant role in the initiation of the warm rain process and the development of radar first echo (Fig. 2). In addition, large concentrations of nuclei in the presence of increased numbers of giant nuclei do not significantly effect the development of precipitation (Fig. 4).

7. ACKNOWLEDGEMENTS

The authors are indebted to R. R. Braham and his colleagues at the University of Chicago for providing their observations of nuclei for these calculations. We are also grateful to R. L. Reinhardt of Sierra Nevada Corporation for making available his work on the microphysical problems addressed in this paper. This research was performed under Grant ENV73-07882 as a part of the research on METROMEX, sponsored by the Weather Modification Program, Research Applications Directorate, National Science Foundation, and under Energy Research and Development Administration contract E(11-1)-1199.

8. REFERENCES

Berry, E. X., and R. L. Reinhardt, 1974: An analysis of cloud drop growth by collection: Part I. Double distributions. J. Atmos. Sci., 31, 1814-1824

Braham, R. R., 1974: Cloud physics of urban weather modification: A preliminary report. Bull. Amer. Meteor. Soc., 55, 100- 105.

Brazier-Smith, P. R., S. G. Jennings, and J. Latham, 1972: The interaction of falling water drops: coalescence. Proc. Royal Soc. Lond. A., 326, 393-408.

_____, _____, _____, 1973: Raindrop interactions and rainfall rates within clouds. Quart. J. Royal Met. Soc., 99, 260-272.

Changnon, S. A., and F. A. Huff, and R. G. Semonin, 1971: METROMEX: An investigation of inadvertent weather modification. Bull. Amer. Meteor. Soc., 52, 958-967.

Egan, B. A., and J. R. Mahoney, 1972: Numerical modeling of advection and diffusion of urban area source pollutants. J. Appl. Meteor., 11, 312-322.

Fitzgerald, J. W., and P. A. Spyers-Duran, 1973: Changes in cloud nucleus concentration and cloud droplet size distribution associated with pollution from St. Louis. J. Appl. Meteor., 12, 511-516.

Fukuta, N., and L. A. Walters, 1970: Kinetics of hydrometeor growth from a vapor-spherical model. J. Atmos. Sci., 27, 1160-1172.

Hocking, L. M., and P. R. Jonas, 1970: The collision efficiency of small drops. Quart. J. Royal Met. Soc., 96, 722-729

Huff, F. A., and S. A. Changnon, 1972: Climatological assessment of urban effects on precipitation at St. Louis. J. Appl Meteor., 11, 823-842.

Semonin, R. G., and S. A. Changnon, 1974: METROMEX: Summary of 1971-1972 results. Bull. Amer. Meteor. Soc., 55, 95-99.

Shafrir, V., and M. Neiburger, 1963: Collision efficiencies of two spheres falling in a viscous medium. J. Geophys. Res., 68, 4141-4147.

Srivastava, R. C., 1971: Size distribution of raindrops generated by their breakup and coalescence. J. Atmos. Sci., 28, 410-415.

Young, K. C., 1975: The evolution of drop spectra due to condensation, coalescence, and breakup. J. Atmos. Sci., 32, 965-973.

TURBULENCE EFFECT ON CLOUD DROPLET SPECTRUM DURING CONDENSATION

A.S. Stepanov

Institute of Experimental Meteorology
Obninsk, USSR

1. INTRODUCTION

Recently a number of authors discussed the theory of condensation and turbulence effects on the basis of different approaches and different physical representations. Fairly recently this problem has caught the attention of research workers. V.I.Belyev (1961) was the first to indicate the advantage of the probabilistic description of a single cloud droplet growth. The discussion made was based on the assumption that water vapour supersaturation in a single droplet growth equation was subjected to the normal distribution with an arbitrary variance. The Lagrangian approach to the cloud droplet spectrum change description was developed in works by Y.S.Sedunov(1965) and I.P.Masin (1965). The structural functions of temperature, liquid water content and supersaturation in cloud were found and correlation of supersaturation and velocity fluctuations was obtained. The condensation growth rate appeared to be the linear function of velocity. The integration of this expression over time and the use of the normal distribution for the droplet coordinate has led to the linear growth of the cloud droplet spectrum width in time (Y.S.Sedunov, 1965).

Eulerian description of the cloud droplet size distribution in turbulent conditions was used in the works by Y.S.Sedunov and L.M.Levin (1966), M.V.Bujkov and M.I.Dekchtyar(1968), T.L.Clark (1974). On the basis of semi-empirical turbulence theory the transport equation characterized by the second derivatives with respect to space variables and droplet sizes was written for the spectrum by Y.S.Sedunov and L.M.Levin (1966). The solution of this equation for a spatially homogeneous medium has shown the expansion of the spectrum. The necessity to complement the transport equation for the cloud spectrum by the equations for temperature, supersaturation was shown by M.V.Bujkov, M.I.Dekchtyar(1968), but the turbulence effect on cloud droplet spectrum was reduced only to turbulent mixing in space. To receive the transport equation T.L.Clark(1974) has used the standart procedure of the linear treatment of turbulent fluctuations and averaging. Nevertheless the attempts to express the correlation of the vapour supersaturation and droplet size distribution in terms of averaged characteristics of the cloud medium failed. Therefore the transport equation has not been derived.

The conclusions by Y.S.Sedunov(1965), I.P.Masin(1965), L.M.Levin and Y.S.Sedunov(1966) concerning the turbulence effect on the cloud droplet size spectrum expansion were argued by J.T.Bartlett and P.R.Jonas(1972), by J.Warner(1969). In the paper by J.T.Bartlett and P.R.Jonas (1972) a single droplet growth equation and the equations for temperature and water supersaturation were numerically solved and characteristics of adiabatically isolated air parcels which move stochastically in the cloud were obtained. The main conclusion is: turbulence does not influence practically the droplet size width.

The discrepancy of the conclusions about the turbulence effect on the cloud droplet spectrum can be accounted for by the inconsistency of the closed equation set describing both the cloud spectrum and thermodynamic characteristics of the medium and by the fact that the mechanism of the turbulence effect on the cloud spectrum is not clear completely. In work by A.S.Stepanov(1975a) a scheme of deriving a closed equation set for the cloud droplet spectrum, thermodynamic characteristics of the turbulent medium, based on the linear treatment of the fluctuation in the initial equations of regular condensation growth, on the solution of the equation set for fluctuations and on the application of these solutions to the equations for the averaged fluctuation values was suggested. The equation sets for the turbulent medium for different ratio of the time of phase relaxation τ, the Lagrangian turbulence scale T_L and the time of vapour and heat exchange between parcel and medium (for nonadiabatic fluctuations (A.S.Stepanov, 1975b)) are different. A.S.Stepanov(1975a) has shown that turbulence does not effect the cloud droplet spectrum if the cloud medium is homogeneous, i.e. there are no gradients of the specific droplet concentration n/ρ, the specific water content $P+m/\rho$ and the pseudopotential temperature θ_e (ρ is air density, P is liquid water content, m is equilibrium vapour concentration above the flat water surface). It is this state of the cloud medium that was numerically analyzed by J.T.Bartlett and P.R.Jonas(1972).

The main purpose of this paper is to analyze and evaluate the effect of the non-uniformity of the cloud medium, droplet sedimentation and of the fluctuation averaged air movement on the cloud spectrum in the turbulent conditions.

2. THE MAIN EQUATIONS

The initial equation set for vapour concentration C, temperature T, liquid water content P, droplet concentration n, droplet size distribution $f(\vec{x},S,t)$ (R, S, V are radius, surface and droplet volume respectively) is

$$\left(\frac{\partial}{\partial t} - \vec{v}\frac{\partial}{\partial \vec{x}}\right) A_i = B_i \qquad (1)$$

$$A_i = \left(\frac{P+C}{\rho}, T - \frac{L}{C_p}\frac{P}{\rho}, \frac{P}{\rho}, \frac{n}{\rho}, \frac{f}{\rho}\right),$$

$$B_i = \left(0, \frac{\vec{v}\vec{g}}{C_p}, \frac{\delta}{\rho}\frac{1}{\tau}, 0, -\frac{8\pi D}{\rho_e}\frac{\partial}{\partial S}\delta\frac{f}{\rho}\right) \qquad (2)$$

where ρ_e is water density, $\delta = C - m$ is water vapour supersaturation, D is molecular diffusion factor for water vapour, L is latent heat of water vapour condensation, C_p is specific heat capacity of air at a constant pressure, $\vec{g}$ is the acceleration due to gravity. P, n, τ are associated with the droplet size distribution in the following way

$$P = \rho_e \int dS\, V f, \quad n = \int dS\, f, \quad \tau^{-1} = 4\pi D \int dS\, R f \qquad (3)$$

The contribution of hygroscopicity and surface tension forces to the rate of cloud droplet growth is neglected, i.e. we assume that the droplet size is considerably larger than the condensation nucleus size. The equations for the turbulent medium with $T_L \gg \tau$; $m, P \gg \delta$ ($\mathcal{K} = \mathcal{L}^2 T_L^{-1}$ is turbulent diffusion factor, $\mathcal{L}$ is the characteristic path of mixing) have been derived from the equation sets (1), (2) by A.S.Stepanov(1975a). To close these equations for T, P, n, δ approximate formula for the time τ was used

$$\tau = 4\pi D\left[\frac{3}{4\pi}\left(\frac{n}{\rho}\right)^2 \frac{P}{\rho}\frac{1}{\rho_e}\right]^{1/3} \cdot \rho \qquad (4)$$

Taking $A_i = \bar{A}_i + A_i'$, where A_i' are turbulent fluctuations, and treating the equations (1),(2) as linear, one can find A_i' in the form of the functionals of the velocity fluctuations. The substitution of the latter in the equations for the averaged values and the use of the equations

$$\overline{v_i'(t)\, v_j'(t')} = v'^2 \delta_{ij}\, \exp\left(-\frac{|t-t'|}{T_L}\right),$$

$$\mathcal{K} = v'^2 T_L \qquad (5)$$

allow to express all the functions through $\mathcal{K}$. In contrast to the work by A.S.Stepanov(1975a) introduce now the mean velocity of the air movement $\vec{\overline{v}}(\vec{x},t)$ and the droplet sedimentation velocity

$$\vec{W}(s) = \frac{1}{18\pi\eta}\, \rho_\ell\, s\, \vec{g} \qquad (6)$$

where η is air viscosity.

With $\bar{v}, W \ll v'$ one can ignore these velocities in the equations for fluctuations. Besides the diffusion limit $\ell \gg \mathcal{L}$ will be considered, where ℓ is the characteristic distance of variations of the averaged fields P, n, T, δ, $\vec{v}$ (for simplicity everywhere below the average values are written without bars). Therefore the equation set for the turbulent medium will have the form:

$$\left(\frac{\partial}{\partial t} + \vec{v}\frac{\partial}{\partial \vec{x}} - \mathcal{K}\frac{\partial^2}{\partial x^2}\right)\frac{P+m}{\rho} + \frac{\partial}{\partial \vec{x}}\rho_\ell\, \overline{V\frac{f}{\rho}} = 0, \qquad (7)$$

$$\left(\frac{\partial}{\partial t} + \vec{v}\frac{\partial}{\partial \vec{x}} - \mathcal{K}\frac{\partial^2}{\partial x^2}\right)\frac{n}{\rho} + \frac{\partial}{\partial \vec{x}}\overline{\vec{W}\frac{f}{\rho}} = 0, \qquad (8)$$

$$\gamma\frac{\partial T}{\partial t} + \vec{v}\gamma\frac{\partial \theta_\ell}{\partial \vec{x}} - \mathcal{K}\frac{\partial}{\partial \vec{x}}\gamma\frac{\partial \theta_\ell}{\partial \vec{x}} = 0, \qquad (9)$$

$$\frac{\delta}{\rho} = \tau\frac{c_p}{L}\, v\frac{\partial}{\partial \vec{x}}\left(\theta_c - \theta_\ell\right) + \mathcal{K}\tau\frac{c_p}{L}\frac{\partial \theta_\ell}{\partial \vec{x}}\frac{\partial}{\partial \vec{x}}\ln\gamma - \tau Q, \qquad (10)$$

$$\frac{\partial}{\partial t}\frac{f}{\rho} + \frac{\partial}{\partial \vec{x}}\left(\vec{v}+\vec{W}\right)\frac{f}{\rho} + \frac{8\pi\mathcal{D}\delta}{\rho_\ell}\frac{\partial}{\partial s}\frac{f}{\rho} - \mathcal{K}\left[\frac{\partial}{\partial \vec{x}} + \frac{8\pi\mathcal{D}\rho\tau}{\rho_\ell}\left(\frac{\partial\theta_c}{\partial \vec{x}} - \frac{\partial\theta_\ell}{\partial \vec{x}}\right)\frac{\partial}{\partial s}\right]^2\frac{f}{\rho} = 0 \qquad (11)$$

Here the potential θ_c and the pseudopotential θ_ℓ temperature, the function connecting the phase transition frequence and the supersaturation Q are introduced

$$\frac{\partial\theta_c}{\partial \vec{x}} = \frac{\partial T}{\partial \vec{x}} - \frac{\vec{g}}{c_p},$$

$$\frac{\partial\theta_\ell}{\partial \vec{x}} = \frac{\partial T}{\partial x} - \frac{\vec{g}}{c_p\gamma}\left(1 + \frac{m}{\rho}\frac{L}{R_\ell T}\right),$$

$$\gamma = 1 + \frac{m}{\rho}\frac{L}{c_p T}\frac{L}{R_n T},$$

$$Q = \mathcal{K}\frac{c_p}{L}\left(\frac{\partial\theta_c}{\partial \vec{x}} - \frac{\partial\theta_\ell}{\partial \vec{x}}\right) \times \left[-\frac{2}{3}\frac{\partial}{\partial \vec{x}}\ln\frac{n}{\rho} - \frac{1}{3}\frac{\rho}{P}\frac{\partial}{\partial \vec{x}}\frac{P+m}{\rho} + \frac{1}{3}\frac{m}{P}\frac{L}{P_n T^2}\frac{\partial\theta_\ell}{\partial \vec{x}}\right] \qquad (12)$$

R_n, R_ℓ are gas constants of vapour and air. Similar to (4) one can use the relations

$$\overline{\vec{W}\frac{f}{\rho}} = \frac{1}{3}\frac{\rho_\ell\vec{g}}{\eta}\left(6\pi^2\rho_\ell^2\right)^{-1/3}\left(\frac{P}{\rho}\right)^{2/3}\left(\frac{n}{\rho}\right)^{1/3},$$

$$\rho_\ell\overline{\vec{W}V\frac{f}{\rho}} = \frac{1}{3}\frac{\rho_\ell\vec{g}}{\eta}\left(6\pi^2\rho_\ell^2\right)^{-1/3}\left(\frac{P}{\rho}\right)^{5/3}\left(\frac{n}{\rho}\right)^{-2/3} \qquad (13)$$

for the integrals over $\vec{W}$ in the equations (7),(8). The equations (7),(8) describe the turbulent diffusion of the specific liquid water content and droplet concentration, (9)- the turbulent heat conductivity with consideration of phase transitions in fluctuations. In contrast to the work by L.M.Levin, Y.S.Sedunov (1966)in equation for spectrum (11) the part of supersaturation due to turbulent mixing is not neglected. The fluctuation averaged supersaturation comes into being due to the medium movement and turbulent mixing in the non-uniform fields $\frac{P+m}{\rho}$, $\frac{n}{\rho}$, θ_ℓ. If the medium is homogeneous and the space distribution of the droplet size spectrum is preselected, i.e. if

$$\frac{\partial}{\partial \vec{x}}\frac{n}{\rho} = 0, \quad \frac{\partial}{\partial \vec{x}}\frac{P+m}{\rho} = 0, \quad \frac{\partial}{\partial \vec{x}}\theta_\ell = 0,$$

$$\frac{f}{\rho} = \frac{f}{\rho}\left[s - \int^{\vec{x}} d\vec{x}\, \frac{8\pi\mathcal{D}\rho\tau}{\rho_\ell}\left(\frac{\partial\theta_c}{\partial \vec{x}} - \frac{\partial\theta_\ell}{\partial \vec{x}}\right)\right], \qquad (14)$$

the turbulence does not influence the cloud medium state.

3. THE CLOUD SIZE SPECTRUM AND TURBULENT FLUCTUATION AVERAGED SUPERSATURATION

The equations (7)-(12)show that the cloud spectrum width in the turbulent medium is increased due to non-uniformity of $^{P+m}/_\rho$, $^n/_\rho$, θ_ℓ and due to the combined effect of this non-uniformity, medium movement and droplet sedimentation. It is more simple to study these effects separately. At first we suggest in the cloud medium only the temperature field disturbed (γ = const)

$$\frac{\partial}{\partial \vec{x}}\frac{P+m}{\rho}=0, \qquad \frac{\partial}{\partial \vec{x}}\frac{n}{\rho}=0,$$

$$\vec{v}=\vec{w}=0, \quad \gamma\frac{\partial \theta_\ell}{\partial \vec{x}}=const. \qquad (15)$$

The cloud droplet spectrum is defined from (14) as δ-function varying in space according to changes of P , m , T . The state of (15) will not change with time according to (7)-(9). But according to (10) the supersaturation arises

$$\frac{\delta}{\rho}=-\mathcal{K}\left(\frac{\partial\theta_\ell}{\partial\vec{x}}-\frac{\partial\theta_c}{\partial\vec{x}}\right)\frac{\tau\rho}{3P}(\gamma-1)\left(\frac{c_p}{L}\right)^2\frac{\partial\theta_\ell}{\partial\vec{x}}. \qquad (16)$$

This result can be explained on the basis of the phenomenological theory of turbulence. At a certain defined point the supersaturation is created by the mixing of the air parcels which arrived here for the period T_L from the points located at a certain distance $\mathcal{L}$ from it. In one of these turbulent parcels the supersaturation is negative and drops evaporate, in another one supersaturation is positive and droplets grow. The absolute value of the supersaturation is larger in that parcel for which according to (4) the time τ is larger and the liquid water content is smaller. That is why $\delta>0$ with wet-unstable distribution of temperature ($\frac{\partial\theta_\ell}{\partial\vec{x}}\parallel\vec{g}$) and $\delta<0$ when the temperature field is wet-stable ($-\frac{\partial\theta_\ell}{\partial\vec{x}}\parallel\vec{g}$). If $\frac{\partial\theta_\ell}{\partial\vec{x}}=0$ the supersaturation accurate to the terms τ/T_L will be $\delta=0$. From equation (11) one can find the variations of the droplet spectrum width. So we have the following equation for the droplet surface distribution variance:

$$\Delta\sigma^2=2\mathcal{K}t\left[\frac{2}{3}s\frac{c_p}{L}\frac{\rho}{P}(\gamma-1)\frac{\partial\theta_\ell}{\partial\vec{x}}\right]^2 \qquad (17)$$

accurate to the first order terms. The spectrum at this time moves to smaller sizes S so that the liquid water content remains constant.

The analogous change of the spectrum is found, if there is the liquid water content gradient in the cloud medium:

$$\frac{\partial}{\partial\vec{x}}\theta_\ell=0, \qquad \frac{\partial}{\partial\vec{x}}\frac{P+m}{\rho}=const,$$

$$\frac{\partial}{\partial\vec{x}}\frac{n}{\rho}=0, \quad \vec{v}=\vec{w}=0. \qquad (18)$$

The equations for the supersaturation and variance ($\Delta\sigma^2=0$ at $t=0$) are as follows

$$\frac{\delta}{\rho}=\mathcal{K}\left(\frac{\partial\theta_c}{\partial\vec{x}}-\frac{\partial\theta_\ell}{\partial\vec{x}}\right)\frac{\tau}{3}\cdot\frac{\rho}{P}\frac{c_p}{L}\frac{\partial}{\partial\vec{x}}\frac{P+m}{\rho}, \qquad (19)$$

$$\Delta\sigma^2=2\mathcal{K}t\left[\frac{2}{3}s\frac{\rho}{P}\frac{\partial}{\partial\vec{x}}\frac{P+m}{\rho}\right]^2 \qquad (20)$$

It is this expansion of the droplet size spectrum that in fact was investigated in works by Y.S.Sedunov (1965), I.P.Masin (1965), Y.S.Sedunov and L.M.Levin (1966).

If to assume the δ-spectrum of the droplet size similarly to (14), the constant gradient of the specific droplet concentration and the uniformity of the remaining parameters of the medium, we have

$$\frac{\delta}{\rho}=\mathcal{K}\left(\frac{\partial\theta_c}{\partial\vec{x}}-\frac{\partial\theta_\ell}{\partial\vec{x}}\right)\frac{2}{3}\tau\frac{c_p}{L}\frac{\partial}{\partial\vec{x}}\ln\frac{n}{\rho}, \qquad (21)$$

$$\Delta\sigma^2=2\mathcal{K}t\left[\frac{2}{3}s\frac{\partial}{\partial\vec{x}}\ln\frac{n}{\rho}\right]^2 \qquad (22)$$

As it is seen from (17), (20), (22) the variance growth rate is squared to the gradient disturbing the medium. For $\mathcal{K}$ = 100 m^2sec^{-1}, P = 0,42 $g\cdot m^{-3}$, R = 10 μm, T = 273°K and $\frac{\partial\theta_\ell}{\partial\vec{x}}$ = 1 °K/100m, $\frac{\rho}{P}\frac{\partial}{\partial\vec{x}}\frac{P+m}{\rho}=\frac{\partial}{\partial\vec{x}}\ln\frac{n}{\rho}$=1/100m the rate of variance variations $\frac{\partial}{\partial t}\Delta\sigma^2$, calculated from (17), (20), (22)equal to 0,99.10^4, 1,41.10^4, 1,41.10^4 μm^4/sec respecpectively.

From (16), (19) it follows that with $\frac{\partial\theta_c}{\partial\vec{x}}$ =0 and $\frac{\partial}{\partial\vec{x}}\frac{P+m}{\rho}\parallel\vec{g}$ supersaturation $\delta<0$. That is why the initial stage of the cloud formation (dry-adiabatic gradient of temperature, upward diffusion of vapour) takes place with negative average supersaturation within the cloud. It should be noted that in the boundary region of a cloud the equations (7)-(11) are not applicable.

The combined effect of the medium movement velocity $\vec{v}$,turbulent mixing and non-uniformity are studied on the example of non-uniformity of the temperature field. Let's define the constant gradient of temperature as

$$\gamma \frac{\partial \theta_6}{\partial \vec{x}} = \frac{\partial \theta_c}{\partial \vec{x}}$$

In this case space coordinate dependence dissapears in the coofficients of the equation (11). The δ -spectrum,defined at $t = 0$, expands at $t > 0$, displacing towards the smaller droplet sizes. With assumption

$$\left(\gamma - 1\right) \frac{\partial \theta_6}{\partial \vec{x}} \frac{c_p}{L} \frac{\rho}{P} \vec{v} t \gg 1 \tag{23}$$

the droplet size spectrum width grows

$$\Delta 6^2 = \frac{8}{3} \mathcal{K} \left[\left(\gamma - 1\right) \frac{\partial \theta_6}{\partial \vec{x}} \frac{c_p}{L} \frac{\rho}{P} \frac{t^{1/4}}{v^{1/2}} \right]^{4/3} \tag{24}$$

where v is g - component of the velocity. For the above mentioned parameters and with $v = 1$ cm sec^{-1}, $t = 10^3$sec $\Delta 6^2 = 5{,}5.10^7 \mu m^4$.

The sedimentation of cloud droplets forms gradients of specific droplet concentration and of a specific liquid water content in a homogeneous cloud medium (14). It is evident that turbulent mixing should lead to the expansion of the droplet size spectrum. From (7), (8), (11) one can evaluate the rate of the spectrum expansion at the expense of the sedimentation and turbulent mixing

$$\Delta 6^2 = \frac{8}{27} \mathcal{K} W^2 \left(\frac{\partial \theta_c}{\partial \vec{x}} - \frac{\partial \theta_6}{\partial \vec{x}} \right)^4 \times \left(\frac{c_p}{L} \frac{\rho}{P} \right)^4 S^2 t^3 \tag{25}$$

Such growth of droplet size distribution width is not great. For the above parameter values $\partial \Delta 6^2 / \partial t = 4{,}7.\ 10^{-6} \mu m^4$ sec^{-1} t^2(sec). For $t = 10^4$-10^5sec sedimentation forms gradients

$$\frac{1}{P} \frac{\partial}{\partial \vec{x}} \frac{P+m}{\rho} \sim \frac{\partial}{\partial \vec{x}} \ln \frac{n}{\rho} \sim 1/100\text{m},$$

and spectrum width growth rates, found from formulas (20), (22), (25) are of the same order of magnitude.

In the above cases the cloud medium was disturbed everywhere in space. Therefore the cloud droplet size spectrum expanded without any limit due to turbulent mixing both in the direction of small sizes and in direction of large ones. If to create local disturbances (e.g. of temperature or of specific liquid water content) in a limited area of space, the cloud droplet size spectrum appears to be limited upwards and downwards in the droplet size space. At this time turbulence leads to a gradual decrease of distarbance. The droplet size spectrum width grows in time, reaches maximum and then decreases again. In this cases the spectrum width limitation is accounted for by the limitation of the maximum value of the disturbancy of the fields of pseudopotential temperature θ_6 , specific liquid water content $P+m/\rho$, specific droplet concentration n/ρ in space. The maximum value of the spectrum width will be reached at different points of space at different moments of time.

From the analysis of equation (11) and correlations (17), (20), (22) one can find that maximum and minimum droplet sizes at a given point of space are defined by the disturbance values for the fields of pseudopotential temperature, specific liquid water content, specific droplet concentration in the cloud medium. These are all the possible maximum and minimum droplet sizes which are comprised in the turbulent cloud air parcels adiabatically displaced towards a given point in space.

References

Bartlett, J.T. and P.R. Jonas, 1972: On the dispersion of the sizes of droplets growing by condensation in turbulent clouds. Quart. Roy. Met. Soc., 98, 150-164.

Belyev, V.I., 1961: On the cloud droplet size distribution at the condensation stage of cloud development. Izv. AN SSSR, FAO, 8, 1209-1213.

Bujkov, M.V. and M.I. Dekchtjar, 1968: To the theory of stratiform clouds. 3. Turbulent diffusion effect on cloud droplet size distribution. Tr. Ukr. NIGMI, vyp. 70, 50-66.

Clark, T.L., 1974: On modelling nucleation and condensation theory in eulerian spatial domain. J. Atmos. Sci., 31, 2099-2117.

Levin, L.M. and Y.S. Sedunov, 1966: Transport equation for microphysical processes in clouds. Dokl. AN SSSR, 170, 323-327.

Masin, I.P., 1965: To the theory of particle size distribution formation in clouds and precipitation. Tr. TsAO, vyp.64, 57-70.

Sedunov, Y.S., 1965: The fine cloud structure and its role in the formation of the cloud droplet spectrum. Izv. AN SSSR, FAO, 1, No 7, 722-731.

Stepanov, A.S., 1975a: Condensation growth of cloud droplets in the turbulent atmosphere. Izv. AN SSSR, FAO, 11, No1, 27-42.

________ 1975b: Condensational growth of cloud droplets in turbulent medium taking into account nonadiabatic effects and in the approximation of smallness of water content. Izv. AN SSSR, FAO, 11, No 3, 267-277.

Warner, J., 1969: The microstructure of cumulus cloud. Pt.1. General feature of droplet spectrum. J. Atmos. Sci. 26, 1049-1069.

DROPLET SIZE DEVELOPMENT IN WARM CUMULUS CLOUDS

A.N. Dingle

and

D.D. Harding

University of Michigan
Ann Arbor, Michigan

Cloud droplet size distributions in convective clouds are observed [see, e.g., Diem (1942), Weickmann and aufm Kampe (1953), Warner (1969)] to be considerably broader than the size distributions computed from condensation nuclei distributions by means of the microphysical equations [Howell (1949), Mordy (1959), Neiburger and Chien (1960)]. The problem of explaining the difference and/or modeling the generation of size distributions similar to the observed ones has been addressed in several previous papers [e.g., Mason and Ghosh (1957), Mason and Chien (1962), Sedunov (1965), Kornfeld (1970), Paluch (1971), Fitzgerald (1972), Mason and Jonas (1974)]. For the most part, these efforts fall short of the mark. The entrainment models [Mason and Jonas (1974), Warner (1973)] tend to show relatively good promise, particularly when provision is made for the introduction of fresh nuclei with the entrained air, but these appear to apply mainly to the outer portion of the cloud sides and top. The model of Paluch (1971) couples droplet sedimentation and small local humidity fluctuations together and shows a drop-size spectrum broadening effect as well as an effect of fluctuating droplet number concentrations and liquid water content. The effect of a varying vertical velocity upon a sample of cloud volume was briefly treated by Kornfeld (1970), but her choice of droplet size classes for the model is too restricted to yield a convincing result.

The details of the motion field in convective clouds are known to be quite complicated. Generally they are characterized as "turbulent" without further elaboration. This implies an indefinite field of upward, downward and lateral motions of varying speeds and reversal frequencies. It is clear that such motions can affect the local environemtns of the cloud droplets. Storebø and Dingle (1974) and Storebø (1976) noted a prominent effect in their models of orographic cloud which tended strongly to favor the persistence of the larger cloud droplets and the deactivation of the smallest droplets in a very short downward displacement of a cloud sample. The present effort is an attempt to determine the effects upon the droplet size distribution of the more or less oscillatory vertical displacements that a cloud sample might undergo in a convective cloud.

The computational model is a modified version of that used by Kornfeld (1970) and Fitzgerald (1972), and is based upon thirty simultaneous ordinary differential equations: for the ambient temperature

$$\frac{dT}{dt} = -\frac{(1+x)(g+\frac{dw}{dt})\,w + L\frac{dx}{dt}}{c_{pd} + xc_{pv} + x_l\, c_w} \tag{1}$$

the pressure

$$\frac{dp}{dt} = \frac{-p}{R_m T}\,(g + \frac{dw}{dt})\,w \tag{2}$$

the growth rate for each of 27 droplet size categories

$$\frac{dm_i}{dt} = \frac{4\pi r v (e_a - e_s(T)\; a \exp[\frac{2\sigma}{r\rho R_v T}]}{\frac{R_v T}{DF_v} + \frac{T^* L\, e_s(T)\; a \exp[\frac{2\sigma}{r\rho R_v T}]}{KF_h(T-35.86)^2}} \qquad (3)\text{-}(29)$$

and the conservation of water mass

$$\frac{dx}{dt} = -\sum_i n_i \frac{dm_i}{dt} \tag{30}$$

The water activity, $\underline{a}$, values tabulated by Low (1969) are used to express the depression of vapor pressure by electrolytes in solution. The condensation nuclei spectrum is defined by a Junge (1963) distribution of ammonium sulfate particles ranging from 0.015μm to 3.9μm radius in 27 size categories such that the individual particle mass is increased by a factor of 1.9 for each succeeding category. At cloud base, defined at 283.16K, 900 mb, and 100% relative humidity, there are 386 particles cm^{-3} giving a total particulate loading of $3 \times 10^{-12} g\ cm^{-3}$.

To obtain comparisons among cloud droplet size distributions generated within various conceivable turbulent flow regimes in cumulus clouds, we have simulated these by assuming hypothetical trajectories and speeds in a series of case studies. The results of these studies are then compared against simulated results of a monotonic lifting-condensation process (Case A). The trajectories are described in Table I for five additional cases.

Table I

Case	height (m)	velocity	time to reach 100 m level(s)
A	0-100	100	100
B	0-20	100	
	20-0	-20	
	0-100	100	220
C	0-20	100	
	20-0	-20	
	0-20	100	
	20-0	-20	
	0-100	100	340
D	0-20	100	
	20-0	-20	
	0-30	100	
	30-10	-20	
	10-100	100	340
E	0-10	100	
	10-0	-100	
	0-20	100	
	20-10	-100	
	10-30	100	
	30-20	-100	
	20-40	100	
	40-30	-100	
	30-50	100	
	50-40	-100	
	40-60	100	
	60-50	-100	
	50-100	100	220
F	$w = 100 + 300 \sin(0.15t)$		61

Figures 1 and 2 show the resulting droplet size distribution, achieved within each cloud sample at the 100 m level (above cloud base). The mode at small size that is made up of nonactivated haze particles is omitted from each of these curves. In the cloud droplet size ranges, cases B and C both give bimodal distributions. The largest droplets, $r = 24\mu m$ are generated in case D, which also gives 0.9 droplets per liter of $20\mu m$ radius or larger.

The broadening effect upon the droplet-size distribution is conveniently expressed (Twomey, 1966) by the dispersion, defined by

$$\delta = \sigma/\overline{r}$$

where σ is the standard deviation of the distribution and $\overline{r}$ is the mean radius. Table II gives the values of these three statistical parameters for the drop-size distribution generated by each case up to 100 m. Figure 3 shows the measured values of dispersion obtained by Warner (1969).

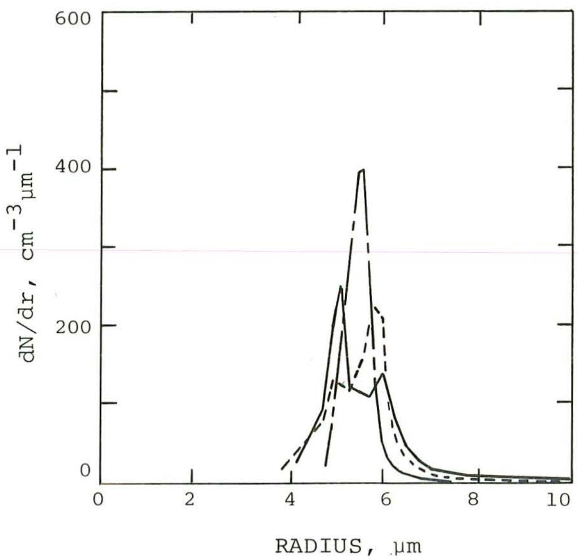

Figure 1. Droplet size distributions at 100 meters. Case A ——— - ———, Case B -----, Case C ———.

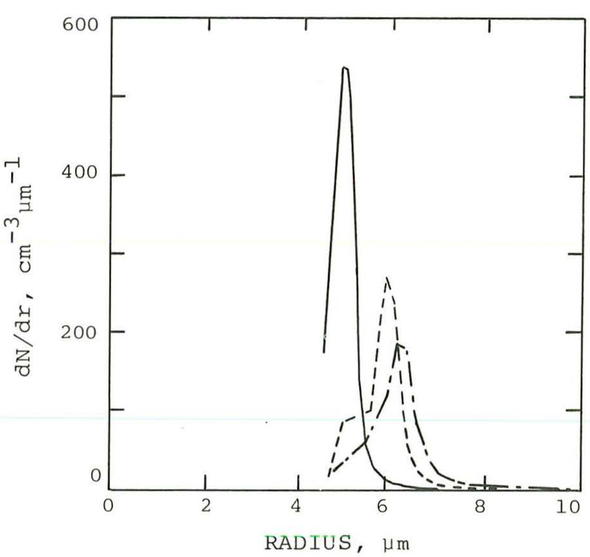

Figure 2. Droplet size distributions at 100 meters. Case D ——— - ———, Case E -----, Case F ———.

Table II

case	$\bar{r}$	σ	δ
A	5.46	.245	.045
B	5.59	.554	.099
C	5.37	.613	.114
D	6.14	.457	.074
E	5.82	.400	.069
F	4.93	.216	.044

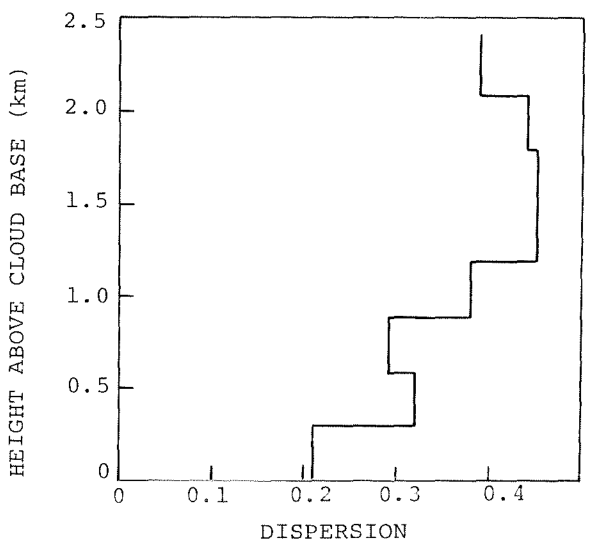

Figure 3, Average coefficient of dispersion as a function of height above cloud base, Warner (1969).

Although the cases treated are distinctly limited, a diversity of effects emerges: on the one hand the mean radius and dispersion are enhanced, and on the other they are diminished. Further study is obviously needed, but the present work at least suggests that the turbulence of a convective cloud can contribute to broadening of the droplet size spectrum in some regions of the cloud, and narrowing in others. Noteworthy is the fact that the dispersion for Case C, while still less than 0.2, is some 2.5 times larger than that for the steady updraft case. The values of the mean radius and standard deviation are not a simple function of time. For example, Case C has a smaller mean radius and larger standard deviation than does Case D although they require the same amount of time to reach the 100 m level. On the other hand, Case F, which takes the shortest time to reach 100 m also has the smallest values of $\bar{r}$ and σ.

There are many complicated features of the microphysics so that predicting the droplet distribution is not a simple matter. It should be recognized that only the smallest droplets are at equilibrium with their environment. The large droplets lag well behind their respective equilibrium radii, and this fact is responsible for the finding that the large droplets can continue to grow during the downward phase while smaller droplets are evaporating.

Further, since a droplet is not activated until both its critical radius and saturation ratio are exceeded, it is neither the largest nor the smallest droplets which first become activated, but rather some intermediate sized droplet. The pattern of the saturation ratio as well as the amount of time spent in the evaporation and condensation phases determine the final droplet distribution. This in turn affects the behavior of the large droplets which are few in number but individually have a large proportionate mass of water. As the small droplets become deactivated, the water attached to them is to some extent transferred to larger droplets. Upon reentering the updraft, the deactivated haze particles will reactivate only if the saturation ratio attains a high enough value.

For example, in Cases A, B, and C only the two smallest categories were never activated. In Case D, size categories 3 and 4 did not reactivate after the second cycle, leading to the largest value of $\bar{r}$ of all the cases. In Case E in which the cycles are small but rapid, size class 3 did not survive the cycling. All particles were activated in Case F, mainly as a result of the fast updraft and resulting high saturation ratio.

Because of the complexity of the problem, the relative roles of the basic parameters can be studied conveniently by means of numerical experiments. It is our intent to pursue these studies.

References

Diem, M., 1942: Messungen der Grösse von Wolkenelementen. I. Ann. Hydrogr. Berl., 70, 142-150.

Fitzgerald, J.W., 1972: A study of the initial phase of cloud droplet growth by condensation: Comparison between theory and observation. Ph.D. dissertation. University of Chicago, xi + 144 pp.

Howell, W.E., 1949: The growth of cloud drops in uniformly cooled air. J. Meteor., 6, 134-149.

Junge, C.E., 1963: Air Chemistry and Radioactivity. Academic Press, New York, xii + 382 pp.

Kornfeld P., 1970: Numerical solution for condensation of atmospheric vapor on soluble and insoluble nuclei. J. Atmos. Sci., 27, 256-264.

Low, R.D.H., 1969: A generalized equation for the solution effect in droplet growth. J. Atmos. Sci., 26, 608-611.

Mason, B.J., and C.W. Chien, 1962: Cloud droplet growth by condensation in cumulus. Quart. J. Roy. Meteor. Soc., 88, 136-142.

Mason, B.J. and D.K. Ghosh, 1957: The formation of large droplets in small cumulus. Quart. J. Roy. Meteor. Soc., 83, 501-507.

Mason, B.J., and P.R. Jonas 1974: The evolution of droplet spectra and large droplets by condensation in cumulus clouds. Quart. J. Roy. Meteor. Soc., 100, 23-38.

Mordy, W., 1959: Computations of the growth by condensation of a population of cloud droplets. Tellus, 11, 17-44.

Neiburger, M., and C.W. Chien, 1960: Computations of the growth of cloud drops by condensation using an electronic digital computer. Physics of Precipitation, Washington, D.C., Amer. Geophys. Union, 191-210.

Paluch, I.R., 1971: A model for cloud droplet growth by condensation in an inhomogeneous medium. J. Atmos. Sci., 28, 629-639.

Sedunov, Y.S., 1965: Fine cloud structure and its role in the formation of the cloud particle spectrum. Izv. Atmos. Oceanogr. Phys., 1, 722-731.

Storebø, P.B., 1976: Small scale topographical influences on precipitation. Tellus, 28, 45-59.

Storebø, P.B., and A.N. Dingle, 1974: Removal of pollution by rain in a shallow air flow. J. Atmos. Sci., 31, 533-542.

Twomey, S., 1966: Computations of rain formed by coalescence. J. Atmos. Sci., 23, 405-411.

Warner, J., 1969: The microstructure of cumulus cloud, Part I. General features of the droplet spectrum. J. Atmos. Sci., 26, 1049-1059.

Warner, J., 1973: The microstructure of cumulus cloud, Part IV. The effect on the droplet spectrum of mixing between cloud and environment. J. Atmos. Sci., 30, 256-261.

Weickmann, H.K., and H.J. aufm Kampe, 1953: Physical properties of cumulus clouds. J. Meteor., 10, 204-211.

ON THE DECREASE OF DROPLET NUMBER WITH HEIGHT IN THE EARLY STAGE OF GROWTH IN A CONVECTIVE WARM CLOUD

YOSHIHIKO TAKAHASHI

Independent Research Laboratory for Meteorology

Tokyo, Japan

1. Introduction

A general physical structure of cumulus clouds has been disclosed by the laborious observations of Zaitsev (1950), Weickmann and aufm Kampe (1953), and Squires (1958). The droplet number, for example, decreases with height from cloud base up to some level and then turns to be constant or rather increase.

Weickmann and aufm Kampe in their paper have pointed out that such a trend of droplet number indicates the effectiveness of a process of coalescence.

Formerly, Smolukovski (1916) presented a theory for the purpose of explaining Paine's interesting experiment on the effect of strong stirring upon the coagulation of a hydrosol; that is, the collisions between particles would become significant owing to the velocity gradient existing in the shearing laminar flow of a fluid. Based on this theory, Wigand and Frankenberger (1930) dealt with the effect of electrification upon the stability of fog and cloud; the velocity gradient on a length of less than 1 mm was linearly interpolated from the maximum gradient 0.5 m/sec per m observed in the surface wind of mean velocity 2 m/sec, because of the absence other available data. The gradient was assumed to be proportional to the mean wind velocity.

This paper treats the decrease of droplet number by Smolukovski's collision taking account of their growth by condensation associated with adiabatic expansion of a mass of moist air carring them along. Here, eddies of minimum sizes are supposed in relation with the velocity gradient on a small length comparable to droplet diameter.

2. Velocity gradient

Fig. 1 schematically shows a profile of turbulent velocity of the wind along an arbitrary axis of x which would be obtained by observing selectively the gusts and lulls referred to the eddies possessing the sizes of a certain definite magnitude; the wind direction would be constant or gradually change during a gust or lull.

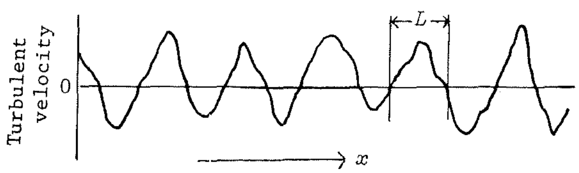

Fig. 1. Schematic profile of turbulent velocity of the wind along an arbitrary axis of x.

Now, assume a similar profile for eddies of minimum sizes and, for simplicity, express it by

$$c = A \sin(\pi x/L) \tag{2.1}$$

where c denotes the turbulent velocity, L the mean dimension of the eddies measured along the x-axis, and A the constant depending on the intensity of turbulence. Then, on the assumption that the turbulence is of an isotropic structure, we have

$$\overline{(\nabla c)^2} = 3(\pi/L)^2\, \overline{c^2} \tag{2.2}$$

or, putting $\left[\overline{(\nabla c)^2}\right]^{1/2} = \nabla C$ and $(\overline{c^2})^{1/2} = C$,

$$\nabla C \approx \sqrt{3}\,\pi\, C/L \tag{2.3}$$

3. Smolukovskian collision of small cloud droplets

We shall consider the small cloud droplets decreasing in concentration by the Smolukovskian collisions. In this case, the collision number of a droplet of radius r_i with those of radius r_j and concentration n_j in unit volume is

$$\frac{4}{3} E_{ij}\, n_i (r_i + r_j)^3\, \nabla C \tag{3.1}$$

per unit time, where ∇C is given by Eq. (2.3) and E_{ij} the collision coefficient depending on r_i and r_j.

When droplets of various sizes are present the collision number in unit volume per unit time is

$$\frac{2}{3}\nabla C \sum_i \sum_j E_{ij}\, n_i\, n_j (r_i + r_j)^3 \tag{3.2}$$

Let n denote the total number of droplets and take E_{ij} constant and equal to E, Eq. (3.2) becomes

$$\frac{16}{3} E\, \nabla C\, n^2\, \overline{r^3}\left[1 + \frac{3}{4}\left(\frac{\bar{r}\,\overline{r^2}}{\overline{r^3}} - 1\right)\right] \tag{3.3}$$

The second term in the bracket will vanish as far as the droplets possess a narrow size distribution. After all, we have the number of collisions between small droplets

$$\frac{4}{\pi\rho} E\, \nabla C\, n\, w = 4\sqrt{3}\, \frac{EC}{\rho L}\, n\, w \tag{3.4}$$

in unit volume per unit time, where w is the liquid water amount in unit volume and ρ the density of water.

4. Decrease of droplet number with height

We now consider a convective cloud in the stage of development with no entrainment and calculate the decrease of droplet number with height by the Smolukovskian collisions. In this case it is necessary to take into account the number of droplets in unit mass of dry air by analogy with humidity mixing ratio.

Accordingly, the decrease of droplet number with height is given by the equation

$$-\frac{d}{dz}(vn) = \frac{4\sqrt{\pi}\,CE}{\rho UL}\, v\, n\, w \qquad (4.1)$$

where z represents the height above condensation level, v the specific volume of dry air at its partial pressure, U the updraught velocity, and others the same as before. Condensation level may be taken as a cloud base in the following discussions.

If we put

$$K = \frac{4\sqrt{\pi}}{\rho}\frac{EC}{UL} \qquad (4.2)$$

and

$$W = \int_0^z w\, dz \qquad (4.3)$$

Table 1. a_1 and b_1 in Eq. (5.1)

Base temp. °C	a_1 g km^{-1}	b_1 g km^{-2}	Error g m^{-3}	
30	2.724	-0.2435	-0.00	0.01
25	2.602	-0.2379	-0.01	0.03
20	2.470	-0.2408	-0.02	0.01
15	2.315	-0.2491	-0.03	0.01
10	2.098	-0.2468	-0.04	0.01
5	1.837	-0.2376	-0.02	0.03
0	1.582	-0.2242	-0.02	0.03
-5	1.302	-0.1971	-0.01	0.01

Table 2. a_2 and b_2 in Eq. (5.2)

Base temp. °C	a_2 km^{-1}	b_2 km^{-2}	Error	
30	-0.0947	0.00358	-0.0001	0.0002
25	-0.0945	0.00326	-0.0002	0.0001
20	-0.0966	0.00366	-0.0002	0.0002
15	-0.0978	0.00380	-0.0001	0.0001
10	-0.0982	0.00393	-0.0001	0.0001
5	-0.0983	0.00394	-0.0001	0.0001
0	-0.0980	0.00385	-0.0001	0.0001
-5	-0.0970	0.00272	+0.0003	0.0001

the integration of Eq. (4.1) gives

$$\ln(n/n_0) = \ln(v_0/v) - KW \qquad (4.4)$$

where n_0 and v_0 are the initial values of n and v at cloud base respectively. v_0/v and W as functions of z can be determined if pressure and temperature at cloud base are given.

5. Computations of W and v_0/v

We have computed W and v_0/v as functions of z, taking cloud base at a height of pressure 950 mb and giving various temperatures to the cloud base. Then, putting

$$W = a_1 z + b_1 z^2 \qquad (5.1)$$

and

$$v_0/v = 1 + a_2 z + b_2 z^2 \qquad (5.2)$$

we have determined the most appropriate values of the coefficients a_1, b_1, a_2, and b_2 as given in Table 1 and 2.

Thus, W and v_0/v can be easily computed with errors less than fractions of a per cent up to about 2.5 km above base but not exceeding a height of -10°C.

6. Comparison with the observations

Fig. 2 illustrates the theoretical log $(n/n_0)-z$ curves for pressure 950 mb, temperature 20°C at cloud base, and various values of K. In comparing with the observations the followings should be noticed.

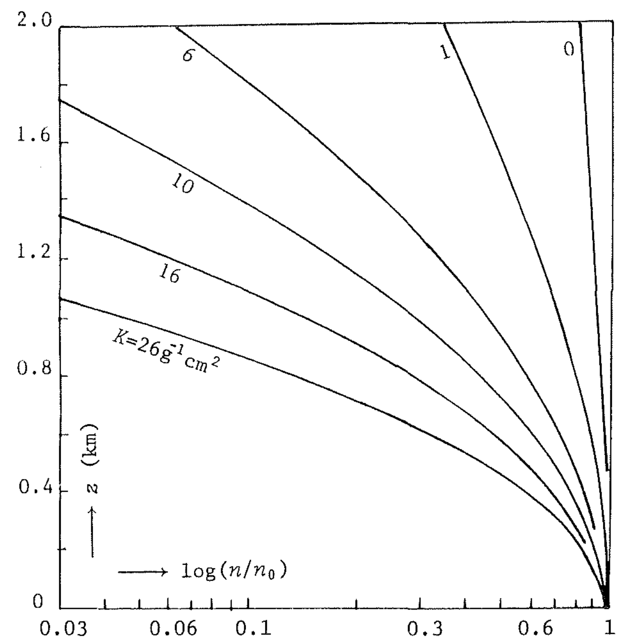

Fig. 2. Diagram showing log(n/n_0) vs. z according to computations by taking pressure 950mb and temperature 20°C at cloud base and giving various values to K (g^{-1} cm^2). Altering the values of K assigned to the curves, this diagram will be used for cases of various base temperatures and, as far as ordinary cumulii are concerned, disregarding base height.

Firstly, 950 mb in pressure is equal to about 500 m in height above sea level in the standard atmosphere. For most of cumulus clouds, however, the height of base may be disregarded with no significant error in computing w and v_0/v. Secondly, the coefficients a_2 and b_2 of Eq. (5.2) are almost constant in respect with base temperature and hence the term v_0/v in Eq. (4.4) is practically independent of base temperature. Thirdly, the ratio of W for any base temperature to that for 20°C are practically constant with respect to z as will be described in next section.

For these reasons the theoretical log $(n/n_0)-z$ diagram in Fig. 2 will be available for the comparison with the diagram of any observed cumulus clouds irrespectively of base height and temperature.

Now, the points of observed values reported by the workers mentioned in the first section will be plotted parallel to one of the curves or interpolated curves up to some heights respectively on the diagram in Fig. 2. In Fig. 3 the identifications are shown by shifting the theoretical curves along the horizontal axis. In case of Zaitsev's cumulus, the theory holds up to the level at which the liquid water content turns to decrease with height.

This evidently indicates the agreement of the present theory with the observations.

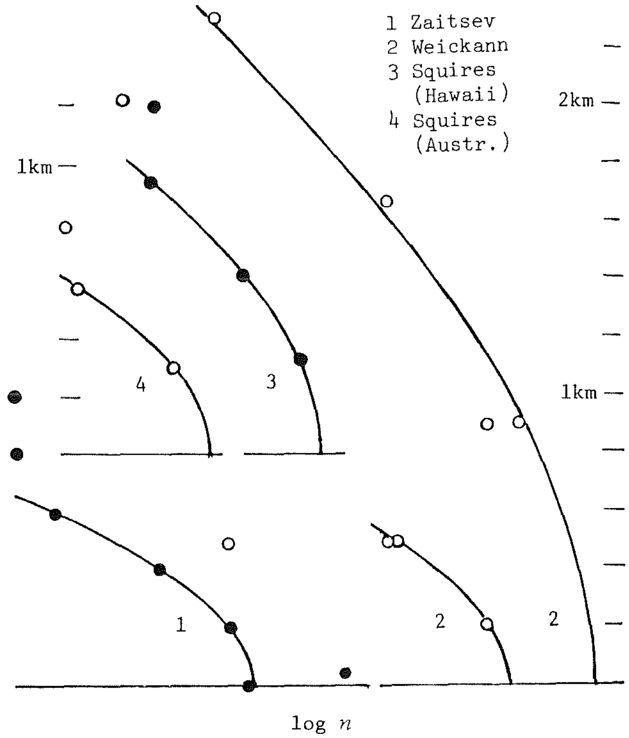

Fig. 3. Identifications

7. Determination of K and n_0

By means of the identification described in the above section numerical values of K can be determined for the clouds under consideration. For Example, $K_{20}=28$ g^{-1}cm^2 for Zaitsev's cumulus as seen from Fig. 3. K thus obtained is obviously nothing but an apparent or virtual one for this cumulus of base temperature 7.5°C and shall be specified by subindex 20. True K, however, can be easily known as follows.

From the numerical data presented in section 5 we have deduced the equation independent of

$$\frac{W_{20}}{W_T}=\frac{60+T}{38+2.1T} \qquad (7.1)$$

where W_T denotes W for base temperature T°C and accordingly W_{20} for 20°C. This equation holds with errors less than 5%. And hence, true K is given by

$$K=K_{20}\frac{W_{20}}{W_T}=K_{20}\frac{60+T}{38+2.1T} \qquad (7.2)$$

For example, K = 35 g^{-1} cm^2 for the above Zaitsev's cumulus.

Initial droplet number at the base of a cloud can be known on the log$n-z$ diagram, namely, it will be equal to n_0 of a shifted and identified theoretical curve. For example. we read n_0= 320 cm^{-3} for Zaitsev's cumulus while its observed number is 300 cm

Table 3.

Observer(s)	K (g^{-1}cm^2)	K (g^{-1}cm^2)	z_m (m)	n_0 (cm^{-3})	r_m (μm)	H_t (m)	H_0 (m)	T_0 (°C)	Cloud type
Zaitsev	28	35	600	300*	8	2950	1150	7.5	congestus
Weickmann	4	4	-	500	8	(upper layer)		20	fair-weather
and aufm Kampe	23	23	-	290	10	(lower layer)			
Squires	10	12	1000	86	15	2900	670	11	trade-wind Hawaii
Squires	20	25	600	600	6	3660	2200	7	mountain Australia

z_m maximum height above base the theory applies, n_0 droplet number estimated at base (* observed), r_m meandroplet radius at H_m, H_t cloud top height above sea level (?), H_0 base height, and T_0 base temperature.

K_{20}, K, n_0, and specifications of the cumulus clouds we have examined are given in Table 3. The temperatures of cloud base with an exception of Weickmann's 20°C have been estimated from the height above base of freezing level or temperature of cloud top on the assumption of wet adiabatic lapse-rate.

8. Discussions

Eq. (4.2) is rewritten as

$$C = 0.14 \rho L U K/E \tag{8.1}$$

Bowen (1950) has estimated an updraught velocity of 1 m sec^{-1} in an Australian mountain cumulus which is similar to Squires's. If put U = 1 m sec^{-1}, L = 1 cm, E = 1, and K = 25 g^{-1} cm^2 (ρ = 1 g cm^{-3}) into the above Eq. (8.1), we have C = 350 cm sec^{-1} and $C = 1.8 \times 10^3$ cm sec^{-1} per sec. These are extraordinarily large values for smallest eddies. A cumulus cloud as a whole might possess smaller velocity of updraught or smallest eddies might be regarded to be of less dimension.

Now, Smolukovski's theory stands on the assumption that the shearing flow is in a stationary laminar state and particles never deviate from stream lines in their movements. But a turbulence is an unstationary phenomenon, stream lines are in rapid and irregular fluctuations as if they are tangling and even small droplets will be forced into collisions not only by the shearing of flow but also by their irregular inertia motions deviating from stream lines. It must be quite different from the case of droplets falling in stil air. In forced collision its coefficient might be not small even for small droplets.

On such a collisions Takahashi (1965, 1974), the present author, has presented a theory. According to this theory, probability that a droplet of radius 10 μm will collide with droplets of the equal radius whose number is unity in cm is 4×10^{-6}sec in moderate turbulence. Smolukovski's theory gives 2×10^{-5} sec^{-1}, if put K = 25 $g^{-1}cm^2$ just obtained and L = 1 cm into (3.1). Consider the roughnesss of both estimations, the above probabilities may be of the same order of magnitude.

Entrainment will bring less increase rate of liquid water content with height and larger decrease rate of droplet number, resulting in positive contribution to K. Houghton and Cramer (1951) by calculation and Zaitsev and Weickmann-aufm Kampe by observation have shown its significant effect upon liquid water content of cumulus clouds. However, if entrainment were all that brings the decrease of droplet concentration such s actually observed, cumulus clouds would not remain so long to develop. Nevertheless, a large overestimation of K will owe partly to the entrainment.

After all, it may be stated that the equation (4.4) which has been derived from Smolukovski's collision theory on the assumption af adiabatic ascent of air will be practically satisfactory, but it is necessary to have a new definition of K taking into consideration microscopic irregular movements of small droplets in a turbulent air and in addition entrainment, mixing, and other macroscopic structure or state of a convective cloud.

REFERENCES

Bowen, E. G. (1950): The formation of rain by coalescence. Aust. J. Sci. Res., A, 13,193.

Houghton, H. G. and Cramer, H. E. (1951): A study of entrainment in convective currents. J. Meteor. 8, 95.

Smolukovski, M. von (1916): Drei Vortrage uber Diffusion, Brownsch Molekularbewegung und Koagulation von Kolloidteilchen. Phys. Zeitschr. 17, 585.

Squires, P. (1958): The microstructure and colloidal stability of warm clouds, Part I. Tellus 10, 256.

Takahashi, Y. (1965): Macro-, meso-, and microphysics of "saiu". Pro. Int. Conf. Cl. Phys., Tokyo-Sapporo, 1965, Suppl., 147.

__________ (1974): On the efficient size and concentration of spray drops for stimulating warm clouds. Proc. WMO/IAMAP Sci. Conf. Weather Modif., Tashkent, 1973, 70.

Weickmann, H. K. and aufm Kampe, J. (1953): Physical properties of cumulus clouds. J. Meteor. 10, 205.

Wigand, A. and Frankenberger, E. (1930): Uber Bestandigkeit und Koagulation von Nebel und Wolken. Phys. Zeitschr. 31, 204.

Zaitsev, V. A. (1950): see Weickmann and aufm Kampe (1953) and Mason, B. J.: The Physics of Clouds, 2nd ed., 1971.

1.3.4

ACCELERATED MOTION OF CLOUD AND PRECIPITATION DROPS

J. Doyne Sartor

National Center for Atmospheric Research*
Boulder, Colorado 80303

1. INTRODUCTION

The motions of cloud and precipitating drops undergo acceleration much of their lifetimes due to turbulence and organized buoyant acceleration of the cloud air, rapid changes in their charge, rapid ambient electric field changes, and during coalescence and accretion. Using an approximation for the drag coefficient for spheres due to Abraham (1970), the accelerated motions of cloud and raindrops are obtained analytically for Reynolds numbers from 0 to 5000. Previous work [Sartor and Abbott (1975)] gives solutions for the velocity and distance traveled as functions of time for Reynolds numbers from 0 to 5. The present work extends the velocity vs. time solution to include raindrops and approximately spherical ice particles with Reynolds numbers up to and including 5000.

Analytical solutions for the interaction of two drops and the resistance of the medium in which they are moving are frequently possible if steady state drag force can be assumed. A similar assumption is made in the numerical calculations of aerosol and cloud drop collision probabilities. The steady state resistance of the medium is used in equations of motion for the particles in which the accelerations of the particles are integrated to obtain their relative trajectories and thereby their collision probabilities. Almeida (1975) has recently completed a definitive work on the effect of atmospheric turbulence on the calculations of collision probabilities. Almeida finds an important increase in the collision probability of cloud droplets for weakly turbulent air streams with eddy dissipation rates of 1 and 10 $cm^2 sec^{-3}$.

2. ACCELERATIONS IN THE EQUATIONS OF MOTION FOR THE CALCULATION OF COLLISION PROBABILITIES

The equation of motion for each drop can be written as

$$(\sigma + \tfrac{1}{2}\rho) V \frac{d\vec{v}}{dt} = (\sigma - \rho) V \vec{g} - \vec{F} \qquad (1)$$

where: σ = density of the drops,
ρ = density of medium (air),
V = volume of the drops,
$\vec{v}$ = the velocity of the drops,
$\vec{g}$ = acceleration of gravity and
$\vec{F}$ = external forces and resistive forces due to the medium.

The left-hand side of the equation contains the net force on the drop and the force on the drops due to the net accelerations in the fluid, commonly referred to as the effect of the induced mass of fluid displaced by the drop. The first term on the right represents the gravitational and buoyancy forces. The second term on the right contains other external forces (e.g., electrical forces) and resistive viscous forces of the medium. For the case of steady state, the drag force on a single sphere sufficiently isolated from other objects and boundaries, the total resistive force on a freely falling drop is written,

$$F = 6\pi\eta r v \left[1 + f(Re)\right]$$

where: η = viscosity of the medium,
r = radius of drops,
v = velocity of drops and
Re = Reynolds number.

The function, $f(Re)$, is empirically determined for steady state but depends only on the Reynolds number, Re, and becomes the Stokes drag force, $6\pi\eta rv$, when Re is very small. This form of the steady state drag force is used frequently to compute the instantaneous velocity of accelerating and decelerating particles using experimentally determined drag coefficients. In our previous work, Sartor and Abbott (1975), we found, using the experimental results of LeClair, Hamielec and Pruppacher (1970), that for $Re \leq 5$, the error in the calculated velocity to be within experimental error. The velocity-time solution for accelerating drops reported in Sartor and Abbott (1975) for $0.01 \leq Re \leq 5$ is

$$v = \frac{(B-Q)\exp\left[\frac{Q}{m}(t-t_0)\right] - K(B+Q)}{2A\left\{K - \exp\left[\frac{Q}{m}(t-t_0)\right]\right\}}$$

where $A = 12(0.0916)\pi\rho r^2$
$B = 6\pi\eta r$
$C = -\frac{4}{3}\pi r^3(\sigma-\rho)g$
$m = \frac{4}{3}\pi r^3\sigma$

*The National Center for Atmospheric Research is sponsored by the National Science Foundation.

and where

$$Q = (B^2 - 4AC)^{1/2}$$

$$K = \frac{2AV_0 + B - Q}{2AV_0 + B + Q}$$

v_o = initial velocity at $t = t_o$.

For Re > 5, Abraham's approximation to the steady state drag is used as the drag coefficient in the equation of motion for accelerating drops.

3. AN ANALYTICAL SOLUTION FOR $5 \leq Re \leq 5000$

Using dimensional analysis and boundary layer theory, Abraham (1970) derives the expression

$$C_D = C_o \left(1 + \delta_o Re^{-1/2}\right)^2 \tag{2}$$

for the drag coefficient for spheres, where $C_o\delta_o^2 = 24$, the Reynolds number, Re, and $\delta_o = 9.06$. Abraham's expression for the drag coefficient is a reasonably good fit to the experimentally determined drag coefficients for uniform motion for Re < 5000. It fits remarkably well for 5 < Re < 5000 but is not as accurate as that of Le Clair et al. for $0.01 \leq Re \leq 5$.

Using Abraham's expressions for the drag coefficient, Eq. (2), and following Abraham (1970) we write

$$F = C_o \frac{\pi}{2} \rho v^2 (r + \delta)^2$$
$$= C_o \left(1 + \frac{\delta}{r}\right)^2 \left(\frac{\pi \rho r^2}{2} v^2\right) \tag{3}$$

where $\frac{\delta}{r} = \delta_o Re^{-1/2}$ and $Re \equiv \frac{2\rho v r}{\eta}$,

with η = viscosity. Abraham identifies δ with the boundary thickness at the waist of a sphere and C_o and δ_o with the Stokes drag coefficient ($C_o = 24\,Re^{-1}$) and "boundary layer," respectively, so that $C_o\delta_o^2 = 24$ giving $\delta_o = 9.06$. Equation (3) can be rewritten in the form

$$F = 12\pi \rho a^2 \left[\frac{v}{\delta_o} + \left(\frac{\eta v}{2\rho r}\right)^{1/2}\right]^2,$$

which when introduced into Eq. (1) gives

$$\frac{dv}{dt} = g - \left[\frac{3}{\delta_o}\left(\frac{\rho}{r\sigma}\right)^{1/2} v + \frac{3}{r}\left(\frac{\eta}{2\sigma}\right)^{1/2} v^{1/2}\right]^2$$

or by letting $u = v^{1/2}$, $2u\,du = dv$,

$$a = \frac{3}{\delta_o}\left(\frac{\rho}{r\sigma}\right)^{1/2} \qquad b = \frac{3}{r}\left(\frac{\eta}{2\sigma}\right)^{1/2},$$

$$\frac{2u\,du}{(au^2 + bu)^2 - g} = -dt \tag{4}$$

Equation (4) can be integrated by factoring and the method of partial fractions to give:

$$a \exp\left(-\frac{\sqrt{g}}{2a}(t - t_o)\right) = $$
$$= (2au + b + \beta)^{\left(1 + \frac{b}{\beta}\right)} \cdot$$
$$(2au + b - \beta)^{\left(1 - \frac{b}{\beta}\right)} \tag{5}$$

where $\beta = \sqrt{b^2 + 4a\sqrt{g}}$.

Equation (5) produces correct terminal velocities in the range 5 < Re < 5000. But it has not been possible so far to compare the computed results with experimental data. As Fuchs (1964) comments, the accelerated rectilinear motion at high Reynolds number such as encountered in the mechanics of aerosols (up to about Re = 1000) has not been studied theoretically, and experimental data on this problem are insufficient and contradictory. This seems to be the situation at the present time also.

Another problem appears when the solution is applied to drops larger than a few hundred micrometers radius, when they become subject to forces that significantly deform them from the spherical. The solution, however, would still apply in the larger Reynolds number range for rigid spheres.

The question of whether this type of solution for accelerating cloud and precipitation should be pursued farther will depend on the importance that future theoretical and experimental studies in cloud physics find for the role of turbulence and other accelerations in the collision-coalescence growth of cloud droplets and other accreting cloud particles.

4. REFERENCES

Abraham, F. F., 1970: Functional dependence of drag coefficient of a sphere on Reynolds number. The Physics of Fluids, 13(8), 2194-2195.

Almeida, F. C. de (1975): On the effects of turbulent fluid motion in the collisional growth of aerosol particles, Report 75-2, Department of Meteorology, Univ. of Wisconsin, Madison, Wisconsin, 185 pp.

Fuchs, N. A. (1964): The Mechanics of Aerosols, The Pergamon Press, N.Y., 408 pp.

LeClair, B. A., A. Hamielec and H. R. Pruppacher, (1970): A numerical study of the drag on a sphere at low and intermediate Reynolds numbers. J. Atmos. Sci., 27, 308-315.

Sartor, J. D. and C. E. Abbott, Jr. (1975): Prediction and measurement of the accelerated motion of water drops in air, J. Appl. Meteor., 14(2), 232-239.

2.1.1

ICE NUCLEUS MEASUREMENTS - WORKSHOP SUMMARY AND CURRENT STATUS

Gabor Vali

University of Wyoming
Laramie, Wyoming 82071

The Third International Workshop on Ice Nucleus Measurements was held in Laramie, Wyoming, in June 1975. The motivation for holding this workshop, as for the two earlier workshops held in 1967 and 1970, was to arrive at a clearer picture for the validity of nucleus measurements and to delineate problem areas in need of improvement. The earlier workshops encompassed condensation as well as ice nucleus measurements. The Third Workshop involved only ice nucleus measurements since it was felt that that area was in the greatest need of clarification and improvement. Indeed, the results of the Second Workshop (Bigg, 1971) showed an alarming degree of disagreement among the various ice nucleus measuring instruments, and progress afterwards was also slow.

The Second Workshop's results did show indications that vapor supersaturation plays an emphatic role in determining the numbers of activated ice nuclei. Subsequently, more attention was paid to the control of this parameter in the various instruments. The large isothermal chamber at the Colorado State University was modified (Garvey, 1975) to precool the cloud prior to reaching the zone where the nuclei are injected. The membrane filter technique, while offering the best hope for accurate control (to $\pm$ 1%, in principal) of the supersaturation, was found to be limited in actual accuracy because of vapor depletion problems which result from the close proximity of aerosol particles on the filter surfaces. A filter processing device operating at reduced air pressures was constructed by H. Georgii and his colleagues at the University of Frankfurt with the expectation that more rapid diffusive transport at low air pressures would help to curcumvent the vapor depletion problem.

Instruments which could respond to contact nuclei at the Second Workshop were of the cloud chamber type, and in these it is difficult to isolate the major operating processes. A device, specifically designed to measure contact nuclei was built following the Second Workshop by Vali (1971).

It was with such backgrounds that the Third Workshop was convened. Represented at this workshop were the instrument types referred to above, the settling cloud chamber by T. Ohtake, the "puff" chamber of H. Gerber and two centrifuge devices for determining the size-dependence of ice nuclei. A complete list of the participants is given in Table 1.

An analytical approach was taken at the workshop, i.e. the instruments were probed extensively to delineate their operating characteristics and sensitivities. Measurements were made at as wide a range of temperatures and supersaturations as the devices permitted. The relative concentration of ice nuclei to condensation nuclei was varied. Procedures were manipulated, instrument dimensions altered, time scales were varied. Tests were conducted with different types of nuclei: outdoor air, silver iodide and an organic nucleant.

It is not possible here to present in detail the results of the workshop. A preliminary analysis of the results has already been published (Vali, 1975). A report containing contributions by workshop participants is also available (Vali, 1976). The main findings can be summarized in the following list:

1. The activity of nuclei in thermal-gradient diffusion chambers (A in Table 1) depends on supersaturation with respect to ice (S_i). For silver iodide there is a factor of 10^1 to 30 increase in the numbers of active nuclei for each 5% of S_i. For outdoor air a factor of 6 to 10 increase was found. The low-pressure diffusion chamber showed essentially the same effect, but with a clear difference in detail.

2. Increasing the proportion of CCN to ice nuclei created dramatic increases in the numbers of activated ice nuclei in the diffusion chambers (A and B) and in the cloud chambers (E and G).

3. A large difference has been found between the numbers of nuclei activated on different filter substrates. The lowest counts were obtained with Millipore Type HA filters and the highest counts with Sartorius Type 133 filters. Sartorius Type 144 being intermediate. All of these filters have 0.45 μm nominal pore sizes.

4. Equivalent results were obtained with aerosols deposited onto solid surfaces or aerosols caught on filters.

TABLE 1. WORKSHOP PARTICIPANTS

Name	Affiliation	Equipment
H. Weickmann	President, Commission of Cloud Physics (IAMAP)	
T. Ohtake	University of Alaska	E
G. G. Lala, J. E. Jiusto, J. Zamurs	State University of New York at Albany	A
K. Young, J. Bolkcom	University of Arizona	B
W. D. King, S. C. Mossop	CSIRO, Australia	
D. Garvey	Colorado State University	A*, G
G. Gravenhorst, D. Meyer	University of Frankfurt	B
A. Gagin	Hebrew University of Jerusalem	
T. R. Mee	Mee Industries	G
C. A. Knight	National Center for Atmospheric Research	
G. Langer	National Center for Atmospheric Research	C*
H. Gerber	Naval Research Laboratory	D
P. A. Allee	NOAA	A*
W. A. Cooper, D. Rogers, G. Vali	University of Wyoming	A, F

*Equipment not present at Workshop - Operated at own laboratory with samples taken during Workshop

Equipment Types:

A: Thermal-gradient diffusion chambers for processing of membrane filters or metal foils.
B: Low-pressure diffusion chambers for filters or foils.
C: Continuous-flow humidification of filters.
D: "Puff" humidification of aerosol sized by Götz centrifuge.
E: Settling cloud chamber (SCC).
F: Drop freezing by contact (DFC).
G: Continuous-flow cloud chamber, Mee Model 140.

5. Reducing the separation between the plates of the thermal-gradient diffusion chambers (A) resulted in increases in nucleus counts.

6. The different methods of sealing filters were found to be equivalent.

7. The dependence of measured ice nucleus concentrations on the volume of air sampled on filters was confirmed for the diffusion chamber instruments (A and B).

8. The rate of humidification of filter samples was shown to influence the results in the low pressure diffusion chambers (B). A rapid approach to the desired humidity results in higher nucleus counts than a slow approach.

9. A fair degree of agreement was found among the different filter processing devices (A and B) for all types of aerosols. The maximum scatter in measured concentrations amounted to one order of magnitude.

10. The Settling Cloud Chamber and DFC instrument (E and F) gave comparable results for all types of nuclei, provided copious numbers of CCN were added to the Settling Cloud Chamber.

11a. The type A, B, D, E and F instruments (see Table 1) gave comparable results for outdoor air, the worst scatter among instruments being about a factor of 20.

b. With silver iodide nuclei there was about a four order of magnitude difference between the concentrations detected by the filter processing instruments (A and B) on the one hand, and the settling cloud chamber, DFC, and "puff" instruments (E, F and D) on the other. The Mee continuous flow cloud chamber (G) indicated intermediate concentrations.

c. Detection of nuclei was accomplished at the following warmest temperatures: diffusion chambers (A) -12C; puff chamber (D) -10C; Mee counter (G) -10C; settling cloud chamber (E) -9C; DEF instrument (F) -6C.

These results have a number of important implications concerning the processes of activation in the instruments and concerning the nature of ice nuclei. In the following, some of these points are discussed, not with reference to specific instruments but rather emphasizing where ice nucleus measurements stand with respect to providing the answers needed for the resolution of cloud physical problems.

It now appears that measurements of natural nucleus concentrations are possible with fair agreement among different techniques of measurement for air which has relatively low concentration of aerosols, such as is normally present in Laramie, Wyoming. Judgement has to be reserved on whether the same would hold for air of higher aerosol content or for heavily polluted urban atmosphere. It has been clearly shown by the workshop results that special problems exist in the measurement of the activity of silver iodide nuclei; large discrepancies among the different instruments were found and could not be resolved. This fact clearly points out the dependence of how nucleation measurements are to be interpreted on the nature of the test aerosols. Improved understanding of these dependences remains the pivotal question in ice nucleus measurements.

Could it be said that, at least for the simpler situation - natural air of moderate aerosol content, nucleus measurements can predict the concentrations of ice crystals in clouds: Even if secondary ice production mechanisms (other than heterogeneous nucleation) are set aside for the moment, the answer seems to be still in the negative. First of all, for many cases the comparison cannot even be made, since no measurement techniques are currently available for detecting nucleus concentration much below 0.1 ℓ^{-1}, whereas such ice crystal concentrations and lower frequently occur in clouds, predominately, of course, at the warmer temperatures (about -10C). Second, for colder cloud temperatures, where the nucleation measurements can be performed, the measurements still lack a great deal of realism in matching natural clouds. The deviation from real conditions are in slightly different directions, and to differing degrees, in the various instruments.

The last point deserves further elaboration. The fact that for natural nuclei some degree of agreement has been found among instruments of varied operating principles must be indicative of some measure of insensitivity of the nuclei to the variables in question. Taking a factor of ten in concentration as the degree of confidence in the measurements, it can be said that, in the instruments used at the workshop, the following list of variables caused less changes (in the temperature range -10 to -20C):

a. Supersaturation - within about $\pm 2\%$
b. Droplet sizes - from few micrometers (settling cloud chamber) to a few millimeters (drop freezing counter).
c. Time scale of humidification - from essentially instantaneous to about 20 sec.
d. Total air pressure - from few millibars to 800 mb (and most likely to 100 mb).
e. Aerosol dispersion - from natural concentrations to about 10^6 times greater compaction (on the membrane filter).

These variations represent, somewhat crudely, the combined ranges and accuracies of the measurement conditions.

If one is unwilling to accept the proposition that natural ice nuclei lack sensitivity to changes within these ranges, then the possibility has to be considered that the agreement among measurement devices was the result of compensating errors. This is an unlikely situation but one that cannot be dismissed lightly, especially in view of the disagreements in the measurements for silver iodide nuclei. Resolution of this question is crucial to further advances in ice nucleus measurements, and actually involves the answering of a host of subsidiary questions.

The capabilities of current instruments may be contrasted to what can be conceived as the requirements for the "ultimate" device for measurements of natural ice nuclei. Such a list would include, among others, the following items:

1. Capability to measure nucleus concentrations at temperatures up to -5C, i.e. concentrations of about 10^{-3} to 10^{-2} ℓ^{-1},
2. capability of resolving spatial variations on cloud scales, i.e. few hundred meters and larger,
3. size and weight compatible with airborne operation,
4. clearly enough defined processes of activation to allow extrapolation of the results to longer time scale, different cloud droplet spectra, etc.

These are very difficult requirements to meet. Starting from the perspective provided by the capabilities of current instruments, it is fair to predict that several years to perhaps a decade of development will be needed.

What avenues look the most promising? Individual opinions will vary widely on this question. In my view, the membrane filter technique is not a good prospect for further development because of the intractability of the vapor depletion problem (that problem getting more severe the lower is the ice nucleus concentration we desire to detect). It seems that cloud chamber type devices will remain impractical for the detection of low nucleus concentrations; also, the definition of processes in such chambers is not likely to be possible. Outside of these approaches, what is left is the hope that devices will be built which break down the overall task into manageable parts.

Turning to the measurement of activity for artificial nuclei, we find that in some respects the situation is easier, in others it is more difficult than for natural nuclei. Nucleus concentrations being usually orders of magnitude higher, the sampling rate requirements are much less severe and therefore measurements at warmer temperatures are possible even with current instruments. On the other hand, the sensitivity of the nuclei to various parameters can be much greater than for natural nuclei. The great influence of supersaturation on the activity of silver iodide is a case in point. The Third Workshop produced clear evidence on this factor. The current situation for the measurement of artificial ice nuclei is not very promising. While the workshop results did help to clarify many problems, a great deal of further study of current measurement techniques will undoubtedly be necessary to learn just what the measurements mean and the variables whose accurate control would insure clear results. Considerable promise is held by the large cloud simulation chambers for at least the laboratory measurement of artificial ice nuclei.

The ultimate question in connection with ice nucleus measurements is how will we ever know whether the measurements are right or not. There is no absolute measurement against which other measurements could be compared. Two approaches involving comparisons with real clouds appear possible:

- comparison of prediction based on models and using measured inputs for nuclei active in the different modes,
- establishment of budgets of ice nuclei for given cloud situations.

The first approach requires the acquisition of measurements of nuclei in air in which cloud formation is imminent, together with observations of the ice content of the resulting cloud. These observations then need to be reconciled with a model which accounts for the nucleation processes in terms of temperature and supersaturation histories together with auxiliary factors such as evolution of the cloud droplet spectrum, aerosol to hydrometeor transfer rates, possibly the chemical composition of the droplets, and others. The second approach is essentially an elaboration of the first but one that allows the circle to be closed, and in its less than complete form permits check if a particular measurement technique is responding to the cloud-active nuclei or not. Considering this latter aspect, suppose that a measurement were perfomred in air feeding into a cold cloud in which ice formation can be shown to be taking place, and that an identical measurement of nuclei were to be made inside the cloud by sampling the air space between hydrometeors. If the type of nuclei detected in the measurement contribute to the population of ice crystals in the cloud, there should be a reduction in the measured concentrations between pre-cloud and cloud environment. This sort of test, while difficult to perform would be extremely useful in eliminating from consideration measurement techniques whih activate ice nuclei by unrealistic conditions in the instrument. When carried to full potential the nucleus measurements in the precloud and cloud environment should give the same quantitative difference as can be predicted by modeling, and confirmed by observation, to be the number of ice crystals nucleated. Yet further checks on the system are possible by also considering the structure and sizes of the ice crystals. These comparisons call for clouds of fairly simple airflow structure in which the two sets of measurements can be performed at points not too widely separated from one another. It is to be hoped that experiments of this nature will be performed, and together with laboratory evaluations will eventually lead to techniques for reliable measurement of atmospheric ice nucleus concentrations.

This discussion extended a fair distance from the products of the Third Workshop: the positive results of that workshop offered the encouragement to engage in such a discussion. The problem of ice nucleus measurements cannot be said to be solved, but the course of research ahead seems to be clearer now that it was prior to the workshop.

ACKNOWLEDGEMENTS

The results of the workshop are due to the sincere efforts of all of the participants. The advances that will accrue from the workshop will have to be credited to them. Organization of the workshop was made possible by support from the Meteorology Program, Atmospheric Sciences Section, National Science Foundation, through Grant DES575-13785.

REFERENCES

Bigg, E. K. 1971: Report on the ice nucleus workshop Fort Collins, 1970. In the: Report on Workshop Goals, Program, Instruments, Observations, and Preliminary Analyses.

Garvey, D. M., 1975: Testing of cloud seeding materials at the cloud simulation and aerosol laboratory. Jour. Appl. Meteor., 14, 883-890.

Vali, G., 1971: A three-component system for measurements of ice nucleus concentrations. Proc. Inter. Conf. Weather Modification, Canberra, Australia, 36-37.

______, 1974: Workshop Summary. Bull. Amer. Meteor. Soc., 56, 1180-1184.

______, 1976: (Editor) The Third International Workshop on Ice Nucleus Measurements. Report.

ICE NUCLEATION BY AEROSOL PARTICLES

N. Fukuta and R.C. Schaller

Denver Research Institute, University of Denver, Colorado 80210

1. INTRODUCTION

Ice nuclei occupy a small fraction of the population of atmospheric particles in most circumstances, and occur in small sizes. They are freely suspended in air and nucleate ice under the influence of different temperatures and supersaturations. There have been three main kinds of experimental methods used in heterogeneous ice nucleation studies: the cloud chamber method, in which a supercooled cloud is utilized; the filter or precipitation method, in which ice nuclei are captured and tested on a filter surface or in droplets on a substrate surface; and the large crystal method, in which ice nucleation on a macroscopic surface of ice nuclei compound is examined. Cloud chamber methods fail to reproduce a clearly defined and stably sustained supersaturation for nucleation. Filter methods suffer from the substrate effect and the droplet method does not determine the probability of ice nuclei to be found in droplets in the atmosphere. Techniques using large surfaces of crystals (often single crystals) are unable to incorporate the size effect. Although these methods have their own merits, none can provide a well-defined condition for ice nucleation without inherent shortcomings. It appears that the current contradictory results of ice nucleation studies have arisen from these inherent shortcomings of the experimental methods used. Therefore, it is clear that the key to the problem of heterogeneous ice nucleation is to devise a new method which can provide clearly defined environmental and ice nuclei surface conditions for ice nucleation, avoiding previous difficulties, and then to proceed with the gathering of data rather than trying to increase knowledge by continuing current methods with their shortcomings.

With regard to the theory, the thermodynamical treatment of ice nucleation by Fletcher (1958, 1962) has met with some limited success. The theory has received refinements from time to time (Fletcher, 1969; Fukuta, 1966; Evans and Lane, 1972) but all these treatments hold only under simplified or ideal conditions. Furthermore, largely due to confusion among experimental data, theory and experiments do not appreciably substantiate one another.

Against this background, the present study has been carried out with three main purposes: first, to build and operate a new ice thermal diffusion chamber which is capable of precisely controlling a range of supersaturations under steady-state conditions at a given temperature for an ice nucleant smoke (no substrate effect); second, to experimentally identify the mechanisms of ice nucleation under the defined environmental conditions of the experiment; and, third, to develop a theory which could describe the obtained quantitative data. The last task involves development of analytic and empirical formulas for various ice nucleation mechanisms which are usable for related atmospheric phenomena. We shall refer to the theoretical development only briefly here due to space limitations.

2. EXPERIMENTAL

2.1 The New Wedge-Shaped Ice Thermal Diffusion Chamber

In order to avoid inherent difficulties associated with current methods of ice nucleation study, nucleation must be carried out under closely simulated atmospheric conditions, i.e., with aerosol particles freely suspended in an environment of controlled supersaturation and supercooling. The thermal diffusion chamber method operated below $0^{o}C$ provides the condition for this study. However, the commonly used parallel plate thermal diffusion chamber permits only one combination of temperature and supersaturation. Therefore, we advanced the method with a new wedge-shaped ice thermal diffusion chamber, in which we have a range of supersaturations at the set temperature. Figure 1 illustrates the structure of this chamber. The top and bottom walls of the wedge chamber are made of 3.1 mm thick copper, with filter paper on their inside surfaces. The filter papers are wetted and frozen. Heating of the upper edge and cooling of the lower edge of the wedge chamber are provided by a thermoelectric unit, so that heat flows steadily along the copper plates from the upper edge to the lower, as well as through the wedge shaped chamber space in the vertical direction. As a result, a steady-state vapor field develops in the space, creating a range of supersaturations along the median plane of the chamber where temperature is constant. Since the vapor pressure of ice is only a function of temperature, one can accurately estimate the supersaturation from the conditions of steady state flow of heat and vapor (see Figure 2). This estimation can be checked and calibrated from the position of the leading edge of the fog formed in the absence of ice nuclei. This can be considered as a built-in standardization point for supersaturation.

Although this wedge chamber can be operated in a number of ways, the standard method of operation is to cool the entire chamber isothermally, inject dry aerosol sample, and then increase the temperature gradient after turbulence has died down. Ice crystals nucleated are illuminated with a microscope lamp or a laser beam, and visually counted in a known volume of the light beam. If nucleation occurs in the zone super-

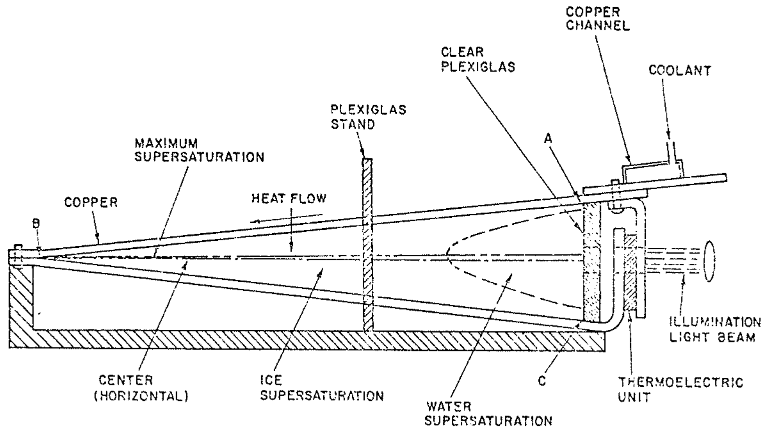

Fig. 1. Schematic description of the Wedge-Shaped Ice Thermal Diffusion Chamber. The inside dimensions of the chamber are 18 cm x 18 cm and the maximum height is 4.5 cm.

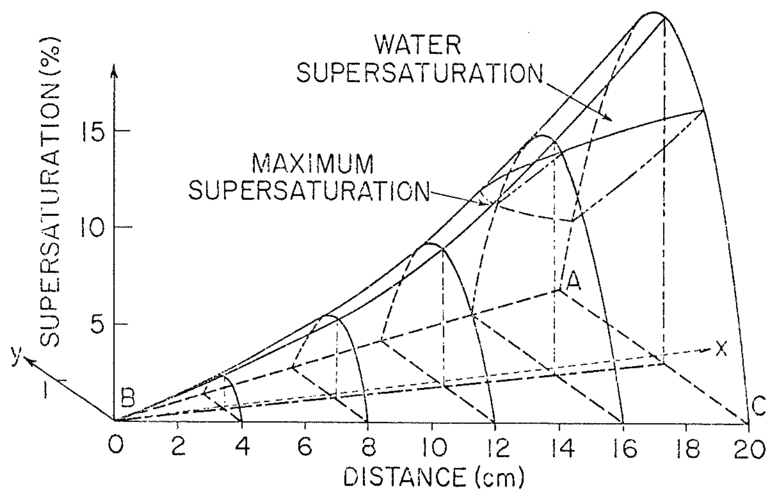

Fig. 2. Profile of supersaturation with respect to ice in the wedge-shaped thermal diffusion chamber. A, B, and C are, respectively, the highest, the apex and the lowest positions of the chamber and their temperatures are -3, -10 and -17°C (cf. Fig. 1).

saturated with respect to ice, but undersaturated with respect to water, deposition must be the mechanism of ice nucleation. If ice is nucleated in the region supersaturated with respect to water, the mechanism observed can be either contact, condensation-freezing, or deposition nucleation.

2.2 Sample Smoke Preparation

Two kinds of air were used for sample preparation: room air and cloud condensation nuclei (CCN) - free air. The samples of AgI, 1,5 - dihydroxynaphthalene (DN), PbI_2 and phloroglucinol (PG) were prepared by heating a platinum wire coated with these chemicals. Metaldehyde (MA) smoke was prepared by placing a small amount of powder in the end of a coil of 3.2 mm ID copper tubing wound around a soldering iron, and then blowing the powder through the coil using a syringe. For preparation of non-volatile samples such as kaolinite (KA) and local soil (LS), the powder was placed in a flask containing dry nitrogen and shaken, and a syringe was used to collect sample aerosol after allowing large particles to settle.

2.3 Contact Nucleation Study

Selecting a zone below water saturation where the temperature is high enough so that deposition nucleation is not possible but is low enough so that ice can form if the liquid phase exists, NH_4Cl smoke is injected in the chamber. The hygroscopic smoke particles become small solution droplets. A dry nuclei sample is then introduced. In this zone, condensation-freezing and deposition nucleation cannot take place. Thus, if ice forms, contact freezing nucleation must be the mechanism, since it is the only possible mechanism under such conditions.

3. RESULTS AND DISCUSSION

3.1 Condensation-Freezing and Deposition Nucleations

Figure 3 shows the experimental results for Ag I in comparison with prior works. The data points represent ice nucleation on 1.3% of the smoke particles in one minute. It is apparent in the figure that there are two different zones of ice nucleation. Ice nucleation which occurs above water saturation at relatively high temperatures always followed water condensation or fog formation. Therefore, the nucleation mechanism is condensation-freezing. Nucleation that takes place at lower temperatures below the water saturation line must be deposition since this is the only possible mechanism here. Previous works using precipitated aerosol (Isono et al, 1966) and large single crystals (Bryant et al, 1959) reported condensation-freezing nucleation limit down to water saturation line. However, accurate control of supersaturation around freely suspending aerosol particles in the present chamber led us to discover the small but significant water-supersaturations required for condensation-freezing to occur. The necessary water-supersaturation decreases as temperature lowers. Of course, as the water-supersaturation approaches zero, condensation-freezing nucleation ceases completely. Thus, condensation-freezing is highly water-supersaturation dependent, and the present experimental results clearly explain why previous studies without water supersaturation control produced extremely scattered data in ice nucleation. It is meaningless to discuss ice nucleation in terms of only the supersaturation or the temperature; both are necessary.

Another important feature discovered is the upward curvature of the deposition nucleation threshold line as temperature increases

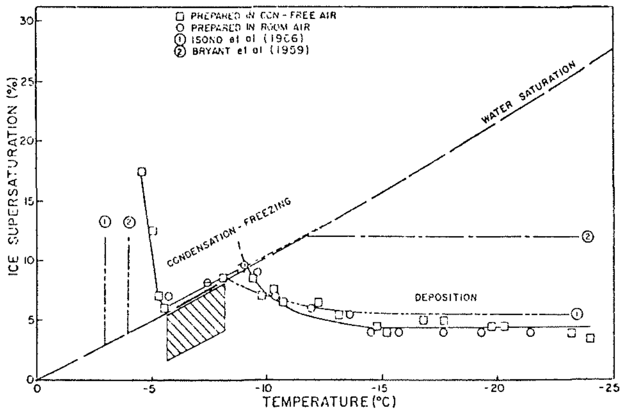

Fig. 3. Threshold curves for ice nucleation by silver iodide. Hatched zone is where contact nucleation was observed.

just below water saturation. Isono et al (1966) also observed this effect but offered no explanation for it. This behavior cannot be explained by the classical nucleation theory.

Figures 4, 5 and 6 show contour lines for three different nucleation rates for AgI , MA and DN, respectively.

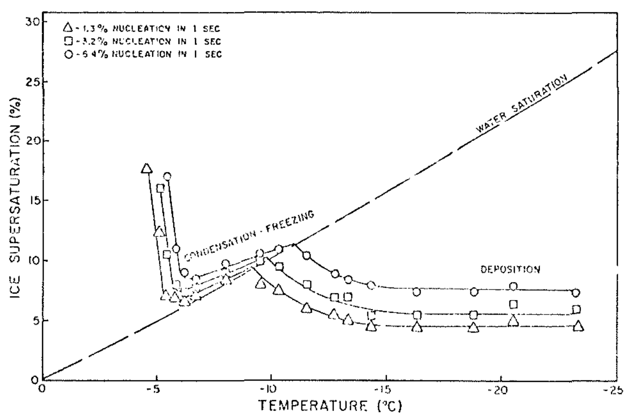

Fig. 4. Ice nucleation rate contour curves for AgI smoke.

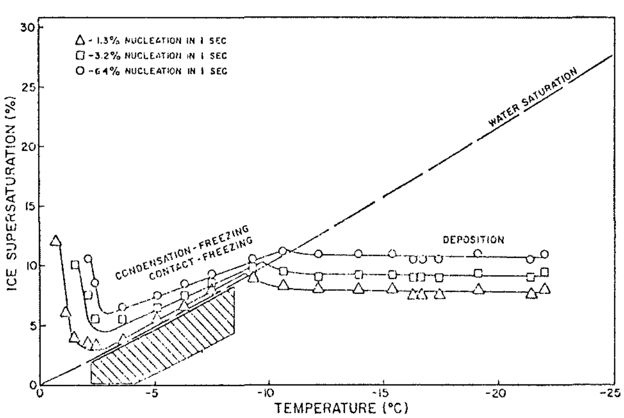

Fig. 5. Ice nucleation rate contour curves for metaldehyde smoke.

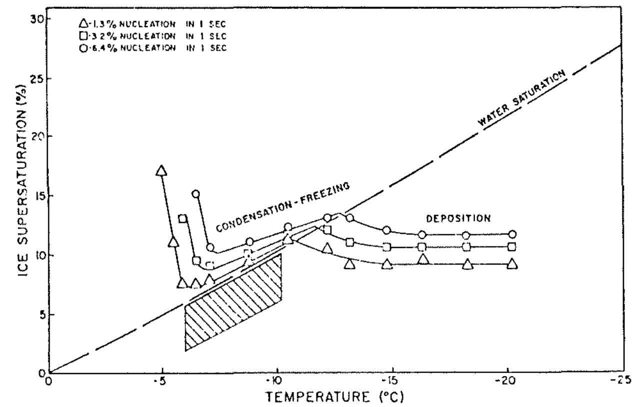

Fig. 6. Ice nucleation rate contour curves for 1,5 - dihydroxynaphthalene smoke.

The contour lines for MA above water saturation include both condensation-freezing and contact nucleation, since MA particles are electric dipoles and coagulate rapidly with fog droplets (Fukuta, 1963).

3.2 Contact Nucleation

When a dry aerosol of ice nucleant is introduced in the wedge chamber under normal operating conditions, a large number of ice crystals appear in a short time. After they fall out, ice nucleation almost ceases. However, a small number of ice crystals keeps appearing, and they appear to be nucleating through the contact-freezing mechanism. The contact nucleation effect is particularly strong with MA. Figure 7 shows the ice nucleation behavior of MA smoke. After

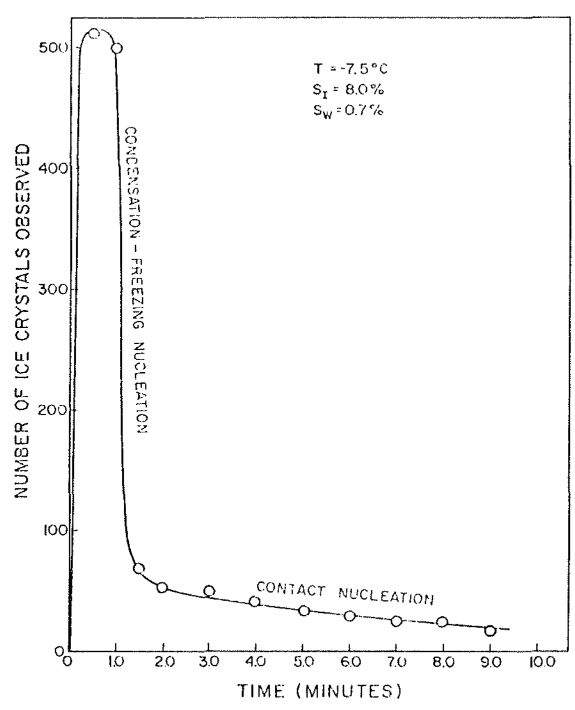

Fig. 7. Condensation-freezing and contact nucleation for metaldehyde smoke.

the initial peak of condensation-freezing nucleation, the smoke particles continue to nucleate ice by contact.

In order to clearly isolate contact nucleation from other mechanisms, we selected zones where neither condensation-freezing nor deposition nucleation takes place (hatched zones in Figs. 3, 5 and 6), and carried out nucleation studies over prolonged periods of time with NH_4Cl solution droplets in the chamber. Figure 8 shows the results.

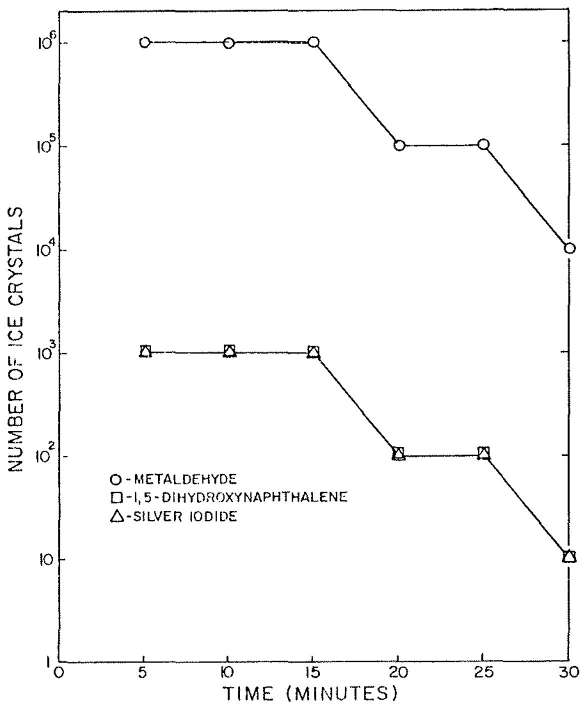

Fig. 8. The time variation of the number of ice crystals formed in five-minute intervals at -6.5°C.

As can be seen in the figure, a nearly constant ice nucleation rate persisted for 20 minutes. It should be noted that MA smoke at the same number concentration nucleated about 1000 times more than the DN and AgI smokes. No contact nucleation was observed with PG for temperatures between -6.0 and -8.9°C and a maximum supersaturation in the chamber of -0.1% with respect to water. This is probably due to the solubility of PG in water.

3.3 Comparison of Nucleation Behaviors Among Different Smokes

Figure 9 is a composite of the nucleation threshold curves of all seven samples studied. A remarkable feature shown in this figure is that regardless of whether it is organic or inorganic, natural or artificial, every nucleant shows two zones of ice nucleation, corresponding to condensation-freezing and deposition nucleation. Both the condensation-freezing and deposition curves show the necessity of higher supersaturations as the temperature increases. On the condensation-freezing threshold curves, the needed supersaturation with respect to water decreases and approaches the water saturation

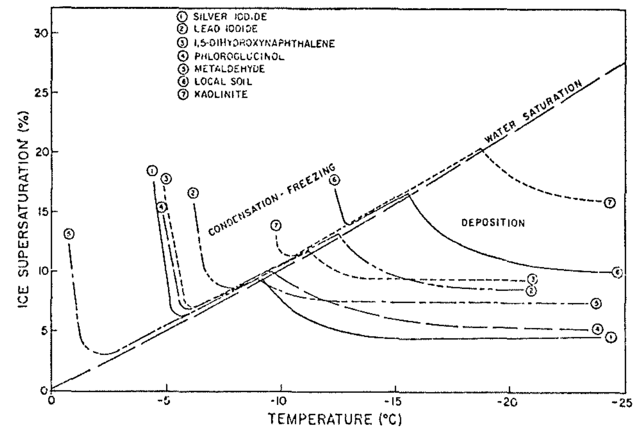

Fig. 9. Fundamental behavior of ice nucleants. The threshold curves represent 1.3% of nucleation in the smoke particles in one minute.

line as the temperature is lowered. The deposition curves show an initial decrease in ice supersaturation with decreasing temperature, but they level off to a constant value of the supersaturation with respect to ice. As will be seen later, these curves of condensation-freezing and deposition nucleation lie on a very steep "mountain" in the nucleation rate surface, where a slight change in ice supersaturation results in a great change in the nucleation rate.

4. NUCLEATION THEORY

With this accurate information about heterogeneous ice nucleation obtained under clearly identified conditions of supersaturation and supercooling, it is possible to test existing theories of ice nucleation. However, since such an analysis requires a lengthy treatment (Schaller, 1975), and will be published elsewhere (Fukuta and Schaller, to be published), we shall briefly discuss only the main conclusions here.

4.1 Condensation-Freezing Nucleation

Separate thermodynamic theories of condensation or freezing exist but in order to describe ice nucleation due to condensation followed by freezing, a new physical concept is necessary. Our physical model assumes flickering clusters of liquid on an ice nucleus particle, in which ice embryos try to form. In this system, ice embryo formation by fluctuations is difficult due to the capillary pressure of the curved liquid cluster surface (Fukuta, 1966). However, when condensation nucleation takes place on the surface, the capillary pressure restricting the ice embryo formation, or freezing nucleation, is removed and the system moves toward freezing nucleation if other conditions permit it to do so. Then, the rate of condensation-freezing J_{CF} can be expressed as the product of the condensation nucleation rate J_C, and the freezing nucleation rate J_F, as

$$J_{CF} = KJ_CJ_F,$$

where K is a constant. This expression describes the experimental data well.

4.2 Deposition Nucleation

The classical thermodynamic nucleation theory of deposition states that the nucleation rate is virtually a function of supersaturation with respect to ice and does not depend on the temperature as long as the ice phase formation is thermodynamically possible. However, as can be seen in the experimental data, the nucleation rate shows temperature dependency in the vicinity of water saturation. This suggests a change in the nucleation mechanism, perhaps due to accumulating adsorbed layer (Schaller, 1965). We shall not discuss the possible mechanism here. Instead, we devised an empirical form to describe the behavior. The empirical formula one can use to describe the ice nucleation behavior below water saturation is

$$S_I = S_{IO} + \frac{A}{T-T_0} \qquad (2)$$

where S_I is the ice supersaturation, T is the temperature, S_{IO}, A, and T_0 are constants to be determined from experimental data.

4.3 Heterogeneous Ice Nucleation by Aerosol Particles

Theoretical analysis of present experimental data permits us to reconstruct the general nucleation behavior of aerosol particles. Figure 10 reveals two "mountains of nucleation rate" for AgI aerosol particles on the supersaturation-temperature plane.

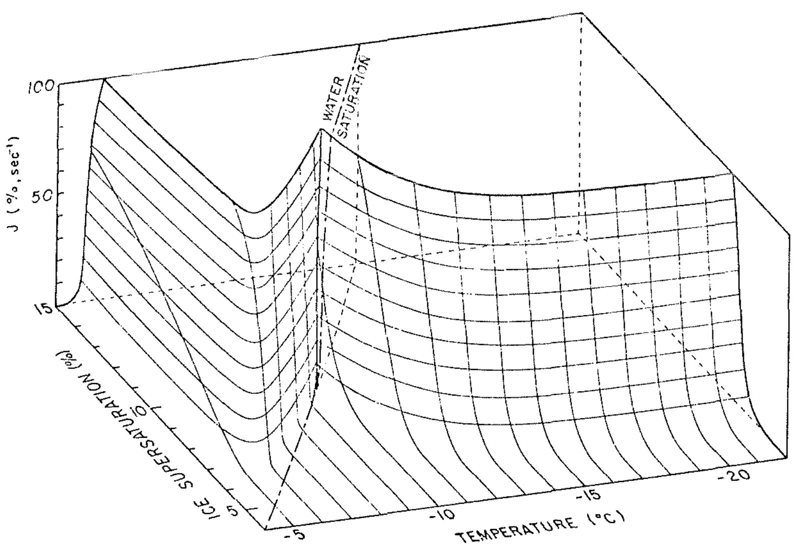

Fig. 10. Three-dimensional plot of nucleation rate on ice supersaturation-temperature plane for AgI smoke particles.

The plateau is that level where all available particles are nucleated. Note that above water saturation at relatively high temperatures, a slight increase in supersaturation greatly increases the nucleation rate. The strong supersaturation dependency of the condensation-freezing nucleation rate in this temperature zone, the water saturated condition providing <u>zero</u> nucleation rate, probably indicates the <u>very</u> origin of serious errors and confusions in previous ice nuclei counting methods.

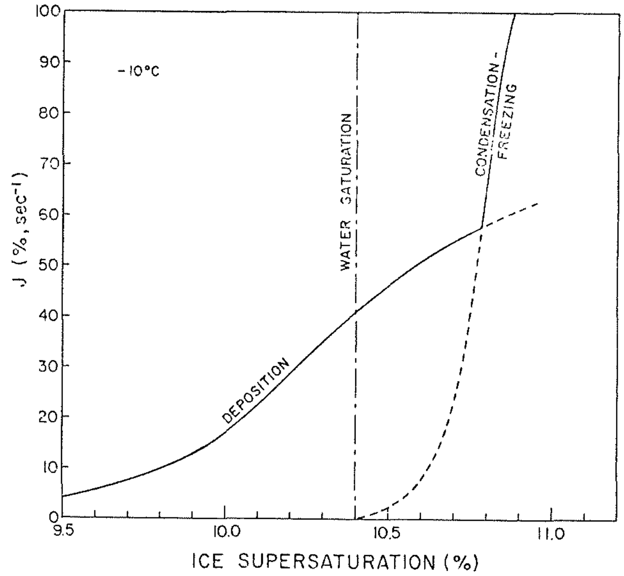

Fig. 11. The nucleation rate of AgI smoke particles at -10°C as a function of ice-supersaturation (cf. Fig. 10).

Figure 11 is a cross-sectional view of Figure 10 at -10°C. It clearly indicates the change in nucleation rate as one passes into a region of water supersaturation from below. In our atmosphere, this corresponds to the change in slope of the nucleation rate curve and the increase in the rate as one enters into a supercooled cap cloud following the air stream. This has been observed indeed in the real atmosphere by scientists of the University of Wyoming. The Wyoming field observation had remained unexplained until we carried out the present work since no previous laboratory works have reproduced this effect due to the difficulty of controlling the supersaturation or substrate effect.

5. SUMMARY AND CONCLUSIONS

The main conclusions in this study are as follows:

(1) The feasibility and accuracy of the new wedge-shaped ice thermal diffusion chamber in an ice nucleation study have been demonstrated.

(2) The importance of supersaturation control without substrate in heterogeneous ice nucleation studies has been shown.

(3) The universal existence of two mechanisms of heterogeneous ice nucleation, <u>viz.</u>, condensation-freezing and deposition nucleations, has been discovered. Conditions for their existence have been identified, the former occurring above water saturation at warm temperatures and the latter below water saturation at lower temperatures.

(4) The forbidden zone for condensation-freezing nucleation above water saturation, the temperature dependency of the zone, and the extremely steep rise of nucleation rate when the supersaturation increases beyond this zone, have been discovered.

(5) The discovery of a unique deposition nucleation behavior near but below water saturation for freely suspended aerosol particles has been made.

(6) Contact nucleation has been identified experimentally as a very slow process except for the nucleant MA.

(7) A thermodynamic theory of condensation-freezing nucleation has been developed and it has been shown that the theory describes the experimental data well.

(8) An empirical expression for describing the unique deposition nucleation zone just below water saturation has been formulated.

(9) The necessity for nucleation rates of condensation-freezing and deposition to be expressed as a function of two independent variables, namely supersaturation and temperature, has been shown. An example of the computation has been carried out, and a three-dimensional graph showing the relationship has been presented.

Acknowledgement: This work was supported by the Weather Modification Program, RANN, NSF under Grant ENV 73-02910.

References

Bryant, G.W., J. Hallett, and B.J. Mason, 1959: The epitaxial growth of ice on single crystalline substrates. J. Phys. Chem. Solids, 12, 189-195.

Evans, L.F., and J.E. Lane, 1972: Line tension and ice nucleation theory. J. Atmos Sci., 30, 326-331.

Fletcher, N.H., 1958: Size effect in heterogeneous nucleation. J. Chem. Phys., 29, 572-576; 31, 1136.

Fletcher, N.H., 1962: The Physics of Rainclouds. Cambridge, The Cambridge University Press.

Fletcher, N.H., 1969: Active sites and ice crystal nucleation. J. Atmos Sci., 26, 1266-1271.

Fukuta, N., 1963: Ice nucleation by metaldehyde. Nature, 199, 475-476.

Fukuta, N., 1966: Activation of atmospheric particles as ice nuclei in cold and dry air. J. Atmos. Sci., 23, 741-750.

Fukuta, N., and R.C. Schaller: Ice nucleation by aerosol particles II. Theories of condensation-freezing and deposition nucleations (to be published).

Isono, K., T. Tanaka, and K. Iwai, 1966: On the nature of atmospheric ice nuclei and features of ice crystal formation on nuclei. J. Rech Atmos., 2, 341-345.

Schaller, R.C., 1975: A study of heterogeneous ice nucleation mechanisms using a new ice thermal diffusion chamber. Ph.D. Dissertation, University of Denver, Denver, Colorado, December, 1975.

2.1.3

FILTER MEASUREMENTS OF ICE NUCLEI CONCENTRATIONS AND SELECTED COMPARISONS

James E. Jiusto, G. Garland Lala, and John Zamurs

Atmospheric Sciences Research Center
State University of New York
Albany, New York

1. INTRODUCTION - SUNY EQUIPMENT

The static vapor-diffusion chamber used to process membrane filters during the 1975 Ice Nucleation Workshop at Laramie, Wyoming, represents an improved version of that described by Lala (1972). The chamber (Figure 1), of disc shape approximately 12 cm diameter and 3 cm high, is operated within any cold box of suitable size and low temperature capability. Both the bottom filter plate and upper ice surface (3.2 mm thick) are independently temperature regulated by means of heater wire. Temperature gradients across the chamber are less than 0.1^{o} C and the error in ΔT between upper and lower surfaces is less than 0.03^{o} C. Four filters can be processed simultaneously and the developed crystals observed after 45-60 minutes from above with a long working-distance microscope and vertical illumination.

Filters are placed on 1 mm thick aluminum discs, each covered with a 0.5 cm^3 layer of warm petroleum jelly or other filter pore sealant. The 4 discs are inserted in the bottom plate recesses of the chamber which is kept within the cold box. The ice lid is then attached as well as styrofoam insulation surrounding the chamber. For approximately 5 minutes, the bottom plate is maintained 2-3^{o} C warmer than the top ice plate in order to evaporate any cold box droplets that might have settled on the filters during the brief loading process. Thereafter temperature uniformity is achieved, and then the top ice surface is warmed to an elevated temperature corresponding to the desired no-sink relative humidity at the filter surfaces. The time to reach a specified ΔT is approximately 0.5 min. (time constant of 10-15 seconds).

A unique feature of the chamber is the capability of varying the distance between the ice surface and the filters. Various height separation rings from 0.25 cm to 1.5 cm can readily be interchanged, with most measurements to date made at a ΔZ = 0.5 cm. Diminishing chamber height has the net effect of increasing filter humidity and the concentration of activated ice nuclei (Lala and Jiusto, 1972; Zamurs, 1975).

In summary the ice nuclei chamber was designed for: relative simplicity of construction, operation, and transportability; high reliability of temperature control and system performance; flexibility in terms of altering and assessing primary and secondary chamber variables; and routine measurements of ice nuclei (IN) concentrations in various types of synoptic airmasses.

2. WYOMING WORKSHOP AND NEW YORK STATE MEASUREMENTS

During the cooperative Workshop, the SUNY IN detector was used in 18 experiments involving the processing of approximately 150 filters. Our particular objectives, in conjunction with the broader goals of the Workshop, were to:

a. examine IN counts and the performance of our system in the relatively clean airmass conditions of Wyoming versus that of the more populated and industrialized northeastern United States

b. extend our analysis of significant instrument and filter variables

c. compare IN concentrations of similar filter instruments and of those operating on different principles

d. explore our hypothesis that static diffusion chambers to date have provided only relative values of IN concentrations, and to develop techniques for approaching absolute values.

A complete description of these experiments (Jiusto and Lala, 1976) and of all Workshop findings (Vali, 1976) is available upon request. Only selected findings from these experiments and those at Albany, New York, will be given here. The Workshop data are necessarily limited in extent.

a. Chamber Height Effect

Relatively little attention has been paid to the effect of chamber height ΔZ on peak filter humidity achieved and corresponding IN counts in a static diffusion chamber. It was shown theoretically (Lala and Jiusto, 1972) that this variable was highly significant, as was the cooling time constant of the chamber. In short, as ΔZ was decreased, the effective filter humidity reached progressively higher values.

Experiments were run to evaluate theoretical predictions, utilizing data obtained in Laramie, Wyoming, as well as Albany, New York. As shown in Figure 2, the trend was confirmed with IN concentration being an exponential function of height over the range investigated. Thus,

$$N \approx N_o e^{-1.7\,\Delta Z}$$

where N_o is the limiting concentration value as ΔZ approaches zero. We presently interpret this limiting concentration as that for which vapor depletion effects (chamber surfaces, filter, and nuclei) are substantially minimized and the prescribed filter humidity is approached.

For the common temperature and humidity conditions represented (T = -20C, R.H. = 100% nominal), the exponential height function in our chamber appears relatively insensitive to airmass type. For ΔZ = 0.25 and 0.5 cm, $N_o \sim 1.5$ N and $N_o \sim 2.3$ N, respectively. It is evident that a) chamber height should be as shallow as possible and b) an IN concentration correction scheme involving extrapolation of ΔZ to 0 appears appropriate. When so done, Millipore filter concentration values then approach those made with current and historical cloud formation apparatus.

b. Volume Effect

The volume effect of the filter method was measured on natural aerosol in Laramie. For our instrument and a volume range of 105 to 1843 ℓ, the IN concentration-volume dependence was: $N \propto V^{-0.86}$. Preliminary results of the University of Wyoming, which included a composite of these and other data, indicated the comparable relationship $N \propto V^{-0.8}$.

It is interesting to compare the volume effect for Albany, New York, a typical semi-urban area of the northeast where atmospheric turbidity and cloud condensation nuclei (CCN) concentrations are substantially higher than in Laramie, Wyoming. Typical Albany CCN concentrations at 1% S are 2000-3000 cm^{-3}; the corresponding filter volume-effect exponent averages approximately -0.8 to -1.0 in experiments conducted to date. One might have expected a greater difference between the distinctly different air quality regimes. Evidently, even relatively clean continental air possesses sufficient CCN to produce a significant volume effect.

c. Filter Type

In previous correspondence and at the Workshop, A. Gagin reported on favorable results obtained with Sartorius membrane filters. Thus, three experiments were performed using Millipore, Sartorius, and Sartorius-hydrophobic filters, all of 0.45 μ pore size. The Sartorius filter counts were generally greater than those of the Millipore filters, while the hydrophobic Sartorius filters always exceeded the Millipores substantially - by an average factor of 3. (Wyoming tests showed a corresponding average factor difference of about 4.) Cellulose nitrate fibers of a Sartorius filter are rendered "hydrophobic" by coating with a silicone compound, according to the manufacturer. AgI test aerosol was used in all three of these experiments. Regarding natural aerosols in previous Albany studies of ambient air with 16 Millipore vs. 16 hydrophobic-Millipore (teflon) filters, the latter yielded consistently higher IN concentrations by a factor of 2 (Zamurs, 1975). Thus it seems that hydrophobic filters act as less of a vapor sink, allow humidity to reach higher values, and hence activate more ice nuclei. Sartorius hydrophobic filters have superior handling qualities.

d. Filter Pore Sealants and Background

Vaseline and STP, two filter sealants in common use, were compared on several Workshop experiments. The IN concentration results obtained were generally quite similar. Background counts on blank filters were somewhat higher with vaseline, typical values for water saturated conditions being 10-15 at -20 C and 4-9 at -16 C. (We have since observed that high-grade petroleum jelly lowers the background somewhat over its commercial counterpart, vaseline.) STP yielded approximately ½ the background values of vaseline.

Previously in New York State tests, STP had been ruled out because of exceptionally high background and spurious high counts on exposed filters. Upon returning from the Workshop, these experiments were repeated with similar results. It became evident that in the "open" system involved, droplets can settle into the STP under conditions of high ambient humidity and low cold box temperature. Such droplets apparently cannot be evaporated from the oil in the several minute pre-heating cycle as they can be from the hardened vaseline or petroleum jelly surface. Subsequent extraneous nucleation results.

3. SELECTED GROUP EXPERIMENTS

Many of the experiments conducted during the Workshop were concerned with the supersaturation spectrum of ice nuclei and how well they fit the function

$$N_i = \gamma\, S_i^{\alpha} \text{ (Huffman, 1973; Gagin, 1973).}$$

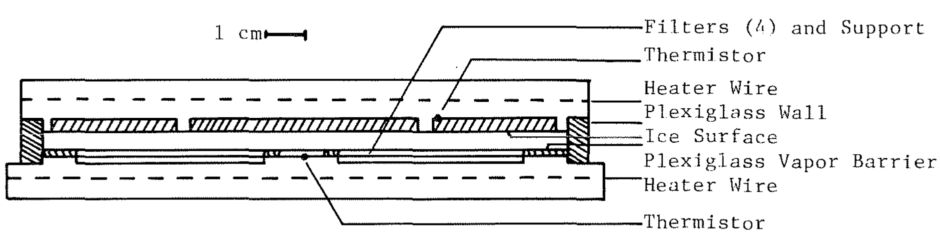

Figure 1. SUNY Static Diffusion Chamber (Cross Section)

The purpose of these experiments was to examine this relationship for various apparatus and to try to define a range over which it can be applied. Comparisons with the Ohtake Settling Cloud Chamber (SCC) and the Wyoming Drop Freezing Counter (DFC) were also made to determine how the results from these drop-freezing instruments compared with filter spectra.

As described earlier, the diffusion chambers indicated a volume dependence of the form $N = N_o V^{-0.8}$. This average volume correction was used to reduce the data to a common volume of 100 liters. Figure 3 shows the spectra for the reduced filter data (SUNY, Wyoming and NOAA) and for the freezing units (SCC and DFC). A least squares fit of the spectrum function to the filter data resulted in a slope of 5.2 while a similar analysis of the SCC and DFC data gave a slope of 11.4. On another day the respective slopes were 5.0 and 11.0, remarkably similar.

A most informative aspect of the experiment is the interpretation of the filter data vs. the DFC and SCC data. The slopes of the spectra differ by a factor of 2 which is partly a result of different modes of nucleation in the three types of instruments. In the static chamber, nucleation occurs primarily by condensation-freezing and deposition while in the SCC nucleation can occur by deposition, freezing or contact nucleation. Perhaps more important, we believe the filter method systematically underestimates, particularly at the higher supersaturations (colder temperatures). However, by applying the SUNY chamber-height effect correction mentioned earlier at $S_i = 21.5\%$ (T = -20C), the filter count becomes approximately 1 ℓ^{-1} - within a factor of two of the drop freezing devices. For concentrations of $N \sim 0.1\ \ell^{-1}$ or less, the sample values of the drop freezing devices are too small for meaningful results (e.g. 10 ℓ volume of the SCC $\equiv$ 1 crystal); here the filter data are far more reliable, though they may be influenced somewhat by an increasing proportion of background counts.

Also shown is a plot of the empirical nucleation function given by Fletcher (1966), $N = 10^{-5} \exp(0.6\ \Delta T)$, which typified many of the IN concentration measurements made to that time. The varying slope of the function tends to support the arguments above regarding the validity and response of each class of instruments over the S_i (T) range indicated.

4. SUMMARY

Some of the conclusions reached on the basis of the Workshop and preceding SUNY analyses of ice nuclei concentration measurements are as follows:

1. The height of a static diffusion chamber strongly influences the peak humidity and the number of activated IN (as does the cooling time constant). The concentration is an exponential function of height in the SUNY chamber such that operation at the shallowest height practical is advised.

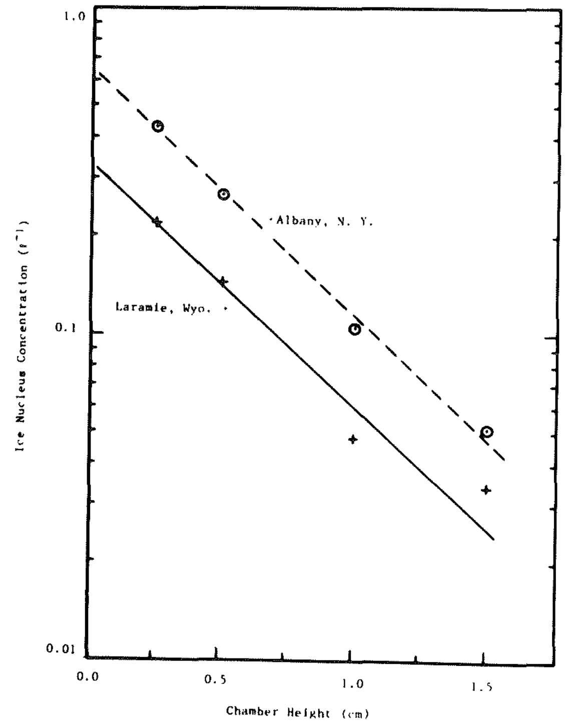

Figure 2. Ice Nuclei Concentration vs. Chamber Height - SUNY ($T = -20C$; $S_w = 1.00$; $V = 394$?, Wyo., 100 ?, N.Y.)

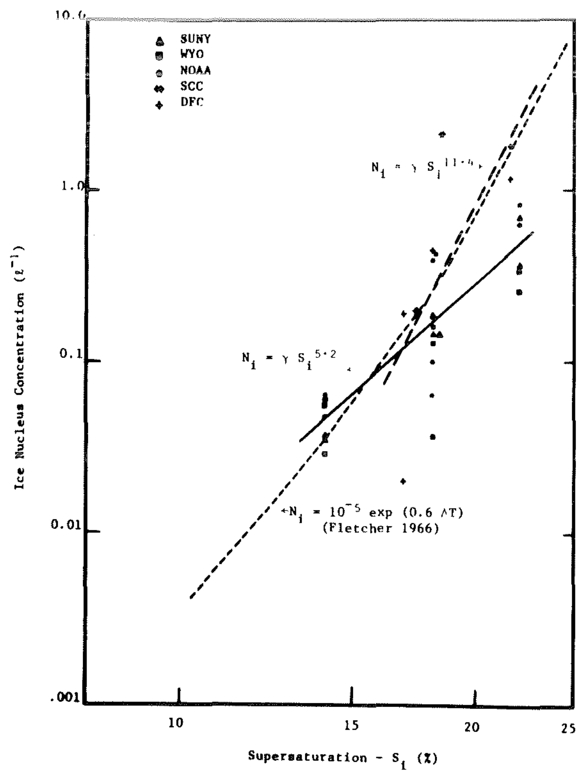

Figure 3. S_i Spectra for Natural Aerosol (Solid line - filter data; long dashed line - drop freezing data; short dashed line - Fletcher, 1966

2. These experiments reaffirm the theoretical prediction (Lala and Jiusto, 1972) that the humidity in filter static-diffusion chambers is overestimated.

3. The ambient filter-volume effect was virtually as pronounced ($N \propto V^{-0.86}$) in Laramie, Wyoming as in Albany, New York, despite a large difference in air quality (CCN concentrations). For pure AgI aerosol, the volume effect was much less (≤ -0.5) reflecting the absence of CCN.

4. Hydrophobic filters (Sartorius), which constitute less of a vapor sink than regular cellulose filters, result in correspondingly greater IN concentrations by at least a factor of 2 to 3. The use of STP or petroleum jelly to seal the filter pores generally gives equivalent results.

5. Though more clarification is needed, the scheme of expressing IN concentration as a function of supersaturation over ice ($N_i = \gamma S_i^{\alpha}$) appears a reasonable approximation provided: a) one operates at temperatures colder than the critical threshold of activation for the aerosol; and b) the dominant nuclei are of the condensation-freezing or deposition types. A small change in R.H. produces large changes in crystal concentrations.

6. A five-instrument comparison (3 static diffusion chamber-filter processors and 2 drop-freezing devices) demonstrated that IN concentration agreement was reasonably good. The drop-freezing chambers gave consistently higher concentrations at colder temperatures (higher S_i) reflecting perhaps their greater response to contact nuclei as well as assured water-saturated conditions, while the filter technique gave higher counts at warmer T (lower S_i). Consistency of the data was generally better with the membrane filters.

7. Membrane filter-static diffusion chambers generally have provided only relative (albeit important) values of IN concentrations due to vapor sinks and overestimated chamber humidity. Evidence suggests that absolute concentration measurements can be approached satisfactorily by including a simple chamber-height (vapor sink) correction.

5. ACKNOWLEDGEMENTS

We gratefully acknowledge the assistance of Dr. Gabor Vali and the University of Wyoming staff and all Workshop colleagues who freely and enthusiastically shared their findings. This research and the development of the diffusion chamber system was supported by the Atmospheric Research Section of the National Science Foundation (Grant DES73-00410-A01).

6. REFERENCES

Fletcher, N. H., 1966: The Physics of Rain Clouds. Cambridge University Press, 396 pp.

Gagin, A., 1973: Studies of the Size and Supersaturation Spectra of Ice Nuclei. Proc. of the 8th International Conference on Nucleation, 24-29, September, 1973, Leningrad, USSR, 294-307.

Huffman, P., 1973: Supersaturation Spectra of AgI and Natural Ice Nuclei. J. Appl. Meteor., 12, 1080-1082.

Jiusto, J. and G. Lala, 1976: SUNY Diffusion Chamber Measurements and Related Analyses. 1975 International Ice Nuclei Measurements Workshop. In Univ. of Wyoming Report to the NSF, ed. G. Vali.

Lala, G. and J. Jiusto, 1972. Numerical Estimates of Humidity in a Membrane Filter Ice Nucleus Chamber. J. Appl. Meteor., 11, 674-683.

Lala, G. G., 1972: A Numerical and Experimental Study of Humidity in a Membrane Filter Ice Nucleus Chamber. Ph.D. Thesis, Dept. of Atmospheric Science, State University of New York at Albany.

Vali, G., ed., 1976: 1975 Ice Nucleation Workshop. Univ. of Wyoming, Dept. of Atmos. Science, Final Report to the NSF.

Zamurs, J., 1975: A Study of Ice Nucleation by the Millipore Filter Technique: Characteristics of the Vapor Diffusion Chamber Method and Synoptic Changes in Ice Nucleus Concentrations. Masters Thesis, Dept. of Atmospheric Science, State University of New York at Albany.

NATURALLY OCCURRING BIOLOGICAL ICE NUCLEANTS: A REVIEW

Russell C. Schnell

NRC Research Associate
NOAA/APCL
Boulder, Colorado 80302

1. INTRODUCTION

It is general knowledge that the atmosphere contains naturally produced terrestrial and marine derived organic material which, according to Hidy (1970), represents an average of between 30 and 40% of the total atmospheric aerosol load. Included in this organic aerosol are large collections of viable microbial life (spores, seeds, bacteria, etc.) which at times are present as dense "microbial cloud systems" over land and sea at all levels up to the tropopause (Gregory, 1967).

Recently, scientists have observed that copious numbers of active ice nuclei may be found in nature closely associated with some species of bacteria, within naturally decayed litters of most plant species, and in association with marine plankton. These ice nucleants may be respectively categorized as Bacteria-derived Nuclei (BDN), Leaf-derived Nuclei (LDN), and Ocean-derived Nuclei (ODN) under the general heading of biological or biogenic ice nucleants. Each nucleant type will be discussed separately below.

2. BACTERIA-DERIVED NUCLEI (BDN)

2.1 BDN In Water

Although Soulage (1957) reported that bacterial cells found in outdoor air could become centers of ice crystals in a cloud chamber, little interest in these observations was aroused until Fresh (1973) isolated a species of ice nucleating bacteria, Pseudomonas syringae (P.s.) from *in vivo* decaying tree leaves. This bacterium was observed to initiate ice in supercooled water (drop freezing technique, Vali, 1971) at -1.3C in concentrations of up to 10^8 nuclei active at -5C. The *in situ* production of active ice nuclei associated with bacteria has been observed in both deciduous and coniferous forest litters (Schnell, 1974, Fresh *et al.*, 1975).

Research into the taxonomy, physiology, and ice nucleation characteristics of P.s. by Maki *et al.* (1974) has shown that: 1. Good ice nuclei could not be observed in P.s. cultures until viable cell counts reached approximately 10^7-10^8 cells per cm^3 of growth media: 2. Approximately 1 in 10^5 of the bacteria in any particular P.s. culture could nucleate ice at temperatures warmer than -10C: 3. The nucleation activity of P.s. was shown to be associated with intact bacterial cells.

Extensive screening of leaf litters and stock cultures of bacteria has resulted in the isolation of another bacterium, Pseudomonas fluorescens biotype G, (P.f.) with ice nucleating activity comparable with that of P.s. (Maki and Garvey, 1975). Numerous species of Pseudomonas as well as other bacteria, in any concentration, do not harbor active ice nuclei (Fresh, 1973, Maki *et al.*, 1974).

Cultures of P.f. have been nebulized and injected into the Colorado State University isothermal cloud chamber where they produced ice crystals at a temperature of -12C. (Maki et *al.*, 1974). It was also determined from these tests that one out of 10^3 P.f. cells was acting as an ice nucleus.

2.2 BDN On Plants

A dramatic aspect of bacterial ice nucleation research has recently been reported by Lindow *et al.*, 1975, plant pathologists studying frost sensitivity of herbaceous plants. Working without knowledge of earlier observations relating bacteria and ice nucleation, they observed that the presence of P.s. on corn and bean leaves increased the plants' sensitivity to frost as did the presence of another bacterium, Erwina herbicola (Lohnis) Dye. They observed that plants with 10^3 bacteria over the total leaf surface suffered some frost damage when subjected to temperatures of -3.5 to -4C (in a mist chamber) for 24 hours, whereas concentrations of 10^7 bacteria per plant ensured virtually 100% frost kill under the same conditions.

Depression of natural bacteria populations on growing field corn by spraying with streptomycin has been shown to reduce the crop's susceptibility to frost. In one case, a mature corn crop sprayed prior to a single radiation frost of -2C exhibited less than one-half the frost damage sustained by adjacent unsprayed corn plants (ibid.) Considering that the unsprayed corn plants sustained 75% loss, the savings inherent in applying bactericides to frost-sensitive crops may make the operation economically attractive.

It is known that living and dead bacteria can be found in air, rain, hail, and snow (Gregory, 1961, 1967; Parker, 1968; Mandrioli et al., 1973). What proportion of the microbes participated in the precipitation formation and what proportion was scavenged from the air beneath the clouds are unknown. In the case of microbes found within the inner layers of large hailstones, the possibility of sub-cloud scavenging does not exist. From all of the above, it appears that ice nucleating bacteria are playing an important role in both cloud physics and Agronomy.

3. LEAF-DERIVED NUCLEI (LDN)

The first strong evidence that naturally occurring organic materials found in soil are a strong source of ice nuclei was presented by Vali (1968) who was able to show that natural soils containing large fractions of organic debris were considerably better sources of freezing nuclei (drop freezing technique)than were the basic clay constituents of these soils. These observations were followed by further study which showed that copious numbers of organic freezing nuclei, some active at temperatures as warm as -4C, were regularly produced during the decomposition of naturally occurring vegetation (Schnell and Vali, 1972).

The ubiquity of LDN was established by finding active freezing nuclei in plant litters collected around the world. The availability of nuclei in the litters was noted to vary according to the climatic zone of the plant's origin; litters from tropical A-type (according to Koeppen classification) climates contain fewer freezing nuclei (10^2 g^{-1} active at -10C) than litters from mid-latitude C-type climates (10^4 g^{-1} active at -10C) which in turn contain fewer nuclei than litters from high-latitude D-type climates (Schnell, and Vali, 1973).

The rates of release of freezing nuclei to the atmosphere from in situ litters from D-type climates has been determined experimently: the fluxes of nuclei active at -12C were found to be 10^1 to 10^3 cm^{-2} day^{-1} during daylight hours. This rate appears to be sufficient to account for the commonly observed concentrations of airborne nuclei (Schnell, 1974; Schnell and Vali, 1976).

Results from simultaneous world-wide measurements of atmospheric ice nuclei at 44 stations around the world were reported by Bigg and Stevenson (1970). Their analysis of these data in light of the biogenic ice nucleus hypothesis has shown that on a world-wide average, stations in tropical A-type climate zones exhibited fewer ice nuclei than mid-latitude B and C-type climates. This is the same trend noted earlier for the availability of LDN on the Earth's surface. Also, results from measurements of the freezing nucleus contents of rainwater (440 samples) collected in four different climate zones in North America were found to exhibit the same close relationship to the local availability of LDN.

Ice nucleus measurements for a three-year period over Australia and the Antarctic Ocean were reported by Bigg (1973). The data presented by Bigg were replotted on a map with outlines of terrestrial climate zones and marine water mass convergence zones. (Fig. 1).

This map shows that on land the lowest atmospheric ice nucleus concentrations are associated with A-type climates, whereas the highest are in C-type climate areas. Dry, dusty B-type climates exhibited nucleus concentrations just larger than those from the A zones and considerably less than those from C zones,thus suggesting that vegetation, not inorganic soil,may be a major source of the ice nuclei observed (Schnell and Vali, 1976). The nuclei associated with the Antarctic Ocean will be discussed in Section 4.

To examine the ice forming ability of LDN as realistically as possible, cloud chamber tests were conducted utilizing the large isothermal chamber at Colorado State University (Garvey, 1975). The ice forming activity of an aerosol produced from litter collected in a D-type climate was observed to be just slightly less active than the activity expressed for the same material tested by the drop freezing technique (Schnell and Vali, 1976).

Limited physical and chemical tests indicate that LDN particles are about 0.1 μm in diameter when suspended in water, are insoluble and stable in all common organic solvents, and begin to loose nucleating activity upon being heated above 60 to 100C. The active LDN component was observed to be less than 1% of the total dry weight of any leaf litter (Vali et al.,1973).

4. OCEAN-DERIVED NUCLEI (ODN)

A possible marine source for atmospheric ice nuclei has been suggested by Brier and Kline (1959) and Battan and Riley (1960) though neither group indicated which marine component may have been the nucleant source. The first firm indications that certain marine waters contained copious numbers of ice nuclei came from Schnell and Vali (1975) who showed that marine waters of high primary productivity contained ice nuclei active at temperatures warmer than -8C. Filtering, concentrating, and then resuspending the plankton into distilled water revealed some nuclei to be active at -4C in concentrations of up to 10^7 to 10^8 nuclei per gram of plankton active at -10C. Marine waters devoid of plankton were found to be free of ice nuclei active at temperatures warmer than -16C.

By screening 23 stock cultures of phytoplankton, Schnell (1975) was able to find one culture, Cachonina Niei (C.n.) that contained ice nuclei active at -5C in concentrations of 10^6 nuclei active at -10C per gram of plankton. Two other cultures showed some ice nucleating ability whereas the other 20 were devoid of ice nuclei active warmer than -15C. Subsequent research on the C.n. culture has revealed the presence of a marine bacterium that when grown in pure culture,initiates ice at -3C in concentrations of up to 10^6 nuclei active at -5C (Schnell, unpublished). This bacterium has not been identified.

During August of 1975, Schnell et al. (1975) collected seawater and fog water samples off the east coast of Nova Scotia (USNS HAYES 1975 Fog Cruise) and tested them for the presence of warm range ice nuclei (drop freezing technique) and the coincident presence of viable bacteria. A number of fog samples were found to contain ice nuclei active at temperatures warmer than -5C. Four out of 15 bacterial isolates separated from these fog samples, when grown on sterile media, were found to initiate ice at temperatures between -2 and -4C.

Figure 1 shows a band of high ice nucleus concentration along the 40°S parallel that coincides with the mean position of the Sub-Tropical Convergence Zone (STCZ). This zone represents an area where the meeting of two oceanic water masses results in continual overturning and mixing of the water. The relatively high nucleus concentrations near the Australian and Antarctic coasts roughly correspond to regions of oceanic upwelling and continental shelf areas. Ryther (1963) noted that Antarctic waters may be the most prolific producers of primary marine plankton in the world, with the output peaking in upwelling zones and to a lesser extent along convergence zones. It has been suggested by Schnell (1974) and Schnell and Vali (1976) that the high ice nucleus concentrations observed over these suspected areas of high plankton growth may be related to plankton-associated ODN.

5. SUMMARY

On the basis of the data and analyses presented in this paper, it is suggested that materials of biogenic origin may be among the more important ice nucleus sources in the Earth's atmosphere. Also, biogenic ice nuclei have been demonstrated to be important in creating low supercooling frost sensitivey in some herbaceous plants. Control of this latter phenomenon appears to be economically within reach.

REFERENCES

Battan, L. J., and J. J. Riley, 1960, Ice crystal nuclei and maritime air. *J. Meteor.*, 17, 675-676.

Bigg, E. K., 1973: Ice nucleus measurements in remote areas. *J. Atmos. Sci.*, 30, 1153-1157.

_____ and C. M. Stevenson, 1970: Comparison of ice nucleus concentrations in different parts of the world. *J. de Rech. Atmos.*, 4, 41-58.

Brier, G. W., and D.B. Kline, 1959: Ocean water as a source of ice nuclei. *Science*, 130, 717-718.

Fresh, R. W., 1973: Microbial production of freezing nuclei from decomposing tree leaves. Report AR106, Department of Atmospheric Resources, University of Wyoming, Laramie, Wyoming, 15 pp.

_____, R. C. Schnell and L. R. Maki, 1975: Highly active ice nuclei produced during tree litter decay. Proceedings, 12th Conference on Agricultural and Forest Meteorology; Tucson, April 14-16, AMS.

Garvey, D. M., 1975: Testing of cloud seeding materials at the Cloud Simulation and Aerosol Laboratory, 1971-1973. *J. Appl. Meteor.*, 14, 883-890.

Gregory, P. H., 1961: *The Microbiology of the Atmosphere*. Leonard Hill, London, England, 251 pp.

_____, 1967: Atmospheric microbial cloud systems. *Science Progr. (Oxford)*, 55,613-628.

Hidy, G.M., 1970: The dynamics of aerosols in the lower troposphere. In *(Third) Rochester International Conference on Environmental Toxicity, 1970, Proceedings*. Charles C. Thomas, Springfield, Ill., pp 81-115.

Lindow, S., R. W. Barchet and C. D. Upper, 1975: The relationship between populations of bacteria active in ice nucleation and frost sensitivity in herbaceous plants, Proc. AGU Fall Meeting, *EOS*, 56, 994.

Maki, L.R., Galyan, E. L., M. C. Chien, and D.R. Caldwell, 1974: Ice nucleation induced by Pseudomonas syringae, *Appl. Micro.*, 28,456-459.

_____ and D. M. Garvey, 1975: Bacterially induced ice nucleation, Proc. AGU Fall Meeting, *EOS*, 56, 994.

Mandrioli, P., G. K. Puppi, N. Bagni and F. Prodi, 1973: Distribution of microorganisms in hailstones. *Nature*, 246, 416-417.

Parker, B.C., 1968: Rain as a source of Vitamin B. *Nature*, 219, 617-618.

Ryther, J. H., 1963: Geographic variation in productivity. *The sea*, Vol. 2, M. N. Hill (ed.), Interscience Publishers, Wiley and Sons, New York, 554 pp.

Schnell, R. C., 1974: Biogenic sources of atmospheric ice nuclei, Report AR111, Department of Atmospheric Resources, University of Wyoming, Laramie, Wyoming, 33 pp.

_____ 1975: Ice nuclei associated with cultured and naturally occurring marine phytoplankton. *Geophysical Research Letters*, 2, 11, 500-502.

_____ and G. Vali, 1972: Atmospheric ice nuclei from decomposing vegetation. *Nature*, 236, 163-165.

_____ and _____, 1973: Worldwide source of leaf-derived freezing nuclei. *Nature*, 246, 212-213.

_____ and _____, 1975: Freezing nuclei in marine waters. *Tellus*, 27, 132-134.

_____ and _____, 1976: Biogenic ice nuclei: Part 1. Terrestrial and marine sources. *J. Atmos. Sci.*, In Press.

_____, J. Carney, and C. Carty, 1975 : Active ice nuclei associated with viable bacteria in Nova Scotia marine fogs. Proc. AGU Fall Meeting, *EOS*, 56, 994.

Soulage, G., 1957: Les noyaux de congelation de l'atmosphere. *Annales de Geophysique*, 13, 103-134.

Vali, G., 1968: Ice nucleation relevant to the formation of hail. McGill University Stormy Weather Group, Science Report MW-58, 51 pp.

_____, 1971: Quantitative evaluation of experimental results on the heterogeneous freezing nucleation of supercooled liquids, *J. Atmos. Sci.*, 28, 402-409.

_____, J. Howatson, and R. C. Schnell, 1973: Development of leaf-derived ice nuclei for weather modification. Report to National Science Foundation, Grant GI-32555X, 32 pp.

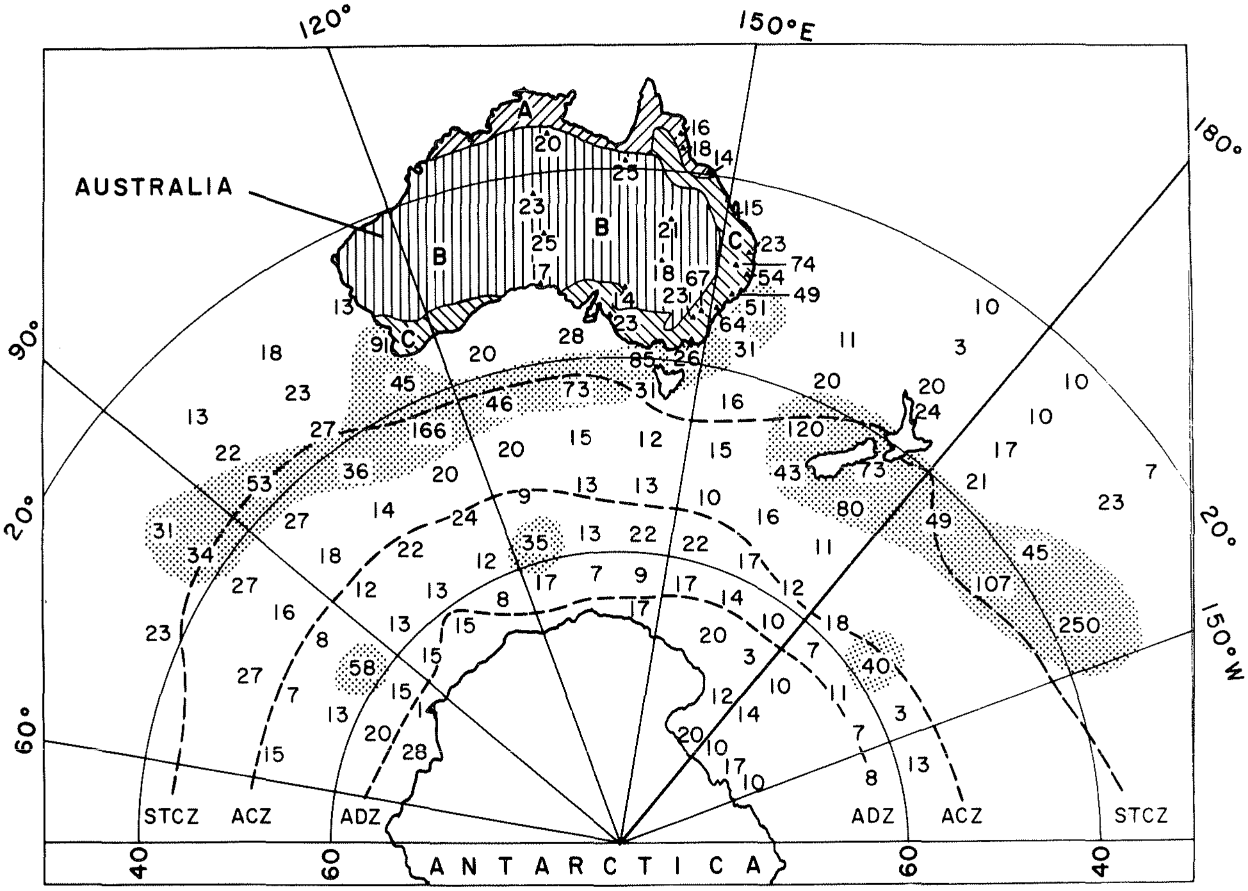

Figure 1. Three-year averages of atmospheric ice nucleus concentrations over Australia and the Antarctic Ocean plotted on a base map illustrating terrestrial climate zones and marine water mass interfaces. The shaded area encompasses atmospheric ice nucleus concentrations greater than 30 nuclei m^{-3} active at -15C. Adapted from Bigg (1973).

ICE-FORMATION BY USE OF SYNTHETIC ZEOLITE NUCLEI

L. Krastanov, L. Levkov

Institute of Geophysics - Bulgarian
Academy of Sciences-Bulgaria

It is known from the available sources of a number of authors that many materials act as artificial crystalisa - tion nuclei of the water at various temperatures below 0°C. Recently /1,2/ we studied the mechanism which may explain the strong ice-formation activity of some unorganic compounds e.g.AgI, PbI_2, CuS. We have come to the conclusion that when the ice crystal appears and grows on on the crystal surface with predominant ion structure the connection of the two contacting surfaces occurs in the following manner: First a dipole-orientated interaction between the polarized molecules of the substrate (cations) and the polar molecules of the water (protones) takes place. Due to this interaction the water molecules at sufficiently low temperature are linked in successive attachment with the ions of the lattice (the cations) and build the first "crystal layer". Further this layer is linked with other water molecules, but this time by way of hydrogen links. Thus the ice embryo is being formed on this primary ice layer on the substrate.

As is known the so called zeolites or molecular sieves have the property of absorbing water even at very low relative humidity even in the form of water vapour from the air without any chemical interaction and to link and hold it in their crystal lattice. The contents of the water therein can vary depending on the temperature and the pressure of the water vapour in the air. When heated the zeolites emit water continuously and can dehydrate but likewise the process can be reversed - the water penetrates into the lattice of the zeolites without destroying the structure of the crystal. It has been established by paramagnetic resonance /3/, that at low temperatures there exist hydrogen links between water molecules and the oxygen ions in the frame of the zeolite. The lattice properties of the zeolites are made use of in our experiments.

The test of the ice nucleation abilities of the zeolite powder particles was carried out (a) by contact of the droplet with the particles in air medium - contact nucleation;(b) by deposition of the water vapour on the nuclei and formation of an ice crystal - deposition nucleation.

The tests were carried out in a microchamber (work volume 15 cm^3) cooled by liquid nitrogen. Single water droplets 2 mm in diameter were trated by suspending them on a thermocouple enveloped in glass, which can measure the temperature of the supercooled droplet to an accuracy of ± 0.2°C. The velocity of cooling was 3°C per minute. The droplet was landed al - ways at the geometrical center of the chamber which was the intersection point of four mutually perpendicular openings used for observation, illumination and manipulation. The temperature of the chamber was measured with the help of a second thermocouple placed 2-3 mm from the chamber wall. Both thermocouples were switched to a "Graphispot" recorder.

Testing of the crystalisation activity of untreated zeolite powder.

A thin glass thread with zeolite powder at its peak was mounted on a micromanipulator opposite one of the chamber openings. A droplet was suspended in the chamber and was cooled down to a certain temperature. The peak of the glass thread was then inserted into the chamber using the micromanipulator until it touched the supercooled droplet. Such a test of zeolite powder z-1 was carried out with as much as 60 droplets divided into 6 series of 10 droplets each depending on the temperature T_k of the droplet at the mo - ment of contact. In this case T_k varied from -10.1 to -16.0°C. Another 40 droplets were experimented with zeopite powder z-2 in 4 series in the interval from -7.1 to -11.0°C. The average temperature which characterises the activity of the samples is given in Table 1 and is defined by the characteristic temperatures of the activity of an ensemble of particles by means of which the droplets were frozen /4/.

Testing of the crystalisation activity of dehydrated zeolite powder.

The experiments were carried out with dehydrated zeolites the treatment being as follows: Powder of z-1 and z-2 was placed consecutively into a glass which is heated to 320-350°C and at the same time evacuated (vacuum 0.1-0.2 mm Hg). After such treatment of 1 hour a sample (crystalsof the powder) is taken on the peak of a glass thread. The thread is brought into contact with a droplet supercooled in the chamber. In the second part of this experiment the dry zeolites are left after the treatment 1) at room temperature t=28°C and relative humidity f=50% from 1 to 3 hours, from 16 to 24 hours and from 60 to 64 hours and 2) at room temperature t=28°C and relative humidity f=98% from 16 to 24 hours and from 42 to 48 hours. Only after that the samples were inserted to contact the supercooled droplets in the chamber. The temperature T_k at the moment of contact was noted at the thermogramme. Several samples of each probe were prepared at equal conditions of treatment. With each sample about 40 experiments of contact influence were carried out at various temperature intervals depending on the activity of the sample. The characteristic average temperatures of activity of the various samples of a same probe at different experimental conditions are shown on Table 1.

It has been established that no ice is formed on a zeolite particle up to -6-8°C from water vapour. This was proved by the experiment described below. Particles of treated z-1 or z-2 are trapped on the tip of a thin glass thread. The thred mounted on a micromanipulator is inserted through the side opening of the chamber until the tip is 1 mm from the surface of the suspended droplet. The temperature of the chamber is decreased to T_o=-6-8°C, that is the temperature of freezing of the droplet if contacted by treated zeolite particle (See the Table). The temperature T_o is controlled by a second thermocouple and is retained for a period of 2-3 minutes. After that the temperature is increased slowly controlled by switching consecutively on and off both thermocouples until it reaches a certain temperature of the droplet T_s within -3-1 degree C i.e. about but always below 0°C. The temperature -3°C is marked by at least one freezing by way of a contact between a waterdroplet and treated zeolite particle. Some time is allowed in order to reach an equal temperature value shown by the two thermocouples thereafter the thread is moved until it touches the droplet. At the above temperature T_o of supercooling of the zeolite no droplet has frozen after 20 trials of touching by both probes.

An electric load was measured on the dehydrated zeolite powder - the carcass of the zeolite lattice after treatment of z-1. The recorded current is of the magnitude 0.1 μA. It has been noticed that on first switch of the galvanometer the impulse is somewhat stronger later decreasing. After a longer stirage of the powder at room temperatures no impulse has been registered.

The most important result obtained by freezing of water droplets by means of dehydrated zeolites can be summerised as follows:

1. The necessary conditions for freezing water droplets by means of zeolite particle (z-1 and z-2) are: the particle should be dehydrated and dry, the droplet should be cooled to a certain temperature: -6-8°C in our experiments and the particle and the droplet should be brought to contact.

The question arises what properties of the dehydrated zeolites could evoke freezing supercooled droplets at relatively high temperatures below 0°C. It is known that many authors identify the properties of water adsorbed in the zeolites with the properties of ice with reference to the arrangement of the water molecules in the lattice of the zeolite and the accuracy of the localisation of the water molecules. It has been established for instance that in the natrolite ($Na(Al_2Si_3O_{10})2H_2O$) the water molecules are definitely localised in the structure of the carcass at room temperature and that they form hydrogen links with oxygen atoms of the carcass of the natrolite which consists of elementary tetraedres as does the lattice of ice.

At our experiments we used dehydrated artificial zeolites z-1 and z-2 which are of the natrolite type. The water molecules and the ions of Na^+ are placed one after the other in the canals of such a zeolite. The analyses of the s spectra of PMR /3/ are evidence that at room temperature the water molecules are exactly localised in the zeolite structure in four positions which differ by p-p vector orientation, the latter being situated in the planes /1̄10/ and /1̄1̄0/ at an angle of +55° towards direction /001/. These directions exactly correspon to the orientation necessary for the water molecule to form hydrogen links with the oxigen atom of the carcass of the natrolite. Because of this when the dehydrated zeolite particles contact the supercooled water it absorbs it into its canals where the water molecules at approprate temperature under 0°C take the order of the ice lattice - the particle becomes ice carrier and induces the freezing of the rest of the supercooled water. So the carcass of the dehydrated particles consists of tetraeders with oxygen atoms at its peaks. Such an elementary tetraeder is a basis of deposition of water molecules which take the same order as in the ice lattice. The more the dimensions of the elementary zeolite tetraeders approach those of the elementary ice crystal tetraeders the higher the temperature of deposition of the water molecules and the nearer the growing crystal will be by its structure to the ice.

Concerning the appearance of negative electric load by the dehydrated zeolites this could be due to the following. Zeolites with Al (cation) in the center of the tetraeder (with ozygen atoms at the peaks - anions) have no full compensation of the electric load. So there are negative load centers in zeolites like AlO_4-tetraeders /5/. The different affinity towards polar molecules like H_2O can be attributed partially to ion-dipole interactions. But the load only cannot be the sole reason for the freezing action of the zeolites.It can be asserted with certitude that the presence of both dehydrated tetraeder structure and negative loaded centers make the zeolite particles active nuclei for ice formation and hence reagents freezing the supercooled water.

REFERENCES
I. L.Krastanov. Compt.rend.Acad.bulg. Sci. 25,I972,II,p.I5I5
2. L.Krastanov,L.Levkov. Compt.rend. Acad.bulg.Sci.29,No I,I976,pp.57-60
3. И.В.Матяш,Киев, Вода в конденсированных средах, 1971,стр.79
4. Н.Генадиев,Л.Левков,Изв.на Геофиз.и-т XIX,25.
5. Вл.Пенчев, Молекулярни сита-зеолити, Наука и изкуство,София, 1973 г.стр.25

Average Values of the Characteristic Temperature of Freezing /°C/ of an Ensemble of Droplets at Contact with Zeolite Powder Particles

kind of sample / material	untreated	treated					
	kept at room condts. /t=22-27°C, f=50%/ unlimited time	kept at room tempt.after treatment /hours/				kept at relative humidity f=98% & room tempt. t=25°C/hs	
		immediatly after treatment	from I to 3	from I6to 24	from 60to 64	from I6 to 24	from 42 to48
z - I	- I3,4	-7,2	-6,8	-6,6	-7,3	-8,6	-I0,4
z - 2	- 9,3	-6,3	-6,3	-6,7	-6,7	-8,7	-9,I

2.1.7

OBSERVING SOUTH FLORIDA'S ICE NUCLEI SPECTRUM

Joe Wisniewski

Department of Environmental Sciences
University of Virginia
Charlottesville, Virginia 22903

1. INTRODUCTION

A Beechcraft Queenair cloud base aircraft supported by the National Center for Atmospheric Research (NCAR)* operated in South Florida for a four week period during summer 1975. The aircraft was equipped with a rainwater collection scoop, a continuous aerosol collector, a NCAR acoustical ice nucleus counter (Langer, 1973), as well as most of the standard meterological instrumentation (Burris et al. 1973).

The rainwater samples were analysed for ice nucleus concentrations using the Vali drop freezing technique (Vali, 1971) and the aerosol samples were analysed for ice nuclei concentrations using the NCAR membrane development chamber (Langer and Rodgers, 1975). Combined with the NCAR acoustical counter results, the ice nucleus data was stratified in various ways to gain a better overall understanding of South Florida's ice nucleus spectrum.

2. OPERATIONS

The aircraft operated within the 13000 km^2 network (Figure 1) covered by digitized radar (Wiggert and Ostlund, 1975) which was used by the National Oceanic and Atmospheric Administration-National Hurricane and Experimental Meteorological Laboratory (NOAA-NHEML) for the rain augmentation cloud seeding study entitled the "Florida Area Cumulus Experiment" (EML Staff, 1974). A total of 89 clouds were worked during 19 flight dates in the period 23 June 1975 through 18 July 1975.

Approximately 310 rainwater samples were collected at the cloud base level (600m) using the same scoop that Wisniewski, Cotton and Sax (1974) used aboard the NOAA-DC6 aircraft during the 1973 Florida Area Cumulus Experiment. The collector was located on top of the aircraft fuselage (Figure 2) with rainwater flowing into the scoop and then into new, washed half-liter bottles. Two five ml vials were separated from each of the bottles, one of which was analysed for silver concentrations as discussed by Wisniewski (1976) and the other analysed for ice

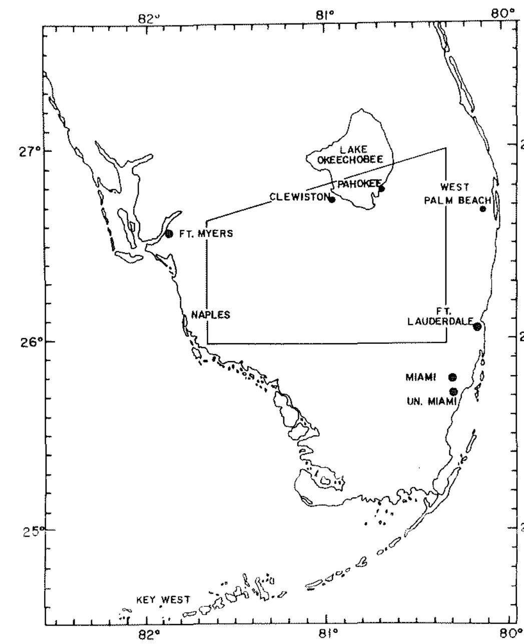

Figure 1. The quadrilateral is the 13000 km^2 network used for operations.

nucleus concentrations as discussed in this paper. The remaining volume in each of the bottles was analysed for a variety of other chemical constituents (NH_4, NO_3, SO_4, Cl, F, Br, Na, K, Mg, Ca, O-PO_4, Total P, Cd, Cu, Fe, Pb, Ni, Zn, conductivity and pH) as discussed by Wisniewski (1976) in a summary paper of the experiment. All samples collected were frozen immediately in Dry Ice and preserved in this state until analysis.

Approximately 390 aerosol samples were collected at the cloud base level (600m) using the Langer sequential membrane filter system with the intake located on the top of the aircraft fuselage behind the rainwater collection scoop (Figure 2). The samples were collected on 0.45 um pore size millipore membrane filters, each being 37mm in diameter. The collector was fixed so that samples could be collected simultaneously with an approximate one second time lag between each sample.

---

*The National Center for Atmospheric Research is sponsored by the National Science Foundation.

Figure 2. The NCAR Queenair aircraft used for sample collection. The rainwater scoop is located on top of the aircraft fuselage in the front while the aerosol intake is located in the rear.

The aircraft flew a varied set of patterns. The predominant pattern was to continuously penetrate a cloud or cloud complex, with the goal of sampling a cloud from its beginning to its dissipation both for rainwater and for aerosol. The second type of pattern was to collect only aerosol samples either in clear air, between clouds or at the perimeter or edge of clouds while circling them.

3. ANALYSES

Three sets of data were obtained from the aircraft for ice nucleus evaluation using the following instrumentation:

1. NCAR acoustical ice nucleus counter - as described in detail by Langer (1975) and in a more concise updated version by Fullerton et al (1975): "The instrumentation provides a continuous real-time ice nucleus count. Air is drawn into the counter where there is a cloud chamber within which a controlled cloud simulates natural conditions. Briefly, the NCAR counter operates as follows. The incoming air sample is humidified to about 80% humidity at 22°C. Cloud condensation nuclei are added to the sample to control cloud density and supersaturation. The air sample then enters the uncooled upper section of the cloud chamber and slowly mixes at -21°C. As the air sample gradually cools, ice nuclei activate the formation of ice crystals, which are detected by an acoustic sensor at the exit of the chamber. The chamber is freon-cooled and lined with a layer of dense polyurethane through which glycol flows slowly to prevent frost from forming on the chamber walls."

2. NCAR membrane development chamber - The instrumentation is described in detail by Langer and Rodgers (1975) but has recently been updated by Langer.* The membranes are placed into the chamber and cooled to some designated temperature. Cold, dry air is passed over the membranes while cooling to prevent active ice nuclei from forming ice crystals that would grow and inhibit the activity of slower ones. Once cooled, moist air is blown in a perpendicular uniform stream onto the membrane's surface at a rather high flow rate of 30 lpm for 15 sec (which provides a strong flux of moisture) giving all nuclei a chance to grow even if they require a maximum supersaturation to initiate condensation. The supersaturation drops by moisture depletion as the droplets grow. Therefore, after the initial burst of 15 sec, the flow is reduced to 5 lpm for approximately 2 min to allow the ice crystals to grow to visible sizes to be counted.

3. Vali drop freezing technique - The technique as described by Vali (1971) was used to analyse all rainwater samples for ice nucleus contents by drop freezing experiments. The procedure was to thaw the five ml rainwater vial, take a small aliquot from it and produce 120 drops on a temperature controlled plate. The number of drops were recorded at quarter-degree intervals as they froze, beginning at -5°C and ending at -25°C, thus giving approximately 80 points for each sample spectrum.

4. RESULTS

Using the instrumentation and analytical techniques described in the last section, results are split into three categories for discussion:

1. NCAR acoustical ice nucleus counter - Preliminary results show the mean ice nucleus concentrations to average approximately five ice nuclei per liter at -20°C. This mean is slightly higher than the one nucleus per liter at -20°C that has been traditionally accepted as a world-wide average; however, nearly all sampling was performed during the convective periods of the day. In addition, a great deal of variability is seen in the data.

2. NCAR membrane development chamber - Approximately 100 membranes were analysed using this technique with very little success. The average sample of air measured was between 70 and 150 liters. Results show that ice nucleus concentrations on the membranes

*Personal communication - Gary Langer, NCAR, Boulder, Colorado.

Table 1. Concentrations of ice nuclei (cm^{-3}) in rainwater samples collected aboard the aircraft

Date	# of Samples	-15°C Mean	-15°C Standard Deviation	-20°C Mean	-20°C Standard Deviation
June 23	7	.60	.85	4.66	2.21
June 25	14	.75	.58	35.56	22.67
June 26	5	4.00	5.24	20.98	8.35
June 28	21	1.75	1.85	11.10	5.42
June 29	18	.58	.55	8.13	6.45
June 30	26	2.60	2.61	34.74	22.88
July 2	13	1.42	1.19	24.92	58.68
July 4	9	3.43	1.81	26.73	15.72
July 5	13	2.35	2.07	32.15	33.84
July 6	17	1.68	1.51	24.54	20.48
July 7	9	1.08	.84	37.17	16.23
July 9	18	1.78	1.97	11.83	6.51
July 10	12	.93	.79	10.14	14.29
July 11	13	.75	.73	6.44	3.43
July 14	24	2.18	1.71	21.35	17.75
July 16	29	5.45	4.37	25.26	11.54
July 17	26	1.30	1.23	14.91	11.76
July 18	31	1.18	1.03	12.00	7.49
Totals:	305	1.97	2.43	19.92	21.09

fall consistently more than an order of magnitude below those recorded by the acoustical counter, with many samples showing concentrations within the background of the membranes. It is interesting to note that Langer* has results from an earlier Hawaii study that show this same discrepancy between the NCAR acoustical counter and the NCAR membrane development chamber while a similar study performed at the HIPLEX project in Montana shows no such discrepancy. Langer hypothesizes that the lower ice nucleus counts result from: 1) the suppression of some nuclei owing to the salts (in this maritime region) collected on the membranes and competing with the nuclei for the vapor supplied during analysis and/or 2) sulphuric acid deposited on the membrane surface which may depress the freezing point. Concerning the South Florida situation, what caused the considerably lower ice nucleus concentration on the membranes as compared to that measured by the acoustical counter is unclear. Whether because of sulphuric acid, salts or another phenomenon, the membrane results show counts so much lower that it appears useless to use this technique in maritime environments. This problem indicates a shortcoming of the membrane technique for ice nucleus analyses. If this technique is to be used in an experiment, it should be thoroughly tested in that specific area beforehand. For example, Mossop (1971) attributed the several order of magnitude difference in ice crystal to ice nucleus concentrations from maritime Australian clouds to an ice multiplication process. These results should be viewed with reservation, however, since the ice nuclei samples were collected on membranes in a maritime environment.

3. Vali drop freezing technique - A summary of the aircraft rainwater ice nuclei concentrations is presented in Table 1 which contains the date of the sample set collected, the number of samples within each set, the mean and standard deviation of ice nucleus samples at -15°C and at -20°C. The results show a good deal of variability between concentrations on the different dates; however, the most important result is that the total overall mean concentrations at both temperatures are considerably lower than those found in other areas (Vali, 1968). The lower concentrations in South Florida agree well with a previous study as documented by Wisniewski, Cotton and Sax (1974). It was attempted to stratify the data according to air mass trajectories as performed by Wisniewski (1976) on silver concentration measurements. Highly significant differences were seen between the silver means and variances using three air mass trajectory paths at two experimental levels. The same stratification applied to the ice nucleus data shows no clear cut trends; however, some differences result:

   1. Significant differences in the variances are seen in the upper level trajectories in comparing each of the three experimental paths.

*Personal communication - Gary Langer, NCAR, Boulder, Colorado.

2. Significant differences in the mean and variances are seen in comparing two air mass trajectory paths at both the upper and lower levels.

Reasons, importance and ramifications of these differences are now being investigated.

5. CONCLUSIONS

Three different techniques were used to collect ice nuclei in South Florida aboard a cloud base aircraft during summer 1975 with the following results:

1. The NCAR acoustical counter showed mean ice nucleus concentrations to be approximately five nuclei per liter at -20°C, a result which seems reasonable compared to other studies.

2. Approximately 100 of the 390 membranes collected were analysed for ice nucleus concentrations using the NCAR membrane development chamber. Very low ice nucleus concentrations were obtained, with many samples showing concentrations not above the background of the membranes. In comparison to the much greater ice nucleus concentrations recorded by the acoustical counter, it appears that the lower concentrations on the membranes may be due to some problem with the detection of the nuclei rather than to their non-existence. This possible ice nucleus suppression on the membranes could be due to interference caused by the maritime environment, since other maritime studies using membranes also show much lower nucleus concentrations.

3. The rainwater samples analysed for ice nuclei using the drop-freezing technique showed much lower concentrations, as compared to other experiments. Whether these low concentrations are real is not clear, since the nuclei may be deactivated by possible interference in the maritime environment, as suggested with regard to the membrane results.

6. ACKNOWLEDGMENTS

The author wishes to thank his closest advisor, Dr. Joanne Simpson, Professor of Environmental Sciences, University of Virginia, for her utmost support and guidance throughout the project. Special thanks are extended to the groups and personnel responsible for sample collection and analyses and for data reduction: the NCAR-Research Aviation Facility for the aircraft that was utilized during the experiment, Mr. Bill Walker whose assistance aboard the aircraft made possible a most successful data collection program, Dr. Gabor Vali who supervised the analyses of all rainwater samples for ice nucleus concentrations at the Department of Atmospheric Science, University of Wyoming and Dr. Gary Langer who supervised the analyses of the membrane samples for ice nucleus analyses at NCAR, Boulder and who helped with overall interpretation of the ice nucleus data. The work was supported under NSF-RANN weather modification grant AEN-75-19817.

7. REFERENCES

Burris, R. H., Covington, J. C. and Zrubek, M. N. (1973): Beechcraft Queen Air Aircraft, Atmospheric Technology-National Center for Atmospheric Research, 1, 25-27.

Experimental Meteorology Laboratory Staff, (1974): 1973 Florida Area Cumulus Experiment (FACE) operational and preliminary summary, NOAA Tech Memo WMPO-12, 257 pp.

Fullerton, C. M., Garcia, C. J. and Langer, G., (1975): Nine months of ice nucleus monitoring at Mauna Loa, Hawaii, Meteorol. Rdsch., 28, 178-190.

Langer, G., (1973): Evaluation of NCAR ice nucleus counter. Part I: Basic operation, J. Appl. Meteor., 12, 1000-1001.

Langer, G. and Rodgers, J., (1975): An experimental study of the detection of ice nuclei on membrane filters and other substrata, J. Appl. Meteor., 14, 560-570.

Mossop, S. C., (1971): The multiplication of ice crystals in clouds, International Conference on Weather Modification, September 6-11, 1971, Canberra, Australia, 1-4.

Vali, C., (1968): Ice nucleation relevant to formation of hail, McGill University-Stormy Weather Group- Report MW-58, 51 pp.

Vali, G., (1971): Freezing nucleus context of hail in Alberta. J. Appl. Meteor., 10, 73-78.

Wiggert, V. and Ostlund, S., (1975): Computerized rain assessment and tracking of South Florida weather radar echoes, Bulletin of the American Meteorological Society, 56, 17-26.

Wisniewski, J., (1976): Tracing of ice nuclei and chemical constituents in South Florida, Tenth Technical Conference on Hurricane and Tropical Meteorology, July 6-9, 1976, Charlottesville, Virginia.

Wisniewski, J., (1976): Variability of rainwater silver concentration in South Florida, International Conference on Weather Modification, August 2-6, 1976, Boulder, Colorado.

Wisniewski, J., Cotton, W. R. and Sax, R. I., (1974): Tracing silver iodide in the South Florida area, Fourth Conference on Weather Modification, November 18-21, 1974, Ft. Lauderdale, Florida, 73-78.

ON ICE NUCLEATION OF SUPERCOOLED FOG

Ken-ichi Sakurai

Hokkaido University of Education
Asahikawa, Japan

1 INTRODUCTION

At Asahikawa, ice fog appears frequently at night on a calm day when air temperature falls lower than about -20°C. Supercooled fog generates initially after the sunset. Then, ice crystals appear in the fog with the falling of temperature. Finally, the fog is made of ice crystals only.

By means of ground observation of the fog, it will be possible to investigate the initial stage of ice crystal formation and to compare ice nuclei with ice crystals in concentration.

2 MEASUREMENTS

Observations were made during the period from 1967 to 1973 at the university campus in Asahikawa. Supercooled droplets were collected on a glass plate coated with cedar oil by an impactor method. Ice crystals and frozen droplets falling gravitationally were collected on a slide glass.

Measurements of ice nuclei were made by a mixing cold chamber. Air containing the ice nuclei was first led into a warm room to be free from any ice particles and then was cooled to the given temperature at which the ice nuclei were activated in the air.

3 RESULTS

3.1 Initial Form of Ice Crystal

Ice crystals in the initial stage were observed at 0625JST. Feb. 14, 1967 as shown in Fig.1. In the photograph, there are frozen droplets, minute columnar crystals and thin plates. Some of the frozen droplets show an intermediate form growing to columnar crystal which has traces of spoke. The concentration of ice crystals including the frozen droplets was 7 X 10^3 per liter at -25.1°C.

Size distributions of the frozen droplets and the columnar crystals are shown in Fig.2. Slopes of both distributions are approximately parallel each other, although the size of columnar crystals is larger than that of frozen droplets as a result of crystal growth. Consequently, it is thought that the minute columnar crystal in which the axial ratio is almost equal to unity may be produced by the growth of frozen droplet.

Thin plates are also seen in

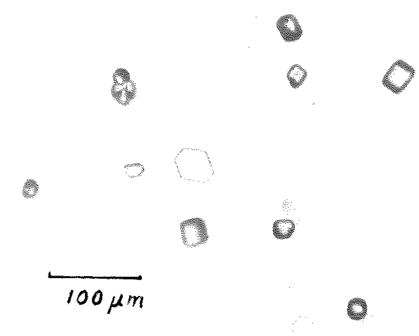

Figure 1. Photomicrograph taken at 0625 Feb. 14, 1967

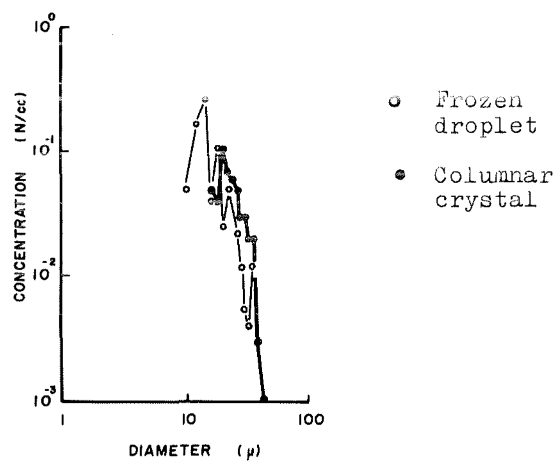

Figure 2. Size distributions of frozen droplet and columnar crystal seen in last figure

Fig.1. Their thickness is about 5 μm. It is reasonable to consider that they are produced by direct deposition of water vapor onto an ice nucleus, because the thickness is smaller than the diameter of the frozen droplet.

3.2 Size Distributions of Supercooled Droplets and Frozen Droplets

Observations of size distribution of supercooled droplets were made before and after the appearance of ice crystals . An example is shown in Fig.3.

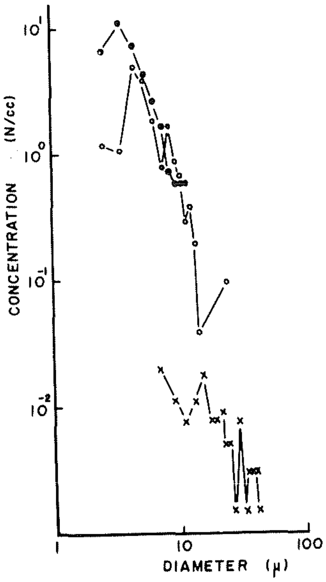

Jan. 16 and 17, 1970

o 2352JST. Supercooled droplets before the appearance of ice crystals
● 0030JST. Supercooled droplets after the appearance of ice crystals
× 0105JST. Frozen droplets

Figure 3. Size distribution of supercooled droplets and frozen droplets

In this figure, size range of supercooled droplets is from 2 to 23 μm before the appearance of ice crystals. The maximum diameter is 12 μm after the appearance of ice crystals in the fog. Moreover, the size range of frozen droplets is from 7 to 41 μm and the mean diameter is about 17 μm.

It will be inferred from these facts that some of supercooled droplets larger than 12 μm freeze and then grow to columnar crystals in the fog.

3.3 Comparison of Ice Nuclei with Ice Crystals in Concentration

Direct comparisons between ice nuclei and ice crystals in concentration were made. The results are shown in Table 1. The last column in the table is the size range of supercooled droplets in diameter before the appearance of ice crystals.

From this table, it will be seen

Table 1

DATE	TIME	TEMP. (°C)	CONCENT. of ICE CRYSTAL (N/L)	CONCENT. of ICE NUCLEI (N/L) (°C ACTIVATION TEMP.)	SIZE RANGE of FOG DROPLET
14 JAN. '73	00 20	-18.7	1		1 - 14 μm
27 JAN. '71	23 40	-18.4	4	2.7 (-20)	1 - 9
12 FEB. '71	05 05	-24.2	5	6.8 (-25)	1 - 11
15 JAN. '71	00 50	-19.2	0.6	0.5 (-18)	1 - 19
16 JAN. '70	23 30	-21.4	200	40 (-20) 150 (-25)	2 - 38
17 JAN. '70	01 33	-22.0	250	9 (-22)	2 - 23
17 JAN. '70	06 00	-25.8	900	100(-26)	
6 FEB. '70	04 40	-19.4	40	1(-18)	4 - 13
13 MAR. '70	05 16	-20.0	280	3(-19)	1 - 21

that the concentrations of ice crystals and ice nuclei are in the same order when the supercooled droplets are smaller than about 20 μm except in the case of Feb. 6, 1970. On the other hand, when the supercooled fog is made of droplets larger than about 20 μm in diameter, the concentration of ice crystals is higher one or two orders than that of ice nuclei.

4 CONCLUSION

From the observations, it is concluded that in the supercooled fog made of droplets larger than about 20 μm ice crystals are produced by freezing when an air temperature is about -20°C or lower and the concentration of ice crystals is higher than that of ice nuclei. Furthermore, it will be supposed that ice nuclei producing frozen droplets or columnar crystals are already immersed in a supercooled droplet and they become to be active with the lowering of air temperature. Thin plates as seen in section 3.1 are produced by direct deposition of water vapor onto ice nuclei.

From the observations at Asahikawa , glaciation from water cloud to ice cloud will closely relate with the size distribution of cloud droplets and the temperature in cloud.

SCAVENGING OF AEROSOL PARTICLES BY GROWING ICE CRYSTALS

Franco Prodi

IFA-CNR Sezione Microfisica
Bologna, Italy

1. INTRODUCTION

Aerosol particles are scavenged by cloud or precipitation elements through a number of mechanisms the most important of which are: aerodynamic capture, Brownian diffusion, phoretic transport of particles due to thermophoresis and diffusiophoresis (directly or through the Stefan flow) and electrostatic capture. The subject is of paramount importance in investigating the removal of particles from the atmosphere (pollutants, microorganisms, radioactive particles)and in following the life hystory of airborne nucleating agents in weather modification experiments. The definition of the role of the different mechanisms deserves also a relevant interest in aerosol physics.

A review of experimental and theoretical studies on scavenging processes has been given by Vittori and V.Prodi (1967). An experiment has been subsequently performed by Sood and Jackson (1970) restricted to the measurements of scavenging efficiency of ice and snow crystals falling at the ground through an aerosol cloud; in their experiment particles are mostly scavenged by aerodynamic capture, as crystals were not, presumably, growing or evaporating in the short time spent in the test chamber. On the other side, Magono et al. (1974) measured the scavenging efficiency of falling snow crystals in a large scale field experiment by combining the data from an aerosol counter and optical microscope observations of particles inside the collected crystals; their results indicate a collection efficiency of several tens percent, one or two orders of magnitude greater than expected from simple aerodynamic considerations. These experiments stress the need to study the role of phoretic forces in the scavenging of particles by growing ice crystals. Furthermore, as scavenging measurements at the ground cannot separate the processes which occur inside and below clouds, a laboratory investigation is demanded.

As a theoretical explanation of the process in terms of the mechanisms involved Vittori and V. Prodi (1967) suggested that growing ice crystals be efficient scavengers of aerosol particles beacause the dust-free space around supercooled cloud droplets should increase the particle concentrations in the vicinity of ice crystals; in support of this interpretation the authors presented an experiment with a fixed crystal growing in a Nakaya chamber. The model has been questioned by Slinn and Hales (1970) 's computations which demonstrated that thermophoresis is the dominant mechanism in most conditions of particle size and conductivity, assuming that the latent heat is transferred to air by conduction alone. In reply, Vittori (1973) pointed out that in the realistic conditions of crystals and droplets falling with a relative velocity in a mixed cloud the relaxation time of water vapor diffusion fields around condensing or evaporating droplets is much shorter than the thermal relaxation time of the droplets and ice crystals. Hence even theoretical investigations give a hint toward conclusive laboratory experiments as simplifying assumptions must be introduced in computations.

To determine the relative importance of the main incloud scavenging mechanisms (Brownian diffusion and phoretic forces) an experiment has been performed which reproduces the conditions of natural mixed clouds with the greatest number of predetermined parameters.

2. EXPERIMENTAL PART

Scavenging experiments with fixed hydrometeors have been frequently criticized on the basis that the heat balance is changed by the conduction through the support. In addition the fields of water vapor concentration and temperature around fixed hydrometeors are not the same as for falling ones in natural clouds where environments not deprived of water vapor are encountered and a heat dissipation by convection is experienced.

In the present experiment a cloud of supercooled droplets and aerosol particles is nucleated and the settling crystals are collected. In such a procedure a limitation derives from the short growth time and consequent small crystal sizes. Therefore the technique for detecting and locating the scavenged particles inside crystals becomes decisive. On the other side the small sizes of crystals are an advantage in investigating the role of phoretic forces in scavenging processes as the effect of aerodynamic capture is practically negligible for the very low terminal velocities.

2.1 Cloud chamber

A plexiglass cylinder (22 cm in diameter, 96 cm in height and 36.5 liters capacity) served as cloud chamber, placed in a cold room (16 m^3) the temperature of which could be regulated down to -28°C.

Two thermocouples were fixed close to the top and the bottom of the chamber, and the temperatures were determined within 0.1°C. In the base an opening with a sled allowed microscope slides to be inserted and exposed to collect settling crystals at fixed intervals without changing the conditions inside the chamber. In the upper part an ice corona with an heating cable embedded into it supplied additional water vapor ,when needed, by regulating the current through a variator. Openings were provided for spraying water droplets, injecting the aerosol and inserting the metal rod which, previously cooled in liquid nitrogen,nucleates the ice crystals. A light beam illuminates the chamber to follow the main stages of cloud evolution. Inside the chamber the aerosol is driven through a vertical pipe with holes drilled along it to have a fast mixing. The liquid water content of the cloud has been evaluated by a double weight of the spray nozzle used to generate the supercooled droplets:2.5 g m^{-3} was the liquid water content during all the experiments.

2.2 Generation and assessment of the aerosol

In a scavenging laboratory experiment one has to profit by the possibility of using an aerosol easily identifiable, of known concentration and size distribution.To the purpose monodisperse and polydisperse aerosols of carnauba wax and polydisperse NaCl aerosols have been generated. Carnauba particles have been generated by a monodisperse aerosol generator (V. Prodi,1972) which produces perfect spheres in the size range 0.2 to 2 μm with a relative standard deviation less than 0.2. Particles of NaCl have been generated by the hot wire (NiCr) technique in a flow of dry nitrogen. The aerosol characteristics have been determined by a thermal precipitator (with circular plates and a central inlet) and subsequent electron microscope examination of the deposited particles.

Attempts for producing metal aerosol particles by high voltage discharge through Mg or Fe electrodes were made and abandoned for the unsuitable shape of the aerosol particles (fluffy and chain like).

2.3 Detection and location of scavenged particles

To detect particles scavenged by growing ice crystals three techniques have been followed:

a-Electron microscope investigation of the replica of individual ice crystals. Microscope slides covered with formvar solution have been exposed in sequence to settling crystals and the formvar films have been transferred on E.M. grids and examined,(Parungo and Weickmann,1973). The film thickness however is critical as the formvar layer is thinner in correspondence with medium or large crystals and deforms under the E.M. beam. So only small (<20 μm) crystals have been successfully inspected by this technique.

b-Electron microscope investigation of the residues on slides after sublimation of the collected crystals. Clean microscope slides are located on the base of the chamber and left untill all crystals fell. The crystals collected sublimate and the residues are shaded with platinum-carbon. The film is then transferred to E.M. grids and replicas of particles counted. The population of particles sedimented or attached to the bottom of the chamber by other mechanisms than crystal scavenging has been determined by an identical experiment except the nucleation, and has been subtracted to the original population. It is difficult however by this technique to exactly locate the particles inside crystals without the corresponding replica of the original crystal.

c- Microchemical reaction on scavenged particles. A different and new approach has been given to the problem of detecting and locating submicron aerosol particles inside individual ice crystals by magnifying them to sizes observable under optical microscope. This has been obtained by modifying a technique previously developed (Prodi F. and Nagamoto,1971) to detect chlorides on any prepared extended ice surface (hailstone cross sections, sea or laboratory ice). A membrane filter, previously embedded into a solution of $AgNO_3$ and dried, is superposed to the slides on which the crystals settled and heated in a way that crystals melt through it. The filter is immediately exposed to ultra violet light and the silver chloride formed in the meanwhile is reduced to metallic silver of typical brown color. When tested for NaCl submicron particles scavenged by ice crystals the results are striking as two magnifying effects superpose: the formation within the ice matrix of a brine droplet from the original scavenged particle and the magnification of the chemical reaction on the membrane filter. At temperatures where ice and brine coexist(above the eutectic point) the salt-water systems are invariate: the temperature determines the concentration of the solution. For NaCl, the concentration of the brine droplet is 3.05 mole l^{-1} at -14°C and 1.1 mole l^{-1} at -4°C (Hoekstra et al., 1965). As an example, at -4°C the brine droplet has a volume which is 32.5 times the volume of the original dry NaCl particle; this corresponds to a magnification factor of 3.2 for the radius. This however underestimates the actual magnification factor as the brine volume is much higher close to 0°C and is difficult to evaluate. Also difficult to be determined exactly is the magnification factor by the microchemical reaction and the absorption through the filter. A total magnification factor of 10-15 is probably experienced. A problem arises in the use of a deliquescent aerosol as NaCl, which may produce, once injected into the cloud of supercooled droplets,a different size distribution. The variation in size distribution of a deliquescent aerosol with the relative humidity is recently investigated for the effects on light scattering and extinction coefficients. The theoretical lowering of vapor pressure over solutions,

$$\frac{d \ln p/p_o}{dT} = \frac{L - L_o}{R\,T^2}$$

must be supplemented in computations with the effect of droplet curvature. Hanel(1971) gives a ratio r/r_o , the wet and dry particle radius, of 5 close to 100% relative humidity. However even considering the extreme situation of all the liquid water inside the chamber redistributed over the NaCl particles,with the 7 10^4 cm^{-3} particles in the present experiment, droplets of 2 μm average radius would result; once the ice phase is initiated in the chamber the solution droplets in the small size range would be soon reduced to a size close to that of the original particle (not exactly the original size due to an hysteresis effect). In fact the lowering of partial pressure on solution droplets is proportional to the concentration of the solution; therefore very small particles cannot grow too much for deliquescence. As an example, in the vicinity of a growing ice crystal at -15°C the relative humidity is reduced to e_i/e_w=0.86, the ratio of vapor pressures over ice and supercooled water; at this relative humidity, according to Robinson and Stokes (1955) m/m_o , the ratio of masses of the droplet and the original NaCl particle, is 4.2, to which a ratio of the radii r/r_o=1.65 corresponds. Hence the use of deliquescent particles in the experiment seems justified.

3. RESULTS

Three tests have been performed.

Test 1.

Experimental conditions:

Aerosol:monodisperse carnauba wax spherical particles, 0.3 μm size,0.2 standard deviation,relative, 10^3 cm^{-3} concentration inside the chamber.

Temperature:-14.6°C .Liquid Water content: 2.5 g m^{-3}.

Results: direct E.M. observation on crystal replicas for scavenged particles was negative in small (<20 μm) crystals; larger crystals could not be observed for the deformation of the formvar film under the E.M. beam.

Test 2

Experimental conditions:

Aerosol: polydisperse carnauba wax spherical particles,of size distribution shown in Fig.1 and concentration inside the chamber of 1.8 10^5 cm^{-3}.

Temperature:-14.6°C.Liquid water content: 2.5 g m^{-3}. Additional vapor has been supplied by heating the ice corona (surface temperature of ice corona:-11°C).

Results: E.M. investigations on slide residues evidenced high scavenging efficiency for the small size particles (<0.2 μm). A quantitative evaluation of the scavenging efficiency gave E= n/n_o= 0.67, where n, the total number of scavenged particles,has been determined by difference from countings on the slides which collected crystals and on the reference ones, and n_o is the number of aerosol particles at the beginning of the experiment.

Test 3

Experimental conditions:

Aerosol:polydisperse NaCl particles of size distribution shown in Fig.1 and concentration inside the chamber of 7 10^4 cm^{-3}.

Temperature:-14°C. Liquid water content: 2.5 g m^{-3} .Additional vapor has been supplied by heating the ice corona (surface temperature of the ice corona:-11°C).

Results: the microchemical reaction on membrane filters proved to be a highly effective technique in detecting and locating scavenged NaCl particles inside crystals.The magnified spots corresponding to the particles are visible at the optical microscope. Photographs of patterns of NaCl particles scavenged by ice crystals are shown in Fig.2 for different plane shapes. As the test is destructive, it is not possible to show the replicas of the same crystals of which the patterns of scavenged particles are presented. However, a correspondence can easily be made with replicas of crystals from the same experiment; in Figs.2a and 2a' the correspondence of patterns of scavenged particles with crystals is given for an hexagonal plate with sectors and for an hexagonal plate with broad branches. It is immediately seen that the crystals are free of particles up to a certain growth stage.Then a sharp contour of scavenged particles is evidenced, which is preferred on tips, branches or dendritic protrusions which enhance the ventilation growth rate as compared with that of solid plates.

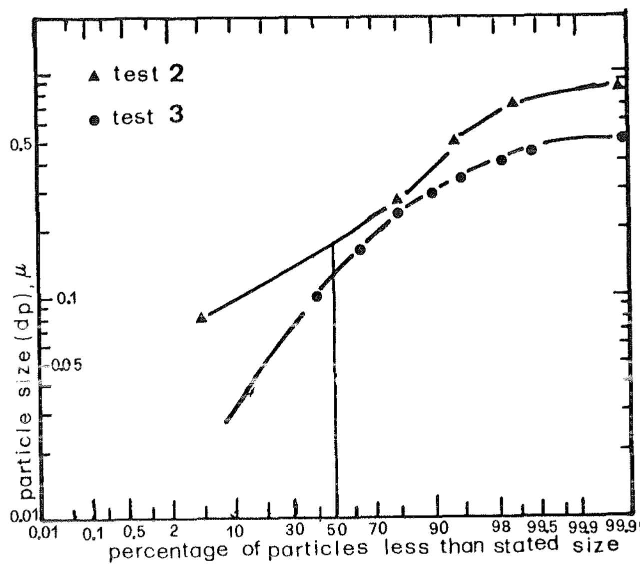

Figure 1. Size distributions of carnauba wax aerosol (triangles,Test 2), and NaCl aerosol (circles,Test 3).

Even for simple hexagonal plates without internal structure,which have a more uniform distribution of particles on the boundary,higher particle concentrations are observed in correspondence of the corners,(Fig.2b).

It is interesting to remark that in the many membrane filters developed on crystals in Test 3, a great number of particle patterns has been observed. Those presented in Fig.2 are only a restricted choice, but are very much representative and many informations can be derived by them.

Fig.2 (Front page): Patterns of microchemical reactions on membrane filters of aerosol particles scavenged by ice crystals during Test 3. Patterns for a broad branched hexagonal plate and for an hexagonal plate with sectors (a),and the corresponding crystals (a');a simple h.plate (b); small plate with tips (c); h.plate with branches (d); composite plate crystal (e).

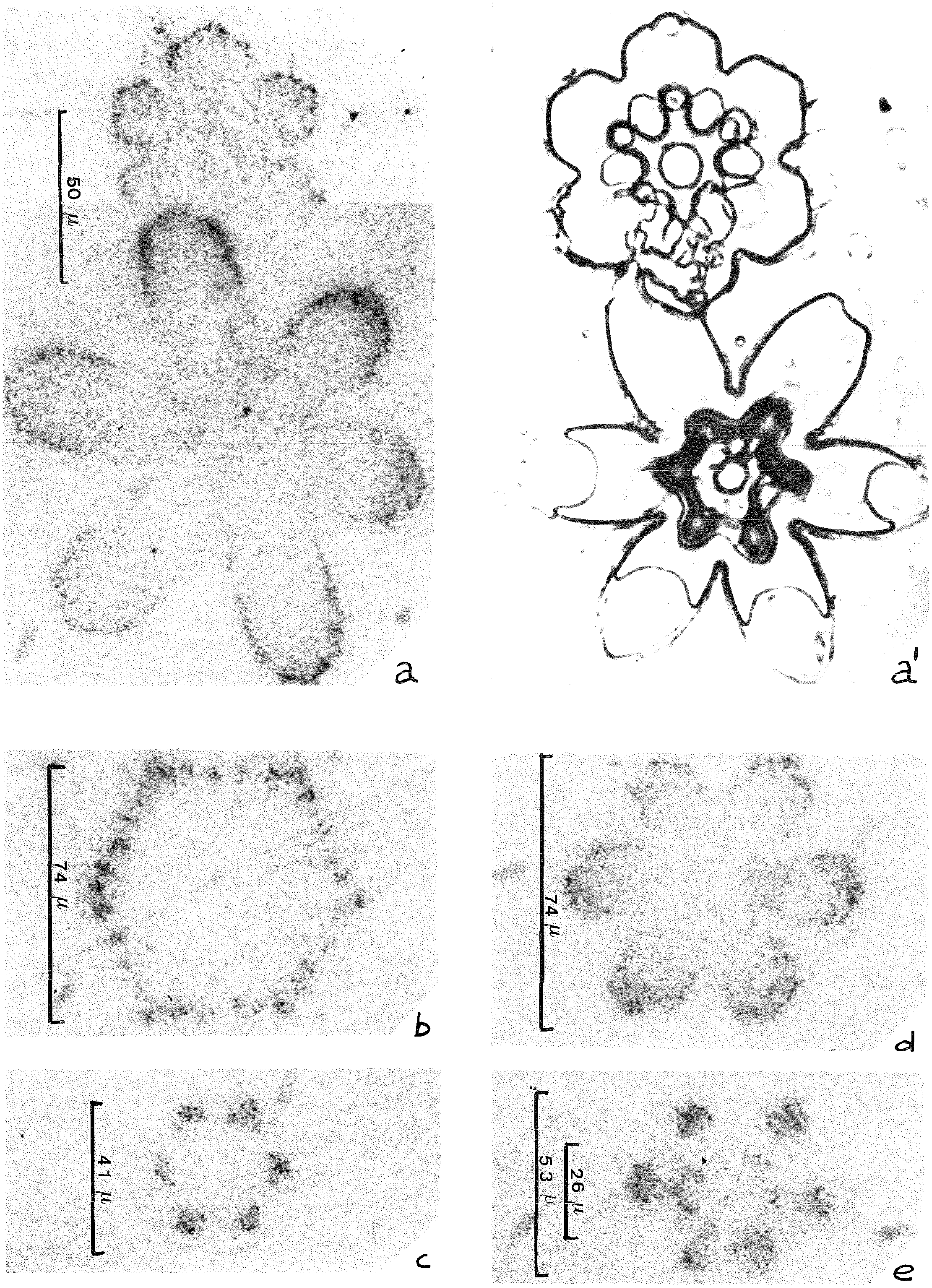
50 μ
a
a'
74 μ
b
41 μ
c
74 μ
d
26 μ
53 μ
e

First the possibility has been considered of determining the scavenging efficiency as the ratio of the number of particles scavenged by crystals and the number of particles initially in the cloud chamber. In fact the spots corresponding with particles are not only observable at the optical microscope but can also be resolved and counted. To the purpose six main crystal forms have been distinguished. A statistic of the occurrence of the different forms on the slides covered with formvar solution and exposed inside the chamber toghether with the clean slides processed by membrane filters. Then average numbers of particles for the different crystal forms have been determined on filters. These data, toghether with the relative occurrence of the different crystal forms and their size ranges are presented in Table 1. The total number of crystals settled is also determined and finally the number of particles scavenged during the experiment is calculated. An efficiency E= 0.25 results.

Table 1

Crystal forms	%	Size range μ m	Min.distance of scav.part. from the center μm	Av.numbers of part. per crystal
Simple Plates	12	75-85	35	126
Small h. plateswith tips	10	32-43	15	
H.plates with sectors	15	50-55	20	
H.plates broad br.	21	70-90	25	159
Stars	19	105-140	27	222
Composite structures	23	53-150	30-75	

A significant figure is also the minimal distance of scavenged particles from the crystal center, which is different for the various forms: shortest in the small plates with tips (15 μm) and highest in simple plates with no internal structure (35 μm). These data are also included in Table 1. The different distances of particles from the center can be explained in terms of the great variety of internal structures, ribbings and thicknesses of crystals which determine different masses, terminal velocities, ventilation, heat fluxes by conduction through the solid ice from the growing boundary toward the center.

4. DISCUSSION AND CONCLUSIONS

The present results clearly indicate that growing ice crystals once reached the size of 25 to 40 μm depending on shapes become very good scavengers of aerosol particles in experimental conditions very close to those experienced in natural clouds. There is also an indication from Test 2 of a dependence on size of the scavenging process, with a limit of 0.2 μm size; this result however needs to be strengthened. From the comparison of reaction patterns with corresponding crystals it is evidenced that particles are collected at the end of growth process: particle patterns are also boundaries of the solid crystals. This is confirmed by the values of ths scavenging efficiency, which is less than 1 in both Test 1 and Test 2 and demonstrate that aerosol is still in the chamber at the end of crystal growth.

To interpret the results it can be noticed that Brownian diffusion is not a relevant mechanism in the present experimental conditions:computations for a plane crystal of 80 μm size and a concentration of 10^4 cm^{-3} ,with 10^2 sec residence time would account for a capture of 2 10^{-2} particles on the crystal. The numbers of particles scavenged and their distributions inside crystals can be better explained in terms of phoretic forces on particles. The results are contrasting with Slinn and Hales (1971) computations which in the case of stationary hydrometeor demonstrated that thermophoresis is dominating and particles can be captured only during evaporation or sublimation. The obvious conclusion is that some of their assumptions are not realistic and need to be reexamined in order to explain the experimental results. The location of particles inside crystals is of help: up to a certain growth stage the crystals are free of particles. It is evident that in the initial stage the model of thermophoresis dominant is correct; the crystal can still be considered stationary. At larges sizes the terminal velocity increases and the assumption of stationary crystal is no more valid. A not negligible terminal velocity affects both heat dissipation and the gradient of water vapor concentration; both effects act in enhancing diffusiophoresis and Stefan flow with respect to thermophoresis. The particle patterns can be interpreted if it is considered that at a certain stage of crystal growth thermophoresis, which rejects particles away from growing surfaces, is overcome by diffusiophoresis which through the Stefan flow attaches the particles to the regions of the crystal where higher growth rates and ventilation is experienced. In fact the velocity of the Stefan flow is

$$U_s = - \frac{D}{p_a} \frac{dp_v}{dr}$$

where D is the mutual diffusion coefficient of water vapor and air, and p_a and p_v the pressure of air and vapor.

Computations on the effect of ventilation in crystal growth are presented by Jayaveera (1970). From Fig.6 in Jayaveera paper it is seen that a crystal of t= 10μm and d= 25μm has a ventilation growth which is 5% of diffusion growth while a crystal of t=20μm and d=100μm has a ventilation growth which is already 12% of diffusion growth. Ventilation affects the heat dissipation and the temperatures on the surface of crystals in a way that is diffucult to study theoretically.

The interpretation of the results in terms of ventilation is confirmed by the data in Tablel on the minimal distance of scavenged particles from the center. The distance is in fact shortest in small plates with tips and ribbings, which for the internal structure (higher masses) and the small drag coefficients experience higher terminal velocities, being equal the cross section area,than simple plates without internal structures.

The present results have important consequences in the problem of removal of aerosol particles from the atmosphere: in natural clouds the efficiency of scavenging should be maximum considering the much longer paths and residence times of crystals in the clouds, and the fact that growth by ventilation is dominant over growth by diffusion in crystals larger than 300μm. In addition it is evidenced that a great fraction of nucleating particles dispersed by various techniques and devices in weather modification experiments cannot be effective as it is scavenged by crystals which nucleated first.

The experiment is going on to test other temperatures and crystal forms, to check the results with measurements of the concentrations of the aerosol left in the chamber, to study the dependence of the efficiency on the size of particles, and to supplement informations on the internal structure of collected crystals.

Finally , an important confirmation of the interpretation of the results could derive from experiments performed in an environment at near zero gravity on orbiting laboratories. By practically eliminating the effect of ventilation only growth by diffusion would be experienced. The assumtion of a stationary hydrometeor would be correct and no particles should be scavenged due to dominating thermophoresis.

5. ACKNOWLEDGMENTS

Mr.Massimo Grisoni provided assistance during the experiments.

6. References

Hänel G.1971: New results concerning the dependence of visibility on the relative humidity and their significance in a model for visibility forecast. Beitr.Phys.Atm. 44, 2/3.

Hoekstra P.T,E. Osterkamp and W.F.Weeks,1965: The migration of liquid inclusions in single ice crystals. J.Geoph.Res. 70,5035-5041

Jayaveera K.O.L.F.,1970: Calculations of ice crystal growth. J.Atm.Sc.,28,728-736

Magono C., T.Endoh,T.Harimaya and S.Kubota,1974: A measurement of scavenging effect of falling snow crystals on the aerosol concentration. J.Met.Soc.Jap., 407-416

Parungo F.P. and H.K.Weikmann,1973: Growth of ice crystals from frozen cloud droplets. Beitr.Phys.Atm.46, 289-304

Prodi F. and C.T.Nagamoto,1971:Chloride segregation along grain boundaries in ice. J. of Glaciology, 10, 299-308

Prodi V.1972:Monodisperse solid aerosol generator. In "Assessment of airborne particles" 169-181. T.T.Mercer,P.E.Morrow,W.Stoeber Eds. C.C.Thomas,Ill.

Robinson R.A. and Stokes R.H.,1955:"Electrolytic solutions", London, Butterworths,476pp.

Slinn W.G.N. and J.M.Hales,1971:A reevaluation of the role of thermophoresis as a mechanism of in and below cloud scavenging. J.Atm.Sc,28,1465-1471

Sood S.K.and R.M.Jackson,1970:Scavenging by snow and ice crystals. In"Precipitation scavenging" AEC simposium series,Conf.700601

Vittori O.,1973:Scavenging of atmospheric particles by growing ice crystals: a contribution to a proposed mechanism. J.Atm.Sc. 30, 321-324

Vittori O. and V.Prodi,1967:Scavenging of atmospheric particles by ice crystals. J.Atm.Sc.24,533-538.

THE KINETICS OF THE HETEROGENIC EMBRYO-FORMATION

G. Miloshev, S. Todorova

Institute of Geophysics
Bulgarian Academy of Sciences
Bulgaria, Sofia, 6 Moskovska str.

In the thermodynamics of the heterogenic embryo-formation,i.e. in the presence of embryos in the atmosphere expressions are given dealing with the work necessary to form embryos which appears as a measure for the stability of the newly created phase /1,2,3,4/.

On the other hand the kinetics of the phase transition investigated by deriving expressions for the rate of formation of stable embryos of the new phase. One should mention here works in this field dealing with the theoretical deriving of the expressions for the rate and calculation of the preexponential factor /5,6,7/ based on the method of Becker-Döring/8/.

In the present work are derived the expressions for the rate of formation of liquid and crystal embryos on incompletely wettable nuclei, including the type of the preexponential factor /9, 10/. These cases are most general since derived on the corresponding boundary conditions all possible cases can be obtained (the rate of embryo formation in homogeneous water vapour on a fully wettable nucleus and an even substrate).

It was shown that liquid embryo does not embrace the nucleus on incompletely wettable nuclei /3,4/, it is formed rather as on a convex substrate (Fig.1) It was shown in the same way that crystal embryos formed on incompletely wettable isomorphous nuclei do not embrace it /11, 12/. Energeticelly the most advantageous configuration between the embryo and the nucleus are shown on Fig.2a,b. To simplify things cubic cristal embryos formed on cubic isomorphous nuclei are considered.

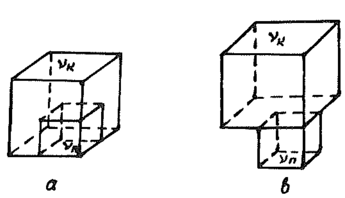

Fig.1

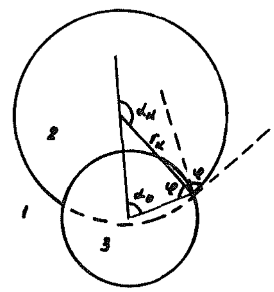

Fig.2

ψ and ψ' denote respectively work for the rupture of the bonds between two adjacent constructive elements in the lattice of the depositing crystal and between the constructive element of the depositing crystal and the constructive element of the isomorphous nucleus. The ratio ψ'/ψ in the molecular kinetic theory of Stranski-Kaishev/13/is a measure of wettability of the substrate of a crystal. When $\frac{\nu_n}{\nu_k} \lessgtr \frac{\psi'}{\psi}$ (ν_n - the number of constructive elements in the edge of the nucleus, ν_k - the number of constructive elements in the edge of the equilibrium embryo),i.e. the nucleus is smaller or greater of a given value,the respective configuration a) or b) on Fig.2 is being realised.

These preconditions were used to derive the expressions for the rate of formation of liqid and crystal embryos on incompletely wettable nuclei applying the method of Becker-Doering.A stationary condition is considered introducing in the system vapours of the liquid and incompletely wettable nuclei, later the liquid droplets and small crystals with a radius r_s are taken away, r_s being much greater than the radius r_k of the equilibrium embryo. New quantities of vapour and embryos are introduced into the system.

The rate of formation of liquid embryos (i.e. the difference in the number of droplets passing in one second in a unit of volume from class ν into class $\nu + 1$, by afixing of a new molecule to the surface and the number of droplets passing in one second in a unit of volume from class $\nu + 1$ to class ν by evaporating of one molecule) is given by the epression:

$$J = \frac{z_n a_{\nu_k}\, 2\sqrt{\frac{3A_k}{\pi kT}}}{2\frac{a_{\nu_k}}{a'_{n\to\nu_k}}\sqrt{\frac{3A_k}{\nu_k^2 \pi kT}} + \exp\left[\frac{\hat{A}_k^*}{kT}\right]\left[1-\Phi(t_0)\right]} \qquad (1)$$

where $A_k = \frac{4}{3}\pi r_k^2 \sigma$ is the work for the homogeneous formation of liquid embryo, z_n - the number of condensational nuclei introduced, a_{ν_k} - the probability of passing of the embryo to a higher class, $\Phi(t_0)$ - the integral of the fault, $\hat{A}_k^*$ - the work for the formation of embryo-freckle on an incompletely wettable embryo. (2)

$$\hat{A}_k^* = \frac{2}{3}\pi r_k^2 \sigma\left\{\left[1+\left(\frac{1-xm}{g}\right)^3 + 3x^2 m\left(\frac{x-m}{g}-1\right)\right] + x^3\left[2-3\frac{x-m}{g}+\left(\frac{x-m}{g}\right)^3\right]\right\}$$

where $x = \frac{r_0}{r_k}$, $m = \cos\varphi$, $g = \sqrt{1+\frac{r_0^2}{r_k^2}-2\frac{r_0}{r_k}\cos\varphi}$,

φ - angle of wettability.

The expression

$$\frac{a_{\nu_k}}{a'_{n\to\nu_k}} = \exp\left[\frac{2\pi r_k^2\sigma}{kT}x^2\left(1-\frac{x-m}{g}\right)(1-m)\right] \qquad (3)$$

is the ratio of the probability of passing of the embryo to a higher class and the probability of formation of preembryo on the nucleus.

Fig. 3 shows the dependence of

$$-\lg\varphi = \lg J + const = -\lg\left\{2\frac{a_{\nu_k}}{a'_{n\to\nu_k}}\sqrt{\frac{3A_k}{\nu_k^2\pi kT}} + \exp\left[\hat{A}_k^*/kT\right]\left[1-\Phi(t_0)\right]\right\} \qquad (4)$$

on the radius and angle of wettability.

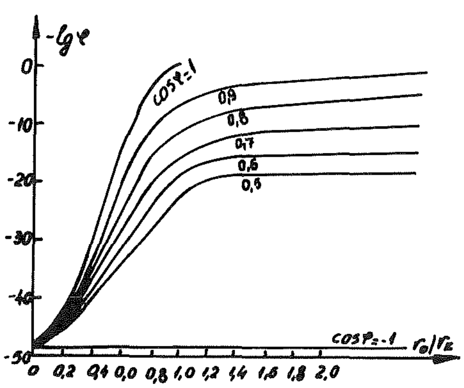

Fig.3

From expression(1) at adequate boundary conditions the expressions for the rate of formation of embryos in homogenious water vapour (r_0=0), on fully wettable nucleus (φ=0) and on an even substrate ($r_0 \to \infty$) can be formulated. The expression is given in the following way:

$$J = \frac{2z_n a_{\nu_k}\sqrt{\frac{3A_k}{\pi kT}}}{2\sqrt{\frac{3A_k}{\pi kT}}\exp\left[-\hat{A}_k^0/kT\right] + \left[1-\Phi(t_0)\right]}\cdot\exp\left[-\hat{A}_k^*/kT\right] \qquad (5)$$

where $\hat{A}_k^0$ is the work for the formation of an embryo freckle on a substrate of its own. The multiplier before $e^{-\hat{A}_k^*/kT}$ by analogy with the expression for the rate of formation of embryos in homogenious water vapour, given by Volmer/14/ can be called kinetic factor, which depends on the number and the size of the nuclei and on the manner of formation of the embryo.

The rate of formation of crystal embryos on incompletely wettable isomorphous nuclei is given by the expression:

$$J = \frac{z_n a_{\nu_k}}{\nu_k}\,\frac{2\sqrt{\frac{3A_k}{\pi kT}}}{2\frac{a_{\nu_k}}{a'_{\nu_n}}\sqrt{\frac{3A_k}{\nu_k^2\pi kT}} + \left[1-\Phi(t_0)\right]\exp\left[A_k B/kT\right]} \qquad (6)$$

$A_k = \nu_k^2\psi$ is the work for formation of a cubic crystal embryo in homogenious water vapour with ν_k constructive elements in the edge; B is a factor which accounts for the presence of nuclei with a definite size and wettability.

refers to the size of $B = 1+2\frac{\nu_n^3}{\nu_k^3} - 3\frac{\nu_n^2}{\nu_k^2}\frac{\psi'}{\psi}$ nuclei with $\frac{\nu_n}{\nu_k} < \frac{\psi'}{\psi}$

$B = 1 - \frac{\nu_n^2}{\nu_k^2}\frac{\psi'}{\psi}$ for nuclei with $\frac{\nu_n}{\nu_k} > \frac{\psi'}{\psi}$

The ratio of probability a_{ν_k} of passing of the crystal to a highes class and the probability a'_{ν_n} of formation of the first layer on an alien nucleus with $\frac{\nu_n}{\nu_k} < \frac{\psi'}{\psi}$ is

$$\frac{a_{\nu_k}}{a'_{\nu_n}} = \exp\left\{\frac{3\nu_n^2\psi}{kT}\left(1-\frac{\psi'}{\psi}\right)\right\} \qquad (7)$$

and for nuclei with $\frac{\nu_n}{\nu_k} > \frac{\psi'}{\psi}$ is

$$\frac{a_{\nu_k}}{a'_{\nu_n}} = \exp\left\{\left[\nu_n^2\psi\left(1-\frac{\psi'}{\psi}\right) + 2\nu_n^2\psi\left(1-\frac{\nu_n}{\nu_k}\right)\right]/kT\right\} \qquad (8)$$

The expression (6) gives a possibility to derive particular cases for the rate of formation of crystal embryos in homogenious water vapour (ν_n =0), on a completely wettable nucleous (ψ'/ψ=1) and on an even substrate ($\nu_n = \nu_k$).

Fig.4 shows the dependence of

$$-\lg\varphi = \lg J + const = -\lg\left\{2\frac{a_{\nu_k}}{a'_{\nu_n}}\sqrt{\frac{3A_k}{\nu_k^2\pi kT}} + \exp\left[A_k B/kT\right]\left[1-\Phi(t_0)\right]\right\} \qquad (9)$$

on the size and the degree of wettability of the nuclei.

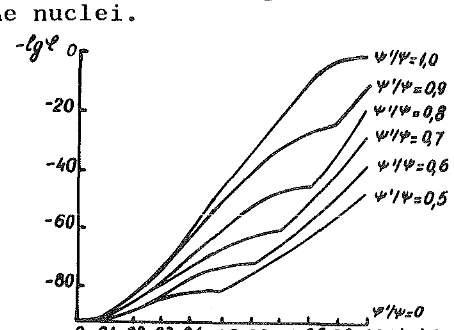

Fig.4

The expression (6) can be written in the following way:

$$J = \frac{2 Z_n a_{\nu_k} \sqrt{\frac{3A_k}{\pi kT}}}{2\sqrt{\frac{3A_k}{\pi kT}} \exp(-A_k B^0/kT) + [1-\Phi(t_0)]} \cdot \exp[-A_k B/kT] \quad (10)$$

where $A_k B^0 = \frac{\nu_k^2 \psi}{kT}\left(1 + \frac{\nu_{11}^3}{\nu_k^3} - 3\frac{\nu_n^2}{\nu_k^2}\right)$ is the work for formation of a crystal embryo with the size of a nucleus as on a substrate of its qwn. Again, as in the case of formation of liquid embryos the multiplier before $\exp[-A_k B/kT]$ is the kinetic factor, which can not be taken as a constant with a definite numeric value, as it depends on the number and size of the nuclei, the manner of embryo formation, the temperature and the saturation.

REFERENCES

1. Krastanov,L.Meteorol.Zeitschr.58 (2) 37,1947.
2. Krastanov,L.Annuaire de l'universite de Sofia t.XLIV,1.
3. FletcherN.H. Journal of chemical physics, vol.29,3,1958.
4. Krastanov,L.and G.Miloshev,C.R. de l'Acad.bulg.des Sciences,t.16 No3,1962.
5. Kaishev R.and I.Stranski.Annuaire de l'universite de Sofia t.XXXII,2 (203-234).
6. Kaishev R.,Zeitschr.Elektrochem; 61,35, 1957.
7. Kaishev R. and B.Mutafchiev,Proc. chem.Inst.t.VII.
8. Becker R.and W.Doering.Ann.d.physik 24,719,1935.
9. Miloshev G.,S.Todorova, C.R.de l'Akad. des Sciences,t.28,No2,1975
10. Miloshev,G.,S.Todorova, C.R.deL'Akad des Sciences,t.28,No3, 1975.
11. Miloshev,G.C.R.de l'Acad.bulg.des Sciences,t.16,No5,6,1963.
12. Милошев Г. Труды Главной Геоф. Обсерв.,Ленинград 176, 1965
13. Странски И.,Каишев УФН,т.21,№4 1939
14. Volmer,M.Kinetik der Phasenbildung, Dresden u.Leipzig,1939

GROWTH MODES OF ATMOSPHERIC ICE CRYSTALS

Helmut K. Weickmann

Atmospheric Physics and Chemistry Laboratory
National Oceanic and Atmospheric Administration
Boulder, Colorado U.S.A.

1. INTRODUCTION

Nature has an almost limitless wealth of snow crystal forms which are to a certain extent reflected in Figure 1 (Nakaya, 1951).

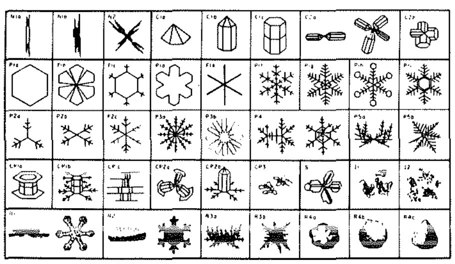

Figure 1. Snow Crystal Habits According to Nakaya, 1951.

We note from the figure that dendritic forms have the greatest variety as stars, sector stars, branched stars, and fernlike branched stars. These forms occur also as spatial dendrites. If the forms are plotted in a diagram which has the temperature as abcissa and a humidity term as ordinate, a certain system appears in which dendrites occupy the temperature range between about -10 and -20 °C, Figure 2 (Magono and Lee, 1966).

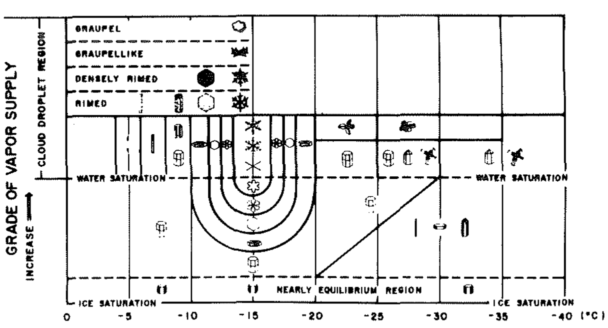

Figure 2. Temperature and Humidity Conditions for the Growth of Natural Snow Crystals of Various Types. (Magono and Lee, 1966)

The wealth of crystal shapes and habits follows from the fact that atmospheric crystals mostly grow in a water saturated environment, i.e., in a water cloud, and consequently develop supersaturation forms. It is often overlooked that crystals growing at or near ice saturation over the entire atmospheric temperature range develop a prismatic habit. Subsequently we are mainly interested in the supersaturation growth process inside a water cloud as these crystals are designed to be nature's "workhorses" for scavenging the water content of the clouds and bringing it down to the ground as precipitation. The significance of these crystal types is by far not yet understood, but their habit has the flexibility of compensating for crystal concentrations which seem either too high or too low for an efficient precipitation process.

We are convinced that intensive research into growth of atmospheric ice crystals will occupy cloud physicists over the next 10 to 15 years and that only in the understanding of these processes will artificial cloud modification be put on a sure footing. In atmospheric ice crystals we find 3 major modes of growth: 1) the strictly crystalline growth, 2) the dendritic growth in which a thin water film over the base plane plays a decisive role, and 3) growth from the melt, in which the water film spreads over the entire crystal.

2. THE CRYSTALLINE GROWTH MODE

Two schools exist which explain the growth of crystal surfaces: one school goes back to analytical developments of Volmer, Stranski, Kaishev, and others. It claims that for the development of a new crystal surface a two-dimensional nucleus must form on the crystal surface which is sufficiently large to bind the condensing molecules and to start a new plane. The other school leads to Frank who postulates that the new plane may begin at any dislocation without the formation of a two-dimensional nucleus and that the growth proceeds from this dislocation in a spiral form.

The formation of the two-dimensional nucleus requires energy which is expressed as supersaturation much the same way as supersaturation occurs for a three dimensional nucleus which is required for the phase transition from vapor to water or ice. The idealistic concept of the nature of a two-dimensional nucleus is that it consists of a sufficiently large number of molecules, so that arriving molecules do not re-evaporate but become attached to it. Since it is, however, known that the steps in which new crystal surfaces grow can consist of a great number of individual layers, it is quite possible that aerosol particles adsorbed on the surface can also act as two-dimensional nuclei. Depending on the binding forces of the molecules in the crystal lattice certain areas exist on the crystal surface where the formation of two-dimensional nuclei is favored. For metallic crystals the binding forces are Van der Waals forces, consequently two-dimensional nuclei are preferably formed in the center of the plane where all neighbors help to bind the nucleus, for ionic crystals whose binding forces are electrostatic, these preferred locations are however the crystal corners and edges and at last the center. Here, the fields of many neighbors unfavorably affect the binding of the new two-dimensional nucleus. Since the binding forces in ice are electrostatic, ice crystal planes should therefore be expected to grow from the corners and along the edges. The energy which is required to form two-dimensional surface nuclei is proportional to the ratio $\frac{p_W}{p_E}$, of the vapor pressure over water and ice, while the number of molecules ready to condense is proportional to the difference of the vapor pressures, $p_W - p_E$. Both magnitudes are shown in Figure 3.

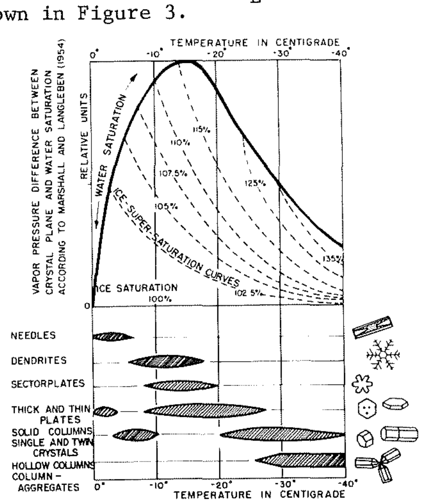

Figure 3. Ice Crystal Habits Depending on Relative and Absolute Ice Supersaturation.

The relative supersaturation available at water saturation for the formation of two-dimensional nuclei is determined by the intersections between the dashed curves and the solid curve while the solid curve reflects $p_W - p_E$ which is proportional to the number of condensable molecules. The diagram illustrates the importance of the 3 parameters: temperature, relative supersaturation, and difference between p_W and p_E. We understand that a delicate equilibrium condition may be required to complete the growth of a crystal plane: the frequency with which two-dimensional nuclei form must be linked to the time period which is necessary to fill in the surface with molecules. One can think of a growth condition where the supersaturation with respect to ice is sufficiently high that the formation of two-dimensional nuclei occurs so frequently that the availability of molecules is insufficient to complete the crystal plane before a new plane starts. In the case of the base plane of the ice crystal this means that it remains unfinished at the center, while the prism plane grows from the upper edge and the corners and ends up in the form of a two-pronged fork. If the planes become finished, a center hole remains in the base plane and a slit in the lower part of the prism plane. Figure 4 shows this growth mode schematically,

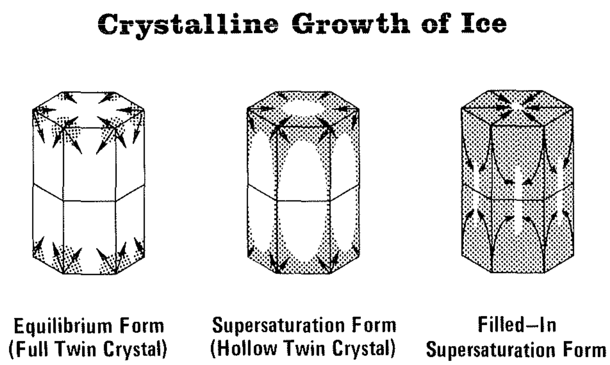

Figure 4. Schematic Crystalline Growth Process of Ice Crystals.

while Figure 5 and Figure 6 show the corresponding crystal surfaces as we photographed them in Cirrus clouds. Figure 5a shows a typical fork-like prism plane, while Figure 5b shows the prism plane closed except for a slit near the original crystal base. Figure 6a shows two ring-like hexagonal base planes; note that the hexagons are not very symmetrical. Figures 6b and 6c are crystals which have been collected in a Cumulonimbus anvil at -15 to -20 °C. They essentially show base planes in various stages of completeness. The crystals shown in Figures 5a, 5b, and 6a have grown in a Cirrocumulus cloud of a mountain wave with an updraft of about 1 m/sec. and at a temperature of -37 to -41 °C.

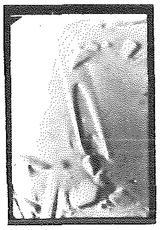

5a

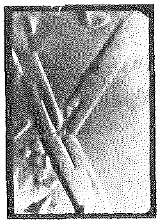

5b

Figure 5. Prism Planes of Cirrus Crystals in Various Stages of Growth.

6a

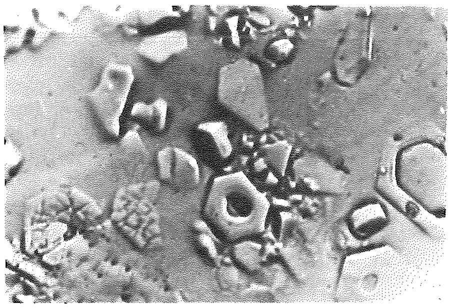

6b

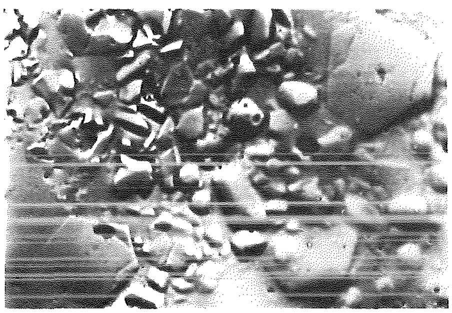

6c

Figure 6. Base Planes of Ice Crystals in Cirrus Clouds and Cumulonimbus Anvil in Various Growth Stages.

The conclusion from these figures is apparently that the two-dimensional surface nucleation process applies for the growth of ice crystals at low temperatures.

3. THE DENDRITIC GROWTH MODE

Coming from low temperatures and going to higher ones, we find that -20 °C is an interesting threshold. Here, richly branched crystals appear which have grown essentially in the direction of the secondary axes. This habit change appears to be the consequence of a semiliquid film which spreads over the base plane and which greatly improves the surface diffusion of the H_2O molecules. They appear to move easily in the base plane and along the edges onto the almost non-developed prism planes. This range of dendritic growth extends from -20 to about -10 °C with strong dependence on the relative humidity.

The Magono and Lee (1966) diagram, Figure 2, shows the habit dependence of snow crystals on both the temperature and humidity. The importance of humidity is shown particularly in the crystal ladder for -15 °C which reaches from ice saturation to the cloud droplet region or from prisms to the richly branched (and rimed) dendrites. The existence of a quasi-liquid water film on an ice surface at conditions near water saturation has been anticipated by Nakaya, Hanajima and Muguruma (1958). At temperatures between -5 and -20 °C they observed that water droplets tended to roll or glide over a clean ice surface - not freeze to it! - becoming smaller and disappearing within about 1/4 sec. Their track remained visible as a little ridge for a few minutes. Only droplets smaller than 5 μm in diameter behaved like this, larger ones fell onto the surface and froze. We have observed the same phenomenon at temperatures above freezing on the glassplate of an Aitken or Scholz-type nucleus counter. The small droplets which formed on nuclei seemed to roll for awhile over the surface until they disappeared. The theory of the quasi-liquid film has been developed by Lacmann and Stranski (1972). They define an equilibrium film thickness δ_{GL} as

$$\delta_{GL} = -A + \left[\frac{A\ \Delta\sigma_{\infty} V_m}{kT\ \ln\ (p_w/p_E)}\right]. \qquad (1)$$

Here A is a parameter of the radius of action of the intermolecular forces.

$\Delta\sigma_{\infty}$ is defined by

$-\Delta\sigma_{\infty} = \sigma_E - \sigma_w - \sigma_{E/w}$ (σ being the specific interfacial free energy, $E \rightarrow$ ice, $w \rightarrow$ water; E/w interface ice/water).

$\Delta\delta(\sigma)$ must be equal to zero at $\Delta\sigma = 0$ and it must be constant for great σ-values ($-\Delta\sigma_{\infty}$).

V_m is the molecular volume in the quasi-liquid film

k is Boltzmann constant

T is temperature

p_w vapor pressure with respect to a water surface

p_E vapor pressure with respect to an ice surface

For p_E equal p_w the film thickness becomes infinite, with decreasing temperature δ_{GL} decreases too. Of special importance becomes the behavior of the film near the corners of the crystal. The authors show that near the melting point the film is so thick that it covers the corners, Figure 7a, while in the temperature range of -15 °C with diminishing film thickness the corners remain unwetted, Figure 7b. At the corners the crystal realizes therefore the full supersaturation while in the surface the supersaturation of the vapor phase in reference to the quasi-liquid film is smaller than that with reference to the ice phase.

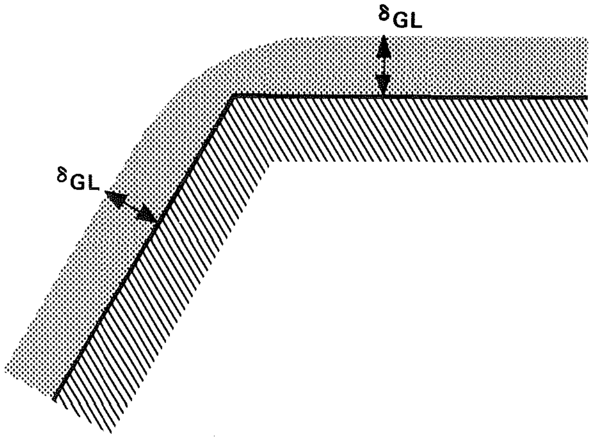

7a

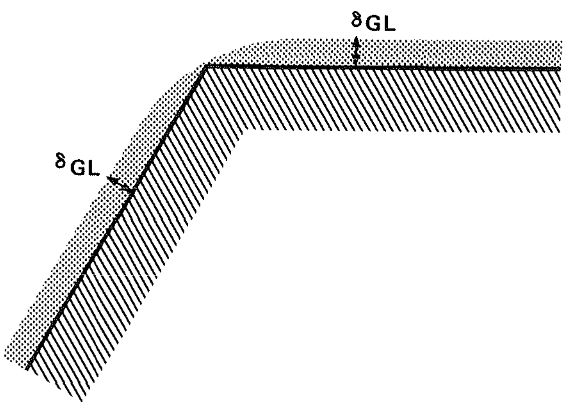

7b

Figure 7. Schematic Drawing of Liquid Film on Ice Crystal at Warm and Cold Temperatures.

Following Figure 8 these conditions cause the formation of dendrites.

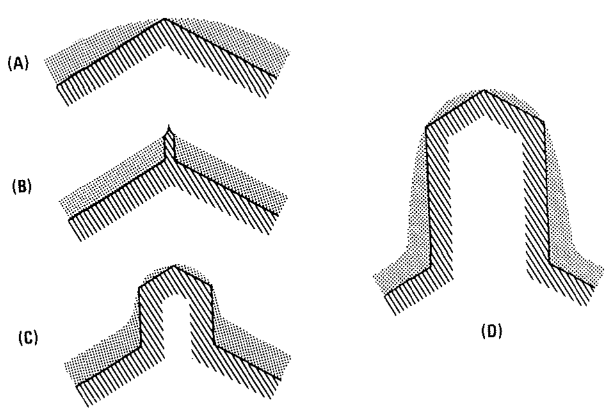

Figure 8. Schematic Development of Dendrites According to Laemann and Stranski, 1972.

In reality, the conditions for the establishment of a liquid film will vary for base planes and prism planes of an ice crystal. Apparently in the dendrite growth mode the film is established over the base plane causing the striking molecules to be bound primarily along the edges and the thin ($10\bar{1}0$) surfaces. This appears to follow from the Nakaya and Terada (1935) observation that dendrites hardly grow in thickness, but essentially in size, Table 1.

Diameter mm	Mean Thickness mm	Mean Value mm
2.35	0.009	
2.5	0.012	
2.8	0.011	
2.9	0.015	0.011 ± 0.0015
3.0	0.009	
3.5	0.011	
5.0	0.010	

According to Nakaya and Terada (1935)

Table 1. Thickness of Dendrites Versus Diameter.

4. GROWTH MODES AT TEMPERATURES WARMER THAN -10 °C

The proximity to Boulder of the Denver Weather Office with its radiosonde station permits correlation, during a snow fall event, of the lapse rate and humidity conditions with the crystal habits that formed in the corresponding clouds. At temperatures warmer than -10 °C for the cloud top temperature we observed a phenomenon which was in the beginning surprising: the crystals that fell from such clouds always consisted of little graupels which seemed to be frozen together from small prisms - if a habit of the individual particles could be established at all. We assume that the quasi-liquid film extends now over the base and prism planes; then none of the crystal planes will realize the full supersaturation of the vapor pressure difference between ice and water and the entire crystal will grow very slowly, much like a water droplet. Then riming will become the more efficient growth process. In this temperature range it may also become significant how the original crystal formed: through an embedded freezing nucleus or through contact from the outside. In the former case a unit crystal or poly-crystal may develop around the freezing nucleus, while in the latter case a thin frozen shell may develop and burst causing the formation of a needle-like whisker.

It appears that in the case of ice, whisker formation is essentially limited to warm temperatures on a base of rotten wood, a moist soil, and the water for the growth of the ice columns must be delivered through a small capillary opening (Nabarro and Jackson, 1958; Muehleisen and Lämmle, 1975). The latter authors emphasize also the need for temperatures between 0 °C and -4 °C, and the existence of capillary openings.

Of course in this temperature range very few ice nuclei exist and it could very well be that a capillary could be replaced by a lone freezing nucleus as was actually observed by Serpolay and Toye (1962). Once a whisker, or thin needle, starts growing in the atmosphere the pointed tips may pierce the water film and realize the ice supersaturation for growth from the vapor aside from their riming efficiency. The whisker character of ice needles would follow from the contact nucleation of a large cloud droplet causing the freezing of a thin shell around the droplet which breaks somewhere, thus allowing the water to squeeze out as whisker.

5. CORRECTION TERMS FOR VENTILATION AND CLOUD DROPLET ENVIRONMENT

It would appear that nature is missing something in the temperature range warmer than -10 °C, as here the account of precipitable water increases while not only the ice nucleation becomes inefficient, but also dendrites no longer form. Needles do appear sometimes near -4 °C, but they are somewhat "unreliable." Apparently we cannot consider each temperature interval by itself, we have to consider them in their larger context within the precipitating cloud system. This usually reaches at least to the -15 to -20 °C levels. Then nature can produce all kinds of dendrites - stellar, spatial, or rimed which the precipitation system permits. These dendrites are not only crystals whose surface is maximum for a given volume and is therefore most effective for diffusional growth from the vapor, but whose surface is on top richly branched thus making the crystal an excellent scavenger of all cloud droplets. These efficient particles then fall through the water clouds below the -10 °C level and collect through riming many more cloud droplets than the "virgin" little graupels would do which form originally in this temperature range. The dendrites also grow through aggregation by interlocking and adhesion. In the needle range, sufficiently large droplets produce needles upon riming, thus continuously improving the scavenging of cloud droplets. Large to giant flakes appear to form in this way.

It is here where we would like to call attention to two important corrections in the growth equation for snow crystals: the ventilation term and the cloud droplet term.

The Ventilation Term

Following Cotton (1970) the rate of mass growth of an ice crystal is given by

$$\frac{dX_i}{dt} = 4\pi\, CD_v \left[\rho_w - \rho_w(r) \right] . \qquad (2)$$

Where C represents the capacitance of the crystal corresponding to an electrostatic analog,

D_v is the diffusivity of water vapor in air

ρ_w is the vapor density at some distance from the crystal, and

$\rho_w(r)$ is the vapor density at a distance from the surface of the crystal corresponding to the mean free path of a molecule.

Considering the heat released by condensation and riming on the crystal and the molecular diffusion on the crystal the rate of mass growth becomes eventually

$$\frac{dX_i}{dt} = 4\pi\, C(S - 1)\, G(T,P) - F(\dot{x}_R,T,P) \qquad (3)$$

whereby

$$G(T,P) = (A_k + B_k)^{-1} = \left\{ \frac{m_w L_s^2}{k_i R_a T^2} + \frac{R_a}{m_w} \frac{T}{D_v e_s(T)} \right\}^{-1} \qquad (4)$$

$$F(\dot{x}_r,T,P) = \frac{\left.\frac{m_w}{R_a} L_s L_f \frac{dX_i}{dt}\right]_R}{k_i T^2 (A_k + B_k)} \qquad (5)$$

The following denominations apply:

X_i mass of an individual ice crystal

S cloud saturation ratio

m_w molecular weight of water

L_s latent heat of sublimation

L_f latent heat of fusion

k_i molecular thermal conductivity

R_a gas constant of air

T cloud temperature

e_s saturation vapor pressure

$\dot{x}_R$ rate of crystal growth by riming

If the crystal develops a significant fall velocity, its diffusion field becomes deformed and a ventilation convection factor must be applied (Shiskin, 1965; Thorpe and Mason, 1966). The mass growth equation becomes then

$$\left.\frac{dX_i}{dt}\right]_s = [4\pi\, C(S - 1)\, G(T,P) - F(\dot{x}_r,T,P)](1 + 0.229 \sqrt{R_e}). \qquad (6)$$

This is valid for $10 < R_e < 200$ and for air temperatures between 0 and -20 °C.

The Cloud Droplet Term

The cloud droplet term has been derived by Marshall and Langleben, (1954) in due consideration that, for crystals growing in a water cloud, the cloud droplets present individual sources of water vapor in the immediate proximity of the crystal. The correction becomes $1 + ka$, where $k = (4\pi\, \Sigma r)^{1/2}$ and a is the radius of the crystal and snowflake, respectively. C in equation (3) would be replaced by a, assuming a roughly circular snowflake shape. Table 2 shows that

The correction depends on both concentration and cloud droplet radius, r.

W g/m^3	N ml^{-1}	r x 10^{-4} cm	k
4	100	22	1.66
4	1,000	10	3.55
4	4,000	6	5.5
4	10,000	4.6	7.6

Table 2. Cloud Droplet Correction of Crystal Growth According to Marshall and Langleben, 1954.

It is also highly dependent on the snowflake size as the rate of growth of a snowflake with 1 cm diameter and for average continental microphysics for a convective cloud (4 g/m^3, 1000 droplets/ml, 10 μm radius) becomes 4.55 times that of a snowflake growing at water saturation but without cloud.

We felt is is necessary to call attention to this little known correction which will play a role in convective clouds where at times giant snowflakes, consisting of dendrites, rimed droplets and needles, form. Studies in the laboratory of the significance of the Marshall-Langleben correction have been carried out by Glicki (1959).

6. CONCLUSIONS

We hope to have shown that the forms of ice and snow crystals in the atmosphere take part in various crystallographic growth processes such as normal crystallographic growth from vapor, dendritic growth, growth from the melt and whisker-type growth. Various nucleation processes contribute in still further increasing the crystal varieties - deposition, freezing, and contact nucleation. Important corrections affecting the rate of growth are the ventilation factor and a cloud droplet term. It appears that the great variety of crystal habits is nature's solution for an optimum scavenging efficiency for precipitable water.

REFERENCES

Cotton, W.R., 1970: A numerical simulation of precipitation development in supercooled Cumuli, Report No. 17, NSF GA-13818, Department of Meteorology, The Pennsylvania State University, 178 pp.

Glicki, N.G., 1959: Growth of ice crystals from the vapor, in A.V. Shubnikov and N.N. Sheftal (ed) 1962, Growth of Crystals; Reports Second Conf. on Crystal Growth, Moscow, USSR, 1959, Consultants Bureau, New York, 1962, 96-100.

Lacmann, R. and I.N. Stranski, 1972: The growth of snow crystals, *J. of Crystal Growth*, 13/14, 236-240.

Magono, C. and C.W. Lee, 1966: Meteorological classification of natural snow crystals, *J. Faculty of Science*, Hokkaido University Series VII (Geophysics), Vol. 2, 321-335.

Marshall, J.S. and M.P. Langleben, 1954: A theory of snow-crystal habit and growth, *J. Meteorology*, 11, 104-120.

Muehleisen, R. and A. Lämmle, 1975: Nene Untersuchungen zur Entstehung von Kammeis (Haareis), *Meteorolog. Rundschau*, 28, 55-60.

Nabarro, I.R.N. and P.J. Jackson, 1958: Growth of crystal whiskers, in Growth and Perfection of Crystals, editors R.H. Doremus, B.W. Roberts, David Turnbull, Proceedings of Int'l. Conf. on Crystal Growth, August 27-29, 1958, New York, John Wiley and Sons, Inc., 13-101.

Nakaya, U. and T. Terada, Jr., 1935: Simultaneous observations of the mass falling velocity, and form of individual snow crystals, *J. Faculty of Science*, Hokkaido University, Series II, (Physics), Vol. 1, 191.

Nakaya, U., 1951: The formation of ice crystals, in Compendium of Meteorology, American Meteorological Society, Boston, p. 207.

Nakaya, U., M. Hanajima, and J. Muguruma, 1958; Physical investigations on the growth of snow crystals, *J. Faculty of Science*, Hokkaido University, Series II (Physics), Vol. 5, 87-118.

Serpolay, R. and M.J. Toye, 1963: Un noveau processus pour la croissance de la glace sur les noyaux glacogenes, *J. de Recherches Atmospherique*, 1963, 85-91.

Shiskin, N.S., 1965: On snow crystal growth in clouds, Supplement Proceedings, Int'l. Conf. Cloud Physics, Tokyo, 136-146.

Thorpe, A.D. and B.J. Mason, 1966: The evaporation of ice spheres and ice crystals, *British J. Appl. Phys.*, 17, 541.

SNOW CRYSTALS PHOTOGRAPHED IN SITU IN WINTER STORMS

Nicholas J. Carrera

Cloud Physics Laboratory
University of Chicago
Chicago, Illinois

1. INTRODUCTION

Natural snow crystals have been studied in diverse ways by many researchers both at ground level and in the air (e.g., Bentley and Humphreys, 1931; Schaefer, 1941; Weickmann, 1947; Borovikov, 1953; Nakaya, 1954; MacCready and Todd, 1964; Magono and Tazawa, 1966). We have constructed an airborne particle camera, following the design of Cannon (1974, 1975) for use in the University of Chicago cloud physics research aircraft. On flights in winter storms in central Illinois we have obtained photographs of snow crystals which differ from those obtained previously, in that the present pictures are of crystals which remained in situ in the free air outside the aircraft. This method has yielded photographs of large, delicate crystals and aggregates which were unobtainable using previous techniques of airborne sampling.

2. SNOW CRYSTAL GROWTH

Investigations of growth under natural and laboratory conditions have established the nature of the variation of snow crystal habit with temperature and supersaturation (Kobayashi, 1961; Ono, 1970; and previous references). Planar growth by vapor deposition takes place between 0 and -4C and between -10 and -22C; prismatic growth occurs from -4 to -10C and at temperatures below -22C. Secondary growth features are determined by the degree of supersaturation with respect to ice. One feature worth noting is that at sufficiently high supersaturation (typically attained in low and mid-level clouds) dendritic growth takes place at temperatures from -12 to -16C, which also corresponds to the temperature region of highest growth rate by vapor deposition (Mason, 1953).

3. DISCUSSION OF THE PICTURES

3.1 Flight 14: Figure 1

All crystals seen during this flight were prismatic. At 9000 ft only individual prisms were seen, but aggregation was seen below this altitude. Of 20 aggregates consisting of two prisms of nearly equal size, the most common juncture was at a 90° angle, in a "T" or "L" configuration, as shown in pictures 10 and 17. "Y" and "V" patterns were also seen, as in pictures 12 and 13. We saw no clear examples of the "X" configuration (two prisms mutually bisecting at 90°) described by Jayaweera and Mason (1965, 1966) and by Nakaya (1954).

Considerable cloud water was present, as evidenced by the impaction of droplets on the aircraft windshield and by the occurrence of airframe icing. At least eight double-dot images like that in picture 5 were obtained. These images result from the refraction of light by water drops (Cannon, 1970) and those seen in our photographs correspond to drops ranging from 300 to 800 μm in diameter. A rough calculation (good to within a factor of 5) indicates that the concentration within cloud from 7000 to 9000 ft of drops larger than 300 μm was about 0.1/liter. The presence of smaller cloud droplets is indicated also, by the numerous dots due to rime droplets, as seen, for example in pictures 3 and 13.

3.2 Flights 15-17: Figure 2

Flight 15 yielded only a few pictures of interest, but one of them, picture 1, is a gem. It is composed of two particles, a stellar and an aggregate of perhaps one or more stellars and columns, linked together by the merest touch of a fingertip. This instance of Nature imitating Art must certainly approach the lower limit of contact necessary to cause aggregation!

Flight 16 was made in cloud which was being seeded by fine ice crystals from a much higher cloud. Despite this seeding, snow crystal concentration in the mid-level cloud was not especially high, and few pictures of crystals were obtained. Most crystals were planar. A particularly nice example of plane dendritic growth is seen in the extensively rimed aggregate in picture 3.

Flight 17 was made in the same storm system as was flight 16, but some important changes had occurred between flights: the tops of the mid-level clouds we flew in had become higher and

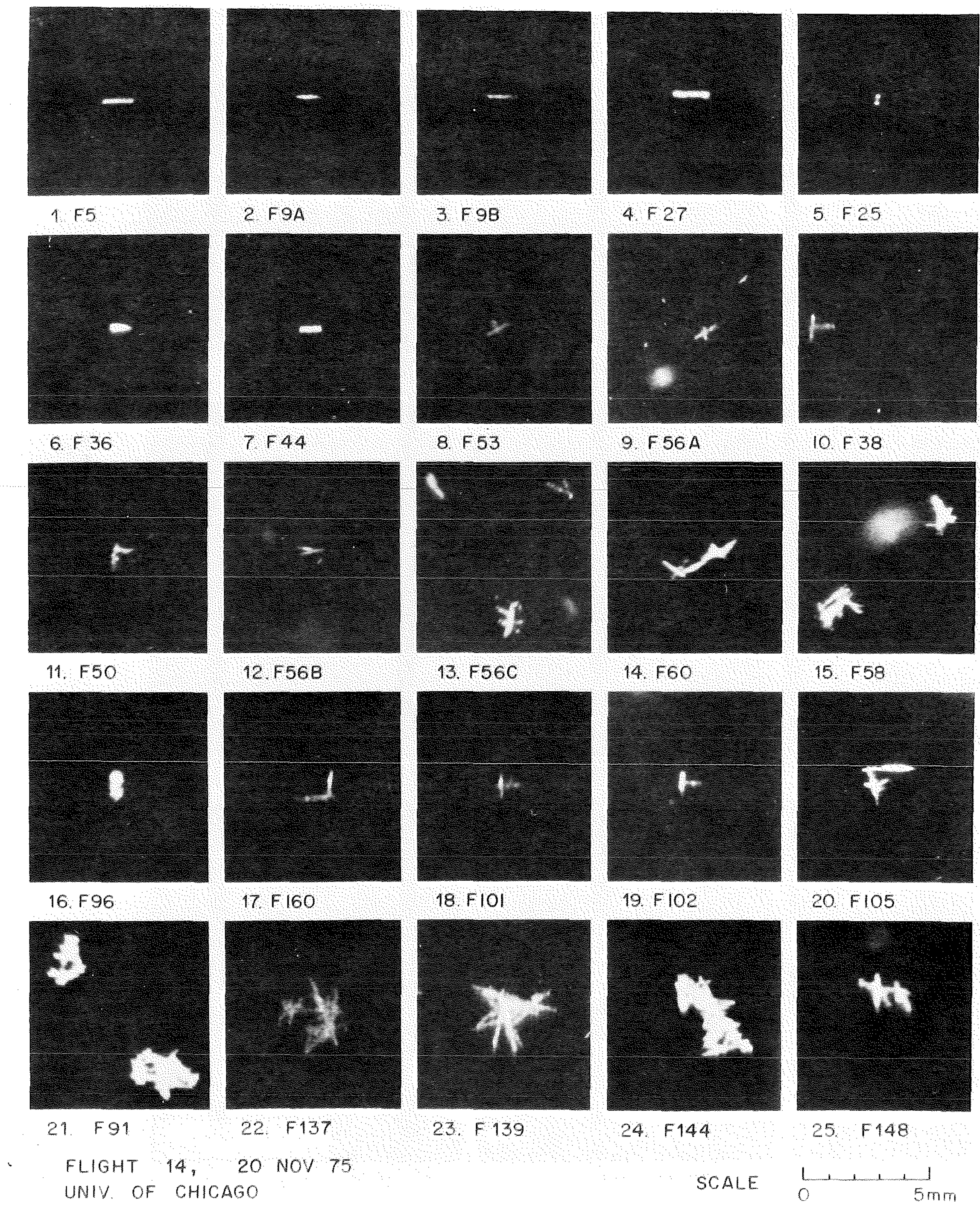

Figure 1. Photographs taken on flight 14, November 20, 1975, 1122 to 1234 CST. Altitudes (msl) and temperatures are as follows: pictures 1-5, 9000 ft (2700m), -4.9C; pictures 6-15, 8000 ft (2400m), -2.7C; pictures 16-25, 7000 ft (2100m), -1.2C. Conditions: mid-level clouds extended from 7000 to 9500 ft; temperature at 9500 ft was -5.5C.

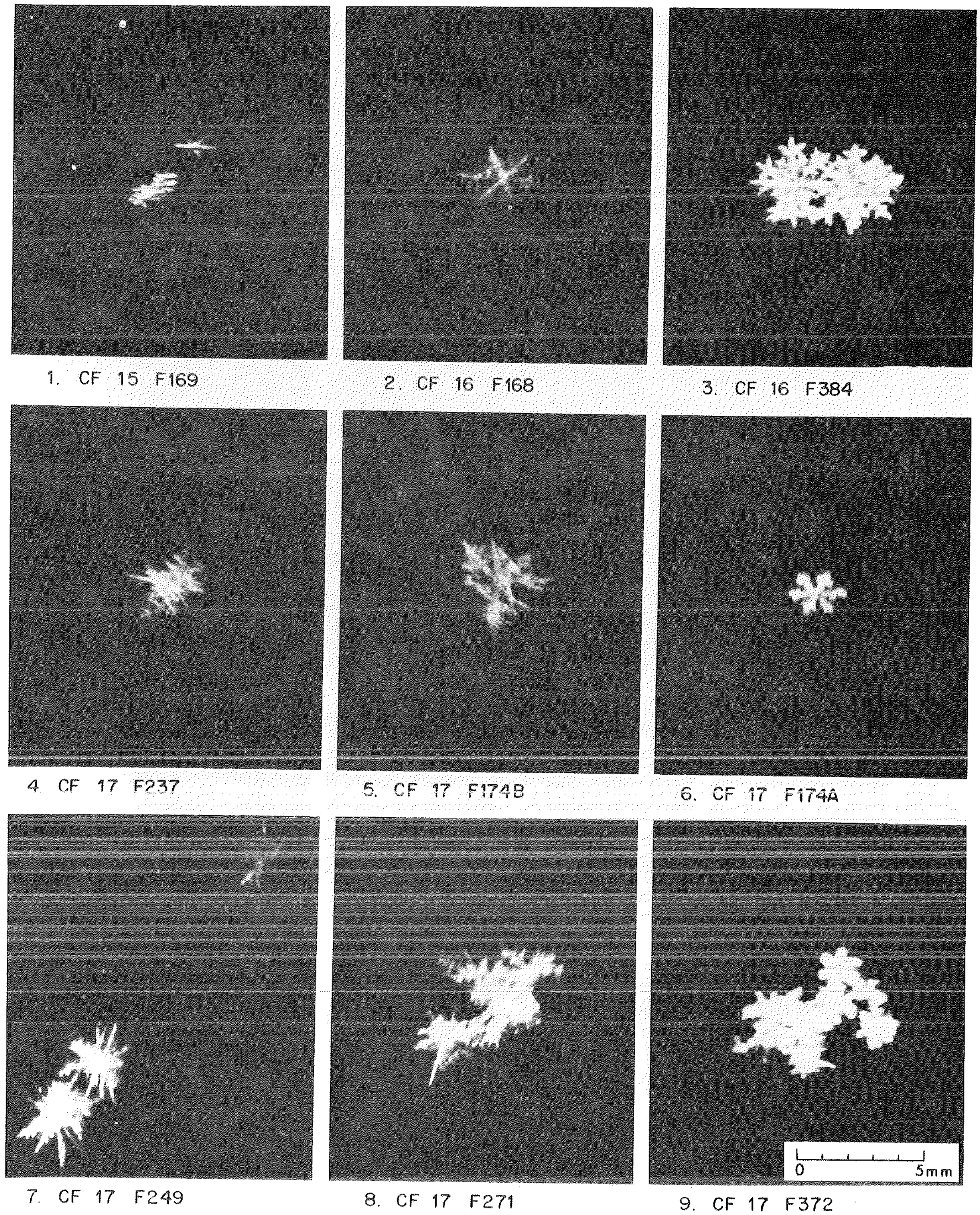

Figure 2. Picture 1, flight 15, November 21, 1975, 0914-1055 CST; altitude, 9000 ft msl (2700m), temperature, -8.1C. Conditions: snow falling from higher cloud whose base was 11,000 ft, -10C (est). Pictures 2 & 3, flight 16, November 24, 1975,1709-1914 CST; picture 2 taken at 7000 ft (2100m), -10.3C; picture 3 taken at 4000 ft (1200m), -3.7C. Conditions: mid-level cloud tops at 9000 ft, -12.5 to -13.5C; small crystals observed falling from thin cloud above,whose base was 15,000 ft (4600m), -28C (est). Remaining pictures taken on flight 17, 2329 CST November 24 to 0109 CST November 25, 1975: picture 4, 8000 ft (2400m), -12.0C; pictures 5 & 6, 7000 ft (2100m), -9.9C; pictures 7 & 8, 6000 ft (1800m), -7.9C; picture 9, 4000 ft (1200m), -4.2C. Conditions: mid-level cloud tops at 12,000 ft (3700m), -20.3C; thin cloud above, with base at 15,000 ft, -28C (est); no observed precipitation from this higher cloud.

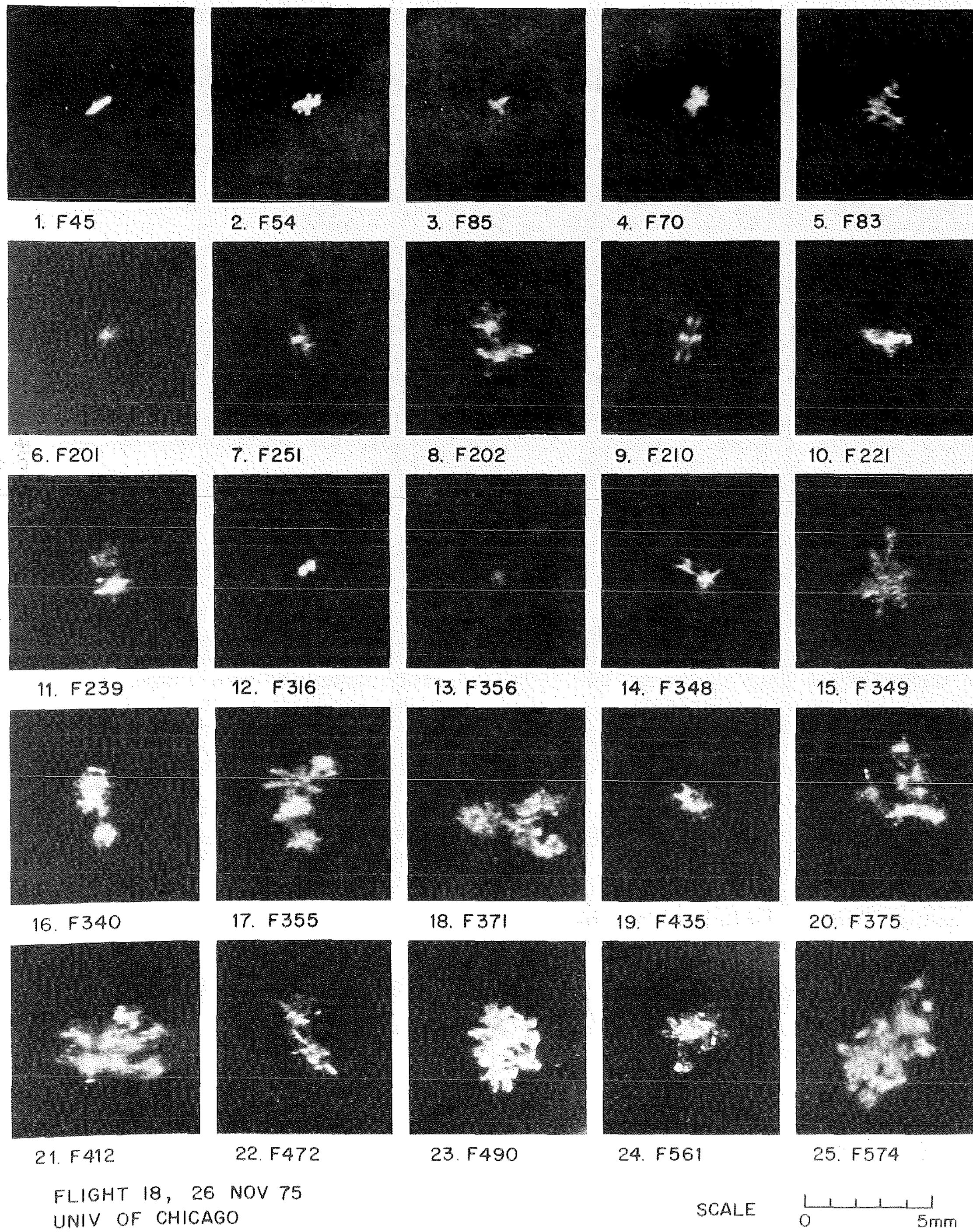

Figure 3. Photographs taken on flight 18, November 28, 1975, 1200-1343 CST. Altitudes (msl) and temperatures are as follows: pictures 1-5, 15,000 ft (4600m), -17.0C; pictures 6-11, 11,000 ft (3400m), -11.8C; pictures 12-18, 9000 ft (2700m), -8.7C; pictures 19-21, 8000 ft (2400m), -7.0C; pictures 22-25 taken during descent from 8000 to 6000 ft (2400-1800m), temperature, -7.0 to -5.0C. Conditions: mid-level clouds extending from 8000-9000 ft to above 15,000 ft (highest altitude flown); sun barely visible through cloud; moderate to heavy snow at all flight levels; radar indicated snow extended to 22,000 ft, -38C (est).

colder; the higher layer of cloud seen earlier persisted, but no longer seeded the lower cloud; mid-level clouds contained more water and had considerably higher snow crystal concentrations than on the earlier flight; and spatial dendrites were seen (pictures 4, 5, and 7).

Spatial dendrites are polycrystalline snow forms and can arise in two ways--by polycrystalline freezing of an isolated drop, or by a drop's freezing under suitable conditions onto an existing ice particle. Both forms have been observed by Nakaya (1954), and it appears that both forms occurred on this flight.

Studies have shown that a critical degree of supercooling is necessary for polycrystalline freezing to occur (Magono, 1968; Pitter and Pruppacher, 1973); and the degree of supercooling required is greater, the smaller the size of the drop involved. Moreover, for any given size drop, the critical supercooling for polycrystalline riming to take place is smaller than that required for polycrystalline freezing of an isolated drop. Alternatively, for a given temperature, a particular size drop can rime to produce a polycrystal, while to produce a polycrystal by isolated drop freezing a much larger drop would be required. Whichever type of freezing occurs initially, subsequent dendritic growth by vapor deposition is necessary in order to produce a spatial dendrite.

Since the changes in both temperature and cloud water between the time of flight 16 and that of flight 17 were such as to make polycrystalline freezing more likely, they are consistent with our seeing spatial dendrites on the later flight. What is not clear, without further information on the cloud droplet spectrum, is whether polycrystalline freezing of droplets or polycrystalline riming was principally responsible for the spatial dendrites observed.

3.3 Flight 18: Figure 3

This flight produced the richest diversity in snow crystal habit of all the flights considered, and it appears it encompassed the widest temperature range as well. Although the highest altitude flown was 15,000 ft, radar on the ground indicated that particles extended as high as 22,000 ft in the region of our flight. The temperature obtained from the 0600 CST Peoria sounding was -38C at this altitude. Thus, many crystals seen at our flight altitudes probably originated at much colder levels.

Pictures 1-3 show prismatic growth had occurred and that riming and aggregation had already taken place by the time crystals were seen at 15,000 ft. Capped columns or tsuzumis are seen in pictures 6, 7, 14, and 19; a stellar tsuzumi, a column capped with stellars, is seen in a tilted attitude in picture 8.

Planar forms shown include a stellar with plates (picture 9), stellars and plane dendrites (pictures 11, 15, 17, and 24), and a plate (picture 16). Riming is evident on nearly all particles. Aggregation is seen to increase markedly at lower altitudes.

4. SUMMARY

The characteristics of the snow crystals seen in these photographs taken in situ agree in general with those found by previous researchers using different methods of observation. Some questions are prompted by differences in detail, however, and these and other questions of interest which may be pursued using this method include the following:

1) What configurations are favored in the aggregation of natural snow prisms and planes? What concentrations of individual crystals are necessary for significant aggregation to occur?
2) What is the initial process of formation of polycrystals? Does polycrystalline riming always occur too, if cloud droplets are large enough for polycrystalline drop freezing to occur? Are spatial dendrites resulting from polycrystalline riming always distinguishable from those initiated by polycrystalline drop freezing?
3) To what extent does cloud droplet growth by coalescence continue in clouds which have entered the ice phase?

5. ACKNOWLEDGMENTS

I thank T. W. Cannon and the NCAR machine shop facility for their considerable help in constructing the airborne particle camera used in this work. Field work was a group effort and depended on R. E. Passarelli, Jr., T. R. Morris, and R. C. Kukuk to be ready for the snowstorms, and on pilot R. C. Townsend to negotiate them with safety. Especially I thank Professor Roscoe R. Braham, Jr., whose stimulus and encouragement made this work possible.

This work was sponsored by the National Science Foundation, RANN, under Grant AEN72-03399-A03, and by the National Science Foundation, Atmospheric Sciences Division, under Grant DES75-14225. The National Center for Atmospheric Research is sponsored by the National Science Foundation.

6. REFERENCES

Bentley, W. A., and W. J. Humphreys, 1931: Snow Crystals. McGraw-Hill, 227 pp.

Borovikov, A. M., 1953: Some results on an investigation of the structure of crystal clouds. Trudy Tsentral. Aerolog. Obs. No. 12.

Cannon, T. W., 1970: A camera for photographing airborne atmospheric particles. Image Technol., 12, 37-42.

Cannon, T. W., 1974: A camera for photography of atmospheric particles from aircraft. Rev. Sci. Instrum., 45, 1448-1455.

Cannon, T. W., 1975: A photographic technique for measurements of atmospheric particles in situ from aircraft. J. Appl. Meteor., 14, 1383-1388.

Jayaweera, K. O. L. F., and B. J. Mason, 1965: The behaviour of freely-falling cylinders and cones in a viscous fluid. J. Fluid Mech., 22, 709-720.

Jayaweera, K. O. L. F., and B. J. Mason, 1966: The falling motions of loaded cylinders and discs simulating snow crystals. Q. J. Roy. Meteor. Soc., 92, 151-156.

Kobayashi, T., 1961: The growth of snow crystals at low supersaturations. Phil. Mag., 6, 1363-1370.

MacCready, P. B., Jr., and C. J. Todd, 1964: Continuous particle sampler. J. Appl. Meteor., 3, 450-460.

Magono, C., 1968: On the additional nucleation of natural snow crystals. J. Rech. Atmos., 3, 147-152.

Magono, C., and S. Tazawa, 1966: Design of "snow crystal sondes." J. Atmos. Sci., 23, 618-625.

Mason, B. J., 1953: The growth of ice crystals in a supercooled water cloud. Q. J. Roy. Meteor. Soc., 79, 104-111.

Nakaya, U., 1954: Snow Crystals. Harvard Univ. Press, 510 pp.

Ono, A., 1970: Growth mode of ice crystals in natural clouds. J. Atmos. Sci., 27, 649-658.

Pitter, R. L., and H. R. Pruppacher, 1973: A wind tunnel investigation of freezing of small water drops falling at terminal velocity in air. Q. J. Roy. Meteor. Soc., 99, 540-550.

Schaefer, V. J., 1941: A method of making snowflake replicas. Science, 93, 239-240.

Weickmann, H. K., 1947: Die Eisphase in der Atmosphäre. Völkenrode Reports and Translations No. 716, Ministry of Supply, London.

3.1.3

ICE CRYSTAL CONCENTRATIONS IN WINTERTIME CLOUDS

William A. Cooper and Gabor Vali

University of Wyoming
Laramie, Wyoming 82071

1. INTRODUCTION

Snowfall over the Rocky Mountains is the most important source of moisture for a many-state area of the United States. This snowfall undoubtedly forms via a Bergeron process involving the ice phase, yet there have been only limited observations of the ice crystal concentrations in the clouds of this area, and we still have a poor understanding of the origin of the ice in these clouds.

From 1973 to 1976, a field study has been conducted to collect improved observations of ice crystal concentrations in these clouds. Aircraft probing and surface observations were combined to obtain comprehensive data; emphasis was laid on the development of new observation techniques. This paper will present examples of the data obtained during the project, and set forth some preliminary conclusions.

2. AIRCRAFT INSTRUMENTATION

The research aircraft used in this project is equipped with a complete array of sensors for state parameters, including a Doppler wind-measuring system. These sensors are coupled to an onboard computer-directed data recording system. The aircraft also has special instrumentation for the measurement of cloud droplets and of ice crystals. The ice concentrations to be reported here were obtained in two ways:

a. A 2-D Probe (Particle Measuring Systems, Inc.). This probe is able to detect the two-dimensional image of ice crystals passing through its senstive volume, and to record those images on magnetic tape. It provides a continuous record of ice crystal concentration, and the sizes and shapes of the ice crystals can be determined from the recorded images. The sensor contains a 32-element optical array onto which the magnified shadow of a crystal is focused. Each element covers a region of the shadow corresponding to a 25 μm square on the ice crystal, so 25 microns is both the minimum size detectable and the resolution for features on the ice crystal. Under normal flight conditions, the probe samples 4 liters per second, which corresponds to 50 liters per kilometer of flight path. The sample volume is smaller for crystals smaller than 150 μm, because of changes in the effective depth of field. There is some uncertainty in using the measurements at sizes smaller than 50 microns.

b. Oil-coated slides sampled in a decelerator. Our decelerator reduces the impact speed of the ice crystals of about 7 meters/second, and allows us to collect intact surprisingly fragile crystals. The slide exposed in the decelerator samples about 5 liters per second, or about 60 liters per kilometer of flight path. The slides are coated with oil so crystals will adhere to them and are preserved in cold hexane or silicone oil. After the flight the crystals on the slide are photographed under a microscope. This technique provides excellent detail regarding the habits, sizes and degree of rime of the ice crystals, and can be used to measure crystal concentrations as well. The collection efficiency of the slides in the decelerator has been measured experimentally and found to be near-unity for sizes above 50 microns. There are some uncertainties in the collection efficiency for crystals smaller than 50 microns, because the influence of different crystal shapes is difficult to evaluate.

The concentrations obtained by these two different methods have been compared with each other. For a set of 12 such detailed comparisons, we have found the concentrations to have the ratio (2-D:slide) of 1.7, with a standard deviation of 0.9, for crystal sizes greater than 50 microns. We are confident of these ice concentration measurements to within a factor of 2; the order of magnitude is certainly right.

3. OROGRAPHIC CAP CLOUD

Elk Mountain is an isolated peak at the northern end of the Medicine Bow Range, in southern Wyoming. During the wintertime, the peak is often enveloped in an isolated cap cloud. This cloud has many advantages for studies of the development of ice:

a. The airflow is often unchanged for periods of many hours.

b. The transit time for any parcel through the cloud is relatively short, often on the order of 10 minutes or less.

c. The airflow is frequently smooth and simple, so that air trajectories can be defined and followed through the cloud.

d. We operate a mountain-top observatory near the summit, and can supplement the aircraft observations with detailed surface observations extending over a longer period than the aircraft can study.

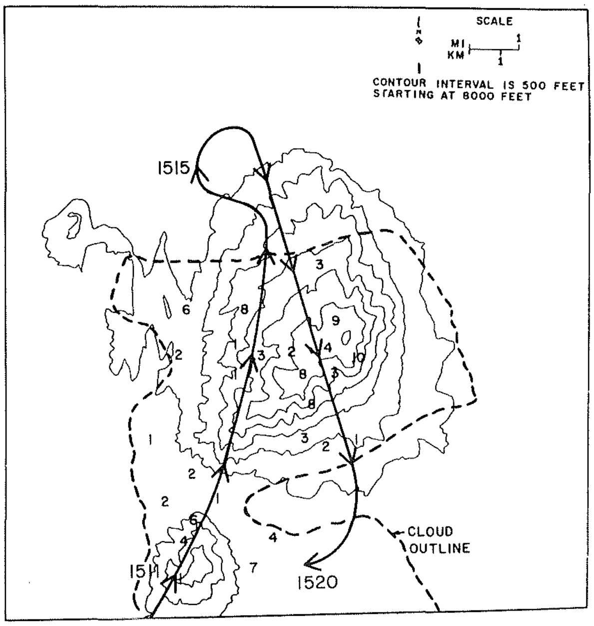

FIGURE 1. The Elk Mountain cap cloud of 18 FEB 1975. The dashed line is the cloud outline, superimposed on the topographic map of the mountain. The summit is at 3400 meters MSL, and the contour interval is 150 meters; the elevation in the valley to the west (left) is 2400 meters MSL, and the wind is from the west. The solid line with arrows indicates a typical aircraft penetration of this cloud. The small numbers throughout the cloud indicate the ice crystal concentrations (per liter) measured on various aircraft passes. Cloud base was 3300 m, and cloud top was at 3650 m.

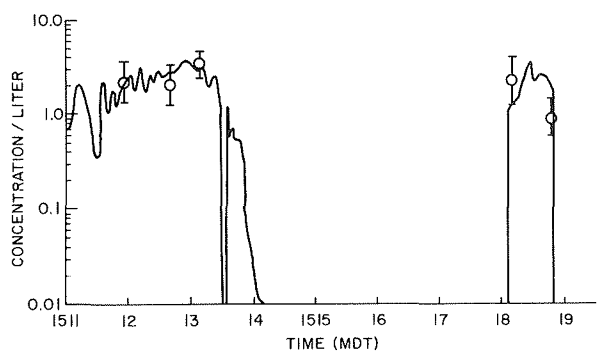

FIGURE 2. Ice crystal concentration observed during the aircraft penetrations shown in Figure 1. The solid line is the concentration as determined from the 2-D probe, and the points with bars are the concentrations obtained from oil-coated slide samples.

The cap cloud of 18 Feb 1975 is an example of this type of cloud. Figure 1 shows the topography of the mountain and the cloud cover. Also shown in this figure is an example of our aircraft penetrations through this cloud. The flight track shown was at an altitude of 3500 m for 1511-1515, and approximately 3600 m for 1516-1520. The temperatures were near -18C.

A plot of the ice crystal concentration observed on this pass is shown in Figure 2. Notice that the ice crystal concentration rapidly increases to about 1 to 3 per liter, and remains relatively constant for the entire first pass. It appears that ice crystal concentrations of about 1 or 2 per liter are observed within about 1 km of the cloud edge. This corresponds to about one minute of growth time for ice from the cloud edge; if a crystal size of about 50 microns is required for detectable crystals, this observation is consistent with an origin for the crystals very near the leading edge of the cloud. Further into the cloud the ice crystal concentration does not increase significantly. On the subsequent pass over the top of the mountain (during which we only dipped into the top of the cloud for a short time), the crystal concentration found was still approximately the same, 3 to 4 per liter.

The crystal sizes were just detectable near the upwind cloud edge. Further into the cloud, there was generally a narrow range of ice crystal sizes at any location, and this size increased with distance from the cloud edge. Over the mountain top, there were few small crystals, and most of the crystals were 200-300 microns in diameter, suggesting that most of these crystals originated near the upwind edge of the cloud. On Figure 1 are shown the ice crystal concentrations observed at various locations in the cloud during a series of aircraft passes. Notice that there seeems to be little increase in the ice crystal concentration downwind from the cloud edge.

A different aircraft penetration, flown more along the airflow, yielded the following sequence of observations:

a. We first encountered the upwind boundary of the cloud, at which point we found a low concentration of liquid (about 0.05 gm/m^3).

b. This liquid region ended, and a 2 to 4 per liter concentration of small ice crystals appeared.

c. These crystals grew to larger sizes, with no significant increase in the ice crystal concentration.

d. Additional liquid water appeared as the updraft increased over the mountain.

d. No significant additional increase in the ice crystal concentration through the remainder of the cloud was seen.

This case suggests that the ice crystals are originating near the leading edge of the cloud, in association with the initial condensation process.

Ice nucleus measurements in this air are well below these ice crystal concentrations. Typical ice nucleus measurement (obtained with Millipore filter samples and subsequent diffusion chamber processing) indicate nucleus concentrations of 0.1/liter or less, well below the observed ice crystal concentrations.

The case shown is only one of many cap clouds we have studied. It is difficult to reach generalized conclusions regarding the concentrations observed in these clouds, because the variability in the concentrations is great even for seemingly similar situations. Cases have been observed with

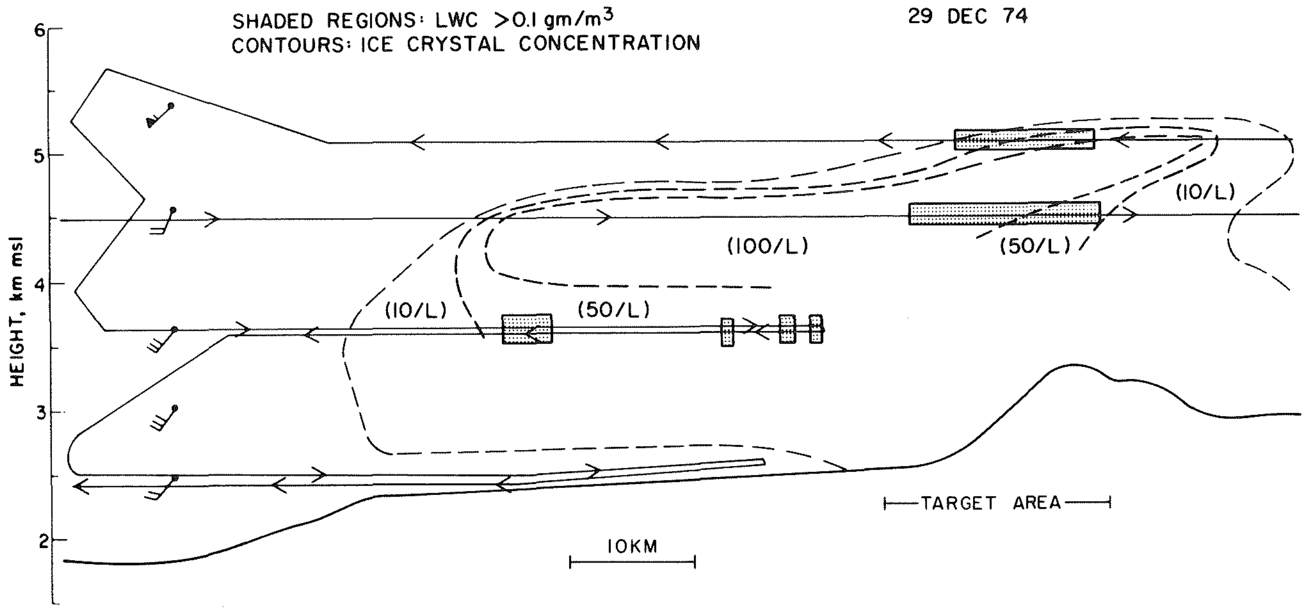

FIGURE 3. Vertical cross section for San Juan Mountains storm of 29 DEC 1974. The outer dashed line is the cloud boundary, and inner lines show ice crystal concentration contours. Shaded regions indicate regions of significant liquid water content. The airflow is from the southwest, or from the left in the diagram. The solid line with arrows indicates our flight track through this storm. (The winds indicated upwind of the cloud are plotted as if north were up and west were left in the diagram.)

ice crystal concentrations from 0.1 to 100 per liter, throughout the temperature range from -12C to -20C, with little apparent correlation between average concentrations and temperature. However, almost all cases are in significant disagreement with the ice nucleus measurements.

4. DEEPER OROGRAPHIC SYSTEMS

During the winter of 1974-75, we studied a variety of different storms in the San Juan Mountains in southwestern Colorado. These storms were frequently 3000 m or more deep, and produced significant precipitation. Figure 3 shows a typical flight track through one storm. The regions where liquid water was observed along our flight track are indicated, as are ice crystal concentrations. Ice crystals were measured only along the flight tracks, but contour lines have been drawn to indicate a likely distribution for the concentrations. The temperature at the 4.5 km flight level was -19C, and at the 5 km level was -23C. The airflow through this storm was mostly smooth, with regions of embedded convection.

Ice crystal concentrations were surprisingly high. The initial pass into the cloud at 4.5 km was especially interesting, because a pattern similar to the Elk Mountain cloud was seen. A region of low liquid water content (about 0.05 gm/m^3, and therefore not shown in Figure 3) was located at the cloud edge, and extended for approximately 3 km. Soon after this region was encountered, a quite high ice crystal concentrations developed. The liquid water was apparently completely converted to ice, so that along this flight track no subsequent liquid water was encountered until the greater updrafts over the mountain were reached. The ice crystal concentration surpassed 100 per liter within 5 km of the leading edge of the cloud, and apparently did not increase significantly after that. We verified that there was no ice falling into the top of this system and found that the air above the cloud was very dry. The ice seems to originate in a manner similar to that in the Elk Mountain cap cloud.

The concentrations we measured were well above our ice nucleus measurement. At -19C, our Millipore filter measurement indicated nucleus concentrations of about 0.1 per liter, or three orders of magnitude below the observed ice crystal concentrations. Additional filters processed by G. Langer using a "puff" technique yielded concentrations of about 1 per liter, still well below the observed ice crystal concentrations.

It is again difficult to make generalizations regarding the ice crystal concentrations observed. All storms we observed had concentrations of 10 per liter or more in parts of the cloud, although some of the warmer and shallower cases had regions where the concentrations were only 1/liter. Characteristic concentrations were 100/liter at -20, 10/liter at -16, and 1/liter at -12, but significant exceptions were noted.

5. AN UPSLOPE-FRONTAL STORM

On 3 Feb 1976, we studied a situation in which snowfall was produced over a large region by a cold and moist airmass advancing over gradually rising terrain. The air above the front was fairly dry. Figure 4 depicts equivalent potential temperature contours along the direction of motion of the front. Clouds were forming within the cold air mass; no clouds were observed above the front surface.

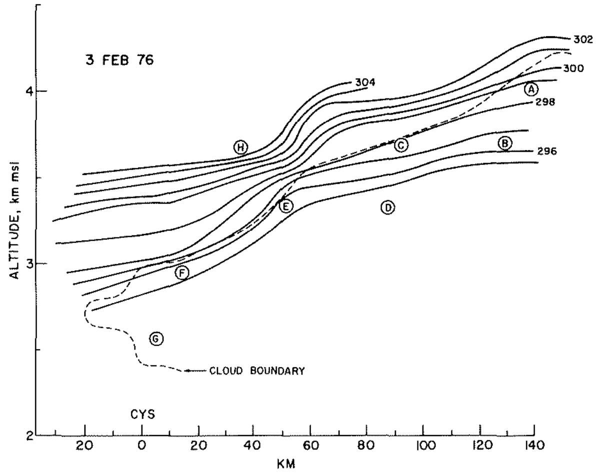

FIGURE 4. θ_E contours for the upslope system of 3 FEB 1976. The vertical cross section passes through Cheyenne, and is taken along a line from 150° (left) to 330° (right in the diagram). Letters refer to locations discussed in the text.

Point H in Figure 4 is ahead of the front, and the air here is warm and dry. The temperature was about -9.5C, and the dew point -15.5C; winds were southwesterly at 25 knots. In contrast, at point G the winds were from the northeast (which is an upslope direction), at 10 knots. The temperature at G was about the same as at H.

Points A, C, E and F represent points near the cloud edge. The front was advancing to the left in Figure 4, so these points represent regions of new cloud formation. The droplets at these locations were relatively small in comparison with the interior of the cloud. The ice crystal concentrations, however, are high: at point A (with temperature -17C) there were 10 per liter, at point C (-15C) there were 5 per liter, at point E (-13C) there were 2 per liter, and at point F (-10C) there were less than 0.1 per liter.

In a system such as this, one might expect that the formation of ice crystals would deplete the ice nuclei during the long lifetime of the storm, and that the air would be deficient in nuclei. There is no evidence of this in the storm we studied. This appears to be due to mixing at the front surface. If the frontal surface were a true barrier, there would be no new source of ice nuclei in the cloud at locations near the front, and as the ice crystals formed earlier fell out we would expect low ice concentrations near the front. However, the ice crystal concentrations here are high. We suggest that these ice crystals are formed on nuclei mixed through the frontal surface from above. That such a mixing process was occurring are supported by the great variability in parameters near the front, by turbulence in this region, and by the visual appearance of the cloud in this region.

This interpretation is supported by our observations at points B and D. The crystals at B originated at some temperature intermediate between the temperatures of A and C, and subsequently fell to B, so the observed concentration at B should be that of some position along the front between A and C. The observed ice concentration at B was indeed intermediate between those at A and C; the same applies to the concentration at D, which was intermediate between the concentrations at C and E. Because the vertical rise of the front proceeds with a speed comparable to the fall velocity of the snowflakes, this provides a possible mechanism for mixing enough nuclei into the cloud to provide a continuous source of ice.

This argument predicts that the ice crystal concentrations in this system will be lower than nucleus concentrations in the air above the front, but not necessarily more than about a factor of two lower. The observed crystal concentrations are within the range found in the other cloud systems.

6. WAVE CLOUDS

Wave clouds bear much resemblance to the cold orographic clouds in that the air flow follows a similar path and the cloud forms initially at cold temperatures. Ice crystals have in most cases even less time to grow than in the cap cloud.

One example occurred on 16 Mar 1976. A wave cloud formed with a long axis of 30 km nearly perpendicular to the wind and a short axis of about 10 km along the wind direction. Cloud base was at 5000 m, much higher than in the orographic clouds we have studied. The temperature at cloud base was -18.5C, and the cloud extended to about 6000 m where the temperature was -24C.

In a pass through this cloud at 5500 m we encountered 5 m/sec updrafts ahead of and at the edge of the cloud. The upwind edge of the cloud was entirely water; there was no ice found.

Near the center of the cloud, we began to encounter ice, initially in the form of small crystals. The concentration was about 1 to 2 per liter, and was rather constant through this pass. The liquid water content was also relatively constant along the flight track. At the downwind edge of the cloud, as we encountered downdrafts, the liquid water ended, but the ice remained for several hundred meters beyond the boundary of the liquid cloud. Ice crystal sizes became smaller as we continued downwind, and the ice ended altogether within about 400 meters of the liquid cloud edge.

The maximum size of the ice crystals was about 200 microns, and at any point the sizes were relatively uniform, indicating a common origin for the crystals. Estimates of growth time based on the distance from cloud edge indicate that if the cloud base were the origin of the ice the crystals should have grown to detectable size in portions of the updraft where we did not find any ice, but this conclusion cannot be drawn with any confidence because of the variability of the cloud outline and flow.

The ice concentrations were unusually low.

In the downdraft portions of the cloud at -22C we only found 1 to 2 per liter ice crystal concentrations. The liquid water content and available growth times for this cloud were similar to the Elk Mountain cap cloud, and yet this is at the lower end of the range of concentrations measured in cap clouds.

7. WINTER CUMULUS CLOUDS

We have also studied some convective wintertime clouds that form at cold temperatures. One such case was encountered on 19 Mar 1976. At a temperature of -19C, and an altitude of 4000 m, we found concentrations of 10-20 per liter. Higher in the cloud, at -22C, we found 80 per liter. This is almost two order of magnitude higher than the concentration found at a similar temperature in the wave cloud discussed above. On another day, we found an even sharper contrast. On 17 Feb 1976 we studied both the cap cloud over Elk Mountain and the convective cells that formed in the valley to the west of the mountain. In the cap cloud, we found unusually low concentrations of ice, on the order of 2 per liter at a temperature of -21C and an altitude of 3950 m. However, in the nearby convective clouds we found concentrations of 50/liter at a temperature of -24C and an altitude of 4250 m. Since the ice crystals were found in a moderately strong (3 m/sec) updraft region, they must have formed initially at a level below this, probably comparable to the region where the cap cloud was observed. This is consistent with the trend which we observed: most convective clouds produced higher ice crystal concentrations than orographic or wave clouds at similar temperatures and altitudes.

8. DISCUSSION AND CONCLUSIONS

The ice crystal concentrations we measured in wintertime clouds over the Rocky Mountain region of the U.S. were frequently surprisingly high in comparison with ice nucleus measurements. Ice nucleus concentrations indicated by the membrane filter technique are nearly a factor of 100 too low in many cases; the extreme discrepancy was found in the case of the San Juan storms, where the ice crystal concentrations exceeded the membrane filter measurements by a factor of 1,000. Measurements by a contact nucleation device have indicated a lesser disagreement, but there is still about a factor of 10 between the median ice nucleus concentrations and the median ice crystal concentrations at a given temperature.

We have observed clouds in which the observed ice crystal concentrations were comparable to measured ice nucleus concentrations. However, the cases where a discrepancy was found are more common, and it is for those situations that an explanation must be sought.

In the orographic cap cloud and in the San Juan storm case presented, the ice apparently originated near the upwind edge of the cloud. This suggests considering which nucleation modes could give the observed pattern:

a. Deposition nucleation is probably not responsible. It is unlikely that deposition nucleation (which should depend primarily on ice supersaturation) would exhibit this behavior at water saturation. The air supersaturated with respect to ice far ahead of the liquid cloud boundary, and deposition nucleation should give a gradually increasing concentration throughout this region. In addition, the filter measurements suggest that deposition nucleus concentrations are too small.

b. Contact nucleation may be responsible, but if so, the nuclei would have to be surprisingly small. To give the observed increase in concentration at the upwind edge, but no further increase in concentration within subsequent liquid water regions, the contact nuclei should almost all be scavenged in a short time. Also, concentrations of contact nuclei would have to be substantially higher than ice crystal concentrations unless almost all are collected early in the cloud. The collection rate for contact nuclei may be estimated, for collection by Brownian motion, as:

$$\frac{dn}{dt} = \frac{nkT}{\sqrt{2\pi mkT}} \; 4\pi r_d{}^2 N$$

where n is the number of contact nuclei per volume, m is the mass of the contact nuclei, N is the number of cloud droplets per unit volume, and r_d is their radius. (This is a rate considerably higher than estimated, for example, by Young (1974), but that calculation assumed steady state collection of nuclei, while for these cases we must consider the first instance of collection of a nucleus by a droplet, since the droplet is forming at a cold temperature.) This give a characteristic time for nucleus collection of:

$$\tau = \sqrt{\frac{m}{2\pi kT}} \; \frac{1}{2r_d{}^2 N}$$

For N = 200 droplets per cm^3 and r_d = 4 μm, this time is about 10 minutes for 0.1 micron diameter nuclei, and about one minute for 0.02 micron diameter nuclei. Unless the nuclei are exceptionally small, the observed ice development in about one minute is not possible. Also arguing against this possibility is the direct measurement of contact nuclei, on top of Elk Mountain and in Laramie. The measured contact nucleus concentrations have never been high enough to account for the higher ice crystal observations, although they are consistent with the lower concentrations.

c. A condensation-followed-by-freezing sequence would behave as observed. If the same particles cause the condensation and subsequent freezing, the association of the ice formation with the leading edge would be predicted. Note that the temperature of any parcel in the orographic clouds changes little during its passage through the cloud, so that few immersion freezing nuclei will be activated at a time later than when they are first immersed in a cloud droplet.

The same pattern can account for the ice concentrations observed in the upslope case we studied. The ice apparently originated at the boundary of the cold air, and may be associated with the condensation and mixing process at this boundary. There was no apparent further increase in the concentration of ice within the cloud. In the wave cloud cases it was more difficult to study the origin of the ice, but the uniform sizes of the crystals argues for a common origin for most of the ice. The convective clouds studied were still more complicated, and the origin and trajectories could not be determined.

The cloud types could be ordered with regard to their ice crystal concentrations as follows, in increasing ice crystal concentration: wave clouds, orographic cap cloud, upslope cloud (1 case), more extensive orographic systems (in a different area), and wintertime cumulus. However, many exceptions could be found to this ordering.

It is possible to rule out many multiplication mechanisms for these clouds. Any mechanism would have to act very rapidly at the leading edge of the cloud, but not operate further into the cloud so that no further increase in crystal concentration would take place. This makes it unlikely that any ice multiplication mechanism is occurring. In particular, we can rule out the Hallett-Mossop (1974) multiplication mechanism for all of the clouds observed. Most of them are everywhere too cold, and where regions warm enough exist the droplet spectrum is too small. Furthermore, in most clouds there are no riming objects present in the area where the ice crystal concentration increases.

The high variability in the concentrations observed under seemingly similar conditions (similar temperature, altitude, and location) suggests that additional studies be performed to search for the causes of this variability. At present, however, we must conclude that we cannot predict the ice crystal concentrations that will result in a given situation, to better than plus or minus an order of magnitude. Our studies seem to indicate that the problem is still our poor understanding of the nucleation process in these situations.

9. ACKNOWLEDGEMENTS

This research was supported by the Meteorology Program, Atmospheric Science Section, National Science Foundation Grant ATM75-02515. The San Juan studies were sponsored by the Division of Atmospheric Water Resources, Bureau of Reclamation, Department of the Interior, Contract 14-06-D-6801.

10. REFERENCES

Hallett, J. and S. C. Mossop, 1974: Production of secondary ice particles during the riming process. Nature, 249, 26-28.

Young, K., 1974: The role of contact nucleation in ice phase initiation in clouds. J. Atmos. Sci., 31, 768-776.

EXPERIMENTAL STUDIES ON THE INFLUENCE OF CRYSTAL DEFECT AND SURFACE NUCLEATION MECHANISMS ON THE GROWTH HABIT OF ICE CRYSTALS

B.J. Anderson*, V. Keller, C. McKnight and J. Hallett

Desert Research Institute
University of Nevada System
Reno, Nevada 89507

1. THE PROBLEM

Laboratory experiments and field studies of the habit of ice growing from the vapor have shown a dependence on temperature, which controls the primary habit (plate-like or column-like) and supersaturation which controls the ratio of the growth rate in "a" and "c" axis directions and the transition from solid to skeletal shapes. The detailed molecular mechanisms responsible for these complex changes have been the object of much interest over the years. The problem has posed a challenge to those who would understand the kinetics of the growth mechanism itself; it has posed a challenge to those who would apply the detail of the habit change to crucial problems of cloud physics such as the relation of column habit to the onset of riming.

Current ideas of crystal growth mechanisms differentiate between growth which takes place by a process of surface or two-dimensional nucleation, and growth which takes place by propagation of discrete steps on an otherwise molecularly smooth surface. Surface nucleation is a process which is strongly dependent on supersaturation, and is assessed analytically in terms of surface energy between the surface - which may consist of an adsorbed layer of intermediate solid-liquid characteristics - and the vapor and solid. Steps grow by incorporation of molecules both directly from the vapor environment and also by diffusion of molecules adsorbed on non-growing faces adjacent to the step. Steps originate from screw dislocations (in which case they perpetuate), from surface accidents - particulate or molecular impurity, or from regions elsewhere at higher supersaturation where surface nucleation has already taken place.

Evidence exists that growth on ice crystal basal surfaces occurs both by surface nucleation and by defects. Shaw and Mason (1955) and Lamb and Scott (1972) both found that crystal surfaces changed growth velocity discontinuously under constant environmental conditions, a possible consequence of change of defect structure; Hallett (1961), and Mason, et al. (1963), found that non-thickening crystals could be caused to thicken by increasing the supersaturation. Both theory (Fletcher, 1972) and experiment (Kulividze et al., 1974) support the existence of a temperature and supersaturation dependent adsorbed non-crystalline layer whose properties may be important both for growth of steps and critical surface nuclei. Bernal (1958) suggested that habit variations were consistent with different temperature dependence of surface energy on "a" and "c" faces; Frank (1975) applied these concepts to interpret a variety of skeletal ice crystal forms, by surface nucleation at those crystal surfaces with lower surface energy which, of course, extend further into the vapor field with consequent growth of layers to other parts of the crystal at lower supersaturation.

The experiments described here demonstrate the role of defects for vapor growth and delineate conditions where distinct growth mechanisms may be important under atmospheric conditions.

2. EXPERIMENTAL STUDIES

Three distinct experimental approaches yield evidence on growth mechanisms:

2.1 Epitaxial Growth of Ice

Ice crystals growing epitaxially on covellite and silver iodide single crystals 3 mm diameter with "c" axis perpendicular to the base crystal show thin film interference colors which give a measurement of crystal thickness to an accuracy of ± 0.02 μm. Temperature and ambient supersaturation are controlled independently; supersaturation can be changed (at constant temperature) with time required to reach a new equilibrium of 10 s. Crystals grow as thin plates within temperature range -10 to -22°C, typical dimension 100 x 0.5 μm. While many plates grow in both crystal directions with typical "a" axis growth rate 0.5 μm s^{-1} and "c" axis growth rate $\sim$0.05 μm s^{-1} at water saturation, a number of crystals (10% at -10°C; 30% at -20°C midway between ice and water saturation) fail to grow at all in the "c" axis direction although still growing laterally. A few crystals sustain close to water saturation without thickening. These crystals can be caused to thicken by increase of supersaturation. Step increase from low values to beyond water saturation leaves progressively fewer non-thickening crystals. Figure 1a shows changes of crystal dimensions as supersaturation is increased. The growth rate of the crystal increases and at the same time the crystal begins to thicken; 1b shows the mass increase of each face and the total mass increase of the crystal. For a non-thickening crystal the growth rate is constant under constant environmental conditions; thin crystal interaction

*Present Address: Marshall Space Flight Center
Huntsville, Alabama

usually begins only on close approach ($\sim$ 1 μm) or within $\sim$ one diameter of a much thicker crystal.

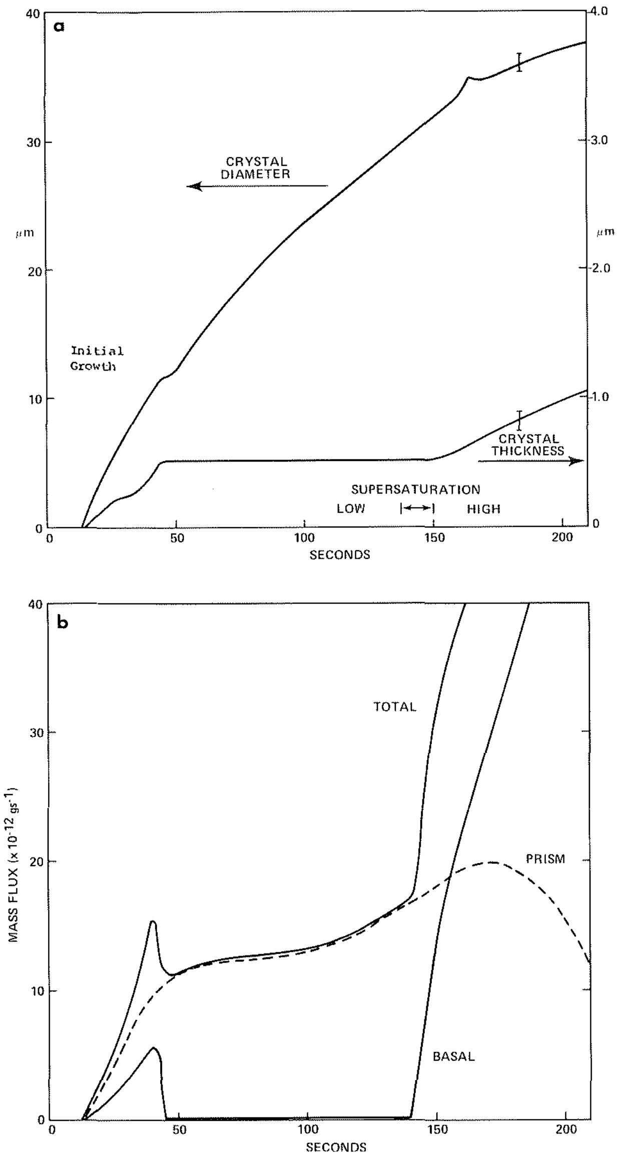

Fig. 1a,b. Initiation of growth in the "c" axis direction of a non-thickening crystal by sudden increase of supersaturation. Low, 0.2; High 0.4 g m^{-3} excess vapor density. Note that the crystal grows at almost constant velocity until it begins to thicken.

The "a" axis growth rate of these crystals under constant conditions shows some variability well outside experimental error; these results are interpreted as caused by a strain in these crystals; evidence for this comes from evaporation of crystals in an ambient supersaturation (Kobayashi, 1965).

2.2 Growth Habit at Low Supersaturation and Temperature

Previous laboratory studies of ice crystal habit have investigated the changes which occur with temperature and supersaturation; supersaturation has been controlled as an independent parameter, for example by the temperature of ice plates in static diffusion chambers. In the atmosphere crystals fall at terminal velocity; in the static diffusion chamber crystals are ventilated by natural convection. In either case the ventilation is not uniquely defined. Crystal growth in the dynamic ice diffusion chamber (Gamara and Hallett, 1972) enables temperature, ambient supersaturation and ventilation velocity to be specified independently. In practice increased ventilation is equivalent to an increased supersaturation in unventilated growth. The effect of supersaturation and ventilation velocity on the growth habit of crystals has been explored in a dynamic diffusion chamber at -30°C and is shown in the table.

TABLE I. Habit of Ice Crystals Growing at -30°C.

"Effective" ice supersaturation	Habit	c/a
0		1
5	equiaxed	
10	simultaneous	1.0
15	solid	to
	columns and	0.3
20	plates	
25		
	hollow	5
30 water saturation ← (zero velocity)		10
>35	columns	>20

At low ice supersaturation the crystals are equiaxed; between 10 and 20% ice supersaturation crystals of both plate-like habit and column-like habit grow simultaneously; beyond 20 to 30% supersaturation crystals grow as hollow columns. (Fig. 2a,b).

Temperature	Ice Supersaturation
-30.6°C	9.5%
-31.5°C	9.7%
-32.3°C	9.0%

(a) static

-30°C	9%

(b) ventilation 6 cm s^{-1}

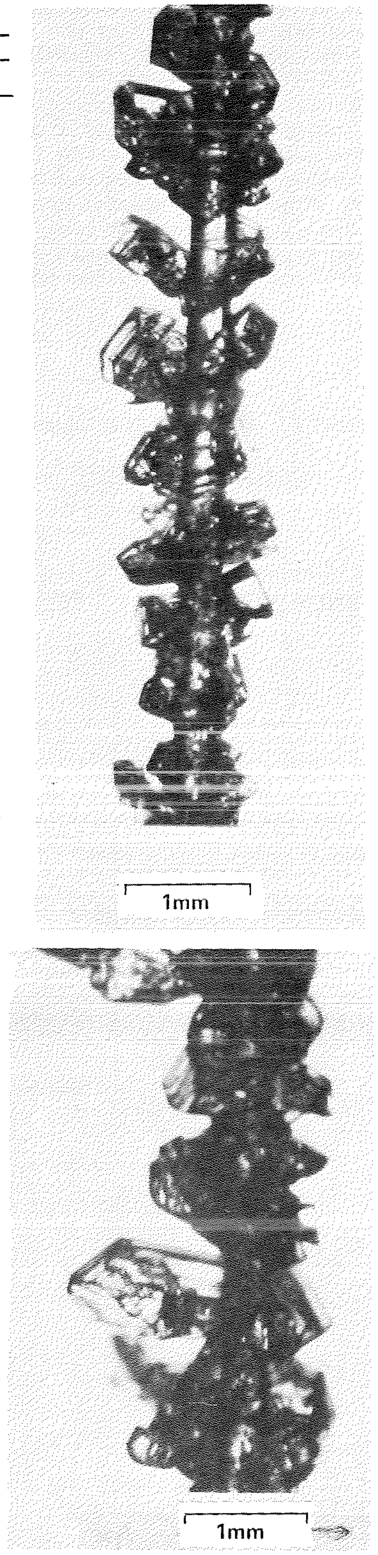

Fig. 2. Ice crystal growth in dynamic diffusion chamber showing simultaneous growth of equiaxed columns and plates at low supersaturation.

2.3 X-Ray Topography Study of Defects

The presence of dislocations in crystals may be detected by scanning x-ray topography whereby defects scatter additional intensity into the direction of a Bragg angle reflection. Vapor grown plate crystals from the dynamic diffusion chamber, from an isothermal chamber containing a little supercooled water or supersaturated sugar solution (after a technique suggested by C. Knight), natural frost crystals, and crystals from slightly supercooled water have been examined. By taking two topographs of each crystal after 120° rotation, defects in the basal plane can be located. Fig. 3a shows vapor grown crystals containing a large number of defects, some emerging from the basal plane and on a step; 3b shows dislocation lines emerging on the prism plane which form loops inside the crystal. Figure 4a shows a defect free plate crystal grown at -18°C, 15% supersaturation over ice. Figure 4b shows a plate grown at -2°C, 2% supersaturation over ice which is possibly defect free - although it could contain defects associated with the visible rib structure. Figure 5 shows a natural frost crystal, also defect free. The full range of plate growth has not yet been fully investigated, but crystals growing at water saturation and midway between ice-water saturation have been found defect free. The radial growth rate of plates is not entirely dependent on growth conditions, but appears inversely related to thickness.

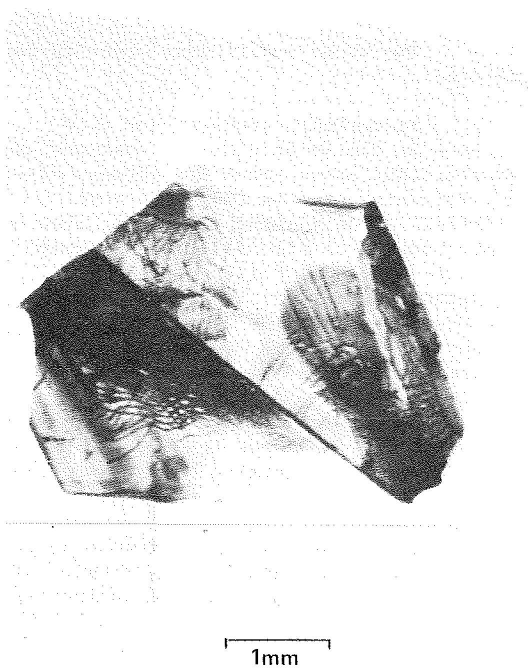

Fig. 3a. Vapor grown crystal with dislocations emerging at steps, prism faces and apparently on basal faces. Grown at -1.5°C and 1.5% ice supersaturation.

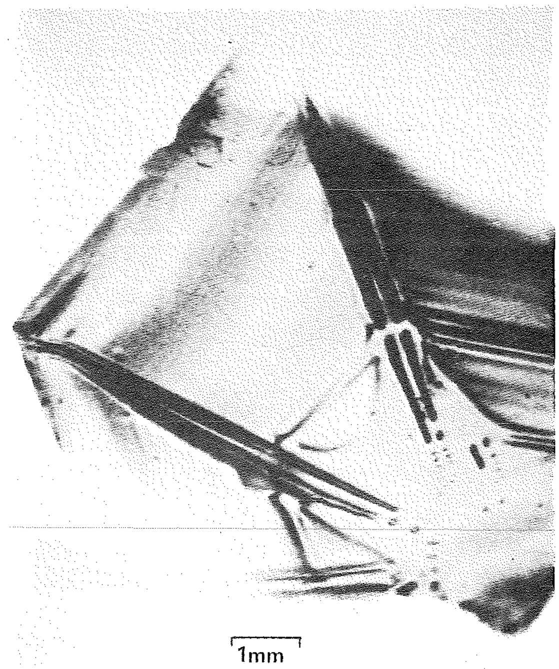

Fig. 3b. Vapor grown crystal showing dislocations associated with ribs, which form internal dislocation loops near the crystal center.

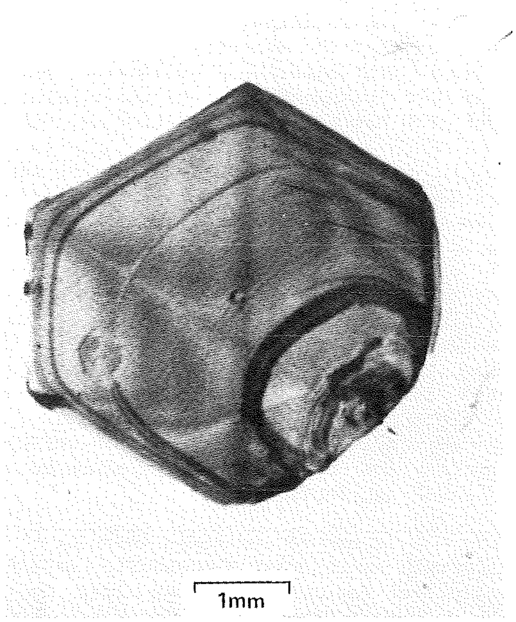

Fig. 4a. Diffusion crystal apparently dislocation free. Grown at -18°C and 15% ice supersaturation.

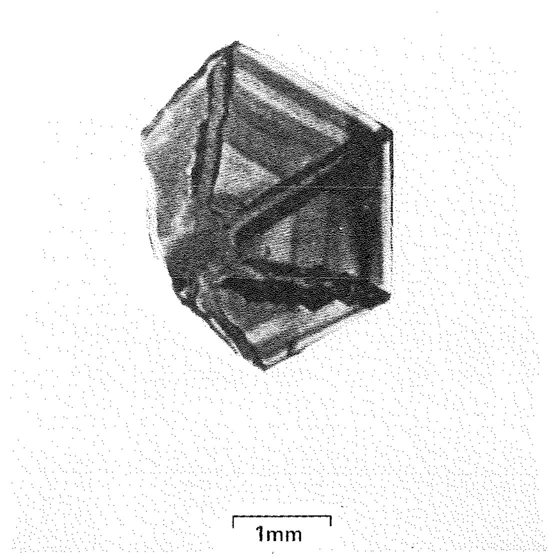

Fig. 4b. Diffusion crystal with visible steps and ribs - possibly dislocation free. Grown at -2°C and 2% supersaturation.

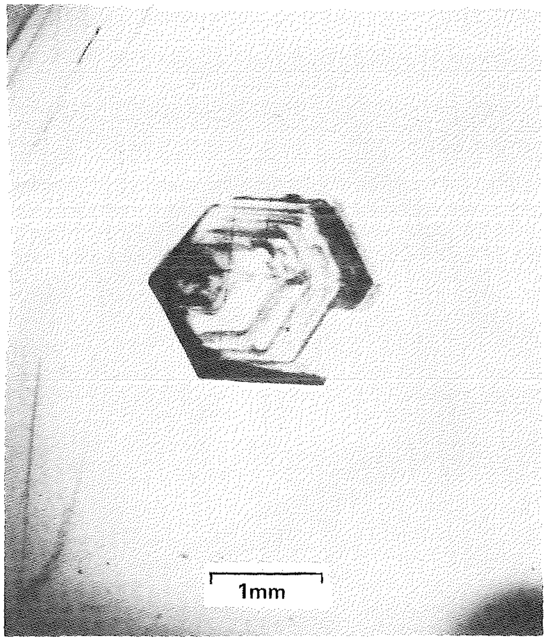

Fig. 5. Frost crystal, defect free. Growth temperature -11 to -13°C.

3. DISCUSSION

The above experimental results may be summarized:

Topographic studies show that crystals grow in the absence of dislocations and at supersaturation above about 0.5 between water and ice. Epitaxial studies show that some crystal (basal) faces exist which do not grow at all in the presence of supersaturation between water and ice; growth can be initiated at a supersaturation which is critical for each crystal. Low supersaturation studies show that crystals may take different habits under the same ambient conditions.

These observations are consistent with the following hypotheses for growth within the range of conditions covered by the experiments:

(a) growth at and somewhat below water saturation is initiated in the absence of defects by a two dimensional surface nucleation process.

(b) some crystal surfaces fail to grow at all at small ice supersaturation; finite growth requires the presence of defects.

(c) growth habit under low supersaturation will be determined by the presence of defects; presence of defects in only "a" or "c" direction will lead to growth only on that face and could give rise to crystals of habit opposite to that usually observed for a crystal with defects in both directions.

(d) habit at high supersaturation and the details of the skeletal growth will be controlled by two dimensional nucleation processes at the crystal edges where the crystal protrudes into higher supersaturation regions.

Earlier studies relating the temperature dependence of the molecular surface migration distance on the basal plane would have bearing in each case - first for the growth of steps as was originally hypothesized, and secondly from the viewpoint that surface nucleation will be much more likely for a higher molecule residence time in an adsorbed layer. For this case the surface energy (as it enters the nucleation analysis) will be related to this migration distance. In either case, however, the complicated variation of surface migration distance and surface energy with temperature require further explanation.

It may be concluded that for crystal growth habit under atmospheric conditions the controlling factor will almost always be the surface nucleation process since most cloud processes take place at or a little below water saturation. In those regions of the atmosphere at small ice supersaturation, probably confined to slow cooling by radiation or slow ascent situations with a plentiful concentration of ice crystals, the habit may be controlled by the initial defect distribution, which is retained during growth and be opposite to that usually (observed.

4. REFERENCES

Bernal, J.D., 1958: Comments on the paper of Hallett & Mason. Proc. Roy. Soc. A 247, 534-536.

Fletcher, N.H., 1970: The Chemical Physics of Ice. Cambridge University Press.

Frank, F.C., 1975: Snow Crystals. I.U.G.G. XVI General Assembly, Grenoble, France, 278.

Gamara, K., and J. Hallett, 1972: The Dynamic Diffusion Chamber for Laboratory Studies of Cloud Processes. International Cloud Physics Conference Proceedings, London, 131-132.

Hallett, J., 1961: The growth of ice crystals on freshly cleaved covellite surfaces. Phil. Mag., 6, No. 69, 1073-1087.

Kobayashi, T., 1965: The Growth of Ice Crystals on Covellite and Lead Iodide Surfaces. Contributions from the Institute of Low Temperature Sciences, Series #20, 1-22.

Kvlividze, V.I., V.F. Kiselev, A.B. Kurzaev and L.A. Ushakova, 1974: The mobile water phase on ice surfaces. Surface Science, 44, 60-68.

Lamb, D., and W.D. Scott, 1972: Linear growth rates of ice crystals grown from the vapor phase. J. Crystal Growth, 12, 21-31.

Mason, B.J., G.W. Bryant and A.P. Van den Heuvel, 1963: The growth habits and surface structure of ice crystals. Phil. Mag., 8, 505-526.

Shaw, D., and B.J. Mason, 1955: The growth of ice crystals from the vapour. Phil. Mag., 46, 249-262.

5. ACKNOWLEDGEMENTS

This work was supported by a grant from the Atmospheric Sciences Division, National Science Foundation, Washington, D.C.

3.1.5

SHAPES OF SINGLE ICE CRYSTALS ORIGINATED FROM FROZEN CLOUD DROPLETS

Choji Magono, Shin-ichi Fujita and Takashi Taniguchi

Department of Geophysics, Hokkaido University
Sapporo, JAPAN

1. INTRODUCTION

It is well known that supercooled cloud droplets first become polyhedrons with 20 faces when they are frozen, then become ice crystals of short column type, their unstable crystal faces of higher orders like pyramidal faces being rapidly disappeared. If the environmental air temperature is around at -15°C, the short columnar ice crystals develop to double plates, as pointed out by Auer (1971). However the formation process for ice crystals of types other than those two types are still not clear.

When the authours examined the relation between the shape of ice crystals and their nucleation mechanisms, utilizing a cloud chamber of diffusion type, they obtained a few hints about the formation processes of ice crystals of types other than short columns and double plates. The supposed processes will be described below.

2. APPARATUS

The vertical crosssection of the cloud chamber used is shown in Fig.1. The chamber was in a cold room, by the temperature of which the air temperature within the cloud chamber was roughly controlled in a range between -5 to -25°C. Water vapor was supplied from a heated water reservoir from above, if required. The cloud chamber was filled up, in general by supercooled cloud droplets, unless the droplets were removed by a special device. The seeding was made, for a few seconds by inserting a metal wire which was previously cooled by dry ice (spontaneous seeding), by AgI smoking or by atomizing water droplets with AgI colloids.

Fig. 1

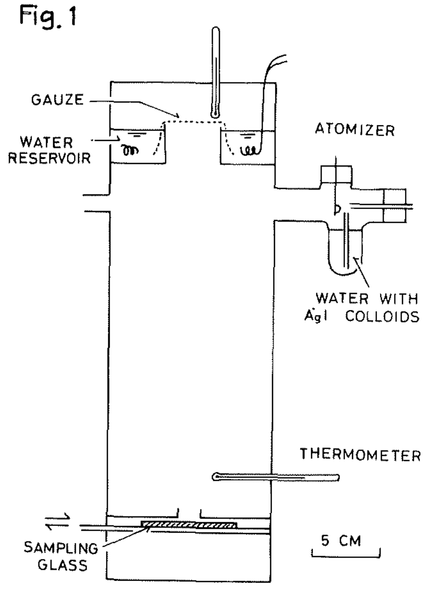

3. ICE CRYSTALS OF STEPPED COLUMN TYPE

In a certain frequency, columnar ice crystals with a thinner co-axial extension are observed in natural ice crystals, as seen in the book of Klinov (1960). This shape of ice crystals are called as "stepped columns" in this paper.

When water droplets with colloidal AgI were atomized at air temperatures of -20 or -25°C, spicules were produced on freezing droplets as seen in Figs.2a and 2b. If supercooled water droplets are rapidly frozen, a spicule is produced from the droplets with diameter of several ten micrometers, as recognized by Iwabuchi and Magono (1975), and the direction of spicule is in agreement with the c-axis of frozen droplets, as demonstrated by Uyeda and Kikuchi (1975).

Frozen droplets with a spicule in

Fig. 2a 2b 2c 2d

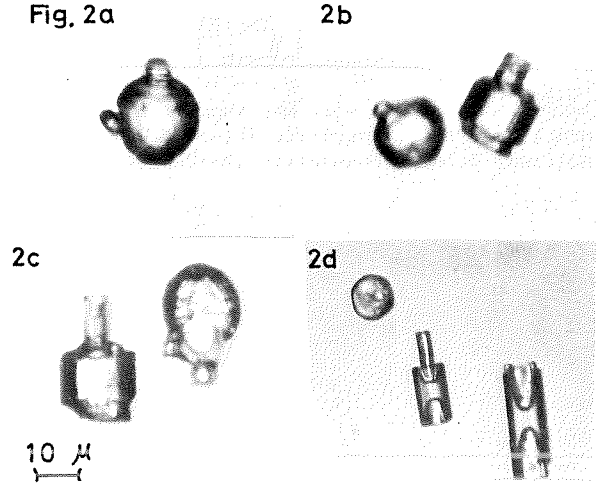

Figs.2a and 2b were obtained by seeding water droplets with AgI colloids, in the same run which was made at around -20°C temperature. In the figures, it may be seen that both the spicules and frozen droplets already have partial crystal faces, and that these faces are parallel with each other. Figs.2c and 2d also show frozen droplets obtained at -24°C temperature. In case of an ice crystal to the left in Fig.2c, the process of stepped column was almost completed, and a frozen droplet to the right is in the process. A completed stepped column is seen in the center of Fig.2d, together with a regular column and a frozen droplet.

Four pictures in Fig.2 are not successive pictures of the same droplets, but were composed from pictures in two runs, however the series of pictures suggest a successive process of forming stepped columns, that is to say, first a spicule is produced on a freezing droplet, then both the spicule and the mother droplet develop to a columnar shape respectively in a condition of column development, in other words, at a temperature region of around -20°C. However the authors do not deny the possibility of other processes forming such stepped columns, for example the attachment of a supercooled cloud droplets to the basal plane of a column.

4. PLATES IN A COLDER TEMPERATURE REGION

It is well known that six branches of this planes or dendrites symmetrically develop sidewards from the center of a snow crystal around air temperature of -15°C (Nakaya, 1954 and Magono and Lee, 1966). However it was found that such planes (at most six) extended from a neck at the center of a twin of columns in temperatures of -20 and -22°C nearly at the water saturation humidity.

A pair of such ice crystals are illustrated in Figs.3a and 3b. These ice crystals were also formed by seeding water droplets with AgI colloids at temperatures of -20 and -22°C in a supersaturated condition. One shows the side view and another, the vertical view of ice crystals which fell side by side on nearly the same place of a sampling glass. In case of Fig.3a, the ice crystal has four branches, and in case of Fig.3b, two branches of plate form are seen to extend.

Side views of thin type of ice crystals are illustrated in the book of Klinov, and Kikuchi and Hogan (1975) took a picture of a snow crystal with five such branches.

The occurrence of ice crystals of this type were also frequently in laboratory experiments, however such sidewards extending branches were not noted, or

Fig. 3a

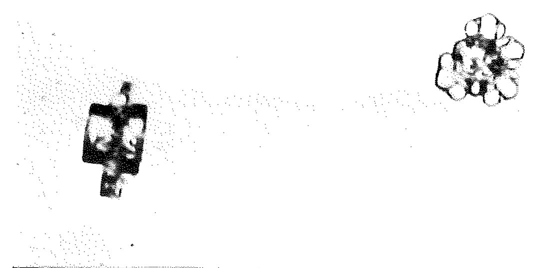

3b

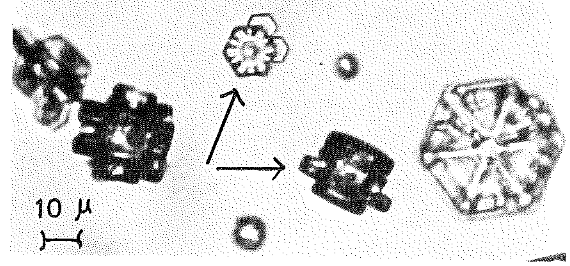

might be misunderstood as usual plane branches which develop in a temperature region around -15°C. However this type of plane branches are entirely different from usual plane branches in following points. The branches extend at temperatures of around -20°C in which ice crystals usually develop to columns. The branches do not extend from the corner of upper or bottom basal plane of a column, but from the neck at the center of a twin column. It is considered that the branches are belonged to the kind of the side plane.

5. ICE CRYSTALS OF SINGLE BULLET TYPE

Two kinds of snow crystals of bullet type are observed in natural snow, i.e. single bullets and combination of bullets (Nakaya, 1954 and Magono and Lee, 1966). Kikuchi (1968) considered that single bullet snow crystals are only fractions of bullets which were disrupted from snow crystals of combination of bullets. However the possibility of existence of single bullets are still left in the case of "ice crystals" which mean diamond dusts or ice particles in cirrus clouds.

In our laboratory experiment, ice crystals of single bullet type were frequently produced by spontaneous seeding, occasionally predominantly at air temperatures around -25°C, and a hint was obtained regarding the formation process of single bullets. In Fig.4a, it may be seen that frozen droplets have a spicule with a sharp pointed top. The frozen droplets were obtained by seeding AgI smoke at a temperature of -25°C nearly at the ice saturation humidity. Single bullet ice crystals were obtained by seeding with a cooled metalic wire, as seen in Fig.4b in which pyramidal ice crystals with a basal plate are also seen. Occasionally ice crystals of single bullet type were predominantly produced, as seen in Fig.4c in nearly the same condition. These figures

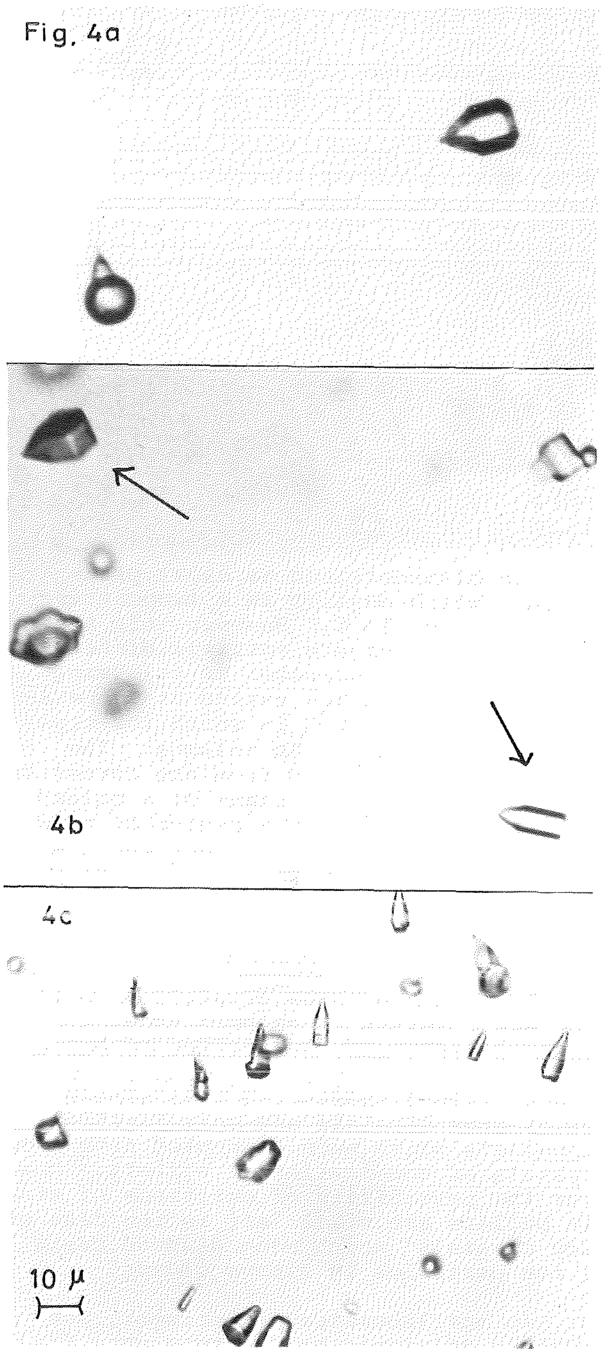

suggest a process that ice crystals of bullet type were originated from frozen droplets with a spicule of a sharp pointed top at a cold temperature which is favourable for the formation and survival of the pyramidal crystal faces. It is very strange that the combination of bullets was not observed in the experiment.

6. PYRAMIDAL ICE CRYSTALS

The occurrence of snow crystals of pyramidal shape is very rare in natural snow, however this shape of ice crystals were frequently observed in the condition of -25°C air temperature with a humidity of nearly the water saturation, by the spontaneous nucleation.

Semi-spherical frozen droplets are seen in Fig.5a. Regarding the semi-spherical shape of the droplets, two possible mechanisms are considered. One is that these frozen droplets are only fractions of disrupted droplets during freezing. Another is that the flat surface at the semi-sphere is a developed crystal surface. Ice crystals of complete pyramidal shape in Fig.5b were obtained in nearly the same condition as in Fig.5a.

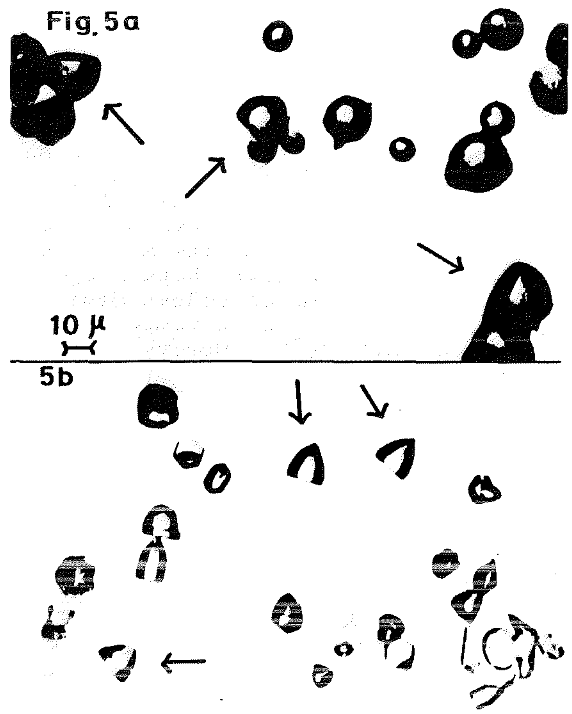

Some of them have a plate at the bottom. Comparing Fig.5b with Fig.5a, it is supposed that these pyramidal ice crystals as seen in Fig.5b were originated from semi-spherical frozen droplets as seen in Fig.5a. This supposition will be accepted after the consideration of formation process of pyramidal ice crystals with a plate or a short column, below.

7. PYRAMIDAL ICE CRYSTALS WITH A PLATE OR A SHORT COLUMN

Ice crystals shown in Figs.6a, 6b and 6c were obtained by the spontaneous seeding at the same run in condition of -25°C and the water saturation. It may be seen that the crystalization just started to take place in a frozen droplet with a plate in Fig.6a, pyramidal faces are partially seen in ice crystals in Fig.6b and pyramidal faces were already completed in ice crystals in Fig.6c.

Throughout ice crystals with pyramidal faces in Figs.4, 5 and 6, it is considered that the pyramidal face can sur-

Fig. 6a

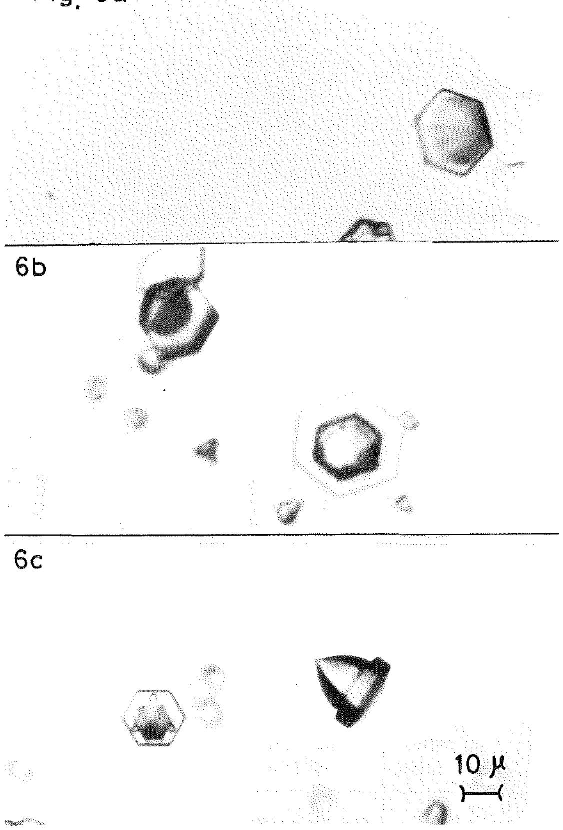

vive in temperatures lower than -25°C in the humidity of nearly the ice saturation, and that the final shape of ice crystals with pyramidal faces is determined by the initial shape of frozen droplets. The proposed processes of ice crystals of cold temperature region are summarized schematically in Fig.7.

Fig. 7

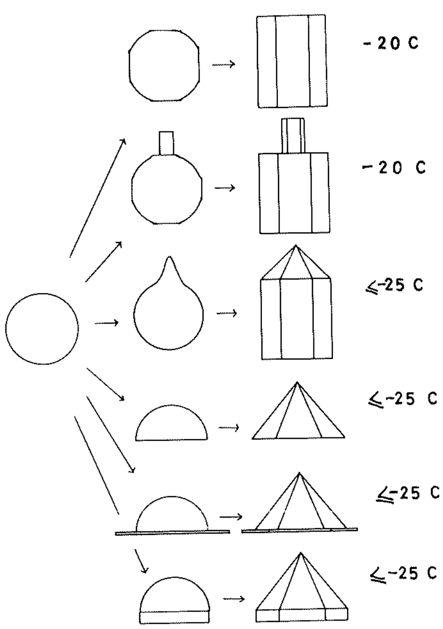

8. CONCLUSIONS

Even when the authors intended to completely remove aerosols or water droplets from the cloud chamber, by keeping it moist and cold for a day, a few minute droplets were recognized on the sampling glass. Accordingly it is considered that almost all ice crystals observed, were originated from frozen droplets. Although the reproduction of the results obtained is not yet perfect, it may be concluded that the ice crystals of stepped form are originated from frozen droplets with a spicule, and that the pyramidal face can survive at temperature range lower than -25°C.

References

Auer Jr., A.H., 1971: Observation of ice crystal nucleation by droplet freezing in natural clouds. J. Atmos. Sci., 28: 285-290.

Iwabuchi, T. and C. Magono, 1975: A laboratory experiment on the freezing electrification of freely falling water droplets. J. Met. Soc. Japan, 53: 393-401.

Kikuchi, K., 1968: On snow crystals of bullet type. J. Met. Soc. Japan, 46: 128-132.

Kikuchi, K. and A.W. Hogan, 1975: Observations of ice crystals in the South Pole in the summer season. Proc. Spring Meeting of Met. Soc. Japan, 27: 89.

Klinov, F.Ja, 1960: Voda v Atmosfere pri Nizkikh Temperaturakh. Acad. Nauk, USSR, pp.171.

Magono, C. and C.W. Lee, 1966: Meteorological classification of natural snow crystals. J. Fac. Sci., Hokkaido Univ., Ser.VII, 2: 321-335.

Nakaya, U., 1954: Snow Crystals. Harvard Univ. Press, Cambridge, pp.510.

Uyeda, H. and K. Kikuchi, 1975: On the direction of crystal axes of frozen water drops. Proc. Autumnal Meeting of Met. Soc. Japan, 28: 188.

3.1.6

ON MORPHOLOGY OF SNOW CRYSTALS

T. Kobayashi

Institute of Low Temperature Science
Hokkaido University, Sapporo, Japan

1. INTRODUCTION

Studies have been made on the morphology of snow crystals on the basis of their groupings categorized by the habit and the type of growth, not drawing on the 41 classes classified by Nakaya (1954) or the 80 classes by Magono and Lee(1966) according to the shapes of natural snow crystals, which were found too complicated to serve for the discussion of the morphology, whereas the eight groups of artificial snow crystals by Nakaya on his T_a - s diagram are found to be inadequate for this purpose, only showing the "overall shapes" of crystals in relation to certain environmental conditions with no fundamental basis to categorize.

Studying the growth of ice crystals, Mason (1955, 1958) stated clearly in his earlier papers that the habit and therefore whether a crystal develops as a prism or a plate is determined by the temperature. Later, Kobayashi(1961) consolidated his experimental results and those of Nakaya, Shaw and Mason(1955), Hallett and Mason(1958), as shown in Fig. 1, whereby he established a diagram, which shows that the temperature determines the habit* of a crystal, while the excess vapour density controls whether a crystal develops as a bulky, a hopper, or a dendritic one, which he refers to as the type of growth or growth feature.

The change of habit with temperature and the change of growth type with excess vapour density have been discussed by Mason et al.(1963), Hobbs (1965, 1971), Frank(1974) and Chernov(1974). The change of habit may be explained by surface diffusion, while the change of growth type may be explained in such a way that a bulky growth is controlled by dislocations which emerge on the faces and the hopper and a dendritic growth is controlled by two-dimensional nucleation which takes place at the edges and corners of the crystals.

The diagram(Fig.1) and these discussions, however, are simply concerned with the growth morphology of single crystalline snow crystals, while many types of polycrystalline snow crystals have been observed. They are "twin prisms", combination of bullets, twelve-branched crystals, assemblage of plane branches in radiating and spatial types, as well as some other peculiar shaped crystals.

The growth morphology of snow crystals should then be reviewed from a simple basic foundation, though their overall shapes are very much complicated. The habit and the growth type of each component crystal in the polycrystalline type of snow are duely considered to obey the diagram in Fig. 1, but considerations have to be given to the formation and structure of polycrystalline germs of the crystals. Some evidence is given in this paper to show the growth of re-entrant twin edge and the growth controlled by dislocation for the natural snow crystals observed.

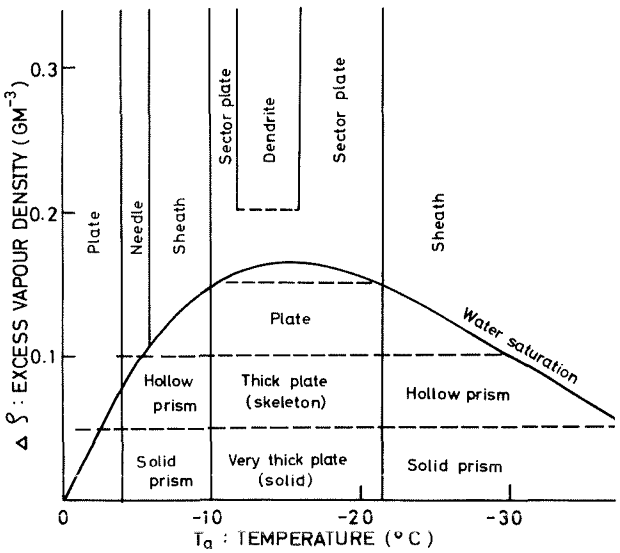

Fig. 1. The variations of snow-crystal habit with temperature and growth type with excess vapour density.

2. TWINNED STRUCTURES IN SNOW CRYSTALS: GENERALIZED-CSL THEORY

When an ice germ is formed by freezing of a cloud droplet or it is nucleated on some other material so that it develops into a polycrystalline state, a twin is likely to come out of it, as Buerger(1945) suggested, "if the structure is of such nature that it permits a continuation of itself in alternative twin junction configuration without involving violation of immediate coordination requirements of its atoms, the junction has low energy and the twin is energetically possible". This will be a leading principle in considering the polycrystalline structures of snow crystals in this paper.

* Although it appears that the word habit has been used in a rather ambiguous way in cloud physics, this word is referred to in this paper as an overall shape of a crystal which undergoes changes depending on different degree of development in different crystallographic faces; its corresponding term is Tracht in German and Shūsō in Japanese.

Kobayashi and Furukawa(1975) proposed a possible mechanism for the formation of a centered twelve-branched crystal; that is, this crystal consists of two components, each of which is a six-pointed crystal and develops from the base at either end of a twinned short prism at the center. They showed that the angle between the counterpart branches of each component, in effect, is equal to the rotation angle about [0001] of the twinned prism, which was expected by the Coincidence-Site Lattice(CSL) concept originally proposed by Kronberg and Wilson(1949) and later discussed by Price(1959) and Fletcher(1971). The results are summarized in Table 1.

Kobayashi and Ohtake(1974) explained the formation of a groove during evaporation on the faces of an ice prism("twin prism") by a rotation twinning about [11$\bar{2}$0] which brings about a stacking fault on the plane (0001). This twinning structure is now understood as a special case of those proposed by Kobayashi and Furukawa(1975).

In these examples the CSL concept was applied only to (0001) of an ice crystal as a composition plane in twinning. This is a very simple case, where the multiplicity Σ, which is proportional to the reciprocal density of the coincidence sites, is assumed to be a measure of energy of an interfacial boundary, because bond arms extended from O-atoms at the boundary are perpendicular to (0001) so that the bonding is perfect at each coincidence site.

As the next step of approach the CSL concept was generalized and applied to any other crystallographic plane $\{h_1h_2\bar{h}_3k\}$ so that the crystallographic orientations and structures of polycrystalline types of snow crystals were explained on the basis of a rotation twinning, with its twin axis perpendicular to the plane $\{h_1h_2\bar{h}_3k\}$.

When an ice crystal is cut along any crystallographic plane $\{h_1h_2\bar{h}_3k\}$ and the upper half crystal is rotated by an angle of 180° about the axis $\ll h_1h_2\bar{h}_3k \gg$* all the lattice points along the composition plane will exactly coincide with each other. Since the area of the CSL is different on each different composition plane, the reciprocal density of the coincidence sites, λ, may be given as the area of the CSL divided by $\underline{a} \times \underline{c}$, where $\underline{a}$ and $\underline{c}$ represent the lattice unit length in $\underline{a}$-axis and $\underline{c}$-axis directions respectively. In this case, however, the orientation of a pair of bond arms across the composition plane does not always coincide with each other after the upper half of the crystal is rotated by 180° about the axis $\ll h_1h_2\bar{h}_3k \gg$, because the directions of the bond arms are not perpendicular, in general, to $\{h_1h_2\bar{h}_3k\}$. Let the angle between each pair of bond arms facing each other be defined as "bond misorientation" β.

In order that the O-O bonding is accomplished at the coincidence sites, β must be small. And it may be assumed that the bonding which has the minimum bond misorientation β will be realized at each pair of the bond arms. Then β may be obtained by the stereographic projection method.

As the reciprocal density of the coincidence sites, λ, and the bond misorientation β may be considered to be a measure of energy of a composition boundary, it will be possible to conclude that two parts of a crystal rotationally displaced about $\ll h_1h_2\bar{h}_3k \gg$ by an angle of 180° can form a twin only if both the values of λ and β are small. An abbreviation is introduced here to call this an $\ll h_1h_2\bar{h}_3k \gg$ twin, its twin axis then being $\ll h_1h_2\bar{h}_3k \gg$. The number of the bond arms accom-

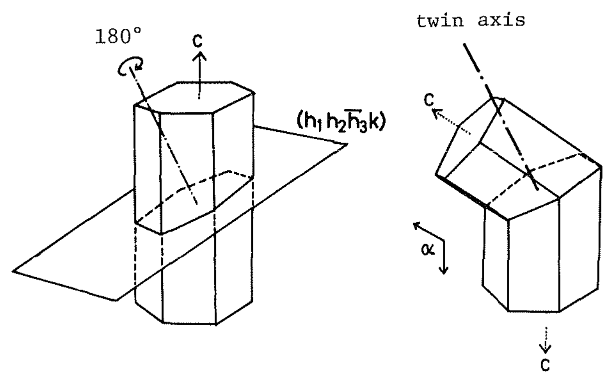

Fig. 2. Illustration of formation of $\ll h0\bar{h}k \gg$ twins.

* For convenience the notation $\ll h_1h_2\bar{h}_3k \gg$ is used in this paper as an axis perpendicular to the plane $\{h_1h_2\bar{h}_3k\}$.

Table 1. CSL relationships for possible coincidence boundaries on (0001) in rotation twinnings.

Rotation angle about [0001](deg)	Multiplicity[a] Σ	Σ'	Axial ratio of twin axis	Corresponding crystal form and angle observed
60	1 (stacking fault)		[11$\bar{2}$0]	Twin prism with identical $\underline{c}$- and $\underline{a}$-axis orientation.
38.2 (21.8)	7		[21$\bar{3}$0]	Twist prism and twelve-branched crystal, each six-pointed component being rotationally displaced by 22°.
27.8	13		[31$\bar{4}$0]	Twist prism and twelve-branched crystal, rotationally displaced by 27°.
30.6	93	14	[8,3,$\overline{11}$,0]	Twelve-branched crystal, rotationally displaced by 30°.
30.0	(square)[b]	11	Diagonal to the square cell	

a), b) See, ref. Kobayashi and Furukawa(1975) plished at a boundary may also be considered as a factor accounting for the probability of twinning realized in nature. The angle α between the two c-axes of each component crystal composing an $\ll h_1 h_2 \bar{h}_3 k \gg$ twin may be calculated.

In this twin relation, each component crystal possesses a common axis which is perpendicular to the plane composed by the two c-axes of the components.

2.1. $\ll h0\bar{h}k \gg$ twins

An $\ll h0\bar{h}k \gg$ twin has the common a-axis $[11\bar{2}0]$ and the rectangular CSL along the composition plane $\{h0\bar{h}k\}$.

Table 2 gives a set of values α_a, λ_a, and minimum β_a, where the suffix a denotes the common axis in the twin relation for possible twinned structures of snow crystals to be expected in nature.

Table 2. CSL relationships for possible $\ll h0\bar{h}k \gg$ twins.

Composition plane	α_a (deg)	$\alpha'_a = 180° - \alpha_a$ (deg)	λ_a	β_a (deg)	number of bondings
$10\bar{1}1$	55.7		1.13	9.5	2
$10\bar{1}2$	93.1	86.9	1.45	8.0	2
$10\bar{1}3$	115.5	64.5	1.87	4.0	2
$20\bar{2}1$	29.6		2.07	8.5	1
$20\bar{2}3$	76.8		2.55	3.0	2
$20\bar{2}5$	105.7	74.3	2.31	2.0	2
$30\bar{3}2$	38.8		3.18	0.0	1
$30\bar{3}4$	70.3		3.67	0.0	2
$30\bar{3}8$	109.2	70.8	5.18	0.0	2

As Table 2 shows, O-O bondings are perfect in $\ll 30\bar{3}4 \gg$, $\ll 30\bar{3}8 \gg$ and $\ll 30\bar{3}2 \gg$ twins at the coincidence sites, β_a being 0.0°.

Even when $\beta_a \neq 0.0°$, a minor adjustment may be allowed in the bond orientation in order that the twinning structure is achieved at the boundary. However, it may be difficult to evaluate the extent of allowances which can be made.

The twins shown in Table 2 may be predicted as possible ones, considering the values of λ_a and β_a as well as the number of the bond arms accomplished at the boundary. Some of these twinning relations may be supported by the observational evidence that angles 70°, 110°, 90° and 55° have been frequently reported as the angle between the c-axes of each component crystal of the polycrystalline type of snow crystals.

An $\ll h,h,\bar{2h},k \gg$ twin has the common b-axis $[10\bar{1}0]$. Only $\ll 11\bar{2}8 \gg$ and $\ll 33\bar{6}4 \gg$ twins might be possible ones.

3. COMPARISON OF OBSERVATIONAL RESULTS WITH THEORETICAL FINDINGS

Detailed discussions on formation of "twin prisms", twist prisms and twelve-branched crystals can be seen in the previous papers (Kobayashi and Ohtake 1974; Kobayashi and Furukawa 1975) and a part of their findings is summarized in Table 1.

3.1 Combination of bullets

A possible mechanism is proposed as to the formation of a combination of bullets; it originates from a polycrystalline ice seed and some of the components may have such twin relations with each other as are described in the previous section. They grow to form a combination of columns or prisms when the ambient temperature is in the range amenable to the growth of prism, leaving sublimated portions behind along the composition boundaries (Fig. 4). In order that the above proposed mechanisms were checked, the c-axes angles between each component bullet lying on one and the same plane of this type of crystals were measured on the photomicrographs of the crystals naturally observed.

The results of measurements are shown in Fig. 3, where the supplement was taken for the angle α_{obs} larger than 90°; mutual a-axes orientations were not examined in these measurements. It must be noted that the observed peaks around 90°, 70°, 65° and 55° for the angle α_{obs} are in good agreement with the angles predicted by the twinning relation in $\ll 10\bar{1}2 \gg$, $\ll 30\bar{3}4 \gg$ or $\ll 30\bar{3}8 \gg$, $\ll 10\bar{1}3 \gg$ and $\ll 10\bar{1}1 \gg$ twins respectively. Lee (1972) also found high peaks around 70° and 55° on his histogram for crystals of the type of a combination of the capped bullets.

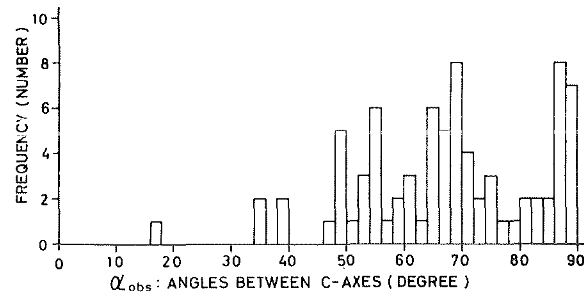

Fig. 3 A frequency histogram of measured angles between the c-axes of each component in crystals of the type of a combination of bullets lying on the same plane of a photomicrograph.

There have been observed many examples of such a crystal type of a combination of bullets or prisms that forms a penetration twin. Illustrated in Fig. 4 are interfaces of an ice crystal in the possible form of such a crystal. In this figure interfaces aa' and bb' intersect perpendicularly each other. The pairs of crystals A - B and C - D compose rotation twins with the composition plane aa' and with the twin axis perpendicular to the plane. The other pairs of crystals A - D and B - C compose rotation twins with the composition plane bb' and with the twin axis perpendicular to the plane.

The c-axes angle for each pair of crystals, α and α' in Fig. 4 are in a supplementary relation. As for $\ll 30\bar{3}4 \gg$ and $\ll 30\bar{3}8 \gg$ twins, they are in the most probable twinning relation, because both the c-axes angles between each component are 70.3° and 109.2° being in an almost supplementary relation.

A penetration twin may possibly be composed of two $\ll 10\bar{1}2 \gg$ twins, since the c-axes angle in the ≪$10\bar{1}2$≫ twin is 93.1°, which is very approximate to 90°.

A single bullet crystal may then be a detached one from a primary growth structure; this detachment may reasonably be attributed to a gross weakening of the structure at the center of the combination due to prolonged evaporation along the composition plane. The evaporation along the boundaries is considered to be primarily responsible for the formation of a round cone-shaped head of bullet(Gow 1965).

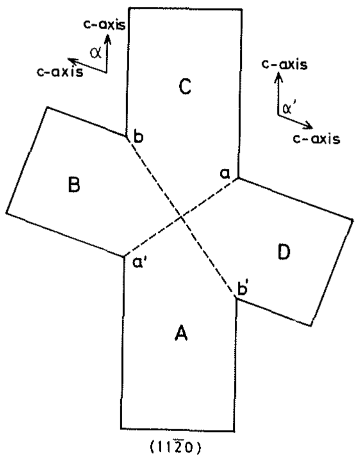

Fig. 4. Illustration of a penetration twin.

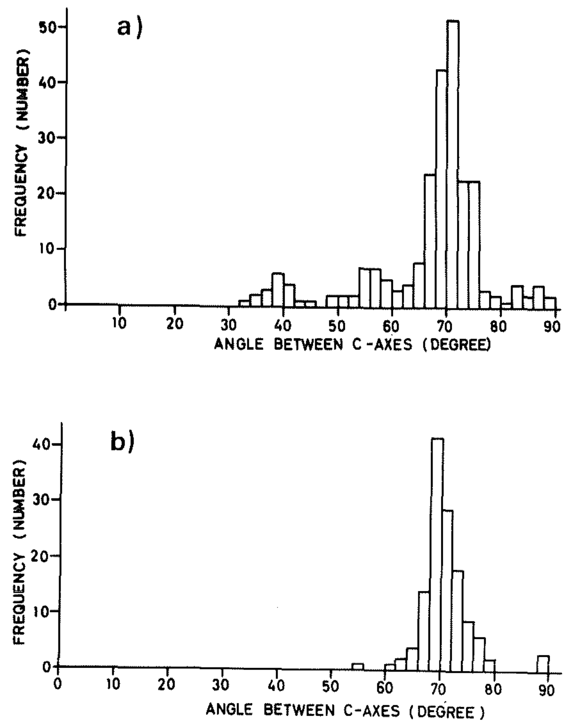

Fig. 5. Distribution of c-axes angles between different branch planes in snow crystals of a)radiating type and b)spatial type(after Lee 1972).

3.2 Spatial assemblage of plane branches in a radiating type and in a spatial type (types P5b and P5a by Nakaya's classification respectively)

A twinned seed probably formed by freezing of a cloud droplet*, may develop into an assemblage of plates or dendrites when ambient temperatures are in the range amenable to the growth of plate. The penetration structure composed of ≪$30\bar{3}4$≫ and ≪$30\bar{3}8$≫ rotation twins may be a probable one for the radiating type and the angle of 70° predicted by this model as the c-axes angle between two components is in good agreement with Lee's observation(Fig. 5).

Formation of an assemblage of plane branches in a spatial type may be explained in the same way, being attributed to the contact and freezing of cloud droplets onto any spots on the dendritic branches in the twin relation such as ≪$30\bar{3}4$≫ and ≪$30\bar{3}8$≫ types. Lee's report is interesting to note. Namely, he found a single predominant peak on his frequency histogram around 70° also for this type of crystals and confirmed that the a-axes of the secondary branches were always in parallel with that of the substrate crystals, which gives another evidence to support the formation of the ≪h0hk≫ type of the rotation twins.

4. A CONTINUOUS STRUCTURE MODEL FOR EXPLAINING C-AXES ANGLE OF 70° BETWEEN EACH COMPONENT

It is very interesting and suggestive to note that the distribution of c-axes angle between each component is predominantly concentrated at 70° for the combination of bullets, plane assemblages in radiating and spatial types, as shown in Figs. 3 and 5. The models of the ≪$30\bar{3}4$≫ and ≪$30\bar{3}8$≫ rotation twins may be possible ones to explain this angle in view of the GCSL theory, because $\beta_a = 0.0°$ and $\lambda_a = 3.67$ and 5.18, which are small. However, a judgement on whether values of λ_a are small or large cannot be formed by other ways than examining the frequency in appearance of crystals in nature.

Buerger's continuation principle is now recalled. If we consider something apart from the GCSL theory, it may be possible to propose more continuous structures in an alternative twin junction configuration without violating the immediate coordination requirement.

It may be considered that the angle 70° is related to 110° as the supplementary angle, which

* Recently Uyeda(Kobayashi et al. 1976) measured the number of component crystals and the angles between the c-axes of neighbouring crystals when a water drop of 1.0 - 1.7mm in diameter was frozen under controlled rates of cooling. He found there are two peaks in a frequency distribution of the c-axes angles, one at 60 - 80° and the other at 20 - 30°.

is quite close to the tetrahedral angle 109°28'.

Neglecting minor differences (less than 1 %) in distances and angles between O and O atoms tetrahedrally arranged in an ice structure, it may be easily understood, as shown in Fig. 6, that any of three O - O bonds, each oriented in a-axes directions, can behave as a c-axis of a second component with the angle 110° against that of the original one, forming a continuous structure in an alternative twin junction. In Fig. 6 a component crystal A has a hexagonal stacking order abba... with the c-axis in the direction from bottom to top in the figure and another component B has a hexagonal stacking order abba... with the c-axis inclined at 110° to that of A, while the junction J has a cubic stacking order abbcca... in both the c-axes directions.

The entire crystal will grow in the shape of the penetration twin shown in Fig. 6, leaving behind offset planes EE', FF', GG' and HH' which emerge from the intersections of the junction planes between the hexagonal and cubic portions. When a crystal grows as a penetration twin prism and thereafter begins to evaporate depending upon the environmental conditions, evaporation will proceed along the offset planes to produce bullet head with a round corn-shape; then an individual bullet will be formed by disintegration due to a gross weakening of the structure at the center.

It may be understood that, as an extreme case, at least one layer of a stacking fault can produce a penetration twin; namely, elements A and C are in a relation of a rotation twin and elements B and D in a relation of another rotation twin. This is just a combination of the "twin prism" model which was fully described in the previous paper (Kobayashi and Ohtake 1974). If the junction has a sequence of the stacking fault in any number of layers, it just forms a repetition of the rotation twin relations.

This structure model suggests a formation of an ice cluster in a cubic system, which is a metastable structure in ice and may probably be formed when an ice crystal is nucleated at a high degree of supersaturation and at low temperatures.

5. STRUCTURE DEPENDENT SHAPES IN SNOW CRYSTALS

A growth morphology of snow crystals has been discussed in view of the habit, growth type and twinning structures in crystal germ. An immense variety in the shapes of single crystalline snow crystals is attributed to the changes of the habit with temperature and the changes in the growth type which are controlled by two-dimensional nucleation processes. Spatial dispositions in polycrystalline

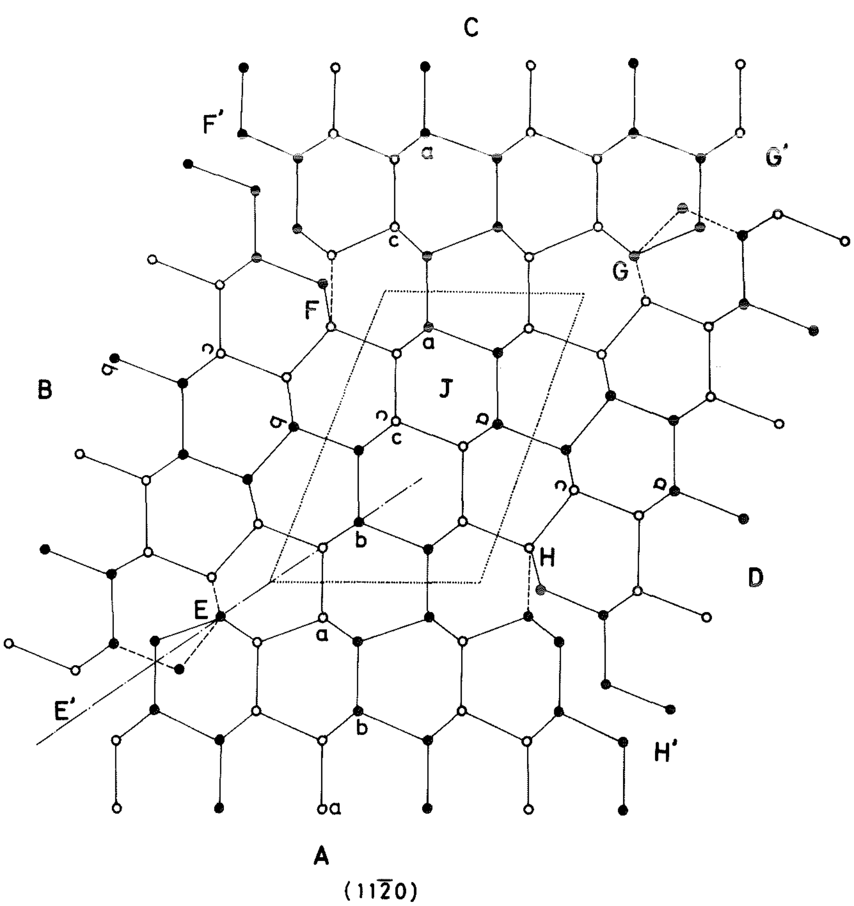

Fig. 6. A continuous structure model for twinning whose c-axes angle between each component is 70°: projection along [11$\bar{2}$0].

types of the crystals may be controlled by the twinning structure of their germs when they are nucleated.

Kobayashi et al.(1976) explained some of peculiar shaped snow crystals on the basis of a re-entrant twin edge growth as suggested by Wagner(1960). Characteristic shapes in a linear assemblage of twinned columns and scrolls (see, Figs. 15 - 17 in ref. Kobayashi et al.(1976)) may be attributed to "ribbon growth" at the re-entrant edges and the shape of each component crystal may depend on the habit and growth type under the environmental conditions.

Another interesting shape of a snow crystal was found by Y. Furukawa at Mt. Taisetsu, Hokkaido in Feb. 1976 and is shown in Fig. 7. This was a plane dendritic crystal with a whisker appearing to grow at its center vertically to the plane ; the whisker began to broaden in thiskness as it grew (Kobayashi 1965) and the small dendrite started to develop at the end of the whisker when it stopped to grow.

Dendrite branches develop by the growth of layers started at their edges and corners by the two-dimensional nucleation mechanism, while at the center part of the growing crystal the growth can be controlled only by dislocations due to a very low supersaturation. The crystal may grow at the center if dislocations take part in producing a whisker vertically to the surface. Detailed discussions will be given in another paper : however, Fig. 7 clearly indicates that another important and interesting target to study hereafter will be about the dislocation-controlled growth and morphology of the snow crystal which may not depend on the ordinary habit and growth type.

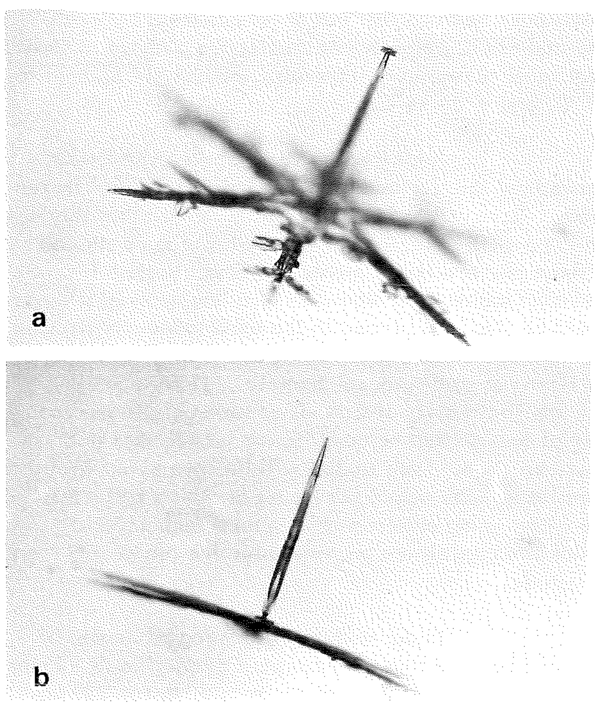

Fig. 7. Growth of a whisker at the center of a dendrite crystal: a) oblique view, and b) side view.

Acknowledgements

The author wishes to express his thanks to Yoshinori Furukawa for his assistance through the observation of snow crystals at Mt. Taisetsu and also for his help in preparing the manuscript.

References

Buerger, M.J., 1945:The genisis of twin crystals. Ameri. Mineralogist, 30, 469-482.

Chernov, A.A., 1974:Stability of faceted shapes. J. Crystal Growth, 24/25, 11-31.

Fletcher, N.H., 1971:Crystal interface models. Adv. in Material Res. 5, 281-314.

Frank, F.C., 1974:Japanese work on snow crystals. J. Crystal Growth, 24/25, 3-5.

Gow, A.J., 1965:On the origin of bullet crystals at the south pole. J. Glaci. 5, 461-465.

Hallett, J. and B.J. Mason, 1958:The influence of temperature and supersaturation on the habit of snow crystals grown from the vapour. Proc. Roy. Soc. 247, 440-453.

Hobbs, P.V. and W.D. Scott, 1965:A theoretical study of the variation of ice crystal habit with temperature. J. Geophys. Res. 70, 5025-5034.

Kobayashi, T., 1961:The growth of snow crystals at low supersaturation. Phil. Mag. 6,1363-1370.

Kobayashi, T., 1965:Vapour growth of ice crystals between -40° and -90°C. J. Meteor. Soc. Japan, 43, 359-367.

Kobayashi, T. and T. Ohtake,1974:Hexagonal twin prisms of ice. J. Atmos. Sci. 31, 1377-1383.

Kobayashi, T. and Y. Furukawa, 1975:On twelve-branched snow crystals. J. Crystal Growth, 28, 21-28.

Kobayashi, T., Y. Furukawa, K. Kikuchi and H. Uyeda, 1976:On twinned strucutres in snow crystals. J. Crystal Growth, 32, 233-249.

Kronberg, M.L. and F.H. Wilson, 1949:Secondary recrystallization in copper. Matals Trans. 185, 501-514.

Lamb, D. and P.V. Hobbs, 1971:Growth rates and habits of ice crystals grown from the vapor phase. J. Atmos. Sci. 28, 1506-1509.

Lee, C.W., 1972:On the crystallographic orientation of spatial branches in natural polycrystalline snow crystals. J. Meteor.Soc. Japan, 50, 171-180.

Magono, C. and C.W. Lee, 1966:Meteorological classification of natural snow crystals. J. Fac. Sci. Hokkaido Univ. Ser.VII, 2, 321-335.

Mason, B.J., 1958:The growth of ice crystals from the vapour and the melt. Adv. in Phys. 7, 235-253.

Mason B.J., G.W. Bryant and A.P. Van den Heuvel, 1963:The growth habits and surface structure of ice crystals. Phil. Mag. 8, 505-526.

Nakaya, U., 1954:Snow Crystals. Harvard Univ. Press, Cambridge, pp.510.

Price, P.B., 1960:On the growth of cadmium crystals from the vapour. Phil. Mag. 5, 473-484.

Shaw, D. and B.J. Mason, 1955:The growth of ice crystals from the vapour. Phil. Mag. 46, 249-262.

Wagner, R.S., 1960:On the growth of germanium dendrites. ACTA Met. 8, 57-60.

3.1.7

A WIND TUNNEL INVESTIGATION OF THE GROWTH RATE AND GROWTH MODE OF ICE PARTICLES BY RIMING

J. C. Pflaum and H. R. Pruppacher

University of California
Los Angeles, California

1. INTRODUCTION

The riming process during which hexagonal ice crystals and frozen drops collide with supercooled water drops is of considerable importance to the formation of precipitation in atmospheric clouds in that it is the process by which graupel particles and hailstones are formed. Although much work has been done on the "hail-stage" of this riming growth by List, Macklin, Knight, Gokhale, and others (for a summary of past work see Mason, 1971), relatively little attention has been paid to the "graupel-stage" of riming growth. Recently, Pitter and Pruppacher (1974) and Schlamp et al. (1975) reported the results of their numerical model for determining the efficiency with which ice plate-like and columnar crystals initially collide with supercooled water drops. In addition, these authors predicted that, in agreement with the field observations of Hobbs (1971), Kikuchi (1972), Ono (1969), and Wilkins and Auer (1970), the collision process between ice crystals and water drops exhibits a rather sharp cut-off which, for columnar crystals (independent of their length) is near a columnar diameter of 50 μm, and for plate like crystals (independent of their thickness) is near a plate diameter of 300 μm. In agreement with the field observations the theoretical results also demonstrate that drops smaller than 10 μm are captured with practically negligible efficiency even by relatively large ice crystals.

This behavior is in strong contrast to the collision behavior of drops colliding with drops which is characterized by considerably different collision efficiency values showing no cut-offs. Wind tunnel studies of Pitter and Pruppacher (1973) and of Pruppacher and Schlamp (1975) further show that the efficiency with which frozen drops collide with liquid supercooled drops cannot a priori be assumed to be given by the efficiency with which two liquid water drops collide, because of their observation that frozen drops spin and tumble in various modes while liquid drops exhibit no such motion except internal circulation.

In order to quantitatively determine the growth rate and collection efficiency of riming ice crystals and frozen drops, both of which have been found by field studies to serve as graupel and hailstone embryos, we began a series of wind tunnel investigations. A few preliminary results and some tentative conclusions are summarized below.

2. EXPERIMENTAL SET-UP

The present study was carried out by means of the UCLA cloud tunnel described in detail by Pruppacher and Neiburger (1968), Beard and Pruppacher (1969), and in its modification for work at temperatures below 0°C by Pitter and Pruppacher (1973). This set-up allows studying the growth of ice particles of various sizes and shapes by collision with supercooled drops under controlled temperature and humidity conditions. The cloud of supercooled drops injected into the tunnel air stream was produced by a steam condensation method. The size distribution of the cloud drops was determined by the rod impaction method described by Beard and Pruppacher (1971). This method was checked by a laser diffraction technique, and satisfactory agreement was obtained. The drop sizes ranged between 4 and 15 μm radius but were strongly peaked at ~ 7 μm radius. The liquid water content of the cloud was inferred from the dew point of the air which contained the moisture of the evaporated cloud. Although thus far most experiments have been carried out at temperatures between -16 and -13°C, growth rate studies are planned at three additional temperature intervals: -20 to -17°C, -11 to -8°C, and -7 to -4°C.

Additionally, most of the experiments carried out thus far involved the riming growth of frozen drops. However, a feasibility study showed that the riming growth of plate like ice crystals can be studied without any additional problems. Small plates of cadmium iodide with diameters of a few hundred microns could be stably suspended in the wind tunnel air stream. In the presence of a supercooled cloud they quickly grew by riming to small graupel particles. Unfortunately, the specific gravity of CdI_2 is considerably larger than that of ice, so that no quantitative growth rate studies could be done. Such studies will be carried out in the near future with actual ice plates as riming collectors, the latter being obtained by a special technique in which the crystals are grown outside the tunnel and then injected.

In our study of the riming properties of frozen drops, we thus far have used drops of radii 225 μm. We plan to extend this study to drops of 100 to 300 μm radius. The drops are injected into the tunnel with a hypodermic needle carrying an insulated metal screen hood which allows exposing the detaching water drops to an electric potential in order to counteract drop charging in shape, and as there is little doubt that the freeze-on "coalescence" efficiency is different from unity. One might have even expected that the collection efficiency would be somewhat greater for these "graupel" particles. Through consideration of the hydrodynamic motions as well as the surface texture of the riming particles, the low collection efficiencies become more understandable.

As found in previous wind tunnel studies (Pitter and Pruppacher, 1973), the frozen drops presently observed exhibited various spinning and tumbling motions which continued through most of the riming process. These rotational motions inevitably modify the flow fields around a particle which neither spins nor tumbles. The possibility that these motions reduce the collection efficiency can not be disregarded, although the physical mechanisms responsible for a reduction remain unclear at the present time.

A more tangible explanation for the lowered collection efficiencies involves the surface texture of the rime. Visual examination immediately indicated that the rime surface is very irregular and rough with many small protuberances. If we consider for a moment an isolated protuberance, an approaching cloud droplet would be subjected to an additional outward radial component of the flow just prior to collision. Downstream of the protuberance, one would expect a wake region where droplets would have only a small chance of landing due to their inertial tendencies. For many proturberances, it is difficult to speculate on actual flow fields. However, it is reasonable to expect the most favorable regions for collection to be at the ends of the protuberances (Macklin, 1961). This would lead to preferred growth propagation at these spots and development of a rather loosely structured rime. This is apparently substantiated by an examination of the rimed particle's density.

(2) The density of the grown graupel particles was calculated from the following relations:

$$\bar{\rho}_{rime} = \frac{\rho_w(r_f^3 - r_i^3)}{r_{gr}^3 - r_{ice}^3} \quad (3) \qquad \bar{\rho}_{graupel} = \frac{r_f^3}{r_{gr}^3} \quad (4)$$

where r_i is the initial water drop radius, r_f is the final water drop radius, r_{ice} is the initial frozen drop radius, r_{gr} is the final "graupel" radius, and ρ_w is assumed to be 1 g cm^{-3}. For the specific set of conditions mentioned above, $\bar{\rho}_{rime} \approx 0.15$ and $\bar{\rho}_{gr} \approx 0.21$.

If the riming particle collected cloud droplets non-selectively, one would expect a rime density near the "close-packed" limit for ice of 0.67. Since observed values are considerably lower, they lead to the conclusion that collision with a riming particle is a rather selective process. The rough, irregular structure apparently only allows for effective collisions on the tips of the protuberances. The reduced surface area able to collect droplets must then account for the lowered collection efficiencies.

(3) During initial stages of growth, most frozen drops appeared to rime rather uniformly and are characterized by rapid spinning and tumbling motions. Some traveled on horizontal helical trajectories as well. As the growth continued, the "graupel" particle showed evidence of rotating more slowly. Further growth led to an increased likelihood of rigid orientation coupled with a much greater tendency for horizontal excursions. It is important to note that these tendencies were by no means characterized by smooth transitions from one fall mode to another. Instead, they typically exhibited very erratic and sudden changes in their fall pattern. It was very common for rapidly rotating particles to suddenly stop their rotation and fall with a preferred orientation. A short time later they could suddenly start rapid rotation once again. Rotation of the "graupel particles" led to the development of roughly spherical shapes. Rigid fall contributed to the development of irregular shapes. Several of the "graupel" particles assumed conical shapes, and it was not uncommon to observe deviation from a basic spherical shape. It is reasonable to expect that longer growth times would result in a greater proportion of irregular shaped "graupel".

Although all preliminary work on plates was done with cadmium iodide crystals, and it would be unfair to discuss any collection results concerning them, the basic mechanism by which plates rime should remain unchanged. Initially, the plate was spinning horizontally, oriented in a position of maximum drag. The upstream side grew by riming for a short time period. Suddenly, the spinning plate flipped over and rimed on the other side. This process alternated and the heavily rimed plate showed an ever increasing tendency to tumble. This tumbling led to the development of a rather spherical "graupel" particle behaving in much the same fashion as the previously described frozen drop "graupel".

A short film will be shown illustrating the various fall modes of frozen drops and plates as they are freely growing by riming in the UCLA cloud tunnel.

(4) The most interesting aspect concerning the riming of frozen drops involved the variation in terminal velocity during growth. During the initial stages of riming, there was a very rapid decrease in the terminal velocity of the particle. For the specific set of conditions outlined above, the first 60 seconds of growth typically produced a 25% reduction in the terminal velocity. The next 60 seconds of growth resulted in the terminal velocity remaining fairly constant, and in the final 60 seconds the velocity began to slowly increase. If one considers a simplified situation where the density of the rime remains constant, it is easy to understand why riming praticles exhibit such behavior. Concentric shells of equal mass will have a progressively smaller thickness as the particle grows. Hence, initially, the cross sectional

by contact potentials. In this manner it was insured that the drop charge was less than 10^{-6} esu. At the same time tests revealed that the drops of the steam cloud also had charges less than 10^{-6} esu. From the studies of Schlamp et al. (1976), one can readily infer that the collision growth of the ice particles was not affected by the remaining (if any) electric charge.

3. EXPERIMENTAL PROCEDURE AND RESULTS

We present below the results of a particular growth experiment, involving 225 μm radius frozen drops. They were grown for 180 sec in a super-cooled cloud ($\bar{a} = 7$ μm) of L.W.C. 1.8 - 2.2 g m^{-3} with an ambient temperature between -16°C and -13°C. The charge on the frozen drops as well as on the individual cloud droplets was $< 10^{-6}$ esu.

A typical experiment proceeded as follows. Steam was allowed to enter the humidifying section of our tunnel well upstream of the observation section. This provided ample time for the cloud to reach thermal and vapor equilibrium with the tunnel air. After a brief period of time, conditions stabilized at a T ~ -16°C, L.W.C. ~ 1.8 g m^{-3}, and the environment at water saturation. A water drop was then injected into the wind tunnel and was immediately brought to its equilibrium terminal velocity by adjusting the tunnel air speed. From this air speed and the drag-size relationships of Beard (1974), the initial mass of the drop was identified. A few seconds later, as the drop approached thermal equilibrium, the few impurities in the drop initiated freezing and the timer was started. The riming drop was prevented from colliding with the surrounding walls by manipulating the direction of the air stream. This was accomplished by means of an adjustable inner tunnel (Pitter and Pruppacher, 1973). Thus, at all times during the particle's growth, it remained freely floating in the air stream. At the end of the 180 sec, the particle was drawn out by means of a suction device and allowed to settle into a subzero, layered mixture of xylene and diethyl phthalate. It came to rest near the interface between these two liquids. At no time during the capture process did the rimed particle come into contact with the walls of the set-up ducting the particle into the organic liquids. This eliminated the possibility of mass loss due to collisional fragmentation. Additionally, there were never any fragments of ice found in the collection cup. In view of these precautions and observations, we feel secure that our mass measurements are accuate.

After capture the collection cup was quickly brought into a walk-in cold chamber where the "graupel" particle was photographically studied. The particle was then melted by placing it in a warm mixture of xylene and diethyl phthalate. This solution was characterized by a gentle density gradient from top to bottom and allowed the liquid drop to float undistorted in an easily photographable position. The final mass was determined from these photographs. Knowing the initial and final mass, along with the time of growth, yielded values of $\frac{dm}{dt}$ between 4×10^{-7} g sec^{-1} and 7×10^{-7} g sec^{-1} for this particular set of conditions. All of this mass change was credited to the riming process. It must be remembered that the environment was water saturated and diffusional growth was occurring on the accreted droplets. Rough estimates suggest that the contribution from diffusion was less than 10% for the present set of conditions. We have chosen to ignore this at the present time.

Due to the inherent nature of the cloud tunnel, during any particular experimental run, the temperature of the tunnel air stream gradually rose from -16°C to -13°C, while the liquid water content rose from 1.8 to 2.2 g m^{-3}. All of the results presented below apply to this temperature and liquid water content range.

(1) The collection efficiency was determined by assuming a freeze-on "coalescence" efficiency of unity and calculating the collision efficiency from the following equations:

$$E = \frac{K}{\pi \bar{A}^2 \bar{V}_\infty} \quad (1) \qquad\qquad K = \frac{\overline{\left(\frac{dM}{dt}\right)}}{\bar{L}} \quad (2)$$

where $\bar{L}$ and $\bar{V}_\infty$ are weighted averages of the liquid water content and terminal velocity of the collector. $\bar{A}$ is the average radius of the rimed drop during its growth. The radius and terminal velocity of the cloud droplets have been neglected in the present calculations. Considering the low p-ratios involved (.02), this omission seems well justified.

For this particular set of conditions our calculated results for $\bar{E}$ range from 0.25 to 0.35 with 75% of the results lying between 0.27 and 0.30. It is important to recognize that these efficiencies represent an average over the entire growth period of the riming particle. There is no reason to expect the collection efficiency to remain constant throughout the growth period. In the future by measuring mass changes over variable time increments, we hope to illucidate any possible variations in collection efficiency as the particle grows. Nevertheless, the values obtained are significant for what they represent, and it is instructive to compare them with the collision efficiency theoretically predicted for a water drop under identical conditions. Recent calculations by Beard and Grover (1974) of low p-ratio collision efficiencies indicate that a water drop (A = 353 μm) having the same N_{Re}(100) as the average rimed particle in our data set, should exhibit collision efficiencies for a = 7 μm of between 0.7 and 0.8. These results are much larger than those obtained from the experimental riming growth. Thus, for similar conditions to those described above, the collisional growth of water drops dominates the riming process when considering the efficiency of mass accumulation.

This was initially somewhat surprising as most of the rimed particles remain relatively spherical area of the "graupel" particle will increase at a faster rate than later on in the growth process. Since the drag on a particle is a strong function of the cross sectional area, it will increase at the same rapid rate. So rapid, in fact, that it overpowers the additional mass that has accrued, leading to a terminal velocity decrease. During later states of growth, the cross sectional area increases at a slower rate so that the accretion of mass assumes the dominant role thereby forcing an increase in the terminal velocity. Quantitative theoretical evaluation of this process over a wide range of conditions will be presented at a later date.

REFERENCES

Beard, K. V., and Pruppacher, H. R., 1969: A determination of the terminal velocity and drag of small water drops by means of a wind tunnel, J. Atmos. Sci., 26, 1066-1072.

Beard, K. V., 1974: Terminal velocity and deformation of raindrops aloft, Preprints, Cloud Phys. Conference, Oct. 21-24, 1974, Tucson, Arizona.

Beard, K. V., and Grover, S. N., 1974: Numerical collision efficiencies for small raindrops colliding with micron sized particles, J. Atmos. Sci., 31, 543-550.

Hobbs, P. V., 1971: Studies of winter cyclonic storms over the Cascade Mountains, Res. Rept. No. 6, University of Washington, Dept. Atm. Sci., Seattle, Wash.

Kikuchi, K., 1972: Snow crystals with small raindrops, J. Meteorol. Soc., (Japan), 50, 142-144.

Macklin, W. C., 1962: The density and structure of ice formed by accretion, Quart. J. Meteorol. Soc., 88, 30-50.

Mason, B. J., 1971: Physics of Clouds, Oxford University Press, London.

Ono, A., 1969: The shape and riming properties of ice crystals in natural clouds, J. Atmos. Sci., 26, 138-147.

Pitter, R. L., and Pruppacher, H. R., 1973: A wind tunnel investigation of freezing of small water drops falling at terminal velocity in air, Quart. J. Roy. Meteorol. Soc., 99, 540-550.

Pitter, R. L., and Pruppacher, 1974: A numerical investigation of collision efficiencies of simple ice plates colliding with supercooled waterdrops, J. Atmos. Sci., 31, 551-559.

Pruppacher, H. R., and Neiburger, M., 1968: Design and performance of the UCLA cloud tunnel; Preprints, Int. Conf. on Cloud Phys., Toronto, Canada, 389-392.

Pruppacher, H. R. and Schlamp, R. J., 1975: A wind tunnel investigation on ice multiplication by freezing of waterdrops falling at terminal velocity in air, J. Geophys. Res., 80, 380-386.

Schlamp, R. J., Grover, S. N., Pruppacher, H. R., and Hamielec, H. E., 1976: A numerical investigation of the effect of electric charges and external electric fields on the collision efficiency of cloud drops, J. Atmos. Sci., submitted for publication.

Schlamp, R. J., Pruppacher, H. R., and Hamielec, A. E., 1975: A numerical investigation of the efficiency with which simple columnar ice crystals collide with supercooled water drops, J. Atmos. Sci., 32, 2330-2337.

Wilkins, R. I., and Auer, A. H., 1970: Riming properties of hexagonal ice crystals, Preprint; Conf. Cloud Phys., Fort Collins, Colo., Amer. Meteorol. Soc., 81-82.

Beard, K. V., and Pruppacher, H. R., 1971: A wind A wind tunnel investigation of collection kernels for small water drops in air, Quart. J. Roy. Meteorol. Soc., 97, 242-248.

ON THE DISTRIBUTION OF ADSORBED MOLECULES ON THE CRYSTAL FACE

T.G. Gzirishvili, T.N. Balakhvantseva, M.F. Basilashvili

Institute of Geophysics of the Academy of Sciences of the Georgian SSR.

Tbilisi, U.S.S.R.

The investigation of the mechanism of vapor phase molecules building into the crystalline lattice is the principal task in the research of crystal growth phenomenon.

It was reported Lamb and Hobbs(1971) Lamb and Scott (1972) that the curve of the linear growth rate of individual ice crystal basic and prism faces temperature T has its maximum and minimum. During the last years some attempts have been undertaken to interpret this peculiar dependence. We think that only those models should be outlined among them which are based on the phenomena of mono and polymolecular adsorption Hobbs and Scott (1965);Lamb and Scott (1973). The outhors of those reports used the model of "immovable adsorption", the reality of which is seriously questionable (Bruckhoff, Van--Dongen, 1973) moreover because the sense of lokalized adsorption is not consistent with the concept of molecule migration on the surface. In order to take into account the interaction between adsorbate and absorbate the authors in their work Lamb and Scott(1973) used the BET theory of polymolecular adsorption. But it is known that the theory mentioned above assumes the absence of lateral interaction between the molecules in the layer, the constancy of the heat of adsorption of molecules of the first layer and in the range of each of the following layers.

Generally in the solution of fundamental differential equation, which defines the correlation between the values of surface density σ of absorbed molecules and the distance Z between the steps on the crystal face the relative pressure is an external parameter (Strickland-Konstable, 1971).

The equation has the following form:

$$\frac{d^2\theta}{dz^2} = \frac{2}{X^2}\theta - \frac{2}{X^2}\frac{P}{P_\infty} \qquad (1)$$

where $\frac{P}{P_\infty}$ is the relative pressure; θ is the filling degree of adsorhent by adsorbate; $\theta = \sigma/\sigma_0$ where σ_0 is the maximally possible density of adsorbed molecules.

To have a more complete information on the mechanism of step movement we have to analyze the system consisting of three equations. equation (1) Hill's equation for polymolecular adsorption (Berezin, Kiceliov, 1968)

$$h = \frac{P}{P_\infty} = K_2 \frac{\theta(1-h)^2}{1-\theta+\theta h} \exp\left[\frac{\theta(1-h)}{1-\theta(1-h)} - K_1\theta\right] \qquad (2)$$

and the equation of the dependence of heat of adsorption on the filling degree,(Berezin, Kiceliov, 1968)

$$(Q-L)\left\{1 + \frac{h}{1-h}\left[1 + \frac{1}{(1-\theta')^2}\right] - K_1\theta h\right\} = Q - L + K_1 K T\theta' \qquad (3)$$

which is received by means of differentation of eq.(2) according to T with constant θ and assuming the independence of a_2 on T; a_2 is the two-dimentional analogue at the constant "a" in Van der Vaals' equation; L is the coefficient of condensation; $\theta' = \theta(1-h)$

In the eq.(2) K_2 is the measure of adsorption stability on the surface

$$K_2 = \frac{\sigma_0}{P_\infty} \frac{\sqrt{MT}}{3{,}52 \cdot 10^{22} \tau_0} \exp\left[-\frac{Q}{KT}\right]$$

where σ_0 is the number of molecules necessary for filling of $1 cm^2$ of the surface by monomolecular layer and is expressed by means of the relation $\sigma_0 = \frac{1}{1{,}57 d^2}$; d is the molecule diameter; P_∞ (mm of mercury column) is the saturated liquid vapor pressure at temperature T; M is the molecular weight; τ_0 is the oscillation period of an adsorbed molecule in the direction perpendicular to the surface; Q is the heat of adsorption; K is Boltsman's constant. The expression for K_1 has the following form:

$$K_1 = \frac{2 a_2 \sigma_0}{KT}$$

De Boer equation of monomolecular adsorption (De Boer, 1962) is the particular case of equation (2)

$$\frac{P}{P_\infty} = K_2 \frac{\theta}{1-\theta} \exp\left(\frac{\theta}{1-\theta} - K_1\theta\right) \qquad (4)$$

The aim of the present paper is to solve the non-linear differential equation of the second order

$$\frac{d^2\theta}{dz} = \frac{2}{X^2}\theta - \frac{2}{X^2}\left[K_2 \frac{\theta}{1-\theta} \exp\left(\frac{\theta}{1-\theta} - K_1\theta\right)\right] \qquad (5)$$

received on the basis of eq.(1) and (4) Equation (5) in which X is the migration length of an adsorbed molecule $X = 10^{-3} cm$ was numerically solved on a computer with the following boundury conditions: at $z = 0$ and $z = y_0$ where y_0 is the distance between the steps ($y_0 = 10^{-1} cm$), θ varied in the range from 0.1 to 0.9.

The examination of the equation (5) showed that the solution exists only for those values of K_1 and K_2 when the two-dimentional phase transition vapor-water takes place. on ice crystal surface(Fig.1)

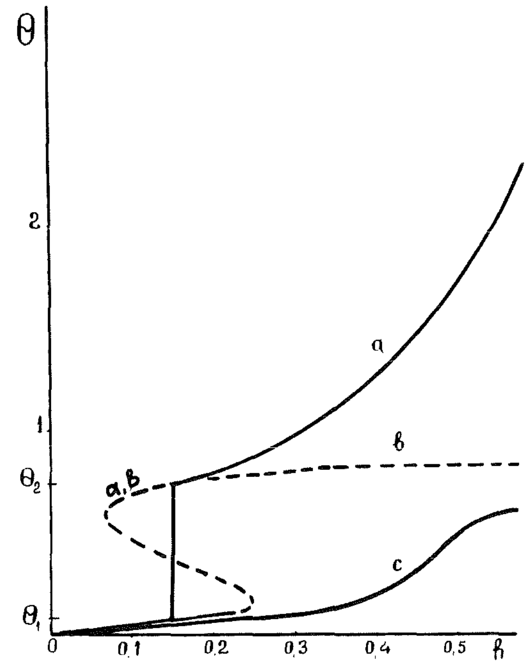

Fig.1
Adsorption isotherms

The curve "a" computed by (2)
The curve "b" and "c" computed by (4).
The curves "a" and "b" correspond to the case when the two-dimetional phase transition takes place: $K_2=5$, $K_1=10$
The curve "c" is obtaines in the absence of the two-dimetional phase transition: $K_2=5$, $K_1=6{,}5$

Fig.2 shows the curves of the fil-

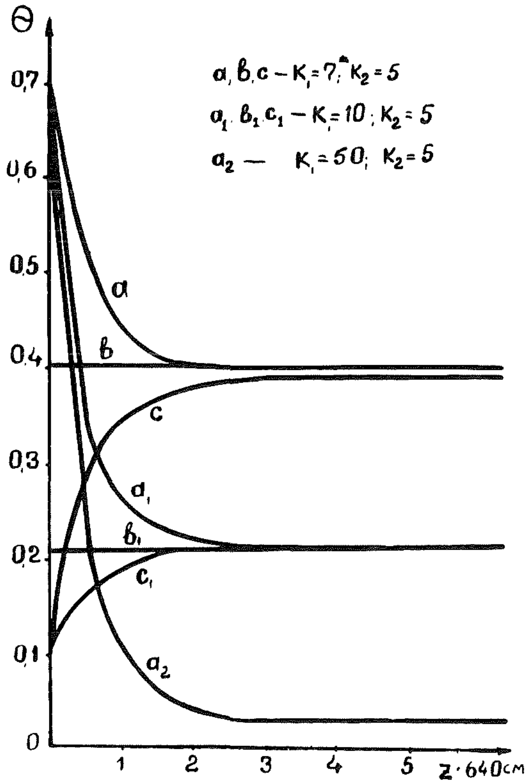

Fig. 2

The distribution of adsorbt moleculs along the crystal face.

ling degree θ versus the values of Z for the case when $K_1 = 7, 10, 50$ and $K_2 = 5$ at $Q = 3\ ^{kcal}/_{mol}$ and $T = 268^\circ$.

The values of K_1 corespond to different orientation of adsorbed molecules on the surface i.e. $K_1 = 50$ corresponds to vertical orientation, $K_1 = 7$ to plane orientation, $K_1 = 10$ to orientation at some angle (Gzirishvili, Ridjamadze, Balakvantseva, 1976).

We took only four boundary values of the magnitude of $\theta = 0{,}7; 0{,}4; 0{,}21; 0{,}1$ not to overload the plot. The two-dimentional phase transition takes place at staggered variation of the magnitude of adsorbate filling degree θ from $\theta_1 = 0{,}25; 0{,}05; 0{,}003$ to $\theta_2 = 0{,}45; 0{,}75; 0{,}91$ respectively for given values of K_1 and K_2.

θ_1 is rhe filling degree of the surface only by saturated two-dimentional vapor and θ_2 is the filling degree of the surface only by two-dimentional condensate.

The couse of the curves (Fig.2) shows that depending on the boundary values of θ the concentration of adsorbed molecules either increases (curves c and c_1), is constant (curves b and b_1) or decreases (curves a , a_1 and a_2).

The comparison of the curves of Fig. 2 with those of eq (4) shows that the increasing portions of the curves of fig. 2 correspond to the portions of curves of eq. (4) limited at the top by the concentration value θ_1 and the portions parallel to the ordinate axis correspond to the portions deflecting the phase transition between the values of θ_1 and θ_2 when Q is not dependent on T (Berezin, Kiseliov, (1968)) and decreasing portions correspond to the curves limited by condensation value θ_2 underneath.

Summurizing the present work it can be pointed out that the appearance of quazi-liquid layer of water on the crystal surface can become the reason of inhibition of growth rate of individual crystal faces and this would give rize to maximums and minimums on the growth rate curves. The further examination of this problem includes the solution of the system consisting of equations (1), (2) and (3) and this will allow to give a quantitative evaluation of ice crystal growth.

REFERENCES

Berezin T.I., Kiseliov A.V., 1969: "Zavisimost teploti adsorbtsii u teploiomkosti adsorbata ot velichini adsorbtsii" Journal Phisicheskoi Khimii 43, 1228

Bruckhoff I.K.P., R.H. van Dongen 1970: Physical and chemical aspects of adsorbents and catalysts. Edited by B.G. Linsen, Chapter 2, Academic Press London and New York.

Gzirishvili T.G., Ridjamadze M.B., Balakhvantseva T.N., 1976: K voprosu dvumernoi condensatsii na yadrakh crystallizatsii - - Izvestia Akademii nauk Gruzinskoi SSR, seria Khimicheskaia, tom 1.

De Boer T.H., 1953: The dynamical character of adsorption. Oxford at the Clarendon press.

Hobbs P.V., and W.D. Scott, 1965: A theoretical study of the variation of ice crystal habits with temperature. J, Geophys. Res. 70. 5025-5034 .

Lamb D., and P.V. Hobbs, 1971: Growth rates and habits of ice crystals grown from the vapor phase. J. Atoms. Sci. 28, 1506-1509.

Lamb and W.D. Scott, 1972: Linear growth rates of ice crystals, grown from the vapor phase J. Crystal Growth 12, 21-31.

Lamb D., and W.D. Scott, 1972: The mechanism of ice crystal growth and habit formation. J. Atoms. Sci. 31. 570-580.

Strickland - Constable R.F., 1968: Kinetics and mechanism of crystallization. Academic Press, London and New York.

3.1.10

DETERMINATION OF THE RATES OF ICE CRYSTAL FORMATION IN TWO LARGE CLOUD CHAMBERS

Dennis M. Garvey, Lyle E. Lilie, Thomas C. Grove and Lewis O. Grant
Department of Atmospheric Science
Colorado State University
Fort Collins, Colorado

1. INTRODUCTION

The testing and calibration of cloud seeding materials is continuing at the CSU Cloud Simulation and Aerosol Laboratory. Parallel research is aimed at relating the test results to expected natural cloud responses to artificial ice nuclei. Generally, our approach involves a physical simulation as opposed to the isolation of separate prosesses. Nevertheless, it provides information concerning nucleation mechanisms for conditions under which the various modes, i.e., deposition, condensation-freezing, and contact freezing, are competing. The purpose of this paper is to present experimental results obtained using this kind of approach, to relate them to natural cloud glaciating behavior, and to study them for information concerning nucleation mechanisms. The work falls into two categories:

A. Experiments in which sized aerosols were tested in the CSU isothermal cloud chamber, in which the drop sizes were known and the temperature kept constant. Aerosols from three pyrotechnics and one airborne generator were studied in these experiments.

B. Experiments in which aerosols from a ground generator burning solutions of AgI-NaI and $AgI-NH_4I$ in acetone were tested in air parcels subjected to simulated ascents in the CSU slow expansion cloud chamber. Variations in effectiveness between in-cloud and pre-cloud seeding material releases were examined.

2. ICE CRYSTAL FORMATION RATES IN ISOTHERMAL CHAMBER

2.1 Background

Vonnegut (1949) first noted that when nucleating aerosols are injected into supercooled clouds, ice crystals continue to form for a number of minutes. He attributed this effect to the probabalistic nature of the nucleation process. Fletcher (1958) investigated this suggestion theoretically and concluded that the nucleation time lag at any temperature should be a function of the temperature activation spectrum for the nucleating aerosol and, in particular, that the time lag should be large at temperatures for which the slope of the activation spectrum is large. The theory was invoked to explain the experimental results of Warner and Newnham (1958) for atmospheric aerosols. The theory was tested for AgI aerosols by Warburton and Heffernan (1964), and qualitative but not quantitative agreement was attained. A disturbing aspect of this work was the fact that the time lag differed for two aerosols whose activation spectra had nearly identical slopes at all temperatures. Vonnegut (1949) had also suggested the possibility that the time lag is a result of the time needed for collisions between aerosol particles and cloud droplets. Isaac and Douglas (1972) referred to this effect as another "time lag" and, considering coagulation due to both Brownian and turbulent motion, they derived theoretical collection efficiencies for clouds of different droplet sizes and concentrations and aerosol particles of different sizes. This viewpoint received some support from the work of Steele and Davis (1969) and Garvey and Davis (1973). The first paper demonstrated an increased nucleating effectiveness with increased liquid water contents, i.e., cloud droplet densities, at a chamber temperature of -12C. The second showed increased crystal fallout times for clouds of lower liquid water contents and larger aerosol particle sizes at a chamber temperature of -20C. Note that this time lag should be relatively independent of temperature. A further possible explanation for the observed time lags is a change in the surface characteristics of the aerosol particles. Such an effect ought to be relatively independent of both temperature and cloud density.

2.2 Experimental Results

Ice crystal fallouts as a function of time for aerosols produced by presently used cloud seeding devices are measured as part of the calibration procedure at the Cloud Simulation and Aerosol Laboratory (Garvey, 1975). Until now, however, this information has not been analyzed in a formal manner. Presented in Table 1 are such data obtained for four devices tested in 1975. The τ given in column 6 is determined by obtaining a linear fit to ln $(\Delta N/\Delta t)$ as a function of time. τ is the time after sample injection for which the fallout rate is 1/e of the initial value. In many cases (type A) the fit is very good, indicating that the fallout rate does indeed decrease exponentially; in other cases (type B) there is a very high fallout rate initially, followed by much lower values which fall off at an exponential rate which is less than that ogtained by the above analysis. Such contrasting "signatures" can be seen in Fig. 1 for the four aerosols of Table 1. These data are all for a cloud temperature of -12C and a cloud liquid water content of approximately 1.5 g/m^3. (The LWC is not varied independently because a standard cloud is desired for the calibration procedure.) It is seen that the fallout rates for the NEI TB-1, the Olin WM-105, and the NOAA airborne generator all follow an exponential pattern, the fallout rate decreasing more rapidly for the particles produced by the acetone burner than for those produced by the pyrotechnics. The Navy TB-1, on the other hand,

Table 1

Device	Run #	T(C)	LWC (g/m^3)	Time (min)	τ (min)	Type
Olin WM-105	371	-16	1.5	28	6.8	A
	372	-16	1.5	41	9.7	B
	379	-12	1.2	42	15.9	A
	384	-8	1.0	27	6.9	A
	386	-8	1.0	46	9.1	A
	407	-20	1.2	52	7.5	B
	410	-20	1.5	30	6.5	B
	413	-16	1.2	38	9.1	A
	417	-16	1.2	27	7.1	A
	421	-12	1.5	39	14.2	A
	605	-8	1.5	30	8.1	A
	620	-16	1.5	53	9.2	B
	622	-16	1.5	54	10.1	A
	631	-12	1.5	36	9.4	A
Navy TB-1	373	-16	1.5	31	6.1	B
	374	-16	1.5	42	8.1	B
	375	-12	1.5	35	8.1	B
	377	-12	1.5	28	5.6	B
	383	-8	1.0	32	5.6	B
	385	-8	1.0	23	4.3	B
	408	-20	1.2	44	7.1	B
	607	-8	1.6	30	12.1	A
	611	-8	1.5	9	1.2	A
	621	-16	1.5	60	8.7	B
	624	-16	1.5	39	6.2	B
	625	-12	1.5	44	9.7	B
	630	-12	1.5	31	5.2	B
NEI TB-1	389	-8	1.0	86	10.8	A
	392	-8	1.0	58	10.2	A
	406	-20	1.0	34	4.5	B
	412	-16	1.2	49	10.1	B
	416	-16	1.2	37	6.6	B
	419	-12	1.5	89	16.4	A
	422	-12	1.5	56	10.5	A
	437	-8	1.5	79	13.1	A
	438	-8	1.5	63	12.8	A
	439	-8	1.5	59	12.3	A
	440	-8	1.5	52	16.9	A
	442	-7	1.5	46	16.7	A
	608	-8	1.6	43	13.1	A
	609	-8	1.6	47	13.1	A
	614	-6	1.5	46	13.1	A
	617	-6	1.5	58	11.4	A
	626	-12	1.5	50	10.0	A
	629	-12	1.5	45	8.5	A
	769	-20	1.5	26	3.3	B
	770	-20	1.5	33	5.5	B
	771	-20	1.5	32	5.6	A
	772	-20	1.5	33	6.1	B
	773	-20	1.5	26	5.2	A
NOAA Air-borne	506	-20	1.5	24.6	3.6	A
	509	-20	1.5	20.2	4.5	A
	510	-16	1.5	16.5	3.8	A
	511	-16	1.5	30.0	6.1	A
	512	-14	1.5	31.0	6.2	A
	513	-12	1.5	25.0	3.9	A
	514	-12	1.5	23.0	3.9	A
	515	-10	1.5	14.0	2.6	A
	518	-8	1.5	34.0	5.2	A
	519	-8	1.5	25.0	4.6	A
	524	-10	1.5	17.0	3.3	A
	525	-10	1.5	18.0	3.3	A
	526	-8	1.5	21.3	3.2	A
	527	-7	1.5	17.7	2.9	A
	528	-7	1.5	20.4	2.7	A

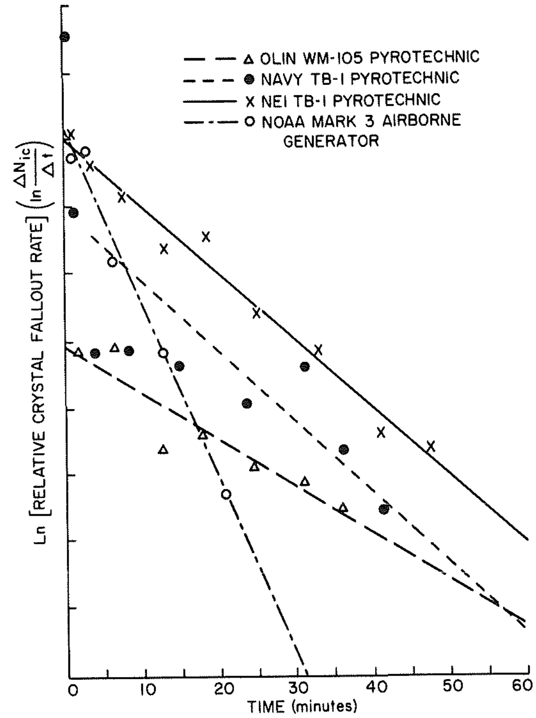

Fig. 1. Typical crystal fallout rates for four cloud seeding devices.

has a clearly defined type B signature. Interestingly, the signature types for the Navy TB-1 and the NOAA airborne generator appear to be independent of temperature (except for two anomalous runs with the TB-1 at -8C), while those for the other pyrotechnics have a temperature dependence. For the Olin flares the signature changes from type A to type B as the temperature decreases to -16 and -20C. For the NEI flares, too, -16C appears to be the transition temperature.

2.3 Discussion

Following section 2.1, a type B signature indicates one of three things: (a) either the nucleation temperature is at a point on the activation spectrum where the slope is very small so that almost all nucleation occurs immediately, the remaining part of the fallout being insignificant compared to that of the first few minutes; (b) or the first part of the fallout represents nucleation due to a fast-acting mechanism, deposition or condensation-freezing, and the remainder is that due to contact nucleation alone; (c) or the particles quickly lose their nucleating effectiveness in the cloud environment, and the two kinds of fallout rates are due to nucleation rates by active particles and relatively inactive ones.

This fallout behavior, which is most pronounced for the Navy TB-1, is relatively independent of temperature, so that for this device explanation (a) can be ruled out. For the Olin and NEI flares this type of signature does occur at -16C and -20C, where the cumulative activation spectra are relatively flat (Fig. 2), but fallout after the first few minutes is still fairly large and cannot be termed insignificant.

Explanation (b) has been proposed by Fukuta (among others) and certainly appears attractive qualitatively. Thus the acetone burner, which produces small particles, has a signature indicating relatively rapid contact nucleation, evidently at all temperatures. The larger particles produced by the pyrotechnics, however, have relatively small collision efficiencies, and unless they produce ice nuclei by either deposition or condensation-freezing, have large time constants. The Navy TB-1 flare is capable of acting quickly at all temperatures, whereas the other flares can only act by deposition or condensation-freezing at temperatures of -16C and colder. By ignoring the first part of the type B signatures, new time constants can be calculated for the second part of the curves only. These are plotted as a function of temperature in Fig. 3. It is seen that the time constants are between 7 and 15 minutes for the Olin and Navy flares with no apparent temperature dependence. For the NEI flares the time constants are about the same as for the other flares except at -20C, where they fall below 7 minutes. The time constants for the acetone burner particles are also relatively independent of temperature and fall between 3 and 6 minutes.

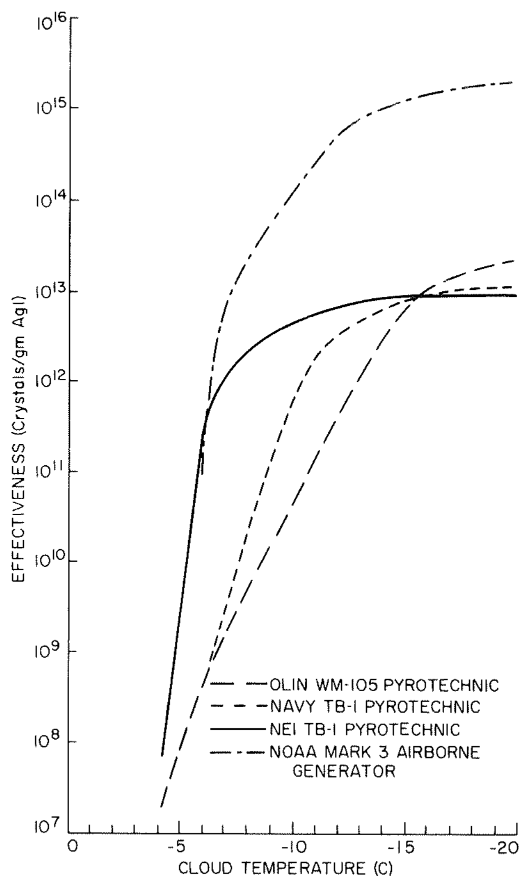

Fig. 2. Temperature activation spectra for four cloud seeding devices.

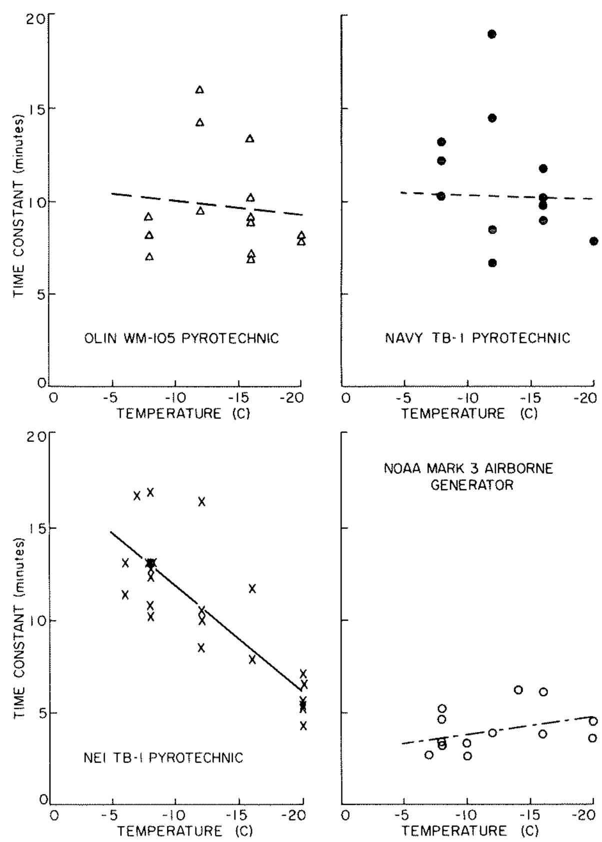

Fig. 3. Time constants for ice crystal fallout as a function of temperature for four cloud seeding devices.

Explanation (c) cannot be ruled out and will have to be considered if quantitative agreement between theoretical collision efficiencies and measured time constants is not found. Even so, a number of questions remain unanswered. Why is there such a large difference in the behavior of the aerosols generated by the NEI TB-1 flares and those produced by the Navy? Why is there an apparent temperature dependence in the time constants for the NEI TB-1 flares? The point to be emphasized here, however, is that the measured time constants obtained in these tests may well be important considerations in the design of weather modification experiments involving injection of artificial aerosols into relatively stable supercooled clouds, orographic clouds being a case in point (Young, 1974). For the seeding of cumulus clouds from below, such information is probably not pertinent, and crystal formation rates as a function of ascent parameters of temperature and CCN activation become of paramount interest. To gain such information a slow expansion chamber has been designed and built. The results of a series of experiments using this device together with an ice crystal counter described by Lilie et al (1976) are presented in the next section.

3. ICE CRYSTAL FORMATION RATES IN EXPANSION CHAMBER

3.1 Procedure

Samples of aerosols produced by burning acetone solutions of AgI-NaI and AgI-NH_4I in 2:1 molar ratios were tested in the slow expansion cloud chamber described by Garvey (1975). The solutions were burned in a "standard" generator and 4 liter samples were taken from a vertical dilution tunnel. The aerosols were then diluted with clean, dry air and injected into an air parcel subjected to the ascent profile shown in Fig. 4. The programmed ascent began at a pressure of 830 mb and a temperature of +20C. Wall temperature was controlled so that cooling corresponded to a dry adiabatic ascent down to a temperature of +15C and a pressure of 780 mb (the LCL), after which cooling corresponded to a moist adiabatic ascent. The figure shows how closely the measured profile followed the programmed profile for a simulated ascent rate of 10 m/s (~4C/min). Twelve tests were performed with each aerosol. In half of these the sample was injected shortly after the simulated ascent had begun (+18C) before the cloud had formed; in the remaining tests the sample was injected into a cloud which had already been supercooled to -10C. It was found that if room air was injected from ambient conditions into the supercooled cloud, expansion cooling was sufficient to produce copious nucleation events immediately. To prevent this from occuring when the sample was injected at cold temperatures, a heating element was placed around the injection tube to balance the expansion cooling. The cloud formed on propane generated CCN and/or the sample aerosol, and the cloud density was monitored using a transmissometer. Care was taken to regulate the concentration of nucleating aerosol so that liquid cloud droplets remained in the chamber until near the end of each experiment.

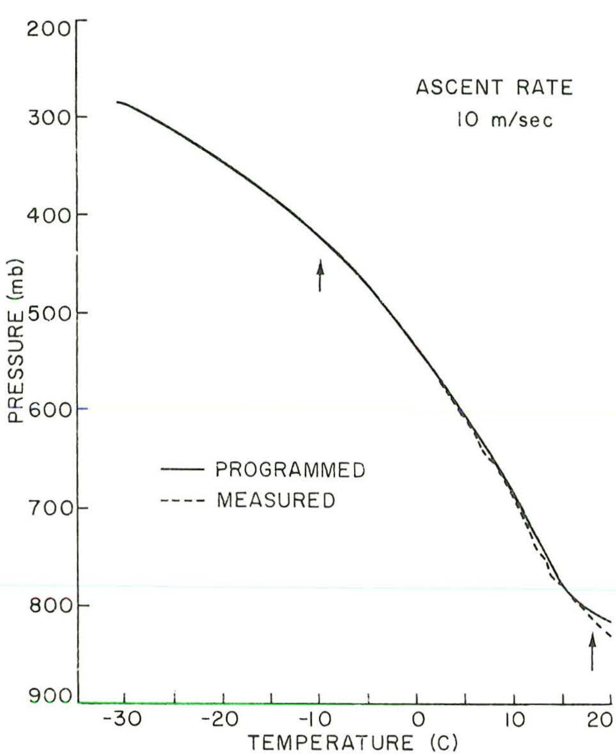

Fig. 4. Programmed and actual pressure-temperature ascent profiles for experiments in slow expansion cloud chamber. Arrows indicate sample injection points.

3.2 Experimental Results

Typical results showing relative ice crystal concentrations as a function of temperature for a pair of runs with each solution are shown in Fig. 5. For runs in which no artificial nuclei were injected, ice crystal concentrations on this scale remained neglibible down to temperatures near -30C. The figure shows clearly the principal finding of this series of tests. For the NH_4I-AgI complex the in-cloud (-10C) injection produces higher ice crystal concentrations and produces them at warmer temperatures than do the same nuclei injected before cloud formation (+18C). The NgI-AgI complex shows a similar effect, but it is much less pronounced than with the NH_4I-AgI complex. A few tests in which injection took place at intermediate temperatures indicated the principal variable affecting the effectiveness was whether the sample injection took place before or after cloud formation.

3.3 Discussion

These results are important for weather modification purposes because they indicate that effectiveness values for cloud seeding devices obtained in the isothermal cloud chamber may overestimate the actual glaciating behavior when these materials are used to seed cumulus clouds from below. See, for example, Dye et al (1976). They extend the work done by Dunsmore and Steele (1974) to colder temperatures (-10 to -35C). An attempt must now be made to further quantify these results and to extend the range of conditions over which such experiments are performed. Particularly important is the relation between the ambient CCN spectrum and the CCN activity of the sample aerosol. Another important variable to examine is the effect of the cloud formation temperature on ice nucleus activity. The number of experimental permutations is almost infinite. But with certain hypotheses in mind and attention to detail in defining the experimental conditions, the slow expansion cloud chamber, together with improved observational techniques, should prove a valuable tool in our efforts to modify cloud behavior in a predictable manner.

4. ACKNOWLEDGMENTS

This research was performed under Grant GI-32894X2 sponsored under Research Applied to National Needs, National Science Foundation. The authors are indebted to Messrs. C. Swain, P. Fiegen, and R. Horn for their assistance in preparing for and carrying out the experiments.

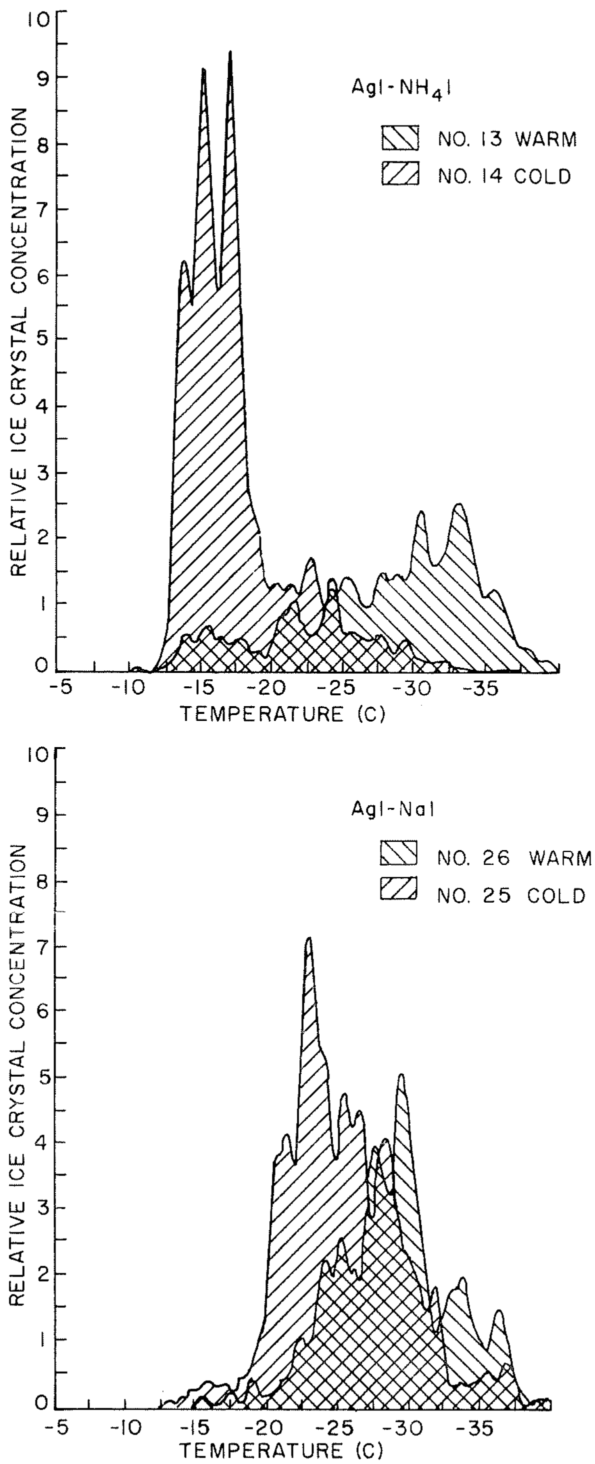

Fig. 5. Relative ice crystal concentrations in the slow expansion cloud chamber for two pairs of experiments.

5. REFERENCES

Dunsmore, H., and R. L. Steele, 1974: An investigation of sequence dependent effects in seeding simulated cumulus clouds. Preprints Fourth Conf. on Weather Modification, Fort Lauderdale, Florida, 183-189.

Dye, J. E., G. Langer, V. Toutenhoofd, T. W. Cannon, and C. A. Knight, 1976: Use of a sailplane to measure microphysical effects of silver iodide seeding in cumulus clouds. J. Appl. Meteor, 15, 264-274.

Fletcher, N. H., 1958: Time lag in ice crystal nucleation in the atmosphere. Part 2: Theoretical. Bull Obs Puy de Dôme, No 1, 11-18.

Garvey, D. M., and C. I. Davis, 1973: Ice nucleating characteristics of AgI aerosols in an isothermal cloud chamber. Proc. 8th Int. Conf. on Nucleation, Leningrad, U.S.S.R., 166-173.

Garvey, D. M., 1975: Testing of cloud seeding materials at the cloud simulation and aerosol laboratory, 1971-1973. J. Appl. Meteor., 14, 883-890.

Isaac, G. A., and R. H. Douglas, 1972: Another "time lag" in the activation of atmospheric ice nuclei. J. Appl. Meteor., 11, 490-493.

Lilie, L. E., T. C. Grove, and D. M. Garvey, 1976: In situ ice crystal counting by means of a laser-television camera system. Proc. Int. Cloud Physics Conf., Boulder, Colorado.

Steele, R. L., and C. I. Davis, 1969: Variation of ice nuclei effectiveness with liquid water. J. Atmos. Sci., 26, 329-330.

Vonnegut, B., 1949: Nucleation of supercooled water clouds by silver iodide smokes. Chem. Rev., 44, 277-289.

Warburton, J. A., and K. J. Heffernan, 1964: Time lag in ice crystal nucleation by silver iodide. J. Appl. Meteor., 3, 788-791.

Warner, J., and T. D. Newnham, 1958: Time lag in ice crystal nucleation in the atmosphere. Part I: Experimental. Bull. Obs. Puy de Dôme, No. 1, 1-10.

Young, K. C., 1974: A numerical simulation of wintertime, orographic precipitation. Part I. Description of model microphysics and numerical techniques. J. Atmos. Sci., 31, 1735-1748.

CRYSTALLINE EMBRYOS AT ICE-VAPOR INTERFACES

David L. Bartley*

University of Missouri
Rolla, Missouri

1. INTRODUCTION

In the present paper we examine a particular crystal growth process which should be significant to the growth of ice crystals in contact with water vapor at high saturations. Specifically, we consider the nucleation of small monolayer ice-like clusters at the basal and prism ice-vapor interfaces. Under the basic assumptions that the ice surfaces are patch-wise smooth and sparcely covered with monomers, dimers, etc., in near equilibrium with the vapor, and that the bond energies and configurational entropy dominate the energy of formation, it is found that the basal surfaces prefer triangular embryos with an orientation which reverses from layer to layer, whereas the most stable clusters on the prism surfaces are rectangular in configuration. At any given saturation ratio, the preferred prism clusters are found to have a critical energy of formation significantly lower than that of the basal clusters, basically because of differences in the cluster corner free energies.

Although refined calculation of temperature dependent growth rates awaits knowledge of the monomer surface densities and diffusion rates, as well as details of vibrational and other contributions to the cluster energies of formation, it appears that these results may have significant implications. The energy gap between prism and basal clusters provides a mechanism for strongly anisotropic crystal growth at high saturations. Moreover, there may be related microscopic aspects of dislocation growth which have been hitherto ignored. Finally, because of their simplicity, the techniques presented for the analysis of cluster shape and configurational entropy may prove fruitful for investigations of heterogeneous ice nucleation and of two-dimensional nucleation phenomena of other materials as well.

2. CALCULATION

2.1 Cluster Energy of Formation

Under the assumptions given in the Introduction, it is possible to show[1] that the Gibbs free energy of formation ΔG of a cluster having a particular molecular configuration is given by the simple expression,

$$\Delta G = -nkT \ln S + |V_b|(2n-n_b). \qquad (1)$$

Here n is the number of water molecules in the cluster, n_b is the number of H-bonds which involve cluster molecules, and S is the supersaturation ratio. The quantity $|V_b|$ is an effective bond energy, which is dominated by the bulk ice H-bond energy at temperature T_o=273K, which is equal to about $10kT_o$. The various T-dependent contributions to $|V_o|$ (for example, an amount equal to -kTln2 due to proton disorder[1]) are ignored in this paper.[2]

The first term in Eq. 1 depends only on the size of the cluster, whereas the second term can be shown[1] to be a function only of the types of molecular arrangements along the cluster perimeter, and thus is reasonably designated the "perimeter free energy." This term is of order $n^{1/2}$ (for large similarly shaped clusters) in this essentially two dimensional situation (analogous to the $O(n^{2/3})$ surface free energy of three dimensional clusters).

2.2 Preferred Cluster Shapes

In order to ascertain the minimal energy cluster configurations for given n, we consider the class of structures which can be formed by straight-line monolayer cleavages which leave closed rings. This will be useful, since a large number of clusters -- namely, all of the irregular 12-sided structures -- can be dealt with analytically.

In Fig. 1 is shown a typical cluster on the basal plane. Here vertices represent water molecules, lines represent hydrogen bonds, and the solid dots show bonds between the cluster and ice surface below. Removing molecules from such a cluster by straight-line cuts leaving closed rings, we obtain duodecagonal clusters which are conveniently parameterized in terms of ten lengths j_o, $\vec{j}$, $\vec{J}$ as seen schematically in Fig. 2.

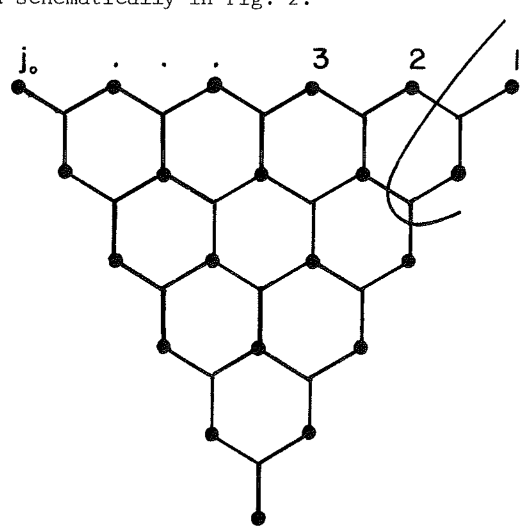

Figure 1. Basal plane ("parent") cluster.

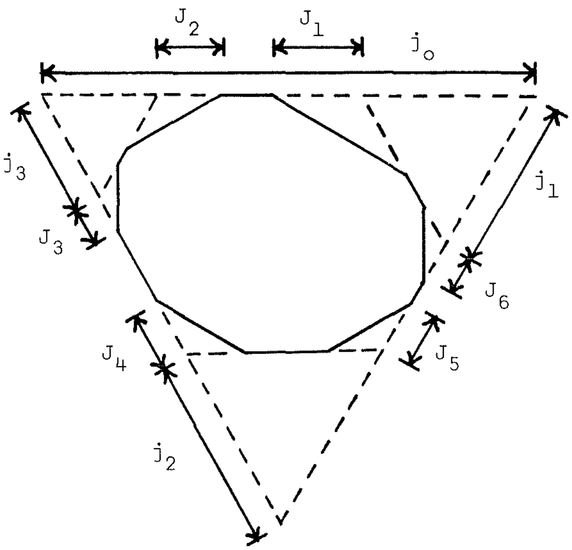

Figure 2. Duodecagonal cluster parameterization.

The number n of molecules in the cluster is found[1] to be a 10-dimensional Lorentz invarient:

$$n = j_o^2 - \vec{j}\cdot\vec{j} - \vec{J}\cdot\vec{J}. \tag{2}$$

Furthermore, the basal cluster perimeter energy ε_{basal} is found[1] to be simply

$$\varepsilon_{basal} = |V_b| j_o\,, \tag{3}$$

analogous to the energy of a relativistic particle of rest mass n and momentum $(\vec{j}, \vec{J})$ which, upon vanishing, yields minimum energy. Thus, the preferred basal clusters of (roughly) fixed n are triangular.

A similar treatment of clusters on the prism surfaces yields a more complicated expression for the perimeter energy ε_{prism} which is given[1] by

$$\varepsilon_{prism} = |V_b|\,[3/2\ j_o - 1/2(j_1+j_2+j_3) - 1/2\ (J_1+J_4)]. \tag{4}$$

Minimizing ε_{prism} at fixed n (given by Eq. 2) gives rectangular structures. Furthermore, ε_{prism} and ε_{basal} for the preferred clusters are assyptotically equal to ε given by

$$\varepsilon = |V_b| n^{1/2}, \tag{5}$$

which (with Eq. 1) gives[3] a critical cluster size n* and energy ΔG*:

$$n^* = (V_b/2kT\ln S)^2, \tag{6}$$

$$\Delta G^* = V_b^2/4kT\ln S. \tag{7}$$

2.3 Configurational Entropy

In the present section the class of structures considered is broadened so that configurational entropy can be reasonably discussed. Further, we no longer make dubious continuous variations over discrete variables. We begin discussion with the basal clusters.

Consider a low energy basal cluster parameterized by j_o as shown in Fig. 1. The number of molecules n and the perimeter energy are given by Eqs. 2 and 3. ($\vec{j} = \vec{J} = 0$).

We now consider all structures which can be made by "decimating" this completed "parent" structure by removing j molecules breaking only two bonds at a time. This procedure yields all of the 12-sided structures considered in Section 2.2 as well as a multitude of others. The rationale here is that removal of a molecule, breaking only two bonds, leaves the perimeter energy exactly invarient and changes the free energy only slightly (as compared, for example, with breaking three bonds) for $kT\ln S \ll |V_b|$, as is always the case in situations of physical interest. If ζ(j) is the number of ways of so decimating a parent triangular structure, then the configurational entropy S_{con} is given by

$$S_{con} = k\ln\,\zeta(j). \tag{8}$$

Subtracting the configurational free energy from the energy of formation (Eq. 1) for a particular cluster, we obtain the energy of formation ΔG_n of an n-cluster in the form

$$\Delta G_n = -nkT\ln S + j_o\,|V_b| - kT\ln\zeta(j) \tag{9}$$

$$n = j_o^2 - j. \tag{10}$$

The difficulty now lies in calculating ζ(j). Focus attention on the upper right corner of the triangle in Fig. 1, and think of rows of molecules running diagonally upward and to the right. We can remove an arbitrary number of molecules from the row labelled 1 (breaking two bonds at a time). If an even number of molecules is removed from row 1 (say, four, as indicated in Fig. 1), then up to an equal number can be removed from row 2. However, if an odd number is taken from row 1, then only up to the odd number minus one can be taken from row 2. The other rows can be considered similarly. The result is that the number η(j) of ways of removing j molecules from a single corner, breaking two bonds at a time, is equal to the number of ways the integer j can be represented as a sum of other integers where odd integers appear only once. The number ζ(j) for the entire triangle can similarly be represented in a simply stated though difficult number theoretic framework. Methods analogous to those employed by Hardy and Ramanujan[4] in their treatment of the theory of the partition of integers give[1] an assyptotic expression,

$$\zeta_{ass}(j) = \frac{3}{16 j^{3/2}} \exp\left(\frac{3\pi^2}{2}\,j\right)^{1/2}. \tag{11}$$

Knowing ζ(j), we can now find ΔG_n by means of Eqs. 9-10, and in Fig. 3 (upper curve) is plotted ΔG_n vs. n at S=3.3 (setting $V_b = -12kT_o$ and $T \sim T_o$) for n in the vicinity of the critical size n* (Eq. 6). As is easily seen, the microscopic

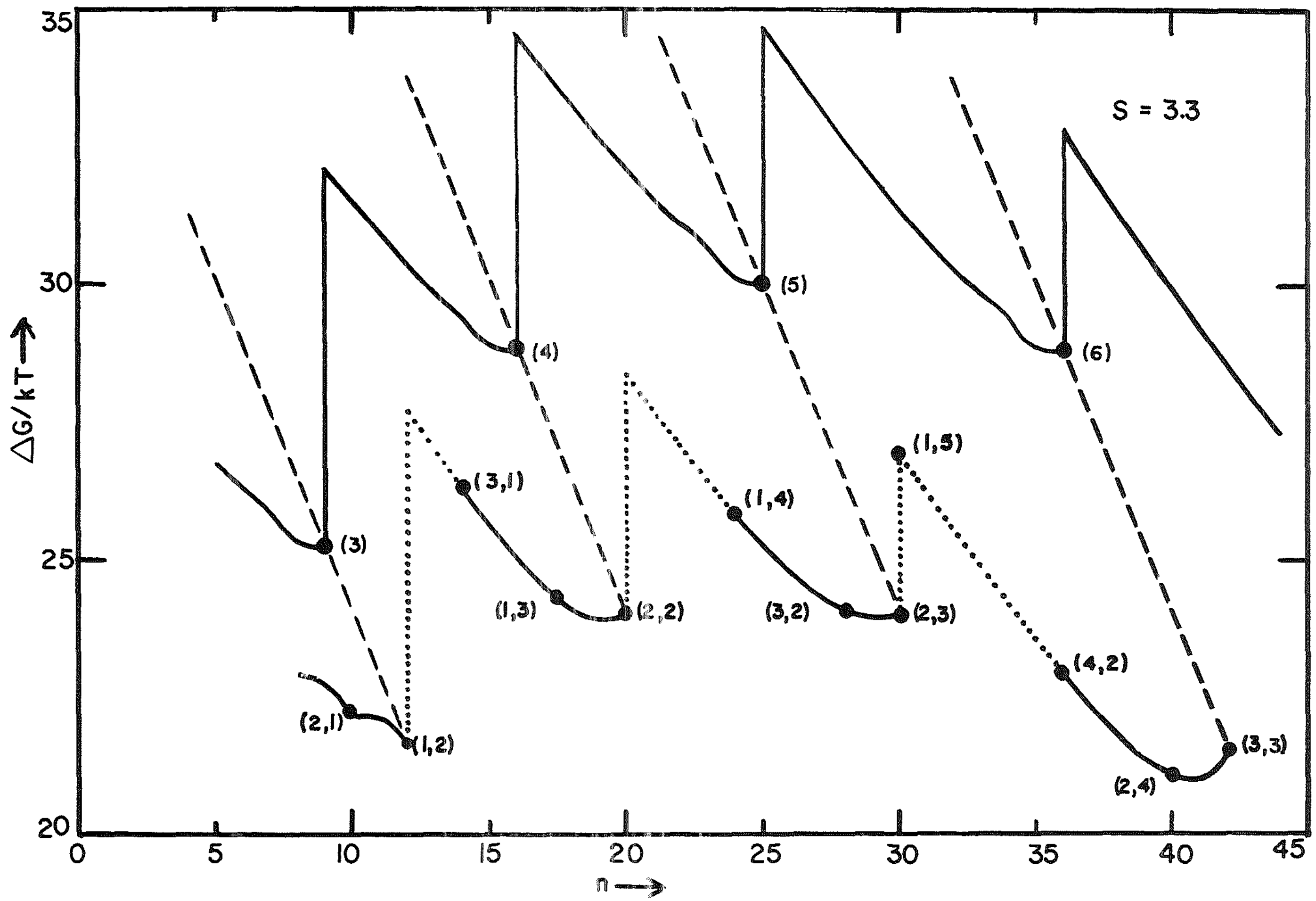

Figure 3. Typical energies of formation of basal and prism clusters.

aspects of this problem yield a discontinuous curve for ΔG_n. Each continuous segment represents decimations of a particular parent triangular cluster (j_o) represented by a solid dot. The jaggedness of ΔG_n may be simply interpreted physically as representing activation barriers to (one-dimensional) nucleation of new cluster edges. Note that the configurational entropy, which, if neglected gives the straight lines in the figure, is clearly significant. In fact, at lower saturations, configurational entropy dominates bond energies and the critical structures "melt" into a more spherical shape as overlapping between the decimations of different parent triangles occurs.

Calculation of the configurational entropy for the prism clusters is considerably more difficult than for the basal clusters. We have, as yet, found no simple number theoretic means of organizing the configurational degeneracy. Moreover, there are various "parent rectangles" for a given perimeter energy, and therefore overlapping between these different rectangles must be accounted for. Furthermore, as rectangle decimations occur through cluster sides, rather than at corners, the configurational entropy depends upon the size of the parent rectangle, unlike the basal cluster case. Nevertheless, by a tedious counting procedure the configurational entropy can be obtained, and in Fig. 3 (lower curve) we have included a plot of the prism cluster energy of formation for comparison with the basal ΔG_n. (The solid dots represent parent rectangles with breadth and width (J_1, J_2).) Lowering of the prism cluster energy of formation with respect to the basal by $|V_b|/2$, due to differences in corner energies and configurational entropy differences, is clearly seen in the figure.

---

*Supported by the National Aeronautics and Space Administration under Grant No. NAS8-31150.

1. Bartley, to be published.

2. For a treatment of oscillations of three-dimensional clusters, see Plummer (1972).

3. Similar expressions can be found in Burton (1951). See also Fletcher (1970) and Zettlemoyer (1969).

4. See Hardy (1917) or Ayoub (1963).

REFERENCES

Ayoub, R., 1963: An Introduction to the Analytic Theory of Numbers. American Mathematical Society, 379 pp.

Burton, W. K., N. Cabrera and F. C. Frank, 1951: The growth of crystals and the equilibrium structure of their surfaces. Phil. Trans. Roy. Soc., 243, 299-358.

Fletcher, N. H., 1970: The Chemical Physics of Ice. Cambridge Press, 271 pp.

Hardy, G. H., and S. Ramanujan, 1917. Proc. London Math. Soc. (2), 16, 131-142.

Plummer, P. L. M., and B. N. Hale, 1972: Molecular model for prenucleation water clusters. J. Chem. Phys., 56, 4329-4335.

Zettlemoyer, A. C., 1969: Nucleation. New York, Marcel Dekker, Inc., 606 pp.

3.1.12

ENERGETICS OF WATER-ICE SURFACE INTERACTIONS: A QUANTUM MECHANICAL STUDY*

P. L. M. Plummer and E. M. Stein
Department of Physics and Graduate Center for Cloud Physics Research
University of Missouri, Rolla, Mo. 65401

1. INTRODUCTION

The initial stages of ice formation and growth are central to the cloud evolution and precipitation processes in continental clouds. Initiation of the ice phase in clouds and the interaction between ice and water particles are fundamental processes which must be understood if we are to successfully model the dynamics of a cloud or subsequently alter its development.

The ice phase in the cloud is produced by freezing of liquid water droplets to form ice crystals and/or the direct formation of ice crystals from the vapor by sublimation (Fletcher, 1966). In forming ice from liquid water, several mechanisms can influence the results, 1) freezing of pure liquid water--homogeneous nucleation of ice from the melt, 2) heterogeneous nucleation of ice from the liquid which contained dissolved materials, or 3) freezing of the liquid layer which originally formed on a condensation nucleus. In this latter case, freezing can then occur by nucleation of the ice phase directly or be initiated by contact nucleation. The direct formation of ice crystals from the vapor can also occur via homogeneous or heterogeneous mechanism. (Previous work on a molecular model for nucleation in water from a supersaturated vapor has indicated that the former is very unlikely; Plummer and Hale, 1972, 1974). The heterogeneous nucleation of ice can occur on an ice crystal already formed by some mechanism or on some other natural or artificial nucleus. Subsequent to the formation of ice crystals, growth and multiplication processes as well as ice-liquid water interactions play major roles in the evolution of the cloud.

In the attempt to understand the details of the microphysical processes involving ice which are important in cloud formation we have simplified the system as much as is feasible while retaining the essential features of the "real" physical situation. Initially we are modelling the energetics of the interaction of water molecules with a variety of surfaces. It is anticipated that these studies can provide the data necessary to predict nucleation rates on these surfaces and to predict whether a given surface could function as an ice or a condensation nucleus.

In this paper we report the first results obtained from modelling the water-ice surface interaction using a small number of water molecules arranged in the lattice positions for ice I_h. The majority of the calculations have been for the basal plane but the prism plane has also been modelled. Semi-empirical quantum mechanical calculations of the CNDO/INDO type (Pople and Beveridge, 1970) are used to obtain interaction energies for a gas phase molecule approaching the surface.

2. THE MODEL

For the calculations of the interaction energies of the vapor phase water monomer with the basal face, a group of ten water molecules were arranged in ice I_h lattice positions as illustrated in Figure 1a. The *c-axis* is normal to the plane. Only the positions of the oxygens are indicated and those represented by filled circles lie 0.9Å below the plane of the open circles. The nearest neighbor distance between molecules in the same plane (dashed lines) was 4.5Å, the lattice constant a_o.

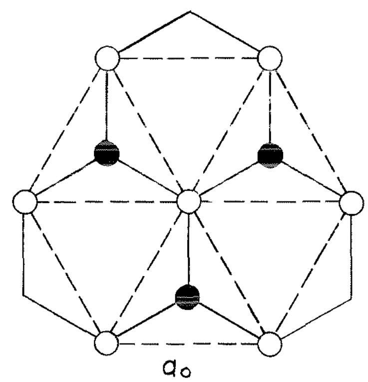

Figure 1a. Ten molecule section of the basal face of ice I_h. The solid lines represent hydrogen bonds between nearest neighbors. The dashed lines connect molecules in the same plane and illustrate the hexagonal symmetry of the lattice.

Figure 1b is a perspective drawing of the basal face. Here the specific configuration of hydrogens used in these calculations are shown. Notice that the hydrogen is not symmetrically placed in the bond but remains much closer to one oxygen with an O-H separation only slightly greater than in the vapor (1.0Å compared with 0.957Å in the free monomer).

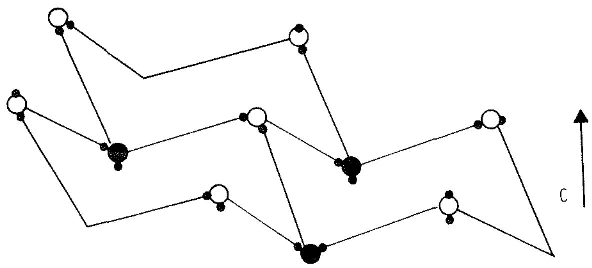

Figure 1b. Perspective drawing of basal face illustrating the relative planes of the oxygen atoms (large circles) and the specific hydrogen positions.

For evaluating the interaction energy of a monomer with a prism face of ice I_h the molecules representing the surface were arranged as shown in Figure 2a. Here as for the basal face only the positions of the oxygens are shown and the plane of the oxygens represented by the filled circles lies 1.38Å below the plane of the oxygens represented by open circles. The *c-axis* is in the plane of the molecules and the nearest neighbor distance is again 2.76Å. Next nearest neighbor distances for molecules in the same plane is 4.5Å. Figure 2b is a perspective drawing of the prism face showing the configuration of hydrogens used in these studies.

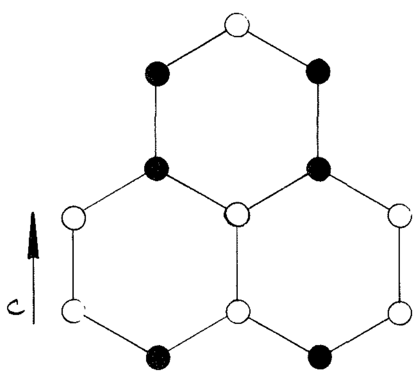

Figure 2a. Prism plane of ice I_h.

Inherent in using a small group of molecules to represent the ice surface either for the basal or prism planes are the assumptions that the oxygen sublattice of ice I_h extends to the surface without rearrangement (which appears to be experimentally justified for sufficiently low temperatures, Firment and Somorjai; 1975) and that a molecule approaching the surface is influenced primarily by first and second nearest neighbors to the approach site (see results and discussion for justification for this assumption).

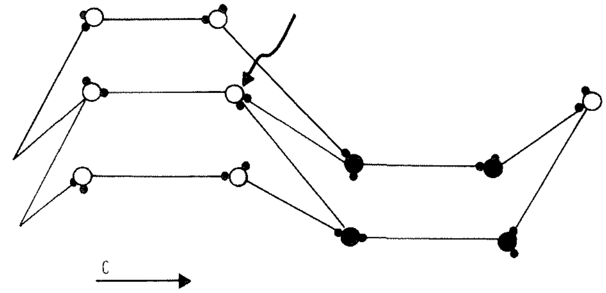

Figure 2b. Perspective view of prism plane showing specific hydrogen configurations.

In these calculations all valence electrons, both of the monomer and of the molecules used to represent the surface, where explicitly included. The basis set consisted of 1s orbitals on all hydrogens and 2s, 2px, 2py and 2pz orbitals centered on each oxygen. Thus the problem consisted of evaluating the expectation values of the energy operator for a variety of monomer-surface distances and orientations overproduct wave-functions describing the 33 nuclei and 264 electrons. In order to make the problem tractable a number of the multi-center integrals were neglected and the two electron repulsion integrals were parameterized from experimental atomic spectral data. The specific technique used has been widely applied to molecular systems and systems of molecular aggregates and is known as the method of 'neglect of differential overlap'. The method is referred to by the acronyms CNDO, INDO or NDDO depending on whether the neglect is 'complete', 'intermediate' or limited to 'neglect of diatomic' differential overlap. (Pople and Beveridge, 1970).

We have used both the CNDO and INDO methods and have found the qualitative predictions to be the same from both. The results reported here are CNDO/2 (the /2 identifies the specific parameterization used for the integrals - QCPE, 1974) calculations which could be more readily compared and calibrated with previous results for water systems (Hoyland and Kier, 1969; Scott, 1975).

For the interaction of the water monomer with the basal face, four types of surface sites were specifically considered.

These are indicated in Figure 3. The site labelled A, directly over the central surface molecule, was considered the primary bonding position and the potential surface was calculated for a variety of rotational orientations of the approaching monomer. Position B is located directly over the nearest neighbor position to site A. Position C is located in the center of the ring. Position D is located half-way between the site A and an adjacent "nearest neighbor" molecule in the same plane. For surface sites A, B and C the incoming monomer was oriented so as to donate one of its protons for hydrogen bond formation with the surface. (A completely symmetric configuration which would give the same results would occur if the protons in the surface molecules were extending out of the surface and the bond to the surface consisted of a proton from a surface molecule with the lone pair electrons of the incoming monomer.) For site D the monomer was oriented with both hydrogens toward the surface.

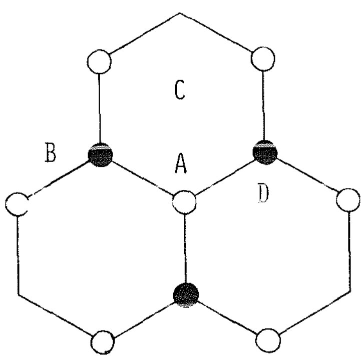

Figure 3. Letters identify the surface sites on the basal plane for which interaction energies with an approaching monomer were calculated.

The primary bonding site on the prism face was located above the central molecule and had the incoming monomer oriented with one hydrogen pointing toward this surface site. (Indicated by the arrow in Figure 2b.)

3. RESULTS AND DISCUSSION

The hydrogen configuration chosen for the basal face (see Figure 1b) provided a charge symmetric environment for the central molecule (the primary bonding site) as well as minimizing the total dipole for the "surface". We believed that this would best represent an *average* surface *seen* by an incoming water molecule. The magnitude of the effects reported can be either increased or decreased if the proton configuration were changed so as to substantially alter the electron density around a given surface site. For the prism face, the surface symmetry is less than for the basal face, so that there is more than one choice of proton configuration, which would result in a "neutral" surface. The configuration used (Figure 2b) had the protons on the molecules in the "nearest neighbor" surface sites to the primary binding site projecting out of the plane. This configuration enhances the bonding to the primary site but also introduces a barrier to the bonding configurations which have both hydrogens of the monomer participating in bonds to the surface.

In these calculations we were attempting to model a water monomer interacting with an infinite ice surface. Thus we needed to know if the small number of molecules used to represent the surface were sufficient to reproduce the short range effects of the interaction with an infinite surface. In all cases, the monomer could interact with the bonding site (nearest neighbor site) as well as next-nearest and third nearest neighbors. If the range of this interaction were sufficiently short range, the use of a limited part of the surface to describe the energetics of the monomer-surface interaction is justified. In the attempt to substantiate this assumption, we repeated the calculations for the primary bonding sites on each surface excluding first, the third nearest neighbors and then the second nearest neighbors.

For the basal plane, 94% of the interaction energy could be attributed to nearest neighbor interaction with an additional 5.4% from second nearest neighbor interactions. Since 99.4% of the binding came from first and second nearest neighbors, the assumption that the energetics of the molecule close to the surface could be modelled using only a small fraction of the surface appears justified. (See also Santry, 1973).

Convergence of the interaction energy for the prism face was not quite so rapid but our limiting of the surface, in this case to fourth nearest neighbors, was again justified. The lower symmetry of the prism face required the inclusion of third nearest neighbors before over 99% of the interaction energy was obtained.

In all of the calculations the molecules representing the surface were held fixed with internal geometries corresponding to those found in ice I_h. The oxygen hydrogen bond length was 1.0Å and the HOH angle was 109.5°. For the approaching monomer the O-H bond length was 1.0Å but the internal angle was reduced to 105°. The total potential energy of the monomer-surface system was calculated for twelve to twenty monomer-surface distances surrounding the minimum separation.

3.1 Basal Plane Calculations

The maximum interaction of the monomer with the basal surface occurred for the monomer approaching site A (Fig. 3) with one of its hydrogens forming a linear hydrogen bond with the surface molecule. For the surface-monomer distance corresponding to the minimum in the potential energy ($R(0\text{-}0)_{scaled} = 2.75\text{Å}$) the monomer was rotated about the hydrogen bond to obtain the most stable orientation for the non-bonded hydrogen. This most stable bonding configuration had a binding energy of 8.0 kcal/mole and had the monomer hydrogen not involved in the surface bond rotated 180° from the bisector of the surface molecule. We found that the energy barrier for free rotation was 0.5 kcal/mole or approximately kT. The potential surface for bond stretching was much steeper and the frequency associated with this motion was calculated to be 280 cm^{-1}.

The second most stable configuration for bonding on the basal plane had the incoming monomer participating in two bonds to the surface and contributing both of its hydrogens to form these bonds. The total bonding interaction was found to be 6.80 kcal/mole or 4.4 kcal/mole per bond. (This value would be increased by 5% to 10% by "relaxing" the monomer bond angle to 109.5°.) We also investigated the potential surface for a monomer bound to site A rotating into a configuration which would permit the formation of a second bond and hence move into the geometry we have described as D. The energy barrier to this motion was found to be 2.7 kcal/mole above the energy minimum at site A.

The remaining two positions considered for monomer approach are not true *bonding* configurations since no surface-monomer hydrogen bond is formed. However, these are both *local* attractive minima in the potential surface. The attractive interaction for these sites is approximately one-half that of site A. (See Table I.) The magnitude of this attraction is highly dependent on the orientation both of the surface hydrogens and of the incoming water monomer.

Table 1
Summary of results for energy calculations.

Site	Energy Minimum[1]	Frequency (Bond Stretch)
Basal A (180°)	-7.98 kcal/mole	280 cm^{-1}
(0°)	-7.45 kcal/mole	
Basal B	-4.05 kcal/mole	180 cm^{-1}
Basal C	-4.45 kcal/mole	
Basal D	-6.80 kcal/mole	
Prism	-7.35 kcal/mole	266 cm^{-1}

[1]This energy is greater than the dis-association energy by an amount equal to the zero point vibrational energy.

3.2 Prism Plane Calculations

For the prism face the most stable configuration had the monomer providing the hydrogen for bond formation to the primary site. The energy of this bond was found to be -7.35 kcal/mole. The characteristic frequency for this bonding site was 266 cm^{-1}. Other bonding sites on the prism face were not investigated in detail but instead we calculated the electron density maps for the prism face. This enables us to visualize the charge distribution for the entire prism face. Figure 4 illustrates the level of detail and information which can be obtained from this approach. Figure 4 is a three-dimensional plot of the total electron density due to the valance electrons. The density is plotted for a plane parallel to the *c-axis* and through the upper layer of molecules as indicated by the open circles in Figure 2. The viewer is oriented 45° clockwise from the *c-axis* and 30° above the plane. The maximum density peaks correspond to the oxygens. The distance between grid points is 0.25Å.

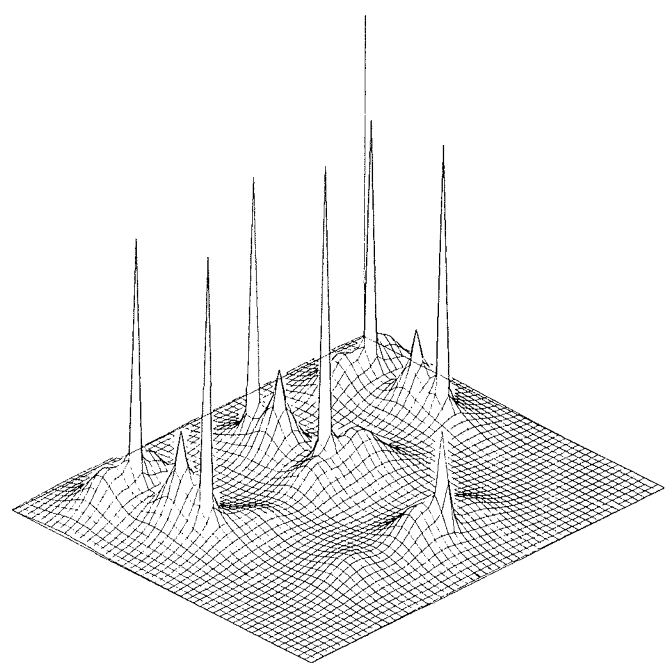

Figure 4. Electron density map of the prism face of ice I_h.

4. CONCLUSIONS

In this study the energetics of the water-ice surface interaction has been modelled using a small number of water molecules arranged in ice I_h lattice positions to represent the surface. The specific hydrogen orientations were chosen so as to provide a *neutral* surface around the bonding sites. The hydrogens at the interaction sites were positioned away from the approaching monomer. This choice seemed appropriate both for an ice surface at low temperatures as well as for the case of a "liquid-like" layer on the surface since such a layer would have its hydrogens pointing preferentially away from the vapor. (Fletcher, 1973.) Thus, an incoming molecule was oriented so as to have one or both hydrogens pointing toward the surface.

The most stable bonding configurations was found for site A on the basal plane. Only slightly less stable (8%) was the primary site on the prism plane. The third most stable configuration (85% of A) was a bifurcated structure with two bonds between the monomer and the surface. The bifurcated structure was separated from the most stable configuration by an energy barrier of less than 1.6 kcal/mole. This configuration is probably most frequently observed as an intermediate or metastable structure for a molecule in the process of forming a single hydrogen bond. This position can perhaps be best regarded as a local minima in the potential for surface diffusion. Its existence and the moderate barrier between it and a more stable single bonded structure, makes reasonable the consideration of a "bipedal walk" process for the surface diffusion of water on ice.

The other binding positions are also local minima with well depths of approximately 50% to 60% of the most stable orientation. In these two orientations the hydrogen finds itself in an attractive potential well of two or more surface molecules. If its incoming energy is not too great, it could reside in such a quasi-bound or "physically adsorbed" position for some time. It would then either be re-evaporated or diffuse across the surface to be incorporated into a more stable "true" bonding configuration. These positions can also provide additional stabilization for the addition of a second molecule to a monomer already bonded to a primary site and therefore enhance the initial stage of cluster formation.

The ice surface should be viewed not as having isolated *strong* bonding sites separated by "inhospitable" regions but rather as consisting of a series of attractive regions separated by low energy barriers. The "nonbonding" local minima provide the energy mechanism whereby a molecule approaching the surface does not have to attach to a primary bonding site but can be attracted and remain in contact with the surface long enough to either move to a more favorable bonding positions on the surface or become attached to a molecule or cluster already bonded to the surface. This, in turn, suggests that surface diffusion would be a primary mechanism for surface cluster formation and crystal growth.

Even though the results reported here are preliminary and certainly do not answer all of our questions about the energetics of the water-ice surface interaction, they do provide much insight into the nature of this interaction and the direction future studies should take. These calculations have shown that there are differences in the strength of the bonds formed between a monomer and the basal face as compared with the prism face. However these energy differences are not large. Therefore other factors such as supersaturation and the flux of monomers to the surface as well as the temperature of the surface and the vapor will play a large role in determining the method of growth of the ice crystal. The differences in surface diffusion mechanisms on the two faces will be very important in controlling the growth habit. Thus these diffusion mechanisms need to be investigated in some detail. To do this we need to calculate the interaction energies for additional surface sites on the prism face. We also need to know the magnitude of the effect of completely *polarizing* the surface. The surface polarization effects will be important in nucleation and growth on artificial nuclei such as silver iodide. (Fletcher, 1959). We are also investigating the effects of monomer relaxation and orientation on the interaction energies of the sites already considered. Work is already in progress to generate electron density maps for the basal surface. We are also calculating electron density maps for the surface-monomer system to better enable us to choose the primary sites for adding second and third molecules to the surface. In the diffusion studies, larger sections of the ice surface will be needed. We will compare the quantum mechanical results for the surface potential with those obtained from empirical potentials such as those developed by Lie and Clementi (1975) and Lemburg and Stillinger (1975). The empirical potentials can then be used to model the dynamics of the surface migration and diffusion by computer simulation on a larger ice surface.

With this data in hand together with our increased understanding of the nature of the ice surface and the water-ice interaction we will be much better prepared to design artificial nuclei for cloud seeding as well as provide the necessary microphysical data necessary for cloud modelling.

ACKNOWLEDGMENTS

The authors wish to thank Kathryn Berkbigler for her help in generating the 3-D plot and for other computational assistance and the computer center at the University of Missouri for providing the computer time for these studies.

5. REFERENCES

*Supported in part by Atmospheric Science Section of NSF, Grant No. GA-32386 and National Aeronautics and Space Administration, Grant No. NAS8-31150.

L.E. Firment and G. A. Somorjai, "Low energy electron diffraction studies of molecular crystals: The surface structure of vapor-growth ice and naphthalene", J. Chem. Phys. 63, 1037-8 (1975).

N. H. Fletcher, "Entropy effect in ice crystal nucleation", J. Chem. Phys. 30, 1476-1482 (1959).

N. H. Fletcher, *The Physics of Rain Clouds*, Oxford Univ. Press (1966).

N. H. Fletcher, "The surface of ice", *Physics and Chemistry of Ice*, ed. by E. Whalley, S. J. Jones and L. W. Gold, Royal Society of Canada, 132-136 (1973).

J. R. Hoyland and L. B. Kiev, "Semiempirical quantum mechanical studies on some hydrogen bonded systems", Theoret. Chem. Acta. (Berl.) 15, 1-11 (1969).

H. L. Lemberg and F. H. Stillinger, "Central force model for liquid water", J. Chem. Phys. 62, 1677-1690 (1975).

G. C. Lie and E. Clementi, "Study of the structure of molecular complexes, XII", J. Chem. Phys. 62, 2195-2199 (1975).

Quantum Chemistry Program Exchange, Indiana University Program 141 by Paul A. Dobosh, (1974).

P. L. M. Plummer and B. N. Hale, "Molecular model for prenucleation water clusters", J. Chem. Phys. 56, 4329-4334 (1972).

________, and ________, "Molecular model for ice clusters in a supersaturated vapor", J. Chem. Phys. 61, 4012-4019 (1974).

J. A. Pople and D. L. Beveridge, *Approximate Molecular Orbital Theory*, McGraw-Hill, New York (1970).

D. P. Santry, "Molecular Orbital Studies on Ice I_h", *Physics and Chemistry of Ice*, ed. by E. Whalley, S. J. Jones and L. W. Gold, Royal Society of Canada, 19-22 (1973).

B. F. Scott, "Molecular Orbital Studies on Ice-Like Structures", Theoret. Chim. Acta. (Berl.) 38, 85-100 (1975).

3.1.13

GROWTH PROCESSES OF ICE CRYSTALS AND A LAW WHICH IS RELATED TO THE SYMMETRIC GROWTH OF PLATE-LIKE SNOW CRYSTALS

Akira Yamashita

Geophysical Institute
Tokyo Univ., Tokyo

1. INTRODUCTION

By the experimental studies using a large cloud chamber of 14.7 meters high Yamashita (1971) has shown trapezoidal ice crystals, V-shaped ice crystals, trigonal ice crystals, tetragonal ice crystals named "inside plate" and several types of poly-crystals of ice. About trigonal ice crystals Yamashita (1973) has described their growth mode, their dendritic growth and their change of growth from trigonal to hexagonal nature in detail. Series of this experimental studies, however, were carried out not only about these rather special ice crystals but also about detailed growth mode and nature of hexagonal shaped ice crystals. Namely Yamashita (1974a) has shown this work as a preliminary paper. The work showing how the initial seedings or the nuclei had effects on the growth of ice crystals was also presented at ICCG-4 (Yamashita, 1974b).

Meanwhile Frank (1974) has introduced the three dimentional-nature of snow crystals, which has been elucidated by Nakaya (1954), and has developed the theme further. Using the concept of "lacunary growth" he has explained the growth of several types of snow crystals and has also shown how ridges are formed in snow crystals.

In this presentation inference of small ice crystals' lacunary growth, analysis of growth directions* of ice crystals obtained in the series of experiments and a law which is related to the hexagonally symmetric growth of ice crystals will be shown.

2. INFERENCE OF SMALL PLATE-LIKE ICE CRYSTALS' LACUNARY GROWTH

In the volume of abstracts of the previous international cloud physics conference Yamashita (1972) briefly described the initial growth processes of ice crystals from frozen water droplets. This work is also shown in the preliminary paper (Yamashita, 1974a) although the growth of lacunae and gas enclosures are neglected. The growth processes are reproduced in Appendix for the purpose to show the morphology of these growing ice crystals with lacunae and gas enclosures.

Since this growth process of ice crystals from frozen water droplets were investigated for water drops of sizes between about 30 and 150 μm in diameter, it was not always appropriate to show the lacunary growth of Frank experimentally although double layered stellar ice crystals were grown. In order to infer lacunary growth from initial ice crystals to snow crystals, about 100 photographs of plate-like single crystals of ice were selected for analysis from the previous work (Yamashita, 1973) because ice crystals grown by the seeding of employing adiabatic cooling were grown from sub-micron sized ice particles. These were the ice crystals grown for about 200 seconds in a supercooled cloud of −10.3, −12.5, −15.1 or −17.8°C in free fall. Almost all of them were double layered hexagonal plates of sizes between 100 and 660 μm. As the analysis of these comparatively large crystals, however, was not sufficient for the purpose, an additional experiment was made.

Experiment: Ice crystals were produced by breaking a glass tube which had contained 1 cc of compressed air (3 atm.). They were grown at −16°C in a cloud chamber No.2 (Yamashita, 1974a) of 650 ml and 265cm high. In this case so many ice crystals (about 1×10^{10}; counted value) grew mixed with a supercooled cloud that they did not become large like those in the work shown above. Ice crystals grown for 304~314 seconds were selected for analysis. Their sizes distributed between 30 and 100 μm. Photomicrographs in Fig.1-1~30 show examples of them.

Inference of small plate-like ice crystals' lacunary growth was made by using both the ice crystals selected from the previous work and these ice crystals in the figure. Result is summarized in Fig.2. A submicron sized ice crystal grows to a hexagonal solid plate and then to a hexagonal solid plate with a small lacuna on every prismatic face (a). Although a lacuna frequently grows to a gas enclosure (see Fig.1 1~7) it becomes relatively large when the ice crystal grows further. A lacuna of this stage has sphere-like stepped structure (b). Then six lacunae come to be connected each other to make a double layered ice crystal (c). One of doubled plates grows thicker and larger than the other (d) (e), and it grows to a stellar

* Note: "Growth direction" of plate-like ice crystals is not of prismatic faces but of the $\langle(10\bar{1}0)(01\bar{1}0)\rangle$ edges in this article.

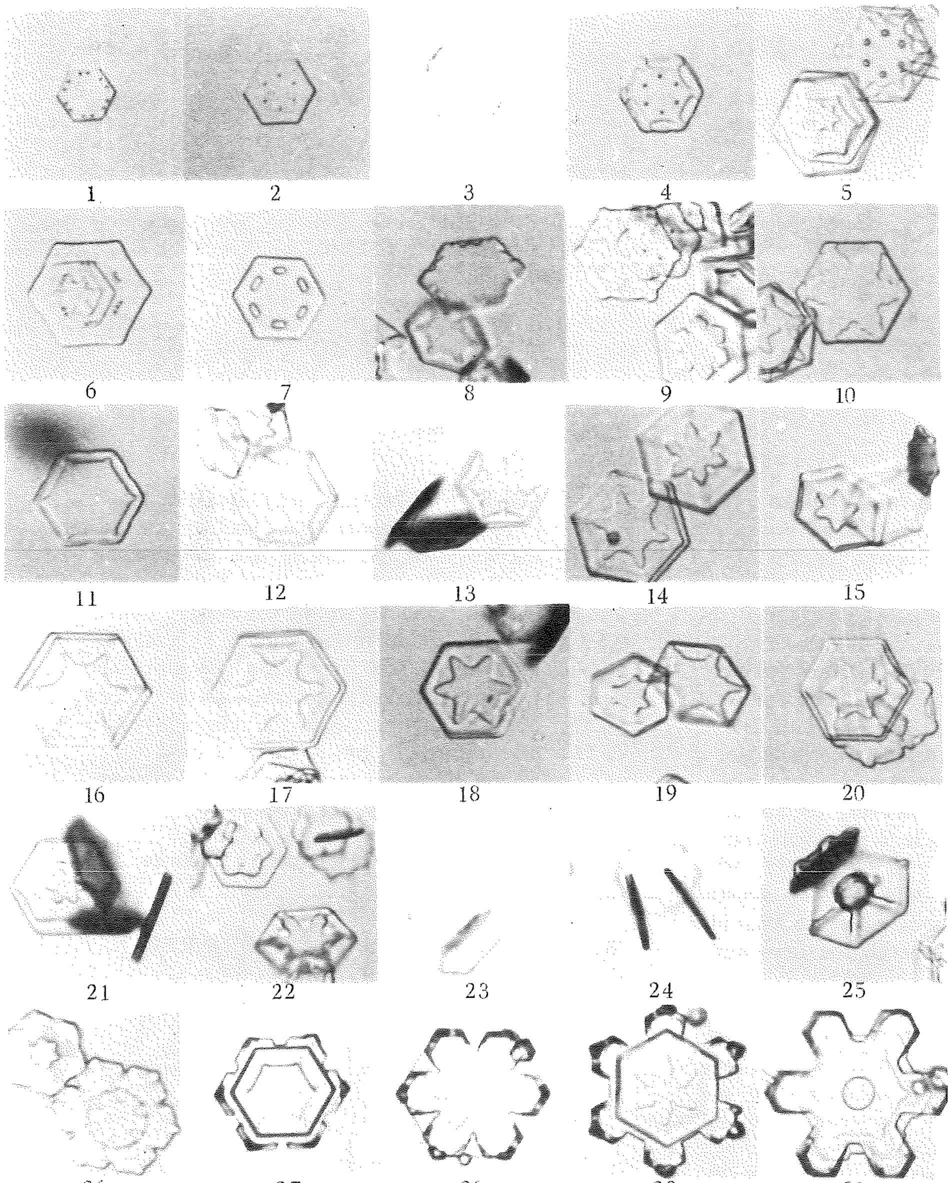

Fig. 1

1 - 30

Ice crystals grown for about 310 seconds at −16 °C. Seeding: adiabatic expansion of room air compressed in a glass tube. A comparison scale of 100 μm is

Size: basal face; 30 ~ 100 μm thickness of double plate; about 5 μm, thickness of a plate; 1 - 2 μm (thickness is the mean value of 23 ice crystals as those shown in 21 and 24.)

Size of flower-like, stellar or round markings at the center: about 15 ~ 50 μm (this suggests that these ice crystals were grown from 15 ~ 50 μm size solid plates)

(1, 2, 3, 4, 5-upper, 6 and 7 have gas enclosures. 9-upper left and 10 have lacunae of rather round steps. 21-right and 24 show side-views of double plates. 25 is a single plate, which may be grown from a frozen water droplet, shows ridges. - - - - -)

31 - 33

Ice crystals grown for about 200 seconds. Comparison scales are 100 μm.

31; about −13°C, (See that a plate has grown larger than the other plate only at a corner.)

32; −16.1°C   33; −14.1°C

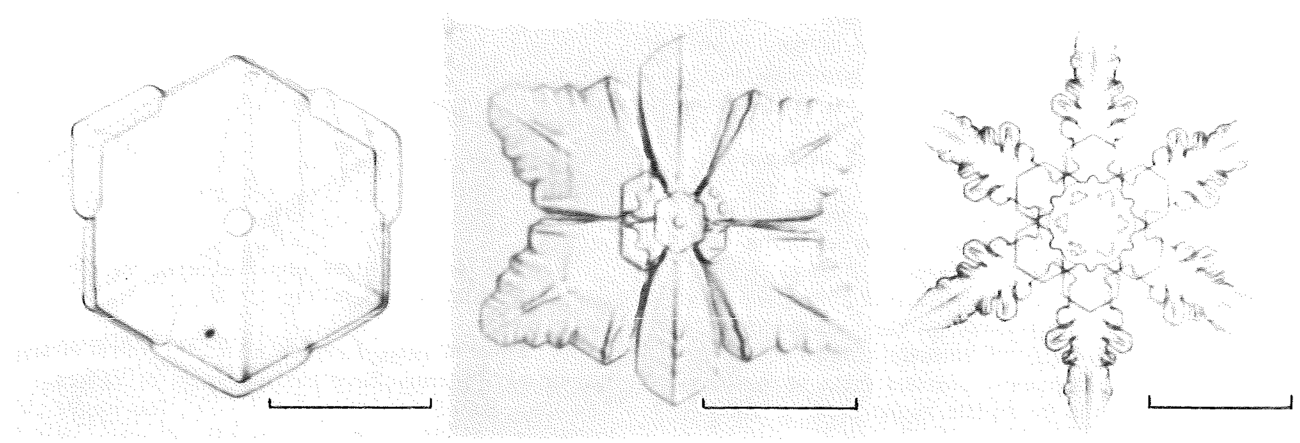

31   32   33

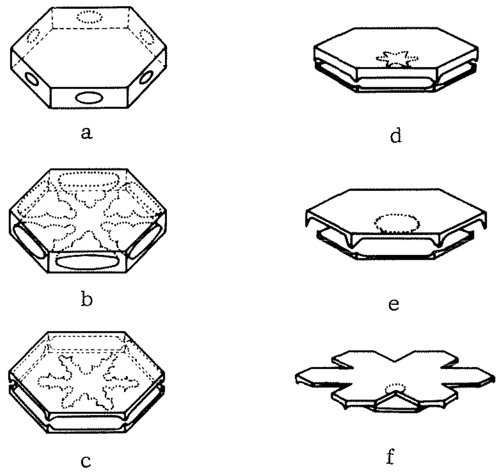

Fig.2 Six representative shapes of plate-like ice crystals with lacunae. An ice crystal grows from a small solid plate to a snow crystal changing its shape $a \rightarrow b \rightarrow c \rightarrow d \rightarrow e \rightarrow f$.

plate (f). Thus, as an ice crystal grows inside structures of it develop . Now it becomes natural to look into the relation between markings of investigated ice crystals and the lacunary structures shown in Fig. 2. This relation is summarized and explained in Fig.3 . The central marking of flower-like or stellar shape was found in small and thin ice crystals like those in Fig.1-1~30 and that of rather round shape was found in large and thin ice crystals grown at $-15.1°C$. The marking of ridge was not always vague for comparatively large ice crystals.

This lacunary growth model of small plate-like ice crystals agrees quantitatively with the lacunary growth of Frank (1974), which is mainly based on the three dimentional structure of snow crystals shown by Nakaya (1954), except the result that with enlargement the lacunae $\langle(10\bar{1}0)(01\bar{1}0)\rangle$ edges are breached at first and the $\langle(0001)(10\bar{1}0)\rangle$ edges of a larger plate of the two layers are breached at second. This order of breaching is correct even for the thin ice crystals of thickness about $5\mu m$.This breaching process may be one factor for production of so many double layered snow crystals in nature. Lacunae usually appear in the centers of the prism faces at first, several ice crystals, however, which have two or three small lacunae on every prism face are also found. (The crystal in Fig.1 - 1 has 12 gas enclosures, a kind of lacunae, for example.)

There are differences morphologacally between the lacunae in this study and the skeleton structures of stepped shapes drawn by Nakaya (1954). The difference of rather round structure and stepped structure should be attributed to the difference of crystal sizes, although the lacunae almost enclosed in concaves have possively changed their shapes from rather stepped form to rather round form of comparatively equilibrium state. In this work neither crystal faces nor sharp edges observable under an optical microscope were found in lacunae.

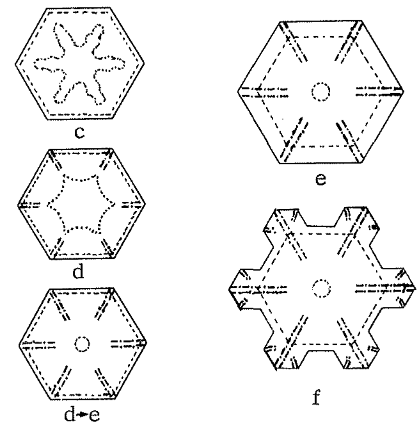

Fig.3 Markings of plate-like ice crystals. Flower-like, stellar or round markings at the center are the figure which shows the boundary of lacunary growth (the figure of thick part connecting upper and lower plates). Hexagonal marking shown by dotted lines are the figure of the smaller one of two layers. Fat and rather vague markings,=:=:=:= , are the figure of ridges. (c, d - - - in the figure correspond to the shapes c, d - - - in Fig.2 respectively)

3. ANALYSIS OF GROWTH DIRECTIONS OF ICE CRYSTALS

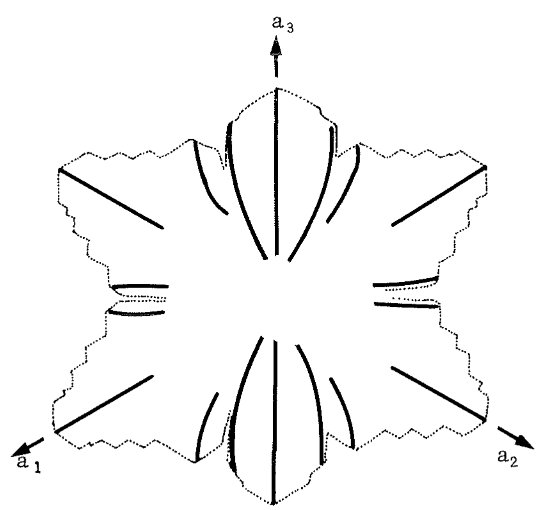

Fig. 4 Ridges observable in the ice crystal shown in Fig.1 -32.

Most of plate-like ice crystals grown in free fall of 14.7 meters have the markings of ridges. The ice crystal shown in Fig.1 - 31 has vague ridges radiating from the center to the six corners and the crystal in Fig.1 -33 has also ridges in six main branches and in subsidiary branches. Ridges of the crystal shown in Fig.1 -32 are drawn in Fig.4. A ridge which lies in the center of a branch has the orientation parallel to a - axes There are three types of branches (Fig.5) whose subsidiary ridges curved in different ways.

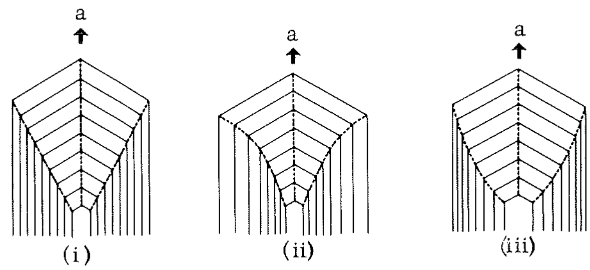

Fig.5 Three types of branches (Dotted lines show ridges.)

Orientations of ridges were also investigated for snow crystals in the text books (Bentley and Humphreys, 1931, Nakaya, 1954). Results are summarized in Fig.6.

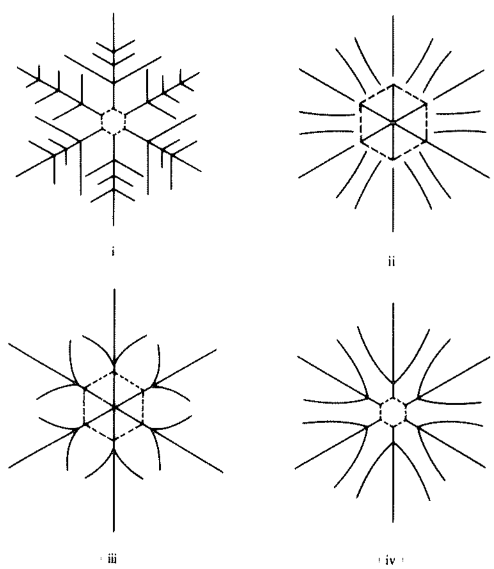

Fig.6 Orientations of ridges found in plate-like snow crystals. (i); Dendrites or sectors whose six main branches have many secondary branches. All ridges are parallel to the crystallographic orientation of a-axes. (ii), (iii) and (iv) ; Stellar crystals of six main branches. There are two kinds of ridges in a branch. One is a straight line parallel to a-axis and the other is curved.

Secondary branches of dendrites or sectors have ridges parallel to a-axes. However, they are inferred to have grown not to the direction of the most favoured access of water vapour. These branches usually have the shape which has not the axis of symmetry. (The growth direction, the direction a ridge leaded the growth, does not make the axis of symmetry.) Fig.7 shows three types of such a secondary branches.

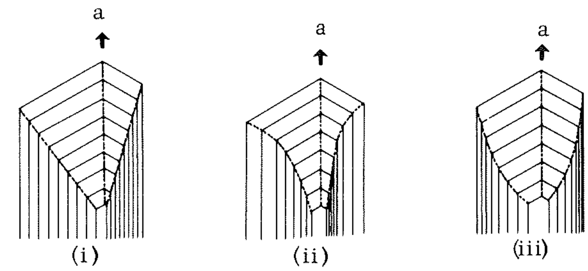

Fig.7 Three types of (secondary) branches. (Dotted lines show ridges)

In the photogragps of natural snow crystals it was difficult to find those branches had clearly changed their growth directions. However, in the photographs of Nakaya's artificial snow crystals we can find a few such a crystals. An example is shown in Fig.8.

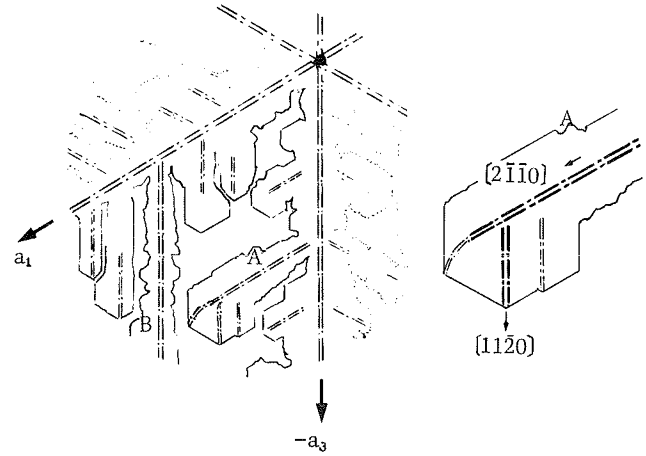

Fig.8 Sketch of an artificial snow crystal. From Nakaya (1942); No.1412. The secondary branch A is shown enlarged (right). The direction of the ridge leading from the main branch to the corner is [2$\bar{1}\bar{1}$0] at first and then is curved. On the other hand another ridge directing the direction [11$\bar{2}$0] is clearly recognized. This change will be explained as follow. The branch A had started to grow toward [2$\bar{1}\bar{1}$0] However, by the effect of the branch B the growth toward [11$\bar{2}$0] became more favourable than the former growth. This change of growth direction is not gradual but should be recognized a clear change.

From the structure of ridges the branch A in the figure seems to have changed the growth from the direction [2$\bar{1}\bar{1}$0] to the direction [11$\bar{2}$0]. There may be a transient stage when the branch has grown toward both the directions at the same speed.

These analyses (including inferences) can be condensed to a law.

Law: The most rapidly growing portion of plate-like ice crystals grows towards one of $\langle 11\bar{2}0\rangle$ directions. (The portion is represented by one of $\langle\!\langle 10\bar{1}0)(01\bar{1}0)\rangle\!\rangle$ edges.) This law can be applied to every branch. That is , it is possible to apply the law restricting portions. In the case of sector plates the portions of edges neighbouring to the most rapidly growing portion grow curved usually making ridges frequently.

For the purpose to confirm the correctness of the law photographs of artificial snow crystals and artificial frost crystals of Nakaya were investigated. These crystals have not such a smmetric shapes as snow crystals in nature, however, the law is correct even for them. The law seems to be contributing to the production of beautiful crystals grown suspended on substances.

The commercial movie of snow crystal growth taken in Nakaya's laboratory gives us a proof for the inference that ridges show growth history of $\langle\!\langle 10\bar{1}0)(01\bar{1}0)\rangle\!\rangle$ edges. The law can be confirmed again.

3. MECHANISM OF THE GROWTH

The law shown in the previous section suggests that growth of prism faces can not be independent in any case. Origins of growth, surface nucleations on crystal faces, will be also related to the law. (Here, growth which is not dislocation-aided is considered only.) As Frank (1974) has suggested about fastly growing snow crystals, surface nucleation occurring near the corner will be considered.

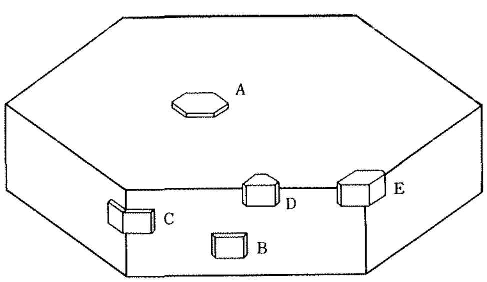

Fig.9 Surface nucleations

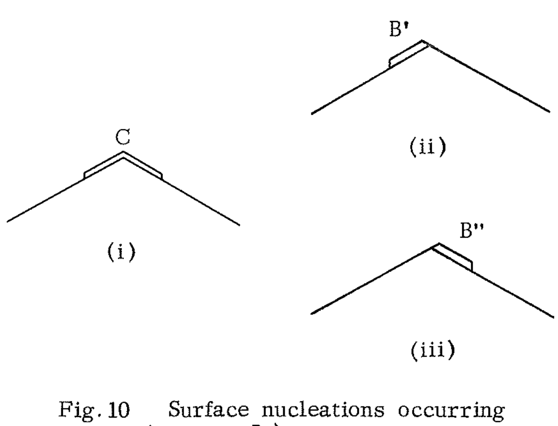

Fig.10 Surface nucleations occurring at the $\langle\!\langle 10\bar{1}0)(01\bar{1}0)\rangle\!\rangle$ edges.

Five types of surface nucleations are shown in Fig. 9 and two dimensional figures of surface nucleation at an edge of $\langle\!\langle 10\bar{1}0)(01\bar{1}0)\rangle\!\rangle$ is shown in Fig.10. For the growth of plate-like ice crystals surface nucleations on prism faces would be contributing and those on basal faces may be neglected for consideration for a while(E should be considered to be one of C,for example , in Fig.9).

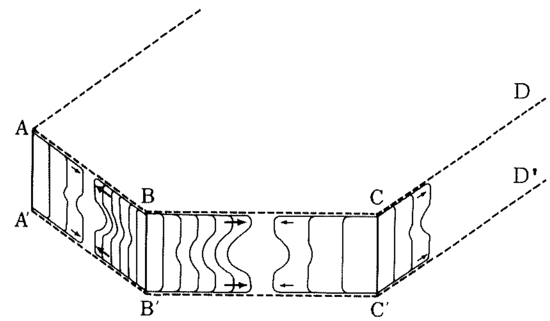

Fig.11 A model of layer by layer growth of prism faces. If the production rate of new layers at the edge BB' is larger than those of AA' and CC' and the rate is equal for both the prism faces, the prism face (BCB'C') and the prism face (ABA'B') grow only by the layers which come from BB' and grow at the same speed. This agrees with the law in the previous section. (In this case the face CDC'D' grows by the layers from CC')

If the surface nucleation of C ((i) in Fig.10) of a single layer occurs one by one and other surface nucleations are negligible, the growth shown in fig. 11 will occur. It may also occur if the two types of surface nucleations (ii)and(iii) occur at just the equal rate. These mechanisms agree with the law.

4. CONTRIBUTION OF THE LAW TO GROWTHES OF ICE CRYSTALS

Only a short consideration will be given. The law should be applied to such ice crystals as aggregated plates , frost of plate-like shapes , ice crystals grown suspended on something(or grown on substrates) or window hoar crystals. Except plate-like ice crystals grown at temperatures lower than -20°C and window hoar crystals (or the like) the law seems to be closely related to their hexagonally symmetric growthes. Consideration how ice plates grow when they have fallen on a flat substrate(or the case an ice plate has aggregated to a larger ice crystal) is shown in Fig.12.

Even ice crystals of plate-like shapes grown in comparatively low humidity (whose growth speed was controlled to be about 1/10 of that in a dense supercooled cloud) obey the law. Considering that some plate-like snow crystals may have grown in such a low humidity, the law seems to be correct for a wide range of humidity.

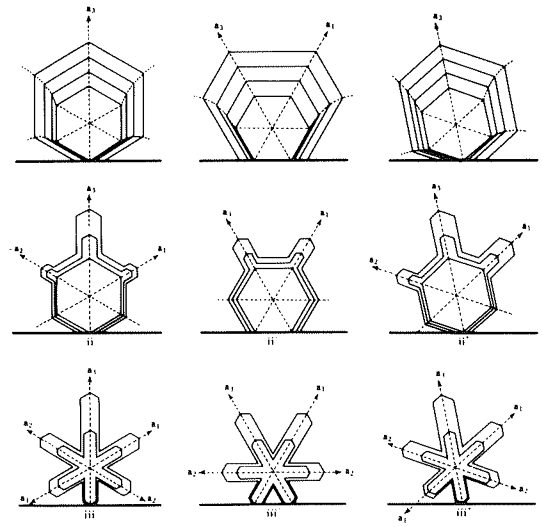

Fig. 12 Inferred growth processes of ice crystals after they have fallen on flat substrates (or on larger ice crystals). Hexagonally symmetric ice crystals grow gradually changing their shapes obeying the law. (Supply of water vapour is assumed to be interrupted by substrates shown by thick solid lines.)

REFERENCES

Frank, F.C., 1974: Japanese work on snow crystals. Crystal Growth, Proceedings of ICCG-4, Tokyo. (North Holland Co.) 3-5.

Nakaya, U., 1942: Snow crystals (in japanese) Iwanami, Tokyo, Photo. No. 1412, 283p.

———————, 1954: Snow crystals. Harvard Univ. Press.

Bentley, W.A. and W.J.Humphreys, 1931: Snow Crystals. MacGraw-Hill, London and New York.

Yamashita, A., 1971: Skeleton ice crystals of non-hexagonal shape grown in free fall. J, Meteor. Soc. Japan, 49, 215-231.

————————, and Takahashi, C., 1972: Initial growth process of snow crystals from frozen water droplets. Volume of abstract. The international cloud physics conference. London, 50-51.

————————, 1974a: Study of ice crystals using a large cloud chamber. (in japanese) Kisho-kenkyu Note No.123, Meteor. Soc. Japan. 813-860.

————————, 1974b: Ice crystals grown from the vapour in free fall: the influence of nucleation methods. Collected Abstract, ICCG-4, Tokyo, 492-593.

————————, 1973: On the trigonal growth of ice crystals. J.Meteor. Soc. Japan, 51, 307-317.

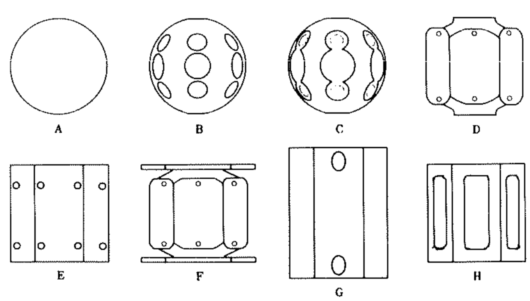

Fig. 13. Ice crystals of various growth stages with lacunae and gas enclosures. Growth from 30 ~150 µm size water droplets. (c-axes: vertical in the figure)

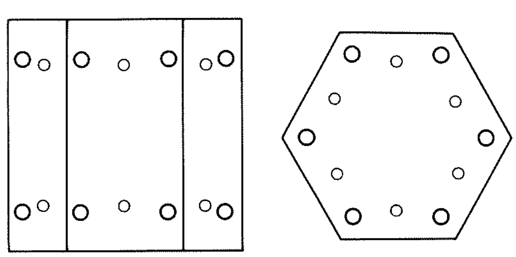

Fig.14 Details of the stage E in Fig.13. There are two kinds of gas enclosures. Right; a section of a level of containning gas enclosures.

Appendix : Growth process of snow crystals from frozen water drpolets of about 30 ~ 150 µm with lacunae is as follow (see Fig. 13) : at −10.5 ~ −20°C and 0 ~ −3.5°C; A→B→C→(D)→F, at −8.0 ~ −10.5°C and about −3.5°C; A→B→C→D→E→H , at −3.5 ~ −8.0°C; A→B→C→D→(E)→G. ();can be skipped

At first, 20 circular low indice faces appear on a spherical ice crystal. Then, as it grows lacunae are recognized on 12 pyramidal faces (shown by dotted lines in C). With further growth the lacunae grow to gas enclosures (D) if the crystal is larger than about 50 µm in diameter. With yet further growth of curved faces the change of the famous habit of snow crystal with temperature becomes to be recognized.

G is shown with two gas enclosures which are grown from lacunae on basal faces and H shows a crystal with large lacunae on their prism faces.

Fig.14 shows two kindsof gas enclosures of the growth stage E. Gas enclosures of thinner circles are those grown on pyramidal faces. Those of the thicker circles are gas enclosures which are observed frequently and are larger than the former usually

In conclusion (about lacunary growth) , lacunae grow on every three kind of low index face and they frequently grow to gas enclosures in the case of ice crystals growing from frozen water droplets. The other lacunae begin to develop between every two pyramidal faces . These lacunae , and those developed on pyramidal faces can not remain stable and they disappear eventually unless they grow to gas enclosures. What should be noted is the disappearance of pyramidal faces. They, though at first clear, disappear surrounded by curved faces. The theory of the disappearance of faster growing faces cannot be applied.

3.1.14

ON THE ANGLES BETWEEN PRINCIPAL AXES OF NEIGHBOURING CRYSTALS OF FROZEN WATER DROPLETS

Katsuhiro Kikuchi and Hiroshi Uyeda

Department of Geophysics, Hokkaido University
Sapporo, JAPAN

1. INTRODUCTION

Recently, there seems to be a special interest in the mechanisms of origin of polycrystalline snow crystals, namely, spatial dendrites, radiating assemblage of dendrites, combination of bullets and so on. Lee (1972) made careful measurements of the angle between spatial branches of natural polycrystalline snow crystals under a microscope using a universal stage. He found that the predominant angle varied according to the crystal shape of snow crystals, however, he noted that the highest peak in the distribution of the angle was recognized around 70° in all types of spatial dendrites, radiating assemblage of dendrites, side planes and combination of bullets. Furthermore, his results were reconfirmed through the measurements at the same location on top of Mt. Teine, Hokkaido during two winter seasons of 1974 and 1975 by the authors (Uyeda and Kikuchi, 1976).

On the other hand, laboratory experiments regarding crystal structure and orientation of frozen supercooled drops on an ice surface were carried out by Hallett (1964), however, he did not measure the angle between the c-axis direction of the frozen drop and ice substrate. Higuchi and Yosida (1967) made grow prism crystals from frozen droplets on impaction onto an ice substrate and they measured the angle between c-axes of prism crystals and the orientation of the ice substrate. As a result, it was determined that the peaks of the measured angle were approximately 20°, 30°, 60° and 90°. The same experiment in the case of dendritic crystal was done by Magono and Aburakawa (1968) and Aburakawa and Magono (1972). They measured the angle between dendritic branches grown from frozen droplets impacted and ice substrate and they obtained the result in which the peaks of the angle were approximately 80° at -20°C and -28°C and within a range of 40° and 50° at -10°C. Murray and List (1972) carried out investigations of water drops frozen freely-floating in purified air in a vertical wind tunnel. In their experiments, the drop diameters varied from 1 to 8 mm and air temperature varied from -1° to -18.5°C, and the ice phase was initiated artificially. Especially, they made etch pits on the frozen water drops at an arbitrary air temperature and obtained the distributions of crystallographic orientation namely the angle between the c'-axis and a radial line from the assumed growth center in a temperature range from -2° to -12.8°C. However, they did not measure the angle between crystals against each other. The idea that polycrystalline snow crystals, especially, spatial dendrites and combination of bullets grew from polycrystallized droplets was set forth by Weickmann (1972) and Parungo and Weickmann (1973), and Kikuchi and Ishimoto (1974) confirmed this in a laboratory experiment. In this paper, investigations of crystallographic orientations of c-axes of polycrystallized water droplets and the angle between neighbouring crystals against each other will be described.

2. EXPERIMENTAL APPARATUS AND PROCEDURE

A droplet container for freezing of water droplets is placed in freezing box

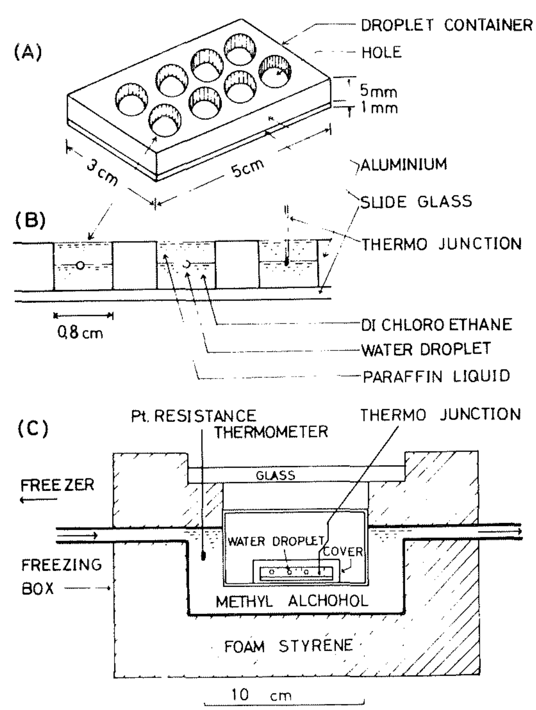

Fig.1 Experimental apparatus.

cooled by circulating cold methyl alcohol. The circulating methyl alcohol is chilled in a freezer controlled by a programmer and a temperature controller. Temperature controller regulated the temperature of methyl alcohol within a range of ±0.01 °C. And a programmer was used for the adjustment of the rate of cooling of the freezer. The schematic figure of the experimental apparatus, a droplet container (A, B) and freezing box (C), is shown in Fig.1. The container was constructed from aluminum plate and the size is 3 cm X 5 cm X 0.5 cm having 8 holes. The diameter of each hole is 0.8 cm. One of the holes was used for the temperature measurement by means of a thermo-junction. Freezing temperature of each droplet was decided by the temperature when the droplet become opaque. The accuracy in the temperature determinations is considered to be of an order of 0.5°C. Water droplets were made of distilled and de-ionized water and they were inserted by a hypodermic syringe and suspended either at the interface of two immiscible liquids, one heavier and one lighter than water, or on dichloroethane covered with liquid paraffin. Thus, they are sandwitched by both liquids. This is almost the same as in Bigg's experiment (1953). Freezing experiments were carried out by rates of cooling of -12°C/h, -30°C/h and -60°C/h. The sizes of frozen water droplets were mainly 1.0~1.7 mm in diameter and for special purposes were 0.4~0.65 mm. When the supercooled water droplets were frozen, the record of the thermo-junction was checked for each droplet individually. Then each frozen droplet was collected using a small pair of tweezers and transferred onto a slide glass. On the slide glass, the droplet was fixed by solidified aniline ($C_6H_5NH_2$) (Kinoshita and Wakahama, 1959) and was cut into thin sections with a small safety razor blade. The thin section of the frozen droplet was fixed using viscous cedar oil on a universal stage under a polarizing microscope and photographs in color and monochrome were taken. Then the number of component crystals was counted. On the other hand, the principal axis of the thin section of a frozen droplet was determined from an extinction position under a polarizing microscope and corrected by Langway's correction table (1958). Then this was projected on Wulff's stereographic net and the angles between c-axes of neighbouring crystals were measured. The measuring accuracy by this method is 5 degrees at its maximum. A series of measurements from the termination of freezing to the finishing of determination of the angle was completed in less than two hours.

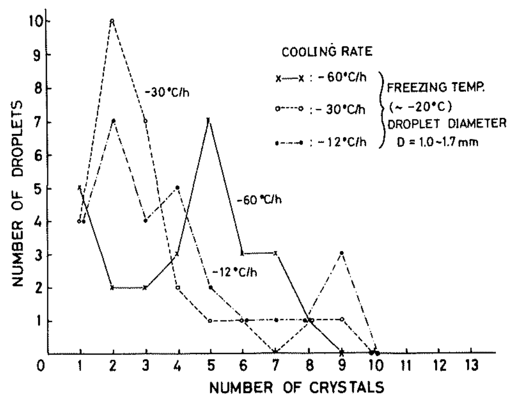

Fig.2 Frequency distributions of the number of component crystals at each cooling rate.

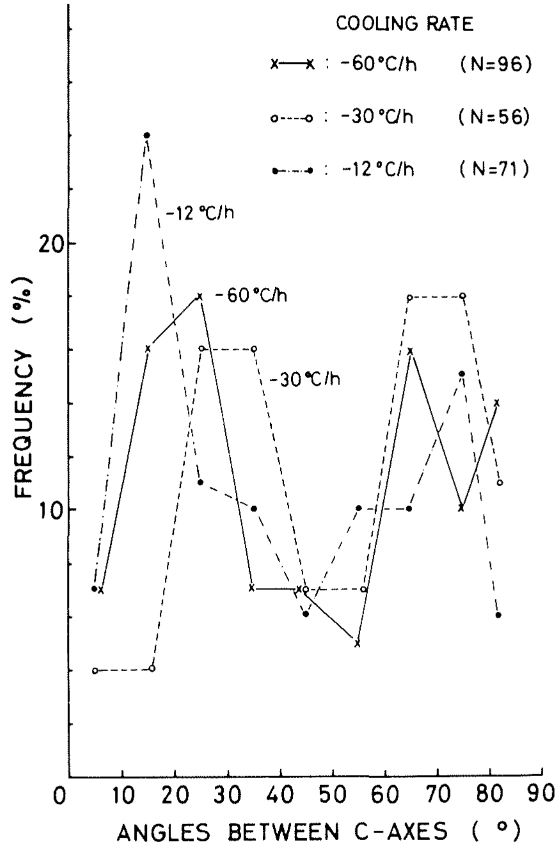

Fig.3 Frequency distributions of the angle between c-axes of neighbouring crystals at each cooling rate.

3. RESULTS

3.1. The number of component crystals and the angle between neighbouring crystals on the thin sections of frozen droplets

Fig.2 shows the distribution curves of the number of crystals on the thin section of frozen droplets at each cooling rate. As seen in this figure, remarkable peaks were recognized in 2 to 3 crystals in the cases of -12°C/h and -30°C/h. However, in the case of -60°C/h, remarkable peak was seen in 5 crystals. In this measurement, a number of crystals in which the direction of the principal axis changed continuously or had small angle grain boundaries was omitted from the frequency curves.

The measured results of the angle be-

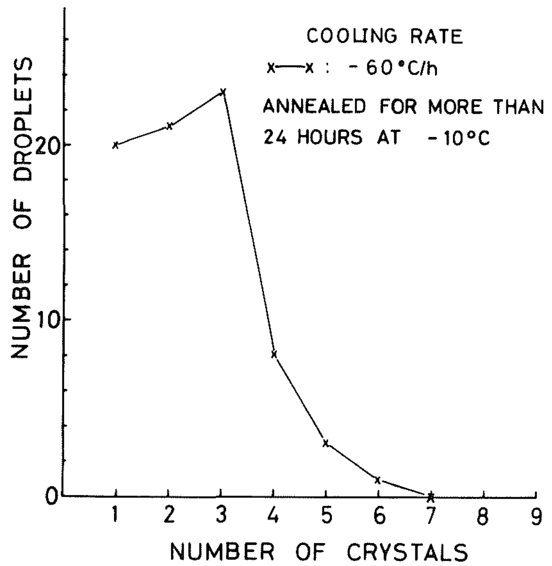

Fig.4 Frequency distribution of the number of component crystals under the condition of annealing for more than 24 hours at -10°C.

tween the principal axes of neighbouring crystals using the same specimen as described above are shown in Fig.3. The ordinate and abscissa shows the frequency distributions and the angle for each 10 degrees, respectively. A sample population for each cooling rate is placed in the upper right of the figure. As may be seen, there were remarkable peaks around 20° to 30° and 60° to 80° irrespective of

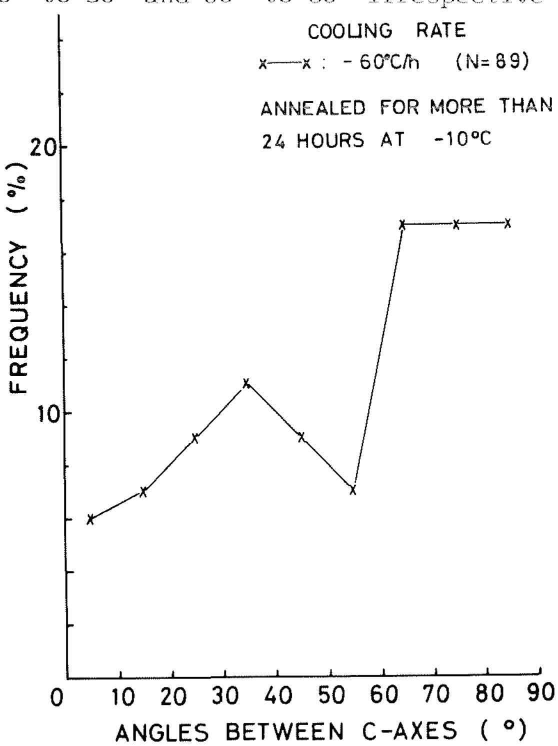

Fig.5 Frequency distribution of the angle between c-axes of neighbouring crystals under the condition of annealing for more than 24 hours at -10°C.

cooling rates. Especially, in the same manner for all cooling rates, the frequency distributions showed an extreme reduction at 10° and 50°.

3.2. Crystal growth by recrystallization

It is well known that a number of minute crystals in an ice specimen are recrystallized to a few relatively large crystals with the advance of time. Thus, the following experiment was carried out for the examination of this effect to 1 mm size frozen water droplets. At first, the water droplets were frozen at a rate of cooling of -60°C/h and afterwards they were warmed at the rate of +12°C/h to -10°C. After a lapse of time, the droplets were kept at a temperature of -10°C for a duration not more than 72 hours, and not less than 24 hours. Subsequently the same technique described in the previous section was applied. The results are shown in Figs.4 and 5. Compared with Fig.4 and the distribution curve of cooling rate of -60°C/h in Fig.2, a remarkable difference in the distribution was recognized. The decrease of the number of crystals in each thin sections of frozen droplets, namely, the movement of peak value from 5 in number of crystal to from 1 to 3 means that the recrystallization under conditions of temperature at -10°C and annealing for more than 24 hours progressed. And further, the effect made its an appearance in the distribution of angle between neighbouring crystals. Compared with Fig.5 and Fig.3, it may readily be seen that a remarkable peak around 20° and 30° in the frequency curve of the cooling rate of -60°C/h in Fig.3 had diminished and another peak at 70° remained and further the peak increased more evidently in Fig.5. That is to say, it was shown that the effect of annealing was recognized in the case of small sized frozen droplets of about 1 mm in diameter, especially, it is interesting to note that the small angle between c-axes of neighbouring crystals diminished and the large angle alone remained.

3.3. Freezing experiments at relatively high temperature

We know the experimental results when supercooled water drops were impacted on an ice surface, where the number of crystals of the frozen drops were supercooling dependent, namely, with the decrease of temperature increasing numbers of crystals appeared. Conversely, with the increase of temperature decreasing numbers of crystals was found to be remarkable (Hallett, 1964; Magono and Aburakawa, 1968). And then, the freezing experiments carried out the same manner as described in the above section was undertaken at relatively high temperatures in the same size range, namely, 1.0∿1.7 mm in diameter. At first, the temperature decreased at the cooling rate of

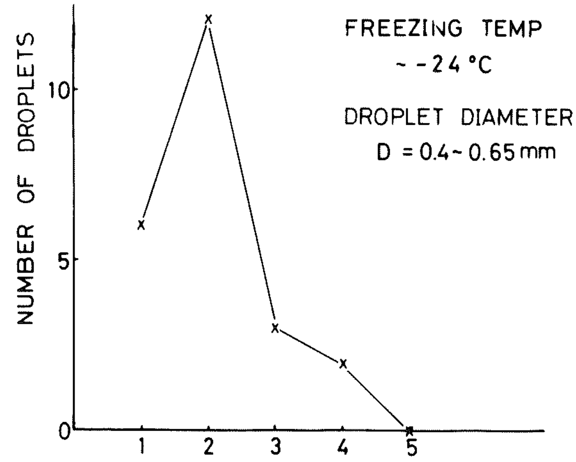

Fig.6 Frequency distribution of the number of component crystals of relatively smaller sized frozen droplets.

-60°C/h from room temperature till the temperature of the droplet container reached -10°C. And thereafter the temperature of -10°C was maintained until the supercooled droplets were frozen. Consequently, in the case of this experiment, a few droplets required more than two days to freeze. After that the frozen droplets were selected and thin sections were made. As a result, 20 out of 27 of frozen droplets were crystallized in a single crystal and another 7 droplets were composed of 2 crystal components. It was possible to measure the angle between two crystal components in 5 droplets out of 7. The angle was within a small range such as 17°, 17°, 18°, 19° and 26° respectively and a remarkable peak around

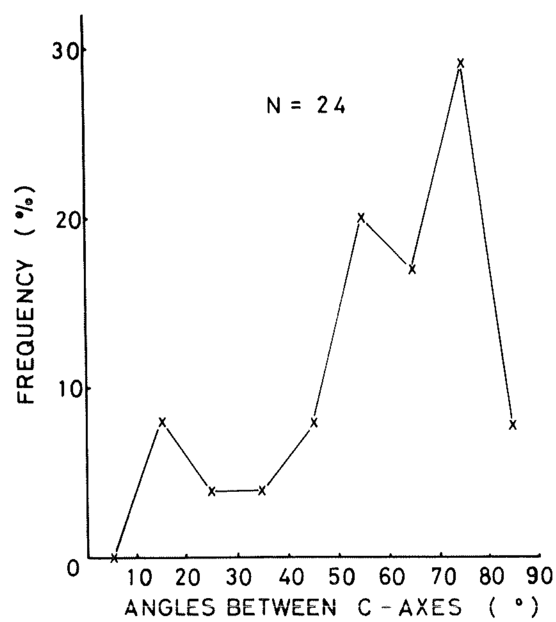

Fig.7 Frequency distribution of the angle between c-axes of neighbouring crystals of relatively smaller sized frozen droplets.

70° pointed out in the previous sections was not recognized in this experiment.

3.4. Freezing experiment of smaller sized droplets

In the experiment of the previous sections, water droplets of a size range of 1.0 to 1.7 mm in diameter were used. The size range used, however, was somewhat too large to apply to the center droplet of a combination of bullets and radiating assemblage of dendrites in nature. Regarding this, we have previously performed the same experiment in a somewhat smaller sized droplets, namely 0.40 to 0.65 mm in diameter. The rate of cooling was selected as -60°C/h in this experiment. The average freezing temperature in this cooling rate was -24°C in a range between -22° and -26°C. As for the number of crystals in the thin section of frozen droplets 2 crystals were prominent and more than 4 crystals were not observed in this experiment as shown in Fig.6. The angle between the principal axes of neighbouring crystals was predominant at 50° to 80° as shown in Fig.7. However, the sample population in this experiment was only one third less than in the previous experiment. Because, it was very difficult to produce a thin section of frozen droplets as small as 0.40 mm in diameter in this manner and we failed at this stage on numerous occasions.

4. CONSIDERATIONS

As a matter of course it was considered that the number of the component crystals in the thin section is smaller than the number of crystals on the surface of a frozen droplet. According to Kikuchi's observation (1968), however, the number of bullet crystals composing a combination of bullets was 2 to 4 crystals in nearly 90 % of the cases. Therefore, the number of component crystals of 2 to 4 in this experiment coincides with the previous observation except for the diameters. This fact means that the number of the component crystals on the thin section does not vary with the number on the surface of a droplet because the size of the frozen droplet examined was not large compared with the natural frozen water droplets of relatively large sizes. On the other hand, the number of component crystals in this experiment was smaller than those in Hallett's experiment (1964). In the latter case, the freezing temperature was close to homogeneous nucleation, however, in the case of temperatures above -20°C, the difference of the number of crystals was not so large between each other.

The frequency distributions of the angle between neighbouring crystals on the thin sections of frozen droplets were remarkable in a range of 60° to 80°, and 20° to 30° for all cooling rates. In these frequency distributions, it is considered that the angle between 60° and 80° corresponds to the angle of about 70 in natural polycrystalline snow crystals (Lee, 1972: Uyeda and Kikuchi, 1976). However, the smaller angle of 20° to 30° is rarely found in nature. It is expected from this fact that the frozen cloud droplets underwent recrystallization during their descent. Crystal growth by recrystallization was described in the previous section already. If a small angle between the neighbouring crystals is present on the surface of frozen droplets, two branches or two bullets of snow crystal may not grow from the surface of the droplet because the diffusion vapor flux is restricted to a small area. Further, as anticipated in the experiment of smaller sized droplets, natural frozen cloud droplets in small sizes may not crystallize with a small angle within each other.

Lee (1972) developed a matching theory to interpret the 70° angle between the spatial branches and he calculated the misfit factor. According to his conclusion to the snow crystal of spatial dendrites, a misfit of basal plane to $(30\bar{3}2)$ plane was 0.0 where the angle between $\underline{c}$-axes of both planes was 70.5°. That is to say, the angle of 70.5° calculated from the matching theory corresponded to the observation angle of 70°. There is another plane of misfit factor of zero, namely, $(30\bar{3}7)$. In this case, the angle between $\underline{c}$-axes is 38.9°. Further, the misfit of the basal plane to $(40\bar{4}5)$ plane is 0.4 and the angle between both planes is 56.4°. From these results, Lee (1972) concluded that the peaks at the 70° of the frequency distributions of angle between $\underline{c}$-axes of the polycrystalline snow crystals showed a matching of $(30\bar{3}2)$ plane to basal plane (0001). And the respective planes of $(30\bar{3}7)$ and $(40\bar{4}5)$ corresponds to the peaks of 40° and 56° respectively.

Although the matching theory is suitable to apply to the polycrystalline growth such as in the case of shape of spatial dendrites which are the supercooled cloud droplets colliding and frozen onto the basal plane of dendritic single crystal and which grew the branches from the frozen droplets. However, there is no inevitability in applying the matching theory to the shapes of radiating assemblage of dendrites and combination of bullets which are considered to grow from frozen cloud droplets. Regarding this, Iwai (1971) introduced the idea of penetration twin theory. According to his opinion, the angle of 70° between both planes or branches is the result of twin relation of $(30\bar{3}8)$ planes.

Recently, Kobayashi et al (1976) developed a theory of the twin relation based on the CSL relationships to the polycrystalline snow crystals including the shape of the combination of bullets. And they suggested that component crystals having an angle of about 70° may be in «$30\bar{3}4$» and «$30\bar{3}8$» twin relation and 30 may be in «$20\bar{2}1$» twin relation with each other.

5. CONCLUSIONS

Freezing experiments were carried out from the point of view of the mechanisms of origin of polycrystalline snow crystals, namely, spatial dendrites, radiating assemblage of dendrites, combination of bullets and so on. Especially, a detailed examination was made on the number of component crystals and the angles between $\underline{c}$-axes of neighbouring crystals when water droplets of $0.40 \sim 1.7$ mm in diameter were frozen under controlled rates of cooling. The results were as follows; Most of the water droplets froze in a range of $-17^\circ \sim -23^\circ C$ at all rates of cooling, namely $-12^\circ C/h$, $-30^\circ C/h$ and $-60^\circ C/h$. The number of the component crystals was $2 \sim 3$ for the cooling rates of $-12^\circ C/h$ and $-30^\circ C/h$, and $5 \sim 6$ for the rate of -60 C/h, respectively. These numbers coincided with the number of bullet crystals in natural falling snow crystals. As shown in Fig.3, there were two peaks in the frequency distributions at $20^\circ \sim 30^\circ$ and $60^\circ \sim 80^\circ$ for the angle between $\underline{c}$-axes of the neighbouring crystals. However, under annealing conditions, the remarkable peak around $20^\circ \sim 30^\circ$ diminished and another peak at $60^\circ \sim 80^\circ$ remained alone and further the peak increased more prominently. The result seems to support the theory on twinned structures by Kobayashi et al (1976) in which the component crystals may be in «$30\bar{3}4$» and «$30\bar{3}8$» twin relation for the angle of 70° and «$20\bar{2}1$» twin relation for the angle of 30°. However, the small angle of about 30° corresponding to «$20\bar{2}1$» twin relation is not clear in natural falling snow crystals. The reason is considered as follows; Frozen cloud droplets in nature undergo recrystallization during their descent or if only a small angle between the neighbouring crystals is present on the surface of frozen droplets, two branches or two bullets of a small crystal may not grow from the surface of the droplet because the diffusion vapor flux is restricted to a small area.

Acknowledgments

The authors express their hearty thanks to Profs. C. Magono and T. Kobayashi, Hokkaido University, for their encouragement and discussions throughout the course of this study. A part of the expense of this study, especially, the equipment used for this experiment was defrayed by the Special Funds given to Kikuchi at 1972 from the Ito Science Fundation.

References

Aburakawa, H. and C. Magono, 1972: Temperature dependency of crystallographic orientation of spatial branches of snow crystals. J. Meteor. Soc. Japan, 50, 166-170.

Bigg, E.K., 1953: The supercooling of water. Proc. Phys. Soc., B, 66, 688-693.

Hallett, J., 1964: Experimental studies of the crystallization of supercooled water. J. Atmos. Sci., 21, 671-682.

Higuchi, K. and T. Yosida, 1966: Crystallographic orientation of frozen droplets. Physics of Snow and Ice, Vol.1 (Inst. Low Tem. Sci. Hokkaido Univ., Sapporo), 79-93.

Iwai, K., 1971: Note on snow crystals of spatial type. J. Meteor. Soc. Japan, 49, 516-520.

Kikuchi, K., 1968: On snow crystals of bullet type. J. Meteor. Soc. Japan, 46, 128-132.

Kikuchi, K. and K. Ishimoto, 1974: Role of frozen cloud droplets on the growth of snow crystals of certain shapes. J. Fac. Sci., Hokkaido Univ., Ser.VII, 4, 69-80.

Kinoshita, S. and G. Wakahama, 1959: Thin sections of deposited snow made by the use of Aniline. (in Japanese with English résumé) Low Temp. Sci. Hokkaido Univ., Ser.A, 18, 77-96.

Kobayashi, T., Y. Furukawa, K. Kikuchi and H. Uyeda, 1976: On twinned structures in snow crystals. J. Crystal Growth, 32, 233-249.

Langway, C.C. Jr., 1958: Ice fabrics and universal stage. SIPRE Tech. Report, 62, 16pp.

Lee, C.W., 1972: On the crystallographic orientation of spatial branches in natural polycrystalline snow crystals. J. Meteor. Soc. Japan, 50, 171-180.

Magono, C. and H. Aburakawa, 1968: Experimental studies on snow crystals of plane type with spatial branches. J. Fac. Sci., Hokkaido Univ., Ser.VII, 3, 85-97.

Murray, W.A. and R. List, 1972: Freezing of water drops. J. Glaciology, 11, 415-429.

Parungo, F P. and H.K. Weickmann, 1973: Growth of ice crystals from frozen cloud droplets. Beit. zur Phys. Atmos., 46, 289-304.

Uyeda, H. and K. Kikuchi, 1976: Remeasurement of axial angle between spatial branches of natural polycrystalline snow crystal. (to be published)

Weickmann, H.K., 1972: Snow crystal forms and their relationship to snowstorms. J. de Recherches Atmosphériques, 603-615.

RECENT EXPERIMENTS ON "SPLINTER" PRODUCTION DURING RIMING

S.C. Mossop and E.R. Wishart

Division of Cloud Physics, CSIRO, Sydney, Australia

1. INTRODUCTION

Evidence that secondary ice particles are ejected when a moving body gathers rime in a supercooled cloud at about -5C was first presented by Hallett and Mossop (1974). The main experimental findings to date are as follows.

(a) "Splinter" production is confined to the temperature range -3 to -8C; the production rate is greatest at about -5C, regardless of target velocity (over the range 1.4 to 3 m s^{-1}) (Mossop, 1976).
(b) This phenomenon is found only in clouds which contain large drops. The rate of splinter production is most closely correlated with the concentration of drops ⩾24 μm in diameter (Mossop and Hallett, 1974).
(c) At a temperature of -5C one splinter is produced for about every 200 drops of diameter ⩾24 μm accreted, regardless of the target velocity (Mossop, 1976).

In the present paper we report new results on the effect of drop size and other variables on the production of secondary ice particles.

2. EFFECT OF CLOUD DROP SPECTRUM ON PRODUCTION OF SECONDARY ICE PARTICLES

In the work cited above the riming experiments were carried out in a chamber of volume about 4 m^3 in which a cloud was formed by introducing steam from a boiler. The riming body was a vertical metal rod 30 cm long and 0.2 cm in diameter which moved about a vertical axis at the desired speed. Ice crystals ejected were detected as they passed through a light beam and the rate of production could be determined by calibration experiments in which the crystals fell into trays of supercooled sucrose solution on the floor of the chamber.

With this apparatus we have determined the number of secondary crystals produced per milligram of rime accreted, and this is plotted as a function of temperature in Fig. 1. The target velocity was 1.4 m s^{-1}, the radius of rotation being 15.3 cm. The average drop size distribution is plotted in Fig. 2 as spectrum A. This was obtained with a single-stage impactor using MgO-coated slides (May, 1945; 1950).

The mean drop size was then reduced by providing a source of condensation nuclei within the chamber. A small coil of platinum wire heated electrically to a yellow heat was kept on the floor of the cloud chamber about 30 cm from the steam inlet. A reproducible drop size distribution was obtained in this way (Fig. 2, spectrum B). The rate of splinter production with a 30 cm rod moving at 1.4 m s^{-1} through this cloud was less than with the "standard cloud" as shown in Fig. 1 and the peak appeared to have shifted to about -6C.

Finally, a still smaller mean drop size was obtained by making a cloud in the 300-ℓ cloud chamber described by Mossop, Brownscombe and Collins (1974). This is capable of detecting much smaller splinter production rates since every ice particle falls into a tray of sugar solution at the bottom of the chamber and can be counted. The drop spectrum (C) is shown in Fig. 2 and the splinter production per unit weight of rime is plotted in Fig. 1. Cloud parameters are summarized in Table 1.

The following conclusions may be drawn from this work.

(a) The temperature for peak splinter production may vary from about -5 to -6C depending on the drop size distribution, clouds with more large drops giving the higher peak temperature. The temperature limits for splinter production are unchanged at -3 and -8C.

(b) The rate of splinter production depends upon the drop size distribution in the cloud, bigger drops producing more splinters. There is no sharp cut-off at 24 μm and splinters can be produced at a low rate even in a cloud such as C, where drops >24 μm are very rare.

If we confine our attention to measurements at a particular temperature, say -5±0.5C, we can plot the number of crystals produced per second by a 30 cm riming rod as a function of the concentration of large drops in the various clouds. Since the target velocity is constant the rate at which drops are swept up should be proportional to concentration. When this is done for drops ⩾23.5 μm we get Fig. 3. (This curious diameter, 23.5 μm, arises merely from the microscope graticule used in sizing the drops.)

This shows that though the rate of splinter production is related to the rate at which these large drops are swept up, the linear relationship suggested by Mossop and Hallett (1974) is probably incorrect. It appears that the splinter production per drop is a function of drop size. The nature of the relationship may throw light on the splintering mechanism and needs to be explored further.

3. EFFECT OF CIRCULAR MOTION ON SPLINTERING

In our experiments the riming rod moves in a circular path gathering rime on the leading edge. Newly accreted drops would have a tendency to flow away from the centre of rotation and this could

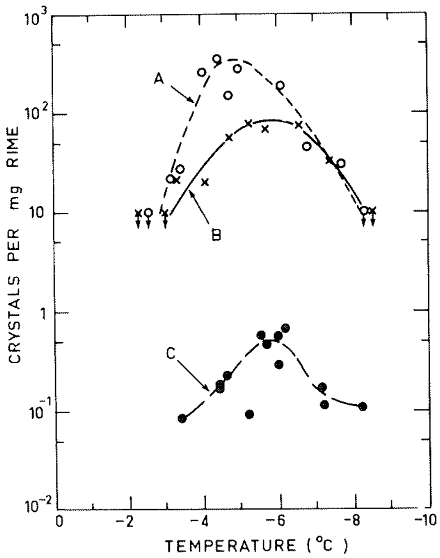

Fig. 1 - Crystals produced per unit weight of rime as a function of temperature for three different drop spectra. The riming bodies were metal rods 0.2 cm in diameter moving at 1.4 m s^{-1} through the supercooled cloud.

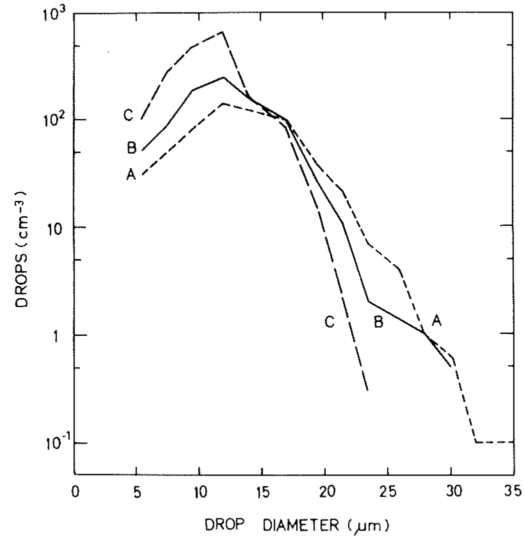

Fig. 2 - Drop size distribution plotted at diameter intervals of about 2.5 μm for the three artificial clouds referred to in Fig. 1. The values from which these spectra were plotted are given in Table 1.

Table 1. Average values of cloud parameters

Cloud	Drop concentration (cm^{-3}) for various diameters (μm)														Drops	L.W.C.
	5.5	7.5	9.5	12	14	17	19.5	21.5	23.5	26	28	30	32	34.5	(cm^{-3})	(gm m^{-3})
A	30	80	78	138	128	96	37	21	7	4	1	0.6	0.1	0.1	621	0.97
B	50	88	178	347	155	96	26	11	2	1.4	1	0.5			956	1.08
C	100	273	454	687	164	86	15	2.3	0.3						1782	1.42

affect the structure of the rime and hence the rate of splinter production. Mossop (1976) gave reasons why this is not thought to be of great importance. Nevertheless, it was thought advisable to make a direct experimental test.

In the experiments described above the target velocity was 1.4 m s^{-1} and radius of rotation 15.3 cm, giving a centripetal acceleration of 1280 cm s^{-2}. In a new series of experiments the velocity was kept constant but the radius of rotation was reduced to 9.5 cm, giving a centripetal acceleration of 2060 cm s^{-2}. The rate of secondary crystal production was determined at a number of temperatures and the results are compared with the "standard conditions" in Fig. 4. It is apparent that increasing the centripetal acceleration by 60% had no appreciable effect on splinter production.

4. TEST OF "GLANCING-CONTACT" THEORY OF SPLINTERING

If a supercooled drop makes only glancing contact with an ice surface it may be possible for the drop to carry away with it the ice which has started to grow into it from the original surface. This theory of the origin of splinters was rejected by Mossop (1976) on the grounds that the

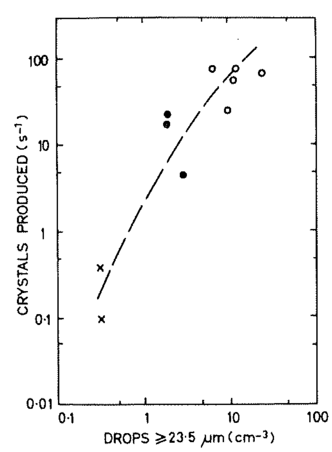

Fig. 3 - Relationship between crystals produced per second by a metal rod moving at 1.4 m s^{-1} through a cloud for various values of large drop concentration (diam. ⩾23.5 μm); temperature -5±0.5C. Results with spectra A, B, C are represented by open circles, closed circles and crosses respectively.

time of contact was so short that the new growth would extend <1 μm into the drop and was therefore unlikely to be detached.

The glancing-contact mechanism may be feasible if one postulates two drops arriving on virtually the same spot in quick succession. A dendrite will grow into the water film produced by the first drop and this could be long and frail enough to be detached by the glancing collision of a second, comparatively large drop. The time for dendrite growth could be much longer than that visualized in the single-drop situation.

The probability of a second drop being accreted on top of a still unfrozen drop before dendritic growth has reached the surface of the liquid film can be evaluated following Macklin and Payne (1967, 1968). This probability decreases rapidly with temperature, thus providing a possible explanation for the cut-off of the splintering mechanism at temperatures below -8C.

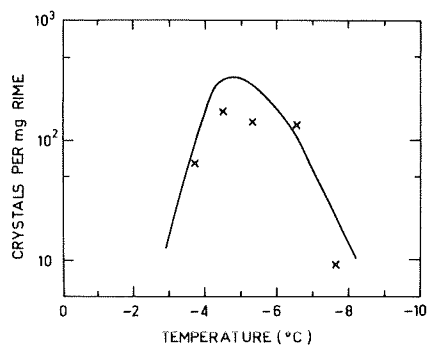

Fig. 4 - Experiments with riming rod moving at 1.4 m s^{-1} through "standard cloud" spectrum A. Full line is curve A from Fig. 1 and applies to a radius of rotation of 15.3 cm. The crosses represent results with a radius of rotation of 9.5 cm.

Where rime is growing upon a rod the glancing-contact mechanism will act along the two edges of the rime. This suggests a practical test of the theory if the edge length of the riming body can be increased without proportionately increasing the cross-section. In this way the probability of glancing collisions could be increased in relation to the number of drops being accreted.

A new riming body was therefore constructed from the original riming rod by fixing to it 178 cross-wires each 1.7 cm long and 0.025 cm in diameter. In this way the edge length was multiplied by a factor of about 10 but the sampling cross-section was only doubled. The rate of splinter production during the growth of rime on this array was investigated for a velocity of 1.4 m s^{-1}, liquid water content about 1 gm m^{-3} and a number of different cloud temperatures. A comparison with results obtained under similar conditions with the simple riming rod is shown in Fig. 5.

The crystals produced per unit weight of rime accreted are actually fewer with the new riming array, providing no support for the glancing-contact theory. The decrease is probably due to the greater proportion of small drops accreted by the array, so that per unit weight of rime the large drops are fewer. This agrees with the postulate that the splinters are produced by the larger drops.

5. RIME STRUCTURE

In many of our experiments on splinter production during rime growth we have examined fragments of the rime under a microscope. The fragments were embedded in silicone fluid and sandwiched between two glass plates.

For a given drop size distribution the structure of the rime is influenced by two variables, the surface temperature of the rime and the velocity of impact of the drops (Macklin, 1962; Macklin and Payne, 1968). The rime is built up of an elaborate interconnected mesh of ice branches growing forward into the airstream. The higher the temperature and the greater the velocity, the more massive and smooth these ice elements are and the smaller the air spaces between them. At lower temperatures and velocities the structure becomes frailer and more

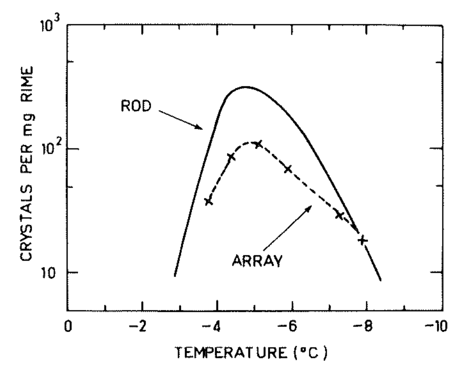

Fig. 5 - Experiments with riming body moving at 1.4 m s^{-1} through "standard cloud", spectrum A. Full line is curve A from Fig. 1 and applies to a cylindrical metal rod. The broken line applies to an array which has many thin cross-wires attached to the rod.

open and the individual frozen drops become more obvious. A typical example of the surface structure of the rime is shown in Fig. 6.

The following findings are relevant to the splintering problem.

(a) No frail, needle-like growths have been seen under any of our experimental conditions. There is evidence of diffusional growth of the rime ice from about -5C downwards, but only at the lowest velocity (1.4 m s^{-1}). Flat faces can be seen on some of the ice branches.
(b) At a liquid water content of 1 gm m^{-3} and over the range of velocities 1.4 to 3.0 m s^{-1} the rime branches have a sausage-like form at temperatures down to -8C. Individual frozen drops are not obvious within the rime structure. Only at the rime surfaces can protuberances such as frozen drops on frail stalks sometimes be seen and then only from about -5C downwards.
(c) At temperatures warmer than -3C the rime structure is smooth and massive so that any detachment of frail structures seems most unlikely. However, this is likely to become easier as the temperature is lowered.

6. CONCLUSIONS

New experiments confirm that the production of secondary ice particles during the growth of rime at about -5C depends upon the presence of big drops in the cloud. There is evidence that the splinter production per drop accreted is a function of drop size and that it falls off rapidly for drops smaller than about 24 μm diameter.

The mechanism of splinter production is not yet understood. An experimental test failed to confirm the hypothesis that drops making glancing contact with the rime may carry away ice fragments.

Fig. 6 - A fragment of rime grown on a rod moving at 1.4 m s^{-1} through a cloud of temperature -6.1C, liquid water content ~1 gm m^{-3}. Experiment 3 of 22 October 1974.

REFERENCES

Hallett, J. and S.C. Mossop, 1974. Nature, 249, 26-28.

Macklin, W.C., 1962. Quart. J. R. Meteorol. Soc., 88, 30-50.

Macklin, W.C. and G.S. Payne, 1967. Quart. J. R. Meteorol. Soc., 93, 195-214.

Macklin, W.C. and G.S. Payne, 1968. Quart. J. R. Meteorol. Soc., 94, 167-175.

May, K.R., 1945. J. Sci. Instrum., 22, 187-195.

May, K.R., 1950. J. Sci. Instrum., 27, 128-130.

Mossop, S.C., 1976. Quart. J. R. Meteorol. Soc., 102, 45-57.

Mossop, S.C., J. Brownscombe, and G.J. Collins, 1974. Quart. J. R. Meteorol. Soc., 100, 427-436.

Mossop, S.C. and J. Hallett, 1974. Science, 186, 632-634.

3.2.2

ICE MULTIPLICATION THROUGH GRAZING COLLISIONS

Armin N. Aufdermaur and Howard R. Larsen
Osservatorio Ticinese, 6605 Locarno-Monti, Switzerland

1. INTRODUCTION

An understanding of the issues of the origin and initial growth of ice in natural clouds has been identified as a crucial problem in recent reviews in cloud physics (Braham and Squires 1974, Cotton et al, 1975). A major problem is the hypothesised 'ice multiplication' process whereby an apparently few freezing nuclei may give rise to many ice particles. Mossop et al. (1970, 1972) for example report a series of observations in which ice crystals have been found in aged cumulus clouds in concentrations up to 10^5 m^{-3} at temperatures around -10°C, although the concentration of active freezing nuclei hardly exceeded 10 m^{-3}. Earlier in the life cycle of these clouds, relatively large supercooled water drops (d>0.3 mm) and rimed ice pellets in concentrations of several 100 m^{-3} were observed. Koenig (1963) and Braham (1964) have recorded similar results, associating ice multiplication with the presence of rimed ice particles and a significant number of large (d>1 mm) supercooled drops.

It has long been suggested (Brewer and Palmer, 1949) that the multiplication might occur as supercooled droplets freeze on collision with ice pellets, if the freezing leads to the ejection of ice splinters. However, most laboratory studies (Aufdermaur and Johnson, 1972; Bader et al. 1974; Mossop et al. 1974) involving the riming of supercooled droplets have failed to confirm a significant splinter ejection process. Recently Hallett and Mossop (1974) observed a relatively large multiplication effect (several hundred secondary ice particles per mg of rime), when a metal rod was swung in a cloud of very small droplets (d<35μm) at around -7°C but the mechanism of multiplication was not clear. Further experiments (Mossop 1976) have confirmed the operation of a multiplication process under very specific conditions of temperature and cloud droplet spectrum, but have failed to throw any light on the mechanism involved.

All these studies have concentrated on collisions between ice pellets and relatively small supercooled droplets (d<100 μm). On the other hand, we have studied a process in which the production of secondary ice particles occurs when larger drops are involved. In subsequent sections of this paper, we describe first an experiment in which collisions between a simulated hailstone and supercooled water drops produced secondary ice particles, secondly a theoretical examination of some aspects of this process, and thirdly an evaluation of the significance of the process in natural clouds.

2. THE EXPERIMENTS

2.1 Equipment

A drop is formed and suspended on the end of a fine teflon tube at the ambient cold room temperature of -1 to -12°C. An ice sphere swings down on the end of a short pendulum, which also carries a projection to knock the tube out of the way just before the collision. The ice sphere is aimed to overlap about half the drop looking in the direction of the relative motion, so that a grazing collision occurs with the now freely falling drop. A photograph of the splash products taken some 20 ms after the collision indicates whether the water splashing off is freezing or not. The splash product is also allowed to fall on to a sheet of blotting paper, where a liquid product is absorbed while any ice structure present is retained at the surface. Thus there are two independent indicators of whether the collision resulted in secondary ice production or not.

The drop is formed from de-ionized tap water which has been passed through a two stage, Millipore filter (pore size 0.1μm) into a micropump from which it is forced through the 0.2 mm diameter teflon tube. The micropump is electronically controlled, so that the drop diameter is known and reproducible (typically 1.4 mm). In early experiments (included in the results below).The drop was suspended from the end of a fine nylon fibre; in this case it was formed by spraying warm water on to the fibre. The drop was given time in both cases to reach thermal equilibrium, which was 1 to 2 ^{o}C colder than the environment because the air was not water saturated. The end of the tube can be positioned by micrometer adjustment in the plane perpendicular to the line of collision, so that the overlap and position of collision on the ice sphere can be varied. The tube is knocked out of the way some 2 ms before the collision, and photographs of the drop in this period show very little distortion of the drop following shearing off of the tube.

The 'ice sphere' generally consisted of an ice shell over a metal surface, and was usually formed by dribbling water from a syringe over a cold steel sphere already mounted on the pendulum. This produced a rather irregular surface typically 0.5mm thick. A more regular surface has been produced for later experiments by plunging a brass sphere cooled to -30^{o}C into water at +1^{o}C, when a smooth shell some 0.5mm tick is formed. The water used was de-ionized and efforts were made to ensure it did not contain organic impurities, particularly oils, which could act as surface contaminants.

A photograph of the drop and the ice sphere is made immediately before collision, from which the degree of overlap can be measured. The collision velocity was determined by the height from which the pendulum was released; three different velocities (nominally 1,2, and 3m/s) were obtained in this way. As the collision occured a projection from the pendulum passed successively two photoelectric sensors, from which an accurate measure of the actual collision velocity could be derived.

2.2 Results:

At relative velocities of 1 to 3m/s, the collisions usually resulted in the production of a single large splash product. In a few cases several small products were also detected, but their nature (water/ice) could not be determined.

The results of 267 collisions at one velocity (approximately 2 m/s) and 50% drop overlap are summarized in Table I, grouped according to the ambient air temperature. Cases where the nature of the splash product was uncertain have been included to give some idea of the reliability with which the results could be determined. The results indicate an increasing probability of secondary ice production with decreasing temperature over the temperature range -5^{o}C to -12^{o}C.

Less well defined results were obtained when ice production was considered as a function of velocity. Table II shows the data for collisions at -10^{o}C subdivided according to velocity. More results are necessary to establish a relationship between freezing and velocity.

To verify that the ice generation

TABLE 1. Results from 267 grazing collisions of water drops (1.1 to 1.6 mm diameter) with ice coated spheres (7 mm diameter) at a relative velocity of 2 m/s, grouped according to ambient temperature ($\pm$ 1.25 ^{o}C)

Air temp ^{o}C	Total no of collisions	Splash product			% Ice
		Water	Ice	?	
-5	112	102	8	2	7
-7.5	42	33	7	2	17
-10	54	42	12	0	22
-12.5	59	40	19	0	32

occurred not as a result of e.g. mechanical shock forces but because of an ice/water interaction two more experiments were performed:
i) The overlap was reduced until the drop failed to collide with the sphere, and a further 132 runs made. An ice product was never observed.
ii) A clean metal sphere was used in place of the ice target, when no ice was observed in 55 collisions.

In an attempt to determine the controlling parameter governing the production of secondary ice, monocrystaline ice hemispheres of different orientations were used as targets. The ice hemispheres, of approximately the same diameter as the earlier targets, were formed by carefully nucleating slowly cooling water in suitable plastic moulds. Ninety collisions were performed, approximately 30 at each of three perpendicular c-axis orientations (in the direction of relative motion, in the direction of the pendulum arm, and normal to the ice surface at the center point of the collision). No effect of orientation was found.

The effect of surface roughness on the nucleating ability of the ice was then examined. Rough ice coatings were made and secondary ice was found to be frequently produced. However there was the residual possibility that some loose ice was left on the surface in the process of forming the rough surface. The effect of a highly curved ice surface was therefore studied directly by using needles carrying sharp ice edges or points

TABLE 2. Results from 128 grazing collisions at -10 ^{o}C, grouped according to collision velocity.

Velocity m/s	Total no of collisions	Splash product			% Ice
		Water	Ice	?	
1	47	42	5	0	10
2	54	42	12	0	22
3	27	24	2	1	7

mounted on the pendulum in place of the large ice sphere. Steel meedles with rounded tips of 150 μm radius coated with a 20 to 30 μm thick layer of ice were tried, but they proved not to be efficient nucleators. The efficiency could be increased by producing sharper edges on the rounded tip by careful melting or grinding, but this was an extremely difficult process. However by cooling the needle to -40°C and then touching only the very tip in water, a small and sharp edged cap, almost a disc, of ice could be reproducibly formed which gave greatly enhanced secondary ice production. These experiments are summarized in Fig. 1. The freezing probability is plotted versus the smallest radius of curvature found on the ice. (The shape of each needle was recorded on two mutually perpendicular photographs immediately before a collision run).

The results of Fig. 1, obtained at 2 m/s relative velocitiy and at different temperatures, show that the curvature of the mother ice surface is a controlling parameter in the secondary ice production we observed. It should be noted that a freezing probability of 0.2 resulted from collisions with surfaces of radius of curvature larger than 200 μm and at air temperatures around -10°C. This agrees with the results of the earlier experiments of Table 1, where the surface of the ice targets was not controlled, but relatively smooth.

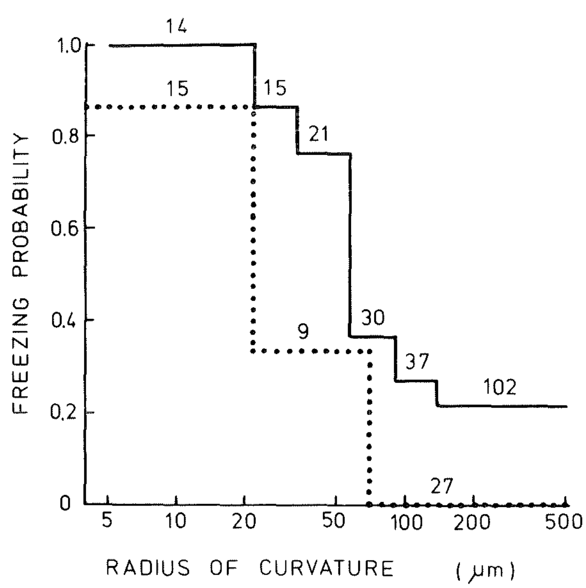

Fig. 1. Probability of freezing after collision versus smallest radius of curvature on the ice substrate, for two temperature ranges:
—— air -7.5 to -12, drop -9 to -13 °C
--- air -1.2 to -4.5, drop -3 to -5.6 °C
Probabilities are derived from number of collisions indicated above the curves.

3. THEORY

3.1 The nucleation mechanism

Because collisions with substrates other than ice did not lead to freezing, we attribute the freezing of a supercooled drop after a grazing collision specifically to the fact that it was in contact with ice and not to other effects such as mechanical shock. The most plausible hypothesis is that the drop carries away an ice nucleus, either one already existing on the surface or one created during the collision. In the following section we investigate this latter possibility.

It is presumed that when the collision occurs dendritic growth takes place from the ice surface into the supercooled water, and we calculate first the length a dendrite crystal must reach in order to be broken off by the drag forces of the moving water. It is assumed that the bulk of the water continues to move at the pre-collision relative velocity V. The water immediately in contact with the ice will be at rest, with the velocity v in the boundary layer increasing with increasing distance y from the interface at the rate:

$$dv/dy = V\ (\rho V/s\eta)^{1/2}$$

Here s is a characteristic length wich depends on the flow conditions (see Meksyn, 1961). ρ is density, η viscosity of water. If we assume that the dendrite is a cylinder of diameter b and length l growing normal to the interface, and with a drag coefficient approximated by $10\ (\eta/\rho b v)^{1/2}$, we can integrate the torque in the boundary layer and obtain

$$I = 1.4\ \rho^{5/4}\ b^{1/2}\ V^{9/4}\ \eta^{-1/4}\ s^{-3/4}\ l^{7/2}$$

The torque required to break such a cylinder is

$$I = \sigma\ b^3 \pi/32$$

where σ is the breaking stress, for which a reasonable value is $1.5 \cdot 10^6$ N m^{-2} (see Hobbs, 1974, p.333). The critical length of dendrite for fracture is then (eliminating I from the last two equations):

$$l_c = 0.47\ b^{5/7} V^{-9/14}\ s^{3/14}\ \sigma^{2/7}\ \rho^{-5/14}\ \eta^{1/14}$$

Taking a dendrite diameter of 1 μm, we evaluate this expression for 2 m/s relative velocity, typical of our experiments. For flow over an effectively plane surface s = 9 x where x is the distance from the start of the boundary layer, downstream to the location of the dendrite. Taking x = 0.5 mm gives

$$l_c = 14\ \mu m$$

For flow around a spherical cap s = r/2, where r is the cap radius of curvature, so that for a 20 μm radius cap

$$l_c = 4\ \mu m$$

It is now necessary to examine whether a dendrite can grow to these critical lengths during the short time a drop flows over it. That time is typically 0.5 ms in our experiments. Measurements of the free growth rate of dendrites in supercooled water (Hobbs, op. cit., p. 587) indicate that the dendrite tip advances at a velocity dependent on the supercooling and given approximately by

$$v_d = k \cdot \Delta T^2$$

with $k = 5 \cdot 10^{-4}$ ($m\ s^{-1}\ {}^{o}C^{-2}$), (see Hobbs, op. cit., p. 587). The critical lengths of 14 and 4 μm are reached in the available time at temperatures of -8 and -4°C respectively. However to assume growth at the original drop temperature neglects that the whole interface will start to freeze almost instantaneously, which forces its temperature to a value close to 0°C. A thermal boundary layer develops in the flowing water whose thickness δ_T is given by

$$\delta_T = (q\eta/V\rho)^{1/2} \quad Pr^{-1/3}$$

q is the same as s for the flat case (i.e. 9 x) but is 4 s (i.e. 2 r) for flow over a spherical cap. For the flat case, x = 0.5 mm, we obtain δ_T = 27 μm and for the cap, r = 20 μm, δ_T = 3 μm. This warm boundary layer will slow down the growth of dendrites within it. In fact since the interface is close to 0°C dendritic growth from the interface will be too slow to have any relevance unless there are microscopic roughness elements on the surface which can give the dendrite a 'head start'. Such elements are actually expected on the surface (Hobbs, op. cit., p. 430). A headstart of 2 μm would allow a dendrite to reach the critical length through the thin boundary layer over a 20 μm radius cap at -5°C, but in the much weaker gradients over a plane surface the critical length could not be reached even at very low temperatures. At -20°C for example it grows just 0.7 μm. In the flat case there is only a small region where the boundary layer may be thin enough for dendrites to grow and to break off ($x \to 0$, start of boundary layer) and it must remain stable a rather long time while the dendrites grow. This leaves a small probability for the process to occur even in the flat case, which we believe is responsible for the results obtained with 'smooth' ice spheres (Tables 1 and 2).

We conclude therefore that dendrites may grow and be broken off particularly if the ice particle shows protrusions with a radius of curvature of the order of 20 μm, which creates thin viscous and thermal boundary layers. Increasing relative velocity would further reduce the thickness of these boundary layers, but also reduce the time available for dendrites to grow, so a straightforward dependence on velocity is therefore not expected. A similar reduction of the time available for dendrite growth happens also in grazing collisions with smaller drops. We expect therefore a lower limit on the drop size favourable for this mechanism of ice multiplication. For the following discussion we assume this lower limit to be 0.5 mm diameter.

3.2 Significance of this process in nature

In order to evaluate the significance of an ice multiplication process involving large drops we consider in this section the situation of a graupel growing in a cloud containing supercooled precipitation. We note first that the accretion of cloud droplets will lead to surface roughness well suited to the proposed process. The average time between collisions of a spherical ice particle of diameter D with raindrops larger than some limit diameter d_m is found in Fig. 2. We assumed a drop concentration equivalent to a rain intensity of 10 mm/hr distributed in drop size as proposed by Marshall and Palmer (1948). The calculation is similar to those described by List et al. (1970). However, we have to make a correction to allow for the fact that only partial coalescence fulfills the requirements of our multiplication mechanism. As experimental results are not available for the range of drop and target sizes under consideration, we used a crude model to estimate the probability that a collision results in only partial coalescence. The model, which considers the energetics of grazing collisions, will appear elsewhere.

For a cutoff (d_m) of 0.5 mm the mean time between partial coalescence collisions is of the order of 10 to 100 s, depending on the diameter of the hailstone. Similar calculations have also been made for a drop concentration typical of those found by Koenig (1963) in ice-enhanced clouds. The mean time found is only 10 s for a 2 mm ice particle and 0.5 mm drop cutoff (using data from Koenig's Fig. 11; Cloud Dog, pass 7, time circa 1095 s).

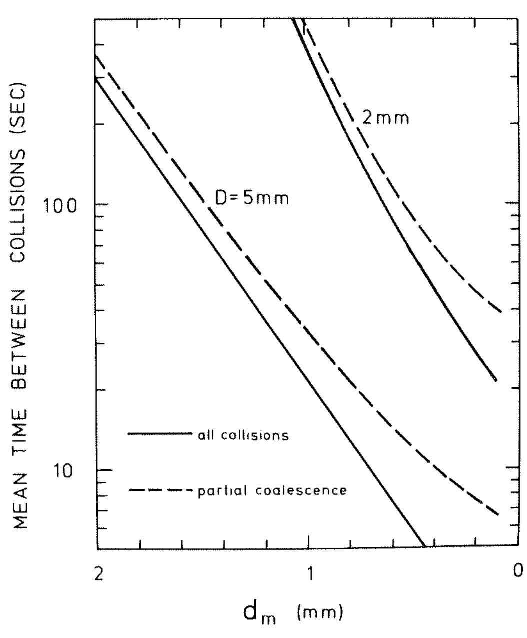

Fig. 2. Mean time between collisions of a 2 or 5 mm ice sphere and raindrops larger than diameter d_m. Drop concentrations according to Marshall and Palmer for 10 mm/hr rain.

If each of these partial coalescence collisions results in the production of a secondary ice particle, the number of ice particles will double in 10 s. However, the chain reaction to produce further ice does not proceed at the same speed, because the secondary ice particles are smaller than the mother hailstone. This complication makes it difficult to compare the present mechanism with that found by Hallett and Mossop (1974). Their secondary ice particles are more than 10 times smaller again than ours, but their rate of production is at least 10 times faster. The problem has recently been considered by Chisnell and Latham (1976).

4. CONCLUSIONS

The experiments described in this paper have shown that a supercooled water drop after colliding with and splashing off an ice pellet has a certain probability of freezing. This probability is greatly enhanced when areas of the ice surface are highly curved, with radii of curvature of the order of 50 µm or less, and also increases with decreasing temperature.

It is shown theoretically that these conditions favour the growth and breaking of dendrites during the time of contact, so that these fragments may induce freezing of the drop after collision. However it appears to be difficult for this mechanism to work when the droplet is below a certain size, as the time available for a dendrite to grow would become too small. For this reason the secondary ice particles produced in the experiments of Hallett and Mossop (1974) are unlikely to be created by the present mechanism.

Nevertheless the present process is likely to be significant in a cloud containing large drops. It operates over a wide temperature range and produces relatively large secondary ice pellets.

ACKNOWLEDGEMENTS

We thank Mr. R. Lüthi for his valuable technical assistance. This research was supported by the Swiss National Fund.

REFERENCES

Aufdermaur, A.N. and Johnson, D.A., 1972: 'Charge separation due to riming in an electric field'. Quart.J.R. Met.Soc., 98, pp 369-382.

Braham, R.R.Jr., 1964: 'What is the role of ice in summer rain showers?' J.Atmos. Sci., 21, pp 640-645.

Braham, R.R.Jr. and Squires, P., 1974: 'Cloud physics - 1974'. Bull.Amer. Meteor.Soc., 55, pp 543-556.

Brewer, A.W. and Palmer, H.P., 1949: 'Condensation processes at low temperatures and the production of new sublimation nuclei by the splintering of ice'. Nature, 164, pp 312-313.

Chisnell, R.F. and Latham, J., 1976: 'Ice particle multiplication in cumulus clouds'. Quart.J.R.Met.Soc., 102, pp 133-156.

Cotton, W.R., Jiusto, J.E. and Srivastava, R.C., 1975: 'Cloud physics and radar meteorology'. Rev.Geophys. Space Phys., 13, pp 753-760.

Hallett, J. and Mossop, S.C., 1974: 'Production of secondary ice particles during the riming process'. Nature, 249, pp 26-28.

Hobbs, P.V., 1974: 'Ice physics'. Clarendon Press, Oxford, p 837.

Koenig, L.R., 1963: 'The glaciating behaviour of small cumulonimbus clouds'. J.Atmos.Sci., 20, pp 29-47.

List, R., MacNeil, C.F. and McTaggart-Cowan, J.D., 1970: 'Laboratory investigations of temporary collisions of raindrops'. J.Geophys.Res., 75, pp 7573-7580.

Marshall, J.S. and Palmer, W.McK., 1948: 'The distribution of raindrops with size'. J.Meteor., 5, pp 165-166.

Meksyn, D., 1961: 'New methods in boundary layer theory'. Pergamon Press, Oxford, p 294.

Mossop, S.C., 1976: 'Production of secondary ice particles during the growth of graupel by riming'. Quart.J.R.Met.Soc., 102, pp 45-57.

Mossop, S.C., Cottis, R.E. and Barlett, J.M., 1972: 'Ice crystal concentrations in cumulus and stratocumulus clouds'. Ibid., 98, pp 105-123.

Mossop, S.C., Ono, A. and Wishart, E.R., 1970: 'Ice particles in marine clouds near Tasmania'. Ibid., 96, pp 487-508.

3.2.3

AIRCRAFT MEASUREMENTS RELATING TO SECONDARY ICE CRYSTAL PRODUCTION IN FLORIDA CUMULI

John Hallett, Dennis Lamb
Desert Research Institute
Reno, Nevada

A.S. Ramachandra Murty
Indian Institute of Tropical Meteorology
Poona, India

Robert I. Sax
NOAA National Hurricane & Experimental Meteorology Laboratory
Coral Gables, Florida

I. INTRODUCTION

Aircraft measurements of ice particle concentrations in convective clouds have shown that concentrations sometimes occur which are in excess by as much as a factor of 10^4 of the most optimistic ice nuclei concentration measured at the coldest temperature of the cloud (Mossop et al., 1972). These high concentrations were measured at temperatures between -4 and -10°C and were associated with the presence of graupel precipitation particles.

A mechanism for the production of secondary ice crystals was sought to explain these observations. Recent experimental studies by Hallett and Mossop (1974 a,b), Mossop and Hallett (1974) and Mossop (1976) have delineated in detail the conditions under which secondary ice crystal production could take place. In summary, crystals are produced during graupel growth, providing

(a) the temperature lies within the range -4 to -6°C,

(b) the cloud contains drops with diameter $\gtrsim$ 25μm; 200 drops of this size must be accreted to produce one secondary crystal,

(c) droplet accretion occurs at velocity > 0.8 m s^{-1}, impact velocity equivalent to the terminal velocity of a graupel particle ∿ 0.5 mm in diameter (Zikmunda and Vali, 1972). The rate of production of ice particles is then independent of velocity up to 3 m s^{-1} in cloud of L.W.C. ∿ 1 g m^{-3}.

Clouds containing significant concentrations of drops with diameter > 25 μm form under quite distinct conditions:

(a) cold ($\lesssim$ +4°C) base and maritime CCN spectrum as in the case of the original study of Mossop et al. off the coast of Tasmania.

(b) warm base $\gtrsim$ +20°C where some drops of this size will always form, although a maritime CCN spectrum will favor a higher concentration.

Conversely, large drops would not be expected in situations with continental aerosol and cool bases.

A simple model for the production of secondary ice crystals and their subsequent concentrations may be constructed as follows:

Consider a spherical graupel particle of radius r_g falling with terminal velocity V_g through air containing a concentration n_d of cloud drops of diameter >25 μm. With the collection efficiency of the particle taken as E and the splinter production rate per graupel-drop collision as α, (α = 1/200 for -4>T>-6°C and α = 0 otherwise), the number of splinters produced per graupel particle per unit time, neglecting the drop fall speed, is

$$S = E\,\alpha\,\pi\,r_g^2 V_g n_d \qquad (1)$$

Assuming a steady state concentration n_g of graupel particles in a generating column lying between the -4 and -6°C isotherms and of thickness h, secondary ice particles will be produced as air rises through this column to give a concentration above the generating zone of

$$n_s = \frac{S\,n_g\,h}{w}\,. \qquad (2)$$

The concentration is seen to vary inversely as the instantaneous updraft velocity w.

With E = 0.5 and h = 500 m, this gives

$$n_s = \frac{(3.9)\,r_g^2\,n_g\,V_g\,n_d}{w}\ m^{-3}, \qquad (3)$$

or, taking the additional values of

r_g = 0.5 mm,

V_g = 1.0 m s^{-1}

n_d = 50 cm^{-3}

w = 5 m s^{-1},

it follows that $\frac{n_s}{n_g} \approx 10.$ (4)

Within the temperature range -4 to -6°C, crystals grow near water saturation as columns with velocity along the "C" axis of 1.5 to 0.8 $\mu m\ s^{-1}$, (Ryan et al., 1974); crystals of 100 µm length would therefore be present after a growing period of 1 to 2 minutes. Observation of cloud and precipitation particles above the generating level should show the presence of such secondary particles should generation be taking place at lower levels. Since cumulus clouds which fulfill the criteria for production of secondary ice particles occur in Florida during summer, opportunity was taken to make specific measurements which could give evidence of this process during the NOAA aircraft program in July 1975.

2. AIRCRAFT OBSERVATIONAL PROGRAM

As part of the 1975 Florida Area Cumulus Experiment (FACE), NOAA's specially-instrumented DC-6 aircraft was used as a research platform to collect microphysical data bearing on the internal microstructure of Florida cumuli. Since the cloud physics program of FACE was conducted with the area-wide seeding experiment, the usual flight procedure was to penetrate as many clouds as possible in the shortest time. However, several occasions existed when the DC-6 carried out special penetrations into clouds of interest and repenetrated the same cumulus towers to obtain data relevant to the evolution of their microstructure. The flight altitude typically was at 5.8 km (-8°C to -10°C), but numerous penetrations were also conducted at 5.2 km (-4°C to -6°C). It should be emphasized that all microphysical data from a particular tower were collected at a single level. The aircraft was operating near its ceiling altitude at 5.8 km and did not have the performance capabilities to enable multi-level penetrations within the same cloud.

These studies were carried out during the month of July within the 13,000-km^2 FACE target area of the south Florida peninsula. The aircraft normally began making cloud penetrations at the 5.2-km level during early afternoon (1400 local time) and at the 5.8-km level by mid-afternoon (1500 local time). On most days this was the time period that convection over the south Florida peninsula was becoming sufficiently well organized to produce a moderate number of cumulus towers growing through the respective flight altitudes. As a general rule, the aircraft penetrated towers within 0.5 km of their tops, although a few, especially those which were repenetrated, had grown 1 to 2 km above the flight altitude. Towers in an active stage of development not associated with larger convective systems were selected preferentially for initial penetrations. The diameters of the towers encountered varied widely, ranging from a few hundred meters, when traversed close to the tower top, to as much as three of four kilometers when traversed closer to cloud base. Cloud bases on all days were at altitudes within the range 0.7 to 1.0 km (approximately 20 to 22°C). A detailed description of the flight procedures, the target area, and the experimental design of FACE is available elsewhere (Woodley and Sax, 1976).

Since the conversion of supercooled water to ice is the vital first link in a sequential chain of events hypothesized to lead to increased localized rainfall through dynamic seeding, the FACE program has focused considerable attention on obtaining the microphysical measurements necessary to characterize the glaciating behavior of Florida cumuli, both seeded and unseeded. The DC-6 aircraft was instrumented for FACE 75 with a formvar replicator of the DRI design (Hallett et al., 1972), a foil impactor, and conventional water measuring devices (Johnson-Williams hot wire and lyman-alpha evaporator). The replicator data were examined frame by frame for the concentration of graupel, vapor-grown columns and cloud drops of diameter >25 µm; in all, 106 penetrations were analyzed. Vertical velocity was computed using the measured aircraft pitch and attack angles combined with filtered values of changes in radar altitude. Spatial resolution of electronically recorded data was of the order of 100 m with the aircraft data system accessed once per second. All cloud penetrations discussed were purposely selected either on days when no seeding was taking place or else prior to any release of silver iodide on seeded days.

3. RESULTS

Aircraft penetration at the secondary ice crystal generation level (-4 to -6°C) on 22 July showed the presence of cloud drops having diameters greater than 25 µm in concentration which ranged from 20 to over 100 cm^{-3} (Fig. 1, 2a). These concentrations are well within the range which could lead to significant production of secondary particles. Graupel concentration at this level was highly variable. The cloud penetrated in Fig. 1 was in its initial growth period and shows an almost complete absence of graupel (Fig. 1 b). As this cloud evolved, a second penetration 4 minutes later (Fig. 2) shows a rapid increase in the concentration of graupel particles between 1 and 5 ℓ^{-1}, most with diameters greater than 0.5 mm, uniformly distributed throughout the cloud. The first penetration showed peak updrafts of about 10 $m\ s^{-1}$, while the second penetration showed a broad updraft region in excess of 10 $m\ s^{-1}$ with peak value >20 $m\ s^{-1}$; cloud L.W.C. >1 $g\ m^{-3}$ was associated with updraft regions (Figs. 1, 2 c). The maximum height of cloud above flight level (estimated from time-lapse nose camera film) was about 500 m.

Figs. 3 and 4 show data from penetrations of cumuli on 24, 27 July above the ice generating level, at temperatures ∿ -9°C. Both of these passes show the simultaneous presence of column crystals (Fig. 5) in concentrations ∿30 ℓ^{-1}, of graupel particles >0.5 mm with a maximum concentration ∿20% of this value, and larger cloud drops with diameters >25 µm, with concentration of 50 cm^{-3}. These values are consistent with the estimates of Eq. (4). The concentration of the graupel in the updraft would be representative of that at the -4°C level as the growth rate during ascent would not significantly change their diameter in the available time. Figs. 3 and 4 demonstrate the following features:

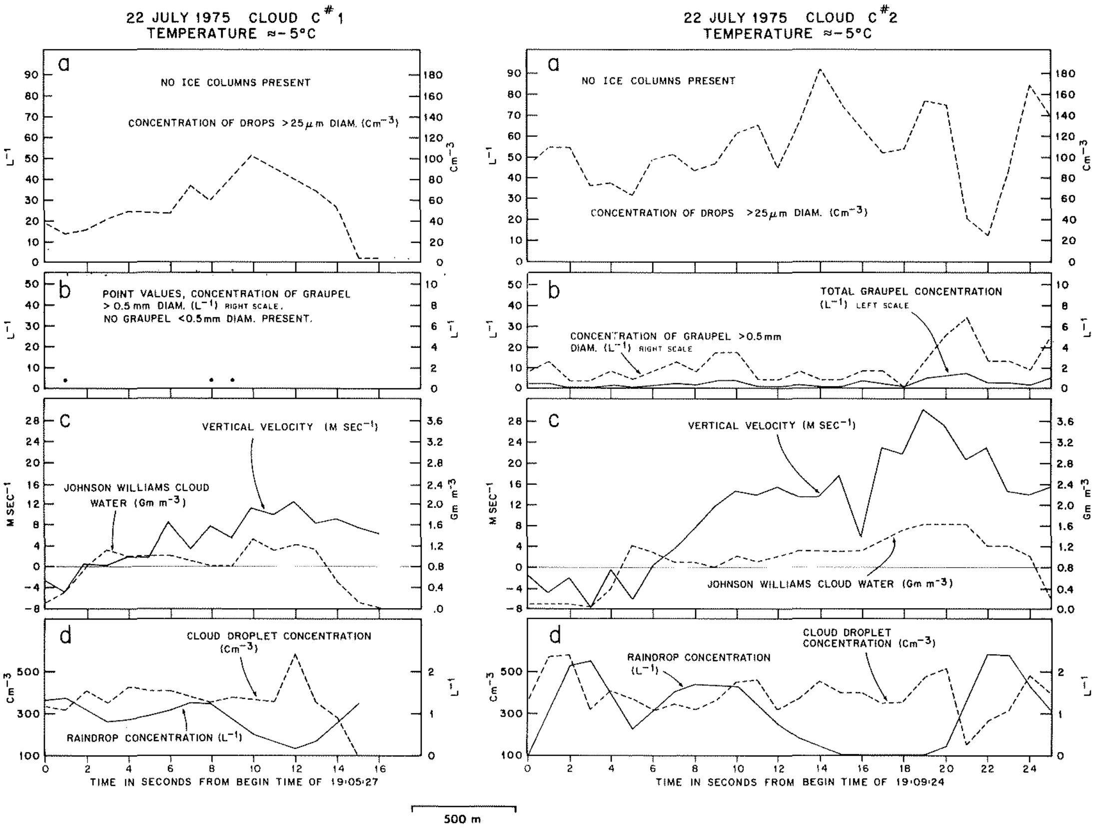

Fig. 1,2. Successive penetrations through a developing cumulus at -5°C level, separated by 4 minutes. During initial penetration only low concentrations of graupel are found; during the second penetration the cloud contains both graupel and cloud drops diameter > 25 μm and satisfies the criteria for ice multiplication processes.

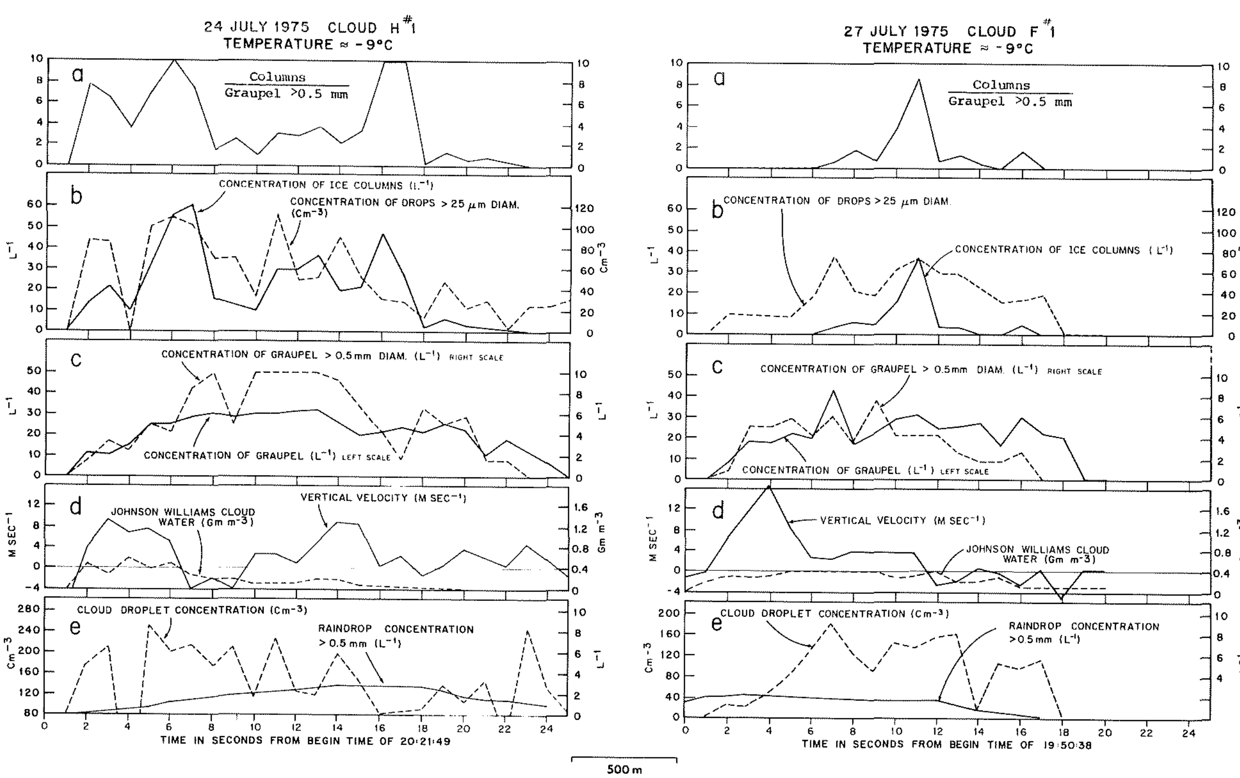

Fig. 3,4. Penetration of two clouds (on different days) at the -9°C level showing the simultaneous occurrence of graupel, vapor grown columns and drops diameter > 25 μm. The upper curves show the ratio of columns to graupel.

(i) The region of occurrence of ice columns corresponds roughly with that of high concentrations of drops of diameter >25 μm and of graupel particles.

(ii) The highest column concentrations tend to be in regions of lower updrafts.

(iii) Graupel and raindrop concentrations are fairly uniform over significant regions of the cloud (c,e).

Fig. 6, a repenetration of the cloud in Fig. 3 after 10 minutes, shows a new thermal rising through the debris of the earlier cloud, still with graupel concentration in excess of 10 ℓ^{-1} but not containing any ice columns. This is to be contrasted with Fig. 7 which shows a vigorous growing tower on the flank of a larger system and a sustained updraft of 10 to 20 m s^{-1} and L.W.C. >2 g m^{-3} over a width of 1 km. No rain water is present and there is an almost complete absence of graupel (less than 0.1 ℓ^{-1}). Measurement of column dimensions averaged over the one penetration pertaining to Fig. 3 showed that the crystals had major axes extending from 50 to 250 μm (Table 1) and minor axes mostly (97%) less than 50 μm. Crystals were in the form of solid columns, with less than 1% showing hollow ends. The few crystals with larger minor axes (∿75 μm) were associated with lower temperatures (-10 to -12°C).

TABLE 1. Frequency of Occurrence of Column Dimensions (μm) (penetration H 1, 24 July 1976; temperature -8 ± 1°C).

Major Axes	Minor Axis 20	40	50	60	75	100
50	232	4				
75	174	60				
100	1	2				
150	40	58	5	2	2	2
200		8		3	1	
250		5		3	1	4

The spatial distribution of vapor grown crystals was by no means uniform, as shown in Fig. 3; of four "ideal" clouds penetrated, two showed no crystals at all.

4. DISCUSSION

Although the attempt was to select isolated towers for penetration, the presence of earlier towers prior to the formation of the penetrated cloud cannot be excluded, and may indeed have been a source of the graupel concentrations which were subsequently observed. Fresh towers growing through the -4°C level are often ice free (<0.1 ℓ^{-1}) and it is inferred that the high concentration of graupel which does occur is related to ice particles formed elsewhere, at higher levels, and subsequently brought to this level. On many occasions there were no (<0.1 ℓ^{-1}) primary ice crystals present at this level.

The variance of the measured updraft is much greater near cloud tops to within one cloud diameter below cloud top; the variance of updrafts below was much lower. This leads to a simplified picture of the cloud extending through a region of continuous upward motion, manifested at upper levels by the periodic emergence of towers. The uniform updraft regions lack mixing with graupel only in the low velocity edges; the upper regions are highly turbulent with a much more uniform distribution of graupel in the horizontal. The source of column ice may be sought in the interaction of graupel with large drops in the developing cloud - first, throughout in the more turbulent regions where graupel is mixed down from higher levels; second, as the cloud evolves, from the lower velocity regions surrounding the steadier central updraft. The dimensions of the observed crystals and the time available for growth deduced from the updraft velocity are consistent with this picture.

The transition of vapor grown crystals to graupel raises some interesting questions. Ono (1969, 1970) has shown that the initial collection of drops, as does the fall velocity of column crystals, depends essentially on the minor axis dimension, no collection occurring for widths less than ∿50 μm even for crystals as long as 500 μm. Table 1 shows that the minor axis of crystals observed at -8°C were mostly less than this value and would not be expected to rime. Lightly rimed columns were rarely observed. This leads to the question of graupel origin. No sustained data collection was made at temperatures less than -9°C, but it may be inferred from laboratory studies that at slightly lower temperatures the habit will become more plate-like with a consequent onset of drop collection. Even near -8°C a period of extended growth at sub-water saturation would eventually lead to crystals with minor axis dimensions > 50 μm. Once accretion begins, subsequent growth should occur quickly. Inserting values from the measurements of Fig. 3 into Eq. (3), one obtains a multiplication factor X of 5 to 10; an increase over the proto-ice concentration at -8°C by this factor when taken down to the -4°C level would lead to an increase of X^n in an n-stage process. It follows that the ultimate ice concentration at the -4°C level will depend on the proto-ice concentration at -8°C (or colder, if appropriate) and the number of cycles. Clouds which fail to reach these cold levels, although containing secondary particles which have grown to columns, would be incapable of growing these crystals to a sufficient width to begin riming and so would not satisfy the criteria for a continuing ice crystal multiplication process.

5. CONCLUSIONS

In these observations:

(i) graupel and drops > 25 μm occur at -4°C in concentrations which are consistent with laboratory derived criteria for the occurrence of secondary ice production.

(ii) Unrimed columns occur at temperatures ∿ -9°C, a fact consistent with a generating level at lower altitude, with more crystals in the lower updraft regions (in accordance with Eq. 2).

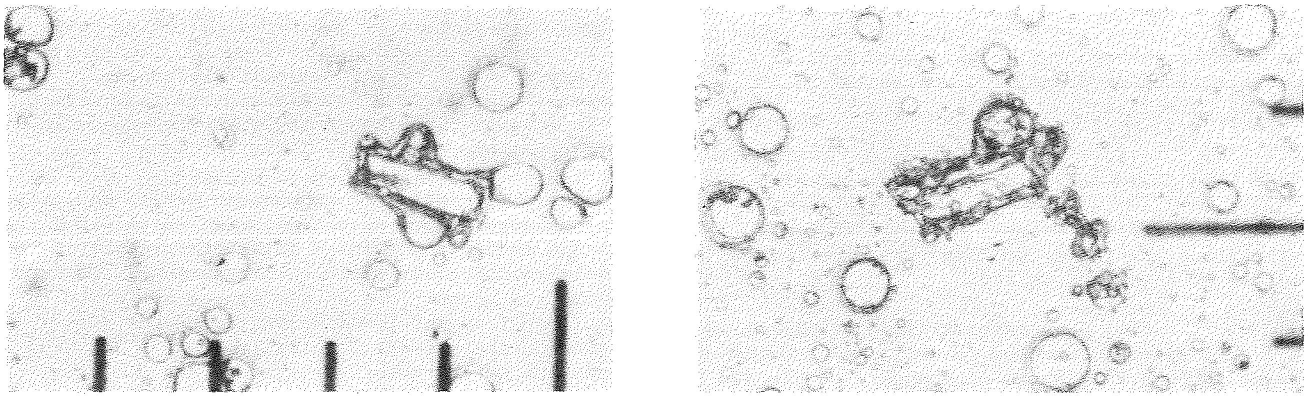

Fig. 5. Formvar replica showing simultaneous occurrence of cloud drops >25 µm and vapor grown ice columns with distinct crystal facets. Droplets on the columns do not necessarily give evidence of riming. Graupel was also present during this penetration. Scale: 100 µm

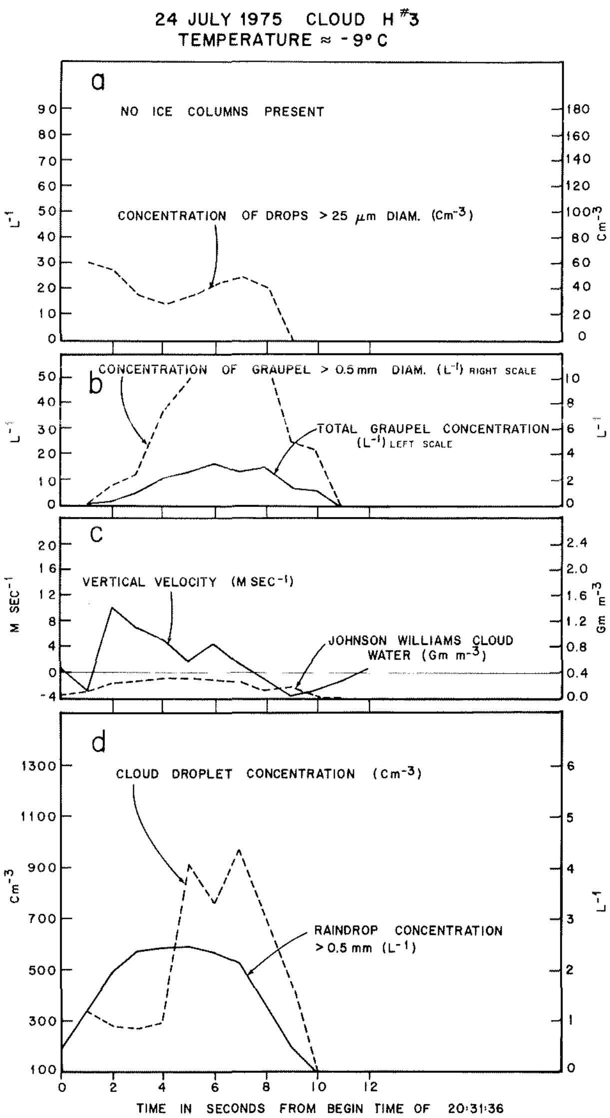

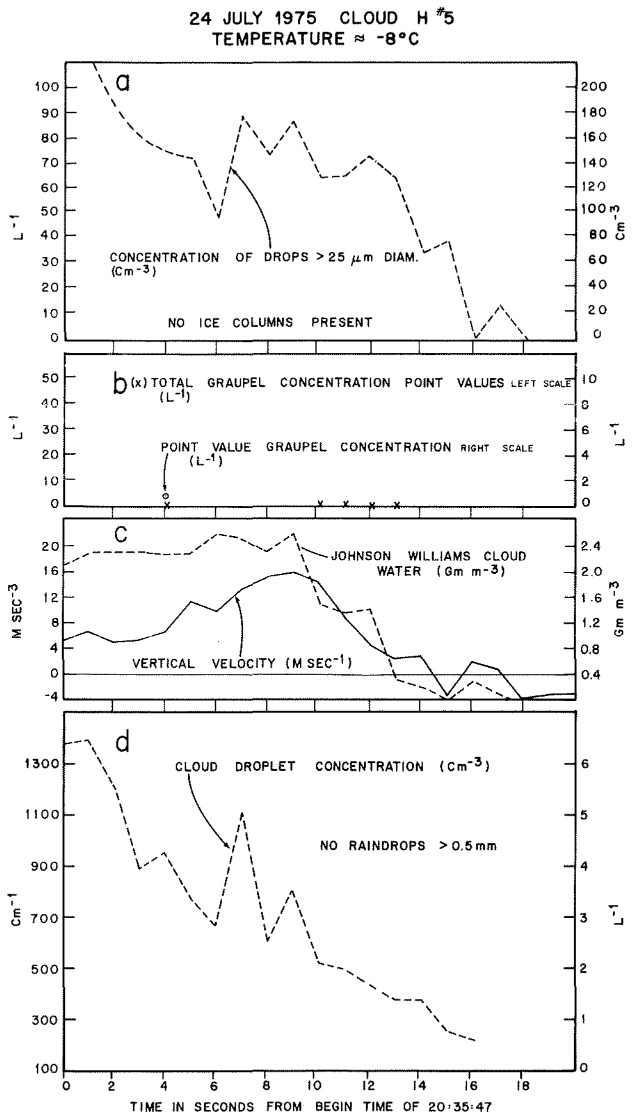

500 m

Fig. 6. Penetration of a new tower growing through the debris of Fig. 3 some 10 minutes later. Graupel particles have been reincorporated into the growing cloud.

Fig. 7. Penetration of a vigorous growing tower from the flank of an extensive older cloud mass which shows a very low graupel concentration.

(iii) Clouds must penetrate to a temperature of -8°C or lower to permit columns to thicken for a finite collection efficiency and subsequent transport to lower levels in updraft weak regions and so initiate a further stage of secondary ice production.

6. REFERENCES

Hallett, J., R.W. Hanaway and P.B. Wagner, 1972: Design & Construction of a New Cloud Particle Replicator for Use on a Pressurized Aircraft. Air Force Cambridge Research Laboratory, Report AFCRL 72-0410.

Hallett, J., and S.C. Mossop, 1974a: Production of secondary ice particles during the riming process. Nature, 249, 26-28.

Hallett, J., and S.C. Mossop, 1974b: Secondary ice particle production during the riming process. Preprints Conf. on Cloud Physics, Tucson, American Meteorological Society, Boston, 165-168.

Mossop, S.C., R.E. Cottis and B.M. Bartlett, 1972: Ice crystal concentrations in cumulus and stratocumulus clouds. Quart. J. Roy. Meteor. Soc., 98, 105-123.

Mossop, S.C., and J. Hallett, 1974: Ice crystal concentration in cumulus clouds: influence of the drop spectrum. Science, 186, 632-634.

Mossop, S.C., 1976: Production of secondary ice particles during the growth of graupel by riming. Quart. J. Roy. Meteor. Soc., 102, 45-57.

Ono, A., 1969: The shape and riming properties of ice crystals in natural clouds. J. Atmos. Sci., 26, 138-147.

Ono, A., 1970: Growth mode of ice crystals in natural clouds. J. Atmos. Sci., 27, 649-658.

Ryan, B.F., E.R. Wishart and E.W. Holroyd, 1974: The densities and growth rates of ice crystals between -5C and -9C. J. Atmos. Sci., 31, 2136-2141.

Woodley, W.L., and R.I. Sax, 1976: The Florida Area Cumulus Experiment: Rationale, Design, Procedures, Results, and Future Course. NOAA Technical Report ERL 354-WMPO 6.

Zikmunda, J., and G. Vali, 1972: Fall patterns and fall velocities of rimed ice crystals. J. Atmos. Sci., 29, 1334-1347.

7. ACKNOWLEDGEMENTS

A.R.S.M., participated through the award of W.M.O. fellowship.

J.H., D.L., were supported by a grant from the Atmospheric Sciences Section, National Science Foundation, Washington, D.C.

We wish to express our appreciation of the staff of NOAA Research Flight Facility in their efforts which contributed to this investigation.

3.2.4

THE ICE PHASE IN CLOUDS

P. Goldsmith, J. Gloster, C. Hume

Meteorological Office, Bracknell,
Berks. UK.

1. INTRODUCTION

In this paper we report two sets of experimental results pertinent to the ice crystal budget in clouds. In one we are dealing with the actual measurement of the concentration of freezing nuclei and in the other on factors which may lead to a multiplication of ice particles when supercooled droplets freeze on riming.

2. FREEZING NUCLEI MEASUREMENTS

One of the most convenient methods of measuring the concentration of freezing nuclei is by means of the membrane filter method in which a known volume of air is filtered by means of a suitable absolute filter and the freezing nuclei are subsequently detected on the filter surface by subjecting that surface (and the particles captured on it) to conditions of temperature and supersaturation appropriate to the atmosphere. Ice crystals grow around the active nuclei which can then easily be counted.

Various modifications of this technique have been developed at different laboratories but all follow this general principle but detail of temperature and supersaturation control differ from laboratory to laboratory. In this work basically the method of Stevenson (1968) is adopted.

One of the difficulties with the membrane filter method is the so-called volume effect in which differing concentrations are obtained when different volumes of air are sampled. This has been overcome in the past in a number of ways, for instance Stevenson (1968) found that by obtaining better thermal contact between the filter and the cooling surface by means of impregnating the back of the filter with vaseline the volume effect was reduced or obviated. Gravenhorst et al (1975) realising that a major cause of the volume effect in polluted air was competition for the available water in the development apparatus between freezing nuclei and hygroscopic particles on the filter reduced the influence of this competition by developing at lower pressures. Gagin and Aroyo (1969) recognising the volume effect as common applies an empirical correction to bring their results to a standard volume. However, all these and other workers in general operated by sampling something between 50 and 200 litres of air on each filter. In the work described here, series of measurements were made at much lower volumes and evidence was found that the volume effect could extend down to volumes of as little as 200 ml. In Figure 1, is shown a typical example of this effect. The concentration of freezing nuclei is shown as a function of volume sampled between 200 ml and 200 litres. The results are normalised to the concentration at 100 litres (where the concentration was measured at 2.2 nuclei/litre). It is seen that concentration when measured at low volumes is nearly 40 times greater than that when the volume sampled is 100 litres. Clearly if this result is common then it would appear that the membrane method is capable of considerably underestimating the concentration of natural ice and freezing nuclei when operated with the standard 100 litre sample.

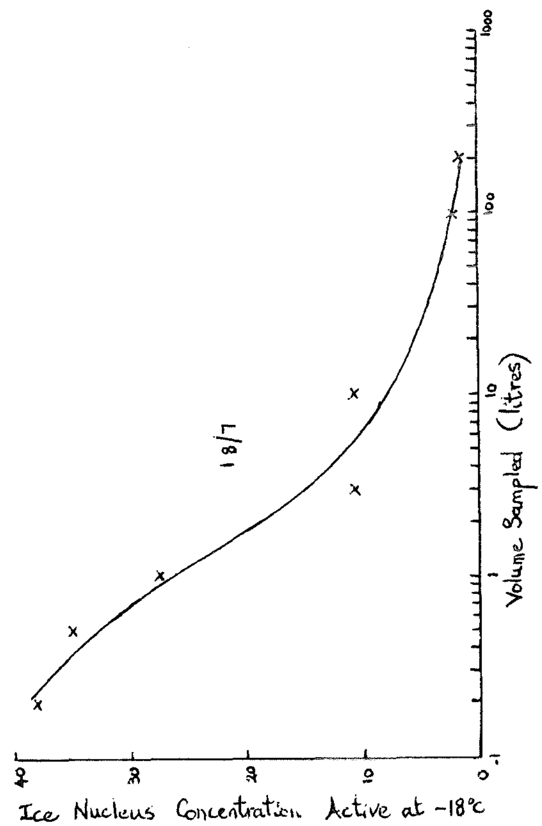

Fig. 1 Apparent ice nucleus concentration as a function of the volume of air sampled on 18.7.75

Some 23 studies, similar to that giving the results of figure 1, in which simultaneous samples were taken at a series of volumes have been carried out. It already having been confirmed that the sampled concentration was not a function of the volume flow rate through the filter. Of these 23 experiments 14 showed a significant amplification over the concentration as measured at 100 litres whilst the other 9 samples, although generally showing an increase, gave results within about a factor of 2.

The results are summarised in Table I in which the date, concentration at 100 litres, the concentration relative to that at 100 litres measured at 10 litres and 1 litre together with the maximum relative concentration (or amplification factor) measured on each experiment are listed of those 14 experiments giving a markedly positive effect.

TABLE I

Relative concentration of freezing nuclei at a number of sampled volumes.

Date	Concentration at 100 litres	Concentration 10L/100L	1L/100L	Ratio MAX
18-4-75	1.0	1.7	12	12.0
25-4-75	4.5	-	9.6	9.6
30-5-75	2.0	5.0	23.5	47.0
3-6-75	3.3	10.6	27.3	106.0
6-6-75	2.5	3.6	20.0	80.0
12-6-75	5.5	-	7.3	80.0
18-6-75	5.4	2.7	-	3.0
2-7-75	3.2	1.9	-	12.0
10-7-75	1.0	3.8	8.0	10.0
14-7-75	4.4	-	-	6.0
18-7-75	2.2	5.0	12.3	38.0
22-7-75	1.1	4.7	-	6.0
25-7-75	0.7	-	14.3	14.3
12-11-75	0.6	3.3	-	9.0

In Table II are listed the dates and concentrations at 100 litres of those experiments giving a minimal or no volume effect.

TABLE II

Concentration of nuclei on these days with a minimal volume effect.

Date	Concentration at 100 litres
12-6-75	5.6
25-6-75	1.1
30-6-75	3.6
8-7-75	5.0
11-7-75	8.7
16-7-75	1.4
17-7-75	1.3
21-7-75	1.0
29-10-75	0.5

It is immediately apparent that the presence or other-wise of a decreasing volume effect is not dependent on the concentration measured at 100 litres and that the amplification factor is rather variable but measurements indicating a factor of eighty or over have been made on a number of occasions. However, it is quite possible that the maximum amplification on virtually all occasions was not observed, since the limitation of measurement is decided by the background count of ice crystals grown on a filter without having had any air passed through it. This background is variable from filter to filter in the same box from the manufacturer and the general procedure is to measure the background on a number of filters from the same box as that used in the experiment and if the variation in this background count is comparable with the number of ice nuclei expected on the sample then that sample cannot be regarded as significant. This limits how low a volume of air can be sampled with any degree of confidence.

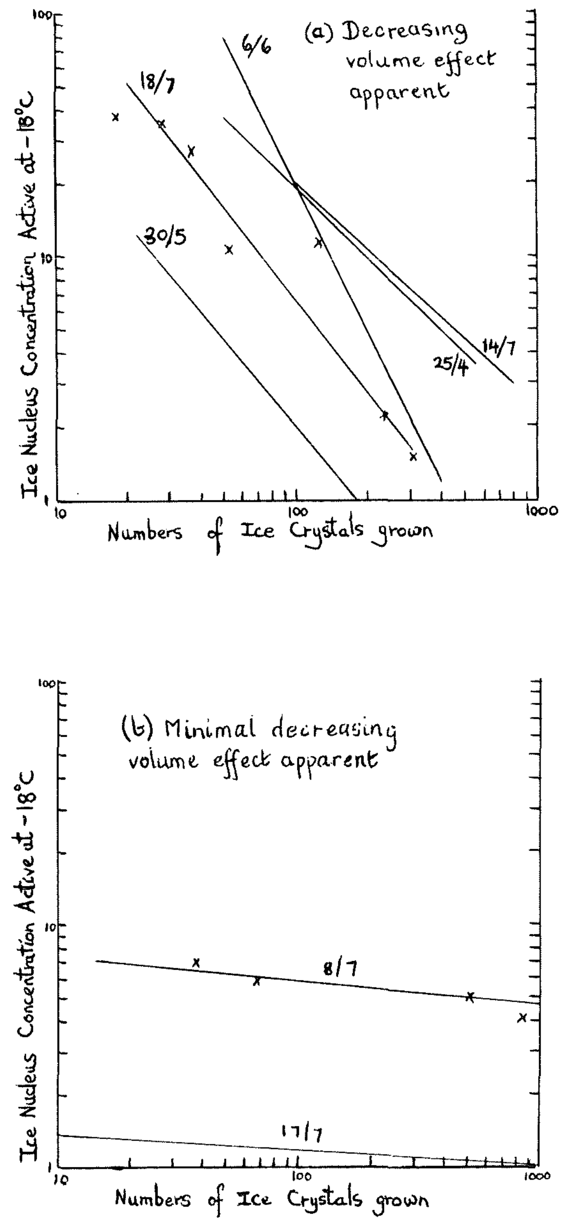

Fig. 2 Ice nucleus concentration as a function of the number of ice crystals grown on the filter.

Clearly a combination of low background, low background variability and high freezing nucleus concentration is the ideal for stretching the sampling procedures to the lowest possible volumes. Generally speaking it was only occasionally that we were able to obtain significant samples at volumes lower than about 500 ml. In figure 2(a) typical results are plotted on a log/log presentation of the apparent ice nucleus concentration as a function of the total number of ice crystals grown on each filter. The crosses refer to the actual points measured on 18.7.75, the other four lines represent the best fit to a similar array of points. The date in 1975 of each experiment is given by the side of each line.

It might be argued that there is an optimum number of ice crystals that can be grown on any filter and that any attempt to grow more than this optimum number is limited because of competition. If this were so then it should be apparent from a graph such as that of Fig. 2a where one would expect the true ice nucleus concentration to be measured when the total number of ice crystals grown is below this optimum. There is little evidence for this in fig. 2(a) because if there is such an optimum number it must be at about 20/30 crystals, which generally is within the range of uncertainty dictated by the background counts. However, if this argument is true then it means that the maximum amplification of concentration over that at 100 litres was generally not reached with perhaps the data obtained on 18/7 and 30/5 being the exceptions. Further work on this point is being done.

For completeness in fig. 2(b) are shown two examples from these experiments showing a minimal volume effect. It is seen that each ice nucleus concentration although showing a typical upward trend is always within a factor of two of the mean value. The factors leading to this marked difference is the characteristics of ice nuclei as measured by the membrane filter method from day to day continue to be studied. But all the main features of the results shown here do not appear to be dependent upon detail of the filter development. Much improved temperature and supersaturation control have yielded similar results just as a change from vaseline backed filters to an oil based system has not changed the basic findings.

In summary then, experimental evidence is given in this paper which suggests that there are occasions when the conventional membrane filter method of measuring the concentration of ice freezing nuclei apparently considerably underestimates the true concentration by well over an order of magnitude.

3. Ice crystal multiplication on riming

Considerable attention has been directed recently on the laboratory results of Hallett and Mossop (1974) and Mossop (1976) which show that there is an ice multiplication process when a moving target gathers rime in a supercooled cloud at a temperature of around -5°C. They also show that the rate of production of ice splinters is dependent upon the size of the cloud droplets and in particular on the rate of accretion of drops $\geqslant$ 24 um diameter. These results have been used to help understand why some continental cumuli, containing mainly small droplets, have a low ice crystal concentration whilst more maritime cumuli containing significant numbers of larger droplets have higher natural ice crystal concentrations.

In the work described here we repeat the work of Hallett and Mossop using a very similar apparatus in which two rods, 30 cm long are rotated in a supercooled cloud at a speed of about 2 ms^{-1}. The droplet size spectra of the clouds are measured by a Knollenberg Axial Scattering Probe modified in the way described by Ryder (1976)

In figure 3 are shown the results of a typical run in a cloud with liquid water content of about 1.5 gm^{-3} as measured by an absolute device. The production rate of secondary ice crystals is seen to peak at a temperature of about -5°C in confirmation of the Hallett and Mossop results.

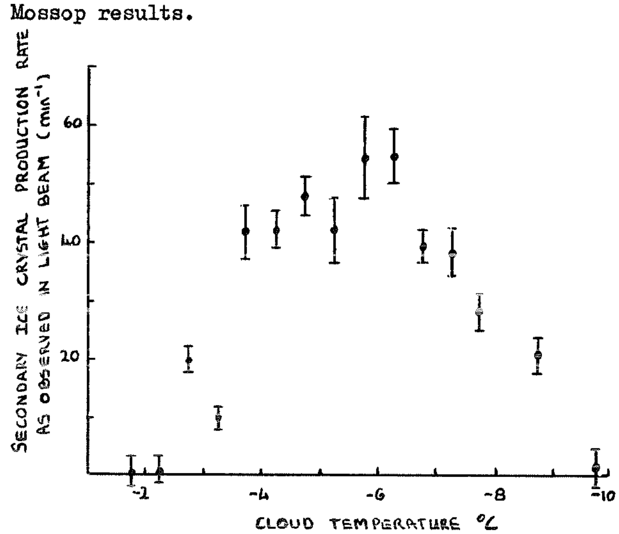

Fig. 3 Dependence of ice splinter production on temperature.

NUMBER OF LARGE DROPLETS ACCRETED PER ICE SPLINTER

	Rod Diameter	
	2 mm	10 mm
	98	216
	58	165
	115	114
	87	133
	56	50
	78	61
		146
		109
MEAN	82	124
STD DEVN	10	21

TABLE III

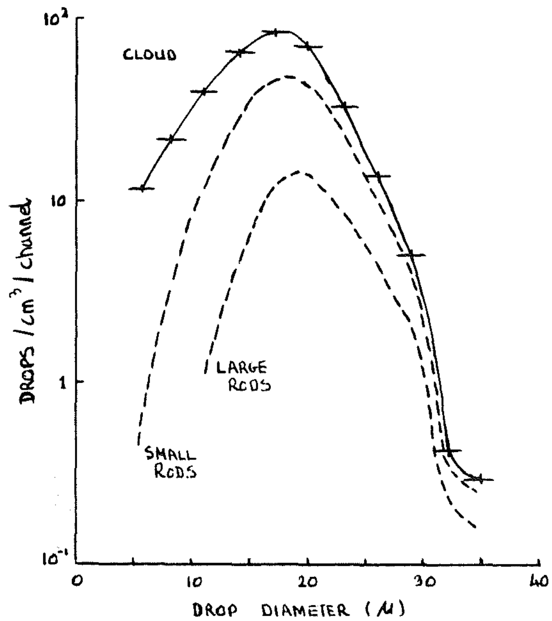

Fig. 4 Typical spectra of cloud and accreted droplets.

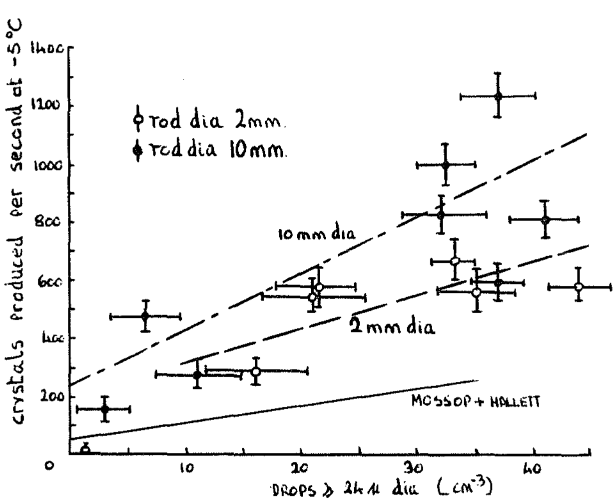

Fig. 5 Dependence of ice splinter production on concentration of large cloud droplets.

However, when considering the effect of the spectra of the supercooled cloud droplets it is the spectra of the accreted droplets that is important. In particular it may be the strength of the structure of the rime, as dictated by the relative number of large and small droplets accreted, which decides the probability of mechanical breakage leading to ice splinters.

We therefore devised an experiment to vary the large to small accreted droplet ratio without changing the cloud spectra itself. This was achieved by comparing results with riming rods of different diameters. Since the collection efficiency is a function of this diameter and the diameter of the cloud droplets it is possible to modify the accreted droplet spectra quite significantly in this way.

In fig. 4 this effect is demonstrated. A cloud droplet spectra typical of these experiments is shown together with the calculated accreted droplet spectra for rods of diameter 2 mm and 10 mm respectively using the Langmuir collection efficiencies for a cylinder. The accreted spectra must be regarded as approximate since the cylinder shape will be modified during riming.

In fig. 5, a comparison is given of the ice crystal production rate for a whole series of different cloud droplet spectra for the two different rods. The ice crystal production being given as a function of the concentration of droplets in the supercooled cloud with diameters greater than 24 um.

The results confirm those of Mossop and Hallett (1974) in that a clear dependance of secondary ice crystal production on the number of large droplets is discernable. However, the results of Mossop and Hallett, obtained with a 1.8 mm rod also plotted on fig. 3 are significantly lower than our results with a 2 mm rod. This is probably largely due to the different shape of the cloud spectra involved in the two cases.

At first sight it would appear that the 10 mm diameter rod gave a production rate significantly greater than that of the 2 mm rod, but it must be remembered that this figure shows that results plotted as a function of the droplet spectra in the cloud. If we now take into account the differing collection geometry and collection efficiencies appropriate to the two rods, then we can obtain a production rate as a function of the number of accreted drops.

This is given in Table III which lists the number of large droplets (≥ 24 um) accreted to produce one secondary ice splinter obtained in each experimental run with both 2 and 10 mm rods. The results are that for the 2 mm rod it requires 82 ± 10 large droplets to be accreted to produce each ice splinter whilst for the 10 mm rod the equivalent number is 124 ± 21. This result is not inconsistent with our thesis that the relative number of large to small accreted droplets is an important factor in determining the ice splinter production rate.

In conclusion, results are presented herein which confirm the work on Hallett and Mossop of a preferred temperature region for secondary ice particle production on riming at about $-5^{o}C$. Furthermore the results with riming rods of different diameters operated within clouds containing similar droplet spectra indicate that not only is the ice splinter production dependent upon the absolute number of large droplets accreted but also upon the relative number of large to small droplets. The more small droplets accreted for each large droplet the weaker the structure of the rimed ice and so the greater the possibility for splintering. Having said this, it should be emphasised that as yet there is no satisfactory physical explanation as to why the ice crystal multiplication on riming peaks at a temperature of about $-5^{o}C$.

REFERENCES

Gagin A, and M Aroyo (1969) J. Rech. Atmos., 4, pp. 115-122

Gravenhorst G., H W Georgii, M Grasch and D. Meyer (1975) Proc. VIII, International Conference on Nucleation. Leningrad 1973. pp. 283-286

Hallett, J. and S C Mossop (1974) Nature 249 pp. 26-28

Mossop S.C. and J Hallett (1974) Science 186, pp. 632-634

Mossop S.C. (1976) Quart. J. Roy.Met.Soc. 102, pp. 45-57

Ryder P. (1976) This conference.

Stevenson. C.M. (1968) Quart. J. Roy.Met.Soc., 94, pp. 35-43

ICE CRYSTAL MULTIPLICATION BY CRYSTAL FRACTURE

Larry Vardiman

Bureau of Reclamation
Denver, Colorado

1. INTRODUCTION

Evidence has accumulated over the last twenty years that in some clouds the concentration of ice crystals may be a factor of four or five orders of magnitude greater than the concentration of observed ice nuclei apparently available to the cloud. One of the earliest and most persistently proposed mechanisms to explain this disparity has been the mechanical fracturing of fragile ice crystals (Findeisen, 1943; Grant, 1968; Vardiman, 1972; Hobbs and Farber, 1972). However, only very rough approximations have been used to determine if collisions between crystals can generate sufficient numbers of fragments to explain "ice multiplication."

This paper will describe the formulation of a model to predict generation rates of fragments by crystal-crystal collision, experimental data obtained to initiate the model, results of the model calculations, and applications of these results.

2. THEORY

In a cloud of particles varying in size, two basic types of collision processes are possible-random collisions and ordered collisions. Random collisions are associated with turbulent motions in the air caused by vertical and horizontal wind shear. Ordered collisions are caused by the difference in terminal fall velocity between particles. Although random collisions may be of the same order of magnitude as ordered collisions in turbulent clouds, only ordered collisions have been treated in this study due to the inability to formulate random collisions in an analytic manner.

The formulation of the generation rate of secondary particles requires knowledge of the collision frequency among crystals and the number of fragments generated per collision. The collision frequency has been treated in a manner similar to Austin and Kraus (1968) and is given by;

$$F_{ijkl} = EC_{ij}C_{kl}A_{ijkl}|v_{ij}-v_{kl}| \qquad (1)$$

where F_{ijkl} is the collision frequency between crystal types i and k of sizes j and l, E is the collision efficiency, A_{ijkl} is the collision cross section between the crystals, and $|v_{ij}-v_{kl}|$ is the relative fall velocity. The number of fragments generated in a given collision has been found experimentally to be a function of the change in momentum produced in a collision between two crystals. The term "fragment generation function" is used to describe this factor. Each crystal type was found to possess a different fragment generation function depending primarily on the degree of rime. The functions for five different crystal types and degree of rime are shown in Figure 1. They were determined by assuming similarity between collisions of crystals falling onto a fixed plate and collisions between crystals in a cloud. Details of the similarity assumptions will be discussed in section 3.

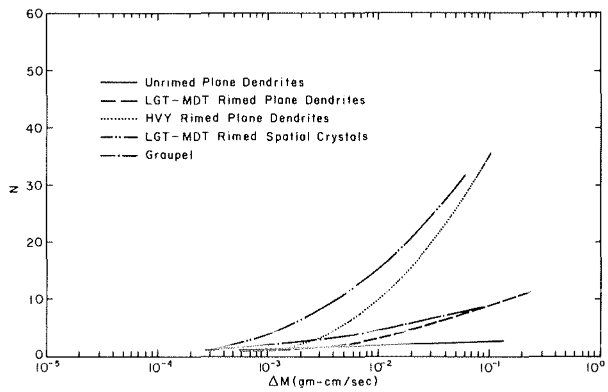

Figure 1. Fragment generation functions for five crystal types. N is the number of fragments generated per collision as a function of the change in momentum, ΔM.

Once the collision frequency and fragment generation functions have been determined the total fragment generation rate may be computed as follows. The fragment generation rate between two crystals is;

$$(dC/dt)_{ijkl} = C_{ij}C_{kl}A_{ijkl}|v_{ij}-v_{kl}|N_{ijkl} \qquad (2)$$

where C is the total crystal concentration, E has been assumed equal to 1 and N_{ijkl} is the fragment generation function for the collision between crystal types i and k of sizes j and l. The total fragment generation rate for crystal type i and size j is;

$$(dC/dt)_{ij} = \sum_{k}\sum_{l} C_{ij}C_{kl}A_{ijkl}|v_{ij}-v_{kl}|N_{ijkl} \qquad (3)$$

The total fragment generation rate for all types and sizes in a cloud is;

$$dC/dt = \sum_{i}\sum_{j}\sum_{k}\sum_{l} C_{ij}C_{kl}A_{ijkl}|v_{ij}-v_{kl}|N_{ijkl} \qquad (4)$$

Now, if a size distribution for each crystal type is defined as follows;

$$P_{ij} = C_{ij}/\ C \quad \text{or} \quad P_{kl} = C_{kl}/\ C \qquad (5)$$

Then,

$$dC/dt = C^2 \sum_{ijkl}\sum\sum\sum P_{ij} P_{kl} A_{ijkl} |v_{ij} - v_{kl}| N_{ijkl} \quad (6)$$

The terms in the summations are functions of crystal type and size distributions only. These may change in time but are independent of C. Equation (6) may now be written;

$$dC/dt = K(t)C^2 \quad (7)$$

where K(t) is equal to the terms in the summation portion of equation (6). The general solution to this equation is;

$$C = C_o/(1 - C_o \int_0^t K(t)dt) \quad (8)$$

Equation (8) is plotted in Figure (2) and shows several possible ways K(t) may vary. The decision whether mechanical fracturing of fragile crystals by crystal-crystal collision is sufficiently great to contribute to ice multiplication must be made by evaluating the magnitude of K(t) and its variation with time.

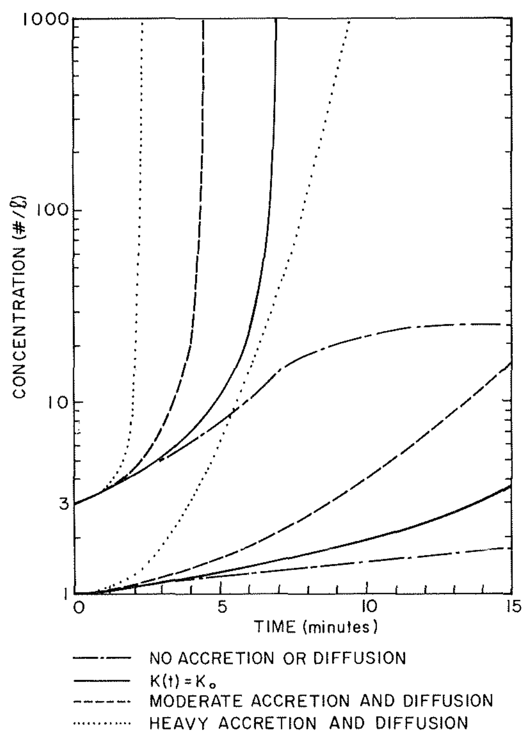

Figure 2. The change in crystal concentration as a function of time.

3. EXPERIMENTAL DATA AND PROCEDURES

The fragment generation functions for five crystal types were determined by the observation of ice crystals colliding with a fixed plate. The number of fragments generated was measured as a function of the change in the vertical component of the particle's momentum. A 16-mm high-speed camera with a resolution to 50 microns was used to observe the collisions. Fragment generation functions were obtained for unrimed, moderately rimed, and heavily rimed plane dendrites; lightly rimed spatial crystals; and graupel. Several interesting facts were discovered from this experiment.

The greater the degree of rime on plane dendrites, the greater the fragmentation.

Lightly rimed spatial crystals are the most effective crystals studied for generating fragments at a given change in momentum.

Graupel are surprisingly ineffective in generating fragments. Since many graupel appear to originate on spatial crystals, the comparison between the results for graupel and spatial crystals is striking. It would appear that rime causes a crystal to become more fragile until the rime begins to fill-in the spaces of a crystal sufficiently that a "cementing" effect becomes predominant. At this point, the crystal appears to become stronger again and only weakly bonded surface rime may break off, rather than fracturing of the internal structure.

Unrimed plane dendrites, which have been proposed for so many years as a possible source of secondary ice crystals, are dramatically ineffective in generating fragments.

The similarity between the collision of a crystal with a fixed plate and a collision between crystals in a cloud may at first appear slight. However, the number of fragments was determined as a function of the change in momentum. Therefore, the apparent difference in the magnitude of the change in momentum may be treated mathematically for the case of the crystal collisions in clouds. The remaining differences involve the collision orientation, shape effects, and the coefficient of restitution. Collision orientation differences appeared to be minor and the coefficient or restitution was approximated by a special treatment of the graupel data. Shape effects were not taken into account but appeared to be important only in the case of spatial crystals. This may be part of the reason why spatial crystals fragmented so easily.

4. NUMERICAL MODELING

A numerical model was constructed based on equation (6). The fragment generation functions for the five crystal types were obtained in analytic form. The fall velocities for unrimed plane dendrites were modeled after Brown (1970) and for graupel after Zikmunda and Vali (1972). No standard fall velocity equations are available for moderately rimed and heavily rimed plane dendrites and lightly rimed spatial crystals. Therefore, a least-squares approximation to the terminal velocities observed in association with the determination of the fragment generation functions was used. The collision cross sections were approximated by the area of a disc whose diameter is equal to the sum of the diameter of the two colliding particles.

Several size distributions from very narrow to very broad with modes at small sizes and large sizes were used. K(t) is independent of C and can be treated separately in an analytic manner. The value of C strongly determines the critical magnitude of K(t) for significant secondary particle generation.

The model describes a situation where an initial distribution of particles begins to collide and fragments are produced which reduce the concentration of large particles and increase the concentration of small particles. The expected result is for K(t) to approach zero from an initial positive value. Numerical integration in time determines the rate of change in K(t) and thereby the rate of change in C.

The model was found to be stable but did require small time steps for large initial crystal concentrations when K(t) was large. This was due to the dependence of the collision frequency on C^2. If the time step is too large, the change in K(t) is not sufficient to restrict the change in C.

5. RESULTS

The most critical parameters in this study were found to be the relative velocity between crystals and the degree of rime. If the relative velocity for all crystal sizes is increased by 10% the rate of fragment generation increases by 50%. This is true because an increase in relative velocity affects both the collision frequency and the fragment generation function. The effect on the collision frequency is straightforward in equation (1). The effect on the fragment generation function is to increase the change in momentum which produces a nonlinear change in the number of fragments generated.

The crystal combination which has the greatest relative velocity between crystals is graupel and unrimed plane dendrites. However, neither graupel nor unrimed plane dendrites generate a large number of fragments, so a greater effect was found between graupel and rimed crystals. The greatest rate of secondary particle generation was found between heavily rimed plane dendrites and graupel although there was little difference from that between moderately rimed plane dendrites and graupel or lightly rimed spatial crystals and graupel. Apparently, the reduction in relative velocity is more than compensated for by the ability of rimed crystals to produce fragments.

The magnitude of ice multiplication due to the generation of secondary particles is less than a factor of ten for every possible combination of crystal types and size distributions without accretion and diffusion. The broader the distribution of either or both crystal types colliding in a cloud, the greater the rate of fragmentation. This is apparently an effect of shifting a greater concentration of crystals to larger sizes by a broader distribution. The larger the crystals, the greater the relative velocities and the greater the ability to produce fragments. Ice multiplication becomes less for smaller and narrower size distributions and lighter rimed crystals. The generation of secondary particles is effectively zero unless graupel or heavily rimed particles are present.

When accretion and diffusion are allowed to occur during fragmentation the concentration of crystals continues to increase as a function of the rate of accretion and diffusion and the ice multiplication can become greater than a factor of ten.

The following results summarize the main findings of the numerical study:

The magnitude of K required to generate secondary particles appears to be insufficient to generate more than a ten-fold increase in crystal concentration in most stratiform clouds.

Convective clouds may have K's large enough to generate many more secondary particles due to larger crystals and high rates of accretion and diffusion.

Continued accretion and diffusion are required to obtain ice multiplication ratios greater than ten.

Initial crystal concentrations greater than 1/liter are required to generate significant numbers of fragments in short periods of time (less than 10 minutes).

6. DISCUSSION OF RESULTS

The results of this study were somewhat different than had been expected. The presence of fragments and numerous irregular crystals beneath convective cells (Vardiman, 1972) led to the belief that mechanical fracturing of unrimed dendrites would explain part of the observed excess in ice crystal concentrations. It was also thought that this process might possibly be general enough to explain high crystal concentrations observed in many other cloud conditions. The findings from the model, based on experimentally derived fragment generation functions, eliminate further consideration of unrimed crystals as a source of more than minor numbers of in-cloud fragments. The model does predict, however, that under certain cloud conditions, significant fragmentation can occur - namely when relatively large concentrations of rimed crystals are present. Since relatively large concentrations of rimed crystals are required before secondary particle generation can proceed, this mechanism cannot explain the occurrence of excess crystal concentrations at warm temperatures, as observed by Mossop. Even though mechanical fracturing of rimed crystals by crystal-crystal collision cannot explain ice multiplication in general, it may still be important in certain cloud situations.

The following cloud types exemplify the possible contribution mechanical fracturing can play in crystal concentration:

6.1 Stratiform Clouds

Changes in crystal concentration for natural stratiform clouds due to mechanical fracturing appear to be limited to less than a factor of 10. A stratiform cloud is probably highly self-limiting in the process. If the cloud top is not sufficiently cold to generate enough crystals from natural ice nuclei and utilize all of the condensate, the crystals will become rimed and begin to generate secondary particles by mechanical fracturing. Since the growth time is limited in the slow updraft of a normally shallow stratiform cloud, the generation of secondary particles should reach peak efficiency only near the base, and only a small fraction of the cloud will be affected by this mechanism.

6.2 Isolated Convective Clouds

Convective clouds contain several features which would at first appear to make them very efficient in generating secondary particles by mechanical fracturing compared to stratiform clouds. The turbulence in a convective cloud should increase the collision frequency over that of a stratiform cloud and the collisions should be more forceful. Convective clouds normally have higher liquid water contents which allow accretion and diffusion to proceed at an accelerated pace. Crystal sizes are normally larger and many convective cells contain large graupel.

On the other hand, the updraft is sufficiently strong so that crystals do not reside in a favored growth region very long unless they are falling at the same speed as the updraft. In addition, most of the fragments are probably blown out the top and sides of a convective cloud and sublimate before being reincorporated into the cloud. The results of this study on secondary particle generation should be put into a convective cloud model before definite conclusions can be drawn, but the characteristic features of an isolated convective cloud seem to indicate that the generation of secondary particles by mechanical fracturing has little effect on the main portion of the cloud.

6.3 Embedded Convective Clouds

Embedded convective clouds should contain the same favorable features for secondary particle generation that isolated convective cells contain, but should also be able to retain the fragments before sublimation in the surrounding environment. Fragments generated near the sides and top of an embedded convective cell will be continually mixed into the surrounding stratiform deck or into new cells. As the fragments grow, rime, and generate new fragments in turn, the background concentration of ice crystals in the cloud will rise above that expected from natural ice nuclei. As the concentration increases, the collision frequency increases. When a relatively high crystal concentration is reached the reduced liquid water content of the cloud limits further mechanical fracturing. Crystal concentrations could reach 100 to 1,000 times that expected from natural nuclei.

7. CONCLUSIONS

The multiplication of ice crystals by mechanical fracturing of fragile crystals during collisions with other crystals has been shown to be important only in rather specialized conditions. This mechanism cannot explain high concentrations of crystals at warm cloud temperatures. However, multiplication of crystals may still occur as follows:

7.1 Smooth stratiform clouds should be moderately affected by mechanical fracturing near cloud base if riming is present. Increases in crystal concentration appear to be limited to less than a factor of ten unless recirculation of the fragments to higher levels of the cloud can occur.

7.2 Isolated convective cells should not be strongly affected by mechanical fracturing because the fragments would be generated near the top of the cloud and would probably be evaporated at the top or edges without being reincorporated into the cloud circulation.

7.3 Convective cells embedded in a stratiform layer appear to provide the greatest opportunity for secondary particle generation by mechanical fracturing. The fragments would be generated at or near the top of a convective cell which could then be recirculated in the cell or dispersed out into the surrounding stratiform deck. By continued riming, fragmentation, and recirculation the crystal concentration could reach 100 to 1,000 times the natural concentration.

8. ACKNOWLEDGEMENTS

This research was sponsored by the Atmospheric Sciences Section, National Science Foundation, under Grant GI-31460 and the State of Colorado, Weather Modification Research Funds.

9. REFERENCES

Austin, P. M. and M. J. Kraus, 1968: Snowflake Aggregation-A Numerical Model, Proceed. of the International Conf. on Cloud Physics, Toronto, 300.

Brown, S. R., 1970: Terminal Velocities of Ice Crystals, Atmospheric Science Paper No. 170, Colorado State University, Ft. Collins.

Findeisen, W., 1943: Untersuchungen uber die Eissplitterbildung an Reifschichten, Meteorologische Zeitschrift, 5, 145.

Grant, L. O., 1968: The Role of Ice Nuclei in the Formation of Precipitation, Proceed. of the International Conf. on Cloud Physics, Toronto, 305.

Hobbs, P. V. and R. J. Farber, 1972: Fragmentation of Ice Particles in Clouds, H. Dessens Memorial Vol., J. Atmos. Rech., 6, 245.

Vardiman, L., 1972: A Case Study of Ice Crystal Multiplication by Mechanical Fracturing, Proceed. of the International Cloud Physics Conf., London, 22.

Zikmunda, J. and G. Vali, 1972: Fall Patterns and Fall Velocities of Rimed Ice Crystals, J. Atmos. Sci., 29, 1334.

3.2.6

ICE PARTICLE MULTIPLICATION BY RIMING IN CUMULUS CLOUDS

R.F. Chisnell and J. Latham

Department of Mathematics
University of Manchester
England

Department of Physics
University of Manchester
Institute of Science and Technology
England

April 1976

1. INTRODUCTION

There now exists a substantial body of evidence showing that the concentration of ice particles in some fairly shallow supercooled clouds can be a factor, f, of up to 10^4 times the measured concentration of ice nuclei effective at the cloud top temperature. Particularly detailed field investigations have been reported recently by Mossop, Ruskin and Heffernan (1968), Mossop, Ono and Wishart (1970) and Mossop, Cottis and Barlett (1972). The time available to produce these high concentrations is in the region of 50 minutes.

In these clouds the measured values of the concentration of small ice particles were typically in the range 10 to 100 ℓ^{-1}. Such clouds were generally found to contain large supercooled drops and rimed ice particles each usually in concentrations of 0.1 to 1 ℓ^{-1}.

In this article we discuss a stochastic model of ice particle multiplication, in which supercooled drops and rimed ice particles can both play a central role. Splinters are produced by riming, a process shown by Hallett and Mossop (1974) and Mossop and Hallett (1974) to be very efficient under certain conditions. Although a splinter will eventually grow into a rimer if it is not captured by a supercooled drop, drop capture enables splinter production by the riming process to start at once. By introducing the dimensions of the cloud and simplified models of the airflow, account is taken of the growth and finite lifetimes of the rimers formed within it and hence no unrealistically large ice particles occur in the model.

2. THE PHYSICAL MODEL

In this section we outline the chain of processes starting with one small ice particle, by which multiplication occurs within a model cloud of dimensions and microphysical properties based on the observations of Mossop et al (1972).

The cloud has a supercooled depth Z = 1.2km, a summit temperature $T_s = -10^{\circ}C$, and a cloud droplet water concentration C = 1.0g m^{-3}. An important feature is the assumed presence of a significant concentration of supercooled rain-drops. Their diameter, d, generally ranges from 60μm to 1mm. The lower diameter of 60μm marks the boundary between the cloud droplets and rain-drops. The droplets have negligible fall velocities and may be swept out by the much larger falling rimed particles. By contrast the rain-drops, particularly the larger ones, have significant fall velocities in comparison with the ice splinters which may have been formed in the riming process. When such a collision occurs it is assumed that the drop freezes immediately, thereby becoming an ice particle of mass equal to that of the drop; the splinter remains embedded within the frozen drop. We have divided the drops into two categories, 'small drops' with 60μm < d < 250μm, and 'large drops' having d > 250μm. A distribution of sizes of large drops is utilized in order to take account of the observations of Mossop et al (1972). In most calculations these drops are confined within the diameter range 0.5 to 1mm. In this paper the results presented relate to a 'top-hat' distribution of water drops, in which all drop size intervals make uniform contributions to the volume sweepout rate. The concentrations of water particles of all types are constant in space and time.

We now consider the possible life histories of an ice splinter and the assumed process of secondary ice particle production. The splinter may have been formed by the activation of an ice nucleus or by the riming process. There are four possible stages in the development of this ice particle.

Stage 1 The particle is small and grows principally by vapour diffusion. This type 1 particle is termed a 'small splinter'. If it avoids capture by raindrops it grows for a time T_1 before achieving a mass W_1 and entering the second stage. In all calculations of ice particle growth made in this paper considerable use is made of the detailed computations of Koeing (1972). W_1 is chosen to be 2μg, which is the typical mass of a small raindrop; inspection of Koenig's growth curves for a mean temperature of $-5^{\circ}C$ and a cloud-water concentration of 1g m^{-3} shows that $T_1 \approx 8$ minutes. If, however, the ice splinter collides with a supercooled raindrop before the time T_1 has expired, the raindrop will freeze and capture the splinter. If the collision is with a small raindrop the resultant particle enters Stage 2 immediately. If the collision is with a large raindrop the resultant frozen drop enters Stage 4 directly. The small splinter is assumed to have a negligible fall velocity compared with all water drops, so that the probability of it being captured in an elementary time interval is given by the proportion of volume swept out by the drops in that time. We denote the proportional volume sweepout rate by λ. The separate contributions to λ from small and large drops are denoted by λ_1 and λ_2 respectively, with $\lambda = \lambda_1+\lambda_2$.

Stage 2 The particle has an initial mass W_1, having been formed either by continuous growth of a small splinter, or by the freezing of a small raindrop. This type 2 particle is termed a 'large splinter'. It may grow by diffusion and accretion for a time T_2 before it achieves a mass W_g(0.1mg) and enters Stage 3. Koenig's work shows that $T_2 \approx 4.8$ minutes. The amount of rime deposited on the large splinter during its lifetime is so small that the possibility of associated splinter production can be neglected. Since its fall velocity will be comparable with that of a small raindrop we assume that collisions between such particles will not occur. However, collision between the large splinter and a large raindrop may occur at any time in the growth period T_2. This collision is considered as large raindrops have much higher fall velocities than the large splinters. By neglecting the fall velocity of large splinters in comparison with that of large water drops the probability of collision is determined by λ_2. In this event the large raindrop will freeze, and the resulting frozen drop enters Stage 4.

The last two stages of growth are alternates and are populated by rimers.

Stage 3 The particle is formed by the growth of a large splinter. This type 3 particle is called a 'growth rimer' and has an initial mass W_g = 0.1mg. Type 3 particles remain within the supercooled region of the cloud, growing exclusively by accretion for a time T_3, until they fall through the 0°C isotherm with a mass W_f and are removed from the system. For any given calculation it is assumed that all growth rimers, and also all Stage 4 particles, achieve the same final mass W_f. Values of W_f ranging from 1.0 to 15.7mg have been employed in the calculations. Koenig's growth curves have been used to estimate the rate of growth of these particles. The number of splinters ejected by a rimer is governed by M_p, the number of splinters ejected per unit mass of accreted rime. Since $W_f >> W_g$ the number ejected is approximately M_pW_f.

Stage 4 This stage is populated by 'capture rimers'. It is entered by a small or large splinter being captured by a large drop; its initial mass w is that of the drop. Since a range of values of w is considered there is a range of values of growth time $T_4(w)$ before the final mass W_f is achieved. The growth and splintering behaviour of these type 4 particles is assumed to be identical to that of the growth rimers.

3. MATHEMATICAL TREATMENT

The ice particle multiplication has been treated as a stochastic process. Generating functions have been formulated for the probabilities of particular numbers of the various categories of ice particle existing at a general time t, as a consequence of one initial ice particle. The formulation is in terms of (i) the probabilities of collision between ice splinters and small and large water drops, described by λ_1 and λ_2 respectively (ii) the splintering number M_p, the number of splinters ejected by a rimer per unit mass of accreted rime. These generating functions lead to a set of renewal equations for the estimated mean numbers of ice particles at time t. The Laplace transforms of the renewal equations have been studied and show that a simple large time analysis gives a good description of the growth mechanism, except for the small time behaviour described by a marching technique. The large time analysis predicts that $A_1\exp(p_0t)$ ice particles exist at time t as a consequence of one initial small ice splinter.

The details of this mathematical treatment have been presented by Chisnell and Latham (1976). Herein we simply present some values for the important parameter p_0 for various W_f, M_p, λ_1 and λ_2. These are given in Table 1. The largest value of M_p employed, 60mg^{-1}, is based on the measurements of Hallett and Mossop averaged over the life history of a rimer within the cloud. Recently the model has been extended to take account explicitly of variations of M_p with temperature

W_f (mg)	λ_2^{-1} (min)	λ_1^{-1} (min)	M_p (mg^{-1}) 3	10	30	60
15.7	11.2	28	.32	.49	.73	.94
	21	28	.27	.41	.59	.76
	70	28	.21	.30	.42	.52
	∞	28	.18	.24	.30	.34
	∞	∞	.17	.22	.27	.31
8.6	11.2	28	.29	.48	.72	.94
	21	28	.24	.39	.58	.75
	70	28	.19	.28	.40	.51
	∞	28	.16	.23	.29	.33
	∞	∞	.14	.21	.26	.30
3.0	∞	28	.12	.19	.26	.31
	∞	∞	.11	.18	.24	.27

Table 1 Values of the growth parameter p_0(min^{-1}) for ranges of the primary parameters M_p and λ_2. Values of p_0 in the absence of drops, $\lambda_1 = 0$, $\lambda_2 = 0$ are also included.

Table 1 lists values of p_0 for various values of the three parameters M_p, λ_2 and W_f. We note that although W_f has some importance for small M_p, W_f changes have a very small effect when M_p is large, especially when λ_2 is also large. By contrast it is noted that λ_2 and M_p cause significant changes in p_0 throughout the whole of their ranges, with variations due to M_p being the more pronounced. Thus M_p emerges as the dominant parameter, with the presence of large water drops significantly enhancing the multiplication process. The role of the large water drops is to reduce the time interval between the birth of some splinters and their transition to rimers, and that of the small drops is to hasten the transition of some small splinters to large splinter status. The importance of the presence of small drops in the model is seen by comparing the last two rows of the results for each W_f section of Table 1. Removal of the small drops is achieved by putting $\lambda_1 = 0$ and is seen to be a significant effect, though of less importance than the removal of the large drops.

4. MULTIPLICATION TIMES

The calculations so far presented give the estimated number of ice particles resulting from one initial splinter. As the progeny of any ice particle exist independently of those originating from any other ice particle, the results of the previous section may be used in a cloud where many primary ice particles are formed. The experimental data relates to the multiplication factor f, the ratio of the concentrations of ice particles to ice forming nuclei effective at the cloud top temperature T_s. To derive an expression for f, we now embed the results of the previous section in a rudimentary model of the airflow within the cloud. We shall see that the form assumed for the airflow does not have a major effect upon the multiplication rate, a constant updraught and a thermal model giving similar results.

For some calculations we assume that an updraught of constant speed U passes through the cloud except in a thin layer at the summit, where the airflow becomes horizontal and the vertical speed falls to zero. For the cloud properties assumed, the values of W_f = 15.7, 8.6 and 3.0mg can be shown to correspond to U = 2.0, 1.3 and 0.5ms^{-1} respectively. In this model we assume that a concentration, n_i, of ice nuclei effective at T_s is carried to the cloud top by the updraught U. The ice nuclei are all assumed to form ice particles on arrival at the cloud top, so that the rate of formation of small splinters per unit cross-sectional area of the cloud is Un_i. If the nucleation commences at t = 0, the estimated number of resulting ice particles per unit area at time t is given as

$$N \approx U n_i A_1 e^{p_0 t}/p_0, \tag{4.1}$$

$A_1 \exp(p_0 t)$ arising from each nucleus. These particles are distributed over the height Z between the T_s and 0°C isotherm. Hence the overall cloud multiplication factor is

$$f = \frac{UA_1}{Zp_0} e^{p_0 t}. \tag{4.2}$$

The largest multiplication factor measured by Mossop et al.(1972) is about 10^4 and the time taken for f to reach this value is

$$\tau = \frac{1}{p_0} \ln\{\frac{10^4 Z p_0}{UA_1}\}. \tag{4.3}$$

This formula for τ emphasizes that p_0 is the key growth parameter. For typical physical situations $(Zp_0)/(UA_1)$ is of order 1 and

$$\tau \approx \frac{1}{p_0} \ln 10^4.$$

To achieve multiplication factors of 10^4 within 50 mins. it is concluded that p_0 must be in excess of about 0.2 min^{-1}.

Values of τ are presented in Table 2 for two different models of ice particle multiplication.

Model	λ_1^{-1} (min)	λ_2^{-1} (min)	U (m/sec)	τ(min) M_p(mg^{-1}) 3	60
A	∞	∞	0.5	103	48.2
			2	66.5	39.8
B	28	∞	2	62.0	35.5
		70		52.7	23.1
		21		41.4	16.2
		11.2		35.3	13.1

Table 2 Values of τ, the number of minutes required to achieve a multiplication factor of 10^4, for various values of λ_1, λ_2 and U. Model A relates to riming in the absence of drops and model B in their presence.

In model A no drops are present in the cloud. It is seen that for M_p = 3mg^{-1}, a value based on the experiments of Bader et al. 1974 the growth process is too slow. However, for M_p = 60mg^{-1}, a value based on the work of Hallett and Mossop, the multiplication rate is adequate for both values of U. In model B supercooled raindrops are present in the cloud. Results are shown for the standard value λ_1^{-1} = 28 min covering the cited range of λ_2 values, with an updraught of 2m sec^{-1}. A comparison with the results for Model A, reveals that the presence of the raindrops has a marked effect, the time to achieve a multiplication factor of 10^4 is significantly reduced for both values of M_p. The influence of U, or the related parameter W_f, on τ is much less pronounced.

On a 'thermal' model of the particle multiplication we assume, following Mason (1975), that the concentration of ice forming nuclei at a depth z below the cloud top is $n_i \exp(-\alpha z)$, where $\alpha = 2.9 \times 10^{-5}$cm^{-1}. The total number of ice nuclei activated during the ascent of a thermal is approximately n_i/α per unit area, as $\exp(-\alpha Z)$ is small if the cloud depth Z is a kilometre or more. Each of these activated nuclei results in $A_1\exp(p_0 t)$ ice particles at time t and the multiplication factor is $f = (\alpha Z)^{-1}\exp(p_0 t)$. Thus the multiplication time is

$$\tau = \frac{1}{p_0}\ \ell n\left(\frac{10^4\alpha Z}{A_1}\right) . \qquad (4.4)$$

Following Mason we assume that each ice particle formed by nucleation will achieve a radius of 0.1mm after 10 minutes and then begin to fall through the quiescent cloud. If Z = 1.2km, $\rho = 0.3\text{g cm}^{-3}$ and the collection efficiency is unity we estimate that the exit mass W_f of rimers formed at the top of the cloud is 1.7mg. We adopt this value of W_f for all rimers, as we believe that following the ascent of the thermal there will be a considerably reduced updraught, possibly arising from the same energy source as the thermal. This reduced updraught will carry splinters towards the cloud top. We take the same value of $T_1 + T_2 = 12.8$ min as before and estimate from the data of Koenig that $T_3 = 5.2$min. The estimated weighted average value of M_p is 60mg^{-1}. Assuming $\lambda_1 = 0 = \lambda_2$, there following $p_0 = 0.28\ \text{min}^{-1}$, $A_1 = 0.22$ and from equation (4.4) $\tau = 42.8$ minutes. This agrees well with the value of $\tau = 48.2$ minutes calculated on the constant updraught model for identical parameter values. If we permit small drops to be present within the cloud and take $1/\lambda_1 = 28$ minutes the growth parameter is increased from 0.28 to 0.33 min^{-1}.

ACKNOWLEDGMENT

We are grateful to Mr. J. Siemieniuch for writing the programme used to obtain most of these numerical results. This work was in part carried out within the research programme supported by NERC under grant GR3/2425.

REFERENCES

Bader M., Gloster J., Brownscombe J.L., & Goldsmith P,.(1974) 'The production of sub-micron ice fragements by water droplets freezing in free fall or on accretion upon an ice surface'. Quart.J.R.Met.Soc., 100, 420-426.

Chisnell R.F., & Latham J., (1976) 'Ice particle multiplication in cumulus clouds'. Quart. J.R.Met.Soc., 102, 133-156.

Hallett J., & Mossop S.C., (1974) 'Production of secondary ice particles during the riming process' Nature, 249, 26-28.

Koenig L.R., (1972) 'Parameterization of ice growth for numerical calculations of cloud dynamics' Monthly Weather Rev., 100, 417-423.

Mason B.J., (1975) 'Production of ice crystals by riming in slightly supercooled cumulus' Quart.J.R. Met.Soc., 101, 675-679.

Mossop S.C., Cottis R.E., & Barlett J.M., (1972) 'Ice crystal concentrations in cumulus and stratocumulus clouds' Quart.J.R.Met. Soc., 98, 105-123.

Mossop S.C., & Hallett J., (1974) 'Ice crystal concentration in cumulus clouds: Influence of the drop spectrum' Science.

Mossop S.C., Ono A., & Wishart E.R., (1970) 'Ice particles in maritime clouds near Tasmania' Quart.J.R.Met.Soc., 96, 487-508.

Mossop S.C., Ruskin R.E., & Heffernan K.J., (1968) 'Glaciation of a cumulus at approximately -4°C'. J. Atmos.Sci., 25, 889-899.

3.2.7

ICE PARTICLE MULTIPLICATION IN MOUNTAIN CUMULUS CLOUDS

John LeCompte and Lewis O. Grant

Department of Atmospheric Science
Colorado State University
Fort Collins, Colorado

1. INTRODUCTION

For more than a decade ice crystal concentrations larger than ice nuclei concentrations have been observed in some clouds (Koenig, 1963; Mossop, et al., 1970; Ono, 1971; Auer, et al., 1969). Many hypotheses (Koenig, 1962; Hallet and Mossop, 1974; Gagin, 1971, 1973; Henmi, 1974; Vardiman, 1974) have been proposed to explain the conditions under which secondary ice particles may be generated or ice nucleation enhanced. To date, no one hypothesis has gained general acceptance. To reach a better understanding of the microphysical processes responsible for the generation of secondary ice particles, more field documentation of actual clouds is needed to provide a better basis for evaluating the proposed multiplication hypotheses, particularly for continental cumulus clouds.

Observations of ice particle concentrations and ice nuclei concentrations were made during the 1975 South Park Area Cumulus Experiment (SPACE) in small mountain cumuli. Complementary observations show that large water drops were not present in these clouds. This paper considers the various ice multiplication and nucleation enhancing mechanisms within the framework of these observations.

2. ICE MULTIPLICATION PROCESSES

The most common microphysical trait of clouds in which ice multiplication has been observed is the presence of large water drops (Braham, 1964; Mossop, et al., 1970; Koenig, 1963; Ono, 1971). Several interpretations of how this microphysical trait generates numerous secondary ice particles have been suggested. One hypothesis is that the shattering of these drops as they freeze ejects ice splinters, hence multiplying the amount of ice seen in the cloud (Koenig, 1962). The drop initially freezes on the outside with the freezing process progressing inward. As the freezing continues, internal pressures build causing the ice shell to fracture. A uniform ice shell aides the shattering process. Studies by Dye and Hobbs (1968), and Johnson and Hallet (1968) on the freezing of drops suspended from a support produced few shatterings. However, these experiments did not simulate in cloud conditions well since the drops were supported and not in free fall. Experiments by Takahashi and Yamashita (1970) have shown drops between 75 and 175 μm diameters did shatter while freezing in free fall at -16C. The number of splinters produced was not measured.

A second hypothesis is that multiplication occurs when ice fragments are ejected as large drops become active in the riming of existing ice particles (Mossop, et al., 1970; Ono, 1971). Laboratory evidence by Hallet and Mossop (1974) supported this hypothesis. They found that under conditions where the drops were greater than 23 μm in diameter and the environmental temperature was between -3C and -8C numerous secondary ice particles were produced during the riming process. The reason for ice splinter ejection during the riming process is not clear. Recently King and Fletcher (1976) investigated the thermal shock generated during the riming process. This was found insufficient to cause the ejection of ice splinters.

There is also evidence of ice multiplication in clouds with no large drops, suggesting that other mechanisms may be important at least under some conditions. One such experiment (Auer, et al., 1969) reported three orders of magnitude more ice particles than ice nuclei in clouds with temperatures warmer than -10C. Although drop size distributions were not measured, it is unlikely that these stable cap clouds contained any large water drops. Gagin (1971, 1973) has proposed a nucleation enhancement mechanism which is not dependent on the presence of large water drops. He has shown that the ice nuclei spectrum is both temperature and supersaturation sensitive. Local transient areas of high supersaturation may activate more ice nuclei than would be expected from the measurements from ice nuclei counters operating at lower supersaturations. The result would be what appears to be ice multiplication, but is really an enhancement of ice nucleation.

Henmi (1974) proposed an ice multiplication mechanism based on laboratory evidence that rimed particles produce secondary ice particles during the evaporation of the rime. The hypothesis is dependent on the formation of low density rime on the ice particles and subsequent exposure to undersaturated regions in the cloud.

An additional ice multiplication hypothesis not dependent on the presence of large water drops is that investigated by Vardiman (1974). Numerous fragmented crystals have been observed from cumulus cells embedded in orographic clouds (Grant, 1968; Vardiman, 1972). It has been suggested that the number of ice particles may be multiplied by the collision and mechanical fracturing of rimed crystals in the cloud. The amount of multiplication is dependent upon the amount of riming and the crystal habit involved.

3. PROCEDURE

The NOAA/NCAR Explorer instrumented sailplane was flown during the 1975 South Park Area Cumulus Experiment (SPACE), from July 7 until August 8. The sailplane was towed aloft during the initial stages of cumulus development, and released near the base of a growing cumulus cloud. It then proceeded through the base of the cloud, spiralling upwards, sampling through the entire cloud depth. The advantages of using the sailplane are the lack of engine pollutants, the formation of a minimum of cloud turbulence, and the slower velocity allowing for a longer sampling time.

The sailplane simultaneously measured temperature, drop concentration, liquid water content, pressure-altitude, airspeed, sailplane rate of climb, and sailplane attitude. These were telemetered to a surface data recording station. Drop size distributions were measured with an electrostatic disdrometer (Abbot et al, 1972) mounted on the sailplane. The instrument cannot distinguish droplets below 4 μm radius and groups all drops greater than 19 μm radius into one size range. Its sampling volume is dependent upon the speed of the aircraft. At an aircraft speed of 75 m sec^{-1} it has a sampling volume of 3.75 cm^3 sec^{-1}.

The Cannon "in situ" cloud particle camera (Cannon, 1974) was used to measure ice particle concentrations in the cloud, and was used as a check for large water drops. At a magnification of 1/2 the smallest particle the camera can resolve is 16 μm in diameter. However, the film analysis system cannot detect particles below 100 μm in diameter. Both concentration and size distribution of ice particles can be determined.

While the sailplane sampled the cloud, support aircraft (the C.S.U. Aerocommander and, for a one week period, the University of Wyoming Queen Air) were in the air sampling the surrounding environment, observing the cloud, and on occasion entering it after the sailplane had exited.

Ice nuclei measurements were taken with a Mee ice nucleus counter mounted onboard the C.S.U. Aerocommander. Some filters were also exposed by the sailplane for ice nucleus measurements.

Stereo photographs of the research area were taken at one minute intervals to provide information on cloud dimensions (top, base, and sides). These measurements, along with radiosonde observations taken twice during the day, were used to verify aircraft measured cloud top and base temperatures.

4. THE OBSERVATIONS

Natural (non-seeded) clouds were penetrated on 13 days. Two clouds, one entered on July 9 and one on July 14, are discussed in this paper. These two clouds were chosen because both were within the desired temperature regime, and both posessed fairly complete data sets.

On July 9 the sailplane did not follow its usual proceedure. Rather, it entered the cloud near cloud top at a temperature of approximately -9C. For the next 13 minutes the sailplane spiralled within the cloud between temperatures of -7C and -9C. The cloud particle camera was operated during this time. The other 12 minutes were spent spiralling down through the cloud and exiting near the base, during which the cloud particle camera became inoperative. Only the portion of the flight while the cloud particle camera was in operation will be used in this study. On July 14 the sailplane did follow the normal proceedure. It spiraled up through cloud base at approximately 0C, reached a minimum incloud temperature of -1.5C, and exited back through cloud base. The cloud particle camera was operated during the entire flight.

The sounding on July 9 showed substantial moisture in the lower levels with a stable layer beginning around 5500 meters. Observations by the crew of the University of Wyoming Queen Air research aircraft substantiated parcel theory estimates of cloud tops reaching 6500-7500 meters. Bases were observed near 4000 meters. According to these observations cloud top temperatures were -10C.

Ice nuclei data measured with the Mee ice nucleus counter showed little variation with time. At -19C, 40 nuclei per liter were observed and at -15C, 1 nucleus per liter was observed. At temperatures warmer than -15C fewer nuclei per liter would be expected. If the number of nuclei per liter at warmer temperatures can be calculated by extrapolating to warmer temperatures using the equation

$$N(\Delta T) = N_o \exp(\beta \Delta T) \quad \text{(Fletcher, 1969)}$$

with values of $\beta = .8$ and $N_o = 1 \times 10^{-5}$ $liter^{-1}$, then 1×10^{-2} and 5×10^{-5} active nuclei per liter would be expected at temperatures of -9C and -2C respectively. If each nucleus is assumed to generate one ice particle, the same concentrations of ice particles would be expected in the clouds with these temperatures.

The ice particle data from the Cannon cloud particle camera for July 9 showed $1 \times 10^{-2} \pm 5 \times 10^{-3}$ particles per liter, the error being caused by possible sizing errors which will affect the sampling volume for that particle. No ice particles were observed in the July 14 cloud.

Table 1

Drop size distributions

Size Range (μm)	Droplets cm^{-3} July 9	July 14
4.0-5.5	20.60	40.68
5.5-7.0	4.89	.78
7.0-8.5	.62	.03
8.5-10.0	.05	.03
10.0-11.5	.02	.02
11.5-13.0	.02	.02
13.0-16.0	.00	.00
16.0-19.0	.00	.00
> 19.0	.00	.00

The electrostatic disdrometer average drop size distribution data outlined in Table 1 shows no drops larger than 13 μm radius. The July 9 cloud shows the wider distribution with greater concentrations in the 5.5 - 10.00 μm size ranges. From the difference between the liquid water content calculated from the drop size spectrum, and that measured independently by the sailplane, a concentration can be estimated for the 0 - 4 μm size range not measured by the disdrometer. This calculation shows both clouds to have similar concentrations (greater than 1×10^3 drops cm^{-3}) in this size range. These drop size distributions are clearly characteristic of continental cumulus clouds.

The ratio of the liquid water content to the adiabatic liquid water content (Q/Qa) averaged over the entire cloud depth sampled was calculated (see Table 2). Both the mean liquid water content and the mean Q/Qa are larger for the July 9 cloud than that of July 14. In Figure 1 the liquid water content is plotted as a function of time into the cloud. The July 9 cloud appears to consist of a vigorous, slightly diluted core region bordered by a narrow, well mixed region. The July 14 cloud, on the other hand, does not show this structure, but is well mixed throughout.

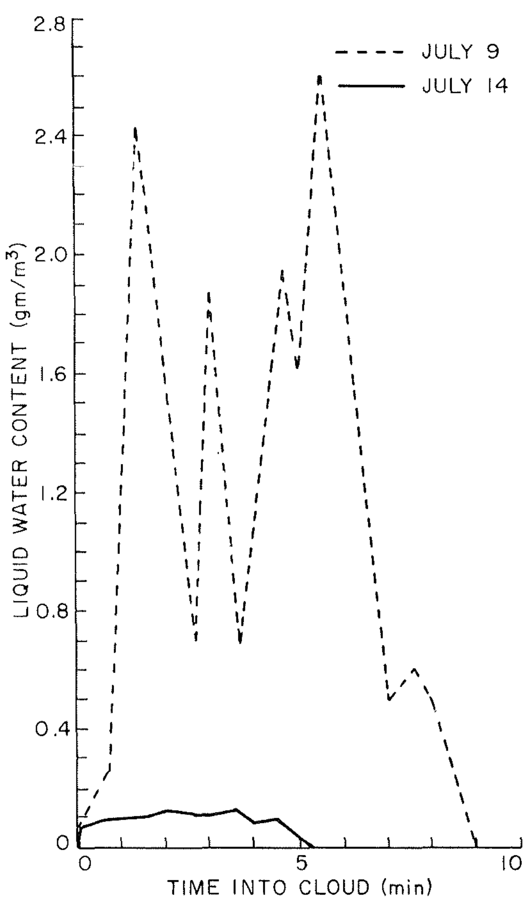

Figure 1. Smoothed values of liquid water content measured by the sailplane during cloud penetration.

Table 2

Average liquid water water content, updraft, and Q/Qa for the July 9 and July 14 cloud.

Cloud	$\overline{LWC}$ (gm m^{-3})	$\overline{W}$ (m sec^{-1})	$\overline{Q/Qa}$
July 9	1.2	3.20	.76
July 14	.1	1.66	.45

5. DISCUSSION

The ratio of the sampled ice particle concentration to the sampled ice nuclei concentration for July 9 was near one. No ice particles were observed in the July 14 cloud, as was expected. Obviously, these observations indicate no ice multiplication in the July 9 or July 14 clouds. However, there are factors which may have caused errors in calculating this ratio. Some of the larger ice particles may have fallen out of the sampling volume depleting the ice particle concentration observed. Another error may have been that some of the ice particles were smaller than the detection limit of 100 μm of the OD^3 analysis system used to analyze the cloud particle camera film. These factors, along with the possible ice nucleus counter error and the error in extrapolating the measurements to warmer temperatures, could have affected this ratio. However, the several orders of magnitude of multiplication found by other observers (Mossop et al, 1970; Ono, 1971; Auer et al, 1969), and not observed in these measurements, cannot be accounted for by this error.

Neither cloud contained any water drops larger than 13 μm radius. Therefore, ice multiplication theories (Koenig, 1962; Hallet and Mossop, 1974) necessitating the presence of large water drops cannot be considered to have been active in these clouds. Ice particles in the sampled volume of the July 9 cloud may have passed through the -3C to -8C temperature regime, but the July 14 cloud does not meet these temperature requirements necessary for the Hallet and Mossop multiplication theory.

The ice crystal habit necessary to generate fracturing collisions with graupel particles for the Vardiman (1974) ice multiplication hypothesis was not observed in these clouds. Vardiman had concluded that it was unlikely that his proposed multiplication mechanism would be observed in isolated cumulus clouds.

The cloud volume sampled in the July 9 cloud was a dynamic, slightly diluted updraft bordered by a narrow more strongly mixed region. The mean liquid water content was 1.2 gm m^{-3}, and the Q/Qa value has been computed to be .76 for the entire cloud volume sampled. If the cloud is separated into a central region (from minute one to minute seven in Figure 1), and a peripheral region, the mean liquid water contents are 1.5 and .5 gm m^{-3} respectively. This reflects the difference in these two cloud regions.

The liquid water content and Q/Qa values are much less for the sampled volume of the July 14 cloud. If Q/Qa is assumed to decrease from unity as more dry air is mixed into the cloud, then the July 9 cloud has experienced much less mixing than the July 14 cloud. The Henmi (1974) hypothesis is based on low density rimed particles contacting undersaturated regions of the cloud and experiencing evaporation. The July 14 cloud meets the liquid water content, drop size, and updraft requirements necessary for the production of low density rime. The Q/Qa value for this cloud shows that the dry air has been mixed into the cloud to provide undersaturated regions. But, at such warm temperatures, no ice particles are present for riming to occur. The July 9 cloud with larger liquid water contents and stronger updrafts would produce a much denser rime hindering this mechanism. The conditions in the July 9 cloud, therefore, are more suitable for the formation of a liquid-coated ice particle necessary to enhance nucleation within local transient areas of high supersaturation as proposed by Gagin (1971). However, this mechanism does not appear to have been a factor in these clouds since no nucleation enhancement was observed.

6. CONCLUSIONS

The ice particle concentration to ice nuclei concentration ratio for the July 9 cloud, a small cumulus cloud with cloud top temperature near -10C, was near one indicating no ice multiplication or nucleation enhancement. The July 14 cumulus cloud extending to about -2C was observed, as would be expected, to have no ice particles.

Of the various hypothesis proposed, only the Henmi (1974) and Gagin (1971) hypotheses could have occured in these clouds. There was no evidence, however, that they were operative.

Other clouds observed during the 1975 South Park Area Cumulus Experiment (SPACE) are being investigated for ice multiplication evidence and possible mechanisms associated with the phenomenon.

7. ACKNOWLEDGEMENTS

This work was partially supported by National Science Foundation Grants ERT 71-01885 and DES 75-17313, and by the State of Colorado.

8. REFERENCES

Abbot, C. E., J. E. Dye, and J. D. Sartor, 1972: An electrostatic cloud droplet probe. J. of Appl. Meteor., 11, 1092-1100.

Auer, A. H., D. L. Veal, and J. D. Marwitz, 1969: Observations of ice crystals and ice nuclei concentrations in stable cap clouds. J. of the Atmospheric Sciences, 21, 640-645.

Braham, R. R., 1964: What is the role of ice in summer rain showers? J. of the Atmos. Sci., 21, 640-645.

Cannon, T. W., 1974: A camera for photography of atmospheric particles from aircraft. Rev. of Scientific Instruments, 45, No.11, 1448-1455.

Dye, J. E., and P. V. Hobbs, 1968: The influence of environmental parameters on the freezing and fragmentation of suspended water drops. Journal of the Atmos. Sciences, 25, 82-96

Fletcher, N. H., 1969: The Physics of Rainclouds, Cambridge University Press.

Gagin, A., 1971: Studies of the factors governing the colloidal stability of continental cumulus clouds. Proc. of the Int'l Weather Mod. Conf. Canberra, Australia, 5-11.

Gagin, W., 1973: Studies of the size and supersaturation spectra of ice nuclei. Proc. of the 8th Int'l Conf. on Nucleation, Leningrad, 77-78.

Grant, L. O., 1968: The role of ice nuclei in the formation of precipitation. Proc. of the Int'l Conf. on Cloud Physics, Toronto, 305-310.

Hallett, J., and S. C. Mossop, 1974: Production of secondary ice particles during the riming process. Nature, 249, 26-28.

Henmi, T., 1974: Secondary ice particle production from rimed ice. Atmos. Sci. Paper, No. 220, Dept. of Atmospheric Science, Colorado State University, Fort Collins, Colorado.

Johnson, D., and J. Hallet, 1968: Freezing and shattering of supercooled water drops. Quart. J. of the Royal Meteor. Soc., 94, 463-482.

King, W. D., and N.H. Fletcher, 1976: Thermal shock as an ice multiplication mechanism. Part I. Theory. J. of the Atmos. Sci., 33, 85-96.

Koenig, L. R., 1962: Ice in the summer atmosphere: an inquiry into its structure, genesis, and metamorphosis. Tech. Note No. 24, Cloud Physics Laboratory, The University of Chicago, Department of Geophysical Science.

Koenig, L. R., 1963: The glaciation behavior of small cumulonimbus clouds. Journal of Atmos. Sciences, 20, 29-47.

Mossop, S. C., A. Ono, and E. R. Wishart, 1970: Ice particles inmaritime clouds near Tashmania. Quart. Journal of the Royal Meteor. Soc, 96, 487-508.

Ono, A., 1971: Some aspects of the natural glaciation processes in relatively warm maritime clouds. Journal of the Meteor. Soc. of Japan, 49, Special Issue, 845-858.

Takahashi, C., and A. Yamashita, 1970: Shattering of frozen water drops in a supercooled cloud. J. of the Meteor. Soc. of Japan, 48, 373-376.

Vardiman, L., 1972: Ice crystal multiplication in convective elements of winter orographic clouds. Atmos. Sci. Paper, Dept. of Atmos. Sci., Colorado State University, Ft Collins. CO.

Vardiman, L., 1974: The generation of secondary ice particles in clouds by crystal-crystal collision Atmos. Sci. Paper No. 230, Dept. of Atmos Sci. Colorado State University, Ft Collins, CO.

3.3.1

NEW TECHNIQUE FOR STUDYING THE DEPOSITION OF DROPLETS ON THE ICE CRYSTAL SURFACE

P. Yue and J. Podzimek
Graduate Center for Cloud Physics Research
University of Missouri-Rolla
Rolla, Mo. 65401

I. INTRODUCTION

The aim of this contribution is to call attention to a new technique enabling the visualization of impacted cloud drops on the crystal surface. The pattern of cloud drops on the crystal surface might be important for the study of the early stage of the riming of the crystals in a mixed cloud.

In order to show the capabilities of the new technique we have chosen the disc and hexagonal plate as the models on which the deposited drops were identified. As long as these models fall quietly in the atmosphere we can describe their fall in simple terms. Actually, the drag and the aerodynamic moment are sufficient for the characterization of their paths. The corresponding drag coefficients deduced by several authors (Willmarth et al., 1964; Jayaweera et al., 1965; Podzimek, 1968 and List et al., 1971) were not much different and varied approximately from 1.5 (for $Re=3x10^2$) to 9.0 (for Re=10). From observations in nature (i.e., Podzimek, 1965) and in the laboratory (i.e., Podzimek, 1968; Jayaweera, 1972) one can conclude that unrimed hexagonal plate-like crystals settle quietly in calm air with their base perpendicular to the direction of fall unless Re exceeded 100.

For these reasons an attempt is made to place an ice crystal model in a wind tunnel in which salt solution droplets carried in an air flow will impact on the model. Evaluating their spots and positions in a sensitized gelatin layer on the crystal surface enables us to judge the crystal collision efficiency and to compare with simple theoretical models.

2. ARRANGEMENT OF THE EXPERIMENT

For a low velocity wind tunnel we used the Turbofan system of Scott-Engineering Sciences, Model 9005. The diameter of the test section is 13.02 cm (5.125 inches). A humidifying unit is added to the air inlet of the wind tunnel (Fig. 1). Humidification is effected by the evaporation of water in the humidification box. The relative humidity was continuously measured by the Cambridge dew point hygrometer, Model 880 and was maintained above 75 per cent. The accuracy in keeping the humid air velocity constant was approximately $\pm 5.0\%$, (for air velocity of 10 cm/sec and less for higher velocity).

The ice crystal models were made of plexiglass. Their diameters were 1.27 and 0.635 cm which enable us to reach Re of several tens to several hundreds. Models were mounted

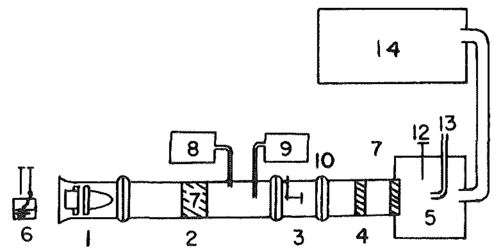

Fig. 1. Arrangement of the Experiment.
1. Rotor Housing; 2. Wind Tunnel;
3. Test Section; 4. Channel Extension;
5. Humidifier; 6. Wet and Dry Bulb Thermometers; 7. Flow Straightener Tube;
8. Dew Point Hygrometer; 9. Climet Particle Counter; 10. Model Support;
11. Thermometer; 12. Aerosol Inlet;
13. Filtered Air Storage Chamber.

in the center of the test section supported by stainless steel rods. A 0.16 and a 0.08 cm diameter rod was used in supporting the larger and smaller models respectively. The model is placed at least 5 cm away from the ceiling support. The diameter of the models are less than 0.1 of the diameter of the test section. Hence, no correction was considered for the effect of the tunnel walls.

The crystal models were coated with film formed from a solution containing 5% by weight of silver nitrate and 8% by weight of gelatin. This sensitized gelatin sheet was investigated under the microscope at a magnification of 128X and photographed for evaluation of the sizes of individual salt solution drops and of their position on the model surface. However, the evaluation of the size of cloud drops assumed that we know the magnification factor which is defined as the ratio of the spot (Liesegang Circle) diameter to the solution droplet diameter.

3. MAGNIFICATION FACTOR OF CAPTURED DROPS

Different techniques have been used in the past for the determination of the magnification factor of salt crystals or salt solution drops captured in the sensitized gelatin sheet (i.e., Preining et al., 1976). It seems to be useful to have the magnification factor related to the aerodynamic diameter of particles and for this aim we made measurements with the aerosol centrifuge (Preining et al., 1976). Also, we investigated the important problem of how far the environmental humidity influences the established magnification factors for sodium chloride aerosol (Yue, 1976).

It was found that spots formed by chloride solution drops deposited on sensitized gelatin film will not be further affected by the change of environmental humidity. On the other hand, droplets injected into an air stream of relative humidity around 72%, the deposition is in crystal form and this will form spots when further exposure to vapor saturated environment. The spots thus formed will give a different magnification factor.

4. EVALUATION OF DEPOSITED DROPS ON CRYSTAL MODELS

The sizes of salt solution drops deposited on the crystal surface were calculated from the "Liesegang's circles" in the sensitized gelatin layer using the magnification factor as was described before. The exposed models with the sensitized sheets were first put under a mercury lamp for 10 minutes to obtain brown circles of insoluble AgCl through photochemical reaction. Then the models (with the diameters R_1 = 0.635 cm and R_2 = 1.27 cm) were evaluated in the microscope at a magnification 128X. Several passages were made across the model surface from the edge through the center and all spots lying within a strip of 1.5 mm wide were counted. In the pilot experiment we used two models of circular disc and one hexagonal plate type model with an air flow velocity of 10 cm sec^{-1}. These yielded Reynolds numbers of 44.0 and 88.00 for the two model sizes. Two runs were made with each model in order to check separately the catching efficiency on the frontal and rear side of the models.

The main results are plotted in Fig. 2, 3, 4, 5, 6, and 7. In each figure the mean number of drops counted with diameters smaller than 5 μm, 5 to 10 μm, 10 to 15 μm, 15 to 20 μm and 25 to 30 μm are plotted. The total number of drops counted on each model is usually over 1,000. In spite of this laborious evaluation, the mean statistical error in deducing the size distribution of drops was greater than $\pm$10%. However, in several size classes, this error is even greater than $\pm$30%.

There is higher catching efficiency for the smaller models on small sizes of solution drops as one would anticipate. In general, we found surprisingly high deposition of drops on the rear side of the models. The total number of drops is smaller on the rear side, however, some distortion on the pattern of deposited drops might be caused by the supporting rod which is attached to the center of the model. The pattern of deposition is similar to that of Sasyo's (1971), also using a wind tunnel, and of Podzimek's observations (1970) in nature. Both authors found the highest concentrations of the deposited drops close to the borders of the frontal side and in

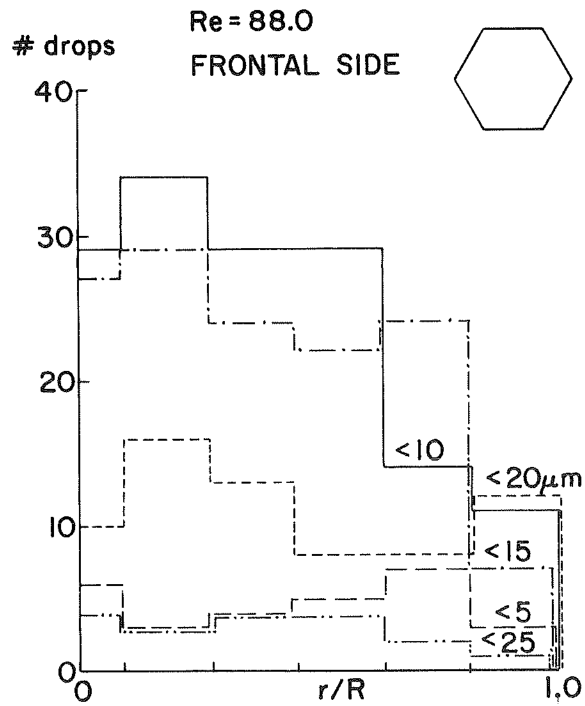

Fig. 2. Distributions of frontal deposition of drops on a hexagonal plate of diameter 1.27 cm.

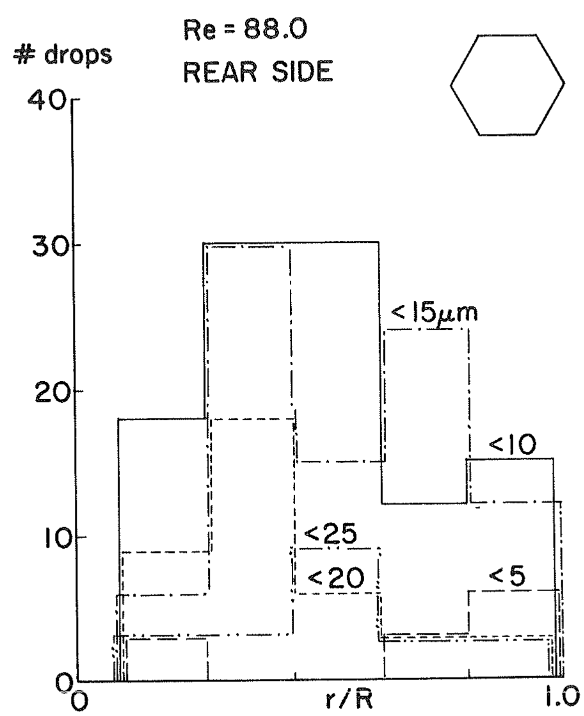

Fig. 3. Distribution of rear deposition of drops on a hexagonal plate of diameter 1.27 cm.

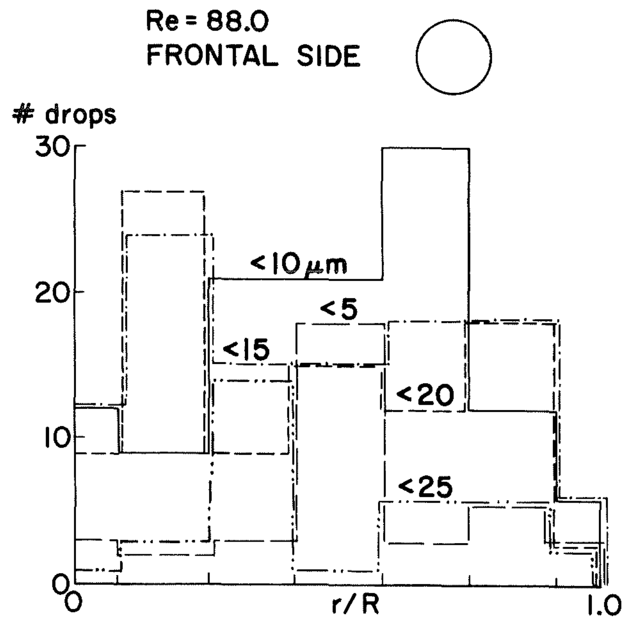

Fig. 4. Distribution of frontal deposition of drops on a circular disc of diameter 1.27 cm.

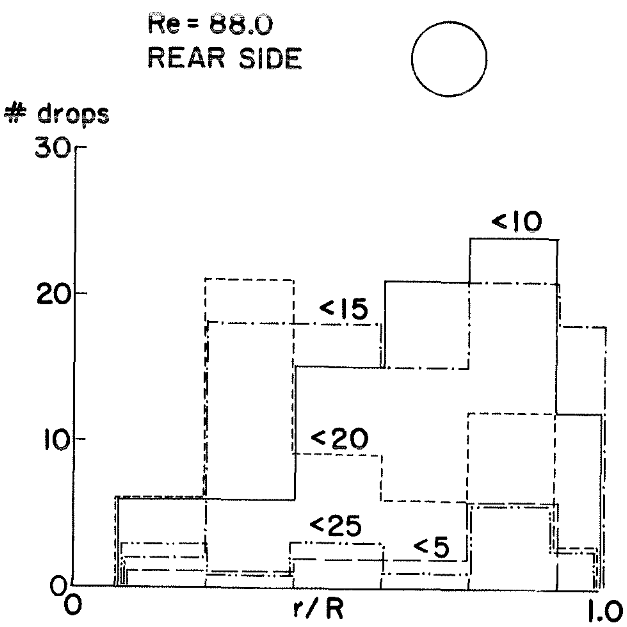

Fig. 5. Distribution of rear disposition of drops on a circular disc of diameter 1.27 cm.

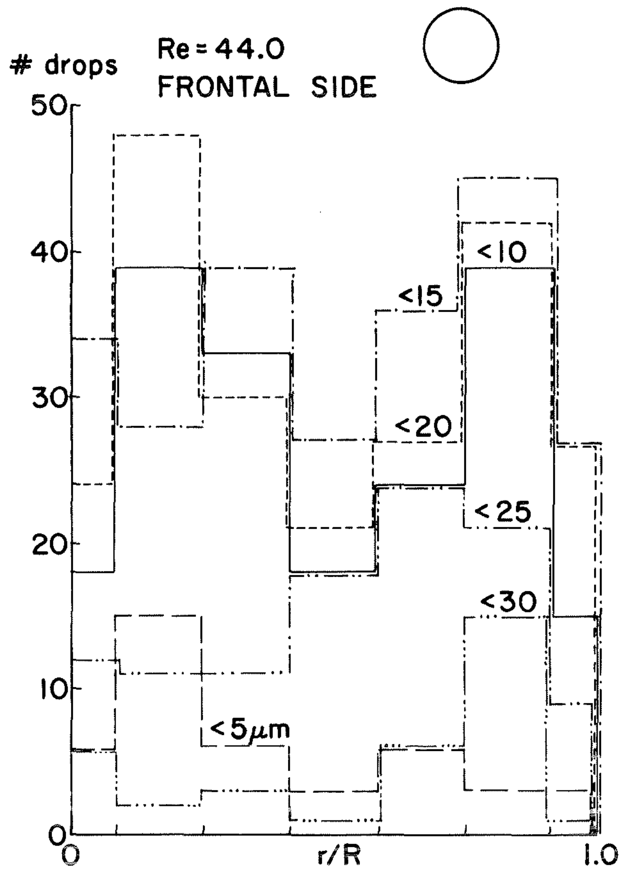

Fig. 6. Distribution of frontal deposition of drops on a circular disc of diameter 0.635 cm.

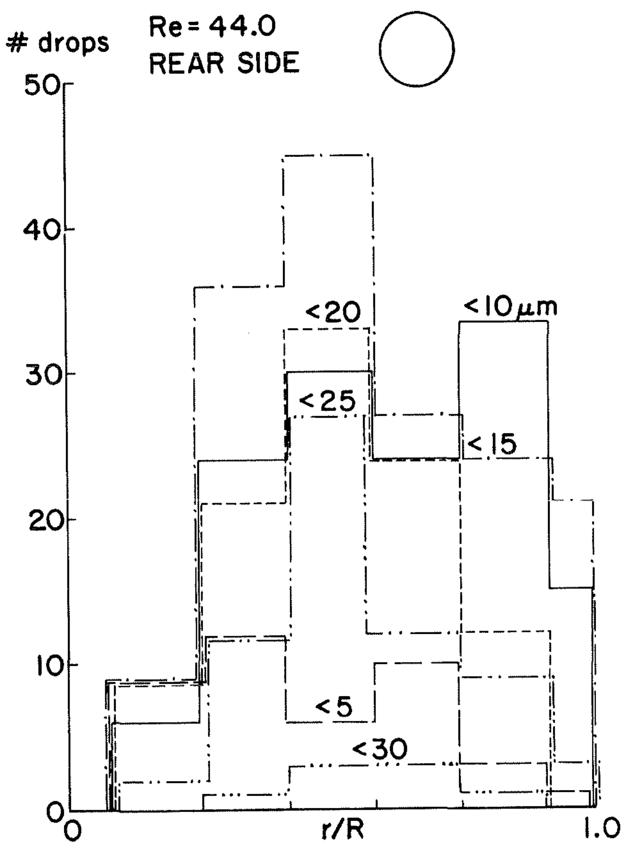

Fig. 7. Distribution of rear deposition of drops on a circular disc of diameter 0.635 cm.

the middle section of the rear side. However, there are strong deviations from this rule, which might be explained by the changing of aerodynamic characteristics of the rimed crystal in nature and by different conditions in Sayso's experiment.

Sayso (1971) investigated the deposition of simulated cloud drops of mean size of 25 μm on a hexagonal plate of 1 cm in diameter. The airflow velocity in the wind tunnel was 50 cm sec^{-1}, so that the corresponding Re = 330. Also, the Stokes numbers of the individual droplets impacting the model were about 5 times larger than ours for the same size of droplets.

Unlike the observation in nature (Podzimek, 1976) our drop size spectrum from the rear side was not much narrower than that of the frontal side. The rates of the number of drops on the front side of a natural crystal to the number on the rear side varied from 3.5 to 7.0 at Re between 2.0 and 20.0. However, riming and co-growing of the frozen drops on a natural crystal might strongly influence the deposition of drops.

CONCLUSIONS

The described simple method for the investigation of the cloud drop deposition on ice crystal models seems to be suitable for the study of the early stage of crystal riming.

It is necessary to consider the deposition of cloud drops on both sides of the falling crystal in calm air. The frontal side of a hexagonal plate collects more drops than the rare side. For Re = 44, the deposition on both the front and the rear sides roughly correspond to the simple theoretical models for drops between 10 to 25 μm, namely, higher concentration should be found near the edge for frontal deposition and mid-way from the center for rear deposition. However, we often found several very small droplets close to the center of a hexagonal plate or a disc. We hypothesize that this anomalous occurrence of small droplets at the center might be explained by the interaction between small and large drops which are impacting the surface at the same time. This could also explain why there are two peaks on several of the distribution histograms.

REFERENCES

Podzimek, J., 1970, Contribution to the problem of the collection efficiency of the falling ice crystals, Conf. on Cloud Physics, Fort Collins, Aug. 1970, AMS, 13.

Sasyo, Y., 1971, Study of the formation of precipitation by the aggregation of snow particles and the accretion of cloud droplets on snow flakes, papers in Meteor. and Geophys., Japan, 22, 69-142.

Jayaweera, K. O. L., and R. E. Cottis, 1969, Fall velocities of plate-like and columnar crystals, Quart. J. Roy. Meteor. Soc., 95, 703-709.

List, R. and R. S. Schemenauer, 1971, Free fall behavior of planar snow crystals, conical graupel and small hail, J. Atmos. Sci. 28, 110-115.

Podzimek, J., 1965, Time sequence of shapes of ice crystals at transition of frontal systems on 5. and 6.2, 1963, Travaux de l'Inst. Geophys. ATS, Geofysikalni Sbormik, Prague, 239, 613-627.

Jayaweera, K. O. L., 1972, An equivalent disc for calculating the terminal velocities of plate-like ice crystals, J. Atmos. Sci., 29, 596-598.

Podzimek, J., 1968, Aerodynamic conditions of ice crystal aggregation, Proc. Int. Conf. Cloud Physics, Univ. of Toronto, 295-299.

Preining, O., J. Podzimek, and P. C. Yue, 1976, Magnification factor for sodium chloride Liesegang circles established with the aid of aerosol centrifuge, Aerosol Science, (in print).

Yue, P. C., 1976, Chemical spot test method for droplet size determination - humidity effect, presented at the Ann. Mtg. of Missouri Academy of Science, Univ. of Mo.-Rolla, April 22-24, 1976.

3.3.2

INFLUENCE OF ELECTRICAL FIELD ON AGGREGATION OF LARGE AND SOLID PARTICLES

V.M. Muchnic, V.A. Djachuk

Ukrainian Hydrometeorolgical Research Institute, Kiev, USSR

It is maintained a point of view that the influence of the electric forces on the processes of a growth of the hydrometeors in clouds, including thunderclouds, is small. This opinion has a theoretic base, that at the increasing of drop sizes a relative decreasing of the influence of the electric forces on a coagulation velocity of drops with droplets takes place, Levin (1961). But such conclusion is not applicable to the drops of the comparable sizes, the intensive fields and the big charges, i.e. for conditions which are the same in regions of the thunderclouds.

Hydrometeors which occur very often in the thunderclouds are hails, Musil and oth.(1974). At the wet growth and the melting large drops are tearing off of them, because of this the hails are the intensive generators of the large drops. By the wet growth and the melting a hailstone radius of 0.66 cm in a cloud at the height of 10 km(with a base of 1 km height, a level of $0^{o}C$, the height of 3.5 km, the maximum liquid-water content of 6 g/m^3 and an ascendant velocity 25 m/s) is to R=1.52 cm. By the fall it is teared off the hail of 120 g of water in the form of the drops, Budak and oth.(1972). If the mean radius is 0.5 mm, Blanchard (1955), then during the fall time of a hail $2\cdot 10^5$ of drops are formated. Because of this an increase of the drop concentrations will take place in the ascendant currents.

In the thunderclouds the electric fields of $E=3\cdot 10^5$ V/m are observed between the levels of $+10^{o}C$ and $-20^{o}C$. That is why in this region the role of the aggregation of the large particles on the influence of gravitational, turbulent and electric forces must be considerable.

In the intensive electric fields it is observed a large deformation in the gap between the drops up to a formation of a dam. Therefore calculations of a coagulation in the electric field are not correct if it is assumed that drops are hard spheres, Levin (1961), Sartor and Miller (1965), Krasnogorskaya (1967) and oth. Owing to this it is necessary to examine the peculiarities of the aggregation and the disaggregation of hydrometeors in the various phases of water at the influence of electric forces.

In order to investigate the drops of r=0.25 ÷ 2.0 mm are suspended on capron threads of the diameter of 10 μ and the length of 3 cm in the centre of a condenser with a horizontal electric field. The charges on the drops and the threads were taken off by air ionization by a radioactive source. The processes of the aggregation were photographed in a transmitted light with the frequency of surveying of 4500 frames/s. For the present investigations there are an estimation of the resistance force of air for the motion and the force of the deviation of the drops from a vertical. They are very small in comparison with the force of the electric interaction of drops. Consequently the processes of the approach of drops, the dam formation and the aggregation occur only at the action of electric forces and a surface tension forces. That is why for constant E and T the value of the dam length (L) must be constant. Really, for the drops $r=1 \div 1.3$ mm and $E=2.5 \cdot 10^5$ V/m, $L=2.25 \cdot 10^{-2}$cm (at the accuracy to 2%) though the start gap between the drops varied from $2.6 \cdot 10^{-2}$ to $9.8 \cdot 10^{-2}$cm.

We have obtained the dependence of L from E ($0.5 \cdot 10^5 \div 8 \cdot 10^5$ V/m) and r ($0.25 \div 1.25$ mm). One can see from Fig.1 that ratio L/r may be present as a single-value function of E. In this figure there is a plot of a value obtained from Sartor's and Abbot's experiments (1968) for the case of a free fall of water drops at r=0.78 mm in a field of $E=3.85 \cdot 10^5$V/m. It is obvious that this value is in a good agreement with our data.

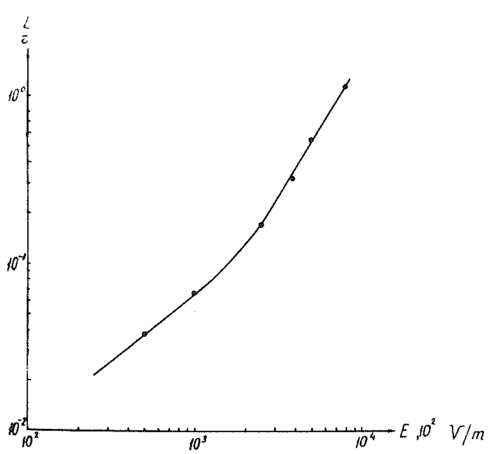

Figure 1. The dependence of the ratio of the dam length L between two collision drops of equal size to their radius r from the external electric field strength E.

At the influence of an electric field in the gap between the drops it takes place a conical deformation of the surface that results in a significant increase of the field strength in the gap. The last is accompanied by the rise of an instability and from the cone peaks the water jets tear out at the velocity of 1 m/s, Djachuk (1971). A corona or a spark discharge makes equal the potentials on the poles of cones before of their contact. By this the electric force disappeared in the gap, which caused the instability. From this moment the formation of the dam occurs at the acceleration forces of jets and surface forces of drops.

When the dam is formed it is occured an increasing of the diameter of a dam, which depends on the field strength counteracting to the drop aggregations. It was obtained by us that the dam cros-section surfaces are a linear time function for E from 0 to $5 \cdot 10^5$V/m (Fig.2), that is in an agreement with Frenkel (1946). This regularity is disturbed for the high field strength, for which the counteracting forces are large, Djachuk (1975).

We have obtained also that the velocity of rapprochement of the drops boundaries in the gap has appreciable pulsations. It is possible that these pulsations depend on the influence of electric forces in according to Latham's and Brasier's-Smith's (1969) data for the drop, which is destroyed in an electric field. It is interesting to note that in our experiments the pulsation frequency for pair of drops of r=1.34mm and $E=8 \cdot 10^5$ V/m was the same which was calculated by Latham and Brasier-Smith for a single drop of r=2 mm and $E=9.5 \cdot 10^5$ V/m.

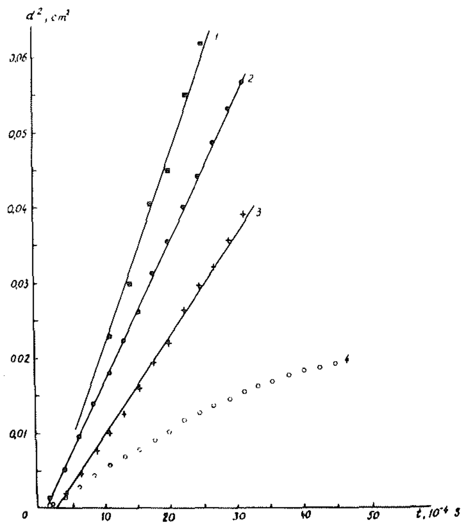

Figure 2. The dependence of the square of dam diameter d^2 between two drops of equal size from time of it formation: 1 - E=0; 2 - E= $2.5 \cdot 10^5$ V/m; 3 - E=$5 \cdot 10^5$ V/m; 4 -E= $8 \cdot 10^5$ V/m.

In the process of a confluence of two drops a single resulting drop is occured which is elongated in the direction of the electric field. In intensive electric fields on the drop poles the sharpenings and the ejections of water jets arose. These ejections arose in turns from both poles, leading off the positive. The time between the ejections was about 0.5 ms.

All experiments were carried out at the room temperatures and moisture. The research of the aggregation of supercooled drops with each other and with frozen drops were fulfiled at a negative temperature in a metallic chamber. The drops on the capron threads were lowered in the chamber. There they frozen here and after that the drops drew together to the desirable distance between them. Then the electric field and the high-speed camera were swithched on.

We have revealed that by the confluence of supercooled drops the crystallization temperature is considerably higher than for single drops of the same sizes and depends on the field strength. If E=$1 \cdot 10^5$ V/m, then the drops with r=1.25 mm at the supercooling temperature up to -16°C do not freeze by the collision. The freezing takes place at the temperatures of -18°C and below. And if E=$5 \cdot 10^5$ V/m the pair of such drops freezes at -8°C. The cause of this increase of a freezing temperature may be the formation of crystallits in the thin jet of water which according to Leb(1963) may be effective centres of a crystallization.

The shapes of the hydrometeors, formated at the influence of the electric forces, may be very different. Latham (1969) reported that Smith had obtained the dumb-bell forms of hydrometeors by the collision of supercooled drops of r=100 ÷ 300 μ.

By the collision of artificially crystallized drop (at once after appearance of an ice cover) with the supercooled drop the temperatures higher than -5°C in an electric field of any strength it took place the formation of the particle or a glassy ice. In the process of the collision it was occured a destroying of the ice cover, the confluence of water in a single drop and a crystallization from the surface. Sometimes at the temperature below -5°C and always at the temperature below -15°C and E=$1 \cdot 10^5$ V/m by the collision of a completely or considerably frozen drop with supercooled one it resulted in a two-lobe particle. And if E=$5 \cdot 10^5$ V/m then the force of a collision is so big that the water envelops completely the frozen drop. As a result spherical ice particles were formated.

By the collision of two partial frozen drops at $E < 5\cdot 10^5$ V/m dumb-bell particles are formated. The same particles were observed by Mee in the clouds on Caribbean Sea at the temperature of $-5^{o}C$, Latham (1969). If $E \geqslant 5\cdot 10^5$ V/m and the drops have thin ice cover by a collision two - lobe and sometimes spherical particles are created.

The collision of completely frozen drops by $E < 5\cdot 10^5$ V/m at any temperature has brought to their aggregation. The forces of an adhesion were higher than the electric forces which stretched the particles. And if $E \geqslant 5\cdot 10^5$ V/m and the temperature is $-30^{o}C$ and below it then the forces of an adhesion are smaller than the electric forces and the particles after the collision go away.

On the basis of our experiments it follows that the electric field can considerably influence on the conditions of the aggregation of large particles in mature thunderclouds.

REFERENCES

Blanchard,D.C.,1955: The supercooling, freezing and melting of giant waterdrops of terminal velocity in air. Artificial simulation of rain. Eds. H. Weickmann and W.Smith.L.,pp.233-249.

Brasier-Smith,P.R.,and Latham,J.,1969: Numerical computations of the dynamic of the disintegration of the drop situated in an electric field. Proc. Roy. Soc. A.,312,№1509,pp.277-289.

Budak,I.V.,Muchnik,V.M.,and Fishman,B.E., 1972: Computation of growth and melting of ice particles and profiles of radar reflectivity in models of cumuli-nimbus clouds. Trudy Ukrainsk. N.-I. Gidrometeorol. Inst.,№114, pp.14-28.

Djachuk,V.A.,1971:On confluence of two large drops near sizes in an electric field.Trudy Ukrainsk.N.-I. Gidrometeorol. Inst., №103, pp.82-95.

Djachuk,V.A.,1975:The influence of electric field on the interaction of drops. Trudy Ukrainsk. N.-I. Gidrometeorol. Inst., №137, pp.74-88.

Frenkel,J.I.,1946: Viscous flow in crystall body.JETPh,16,№1, pp.29-38.

Krasnogorskaya,N.V.,1967:The influence of electrical forces on coagulation of cloud drops.Meteorol. i Gidrol.,№3,pp.51-59.

Latham,J.,1969: Cloud physics. Rep. Prog. Phys., 32, №1, pp.69-134.

Levin,L.M.,1961: The research of coarse - dispersed aerosols. M., AN SSSR, 267p.

Loeb,L.,1963: A tentative explanation of the electric field effect on the freezing of the supercooled water drops. J. Geophys. Res., 68, №15, p.4475.

Musil,D.J., May,E.L., Smith,P.L., and Sand,W.R., 1974: Measurement of ice and liquid precipitation distributions inside hailstorms. Conf. on Cloud Phys., Amer. Meteorol. Soc., Boston, pp.267-270.

Sartor,J.D., and Abbott,C.E., 1968: Charge transfer between uncharged water drops in free fall in an electric field. J. Geophys. Res., 73, №20,pp.6415-6423.

Sartor, J.D., and Miller,J.S., 1965: Relative cloud droplet traectory computation. Proc. Inter. Conf. on Cloud Phys. Tokyo, pp.108-112.

3.3.3

COLLISION EFFICIENCIES OF DROPLETS WITH DIAMETER BELOW 40 μm FOR NON-GRAVITATIONAL VELOCITIES

Ryszard Balcer* and Jerzy Czyż**
* Institute of Geophysics, University of Warsaw
** Institute of Geophysics, Polish Academy of Sciences
Warsaw, Poland

1. INTRODUCTION

The mechanism of early stages of evolution of droplet spectra in natural fogs and clouds is still mysterious in many respects. The observed speed of formation of relatively large droplets is often much greater, than it follows from estimates based on existing theories of condensation and coalescence. Although some recent numerical experiments (Leighton and Rogers, 1974) seem to indicate, that the simultaneous coalescence and condensation may be responsible for fast shift of the spectrum towards greater sizes, lack of clear physical, qualitative explanation of this effect may cast some doubts, if this is not a purely mathematical property of the computational form of the model. Thus further search for other possible factors of the droplet spectra evolution seems to be justified.

K.E.Haman (private communication) has made a following suggestion: the typical stochastic theory of gravitational coalescence make use of the kinetic equation in the form:

$$\frac{\partial}{\partial x} f(m,t)=\frac{1}{2}\int_{m'=m_0}^{m'=m} K(m-m',m')f(m-m',t)\, f(m',t)\, dm' - \int_{m'=m_0}^{m'=\infty} K(m,m')f(m,t)\, f(m',t)\, dm' \quad \ldots\ldots\ldots\ldots (1)$$

where $f(m,t)$ - time(t) - dependent spectral distribution function of droplets with respect to their mass m; $K(m,m')$ - the so called coalescence kernel. The term "stochastic" is somewhat misleading in this context, since notion of probability is not essential for this approach andis used only as an equivalent of normalized frequency. The kernel K is assumed a deterministic non random function of m and m', free fall velocities of the droplets and their collision efficiences both assumed not random functions of masses only. Collision efficiences are generallydetermined under assumption, that at beginning of computation, the droplets are far from each other and do not interact. The form of Eq.(1) implies also that the droplets are assumed to be randomly distributed in space.

In fact all this assumtions might be questioned. Particularily in turbulent atmosphere, the starting positions and velocities of colliding droplets may differ randomly from those usually assumed in determination of coalescence efficiency and kernels. There is also certain evidence, that the coalescence efficiency might be altered by accelerations. Thus, the kernel as a function of masses, should be considered a random function in strict meaning of this word. Eq.(1) becomes then an essentially stochastic equation for random distribution function $f(m,t)$. Let us notice, that certain type of such on approach can be found in the theory of so called turbulent coalescence investigated many years ago (Saffman and Turner, 1956), but not proved to be very essential in clouds.

In contrary to the concept of turbulent coalescence, in which only the direct effect of air velocity pulsations on droplet collisions has been considered, the present hypothesis states, that microturbulence might enhance the gravitational coalescence by random variations of the coalescence efficiency; this resembles to certain extent the ideas of Woods and al. (1972), who tried to determine the effect of local shear on the collision efficiency.

Confirmation or rejection of this hypothesis and eventual modification of the stochastic coalescence theory requires some knowledge of coalescence efficiency as a function of initial velocities which may differ from the free fall ones, and other factors which independently can affect its value.

The main goal of the present paper is to make the first step towards solution of this rather extensive problem and obtain some experimental and computational estimates of the influence of initial velocities of colliding droplets on their collision efficiences, at least in certain cases relatively easy for investigation. The size of investigated droplets is below 40 μm in diameter, since for larger ones, the classical theory of gravitational coalescence gives satisfactory results.

2. THE EXPERIMENT

2.1. Design of the experiment

The principle of the laboratory experiment is as follows. Small droplets produced by Abbott's-type generator (Abbott, 1972) moove upwards in the airstream produced in small vertical wind tunnel, and collide with the collector droplet, which is hanging on a very fine wire diameter 10 - 15 μm. Vertical velocity of the air may be varried. The motion of droplets is photographed by means of 16 mm movie camera through microscopic lense in two sources of light - continous and stroboscopic on dark background.

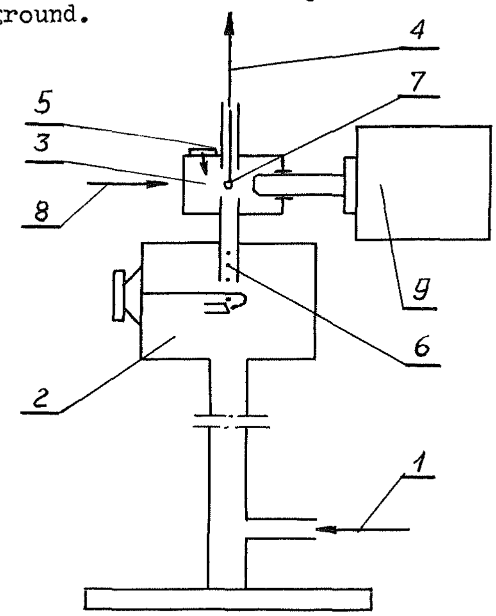

Figure 1. Side view of tunnel.
1.-air inlet, 2.-droplet generator, 3.-observation box, 4.- air inlet, 5.- ^{137}Cs radioactive source, 6.-moving droplets, 7.-collector droplet on the wire, 8.- source of light, 9.-movie camera.

Size of dimensions of objects on the picture are determinated by means of high precision measuring microscope with accuracy of 1.0 µm. Depth of the sharp focus is below 50 µm.

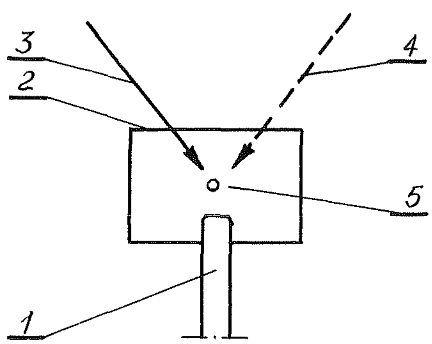

Figure 2. Downview of observation box.
1.-lens of movie camera, 2.-glass window, 3.-continous source of light, 4.-stroboscopic source of light, 5.-collector droplet.

Size of the moving droplets is calculated from the distance between the continous and interrupted traces (see Fig.3) their speed from the lenght of the distance covered by the droplet when it was iluminated by the light pulse. The air speed is determined from the difference between the observed and free fall speed of the moving droplets; its stability can be additionally checked with sensitive hot wire anemoscope. Electrical effects are eliminated by connecting to earth all essential metal parts and the wire with hanging droplet, and introducing a ^{137}Cs radioactive source into the tunnel. Schematic drawing of experimental instalation and its optical cheme is given on Figs 1 and 2.

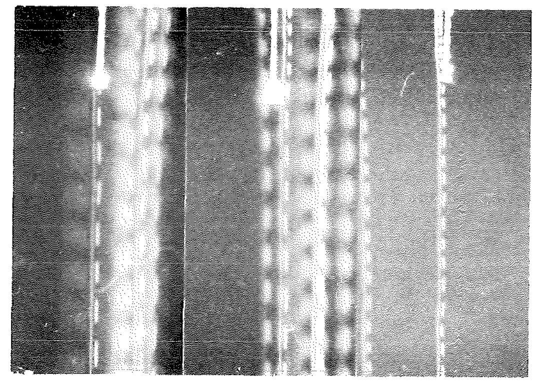

1. 2. 3.

100 µm

Figure 3. Examples of droplets trajectories.
1.-collision, 2.-grazing trajectory, of moving droplet, 3.-variable speed of moving droplet as a result the accoustic effects. This effect - parasitic in present study is going to be investigated as a factor in coalescence in future experiments.

The early idea was use a true water droplet as a collector. However, first experiments indicated, that the cappilary forces between the droplet and wire result in strong deformations of shape; the droplet has tendency to move the wire. Thus a small metal ball, made by melting the end of the wire in electrical discharge has been used instead, although its shape generally was not ideally spherical as well. Sometimes good results were obtained by a drop formed on the metal ball after covering it with water in the first collision.

The supporting wire seems to introduce no essential disturbances of airflow in the front of the hanging droplet though it can considerably obscure eventual wake effects. The changes of dynamics of interaction between the droplets caused by fastening one of them may be more serious particularily when masses of both droplets are close to each other. Thus collision efficiences for such system may differ from those for freely moving droplets .

Though quantitative estimation of this difference was impossible at the time this paper was being written, the authors are aware of this problem and both experimental and computational works are planned to solve it in the nearest future.

The experimental estimation of collection efficiency is made by searching of pairs of nearly grazing trajectories, one with collision and the second without, and by carefully measurements of their parameters. Provided that droplet sizes and speeds in both cases are close to each other, this permitts an under- and overestimation of the collision efficiency, which with some luck may place it within fairly narrow band.

The movie was usually taken with speed of 4 frames per second; light impulse of the stroboscope was 1 ms.

Despite the simplicity of the principle, the experiment is difficult and laborius. The greatest troubles are connected with securing uniform flow in the tunnel, particularily at low vertical velocities, and obtaining sufficiently good pairs of trajectories within reasonable duration of observations.

2.2 Results

For the present analysis more than 5000 frames were taken, for collector "droplets" with diameter D between 20 - 40 µm and air speed V_a equivalent to 0.7 - 6.0 of their free fall speed v_g. Diameters of the moving droplets were (d) in range 15 - 30 µm, permitting the d/D ratio 0.38 - 1.20. Ratio of the width to the droplet diameter was determined by direct measurements on droplets which stuck to the wire, and in present experiment is equal to 0.62 ± 0.01.

In the material analysed till now no pair of trajectories was found, which would permit determination of collision efficiency with meaningful accuracy, but in 6 cases underestimates of the collision efficiences were obtained, with increasing V_a/V_g ratio.

Documentation of these cases is given in Table 1.

Table 1

Case no.	1	2	3	4	5	6
D (±1 µm)	24.4	27.0	34.0	40.0	40.0	40.0
d (±1 µm)	22.8	22.0	22.8	28.0	22.8	20.4
d/D	0.93	0.82	0.67	0.70	0.57	0.51
V_g (±0.1 cm/s)	1.8	2.2	3.5	4.8	4.8	4.8
v_g (±0.1 cm/s)	1.6	1.5	1.6	2.4	1.6	1.3
V_a (±0.1 cm/s)	5.1	4.5	4.7	5.5	5.7	5.1
V_a/V_g	3.7	2.7	1.8	1.6	1.5	1.3
$\underline{E}_a(V_a/V_g)$	0.20	0.09	0.10	0.34	0.67	0.20
E_g	0.07 0.02	0.07 0.02	0.09 0.03	0.20 0.04	0.20 0.04	0.15 0.04

$\underline{E}_a$ - experimental underestimate of the collision efficiency for V_a as above,
E_g - gravitational collision efficiency (Davis & Sartor, 1967/Klett & Davis, 1973)
(V_g, v_g - after Stokes formula)

Values $\underline{E}_a$ given in the Table 1 exceed the known values of E_g so much that it would be probably difficult to attribute this difference only to immobility of the collector droplet. On the other hand no evidence was found in the course of the experiment that for V_a and close to v_g, such difference atributable then to immobility of the collector droplet or other imperfections of the experiment is present, although there was no opposite evidence either. Thus it seems probable that the increase of collection efficiency can be at least partly attributed to the increase of the apparent free fall velocity.*)

It is worth noting, that in course of measurement a number interesting observations concerning the droplet motion and collision process has been made. One of the most interesting is, that at time when the airflow velocity was being increased, the collection frequency looked to be greater than before and after the change of velocity. Unfortunately there was no opportunity to study this effect in detail.

The measurements are being continued with technical modifications directed towards increasing the effectiveness of producing droplet trajectories close to the grazing one and towards improoving the aerodynamics of the tunnel and picture quality.

3. CONCLUSIONS

Experimental results, though only preliminary suggest, that the collision efficiency of colliding droplets with diameters below 40 µm is very sensitive to the value of the free fall velocity in turbulent atmosphere may case, that the collision efficiency as a function of masses or radii of the coliding droplets becomes a random function with large variance. This mass essentially change the conclusions based on stochastic theory of gravitational coalescence in clouds, particulary for its early phase. However the number of results obtained till now is too small, and more experimental and computational work is necessary if the present conclusions are to be accepted with satisfactory degree of certainity.

4. ACKNOWLEDGMENTS

The authors are indebted to Dr. K.E. Haman, University of Warsaw, who initiated this study and actively participated in its developement.

*) Unexpectedly large increase of collision efficiency has been also confirmed in a test computation with mathematical model of collision. For conditions corresponding to the case 5 of Table 1 but with motion and rotation of both droplets allowed, collision efficiency $E=0.91 \pm 0.1$ was found. Unfortunately, shortage of computer time interrupted further computations.

5. REFERENCES

Abbott, C.E. and T.W. Cannon, 1972: A droplet generator with electronic control of size, production rate and charge, The Review of Sc. Instr., Vol.43, pp. 1313-1317.

Davis, M.H. and J.D. Sartor, 1967: Theoretical collision efficiencies for small cloud droplets in Stokes flow, Nature, Vol.215, pp. 1371-1372

Klett J.D. and M.H. Sartor, 1973: Theoretical collision efficiencies of cloud droplets at small Reynolds numbers, J. Atm. Sci., Vol.30, pp. 107-117.

Leighton, H.G. and R.R. Rogers, 1974: Droplet growth in a strong updraft, J.Atm.Sci., Vol.31, pp. 271-279.

Saffman, P.G. andJ.S.Turner, 1956: On the collision of drops in turbulent clouds J. Fluid Mech., Vol.1.

Woods J.D., Drake J.C. and Goldsmith P., 1972: Coalescence in turbulent cloud, Quart.J.R.Met.Soc., Vol.98, pp. 135-149

THE EFFECT OF ELECTRIC FIELDS AND ELECTRIC CHARGES ON THE COLLISION EFFICIENCY OF SMALL AND LARGE CLOUD DROPS

R. J. Schlamp, S. N. Grover, H. R. Pruppacher

Department of Meteorology, University of California
Los Angeles, California

and

A. E. Hamielec

Department of Chemical Engineering, McMaster University
Hamilton, Ontario, Canada

1. INTRODUCTION

It is now well established that some convective clouds are already weakly electrified in their early stages of development, the electrification increasing progressively as the clouds reach their mature stage. An electrified cloud implies that the cloud particles carry an electric charge and are exposed to an external electric field. Electric field strengths in mature convective thunderstorm clouds may be as high as several kilovolts per centimeter (Mason, 1971). Takahashi (1972, 1973) summarized observations of his own and others on the electric charge typically carried by cloud drops, drizzle drops and raindrops of varying size. One notices from Fig. 7 of his summary that the mean drop charge for thunderstorms can be expressed as $Q_{A,mean} \approx 2A^2$, where $Q_{A,mean}$ is expressed in esu and A in cm (Grover and Beard, 1975). It is certainly physically reasonable to find that $Q_{A,mean} \propto A^2$, since a cloud drop can be considered to behave electrically as a conducting sphere where the charge resides primarily on the surface. The constant of proportionality will depend on the maturity of the convective cloud system. Thus, observations suggest that already in the early stages of cloud development the processes which control the growth of cloud particles may be affected by the electric state of the cloud system in which the growth takes place.

At temperatures at which clouds are still not yet glaciated, cloud drops grow predominantly by the collision-coalescence process. Intuitive physical reasoning tells us that electric charges and fields will enhance the collision-coalescence growth. Unfortunately, only a few studies have been reported in literature which elaborate on this intuition in a quantitative manner. In order to improve the presently available models for computing the effect of electric charges and fields on the collision efficiency of cloud drops and to extend the applicability of the results of such models to larger cloud drops, we have combined the electrostatic force model of Davis (1962, 1964a,b) with a numerical model for describing viscous flow past a sphere.

2. THE AERODYNAMIC AND ELECTRIC MODEL

The aerodynamic model in the present computations to determine the trajectory of two interacting cloud drops is basically the same as that used previously by Shafrir and Neiburger (1963), Shafrir and Gal-Chen (1971), and Lin and Lee (1975).

The equations of motion for the collector drop of radius A and for the collected drop of radius a can then be written as

$$m_A \frac{d\vec{V}_A}{dt} = m_A \vec{g}^* - \frac{\pi}{4} c_{D,A} N_{Re,A} A \mu (\vec{V}_A - \vec{U}_a) + \vec{F}_{e,A} \qquad (1)$$

$$m_a \frac{d\vec{V}_a}{dt} = m_a \vec{g}^* - \frac{\pi}{4C_{sc}} c_{D,a} N_{Re,a} a \mu (\vec{V}_a - \vec{U}_A) + \vec{F}_{e,a} \qquad (2)$$

We may non-dimensionalize Eqs. (1) and (2) by setting

$$\vec{V}' = \vec{V}/V_{\infty,A}\,,\quad \vec{U}' = \vec{U}/V_{\infty,A}\,,\quad t' = t V_{\infty,A}/A\,,\quad p = a/A$$

$$(\vec{g}^*)' = \vec{g}^* A/V_{\infty,A}^2\,,\quad \mu' = \mu A^2/m_A V_{\infty,A}\,,\quad \vec{F}_e' = \vec{F}_e A/m_A V_{\infty,A}^2$$

One then finds

$$\frac{d\vec{V}_A'}{dt'} = (\vec{g}^*)' - B_2 (\vec{V}_A' - \vec{U}_a') + \vec{F}_{e,A}' \qquad (3)$$

$$\frac{d\vec{V}_a'}{dt'} = (\vec{g}^*)' - B_1 (\vec{V}_a' - \vec{U}_A') + \frac{\vec{F}_{e,a}'}{p^3} \qquad (4)$$

where $B_1 = (\pi/4p^2 C_{sc})\, c_{D,a} N_{Re,a} \mu'$ and $B_2 = (\pi/4)\, c_{D,A} N_{Re,A} \mu'$. Equations (3) and (4) determine the trajectories of two interacting drops.

Since the two drops accelerate as they approach each other, it was necessary to continually update the quantities B_1 and B_2. In order to do this, $N_{Re,A}$ and $N_{Re,a}$ were re-calculated at each time step along the trajectory from

$$N_{Re,A} = \frac{2A\rho\,|\vec{v}_A - \vec{u}_a|}{\mu} \tag{5}$$

$$N_{Re,a} = \frac{2a\rho\,|\vec{v}_a - \vec{u}_A|}{\mu} \tag{6}$$

and the drag force coefficients $c_{D,A}$ and $c_{D,a}$, being a function only of the respective Reynolds numbers, were then computed from the relations for water drops in air given by Beard (1974).

Values for the velocity field $\vec{u}_A$, $\vec{u}_a$ around the drops were derived from the stream function fields given by LeClair et al. (1970) for selected Reynolds numbers from a numerical solution of the Navier-Stokes equation of motion for air flowing past a rigid sphere. Numerically computed flow fields were used for the following Reynolds numbers: 0.02, 0.03, 0.04, 0.07, 0.1, 0.2, 0.3, 0.4, 0.5, 0.6, 0.8, 1.0, 1.5, 1.75, 2.0, 2.5, 3.0, 4.0, 4.5 and 6.0. For drops with $N_{Re,a} < 0.02$ we assumed that the flow field could be approximated by Proudman and Pearson's (1957) analytic solution to the Navier-Stokes equation of motion which considers only the first two terms of the Stokes expansion.

For the purpose of describing the electrostatic forces $\vec{F}_{e,A}$ and $\vec{F}_{e,a}$ we represented both interacting drops by conducting spheres, an assumption which has been justified by Davis (1969). Davis (1964b) solved for the force between two conducting spheres. Expressing the model of Davis (1964b) in slightly different notation, we find for the electrostatic force on the spherical a-drop

$$\begin{aligned}\vec{F}_{e,a} = -\Big\{&\epsilon a^2 E_0^2 (F_1 \cos^2\gamma + F_2 \sin^2\gamma) + E_0 \cos\gamma\,(F_3 Q_A + F_4 Q_a) \\ &+ \frac{1}{\epsilon a^2}(F_5 Q_A^2 + F_6 Q_A Q_a + F_7 Q_a^2) + E_0 Q_A \cos\gamma\Big\}\,\hat{e}_r \\ &+ \Big\{\epsilon a^2 E_0^2 F_8 \sin 2\gamma + E_0 \sin\gamma\,(F_9 Q_A + F_{10} Q_a) + E_0 Q_A \sin\gamma\Big\}\,\hat{e}_\gamma\end{aligned} \tag{7}$$

where γ is the angle between the local vertical, given by the direction of gravity $\vec{g}$, and the line connecting the centers of the two interacting spheres. We are considering only a vertical electric field, where E_o is taken to be negative when the field points from a positively charged region in the top of the cloud to a negatively charged region in the base of the cloud. The force coefficients F_1 through F_{10} in Eq. (7) are the same as in Davis (1964b), and the analytic expressions for them, which are complicated functions of $p = a/A$ and the distance between the two spheres, are given in Davis (1964a). Once $\vec{F}_{e,a}$ is found, the force on the A-sphere is, according to Davis (1964b), given by

$$\vec{F}_{e,A} = \vec{E}_0 (Q_A + Q_a) - \vec{F}_{e,a} \tag{8}$$

The choices of collector drop radii and Reynolds numbers were constrained by the facts that numerical flow fields of only certain Reynolds numbers were available, and that the collector drop radius and Reynolds number must satisfy the relations

$$\frac{c_{D,A} N_{Re,A}}{24}\, 6\pi\mu A V_{\infty,A} = m_A g^* - Q_A E_0 \tag{9}$$

$$V_{\infty,A} = \mu N_{Re,A}/(2A\rho) \tag{10}$$

where the minus sign in Eq. (9) is the result of our convention, which takes E_o as positive for an upward-pointing electric field. Note that according to Eq. (9), a change in the product $Q_A E_o$ requires a change in the Reynolds number if we wish to keep the collector drop radius constant.

Similarly, the collected drop radius and Reynolds number were constrained by the relations

$$\frac{c_{D,a} N_{Re,a}}{24\, C_{sc}}\, 6\pi\mu a V_{\infty,a} = m_a g^* - Q_a E_0 \tag{11}$$

$$V_{\infty,a} = \mu N_{Re,a}/(2a\rho) \tag{12}$$

Again, the choice of the collected drop radius was dictated by the available Reynolds number flow fields.

3. RESULTS

Equations (3) and (4) were numerically integrated using a stable Hamming predictor-corrector-modifier scheme which was accurate to fourth order. We chose to carry out the present computations for 800 mb and +10°C, for which $\mu = 1.768 \times 10^{-4}$ poise $\rho = 9.79 \times 10^{-4}$ g cm^{-3} and $\rho_w = 0.9997$ g cm^{-3}. We also set $g = 9.8 \times 10^2$ cm sec^{-2}. The initial vertical separation between the two interacting drops was chosen to be 70 collector drop radii. Larger initial vertical separations did not alter the trajectories.

In each case the trajectory computation was repeated until the "critical trajectory" for grazing contract of the two interacting spheres was found. This allowed us to determine the corresponding critical horizontal offset, R_c, of the center of the a-sphere from the center of the A-sphere when the a-sphere is 70 collector drop radii upstream. From a knowledge of R_c, $y_c = R_c/A$ could then be computed. From this the collision efficiency, defined by

$$E \equiv \frac{\pi R_c^2}{\pi (A+a)^2} = \frac{y_c^2}{(1+p)^2} \tag{13}$$

was determined.

Collision efficiencies were computed for collector drop radii $11.4 \le A \le 74.3$ μm and collected drop radii $1 \leq a \leq 66\ \mu m$. Shown in Figs. 1 and 2 are the present results for E for various electric charge and field combinations for collector drop radii of 19.5 and 61.7 μm, respectively. The results may be summarized by stating that external electric fields and electric charges residing on interacting cloud drops may have a profound effect on the collision efficiency of two interacting cloud drops.

4. LIST OF SYMBOLS

$\hat{e}_r$	unit vector pointing from center of large drop to center of small drop
$\hat{e}_\gamma$	unit vector perpendicular to e_r, in direction of increasing γ
m_A, m_a	mass of collector drop, of collected drop
Q_A, Q_a	electric charge on collector drop, on collected drop
q_A, q_a	charge parameter for collector drop $= Q_A/A^2$, for collected drop $= Q_a/a^2$
r	radial coordinate from center of sphere
$V_{\infty,A}$, $V_{\infty,a}$	terminal velocity of collector drop, of collected drop
$\vec{v}_A$, $\vec{v}_a$	instantaneous velocity of collector drop, of collected drop
ϵ	dielectric constant of air
λ	mean free path of air molecules
μ	dynamic viscosity of air
ρ	density of air
ρ_w	density of water

5. REFERENCES

Beard, K. V., 1974: Terminal velocity and deformation of rain drops aloft, Preprints, Cloud Phys. Conference, Tucson, Arizona, October 1974, Am. Meteorol. Soc., Boston, Mass.

Davis, M. H., 1962: The forces between conducting spheres in a uniform electric field, RAND Corp. Publ., RM-2607-10PR, Sept. 1962. [Available from Publications Dept., The RAND Corp., 1700 Main Street, Santa Monica, California 90406.]

Davis, M. H., 1964a: Two charged spherical conductors in a uniform electric field: Forces and field strengths, RAND Corp. Publ., RM-3860-PR Jan. 1964. [Available from Publications Dept., The RAND Corp., 1700 Main Street, Santa Monica, California 90406.]

Davis, M. H., 1964b: Two charged spherical conductors in a uniform electric field: Forces and field strength, Quart. J. Mech. and Appl. Math., 17, 499-511.

Davis, M. H., 1969: Electrostatic field and force on a dielectric sphere near a conducting plane--a note on the application of electrostatic theory to water droplets, Amer. J. Phys., 37, 26-29.

Grover, S. N., and Beard, K. V., 1975: A numerical determination of the efficiency with which electrically charged cloud drops and small rain drops collide with electrically charged spherical particles of various densities, J. Atmos. Sci., 32, 2156-2165.

LeClair, B. P., Hamielec, A. E., and Pruppacher, H. R., 1970: A numerical study of the drag on a sphere at low and intermediate Reynolds numbers, J. Atmos. Sci., 27, 308-315.

Lin, C. L., and Lee, S. C., 1975: Collision efficiency of water drops in the atmosphere, J. Atmos. Sci., 32, 1412-1418.

Mason, B. J., 1971: The Physics of Clouds, 2nd ed., Oxford University Press, London, 671 pp.

Proudman, I., and Pearson, J.R.A., 1957: Expansion at small Reynolds numbers for the flow past a sphere and a circular cylinder, J. Fluid Mech., 2, 237-262.

Pruppacher, H. R., LeClair, B. P., and Hamielec, A. E., 1970: Some relations between drag and flow patterns of viscous flow past a sphere and cylinder at low and intermediate Reynolds numbers, J. Fluid Mech., 44, 781-790.

Shafrir, U., and Neiburger, M., 1963: Collision efficiency of two spheres falling in a viscous medium, J. Geophys. Res., 68, 4141-4147.

Shafrir, U., and Gal-Chen, T., 1971: A numerical study of collision efficiencies and coalescence parameters for droplet pairs with radii up to 300 microns, J. Atmos. Sci., 28, 741-751.

Takahashi, T., 1972: Electric charge of cloud drops and drizzle drops in warm clouds along the Mauna Loa-Mauna Kea Saddle Road of Hawaii Island, J. Geophys. Res., 77, 3869-3878.

Takahashi, T., 1973: Measurement of electric charge on cloud drops, drizzle drops and rain drops, Revs. Geophys. Space Phys., 11, 903-924.

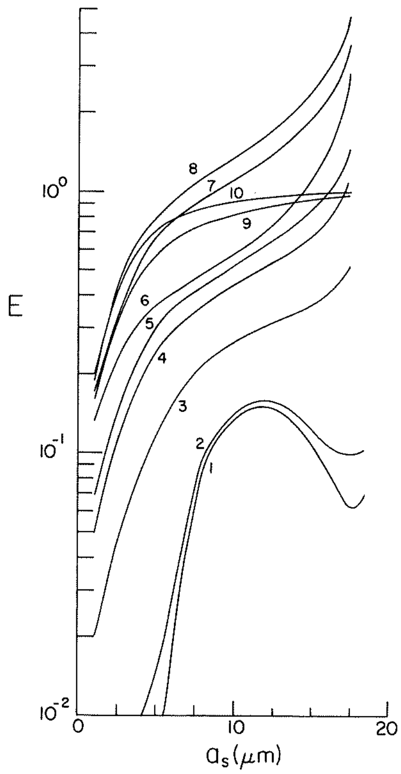

Figure 1. Present results for the efficiency with which a cloud drop of radius A = 19.5 μm collides with smaller cloud drop of radius a.

Curve	q_A (esu-cm^{-2})	q_a (esu-cm^{-2})	E_o (volts-cm^{-1})
1	0.0	0.0	0.0
2	±0.2	∓0.2	0.0
3	0.0	0.0	∓500
4	0.0	0.0	∓1000
5	0.0	0.0	∓1236
6	±2.0	∓2.0	0.0
7	0.0	0.0	∓2504
8	0.0	0.0	∓3000
9	±2.0	∓2.0	∓1236
10	±2.0	∓2.0	∓2504

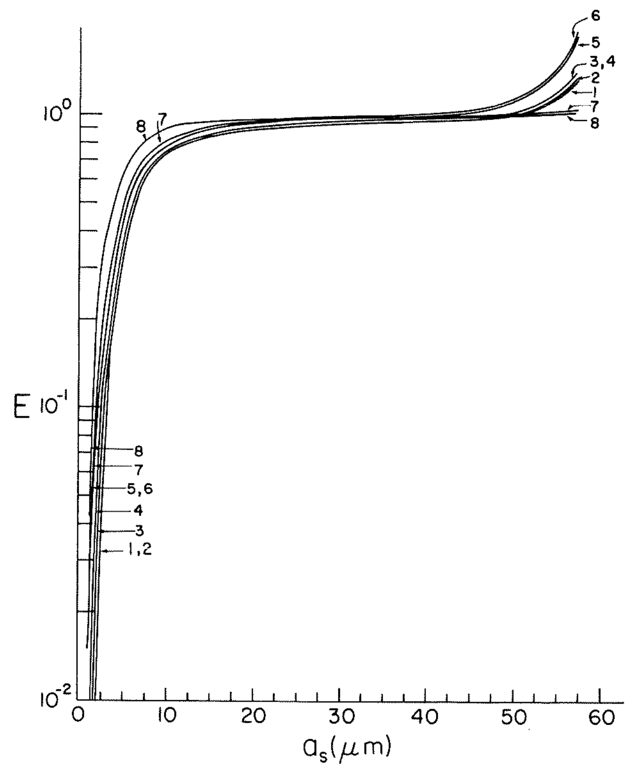

Figure 2. Present results for the efficiency with which a cloud drop of radius A = 61.7 μm collides with smaller cloud drop of radius a.

Curve	q_A (esu-cm^{-2})	q_a (esu-cm^{-2})	E_o (volts-cm^{-1})
1	0.0	0.0	0.0
	±0.2	∓0.2	0.0
2	0.0	0.0	∓500
3	0.0	0.0	∓907
	0.0	0.0	∓1000
4	±2.0	∓2.0	0.0
5	0.0	0.0	∓2842
6	0.0	0.0	∓3000
7	±2.0	∓2.0	∓907
8	±2.0	∓2.0	∓2842

EXPERIMENTAL STUDY OF THE COALESCENCE OF RAIN DROPS

Zev Levin and Benjamin Machnes

Dept. of Geophysics and Planetary Sciences*
Tel Aviv University
Tel Aviv, Israel.

1. INTRODUCTION

The importance of the collection processes in warm cloud development and in the determination of the rain drop spectra is well established. However, the phenomenon of collection is extremely complicated. It includes the hydrodynamic flow around the interacting drops, and, hence, their trajectories, and also the short range forces acting upon the drops when they are close together. These forces, resulting from the deformation of the approaching surfaces and the intervening air layer between them, often prevent the merger of the colliding drops (see Whelpdale and List, 1971, Levin et al, 1973, Foote, 1974, Park 1970). Due to the complexity of the problem it has been divided into two categories; (1) collision and (2) coalescence. The probability for each one to take place during an interaction is obtained separately so that their product represents the efficiency by which drops in free fall merge together.

A great deal of theoretical effort has been devoted to the collision problem of drop in free fall and to the determination of the collision efficiencies (eg. Hocking 1959, Shafrir and Neiburger 1964, Davis and Sartor 1967, and Klett and Davis 1972). However, all these computations assumed solid spheres or at least non-deformable ones, and hence could not be applicable to the situation in which the drops are close together - that is, to the problem of coalescence. Others such as Whelpdale and List (1971) (from here on this reference will be abbreviated as WL) Charles and Mason (1960) and others carried out experiments in which the hydrodynamic flow around the drops was minimized and so looked at the coalescence problem itself. They showed that the efficiency of coalescence is considerably smaller than unity (see WL and Levin et al, 1973). WL, for example, observed coalescence efficiencies which depend on the ratio of the radii of the interacting drops in the following way:

$$E = \frac{1}{(1+p)^2} \tag{1}$$

where $p = r/R$ and where r and R are the radii of the small and the large drop respectively.

Unfortunately their results were based on a limited number of drop radii and p ratios so that the extrapolation of their results to larger p ratios was only speculation. Considerably lower efficiencies were observed by Levin et al (1973) when smaller drop sizes and larger p ratios than WL were used. However, their results were based on measurements of collection and not on coalescence alone and therefore were forced to assume that the theoretical values of collision efficiencies were correct and so deduced the efficiency of coalescence. Recently Braizer-Smith et al (1972) investigated the separation conditions for interacting drops and the number of fragments so produced. However, their results were limited only to p ratios between 0.4-1 and, as a result of their experimental set up, did not eliminate the flow around both interacting drops.

Our aim in this work was to look at the problem of coalescence when a variety of drop sizes, impact angles (angle between the vertical and the line joining the centers of the drops when they touch), impact velocities and p ratios are used. From the results we get an empirical approximation to the coalescence efficiencies. In addition, since many interactions result in partial coalescence (where a fraction of the mass of the incoming droplet is transferred to the collector drop), we obtain an empirical relation that describes the dependence of the efficiency of partial coalescence on other parameters. Such empirical equations are badly needed in numerical models of clouds, and models describing the electrical development in them.

2. THE EXPERIMENT

In order to separate the problem of coalescence from that of the collision we used a similar approach to that of WL. In this experiment large drops were suspended from a small capillary tube. A small droplet generated by a drop generator, impacted the larger drop on its lower hemisphere. Viewing the interactions from two perpedicular directions permitted the identification of the angle of impact. The interactions were simultaneously photographed by a 35mm camera and by a television camera. This method of viewing was thought to be an improvement over the method used by WL who observed the interaction from a single direction and, hence, could have had difficulties in determining the exact impact angle. As will be shown later the impact angle is an important parameter for the coalescence and uncertainty in its determination could lead to great inaccuracies. In order to separate the collision from the coalescence problem one has to eliminate the flow around the interacting drops. This is an impossible task. However, the method used by WL and also used here seems to be a close approximation to it.

*Formerly called: Environmental Sciences Dept.

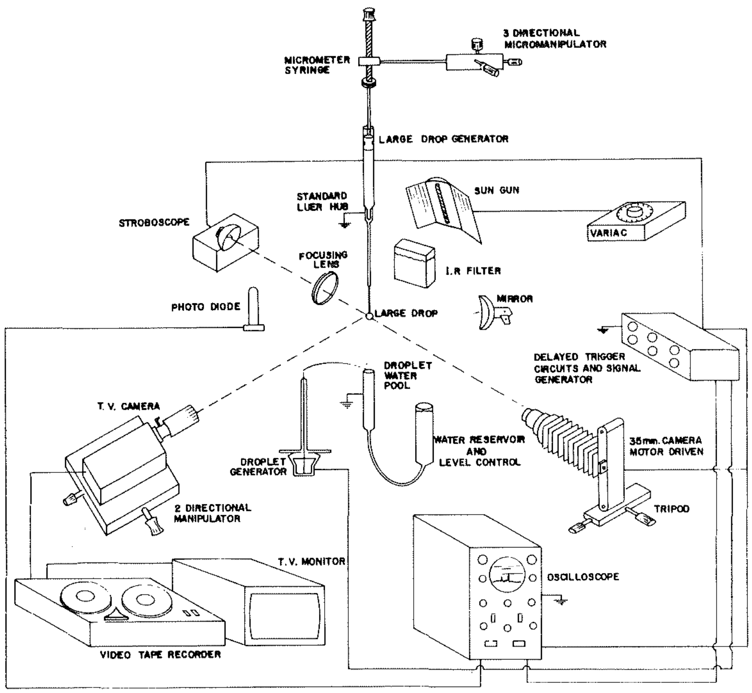

Figure 1. A schematic diagram of the experimental set up.

When a small drop approaches a larger falling drop it enters the region of the boundary layer of the larger drop. Within this region the flow decreases as one approaches the drop surface. For large drops the flow does not diminish at the surface due to internal circulation in them. However, as the drops approach each other the flow between them is probably controlled by the drainage of the intervening air layer. This drainage depends on the speed of the approaching drops and their deformation. It seems therefore that the experiment of WL and the one proposed here are applicable to interaction of drops in the atmosphere, at least for small p ratios. At larger p ratios and larger drops it is possible that the leading surface of the smaller droplet enters the boundary layer while the other side is still affected by the air flow further out. In such a situation the flow will tend to move the droplet sideways and reduce the probability of coalescence. Hence for such cases the results that we obtain here can be considered as an upper limit to the coalescence efficiency.

3. THE APPARATUS

Figure 1 is a schematic diagram of the experimental set up. The size of the larger collector drop was controlled by a micrometer syringe and could be varied from 200 microns to over 2.5mm in diameter. Its position in space could be changed by a micromanipulator. The smaller droplet was generated by a drop generator similar but more powerful than that of Abbott and Cannon (1972). The generator consists of an acoustic suspension speaker with a metal rod connected to the center of its cone. The other side of the rod is bent and immersed in a water bath. An electrical pulse of know amplitude and shape pushes the speaker's cone up and forces the rod out of the water and produces a droplet. The droplet size is controlled by the size of the rod, the pulse shape and its amplitude. It was constructed in such a way as to be able to eject vertically upward single small droplets. The genrator was directed with a slight angle to the vertical and therefore ejected droplets in a parabolic trajectory. This trajectory prevented the droplets from falling back into the water reservoire and disturbing the next generated droplet. By positioning the large drop at different heights along the upward trajectory of the droplet different impact velocities were obtained. By horizontally varying the position of the collector drop the impact angles could be varied. Each interaction was simultaneously photographed on a 35mm film and recored on a video tape by a television camera which was mounted at a right angle to the viewing direction of the still camera. The interation zone was illuminated by a continuous flood light (1000w) with a water filter in front, and by a stroboscope flashing at exactly 1000 cycles per sec. The position of the flood light and the stroboscope were at 160° and 180° from the direction of observation of the 35mm camera.

Once the position of the trajectory was determined the electronic circuit was triggered. The drop generator was the first to be triggered and was followed after pre-set delays by the opening of the camera's shutter and ten flashes of the strobe. Then the camera shutter was closed automatically and the film advanced. During this whole period the television camera continuously recorded the entire event.

By adjusting the position of the impact place so that collisions would occur at precisely the vertical great circle of the collector drop and in the focal plane of the camera, the exact angle and drop size could be determined from the photographs. The impact velocity was determined from the distance between successive light spots on the film. The exact trajectory was determined from the streak produced by the droplet due to the continuous illumination by the flood light.

Both the collector drop holder and the droplet generator were grounded. This eliminated electrical charges from the collector drop but not from the droplets. However, it was estimated that the maximum charge they carried did not exceed 10^{-5} esu and, hence, was believed to have little effect on the coalescence (eg. Neiburger et al, 1974).

4. RESULTS

About 8000 photographs were taken out of which over 3000 were found adequate for analysis. Collisions studied could be classified into three types: (1) those resulting in full coalescence, (2) those resulting in bouncing and (3) those resulting in partial coalescence. The difference between the first and the last two types of interactions could easily be identified from the photographs. However, the differences between the

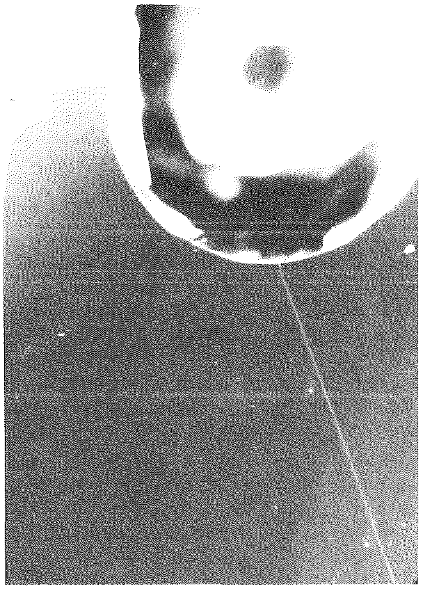

Figure 2. Coalescence event of two drops 2200 and 110 microns diameter impacting at a velocity of 1.1m/sec and angle of 38°.

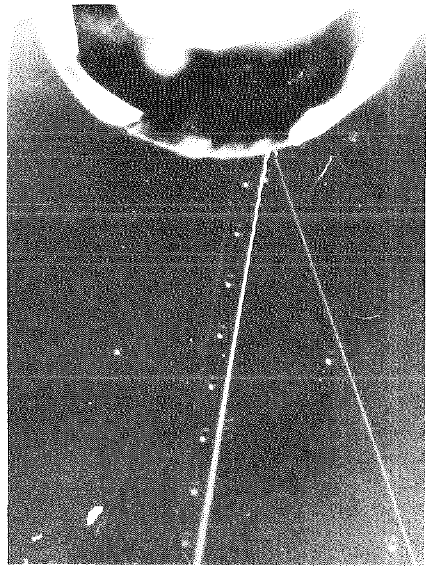

Figure 3. A bouncing of two drops 2180 and 130 microns diameter impacting at a velocity of 1.0m/sec and an angle of 8°.

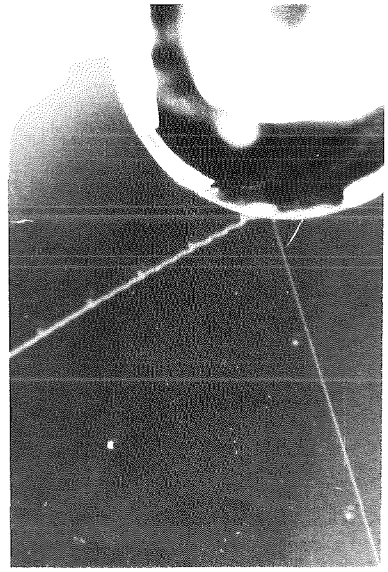

Figure 4. A partial coalescence event when drops of 2160 and 120 microns diameter impact at a velocity of 0.5 m/sec and an angle of 29°. After separation the smaller droplet has a diameter of 80 microns and a velocity of 0.34 m/sec.

last two types was more difficult to resolve. Partial coalescence events where identified as such when the size of the outgoing droplet was smaller than its original size before impact. However, since differences of only about 20 microns in diameter could be resolved, many interaction which actually resulted in partial coalescence may have been classified as bounce. This may mean that the efficiency of partial coalescence we obtained actually represents a lower bound.

Figures 2, 3, and 4 represent interactions which resulted in coalescence, bounce, and partial coalescence respectively (details are given in the figure captions).

Measurements were carried out at a variety of impact angles, impact speeds, and a variety of drops' and droplets' sizes. Within the velocity range (0.15 - 2.5m/sec) tested in our experiment coalescence was negligibly affected by changes in the impact velocity. These velocities included many cases where the impact velocity was equal to the relative terminal velocities of the drops in the atmosphere (Gunn and Kinzer, 1949). Hence data were grouped according to drop size and drop size ratio (p). Figure 5 is an example of the dependence of coalescence (percent of coalescence events out of total number of interactions within a range of impact angles) on impact angle. This figure together with all others, not represented here, show the dramatic dependence of the coalescence on impact angle. They all show that the coalescence probability decreases as the impact angle increases.

Partial coalescence was also strongly dependent on angle of impact but was found to occur primarily between 45° and 67°. Only a relatively few partial coalescence events were observed outside this range.

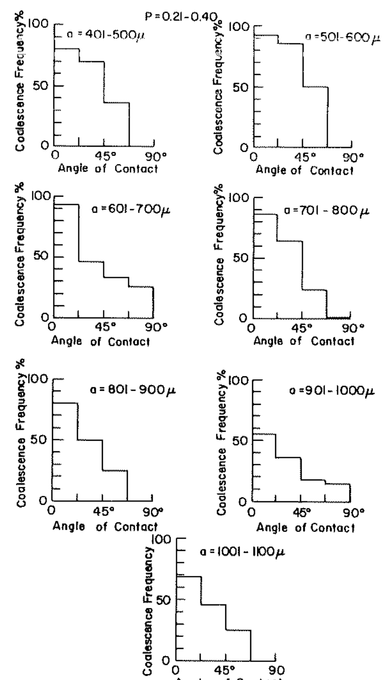

Figure 5. The frequency of coalescence events as a fraction of impact angle. a represents the diameter of the drops.

In order to evaluate the coalescence efficiency we followed a similar procedure to that used by WL. The contribution to the coalescence efficiency of each impact angle interval (22.5°) is computed by the product of the coalescence frequency at that interval and the horizontal projected area of the collector drop seen by the incident droplets. Figure 6 is a representation of the coalescence efficiency as a function of p ratio. It is observed that the efficiency decreases as p increases in general agreement with WL and Levin et al (1973). However, contrary to these works, a dependence of the coalescence efficiency on the size of the collector drop is also observed. Figure 7 is a three dimensional plot of the coalescence efficiency as a function of R and p. The points represent the present experimental results while the curves represent a best fit to the surface. This surface is found to be:

$$E_{coalesce} = 0.65 - 2.08 \times 10^{-3}\, pR + 6.56 \times 10^{-4} p^2 R + 6.07 + 10^{-7}\, pR^2 + 1.17 \times 10^{-2} p^2 - 9.3 \times 10^{-8} R^2 \tag{2}$$

where R is in microns.
In a similar way the analysis of the partial coalescence was carried out. Due to lack of enough data of partial coalescence in each drop size, all the data were merged in order to resolve the dependence of the partial coalescence efficiency on the ratio of the drop size (p ratio). The following equation resulted from a best fit to the data:

$$E_{partial\ coalesce} = 0.22 - 0.23p - 0.025p^2 \tag{3}$$

where here p is restricted to values vetween 0 and 0.87. When Eq. (2) is compared to Eq. (1) it is seen that the coalescence efficiencies predicted by Eq. (2) are lower than those predicted by Eq. (1) for very low and very high p ratios, but are higher than Eq. (1) in other regions. Such differences could be of extreme importance in the development of the size distribution in or below cloud level. To see these possible differences and their effects on the development of the droplet spectrum, the efficiencies predicted by Eqs. (1) and (2) were compared to $E_{coalesce} = 1$ in a stochastic numerical model similar to that of Scott and Levin (1975) except without the effect of electrification. The results are shown in Fig. 8 where G represents the mass of water in gram per m^3 per ln r. It is seen that for E = 1 the spectrum develops very rapidly. When Eq. (1) is used a considerable decrease in the conversion of cloud water to rain water is observed. When Eq. (2) is used an intermediate rate is observed. Of course in this comparison we assumed that the present results and those of WL are applicable to all drop sizes considered in the model. This of course is an extrapolation but it is felt that since the present results show some dependence on size they might be more representative of the actual situation.

Acknowledgment: This work was supported by the European Research Office under Grant No. DA-ERO-124-74-G0058.

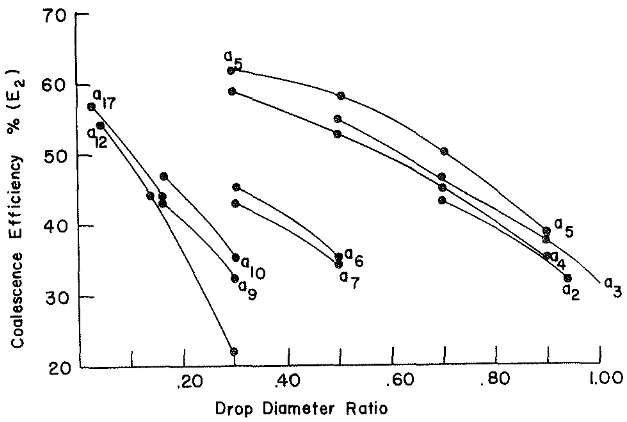

Figure 6. The coalescence efficiency as a function of the ratio of drop diameter for a few drop diameters, $a_2 = 200\mu$, $a_3 = 300\mu$, $a_4 = 400\mu$ and so on.

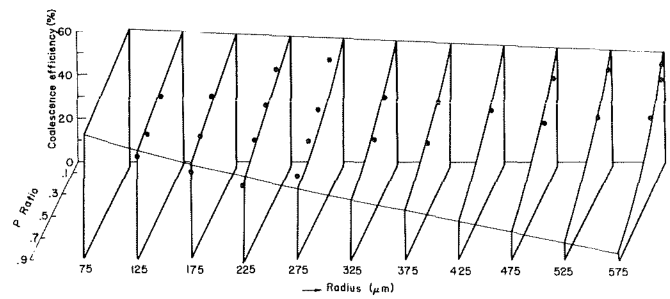

Figure 7. The dependence of the coalescence efficiency on the radius of the larger drop and on p ratio. The dots represent the experimental data and the surface represents Eq. 2.

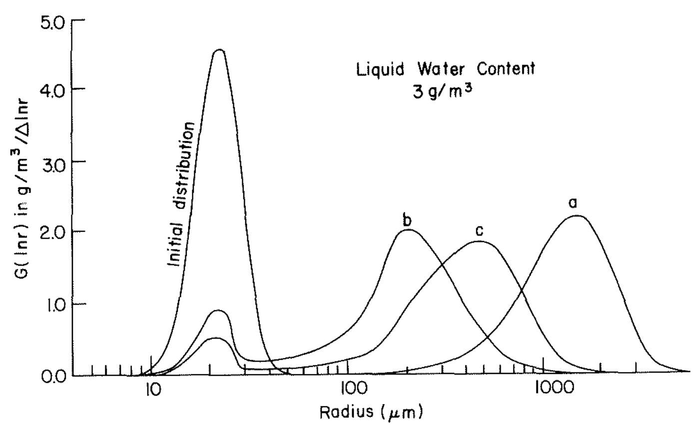

Figure 8. The development of the size spectra after 600 seconds in a stochastic numerical model. (a) $E_{coalesce} = 1$ (b) E as in Eq. 1. (c) as in Eq. 2.

REFERENCES

Abbott, C.E. and T.W. Canon, 1972: A droplet generation with electronic control of size production rate and charge. Rev. Sci. Instr. 43, 1313-1317.

Braizer-Smith, P.R., S.G. Jennings and J. Latham, 1972: The interaction of falling water drops: coalescence. Proc. Roy. Soc. London, A326, 393-408.

Charles, G.E. and S.G. Mason, 1960: The coalescence of liquid drops with flat liquid/liquid interfaces. J. of Colloid Sci., 15, 236-277.

Davis, M.H. and J.D. Sartor, 1967: Theoretical collision efficiencies for small cloud droplets in Stokes flow. Nature, 215, 1371-1372.

Foote, B.G., 1975: The water drop rebound problem: Dynamics of collision. J. of Atm. Sci., 32, 390-402.

Gunn, R. and G.D. Kinzer, 1949: The terminal velocity of fall for water droplets in stagnant air. J. Met., 6, 243-248.

Hocking, C.M., 1959: Theoretical collision efficiencies of small drops. Quant. J. Roy. Met. Soc., 85, 44-50.

Klett, J.D. and M.H. Davis, 1972: Theoretical collision efficiencies of cloud droplets at small Reynolds numbers. J. Atmos. Sci., 30, 107-117.

Levin, Z., M. Neiburger and L. Rodrignez, 1973: Experimental evaluation of collection and coalescence efficiencies of cloud drops. J. of Atm. Sci., 30, 944-946.

Neiburger, M., I.Y. Lea, E. Lobl and L. Rodniguez, 1974: Computed collision efficiencies and experimental collection efficiencies of cloud drops. Conf. Cloud Physics, Tucson, Ariz., Amer. Meteor. Soc. 73-78.

Park, R.H., 1970: Behavior of drops colliding in humid Nitrogen. Ph.D. dissertation, Univ. of Wis.

Scott, W.D. and Z. Levin, 1975: A stochastic electrical model of an infinite cloud: charge generation and precipitation development. J. Atm. Sci., 32, 1814-1828.

Shafrir, U. and M. Neiburger, 1964: Collision efficiencies of two spheres falling in viscous medium. J. Geophy. Res., 68, 4141-4143.

Whelpdale, D.M. and R. List, 1971: The coalescence process in raindrop growth. J. Geophy. Res. 76, 2836-2856.

THE EFFECT OF ELECTRIC CHARGES AND FIELDS ON THE COLLECTION EFFICIENCY OF CLOUD DROPS[1]

Elena S. Lobl

Meteorology Research, Inc.
Altadena, California

1. INTRODUCTION

The initiation of "warm rain" precipitation from clouds that are entirely at temperatures above 0° C, is attributed solely to the collision and coalescence of cloud drops. The collection efficiency, E, defined as the ratio of the number of droplets collected to the number of droplets in the volume swept out by the falling large drop, is the critical parameter in the collection process. Collection efficiency is the product of collision efficiency, E_s, and coalescence efficiency, E_ℓ. Most of the research so far, both numerical and experimental, has investigated the collision process. The numerical studies differ in the computation schemes and the assumptions used. Their results are close for collector drops with radii, A, larger than 40μ. The differences appear in the collision efficiency versus p-ratio (ratio of the cloud droplet radius to the collector drop radius) curves for $A < 40\mu$.

Experimentally, E is measured and compared to E_s, always assuming that E_ℓ is unity. The results obtained by Picknett (1960), Woods and Mason (1964), Beard and Pruppacher (1971), and Abbott (1974) agree with the computed E_s. The Neiburger-Levin group results obtained with the University of California, Los Angeles cloud tunnel (1972, 1973) has found E's much lower than the computed E_s.

The coalescence process was investigated by Whelpdale and List (1971). They conclude: "It is no longer considered adequate to assume a coalescence efficiency of unity for all drop-droplet collisions." Park (1971) studied the coalescence process in detail, concluding that smaller drops coalesce more readily, and at smaller relative velocities, than larger drops. Interactions between equal size drops were sutdied theoretically by Foote (1971) and experimentally by Brazier-Smith, Jennings and Latham (1972).

So far we mentioned interactions between electrically neutral drops. Lindblad and Semonin (1963), and later Plumlee and Semonin (1965) and Semonin and Plumlee (1966), have investigated the electric charges and fields effects on the collection process. They, as well as other researchers (Davis and Sartor, 1968; Sartor, 1970; Paluch, 1970), have found an increase in growth due to an increase in the collision efficiency as an effect of the electrical forces between drops. The latest experimental result (Dayan and Gallily, 1975) is an increased efficiency with an increase of the p-ratio, and no variation with a change in electric charges on the drops.

2. STATEMENT OF THE PROBLEM

From observations it is known that heavy precipitation can fall from warm clouds in just a few hours following the formation of the cloud. The condensation process produces the cloud droplets with radii, a, up to 15μ. Beyond this radius, the growth of the drops is mainly due to the collection process. The computed collection efficiency for the cloud droplets is small. The question we seek to answer is whether electric charges on the droplets, or electric fields of reasonable magnitude can result in the increase of the collection efficiencies to values that will permit the collector drops to grow to precipitation size in a reasonable time. (Reasonable magnitude has here the meaning of electric charges and fields found in a fair weather growing cloud.)

3. CLOUD TUNNEL EXPERIMENTS

The experiments reported in this paper were conducted in the UCLA cloud tunnel (Pruppacher and Neiburger, 1968). Minor modifications were needed in order to be able to stabilize small collector drops ($20\mu \leq A < 40\mu$). Figure 1 shows a layout of the tunnel and the modifications made. The cloud introduced in the tunnel was produced with a De Vilbiss ultrasonic nebulizer (Model 800/882). The electrometer used to measure the charge on the drops was described by Scott and Levin (1970). The liquid water content, lwc, was evaluated with a Cambridge Systems dew point hygrometer (Model 992-4). The collector drops were produced with a modified version of the drop generator described by Abbott and

[1] Research submitted in partial satisfaction of the requirements for the Ph. D. degree in Meteorology at the University of California at Los Angeles, 1975.

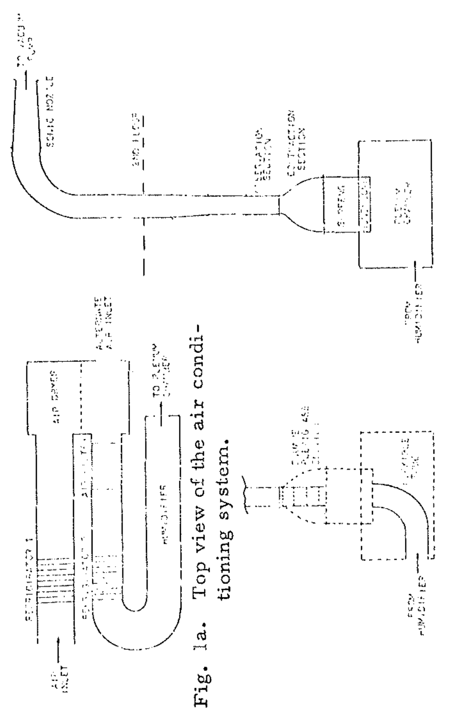

Fig. 1a. Top view of the air conditioning system.

Fig. 1b. Side view of the air flow system.

Fig. 1c. Modifications to the air flow system.

Cannon (1972). The charge and size of the collector drops were varied by adjusting the hood potential, P_H, and the size of the needle forming the drop, respectively. The influence of the electric field on the collection process was tested inside an "inner tunnel" where a uniform electric field could be produced. The design and theoretical background to the calculations of the electric field are described by Cannon and Davis (1971).

The experimental procedure consisted of the following sequence of events:

(1) Measurement of the initial charge of the collector drop was done with the electrometer. Ten drops of known size and with a certain P_H were produced. The size of the collector drops was known from a photographic calibration of the size of drops suspended versus speed of the air inside the tunnel. The charge of the drops was measured in a cloudless tunnel (RH < 95%).

(2) A cloud was produced and a collector drop generated with a similar charge and size to the drops measured in (1).

(3) The drop was suspended and its growth observed. The records of the growth started at the instant the drop was in the observation position, where its terminal velocity matched the updraft speed in the tunnel. A change in the updraft speed needed to keep the drop in the same position meant a change in the drop's terminal velocity and, hence, its size.

(4) After an appropriate growth time (~ 5 min), the nebulizers were turned off, preparing for the final charge measurement. The dV/dt and lwc were monitored continuously, noting the time when the visual cloud disappeared.

(5) Final charge of the collector drop was measured.

The electric field experiments were conducted in a similar fashion. The potential was applied on the rings once the drop was suspended in the observation position inside the inner tunnel.

4. RESULTS

The collection efficiency E was evaluated from the observed rate of growth of the collector drop from one or the other of two equations, depending on whether the rate of collection of the cloud droplets was so rapid that the process could be regarded as continuous, or was so slow as to require each collection of a droplet to be considered as a discrete event.

For the continuous case E is given approximately by

$$E_{cont} = \frac{4\rho}{\mathrm{lwc}\,(1+p)^2(V-v_{\bar{a}})}\,dA/dt \qquad (1)$$

where ρ is the water density at STP and lwc is the liquid water content experienced by the drop in the observation section. The mode radius $\bar{a}$ of the droplet spectrum was used. The terminal velocity V of the collector drop of radius A, and that of a droplet of radius $\bar{a}$, $v_{\bar{a}}$, were obtained using the expressions for the drag experimentally found by Beard and Pruppacher (1969).

For the case of discrete droplet collections

$$E_{disc} = \frac{1}{\bar{N}\,\pi(\bar{A}+\bar{a})^2(V_A - v_{\bar{a}})\,\Delta t} \qquad (2)$$

The collection efficiency in a discrete growth is the probability of one droplet colliding and coalescing with the collector drop in the time interval Δt, when the collector drop is suspended in a cloud of droplets with a number density $\bar{N}$.

It was found empirically that the initial charge induced on the collector drop followed the relationship $q = CA^{n(P_H)}$ where C = 0.75 and $n(P_H)$ varied between 2.10 and 1.35 for zero and 700 V hood potential (P_H). This result corresponds somewhat with Colgate and Romero's (1970) and Twomey's (1956) findings ($q \propto A^2$). The initial charge on the collector drop was slowly lost during the drop's growth. Figure 2 illustrates the rate of charge loss found experimentally for different initial charges. This graph allowed us to evaluate the charge on the collector drop at any time during its growth.

The following six graphs are examples of the experimentally found collection efficiencies versus charge. The main feature of most of these graphs is the collection efficiency less than the computed collision efficiency (marked by the X on the ordinate). In Figure 3 the collector drop size is between 20 and 23μ. It was difficult to produce charge-free ($q < 0.4 \times 10^{-4}$ esu) collector drops of this size. E_x varies as expected, increasing with increasing charge. The following four figures, Figures 4-7, show E_x versus q_A for drops with $29\mu < A < 44\mu$ and $0.2 < p < 0.3$. The collection efficiency in all these graphs starts at values lower than the computed collision efficiency, and increases with an increasing charge. Figure 8 is an example of a 80-83μ drop, p = 0.25. The collection efficiency increase with charge at first stays constant between $0.3 \times 10^{-4} < q < 9 \times 10^{-4}$ esu, and increases rapidly for larger charges.

Table 1 presents the results obtained for the effect of the electric field on the collection efficiency.

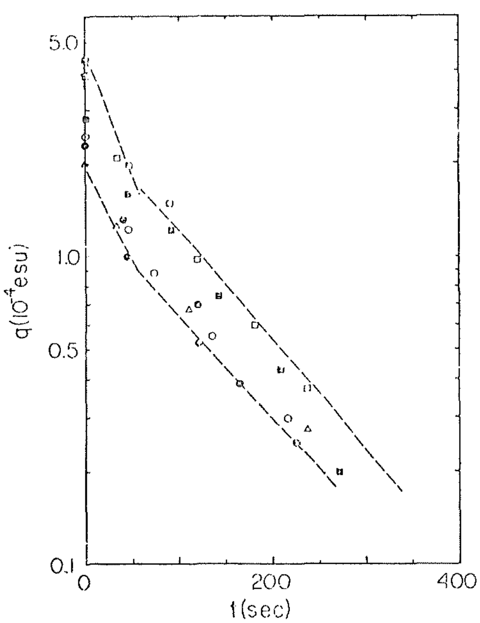

Fig. 2. Charge remaining on the collector drop after a time t has elapsed. The different symbols represent the measurements of charge for different initial charges on the drop.

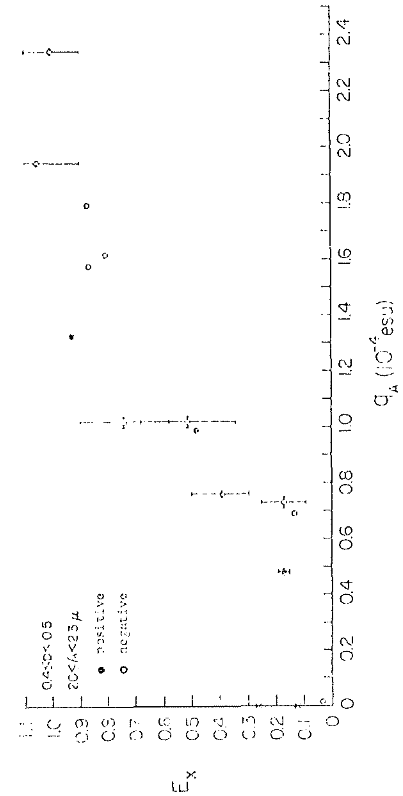

Fig. 3. Experimental collection efficiency vs. collector drop charge.

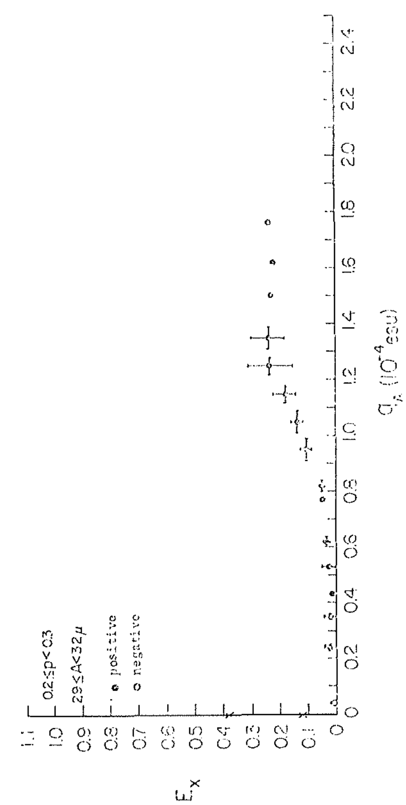

Fig. 4. Experimental collection efficiency vs. collector drop charge.

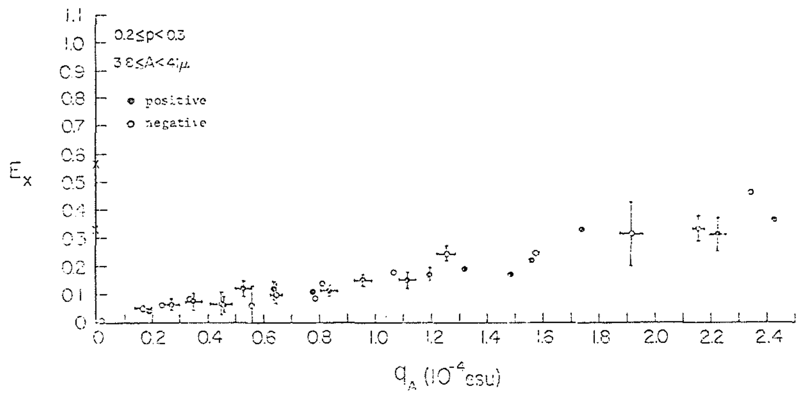

Fig. 6. Experimental collection efficiency vs. collector drop charge.

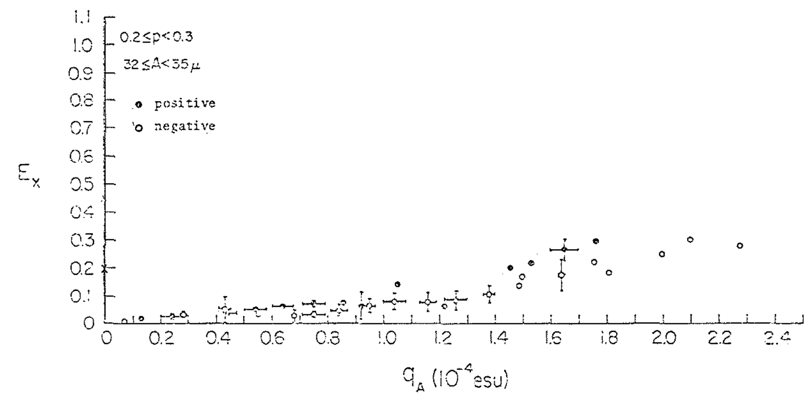

Fig. 5. Experimental collection efficiency vs. collector drop charge.

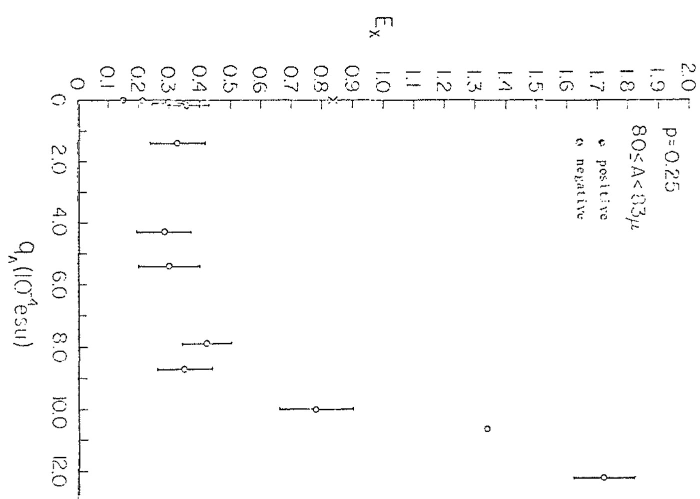

Fig. 8. Experimental collection efficiency vs. collector drop charge.

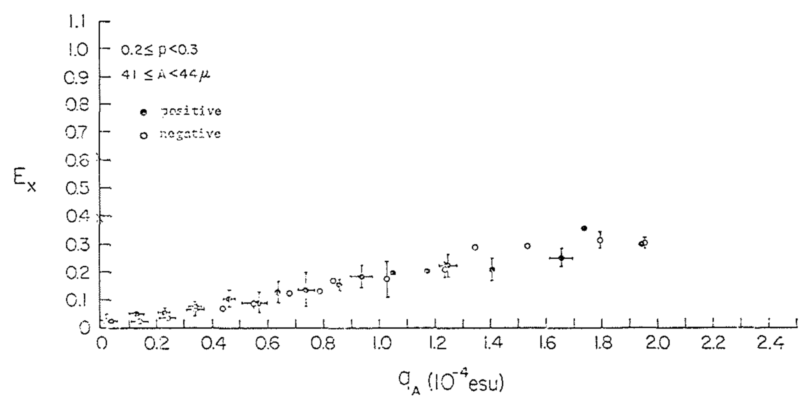

Fig. 7. Experimental collection efficiency vs. collector drop charge.

Table 1

A $0 \le q \le 10^{-4}$ esu

$A(\mu)$	ϵ(V/cm) 0	50	100	150	200	250	300	350	400	450
41-44	.05	.06								.04
44-47	.07	.07		.07		.06		.07		.09
47-50	.09	.08	.06	.08	.11	.03				
50-53	.07	.05	.08		.07	.05				
53-56	.07	.08	.06	.07	.07	.07				
56-59	.08	.06	.08			.06				
59-62	.10									

B $10^{-4} < q \le 2 \times 10^{-4}$ esu

$A(\mu)$	ϵ(V/cm) 0	50	100	150	200	250
47-50				.18		.19
50-53	.07	.08		.16		
53-56	.12	.13	.06	.15	.14	
56-59	.07	.12	.09	.17	.14	.10
59-62	.07	.11	.06		.09	.09

C $2 \times 10^{-4} < q \le 3 \times 10^{-4}$ esu

$A(\mu)$	ϵ(V/cm) 0	50	100	150	200
47-50	.10	.12			
50-53	.14	.14	.14	.19	.21
53-56	.12	.07	.13		
56-59	.10	.15	.12		.15

5. CONCLUSIONS

There is no reason to believe that the calculated collision efficiencies are not correct. Thus, the obvious conclusion from the results obtained in the present research is that bouncing occurred for small charge drop interactions. For uncharged drops, Foote's theoretical study predicts that bouncing occurs when the drops approach at a speed lower than a certain value. For two equal drops 600μ in radius, he found the threshold relative velocity to be 40 cm/sec. Is this critical relative velocity drop size dependent? In a qualitative argument it can be shown that for the same relative velocity larger drops deform more, trapping a larger volume of air, but also having the radial velocity (the velocity due to the motion of the drop surface while deforming) enhance drainage. Smaller drops deform less, trapping less air but also not having the high radial velocity to help drainage. Thus, it seems possible that thinning time, and thus the decision between bouncing and coalescence, rests entirely on the relative velocity between the colliding drops. In our research the experiments yielding low collection efficiencies were conducted with drops interacting at relative velocities lower than 40 cm/sec.

The motivation in undertaking this study was to elucidate the process by which cloud drops grow to precipitation size in warm clouds. While certain aspects of the problem have been clarified, the essential question remains.

(1) We have seen that in the absence of electric effects the experimental collection efficiency for small drops, in the range 20μ to 40μ radius, is less than the computed collision efficiency.

(2) Except possibly for drops smaller than 25μ, the charges found on drops in natural clouds are insufficient to bring the coalescence efficiency to unity.

(3) Electric fields of magnitudes that may be expected in the early stages of cumulus development have no effect on the collection efficiency of drops with charges such as are found on drops in natural clouds.

(4) The charges and fields required to raise the collection efficiency above the computed collision efficiency are much larger than those that occur in the early stages of the development of cumulus clouds.

Thus it would appear that one must turn to other factors in the attempt to explain warm rain. One possibility that may contribute to the answer lies in the collection efficiency of nearly equal drops, which has been found by Abbott (1974) to be large even for drops as small as 25μ in radius.

Our results, together with the results found by Abbott, should be taken into consideration in cloud models simulating warm clouds. If electrical and shear effects are not included in the model, then the collection efficiency of droplets that have reached 25μ should be corrected for the smaller than unity coalescence efficiency found in our experiments.

6. REFERENCES

Abbott, C. E., 1974: Experimental cloud droplet collection efficiencies. J. Geophys. Res., 79, 3098-3100.

Abbott, C. E. and T. W. Cannon, 1972: A droplet generator with electronic control of size, production rate and charge. Rev. Sci. Instr., 43, 1313-1317.

Beard, K. V. and H. R. Pruppacher, 1969: A determination of the terminal velocity and drag of small water drops by means of a wind tunnel. J. Atmos. Res., 26, 1066-1072.

Beard, K. V and H. R. Pruppacher, 1971: A wind tunnel investigation of collection kernels in small water drops in air. Quart. J. Roy. Meteor. Soc., 97, 242-248.

Brazier-Smith, P. R., S. G. Jennings and J. Latham, 1972: The interaction of falling water drops: coalescence. Proc. R. Soc. Lond., A, 326, 393-408.

Cannon, T. W. and M. H. Davis, 1971: Calculation of the Electrostatic Field within a Structure of Uniformly Spaced Coaxial Conducting Loops, NCAR-TN/STR-59, NCAR Technical Notes, Boulder, Colorado.

Colgate, S. A. and J. M. Romero, 1970: Charge versus drop size in an electrified cloud. J. Geophys. Res., 75, 5873-5881.

Davis, M. H. and J. D. Sartor, 1968: Fast growth rates for cloud droplets due to electrical forces in thunderstorms. Planetary Electrodynamics, Coroniti and Hughes, p. 339.

Dayan, N. and I. Gallily, 1975: On the collection efficiency of water droplets under the influence of electric forces I: experimental, charge-multiple effects. J. Atmos. Sci., 32, 1419-1429.

Foote, G. B., 1971: A theoretical investigation of the dynamics of liquid drops. Ph.D. Thesis, Dept. of Atmospheric Sciences, University of Arizona.

Levin, Z., M. Neiburger and L. Rodriguez, 1973: Experimental evaluation of collection and coalescence efficiencies of cloud drops. J. Atmos. Sci., 30, 944-946.

Lindblad, N. R., and R. G. Semonin, 1963: Collision efficiency of cloud droplets in electric fields. J. Geophys. Res., 68, 1051-1057.

Neiburger, M., Z. Levin and L. Rodriguez, 1972: Experimental determination of the collection efficiency of cloud drops. J. de Rech. Atmos, VI, 391-397.

Paluch, J. R., 1970: Theoretical collision efficiencies of charged cloud droplets. J. Geophys. Res., 75, 1633-1640.

Park, R. W., 1971: Behavior of water drops colliding in humid nitrogen. Ph.D. dissertation, Dept. of Chemical Engineering, University of Wisconsin.

Picknett, R. G., 1960: Collection efficiencies for water drops. Intern. J. Air Pollution, 3, 160-168.

Plumlee, H. R. and R. G. Semonin, 1965: Cloud droplet collision efficiency in electric fields. Tellus, 17, 356-364.

Pruppacher, H. R. and M. Neiburger, 1968: Design and performance of the UCLA Cloud Tunnel. Proc. of the Inter. Conf. on Cloud Physics, Toronto, Canada, Aug. 26-30, 389-392.

Sartor, J. D., 1970: Accretion rates of cloud drops, raindrops, and small hail in mature thunderstorms. J. Geophys. Res., 75, 7547-7558.

Scott, W. D. and Z. Levin, 1970: The effect of potential gradient on the charge separation during interaction of snow crystals with an ice sphere. J. Atmos. Sci., 27, 463-473.

Semonin, R. G. and H. R. Plumlee, 1966: Collision efficiencies of charged cloud droplets in electric fields. J. Geophys. Res., 71, 4271-4278.

Twomey, S., 1956: The electrification of individual cloud droplets. Tellus, 7, 445-451.

Whelpdale, D. M. and R. List, 1971: The coalescence process in raindrop growth. J. Geophys. Res., 76, 2836-2856.

Woods, J. D. and B. J. Mason, 1964: Experimental determination of collection efficiencies in small water droplets in air. Quart. J. Roy. Meteor. Soc., 90, 373-381.

THE ONSET AND EARLY GROWTH OF SNOW CRYSTALS BY RIMING*

Roger F. Reinking

U. S. Department of Commerce, NOAA/ERL
Weather Modification Program Office, Boulder, Colorado

1. INTRODUCTION

The growth of snow crystals by riming begins after crystal growth by vapor deposition has progressed for some time. The time elapsed between nucleation of an ice crystal and the onset of droplet accretion is dependent on crystal size and habit of growth, and upon the presence and size distribution of supercooled droplets in the cloud. The size and duration of growth of snow crystals prior to versus after the onset of accretion, and prior to versus after the accumulation of significant rime, are important factors in determining the efficiency with which clouds develop precipitation.

A shift in the relative emphasis on the two processes contributing to the ice crystal growth begins with the onset of riming. The depositional and accretional modes of growth are additive but competitive. The total mass growth rate of a snow crystal is represented by the sum of the contributions from each process, with deposition accounting for the total until the onset of riming. The process of deposition tends to suppress accretion by drawing vapor from cloud droplets. A sufficiently active deposition process can deplete droplet size and population to the point that accretion is prevented. To the contrary, the rate at which liquid water is supplied to supercooled portions of cloud may be sufficient to sustain droplet growth. Crystals are then likely to grow by accretion as well, once they have gained sufficient size to efficiently collect droplets. The droplets accreted and frozen represent direct gains of mass by the crystals, but they also represent a loss from the vapor source for further depositional crystal growth.

The accumulation of significant rime can substantially increase the terminal velocity of a crystal otherwise growing deposition. This increases crystal ventilation and so must enhance the rate of deposition. On the other hand, this velocity effect decreases the residence time of crystals in the cloud. This in turn decreases the time available for depositional growth while possibly more than compensating through additional riming. The increase in terminal velocity due to accretion also results in crystal fallout nearer the position in cloud where the crystals nucleate; in some situations this phenomenon may prevent crystals from blowing into clear air where they could evaporate before precipitating (Reinking, 1975a).

Hallett and Mossop (1974) have experimentally demonstrated that "copious" secondary ice particles are produced as ice particles grow by riming in clouds at temperatures between about -3 and -8 C, when the relative velocity of ice particles and droplets exceeds about 0.7 m sec^{-1}. By means of a simple cloud model that incorporates this mechanism of ice particle generation, Mason (1975) has shown that it is "at least plausible" to produce ice crystal concentrations of the order of 10/ℓ, corresponding to a multiplication factor of 10^4. Thus the onset of riming may signal the start of secondary ice particle production by droplet splintering. The quantities of secondary ice particles produced may be regulated by the accretion rate and therefore by the duration of crystal growth required to accumulate sufficient rime to enhance crystal fallseed and accelerate riming. Jiusto and Lavoie (1975) have concluded that "the riming concept and its further refinement should rank high on or head the priority list for [studies to explain] ice multiplication," and "the critical size and time for riming onset must be considered." Overall, the water budget of a mixed-phase cloud may be as much determined by the process of accretion as by deposition.

In this paper, the onset and early stages of riming of snow crystals are described from field measurements. The study is based on snow crystal data collected during orogenic winter storms of the central Sierra Nevada. Riming on snow crystals with each of the basic growth habits is investigated. For certain types of crystals, some agreement with and some deviations from the empirical results of Ono (1969), Wilkins and Auer (1970) and Iwai (1973) and the theoretical conclusions of Hindman and Johnson (1972), Pitter and Pruppacher (1974), and Schlamp, Pruppacher and Hamielec (1974) are demonstrated.

2. DATA AND METHODS

The data for this study were collected in conjunction with the field weather modification experiments of Project CENSARE (CENtral SierrA REsearch). The project was designed to study snow formation processes and the corresponding potential for enhancing precipitation by cloud seeding. Analyses have continued under new auspices since the termination of the project. Some 14,500 snow crystals were analyzed from 260 individual samples collected during nine synoptically diverse Sierra Nevada snowstorms of the 1971-72 and 1972-73 seasons. Eight of the storms were seeded, one was not. The crystal sampling site was at Tamarack, California (6918 ft MSL) which is located on the western slope of the Sierra Nevada near the mean elevation of maximum snowfall. Crystals were replicated in plastic (1.5% polyvinylformal in ethylene dichloride) on large glass slides. Replicas were obtained at 15-45 min intervals during snowfall.

Data reduction was accomplished by projecting the replicas onto a screen with standard overhead equipment. Magnification of the images of the snow crystals was set at 100X. The replicated crystals were examined for detail with a microscope prior to

*Partially based on a Ph.D. dissertation, Colorado State University (Reinking, 1973).

projection. Size measurements of crystal axes and identifications of individual types of crystals were then made on the screen. A computerized number system equivalent to the Magono and Lee (1966) crystal classification was used to identify diffusional growth habits.

The extent of accretion has normally been empirically classified by simply categorizing snow crystals as rimed or unrimed. Here measurements of the amounts of accretion on individual crystals comprising the field sample are applied to more accurately describe the accretion process. The onset and the progression of the amount of riming for entire crystal populations are thus dipicted. The impracticality of counting and measuring individual droplets on individual crystals was possible to bypass because the crystal sample is large. Studies by Hobbs et al. (1971) and Reinking (1973) demonstrated that semi-quantitative estimates of rime coverage on individual crystals can be obtained on a percent-of-area-covered basis. Amounts of accumulated rime can be visually rated from most to least on a scale of four or five, with reasonable confidence. Therefore, from the Sierran sample, individual snow crystals that formed according to any of the primary, regular growth habits were classified according to rime coverage on their collecting surfaces by using the scale: (1) unrimed, and areal coverages of (2) 1-25%, (3) 25-50%, (4) 50-75%, (5) 75-100%, and (6) 100%-plus for very heavily rimed ice particles.

Single percentages representative of each interval of areal rime coverage were utilized in the analyses. The zero rime category and its separation from the 1-25% category are absolute, so the onset of riming on individual crystals is readily resolved. An areal rime coverage of about 25% represents a somewhat arbitrary but suitable demarcation between insignificant and significant effects of riming on crystal shape, bulk density, aerodynamic behavior, and consequent rates of subsequent riming and possible splinter production. Therefore the unrimed category and the 1-25% category of rime coverage are most important to this study.

The 25-50% and 50-75% categories were weighted at the respective medians. The 1-25% interval was weighted slightly below its median, at 10%; the 75-100% interval was weighted slightly above the median, at 90%. The latter two weights do not produce results substantially different from those based on medians, but do serve as indicators of the following factors:

(1) Crystals in the light rime category frequently have just encountered the onset of riming and have collected only a few droplets. The weight at 10% indicates this phenomenon.

(2) Rime coverage on heavily rimed crystals is particularly uneven. For example, rime near the center of a planar crystal in the 75-100% category may be light, while that near the edges, if visualized to spread out evenly, may more than cover the whole collecting surface. The weight at 90% indicates that many of the crystals in this category have collected rime sufficient to cover their surfaces, even though the surfaces were not totally obscured.

Graupel is represented in the 100%-plus category. Also included in this category are the few snow crystals that remain recognizable by growth habit despite extremely heavy riming.

The observed snow crystals of the various growth habits were grouped according to similarities in formation temperatures, shape and fallspeed (for details, see Reinking, 1973). The grouped samples are summarized in Table 1. Crystal formation temperatures given in the table correspond to water saturation.

Three-dimensional distributions of the areal rime coverage were devised to graphically illustrate the sampled populations of the various planar and columnar crystals. The (x,y,z) coordinates are respectively crystal size, areal rime coverage, and percentage of crystals. For crystals within individual size intervals, the fraction within each percentage category of areal rime coverage was first determined to provide a y-z plot. These two-dimensional distributions were then combined according to crystal size to form a x-y-z surface. As examples, Figures 1 and 2 show the areal rime coverage on elementary needles, in terms of crystal length (c axis) and width (a axis). Graphs of the same type for the habit groups in Table 1, for various subgroups, and for composites of all columnar crystals and all planar and radiating crystals are presented by Reinking (1973, 1975b). The distributions are for the seeded storms, which contributed 96.6% of the total sample. In these distributions, illustration of the areal rime coverage at and following the onset of accretion on the smallest crystals has been enhanced by the use of size intervals for the smallest crystals that are narrower than those used for the larger sizes. The plotted crystal sizes correspond to the mid-points of the size intervals. The surface defined by each three-dimensional distribution shows (1) the size distribution of crystals with any given rime coverage, (2) the dispersion and mode in the amounts of rime on the crystals of any given size, and (3)

TABLE 1

GROWTH HABITS AND OCCURRENCE OF SNOW CRYSTALS AT TAMARACK

	HABIT GROUP	FORMATION TEMPERATURES (C)	SAMPLE SIZE	PERCENT OF TOTAL SAMPLE
N	NEEDLES AND SHEATHS (N1a-d; N2a,b)*	-4 to -8	6925	47.7
C	HOLLOW COLUMNS (C1f)	-8 to -10, -20 to -30	1345	9.3
P1A	HEXAGONAL PLATES (P1a)	-11.5 to -12.5, -17.5 to -18.5	706	4.9
P1B	BRANCHED PLANAR CRYSTALS (P1b-f, P2a-g; P3a-c; P4a,b; CP3a-d)	-12.5 to -17.5	1256	8.6
P1C	FRAGMENTS OF BRANCHED PLANAR CRYSTALS (fP1b-f; fP2a-g; fP3a-c; fP4a,b; fCP3a-d; I3)	-12.5 to -17.5	1584	10.9
P2	RADIATING ASSEMBLAGES OF PLATES AND DENDRITES (P7a,b)	-13.5 to -22.5	276	1.9
CP	CAPPED COLUMNS (CP1a-c)	-8 to -10, -20 to -30 (col) -11.5 to -18.5 (cap)	220	1.5
O	OTHER REGULAR CRYSTALS	....	66	0.4
R	GRAUPEL (R4a-c)	....	1061	7.3
I	MISCELLANEOUS ICE PARTICLES (I1)	....	1082	7.5
	TOTAL SAMPLE SIZE		14521	100.0

*Magono and Lee classification; codes preceded by "f" indicate crystal fragments.

the trends of both the dispersion and the mode with increasing crystal size (or equivalent depositional growth time, assuming reasonable correlation between time and size).

The general patterns and magnitudes of dispersion in these distributions are common to the crystals sampled in individual precipitation periods; they are not the results of scatter due to differences among individual periods of precipitation with crystal populations having narrow dispersions of rime (Reinking, 1973). The composites do, of course, smooth the data from individual periods, and are therefore more readily interpreted.

The analyses were extended to compute the average rime coverage as functions of crystal size. For each basic type of crystal, a mean degree of rime for the crystals in each of several individual, uniform size intervals was computed by weighting the number of crystals in each category of rime coverage with the appropriate percentage. A polynominal was then fit to each set of means to provide a curve of average rime coverage versus crystal size, for each of the crystal types. The category for more than 100% rime could not be assigned a fixed weight so it was excluded from these computations; the resultant errors are not regarded as significant because only 0.1 to 0.3% of the crystals in any given habit group were included in this category (graupel is considered by Reinking, 1975b).

Figures 3, 4 and 5, for elementary needles and branched planar crystals, are examples of the curves of mean rime coverage. Curves for the other basic crystal types are presented by Reinking (1973).

Root-mean-square errors for the curves define the dispersion of the means for the individual size intervals. The points in the graphs designated by triangles are mean values based on fewer than five crystals. These points were excluded in computation of the fitted curves.

Crystal growth times equivalent to the observed crystal sizes are included on the graphs of mean rime. The growth times for crystals with the various habits were computed using the temperature-dependent parameters for depositional growth rates at water saturation as given by Hindman and Johnson (1972). Procedural details are given by Reinking (1973).

The curves of mean rime coverage are most accurate, in relation to both crystal size and growth time, between the onset and the intermediate stages of of accretion. The non-uniform buildups of rime that occur particularly on the planar crystals probably did lead to numerical weighting that was too light at the heavier stages of rime, despite the small adjustment made (see above). Therefore, if the larger percentages of mean areal rime coverage were translated into equivalent masses of rime, they would approximate the average lower limits of the accreted water.

3. ACCRETION IN TERMS OF CRYSTAL POPULATION

Consider the distribution of the amounts of accretion collected on elementary needle crystals (Figures 1 and 2). All of the crystals begin to grow by deposition from initial sizes determined by the nuclei (assuming heterogeneous nucleation), with no immediate occurrence of riming. Thus, the beginning of growth of 100% of the crystals is represented by a point near (0, 0, 100). As the needle crystals grow, the accretion rate and the consequent rime coverage remain minimal or zero until the *a* axis of individual crystals exceeds about 200 μm and the corresponding *c* axis exceeds about 25 μm. Continued depositional growth then leads to accelerated riming of more and more crystals. This can be noted in Figures 1 and 2, as follows. First, consider the percentages of crystals with any given small size that are in each of the categories of areal rime coverage; the percentages are at or near zero except in the no-rime category which contains most of the crystals. Next, note how the percentages of crystals with significant rime increase toward larger crystal sizes; as the collecting surfaces of more and more crystals become 25, 50 or 75% rimed, fewer and fewer crystals remain in the unrimed category. For example, only about 25% of the observed needles remained in the unrimed category upon growing to an approximate length of 1 mm and width of 90 μm. The fraction of the needle crystals of any size that have not encountered the onset of riming is represented by the shaded (x,z) plane in each of Figures 1 and 2. Examination of the shaded areas and the discussion thus far lead to two important conclusions: (1) Individual crystals must indeed reach some critical minimum size before significant fractions of a population of snow crystals with a

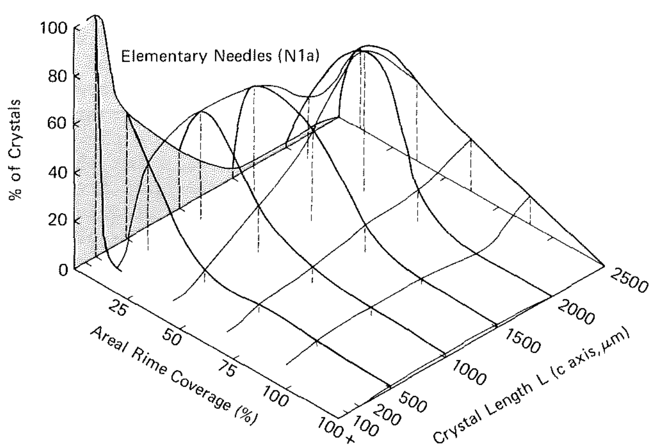

Fig. 1. Distribution of the amounts of accretion (areal rime coverage) on elementary needles, in terms of snow crystal length.

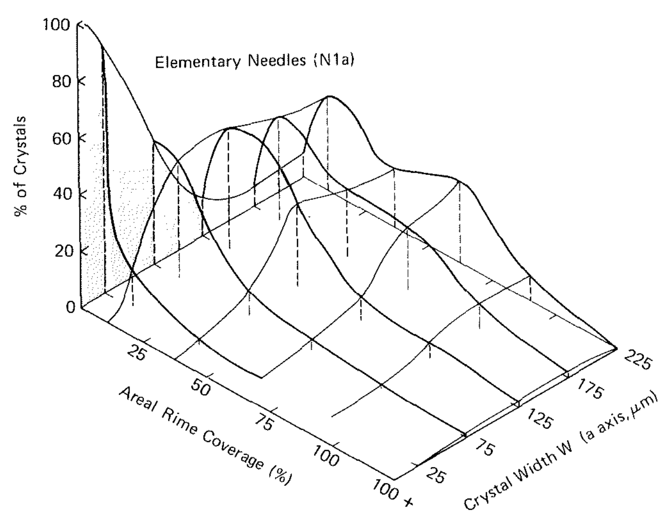

Fig. 2. Distribution of the amounts of accretion (areal rime coverage) on elementary needles, in terms of snow crystal width.

given habit will begin to rime. (2) However, many crystals in a given population do not begin to rime when the critical minimum size is reached. The onset of accretion is delayed over longer growth periods for large fractions of the crystal population, so considerable dispersion occurs in the actual sizes at onset. Indeed, a few crystals approach and sometimes reach the maximum observed sizes without riming.

These conclusions apply at any given time during non-glaciated snowstorms, as well as to the snowfall from several non-glaciated storms considered collectively. None of the storms observed approached total glaciation, even temporarily. The conclusions apply to crystals with all types of growth habits, as is evident from additional graphs like Figures 1 and 2 as presented by Reinking (1973, 1975b).

The onset of accretion is normally presumed to occur during the early stages of growth of all rime-collecting crystals. This is easily, and incorrectly, inferred from current theories and models that predict accretion will begin as soon as crystal growth leads to a non-zero efficiency for the collection of droplets with commonly occurring sizes (Hindman and Johnson, 1972; Pitter and Pruppacher, 1974; Schlamp et al., 1975). These models treat only the growth of single crystals; and the uniform presence of droplets of accretable size is assumed.

Even direct field observations have led some investigators to suggest that crystals in mixed-phase clouds cannot grow beyond a certain size without riming. Ono (1969) and Iwai (1973) empirically estimated that such a limit exists for needles, sheaths and columns at a crystal width (a axis) of 90-100 μm. However, in the Sierran sample, respectively only about 22, 33 and 37% of the needles (Figure 2), sheaths and columns remained unrimed upon reaching a width of 100 μm. Clearly a definite upper limit cannot be assigned.

In natural clouds, populations of snow crystals compete for the droplets; accretion becomes a stochastic process. Among the crystals composing a large population, a few crystals will, with high probability, grow for long times to large sizes without accreting. Clusters of crystals, for example, may shelter other crystals by either collecting droplets of accretable size in the fallpath, or by diminishing the size of droplets to below the accretable minimum size through vapor deposition. Similarly, very localized cells of cloud may be depleted of accretable droplets by intense depositional growth of relatively high concentrations of crystals, so that at least some crystals within are protected from accretion. Spatial variations in the presence of accretable droplets on the microscale can logically introduce the observed variability in the crystal sizes at onset and in the final degrees of riming on crystals of a population such as depected in Figures 1 and 2.

Under such circumstances, in order to prevent accretion, the average vapor levels in the localized portions of cloud are not necessarily diminished to below that for water saturation. A few large but unrimed crystals, with habits that develop only at or slightly above water saturation, can still be observed. The predominance of snow crystals in the Sierra had growth habits that require water saturation or slight supersaturations to develop; and a few of each habit grew to large sizes without riming. Questions could arise regarding the saturation levels responsible for the observed plates and columns. However, these crystals precipitated along with heavily rimed needles, sheaths and dendrites (see Table 3, Reinking, 1975b), so water saturation is definitely indicated.

4. MEAN RIME COVERAGE

The average minimum crystal size and growth time at the onset of accretion may be specified for each principal growth habit by calculating the average rime coverage as a function of crystal size and equivalent duration of growth. Average crystal sizes and growth times at stages of increasing rime load may also be defined in this way. The average areal rime coverage on elementary needles and on branched planar crystals serve as examples; the smallest (and first) crystals to collect rime are specified in each of Figures 3, 4 and 5 by the intercept of the curve with the abscissa.

4.1 Riming of Columnar Crystals

Rime is collected predominantly on the prism faces of the columnar types of crystals. Thus, the a and c axes define the approximately rectangular cross-section presented to the airflow.

Empirically, the average minimum sizes of the c axis and the a axis of needles at the onset of accretion are 220 μm and 31 μm, respectively (Figures 3 and 4). Corresponding growth time to onset is separately estimated to be 4.1 min and 1.8 min from the respective curves. While in a practical sense this discrepancy in time is small, the estimate of 4.1 min, based on the analysis of the c axis, is the most accurate. (A certain absolute error in the measurement of columnar crystal length results in a lesser percentage error than the absolute error in the measurement of width. Given a measurement of size, the relatively rapid growth per unit time along the length axis allows for greater resolution in the determination of growth time. These factors are reflected in the smaller scatter of points and the consequent smaller r.m.s. error in mean rime for the curve fitted to the data on lengths of the needles. Considering the natural scatter in c/a ratios for all types of columnar crystals, the minimum growth times to onset based on the crystal lengths are accurate to about ± 1 min).

A summary of estimates like these for more types of snow crystals is given in Table 2. Some comparisons reveal differences in accretion due to rates and habits of crystal growth.

The columns, sheaths and needles grew to respective average minimum widths of 30, 36 and 31 μm and lengths of 125, 185 and 220 μm to reach the onset of riming. The respective average minimum durations of growth to onset are 3.1, 3.3 and 4.1 min, assuming the times based on length are most accurate.

The uniformity of the widths indicates that the a axis is the most critical dimension in determining the onset of riming on columnar crystals. The corollary is that the average minimum duration of growth leading to onset of riming on columnar crystals is inversely proportional to the growth rate of the a axis and is influenced relatively little by the growth rates of the c axis or the consequent cross-sectional areas of the crystals. This is reflected in the three respective growth times and more strongly in the respective lengths and areas (length-width products) for these crystals (Table 2).

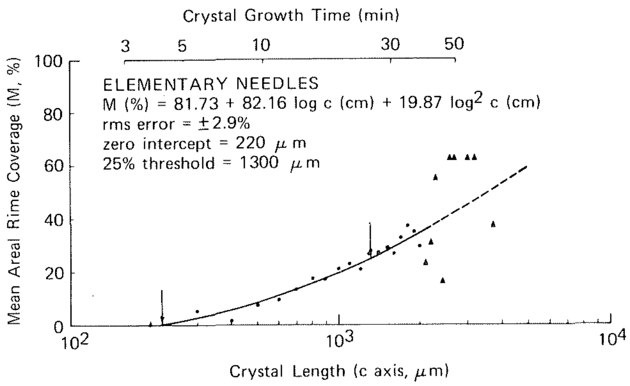

Fig. 3. Mean areal rime coverage, M, on elementary needles as a function of crystal length, **c**, and equivalent duration of growth by deposition.

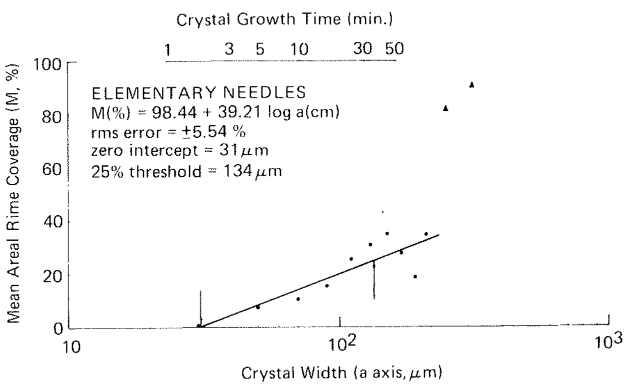

Fig. 4. Mean areal rime coverage, M, on elementary needles as a function of crystal width, a, and equivalent duration of growth by deposition.

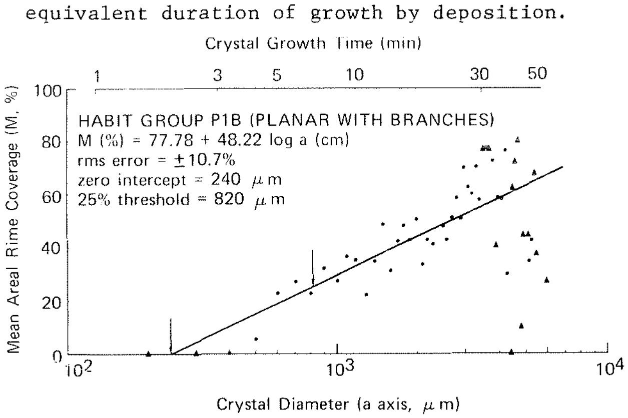

Fig. 5. Mean areal rime coverage, M, on branched planar crystals as a function of crystal diameter, a, and equivalent duration of growth by deposition.

The growth rate used to determine growth time for the columns (habit group C) is based on crystal formation between -8 and -10 C. Most of the observed columns did form here, as is evident from the average length-to-width ratios which substantially exceed unity. Columns that form between -20 and -30 C have c/a ratios near 1.2 (Auer and Veal, 1970; Hindman and Johnson, 1972). According to growth rates of the a axis given by Hindman and Johnson, the columns from relatively cold cloud would require a somewhat shorter time to attain the critical 30-35 μm dimension which would lead to riming, if the same criterion applies when c/a is near unity.

The onset sizes and growth times for habit group N (Table 2) are somewhat less than those for elementary needles and sheaths. Bundles and combinations of needles and sheaths are included in the composite group. These crystals present more irregular obstacles to airflows and thus collect cloud droplets somewhat more efficiently.

The onset of riming on columnar types of crystals has been studied theoretically and in other field situations by other investigators. The field data presented by Ono (1969) and Iwai (1973) have independently verified that the onset is most sensitive to the size of the a axis (width). However, these data indicate that droplets will begin to accrete on the columnar types of crystals only when widths exceed about 50 μm. Rimed columnar crystals narrower than 50 μm were observed in the Sierran snowfall; a few of these were more than 25% covered by rime. The average minimum sizes of 30-36 μm determined here can be allowed a statistical tolerance up to about ±10 μm, and examination of individual crystals suggests that the positive adjustment is the more accurate one. This adjustment sets the onset sizes at 40, 41 and 46 μm for columns, sheaths, and needles respectively; the discrepancy can be reduced but not eliminated.

In clouds containing narrow drop size spectra of very small droplet sizes (diameters <20 μm), the ice crystals must grow by deposition to relatively large sizes in order for riming to commence (Pitter and Pruppacher, 1974). However, differences in the sizes of accretable cloud droplets apparently cannot account for the discrepancy observed here. The rime droplets of the small sample measured by Ono (1969) range in diameter of equivalent spheres from about 12 to 55 μm, whereas those measured from the Sierran data ranged from about 5 to 60 μm (Reinking, 1973). Collection efficiencies of columnar crystals are initially the highest for droplets with diameters of 30 ± 10 μm, according to theory by Schlamp et al. (1975); droplet sizes within this range were heavily represented in both samples.

Schlamp et al. (1975) theorized that the onset of riming on columns will occur when the a axis grows to some dimension between 47.0 and 65.4 μm, as the collection efficiency increases from zero to about 20%. These sizes also exceed the 30-40 μm critical width for columns determined here. Schlamp et al. used the best theories of collection efficiencies available, although even these have room for improvement.

Accretion rates in the crystal growth model of Hindman and Johnson (1972) are estimated from collection efficiencies determined by Ranz and Wong (1952). These efficiencies as applied to snow crystals are generally excessive and very approximate since snow crystals predominantly have Reynolds numbers considerably <100 and the incorporated theory for potential flow is not justified (Reinking, 1973; Pitter and Pruppacher, 1974). Predictions of the columnar crystal riming from the Hindman and Johnson model are most readily compared to the present data for needles. The model computations for crystal growth at -5 C indicate that needles will begin to rime at widths of 32.5 μm. Curiously, despite the dubious collection efficiencies, this estimate is in excellent agreement with the unadjusted 31 μm width found here.

The method of using curves of mean rime coverage to estimate the average minimum sizes and growth times at the onset of riming may have an advantage over establishing a rime/no-rime demarcation by the method of Ono and Iwai. A field sample of snow crystals, however large in a practical sense, is still a minute fraction of all the crystals that precipitate. Thus, a size demarcation like the 50 μm crystal width determined on an absolute rime or no-rime basis, without considering the trend in amounts of rime versus crystal size, may well shift from sample to sample. The larger the total sample, the more crystals there will be in the tail of the distribution that represents the onset of accretion. The method of using the mean rime curve establishes an onset that is based not just on the demarcation separating unrimed and rimed crystals of the sample, but is also based on the whole trend of rime coverage increasing with crystal size from the onset to heavy stages. A smooth continuity is thus established between the onset and the accumulations of rime that follow. Thus, the tail of the distribution is more reliably accounted for, and the critical dimensions so determined are likely to be more representative of the true minimum sizes.

Riming beyond the onset to the 25% threshold of mean areal rime coverage (section 2) is also defined in Table 2. The widths of the columnar types at this threshold are again comparable, in view of the increasing scatter of the data with increasing crystal size. The durations of growth to this stage are also comparable, with the sequence of minor differences still holding true. The columns reach this stage first, followed in order by the needles and sheaths. The bulk densities are respectively smaller, for columns, needles and sheaths, and the terminal velocities of these crystals very directly with the densities. The efficiencies for collecting droplets vary directly with the fallspeeds, relative to the droplet fallspeeds, so the pattern in the growth times to onset is logically explained.

The Sierran data strongly contradict the conclusion of Ono (1969) that riming of needles and sheaths "is very rare because their minor axes [remain] below the riming limit;" rimed needles and sheaths were observed in profusion during the Sierran snowstorms, as shown by Figures 1, 2, 3 and 4.

4.2 Riming of Planar and Radiating Crystals

Rime on a planar crystal is collected primarily on the basal face that encounters the air stream. This face is represented by the a axis. Radiating crystals are very roughly spherically symmetric, so they may be represented by their diameters, D. The average minimum sizes at the onset of riming on branched planar crystals (240 μm) and the radiating crystals (320 μm) are the largest observed (Figure 5; and Table 2, habit groups P1B and P2). The branched planar crystals form in the cloud regime of most rapid depositional growth (-15 ±3 C), and the radiating types of crystals fall into this regime to attain most of their size, after forming at colder temperatures. The consequent average minimum growth time to onset for the branched planar crystals is very short, 1.9 min. Hindman and Johnson (1972) predict that snow crystals growing at -15 C will encounter the onset of riming within 1-2 min, which equates to a size between 150 and 300 μm; agreement of the Sierra data with a time and size near the greater of these is good. Since the radiating crystals must grow slowly and settle for some time before reaching the regime of rapid growth, their growth time to onset is longer; the 4.2 min estimated here for these crystals seems physically reasonable even though it is very approximate.

Habit group P1C represents branches broken from planar crystals. It is very interesting that the average minimum size of these crystal fragments at the onset of riming is only slightly greater than half the size of the whole branched planar crystals at the onset. The data suggest that crystal fracturing occurs simultaneously with or shortly after the onset of riming. A physical connection of the two processes could be implied.

The axial growth rate of hexagonal plates is less than one-third that of the branched planar crystals (Hindman and Johnson, 1972), so the growth time to onset is longer for the plates (3.3 vs 1.9 min).

TABLE 2

ESTIMATES OF THE ONSET AND THE 25 PERCENT THRESHOLD OF ACCRETION

CRYSTAL HABIT GROUP	(a) Maximum Crystal Dimension					(b) Crystal Width			(c) Cross-sectional Area	
	Crystal Dimension	Average Minimum Size at Onset (μm)	Average Minimum Growth Time at Onset (min)*	Average Size at 25% Rime Coverage (μm)	Average Growth Time at 25% Rime Coverage (min)	Crystal Dimension	Average Minimum Size at Onset (μm)	Average Size at 25% Rime Coverage (μm)	Average Minimum Area at Onset ($mm^2 \times 10^3$)	Average Area at 25% Rime Coverage ($mm^2 \times 10^3$)
All Planar and Radiating Crystals	(D)	95	---	1080	----	---	--	---	----	---
All Columnar Crystals	(L)	120	---	900	----	(W)	30	160	4.8	132
N(Needlelike)	(L)	140	2.6	1100	25.0	(W)	34	120	6.8	174
N1a (Needles)	(c)	220	4.1	1300	25.0	(a)	31	134	6.7	79
N1c (Sheaths)	(c)	185	3.3	720	19.0	(a)	36	110	3.8	70
C (columns)	(c)	125	3.1	450	17.0	(a)	30	155	15.0	---
P1A (Plates)	(a)	150	3.3	None	----	---	--	---	21.0	239
P1B (Branched Planar)	(a)	240	1.9	820	6.6	---	--	---	----	---
P1C (Broken Branches)	(L)	125	---	730	----	---	--	---	----	---
P2 (Radiating)	(D)	320	4.2	700	9.9	---	--	---	----	---
CP (Capped Columns)	(c)	115	2.7 (a)** 9.5 (b)	200	5.7 (a)** 29.0 (b)	(a of cap)	34	53	----	---

*Based on c axis for columnar types of crystals.

**For capped columns, growth time (a) corresponds to formation of columnar part at -8 C to -10 C, and (b) corresponds to formation at -20 C to -30 C.

However, the size of plates at the onset is only about two-thirds that of the branched crystals (150 μm vs 240 μm); the aerodynamics of the simple hexagonal shape apparently lead to collection efficiencies exceeding zero at a considerably smaller size.

Measurements by Wilkins and Auer (1970) reveal a minimum onset size of about 200 μm for plates. The sample used to determine this size was extremely small so this size cannot be regarded as an absolute minimum, and the difference between this size and the 150 μm determined from the Sierran data cannot be argued as significant. From another small sample, Ono (1969) suggested that riming is rare on plates with the a axis <300 μm. Both the data of Wilkins and Auer and the Sierran data clearly show that significantly smaller plates will rime.

The most up-to-date theoretical estimates of accretion efficiencies for plates have been calculated by Pitter and Pruppacher (1974). They find that the efficiency begins to exceed zero and plates begin to rime only when the a axis grows to a size within the 294-320 μm range. This estimate is too large, as the observations of natural crystals show.

The effect of the rapid growth of branched planar crystals and radiating crystals on droplet collection after the onset of riming is evident in the growth times required to reach the 25% threshold of rime coverage (Table 2). The respective total growth times of only 7-10 min may be compared to the 17-25 min required by the basic columnar types of accumulate the same coverage on their collecting surfaces. The branched planar and radiating crystals types accumulate water by accretion at rates much faster than those for all the other types of crystals, with the possible exception of capped columns which begin growth in clouds at -8 to -10 C (see below).

After 3 or 4 minutes of growth, the areas of the droplet-collecting faces of branched planar crystals exceed those of plates with similar growth times by more than an order of magnitude (Reinking, 1974). Thus, it is not surprising that the observed plates did not, in the mean, accumulate sufficient rime to cover 25% of their surfaces (Table 2). A more detailed description of the relative rates of accretion by the various types of crystals is given by Reinking (1974).

4.3 Riming of Capped Columns

Accurate estimation of the riming characteristics of capped columns was complicated by the complex shapes and generally heavy accumulations of rime on these crystals. Combined data for plate-capped and dendrite-capped columns indicate that the columnar sections must reach an average minimum length of roughly 115 μm to start to accrete droplets. The caps only slightly exceed the dimensions of the columnar sections at this time.

Caps would normally be expected to form on columns that nucleate between -20 and -30 C and then settle down to warmer regimes where the planar habits develop; however, growth times based on columns nucleated between -8 and -10 C are physically in much better accord with the averages of the observed c/a ratios. Both possibilities are presented in Table 2. Imbedded convection could have carried warm zone columns up to the regimes for planar cap growth; the 2.7 min time to onset is regarded as the best estimate.

At the 25% threshold of rime coverage, the c axes of the capped columns are substantially smaller than the c axes of ordinary columns. The caps, however small, do definitely and profoundly increase the efficiency for collection of droplets.

5. CONCLUSIONS

Individual snow crystals must grow by deposition to at least a critical minimum size before they can begin to collect cloud droplets. Many of the crystals comprising a population in a mixed-phase cloud grow well beyond the critical minimum size before they begin to rime; this is apparently a result of the stochastic nature of accretion, the competition among crystals for cloud water, and a consequent non-uniform spatial distribution of droplets of accretable size even in clouds that on the average contain large quantities of liquid water. Empirical estimates and theoretical models that depict the onset of accretion only on crystals of small size should by no means be used to describe all the crystals that rime in a given cloud system. The models need to be expanded to account for the whole distribution of crystal sizes at the onset of riming, as shown, for example, in Figures 1 and 2.

The critical minimum sizes of snow crystals at the onset of accretion are reported above as averages for the basic growth habits from the Sierran snow sample. These estimates show that minimum lengths or diameters of crystals within the approximate range of 115-320 μm have to be attained before any crystals will begin to rime. The widths of columnar types of crystals must grow to a minimum of 30-34 ± 10 μm; the onset of riming on these crystals is regulated primarily by this dimension with little influence from the lengths or cross-sectional areas.

The critical minimum sizes of specific types of crystals determined from the Sierran field sample are somewhat less than those observed by Ono (1969), Iwai (1973) and Wilkins and Auer (1970), and those predicted by the theories of Pitter and Pruppacher (1974) and Schlamp et al. (1975), but are comparable to those predicted by Hindman and Johnson (1972). Curiously, the Hindman and Johnson model of accretion has the least sound basis of the theories. Some improvement of the theoretical accuracies is apparently still warrented. Also, the theories need to be expanded to account more specifically for more of the basic types of crystals.

The average minimum durations of depositional crystal growth prior to riming are estimated to be between 1.9 and 4.2 min and are thus quite similar for all crystal types. However, systematic variations with crystal habits are evident in both the growth times and the minimum sizes required for riming. Columns, needles and sheaths, with respectively lesser bulk densities, do respectively grow to larger minimum lengths and require longer minimum times to reach the onset of accretion. Bundles and combinations of needles and sheaths reach the critical size sooner than single needles and sheaths. Branched planar crystals grow to minimum droplet collecting sizes in relatively short times. Hexagonal plates must grow for longer times, but to lesser sizes than the branched crystals.

The relative differences observed among the various basic crystal types at the onset of riming are carried through to at least the stage when 25% of the collecting surfaces of the crystals become covered with rime. However, the average capped columns have only small caps and follow the minimum size characteristics of ordinary columns at the rime onset, but develop much accelerated accretion rates as the caps grow and 25% rime coverage is approached. Roughly at this 25% stage, the effects of riming on crystal aerodynamics begin to significantly affect further crystal growth, and accretion becomes a major contributor to total precipitation. The average patterns of riming to and beyond the 25% stage show that the branched planar and radiating crystals and the capped columns develop the most significant rates of accretion and precipitate the greatest masses of water in the form of rime.

The crystal multiplication study of Hallett and Mossop (1975) indicates that riming of needles and sheaths contributes more significantly than riming of other crystals to new crystal production and an accelerated deposition process. The data presented here show that this multiplication process is likely to be encouraged by frequent collection of heavy rime on needles and sheaths.

REFERENCES

Auer, A. H. and D. L. Veal, 1970: The dimension of ice crystals in natural clouds. J. Atmos. Sci., 27, 919-926.

Hallett, J. and S. C. Mossop, 1974: Production of secondary ice particles during the riming process. Nature, 249, 26-27.

Hindman, E. E., II, and D. B. Johnson, 1972: Numerical simulation of ice particle growth in a cloud of super-cooled water droplets. J. Atmos. Sci., 29, 1313-1321.

Hobbs, P. V. et al., 1971: Studies of winter cyclonic storms over the Cascade Mountains (1970-71). Rpt. VI, Dept. Atmos. Sci., Univ. Washington, Seattle, 306 pp.

Iwai, K., 1973: On the characteristic features of snow crystals developed along c-axis. J. Meteor. Soc. Japan, 51, 458-465.

Jiusto, J. E. and R. L. Lavoie, 1975: American Met. Soc. symp. on the prediction and measurements of ice crystal concentrations in clouds (summary). Bull. Amer. Meteor. Soc., 56, 1175-1179.

Magono, C. and C. W. Lee, 1966: Meteorological classification of natural snow crystals. J. Fac. Sci., Hokkaido Univ., Ser. VII, 2, 321-335.

Mason, B. J., 1975: Production of ice crystals by riming in slightly supercooled clouds. Quart. J. Roy. Meteor. Soc., 101, 675-679.

Ono, A., 1969: The shape and riming properties of ice crystals in natural clouds. J. Atmos. Sci., 26, 138-147.

Pitter, R. L. and H. R. Pruppacher, 1974: A numerical investigation of collision efficiencies of simple ice plates colliding with supercooled water droplets. J. Atmos. Sci., 31, 551-559.

Ranz, W. E. and J. B. Wong, 1952: Impaction of dust and smoke particles. Ind. Eng. Chem., 44, 1371-1380.

Reinking, R. F., 1973: Empirical assessment of accretion microphysics. Ph.D. dissertation, Colorado State Univ., 342 pp.

----1974: Cross-sectional areas of snow crystals and the accretion process. Preprints Conf. Cloud Physics, Tucson. Amer. Meteor. Soc., 185-190.

----1975a: Microphysical processes of snow formation. Preprints, Spec. Regional Weather Modification Conf. on Augumentation of Winter Orographic Snowfall in the Western United States., San Francisco, Amer. Meteor. Soc., 85-93.

----1975b: Formation of graupel. J. Atmos. Sci., 14, 745-754.

Schlamp, R. J., H. R. Pruppacher and A. E. Hamilec, 1975. A numerical investigation of the efficiency with which simple columnar ice crystals collide with supercooled water droplets. J. Atmos. Sci., 32, 2330-2337.

Wilkins, R. I. and A. H. Auer, 1970: Riming properties of hexagonal ice crystals. Preprints Conf. Cloud Physics, Ft. Collins, Colo., Amer. Meteor. Soc., 81-82.

3.3.8

WATER DROP SEPARATION PROBABILITIES

C. P. R. Saunders*, S. Al-Said, M. Gay

University of Manchester
Institute of Science and Technology
Manchester, England

1. INTRODUCTION

The separation of water drops and droplets following their interaction inside a cloud plays an important role in the rate of drop growth and hence, cloud development. Of importance in electrified clouds is the separation of electric charge on the two drops; the sum of many such interactions will then influence the overall electrification of the cloud. The intensity of the electrification will, in turn, influence significantly the collision and coalescence efficiency of the interacting drops and droplets.

2. DROP-DROP INTERACTIONS

Brazier-Smith, Jennings and Latham (1973) showed that a drop in the size range 0.46 mm to 2.33 mm interacting with a smaller drop in the size range 0.24 mm to 1.81 mm has a finite separation probability as shown in Table 1. Their work was based on the theoretical assumption and experimental verification that two drops, which upon collision have sufficient rotational energy to provide the excess surface energy required to reform two drops, would separate.

Table 1. Water drop separation probabilities.

r mm	R mm 0.46	0.64	0.91	1.28	1.81	2.33
.24	.046	.032				
.33	.030	.573	.536	.251		
.46		.55	.787	.742	.512	
.64			.761	.873	.816	.553
.91				.842	.896	.795
1.28					.837	.836
1.81						.504

Utilizing these values of separation probability and postulating a realistic drop-size distribution, Jennings (1971) calculated that for a cloud with a liquid-water content of 3 gm m^{-3} and electric field 10 kv m^{-1}, the rate of charge separation due to the induction process is $\sim$0.5C km^{-3} min^{-1}. This rate is of the same order as that shown by Mason (1953) to be a requirement of theories which attempt to explain thunderstorm electrification. However, the manner in which two large drops separate is such to decrease the existing electric field; the upper drop of a separating drop-pair experiences a negative induced charge and the lower drop a positive charge inside a typically electrified cloud exhibiting an enhanced field with an upper positive charge and negative lower charge. After separation, the two drops help to dissipate the electric field.

When two drops separate, a filament is pulled out between them. Al-Said and Saunders (1976) have shown experimentally that the charge residing on the separated drops is enhanced, because of the filament, compared with the theoretical charge calculated with the assumption that the drops separate as rigid spheres. Latham and Mason (1962) showed that the charge separated, q, in an electric field E v m^{-1} at an angle, θ, to the line of centres of two initially uncharged contacting drops of large radius, R, and small radius, r, treated as rigid spheres, is given by

$$q = 1.1 \times 10^{-10} \gamma_1 E r^2 \cos\theta \quad \text{Coulombs.} \qquad (1)$$

γ_1 is a function of r/R. (This is the equation used by Jennings (1971), who assumed $\cos\theta = 1$.) A theory of charge transfer put forward by Censor and Levin (1973) for water drops separating with a filament between them was verified to within 10% by the measurements of Al-Said and Saunders (1976). The 10% difference is probably due to the fact that separating drops do not take up the idealized drop shape on separation which Censor and Levin had to assume to make their theory tractable (Figure 1). They assumed that the outer positions of the drop-pairs are hemispheres while the filament is described by a cosine function of half-cycle length λ. Al-Said and Saunders pointed out that the complex theoretical equation of Censor and Levin (1973) could be represented, for some particular cases by

$$Q = \alpha \times 10^{-10} E r^2 \cos\theta \quad \text{Coulombs.} \qquad (2)$$

α is a function of the undistorted drop radius ratio R/r and of the non-dimensional filament length, n, which is effectively the separation of the drop centres $(\lambda_1 + \lambda_2)$ divided by $(R + r)$. Table 2 presents values of $1.1\gamma_1$ and α which permits a comparison to be drawn between the predictions of the rigid sphere and filament theories for the same values of E, r^2 and $\cos\theta$. The values of the ratio (R/r) are appropriate to the values of R and r which result in separation, from Table 1.

*At present at the University of Wyoming, Department of Atmospheric Science, Laramie, Wyo.

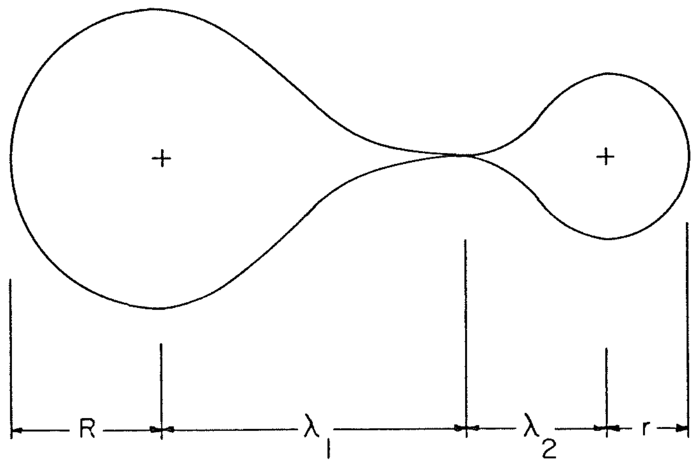

Figure 1. The configuration of the drops at the moment of separation.

Table 2. Values of $(1.1\gamma_1)$ and α_n for various values of R/r and n.

	R/r	1	2	3	4
n	$1.1\gamma_1$	1.80	3.1	3.66	4.04
1	α_1	2.1	3.86	5.78	8.20
2	α_2	2.74	5.18	8.16	12.67
3	α_3	3.38	6.49	10.55	17.13
4	α_4	4.02	7.80	12.93	21.60
5	α_5	4.66	9.11	15.32	26.07
6	α_6	5.30	10.43	17.71	30.54

The table shows how for any given value of R/r the charge transfer multiplication factor, α, increases with filament length, n. A comparison of the values of α and $1.1\gamma_1$, for the case when the drop centres for both theories are separated by (R + r) and n = 1, shows that the filament theory enhances the charge transfer relative to the solid sphere theory even when the overall length of the drop-pair is 2(R + r) for both theories; this shows that the enhanced charge on the two drops in the filament configuration is not due simply to an extension of the drop-pair. Both $1.1\gamma_1$ and α increase for increasing values of R/r as does the ratio of $(\alpha/1.1\gamma_1)$. Larger values of α will occur for values of (R/r) greater than 4; however, the separation probabilities of drops in this category is very small. All drop-drop interactions in clouds which result in separation will involve the formation of filaments with values of n between 1 and 6; the more glancing the collision the higher is the value of n at separation. Thus, the discharge rate within electrified clouds will be enhanced significantly above that predicted by Jennings (1971) due to the formation of filaments between separating drops.

3. DROP-DROPLET INTERACTIONS

In contrast with the drop-drop interactions described above, drop-droplet interactions do not involve sufficient rotational energy for the temporarily coalesced drop-pair to revolve. When separations occur, in most cases the droplet bounces from the underside of the drop. In a vertical electric field, for initially uncharged drops, this will result in charge separation in a direction which enhances the existing field. Whelpdale and List (1971) measured the coalescence efficiency, E_f, for drops in the size range 400 μm < R < 2000 μm with droplets in the range 20 μm < r < 100 μm. They determined that $E_f = R^2/(R + r)^2$, which implies that separation occurs when the centre of the droplet is outside the diameter of the drop.

Separation will occur between drops and droplets whose line of centres on impact makes an angle, θ, relative to the vertical, where θ has a maximum value of 90° and a minimum value, θ_{min}, of $\tan^{-1} (R^2/(r^2 + 2Rr))^{1/2}$. The smallest value of θ_{min} for pairs of drops in the size ranges investigated by Whelpdale and List (1971) occurs for R = 2000 μm and r = 100 μm when θ_{min} = 63°. The charge transfer is proportional to cosine θ, which is zero for θ = 90° and reaches a maximum of only 0.45 for θ = 63°. It is, therefore, very important, when calculating the charge transfer between a drop and droplet, to take account of the range of values of θ for which separation will occur for the particular values of R and r being considered. Ziv and Levin (1974) and Levin and Scott (1975) have used 45° as an arbitrarily assigned mean collision angle, θ_A, for which separations occur when calculating electric field growth by charge transfer between drops and droplets. The use of 45° leads to an overestimation of the rate of charge transfer when compared with the true mean collision angle for which separations occur, θ_T, which, averaged over all drop-droplet interactions in the range investigated by Whelpdale and List (1971), is close to 80°. Scott and Levin (1975) show that θ_A = 79.5° reduces the rate of electric field growth and the maximum field attained compared with their predictions for θ_A = 45°, but believe that 45° is a more reasonable angle to assume than 79.5°.

In order to assess the possibility of utilizing correct values of the angle, θ, for which separation occurs in calculations of charge separation rates in electrified clouds, the following analysis was performed. Some of the many simplifications in this calculation will be discussed later. Using the observed size distribution of cloud drops (N_R) and droplets (N_r) in electrified clouds from Weickmann and aufm Kampe (1953) and Blanchard (1953), the rate of charge transfer due to collisions and separations of drops and droplets was determined from the following equation which takes into account the separation probability $(1 - E_f)$

$$\frac{dq}{dt} = \sum_{r=20}^{100} \sum_{R=400}^{2000} \pi V N_R N_r (2R + r)\gamma_1 E r^3 \cos\frac{1}{2}(\theta_{min} + 90) \tag{3}$$

V is the relative velocity of the drop and droplet for the particular values of R and r being considered. The charge separated in the vertical electric field, E, is assumed, until better resolution of the configuration of the drops at the moment of separation is obtained, to be given by the Latham-Mason equation. For those interactions which result in separation, the average of the extreme values of θ was used, θ_{AV}; thus, a typical value of θ was 80° for which $\cos\theta = 0.17$. Strictly, θ_T should be used here, but the other simplifications implicit in this calculation make the error negligible. For example, for the worst case of $\theta_{min} = 63°$, θ_{AV} as used in equation (3) is 76.50°, while θ_T is 74.45°.

For an electric field of 10 kV m^{-1} the rate of charge transfer in the cloud due to drop-droplet interactions is $\sim$0.6C km^{-3} min^{-1}.

4. DISCUSSION

Both the charge generation and dissipation rate for the two processes considered here are of the same order. Serious criticisms of both of the calculations are justified and are now listed. 1) The cloud is not depleted by sweep-out. 2) Despite interactions which result in coalescence, no particles change their size ranges. 3) No recombination of charge is considered when particles coalesce after a previous charge separation interaction. 4) In the case of the drop-drop interactions, the electric field has been taken as parallel to the line of centres of the separating particles; this will not generally be the case. The following points refer to the drop-droplet interactions. 5) The electric field and particle charges will promote coalescence and thus decrease further charge separation. 6) The collision efficiency, assumed to be unity, will be less than unity for small, uncharged droplets in zero electric field, but will be increased as the charges and field develop; thus, the total number of interactions is in error. 7) The electric field is assumed to be vertical; this is unlikely to be the case so that in a vertical airstream interactions on opposite sides of the drop will lead to charge transfer of opposite signs. For the drops and droplets in the ranges investigated by Whelpdale and List (1971) for which θ_{min} is 63°, variation of the electric field direction from 0° to 27° with respect to the fall direction of the drops and droplets, results in a progressively reduced charge transfer rate from its maximum at 0° to zero at 27°. For angles greater than 27°, net charge transfer due to the induction process remains at zero. Tilted electric field vectors are common in electrified clouds (Ogawa and Brook, 1969) and frequently may differ by more than 27° with the particles' fall direction. 8) The drops remain uncharged for the initial and subsequent interactions and thus maintain an internal horizontal balance level of charge with their top and lower halves, relative to the field, carrying equal and opposite charges. In reality, once charged, the balance level will descend, as pointed out by Moore (1975) and many interactions at high values of θ will remove charge from above the balance level of such a sign to help dissipate the electric field.

5. CONCLUSION

The calculations here presented indicate that both charge separation and dissipation processes are important in electrified clouds. In some respects, both models suffer from the same simplifications which perhaps makes it more justifiable to compare their results. A dissipation rate due to drop-drop interactions of more than 0.5C km^{-3} min^{-1} is sufficiently significant to warrant its inclusion in complete electric field-growth models. The growth rate of 0.6C km^{-3} min^{-1} is an overestimation because of the simplifications pointed out in the discussion. However, of greatest importance to the effectiveness of drop-droplet interactions in separating charge in clouds is the particular value of the coalescence efficiency adopted. Recent work by Lobl (1975) has suggested that the coalescence efficiency may be less than that determined by Whelpdale and List (1971) with separations occurring at smaller values of θ than those considered here. This will cause both more charge transfer and less coalescence; thus enhancing the charging rate of particle growth by collisions and coalescence. Therefore, it is most important to perform further experiments on drop and droplet collisions to determine both their shape and charge transfer on separation and to reproduce as closely as possible the in-cloud parameters such as relative velocity, particle charge and electric field. The results of such experiments can then be incorporated with the dissipation data into an improved model of electric field growth.

REFERENCES

Al-Said, S. M. and C. P. R. Saunders, 1976: Electric charge transfer between colliding water drops. J. Geophys. Res., in press.

Blanchard, D. C., 1953: Raindrop size-distribution in Hawaiian rains. J. Meteor., 10, 457-473.

Brazier-Smith, P. R., S. G. Jennings and J. Latham, 1973: Raindrop interactions and rainfall rates within clouds. Quart. J. Roy. Met. Soc., 99, 260-272.

Censor, D. and Z. Levin, 1973: Electrostatic interaction of axisymmetric liquid and solid aerosols. Pub. Dept. Env. Sci. Tel Aviv Univ., ES 73-015.

Jennings, S. G., 1971: The interaction of falling water drops. Ph.D. Thesis, UMIST, Manchester, England.

Latham, J. and B. J. Mason, 1962: Electrical charging of hail pellets in a polarizing electric field. Proc. Roy. Soc. A266, 387-401.

Levin, Z. and W. D. Scott, 1975: The effect of electrical conductivity on the growth of the electric field in a thunderstorm. Tellus, 27, 497-506.

Lobl, E. S., 1975: The effect of electric charges and fields on the collection efficiency of cloud drops. Ph.D. Thesis, UCLA, Los Angeles, California.

Mason, B. J., 1953: A critical examination of theories of charge separation in thunderstorms. Tellus, 5, 446-460.

Moore, C. B., 1975: Rebound limits on charge separation by falling precipitation. J. Geophys. Res., 80, 2658-2662.

Ogawa, T. and M. Brook, 1969: Charge distribution in thunderstorm clouds. Quart. J. Roy. Met. Soc., 95, 513-525.

Scott, W. D. and Z. Levin, 1975: A stochastic electrical model of an infinite cloud: Charge generation and precipitation development. J. Atmos. Sci., 32, 1814-1828.

Weickmann, H. D. and H. J. aufm Kampe, 1953: Physical properties of cumulus clouds. J. Meteor., 10, 204-211.

Whelpdale, D. M. and R. List, 1971: The coalescence process in raindrop growth. J. Geophys. Res., 76, 2836-2856.

THE NATURE OF HAILSTONE EMBRYOS

V.G. Khorguani and M.I. Tlisov

High Mountain Geophysical Institute, Nalchik, U.S.S.R.

The hailstone embryo investigation is of great significance both for the study of physical formation and active modification of hail processes (by embryo we mean an uniform formation in the hailstone center with mm size). Notwithstanding the achieved success the hailstone embryo nature is not yet known in a proper way. The literature data have descriptive character, not covered statistically and ambiguous in all. Some of the authors consider large drops tobe hailstone embryos (in mm), while the others-grauple, grown on ice dendrits/I/. Generally speaking, the both interpretations may have physical foundation , the drop-embryo being formed as the result of its spontaneous crystallization or the contact with single crystals. The formation of the grauple-embryotakes place on large crystals as the result of watre vapor sublimation and coagulation with supercooled drops.

The investigation of the hailstone embryo was carried in complex. First of all, the possible variants of artificial hailstone embryo generation , stucture and their composition were investigated in a wind tunnel. Then, based on these investigations the natural hailstone embryos were analysed to determine their nature

I. The experiments with artificial hailstone embryo were conducted in a vertical wind tunnel of opened type with closed working section mounted at 300 m over sea level (south Elbrus slope)/2/. Water drops with I-6 mm diameter and temperatures near to zero were hung on glass thread of 28 mkm thickness and were frozen in air stream. After this, tha hailstones of different sizes were grown on them either in dry or in wet regime. The hailstone cuts were investigated in polarized, transmitted and reflected lights.

The study of the cuts showed, that during the large drop freezing the transparent ice is formed at the center of which a large amount of air bubbles concentrates, ice becoming relatively opaque. At considerable supercooling the crystals oriented chaotically.The freezing of the fixed drops takes place in airstream on the frontal side and leads to the assymetric air bubble distribution. At the supercooling larger -I5°C this, in its turn, results in burstlike cracking of nearly 60% of all frozen drops

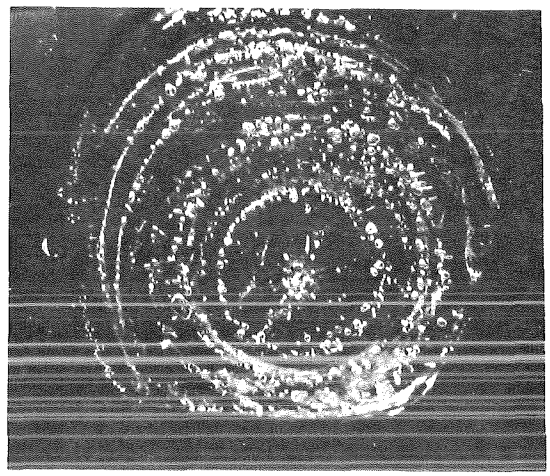

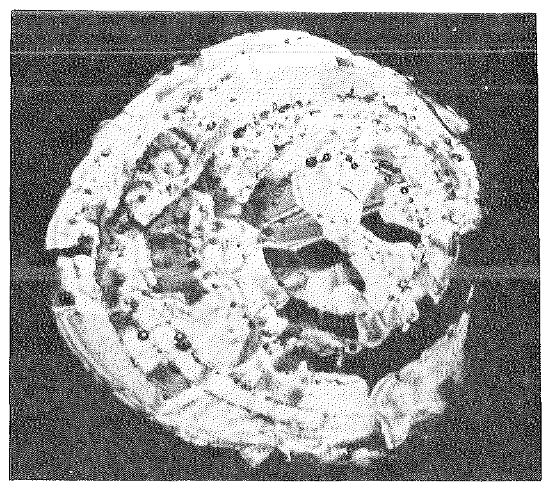

Fig.I. Artificial hailstone cut with large drop-embryo. a-in reflected, b- in polarized light.

If the hailstone grow in dry regime a milky ice layer is formed around the embryo. In wet regime a ring of air bubbles ejected from the hailstone toward the embryo surface is formed betwee ween the embryo andmilky ice layer (fig.I). In both cases the embryos are well seen.

If the freezing of large drops is the result of collision with cloud ice crystals in a wind tunnel at concentration more than 5 sm a mixed drop is formed. In such embryo the crystals have fine stucture, the air bubbles being distributed chaotically. In hailstone cuts it is practically impossible to point out such embryos. The probability of their formation in natural clouds is very small.

A grauple embryo was grown on polydisperce ice crystals with I00-200 mm mean square size when suspended in airstream by means of blowing round the supercooled water fog at various temperatures. As the result a milky ice layer is formed having low density. As the rule , the embryo is easily identified in hailstones. In natural processes when grauple is in the warm part of the cloud it may melt and saturate with water ter. In the case of second supercooling the change of grauple structure is possible. This process modeling showed that crystal structure of secondarily frozen drops is similar to that of air bubble distribution along the section which was chaotical. This embryo is always identified in the hailstone cuts.

2. In the North Caucasus (Krasnodar territory and Kabardino-Balkaria) were collected I5 samples of hailfalls The two of them may be refered as catastrophic ones, that is 0I.07.72 (Kabardino-Balkaria) and I5. 06. 74 (Krasnodar Territory). Based on laboratory experiments the cuts of about 2 I0 hailstones were analysed. Here, the statistically covered hailstone size spectra of all hailfalls were taken into account. Data on thehailstone type of all hailfalls are given in Table (Ngr - grauple embryo in %, N ld- large drop-embryo in %) with the corresponding mean cubic diameter (D sm). The Table shows that in all samples investigated both thw grauple and large drop embryo are the cases, the grauple prevailing the large drop-embryo in I2 hailfalls. It is in three cases only that large drop-embryo prevailed grauple embryo. In average, grauple embryos accounts about 65%, the drop-embryos- 35%. It is likely that this prevailing is the characteristic feature of all hailfalls /3/. Mixed embryos are extremely rare and in some cases they are absent at all.

Figure 2 shows the dependence of grauple embryo ratio on hailstone diameter(in %). Point I corresnonds to averaged data, curves 2,3,4 to the sections of separate hailfalls. Each of the last curve is drawn as the result of more than 2000 hailstone analysis.

Table

No	Date of hailfall	D ,sm	Nld %.	N gr in %.
I.	30.5.72	I,2	37	63
2.	I3.6.72	I,4	43	57
3.	22.6.72	I,6	I9	8I
4.	29.6.72	I,8	I4	86
5.	I.7.72	3,2	55	45
6.	28.8.72	I,5	32	68
7.	I9.6.74	I,I	67	33
8.	II.6.72	0,7	33	67
9.	29.6.72	2,0	I4	86
I0.	I3.6.73	I,0	26	74
II.	26.6.73	0,9	39	6I
I2.	I3.6.74	I,3	36	64
I3.	I5.6.74	3,8	20	80
I4.	23.6.74	0,95	53	47
I5.	9.7.74	2.2	32	68

Notes: I-7 hailfalls in Kabardino-Balkaria, 8-I5 - in Krasnodar Territory.

Fig 2 shows that the grauple embryo ratio increases with the increasing of the hailstone diameter. This regularity is either for single and for averaged hailfalls.

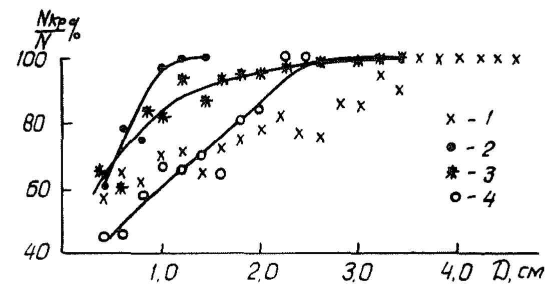

Fig.2 The dependence of grauple embryo number on thehailstone diameter. I- average of 8 hailfalls, others corresponds to hailfall samples; 2- II.6.72, 3- 29.6.72., 4- I3.6.74.

It is followed that the hailstone size is determined by the time of its presence in the cloud /I/, all other conditions being equall grauple embryo forms sooner than drop-embryo. Some other authors' investigations show /4/ that in powerful convective clouds at temperatures - I0°C a considerable amount of large crystals is already present and can be easily converted into grauple embryohailstone as the result of sublimation and gravitational coagulation with supercooled cloud d drops.

Therefore the above mentioned allowes us to make the conclusion that in the convective clouds the grauple particles are " provided" beforehand and that it is on them that the formation of hailstones takes place at hail stage of the cloud. It is likely, that the appearence of the large embryo drops takes place during the transit to the hail stage , when updraft speed is at least of 8-IO m/sec.

References:

I. Sulakvelidze G.K. Livnevie osadki i grad. Gidrometisdat, L., I967.

2. Tlisov M.I. and Khorguani V.G. Trudi Visokogornogo Geofisicheskogo Instituta, vip. 29, I975, str.I22.

3. Knight Ch., Knight N. Journ. Atmos. Scien., v.3I, No 4, I974, p. II74.

4. Hobbs P.V. Journ. Atmos. Sci., v.29, No2, I969.

3.4.2

HAIL EMBRYO STUDIES

Charles A. Knight and Nancy C. Knight

National Center for Atmospheric Research *
Boulder, Colorado 80303

1. INTRODUCTION

Researchers have described and classified hailstone embryos, or "growth centers," for many years (e.g., Weickmann, 1953). The classifications have ranged from "objective" (clear vs cloudy or opaque; e.g., Macklin et al., 1960) to semi-interpretive (rime vs glaze; Carte and Kidder, 1966) to much more detailed interpretations with many categories (e.g., List, 1958). All of the evidence used to place embryos in any genetic category involves some degree of subjectivity. In the discussion which follows, the subjective element is made as explicit as possible.

Hail embryos are studied in an effort to determine where, and by what microphysical processes, they are formed. Our approach has been to look at many hailstone embryos, find what appear to be natural descriptive classifications, and interpret these in terms of origin. It is observed that hailstone embryos may be divided into two major classes with a third, minor, but still distinct class. A small residuum remains unclassified. The classification and its interpretation is given in some detail in what follows and is applied to two large collections of natural hail. Some information about trajectories, inferred from D/H ratios and crystal sizes, is also included.

2. EMBRYO CLASSIFICATION AND INTERPRETATION

Much of the authors' work on hail embryo classification and interpretation has been published (Knight and Knight, 1970, 1973a, 1973b, 1974), so the emphasis here is on clear, brief exposition and and filling in some details. From observation, there almost always exists a distinct, inner growth unit in hailstones, ranging in size from 2-3 to 10-15 mm in diameter. In about 90% of the hailstones sectioned, this growth unit is one of two types, distinguished by shape, bubble organization and content, crystal size, and the presence or absence of internal cracking. "Archetypal" examples of the two types are given in Figs. 1 and 2. The first is conical and bubbly, sometimes having a transition to clear ice at the blunt end and has small or large crystals or transitions from one size to the other and no internal cracks. The other is round or oblate with a ring of clear ice surrounding a bubbly center, always has large crystals and often contains obvious internal cracks.

Interpretation of conical embryos as having originated from graupel and spherical ones from frozen drops may be traced to List (1958) and others and is discussed in the references by the authors given above. We have chosen to apply the term "embryo" to the units illustrated in Figs. 1 and 2. Here the true "graupel" part of the conical embryos are outlined and numbered 1 in Fig. 1. As far as we are aware, there is no evidence which would allow one to determine the true "frozen drop" portion of spherical or oblate embryos and we have used the outermost border of the clear inner ring to delineate these embryos. These boundaries have been chosen because they are almost always unequivocally identifiable. It was perhaps unfortunate to have chosen the words graupel and frozen drop to describe units defined in this way, however, the problem remains of referring to a distinguishable entity and at the time using words previously defined without reference to evidence supplied by the hail itself. We use "graupel embryo" to mean an embryo which originated from a graupel particle and "frozen drop embryo" to mean an embryo originating from a frozen drop.

In applying this classification there are areas of judgement which should be clearly described. A small, porous graupel particle may grow in an updraft, fall a little below the freezing level and melt partially and then enter another updraft and rise again, growing into a hailstone. It is certainly possible to misclassify the resulting embryo as having originated as a frozen drop, but such histories are probably too special to worry about. Classifications are given in statistical form and very particular circumstances such as these will affect them very little. The distinction between a group of air bubbles interpreted as having resulted from the final freezing of a drop and those representing a graupel, is made on the presence or absence of a detectable conical organization. Figure 3 gives two examples in which the conical organization is present but not overwhelmingly obvious.

* The National Center for Atmospheric Research is sponsored by the National Science Foundation. Part of the work reported herein was performed as a part of, and with some support from, the National Hail Research Experiment, managed by the National Center for Atmospheric Research and sponsored by the Weather Modification Program, Research Applications Directorate, National Science Foundation.

Figure 4 illustrates another possible error. Broken halves of drops fall in a constant orientation and may grow into very graupel-like embryos. If the plane of the thin-section shown here had been slightly off from center, the embryo would have been misclassified as a graupel but, again, this is a rare event and not statistically important. Another rare event is that instance when a frozen drop embryo does not freeze completely because the hail growth is always wet. At some stage of such stones the liquid may drain out and the embryo is then hollow.

There are two other embryo classifications, "spherical bubbly" and "other" and these two are occasionally combined. Spherical bubbly embryos are rather structureless, bubbly centers, quite distince from graupel or frozen drops. An illustration is given in Fig. 7.

Four points need to be mentioned. 1) In speaking of graupel, meaning the portions labelled 1 in Fig. 1 and not the whole embryo, the implication is that at one stage the material was loose, porous rime. The evidence for this seems very good (Knight and Knight, 1973b), but there is no evidence preserved of the nature of the ice particle upon which the riming started. It could be a vapor-grown crystal or a small frozen drop. A frozen drop bigger than several hundred microns diameter would be recognized. 2) In cases of doubt, shape itself is a strong reason for classification as one type of embryo or the other. This is because of the very strong observation that conical embryos do not grow from complete, frozen drops big enough to be identified: only from half-drops, whose fall orientation is stabilized by their shape. 3) Embryos of large and giant hailstones are very much more difficult to classify than those of smaller hail (1-3 cm). While part of this difference may be due to recrystallization and generally poorer collection procedures for the large hail, our impression is that this is not sufficient to account for the difference, and the reason for this is unresolved. 4) The problem of whether the orientation and positioning of the thin-section is appropriate to identifying the embryo, is always present. Judgement and care is called for throughout the process of sectioning and classifying. We consider this unimportant as a statistical bias, though a possible factor in individual cases.

3. EMBRYO TYPE STATISTICS

It is interesting to seek relationships between embryo type and climate and storm characteristics. The National Hail Research Experiment is conducted in northeastern Colorado where ground level is about 1.7 km MSL. The cloud base temperatures for hailstorms in this area range from -5 to +10°C and typical cloud droplet concentrations are about 1000/cc, placing the aerosol population well in the "continental" category. We have published (Knight et al., 1974) some results from extensive collections of hail in this area. Partly in connection with another project (Project DUSTORM) and partly to examine hail embryo types from another climatic region, a collection effort was made in Oklahoma in 1975 in cooperation with the National Severe Storms Laboratory. We have sectioned 655 hailstones from Oklahoma, Missouri and vicinity. In these areas the storms have warmer cloud bases and their source air is presumably more maritime. These two hail sources are distinguished in Table I, and the stones are further broken down as to size: greater than or less than 2.5 cm major diameter. The results show what one might expect: graupel embryos predominating in NE Colorado while drops predominate in Oklahoma; and in each region, the large hail is more likely to have drop embryos than the small.

Cloud base temperatures were calculated for as many of the NHRE hail collections as possible, using local soundings and parcel theory. Figure 5 shows a plot of percentage of frozen drop embryos in a storm collection vs the cloud base temperature. While the relation is not perfect, it is clear that warmer cloud base temperatures are conducive to frozen drop embryos.

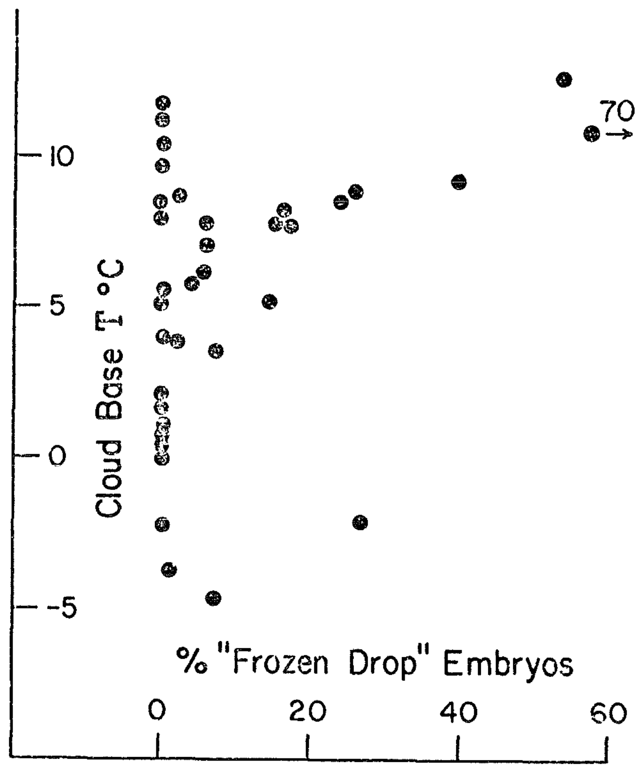

Figure 5. Calculated cloud base temperatures are plotted against percent of frozen drop embryos for 35 hailstorms in NE Colorado.

These results are not really surprising. Warmer cloud bases must surely correlate with stronger updrafts and consequently larger hail. Warmer cloud bases also provide a higher liquid water content and a greater vertical extent for liquid coalescence to operate. If frozen drop embryos are formed by recirculation of ice particles below the freezing level, so that they melt and then refreeze, there is also more opportunity for that process when the cloud bases are warmer.

4. D/H, CRYSTAL SIZE, AND EMBRYO TYPE: CORRELATIONS AND TRAJECTORIES

One of the major unanswered questions in hail research is where and at what time the embryos originate. Any means of interpreting the trajectory of the stone from the stone itself would be very valuable. The deuterium-hydrogen ratio D/H in the hailstone is one way of getting at the answer (Facy et al., 1963 and several later publications from other groups). A lower D/H implies growth higher in the cloud. Crystal size in the accretional (graupel) embryos is also valuable. According to work summarized by Pitter and Pruppacher (1973) and more recent work by Rye and Macklin (1975) and Abbott (unpublished), small crystal size, diameter less than 1 mm, implies growth at cloud temperatures lower than about $-15^{\circ}C$ and crystal size larger than that implies growth at warmer temperatures.

Small, conical hail that grew from graupel often shows sharp grain size transitions. The 1975 hail samples from NE Colorado that were collected in nets and quenched, contained several examples of such transitions. Two of the collections from the storm on July 23 were quite different: in one (#728), the crystal size was large at the start and small at the outside, indicating growth while ascending past the $-15^{\circ}C$ level; in the other (#727), the reverse was true (fig. 6). In each case, six stones were dissected to get large enough samples for D/H analysis, and the results are, in ‰ Standard Mean Ocean Water (SMOW)

#728	large (inside)	: -125.8	small (outside)	: -140.5
#727	small (inside)	: -150.8	large (outside)	: -128.6

One more collection, from July 22, 1975, had large crystals in the inside, and D/H for that layer was -116.8, while that for the outer layer of small crystals was -118.3. The agreement in trend between the D/H and the crystal size interpretation of the trajectory is encouraging, and more such checks are planned.

D/H in embryos may also by correlated with embryo type. Deuterium profiles have been measured on six giant hailstones that fell near Sterling, Colorado, on August 15, 1974. These results will be analyzed in detail and reported elsewhere by D. Ehhalt and the present writers, but the analyses of the embryos themselves are of interest here. The six stones had three embryo types, whose δD values, again in ‰SMOW, are given below.

Spherical bubbly (3)	-69.4, -72.5, -72.9
Graupel (2)	-57.4, -44.4
Frozen drop	-53.4

Several of these embryos are shown in Fig. 7. It is remarkable that in all six cases, the embryo δD value is an extreme for the entire stone: three times the highest value, three times the lowest. The frozen drop embryo is expected to have a high value if it shows anything approaching equilibrium with the lower levels in the storm where liquid drops are to be expected. The very low values for the spherical bubbly embryos would be consistent with formation high in these storms, and are no doubt one clue to how this rather minor embryo type originates.

5. CONCLUSION

Progress in understanding hail embryo formation hinges upon the kind of analysis in the last section: using structural features, deuterium (or O^{18}) content, and any other means to deduce some features of their histories. This kind of study must be done on hailstones properly collected at accurately known times and locations, from storms that are documented in other ways; especially storms with detailed radar reflectivity coverage, as well as Doppler coverage and data from penetrating aircraft. The paper by Musil et al., (1976) in these proceedings is a first try at such a synthesis, and efforts to obtain data sets of this kind will continue in NHRE.

REFERENCES

Carte, E. and R. E. Kidder, 1966: Transvall hailstones. Quart. J. Roy. Met. Soc., 92, 382-391.

Facy, L., L. Merlivat, G. Nief and R. Roth, 1963: The study of formation of hailstones by isotopic analysis. J. Geophys. Res., 68, 3841-3848.

Knight, C. A. and N. C. Knight, 1970a: Hailstone embryos. J. Atmos. Sci., 27, 659-666.

_____, and _____, 1973b: Conical graupel. J. Atmos. Sci., 30, 118-124.

_____, and _____, 1973b: Quenched spongy hail. J. Atmos. Sci., 30, 1665-1671.

_____, and _____, 1974: Drop freezing in clouds. J. Atmos. Sci., 31, 1174-1176.

_____, and _____, J. E. Dye and V. Toutenhoofd, 1974: The mechanism of precipitation formation in northeastern Colorado Cumulus. I. Observations of the precipitation itself. J. Atmos. Sci., 31, 2142-2147.

List, R., 1958: Kennzeichen atmosphaerischer Eispartikeln, I. Teil. Z. angew. Math. Phys., 9a, 180-192.

Macklin, W. C., E. Strauch and F. H. Ludlam, 1960: The density of hailstones collected from a summer storm. Nubila, 3, 12-17.

Musil, D. J., C. A. Knight, W. Sand, A. Dennis and I. Paluch, 1976: Radar and related hydrometeor observations inside a multicell hailstorm. Proc. Int. Cloud Phys. Conf., Boulder, Colorado, 1976.

Pitter, R. L. and H. R. Pruppacher, 1973: A wind tunnel investigation of freezing of small water drops falling at terminal velocity in air. Quart. J. Roy. Met. Soc., 99, 540-550.

Rye, P. J. and W. C. Macklin, 1975: Crystal size in accreted ice. Quart. J. Roy. Met. Soc., 101, 207-215.

Weickmann, J., 1953: Observational data on the formation of precipitation in cumulonimbus clouds. In Thunderstorm Electricity, ed. H. R. Byers, University of Chicago Press, 1953, 66-138.

TABLE I

		Graupel # (%)	Frozen drop # (%)	Other # (%)	Total
≤2.5 cm	NE Colo.	1982 (86)	197 (8)	127 (6)	2306
	Okla. +	69 (25)	151 (55)	54 (20)	274
	Total	2051 (80)	348 (13)	181 (7)	2580
>2.5 cm	NE Colo.	80 (52)	46 (30)	29 (18)	155
	Okla. +	70 (18)	259 (68)	52 (14)	381
	Total	130 (28)	305 (57)	81 (15)	536
All	NE Colo.	2062 (84)	243 (19)	156 (6)	2461
	Okla. +	139 (21)	410 (63)	106 (16)	655
	Total	2201 (71)	653 (21)	161 (8)	3116

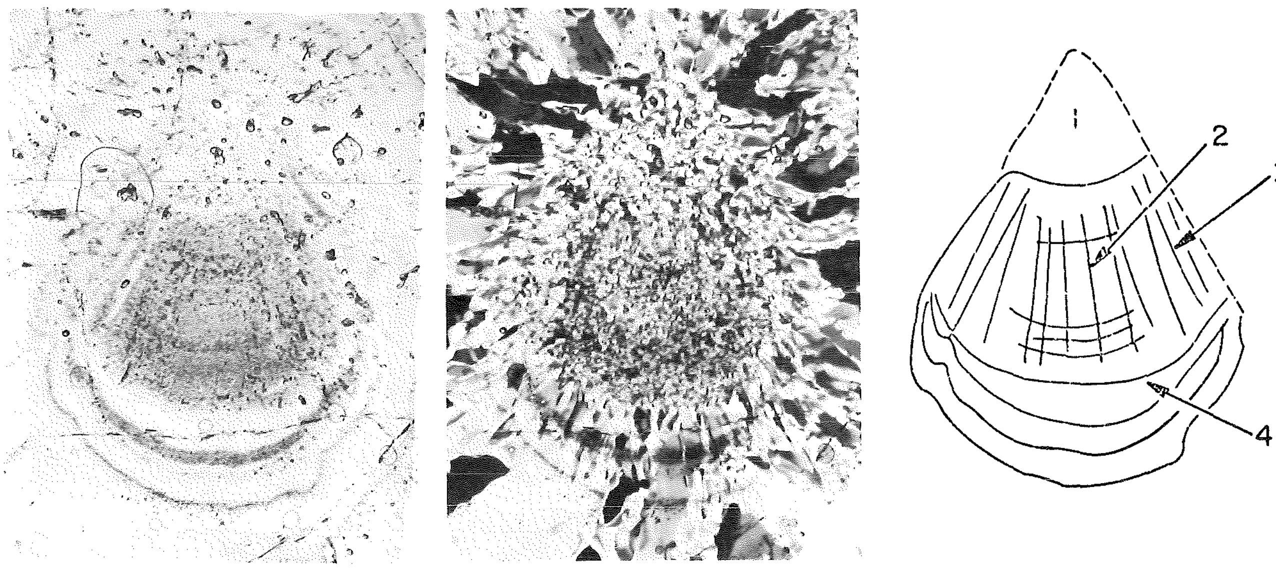

a)

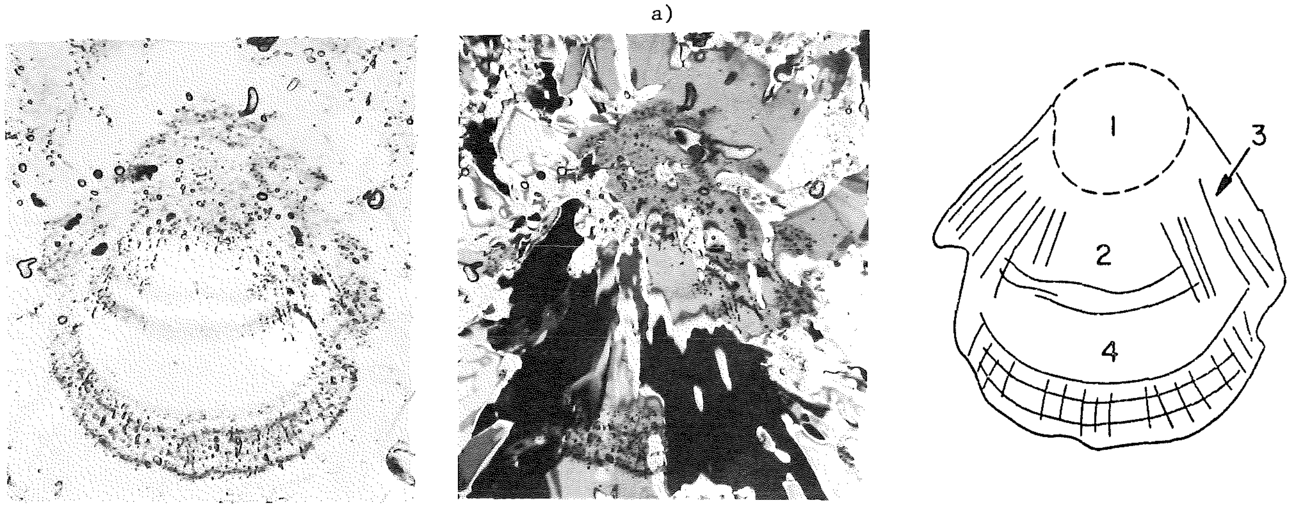

b)

Fig. 1. 3.4x. Two typical examples of graupel embryos: embryos that originate from graupel particles, labelled number 1 in the sketches. (June 11, 1973, Colorado).

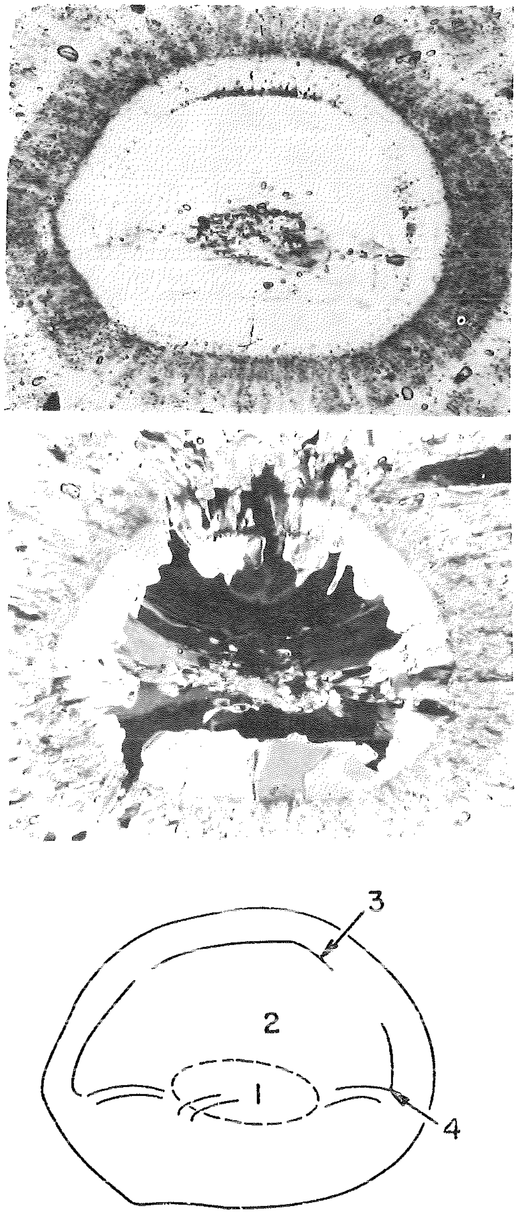

Fig. 2. 2.5x. A typical frozen drop embryo (June 4, 1973, Oklahoma).

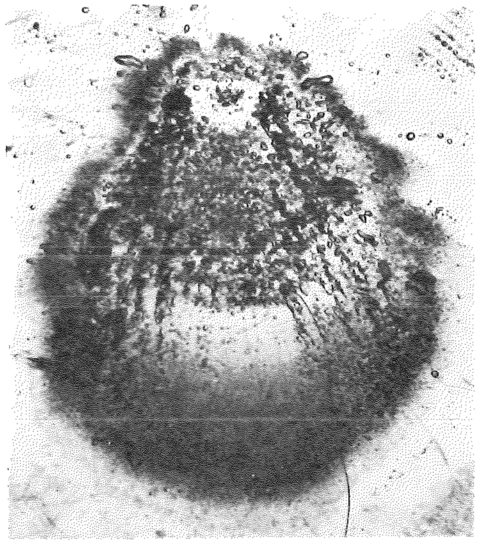

Fig. 4. 9x. Graupel-like embryo grown from a half of a frozen drop. (June 6, 1975, Oklahoma).

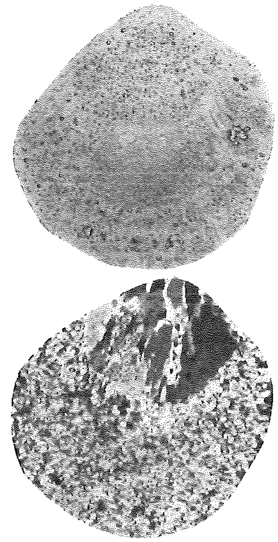

Fig. 6a. 1.8x. Typical hailstone from collection #728 (July 23, 1975).

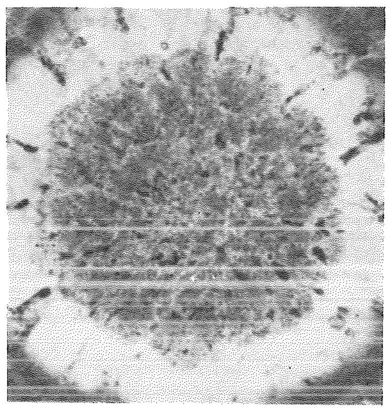

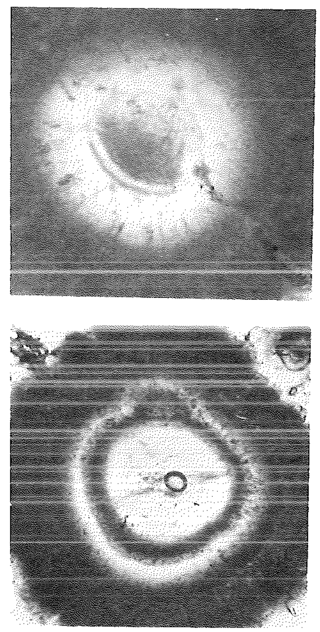

Fig. 7. 3.5x. The three embryo types from August 15, 1974, near Sterling, Colorado.

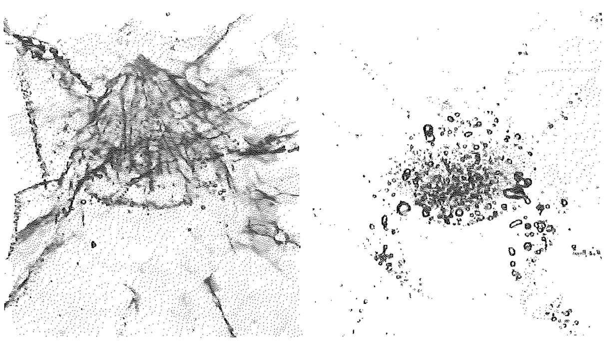

Fig. 3. 3.4x. Two graupel embryos, the left one quenched, the right one not. (June 11, 1973, Colorado).

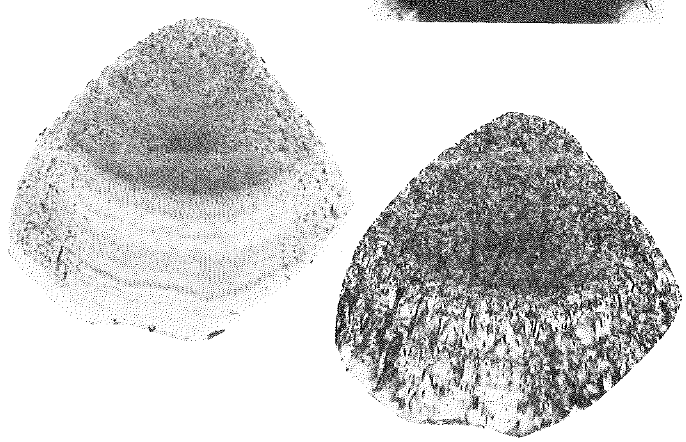

Fig. 6b. 1.8x. Typical hailstone from collection #727 (July 23, 1975).

3.4.3

CRYSTALLOGRAPHIC STRUCTURE OF SOME LARGE HAILSTONES AND ITS CORRELATION WITH ATMOSPHERIC CONDITIONS.

Laura Levi* - Elena M.de Achával - Luisa Lubart - María E.Saluzzi**.

Servicio Meteorológico Nacional - Buenos Aires - R.Argentina.
* Comisión Nacional de Energía Atómica.
** Comisión Nacional de Investigaciones Espaciales.

1. THE HAILSTORM

In the present work, several large hailstones, precipitated during two minutes from a highly developed air mass convective hailstorm, are analysed and their growth conditions are discussed

The storm took place under the lee of the Andes chain at Rama Caída - Mendoza - Argentina, on 8 January 1975. Storms of this type are frequent in this region when the following conditions are given (Saluzzi et al.1973):
1) A favourable thermodynamic pattern in low levels, i.e. the atmospheric circulation near the ground has already produced the advection of temperature and humidity necessary to establish the above mentioned thermodynamic pattern.
2) The entrance of an intense upper level trough.

The values of some cloud parameters, derived from the nearest radio sounding, are given in Table 1, where : h=height from the sea level; p=pressure; T_e=sounding temperature; T_i=temperature inside the parcel in adiabatic ascent; U=adiabatic updraft; w=adiabatic liquid water content.

Table 1 - Cloud Parameters

h (km)	p (mb)	T_e (°C)	T_i (°C)	U (ms^{-1})	w (gm^{-3})
3.90	640	6	6	2	0
4.60	580	- 1	1.5	7.9	2.2
5.45	520	- 8.5	- 3	13.9	3.5
6.40	460	-16	- 8.5	23.7	4.2
6.90	430	-20	-12	28.2	4.3
7.45	400	-24	-15	34.2	4.2
7.90	380	-26.5	-18	37.7	4.2
<u>8.20</u>	<u>360</u>	<u>-29</u>	<u>-21</u>	<u>40.6</u>	<u>4.1</u>
9.00	320	-34	-26.5	44	3.9
10.05	278	-40	-34.5		3.5
11.30	230	-45	-45.5		3.1

In the Table the underlined values correspond to the level h_m of maximum updraft U_m obtained on the assumption that the updraft speed decreases near the top of the cloud (English, 1973). Since the value of U_m, according to the modified updraft profile proposed by English, differs slightly from the value of U at $h=h_m$, it may be considered in the present case $U_m=40ms^{-1}$.

2. HAILSTONE ANALYSIS

A photograph of the hailstone sample is shown in Figure 1. The stones were oblate spheroids with maximum diameter of 5 to 7 cm and marked excentricity which reached, for the largest hailstones, a value of about 0.5. The opposite surfaces of the spheroids differ, one of them being knobby, the other smooth. Note that in the figure only H6

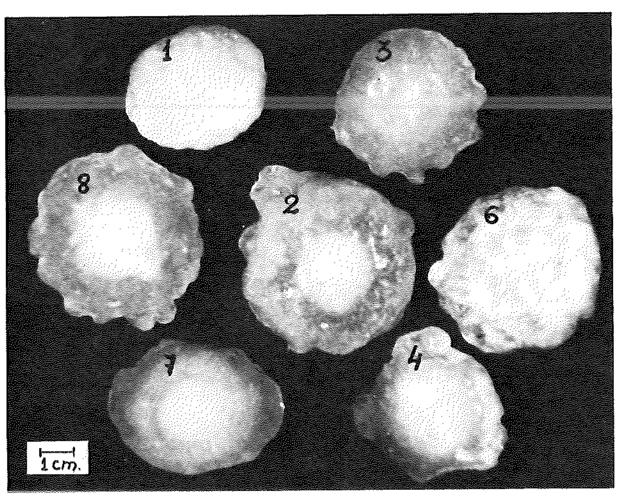

Figure 1 - External hail structure.

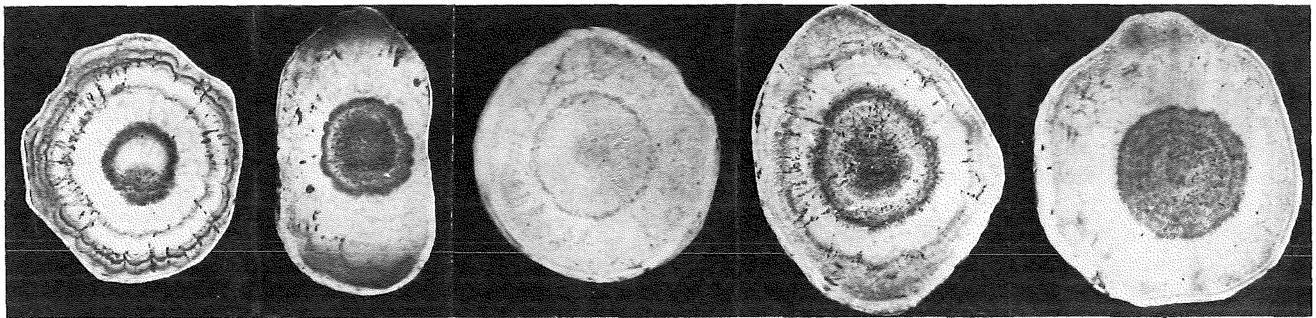

H1 H2 H3 H7 H8

Figure 2a - Hailstone sections in transmitted light. Note that the extremities of H2 are dark due to the weak illumination.

shows its knobby surface up. More pronounced knobs protrude from the lateral surfaces of the hailstones.

2.1. Crystal Structure

Figure 2a shows several hailstone sections observed in transmitted light. All sections contain the equatorial plane of the spheroids, except H2 that was cut through the plane containing the maximum and minimum diameters. Two thin sections observed by polarized light are given in Figure 2b. Here, weakly marked dark crosses may be noted, formed near the centre of H7 and in the peripheric zone of H8.

It may be noted that all samples, except H1, are mainly transparent and formed by large crystals in their peripheric zones. Their central zones or graupels present, however, some interesting differences. In fact, they can be characterized as opaque ice centres mainly formed by small crystals (H2,H6,H7,H8) and as transparent ice centres formed by large crystals (H1,H3,H4).

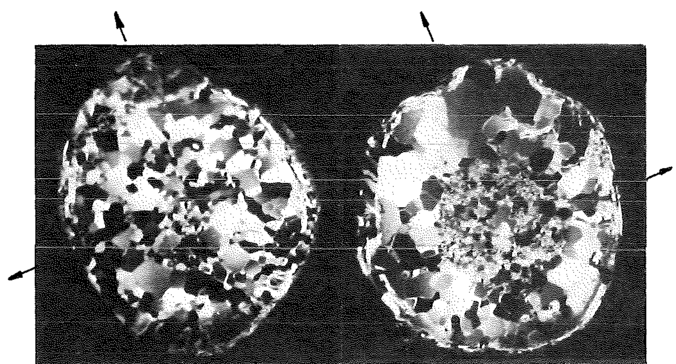

H7 H8

Figure 2b - Hailstone sections observed by polarized light. The arrows indicate the dark cross arms.

Some conical graupels, with their axes approximately in the ecuatorial plane of the spheroid, were also observed in a few cases (see H1 and H7 in Fig.2a). In the other samples the central zones appeared nearly spherical.

Table 2 shows the results obtained from the replica analysis of some

Table 2 - Crystal size and orientation in successive hailstone zones

Zone	H8 r (mm)	H8 $\bar{\sigma}$ (mm^2)	H8 $\bar{\varphi}$ (°)	H3 r (mm)	H3 $\bar{\sigma}$ (mm^2)	H3 $\bar{\varphi}$ (°)	H1 r (mm)	H1 $\bar{\sigma}$ (mm^2)	H1 $\bar{\varphi}$ (°)	H7 r (mm)	H7 $\bar{\sigma}$ (mm^2)	H7 $\bar{\varphi}$ (°)
0	0- 3	2.0	-	0- 4	0.4	-	0- 6*	22.0	-	0- 5*	0.8	-
1	3-10	0.1	-	4- 9	2.5	<30	6-13*	2.0	<30	5-11*	0.1	-
2	10-16	2.0	25	9-12	2.5	-	6- 7	0.1	-	6- 9	1.0	<30
3	16-23	5.0	42	**	0.3	-	7-13	2.0	<30	9-12	0.2	-
4				12-20	2.0	>40	13-20	2.0	>40	12-22	1.0	>40

* The radial distance is taken from the apex of the graupel.
** Discontinuous layer of small crystals.

hailstones. The table gives, for successive hailstone zones, the minimum and maximum radius r of the zone, the mean crystal surface $\bar{\sigma}$ and the mean value of the angle $\bar{\varphi}$ formed by the crystal c-axis with the radial direction. Notice that some melting, occurring during the preparation of the samples, reduces slightly the replica radii with respect to those of the stones.

In each sample, $\bar{\varphi}$ was only obtained for a few zones where crystals were satisfactorily etched. Both, $\bar{\varphi}$ and $\bar{\sigma}$ have been carefully determined for Zones 2 and 3 of H8, where about 100 crystals have been analysed in each zone. For other samples, $\bar{\varphi}$ has been evaluated analysing a smaller number of crystals. In these cases it has been indicated in Table 2, $\bar{\varphi} < 30°$ or $\bar{\varphi} > 40°$, according to the interval where this angle is found. As it is known, (Levi and Aufdermaur, 1970), $\bar{\varphi} < 30°$ corresponds to dry growth, while $\bar{\varphi} > 40°$ must be interpreted, in the present case where crystals are large, as an evidence of wet growth.

The evaluation of $\bar{\varphi}$ was mainly used to recognize dry and wet growth regimes, while the determination of $\bar{\sigma}$ was used to evaluate the air temperature T_a prevailing during growth. This has been done on the basis of Figure 3 obtained by the present authors from the analysis of some artificial accretions.

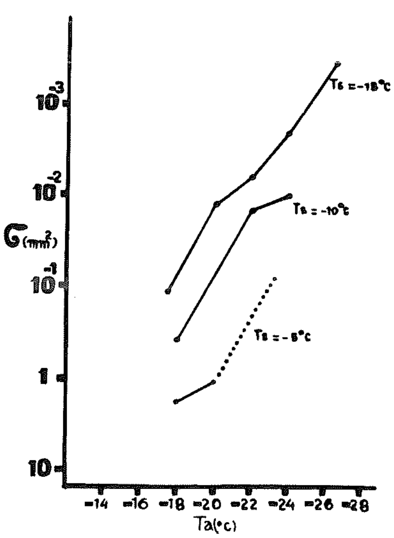

Figure 3 - Crystal size as a function of T_a for different values of T_s.

For some zones of dry growth formed by elongated crystals, the mean value of the crystal width ($\bar{d}$), was also determined (Rye and Macklin, 1975). The results are given in Table 3

Table 3 - Mean crystal width

	H1	H3	H7	H8
Zone	1	1	2	2
$\bar{d}$ (mm)	0.9	1.1	0.7	1.0

2.2. Growth conditions

In order to correlate the growth conditions with the crystal structure, hailstones may be classified as follows:

a) Hailstones with opaque centre H2, H6, H7 and H8.- The structure of H8 is taken here as a representative example of this kind of hailstones. It may be noted that its transparent peripheric region appears uniform by observation in transmitted light (Fig.2a) though crystals are getting larger with increasing diameter as it is shown in Figure 2b.

In Table 2 this region has been divided in Zone 2 and 3, each of them characterized by a different crystal orientation and size. The value $\bar{\varphi} = 25°$ found for Zone 2 indicates that this was formed in dry growth regime, whereas the change to $\bar{\varphi} = 42°$ observed in Zone 3 suggests a transition from dry to wet growth. This indicates that the temperature T_s which prevailed during growth of Zone 2 was just under 0°C.

The weak dark cross, shown in Figure 2b in the peripheric region of H8, is in agreement with these results and show that some of the crystals nucleated in Zone 2 with dry growth orientation continuate in Zone 3, though wet growth conditions were established in the latter. Thus, crystals showing the dry and the wet growth orientations would both occur in this zone. The pronounced scattering of the crystal orientation resulting as a consequence, would determine the value $\bar{\varphi} = 42°$ measured in the replica. This value is intermediate between that corresponding to dry and to wet growth.

The results obtained for Zone 2 may now be used to evaluate the temperature T_a prevailing during the growth of this zone. In fact, the mean crystal size $\bar{\sigma} \cong 2$ mm² would give $T_a \cong -18°C$ (Figure 3, curve T_s=-5°C), while a higher value of this temperature, $T_a \cong -10°C$, would result from the mean crystal width,

$\bar{d}$ = 1mm (Rye and Macklin,1975). This difference may possibly be correlated with the limit dry-wet growth conditions prevailing in this zone, where crystals show a more rounded shape (Figure 2a) than typical growth accretions.

On the other hand, from $\bar{\varphi} = 25°$, it is obtained according to Levi et al. (1974), $T_a \cong -22°C$. This temperature is evidently too low for the present zone formed by large crystals and transparent ice. This disagreement could be explained considering that, in dry growth regime , an increased degree of disorder would always determine an increase of $\bar{\varphi}$.

It may be concluded that Zone 2 was probably started at $T_a \cong -18°C$, where the transition occurs from the small crystals of Zone 1 to the large ones of Zone 2. This temperature would increase towards approximately $-10°C$, arriving to Zone 3 where the transition occurs from dry to wet growth regime .

The temperature T_a may also be estimated for Zone 1, which should have grown in dry regime , the same as Zone 2. Assuming $-10 < T_s < 0°C$, it is found from Figure 3 $T_a \cong -22, -24°C$. A similar estimation of T_a is obtained if the crystal mean linear dimension $\sqrt{\bar{\sigma}}$=0.3mm is compared with the values given for $\bar{d}$ by Rye and Macklin.

As for Zone O, probably corresponding to the hailstone embryo, it is formed again by large crystals which indicate $T_a \cong -18°C$.

b) Hailstones with transparent centre H1,H3 and H4.- As noted previously these hailstones are nearly completely formed by large and transparent crystals grown at T_a = -18, -10°C, as it is shown in Tables 2 and 3. Notice that Zone 0 of H1 is rather opaque probably due to riming, but it is formed by a large single crystal.

The analysis of the crystal orientation indicates that, in these cases too, dry growth prevails up to hailstone radii of 15-20 mm, where thin opaque layers formed by small crystals, are usually found. In more peripheric zones large crystals prevail again, showing a scattered orientation, probably corresponding to wet growth.

3. DISCUSSION

The previous analysis of the crystal structure may now be considered, to obtain information about the hail trajectory and about the temperature and the updraft speed existing in the cloud.

3.1. Liquid water content.

The observation that the transparent ice zones, consisting of large crystals, were formed in dry growth regime up to about 10-15 mm radius, has been used to obtain an evaluation of w.

Assuming T_a = -18°C and T_s near 0°C for hailstone radii 10<r<15 mm, it has been found $w \cong 2$ gm^{-3}. This value is lower than the adiabatic values given in Table 1. The difference could be accounted for considering depletion in the region of quick hailstone formation.

3.2. Hailstone trajectory and updraft speed.

It may be noted that the observed different structures of hail central zones indicate that large hailstones, collected on the ground at nearly the same place and time, may have grown along quite different initial trajectories.

Thus, opaque graupels formed by small crystals should have grown around embryos formed inside an updraft strong enough to carry them up quickly into the higher cloud region, where the temperature is low and the updraft speed begins to decrease with increasing height (Gokhale,1969). Here they would spend some time, possibly with small up and down motions. These oscillations may be responsible of the layered structure shown by the graupel of H8 and by the opaque-transparent-opaque transition shown by that of H2 and of other samples.Finally,after reaching balance, the stones would precipitate to the ground crossing warmer regions of the cloud,where clear peripheric zones, consisting of large crystals,would form.

On the other hand, hailstones nucleated at lower cloud levels, would grow to medium size before arriving to regions of high updraft speed. Thus, they would reach balance without penetrating into low temperature regions and would precipitate inmediately after. The transition from the upward to the downward motion of the hailstone, could be recognized by the formation of opaque layers, formed by small crystals which appear as dark rings in the photographs of Figure 2a. H3 may be taken as a representative example of this type of hailstones.

More complex structures were shown by some samples such as H1 and H7, where the presence of successive opaque rings could be considered as an evidence of recicling.

Table 4- Balance radii and updraft speeds

	r_1 (mm)	r_2	U_{r_1} (ms^{-1})	U_{r_2}
H1	1.2	1.7	32	38
H2	0.9	-	28	-
H3	1.1	-	30	-
H4	1.2	-	32	-
H6	1.2	-	32	-
H7	1.0	1.5	29	36
H8	1.1	-	30	-

Table 4 gives the radii of the opaque graupels and those of the successive opaque rings observed in different stones and the corresponding updraft speeds U_r, calculated assuming balance (Knight et al.1975). The first transitions occurring in H1 and H7 (Figure 2a) are not considered here because they could be correlated to the rotation of the conical graupel with respect to the updraft.

It may be seen that all stones show a transition at $r = 10mm$, $U_r=30\ ms^{-1}$ while the second transition shown by H1 and H7 corresponds to $U_r=35-38\ ms^{-1}$.

It is now possible to compare the values of U obtained from the hail structure with those derived from the radiosounding. According to Table 1, the adiabatic updraft would attain 30 ms^{-1} at $h \cong 7$ km. It could be inferred that this level represents the maximum height reached by graupels when they ascend within the cloud. However, if hailstones showing only one balance radius would precipitate to ground from this height, they would only descend through a cloud column of about 2 km before reaching the freezing level, where it is $U \cong 10\ ms^{-1}$. It may be easily calculated that the thick peripheric regions of these stones , partially grown in dry regime, could not have been formed along such trajectories.

On the other hand, the results previously derived from the hailstone structure show that graupels similar to H8 should develope inside cloud regions where $h > h_m$. Thus, a more convenient interpretation of the behaviour observed could be the hypothesis that the updraft speed prevailing during hail growth was lower than its adiabatic value. This could be due to the inadequacy of the adiabatic model, which does not take into account the horizontal distribution and the time dependence of the updraft. Actually, the existence of the second balance shown by H1 and H7 may be interpreted if it is assumed that the updraft was increasing during the development of the phenomenon, determining a second ascent of some stones. The fact that the second balance occurs at $U_r \cong U_m$ supports this interpretation.

3.3. Air temperature in the cloud.

According to the previous discussion, hailstones similar to H8 would spend most of the time needed to form the graupel at cloud levels h > 8.2 km where Table 1 gives $T_e < -29°C$. However, the crystal structure indicates that these graupels were growing at a temperature $-20 > T_a > -25°C$. It may be concluded that the air temperature of the cloud was several degrees higher than the sounding temperature T_e and probably near to the adiabatic temperature T_i.

It may be seen from Table 1 that for h < 8 km, this temperature increases towards ground from -18°C to -8°C, along a cloud column of about 1.5 km. Such temperature distribution would justify the formation of transparent ice zones, formed by large crystals, as they have been observed in the present hailstones.

Acknowledgments - The authors are indebted to G.Leyva and A.Faigon for technical help and to Dr.J.Nuñez for the interest paid to this work.

L.Levi acknowledges the economic support of the National Research Council of Argentina.

REFERENCES

English M.,1973: The growth of large hail. Report MW-78, Stormy weather Group, Mc Gill University,Montreal.

Gokhale N.R. and K.M.Rao, 1969: Theory of Hail Growth. J.Rech.Atmos. 4,153-178.

Knight C.A.,D.H. Ehhalt,N.Roper and N.C. Knight , 1975: Radial and Tangential Variation of Deuterium in Hailstones. J.Atms.Sci.32,1990-2000.

Levi L. and A.N.Aufdermaur, 1970:Crystallographic orientation and crystal size in cylindrical accretions of ice.J.Atmos. Sci. 27,443-452.

Levi L.,E.M.de Achaval and L.Lubart,1974: Structure of ice grown from droplet accretion and solidification process. J.Crystal Growth, 22,303-310.

Rye P.J. and W.C.Macklin, 1975: Crystal size in accreted ice. Quart.J.R.Met.Soc. 101, 207-215.

Saluzzi M.E.,J.M.Nuñez and D.Berger, 1973: Estudio comparado del comportamiento de la convección severa en la zona norte de la Pcia. de Mendoza. Congreso de la Asociación Física Argentina.

3.4.4

ON THE VARIATION OF THE COLLECTION EFFICIENCIES OF ICING CYLINDERS

Roland List, P.I. Joe, G. Lesins, P.R. Kry, M.R. de Quervain*, J.D. McTaggart-Cowan, P.W. Stagg, E.P. Lozowski**, E. Freire, R.E. Stewart, C.G. List, M.C. Steiner, J. Von Niederhäusern*

Department of Physics, University of Toronto, Toronto, Canada

1. INTRODUCTION

The importance of studying the growth of hailstones in the laboratory at pressures equivalent to those occurring in hail clouds has been recognized about twenty years ago. The facilities to perform such investigations became available in 1963 [List, 1966a]; however they have not been used at conditions different from laboratory pressures until 1972 and 1974 when a team from the University of Toronto, reinforced by a participant from the University of Alberta, was allowed to carry out icing experiments in the pressure controlled Swiss hail tunnel.

The need to duplicate atmospheric conditions and not just to simulate them [List, 1966b] arises from the fact that heat and mass transfers, aerodynamics and collection processes may vary with pressure and lead to different artificial ice deposits. If this were the case, any interpretation of ice structures as they are performed now may have to be completely revised.

When the artificial hail growth experiments were carried out in 1972, it became obvious that unexpected insights complicate the generally accepted picture even more. It was found, for example, that the collection efficiencies were substantially lower than expected on the basis of Langmuir and Blodgett [1946] and Macklin and Bailey [1968] and seemed to have a strong dependence on the liquid water content w. Thus, the previously used method [List, 1960] to calibrate the liquid water distribution across the wind tunnel by the icing of cylinders - in which it was assumed that the ice deposit distribution was a true image of the w-distribution - had to be discarded. This procedure relied on the known water injection rate of the nozzles, the assumption that the collection efficiency is constant along the icing cylinder, and that no icing occurs along the wind tunnel walls.

The importance and uniqueness of the artificial hail growth experiments and the anticipated scraping of the pressure controlled icing tunnel made it imperative to properly calibrate the liquid water content distribution. Since this specific investigation leads to insights which are not provided by the hail growth experiments, the calibration aspect - while being important from the point of view of the application - is overshadowed by the physics of the icing.

In the following, the icing of cylinders and its interpretation is discussed. It will be shown that the collection efficiency can be as low as 15% and that it depends on liquid water content, air density and relative velocity. Hence, the results by Carras and Macklin (1973) will be considerably expanded. The results will be far-reaching in terms of our thinking of hail growth and will provide key concepts to be applied in future theories on hail-formation, theories which in addition to new aerodynamic concepts [Kry and List, 1975] will include more adequate consideration of collision and heat and mass transfer processes.

2. THE ICING EXPERIMENT

The geometrical arrangement in the hail tunnel [List, 1966a] is shown in Figure 1. A rotating cylinder with a length of 22 cm and a diameter of 2.2 cm is mounted in the quadratic measuring section which has a width of 22.2 cm. The cylinder can be mounted either in the North-South or East-West direction, the rotation frequencies are between 1 and 2 Hz. The

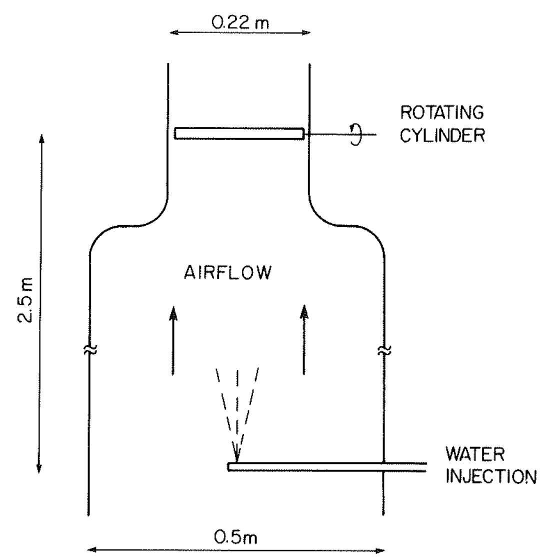

Figure 1. Arrangement of rotating cylinder in the pressure controlled hail tunnel.

*Swiss Federal Institute for Snow and Avalanche Research, Davos.
**University of Alberta, Edmonton.

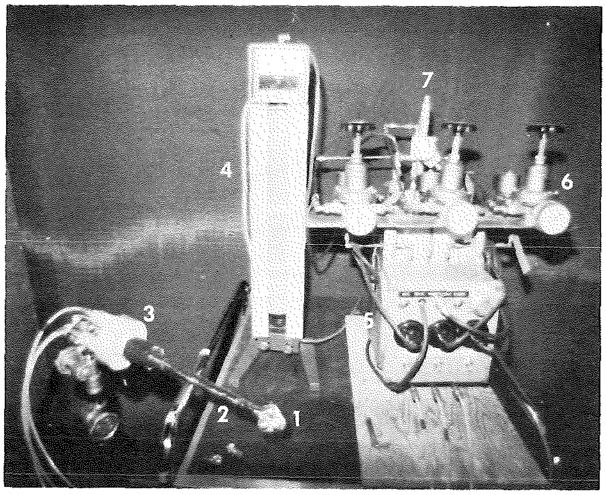

Figure 2. Water injection system with nozzles (1), mounted on heated arm (2), with flange (3) and connecting water purifying system consisting of de-ionizer (4), tank (5), valves for controlling nozzle pressure (6) and connection for controlling tank pressure (7).

water injection occurs 2.5 m below the cylinder in the tunnel section which is 50 x 50 cm wide. Three single nozzles can be mounted simultaneously on the heated head of the injector (Figure 2). De-ionized water [conductivity $\sim 10^6 \Omega^{-1} cm^{-1}$] is supplied from a pressurized vessel and can be injected during pre-selected time intervals. The 5 nozzles used are all of the conical type, their spray angles vary from 60-90^o and their openings allow different flow rates, achieved with different water pressures (4-8x10^{5}Pa). The water is injected without air to avoid disturbing the air flow too much. The flow rates were reproducible within $\pm$5% over a period of three years; they do not depend on pressure head variations as long as they are within 10% of the total pressure. The injection rates are not affected by a change in laboratory pressure from 733 hPa [Hail laboratory, Weissfluhjoch-Davos] to $\sim$ 1000 hPa [University of Toronto].

The droplet spectra produced by the different nozzles were established by exposing oil-covered glass slides into the droplet mainstream. This was difficult to achieve in the wind tunnel; therefore, the data given here are from direct spray measurements outside the tunnel, i.e. without artificial air flow. The droplet sizes seem to be larger than in the wind tunnel tests; collisions and coalescences while impacting and moving on the glass slides have certainly biased the data toward large droplets. In view of these possible errors, no correction seems necessary for the limited evaporation that the spray experiences in the wind tunnel. It may be recognized, however, that the smallest droplets may well have evaporated completely. This does affect the mean but not particularly the median volume diameter.

The droplet characteristics of the five different nozzles (A-E) and their combination ABC is displayed in Table 1. On first sight the diameters (up to $\sim$ 200μm) seem to be quite large. It has to be recognized however, that the large liquid water contents w used in these experiments (up to 50gm^{-3}) inevitably require large droplet sizes since the large values of w have to be accommodated essentially by the same droplet number as small values. Such sizes are not unreasonable also in view of fast acting droplet coalescence mechanisms which occur in nature under such circumstances [Leighton and Rogers, 1974].

In each individual icing experiment an iced cylinder was produced characteristic for nozzles A, B, C, D, E or ABC, dynamic velocity pressures p_{dyn} of 2, 3, 4 or 5 hPa ($p_{dyn} = \rho V^2/2$, where ρ is the air density and V the air velocity) and air densities ρ of 1.005, 0.692 or 0.477 kgm^{-3} corresponding to pressures at the laboratory level and the -10C and the -30C levels respectively, in a hail producing cloud in Colorado (Beckwith, 1960). The cylinders were inserted in the tunnel either in the North-South or the East-West direction. All experiments were carried out at an air temperature in the wind tunnel of -20C. Figure 3 shows a typical iced cylinder. 63 experiments were performed in total.

Nozzle	Injection Rate [gs^{-1}]	$\bar{D}$ [μ]	$D_{\bar{V}}$ [μ]	$D_{V,med}$ [μ]	$D>D_{\bar{V},med}$ [%]	D_{max} [μ]
ABC	15.60	58	100	144	10	215
B	7.64	16	63	118	3	185
A	5.22	51	74	94	11	186
C	2.72	35	73	120	7	180
E	1.22	46	71	98	8	156
D	0.61	17	41	65	4	113

Table 1. Average diameters $\bar{D}$, mean volume diameters $D_{\bar{V}}$, median volume diameters $D_{V,med}$ and maximum diameter D_{max} of drops produced by the different injection nozzles A to E and the combination of nozzles A, B and C.

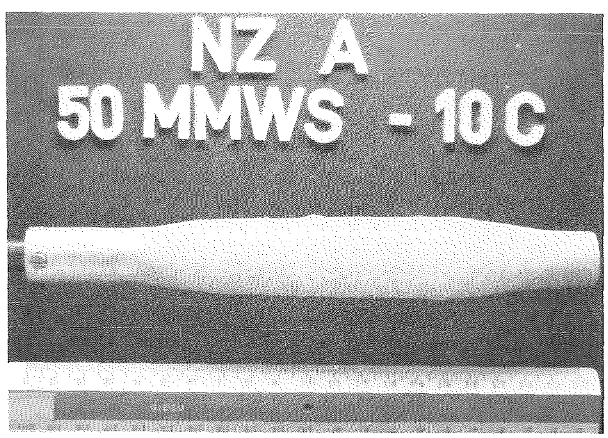

Figure 3. Cylinder iced for 60s by nozzle A at a temperature of -20C and a pressure of 504.7 hPa, equivalent to the -10C level in the atmosphere. The relative air speed was 38.4 m/s with a corresponding velocity pressure of 50mm of water or 4.9 hPa; scale in cm.

3. EVALUATION OF EXPERIMENTS

The photographic record was used to determine the average ice thickness of 19 cylinder segments of a length of 1 cm. Corrections due to distortion had to be considered. The accretion for each element (i) can be characterized by the equation:

$$E_i w_i = K_i = \pi \rho_i \, x_i (V\tau_i)^{-1}, \qquad (1)$$

where E_i is the collection efficiency of the i-th element, w_i the liquid water content to which the i-th element is exposed, ρ_i the ice density, x_i averaged ice thickness of the i-th element, V the velocity, and τ the icing time.

It was assumed that the liquid water content was distributed with a radial symmetry across the tunnel measuring section. This assumption was reasonable in most cases and allowed averaging of the symmetric cylinder segments including the North-South and East-West directions. In a few cases where this assumption was unsatisfactory a more elaborate procedure was applied.

It can then be argued that the percentage distribution of the total accreted water over all 9 radial rings and the inner core might be determined since the total injection is known. Negligible water was accreted occasionally on the tunnel walls, and negligible amounts were evaporated after injection. Hence, no special corrections were considered necessary. But the main problem is still unresolved: the liquid water distribution is not similar to the calculated ice deposit distribution. This would require a constant collection efficiency E.

Interpretations of other icing experiments suggested the following liquid water content dependence on E, with the other parameters being constant:

$$E = E_o + (1 - E_o)/(1+kw), \qquad (2)$$

where E_o is an asymptotic value reached at infinite w, and k is a measure of the curvature by which this limiting value is approached.

Substituting (1) in (2) and solving for w_i one obtains:

$$w_i = [K_i k - 1 + \sqrt{(K_i k-1)^2 + 4E_o K_i k}\,](2kE_o)^{-1}. \qquad (3)$$

Mass conservation requires that the w-flux is equal to the injection rate F. For the specific geometrical arrangement applied here according to Figure 3 this leads to:

$$w_1/8 + \sum_{i=2}^{10} w_i (i-1) = F(2\pi V)^{-1}. \qquad (4)$$

Hence E_i, w_i, k and E_o are the 22 unknowns (i=1 to 10). The set of 21 equations (1, 2 or 3 and 4) is not sufficient to produce unique values for E_o and k. A numerical procedure can now be applied to determine a continuous set

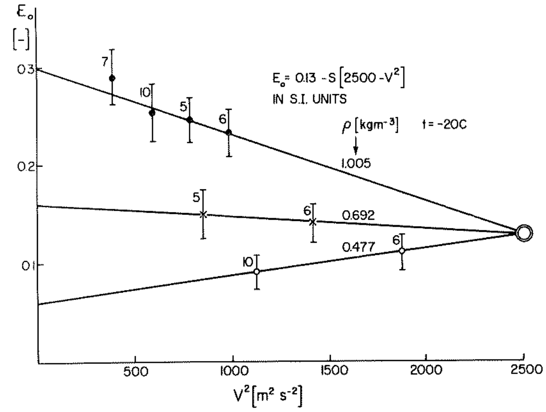

Figure 4. Average calculated asymptotic collection efficiency E_0 as function of V^2, for densities representing the laboratory pressure (733 hPa) and the pressure during haildays at the -10C level (504.7 hPa) and the -30C level (346.1 hPa). All experiments in which the values of E_0 are based were carried out at -20C. The error bars represent the standard deviation from the averages and the associated figures indicate the number of pairs of experiments used to derive the averages.

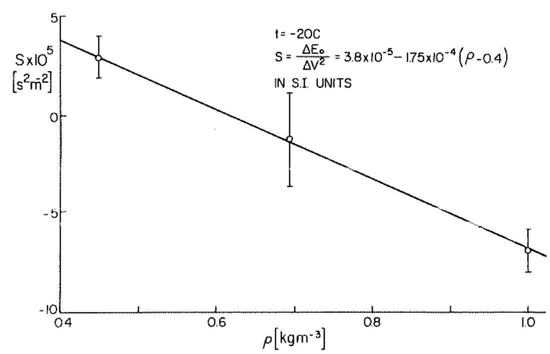

Figure 5. Density dependence of the slopes of the linear relationships E_0 versus V^2. Error bars are calculated with standard regression techniques.

(E_o,k) displaying the best fit to equation (2). In this (E_0,k) plane there is only one point which is physically significant. However, it cannot be found from measurements with one nozzle (with constant injection rate) only. Calculations have to be based on cylinders iced with different nozzles. This can be done if it is assumed that the differences in droplet character as displayed in Table 1 are not of major consequence, and that the function E(w) is essentially the same for all experiments, independent of nozzles. The set of (E_0) for the icing experiments which differed only in nozzles was then averaged over all pairs and plotted for different values of V^2 and air densities (Figure 4). Other functional dependences were also tried graphically but this one gave the best result. For given air densities the asymptotic collection efficiencies vary linearly with V^2, and the resulting lines have one point in common. The slopes of the straight lines show a nearly perfect linear dependence on density (Figure 5), which when combined with the results of Figure 4 leads to the equation:

$$E_o=0.13-[3.8x10^{-5}-1.75x10^{-4}\ (\rho-0.4)](2500-V^2), \quad (5)$$

in S.I. units.

The dependence of the asymptotic collection efficiency E_o on the air density is linear; it decreases with increasing V^2 for $\rho>0.4\ kgm^{-3}$, it increases for $\rho>0.4 kg/m^3$. Within the range of densities encountered in the average atmosphere where icing occurs ($\sim$0.4-0.8 kgm^{-3}) the velocity dependence of E_o is not spectacular.

Applying the same procedure used to determine E_o to the calculation of k leads to Figure 6. This display shows that k is not density dependent. It varies linearly with the V^2 according to:

$$k = 0.425\ V^2, \text{ in S.I. Units} \qquad (6)$$

Substituting (5) and (6) in (2), a general equation is found for the dependence of the collection efficiency on the icing conditions at a temperature of -20C:

$$E = a_1 - S(\rho)\ L(V^2) + \frac{a_2-S(\rho)\ L(V^2)}{1+a_3V^2w}, \qquad (7)$$

in S.I. Units,

where $a_1 = 0.13$, $a_2 = 0.87$, $a_3 = 0.525$,

$S(\rho) = 3.8 \times 10^{-5} - 1.75 \times 10^{-4}\ (\rho-0.4)$,

$L(V^2) = 2500 - V^2$.

4. DISCUSSION OF RESULTS

Equation (7) can be explored by varying either w, ρ or V^2 and leaving the values of the other independent variables constant. The ranges of variation were chosen in view of the artificial hail growth experiment with $0<w<50 gm^{-3}$ (up to $30gm^{-3}$ were measured by Sulakvelidze et al., 1967, and Kyle and Sand, 1973), $0.477 \leq \rho \leq 1.005 kgm^{-3}$ (the low value corresponding to a density at the -40C level in the atmosphere, the higher value given by the laboratory pressure at Weissfluljoch where the experiments were conducted), and $2hPa \leq p_{dyn} \leq 5hPa$ for the velocity pressure range. Rather than velocity, its corresponding pressure was treated as a variable because it remains constant for free falling objects, independent of atmospheric pressure.

Figures 7, 8 and 9 give the variation of E as a function of the liquid water content at different air densities and values of V^2. The low values of the collection efficiency E ($=E_1E_2$) or more precisely the coalescence efficiency E_2 (the observed collision efficiency E_1 is essentially unity) are quite unexpected. They imply that substantial bouncing and/or shedding of some kind has to occur. This is substantiated by photographs taken along the cylinder axis which show streaks of droplets originating at the cylinder surface (Figure 10). According to (7) E(w) is the same for all densities if $V^2 = 2500\ m^2s^{-2}$. The spread of E for different V^2 is larger at laboratory pressure than at $\rho = 0.573$ or $0.494\ kgm^{-3}$.

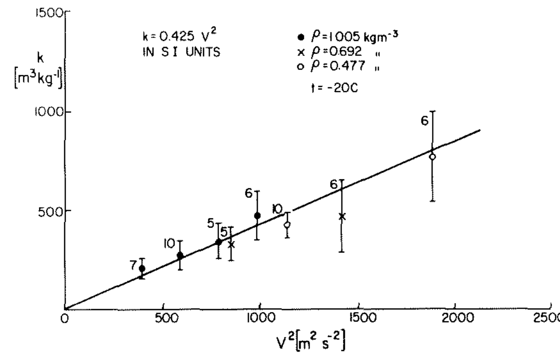

Figure 6. Dependence of curvature factor k on V^2, based on experiments carried out at three densities and a temperature of -20C. The average values were calculated for the number of pairs of experiments indicated.

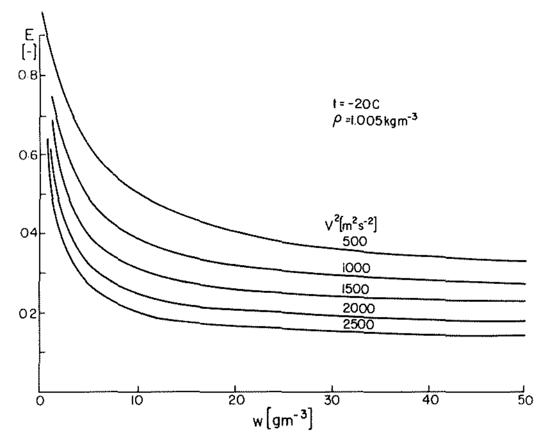

Figure 7. Calculated variation of collection (coalescence) efficiencies as function of the liquid water content, parameter V^2; for laboratory pressure (733 hPa).

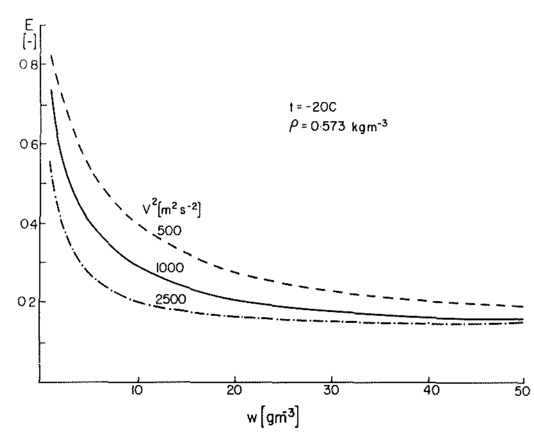

Figure 8. As Figure 7 but for 418 hPa, equivalent to -20C level pressure.

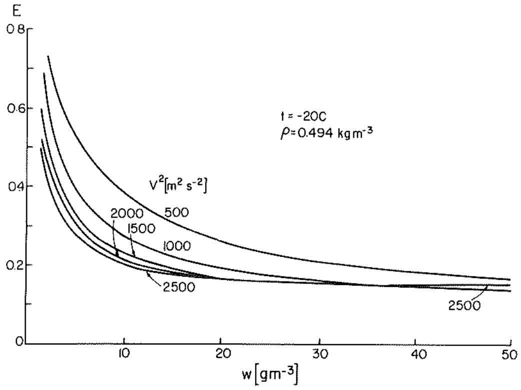

Figure 9. As Figure 7 but for 346.1 hPa, equivalent to -30C level.

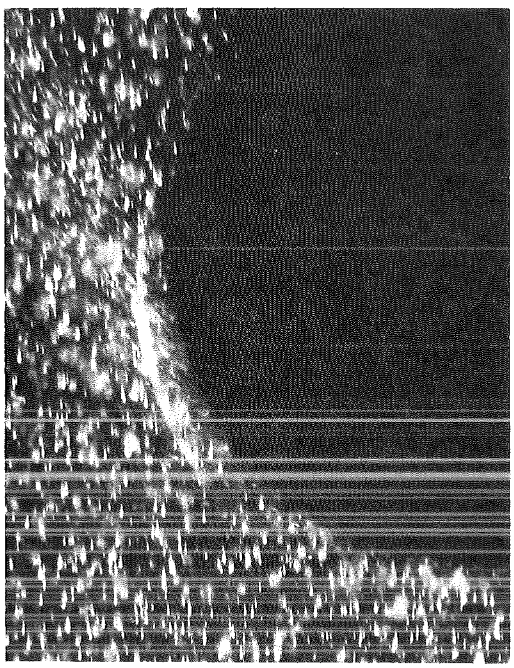

Figure 10. Photograph taken along the axis of a 2.2 cm diameter cylinder rotating at 4Hz; water was injected through nozzle B at laboratory pressure (733 hPa), air velocity 24.2 ms^{-1}, liquid water content $\sim$32gm^{-3}, temperature -20C.

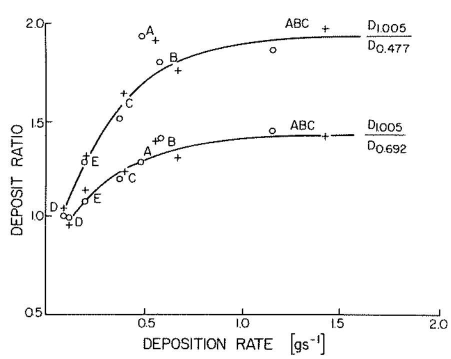

Figure 11. Ratio of ice deposits accumulated on cylinder at different air densities (1.005, 0.692 and 0.477 kgm^{-3}) for the deposition rates associated with Nozzles A, B, C, D, E and the combination ABC; temperature -20C; circles for velocity pressures of 2.94 hPa, crosses for 4.9 hPa.

The observed strong density dependence at high liquid water contents was already suggested by comparison of the total weight of the ice deposits at different deposition rates (Figure 11) calculated for the different icing cylinders. The density effect is reduced more and more as $w \to 0$. This bulk picture is repeated in the detailed analysis of (7) and (2) which confirm that $E \to 1$ as $w \to 0$. Figure 12 demonstrates very clearly that an air density variation affects E more when the liquid water content is high and the farther V^2 deviates from 2500m^2s^{-2}. For V = 50 ms^{-1} the density effect is nil. If the cylinder would be falling freely (with constant drag coefficient) and only infinitesimal deposits were considered, then plotting of E against the dynamic pressure p_{dyn} is logical. This is done in Figure 13, which shows that the collection efficiency is very small for large water contents (>10gm^{-3}) and does not depend much on the free fall speed. E increases with decreasing w and so does its dependence on the dynamic pressure. The density effect at a given w is essentially independent of p_{dyn}.

A comparison of Figure 12 for ρ = 1.25 kgm^{-3} with Carras and Macklin's (1973) Figure 4 for similar values of cylinder diameters (2.5 vs. 2.2 cm), air speed (32-35 vs. 33 m/s), air temperature (-17.5 and -22.5C vs. -20C) and sea level air pressure shows that these authors give a constant collection efficiency of $\sim$0.5 for liquid water contents varying from 1-10 gm^{-3}. The present experiments, however, give E = 0.42 for w = 10 gm^{-3} increasing to E = 0.8 for w = 1 gm^{-3}. It may be added that a variable collection efficiency is easier to accept and explain by considering the dependence of surface conditions from w.

It may be mentioned that no error is expected to contribute to this comparison on the basis of droplet temperatures. In both cases they adjust after injection within about 1C to the air temperature. The heat transfer droplets-air is very efficient; when water was injected at the boiling point no difference in icing appeared

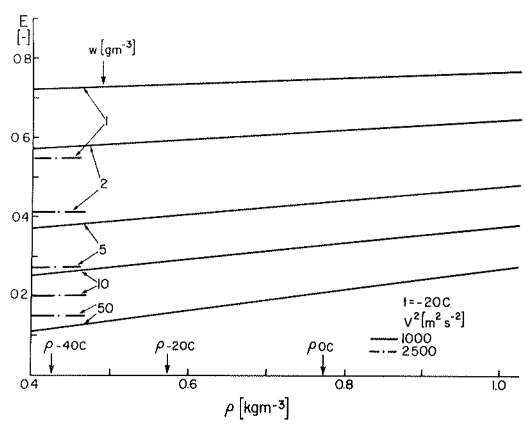

Figure 12. Density dependence of coalescence efficiency ($\equiv$ collision efficiency), for different liquid water contents and air speeds of 31.6 and 50 ms^{-1}. Note that E is independent of density for V = 50 ms^{-1}. Densities corresponding to the hail growth region are bound by the 0C and the -40C level as indicated.

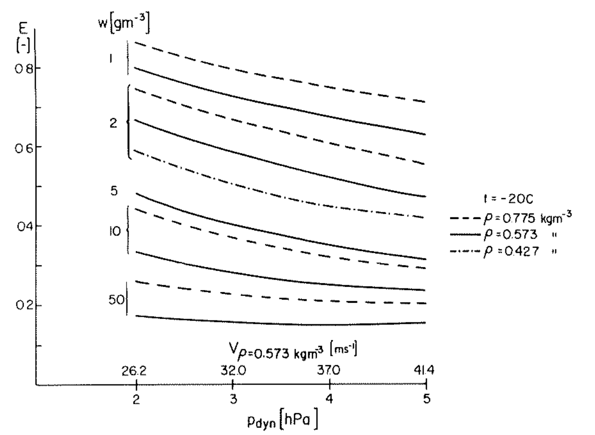

Figure 13. Dependence of the coalescence efficiency on the velocity pressure or dynamic pressure head p_{dyn}, for different liquid water contents and densities, with 0.775 representing the 0C level density and 0.427 the -40C level value. Also indicated are velocities for density 0.573 kgm^{-3} (corresponding to the pressure at the -20C level). Dynamic pressures are constant for given freely falling bodies independent of density or air pressure. Dynamic pressures are constant for given freely falling bodies and are independent of air density and pressure.

as compared with the normal case of water injected just above freezing. To what degree the droplet size affected the collection efficiency is unknown. It may be assumed that Carras and Macklin (1973) used droplets with diameters of the order of 20μ.

5. EXPERIMENTAL ACCURACY

Let us now assess the accuracy of the data. The air velocity is measured with a precision water micro-manometer (< ± 1%), the wind tunnel pressure with a special precision gauge (< ± 0.1%), and the air temperature is known to within 1C. The average thickness of the iced cylinder segment is assessed within 10% and compared and corrected in respect to the total deposit which is weighed to within 0.1%. The biggest error is incurred through the numerical methods in determining E_o and k and equations (1) - (4). However, the extent of the standard deviations shown in Figures 5 and 6 demonstrates that the equations for E and k seem to be more reliable than indicated by the error bars. A statistical assessment of the error would be unsatisfactory because they would give rather meaningless limits. Assuming that the basic model E(w) (equation 2) is correct for w > 1gm^{-3}, then the original uncertainty in E is primarily attached to w and not to E_o and k. Combining the apparent errors in E_o,k and the w-related ones of all the measured quantities with the consistency of the data set and the ease at which it could be repeated, a standard error of ± 20% is suggested for w. While liquid water contents as low as 0.1 gm^{-3} entered the calculations to establish equation (7), it has to be said that the weight of these low values is rather small as compared to the bulkier deposits at higher w's. (Due to this insensitivity at low w the value E = 1 may even be approached with a horizontal tangent, i.e. dE/dw = 0 at w → 0).

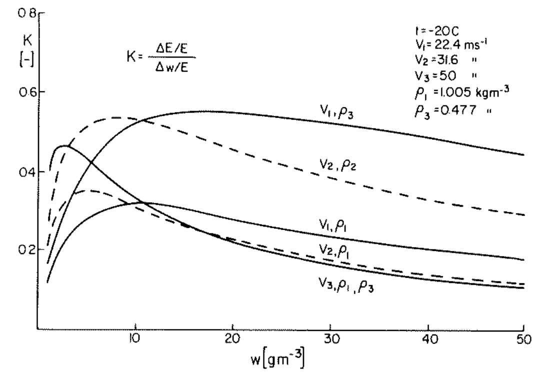

Figure 14. Dependence of the error multiplication factor K on the liquid water content W.

Hence, it is proposed to increase the error for w < 2 gm^{-3} to 50%.

If it is assumed that the spreads in E and k are caused essentially by the error in w then the error of the collection efficiency ΔE is only dependent on Δw and can be assessed through logarithmic differentiation of equation 2:

$$\frac{\Delta E}{E} = \left| \frac{(E_o-1)kw}{E(1+kw)^2} \right| \frac{\Delta w}{w}. \qquad (8)$$

$$\text{Setting } K = (E_o - 1)kw\, E^{-1}(1+kw)^{-2} \qquad (9)$$

the amplification of the error in the liquid water content (Δw/w) can be assessed and leads to an estimate of the error to be expected in E.

Plotting K versus w (Figure 14) shows that the error in the calculated collection efficiency is normally less than half the error in the liquid water content. It is highest for low speeds and low air densities, it is low for V = 50ms^{-1} where it is density independent. Except for one parameter combination (V_1,ρ_3), the error peaks at liquid water contents below 10gm^{-3}. The drop in K at low w (< 2gm^{-3}) is not real because it will be compensated by an increasing error in w. For free fall icing in the atmosphere the error amplification is generally quite less than K = 0.5.

6. CONCLUSIONS

Experiments on the icing of cylinders with diameters of 2.2 cm in a pressure controlled wind tunnel at an air temperature of -20C at different air speeds, air pressures and liquid water contents lead to the following statements:

a) Due to their size and inertia the droplets in the air stream were not deflected by the presence of a slowly rotating cylinder (Collision efficiency ≈ 1). The coalescence efficiency however, was reduced considerably to values as low as 15%.

b) The reduction in the coalescence efficiency is caused by bouncing and shedding processes. Whereas bouncing depends on the size of the colliding droplets, shedding mechanisms mainly depend on the state of the surface water skin or w (see also Joe et al., 1976).

c) The dependence of the collection efficiency E on liquid water content w, air density and air speed is given by a general formula. The w-dependence can best be described by a function of the principal form 1/w, which approaches a limiting value of E, namely E_o, asymptotically for $w \rightarrow \infty$.

d) The collection efficiency E is dependent on air density, except for a speed of $V = 50ms^{-1}$. E can be up to 58% lower (for $V = 33ms^{-1}$ and $w = 10gm^{-3}$) than measurements would indicate at (near sea level) laboratory pressures.

e) The asymptotic value for $w \rightarrow \infty$ of the collection efficiency, E_o, of a cylinder is dependent on air density and air speed. The way E_o is approached starting from 1 at w = 0 is given by a curvature factor k, which is larger for higher speeds and independent of air density.

f) While the water loss is large it is never such that an increase in liquid water content will lead to a decrease in ice deposit growth.

A comparison of theoretical heat and mass transfer calculations with experiments of the type Carras and Macklin (1973) used in respect to a critical water content, separating "wet" from "dry" growth, is unlikely to give satisfactory results because of two reasons: (a) the separation between "wet" and "dry" is very artificial because the surface is always partially "wet" for "dry" growth and (b) the heat and mass transfer calculations assume a temperature of OC for the bouncing or shedding water. This does not seem to be the case.

In summary, the new experiments have demonstrated that icing experiments at laboratory pressures cannot be translated to apply for regions in clouds in which hail is formed. The growth mechanisms are different because the heat and mass transfer is density dependent and, thus, affects collection through changes in surface characteristics.

Acknowledgements. The permission by the Swiss Federal Forestry Administration, Department of the Interior, to carry out the icing experiments in the Swiss Hail Tunnel is greatly appreciated. The help by collaborators at the Swiss Federal Institute of Snow and Avalanche Research was considerable and thanks go also to Mr. M. Kostilek and his colleagues of the workshop of the Physics Department of the University of Toronto who built the measuring section used in the experiment. The operational costs for the experiment were shared by the Swiss Institute, the Atmospheric Environment Service of Canada and the Canadian National Research Council. It should be remembered that the Swiss Hail Tunnel was built under a grant by the Swiss National Fund. The evaluation of the experiment was carried out at the University of Toronto.

REFERENCES

Beckwith, W.B., 1960: "Analysis of hailstorms in the Denver network, 1949-1958", in Physics of Precipitation, Geophysical Monograph No. 5, Amer. Geoph. U., 348-353.

Carras, J.N., and W.C. Macklin, 1973: "The shedding of accreted water during hailstone growth". Q.J.R.Meteor.Soc., 99, 639-648.

Joe, P.I., R. List, P.R. Kry, M.R. de Quervain, P.Y.K. Lui, P.W. Stagg, J.D. McTaggart-Cowan, E.P. Lozowski, M.C. Steiner, J. von Niederhausern, R.E. Stewart, E. Freire, G.Lesins, 1976: "Loss of accreted water from growing hailstones". Proceedings Int'l. Cloud Physics Conference, Boulder, Colorado, July 26-30.

Kry, P.R., and R. List, 1975: "Angular motions of freely falling spheroidal hailstone models". Phys. Fluids, 17, 1093-1102.

Kyle, T.G., and W.R. Sand, 1973: "Water content in convective storm clouds". Science, 180, 1274-1276.

Langmuir, I., and K.B. Blodgett, 1946: "A mathematical investigation of water droplet trajectories". U.S. Army Air Forces Tech. Rep. No. 5418.

Leighton, H.G., and R.R. Rogers, 1974: "Droplet growth by condensation and coalescence in a strong updraft". J. Atmos. Sci., 31, 271-279.

List, R., 1960: "Zur Thermodynamik teilweise wässriger Hagelkörner". Z. angew. Math. Phys., 11, 273-306.

------, 1966a: "A hail tunnel with pressure control". J. Atmos. Sci., 23, 61-66.

------, 1966b: "On the simulation of physical processes occurring in clouds". Bull. Amer. Meteor. Soc., 47, 393-396.

Macklin, W.C., and I.H. Bailey, 1968: "The collection efficiencies of hailstones". Q.J.R. Meteor. Soc., 94, 393-396.

Sulakvelidze, G.K., N. Sh. Bibliashvili and V.F. Lapcheva, 1967: "Formation of precipitation and modification of hail processes". Israel Program for Scientific Translations, Jerusalem, pp. 208.

HAILSTONE GROWTH

D.v/d S. Roos, J.C. Vogel and A.E. Carte

National Physical Research Laboratory, CSIR,
Pretoria, South Africa

1. INTRODUCTION

There are two main approaches to the derivation of quantitative information on the growth environment of hailstones. One method suggested by French workers in 1962 involves measurement of the isotopic content of the various layers of a hailstone (Facy et al., 1963). The other is based on the work of several groups but it was recently put on a more quantitative basis by Macklin et al. (1976). This method involves the measurement of crystal dimensions and concentrations and sizes of air bubbles. Neither method has been fully tested or exploited. The objects of this paper are to compare results for ambient temperatures obtained by the two methods and to relate growth trajectories to the storms from which the hailstones originated.

Information on surface patterns of hailfalls was obtained by a dense network of observers (about 3000 in 3000 km^2) in the vicinity of Johannesburg and Pretoria, South Africa. An S-band radar with a 1.2° beamwidth and a 5-level iso-echo contour system provided data on storm structures. Measurements of deuterium in hailstones were made, and not ^{18}O. Finally, the average lengths of crystals were determined for growth layers and then related to ambient temperature.

2. DEUTERIUM MEASUREMENTS

The deuterium content of hailstone ice was determined for cubes with a side length of about 3 mm cut from various growth layers.

The melted cubes were reduced in an uranium oven to hydrogen which was analysed in a mass spectrometer. Its deuterium content, δD, was calculated from the formula

$$\delta D = 1000\left(\frac{R_s - R_{st}}{R_{st}}\right)‰$$

where R_s and R_{st} are the isotope ratios (D/H), respectively, in the sample and the standard, viz. standard mean ocean water (S.M.O.W.).

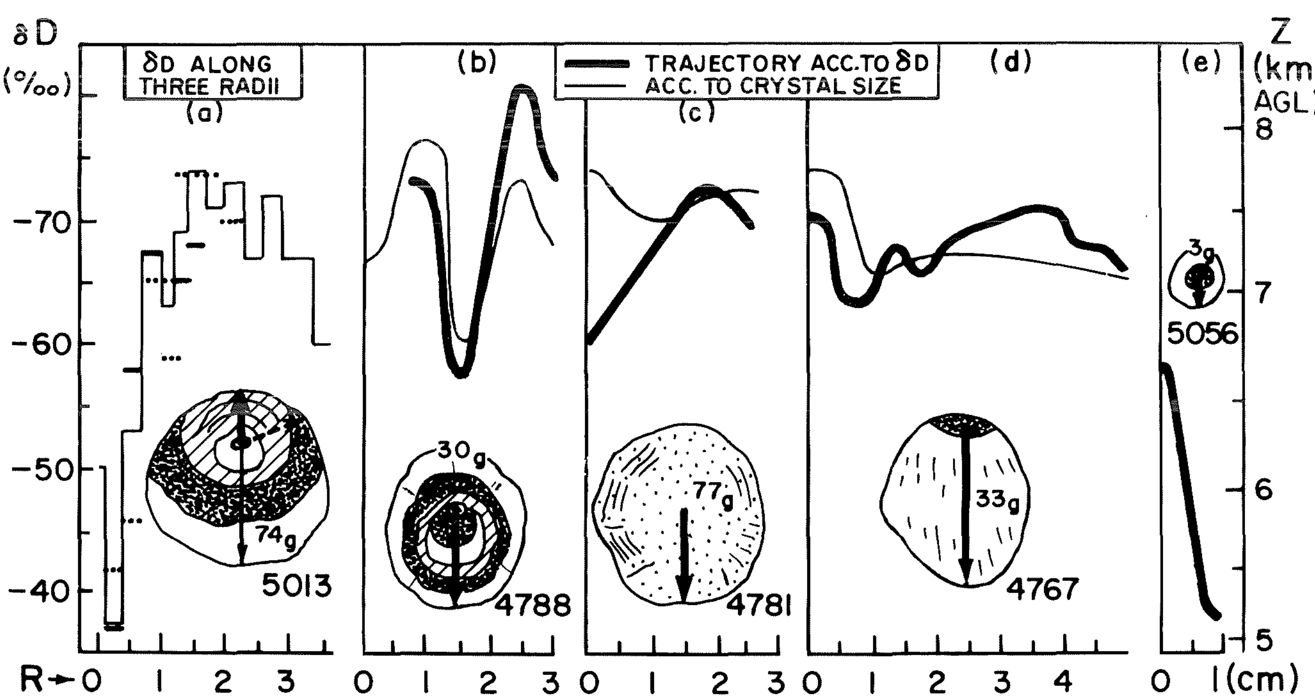

Figure 1. Trajectories of hailstones from storms on 29 November 1972. (a) to (d) were from the same storm. Radial distance from the growth centres was plotted against deuterium content, δD, and height above ground, Z.

Results for about 400 cubes cut from 34 hailstones that originated in 3 different storms on 29 November 1972 were examined in detail (Roos et al.). Firstly, variations in δD within individual layers were investigated. Altogether 75 samples from 16 layers, including asymmetrical ones, were measured. Both opaque and transparent layers were sampled. The mean standard deviation per layer was 2.2 ‰. This figure is only slightly greater than the reproducibility obtained from repeated measurement of the same sample of water but much smaller than the differences between layers. Individual layers of the hailstones investigated were therefore regarded as isotopically uniform.

Variations along different radii within the same hailstone were also investigated. In Fig. 1(a) a schematic drawing of a section through a spheroidal hailstone of 74 g is shown. The δD-profiles presented with it were determined along the 3 radii indicated. Note the good agreement between the 3 sets of measurements, particularly for the dips at $R \approx 0.3$ cm and $R \approx 1$ cm. Similar agreements were generally found where more than one radius was considered.

Jouzel et al. (1973) and others have found a tendency for opaque ice to contain less deuterium than transparent ice, in conformity with the opaque ice having formed at relatively low temperatures. In order to see if a similar tendency could be found for our samples they were subjectively divided into two groups according to whether they comprised opaque or clear ice. Those of intermediate opacity were disregarded. The results for 229 cubes are depicted in Fig. 2 where δD was plotted against radial distance, R, of the sample from the growth centre. The curved band in the figure separates 94 per cent of the samples: opaque samples lay above the band and clear ones below it.

After this, a scale was derived whereby δD could be expressed in terms of the in-cloud ambient temperature T_a, and hence height above ground. It was observed that small crystals (<0.5 mm) were practically never found in ice samples having δD>-61 ‰ while large crystals (>2 mm) were hardly ever found when δD<-73 ‰. From earlier results on crystal size and T_a (Levi and Aufdermaur, 1970), these values were taken to correspond with -18 °C and -24 °C respectively. A linear scale relating δD and T_a based on these two points has a slope of 1 °C per 2 ‰. Extrapolation of this line yielded T_a = -29 °C and -1 °C for the extreme δD values encountered for 317 samples that were measured for one storm on this day. These values seem to be realistic, as limiting temperatures for hailstone growth would be about -35 °C and -5 °C.

The upper air sounding at 1400 SAST on 29 November 1972 was used to relate T_a and hence δD to height Z in km above ground level (AGL), as is presented on the ordinates in Fig. 1. Adiabatic ascent was assumed.

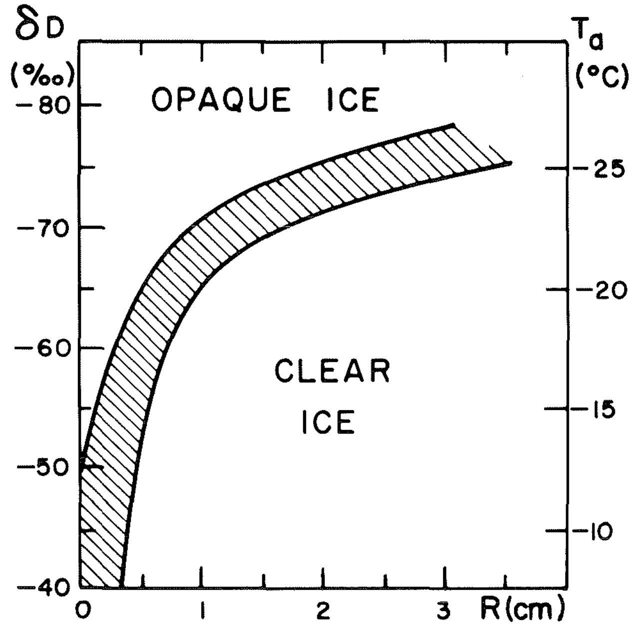

Figure 2. Relationship between opacity, radial distance from growth centre and δD of a sample.

3. GROWTH CENTRES OF HAILSTONES

A fundamental point to establish about hailstones is their position of origin within the cloud. In most hailstones a growth centre of between a few mm and 1 cm in diameter can be detected. Such embryos were found to be conical graupel in 80 per cent of hailstones studied in Switzerland (List, 1960). In the U.S.A., Knight and Knight (1970) classified 60 per cent of their embryos as graupel particles and 10 per cent as spherical, bubbly. These findings were not related to size of the hailstones.

Some 1700 South African hailstones collected from many storms during 7 years were grouped according to size. This revealed that small hailstones are just as likely to have growth centres composed of large-crystal, transparent ice (glaze) as of small-crystal, opaque ice (rime), while rime is much more likely to be found at the centre of large ones. The implication is that large hailstones undergo their first stage of growth at a higher level in the cloud than smaller ones.

Results for the relative frequency of different types of embryos for hailstones of

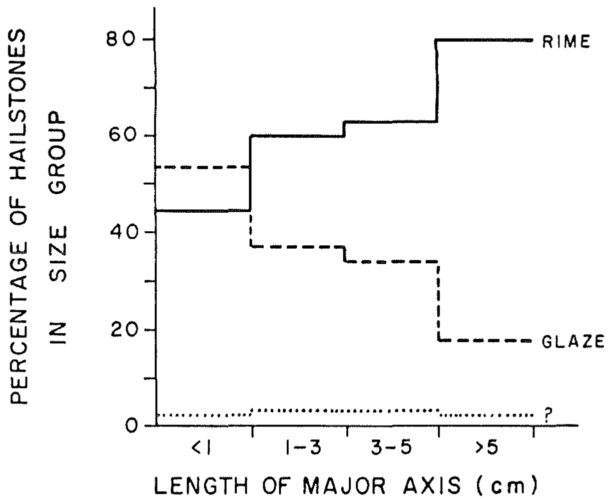

Figure 3. Relative frequencies of rime, glaze and indeterminate growth centres in hailstones of different sizes.

various sizes are presented in Fig. 3, which has been taken from Carte and Kidder (1970).

Practically all embryos of several hundred hailstones from the 3 storms of 29 November 1972 were found to be rime. Both large and small hailstones were examined. A few embryos of hailstones from the most severe storm had the characteristics of frozen drops. The deuterium contents of 16 embryos were measured. All values lay approximately in the middle of the range of δD-values encountered on this day, suggesting that they formed in the vicinity of the mid-level of the region of hail growth, at about -10 °C to -18 °C or 6 to 7 km AGL. Embryos from all three storms were measured, and they included a few frozen drops which did not differ significantly in D-content from the graupels. There was a slight indication of those which came from the earliest stages of the storms having originated at higher altitudes than the ones which came later when the storms were subsiding.

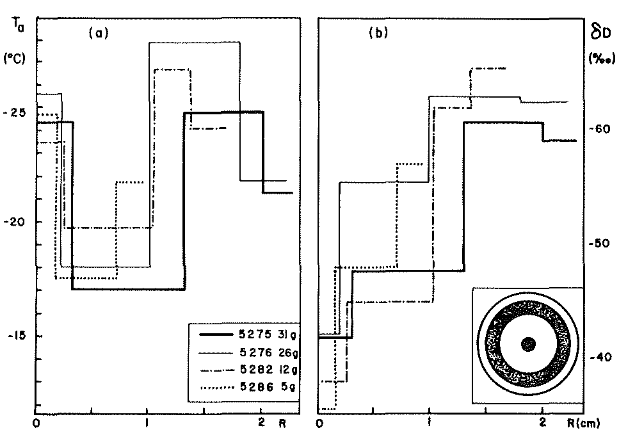

Figure 4. (a) Ambient temperatures (inferred from crystal size) during growth of 4 centro-symmetrical hailstones and (b) approximate δD-values.

Crystal sizes were measured in 4 centro-symmetrical hailstones that came from a storm on 17 January 1975. One had 3 layers and the rest had 4. Results indicated the origins of all to have been high up in the cloud whereas deuterium results pointed to the embryos having grown at a lower altitude than any subsequent layer. See Fig. 4. Results of either method must therefore be interpreted with caution. Another surprising result was found when the trajectories of two large hailstones ($m \approx 50$ g) of almost identical multi-layer structure were compared: while their trajectories (inferred from δD) were very similar during the later stages of growth, the two identical embryos evidently originated at levels differing by 1.5 km in height and 11 °C in temperature.

4. HAILSTONE TRAJECTORIES

4.1 Storms on 29 November 1972

Three hailstorms on 29 November 1972 were studied in detail. The first one (Storm 1) was tracked for 2½ hours and it produced hailstones larger than 5 cm in diameter. It was followed by Storm 2 which travelled along a parallel track 15 km to the north and its hailstones were up to 5 cm in diameter. These two storms ultimately merged and became part of a multicellular complex, part of which gave rise to small hailstones (Storm 3). The tracks taken by these storms and the areas on which they produced hail are depicted in Fig. 5.

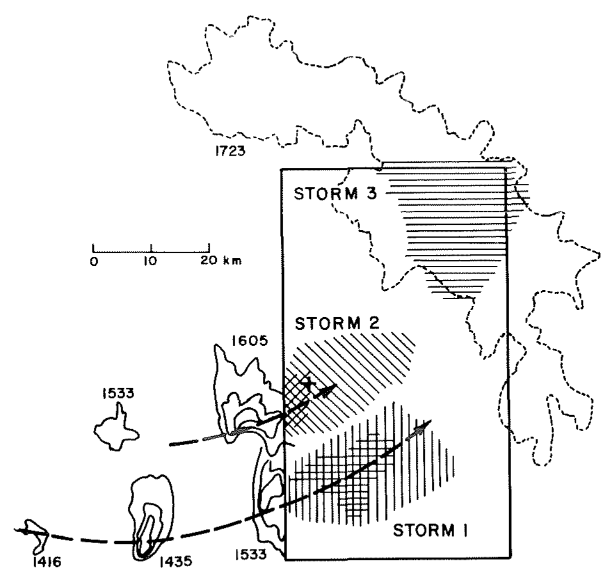

Figure 5. Storms on 29 November 1972. Radar PPI's at 2° elevation are shown for several times. Broken lines are tracks followed by echo cores. Hatching shows where hail fell and cross-hatching where hailstones were >3 cm in diameter.

The structures of several hundred hailstones from these three storms were examined, supplemented by measurements of deuterium content in 34 of them.

Storm 1 comprised a single core of high radar reflectivity throughout its life but various features suggested that discrete growth took place. In particular, tracks of echo tops showed new ones to have originated on the right of older ones at intervals of 6 to 10 min. The largest hailstones fell at the beginning of the hail path after which the path broadened as the severity and echo height declined. Patchiness was evident in the character of the hailfall.

Examples of trajectories of 5 hailstones from the storms on this day are displayed in Fig. 1. The two methods (according to δD and to crystal length) showed the same general trends for Nos 4788 and 4767. For No 4781 and No 5013 (trajectory acc. to crystals not shown) there was, as before, lack of agreement for the smallest diameters. The four large stones all came from Storm 1 from locations within 10 km of one another, and the variety of internal structures and trajectories is to be noted. Two of these stones were non-spheroidal in shape: No 4788 was an "apple" and No 4767 a cone with pointed base.

The graphs in Fig. 6 show fallspeed versus growth time, equivalent spherical radius and mass for three of these hailstones which were practically spherical throughout all stages of growth (even though not necessarily always centro-symmetrical). Their fallspeeds (V) were calculated for different sizes using the expression

$$V \approx 55\ (r/\rho_a)^{\frac{1}{2}} \quad \text{(c.g.s. units)}$$

from Roos and Carte (1973). The updraught experienced by them as they grew was then derived from the expression

$$U = V(1 + 0.278\ EW \frac{dZ}{dr})$$

where

r = equivalent spherical radius

ρ_a = air density

E = collection efficiency

$(0.48 \leq E \leq 0.68)$

and

W = adiabatic liquid water content.

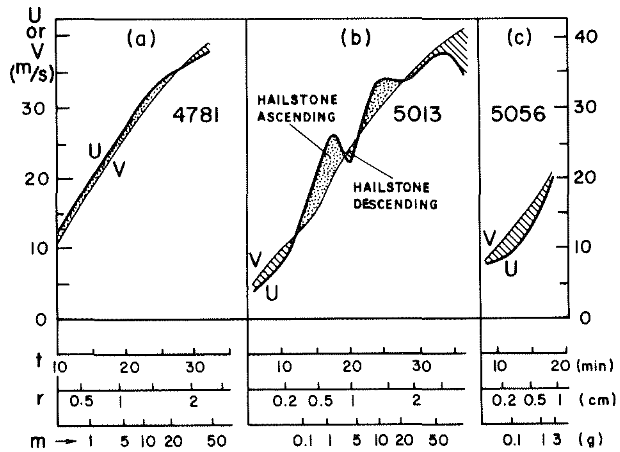

Figure 6. Hailstone fallspeed, V, and updraught speed, U, as functions of growth time t, equivalent spherical radius r and mass m of hailstone. Steadily increasing updraught (a), pulsating updraught (b) and a descending hailstone (c) are depicted.

These examples and others illustrated that large hailstones from not far apart in Storm 1 encountered different updraught conditions: some were swept upwards continuously in an updraught that increased steadily with height and time; others oscillated up and down, two with a period of approximately 8 min. Hailstones which remained suspended at about the same altitude during most of their growth period must have been within an environment where the updraught increased steadily with time and might have moved horizontally towards the region of strongest updraught.

The small hailstone from Storm 3 (Figs 1(e) and 6(c)) was typical of others from the late stage of the storm system in having grown entirely during descent.

4.2 Storms on 17 January 1975

Storms occurred ahead of a cold front on 17 January 1975. Fig. 7 shows how a single-cell storm (Storm A) moved eastwards towards a northward-moving multicellular complex. When the single-cell joined the western flank of the complex it backed abruptly to follow a track nearly parallel to that of cells within the complex. It entered the hail-observing network at the time of the merger and produced large hailstones, up to 5 cm in diameter.

The rest of the complex had taller cells, they were of greater horizontal extent and their maximum radar reflectively was equal to that of Storm A but its largest hailstones were no more than 3 cm in diameter.

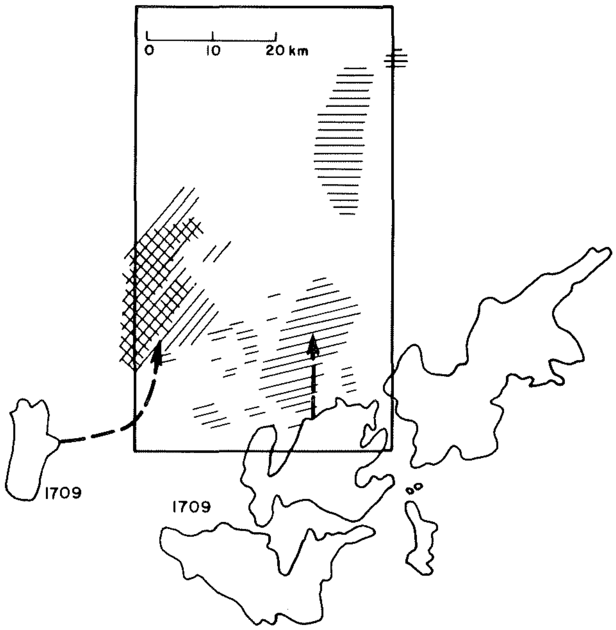

Figure 7. Storms on 15 January 1975. Radar echo outlines at 17h09 are shown for 2° elevation. Broken lines are tracks followed by echo cores. Hatching shows where hail fell. Cross-hatching indicates hailstones >3 cm in diameter.

At the time of the hailfall the storms had structures typical of those within a squall line. Forward overhangs and weak-echo regions indicated that inflow regions were at the leading edge where a gust front was recorded. Continual regeneration was noted ahead of and between existing strong echoes. The radar scanning cycle of 3 to 5 min was too slow for some features to be tracked satisfactorily because of rapid development.

Centro-symmetrical hailstones were selected from several parts of the hail path. The first 4 hailstones analysed came from the same location. They were Nos 5275, 5276, 5282 and 5286 and were structurally similar to the schematic section in Fig. 4. Their masses were, respectively, 31, 26, 12 and 5 g. These hailstones evidently followed very similar trajectories, in spite of large differences in final mass.

An attempt has not yet been made to link δD with T_a for this day because only few results are available at this stage. However, it is obvious from Fig. 4 that the two methods gave different results for the embryo stage. This has already been commented on. Differences for the outer layers appear to occur as well: crystal lengths indicated descent during growth of the outer layers of 3 hailstones, while δD-values showed only slight descent for 2 of them. Both methods showed that all 4 hailstones ascended after the embryo stage. Hailstones of other structures from a number of other localities are being investigated. Preliminary examination of their internal structures suggests that not all will have trajectories as simple as those depicted in Fig. 4.

5 CONCLUSIONS

The two methods for determination of ambient temperature during growth of hailstones agreed well for many samples. Differences for embryos - and outer layers - were found. Measurements of crystal lengths suggested that some embryos had originated at considerably higher altitudes than values resulting from deuterium measurements. Possible reasons for the discrepancies are: accretion by porous embryos of raindrops that were not in deuterium equilibrium with their surroundings; simultaneous accretion of ice crystals and water droplets (perhaps reducing the average crystal size); changes in deuterium content of the input air; and "injection" of embryos into a different part of the dynamic cloud system (Knight and Knight, 1970).

The embryos of large hailstones are likely to have been formed at high levels. In three storms of different degrees of severity on one day for which D-measurements were made, the embryos of hailstones of various sizes all originated at about the mid-level of hailstone growth. Most were graupels but this finding also applied to the few frozen drops that were measured.

Hailstones of a variety of structures fell from one single-cell storm (Storm 1). Various features suggested that its airflow was not steady. Some of the large hailstones (>30 g) apparently remained balanced at about the same altitude during most of their growth. The largest one was restricted to heights between 7.3 and 7.7 km while growing from 5 to 77 g. The updraught in its environment was calculated to have increased at 1.2 ms^{-1} per min and reached a maximum of 39 ms^{-1} at the 330 mb level. Other hailstones from the same storm followed oscillatory trajectories with a period of about 8 min which was in agreement with observed changes in the fine-scale radar structure. In other cases, growth occurred on predominantly ascending trajectories or (for small hailstones) during continuous descent.

Hailstones from a single-cell storm (Storm A), with rapid changes of internal structure during its most intense phase, included large ones. Their growth trajectories, apart from the embryo stage, were simple up-and-down ones. Many of the hailstones had more complex structures than those analysed so far and would not be expected to have such simple trajectories.

Insofar as generalization is possible, the favoured temperature range for hailstone growth was found to be -20 to -25 °C. Growth trajectories have revealed that complex airflow patterns may exist even in storms of apparently simple radar structure.

Deuterium measurements should be supplemented by tritium measurements, which provide information on entrainment (Ehhalt, 1967). Other valuable information would be the exact time of arrival on the ground of hailstones that are analysed. Their location with respect to the radar echo pattern could then be established precisely.

ACKNOWLEDGEMENT

Our thanks are due to Miss H. van Urk who measured the deuterium contents of hailstones from storms on 15 January 1975, some of which are reported in this paper.

REFERENCES

Carte, A.E., and R.E. Kidder, 1970: Hailstones from the Pretoria-Witwatersrand Area, 1959-1969. C.S.I.R. Res. Report 297, Pretoria, 1-42.

Ehhalt, D.H., 1967: Deuterium and tritium content of hailstones: additional information on their growth. Conference of Amer. Geophys. Union, Washington, D.C.

Facy, L., L. Merlivat, G. Nief and E. Roth, 1963: The study of the formation of hailstones by isotopic analysis. J. Geophys. Res., 68, 3841-3848.

Jouzel, J., and L. Merlivat, 1973: Étude isotopique de l'orage à grêle du 19 août 1971 dans la region de Clermont-Ferrand. J. Rech. Atmos., 7, 167-174.

Knight C.A., and N.C. Knight, 1970: Hailstone embryos. J. Atmos. Sci., 27, 659-666.

Levi, L., and A.N. Aufdermaur, 1970: Crystallographic orientation and crystal size in cylindrical accretions of ice. J. Atmos. Sci., 22, 443-452.

List, R., 1960: Growth and structure of graupel and hailstones. Monogr. No. 5, Phys. of Precip., Am. Geophys. Union, 317-324.

Macklin, W.C., J.N. Carràs and P.J. Rye, 1976: The interpretation of the crystalline and air bubble structures of hailstones. Quart. J. Roy. Meteor. Soc., 102, 25-44.

Roos, D.v.d.S., and A.E. Carte, 1973: The falling behaviour of oblate and spiky hailstones. J. Rech. Atmos., 7, 39-52.

Roos, D.v.d.S., H. Schooling and J.C. Vogel: Deuterium in hailstones collected on 29 November 1972. To be submitted for publication.

3.4.6

The Modeling of Hailstone Growth and Melting Processes

A.I. Kartsivadze, A.M. Okudjava, V.A. Lapinskas and V.A. Chikhladze

The Institute of Geophysics of the Georgian Academy of Sciences, USSR, Tbilisi

The formation of clouds and precipitation is the result of a complicated of numerous factors acting in the earth atmosphere. The direct and reverse ties between these factors cannot be easily detected in natural conditions. That is why it is difficult to find out the main nechanisms governing the processes of cloud and precipitation evolution.

The impossibility of getting direct information on microphysical and dynamical processes taking place in clouds at various stages of their development also presents an assential obstacle for the investigation of the nature of these phenomena.

In this highlight we attach great importance to those methods of investigation which allow to disintegrate complex processes, study separate factors to integrate them subsequently and to construct thus a model of natural phenomena. This way of physical experimentation creates wide ample opportunities not only for the investigation of a natural proces but also makes it possible to find out the means for artificial transformation of this process in a dezirable direction.

The realization of such experiments is connected with the necessity of the creation of complex experimental facilities for the reconstruction of a wide range of physical conditions observed in the atmosphere. The laboratory complex of the Institute of Experimental Meteorology in Obninsk, Borovski, Volkovitski (1967), is an exampleof such a facility. To the similar purpose serves the construction of an experimantal facility of the Institute of Geophysics of the Georgian Academy of Sciences.

The facility is accomodated in two buildings, one of which is presented in Fig.1. The main body of the facility is thermo--barochamber (TBC)with the internal volume of about $350m^3$ (Fig.2) It consists of a big cloud chamber(1) with the volume of about $260m^3$ which represents a vertical cylinder with conical bottom (2) 17m high and 4.6 m in diameter; central tube (3) 20m high and 1m in diameter; vertical aerodynamic tube (4) 20m high, 1m in diameter, the aircooler (5); airfilters (6); the powerfool ventilator (7); the system of airconductors(8); the vacuum pumps(9) and freon refrigerators (10).

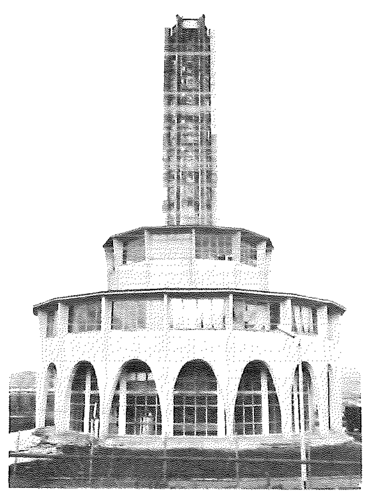

Fig.1

The big cloud chamber, vertical aerodynamic and central tubes have the systems for: the vapor supply, the water spray, the spray of powdered reagents, automatic regulation, recording and monitoring of the chamber's working regime.

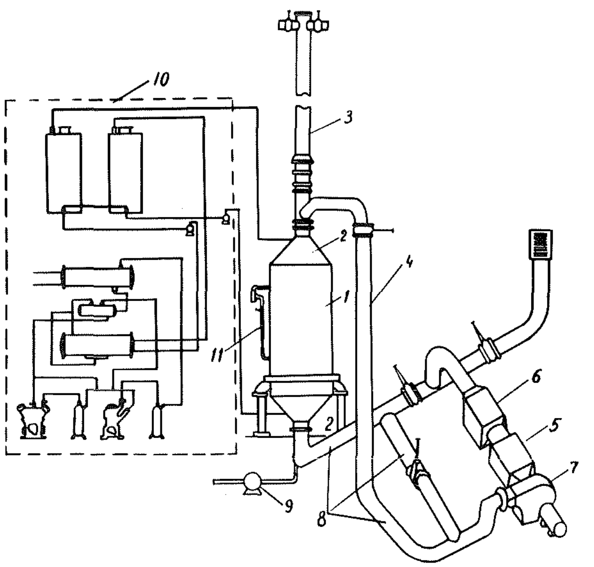

Fig. 2

The creation of a dezired temperature regime is realized through the circulation of freon-30 cooled in refrigerators and blown into the jacket of the big cloud chamber and central tube. In such a way it is possible to lower the temperature down to -40° C in the internal volume of TBC.

The required temperature can be maintained continuously in the whole volume of the TBC to within ± 1°C. An air-mixing device inside the chamber allows to get a sufficiently homogenious temperature field. Special tests have shown that temperature differences in the internal volume of the TBC do not exceed ± 1°C.

The system of vacuum pumps and air compressors makes it possible to change air pressure in the big cloud chamber and central tube in the range of 0.05 to 2.0atm. It is therefore possible to create in the TBC conditions raughly corresponding by temperature to high layers of the troposphere while by preassure they correspond to the hight of about 25 km above the Sce level.

The modelling of cloudy environment in the TBC is realized by adiabatic expansion, water spraying or direct vapor injection. The regulation of water and air pressure by means of different spray nozzles makes it possible to create a cloudy environment with a monodispersed spectrum of droplets of given size, or a polydispersed spectrum very near to those, observed in natural conditions.

The water content of the created environment can be changed within broad limits considerably overpassing natural ones.

In the vertical aerodynamic tube it is possible to create updrafts reaching 40 m s^{-1} and more.

A device for modeling hailstone growth and melting processes(11) is attached to the main body of the big cloud chamber.

Laboratories, working rooms and central operational desk are accomodated on two floors around the TBC while in the ground floor there are machines and aggregates.

In the second building two thermobarochambers with the volume of 8 and 0,5 m^3 are mounted. In these chambers the temperature and pressure can be lowered down to - 70°C and 0.01 atm respectively. This corresponds to the conditions, observed in highest layers of the stratosphere.

Serial experiments on crystallizing activity of various chamical compounds can be conducted in an isothermal cloud chamber with the volume of $2m^3$ while investigations of elementary processes of cloud particles evolution are carried out in a small chamber with the volume of 3 ℓ. Here, besides thermal regime it is possible to create and change air humidity and electric field intensity up to several thousands V cm^{-1}.

The experimental facility allows to conduct investigations by means of lazer technique, the electron mycroscopy, electronography, x-ray analysis, mycrocalorimetry, infrared spectroscopy, spectrophotometry and ect.

Out of the whole complex of experiments here will be discussed preliminary data on the investigation of hailstone growth and melting.

Interesting results have been obtained by several authors through a laboratory modeling of the processes mentioned above, Mason (1956), Muchnik and Shmukler (1954), Khimach (1964), Mossop and Kidder (1962), Browning, Ludlam and Macklin (1963), List(1960), Kachurin and Morachevski (1965). However, a common shortcoming of those investigations is that the experiments were carried out either using fixed hailstone devoid of all degrees of freedom, or using ice cylinders rotating uniformly around their longitudinal axes. Besides that almost in all the experiments there was no required conformation between the measured hailstone sises and airflow velocities. All this did not permit the reproduction of hailstone growth and melting conditions with the sufficient precision which resulted inadequate reliability of experimental results.

During 1963-1967 the first attempt was made in the Institute of Geophysics of the Georgia Academy of Sciences for the investigation of the melting processes of hailstones suspended in the air current, Gvelesiani et.al. (1964), Gvelesiani and Kartsivadze (1964). In the device used for this purpose the air current blowing on the hailstone was characterized by an abnormally high degree of small scale turbulence which resulted in considerable changes of heat transfer conditions and thus affected the rate of hailstone melting.

After the completion of the TBC it became possible to model both the natural processes of hailstone growth and melting since the big cloud chamber is quite suitable for the creation of a cloudy environment. Its parameters almost equal to those observed in natural conditions and it can be used for the realization of an airstream blowing around a growing hailstone.

To carry out those experiments a special device was attached to the TBC (Fig.3). A hailstone in this device is

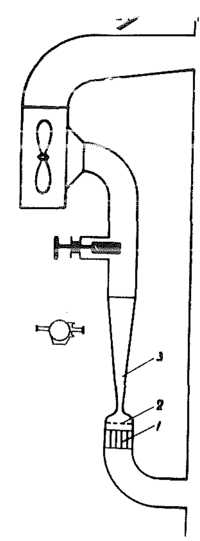

Fig. 3

suspended on an airstream. For this porpose a diffuser with a small apex angle is used in which a laminarized strеem of a cloudy environment is formed. In the diffuser (3) at any given level such a distribution of aircurrent velocity is created that the pressure in the central part of the diffuser is always less than that near its walls. Moreover the airstream velocity in this device decreases with height and that is why the hailstone remaines in the axial part of the diffuser on a corresponding level during the process of its growth or melting.

A problem of liquid movement in a diffuser is theoretically well investigated in the case of source being located in its apex. Under real conditions the cloudy environment gets into diffuser through the entrance section in which the steady regime is characterized with some profile of velocity. If the entrance to the diffuser is smooth enaugh then the flow-velocity U_0 in each point of the entrance section will be nearly constant.

Motion equations for this problem with the assumption of a steady and cylindrically symmetric flow in the absence of mass forces were integrated by Targ (1951). In the equations the approximation consists in a partial account for the inertial terms and terms depending on viscosity. All calculations have been made in polar coordinates (ρ, θ). The solution is true for small apex angles $\delta = 2\alpha$ of the diffuser when it can be considered that $ctg\alpha = 1/\alpha$ For the characteristic dimension of the conical diffuser let us accept $\rho\alpha$, where ρ is counted off an imaginary apex of the diffuser. In this case for Reynolds number we have.

$$R = u\rho\alpha/\nu$$

where ν -is kinematic viscosity of the environment.

The analysis of the solution brings us to the conclusion that a flow in the diffuser is directed towards the decrease of pressure if $\alpha R \leq 4.73$. Besides that if $\alpha R \leq 7.34$ the flow will not be jerky. With the increase of αR the flow is cutting off from the walls and the region of the cut-off gradually approaches the entrance section. When the values of αR are small in the diffuser at a sufficiant distance from the entrance there is established a flow with a parabolic profil of velocities :

$$v_\rho/u_0 \approx 2(1-\theta^2/\alpha^2)\rho_0^2/\rho^2, \qquad (1)$$

where ρ_0 - is the distance from the apex to the entrance section of the diffuser.

Let us take for the initial length of the diffuser the distance L from the entrance section to the point at which the axial velocity of the flow determined by (1) differs from the real axial velocity less than by 1%. In this case according to Targ(1951)

$$L \approx 0.16\rho_0\alpha R$$

Based on the results mentioned above parameters of the diffuser were selected as follows: the apex angle is 8°, the length of the diffuser - - 514 mm, the diameter of the entrance hole 40mm.

The main difficulty in the construction of an experimental device lies in the necessity of getting a laminar air flow brought to the diffuser. To meet this request we instolled honeycombs (1) on the path of the airflow. They served as destructors of large vortexes and evend the airflow. After the honeycombs the grid was placed creating a fild of uniformly distributed velocities along the current crossection and decreasing the initial turbulence.

After that a special profile nozzle with a high degree of compression was mounted. It diminished considerably the consumption of the blower capacity. At the same time it smoothened the velocity profile at the nozzle exit and decreased the turbulence.

The nozzle which meets the above mentioned requirements can computed by Vitoshinsky formula, Krasnov et. al. (1974).

The internal surface of the device where supercooled water aerosol was blown had cryophobic cover which prevented its icing.

Microphysical characteristics of the cloudy enviorenment blowing on a hailstone are formed, measured and controled in the big cloud chamber.

In the divice described above a hailstone is soaring in the diffuser. It rotates freely and the velocity of the air blowing around the surface of the hailstone is established in accordance with its dimensions and density.

By changing temperature, pressure and microphysical characteristics of an initiated cloud environment in the chamber it becomes possible to re-create a complete picture of the natural process of a hailstone growth and melting.

By means of crystallizing reagents it is possible either to crystallize the whole cloudy environment or to create a mixed cloud, i.e. to model a growth process during artificial modification.

The photographs given on Figs.4,5, show the ability of modeling the characteristic structure of Natural hailstones in the device described above.

The data presented presumably can illustrate the opportunities of the Institute of Geophysics facility in cloud physics research.

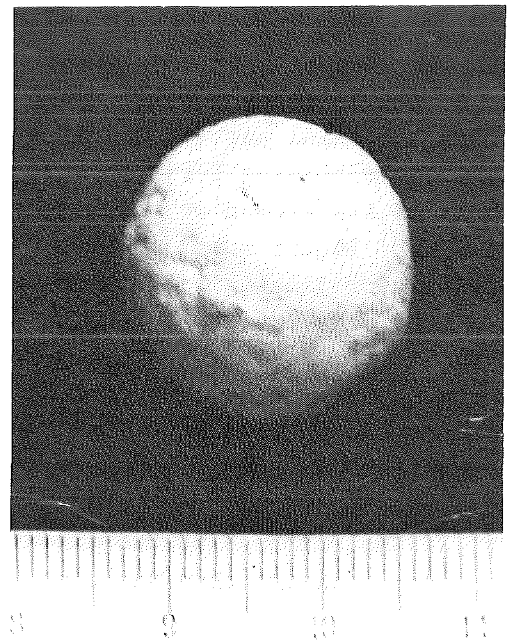

Fig.4

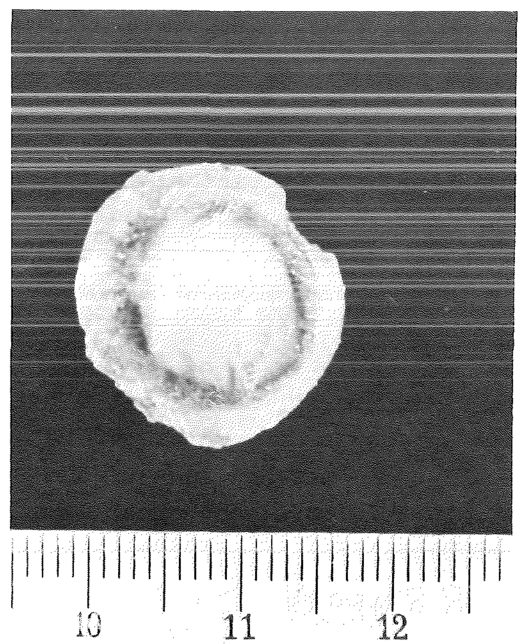

Fig.5

REFERENCES

Borovski, N.V., Volkovitski, O.A., 1967: Termobarocamera dlia issledovanii po fisike oblakov. Trudi IPG, vip.7

Browning, K.A., Ludlam, F.N., Macklin, W.C., 1963: The density and structure of hailstones, QJAMS, 89, n. 379.

Gvelesiani, A.I., Kartsivadze, A.T., 1967: Taiania gradin v potoke teplogo vodnogo aerozolia. Tr. Inst. Geofiziki AN Gruz.SSR,25 vip.1

Gvelesiani, A.I., i dr., 1964: Opiti po izucheniu protsessa taiania gradin. Tr. Vsevoiuznogo Soveshchania po activnim vozdeistviam na gradovie protsessi.Tbilisi

Kachurin, L.G., Morachevski, V.G., 1965: Kinetika fazovikh perekhodov vodi v atmosfere. Izd. LGU.

Khimach, M.A., 1954: Eksperimentalnoe issledovanie taiania sfericheskikh ledianikh chastits.Tr. GGO, vip. 47 (109).

Krasnov, N.F., i dr, 1974: Prikladnaia aerodinamica. Visshaia Shkola, Moskva.

List, R., 1960: Desine and operation of the Swiss Hail tunnel, in Physics of precipitation.Geophys. monograph, n.5, Waverly Press, Baltimore.

Mason, B.G., 1956: On the melting of hailstones Quart. J.Roy. Meteor. Soc., 82

Mossop, S.C., Kidder, R.E., 1962: Artificial hailstones. Buletin de l'Observatoire du Puy de Dome. n.2.

Muchnik, V.M., Shmukler, A.Kh., 1954: O Taianii gradin pri padenii. Tr. UKrNIGMI, vip. 1.

Targ, S.M., 1951: Osnovnie zadachi teorii laminarnikh techenii. GITTL, Moskva-Leningrad.

3.4.7

RAINDROP AND HAILSTONE SIZE DISTRIBUTIONS INSIDE HAILSTORMS

P. L. Smith, Jr., D. J. Musil, S. F. Weber, J. F. Spahn, G. N. Johnson, and W. R. Sand[1]

Institute of Atmospheric Sciences
South Dakota School of Mines and Technology
Rapid City, South Dakota 57701

1. AIRCRAFT INSTRUMENTATION

Numerous hailstorms in northeast Colorado have been penetrated by an armored T-28 aircraft (Sand and Schleusener, 1974) to investigate their internal structure. This work is part of the U. S. National Hail Research Experiment (NHRE). Instrumentation carried by the T-28 senses many variables of meteorological interest. Of principal concern in this paper are the observations of the precipitation particles ranging from small raindrops through large hailstones.

1.1 Precipitation Particles

Two sensors provided most of the data on precipitation particles that are discussed in this paper. One is a continuous hydrometeor sampler (foil impactor) of conventional design. Musil et al. (1976a) discuss reduction and analysis of the foil data. The foil impactor records particles ranging from about 0.25 mm up to more than 1 cm in diameter. The instrument's sampling volume is about 0.14 m^3 per 100 m of aircraft flight path. The nominal T-28 flight speed at the penetration altitudes is 100 m sec^{-1} and the foil data have, in most cases, been analyzed for 12-sec intervals. This corresponds to a spatial resolution along the track of about 1.2 km and a sampling volume of about 1.7 m^3.

To provide a larger sampling volume for the larger hailstones, a laser hail sensor based on the shadowgraph principle discussed by Knollenberg (1970) was developed. A report by Shaw (1974) describes the optical design of this sensor, although some modifications were effected in the flight version. The hail sensor records particles ranging from about 0.46 cm up to several centimeters in diameter. We infer that the particles observed by this sensor are hail and graupel, but there may be some doubt about the smallest size categories (nominally 4.6 and 5.3 mm). The instrument's sampling volume is about 10 m^3 per 100 m of flight path, although the end-element rejection technique used reduces the sample volume for the larger sizes. The data have been analyzed for 5-sec intervals, except for the 10-sec intervals used in computing radar reflectivity factors. This corresponds to spatial resolutions of 0.5 or 1.0 km and to sampling volumes of 50 or 100 m^3.

The T-28 also carries an optical array two-dimensional spectrometer (Knollenberg, 1976). It senses particles from 32 μm up to more than 0.8 mm in diameter, but the sampling aperture is too small to provide meaningful size distributions for the precipitation particles. The two-dimensional data are intended mainly to provide observations in the intermediate range between cloud droplet and precipitation particle diameters and to help in distinguishing between liquid and solid phases of the particles. Analysis of the two-dimensional spectrometer data is being carried out primarily by the NHRE staff.

1.2 Other Variables

The T-28 carries a variety of sensors for other meteorological variables and for aircraft response data. Of main interest in this paper are the measurements of the following variables:

a. Updraft velocity: Obtained from a variometer, with corrections applied for indicated air speed and engine power setting (manifold pressure).

b. Cloud liquid water concentration: Obtained from a Johnson-Williams hot wire sensor.

c. Temperature: Obtained from a reverse-flow temperature probe designed and built by NCAR; this probe was not installed on the T-28 flights prior to 1975.

d. Aircraft icing rates: Obtained from a Rosemount icing rate probe, supplemented by the pilot's observations of airframe icing.

2. OPERATIONAL PROCEDURES

The initiation of a hailstorm penetration is coordinated between the T-28 pilot and a meteorologist located at the NHRE operations center (Grover). The penetration procedures have been changed from time to time, but generally the

---

*Current affiliation: Department of Atmospheric Science, University of Wyoming, Laramie, Wyoming.

objectives have been to penetrate the major updraft regions, the high radar reflectivity regions, or both. The penetrations are made at altitudes between about 5 and 7.5 km MSL, which correspond to environmental temperatures between about 0 and -20°C.

The meteorologist at Grover has access to current quantitative radar reflectivity patterns for the storms on which the aircraft track is overlaid by a computer generated display. Flight safety is a primary consideration, and no penetrations are made in situations which would take the T-28 into or underneath any region in which the equivalent radar reflectivity factor exceeds 55 dBz. This criterion has been fairly successful; the largest hailstones encountered in flight thus far were about 2.5 cm in diameter.

3. OBSERVATIONS

This section sets forth some of the significant observations made during flights in 1972, 1973, and 1975. The most detailed observations were obtained on flights made on 9 and 31 July 1973 and 21 and 22 July 1975. While this may limit their generality, each finding discussed below is based on more than one occurrence unless otherwise noted.

3.1 Hail, if Present, Occurs in the Updraft Regions

Hail is also found along the edges of the updrafts and in the adjacent downdraft regions of mature cells, but whenever hail is encountered at penetration altitudes hailstones occur within the major updraft regions. The T-28 pilot (W. R. Sand) noted the presence of hail in the updrafts in some of the earliest hailstorm penetrations (Sand et al., 1974a) and the foil impactor data discussed by Musil et al. (1976a) show this clearly. Figure 1 shows laser hail sensor observations from a storm in which hailstones up to 2.5 cm in diameter were encountered during penetration at an altitude of about 7 km. The greatest hail mass concentrations were in a region where the updraft speed was between 5 and 10 m sec^{-1}. The maximum updraft speeds were about 15 m sec^{-1}, apart from one spike which exceeded 20 m sec^{-1}. Most of the hail mass was therefore falling against the updrafts, which seems to be the usual case.

3.2 Hail, Rain, and Cloud Water Sometimes Coexist in the Updraft Regions of Newly Developing Cells

The coexistence of hail and liquid water in both raindrop and cloud droplet size ranges was noted by Sand et al. (1974b). In the storm discussed by Musil et al. (1976a), the T-28 penetrated a cell (identified as W5) less than two minutes after the initial radar echo appeared. They found hail (i.e., particles larger than 5 mm in diameter), rain (liquid particles in the range 0.25 to 5 mm in diameter), and cloud liquid water (as indicated by the Johnson-Williams sensor) coexisting in the updraft region of this newly developed cell.

The presence of raindrops was inferred from the shapes of the particle imprints on the foil. It is fair to note that our interpretation

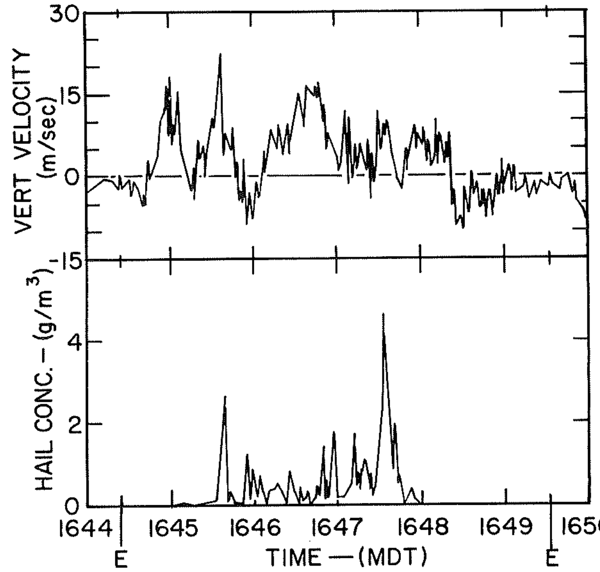

Fig. 1. Updraft speed (top) and hail mass concentration (bottom) data from Penetration 4 at about 7 km MSL on 21 July 1975. Times indicated are MST; the time scales in this and subsequent figures can be converted to approximate distance scales by using a nominal aircraft speed of 6 km/min. Points marked E denote locations of cloud entry or exit. The hail concentrations were computed from size distributions observed by the laser hail sensor.

of the foil imprints in terms of liquid or ice phase of the particles has been questioned (Knight et al., 1976). The presence of liquid water is corroborated in the above cases by the activity of the Rosemount icing rate probe and the accumulation of ice on the airframe. However, further evidence that the liquid particles were of raindrop rather than cloud droplet size is lacking.

3.3 The Time Interval During which Hail, Rain, and Cloud Water can Coexist May Be Very Short

Figure 2 shows data from penetration of a cell only about 8 minutes after it was first identified on radar. Hailstones up to 1.5 cm in diameter were present in the updraft region, along with cloud liquid water concentrations up to more than 1.5 g m^{-3}. However, the foil data showed all the precipitation sized particles to be ice. At this time the radar echo from the cell was already reaching the ground. These facts suggest that the cell had reached a mature stage of development in a matter of less than 10 minutes. This cell appeared to form by propagation from an earlier one, as no distinct first echo could be identified, so the hailstones may have developed from embryos formed in the previous cell.

The conversion of the raindrops to ice may be a function of the time available for freezing to take place as well as the temperature. Thus with the rather weak updrafts in Fig. 2, the ice phase is dominant less than 10 minutes after the cell was identified. In an earlier cell of the same storm with updrafts of 15 m sec^{-1}, penetrated about 12 minutes after the first echo appeared, no hail was encountered and some 10% of the precipitation mass was found to be liquid.

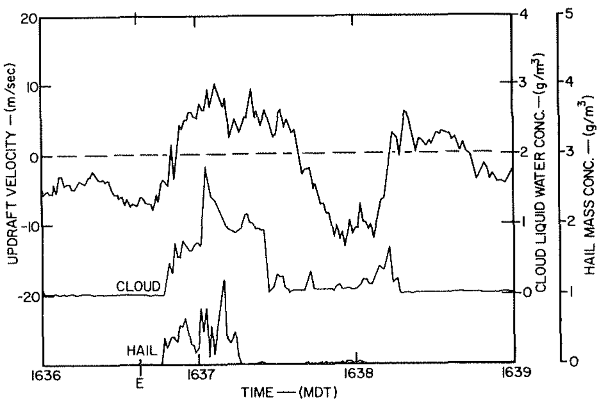

Fig. 2. Updraft speed (top), cloud liquid water concentration (middle), and hail mass concentration (bottom) data from part of Penetration 3 at about 6.5 km MSL on 21 July 1975. Times indicated are MST; the point marked E denotes cloud entry. The hail concentrations were computed from size distributions observed by the laser hail sensor. The cell shown around 1637 was penetrated again about 10 minutes later (see Fig. 1, 1647-164830).

3.4 Cloud Liquid Water Present in the Updraft Regions Can Support Hailstone Growth

Sand et al. (1974a) observed hail and cloud liquid water coexisting in updraft regions. Figure 2 shows the same thing; in that case there were no raindrops but hailstones up to 1.5 cm in diameter were observed in an environment with cloud liquid water concentrations up to more than 1.5 g/m^3. Hailstones up to 2.5 cm in diameter were found when the same cell was penetrated again about 10 minutes later. Even in the mature cells depicted in Fig. 1, all of which were more than 20 min old and contained no raindrops, cloud liquid water concentrations up to 1 g/m^3 were present in the same updraft regions where the hailstones occurred.

Sometimes cloud liquid water is also present in the downdraft regions (see Fig. 2), although in the downdrafts the liquid water concentrations are small, usually less than 0.25 g m^{-3}. Precipitation particles found in the downdraft regions are almost invariably ice.

3.5 Liquid Precipitation Particles (Raindrops) Occur at Temperatures of -12°C or Less

This analysis of the particle phase is based on our interpretation of the imprints in the foil. As noted above, Knight et al. (1976) have reservations about this interpretation. The supporting evidence of the character of the air-frame icing remains, however (Sand et al., 1974a). The optical array two-dimensional spectrometer was intended to help distinguish liquid from solid particles in the precipitation size ranges. Enough ambiguities appear in the two-dimensional images, however, to make this distinction so far unreliable. A particle camera (Cannon, 1976) has been added to the T-28 instrumentation for the current field season in the hope of firmly resolving this question.

3.6 The Precipitation Particle Size Distributions:

a) Are exponential or bi-exponential. Figure 3 illustrates a typical particle size distribution found from analysis of the foil impactor data in a region where particles up to nearly 1 cm in diameter existed. When only raindrop-size particles up to, say, 5 or 6 mm in diameter are present, a single line on the semi-log plot (indicative of an exponential particle size distribution function) tends to fit the data fairly well. When larger particles (graupel or hail) are present, a pair of exponential functions, one for the rain region and one for the hail region as indicated by the two solid lines, provides the most satisfactory representation. This pattern has been observed frequently in the foil data.

b) Show a distinct break in the neighborhood of 3 mm diameter. Examination of many plots like Fig. 3 shows the break between the small and large particle regimes tends to fall near 3 mm. We have therefore divided the precipitation mass into two categories, placing

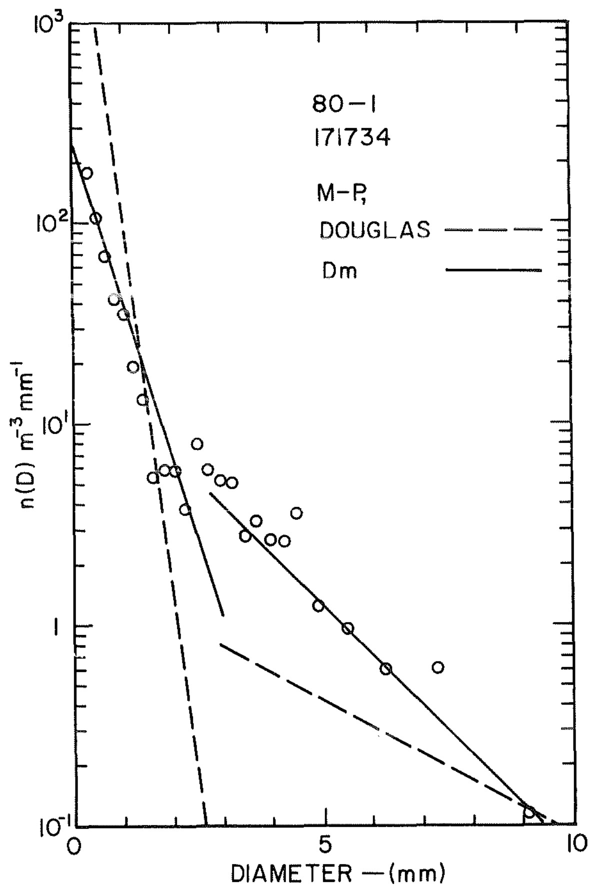

Fig. 3. A precipitation particle size distribution observed with the foil impactor in the updraft region of a mature cell penetrated at about 7.2 km MSL on 9 July 1973. The broken lines represent Marshall-Palmer raindrop and Douglas hailstone size distribution functions corresponding to the precipitation concentrations for particles smaller and larger than 3 mm, respectively. The solid lines represent exponential functions fit using the D_m technique outlined in Appendix A.

the demarcation point at 3 mm, for purposes of further analysis. For convenience we refer to the particles smaller than 3 mm as rain and the larger ones as hail, although we recognize that the smaller particles are often ice and some of the larger ones are frequently liquid.

c) Are not fit very well by either the Marshall-Palmer raindrop or the Douglas hailstone size distribution functions. We use a technique described in Appendix A to develop separate exponential functions for the rain and hail size regimes. That technique, a variation of the one employed by Waldvogel (1974), is less sensitive to sampling volume problems encountered for the larger hailstone diameters. The resulting curves, as shown by the solid lines in Fig. 3, provide a reasonably good fit to the data points in most cases, but they depart appreciably from the Marshall-Palmer and Douglas lines indicated by the broken lines in Fig. 3. In general, the intercept parameters n_o for the rain distributions are smaller than the Marshall-Palmer value, indicating fewer but larger particles than the Marshall-Palmer distributions. The slope parameters for the hail distributions are larger than the Douglas value (Fig. 4), indicating that the number concentrations of large hailstones are smaller than the Douglas function would suggest. This finding is in agreement with Federer and Waldvogel (1975), whose values of the slope parameter were also larger than the Douglas value of 0.309 mm^{-1}. A similar conclusion was reached by Smith et al. (1975) on the basis of an heuristic argument.

d) Show that the precipitation concentration W is dominated by the larger particles (hail) whenever W becomes large. Both the 1973 and 1975 foil data show that whenever the precipitation concentration W becomes large most of the mass is in particles larger than 5 mm in diameter. Examination of the foil data that have been reduced thus far shows no cases in which W exceeds 0.5 g m^{-3}

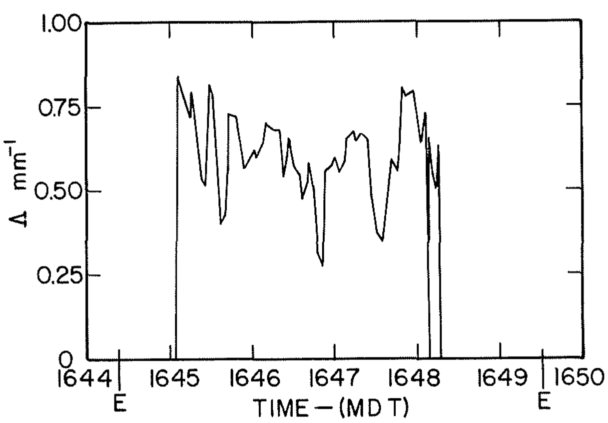

Fig. 4. Plot of the slope parameter Λ for the hailstone size distribution functions obtained with the laser hail sensor during Penetration 4 at about 7 km MSL on 21 July 1975. Times indicated are MST; points marked E denote locations of cloud entry or exit. Values of Λ were obtained from 5-sec running means of the observed n(D), and plotted every second. No values were computed when only the first size category (nominally 0.46 cm) had particle counts. For comparison, Douglas (1964) found a constant value Λ = 0.309 mm^{-1}.

unless there were some particles larger than 5 mm present. When larger values of W do occur, the large particles are dominant and the correlation between W and the number concentrations of particles larger than 5 mm is quite striking (see Musil et al., 1976a).

e) Do not exhibit the roll-off below about 1 mm diameter that is characteristic of many raindrop observations made at the ground. Small number concentrations for raindrops less than about 1 mm in diameter are often noted in surface observations made with raindrop cameras (e.g., Stout and Mueller, 1968) or momentum-type disdrometers (e.g., Martner, 1975). No such roll-off appears in our in-cloud observations made with the foil impactor. Evaporation of the small raindrops below cloud base provides one possible explanation of the difference. On the other hand, there is some suspicion that the roll-off is an artifact of the observing instruments. In any case, the in-cloud particle size distributions do not show these reduced number concentrations of the small particles, a fact that may be significant in relation to the raindrop and hailstone growth processes. Examination of the optical array, two-dimensional spectrometer data also shows large concentrations of sub-millimeter size particles, corroborating this finding.

4. SUMMARY STATISTICS

The extreme observed values of some of the variables indicated in Table 1 may be of interest. With reference to these values, updrafts greater than 20 m sec^{-1} have been observed on numerous occasions. Hailstone number concentrations greater than 10 m^{-3} are frequently observed. However, apart from one storm with 12 g m^{-3}, the precipitation concentrations have all been less than 5 g m^{-3}.

In Table 2, the observed range of the intercept parameter n_o for the raindrop and hailstone size regimes is compared with some other values that have appeared in the literature. A similar comparison is given for the slope parameter Λ, for the hailstone distributions.

5. HAIL RADAR REFLECTIVITY FACTOR COMPUTATIONS

The laser hail sensor provides a sample volume of about 100 m^3 for 1 km of flight path.

TABLE 1

Extreme Values Observed for Some Variables of Interest

Variable	Extreme Value
Updraft speed	25 m/sec
Downdraft speed	18 m/sec
Hailstone diameter	2.5 cm
Number concentration of hailstones (particles > 5 mm in diameter)	22 m^{-3}
Total number concentration of precipitation particles	440 m^{-3}
Precipitation concentration	12 g/m^3

TABLE 2

Values of Parameters in the Exponential Particle Size Distribution Functions

Parameter	Observed Range	Comparison Value	Source
n_o (rain)	10 - 2700 m^{-3} mm^{-1}	8000 m^{-3} mm^{-1}	Marshall and Palmer
n_o (hail)	0.25 - 61 m^{-3} mm^{-1}	30 m^{-3} mm^{-1}	Smith et al. (1975)
Λ (hail)	0.27 - 0.84 mm^{-1}	0.309 mm^{-1}	Douglas (1964)
		0.32 - 0.65 mm^{-1}	Federer and Waldvogel (1975)

This 1 km resolution is comparable to that provided by typical weather radar observations, and the 100 m^3 sampling volume usually contains several hundred hailstones when any substantial amount of hail is present. This sampling volume is also of the same order as that used by Federer and Waldvogel (1975) in their analysis of hailstone observations at the ground. Therefore, a comparison has been made between reflectivity factors computed from the hail sensor data and those observed by the CP-2 radar at Grover.

To make the computations from the hail sensor data, radar cross sections tabulated by Battan et al. (1970) were used. Using the radar cross sections for dry hailstones leads to the equivalent reflectivity factors plotted in Fig. 5. The maximum value of 63 dBz is somewhat higher than the largest value (58 dBz) observed by the CP-2, but the comparison is good considering the possible variations with time and other problems that are involved in making such a comparison.

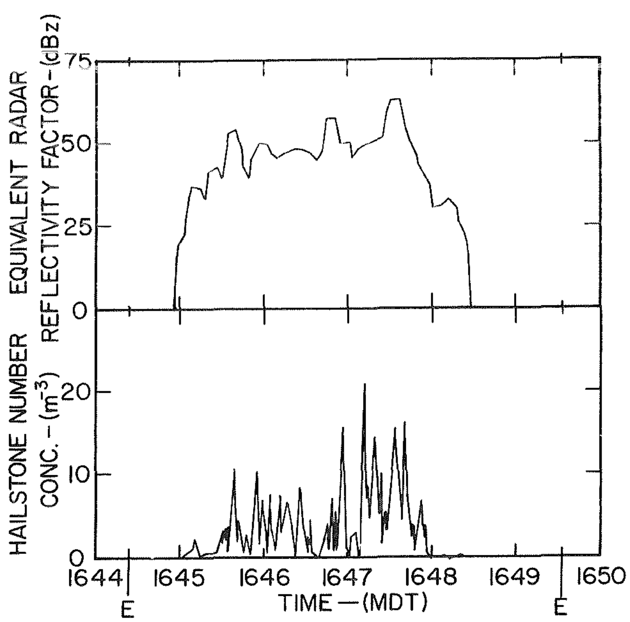

Fig. 5. Equivalent radar reflectivity factors (top) and hailstone number concentrations (bottom) computed from the laser hail sensor data from Penetration 4 at about 7 km MSL on 21 July 1975. Times indicated are MST; points marked E denote cloud entry or exit. The reflectivity factors shown were computed using 10-cm radar cross sections for dry hailstones and 10-sec running means of n(D). The largest hailstones encountered on this penetration, about 2.5 cm in diameter, occurred in the regions with highest reflectivity factors.

Somewhat larger reflectivity factors are obtained if the cross sections for wet hailstones are used. However, by taking the water film thicknesses indicated by the studies of Chong and Chen (1974) we obtained values only one or two dB larger than the dry hail reflectivity factors. This difference is much smaller than that found in earlier studies (e.g., Douglas, 1964). The primary reason is that the hydrodynamic studies of Chong and Chen show that large hailstones cannot support water films of the thicknesses that were postulated in the earlier calculations. With the thinner water films that are more realistic, the differences between radar cross sections of dry and wet hailstones are less pronounced.

6. CONCLUSIONS

This paper has summarized a number of observations of the hydrometeor composition of the interiors of hailstorms at mid-levels. The implications of these and other observations for the hailstone growth mechanism are discussed in a separate paper by Musil et al. (1976b).

Acknowledgment. This research was performed as part of the National Hail Research Experiment, managed by the National Center for Atmospheric Research and sponsored by the Weather Modification Program, Research Applications Directorate, National Science Foundation.

REFERENCES

Battan, L. J., S. R. Browning, and B. M. Herman, 1970: Tables of the radar cross sections of dry and wet ice spheres. Tech. Rept. No. 21: Tucson, The University of Arizona, Institute of Atmospheric Physics.

Cannon, T. W., 1976: A particle camera for powered aircraft. Preprints Int'l. Cloud Physics Conf., (this volume).

Chong, S. L., and C. S. Chen, 1974: Water shells on ice pellets and hailstones. J. Atmos. Sci., 31, 1384-1391.

Douglas, R. H., 1964: Hail size distributions. Proc. 1964 World Conf. Radio Meteor. and 11th Wea. Radar Conf., Boston, Amer. Meteor. Soc., 147-149.

Federer, B., and A. Waldvogel, 1975: Hail and raindrop size distributions from a Swiss multicell storm. J. Appl. Meteor., 15, 91-97.

Knight, C. A., W. R. Sand, W. W. Grotewold, and N. C. Knight, 1976: Interpretation and calibration of foil impactor impressions from water drops, graupel, and slush particles. Preprints Int'l. Cloud Physics Conf., (this volume).

Knollenberg, R. G., 1970: The optical array: an alternative to scattering or extinction for airborne particle size determination. J. Appl. Meteor., 9, 86-103.

________, 1976: Three new instruments for cloud physics measurements: the 2-D spectrometer, the axially scattering spectrometer and the active scattering spectrometer. Preprints Int'l. Cloud Physics Conf., (this volume).

Martner, B. E., 1975: Z-R and Z-W_o relations from drop size measurements in high plains thunderstorms. Preprints 9th Conf. Severe Local Storms, Norman, Oklahoma, Amer. Meteor. Soc., 307-310.

Musil, D. J., E. L. May, P. L. Smith, Jr., and W. R. Sand, 1976a: Structure of an evolving hailstorm. Part IV: Internal structure from penetrating aircraft. Mon. Wea. Rev., (April issue).

________, C. Knight, W. R. Sand, A. S. Dennis, and I. Paluch, 1976b: Radar and related hydrometeor observations inside a multicell hailstorm. Preprints Int'l. Cloud Physics Conf., (this volume).

Sand, W. R., D. J. Musil, and R. A. Schleusener, 1974a: Observed liquid water and ice composition of the high radar reflectivity zones and updraft areas of hailstorms. Preprints Conf. Cloud Physics, Tucson, Arizona, Amer. Meteor. Soc., 263-266.

________, ________, and T. G. Kyle, 1974b: Observations of turbulence and icing inside thunderstorms. Preprints 6th Conf. Aerospace and Aeronautical Meteorology, El Paso, Texas, Amer. Meteor. Soc., 299-304.

________, and R. A. Schleusener, 1974: Development of an armored T-28 aircraft for probing hailstorms. Bull. Amer. Meteor. Soc., 55, 1115-1122.

Shaw, W. S., 1974: Development of an airborne optical hailstone disdrometer. Report 74-16, Institute of Atmospheric Sciences, South Dakota School of Mines and Technology, Rapid City, South Dakota. 35 pp.

Smith, P. L., Jr., C. G. Myers, and H. D. Orville, 1975: Radar reflectivity factor calculations in numerical cloud models using bulk parameterization of precipitation. J. Appl. Meteor., 14, 1156-1165.

Stout, G. E., and E. A. Mueller, 1968: Survey of relationships between rainfall rate and radar reflectivity in the measurement of precipitation. J. Appl. Meteor., 7, 465-474.

Waldvogel, A., 1974: The N_o jump of raindrop spectra. J. Atmos. Sci., 31, 1067-1078.

APPENDIX A

The D_m Method for Fitting Particle Size Distribution Data

The Marshall-Palmer size distribution function

$$n(D) = n_o\, \varepsilon^{-\Lambda D} \qquad \text{(A-1)}$$

has two parameters, the intercept parameter n_o and the slope parameter Λ (those adjectives being applicable to the straight line obtained when n(D) is plotted on semi-logarithmic scales). Using linear regression to fit such functions to experimental data leads to difficulties when some of the data deviate from the line, as often happens at both small and large diameter ends of the distributions. Sensitivity to the influence of individual data points can be reduced by using integral expressions derived from (A-1).

Determination of the two parameters requires two equations. Waldvogel (1974) used expressions for the precipitation concentration W and the radar reflectivity factor Z. Introducing the latter, however, can lead to problems when sample volumes are limited because Z is strongly influenced by the large particles which may be poorly represented in the samples. These problems can be mitigated by using only lower moments of the size distributions.

In particular, we use W and the mass-weighted mean particle diameter D_m defined by

$$D_m \equiv \frac{\int_0^\infty n(D)\, D^4\, dD}{\int_0^\infty n(D)\, D^3\, dD}$$

$$= 4/\Lambda, \text{ for } n(D) \text{ as in (A-1).} \qquad \text{(A-2)}$$

Values of W and D_m are computed from the observed size distributions using summation forms of the integrals in (A-2). Then the slope parameters are obtained from

$$\Lambda = 4/D_m \qquad \text{(A-3)}$$

and the intercept parameters from

$$n_o = 256\, W/\pi\rho\, D_m^4 \qquad \text{(A-4)}$$

When both "rain" (D<3 mm) and "hail" (D>3 mm) are present, separate computations are made for each region. It has become apparent that a decision threshold may be needed so that this separation is only made when particles larger than, say, 5 mm are present.

AERODYNAMICS OF FREELY FALLING BODIES

R.E. Stewart, Roland List and U.W. Rentsch

Department of Physics, University of Toronto, Toronto, Canada

1. INTRODUCTION

Predicting the free fall characteristics of ice crystals, graupel, and hailstones is a necessary step in understanding their growth and, hence, also the growth of rain through the Wegener-Bergeron-Findeisen mechanism. The terminal velocity of such particles and associated secondary motions like oscillations and horizontal movements will affect growth through alterations to accretion and heat and mass transfer. This has been illustrated for hailstones for example, by List et al. (1969).

Up to now, experiments designed to determine free fall characteristics (beyond straight fall) have been conducted in wind tunnels. They allowed the direct measurement of aerodynamic forces and torques acting on spheroidal bodies which were restrained in their freedom of movement (List et al., 1973; Kry and List, 1974a & b). By utilizing similarity theory and assuming that forces and torques depend on position only (and not on history or secondary motions), these results have been used to calculate the behavior of freely falling hailstones. Oscillations, rotations and translations of freely falling particles, however, may cause shifts in the wake and introduce delays in the adjustment of the fluid flow to the continuously changing particle motion and orientation. Therefore, the previous measurements may not give the ultimate answers on free fall aerodynamics of tumbling bodies. In particular, the sensitivity of wind tunnel investigations is not adequate to establish and evaluate any damping effects. Hence a new type of experiment is required.

If oscillations become appreciable, the non-dimensional oscillation frequency of the fluid, the Strouhal number, must be matched in addition to the Reynolds number. This effectively eliminates the possibility of studying the motions of falling particles in a liquid such as water and invoking similarity theory to apply the results to air (List, 1966). Free fall of hailstones can only be understood by investigating models falling freely in air. This paper presents preliminary results obtained from the investigation of the motion of a freely falling disk, using results which have been obtained from a free fall tower with a controlled falling high speed camera. This technique is more convenient than having particles dropped from an aircraft and followed by parachutists (Knight & Knight, 1970) because space, orientation and time are much better defined. The approach to the problem in a free fall tower is quite opposite to the procedure in wind tunnel measurements: instead of measuring forces and torques and calculating movements, the motions are measured and the forces and torques are calculated. A disk has been chosen as test particle to elucidate the new technique because this shape represents an aerodynamically blunt body which is known to carry out secondary motions during its fall (List and Schemenauer, 1971).

2. EXPERIMENTAL SETUP AND ANALYSIS TECHNIQUES

The free fall motion of a disk is studied by a high speed camera (Hycam) which is released at the same time as the particle and is programmed to follow it at the same speed (except perturbations). The disk is always kept in the field of view of the horizontally pointing camera over the entire 3.25 m (vertical) fall distance which is presently available in the laboratory (Rentsch, 1975). The camera is braked at the end of the fall within 1 m through a piston in an air-tight cylinder with a deceleration of ≤ 16 g (where g is gravitational acceleration). Due to the present height limitation, the maximum tracking speeds are ~ 7 m/s over the lowest 1 m of fall before braking (Figure 1).

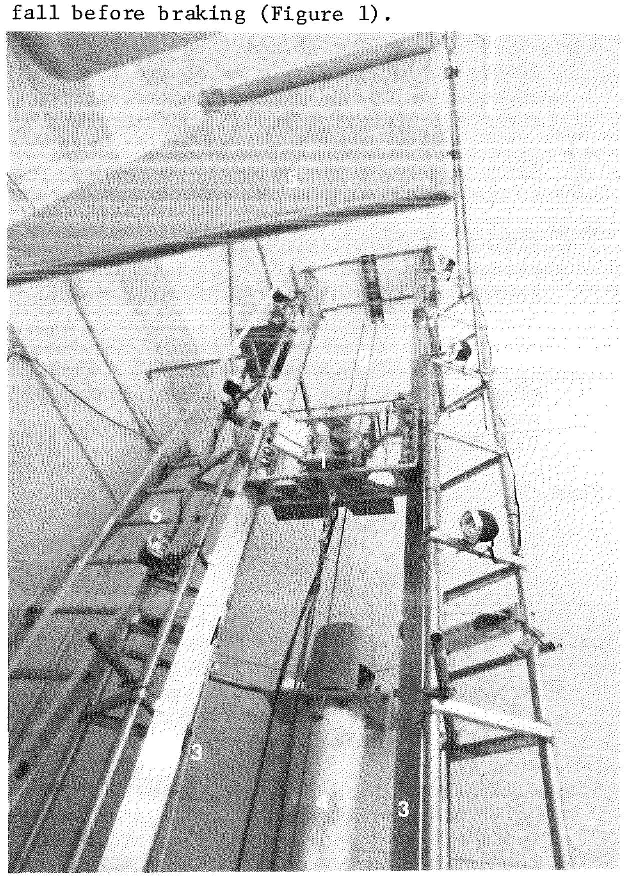

Figure 1. Upper part of free fall tower with the high speed camera (1) mounted on the sled with the driving cables (2), guide rails (3), and braking cylinder (4). (5) is the backdrop for photography and (6) are the flood lamps. Spacing between horizontal supporting bars on the towers is 0.5m.

In order to analyze the motion of the disk during free fall, its space position and orientation must be known as a function of time. An optical system was designed to measure the particle coordinates accurately in each frame of the film (Figure 2). With this arrangement of half-silvered and front-surfaced mirrors, three images of the disk are formed on the film (Figure 3). The measurement of coordinates of a series of characteristic surface points then allows reconstruction of the true spacial position of the particle at the time the frame was made. The individual frames were projected with a magnification 50x onto the screen of a projection microscope (Projectina) and evaluated with a specially constructed digitizer. The X-coordinate of the centre of the mass of the particle can be calculated from the horizontal positions of the direct view image and one of the mirror view images. The Y and Z-positions of the disk's centre of mass is then calculated from the direct view alone. At typical disk distances of 40 cm from the film in the camera, the standard error of reproducibility is 0.4 mm in the X-direction and 0.1 mm in the Y and Z-directions. Calibration curves slightly adjust the calculated X-coordinate across the field of view to account for systematic errors arising from the optical system.

The orientation of the disk is assessed with the help of colour-coded marks (see Figure 3) situated as specific body coordinates on the disk. The space Y and Z-coordinates of these marks relative to the centre of the disk are computed by assuming that all the marks have the same X-coordinate, the centre of mass value. The transformation between the body and space coordinates is described by the Euler angles (Goldstein, 1950), which are calculated by a "trial and error" computer program. The accuracy achieved is about $\pm 3^{o}$.

Free fall aerodynamics is explored in this paper by studying the fall of a very light particle (with a relatively long fall time). A homogeneous plastic material (styrofoam SM) of density 0.0345 gm/cm^3 ±2% was shaped into a disk of thickness 0.85±0.02 cm and diameter 1.95±0.02 cm. Photographs of the free fall motion of this disk were shot at 200 frames per second with a 12.5 mm lens, using Ektachrome 7242 16 mm film. Every second frame of the film was analyzed.

3. RESULTS

Some aspects of the free fall characteristics of the disk for a typical drop are shown in Figure 4. This diagram displays, as smoothed functions of time and vertical position, the horizontal positions, the velocities of the centre of mass, and the components θ_x and θ_y of the inclination of the disk's minor axis from the vertical (attack angle) with respect to the X and Y-axes, respectively. θ_x is defined positive if the outward normal from the lower face of the disk points in the direction of positive values of Y. A similar definition applies to θ_y. The true attack angle can be found if these components are treated as vector components. The horizontal and vertical velocities relative to the camera were calculated by central finite differencing. Maximum errors arising from resolution inaccuracies are ±3 cm/s for X and Z-velocities and ±1 cm/s for the Y-velocities. A numerical averaging, Hanning window (Kanasewich, 1975), was applied to these computed velocities to smooth the curves. The fluctuations of the vertical velocity were calculated only during the portion of the fall time when the camera fell at the selected terminal velocity of 1.96±0.02 m/s (≥0.5s after release). This curve was smoothed by hand to lessen a possible effect of the slight oscillation in the camera's velocity caused by stretching of the driving cable. Smoothing in this and the other curves may have erased physical fluctuations as well.

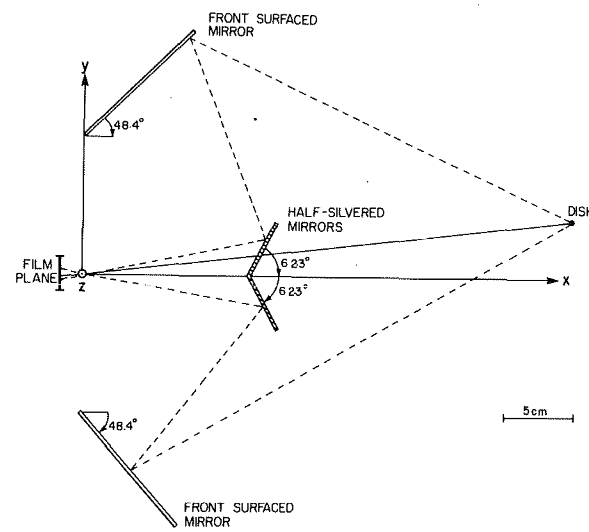

Figure 2. Schematic diagram of the optical system indicating the geometry by which three images of the disk are formed on each frame of the film. The coordinate system used to describe the disk's position is also shown.

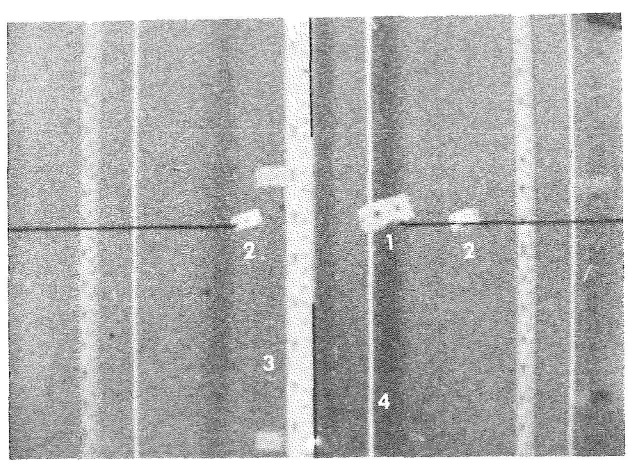

Figure 3. Photograph taken with the high speed camera of the falling disk with the marks used for determining its orientation. The direct view of the disk is the central image (1) and the smaller images (2) are the views through the side mirrors. A ruler (3) and a plumb line (4) and their images help to determine the space coordinates. The cross-hair is from the camera.

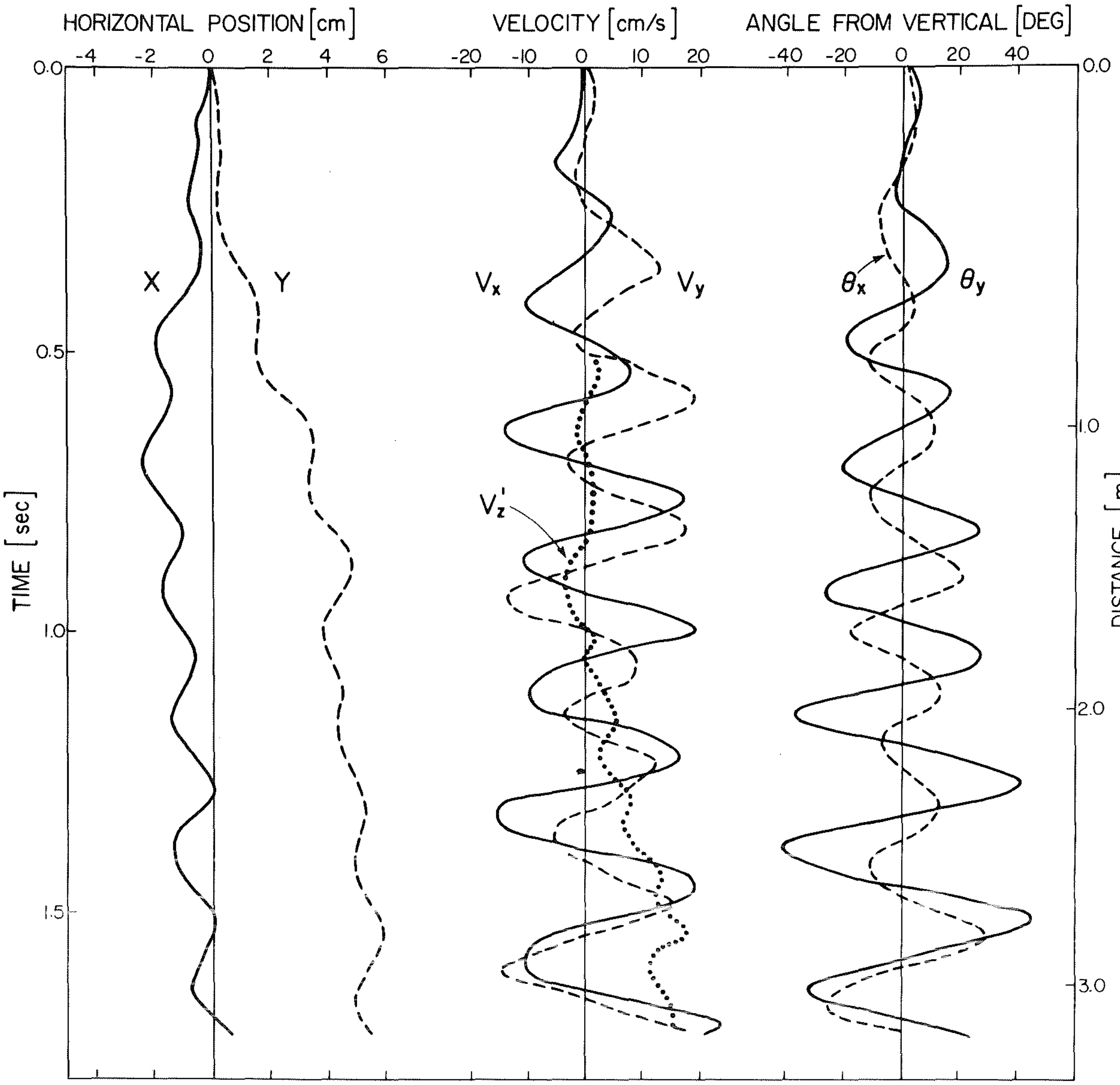

Figure 4. Smoothed characteristics of the disk's free fall motion. V_x and V_y are the velocities in the X and Y-directions, respectively. V_z measures the difference between vertical velocity of the disk and that of the camera, and is only shown for times when the camera fell at constant velocity (1.96 m/s, after 0.5s). θ_x and θ_y are the attack angles of the disk with respect to the X and Y-axes, respectively. Helical motion occurs between 0.25 and 1.15s, essentially planar oscillation starts to dominate the motion afterwards.

The general character of the disk motion is described by the inclination angles θ_x and θ_y. Hence, we will discuss those aspects first. At the point of release, the minor axis of the disk was inclined approximately 5^o from the vertical. During the first 0.1 seconds, this attack angle gradually increased to about 9^o, after which it returned to zero at 0.17s. Afterwards, θ_x and θ_y became out of phase. This is shown in the horizontal velocity curves as well. Both the velocities and the orientation remained out of phase by about 1/4 period until approximately 1.15s. This phase difference implies that a helical type of motion occurred. An oscillation was superimposed since the attack angle was not constant. The rotation about the minor axis was very small. This helical motion may be due to the tilted release position; a disturbance in the air (Willmarth et al., 1964) is less likely the cause because this motion is not accidental as other drops of disks showed. During this helical motion the frequency of the oscillations averaged about 4.3Hz. At 1.15s θ_y peaked at -38^o, representing a 10^o increase in amplitude over the previous oscillation. Neighbouring θ_x peaks decreased. Small frequency changes which accompanied the changes in rotational amplitude (rotation refers to the minor disk axis) brought the two horizontal components closer into phase after this time. The large angular increase may have occurred as a threshold angle was reached (near 30^o) above which the restoring torque acting on the disk decreased. This is in qualitative accord with measurements of the restoring torque acting on a cylinder by Willmarth et al. (1967). The transition of helical to oscillatory motion is in agreement with the case for spheroids as described by Kry & List (1974b), who show that a helical motion is not stable. The individual oscillation amplitudes about both horizontal axes increased after the transition to an oscillatory motion: the total attack angle increased from 26° just before the transition to 49° after 2 oscillations. The individual oscillation frequency decreased slightly to 4Hz for Y-axis rotations but was somewhat larger for rotations about the X-axis. The effect of this is to bring the components more into phase. These frequency changes may be caused by a non-linear dependence of the aerodynamic restoring torque to attack angle, a coupling of the oscillatory and translational motions (List et al., 1973) or hysteresis effects resulting from the oscillations.

The total angular rotation about the minor axis amounted to 120° for the entire fall. During this period, 6 oscillations occurred in θ_x and θ_y.

The trajectory of the disk [X(t),Y(t)] shows an overall horizontal drift of 5.5 cm in the Y-direction and 0.5 cm in the X-direction, although departures from the original X-position reached 2.5 cm at one portion of the fall. Horizontal drifts beginning around 0.3s are in the directions expected for slipping according to the orientation of the disk. At this time θ_x is negative which implies that the lift force is directed towards positive Y and θ_y is positive, inferring motion towards negative values of X. This initial drift, in both directions, was quite large (1.5 cm) even though terminal velocity had not been reached and θ_x and θ_y were both small (8° and 16°, respectively). Later X-drifts became smaller and the disk slowly returned to its initial X value. The systematic Y-drift, away from the initial value, continued throughout the fall, although it was less pronounced after the transition to oscillation occurred.

List et al. (1973) did not obtain net horizontal motions when studying oscillating spheroids at terminal speeds under quasi-steady state conditions. Hence, other factors are needed for explanation. Wake effects may have been responsible for some of the drifts, especially the initial ones. At 0.3s the disk was accelerating towards its terminal velocity and as a result the flow over the leading edge of the inclined disk would be increased, whereas the wake over the trailing edge would lag. The lift would be enhanced by the increased pressure gradient across the disk caused by the non-equilibrium flow velocities. The asymmetry produced would require a certain time to be damped out so that the later large drifts may be related to the initial drift. Some drift may also be due to air motions (which were less than 10 cm/s, as deduced from photographs of smoke), effects from the camera, or asymmetry of the disk itself.

Typical X-coordinate oscillations (peak-to-peak) were 1.5 cm or 75% of the disk diameter D. Peak velocities in this direction were not generally symmetric (reflecting the slight drift) and average speeds were fairly constant around 15 cm/s or 7.5% of the terminal velocity. The accompanying accelerations reach 0.6g for a lift coefficient C_L=0.7. This coefficient is defined as:

$$C_L = F_L \,/ (\frac{1}{8}\, \rho_f U^2 \pi D^2),$$

where F_L is the lift force, U the disk's velocity, and ρ_f the air density. Oscillatory motions in the Y-direction were slightly smaller than those in the X-direction through most of the fall except when θ_x approached θ_y and the horizontal amplitudes were similar. Following the transition to basically planar oscillations, average peak velocities V_y increased steadily from 6 cm/s to over 15 cm/s.

The average vertical velocity V_z=1.96 m/s (Reynolds number 2.6×10^3) was relatively constant during the entire helical motion. Once the more in-phase motion began, V_z increased by up to 15 cm/s, representing 7.5% of the terminal velocity. This corresponds to a decrease in drag coefficient C_D from 1.25 to 1.05, where C_D is defined in an analogous manner to C_L, except that the drag force replaces the lift force F_L. Improved average streamlining of the disk during the large orientation changes accounts for the decreased aerodynamic resistance. The vertical velocity fluctuations result from complex interactions between the changing cross-sectional area, streamlining, and possibly wake effects.

List et al. (1973) predicted, for oscillations confined to a plane, that the angular amplitudes would increase as a result of a coupling between the horizontal and the angular motion. This occurred during the latter portion of the disk's fall. The instantaneous velocity was approximately 5° from the vertical at zero attack angle. The disk therefore was subjected to an accelerating torque until it had rotated about 5° past the vertical. If the restoring torque varied linearly with attack angle, the disk's angular amplitude would increase by approximately 10° per cycle. Actually, above some angle the restoring torque will decrease substantially (Willmarth et al., 1967) so that the assumption of a linear relation corresponds to a lower limit of angular amplification. This limiting amplification was surpassed only over the cycle between 1.03 and 1.27s when the helical motion broke down. In later cycles the largest amplification was 5° per cycle. The planar oscillation state was not achieved exactly in this experiment, however, and the existence of a damping torque could not be established.

The non-dimensional oscillation frequency (defined as Strouhal number S = nD/U where n is the oscillation frequency) varies from about 0.043 during the helical motion to 0.037 during the latter portion of the fall. The non-dimensional inertia of the disk I* (Stringham et al., 1969) is given by $\frac{\pi}{4}\frac{\rho_b}{\rho_f}\frac{T}{D^3}[\frac{D^2}{16}+\frac{T^2}{12}]$ for a thick disk having a thickness T and a density ρ_b. For the disk studied here, I* is 0.77.

Willmarth et al. (1967) made measurements in a wind tunnel in which thin disks (T<<D) were free to rotate about a diametric axis perpendicular to the flow. They found that the two non-dimensional numbers S and I* were related. The predicted oscillation frequency obtained from this relation,

0.04, agrees very well with the oscillation of the freely falling disk, even though the wind tunnel experiments were carried out at Reynolds numbers over an order of magnitude larger and the disks used in these measurements were much thinner than the present one. Willmarth et al. showed that the restoring torques acting on the oscillating disks were about 30% less than those measured for stationary disks. However, these torques both decreased slightly with decreasing Re so that it is not known for sure if the static torque had decreased sufficiently to explain the observed dimensionless frequency at Re for the falling disk.

Delays in the adjustment of the boundary layer and wake due to the changing orientation of the disk and resulting effects on aerodynamic forces and moments should be observable as time delays between translational motions and disk orientations. Assuming no delay or coupling, the maximum horizontal velocity will occur as the attack angle becomes zero and the velocity would vanish at the maximum angles of the oscillations. An analysis of these extreme situations failed to turn up any definite asymmetries.

6. SUMMARY AND COMMENTS

Experience has demonstrated that wind tunnel measurements of forces and torques of fixed or restrained particles can only be used to calculate first order behavior of freely falling particles. In particular, this method is not sensitive enough to measure any damping effects which eventually take control over the particle motion. Considerable advances, however, can be achieved by observing the free fall of particles with a high speed camera and by determining forces and torques on the basis of the particle motion. This, in turn, allows the calculation of drag and lift coefficients (for given particle orientations) and their variation as functions of secondary motions and angular and translatory accelerations.

An apparatus has been described (an extensive description will be published later) which allows the pre-programmed observation of freely falling bodies at an average distance of 40 cm by a controlled falling high speed camera. A mirror system allows the determination of particle coordinates and orientation during its fall.

The power of the method of aerodynamic evaluation has been shown for the case of a disk with a diameter of 1.95 cm and a terminal speed of 1.96 m/s. The disk was released with an original inclination of the minor axis versus the vertical of 5°. After 0.25s, its mode of fall was helical; but since this motion is not necessarily a steady state possibility, it converted after 1.15s to an essentially planar oscillation with continuous acceleration in the vertical and a continuous increase in oscillation amplitude. Provided the observational distance would have been larger, a tumbling might have commenced. The observed maximum horizontal translations were up to 5.5 cm from the vertical, the largest horizontal speeds were up to 20 cm/s, the largest perturbations in the vertical speed 15 cm/s, the highest horizontal accelerations 0.6g, and the largest oscillation angles (from the vertical) 50° at frequencies of $\sim$ 4Hz.

This disk case did not show any clear-cut influence of the wake on the motion through hysteresis effects. Further, the accuracy of the measurements still does not allow at this time consideration of the variation of the drag and lift coefficients at given particle speeds and orientations. Some higher frequency fluctuations of the measured quantities are visible. However, their origin might be coupled with the apparatus. Extended calibration procedures will clarify this point and remedy the problem.

In summary, it can be stated that the newly-developed fall tower - which can easily be extended to a height of 25 m and allow fall speeds of 25 m/s - finally provides the experimental platform to study free fall of particles in a more realistic fashion. It will lead to a more extensive understanding of the fall behavior of models of atmospheric precipitation particles like ice and snow crystals, graupels, hailstones and raindrops.

ACKNOWLEDGEMENTS. The research presented here is supported by a grant from the National Research Council of Canada.

REFERENCES

Goldstein, H., 1950: Classical Mechanics. Addison-Wesley, Reading, Mass., pp. 399.
Kanasewich, E.R., 1975: Time Sequence Analysis in Geophysics. University of Alberta Press, Edmonton, Alberta, pp. 364.
Knight, C.A., and N.C. Knight, 1970: The falling behavior of hailstones. J. Atmos. Sci., 27, 672-681.
Kry, P.R., and R. List, 1974a: Aerodynamic torques on rotating oblate spheroids. Phys. Fluids, 17, 1087-1092.
----, and ----, 1974b: Angular motions of freely falling spheroidal hailstone models. Phys. Fluids, 17, 1093-1102.
List, R., 1966: On the simulation of physical processes occurring in clouds. Bull. Amer. Meteor. Soc., 47, 393-396.
----, R.B. Charlton, and D.F. Parson, 1969: Inertia effects on hailstones in oscillating updrafts. Proc. 6th Conf. Severe Local Storms, Chicago, Ill., 264-266.
----, and R.S. Schemenauer, 1971: Free fall behavior of planar snow crystals, conical graupel and small hail. J. Atmos. Sci., 28, 110-115.
----, U.W. Rentsch, A.C. Byram, and E.P. Lozowski, 1973: On the aerodynamics of spheroidal hailstone models. J. Atmos. Sci., 30, 653-661.
Rentsch, U.W., 1975: Design of an electronic control system for photographic tracking of freely falling hailstone models. Professional engineer's thesis, University of Toronto, pp. 80.
Stringham, G.E., D.B. Simons, and H.P. Guy, 1969: The behavior of large particles falling in quiescent liquids. Geological Survey Professional Paper 562-C, Washington,

D.C., pp. 36.

Willmarth, W.W., N.E. Hawk, and R.K. Harvey, 1964: Steady and unsteady motions and wakes of freely falling disks. Phys. Fluids, 7, 197-208.

----, ----, A.J. Galloway, and F.W. Ross, 1967: Aerodynamics of oscillating disks and a right-circular cylinder. J. Fluid Mech., 27, 117-207.

3.4.10

LOSS OF ACCRETED WATER FROM GROWING HAILSTONES

P.I. Joe, Roland List, P.R. Kry, M.R. de Quervain*, P.Y.K. Lui, P.W. Stagg, J.D. McTaggart-Cowan, E.P. Lozowski**, M.C. Steiner, J. Von Niederhäusern*, R.E. Stewart, E. Freire, G. Lesins

Department of Physics, University of Toronto, Toronto, Canada

1. INTRODUCTION

Icing experiments were performed in the summers of 1972 and 1974 at the Swiss Federal Institute for Snow and Avalanche Research in its three storey high, closed-circuit hail tunnel with pressure control (List, 1966). They involved the icing of 2 and 3 cm oblate ice spheroids of axis ratio 1.0, 0.67 and 0.5 at temperatures from -5 to -30C and liquid water contents between 3 and 50 gm/m^3. The tunnel pressure was adjusted according to mean temperature-pressure profiles found in hailstorms in Colorado (Beckwith, 1960). The oblate spheroids (including spheres) moved with various secondary motions: spin about a horizontal minor axis, spin about a horizontal major axis and symmetric gyration. The latter motion consists of a spin about a minor axis which rotates at a given angle about a horizontal axis such that it describes the surface of a cone with apex at the hailstone centre (Kry and List, 1975a,b). Fixed spheres were also iced to repeat in part the conditions of previous experiments by List (1960).

The purpose of the experiments was to investigate the growth of ice particles, their surface temperatures and deposit properties such as sponginess, air bubble distributions, bubble concentrations, crystal sizes and orientations, and relate them to the icing conditions and modes of free fall motions. The experiments were based on advances made at the Toronto Laboratory with respect to the relation of bubble size distributions with air temperature and liquid water content (List et al., 1972; List and Agnew, 1973), better understanding of hailstone aerodynamics through experiments and modelling (Kry and List, 1974a,b; List et al., 1973) and the availability of a radiometric microscope to measure the surface temperature of growing stones.

Analysis of the results showed that the collection efficiency was low, ranging from 15% to 60% (unpublished results). Photographic evidence obtained during icing revealed that the incident droplets approached in straight trajectories - therefore, the collision efficiency is unity - and that droplets bounced (or shed in various ways) from the surface of the growing hailstone (Figure 1). Hence, this figure clearly demonstrates that the coalescence efficiency is not unity. Bouncing was observed in many other instances and appears to be a common event. This phenomenon was investigated by numerical simulation for its contribution to the coalescence efficiency.

*Swiss Federal Institute for Snow and Avalanche Research, Davos.
**University of Alberta, Edmonton

However, there is also shedding at work. Hence, a discussion of mechanisms by which a growing hailstone can lose already accreted water will round off our conceptual picture of factors involved in the assessment of coalescence efficiency.

Water losses by bouncing and shedding from fixed, growing hailstones have been observed before [List, 1963], while Carras and Macklin (1973) conjectured from their experiments that these processes had to occur also for their hailstones which grew while floating in their tunnel (with bouncing from the walls). Systematic, directly documented investigations however, have not been published.

2. BOUNCING OF DROPLETS FROM A SPHERE

2.1 Phenomenology

The main features of the bouncing of droplets from an icing sphere (Figure 1) are depicted in the conceptual sketch in Figure 2. The suspension of the hailstone was from above. The droplets were injected from below and carried up by the air flow. They appear as tapered streaks due to the nature of the capacitor discharge of the strobe unit. The length of the streaks is proportional to the speed of the droplets, and the incident droplets are assumed to be travelling at the speed of air. Digitization of Figure 1 indicated that the reflected or bounced droplets move at 39-58% of the incident velocity. They appear to reach a constant outward velocity as the angle that their trajectories make with the vertical (the deflection angle, θ) appears to become constant (about $50 \pm 10^{\circ}$). The angle between the incident droplet velocity vector and the normal to the hailstone surface at the point of impact is termed the collision angle (ϕ). There appears to be a central region where reflected streaks do not appear to originate. The boundary of this region is quite well defined ($\phi_{nb} = 25 \pm 5^{\circ}$). In this region dots appear instead of streaks. Because the incoming droplets do not experience any deflection, the collision efficiency is one.

2.2 Numerical Model

The first step in the numerical modelling is the investigation of the collision - coalescence - bouncing mechanism of a single droplet of a given size. The overall effect of a whole droplet spectrum on the coalescence efficiency of an ice sphere can then be assessed by integration.

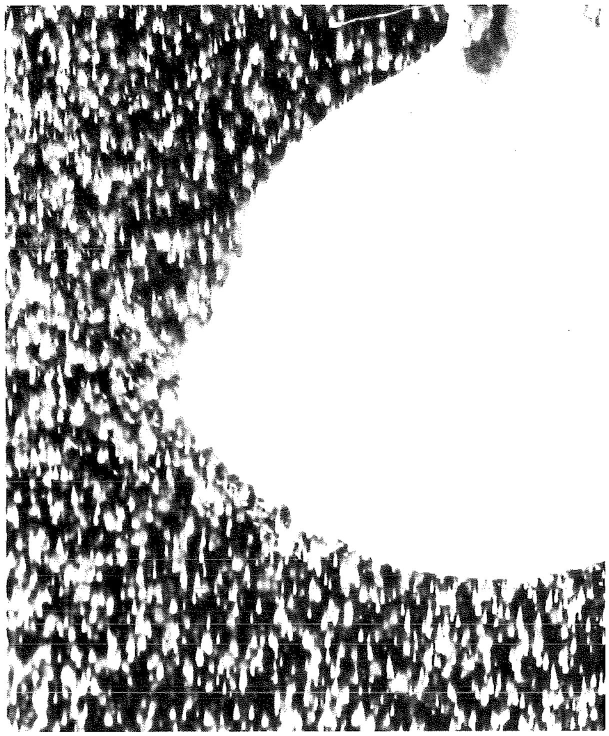

Figure 1. Photograph of the bouncing of supercooled droplets from an artificially growing spherical hailstone embryo. The features to note are the vertical streaks of the incident droplets (A), the reflected streaks (B), the central region and its boundary (C) and the dots representing slowly moving droplets (D).

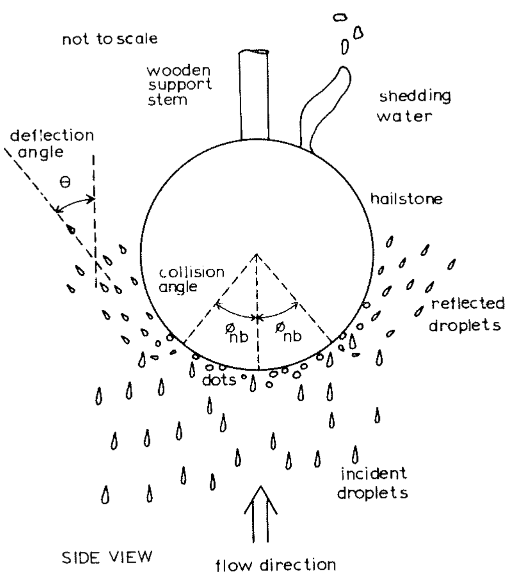

Figure 2. A conceptual sketch of the bouncing of the supercooled droplets, emphasizing and defining some of the details observed in Figure 1.

The external forces on the droplet are the hydrodynamic drag and gravitational forces. The effect of accelerations on the droplet was expected to be significant since the droplet, upon reflection, changes direction quite rapidly. An analytical expression for the drag on an accelerating sphere in Stokes flow was derived by Pearcey and Hill (1956) and was adapted to non-zero Reynolds numbers by replacing the Stokes steady state drag part of the solution by one applicable to the Reynolds numbers encountered along a trajectory; specifically, that of Beard and Pruppacher (1969) and Pruppacher and Steinberger (1968). The resulting equations of motion in two dimensions are

$$\frac{d\vec{v}}{dt} = \vec{g} - \frac{\rho_a}{\rho_d}\frac{d}{dt}(\vec{v}-\vec{u}) - \frac{9}{2}\frac{\rho_a}{\rho_d r}\sqrt{\frac{\nu}{\pi}}\int_{-\infty}^{t}\frac{d(\vec{v}-\vec{u})}{d\tau}\frac{d\tau}{\sqrt{t-\tau}}$$

$$- \frac{9}{2}\frac{\rho_a}{\rho_d}\frac{\nu}{r^2}(\vec{v}-\vec{u})\left[1 + \alpha Re^{\beta}\frac{(\vec{v}-\vec{u})}{|\vec{v}-\vec{u}|}\right], \qquad (1)$$

$$\frac{d\vec{x}}{dt} = \vec{v}, \qquad (2)$$

with $\vec{v}$ the droplet velocity relative to a fixed frame of reference attached to the stationary sphere,

$\vec{g}$ acceleration due to gravity,

$\rho_a\rho_d$ air and droplet densities, respectively,

$\vec{u}$ air velocity,

r droplet radius,

ν kinematic viscosity of air,

t,τ time, and

Re droplet Reynolds number,

$\vec{x}$ droplet position vector in respect to sphere centre,

and $\alpha = 0.102$	$\beta = 0.995$	for $0.01 <$ Re $<$	1.5
0.115	0.802	$1.5 <$	< 20
0.189	0.632	$20 <$	< 400

The first term on the right hand side represents the effect of the weight, the second the fraction of the displaced volume of air which has to be accelerated, the third is a history term and the fourth the Stokes drag as extended by Beard and Pruppacher. The first and fourth terms represent the major contributions to the total acceleration.

Results indicate that the second and third acceleration terms of (1) may change the droplet velocities for trajectories after reflection and in the region of interest by up to 10%. The retention of all four terms is therefore recommended. Figure 4 gives an idea about bounced droplet trajectories as treated along equations by different authors.

The flow field near the boundary of the collector sphere was expected to be crucial. Hence, it was measured for Re = 2.4×10^4 in a horizontal wind tunnel at the University of Toronto (Joe, 1975). Figure 3 shows the streamline pattern for the flow. The streamfunction for the experimentally measured flow may be written as

$$\psi = \frac{1}{2}(R^2 - R^{-1})\sin^2\Omega + a\exp(-b\,x^c), \qquad (3)$$

with ψ the streamfunction,

R distance from sphere centre,

x upstream position,

$\sin \Omega = -x/R$,

a,b,c coefficients equal 0.0812, 3.6779 and 3.7805, respectively.

The flow differs substantially from potential and viscous flows, particularly near the sphere, i.e. in the region which is important for the deflection of bouncing droplets.

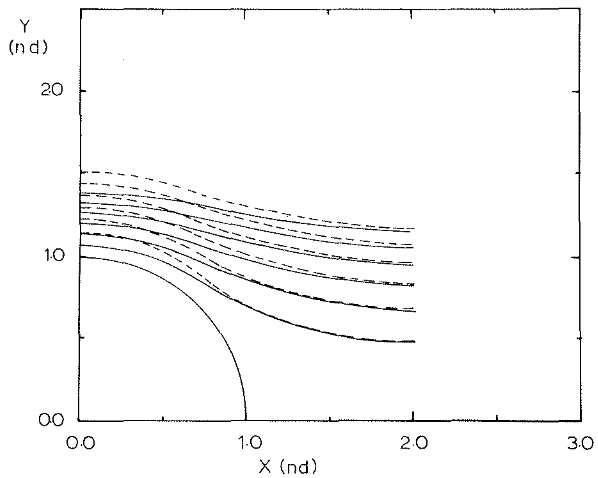

Figure 3. Streamline pattern for the flow around a sphere at Re = 2.4 x 10^4. The dashed lines are the streamlines for ψ = 0.1, 0.2, 0.3, 0.4 and 0.5 of the experimentally measured flow and the solid lines are for potential flow.

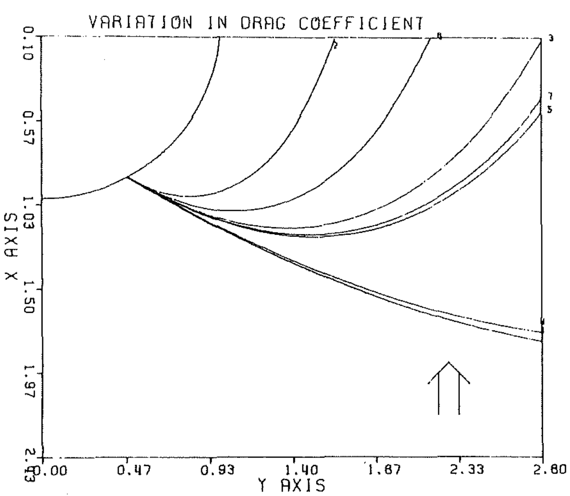

Figure 4. Bounced trajectories calculated with drag coefficients formulated by various authors. The trajectories marked 1 to 7 were calculated with drags by Stokes (1), Oseen (2), Goldstein (as modelled by Langmuir) (3), Pearcey and Hill (4), Beard and Pruppacher (5), Carrier (6) and the modified Beard and Pruppacher (7), respectively. The differences among the various drags are quite significant.

In order to assess the coalescence efficiency, a transformation describing the relation between incident and reflected droplet properties (mass and velocity) is needed. The parameterization scheme applied is based upon classical mechanics and experimental observations (Jeans, 1935). The normal velocities (with respect to the spherical collector) of the incoming droplet, w_n, and the reflected one, w_n', are related by

$$w_n' = -\frac{\varepsilon}{m_{tr}} w_n , \qquad (4)$$

where ε is the coefficient of elasticity and m_{tr} is the mass transfer ratio, i.e. the ratio of the mass of the reflected droplet to the incident droplet. The tangential velocities w_t and w_t' are related by

$$w_t' = \frac{w_t}{m_{tr}} + \mu(1+\varepsilon) \frac{w_n}{m_{tr}} , \qquad (5)$$

where μ is the coefficient of friction, and

$$r' = m_{tr}^{1/3} r , \qquad (6)$$

where r' is the radius of the reflected droplet.

It should be noted that the (smaller) reflected droplet might benefit from the compressional energy of the entire (larger) incident droplet; thus an actual increase in speed is not a priori ruled out. The scheme (eqns. 4–6) relates the incident droplets to the reflected ones in a linear way and is valid since it will only be used to transform one delta-function size distribution into another one when determining the bounds on the coalescence efficiency of droplet spectra.

2.3 Results on bouncing

The simulation of the incident trajectories of the case depicted and specified in Figures 1 and 2 shows that the minimum incident droplet radius for bouncing is 40 $\pm$ 5 μm. If it is smaller then complete coalescence occurs. Further, the droplet velocities in the region of interest depend primarily on droplet size. In order to compare the trajectories after reflection, the droplets have to pass first the point of maximum curvature of their trajectories (the apex), their farthest upstream position after bouncing before they reach the region where the velocities were measured. At the apex, the effect of the initial velocity conditions are essentially forgotten since the radial droplet velocities approach a zero value. Then the speed picks up due to the hydrodynamic drag force at a rate dependent only upon the droplet size (given a flow). It should be noted that the initial conditions control the gross features of the trajectories. The results indicate that the radii of the reflected droplets range from 18 to 30 $\pm$ 3 μm for mass transfer ratio ranging from 0.0044 to 0.422.

The model also explains the presence of dots for collision angles $<\phi_{nb}$: they represent bounced droplets which are moving very slowly and may even have bounced more than once, as shown by trajectory 1 in Figure 5. Therefore, the central region where no streaks appear is a region where bouncing does occur, but droplet speeds are so low that they do not appear as streaks on the photographs. These droplets may collide again with the hailstone and can barely escape complete coalescence. Considering the limited resolution the dots do not appear to have more than 10% of the incident speed. Using this as a numerical definition of a dot, the central region may be simulated with elastic and frictional coefficients ranging from 0.0 to 1.57×10^{-3} and from 4.725×10^{-3} to 3.52×10^{-2}, respectively, using the previously determined values for m_{tr}.

Assuming that upon a second collision the droplet totally coalesces, bounds on the coalescence efficiency may be calculated assuming delta function distributions for the droplets of a spectrum. A central frontal region is then defined where total coalescence may occur. (The

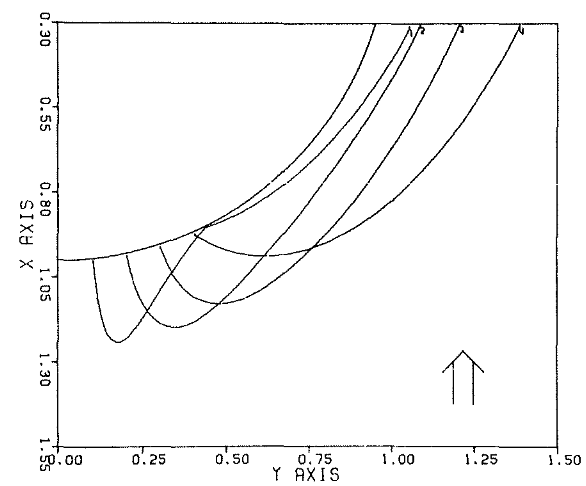

Figure 5. Bounced trajectories simulating the minimum total coalescence region. The initial droplet radius was 40μm. The bounce conditions were ε = 0.112, μ = 0.337 and m_{tr} = 0.422 (therefore, the bounced droplet radius was 30μm). These conditions promote escape of the colliding droplet from the hailstone. This figure indicates that only the droplet trajectory originating at a collision angle of less than 10° (marked 1 on figure) bounces twice, implying that the minimum total coalescence region occurs at a collision angle of less than 10°. Simulation with bounce conditions ε = 0.0, μ = 0.499, m_{tr} = 0.0044 and an initial droplet radius of 110 μm (therefore, the bounced droplet radius is 18 μm) under which escape of the droplet from the hailstone is not favoured indicates that the maximum total coalescence region is just the central region.

actual coalescence may occur elsewhere but is accounted for at the point of first collision). Outside this region the droplets partially coalesce according to the value of the mass transfer ratio. The minimum and maximum total coalescence regions are determined numerically for the minimum and maximum droplet sizes in the spectrum (Figure 5). The coalescence efficiencies thus determined range from 99.7 to 58.2%. This may be compared to a value of ∿16% as calculated from the ratio of the accreted over impacted water mass (Stewart and List, 1974).

3. OTHER MECHANISMS FOR REDUCING THE COALESCENCE EFFICIENCY

Even though the assessment of bouncing is somewhat crude, the obvious conclusion is that there must be other more significant loss mechanisms. A further search disclosed six distinct types in addition to straight bouncing, as illustrated by sketches in Figure 6 and photographs in Figure 7. Of 1,192 photographs, 86 showed evidence of bouncing and 242 exhibited shedding mechanisms. Three types (see Fig. 6abc and 7abc) termed bouncing, crown formation, and Rayleigh jet formation occur on the frontal surface of the hailstone. This type of phenomena can principally occur on dry and wet surfaces (Worthington, 1877, 1908; Harlow and Shannon, 1967; Levin and Hobbs, 1970). In the experiments described, the relevant surfaces were wet. Crowns and Rayleigh jets could both be phenomena related to the same thing, namely bouncing of large "stray" drops which may occasionally be imparted into the air stream by the injection system. The crown of Fig. 7b is 550 ±50μm high with a base width of 850 μm. The jet of Fig. 7c is 1,250 μm long and has a tip diameter of 200 μm. Conclusions about the size of the impacting droplets are difficult to make because the stage of the impact is unknown and the phenomenon also depends upon the surface conditions.

Crowns and jets occur very infrequently and were seen only on 8 out of 1,192 photographs of icing particles. The rolloff of droplets along spikes and spin-off (Fig. 6d and Fig. 7d) occurs perpendicular to the rotational axes and is favoured by a combination of static pressure and centrifugal forces. As the droplets roll along spikes, they continuously lose mass and thus contribute to spike growth. This type of shedding of large (∿300μm) drops occurs only in ice growth on particles whose spin axis remains fixed.

Sheet and drop shedding (Fig. 6 e,f and Fig. 7 e,f) are events observed particularly on the rear of the gyrating or stationary spheroids. These mechanisms clearly demonstrate the presence of a water skin as water must accumulate on the

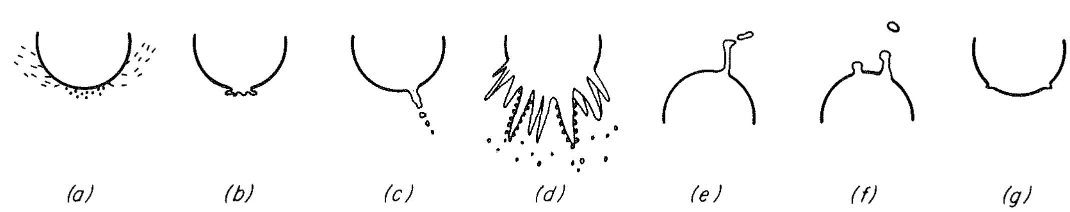

Figure 6. Sketches of the various loss mechanisms affecting coalescence (a) bouncing, (b) crown formation, (c) jet formation, (d) rolloff from spikes, (e) sheet shedding, (f) globule shedding and the (g) pointed protrusions. Compare with the photographs of Figure 7.

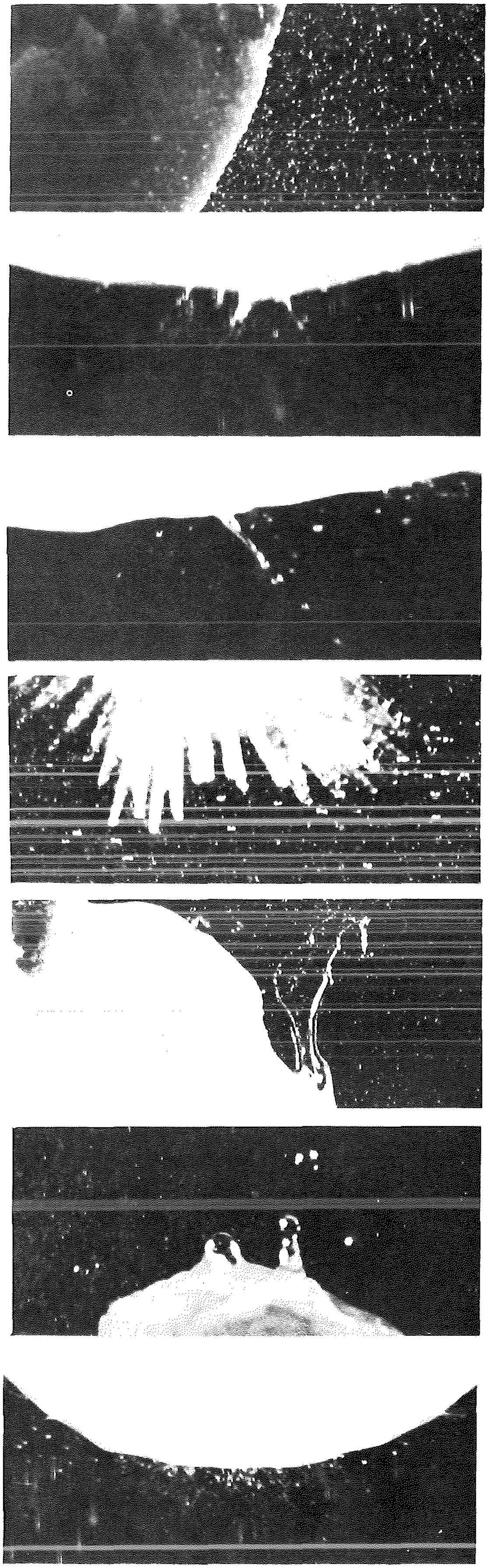

a

b

c

d

e

f

g

Figure 7. Photographs of the various loss mechanisms affecting coalescence. For 7a, b, c, g, the icing conditions were T = -20C, V_s = 33.4 m/s, LWC = 28.5 gm^{-3}, diameter = 2 cm, axis ratio = 0.67, f_{ro} = -190 rpm and f_{gy} = 960 rpm. The icing conditions for Fig. 7e are the same as that for Fig. 1. Fig. 7d occurred with conditions T = -10C, V_s = 23.1 m/s, LWC = 38.7 gm^{-3}, diameter = 2 cm, axis ratio = 0.67, and f_{ro} = 400 rpm. Fig. 7f had conditions T = -10C, V_s = 31.0 m/s, LWC = 51.0 gm^{-3}, sz = 2 cm, AR = 0.67, f_{ro} = 190 rpm and f_{gy} = 960 rpm. The order of presentation is the same as that for Fig. 6.

surface before shedding can occur. They may be related and depend upon what type of instability triggers the shedding. If the build-up of mass, momentum and energy becomes sufficient to overcome the adhesive forces then shedding occurs. Detaching sheets will normally disintegrate quickly into droplets. The pressure field and the tangential stress on the surface seem to favour the release of water from a piece of surface while it is at the rear of the hailstone. Sheet detachment is by far the most common and most effective loss mechanism.

The remaining event (Fig. 6g and Fig. 7g) is rather puzzling. The pointed protuberances appear to consist of liquid water, symmetric about the foreward stagnation point at angles of $\sim\pm 40^{o}$, suggesting a rotational symmetry about the main flow axis. It seems that a continuous stream of droplets is originating in the points (edges for cylindrical symmetry) of the protuberances. The authors have no interpretation for this shedding phenomenon which was consistently observed for growing gyrating ice particles. It may be related to the central no-streak region as observed in Fig. 1.

4. CONCLUSIONS

Based on an examination of photographs taken during the icing of spheres and spheroids in a hail tunnel and a numerical simulation of the bouncing of droplets the following conclusions can be made:

1) The collision efficiency for water droplets >20μm approaching ice particles with sizes of 2cm and more and speeds equal to the difference of their terminal speeds is $E_1 \sim 1$.

2) The particle growth rates are much less than expected from the collision efficiency. Hence, the collection and coalescence efficiencies are considerably less than unity, $E_2 < 1$.

3) An artificially growing hailstone can lose water in two principally different ways:
   - a) by loss of water from the water skin through disintegration of surface skin, detachment of large drops, and/or rolling off of drops along spikes or protuberances;
   - b) by bouncing of fractions of colliding droplets (also in form of jets and crowns).

4) Bouncing occurs only if the colliding droplets have diameters >80μm.

5) Bouncing from a central frontal surface ($\phi_{nb}<25^o$) produces droplets moving at very low speeds relative to the collector particle. Such droplets are normally recaptured later.

6) The diameters of the bounced droplets are within 16 to 75% of the size of the colliding droplets. Corresponding elasticity and friction coefficients are 0 to $1.6x10^{-3}$ and $4.7x10^{-3}$ to $3.5x10^{-2}$ respectively.

7) A numerical simulation of observed trajectories of bouncing droplets can explain a minimum integrated mass accretion of 60%. A comparison of the droplet fluxes before and after bouncing however indicates that only a fraction (20%) of the droplets which could bounce do actually bounce. Hence, the overall effect of bouncing reduces the overall coalescence (or collection) efficiency by no more than 8%. The reduction in cases of actual bouncing is obviously connected with the characteristics of the surface and its water skin. It needs to be remembered that an irregular ice substrate stabilizes the water skin. Hence, bouncing may strongly depend on the exact location of the droplet impact in respect of the underlying ice.

8) Artificial hailstones which rotate around an axis with constant direction in space can grow icicles. In such situations the accreted water forms blobs which roll along the icicles and detach at low speeds (<10% of relative air speed) as drops with diameters >200µm. This shedding is very efficient and accounts for most of the lost water. This mechanism, however, is not of particular importance to hailstone growth in nature.

9) For gyrating bodies, shedding occurs by detachment of pieces of surface skin which disintegrate rapidly into droplets. If this happens repeatedly at a given locale then the detached drops are large. Both mechanisms occur mostly in the rear part of the growing ice particles. This shedding accounts for the bulk loss of water for gyrating hailstones, a mode of motion which leads to the spheroidal hailstones in nature.

10) Since the collection efficiency (the product of the collision and coalescence efficiencies) can be so low that the accreted mass is smaller than the mass of water which could freeze on impact on account of its supercooling, the bouncing drops have to be supercooled or contain ice (which has not been detected yet in bouncing drops).

In summary, shedding and bouncing severely limit the growth rate of hailstone-sized ice particles and also affect their heat and mass transfer.

ACKNOWLEDGEMENTS. The original icing experiments on which this investigation is based were jointly sponsored by the Swiss Federal Institute for Snow and Avalanche Research, the Atmospheric Environment Service of Canada and the Canadian National Research Council. The latter two organizations also supported the evaluation.

REFERENCES

Beard, K.V., and H.R.Pruppacher, 1969: "A determination of the terminal velocity and drag of small water drops by means of a wind tunnel". J.Atmos.Sci., 26, 1066-1072.

Beckwith, W.B., 1960: "Analysis of hailstorms in the Denver network 1949-58". Phys. of Precip., Geoph. Mono. 5, Amer. Geoph. Union, 348-353.

Cannon, T.W., 1970: "A camera for photographing airborne atmospheric particles". Image Technology, April/May.

Carras, J.N., and W.C.Macklin, 1973: "The shedding of accreted water during hailstone growth". Q.J.R.Meteor.Soc., 99, 639-648.

Harlow, F.H., and J.P.Shannon, 1967: "The splash of a liquid drop". J.Appl.Phys., 38, 3855-3866.

Jeans, J.H., 1935: "An elementary treatise on theoretical mechanics". Dover Pub.Inc., 2nd Ed., pp. 364.

Joe, P.I., 1975: "Investigation of the bouncing of supercooled water droplets from an artificially growing hailstone". M.Sc. Thesis, U.of T., Physics Dept., pp.254.

Kry, R., and R.List, 1974a: "Aerodynamic torques on rotating oblate spheroids". The Physics of Fluids, 17, 1087-1092.

---- and ----, 1974b: "Angular motions of freely falling spheroidal hailstone models". The Physics of Fluids, 17, 1093-1102.

Levin, Z., and P.V.Hobbs, 1971: "Splashing of water drops on solid and wetted surfaces: hydrodynamics and charge separation". Phil.Trans.Roy.Soc., 269, 555-585.

List, R., 1963: "Determination of capture probabilities of precipitation particles with the Strobolume". General Radio Experimenter, 37, No. 11, 15-16.

----, 1966: "A hail tunnel with pressure control". J.Atmos.Sci., 23, 61-66.

---- and T.A.Agnew, 1973: "Air bubbles in artificial hailstones". J.Atmos.Sci., 30, 1158-1165.

----, P.I.Joe, G.Lesins, P.R.Kry, M.R.de Quervain, J.D.McTaggart-Cowan, P.W.Stagg, E.P. Lozowski, E.Freire, R.E.Stewart, C.G. List, M.C.Steiner, J.Von Niederhäusern, 1976: "On the variation of the collection efficiencies of icing cylinders". Proc. of International Cloud Physics Conference, Boulder.

----, W.A.Murray and C.Dyck, 1972: "Air bubbles in hailstones". J.Atmos.Sci., 29, 916-920.

----, U.W.Rentsch, A.C. Byram and E.P. Lozowski, 1973: "On the aerodynamics of spheroidal hailstone models". J.Atmos.Sci., 30, 653-661.

Lui, P., 1973: "The growth of artificial hailstones in a wind tunnel". B.Appl. Sci. Thesis, Dept. Eng. Sci., U. of T.

Pearcey, T., and G.W.Hill, 1956: "The accelerated motion of droplets and bubbles". Aust. Journal of Physics, 9, 19-30.

Pruppacher, H.R., and R.Steinburger, 1968: "Experimental determination of the drag on a sphere at low Reynolds numbers". J. Appl. Physics, 39, 4129-4132.

Stewart, R.E., and R.List, 1974: "Collection efficiencies of artificial hailstones". 8th Congress of the Can. Meteor. Soc., York University, Toronto.

Worthington, A.M., 1877: "Forms assumed by drops of liquids falling vertically on a horizontal plate". Proc.Roy.Soc., 25, 261.

----, 1908: "A study of splashes". Longmans, Green and Co., New York, pp. 129.

AIRCRAFT OBSERVATIONS IN THE SUB-CLOUD LAYER OVER LAND

C.E. Coulman and J. Warner

Division of Cloud Physics, CSIRO, Sydney, Australia

1. INTRODUCTION

This paper describes measurements of temperature, pressure and water-vapour mixing ratio made below fields of cumulus clouds which formed over extensive, flat country. The observations were commenced before the formation of fair-weather cumulus clouds and continued until the field had decayed appreciably. The term "sub-cloud layer" is here used to denote the whole depth of atmosphere beneath cumulus cloud base; however, since the operations were made from an aircraft no measurements could safely be taken at heights of less than about 25 m above the surface.

2. OBSERVATIONAL TECHNIQUE

The data reported here were obtained in April 1975 in flights over extensive level plains in the vicinity of Moree, N.S.W., Australia (29°30' S.; 149°50' E.).

The aircraft carried wet- and dry-bulb resistance thermometers and sensors of dynamic and static pressures; observations were recorded at 8-s intervals, which permitted spatial resolution of 0.48 km at a flying speed of 60 m s^{-1}. This equipment has the following performance:

Response time (temperature) ~5 s;
(pressure) ~1 s.
Temperature resolution 0.02 C, accuracy ±0.05 C.
Static pressure resolution 0.4 mb, accuracy ±0.5 mb.
Dynamic pressure resolution 0.07 mb, accuracy ±0.5 mb.

A photoelectric sensor was used to detect the presence of cloud above the aircraft.

Each day's operation comprised a series of horizontal measurement runs at selected heights and either three or four vertical soundings from near the surface to about 3 km altitude. A navigational aid enabled the aircraft to regain a given air-position to within 5 km during any flight.

3. GENERAL METEOROLOGICAL CONDITIONS

Skies were generally substantially free from cloud other than diurnal, fair-weather cumulus, and surface winds were always light, seldom in excess of 3 m s^{-1}. During late morning and early afternoon conditions were predominantly convective.

Throughout the expedition the ground was wet and in places covered with shallow water from previous rain. Daytime rain showers were observed only on two days, after conclusion of measurements.

The synoptic-scale vertical motion field showed downward flow over the region on six days and insignificant motion on the other four. On some days cumulus cloud tops exceeded 3 km, but more frequently did not exceed about 2.3 km.

4. THE MEAN STRUCTURE OF THE SUB-CLOUD LAYER

(a) Vertical Structure

The vertical stratification of the lower troposphere in fair weather over land evolves during the day in a well-recognized sequence. It is therefore meaningful to average vertical profiles of, say, virtual potential temperature θ_v and water-vapour mixing ratio q over a number of days in order to discuss certain of their characteristics.

It is desirable to normalize the height in soundings when averaging observations from several days and a scaling parameter having natural significance is the height, z_c, of the top of the well-mixed convection layer. In Fig. 1 a typical sounding is shown to illustrate how z_c may be determined to within about 50 m. The normalized height ζ is defined as

$$\zeta = \frac{z_j - z_s}{z_c - z_s} , \qquad (1)$$

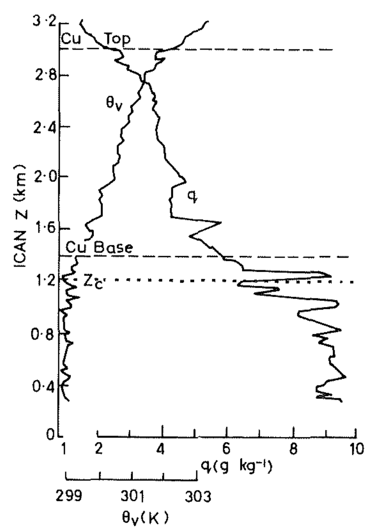

Fig. 1 - Typical afternoon sounding for virtual potential temperature θ_v and mixing ratio q. Top of convection layer is at z_c. Date and time: 16/4/75, 14-30 hrs.

where z_j and z_s are respectively the jth value of height recorded in a sounding and the height of the surface in the vicinity of the sounding. All z-values are calculated from pressure measurements according to the ICAN standard.

Soundings taken in the morning and in the afternoon of each day have been normalized and separately averaged over nine days of observations and are shown in Fig. 2 together with the average heights of cloud base.

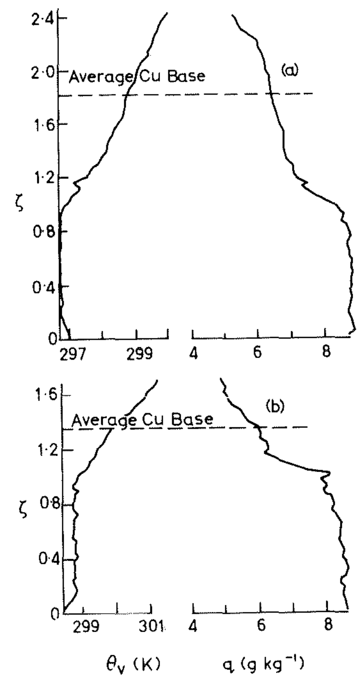

Fig. 2 - Soundings of θ_v and q averaged over nine days and normalized to z_c: (a) mornings; (b) afternoons.

Figures 1 and 2 illustrate some of the already known features of soundings of the planetary boundary layer but there are certain additional points which need some discussion. The sub-cloud layer is seen to comprise a well-mixed convection layer, in which virtual potential temperature θ_v is substantially independent of height and is surmounted by a region which exhibits a stable gradient of θ_v. Throughout each day cumulus cloud base was found to be higher than the top of the convection layer by an amount which generally decreased as time of day advanced. This implies that parcels of air which rise from regions below the top of the convection layer must penetrate a stable gradient to reach the observed condensation level. There is no evidence in any of the soundings, nor in the averaged results, for a sharp inversion layer near or just below cloud base such as that postulated in some models of a sub-cloud layer (e.g. Betts, 1973). Such sharply defined inversions are often characteristic of the early stages of the process of overnight inversion dispersal which sometimes precedes cloud formation by a few hours.

We may calculate a maximum value for the penetration of a stably stratified layer by a parcel which has been accelerated to a vertical velocity w at height z_c by buoyancy forces. If we equate its loss of kinetic energy to its gain in potential energy, without allowing mixing or any other fluid dynamical changes, the penetration d is given by

$$d = w\left[\frac{T}{g\ d\theta_v/dz}\right]^{\frac{1}{2}} . \qquad (2)$$

For typical values, say, $w = 1\ m\ s^{-1}$, $d\theta_v/dz = 1.5\ K\ km^{-1}$, $T = 300$ K and $g = 9.81\ m\ s^{-2}$, we find $d \approx 130$ m.

This is rather less than the afternoon values of (z_b-z_c), where z_b is the height of cloud base. It is much less than typical morning values of (z_b-z_c) when this difference is of the same order as z_c itself (see Fig. 2a). Since d depends on $(d\theta_v/dz)^{-\frac{1}{2}}$ the local gradient of density beneath an incipient cumulus cloud must, presumably, be very small, and it is tempting to speculate that such a modified gradient is the result of a succession of penetrating parcels of air.

It is important to consider in what sense these soundings represent average properties of the sub-cloud layer. The morning soundings were made in almost cloud-free conditions and, with the reservations discussed in Section 4(b), probably represent an average measure of vertical stratification above a large area of level terrain. The afternoon soundings however were made in the same air-position as the morning soundings, and this coincided sometimes with a cloudy patch, sometimes with a clear region. The aircraft always avoided cloud when performing a sounding. The degree to which such soundings represent an area average must be affected by fractional cloud cover and the horizontal variations in properties discussed later in this paper.

(b) Horizontal Structure

The cloud fields observed often exhibited patchiness on a scale of 20 to 50 km and corresponding meso-scale variations in temperature and humidity were detected in the horizontal runs, notwithstanding the choice of an experimental site over extensive, level plains.

If we define horizontal coordinates x and y, respectively parallel to the east and north directions, then we can show that

$${}_x\left(\frac{d\theta_v}{dt}\right)_H - \left(\frac{d\theta_v}{dt}\right)_S = U\frac{\partial\theta_v}{\partial x} , \qquad (3)$$

where t is time and U is aircraft speed along x. The suffix S denotes a derivative calculated from successive soundings in a given air-position and H refers to horizontal runs in the direction denoted by the accompanying suffix. Similar equations hold for other variables and directions.

The values of $|\partial\theta_v/\partial x|$ or $|\partial\theta_v/\partial y|$ encountered in this expedition reached $4 \times 10^{-2}\ K\ km^{-1}$, with a mean value of about $6 \times 10^{-3}\ K\ km^{-1}$. Values for $|\partial q/\partial x|$ or $|\partial q/\partial y|$ averaged about $10^{-2}\ g\ kg^{-1}\ km^{-1}$ and reached $5 \times 10^{-2}\ g\ kg\ km^{-1}$. These gradients have been calculated by fitting a straight line to the data from each run, e.g. as shown in Fig. 3, to determine ${}_x(d\theta_v/dt)_H$ etc. It must be pointed out however that these estimates of gradients sometimes do not faithfully represent the data; sharp, step-like changes in properties

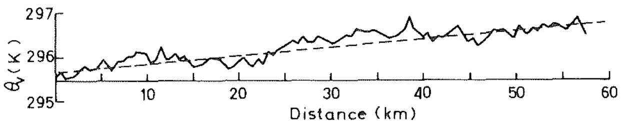

Fig. 3 - Horizontal run in convection layer showing horizontal gradient of θ_v.

are often observed - e.g. as shown in Fig. 4, where the change commences at about 35 km on the x-axis. Such sharp changes in properties in the upper part of the sub-cloud layer are often associated with the transition from cloudy to clear regions with clouds preferentially above the areas of higher q-values.

Clearly, spatial as well as temporal gradients must be taken into account in the analysis of the properties of a sub-cloud layer with this order of meso-scale variability.

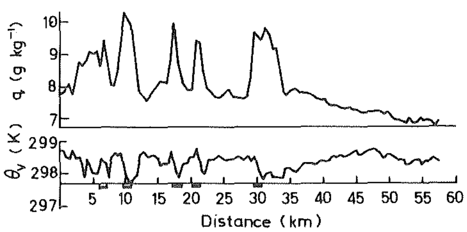

Fig. 4 - Typical run about 70 m below cloud base. Note coincidences of θ_v-minima, q-maxima and positions of clouds shown by bars below distance axis. Date and time: 16/4/75, 12-05 hrs.

5. CLOUD-SCALE STRUCTURE OF THE SUB-CLOUD LAYER

We shall now consider the fluctuations from the mean properties of the sub-cloud layer on scales roughly in the range 0.5 to 5 km. This range embraces the horizontal dimensions of the fair-weather cumulus clouds observed.

(a) Change of Scale with Height

Records of such quantities as potential temperature θ, θ_v and q made in horizontal runs suggest that there is a marked change in scale size when we proceed from the well-mixed convection layer into the stable layer above; Figs. 3 and 4 are cited as examples. In Figs. 5 and 6 respectively, spectra of θ and q calculated from several horizontal runs at each value of normalized height ζ are shown. These spectra have been obtained from the residual fluctuations from a straight line fitted to the data of each run, as described in Section 4(b) and illustrated in Fig. 3. By this means the non-stationarity of each series is reduced; the spectral density estimates have then been normalized by the series variance before averaging over the number of runs indicated in brackets in the figures.

There is, of course, considerable evidence that important contributions to the total variance of temperature and humidity in the convection layer occur at frequencies above the resolution limit of the instruments used in this work (e.g. Coulman, 1969; Warner and Telford, 1967). Nevertheless, Figs. 5 and 6 show a clear shift of the peak values in the spectra towards the well resolved lower frequencies when we compare the results for $\zeta > 1$ with those for $\zeta < 1$. This change of scale is apparent in spectra taken throughout the period of the day encompassed by the present investigation but insufficient data have been analysed as yet to determine whether or not there is any quantitative dependence of the change of scale on time of day or state of development of a cloud field.

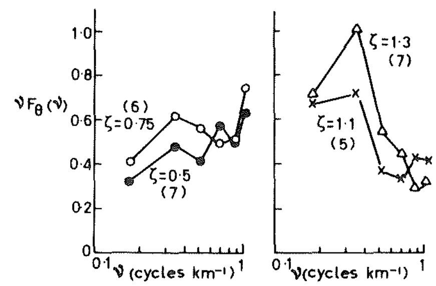

Fig. 5 - Spectra of θ-fluctuations show shift to lower frequencies above the convection layer ($\zeta > 1$) when compared with spectra in that layer ($\zeta < 1$). Spectra are normalized by variance and averaged over number of runs shown in brackets.

Grant (1965) observed moist patches of air from 1 to 3 km in horizontal extent in a sub-cloud layer and radar observations (e.g. Konrad, 1970) have also suggested structure in the temperature and humidity fields on kilometre scales.

Before discussing the significance of this change of scale with height it is desirable to examine some thermodynamic properties of the parcels of air concerned.

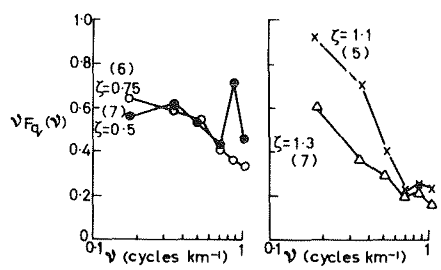

Fig. 6 - Spectra of q-fluctuations show shift to lower frequencies above the convection layer ($\zeta > 1$) when compared with spectra in that layer ($\zeta < 1$). Spectra are normalized by variance and averaged over number of runs shown in brackets.

(b) Correlation between Density, Temperature and Humidity Fluctuations

It is of interest to examine the relative contributions of temperature and humidity to the fluctuations of density observed in horizontal traverses at various heights in the sub-cloud layer.

We have calculated the correlation coefficient $b(\theta',q')$ for the residual fluctuations of θ and q from the straight line fitted to the data from each horizontal run as described in Section 4.

It appears in Fig. 7 that there is a strong negative correlation in the region of the sub-cloud layer between the top of the convection layer and cloud base $\zeta > 1.0$, a weaker negative correlation in the upper part of the convection layer $0.5 < \zeta < 1.0$, and a positive correlation in the lower region $\zeta < 0.5$.

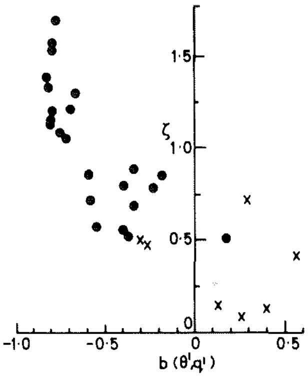

Fig. 7 - Correlation between θ- and q-fluctuations changes sign as ζ increases. x denotes use of 10 Hz sensors; • refers to sensors described in Section 2.

The correlation coefficients for θ_v and q in the region $\zeta > 1.0$ are also always negative and of slightly smaller magnitude than the corresponding $b(\theta',q')$; thus the denser parcels of air are cooler and moister than their neighbouring environment. Deardorff (1974) obtained negative values of $b(\theta_v',q')$ in the upper part of the convection layer he modelled.

These correlations refer, or course, to fluctuations which are resolvable with the present instruments. The points denoted by crosses in Fig. 7 have been calculated from data drawn from another expedition to the same site when faster response instruments, capable of resolving structure at frequencies up to 100 cycle km^{-1}, were used. These also show positive correlation coefficients in the lower part of the convection layer where small-scale fluctuations predominate.

The values of the θ_v-minima, or maximum-density parcels, in Fig. 4 may be compared with the expected values of θ_v in the convection layer $\zeta \leqslant 1.0$ after correction for the temporal and spatial gradients mentioned in Section 4. For this run these θ_v-minima in the first 35 km of the run exceed the value of θ_v in the convection layer by 0.3 to 0.5 K. In some other runs this difference is even smaller; however, it is doubtful whether differences of less than 0.2 K can be confidently detected in view of the corrections mentioned above.

Thus we can identify parcels of air having density very closely similar to that of the convection layer in the region between the average top of the convection layer and cloud base; this is a region which on average is stably stratified according to the soundings. Moreover, the scale of these relatively cool, moist, dense parcels is a kilometre or more. This evidence tends to support the speculation of Section 4(a) that local modification of the stratification below cloud base level occurs through penetration by successive elements from the convection layer. It is worth noting the location of clouds in Fig. 4 in relation to the θ_v-minima and q-maxima; this is characteristic of many of the horizontal runs.

(c) Lifting Condensation Level of Sub-Cloud Air

The correspondence between certain fluctuations in the sub-cloud layer properties and the existence of clouds has already been pointed out in Fig. 4; in Fig. 8 z_a the lifting condensation levels for the samples at each of the data points of the same horizontal run have been plotted against distance, together with indications of the location of cumulus clouds. The upward-facing cloud detector responds instantaneously to the edge of a cloud overhead. There is however an interval of 8 s between successive samples of any particular variable, such as temperature, which is being recorded. The detection of cloud relative to records of θ_v, q etc. therefore has a biased uncertainty of from zero to 8 s in time or 0.5 km in space.

The average height $\bar{z}$ of the run concerned in Fig. 8 was 1.077±0.015 km and the average height of cloud base observed was z_b = 1.150±0.030 km. The variations in z_a are much larger than those of either $\bar{z}$ or z_b and we take z_a/z_b as a convenient normalized measure of z_a-variation which may be used to compare the results of different runs.

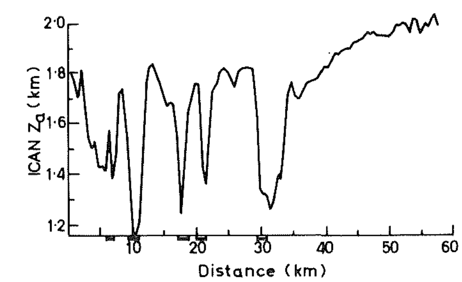

Fig. 8 - Minima in lifting condensation level z_a coincide with occurrence of clouds, denoted by bars below distance axis. Date and time: 16/4/75, 12-05 hrs.

In Fig. 9 values of z_a/z_b have been calculated from three different sources of data, namely the z_a-values under detected clouds, the z_a-values averaged over each run and the z_a-values from soundings; they are plotted against $\bar{z}/z_b$, the normalized average run height. Data from four days' observations are shown in Fig. 9.

As previously found by Warner (1963), air from near the surface, $\bar{z}/z_b \leqslant 1$, would exhibit condensation at or below observed cloud base if lifted adiabatically. The average properties of air in much of the sub-cloud layer however would require a parcel having those properties to be lifted to heights in excess of observed cloud base to form condensate. Air immediately beneath detected clouds has a normalized condensation level very close to 1.0 because as previously noted its properties are closely similar to those of the convection layer.

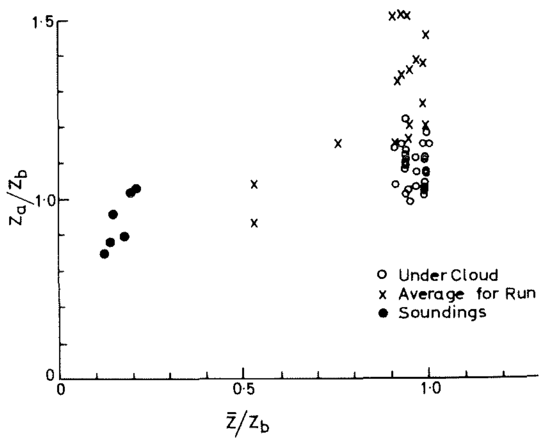

Fig. 9 - Air beneath detected clouds has lifting condensation level z_a close to observed cloud base height z_b, but average lifting condensation level is much higher.

It should be remarked that the possible uncertainty in the values of z_a/z_b is about ±0.03 for values of z_a and z_b of the order of 1 to 2 km. The lifting condensation level can be calculated to about ±0.010 km when wet- and dry-bulb temperatures are known to ±0.05 C but estimation of cloud base is subject to error of the order of 0.030 km.

6. SUMMARY

These observations suggest that on a horizontal scale of 20 to 50 km and in fair weather the subcloud layer consists of a well-mixed convection layer surmounted by a stably stratified region in which cumulus clouds form. However, meso-scale variations in properties are often sufficiently large to cause cloud formation to be patchy on the scale of 20 km or more. On horizontal scales of the order of cumulus cloud dimensions (0.5 to 5 km) the processes of downward entrainment and upward penetration at the top of the convection layer appear to lead to the formation of regions of air having properties very close to those of the convection layer itself. In such regions it can almost be said that the convection layer "extends" right up to cumulus cloud-base.

This result can be expected to influence the scale and properties allocated to the initiating impulse in cumulus cloud models. It is not implied however that an upward flux of heat and moisture, continuous throughout the day, exists in these regions where air from the convection layer appears to have successfully penetrated the stable layer.

Further analysis of the data is needed before the time dependence of these phenomena is elucidated and possible effects of the cumulus clouds themselves on the dynamics of the subcloud layer can be confirmed.

REFERENCES

Betts, A.K., 1973. Quart. J. R. Meteorol. Soc., 99, 178.
Coulman, C.E., 1969. Solar Phys., 7, 122.
Deardorff, J.W., 1974. Boundary Layer Meteor., 7, 81.
Grant, D.R., 1965. Quart. J. R. Meteorol. Soc., 91, 268.
Konrad, T.G., 1970. J. Atmos. Sci., 27, 1138.
Warner, J., 1963. J. Atmos. Sci., 20, 546.
Warner, J., and J.W. Telford, 1967. J. Atmos. Sci., 24, 374.

4.1.2

EFFECTS OF A LARGE CITY UPON CONVECTIVE CLOUDS AND COALESCENCE RAIN

Roscoe R. Braham, Jr.

and

Maureen Dungey

University of Chicago
Chicago, Illinois

1. INTRODUCTION

This report is part of Project METROMEX, a research effort studying the influence of a large metropolitan area, St. Louis, Mo., on the physics and dynamics of clouds. The University of Chicago involvement in METROMEX has been mainly along two lines -- radar mapping of precipitation and cloud microphysical studies based upon data from our cloud physics airplane. Our group was based at Greenville, Ill., about 70 km northeast of St. Louis.

This paper is concerned mainly with findings from our 3-cm TPS-10 radar. This radar was operated on 152 days of convective clouds in June, July, August 1971, 72, 73, 74, and 75. Operations typically began about 0900 LDT and continued through the day until any precipitation echoes had decayed or moved beyond radar range. The radar was calibrated daily to give a minimum detectable equivalent reflectivity factor of 4 dbz at 16 km increasing to 20 dbz at 97 km, the maximum range normally used for data collection. The TPS-10 antenna rotates in azimuth 360 deg in 3 minutes while scanning vertically once every 2 deg of azimuth. Data were recorded via scope photography.

Two types of radar observations are discussed in this paper -- radar first echoes and echoes of maximum height.

2. FIRST ECHO ANALYSES

2.1 Definition of First Echoes

A radar first echo (FE) is defined as the first observed radar signal from a volume of cloudy air which had not previously produced an echo. A reflectivity threshold of about 10 dbz is usually implied since observations of FE's have been most useful in studies of precipitation initiation. To be a valid FE, the "new" FE is required to be separated from existing echoes sufficiently to rule out a mere expansion of an existing echo.

In the summer in midwestern U.S. most FE's originate either as shafts of rain inside developing cumuli or from melting snow streamers in stratified clouds. In METROMEX, we endeavor to restrict analyses to FE's of the first type since we anticipate urban effects to be most noticeable in convective clouds having their roots within the boundary layer.

2.2 First Echo Data Reduction

The characteristics and locations of 4553 FE's have been determined from a frame by frame examination of the data film from 304 hours on 82 days distributed through the summers of 1972 through 1975. Since an effort was made to identify all FE's that developed within the radar range, 10 to 60 statute miles (16 - 97 km), this data set is considered to represent a 100% sample of all FE's within the radar area during the 304 hours. Because of the uncertainty of FE evaluation when many large echoes are present, our data tend to be biased toward the early part of convective days and towards days of isolated rain showers.

The day-to-day variation in the locations of convective clouds is another factor that must be considered in FE analysis. It is well-known that convective showers seldom, if ever, are randomly scattered. Instead, there is a marked tendency for them to occur in lines or clusters associated with mesoscale meteorological structures.

Thus, we tend to find FE's grouped in different parts of the radar area on different days. In studies seeking to isolate FE characteristics that may be associated with some specific area, such as a terrain feature or large city, we need a large sample of days to reduce the effects of sample variability.

2.3 First Echo Characteristics

Sample means for the entire data set of 4553 FE's are as follows:

FE	Base	Top
Height	2350 m	4570 m
Temperature	11.0 C	-2.1 C

Only 5 percent of the FE's were entirely colder than 0C, 50 percent straddled the freezing level and the remaining 45 percent, were entirely warmer than 0C. These data verify previous studies showing that summer FE in this area originate almost entirely through coalescence. Only about one-third of the FE's grew as much as 2000 ft (600 m) in the three minutes following detection. The average top and base characteristics of the FE that grew 600 m or more are fairly similar to those that decline in height continuously following detection. The data show large daily variability in FE heights (temperatures) probably associated with regional meteorological conditions.

2.4 First Echo Location

Figure 1 is a map of the frequency of FE formation within a radius of 97 km of Greenville, Illinois, an area which includes St. Louis and its normal summer downwind. Units are FE/100 mi^2 (FE/259 km^2) summed over the 304 hours of data. St. Louis can be identified as the region near the confluence of the Mississippi, Illinois, and Missouri Rivers along the west side of the map. Attention also is called to the Alton industrial complex on the east bank of the Mississippi River north of St. Louis, and the East St. Louis and Granite City industrial areas on the east bank directly opposite St. Louis.

A uniform distribution of FE's on Fig. 1 would give 41.4 FE/100 mi^2. Obviously the distribution is far from uniform -- the area over and east of St. Louis has values up to 2.4 times the map average. One also notes a tendency for circular symmetry with lower values near and at greatest range from the radar. This suggests two superimposed effects, one associated with the city and/or terrain around the city, and the second associated with a range-dependent radar sensitivity for FE detection. We have experimented with methods for reducing the radar range effect through range normalization techniques, but because of space limitations only the original, non-normalized data are shown here.

We note on Fig. 1 that there are three areas of maximum FE frequencies. Over the city and elongated toward the northeast is a ridge of high

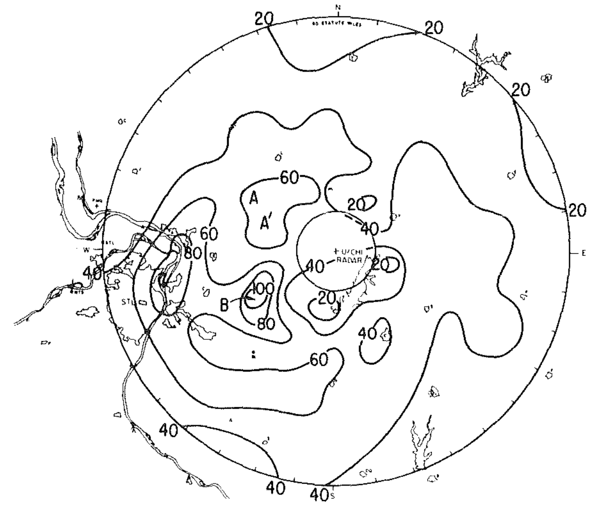

Figure 1. First Echo frequency per 100 mi^2 for 1972-3-4-5. Sample total: 4553 FE's. Map average: 41.4 FE/100 mi^2.

FE frequencies having a point maximum of 90FE/100 mi^2 (2.2 times map average) at point C on the map. About 40 km east-northeast of the Alton industrial area is another broad maximum (A) with a maximum point frequency of 77FE/100 mi^2. About 30 km directly east of downtown St. Louis and the East St. Louis and Granite City industrial areas is the third area with a maximum of 101FE/100 mi^2 (B). It is consistent with our knowledge of urban meteorology to associate the maximum over the city with effects of the urban heat island and release of water vapor. Perhaps areas A and B are associated with microphysical effects arising from anthropogenic particles. However, we must look further to see whether the data are internally consistent with such an interpretation. The major analytic tool is data partitioning on relevant meteorological parameters and on weekend-weekday occurrence. This latter partitioning is based upon the hope that man's activities in the city may differ enough from weekdays to weekends to modulate the data.

Data partitioning on wind direction has been regarded as one of the critical tests of whether observed meteorological conditions may have been influenced by the presence of the city. Partitioning on boundary layer transport winds has not been completed. Partioning on FE movement, which may indicate cloud steering winds, has been completed. The data allow five mutually exclusive partitions involving FE vectors between 131 and 360 deg. The remaining data are scattered through days with echo movements between 024 and 120 deg, and are not used in this partitioning.

Cloud Steering Winds	Days	FE
1. 131-184 deg	7	667
2. 202-249	13	816
3. 250-269	16	954
4. 270-304	22	962
5. 312-360	18	860

Partition 1 is informative because its echo movements are such as to eliminate any simple advective contribution of urban effects to areas A and B. In this parition, area A is reduced in size but clearly present with a point maximum of 3 times map average at point A' (Fig. 1). Area B is decreased in size and intensity with a maximum barely twice map average. Although the numbers of days and FE's are rather small, partition 1 clearly shows that the local maxima in areas A and B cannot be due only to an urban effect.

The maximum over the city in partition 1 is similar to that in Fig. 1, an elongated N-S ridge extending from south of St. Louis to north of Alton.

The map for partition 2 (202-249 deg), and the outer boundaries of the urban plume based upon these directions, are shown in Fig. 2. We note that the ridge of high FE frequencies, oriented with the wind, is clearly shown over the city. Area A is only vaguely indicated, but area B is clearly shown with a maximum of 2.6 times map average at point B'. The other features attracting attention are the broad area of above average FE frequencies southeast of St. Louis and the small intense maximum east of the Greenville radar. The latter is directly off the end of a large, shallow lake whose long dimension parallels the median wind in this partition. This local maximum evidently arose from local increases in moisture following evaporation from Lake Carlyle.

The results of all five echo movement partitions are summarized in Fig. 3. The peak value of each area of FE maxima is plotted in units of map average. (This is done to normalize the differing sample sizes.) The arrow accompanying each plotted value is the inverse median echo movement vector for the partition involved. These arrows point toward possible source regions for the areas of maxima. A distinct pattern emerges. All five partitions show a maximum somewhere over the St. Louis-Alton complex.

Area B shows point values more than twice map average on 4 of 5 of the partitions. Except for the 2.1 value associated with SSE winds, we note an orderly movement of the location of the

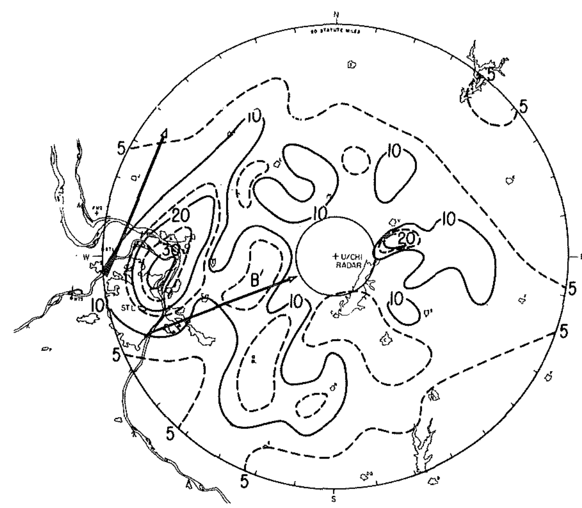

Figure 2. Partition 2 on cloud steering winds 202-249 deg. Units as in Fig. 1.

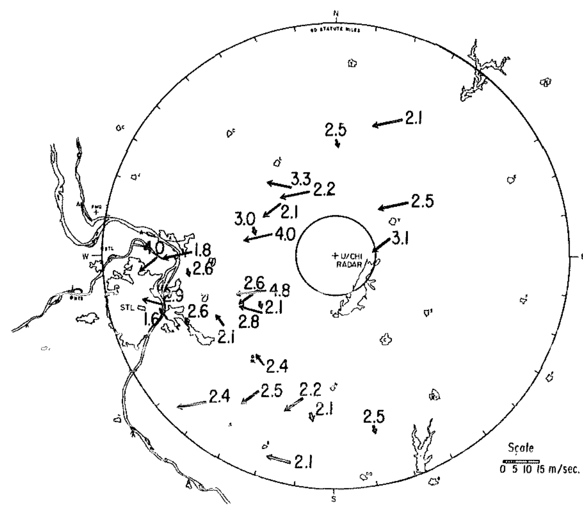

Figure 3. See text for explanation, especially noting that the arrows point toward possible source regions for the areas of maxima -- the solid arrows may be seen to point toward St. Louis.

maximum consistent with a source over the city. The evidence is less conclusive for area A. Although it is clearly present on 4 of the 5 partitions, only two of them suggest a source in the Alton industrial complex. The other two seem to preclude an involvement of the St. Louis metropolitan area. The other areas of FE maxima on Fig. 3 appear at different locations on different partitions and may be interpreted as due to sampling variations.

The weekday-weekend partitioning gives two mutually exclusive subsets: 3399 FE on 57 weekdays, and 1154 FE on 25 weekend days and holidays. When mapped, both show enhanced FE frequencies over the metropolitan area and in the areas identified as A and B on Fig. 1.

3. MAXIMUM HEIGHT ECHOES

In a followup to the Illinois State Water Survey studies indicating above-average frequency of thunderstorms east and northeast of St. Louis, we have used our radar data to study the heights and locations of the tallest echoes present within the radar area on 139 days for which convective echo data are available. We have studied (1) the height and location of the tallest echo on each day, and (2) the height and location of the tallest echo present at each half hour during the radar observations periods. The latter, half-hourly maximum echo events, are called "Hi-Cu." These analyses are restricted to radar ranges of 20 to 60 mi (32-97 km) because of the inability of the radar to adequately sample echoes with tops over 40,000 ft (12 km) inside of 20 mi (32 km). The frequency distribution of top heights of the tallest echoes on each day is shown in Fig. 4a. We note that about half of the summer rainy days at St. Louis produced echoes with tops exceeding 42000 ft (12.8 km), the average tropopause height for this area.

Extending the analysis to include an observation at every half-hour gave data plotted in Fig. 4b. Again we see the peak in frequency corresponding to the tropopause height. For our present concerns, the peak at about 22,000 ft (6.7 km) is more interesting. About half of this mode comes from echoes early in the day on days which ultimately produce storms reaching the tropopause. The other half comes from days on which a mid-troposphere stable layer restricts cloud development all through the day.

The small number of Hi-Cu events makes it necessary to employ different techniques than were used in FE analyses for incorporating day-to-day differences in wind direction into the analysis of urban effect. In one approach to this matter we defined a generalized city area which includes the city of St. Louis, its suburbs and the industrial areas along the Mississippi River. The FE movement vector for each day was used to locate regions that would be 1, 2, and 3 hours of echo movement downwind from the city. The Hi-Cu events then were identified as occurring in one of these areas or in the remainder of the radar areas, which we called the Rural area. Area-weighted relative frequency of Hi-Cu in each of these five areas is given in the following table. The downwind shift and decreasing magnitude of Hi-Cu frequency with increasing wind speed is consistent with an urban effect.

FE Speed	City	Downwind Area (hrs FE travel) 1	2	3	Rural
< 3 mps	2.30				1.00
3 - 9.9	1.45	1.48	1.27	0.95	1.00
> 10 mps	0.76	1.31	1.27	1.25	1.00

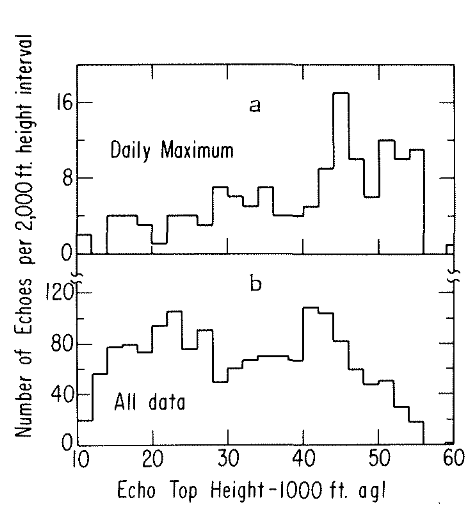

Figure 4. The frequency distribution of top heights a) of the tallest echoes on each day; b) of all observations.

4. SUMMARY

The first echo data show that cumulus clouds near St. Louis in summer initiate precipitation preferentially through the coalescence mechanism. Three favored areas of FE development have been identified: one is over the metropolitan urban-industrial area; another occurs about 30 km east of downtown St. Louis; and the third is about 40 km NE of the Alton industrial complex.

The results of partitioning on weekend-weekday occurrence and on direction of FE movement, seem to suggest that FE enhancement in these areas is due to a combination of urban effects and natural factors which have not yet been identified. The observation of a region of FE enhancement downwind of Lake Carlyle indicates the sensitivity of the atmosphere to local terrain features which can focus or trigger precipitation development, and to the power of radar FE analysis for identifying these areas.

The frequency of tallest echoes is higher over and downwind of St. Louis than it is in the remainder of the radar area. To what extent this is an urban effect, or due to inadequate sample, is not yet clear. The bimodal distribution of echo top heights may give an important clue as to how urban areas increase rain and thunderstorms. The urban heat island could give clouds a slight additional impetus enabling them to overcome a mid-level stable layer and to continue to grow into tropopause-reaching storms.

5. ACKNOWLEDGEMENTS

University of Chicago participation in METROMEX has been supported by the Weather Modification Program, RANN, National Science Foundation, under grants GI 33373 and AEN72-03399.

PHYSICAL STRUCTURE OF CONVECTIVE CLOUDS AND THEIR INFLUENCE ON METEOROLOGICAL FIELDS

I.P.Mazin, S.M.Shmeter

Central Aerological Observatory, Moscow Region, USSR

1. INTRODUCTION

The structure of continental cumulus clouds of temperate latitudes is investigated considerably worse than that of maritime tropical ones. The aim of the present paper is to describe the results of analyses of the experimental data and to fill up partly the existing gap.

The research flights were carried out by IL-14 aircraft in the Ukraine region in summer periods of 1971-1974. The table 1 showes the main parameters measured during the flights.

Table 1

parameter	measurement range	mean square error of measurement	instrument averaging scale (m)
vertical air speed pulsations W	±15 m/s	0.8-1.0 m/s	20
pulsations V' of air velocity in the direction of flight */	±10m/s	0.2 m/s	10
temperature pulsations T	±4°C	0.06°C	5-10
coefficient of visible light attenuation	25-250km^{-1}	20%	10
large particles size distribution	R > 75μm N > 1 m^{-3}	10%	50-100
air humidity */	30-100%	5%	200-300

*/ in clear sky only

Measurements were carried out on the horizontal levels under constant speed inside of them. The experimental data are divided into 3 groups according the cloud thickness H=0.5 - 1 km, H=1-2 km and H=2-3 km. We can consider the 1st group as Cu hum group 2 as Cu med and group 3 - as Cu cong.

In individual penetrations of clouds values of W, V' and T' varied within wide limits even being averaged at distance of 0.1-0.2D (D-cloud diameter), that means usually some hundreds of meters. In spite of such variations some hundreds measurements give the objective features of clouds which are discussed below.

2. VERTICAL VELOCITIES (W)

Vertical velocities in Cu were measured only in 1973 and 1974, i.e. the bank of information about W was half that one of V' and T'. Nevertheless, the results obtained are of considerable interest.

In the central (0.6D wide) part of the horizontal cross-section of Cu hum and Cu med averaged updraft velocities (AUV) are maximum as a rule in the middle or in the lower third part of a cloud (see Fig. 1) where they reach 1.5-2 m/s. In the upper part of a cloud ($z/H > 0.9$) updrafts are replaced by downdrafts. The less the humidity in the vicinity of a cloud, the lower the AUV maximum. In total air rose in the lower two thirds of a cloud in 82% of cases and in the upper one third - in 62%.

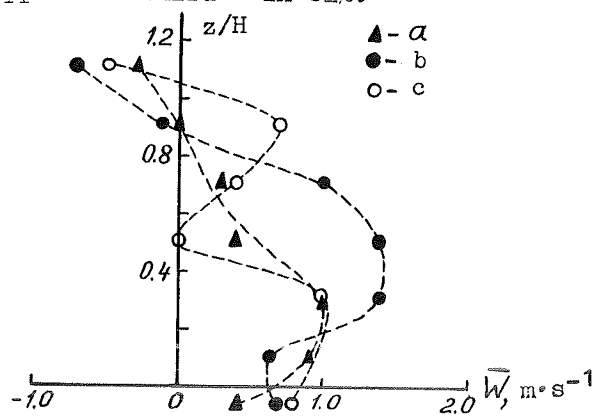

Fig. 1. Vertical profiles of $\overline{W}$ inside of central part of cloud.
a. Cu hum and Cu med, 1973, n=143
b. Cu hum and Cu med, 1974, n=194
c. Cu Cong 1973, n = 56
H - cloud thickness,
Z - height over the cloud base.

Vertical profiles $\overline{W} = f(Z/H)$, and consequently the value of $\partial W/\partial z$ near the vertical boundaries of the cloud differ greatly from profiles W near the cloud axis. The AUV profile in Cu cong is of a double-humped shape with maximums situated in the lower and upper thirds of the cloud. Possibly it indicates the double-layer convection in Cu cong. As a number of measurements in Cu cong was comparatively small (34 penetrations) the further accumulation of information is required to support this hypothesis. The presence of two layers of convection in Cu Cong was also fixed in GATE area (Borovikov et al., 1975).

The variability of W in Cu is rather large: the standard deviation σ_W is of 1.3-1.8 m/s inside the Cu and of 0.6-0.9 m/s - outside. Averaged at the distance 20-30 m the maximum updraft velocities may reach 8-10 m/s.

Close to Cu and just above its top the air usually subsides. The width of downdrafts zone close to the Cu was not less than 0.6D in width in 81% of cases.

3. PULSATIONS OF HORIZONTAL COMPONENT (IN THE DIRECTION OF FLIGHT) OF WIND VELOCITY V' NEAR THE CU.

Near the vertical boundaries of Cu the value $\sigma_{V'} \approx 1$ m/s and maximum individual values V' reach several m/s. Values $\overline{V'}$ with scale of averaging equal to D/5 diminish rather slowly as moving away from the cloud and they are close to 0 at the distance of 1-2D from Cu. It is seen from Fig. 2, that in 1971, 1972 and 1974 the air in average flowes out of the cloud with the velocity of some tenths of m/s through the vertical sides of lower 2/3 of Cu. At upper one third part of Cu the air flowes into the cloud.

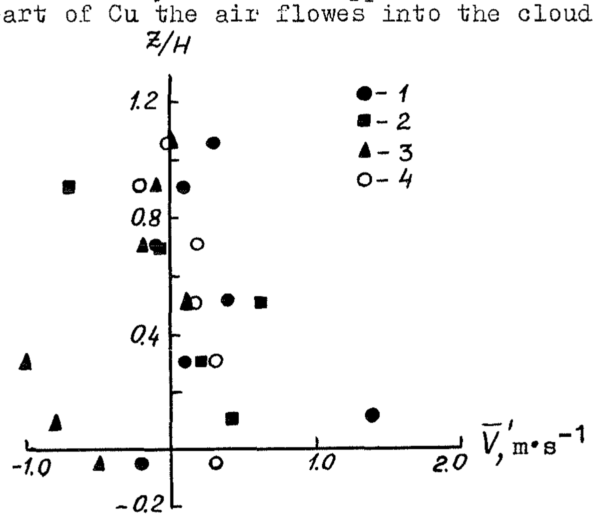

Fig. 2. The values of $\overline{V'}$ averaged over the distance of 0.2D close to the vertical boundary of Cu outside of it.
1. 1971, n=97; 2. 1972, n=33;
3. 1973, n=167; 4. 1974, n=125;

The vertical profile of $\overline{V'}(Z)$ obtained during the measurements in 1973 has another structure. The reason of such a difference demands special analysis and consideration. We shall point out to the fact that in 1973 air humidity in the convection layer was 15-20% less than that during all other periodes of measurements.

In the majority of cases there was air inflow below the cloud and air outflow over it.

It should be mentioned that the measured vertical profiles $\overline{V'}(Z/H)$ quite conform to values $\partial W/\partial z$ near the cloud boundary.
The obtained information does not support the hypothesis of the predominant role of regular entrainment into Cu. Possibly, the main contribution to the entrainment is made by the horizontal turbulent diffusion. The large values of short-period wind pulsations near the vertical boundaries of Cu supports this opinion.

4. TEMPERATURE PERTURBATIONS (TP)
Temperature perturbations are particularly high in clouds, where they can reach +2° and -3°C. In the majority of cases TP in Cu hum is equal to 0.0 ±0.2°C, in Cu med - to -0.1 ±0.3°C, in Cu cong - to -0.4 ±0.3°C.

Virtual temperature pulsations, in the lower two thirds of Cu with correction on weight of cloud water, are usually positive and rarely exceed 0.4-0.6°C. In the upper one third of Cu hum they are negative in 60% cases. Almost the same proportions take place for Cu med. The virtual temperature pulsations in Cu Cong are negative, reaching as a rule -1.5°C in the upper part of a cloud.

It probably indicates the fact that Cu cong were penetrated at the end of mature stage or in stage of dissipation.

Just below the cloud TP are usually negative and equal to -0.3 ± 0.2°C. TP were above zero only in 10% of cases and reached 0.3-0.5°C. The temperature depression lowered under the cloud and $T' \approx 0$ 150-200 m below it base. It mean that the thermals pass the upper part of the layer between the surface and the cloud in stable stratified due to its own momentum being colder then environment air.

T' are negative as a rule, in the layer of 30-40m thick over the cloud, and they are positive higher, at least up to 150m above Cu. Probably air cooling at the top due to evaporation of cloud droplets prevails over the dynamic heating caused by air descending. Higher the picture is vice-versa.

Close to the vertical sides of Cu air temperature is several tenth of a degree lower then temperature of undisturbed air in 75-80% cases. In the direction from the Cu base to the top temperature depression lowers and particularly quickly close to Cu cong. In horizontal direction outside of the cloud the temperature deviations drop to zero at the distance of 0.4-0.6D and then $\bar{T}' \geqslant 0°C$. The reason for the temperature lowering is evaporation of the droplets. The lower is the humidity near the cloud, the lower the temperature.
In average air heating caused by downdrafts compensates the cooling effect at the distance of more than 0.4-0.6D from Cu. Due to the asymmetry of physical processes in the Cu environment, $\bar{T}'$ field characteristics of different sides of the cloud are different and the "cold shirt" round Cu does not necessarily surround the whole cloud.

At the distance of more than 0.6-0.8D from the cloud $\bar{T}' \geqslant 0$ and the most part of the near-cloud environment is warmer than the undisturbed atmosphere, i.e. Cu convection in total heates the convective layer.

5. SOME MICROSTRUCTURAL CHARACTERISTICS OF CU.

The spatial distribution of the coefficient of visible light attenuation γ was investigated much better then other cloud parameters. γ is connected with density of cloud drop size-distribution $n(r,x,y,z,t)$ with relation:

$$\gamma(r,x,y,z,t)=\int_0^\infty \pi r^2 K(\rho)\, n(r,x,y,z,t)\, dr$$

where $\rho=\frac{2\pi r}{\lambda}$ and λ is the wave length. In Cu the drops with radii from 2-3 to 20-30 μm make the main contribution to γ. At $\lambda \approx 0.6\,\mu$m, ρ is greater than 30, and $K(\rho) \approx 2$.
In Cu γ changes within wide limits. Practically there is always a chance to meet sections with $\gamma < 25$ km^{-1} and with $\gamma > 250$ km^{-1} (in such cases meteorological range of visibility $S_m=\frac{3.5}{\bar{\gamma}}$ is less than 14 m.
The curve of the cumulative frequency of γ based on the data of 914 Cu crossings is given in Fig. 3. The average $\bar{\gamma}$ grows from 70-80 km^{-1} to 100-110 km^{-1} with the increasing of cloud thickness H from 0.5 to 1.5 km and then up to H=2.5 km does not almost change and increases again up to $1.3 \cdot 10^2$ km^{-1} with increasing of H up to 3.5 km.

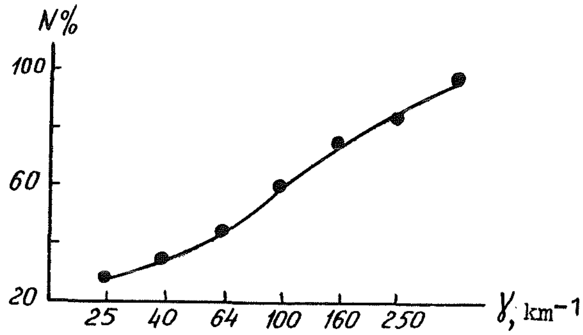

Fig. 3. Cumulative frequency of the coefficient of visible light attenuation in Cu clouds (1973-74)

The averaged vertical profile $\bar{\gamma}(z)$ is of interest. In Cu hum $\bar{\gamma}$ sharply grows up to approximately 1.10^2km^{-1} in the 100-200 m lower layer and it drops more sharply in the uppest layer. Maximum is expressed rather weakly. In Cu med 1.5-2 km thick the process is almost the same, γ reaches $(1.1-1.2) \cdot 10^2$km^{-1}, though at the middle of the upper half of the cloud there is the weak minimum, i.e. curve $\bar{\gamma}(z)$ has a double-humped shape. In more thick clouds (H > 2 km) profile $\bar{\gamma}(z)$ has a pronounced double-humped character with $\bar{\gamma}_{min} \approx (0.8-0.9) \cdot 10^2$ km^{-1} at the height of 1.5-2 km and approximately the same maximums equal to $\bar{\gamma}_{max} \approx 1.2 \cdot 10^2$km^{-1}. It is possible that later the marked minimum of optical density of cloud becomes deeper as a result and the cloud decomposes into two vertically parts due to the process of dissipation.

The scales of correlation of γ in Cu clouds is less than 50 m in 50% cases and more than 400 m in 8% cases.

According to our data the main features of liquid water content (LWC) and spatial distributions are close to each other. But the absence of continuous LWC registration, i.e. discreteness of its information together with large spatial variability of LWC, sometimes led to noticeable differences of LWC and $\bar{\gamma}$ profiles.

The double-humptiness of vertical distribution was ordinally observed not only for γ and LWC curves but also for super-large cloud drop (R > 75μm) concentration.

As a whole, the concentration of these drops changes in average from units in m^3 for clouds with H < 1 km to hundreds in m^3 at H > 2 km.

5. COMMENTS.

The analysis of the obtained results

gives the possibility to imagine the possible Cu cloud formation process.

In the boundary layer up to the height of 0.5-1.0 km before midday time the lapse rate is larger then dry adiabatic one and as a result the first(the lowest)layer of dry convection appears. The dew-point level is 0.5-1.0 km higher than this layer. The thermals being conceived at the ground surface and overheated primarily in relation to the surrounding air accumulate kinetic energy in the layer of instability, that allow them to rise higher than the instability layer due to its own momentum overcoming negative buoyancy. If stratification over the level of condensation is moist-labile the second (now moist-labile) layer of convection appears. Termals of sufficient energy reaching the condensation level enter the second layer of convection forming Cu. As moist-labile layer is usually 1-2 km thick Cu hum and Cu med appear in this layer.

If the second moist-labile layer appears 0.5-1 km higher than the first one the third layer of convection appears. Cloud tops reaching this layer get an additional impulse to development. That is how Cu Cong clouds with two-layers of convection may be formed (see also Borovikov et al., 1975).

In conclusion we underline that the existence of one or two layers of convection in Cu clouds may be seen from in the structure of vertical and horisontal air motions, and their microphysical structure.

REFERENCES

Borovikov A.M., Mazin I.P., Melcnichuk Yu.V., Willis P. GATE report No 14, Jan. 1975, pp. 212-215.

THE INTERACTION OF SMALL CUMULI WITH THEIR ENVIRONMENT

J. W. Telford and P. B. Wagner

Desert Research Institute
University of Nevada, Reno

1. INTRODUCTION

A previous paper by Telford (1975) examined the various mathematical and physical approaches to small convective clouds and showed that they all failed when tested against long-established observational facts. These are:

a. The cloud base of a small cumuli is remarkably constant in altitude; within a few tens of meters.

b. The liquid water content in clouds is not distinguishable between measurements in cloud centers and near their edges (Squires, 1958A, Warner, 1955).

c. The liquid water content becomes, as the height within the cloud increases above the base, a small fraction of the liquid water which would be released by expanding undiluted cloud base air.

Eddy diffusivity integrations fail to simulate these observations as they constrain, for workable grid mesh sizes, the diffusion to proceed only where there is an average concentration gradient. Thus the simulated clouds are wetter in the middle and do not show the dilution actually found from the top down. Entity models suffer similar problems (Warner, 1970, 1972, Simpson, 1971, 1972).

2. THE NEW MODEL

Telford (1975) suggests a new form for the cloud dynamics in which the mean vertical motion is very fast relative to the cloud lifetime, while mixing of dry air from above down into the cloud dominates the dynamics, and initiates the cloud decay. The cloud growth is created by the cloud buoyancy lifting the underflowing air, when any shear exists, so growth only occurs on the side where the underflowing air has passed beneath the cloud. The cloud turret is limited by an overlying inversion and immediately begins to be diluted by the dry air above. This unstable mixing then sinks dry parcels deep into the cloud until the blending with cloud air produces density changes which stop and reverse this motion. This process eventually reaches cloud base and initiates bulk instability downwards and the cloud continues to evaporate until totally gone on this side. Thus a cloud parcel grows on one side of the cloud, dwells in its embedding air mass for a period while it is being diluted from above, and then sinks back and evaporates.

The evaporating side then dilutes the underflowing airstream with dry entrained air from above the inversion brought down with the evaporating cloud and inhibits the cloud renewal growth, so the whole cloud subsides.

3. THE MEASUREMENTS

Previous measurements by Telford and Wagner (1974) are consistent with this picture. Recent analysis of three other cases has been completed by Wagner and Telford (in this volume). In this case no precise calibration of the slip and attack vanes was possible as no turns in clear air were recorded, so the question of convergence or divergence around the cloud cannot be meaningfully discussed because of uncertain accuracy. However, the drift of the cloudy outline through the embedding air at the level concerned, and the lack of air and cloudy air motion at anything like the velocity of outline drift, are well confirmed. This is consistent with the growth and decay pattern discussed above.

In addition, this data shows another vital feature expected from this model. Consistently, for the two passes in each of the three clouds studied, one side of the cloud shows a disturbed velocity pattern in all three velocity components and the other side does not. When the relative velocities in the air are considered the disturbed air is seen to be on the decaying side of the cloud. Thus, in addition to the velocity measurements, we have this solid qualitative evidence, not relying in any way on accuracy of the instrumental performance, which supports the picture of the cloud proceeding through its embedding air mass by a process of decay on one side, and so necessarily growth on the other in the undisturbed air.

4. THE MODEL

This model postulated that mixing

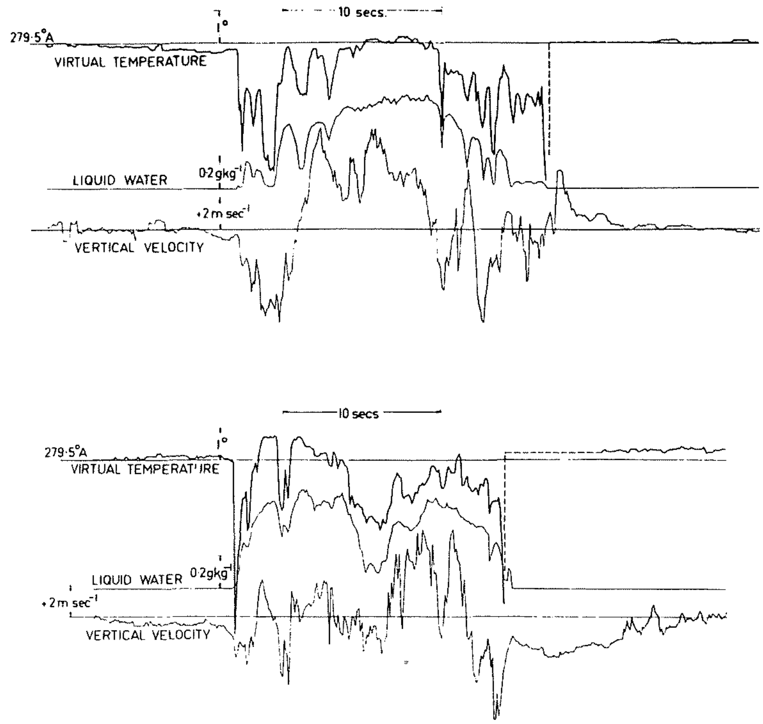

The results from two successive traverses on reciprocal tracks about 250 meters below the top of a fair weather cumulus 1.5 km deep. Note the close correlation between liquid water and virtual temperature. There is some agreement between these two quantities and vertical velocity but clearly regions of strong updraft persist when the buoyancy has become negative, and in some areas little agreement can be seen between the velocity observed at the time of measurement and the buoyancy or liquid water. As is common, the turbulent region is restricted almost entirely to the cloudy area.

Fig. 1 This is Fig. 4 from Telford and Warner, 1962.

occurred downwards from the cloud top, not by the eddy diffusivity process usually incorporated into numerical models, but by a self driven buoyancy process which produces very rapid mixing which quickly approaches buoyancy equilibrium. It must be stressed that this process is not related to the formal eddy diffusivity equation. Squires (1958B) worked out some of the details of such a process, but the details are not necessary to begin with if the process proceeds rapidly to equilibrium. Thus we postulate that the cloud quickly changes its density by mixing in of overlying air until the vertical pressure gradient in the cloud is the same as in the surrounding air.

5. SOME DATA

The density of moist air is measured by its virtual temperature if we ignore the density of the liquid water, which is relatively small. We refer to some previous measurements (Telford and Warner, 1962) in Fig. 1 which shows virtual temperature and vertical velocity towards the top of a fair weather cumulus cloud. The cloudy air shows a density mostly higher than in the surrounding air. The cloudy air of lower density is less than 1 C above the temperature of the surroundings, and air within $\pm$ 1 C of this temperature occupies more than half the cloud area. The remaining cloudy air is appreciably cooler and occurs in small irregular areas. The lack of any resemblance between the two reciprocal passes reinforces the view that the cooler denser cloud air consists of irregular regions, small relative to the cloud as a whole. The sheath of cold air on both sides of the cloud is quite small relative to the internal cold regions. The two passes suggest that statistically there is not much difference between the cloud middle and its edges, apart from the thin outside cold sheath.

However, this data also shows a noticeably greater disturbance in the vertical velocity on the same side of the cloud relative to the other on both passes and virtual temperature as well as the updraft velocity is certainly low on the disturbed decaying side in each case. We do not know how the cloud traverses were lined up with the windshear to check which side was disturbed. This data is consistent with the rapid vertical passage of small regions of cloud cooled by the mixing in of dry overlying air but is quite unrelated to a model in which smooth eddy diffusion dilutes the cloud from the outside inwards.

6. A QUANTITATIVE COMPARISON

In his discussion of models, Warner (1970) provides averages of his data for the cloud environment and the fraction of liquid water measured relative to the computed undiluted value based on no mixing after passing through cloud base. This Table 1 is reproduced here. Warner comments that the variability from one case to another showed that more stable air tended to be moister. He also comments that the

Table 1 The Environment Corresponding to Fig. 2

TABLE 2. Cloud environment parameters.

Pressure (mb)	Height (m)	Temperature (°C)	Relative humidity (%)
925	750	14	85
765	2360	3	85
725	2740	5	15
550	4910	−10	15

individual lapse rates are sensibly constant but, as we will see below small departures of less than say 0.2 C are important.

From Warner's Table 1 we obtain virtual temperatures of 15.61 C and 3.88 C respectively at 750 m and 2360 m in altitude. The virtual temperature in the overlying air at 2740 m in altitude is 5.19 C. Thus the virtual temperature excess in the overlying air is 1.31 C. In a private communication Warner gives an intermediate point as 1500 m altitude and a virtual temperature of 10.11° C. Warner (1970) uses these data to raise serious questions about the validity of entity cloud models to which Simpson (1971, 1972) has replied.

If these data are plotted, using the virtual temperature of 5.19 and -9.92 C at 2740 and 4910 m respectively, and ignoring the 1500 m point, we obtain two parallel straight lines relating virtual temperature to height below and above the inversion. To make comparisons with this model we will assume the cloud mixing is controlled by an environment whose virtual temperature matches the lower line at 750 and 2700 m. The intermediate point is at 1500 m and the discussion considers various simple curvings of the virtual temperature profile towards this point which is about 0.2 C above the linearly interpolated line.

The two lines above and below the inversion are about 4 C apart for an inversion of zero depth so the air mixed down through the cloud top will have a temperature which is certainly less than this. If the inversion transition occurred over 250 m in altitude, at the cloud top, the maximum temperature difference would be 2 C. Since we do not know how much of the lower cooler air is carried up ahead of the cloud to sheath it above, the 2 C figure is probably more realistic, and this gives almost an exact fit for the cloud liquid water. Thus we have some data with which the model can be compared. We should remain aware, however, that non-linear relationships give average results which can differ for the same average input data because the variability in the input changes the average output.

7. TESTING THE MODEL

From the input data discussed above we need to test the predicted ratio of liquid water to adiabatic liquid water, Q/Q_A, against the measured values. Since the prediction is a function of height this function will clearly depend on the function of virtual temperature in the surroundings with height. As small changes in this function are crucial, we have chosen the best fit that can be had by making the virtual temperature exceed the exactly neutral profile for an adiabatic cloud by a power of the height above base. This fit is $\Delta T((Z - Z_B)/(Z_T - Z_B))^{**}1.35$ where Z is the altitude and the subscripts B and T indicate base and top respectively. The temperature increment ΔT ensures the given curve passes through the extrapolated environmental point at 2750 m and 1.4 C. This curve is about 0.1 C warmer than the data given at 1500 m.

Results from variation in this curve are quite large so such variations are examined below. Using these environmental data, however, allows us to examine effects of variations in moisture and temperature excess of the air mixed in from above cloud top on equilibrium values of water content after mixing down through the cloud.

Using Warner's value of a relative humidity of 0.15 for the overlying air and a temperature excess of 2 C, the calculation almost exactly reproduces Warner's 1970 curve of Q/Q_A. This is copied for our Fig. 2. Our curves for this and other conditions can be seen in Fig. 3. Thus granted a variation in environmental temperature of 0.1 C from the given values, which is smaller than the measurement accuracy, and using a 2 C temperature excess for the air mixed in from above, the theory matches the data to better than it can be measured.

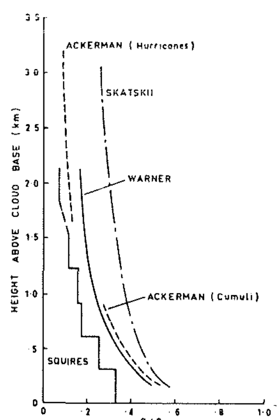

The ratio of the observed mean liquid water content at a given height above cloud base to the adiabatic value. The values attributed to Skatskii were obtained from his published results assuming that the cloud base was at a height of 1 km and at a temperature of 8C.

Fig. 2 This is Fig. 1 from Warner, 1970.

To examine the significance of this matching we need to look at the effects of varying the measured quantities.

7.1 Varying the Overlying Air

We have found that the same water content curve is produced to within about 5% if a certain functional relation between the temperature excess and the relative humidity of the overlying air is maintained. This also applies to different water content curves for the same environmental structure. Thus Fig. 3 shows curves of liquid water with values of Q/Q_A at cloud top of 0.1, 0.2, 0.3 and 0.4. Fig. 4 shows the relationship between relative humidity and temperature excess for each of these curves.

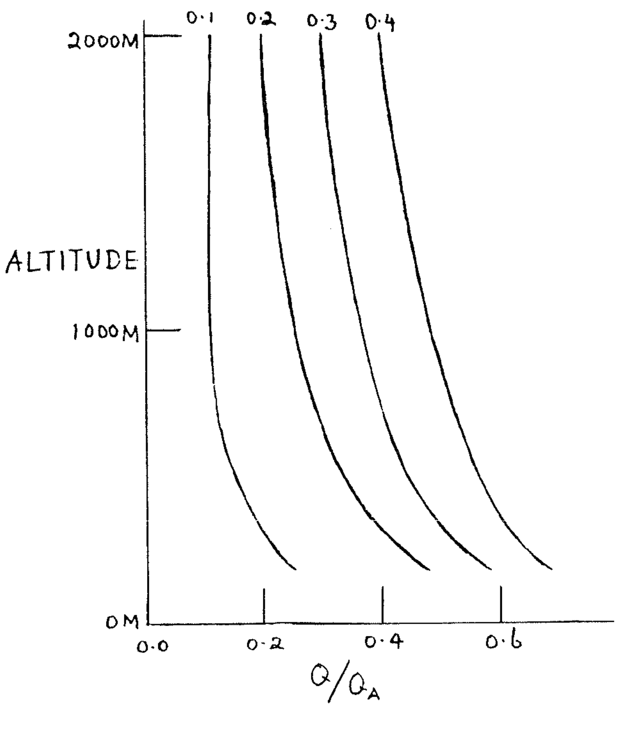

Fig. 3 This figure shows the ratio of actual cloud water to adiabatic water for the theory presented here, using an environment based on that given in Table 1 by Warner. The curve labled 0.2 is a close match to the measured values given in Fig. 2. The other curves relate to different conditions in the overlying air.

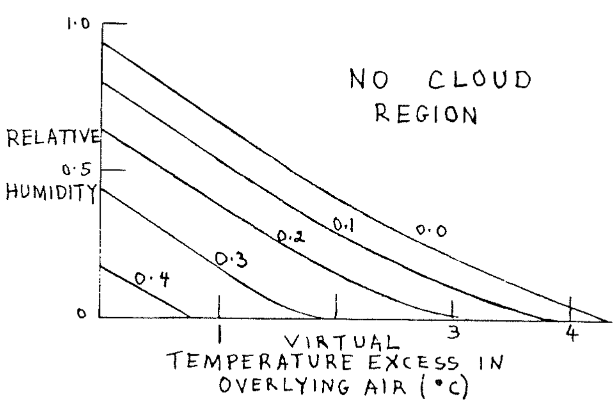

Fig. 4 These curves give the relationship between relative humidity of the overlying air and its temperature excess for each curve of Fig. 3. The same curve of Q/Q_A is produced within about 5% for conditions in the overlying air given by the appropriately labled curve in this figure.

A wet cloud requires dry overlying air with a small temperature excess. For wet air and a strong inversion no equilibrium state in a small cumulus is possible. The region where the overlying air is more than 50% saturated would require the cloud to stop growing below a 2 C inversion; such clouds probably break through to form thunderstorms. Dry air with inversions exceeding 3 or 4 C probably prevent a cloud forming for more than a few minutes. These limits appear fairly reasonable since when small cumuli are formed the overlying air is usually fairly dry, and a few degrees at the inversion is needed to define the cloud top.

7.2 Changing the Environmental Profile

As would be expected the profile of liquid water depends on the exact profile of environmental density. The effects of changing the exponent in the formula given earlier are shown in Table 2.

Table 2

Exponent	1.35		1.00		1.50		2.00	
Altitude	T_v	Q/Q_A	T_v	Q/Q_A	T_v	Q/Q_A	T_v	Q/Q_A
2750	1.40	0.20	1.40	0.20	1.40	0.20	1.40	0.20
2550	2.93	0.21	2.85	0.18	2.97	0.22	3.08	0.26
2350	4.44	0.22	4.30	0.16	4.50	0.24	4.70	0.31
2150	5.93	0.23	5.73	0.14	6.02	0.26	6.26	0.37
1950	7.40	0.24	7.15	0.11	7.50	0.23	7.77	0.43
1750	8.85	0.25	8.57	0.07	8.95	0.31	9.22	0.50
1550	10.27	0.27	9.99	0.03	10.37	0.37	10.61	0.58
1350	11.67	0.32	11.40	0.00	11.75	0.42	11.94	0.67
1150	13.03	0.37	12.81	0.00	13.09	0.50	13.22	0.76
950	14.35	0.46	14.21	0.00	14.39	0.62	14.44	0.88
750	15.61	-	15.61	-	15.61	-	15.61	-

The first example with an exponent of 1.35 is the example used earlier. If we compare the temperatures 1000 m above cloud base, we have 8.57, 8.95 and 9.22 C for Q/Q_A of 0.07, 0.31 and 0.50. The values for the first example are 8.85 and 0.25 respectively. Thus variations of $\pm$ 0.3 C encompass Q/Q_A from almost 0.0 to 0.5. Thus the vertical profile of the stability is of critical importance in determining the profile of in-cloud liquid water and probably calls for an accuracy exceeding the capability of present temperature measurements to determine with confidence. It also illustrates that calculations performed with the common meteorological concepts often used for wet air are of little use.

7.3 The Overall Stability

Using the same stability profile formula with an exponent of 1.35 and with a relative humidity of 0.15 and temperature excess of 2 C in overlying air, let us now examine the effect of changing overall stability in the cloud surroundings. A range of conditions are displayed in Table 3.

Thus we can see that as the environmental air becomes more stable, less dry air has to be mixed into the cloud to achieve stability and so the final mixture is wetter. We see that 1 C in virtual temperature over 2000 m about doubles the liquid water left in the upper half of the cloud so once again temperature and moisture need be measured to good accuracy.

Table 3

Altitude	T_v	Q/Q_A	T_v	Q/Q_A	T_v	Q/Q_A
2750	0.90	0.14	1.90	0.29	2.90	0.52
2550	2.50	0.15	3.36	0.29	4.23	0.51
2350	4.07	0.16	4.81	0.29	5.55	0.51
2150	5.62	0.17	6.24	0.30	6.86	0.51
1950	7.15	0.18	7.65	0.30	8.16	0.51
1750	8.65	0.20	9.05	0.32	9.45	0.53
1550	10.13	0.23	10.42	0.33	10.71	0.53
1350	11.57	0.28	11.77	0.37	11.96	0.55
1150	12.97	0.34	13.09	0.42	13.19	0.55
950	14.33	0.44	14.38	0.50	14.42	0.63
750	15.61	-	15.61	-	15.61	-

8. CONCLUSIONS

The model for the growth of small cumuli given here appears to meet the observational facts far better than other models that have been used. The model postulates that the cloud rapidly builds on one side and that mixing from the top down then dilutes the material. So for most of the life of each column of cloud it is almost in equilibrium with its environment. After some time the dilution reaches cloud base and the overall column is no longer bouyant and it collapses, thus forming the other edge of the cloud. Calculations given above indicate that precise temperature measurements, as well as good measurements of moisture and liquid water will be needed to determine how close the equilibrium state is actually approached in the dynamical conditions in a real cloud.

9. ACKNOWLEDGMENTS

This work was undertaken with the assistance of a grant from the Atmospheric Sciences Section of the National Science Foundation.

10. REFERENCES

Simpson, J., 1971: On cumulus entrainment and one dimensional models. J. Atmos. Sci. 28, 449-455.

Simpson, J., 1972: Reply (to Warner). J. Atmos. Sci. 29, 220-225.

Squires, P., 1958A: The spatial variation of liquid water and droplet concentration in cumuli. Tellus 10, 372-379.

Squires, P., 1958B: Penetrative downdrafts in cumuli. Tellus 10, 381-389.

Telford, J. W., 1975: Turbulence, entrainment, and mixing in cloud dynamics. Pure and Applied Geophysics, 113, 1067-1084.

Telford, J. W. and P. B. Wagner, 1974: The measurement of horizontal air motion near clouds from aircraft. J. Atmos. Sci. 31, 2066-2080.

Telford, J. W. and J. Warner, 1962: On the measurement from an aircraft of buoyancy and vertical velocity in cloud. J. Atmos. Sci. 19, 415-423.

Wagner, P. B. and J. W. Telford, 1976: The measurement of air motion in and near clouds. Proceedings of the International Cloud Physics Conference, 1976.

Warner, J., 1955: The water content of cumuliform cloud. Tellus, 7, 449-457.

Warner, J., 1970: On steady-state one-dimensional models of cumulus convection. J. Atmos. Sci. 27, 1035-1040.

Warner, J. 1972: Comments "On cumulus entrainment and one dimensional models." J. Atmos. Sci. 29, 218-219.

4.1.5

TEMPERATURE AND HUMIDITY SIGNATURES OF SOME SHALLOW FAIR-WEATHER Cu CLOUDS AND THEIR RELATED DYNAMICS AND MICROPHYSICS

R. ROSSET, J.F. GAYET, F. LE DIMET, J. and J. PASTRE

Laboratoire de Dynamique et Microphysique de l'Atmosphère
Université de Clermont-Ferrand - B.P. 45 - (63170) AUBIERE - (France)

1. GENERAL BACKGROUND

A DC7 aircraft instrumented for simultaneous dynamical, thermodynamical and microphysical measurements has been flown through shallow fair weather billowing Cu Clouds often seen topping the planetary boundary layer (PBL). One of the main interests of the present study lies in the high spatial resolution of the microphysical data as given by the Ruskin and Knollenberg (ASSP) sensors, respectively for total water content and droplet spectra. This resolution proves to be sufficient as for the estimation of the importance of entrainment on the development and properties of such clouds, at various stages in their life times.

2. SPECIFIC PURPOSES

Entrainment and its subsequent mixing has long been recognized as a key process in the evolutionary aspects of cloud growth as well as for determining the rate of deepening of the PBL. This latter is locally intensified at certain restricted locations, hummocks (1), (2) or domes (3) protruding from the lower mixed layer into the stable layer aloft. Some of the many aspects observable in the development of these intrusions according to their stability, size and initial momentum can be found in Saunders (4) and Linden (5). At times, shallow Cu clouds are seen rolling and billowing on top of the convective layer, capping the convective intrusions where these latter overshoot the condensation level (6), (2) . So, the study of entrainment in those clouds can give a clue as for the deepening mechanisms of the PBL. As we shall see now, the microphysical data seem to be very sensitive to the degree of mixing of a cloud with its clear air environment.

3. THE EXPERIMENTAL DATA

Fig. 1 is an atmospheric sounding at the time of the flight. A very stable layer with a marked humidity gradient is located between points A and B. The condensation level is at an intermediate position, at C. Shallow Cu clouds are seen billowing between C and a point well below the sharp inversion B where they spread horizontally, as confirmed by pilot observations and photogrammetry. The cloud field appears to be very homogeneous with the same heights for the cloud bases and tops everywhere, a depth of about 100m, a lateral extent between approximately 600m and 1500m and characteristic life times ranging from 3mn to 5mn only.

Typically, for each individual cloud, two phases can be distinguished (2) : a short formative one (lasting for about 1mn or even less) followed by a longer recession phase during which the cloud is spreading laterally due to a "filling-box" mechanism (7) while being dissipated. As an example, fig. 2 (8) gives the time rate of growth of droplet radii due to condensation alone. When comparing with the spectral values of figs. 3 and the duration of the formative phase, one can conclude that two antagonist processes are at work within the clouds : condensation which rapidly builds up the cumili with a peak at 3 µ and mixing with clear air essentially free of condensation nuclei above the inversion base A which tends to dilute them more slowly. Thus, for the spectra of figs. 3, entrainment acts as a modulating process globally reducing and distorting in time the primary spectrum first generated within the updraughts intruding at the condensation level. So, the spectrum and intensity of the vertical velocity at this level are very important to be known, for the further ascent of the convective elements in the stable layer AB is entirely forced by their residual vertical upward momentum there (cf. J_z in fig. 3.3).

It is important to realize that the convective parcels rising above point A are colder and more humid than their environment upon which they impress themselves as wet, negative temperature and potential temperature (Θ) perturbations with relative extrema values where the total water content q_T, the liquid water content q_L, the median volumic diameter d, the total and spectral droplet concentrations N and N_S (3µ, 4µ and 5µ) are maxima themselves, the whole figure being consistent with a reduced entrainment (dilution) at those parts for all the clouds (cf. figs. 3).

All the spectra are unimodal with a very variable concentration in the different droplet sizes (see N_s in figs. 3). The 2μ and 3μ sizes are particularly well suited for our purpose of estimating the degree of entrainment and then, in some way, the phase in the life cycle of the clouds. For example, the cloud of fig. 3.1 is probably decaying with its weak total droplet concentration N, its greater number of 2μ-droplets as compared to 3μ-ones, its marked downdraught and cooling. As for the cloud on fig.3.2, the shifting between the spectral peaks for 2μ on the onehand and 3μ, 4μ and 5μ on the other hand is presumably to be related to the horizontal spreading of the cloud as it begins to roll up rightwards and dissipate on the other side.

To further exemplify the differential role of entrainment on the spectra, we have reported in figs. 4 the ratio R = concentration of 3μ-droplets/ concentration of 2μ-droplets, as a function of the 2μ-droplet concentrations. The 2μ and 3μ ranges have been selected because for all the reported cases they give the absolute spectral maxima. In a sense, the dimensionless number R is representative of the spectral transfers of the water substance as related to entrainment, the 3μ-droplets being essentially generated by condensation whereas, apart from direct condensation, the 2μ range is feeded too by the 3μ-droplets consecutive to mixing of the cloud with clear air. So, values of $R>1$ are indicative of a reduced entrainment while the reverse is true for $R<1$. In fig. 4.1, all the R-values are inferior to 1, in conjunction with weak concentrations, in contrast with fig. 4.3, where R is everywhere greater than 1, whatever the concentrations. Fig. 4.2 gives a composite picture, with a grouping of points in the concentration range 7-9 (in our relative units). On this experimental basis, we can tentatively assert that for the 1st penetration, the 1st cloud has already well decayed (as previously discussed), that the 2nd cloud begun its billowing motion and that for the 2nd penetration, the cloud is still in its formative phase. A direct confirmation of the preceding discussion comes out from the vertical gust velocities J_z: the downdraughts of figs. 3.1 and 3.2 are to be related to the recession phases for the corresponding clouds (stronger in 3.1 than in 3.2 as expected from above) whereas the updraught of fig. 3.3 is characteristic of a formative ascent pulse phase.

4. CONCLUSION

The present study is part of a growing PBL program with consideration of non-perturbed as well as of perturbed conditions (problem of the coupling between the cloud and sub-cloud layers). The humidity and microphysical sensors are still in the process of accurate calibration and testing. So, at the present time, we do not stick so much to the absolute values quoted here as to the relative variability encountered during in -and between- cloud flights within a short period of time. This is particularly true as regards the small droplet sizes and integrated liquid water contents found, however considering we are dealing with very short-lived clouds. Nevertheless, with these restrictions in mind, it is suggested that the time history of shallow billowing fair-weather Cu clouds can be traced out with the aid of droplets as tiny sensitive microphysical tracers. Of crucial importance in the cases reported here is the ratio R between the 3μ and 2μ droplet concentrations as for deciding which phase the sampled cloud is going through.

5. AKNOWLEDGMENTS

This research was supported by D.R.M.E., D.G.R.S.T. and C.N.R.S. under grants 73-34-430-01 and 74-7-0478. We are greatly indebted to Pr R.G. SOULAGE for his advice and constant scientific assistance. Thanks are due to the L.D.M.A. technical staff, AMOR-DC7 crews and to Mrs F. BESSERVE for her typing and drawing of figures.

6. REFERENCES

(1) Carson D.J. and Smith F.B., 1973 : A thermodynamic model for the development of a convectively unstable boundary layer - Proc. 2nd Symp. IUTAM/ IUGG, Charlottesville, Va., USA.

(2) Rosset R., 1975 : Mécanismes, rôle et paramétrisation de l'entraînement au sommet de la couche limite planétaire convective - Thèse de Doctorat d'Etat, Université de Clermont-Ferrand, 125pp.

(3) Konrad T.G., 1970 : The dynamics of the convective process in clear air as seen by radar, Jour. Atm. Sci., Vol. 27, n°11, pp. 1138-1147.

(4) Saunders P.M., 1962 : Penetrative convection in stably stratified fluids, Tellus, Vol. 14, p. 177.

(5) Linden P.F., 1973 : The interaction of a vortex ring with a sharp density interface : a model for turbulent entrainment, Jour. Fluid Mech., Vol. 60, part 3, pp. 467-480.

(6) Ludlam F.H., 1967 : Characteristics of billow clouds and their relation to clear air turbulence, Quarterly Jour. of the Royal Met. Soc., Vol. 93, n° 398, pp. 419-435.

(7) Baines W.D. and Turner J.S., 1969 : Turbulent buoyant convection from a source in a confined region, Jour. Fluid Mech., Vol. 37, pp. 51-80.

(8) Fleagle R. and Businger J., 1963 : An introduction to atmospheric physics, Acad. Press Inc., New York, p.89.

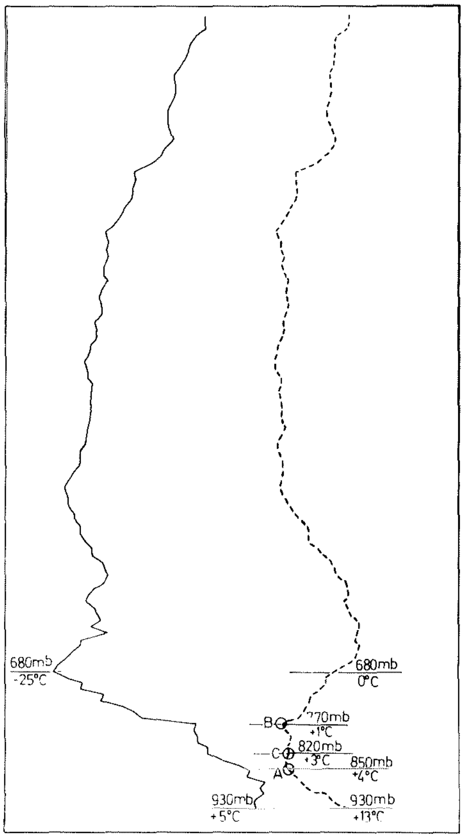

Fig. 1. Emagram of the atmospheric sounding at 9.38 GMT, july 2th 1975 (dashed line : temperature - solid line : dew point temperatures).

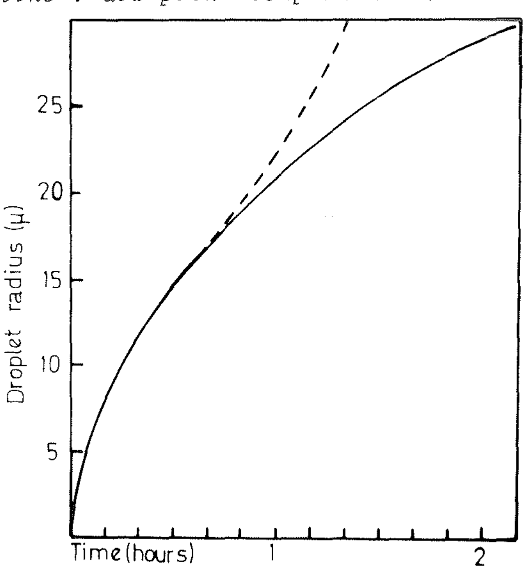

Fig. 2. Solid curve : radius of droplet as a function of time for growth by condensation alone. Dashed curve : estimated radius of droplet as a function of time for growth by condensation and accretion (drawn frome Fleagle and Businger (8)).

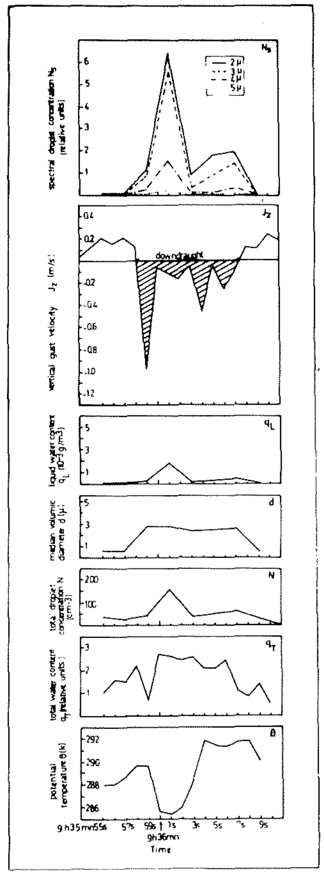

Figure 3.1.
1st penetration
(1st cloud)

Are respectively given vs. time, from top to bottom:

- *Spectral droplet concentration N_s*
- *Vertical gust velocity J_z*
- *Liquid water content q_L*
- *Median volumic diameter d*
- *Total droplet concentration N*
- *Total water content q_T*
- *Potential temperature θ*

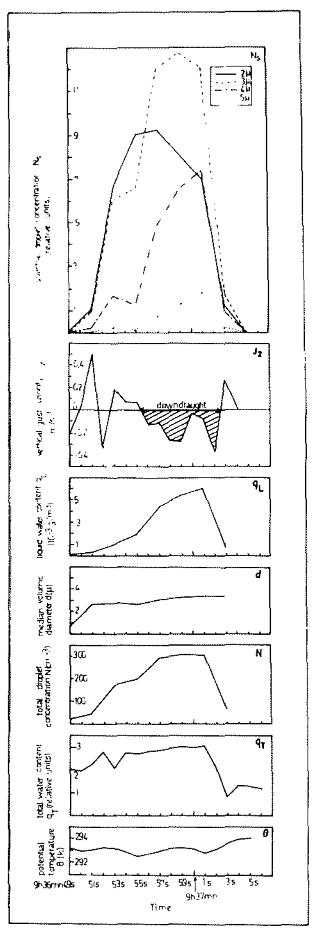

Figure 3.2.
1st penetration
(2nd cloud)

Are respectively given vs. time, from top to bottom:

- *Spectral droplet concentration N_s*
- *Vertical gust velocity J_z*
- *Liquid water content q_L*
- *Median volumic diameter d*
- *Total droplet concentration N*
- *Total water content q_T*
- *Potential temperature θ*

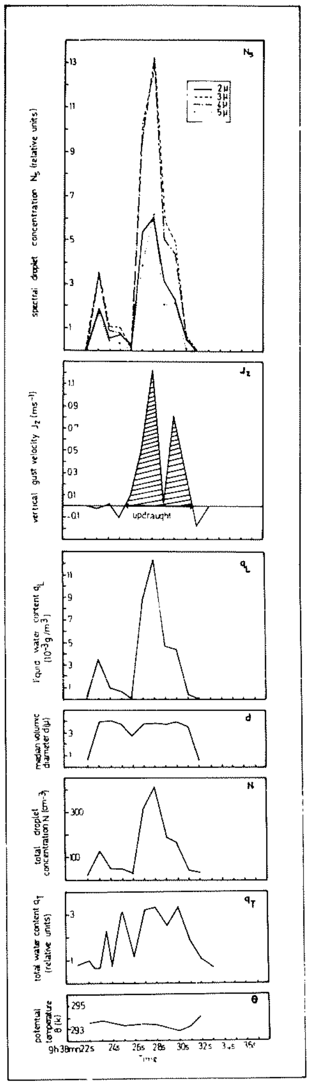

Figure 3.3

2nd penetration

Are respectively given vs. time, from top to bottom :

- *Spectral droplet concentration* N_s
- *Vertical gust velocity* J_z
- *Liquid water content* q_L
- *median volumic diameter d*
- *Total droplet concentration N*
- *Total water content* q_T
- *Potential temperature* θ

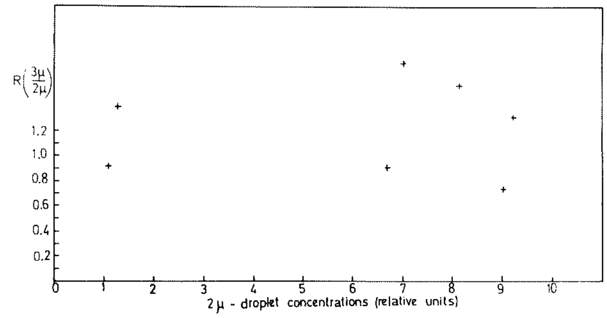

Figure 4.2. R(3μ/2μ) as a function of 2μ-droplet concentration (id. relative units as for N_s*). 1st penetration (2nd cloud).*

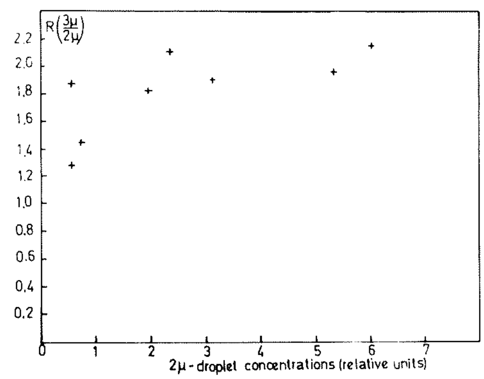

Figure 4.3. R(3μ/2μ) as a function of 2μ-droplet concentration (id. relative units as for N_s*). 2nd penetration.*

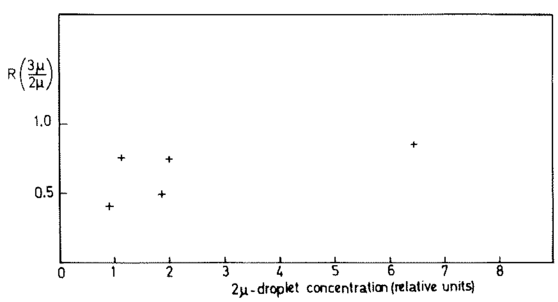

Figure 4.1 R(3μ/2μ) as a function of 2μ-droplet concentration (id. relative units as for N_s*). 1st penetration (1st cloud).*

4.1.6

DESCRIPTION OF MIXING PROCESSES IN INITIAL CUMULUS

Kelvin S. Danielson, Lewis O. Grant and Allan J. Schanot

Department of Atmospheric Science
Colorado State University
Fort Collins, Colorado

1. INTRODUCTION

This paper describes a cumulus cloud in initial growth phases, with particular enphasis on mixing processes through the use of doppler radar and stereo cloud photogrammetry. Radar chaff was dispensed into the sub-cloud layer over a mountain driven cumulus genesis area prior to cloud formation. Initially, the chaff responded to the mean wind flow and the motion of thermals in the clear air of the sub-cloud layer. When the cumulus cloud formed, the chaff was transported vertically with the air which subsequently made up the cloud described in this paper. The ISWS CHILL radar was used to study the reflectivity and motion of the radar chaff. The change in the reflectivity as the air and chaff mixture moved upward is used to estimate the bulk entrainment. The vertical and horizontal continuity or discontinuity of the reflectivity provides insight on the cloud-environment mixing process. The mean horizontal velocity profile of the cloud as determined by radial doppler velocity measurements is also studied. Due to the distance of the cloud from the radar, the radial velocities measured are attributed primarily to horizontal motions of the chaff in the clouds. The doppler spectra used to calculate the mean radial velocities was also recorded by the radar system and is investigated in this study. Emphasis is placed on utilizing the doppler spectra to resolve the turbulence profile of the cloud from analysis of the doppler spectra associated with each mean velocity measurement.

2. ENTRAINMENT PARAMETERIZATIONS

The first attempt to numerically simulate entrainment was made by Stommel (1947) when he developed a graphical technique of computing the rate of entrainment of environmental air into a cloud, based on aircraft soundings of temperature and humidity which compared the values of these variables obtained inside and outside the cloud. Two different conceptual models, and later numerical techniques, were proposed based on the entrainment principle. The "bubble" or "thermal" concept suggested by Ludlem and Scorer (1953) considers a cloud to be made up of a spherical vortex or a series of vortexes which after being heated at the surface become buoyant and begins to rise. Classically, the entrainment or mixing of the bubble as it rises is considered to be a function of the bubble radius. The numerical formulation proposed by Malkus (1960) to simulate this process is:

$$\mu_c = \frac{1}{m}\frac{dm}{dz} = \frac{b}{R} \tag{1}$$

where μ_c is the entrainment rate, m is cloud mass, z is vertical distance, R is the bubble or parcel radius, and b is a dimensionless coefficient. Laboratory experiments by Turner (1962) suggest that b for this formulation should be approximately .6.

Stommel (1947) and Schmidt (1947) argued that clouds, particularly large cumulonimbus clouds, develop a steady persistent structure which is not simulated by a bubble. They suggested that the cumulus cloud would be better simulated by a "steady state jet". To numerically simulate this conceptual model a closed system of equations including a thermodynamic function, vertical mass flux continuity, and vertical momentum were used. The entrainment for this simulation is also assumed to be a function of the "jet" radius and is formulated as:

$$\mu_c = \frac{1}{F_m}\frac{dF_m}{dz} = \frac{b}{R} \tag{2}$$

where F_m is the vertical mass flux in a steady state jet. The coefficient b for this type of model was estimated by Turner (1962) to be .2.

Lopez (1973) parameterized the entrainment and detrainment rates as a function of the turbulent intensity in the cloud parcel and the environment respectively. This formulation is based on laboratory experiments by Scorer and Ronne (1956), Scorer (1957), and Turner (1962a) who suggest that the entrainment is a function of the turbulent intensity in the parcel. Turner (loc cit) in his experiment obtained results which suggest that detrainment is a function of the turbulent intensity of the environment. Following the suggestions of Telford (1966) and Morton (1968), Lopez let the mean velocity of entrainment into the parcel be proportainal to the turbulent intensity in the parcel, and let the mean velocity of detrainment be proportional to the turbulent intensity of the environment.

$$\overline{V}_{ent} = \varepsilon i \tag{3}$$

$$\overline{V}_{det} = \varepsilon e \tag{4}$$

where ε is the entrainment constant, and i and e are the turbulent intensities of the cloud and environment respectively. The turbulent intensity is defined as:

$$i^2 = \overline{u'^2_p} + \overline{v'^2_p} + \overline{w'^2_p} \tag{5}$$

$$e^2 = \overline{u'^2_e} + \overline{v'^2_e} + \overline{w'^2_p} \tag{6}$$

where u', v' and w' are the eddy velocity components. The entrainment rate is the flux of mass into the parcel.

$$\frac{dm_{ent}}{dt} = \rho_e \overline{V}_{ent}\, 2\,\pi\, r\, \Delta z \tag{7}$$

where ρ_e is the density of air in the environment, r is the cloud radius, and z represents the height interval. The detrainment rate is similarly formulated as:

$$\frac{dm_{det}}{dt} = \rho_p \overline{V}_{det} \; 2 \pi r \Delta z \quad . \qquad (8)$$

In order to use this parameterization it was necessary that the turbulent intensity of the cloud and environment be modeled.

Cotton (1975) presents a nonlinear eddy viscosity model in which the mean and turbulent fluxes of the cloud and the environment are modeled. The mean horizontal flux terms of the model are solved by a diagnostic procedure first used by Asai and Kasahare (1967) and later by Ogura and Takahashi (1971,73). In this procedure the air properties are assumed to be environmental properties if there is a net inflow at the edge of the cloud, and to be internal cloud properties if there is a net outflow at the edge of the cloud. The inflow and outflow represent entrainment and detrainment due to mean fluxes respectively. Horizontal turbulent fluxes at the cloud edge are approximated using a method developed by Asui and Kashora (1967) which assumes an eddy exchange hypothesis such that

$$- \overline{u''A''}\Big|_R = K \frac{\partial \overline{A}}{\partial r}\Big|_{r=R} \approx \frac{K(A_o - A)}{R} \qquad (9)$$

where u is a velocity component, R is the cloud radius, A represents each thermodynamic and momentum variable, and K is the eddy viscosity, assumed proportional to the stress at cloud edge.

Several current cloud modeling efforts (Manton and Cotton, 1976a,b,c,d; Sommeria, 1974) are directed at modeling in three dimensions the mean and turbulent fluxes of the cloud and the environment in which it is growing. It is hoped that by developing a fully three-dimensional model, the cloud, the environment, and interactions of the cloud and environment can be better simulated.

The entrainment and detrainment formulations presented suggest two basic relationships. The bubble formulation, the steady state jet formulation and the formulation for the nonlinear eddy viscosity model all inversely relate the entrainment to the radius. One relationship is, therefore, that the entrainment is proportional to the cloud radius. The second relationship suggested by these parameterizations is that the entrainment and detrainment are dependent upon the turbulence of the cloud. Both the Lopez parameterization and the nonlinear eddy viscosity model suggest that this dependency is important.

3. PROCEDURE

The South Park Area Cumulus Experiment (SPACE) is designed to study high elevation mountain cumulus convection with primary emphasis on the initiation phase. South Park is a large (65 km by 40 km) open mountain valley with an average elevation of 3000 meters (MSL) and is located approximately 100 km southwest of Denver, Colorado. The Mosquito Range, located on the western boundary of South Park with a ridge elevation of approximately 4200 meters, is a preferred location for initial cumulus activity on most days during the summer. The procedure used was designed to utilize the preferred location concept by creating a homogeneous chaff field in the subcloud layer over the mountain driven cumulus genesis area just prior to initial cumulus activity. It was reasoned that the chaff would be transported vertically with convective elements and could then be used as a tracer to study the mixing, cloud dimensions, radical velocities, and turbulence of the clouds which resulted from the convective activity.

In order to create a homogeneous chaff field below cloud base just prior to convective activity several variables must be either predicted or measured. These are mean wind speed and wind direction, particularly at or near cloud base level, the cloud base height, and the time of initial convection. Data for estimating these variables was provided, almost exclusively, by a morning rawinsonde. The winds were measured from the trajectory of the balloon. The cloud base height was calculated by averaging the temperature and humidity in a lower layer and then computing the lifting condensation level using the layer averaged values of temperature and dewpoint. The time of initial convection was calculated by determining the time it would take to break the surface temperature inversion and any other temperature inversions below the predicted cloud base height. An emperical formula was developed to calculate the time necessary for sufficient heating.

Once these variables were determined, a small aircraft was dispatched upwind of the cumulus genesis area at a height slightly above the predicted cloud base height. The chaff would then be released in a grid approximately 7 km wide and 15 km long and was oriented parallel with the Mosquito Range. The time of release and the distance upwind were determined by considering both the estimated time of convection and the distance necessary for the chaff to become dispersed into a relatively homogeneous layer.

The chaff tracer was monitored with the CHILL doppler radar from the initial time of release. If the dispersion rate of the chaff was not sufficient, or if the velocity and direction of the tracer were not acceptable, a second chaff release would be made at a corrected position. When it was determined that the tracer was properly positioned, the radar would scan the chaff field, always including in the scan sequence a scan above the general chaff layer. When a chaff echo was observed above the general chaff field, the scan sequence would concentrate on the echo or echoes above the chaff field. The radar was typically operated in a sector scan mode with the scan sequence and doppler gates concentrated on the chaff echo area. The plan was to collect as much data per scan sequence as possible but to keep the time between scan sequences from becoming excessively long.

The experiment utilizes the CHILL (CHicago-ILLinois) dual wavelength pulse doppler radar operated by the Illinois State Water Survey (ISWS) for measuring the extent, mean radial velocity and distribution of radial velocities about the mean of the radar chaff tracer. The radar has 10 and 3 cm. wavelengths with 1° beam width.

The radar is equipped with programmable sector scanning and digital recording. The CHILL radar has been described in detail by Silha and Mueller (1971).

The case studies in this paper utilize only the doppler spectra and the 10 cm power data. Mean velocities and variances are recomputed from the doppler spectra.

4. RESULTS

The chaff tracer experiment described was run on several days during the 1974 and 1975 SPACE project. The results from the experiment of August 26, 1974, are presented in this paper.

The sounding from August 26, 1974, was characterized by an unstable layer from the surface (730 mb) to approximately 520 mb. From 520 mb to 450 mb the atmosphere was conditionally unstable. The sounding showed a slightly stable layer from 450 mb to 250 mb where the atmsophere became very stable. The lifting condensation level (LCL) on this day was at approximately 510 mb. The mixing ratio at the LCL was 3.5 g/kg. The dew point depression did not exceed 13°C at any level of the sounding and was typically at about 6°C. From energy considerations and using parcel theory assuming no entrainment, the cloud top would not be expected to exceed the 550 mb level.

The synoptic weather pattern for the area was dominated by a persistent high pressure area centered 500 km west of the experimental area. This resulted in light northwesterly winds in the mid to upper troposphere.

The subcloud chaff field dispensed for the experiment was well dispersed and occupied a layer from near the surface to approximately 600 mm^6/m^3. Cloud bases were estimated to be 5700 meters (MSL) from the sounding. Aircraft observations and photogrammetric measurements confirm that 5700 meters (MSL) was the general cloud base height. Photogrammetric studies showed that clouds typically grew to approximately 8000 meters. At approximately 12:30 MDT a radar scan above the homogeneous chaff layer detected several echoes approximately 30 km distance and 10° west of north from the CHILL radar site. This is indicative of the fact that several clouds in the vicinity had transported the chaff vertically, since cloud formation from photogrammetric studies was determined to be just initiating and that precipitation would not have had sufficient time to form. Also in areas adjacent to the chaff experiment, clouds also formed but no echoes were detected from those clouds.

4.1 Power Data

Figures 1, 2 and 3 display vertical profiles of reflectivity and cloud radius of a typical actively growing cloud for times 12:50, 12:52, and 12:56 (MST) respectively. The

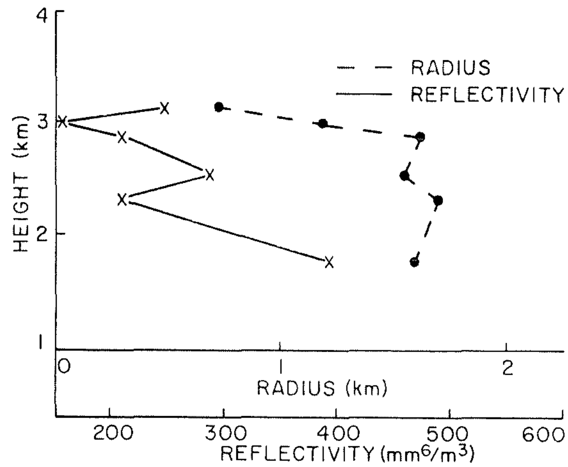

Figure 1. Vertical profile of chaff tracer reflectivity and radius of cloud at 12:50 MST. Height is given with respect to the surface.

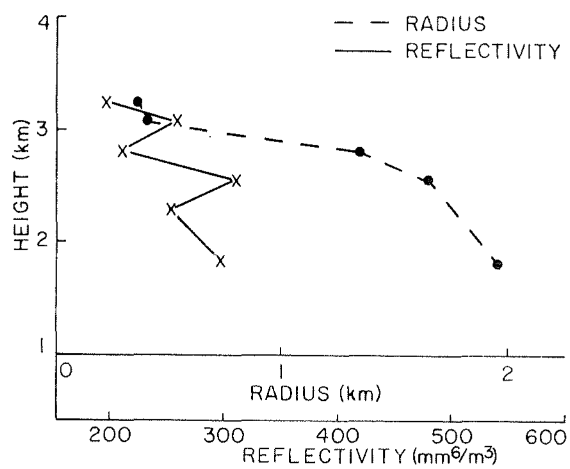

Figure 2. Vertical profile of chaff tracer reflectivity and radius of cloud at 12:52 MST. Height is given with respect to the surface.

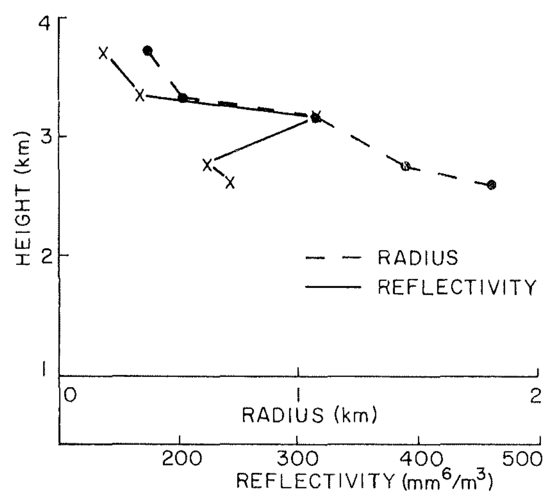

Figure 3. Vertical profile of chaff tracer reflectivity and radius of cloud at 12:56 MST. Height is given with respect to the surface.

measured reflectivity values displayed are averages over the entire extent of the layer being measured. The radius is calculated from the horizontal extent of the chaff field. The scan sequence from which the profiles were ascertained encompassed approximately 90 seconds each. The most distinctive features on the figures is the variability of both average reflectivity and cloud radius, with both height and time. In general, both the cloud radius and the average reflectivity tend to decrease with height. If the cloud were of a steady state nature, the mixing should be definable from the profiles. The variability of these data, however, suggests that the cumulus clouds observed are not in a steady state condition. The large variations in reflectivity with height may be due to a succession of parcels moving upward in the cloud separated by a vertical distance, with higher reflectivity areas corresponding to bouyant parcels, but the data is not conclusive.

The power data can also be analyzed using the conceptual model of buoyant thermals or "bubbles". The only bubble which one can easily distinguish from the data is the top of the cloud.

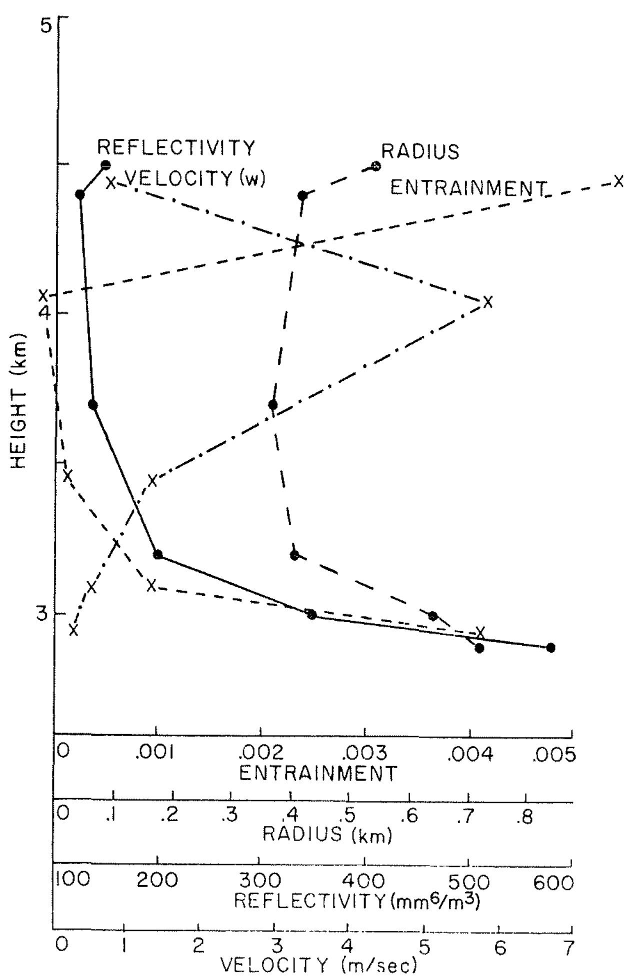

Figure 4. Vertical profiles of reflectivity, cloud radius, vertical velocity, and entrainment following cloud top.

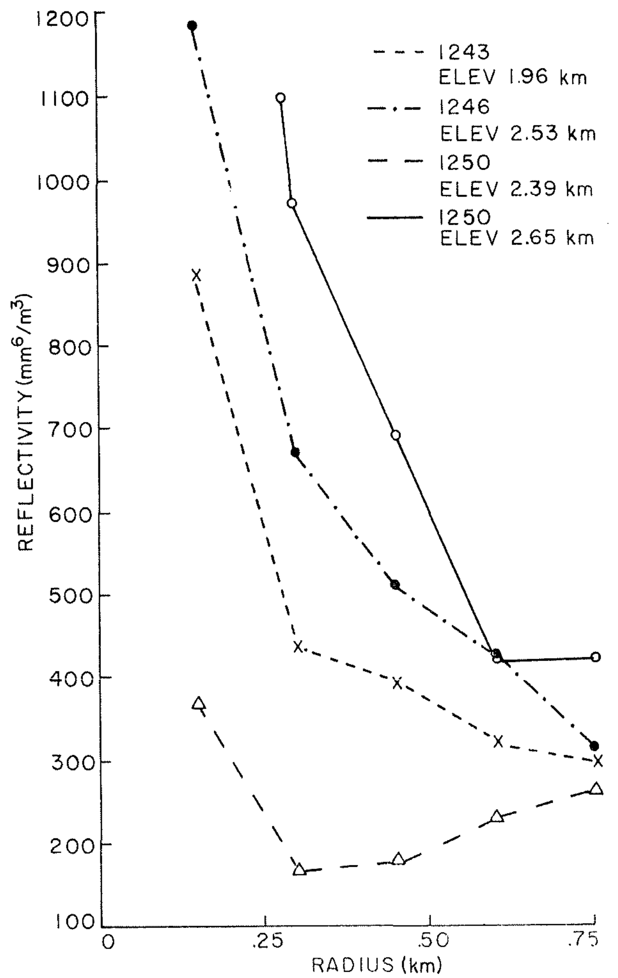

Figure 5. This figure demonstrates the protected core area of mountain cumulus clouds.

From successive scan sequences beginning at 12:37 MDT and ending at 12:59 MDT a plot of the vertical changes of cloud radius, average reflectivity, vertical velocity and entrainment with height is displayed in Figure 4 for the highest scan of the sequence on which a return was detected. The cloud radius is defined by the 18 dbz echo contour since the radar cannot detect a return below 18 dbz. The layers used are the uppermost layer in any scan sequence. The values of reflectivity are averaged over the entire layer. If any value below 18 dbz was noted in the center of the cloud, it was considered to be 16 dbz for the averaging calculation. A single scan had the highest average reflectivities near the center and the lower average reflectivities at the outer portions as is shown in Figure 5. Large variations from this trend were detected, however. The vertical velocity calculation is made by taking the vertical distance between the uppermost layer of successive scan sequences and dividing it by the time between the radar scans during which the data was taken. The entrainment is determined by calculating the volume and the amount of chaff in the volume (chaff density) at the lower level, then allowing for parcel expansion as the parcel rises and for reflectivity changes due to variations in the distance of the cloud

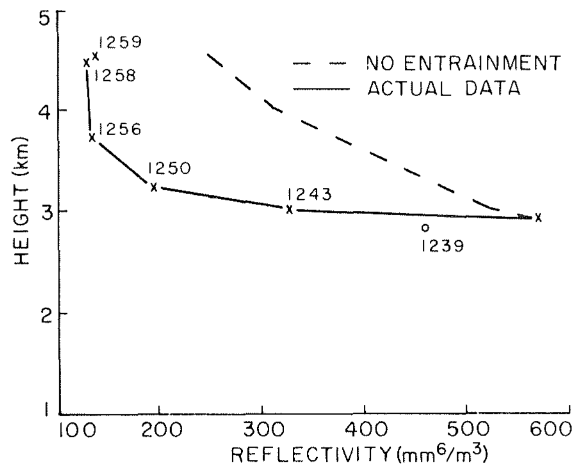

Figure 6. This figure demonstrates how the radar reflectivity observed compared with the radar reflectivity expected for no entrainment.

from the radar, an expected density of chaff and radar reflectivity for no mixing is calculated for the next observed level. This number is then compared with the observed chaff density and reflectivity. If the density is less than the expected value for no mixing, then a calculation is made for the amount of air with no chaff which would have to be mixed in to get the observed chaff density. This volume is then used for the entrainment calculation.

An assumption inherent in considering the cloud top a bubble and measuring the top with a radar is that the radar samples the same parcel with the highest elevation scan on which an echo is detected of successive scan sequences. At the distance of the cloud from the radar (<30 km) with a 1° beam width and a maximum of 2° increments in elevation during the scan sequence, this assumption is not considered caprious.

It should be noted that on Figure 4 the parcel shows a larger velocity in the mid-levels of the cloud. This increase in velocity may result in a change of bubble shape. In all likelihood, the bubble is probably enlongated in the vertical direction. Such a change in shape would probably help account for the curves of radius and reflectivity which at first seem unrealistic, particularly at the mid-levels. No attempt was made to quantify this effect for this paper.

Given these difficulties with the technique, several interesting observations can still be made with a high degree of certainty: (1) mixing of this parcel was large near cloud base; (2) the mixing while the parcel was at mid-levels and had attained a relatively high vertical velocity was small; and (3) the mixing after the parcel stopped moving vertically was high.

Figure 5 is a plot of the average reflectivity versus radius. This figure demonstrates that the core or center of the cloud is protected by the sides of the cloud from mixing. Large variations from these averages are noted in both the center and on the edges of the cloud. Comparison of the two curves from time 1250 shows that below the top of the cloud the mixing is more consistent from the sides to the center than at the top. These two layers are separated by approximately 250 meters (14 km 1° elevation change) which suggests enhanced mixing below the bouyant bubble. It was observed that the protected condition of the core rapidly degraded in the regions below the bouyant parcel and also in the parcel itself after the parcel had stopped moving vertically.

Figure 6 is a plot of the observed reflectivity and the reflectivity expected allowing for parcel expansion but no mixing versus the height. An interesting observation from this figure is that the observed reflectivity at the top of the cloud is approximately one-half the reflectivity of the predicted value for the no entrainment case. This means that for the observed parcel equal volumes of environmental and cloud air were mixed together. In terms of what the Q/Qa values would be this means that if the environmental air were completely dry then the Q/Qa of this parcel would be .5. Since the environment is not completely dry the Q/Qa for the parcel should be somewhat higher. It should also be noted that the center of the cloud parcel had a higher reflectivity than the edge (Figure 4) which implies that at the center of the parcel the Q/Qa would be even higher than .5 for the idealized situation of a completely dry environment. This suggests that the mixing observed in these high elevation mountain cumulus clouds is much less than in cumulus clouds of other observational studies where typical values at comparable cloud locations have been reported as approximately .2 (Warner, 1955).

4.2 Mean Velocity Data

The CHILL radar measures the doppler shift resulting from the radial component of the scatter's velocity for the scatters which are in the radar pulse volume. Since the scatters may have different velocities and radial components of those velocities a distribution of velocities are returned to the radar. From this distribution a mean is calculated, and it is this mean that this portion of the analysis concentrates on.

The mean velocity data from the chaff tracer that was transported vertically with the cloud air was studied to determine which levels of the cloud had convergence and which level of the cloud had divergence. At the relatively low elevation angles used, the velocities measured were attributed mainly to horizontal velocities in the clouds. A layer was determined to exhibit convergence or divergence by noting if the side of the cloud closest to the radar had a higher or lower velocity than the side fartherest away from the radar. Figure 7 demonstrates the basic concept with A and B representing the average magnitude of radial velocity in that portion of the cloud.

The procedure described, clearly defined levels of convergence and divergence. This analysis suggests that most levels of mountain cumulus clouds exhibit divergence. There are certain levels, however, where marked

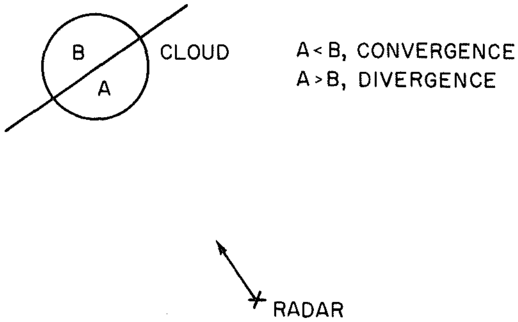

Figure 7. Method used for determining convergence and divergence from mean radial velocities determined by a Doppler radar.

convergence is observed. In several instances the levels of convergence were directly below the level which defined the top of the cloud. Observations of convergence which were not just below cloud top were compared with radar power data to determine if a second thermal might be passing through the existing cloud. The power data showed that the reflectivity in the level above the convergence level was significantly higher. The higher reflectivity may be indicative of a second thermal or bubble. All other levels of actively growing clouds exhibited divergence except for the top level for which neither convergence or divergence could be detected. Also, clouds which were not actively growing did not exhibit any divergence or convergence.

4.3 Turbulence Data

The width and shape of the Doppler spectrum is determined by the distribution of radial velocities of the scatters in the volume being sampled. The width of the velocity spectrum is influenced by turbulence, variable fall velocities of the scatters and wind shear. The spread of the Doppler spectrum due to variable fall velocities is reduced in this study by two factors. One factor is that the scatters in this study are all radar chaff which ostensively all have the same terminal fall velocity. A second factor is that only low elevation angles were used which makes the radial component of vertical velocities very small. The contribution of wind shear to the spread of the Doppler spectrum was estimated using the method of Sloss and Atlas (1968). This calculation showed that the contribution of shear to the spread was an order of magnitude smaller than the contribution from turbulence. Since the contribution of differential fall velocity and wind shear were determined to be small and the spreading due to the radars finite beam width is assumed to be small, the major contributor to the spread of the spectrum is turbulence. For this study, turbulence is assumed to be isotropic.

Figure 8 shows the average variance of the Doppler spectrum for a level in the cloud plotted against the height of that level. The vertical profiles of variance for two clouds are shown. Figure 9 shows the average variance for a single level in a cloud for a time sequence. These two figures

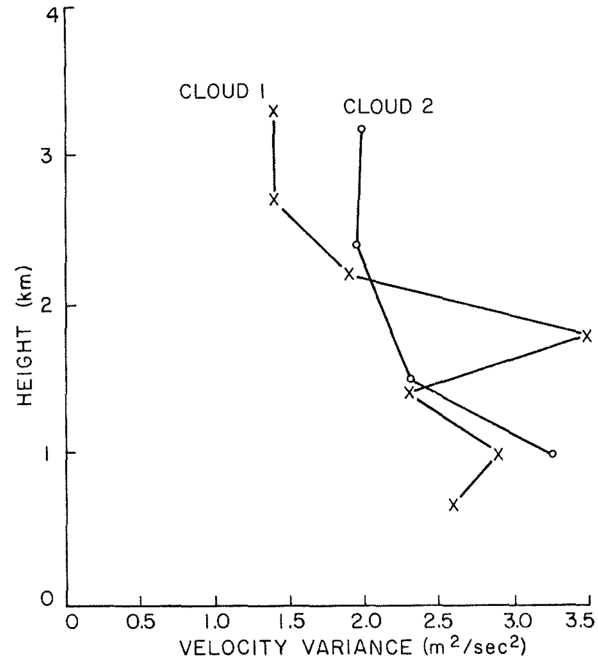

Figure 8. Vertical profiles of velocity variance.

show no trends in the turbulent structure of the cumulus clouds which were studied. Attempts were made to relate the variance of the Doppler spectra to cloud radius, to the vertical position in the lcoud, to the position relative to the cloud top or bubbles, and to areas of convergence and divergence. Relationships of the variance to these physical attributes with respect to time evolution was also investigated. None of the studies showed conclusive results. The magnitude of these data are of interest to cloud modeler and are, therefore, shown in Figures 8 and 9. This data will be analyzed to determine turbulent energy dissipation rates for small mountain cumulus clouds, and these will be used to strengthen numerical simulations of these clouds which are presently being developed in conjunction with the SPACE program. Similar data for clouds in a variety of environments has already been collected during the 1975 SPACE program. Expansion and generalization of the results presented in this paper are expected from analysis of this additional data.

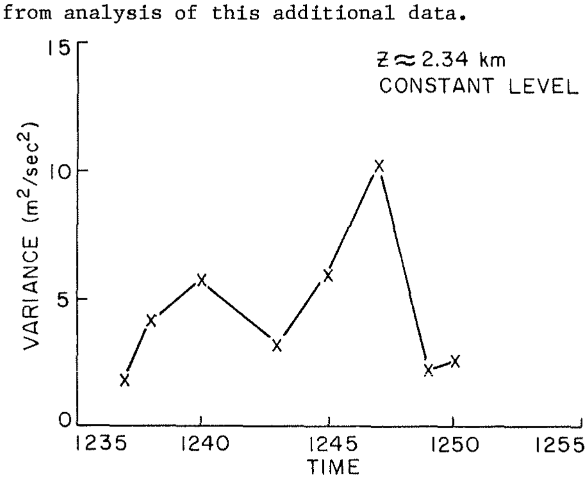

Figure 9. Constant level time series of radial velocity variance for a cumulus cloud.

5. CONCLUSIONS

The chaff tracer reflectivity values observed in this study which utilized the CHILL radar show that the mixing observed for the initial mountain cumulus clouds studied was less than the mixing observed by Warner (1955). This result is in agreement with the other studies of high elevation mountain cumulus which also suggest lower mixing values (Danielson, 1974; Breed, 1976).

The studies of the mixing process indicate that (1) the cloud is more accurately simulated by bouyant thermals than by a steady state jet; (2) that a convergence zone is detected just under the buoyant bubble; (3) that divergence dominates most of the rest of the cloud except for the top which has neither convergence or divergence; and (4) average variances of radial velocities for initial high elevation mountain cumulus clouds is from 1 to 5 m^2/sec^2.

Figure 10 portrays a conceptual model of a cloud which could exhibit these properties. It consists of a bouyant parcel rising with a turbulent wake just beneath the parcel resulting in convergence. An updraft at cloud base following the parcel and divergence over most of the vertical extent of the cloud.

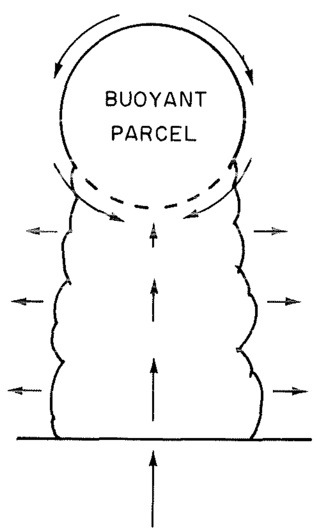

Figure 10. Conceptual model of cumulus cloud air motion.

6. ACKNOWLEDGEMENTS

This work was partially supported by National Science Foundation Grants ERT 71-01885 and DES 75-17313, and by the state of Colorado.

7. REFERENCES

Asai, T., and A. Kasahara, 1967: A theoretical study of the compensating downward motions associated with cumulus clouds. J. Atmos. Sci., 24, 487-496.

Cotton, W. R., 1975: On parameterization of turbulent transport in cumulus clouds. J. Atmos. Sci., 32, 548-564.

Lopez, R. E., 1973: A parametric model of cumulus convection, J. Atmos. Sci., 30, 1354-1373.

Ludlam, F. H., and R. S. Scorer, 1953: Convection in the atmosphere. Quart. J. Roy. Meteor. Soc., 79, 94-103.

Malkus, J. S., 1960: Penetrative convection and an application to hurricane cummulonimbus towers. Cumulus Dynamics, ed. C. F. Anderson, Pergamon, Oxford, 65-84.

Manton, M. J., and W. R. Cotton, 1976: A consistent set of approximate equations for moist deep convection, Part I. To be published in J. Atmos. Sci.

Manton, M. J., and W. R. Cotton, 1976: A consistent set of approximate equations for moist deep convection in the atmosphere, Part II. To be published in the J. Atmos. Sci.

Manton, M. J., and W. R. Cotton, 1976: On the parameterization of rain in cloud models. To be published in the J. Atmos. Sci.

Manton, M. J., and W. R. Cotton, 1976: Parameterization of the atmospheric surface layer. To be published in J. Stmos. Sci.

Morton, B. R., 1968: Non-similar turbulent plumes. Dept. of Mathematics GFDL Paper No. 7, Geophysical Fluid Dynamic Lab., Monash University, Clayton, Victoria 3168, Australia, 50 pp.

Ogura, Y., and T. Takahashi, 1971: Numerical simulation of the life cycle of a thunderstorm cell. Mon. Wea. Rev., 99, 895-911.

Ogura, Y., and T. Takahashi, 1973: The development of warm rain in a cumulus model. J. Atmos. Sci., 30, 262-277.

Schmidt, F. H., 1947: Some speculations on the resistance to motion of cumuloform clouds. Meded. Ned. Meteor. Inst. (b), Deel 1, Mr. 8.

Scorer, R. S., and C. Ronne, 1956: Experiments with convection bubbles. Weather, 11, 151-154.

Scorer, R. S., 1957: Experiments on convection of isolated masses of buoyant fluid. J. Fluid. Mech., 2, 583-594.

Silha, E. G., and E. A. Mueller, 1971: Reflectivity rainfall relationships and reflectivity variability observed with a hybrid video processor. Technical Report, ECOM-0204-F, 66 PP.

Sloss, P. W., and D. Atlas, 1968: Wind shear and reflectivity gradient effects on doppler radar spectra. Preprints 13th Radar Meteor. Conf., Montreal Amer. Meteor. Soc., 297-302

Sommeria, G., 1974: Modele tri-dimensional pour la simulation numeique de la couche limite planetaire. Application a la Couche Limite Tropicale. Ph.D Dissertation, University of Paris.

Stommel, H., 1947: Entrainment of air into a cumulus cloud. J. Meteor., 4, 91-94.

Telford, J. W., 1966: The convective mechanism in clear air. J. Atmos. Sci., 23, 652-666.

Turner, J. S., 1962: The starting plume in neutral surroundings. J. Fluid Mech., 13, 356-368.

Turner, J. S., 1962a: The motion of buoyant elements in turbulent surroundings. J. Fluid Mech., 16, 1-16.

Warner, J., 1955: The water content of cumuliform clouds. Tellus, 7, 449-457.

4.1.7

ALTOCUMULUS AS DISTINCT AIR MASSES IN THE ATMOSPHERE

Marjan Čadež

Faculty of Mathematics and Natural Sciences
Belgrade, Yugoslavia

1. Introduction

During a long period of observations we noticed that the sky often clears up in the evening (see also Hann-Süring 1939 -1951, and Brunt, 1944). It was observed that in these cases clouds transform almost regularly into the altocumulus translucidus (Ac tr) before disappearing. Contrary to the known explanation by Avsec (1939), we suppose here that such a cloud descends as a distinct air mass, through the surrounding air (Čadež, 1948, 1963). At the same time while descending the clouds heat up what causes the water droplets in them to evaporate. Sometimes this phenomenon of descending, can also be detected indirectly by the ground observations. Namely, such conclusion follows from the fact that in these cases the cirostratus transforms into cirocumulus and finally, before disappearing, into altocumulus translucidus.

Ac tr appears in many diverse weather situations. So, at locations where it forms, the atmosphere can be sometimes calm while at some other times the strongest wind can be present. The clouds of this type appear almost always behind the high flying airplanes too (Ludlam, Scorer 1957).

In accordance with the mentioned observations, Ac tr is a cloud composed of small clouds with lower temperature than that of the surrounding air. They are descending while the surrounding lower air which is warmer and unsaturated streams up through the space where the sky is clear. However, we can suppose that these flows of air can get reversed if the small clouds of Ac tr are sufficently heated during the daytime by the direct absorption of solar radiation.

Here we want to explain the described process in more details than it was done in mentioned literature.

2. Equations for Change of Temperature and Water Content in Cloud

We shall consider a part of the cloud which is composed of saturated air having mass m and water-droplets or snow-cristals with mass m_w:

$$M = m + m_w \tag{1}$$

The mass m can further be expressed as a sum of two masses, m_d and m_v, which are related to the dry air and water vapor:

$$m = m_d + m_v \tag{2}$$

Let the total mass M of the considered cloud section as well as the mass m_d of the dry air be constant:

$$dm = - dm_w = dm_v \tag{3}$$

The air is assumed a perfect gas whose temperature T in general case differs from the (mean) temperature T of droplets or ice crystals. In this case the following equation for the added heat (Čadež, 1959) is valid:

$$dQ_M = mc_p dT - Vdp + L(T)dm + c_w(T-T_w)dm + m_w c_w dT_w \tag{4}$$

where

$$mc_p = m_d c_{pd} + m_v c_{pv} \tag{5}$$

and

dQ_M - heat added to the considered system,
c_{pd}, c_{pv} - specific heat for dry air resp. for water-vapour at constant pressure,
V - volume of air mass m,
$L(T)$ - specific latent heat of evaporation at the temperature T,
c_w - specific heat of water.

In our case the last two terms on the

right hand side are relatively small. For this reason we shall neglect them and start from the equ.

$$dQ = c_p dT - \alpha dp + L(T)\frac{dm}{m} \qquad (6)$$

where

α - specific volume of air mass m,
dQ - added heat per unit mass.

The obtained equ. is highly accurate in the case of our system and it becomes exact if $m_w \to 0$. In this case it represents one of the fundamental equations based upon the first low of thermodynamics for saturated air. It would be remarked that the air is assumed to contain a certain amount of water in form of either liquid or ice so that the water-vapour can remains saturated in any process.

A combination of Clausius-Clapeyron equ. and equs. of state for water-vapour and for air yields the following relation:

$$\frac{dm}{m} = Rw\left(A\frac{dT}{T} - \frac{dp}{p}\right)/R_d \qquad (7)$$

where

R, R_d - specific gas constant of the considered air resp. of the dry air,
A - ratio of the latent heat of evaporation to the external latent heat of evaporation,
w - mixing ratio (m_v/m_d).

The expression "external latent heat of evaporation" does not appear in meteorological literature (for example Brunt, 1944, Hess, 1959). However we found it for the first time in the text book by Grimsehl (1938) and also in other books on physics (like Holzmüller, 1966). The external heat $L_e(T)$ can be written approximately as

$$L_e(T) = R_v T \qquad (8)$$

where

R_v - specific gas constant of water vapour.

From equ. (6) and (7) we obtain the equation for change of temperature of saturated air (cloud):

$$dT = (dQ + K\alpha dp)/c_{ps} \qquad (9)$$

where

$$K = 1 + \frac{L(T)w}{R_d T} \qquad (10)$$

and

$$c_{ps} = c_p + AR(K-1) \qquad (11)$$

The obtained value c_{ps} can be interpretated as the specific heat of saturated air at constant pressure (Čadež, 1959).

Eleminating dT from (6) and (9) we obtain the equation for change of water content in cloud:

$$dm_w = - m\Big[\left(c_{ps}-c_p\right)dQ + \left(c_{ps}-Kc_p\right)\alpha dp\Big]/Lc_{ps} \qquad (12)$$

We wish to use equations (9) and (12) to study the development of Ac as it changes the height. For this purpose we take into account that is in our case with sufficient precision

$$\alpha dp = - g dz \qquad (13)$$

where

g - acceleration of gravity,
z - height

Because of that

$$dT = dQ/c_{ps} - \gamma_{as} dz \qquad (14)$$

and

$$dm_w = - m\left(c_{ps}-c_p\right)dQ/Lc_{ps} + mc_p\left(\gamma_a - \gamma_{as}\right)dz/L \qquad (15)$$

Here is

γ_a - dry adiabatic lapse rate (g/c_p)

and

$$\gamma_{as} = Kg/c_{ps} \qquad (16)$$

the saturation-adiabatic lapse rate.

Both, the temperature and the water content depend in large degree on factor K and on the specific heat c_{ps} for saturated air. We present several numerical value for p = 500 mb (Čadež, 1973):

t =	- 40	- 20	0°C	
$c_{ps} - c_p$ =	0,02	0,08	0,33	kcal/kg grad
K =	1,01	1,05	1,24	
γ_{as} =	0,91	0,78	0,51°/100 m	
A =	24,09	21,79	19,84	

Equations (14) and (15) as well as the data presented in the table indicate a great importance of heat exchange with the cloud.

3. Altocumulus as Distinct air mass

"A cloud sheet whose thickness is at least of the order of say 50 meters can be assumed to radiate like a black body" is said in Brunt's text book (1944). This statement already points out the fact that the cloud temperature has to be expected different from the temperature of the surrounding air. The generally known clearing up of the sky in the evenings at various weather situations (for example the days with air-mass thunderstorms) undoubtedly means that then the clouds radiate a large amount of heat energy into upper atmospheric layers and outer space. This further causes relevant changes of temperature and water content of clouds, according to equs. (14) and (15).

A cooled air, i.e. a cloud, descends and during its motion the cloud temperature and the water contents are being effected by both the heat reduction and the atmospheric pressure increase. An estimate of these effects can be obtained from the following calculated example based on equations (14) and (15).

An Ac cloud, composed of droplets, is assumed to be at height where p = 500 mb, T = 253^{o}K and m = 1 kg. In this case we have

$$dT = 3{,}1dQ - 0{,}78dz^{o} \quad \text{and}$$
$$dm_{a} = -0{,}41dQ + 0{,}087dz \text{ gr/kg}$$

Here dQ is given in kcal and dz in 10^2 m. The influence of heat exchange on temperature of the Ac is therefore very important and can significantly effect the cloud development.

Now we are facing an important problem concerning the questions of how the cooled air mass as a cloud moves through the surrounding air, how this effects the shape of the cloud and its growth.

Let us assume that the cloud which is cooler than the surrounding air, initialy takes a spherical shape. Such a cloud now descends at some speed pushing out the air underneath it. Thus the air streams up and around the cloud causing a dynamic pressure depression at its sides. This results into flattering of the cloud and its conversion into altocumulus type (Fig. 1). At the end, this cloud starts splitting, i.e. it transforms from Ac into Ac tr and if the heating due to the descent of the cloud is sufficiently intense the Ac tr disappears.

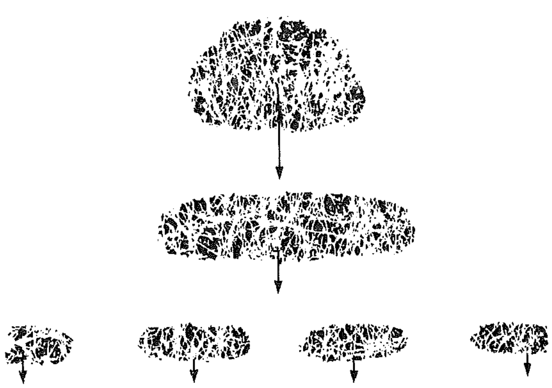

Fig. 1. Shematic presentation of cloud transformation during the descent

Small clouds of Ac tr have well deffined sizes and what the vertical thickness of these clouds depends on, still remains a question that has to be answered. Also the questions whether or not the small clouds stay approximately at the same height and what influences the speed of descent of Ac tr attract our attention, yet we cannot answer them here. In any case it might be expected according to Fig. 2. that the dynamic depressions existing between the small clouds.

$T < T'$ $\qquad p' < p$

Fig. 2. Essential characteristics of temperature, pressure and wind distribution in region of Ac tr

From what we said it can be concluded that altocumulus is a cloud whose temperature differs in general from that of the surrounding air. Such cloud then often moves at various speeds relatively to the ambient medium. To check this mechanism whether it realy exists in the nature, it would be necessary to perform adequate measurements. It would also be worthwille to do related laboratory experiments and in this sense some preliminary attempts were made in the Center for Atmospheric Sciences at the University of Belgrade. Namely, a denser coloured liquid was spread in a thin layer over the surface of water in a tank. Soon a very nice pattern of coloured areas were formed which resembled in certain parts the described atmospheric processes.

We wish to point out that one of the basic atmospheric characteristics is the existence of distinct cold and warm air masses which may have all variety of shapes and sizes. These masses create and disappear under the influence of heating and cooling processes which occur under all kinds of cönditions and at various locations at the ground as well as at the height.

The problem of kinematics of such masses is currently far from being solved and explained. It deserves our special attention and we already derived the related transport equation and the equation of tendency (Čadež, 1966, 1970).

At the end we would call attention to

the work by Vudvord (1964) where the existence of distinct warm air masses in free atmosphere is noticed. Similarly, Karaušev (1969) talks about isolated cold and warm masses in turbulent motions in water.

Acknowledgments. The autor is grateful to his son Vladimir for many helpful suggestions and translation of the manuscript. The author is also indepted to Miss Branka Stevanović for technical preparation and for typing the manuscript.

REFERENCES

Avsec, D., 1939: Tourbillons thermoconvectifs dans l'air - Application a la météorologie. Théses, Série A, 1910, Paris, 184-193.

Brunt, D., 1944: Physical and Dynamical Meteorology. Cambridge at the University Press, 27.

Čadež, M., 1948: O postanku altokumulusa. Astronomska i meteorološka saopštenja, Beograd, 22-24.

——,1959: Uvod u dinamičku meteorologiju - I deo, Osnovi dinamičke meteorologije. Savez studenata PMF Beograd, 78, 85.

——,1963: La formation des nuages Altocumulus translucidus. Geofisica pura e applicata, 54, 182-189.

——,1966: Equation de transport et de diffusion pour l'atmosphére turbulente avec des masses d'air differement échauffées. PAGEOPH, 64, 173-177.

——,1967: Equation générale de transport et de tendence. Geofisica e Meteorologia, 16, 41-44.

——,1973: Meteorologija. Beogradski univerzitet, BIGZ, Beograd, 51.

Grimsehl-Tomaschek, 1938: Lehrbuch der Physik, Band I. B.G.Teubner, 497.

Hann-Süring, 1939-51: Lehrbuch der Meteorologie. W. Keller, 420.

Holzmüller, W., 1966: Technische Physik, Band II, Teil 1 Technische Wärmelehre. B.G. Teubner, 134.

Karaušev, A.V., 1969: Rečnaja gidravlika. Gidrometeorologičeskoe izdateljstvo, 43.

Ludlam, F.H. and R.S. Scorer, 1957: Cloud Study - A Pictoral Guide. John Murray, 78.

Vudvord, B., 1964: in book: Šmeter, F.M., 1972: Fizika konvektivnjih oblakov. Gidrometeoizdat, 17-20.

4.2.1

THE EVOLUTION OF CUMULONIMBUS SYSTEMS IN RELATION TO LOW-LEVEL THERMALLY-DRIVEN MESOSCALE SYSTEMS

William R. Cotton and Raymond L. George

Department of Atmospheric Science
Colorado State University
Fort Collins, Colorado

Roger A. Pielke

Department of Environmental Sciences
University of Virginia
Charlottesville, Virginia

1. INTRODUCTION

The importance of extra-storm scale mesoscale systems to the genesis and propagation of cumulimbus systems is only recently becoming fully appreciated. A number of workers (Malkus and Riehl, 1964; Matsumoto et al, 1967; Lavoie, 1972; and Bhurralkar, 1973) have found that cumulus activity is strongly correlated with mesoscale and synoptic scale convergence zones. Chang and Orville (1973) found that a two-dimensional cumulus model responded much more vigorously and penetrated to a considerable depth when large-scale convergence was imposed on the boundary of the cumulus model. Furthermore, Cotton, Pielke, and Gannon (1976) showed that a one-dimensional time-dependent cumulus model developed a significantly deeper, longer lasting cloud when the initial sounding was replaced by theoretical soundings predicted with the Pielke (1974) mesoscale model in the vicinity of observed cumulus models.

In addition, Cotton et al (1976) found the sea breeze mesoscale system modified the cumulus scale environment by:

1. Increasing the depth of the planetary boundary layer.
2. Inducing larger surface fluxes of momentum, heat, and moisture.
3. Changing the vertical shear of the horizontal wind in lower levels of the atmosphere.
4. Developing intense, horizontal convergence regions of heat, moisture, momentum, and cloud material.

2. INTERPRETATION OF FLORIDA MODELING AND OBSERVATIONAL EXPERIMENT

Still, the primary role of extra-storm scale mesoscale systems is often viewed simply as an initiator of cumulonimbus convection. Once such systems form, they so perturb the planetary boundary layer by means of intense penetrating downdrafts, that the extra-storm scale mesoscale convergence fields are no longer of prime importance. Recently, Pielke (1974) developed a fully three-dimensional mesoscale model of the Florida sea breeze circulation. The sea breeze was initiated and evolved in response to the boundary layer fluxes of heat and momentum and interacted with the large scale flow. The effects of deep, precipitating cumuli and cumulonimbi on the mesoscale circulation were not considered in the simulation. In spite of this neglect, Pielke found that on synoptically undisturbed days with generally weak flow through the depth of the troposphere, the predicted patterns of convergence agreed favorably with the observed locations of clouds and showers throughout an extensive portion of the day. Contrary to the generally accepted view point mentioned above, the agreement between the locations of predicted convergence zones and locations of echo patterns of extensive thunderstorm complexes improved as the day progressed. Figure 1 illustrates such a correspondence.

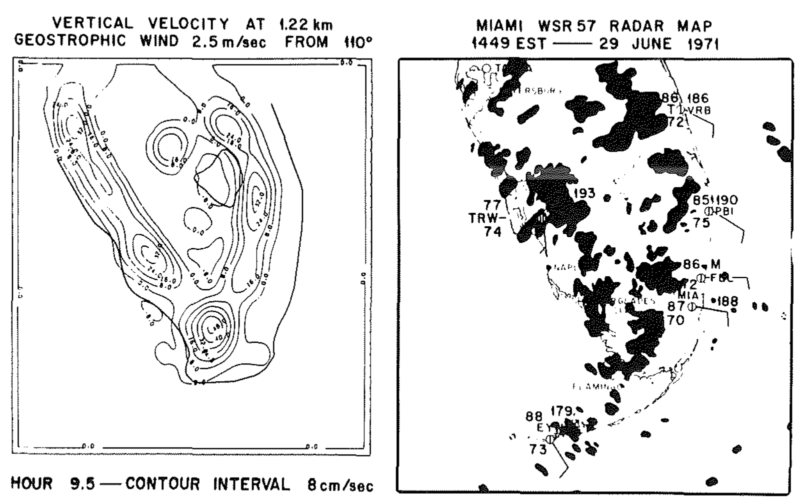

Fig. 1. The model predicted vertical motion field at 1.22 km and the radar echo map at equivalent times for 29 June, 1971.

The interpretation of this result is as follows. Individual cumulus congestus and cumulonimbus clouds can be initiated by small-scale moisture anomalies not necessarily well-defined by a mesoscale model. Once initiated, a cell may survive and propagate by virtue of penetrating downdrafts for periods of 45 minutes to 1 1/2 hours. A complex of cumulonimbus systems, on the other hand, processes so much moisture that they cannot survive for an extensive period (one to three hours) without the enrichment of moisture convergence by extra-storm scale mesoscale systems. This interpretation has been corroborated by the analysis of several case studies, one of which has recently been reported by Cotton and Pielke (1976a,b). In this study, they found that the general complexes of cumulonimbi evolved and migrated across the Florida peninsula in response to the lower tropospheric winds similar to the predictions of the Pielke model. Individual cumulonimbus cells, on the other hand, were observed to propagate in response to deep tropospheric winds 50 to 75 km away from the main centroid of cumulonimbus complexes. In addition, the magnitude of the ratio of eddy transport of moisture at cloud base to the 11 km mean moisture transport was found to be on the order of 2 to 6%. At the same time, it was found that the ratio of eddy kinetic energy to mean kinetic energy ranged from a high of 1700 in the vicinity of cumulus congestus and isolated cumulonimbi to a low of one below extensive cumulonimbus complexes. It is thus seen that thermal scale and cumulonimbus scale eddies make substantial contributions to the kinetic energy budget of the subcloud layer, while the cloud base moisture fluxes are dominated by mesoscale eddies.

3. OBSERVATIONAL AND THEORETICAL STUDIES OF THE COLORADO RIDGE-VALLEY CIRCULATION

We are now in the process of determining whether or now our conclusions from the study of the Florida sea breeze can be generalized to other thermally-driven mesoscale circulations such as the ridge-valley circulation which forms over the Colorado Rockies. As in the case of the sea breeze circulation, the idealized two-dimensional solenoidal field set up by elevated heat sources is fairly well understood. Using a two-dimensional vorticity model, Dirks (1969) showed that a prevailing flow with vertical shear produced a pronounced tilt to the circulation cell above the slope so that part of the cell appeared to break off and form a much larger circulation cell out over the plains. Figure 2 illustrates such a circulation cell. In addition, a simulation of the onset of the nocturál regime demonstrated a strong enhancement of vertical motion over the plains as the downslope flow carried the upper level westerly momentum downward and outward into the plains. This is shown in Fig. 3.

As we have found in the simulation of the Florida sea breeze, the actual three-dimensional flow is considerably more complex. This is particularly true of the mountain-induced mesoscale flow where the complex topography illustrated in Fig. 4 can initiate intense dynamic interactions with the prevailing

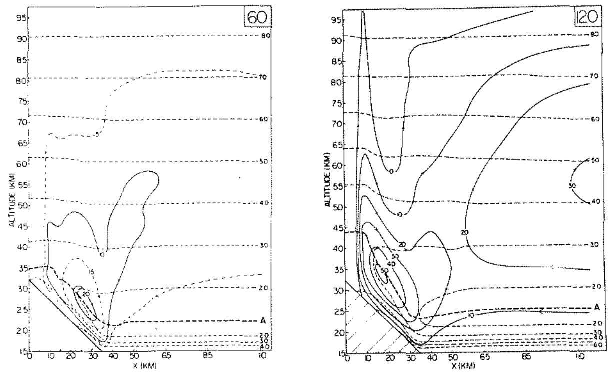

Fig. 2. Evolution of the deviation stream function (solid lines in 10^2 m^2 sec^{-1}) and potential temperature deviation (dashed lines in C deg) fields for Case D. Top of superadiabatic region is shown by heavy dashed line (A).

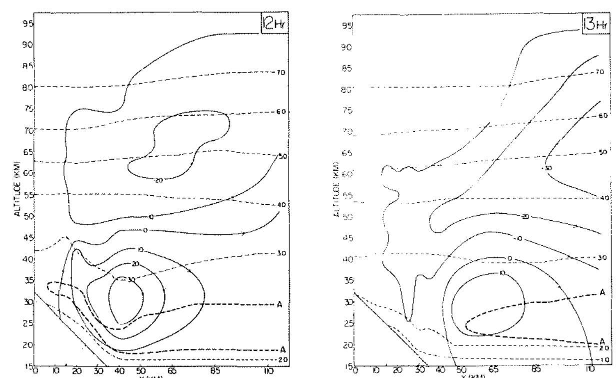

Fig. 3. Evolution of the deviation stream function (solid lines in 10^2 m^2 sec^{-1}) and potential temperature deviation (dashed lines in C deg) fields for Case E. Time is in hours past start of diurnal sine wave.

flow aloft as well as complicated patterns of elevated heating which can drive the upslope flow. To study the spatially and temporally varying pattern of surface temperature, cross sections of surface temperature were measured from aircraft with a Barnes PRT-5 IR radiometer. Figure 5 illustrates an east to west cross section observed at 0900 LST on August 2, 1975, from a point nearly half way between Denver and Colorado Springs, Colorado, over the plains, westward to Leadville, Colorado. The data have been averaged over 11 km intervals and the variance with respect to such an average is shown in Fig. 5c. Not surprisingly, the regions of contrast between the plains and foothills, and mountains and plateau are the regions of maximum temperature variance. What is most surprising, however, is that the South Park elevated plateau heats up considerably faster than any of the surrounding eastward facing slopes or the plains to the east. The magnitude of the difference in temperature between the plateau and the plains to the east reaches its maximum between 0900 and 1100 MST with values greater than 10°C. While the exact reason for the differences in response to solar heating of the relatively horizontal surfaces is not fully understood, it appears to be largely a

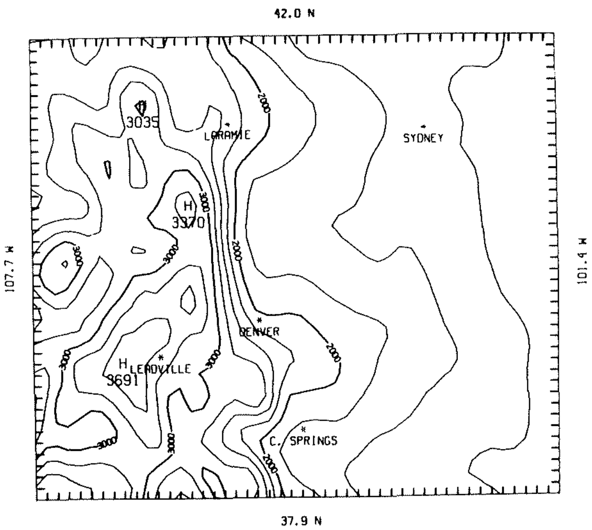

Fig. 4. Smoothed topography (2 and 4Δx trends removed for a 11 km grid) used as input in the Pielke mesoscale model. (contour interval 250 m)

function of differences in thermal inertia of the soil types. The importance of such a temperature difference is even more striking when one realizes that the plateua represents a large-area elevated heat source some 2600 to 4000 feet above the surrounding plains. Thus, it would appear to be a major driving force in the mountain upslope flow.

Another characteristic of the pattern of elevated heating is that the plains to the east rapidly catch up to the elevated plateau exhibiting a surface temperature comparible to the plateau. Shortly after local noon the plateau begins to cool, partly in response to extensive developing cloud cover and precipitation along the higher mountains to the west and partly due to the lower thermal inertia of the plateau soil. During the same period, the plains to the east continue to warm, finally reaching their maximum surface temperature around 1400 LST. Associated with the cooling of the upper level plateau is a reversal in flow from a generally easterly upslope to a prevailing westerly current. The impact of this pattern of elevated heating and associated flow reversal on the genesis of cumulonimbus systems over the western plains will be analyzed by combined numerical experiment with the Pielke model and satellite and radar data analysis.

The SMS-2 satellite photograph at 2145 GMT (1445 LST) illustrated in Fig. 6 shows the extensive cloud cover which shrouds the higher elevations, as well as two preferred regions of convective activity over the western great plains. The regions of cumulonimbus activity are generally located over the Cheyenne ridge to the north and the Palmer ridge to the south. Also of possible importance is the fact that both ridges lie to the east of major plateaus, namely: South Park and North Park.

4. SUMMARY AND CONCLUSIONS

It is clear that thermally driven mesoscale systems such as the Florida sea breeze and Colorado ridge/valley circulations play an important role in the genesis, organization and

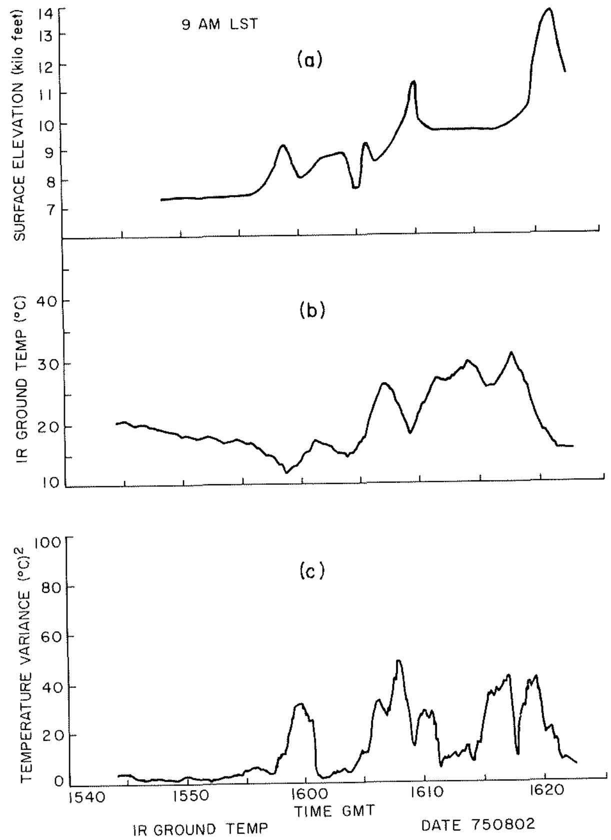

Fig. 5. East-west cross section of IR surface temperature observed at 0900 LST on August 2, 1975. Top represents smoothed elevation of topography. Middle represents 11 km average surface temperature. Bottom represents variance with respect to 11 km smoothed surface temperature.

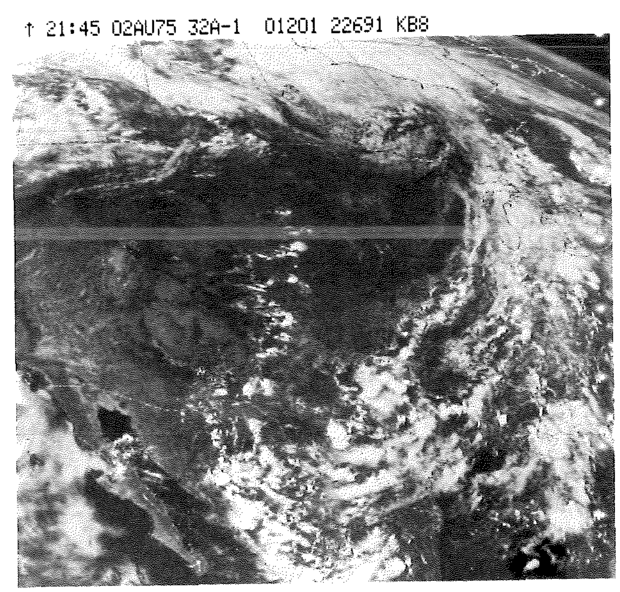

Fig. 6. SMS-2 satellite photograph at 2145 GMT (1445 LST) with 1.85 km resolution .

intensity of cumulonimbus systems. In the case of the Colorado ridge/valley circulation, however, the importance of the circulation to the genesis and propagation of severe storm systems over the western great plains still remains to be demonstrated. The emphasis in the oral presentation will be on the evidence indicating the role of such a circulation in the genesis and propagation of hail producing storms.

5. ACKNOWLEDGEMENTS

A portion of this research was done while Drs. Cotton and Pielke were associated with the Experimental Meteorology Laboratory, NOAA, Coral Gables, Florida. This work was partially supported by National Science Foundation Grants GA-43040X, DES75-17313, and National Aeronautics and Space Administration Grant NSG-5011.

6. REFERENCES

Bhumralkar, C. M., 1973: An observational and theoretical study of atmospheric flow over a heated island. Mon. Wea. Rev., 2, 101, 731-745.

Chang, S., and H. D. Orville, 1973: Large-scale convergence in a numerical cloud model. J. Atmos. Sci., 30, 947-950.

Cotton, W. R., R. A. Pielke, and P. T. Cannon, 1976: Numerical experiments on the influence of the mesoscale circulation on the cumulus scale. J. Atmos. Sci., 33, 2, 252-261.

Cotton, W. R., and R. A. Pielke, 1976a: One day in the life of the Florida sea breeze, Part I: Analysis of mesoscale and synoptic scale observations. Submitted for publication, J. Atmos. Sci.

Cotton, W. R., and R. A. Pielke, 1976b: One day in the life of the Florida sea breeze, Part II: Analysis of sub-cloud fluxes and turbulence spectra. Submitted for publication, J. Atmos. Sci.

Dirks, R. A., 1969: A theoretical investigation of convective patterns in the lee of the Colorado Rockies. Atmospheric Science Paper No. 145, Department of Atmospheric Science, Colorado State University, Fort Collins, Colorado, 122 pp.

Lavoie, R. L., 1972: A mesoscale numerical model of lake-effect storms. J. Atmos. Sci., 1025-1040.

Malkus, J. S., and H. Riehl, 1964: Cloud structure and distributions over the tropical Pacific Ocean. Tellus, 16, 275-287.

Matsumoto, S., K. Nonomiya, and T. Akiyamo, 1967: Cumulus activities in relation to the mesoscale convergence field. J. Meteor. Soc. of Japan, Ser. 2, 45, 292-305.

Pielke, R. A., 1974: A three-dimensional numerical model of the sea breezes over South Florida. Mon. Wea. Rev., 102, 115-139.

4.2.2

AN INVESTIGATION OF THE RELATIONSHIP BETWEEN SURFACE WIND KINEMATICS AND HAILSTORM DEVELOPMENT

J. C. Fankhauser, C. G. Wade, and C. G. Mohr

National Center for Atmospheric Research[1]
Boulder, Colorado

1. INTRODUCTION

Identification of mesoscale atmospheric structure and airflow patterns relevant to hailstorm development and evolution is essential to the effective conduct and evaluation of a hail suppression experiment. A need to locate regions of new storm growth on a near real-time basis arises from research in the National Hail Research Experiment (NHRE) and from earlier hailstorm studies conducted elsewhere. Evidence from case studies of varying storm types (e.g., Browning and Foote, 1976; Browning, et al., 1976) suggests that seeding target regions within the cloud may need to be identified before particles grow to sufficient size and accumulation to produce radar echo. Introduction of artificial nucleants into the newest and weakest updrafts appears to hold the greatest promise for modifying natural hail formation mechanisms from the standpoint of particle competition.

Of the various mesoscale features influencing hailstorm development, surface convergence of air mass and water vapor flux appears to represent one feasible means for improving short-term forecast capability. Streamline confluence zones combined with an adequate low-level moisture supply advecting with an easterly component have proven to be the most consistent subjective indicators of significant convective activity in northeast Colorado (Foote and Fankhauser, 1973; Chalon, et al., 1976). More directly, thermodynamic observations at cloud base indicate that air feeding the updrafts supporting hail growth regions generally originates in the lowest part of the boundary layer (Marwitz, 1972a; Fankhauser, 1976).

Since the roots of convection frequently lie near the surface we should anticipate a correlation between the magnitude of the surface convergence and the favored regions of new storm growth. This paper investigates the relationship between the patterns of radar echo development and surface wind and moisture distributions observed in conjunction with one of the heaviest hail-producing storms since the inception of the NHRE experiment, the case of 7 August 1974. Estimates of horizontal mass convergence derived from streamline, isotach and isogon analyses of surface mesonetwork winds are correlated in time and space with the location of new echo growth and with the evolution of the overall storm system to test the utility of surface mesonetwork observations in predicting regions of new cloud growth.

2. GENERAL DESCRIPTION

2.1 Large-scale Features

On 7 August 1974 the 500-mb charts showed a large cyclone located over the northern portions of the western Canadian Provinces with a trough of fairly large amplitude extending southward into Montana and Idaho. At the surface a cold front of Pacific origin lay from the western Dakotas into eastern Wyoming. Slow eastward progression carried it into northeastern Colorado and the NHRE area by late afternoon.

A sounding representative of thermodynamic conditions and wind shear in the vertical for the region south and east of the storm development is shown in Fig. 1. Surface air and average low-level mixing ratio result in saturation for a lifted air parcel near 640 mb (3.8 km MSL)[2]. Reports by seeding aircraft operating near cloud base agree closely with this estimate of cloud base height. The pseudo-adiabat (Θ = 341°K) representative of cloud base temperature (Θ = 316°K) and moisture conditions (8.2 g kg^{-1}) indicates that the temperature of undiluted parcels ascending in updrafts could be as much as 3°C higher than that of the environment near the 500-mb level.

Wind vectors on the right of Fig. 1 show a southeasterly flow of around 5 m sec^{-1} in the lower two-thirds of the sub-cloud layer and light westerlies from that height upward to cloud base altitude. The flow in the cloud-bearing layer was west-southwesterly averaging near 15 m sec^{-1}. Wind shear in the cloud layer, extending from 3.8 to ~14 km was rather weak (~1 x 10^{-3} sec^{-1}) and characteristic of the shear typically associated with multicell thunderstorms (Marwitz, 1972b).

[1]This research was performed as part of the National Hail Research Experiment, managed by the National Center for Atmospheric Research and sponsored by the Weather Modification Program, Research Applications Directorate, National Science Foundation.

[2]All subsequent references to height will designate height above mean sea level (MSL).

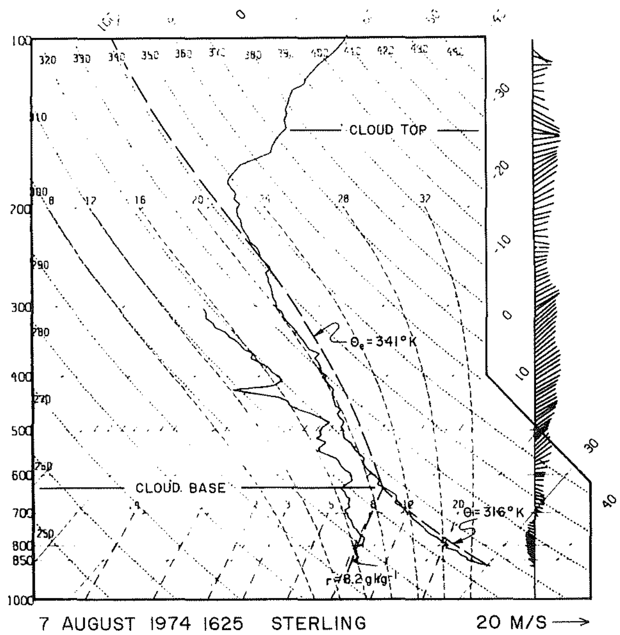

Figure 1. Temperature and dew point curves (irregular, solid) from sounding at Sterling, Colo., 7 August 1974, at 1625 MDT, with wind vectors on the right. Dry and moist adiabats and mixing ratio representative of cloud base conditions are shown as long dashed curves. Pressure altitude of cloud base and cloud top are indicated.

2.2 Radar Echo Development and Movement

Analysis of the high resolution radar reflectivity data from the Grover research radar indicated that storm developments on this day could be treated in three fairly distinct phases:

2.2.1 Phase I (1300-1500 MDT)[3]

First radar echoes of the day appeared at around 1300 from thundershowers developing a few kilometers north of the Grover radar site. A multicellular system comprised of cells oriented in a north-south line soon formed. By 1530 this line had moved in an easterly direction to a position over the NHRE target area (the region where storms were seeded on a randomized basis) shown in Fig. 2. During this period the line evolved in two distinct modes. First, existing cells continually evolved with discrete new echo development occurring in close proximity (within 2 to 5 km) on their right-forward flanks. This gave persistence to line elements for periods longer than the time required for air to move through individual cells as described in the classical single-cell model of Byers and Braham (1949). Second, new cell development took place on the south end of the line at distances of 5 to 15 km away from existing line components. Overall storm motion during Phase I was toward the ESE, and thus to the right of the cloud-layer winds. This movement was the combined result of the advection of existing cells in the general direction of the cloud-layer ambient winds and a progressive growth to the south contributed by propagation through new cell development at the line's southern end. This behavior exemplifies squall line models already well-documented in the literature (e.g., Newton and Fankhauser, 1964).

[3]All subsequent references to time will designate Mountain Daylight Savings Time (MDT).

2.2.2 Phase II (1500-1630)

Between 1500 and 1530 a significantly stronger and more persistent cell developed about 10 km south of the existing line and moved to a position identified as cell M at 1530 in Fig. 2. Subsequent cells merged with it and by 1600 a very intense storm approaching the supercell category had formed. Storm motion changed perceptibly at this time as the steady ESE progression of Phase I changed to a considerably slower motion toward the SE.

2.2.3 Phase III (1630-1730)

Development of the most intense cell of the day occurred during this period over the southeast portions of the grid shown in Fig. 2. Definite supercell characteristics were observed with a large single-cell radar echo structure and a transitory vaulted weak echo region.

In addition to the storm developments already mentioned, two other major events took place. After 1730 a new line of vigorous cells formed ahead of the system described in Phases I-III at the leading edge of the outflow boundary shown schematically in Fig. 2. As this line was moving out of the sphere of surveillance represented by the grid in Fig. 2, a new but weaker

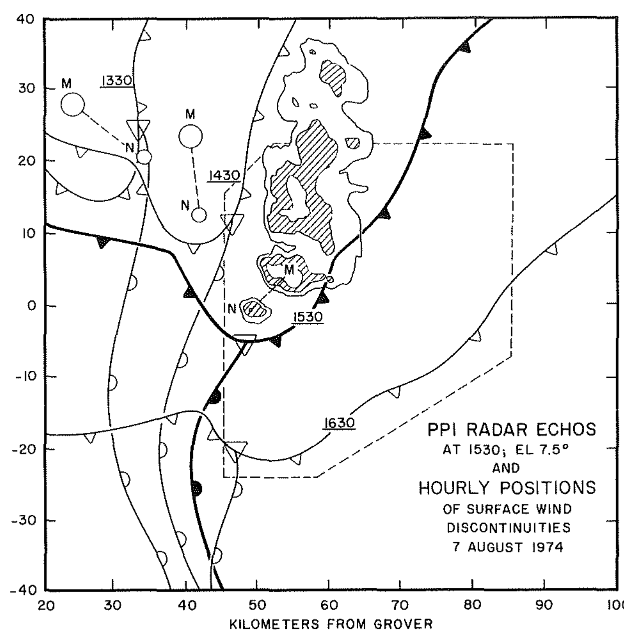

Figure 2. PPI radar echoes at 1530 from Grover radar; antenna elevation, 7.5°. Reflectivity contours are in 1 dB intervals above 25 dBZ. Lines with barbs and warm front symbols denote, at the specified times, the leading edges of thunderstorm outflow and warm dry air, respectively. Inverted triangles show intersection of these air masses with moist air to the southeast. Letters M and N identify locations of mature and new echoes at 1530. Equivalent locations and separations are shown schematically at earlier times. Interior dashed boundary shows location of the NHRE target area.

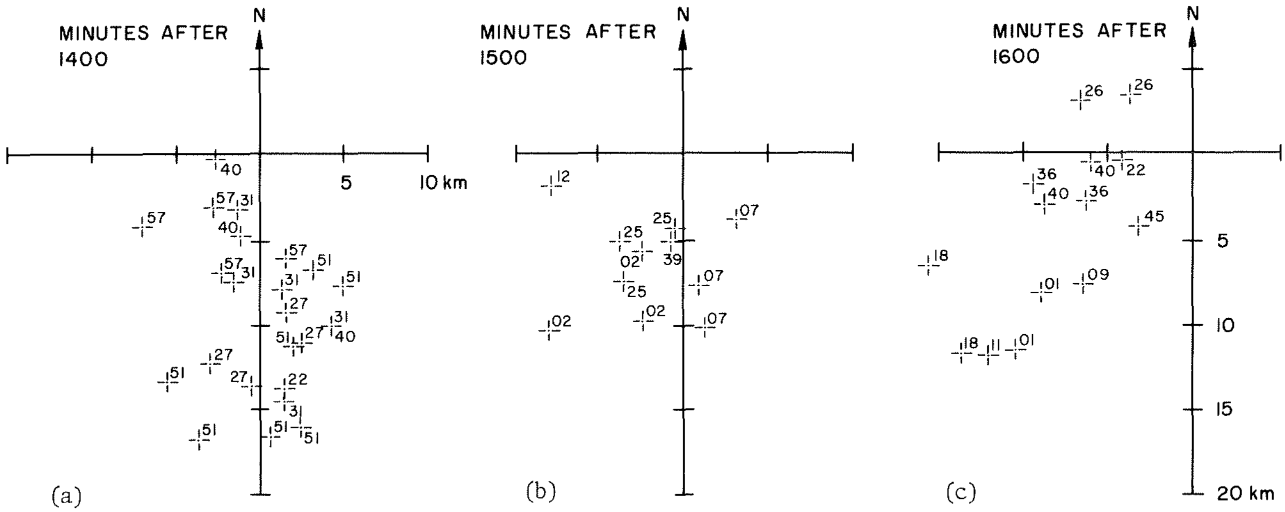

Figure 3. Crosses show the location and time of detection of new echo formations in minutes after the hours of (a) 1400, (b) 1500, and (c) 1600, relative to the nearest mature echo element whose position at any time is represented by the center of the coordinate system.

line formed on the western edges of the area and moved rapidly eastward through the grid. This latest development was apparently associated with the arrival of the cold front mentioned in Section 2.1.

Since events related to the developments associated with Phases I and II occurred over the western and central portions of the grid where surface observations discussed in a following section are more dense, we will focus our discussion on events observed during these earlier phases.

2.3 Characteristics of Individual Cells

During Phase I and in the early part of Phase II new cells appeared with a frequency of 1 every 5 to 10 min and at a preferred distance of 5 to 15 km from existing echo in a quadrant to the south. They generally formed in an altitude range of 6 to 7 km (-12° to -15°C) and at maturity echo tops attained heights of 13 to 14 km. Cells moved generally along the direction of middle level winds (Fig. 1) but their speed was about half that of the ambient flow. The average time interval from first echo appearance to maximum reflectivity near the ground was on the order of 20 to 30 min. This is comparable to the typical period of cell evolution found in other multicellular storm studies (Renick, 1971; Chalon, et al., 1976).

The location of new echo formation with respect to mature or maturing line components is shown for three one-hour intervals in Fig. 3. The origin represents the nearest maturing echo having a radar reflectivity of $\geq$ 45 dBZ, and the relative positions of new echo at the time of first detection are shown as a function of time after the designated hour. In addition to showing the favored location of new cell development, data in Fig. 3 indicate that the cell development cycle decreased with time from about 5 min in Phase I to around 10 to 15 min in Phase II.

For the period 1400-1500, new echo developments are clustered in the southerly quadrant and centered in the range of 5 to 15 km from existing mature neighbors. With time (Figs. 3b and 3c) the favored location of new echo formation shifts from south to southwest (1500-1600) and eventually to west-southwest (1600-1700). This phenomenon is shown schematically for selected times in Fig. 2 by the relationship between features lettered M and N. M represents the mature or maturing cell at any time while N shows the location of the newest echo formation.

3. SURFACE KINEMATICS

3.1 Surface Wind Patterns

Figure 2 shows the history of wind discontinuities associated with the boundaries between three distinct air masses. One, located over the southeast portion of the grid is characterized by comparatively moist air having mixing ratio (r) typically between 7 and 8 g kg^{-1}. This air mass was advecting from the southeast, in agreement with the winds in the lowest layers on Fig. 1. The leading edge of outflow air originating from downdrafts within the storm is shown as a barbed front. A third air mass of distinctly drier (r = 5 to 7 g kg^{-1}) and somewhat warmer air lay over the western portion of the grid. This air presumably originated from katabatic flow off the foothills to the west of the NHRE area. Its eastern boundary is symbolized as a warm front. These three air masses join to form a "triple point" similar to the terminology coined by tropical meteorologists to describe the intersection of three different air masses. Their intersection in this case is marked for the various times by an inverted triangle in Fig. 2.

Although earliest echo formations occurred outside the coverage of the mesonetwork observations, they appear to have been triggered by the convergence at the boundary between the moist southeasterlies and the drier westerlies. The triple point was probably not present in these early stages and formed only after the generation of downdrafts from the earliest cells.

Detailed analysis of the surface wind field is shown at 1445 in Fig. 4. This time was chosen when the positions of discontinuities lay

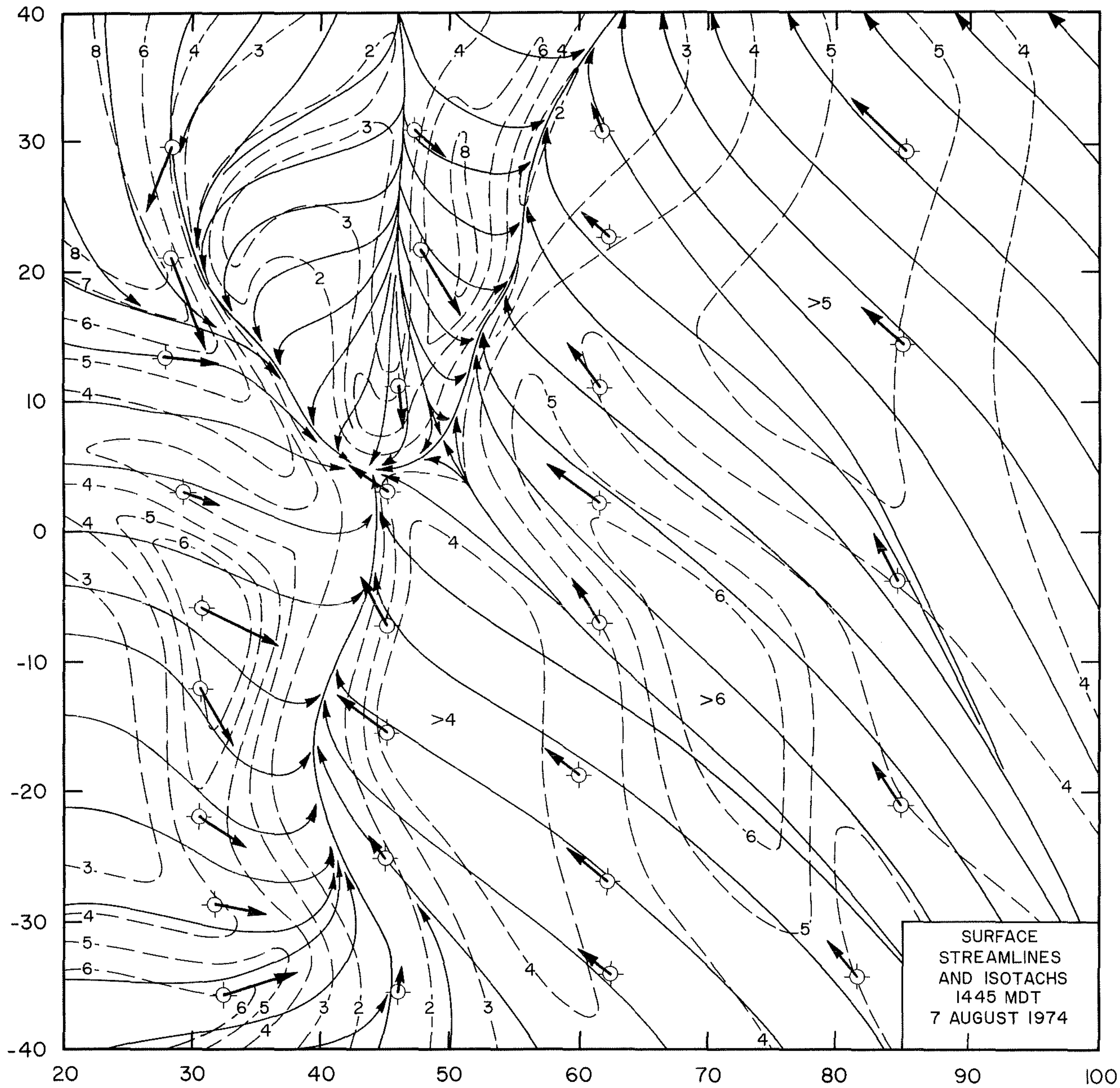

Figure 4. Surface streamlines (solid) and isotachs (dashed) at 1445. Vectors (1 m sec^{-1} $\equiv$ 1 km) representing 1-min wind averages are plotted at the designated mesonetwork sites. Border is labeled in kilometers from the Grover field site.

close to a number of mesonetwork sites which recorded analog wind data across the transition zones. This enabled incorporation of time-to-space transformation of data from these sites to obtain added resolution in areas where the flow was most complicated. Off time data used at each station were displaced according to the local speed of the outflow boundary. A general description of the NHRE surface mesonetwork and a brief discussion of data reduction techniques is given by Nicholas and Fankhauser (1975).

Comparison of features appearing in Figs. 2, 3 and 4 reveals some qualitative correlations between the surface wind fields and the radar echo development patterns discussed in the previous section. Figure 2 shows that at any time there is close agreement between the location of the surface triple point and the favored region of new cell growth. This correlation is strengthened by noting that as the triple point moves with time from the storm's right-forward sector to its right-rear sector the clusters of new echo formations in Fig. 3 show a corresponding shift.

3.2 Surface Divergence Patterns

In this section we seek to establish a quantitative measure of the surface convergence which might fortify the qualitative relationships between the surface flow fields and radar echo development patterns identified in the previous section.

Streamline and isotach fields, as analyzed in Fig. 4, were converted from analog to digital form using a Bendix Datagrid line follower. Streamline coordinates were used to compute isogons numerically and, after objective interpolation of isogon and isotach fields, wind data were obtained at 2-km intervals on an equal-area grid of dimensions 80 x 80 km. From these the kinematic divergence equation in Cartesian form was evaluated straightforwardly.

Figure 5 shows the results of the divergence (units of 10^{-3} sec^{-1}) calculated at 1445, a time late in the period of Phase I. Middle-level (∿7.5 km) PPI echoes at a scan time closest to the time of surface analysis are also shown with the position of surface wind discontinuities as in Fig. 2. Three distinct zones of convergence (shaded regions with light solid contours) are detected; the strongest being at the boundary between moist southeasterly flow and the outflow from maturing and mature cells (again designated by the letter M). The next strongest maximum is found to the rear of the mature cells along the boundary between aging outflow air and the dry westerly current. Confluence toward the triple point (Fig. 4) contributes to the third identifiable maximum located 10 to 15 km south of the mature echoes.

Maximum surface divergence (lightly dashed contours) is comparable in magnitude to that of the strongest convergence and is associated with the oldest echo elements. Here spreading downdrafts are presumably strongest due to the dominance of precipitation processes late in the cell's evolutionary cycle.

The elongated convergence maximum at the leading edge of the outflow undoubtedly plays a role in sustaining convection in the regions of highest radar reflectivity and probably provides the mechanism for developing new growth adjacent to existing cells as was observed frequently in Phase I. The second largest convergence center is located in a region (relative to the active parts of the storm) which is likely to be thermodynamically unfavorable for convective development. The air there was probably more statically stable due to convective overturning by the mature cells. Whatever the cause, no new radar echoes were observed to form in this locale.

A region where dynamic and thermodynamic features complement one another is probable, however, in the vicinity of the third convergent zone. A free access to the highest surface moisture exists here, as well as a possible dynamic driving mechanism of the type proposed by Newton and Newton (1959). We refer to the possibility of vertical non-hydrostatic pressure gradients conducive to vertical accelerations in the southern sector of existing storms.

Lacking adequate three-dimensional data to verify any of the above concepts we see at least a strong correlation between the convergent zone at the surface triple point and the location of new cell growth (N in Figs. 2 and 5). From evidence in Figs. 2 and 3 the link between this surface flow feature and the favored region of new cell growth appears to hold throughout Phase I and early into Phase II of the system's overall development. Late in Phase II these correlations began to break down. Although we

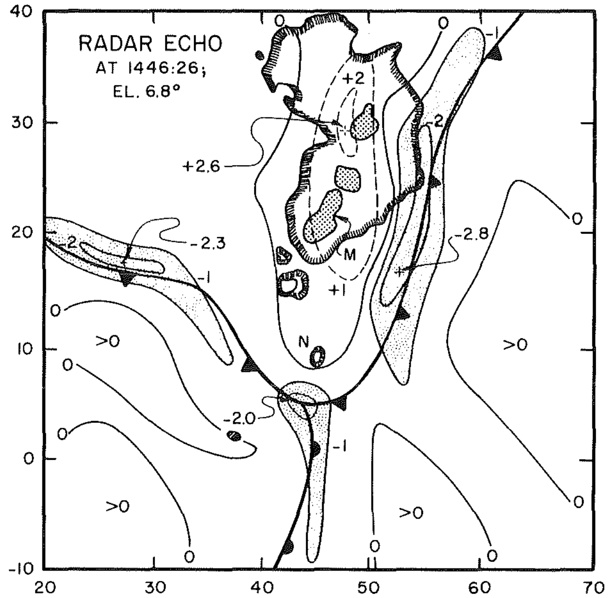

Figure 5. Contours of surface convergence (light, shaded) and divergence (light, dashed) in units of 10^{-3} sec^{-1}, from wind analysis in Fig. 4. Wind discontinuities as in Fig. 2. Outer PPI echo contours designate radar reflectivity of 25 dBZ and stippling shows locations of strongest embedded cells.

have not yet examined the convergence patterns for this later period, progression of the surface outflow boundary to greater and greater distances away from the location of active cells seems to relate to the perceptible change in the storm's character observed late in Phase II and in Phase III.

4. SUMMARY AND CONCLUSIONS

We have noted a strong correlation between a unique surface wind feature and the location of nascent radar echoes associated with a major hailstorm in northeast Colorado. Although we know from overall developments on this day that the simple relationships tested here were not applicable to all stages of storm development, the evidence presented suggests that experimental seeding programs dependent upon identifying regions of new cloud growth in near real-time can benefit from access to mesoscale wind information on an operational basis. A capability for real-time wind assessment exists in the Portable Automated Mesonetwork being tested by the NCAR Field Observing Facility in the NHRE research operations this summer. Assessment of its utility as an operational tool capable of identifying surface features such as those treated in this paper is pending.

Browning, K. A., J. C. Fankhauser, J.-P. Chalon, P. J. Eccles, R. G. Strauch, F. H. Merrem, D. J. Musil, E. L. May, and W. R. Sand, 1976: Structure of an evolving hailstorm, Part V: Synthesis and implications for hail growth and hail suppression. To appear in Mon. Wea. Rev., 104 (in press).

_____, and G. B. Foote, 1975: Airflow and hail growth in supercell storms and some implications for hail suppression. To appear in Quart. J. Roy. Meteor. Soc., 102 (in press).

Byers, H. R., and R. R. Braham, 1949: The Thunderstorm. U. S. Government Printing Office, Washington, D. C., 287 pp.

Chalon, J.-P., J. C. Fankhauser, and P. J. Eccles, 1976: Structure of an evolving hailstorm, Part I: General characteristics and cellular structure. To appear in Mon. Wea. Rev., 104 (in press).

Fankhauser, J. C., 1976: Structure of an evolving hailstorm, Part II: Thermodynamic structure and airflow in the near environment. To appear in Mon. Wea. Rev., 104 (in press).

Foote, G. B., and J. C. Fankhauser, 1974: Airflow and moisture budget beneath a northeast Colorado hailstorm J. Appl. Meteor., 12, 1330-1353.

Marwitz, J. D., 1972a: The structure and motion of severe hailstorms. Part I: Supercell storms. J. Appl. Meteor., 11, 166-179.

_____, 1972b: The structure and motion of severe hailstorms. Part II: Multi-cell storms. J. Appl. Meteor., 11, 180-188.

Newton, C. W., and J. C. Fankhauser, 1964: On the movements of convective storms, with emphasis on size discrimination in relation to water-budget requirements. J. Appl. Meteor., 3, 651-668.

_____, and H. R. Newton, 1959: Dynamical interactions between large convective clouds and environment with vertical shear. J. Meteor., 16, 483-496.

Nicholas, T. R., and J. C. Fankhauser, 1975: The resolution of surface kinematic features of thunderstorms. Preprints, Second Conf. on Wind Engineering Research, Ft. Collins, 22-25 June 1975, pp. II-8-2 to II-8-4.

Renick, J. H., 1971: Radar reflectivity profiles of individual cells in a persistent multicellular Alberta hailstorm. Preprints, Seventh Conf. on Severe Local Storms, Amer. Meteor. Soc., Boston, 63-70.

4.2.3

DISCONTINUOUS ASPECTS OF THE GROWTH OF A CLOUD FROM CuCg to CuCb STAGE

Daniel Ramond, CNRS
Dominique Tixeront

L.D.M.A.

Université de Clermont-Ferrand

France

1. INTRODUCTION

Since the Thunderstorm Project – Byers, Braham (1949)–a number of efforts have been made to improve the knowledge of the structure and the behaviour of storms. Detailed case studies–Fujita (1958), Browning and Ludlam (1960), Chisholm (1970), Marwitz and Berry (1970), Fankhauser (1971) etc – have permitted to recognize different types of storm behaviour – Marwitz (1972) – and to propose well documented and synthesized models for some of them – Browning and Ludlam (1962), Newton (1967)–.

However all these studies were related to storms in their fully mature stage, and very little is known about the early stage of growth. Such a lack of information prohibits partially an actual and realistic classification of the initial conditions which are favorable to deep convection.

The purpose of this paper is to present a case study of a storm in its very early stage of growth, from the time it was a 1500 m deep Cumulus, up to the first hail precipitations.

Simultaneous measurements were made with an AMOR-DC7 aircraft*, the instrumentation of which included a vertically stabilized PPI 3 cm radar, and with terrestrial equipments such as photogrammetric automatic cameras, Rawin-sondes, and a 10 cm radar which was operated by the Institut et Observatoire de Physique du Globe (I.O.P.G. Clermont-Ferrand).

2. CLERMONT-FERRAND STORM, MAY 23, 1973

2.1 Synoptic and local situation

On May 23, 1973, a low-gradient situation with a pressure rising tendancy was prevailing over the French territory where a number of isolated hailstorms were reported.

The Clermont-Ferrand storm developed in the morning and was studied between 9 h 30 and 11 h 15 GMT. Soundings made in the vicinity of the storm are shown on fig. 1. The winds were veering slowly from 230° at the ground to 250° at tropopause level, with a constant vertical wind shear of $3.8 \times 10^{-3} sec^{-1}$

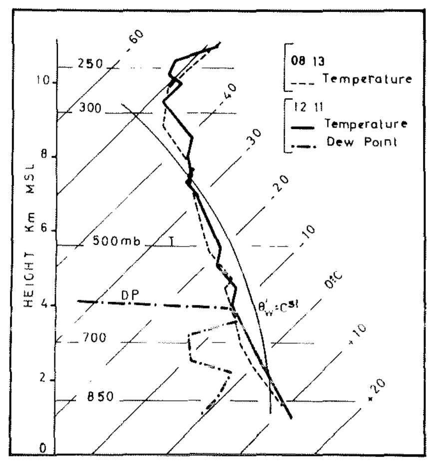

Figure 1. Storm environment soundings of temperature and dewpoint (0813, 1211)

2.2 Storm history

The study of the storm with the AMOR DC7 aircraft started at the very beginning of its growth stage. At that time, it was still an isolated cumulus no more than 1500 m in depth, and gave no echo on the scope of the DC7 airborne radar.

Fig. 2 gives a schematic description of the evolution of the cloud up to the first hail precipitations, as deduced from radar and photographic data. The mature stage appeared to be reached by a discontinuous process, involving four successive cells, in a row, which, in the following, will be referred to as cells A, B, C and D ; the new cells formed, every 10 to 15 minutes, on the upwind flank of the preceding one, as the old ones dissipated downwind and merged in an anvil drifting with the wind aloft.

The maximum altitude reached by the cells increased from 6000 m MSL for cell A to 7500 m for cell D. The cloud system yielded continuous precipitations below base, starting at 9 h 57 under cell A and it is to be noted that hail has been reported under cell C though

*The AMOR DC7 aircraft is sponsored and operated by the Direction des Recherches et Moyens d'Essais and by the Centre d'Essais en Vol/Brétigny.

its top never went higher than the -35° C isotherm level.

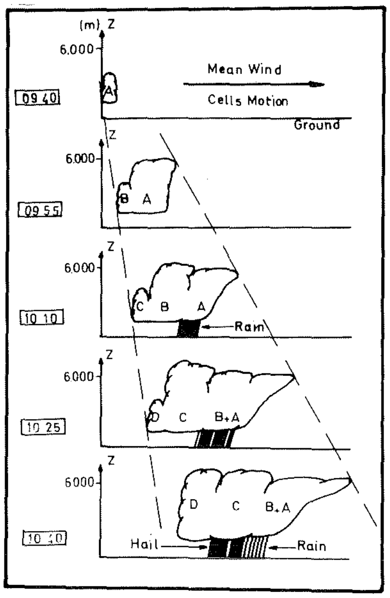

Figure 2. Schematic history of the first four cells of Clermont-Ferrand storm, deduced from radar, airborne and terrestrial cameras.

On fig. 3, contours of radar echoes photographed on the AMOR-DC7 scope, have been drawn at four instants corresponding to each step of the growth. It can be seen that above 4000 m at least, the cells echoes remained distinct except late in their dissipation stage.

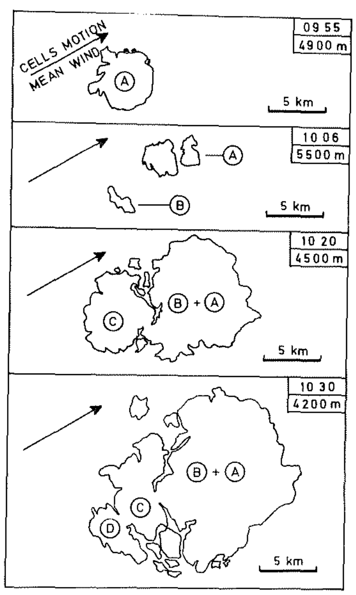

Figure 3. Radar echo contours at various instants of the early stage of growth the Clermont-Ferrand storm.

Cell D was the last of the row, but about 10 h 30, a new cell E formed on the right flank of the system and revealed to be the first cell of a new row parallel to the previous one, and presenting the same periodical scheme of development.

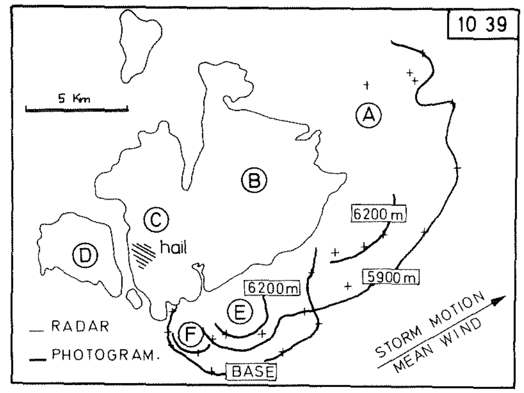

Figure 4. Radar echo contour at cloud base - thin lines - and isolevel contours of the visible cloud - thick lines - as deduced from photogrammetry. Cross marks are measured points.

On fig. 4, data from the AMOR-DC7 radar and from terrestrial stereophotogrammetry are combined to exemplify this extension of the cloud system on its right flank. At 10 h 39, time of the photographs, the AMOR DC7 was flying around the cloud system at 200 m above cloud base and the elevation angle of the radar antenna was set to zero ; the cloud system was positionned about 35 km to the North West of the pair of automatic cameras.

It can be seen on fig. 4 that the radar echoes of cells D, C and B had remained distinct even at base level while the new cloud row, constituted at that time of only two cells E and F, the later being no more than 1200 m deep, gave no radar echo near base though the tops of cell E had reached the height of 6500 m. Four minutes later, at 10 h 43, pea-size hail was encountered by the aircraft as it was exploring the subcloud layer. The area where hail was encountered is indicated on fig. 4, by a dashed area, situated at the rear of cell C and just downwind of cell D.

For technical reasons, measurements on the Clermont-Ferrand storm had to be stopped at 11 h 10, as the second cloud row counted three cells, E, F, G, each of them having reached altitudes higher than 8000 m MSL. Cells A and B had merged in the anvil and cell D echo was slowly dissipating while remaining distinct from C near base level. The later cell, on the contrary had strengthened and its radar echo at base level was merging with that of cell F. Pea-size hail was reported at the ground along its track.

Nevertheless visual observations indicated that the discrete propagation process of the storm on the right flank kept on with time.

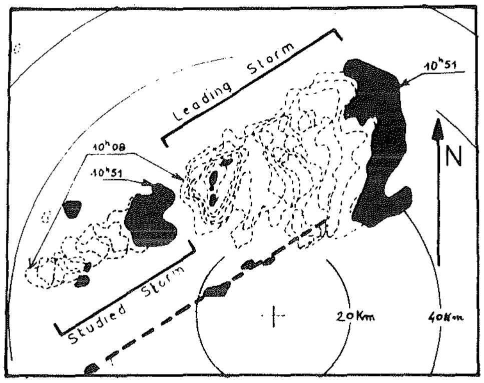

Figure 5. Successive 10 cm radar echoes between 1008 and 1051. Thick doted line indicates a dense line of small cumuli.

Fig. 5 shows successive outlines of the IOPG 10 cm radar echoes of the studied storm at an elevation angle of 2°. It appears that the Clermont-ferrand storm followed exactly the track of a more matured storm which exhibited the same propagation process on its right flank. At 10 h 51, a "hook", as described by Browning (1965) and Marvitz (1972) was clearly visible on its southern edge. Note that during the observations period, the northern flanks of both storms didn't dissipate and remained on the same line parallel to the mean wind andto a continuous and persistant row of short life cumuli which was followed by photogrammetry, as it moved, as a whole, in the mean wind direction. Some of the cumuli constituing this row started to yield radar echoes about 11 h 00.

3. HORIZONTAL SPEED OF INDIVIDUAL CELLS. PERIODIC FLUCTUATIONS.

3.1 Radar analysis - Cells A, B, C, D

Due to the wide spread angle of the IOPG radar antenna (4°), it proved to be impossible to separate on the scope the individual echoes of the cells in the cloud system. The AMOR-DC7 radar, which was always operating in the vicinity of the cloud, was thus used for analysing the horizontal speed fluctuations of each cell.

The scope was photographed every minute in the average, and the shutter release time was recorded to a 1/10th of a second. Using a localisation DELTA system, the aircraft xy-position was known at every instant with an accuracy better than 50 m while the magnetic heading was recorded every 1/10th of a second with a mean .5° accuracy. By selecting various samples of the scope photographs including either all of them, or every second or every third, and averaging the echo centroīds speeds computed from each sample, the final error on the horizontal speed of individual cell echoes was minimized : its maximum value was estimated to 1.5 m sec^{-1}.

The horizontal speed fluctuations of the echo centroīds fo cells A, B, C and D are plotted versus time on fig. 6. As the aircraft altitude was varying during the measurements, and in order to eliminate errors due to eventual echo tiltings or over hangings, the analysis was restricted to layers less or equal to 500 m in depth, for each cell, as indicated on fig. 6. The curves reveal a periodicity of about 10 mn. It is also to be noted that, at least for cells A and C, a speed decrease was measured when a new echo with a lower horizontal speed was appearing upwind. The dotted part of curve C corresponds to the part of the cell C echo just downwind of the new cell D. The right and left flanks of C were actually moving with a slightly higher speed.

The maximum horizontal speed attained by each cell echo was approximatively equal to the environment wind speed at the level of measurements. Thus, during most of its active stage, each cell acted as an obstacle to the environment wind, a fact that has already been noted by various authors for larger storms - Newton (1959, 1963), Hitschfeld (1960), Schmeter (1966), Alberty (1969), Fankhauser (1971). It seems also that each cell acts as a protective barrier against the wind for the cell situated just downwind of it.

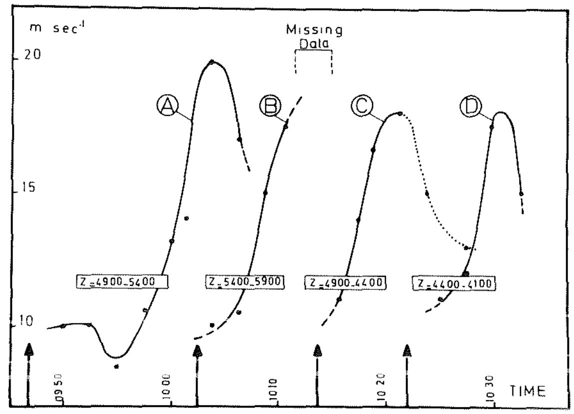

Figure 6. Horizontal speed of the DC7 radar echoes of the successive cells A, B, C, D. Vertical arrows indicate time of appearance of new well-defined echoes upwind.

3.2 Photogrammetric analysis. Cell E

After 10 h 35, the DC7 was ordered to explore the subcloud layer and cell E was analysed by terrestrial photogrammetry. Fig. 7 gives the outlines of the Clermont-Ferrand storm at 10 h 49. Cells E and F were clearly visible on the storm right flank as well as the anvil in which A and B were merging and dissipating (see also fig. 4). In order to characterize the evolution of cell E, four points have been selected which were identifiable for more than 20 minutes. They are numbered from 1 to 4 on fig. 7.

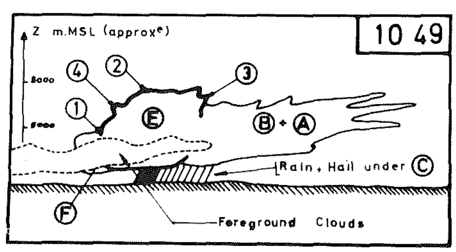

Figure 7. Outlines of the Southeastern flank of the cloud viewed from one of the photogrammetric stations. Points 1, 2, 3, 4, see text.

Point 1, which is the only point not related to a material cloud parcel, is defined as the lowest distinguishable upwind point. Its altitude has never been less than 4700 m due to the masking of low level clouds in the foreground, or the merging of the visible upwind boundary of cell E with the growing cell F.

Point 2 is a materiel point near top.

Point 3 is the farest downwind point.

Point 4 is an ascending protuberance on the upwind flank.

The heights of these points are plotted versus time on fig. 8, between 10 h 30 and 11 h 00. The measured horizontal components of motion of all the points revealed to have the same direction as mean wind but values varying from point to point and with time, as indicated on fig. 9a.

A close examination of fig. 8 and fig. 9a leads up to the distinction of three phases of evolution for cell E :

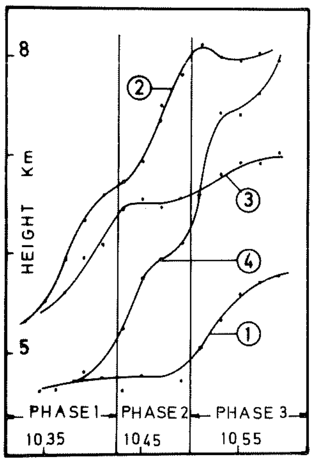

Figure 8. Altitude of cell E selected points versus time

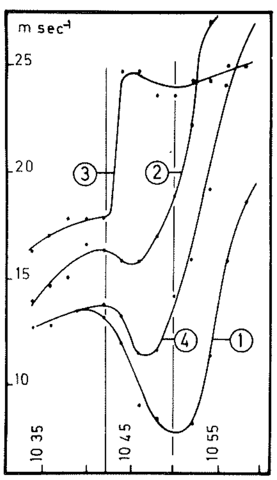

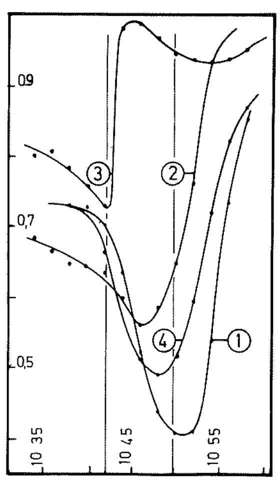

Figure 9a. (left) Horizontal speed of cell E selected points, versus time

Figure 9b. (right) Horizontal speed of cell E selected points reported to wind speed at their level, versus time.

Phase 1 : from 10 h 30 to 10 h 38 the vertical velocity of points 2, 3 and 4 - i.e. cell top, downwind and upwind flanks respectively- was approximatively the same (see fig. 8) while the cell diameter increased, as it can be seen by comparing the horizontal speed of points 3 and 4 (fig. 9a). As compared to the lowest upwind point 1, the horizontal velocity of point 4 increased during its ascent, indicating that the cell was slightly tilting downwind. Fig. 9b, where horizontal speeds are reported to the wind speed at the points levels, shows that the speed of all the points was comprised between 60 and 80 per cent of the environment wind speed.

Phase 2 : from 10 h 38 to 10 h 50, the vertical velocity of the downwind flank (point 3), decreased down to a quasi zero value while its horizontal velocity became equal to the environment wind speed (fig. 9b). The upwind flank kept on rising (point 4, fig. 8) but its horizontal velocity decreased sharply (points 1 and 4) down to 40 or 50 % of the environment wind speed, which suggests that the cell was building up on the upwind flank against the wind. It was about the end of this phase that cell F grew rapidly.

Phase 3 : from 10 h 50 to 11 h00 the altitude of the top of cell E stabilized as the horizontal velocity of all the points tended to become equal to the wind speed at their level (fig. 9b). This phase corresponded to the beginning of the dissipation stage while the new cell F was still in its growing stage.

It results from these data that cell E acted as an obstacle for the environment wind, as it was noted above cells A, B, C, D. More over, these data suggest that such a fact is not only due to a mere transport of lower horizontal moment by rising parcels from the subcloud layer, an hypothesis which couldn't, alone, give a satisfactory explanation of the sharp decrease in the upwind flank horizontal speed during Phase 2.

Aircraft measurements inside cell E might have given the key of the production process of a horizontal momentum component directed windward. In default of these measurements, the analogy between cell A and cell E may nevertheless authorize an extrapolation to cell E of the data collected inside cell A.

As a matter of fact, both cells were the first of a row, and the horizontal speed fluctuations of the centroïd of the cell A echo, represented on fig. 5, are very similar to that of a mean point of cell E, such as point 2 of fig. 9 a, for example.

4. A HORIZONTAL COMPONENT DIRECTED WINDWARD IN THE UPDRAFT

Between 9 h 38 and 10 h 02, four penetrations inside cell A have been performed, at various altitude, by the AMOR-DC7. The data have already been succintly analyzed by Ramond (1975). One of the penetration, however, will be re-analyzed here after in more detail. It took place at 9 h 55, at an altitude of 4900 m MSL - same as that of point 1 of cell E (fig.8) - when the horizontal echo speed was at a minimum (see fig. 5) - i.e. in the middle of phase 2 if the analogy with cell E holds.

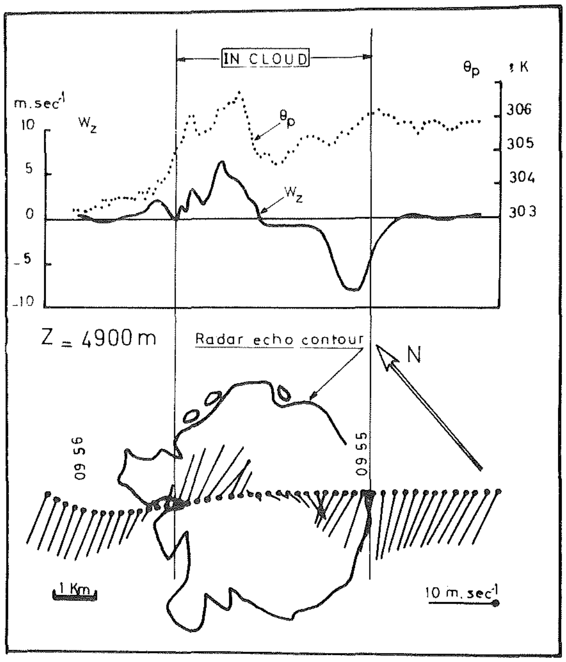

Figure 10. Penetration in cell A. AMOR-DC7 flight track and horizontal winds are relative to the radar echo motion. Potential temperature θ_p and vertical air velocity W_z fluctuations along the track are drawn in the upper half.

Fig. 10 shows the flight track and the horizontal wind vectors relative to the motion of the echo deduced from fig. 6. A critical examination of the Doppler winds, for this case, has been made by Ramond (1975) and concluded to the representativeness of the measured winds inside cell A. The Doppler winds are computed every tenth of a second, averaged over a second and then filtered with a running mean over 5 points. The vertical air velocity plotted on fig. 10, contrary to that given earlier (Ramond, 1975), has been corrected for pilot action, according to a method described by Tixeront (1976) and based on an a posteriori calibration of the pitch and incidence angles correlation.*

It can be seen on fig. 10 that the updraft had a horizontal momentum component in the upwind direction. In the downdraft, on the contrary, the horizontal momentum component is in the direction of the wind. However no rotation was observed on the successive echoes, but a stretching in the downwind direction was clearly visible. Since the echo motion, at the time of the penetration, was about equal to the mean wind in the subcloud layer, the relative horizontal momentum in the updraft cannot be explained by a transport from the lower layers but must have been created during the ascent of the air parcels.

The total momentum in the updraft region, computed from the measured vertical air velocity and the Doppler winds, is plotted versus time on fig. 11, along with the vertical component. The bell-shape curve of the total momentum suggests that at a given level, the updraft had a constant momentum except along the edge where mixing is expected, and that the horizontal momentum is produced by a transfer process from the vertical component.

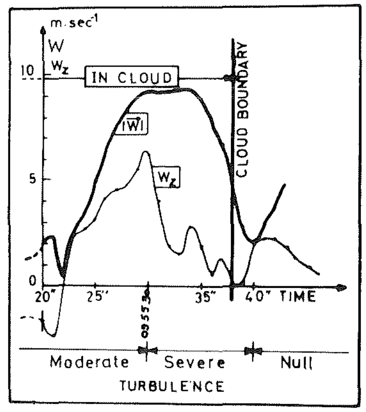

Figure 11. Vertical component of the wind (W_z) and total wind (W) within the updraft zone.

5. ROLE OF PRECIPITATION WATER CONTENT IN A WIND SHEARED CELL

Among all the possible processes which may cause the transfer of momentum from vertical to horizontal component in a wind sheared updraft, the most obvious seems to be the weight of the precipitation water content.

Strivastava (1962) using a one dimensional model showed that the rising concentration of precipitation water content aloft might lead to the inhibition of the updraft, but that the cloud could start a new cycle of life as soon as the precipitations has fallen to the ground. In a wind shear, due to entrainment, the updraft tilts downwind as it can be inferred from the above analysis of phase 1 of cell E (fig. 9a) and the problem is at least two-dimensional. However, a process similar to the one described by Strivastava may apply to explain the behaviour of a wind sheared updraft as that of cells A and E.

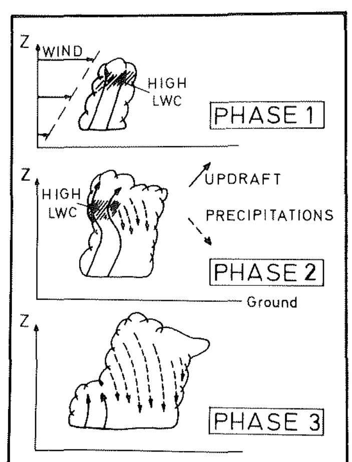

Figure 12. Double mechanism of vertical to horizontal momentum transfer in a tilted updraft, and of generation of a new cell on the upwind flank.

Fig. 12 illustrates schematically the proposed mechanism, in three steps corresponding to the three phases of development of cell E.

* In 1973, the AMOR DC7 was not equipped with incidence vane.

Phase 1 : the cloud grows and tilts downwind due to entrainment and drag. A high liquid water content zone forms aloft in the updraft. No precipitation water content is yet present in the cloud.

Phase 2 : the precipitation water content begins to fall through the downwind part of the updraft, transfering downward its higher horizontal momentum. The downwind part of the cloud stops to rise. Air parcels rising in the updraft and encountering an excessive resistance resulting from drag forces in the precipitation zone, deviate toward the upwind flank. The cloud builds up against the wind and the high liquid water content - and consequently the precipitation zone - is extended windward by the updraft. The precipitation falling from this new extended LWC zone are likely to inhibit the updraft near its root.

Phase 3 : a downdraft establishes in most of the cloud, starting from aloft. But as the downdraft carries down a higher horizontal momentum than that of what remains of the updraft in the lower levels, a horizontal separation of the two occurs. The updraft starts a new cycle and generate a new cell on the upwind flank.

This scheme assumes that the successive two cells share the same updraft root at cloud base, an assumption which has been experimentally verified by photogrammetric data on cells E, F and G.

6. CONCLUSION

Researches are still in progress on the Clermont-Ferrand storm, in order to clarify several points which are not yet clearly understood.

One of these points is the fact that only one of the four first cells actually gave hail precipitations and persisted for a much longer time than the others, acting as the nucleus of the building up storm. Cell to cell interactions are investigated.

An other point to be clarified is the appearance of a different process of growth characterized by a discrete propagation on the right flank which seems to take place as the mature stage is reached.

However, it has been shown, for the case studied above, that the storm growth process, in the early stage was a periodic generation of new cells on the upwind flank. This process has been related to the role of the precipitation water content combined with a wind shear.

7. BIBLIOGRAPHY

Alberty, R.L., 1969, Monthly Weather Review, vol. 97, n° 8, p. 590-596.

Browning, K.A., 1965 : A family outbreak of severe local storms. A comprehensive study of the sotrms in Oklahoma on 26 May 1963, Part I. Special Rept n° 32, AFCRL-65-695(1),346p.

____ and Ludlam, F.H., 1962 : Airflow in convective storms, Quarterly Journal of the Royal Met. Soc., vol. 88, n° 376, p.117-135.

____ and Ludlam, F.H., 1960 : radar analysis of a hailstorm, Tech. Note n° 5, Contract AF61 (052)-254, Dept of Met., Imperial College, London, 109 pp.

Byers, H.R., and Braham, R.R., 1949 : The thunderstorm, Report of the Thunderstorm Project, US Air Force, U.S. Navy, U.S. National Advisory Comittee for Aeronautics, and U.S. Weather Bureau, Washington D.C., 287 pp.

Chisholm, A.L., 1970 : Alberta Hailstorms : a radar study and model, Ph. D. Thesis, Dept of Meteorology, McGill University, 237 pp.

Fankhauser, J.C., 1971 : Thunderstorm-environment interactions determined from aircraft and radar observations, Monthly Weather Review, vol. 99, n° 3, pp. 171-192.

Hitschfeld, W, 1960 : The motion and erosion of convective storms in severe vertical wind shear, Journal of Meteorology, vol. 17, n° 3, pp. 270-282.

Marwitz J.D., 1972 : The structure and motion of severe hailstorms, Part I, II, III, Journal of Applied Meteorology, vol. 11, N°2, pp. 166-201.

____ and Berry, E.X. : The weak echo region and updrafts of a severe hailstorm, Preprints of Papers, Fourteenth Radar Meteor. Conf., Tucson, Ariz., Amer. Meteor. Soc., pp. 43-47

Newton, C.W., 1963 : Dynamics of severe convective storms, Meteor. monogr., n° 27, pp. 33-58

____ 1967 : Severe convective storms, Advances in Geophysics, vol. 12, pp. 257,308.

Ramond, D., 1975 : Variations du vent horizontal à l'intérieur de cellules convectives, Journal de Recherches Atmosphériques, vol. 9, n° 4, pp. 77-85.

Strivastava, R.C., 1967 : A study of the effect of precipitation on cumulus dynamics, Journal of Atmospheric Sciences, vol. 24, n° 1 pp. 36-45.

Tixeront, D., 1976 : Developpement rétrograde et pulsatoire d'un cumulonimbus, Thèse de Docteur-Ingénieur, Université de Clermont-Ferrand, pp. 87.

ACKNOLEDGEMENTS

This research was supported by the Délégation Générale à la Recherche Scientifique et Technique - convention n° 73.7.1325 -, by the Direction des Recherches et Moyens d'Essais - convention 73.34.430 -, and by the Centre National de la Recherche Scientifique.

We are deeply indebted to Pr. Soulage who inspired the best of this work, and we would like to express our appreciation to Mr Pierre Billet for doing a fine job in preparing the figures.

4.2.4

Microstructure of a CuCg cloud

J.F. GAYET

Laboratoire de Dynamique et
Microphysique de l'Atmosphère

Université de Clermont-Ferrand
(France)

1. INTRODUCTION

Only a few measurements have been published since yet on the detailed evolutionary microstructure of CuCg clouds over a wide range of droplet sizes, with a high spatial resolution. Nevertheless, such data would be required to understand the time history of ordinary CuCg cloud not too long in duration, not covering too large an areal extent. In the present paper, I just intend to briefly describe the microstructure of a CuCg cloud as deduced from in situ measurements at different levels and times, with an AMOR-DC7 aircraft (x). Apart from thermodynamic and dynamic sensors, and a 3cm PPI radar, AMOR-DC7 was instrumented with three Knollenberg's spectrometer probes (2) (Axially Scattering Spectrometer Probe : ASSP, $3 \leqslant D$ (xx) $\leqslant 45\mu m$; Optical Array Cloud Droplet Probe : CDP, $20 \leqslant D \leqslant 300\mu m$; Optical Array Precipitation Spectrometer Probe : PSP, $300 \leqslant D \leqslant 4500\mu m$) and with a Total Water Content Probe (General Eastern - Model 184B) similar to the one described by Ruskin (4).

2. EXPERIMENTAL DATA

2.1. Meteorological background and flight procedures

Fig. 1 shows a sounding launched in the cloud environment. The wind was backing from 90° at the ground to 230° at the tropopause level. The CuCg cloud has been developing in the lower zone, of negative vertical wind shear (fig. 1).

The measurements were begun at the time the cloud reached its maximum altitude (4700m MSL, cf. fig. 1). The AMOR-DC7 flight track is plotted in fig. 2.

The successive penetrations within the cloud are denoted by thick lines and numbered 1 to 6. The cloud boundaries along the flight track have been accurately located in relation to the sharp discontinuities observed in the particle counting, with a zero concentration just out of the cloud. From the DC7 radar echoes and from the successive positions of the cloud boundaries along the flight track, the mean horizontal velocity of the cloud has been estimated to be 7m/s-195°,giving a global motion to the left of the mean wind in the cloud layer.

Penetrations were performed at four different levels (n°1 : 4340m, n°2 : 3990m, n° 3 and 4 : 3420m, n° 5 and 6 : 2760m MSL). As the data of only two out of the three Knollenberg's probes could be recorded at a time, the measured diameter range for each penetration laid either from 3 to 300μm (ASSP-CDP) or from 20 to 4500μm (CDP-PSP). During the penetrations 1, 2, 3 and 5, the ASSP-CDP data were recorded whereas for the penetrations 4 and 6 it was the CDP-PSP set which was operated.

2.2. The spatially heterogeneous features of the microstructure

Only the data relative to the 3420m and 2760m levels will be discussed in the following. As a matter of fact, two successive penetrations were performed at each of these levels with different sets of Knollenberg's probes (ASSP-CDP and CDP-PSP) which yielded quasi-simultaneous measurements over the whole diameter range 3 to 4500μm.

On fig. 3 to 6, the fluctuations of various parameters measured during penetrations 3 to 6, are plotted along the flight track ; namely : the drop concentration C, the mean volumic diameter D_o, the liquid water content T_w and the radar reflectivity R which are all computed from the recorded spectra. The flight track is plotted with the DC7 3cm radar echo contour at the time and level of the penetration. The fluctuations of potential temperature TP, the mixing ratio RM, the vertical air velocity WA and the horizontal absolute Doppler wind module VH are also reported on fig. 3 to 6

(x) The AMOR-DC7 aircraft is sponsored and operated by the Direction des Recherches et Moyens d'Essais and by the Centre d'Essais en Vol/Brétigny.

(xx) D = drop diameter

At the 3420m MSL level (penetrations 3 and 4 on fig. 3 and 4) the vertical velocity field within the cloud is characterized in the southern part by important positive fluctuations whereas these fluctuations are damped in the northern part.

At the 2760m MSL level (penetrations 5 and 6 on fig. 5 and 6), the southern part of the cloud is no more characterized by important vertical velocity fluctuations, which is indicative of the great variability encountered either in space or time. On the opposite side, the northern part of the cloud exhibits a light turbulence comparable to the one measured at the 3420m MSL level.

As opposed to the vertical wind field the cloud microstructure exhibited a noticeable persistence of its overall features from one penetration to the next. Fig. 7 represents for penetration 3 the UV signal of the total water content probe along the flight track.

As already shown (1), such a recording gives a qualitative idea of the horizontal distribution of large drops with high amplitude peaks of frequency about 10Hz (aircraft speed = $100 m.s^{-1}$) superimposed on the mean signal, denoting the presence of large drops with a low concentration.

The total water content probe recordings obtained during penetrations 4, 5 and 6 are very similar to the one presented on fig. 7. We can note on fig. 7 that in the southern part of the cloud (refered to as zone A), the UV signal fluctuations of high frequency have a low amplitude. This fact suggests that no large drops were present in this part of the cloud, which is confirmed by the Knollenberg's probe data recorded simultaneously (fig. 3). Zone A is constituted with small drops with a concentration of $50 cm^{-3}$ and a mean volumic diameter D_o = 6µm. An average spectrum sampled in zone A is given on fig. 8 (ASSP set) ; this sample does not extend beyond 15µm with a peak at 3µm. Visual observations aboard the AMOR-DC7 have also suggested that the southern part of the cloud (zone A) was an active bulging zone, which is coherent with the microstructure measurements collected in this zone and discussed above.

A further examination of fig. 7 reveals a sharp discontinuity in the microstructure at the centre of the cloud (zone B). The large fluctuations of the UV signal indicate the presence of large drops. This change of the microstructure is also displayed on the concentration and mean volumic diameter curves of fig. 3 and 5. The mean volumic diameter reaches its highest value : 200µm, whereas the drop concentration falls down to 2 cm^{-3}.

Though penetration 3 (or 5) has been performed with the ASSP-CDP set(restricting the measured diameter range to 300µm), penetration 4 (or 6) performed with the CDP-PSP set immediatly after and at the same level than 3, yielded a UV trace similar to that of penetration 3 (fig. 7), effectively indicating a higher liquid water content ($4 g/m^3$ on fig. 4) located in the centre of the cloud (zone B). An averaged spectrum representative of this zone is shown on fig. 9. It can be seen that the spectrum extends towards the large drop diameters (4500µm), with a bimodal distribution centered on 220 and 3000µm.

It is to be noted that the spectra simultaneously measured by the CDP and PSP (fig. 9 for example) -or by the ASSP and CDP- are overlapping from 150 to 300µm, and that the data in this range must theoretically be similar. In fact, it has be shown (1) that the data of the first channel of each probe are to be taken with caution and that comparisons in the overlapping range are not significant. Nevertheless, this does not affect the fact that large drops were present in zone B which seems to indicate that the latter corresponds to a more mature stage of the cloud.

As to the northern part of the cloud (zone C) it is characterized by a total water content probe UV signal which exhibited high frequency fluctuations of lesser amplitude, the mean value of which were decreasing from the centre to the boundary of the cloud (fig. 7). The liquid water content and the mean volumic diameter as deduced from Knollenberg's probe spectra recorded in this zone are also decreasing from the centre to the boundary of the cloud (fig. 4 and 6). Fig. 10 represents an averaged spectrum for zone C. This spectrum is bimodal and centered on 20 and 200µm approximatively. As compared with the spectra relative to zone B, the peak diameters are considerably reduced. This observation in connection with the fact that no significant vertical velocities were measured in zone C during the period of study suggests that zone C is a dissipating zone in which mixing and evaporation were occurring.

3. CONCLUSION

Though the measurements have been made at different times and different levels, the horizontal heterogeneity of the microstructure of a CuCg cloud is quite obvious. Three adjacent zones can be distinguished :

- An active zone (zone A) characterized by new cells on the southern flank of the cloud (i.e. downwind). This observation agrees with the results obtained by Malkus (1952) about the growth of CuCg clouds in a negative wind shear. This zone is inherently unsteady and it may be difficult to compare measurements performed within it at different times and levels. This has proved to be true for the vertical velocities ; on the contrary, the microstructure has proven to be more steady in character from one penetration to the next. (cf. fig. 3 and 5, zone A). This suggests a greater relaxation time for the microstructure than for the dynamics of the cloud. Entrainment and the subsequent evaporation contributing perhaps to the slowing down of the drop growth.

- A mature zone (zone B) located in the centre of the cloud, the main feature of which consisting of a high liquid water content associated with large drops. This may be attributed to a longer life time of this part of the cloud, an hypothesis which leads one to consider zone B as being in an intermediate stage of the cloud growth.

- A dissipating zone (zone C). This zone as previously seen is relatively stable as far as dynamics is concerned. The bimodal aspect of the microstructure in this zone, as well as in zone B seems to be in good agreement with some results obtained by Warner (1969) in different CuCg clouds. However, the shifting of the diameter peak of the bimodal spectra as compared with those in zone B, may lead to the hypothesis that zone C represents the final stage of evolution of each part of the cloud, stage during which mixing and evaporation processes are prevailing.

4. ACKNOWLEDGMENTS

I am indebted to Professor R.G. SOULAGE for his leading role in the experiments and my colleagues, in particular, D. RAMOND and R. ROSSET for their suggestions and critics of the manuscript. This study was supported by the Direction des Recherches et Moyens d'Essais (Contract n° 73-34-430), by the Délégation Générale à la Recherche Scientifique et Technique (Contract n° 73-7-1325) and by the Centre National de la Recherche Scientifique.

5. REFERENCES

(1) GAYET J.F., 1976, Physique de la mesure du spectre dimensionnel des gouttes de nuages au moyen des capteurs de Knollenberg, Thèse de 3ème Cycle, Université de Clermont-Ferrand, pp. 53.

——— , 1976, Structure microphysique d'un cumulus congestus, Thèse de 3ème Cycle, Université de Clermont-Ferrand, pp. 23.

(2) KNOLLENBERG R.G., 1969, The optical array : an alternative to scattering or extinction for airborne particle size determination, Jour. of Appl. Met., vol. 9, pp.86-103.

(3) MALKUS J.S., 1952, Recent advances in the study of convective clouds and their interaction with the environment, Tellus, vol. 4.

(4) RUSKIN R.E., 1966, Measurements of water-ice budget changes at -5C in AgI-seeded tropical cumulus, Jour. of Appl. Met., Vol. 6, pp. 72-81.

(5) WARNER J., 1969, The microstructure of cumulus cloud. Part I : General features of the droplet spectrum, Jour. of Atmos. Sci., Vol. 26, n° 2, pp. 1049-1059.

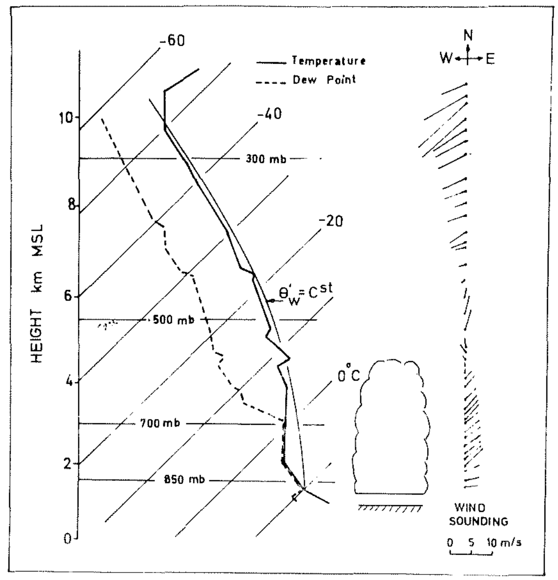

Fig. 1 - Cloud environment sounding (june 11, 1975 ; 14.35)

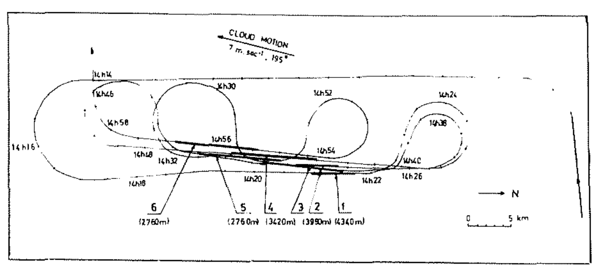

Fig. 2 - The AMOR-DC7 flight track. The penetrations, numbered from 1 to 6, are referred to by thick lines on the flight track.

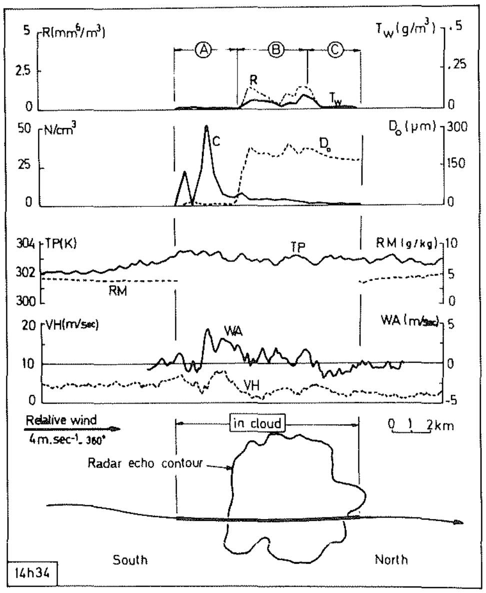

Fig. 3 - Penetration 3 - Height : 3420m MSL - Knollenberg's spectrometer probes : ASSP-CDP (see text for legend)

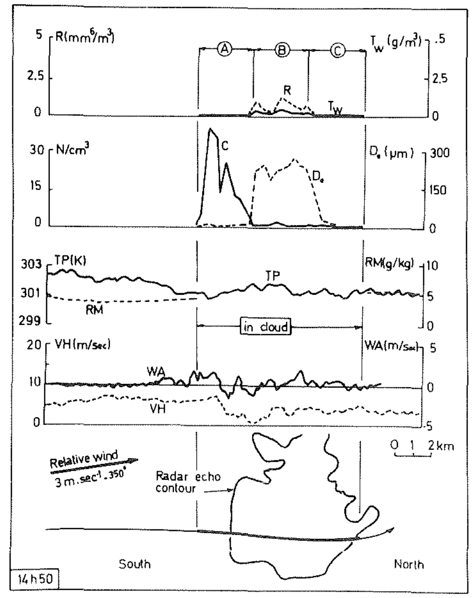

Fig. 5 - Penetration 5 - Height : 2760m MSL - Knollenberg's spectrometer probes : ASSP-CDP (see text for legend)

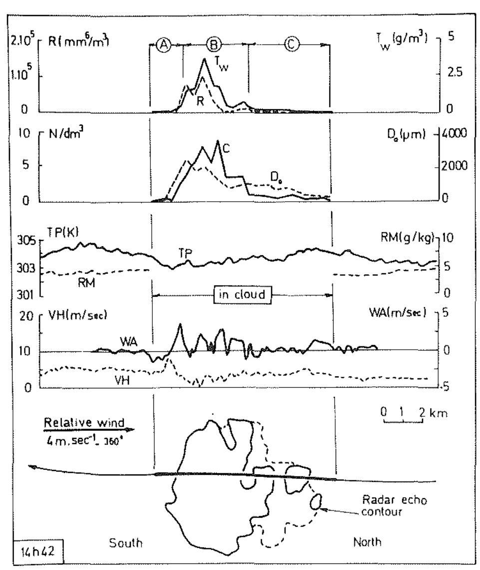

Fig. 4 - Penetration 4 - Height : 3420m MSL - Knollenberg's spectrometer probes : CDP-PSP (see text for legend)

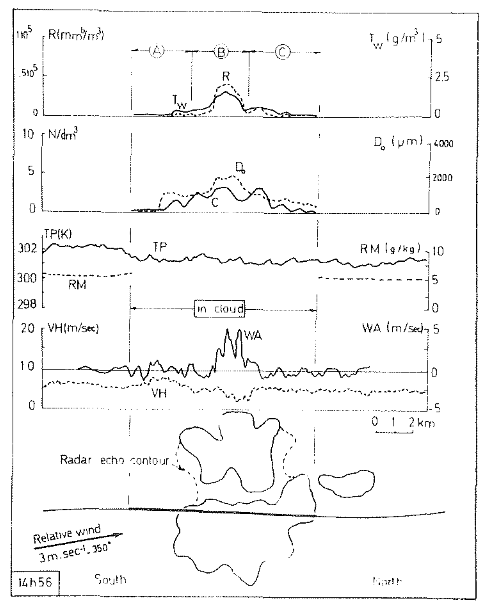

Fig. 6 - Penetration 6 - Height : 2760m MSL - Knollenberg's spectrometer probes : CDP-PSP (see text for legend)

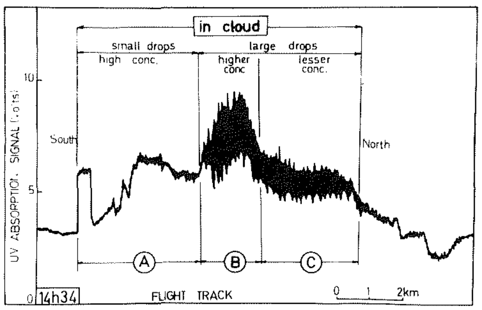

Fig. 7 - UV signal trace (TWC probe) along the flight track during penetration 3.

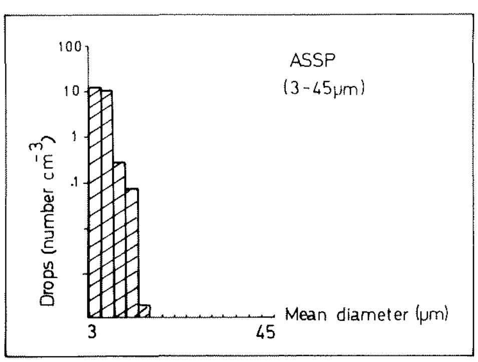

Fig. 8 - Average spectrum in zone A

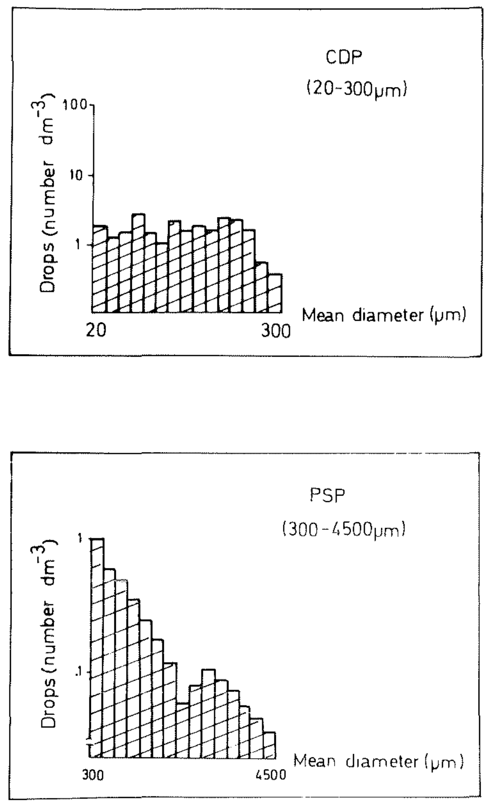

Fig. 9 - Average spectrum in zone B

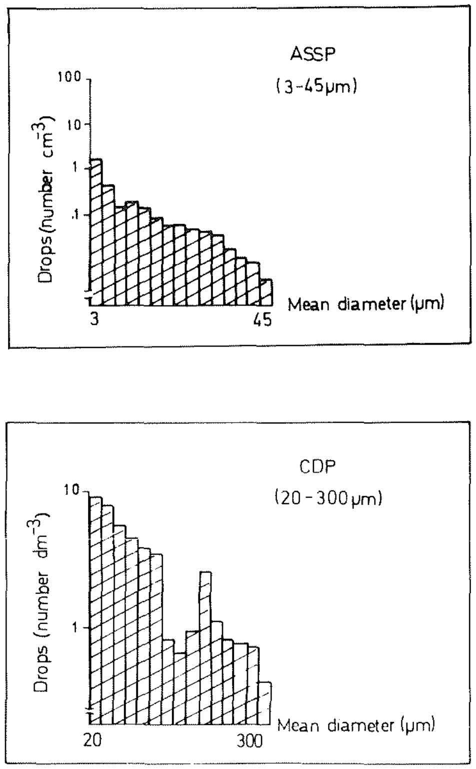

Fig. 10 - Average spectrum in zone C

4.2.5

CLOUD DROPLET SPECTRA MEASURED IN ALBERTA THUNDERSTORMS

J. Carr McLeod

Department of Meteorology
McGill University, Montreal

1. Introduction

Although many in-cloud droplet measurements have been made over the past 25 years, there has been a scarcity of these observations in cumulonimbus clouds, primarily owing to the aviation hazards which exist near these clouds. It was the intention of this study to gain some information on the droplet sizes common in the lowest kilometer of the updraft region of cumulonimbus clouds in Alberta, and to compare these observations with those made in other cloud types and at other locations. The facilities of the Alberta Hail Project (AHP) were made available to the author for this study during the summer of 1975.

2. Equipment

The aircraft flown on all data collection flights was a Cessna 411 operated for AHP by Intera Environmental Consultants Ltd. of Calgary. Most of the supplemental meteorological data such as temperature, pressure altitude, location and updraft speed were read from the standard aircraft sensors. The plane was also equipped with a Bendix RDR 130 radar and a Johnson-Williams liquid water content meter.

The emergency exit door of the aircraft was removed and replaced by a metal panel in which a hole was cut to permit extrusion of a droplet replicator. This device, furnished by the Atmospheric Environment Service of Canada, consisted of a hollow steel tube with two slits cut part way along it and a steel rod capable of holding two glass slides. The slides were exposed to the cloudy air by manually pushing the rod through the tube so that each slide passed by one of the slits.

The slides measured 4 mm x 36 mm. They were coated with a 15-20% solution of gelatin powder in water (after Jiusto, 1965). The gelatin coating was virtually permanent, allowing precoating prior to flight and analysis well after the flight.

3. Procedure and Analysis

The AHP 10-cm weather radar was used for storm surveillance. Once a storm had been selected for aircraft penetration, the plane was launched and the on-board radar was used to zero in on areas of maximum reflectivity gradients, which were invariably located near the updraft region. Upon locating the updraft area, a series of climbing turns and penetrations was made at intervals of about 500 ft (150 m) in the vertical. One pair of slides was exposed on each penetration. Usually, 5-10 minutes elapsed between successive exposures. The experiment was ended when aircraft icing or fuel reserves became critical.

After the flight, the slides were examined and photographed under an ordinary light microscope. A GP3 Graf-Pen digital recorder was used to analyze the photographs. With the photographs taped onto a grid, each droplet replica was circled with this pen and the x-y coordinates of the droplet circumference thus recorded on magnetic tape. Points were recorded at the rate of 140 s^{-1}. The resolution of the recorder was 0.1 mm, which corresponds to a scaled-down resolution of ± 0.25 μm. With this device, over 10,000 droplets were sized in 8 man hours of work and a relatively small amount of computer time.

Another advantage of the gelatin replication method is that the conversion factor of replica to true droplet size is nearly constant at 2:1 over the entire range of measured droplets (Jiusto, 1965; Kumai, 1973). Once a representative sample of droplets from a slide was measured, the droplets were grouped into micron-wide intervals and the number in each category was adjusted according to the Langmuir and Blodgett collection efficiencies (Jiusto, 1965). Since the slides were narrow and the aircraft speeds high, collection efficiencies were close to unity and the corrections consequently small. Graphs of droplet diameter vs. percent of total number of droplets per micron interval were then produced.

4. Case I: July 20, 1975

A cold front passed over central Alberta during the morning of July 20 leaving fairly clear skies in its wake. This permitted considerable daytime surface heating, and with continued cold air advection at high levels an unstable airmass was produced. Several small-hail generating thunderstorms occurred throughout the province on this date.

The storm which was investigated became radar-detectable at 1504 MDT. Until 1700 MDT it was quite small in aerial extent, though some small hail was produced at about 1630. From 1730 to 1845 MDT the storm was apparently in a mature phase with much larger aerial extent and hail falling in a continuous swath. The storm weakened considerably after 1900 MDT and was no longer radar-detectable at 2015. Penetrations were made on the SE corner of this storm from 1720 MDT until 1805.

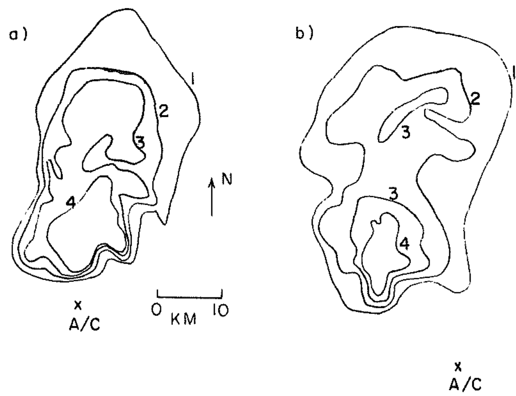

Fig. 1 *a) Radar echo at* 1° *elevation at approximate time of first slide exposure. Contour thresholds are in 10-dB steps, with threshold* 1 *corresponding approximately to* 17 *dBz. Position of airplane relative to echo is noted. b) As in a), with same scale and orientation, but for the fourth penetration at* 183*m above cloud base.*

The first pair of slides was exposed just above cloud base (2255m above sea level). The appearance of the echo at the time of this penetration is shown in Fig. 1a. The plotted aircraft position indicates that the penetration was made near the zone of maximum reflectivity gradient, but in a region that was not radar detectable. Measured updrafts of 2.5 m s^{-1} were encountered.

Only one of the exposed pair of slides captured droplets. The occurrence of blank slides was not uncommon in this study. There were two or three causes of these null samples. Occasionally the slides were inadvertently exposed with the clear gelatin coating facing the replicator, thus making replication impossible. On other slides too many droplets hit the replicator and the gelatin coating was almost completely washed off. Finally, other slides for which neither of these explanations is valid were apparently exposed in areas of cloud where there were no droplets large enough to be captured and recognized. It is into this latter class that the blank slide of this exposure falls.

The spectrum of droplets from the one successful slide in this exposure is curve (a) in Fig. 2. The spectrum has a very small mean diameter ($\bar{d}$) of only 3.3 µm, the smallest mean measured on any slide in any case. The dispersion (ratio of standard deviation to mean diameter) is also the lowest measured, at 0.23. Warner (1969) found a tendency for spectral dispersions to be approximately 0.2 near cloud base but offered no reason for this.

The next two exposures were made at 30 and 60 m above cloud base, but none of the four slides captured droplets. It seems that the droplets in the exposure area were either too small for capture and recognition, or nonexistent, despite the larger droplets found at the lower level.

The fourth penetration and exposure was made at 183 m above cloud base at 1735 MDT. The 1° contoured PPI is shown in Fig. 1b. The reason for presenting this figure is to show the large distance between the position of penetration and the detectable radar echo. Even allowing for possible errors in the aircraft position, a very broad updraft region is indicated.

Both slides of this exposure produced spectra (curves (b) and (c) in Fig. 2). These spectra are quite similar to that of the first penetration, being only slightly broader and having slightly larger mean diameters.

The fifth penetration was at 336 m above cloud base. The resulting droplet distributions are curves (d) and (e) of Fig. 2. Once again a slight broadening and increase in mean diameter is found but these changes are quite small.

The final two penetrations were both made at 488 m above cloud base. Of the four slides exposed, one was loaded incorrectly but the other three produced the distributions shown in curves (f), (g), and (h). These three spectra are similar to one another and markedly different from those at lower altitudes, being broader and with larger mean diameters.

The analysis of these three slides was hampered by some overlapping of replicas, caused by either multiple impacts or droplets running together on the slide after impact. Most replicas were either not affected by this problem or were easily recognizable as individual droplets, yet some information was lost. This problem was more serious in Case III.

5. Case II: August 2, 1975

The airmass over Alberta on this date was cooler, drier and more stable than on July 20. The developing storms were higher based than on the earlier day and had a tendency to form into lines of a few distinguishable cells. The storm investigated formed at 1620 MDT and had dissipated by 1833. Penetrations were made on its SE corner between 1710 and 1740 MDT at altitudes ranging up to 1218 m above cloud base.

As an easy way to summarize the droplet measurements in this case, Fig. 3 gives the mean diameter on each slide as a function of height above cloud base. Since the aircraft took 5-10 times longer to reach a successively higher exposure level than did the droplets, and since there was no way to be sure the aircraft was in the same position relative to the storm and updraft in all penetrations, it is erroneous to interpret Fig. 3 simply as the development of droplet size in an ascending parcel of cloudy air. Even so, it is still possible to accept the results as approximately representing droplet development with height above cloud base. This

SLIDE	HT. ABOVE CLOUD BASE (M)	NO. OF DROPLETS	$\bar{d}$ (μm)	DISPERSION
a	0	281	3.3	0.23
b	183	1230	3.8	0.35
c	183	1293	4.0	0.27
d	336	614	5.5	0.36
e	336	1242	4.5	0.40
f	488	650	9.4	0.42
g	488	924	7.6	0.41
h	488	940	8.5	0.41

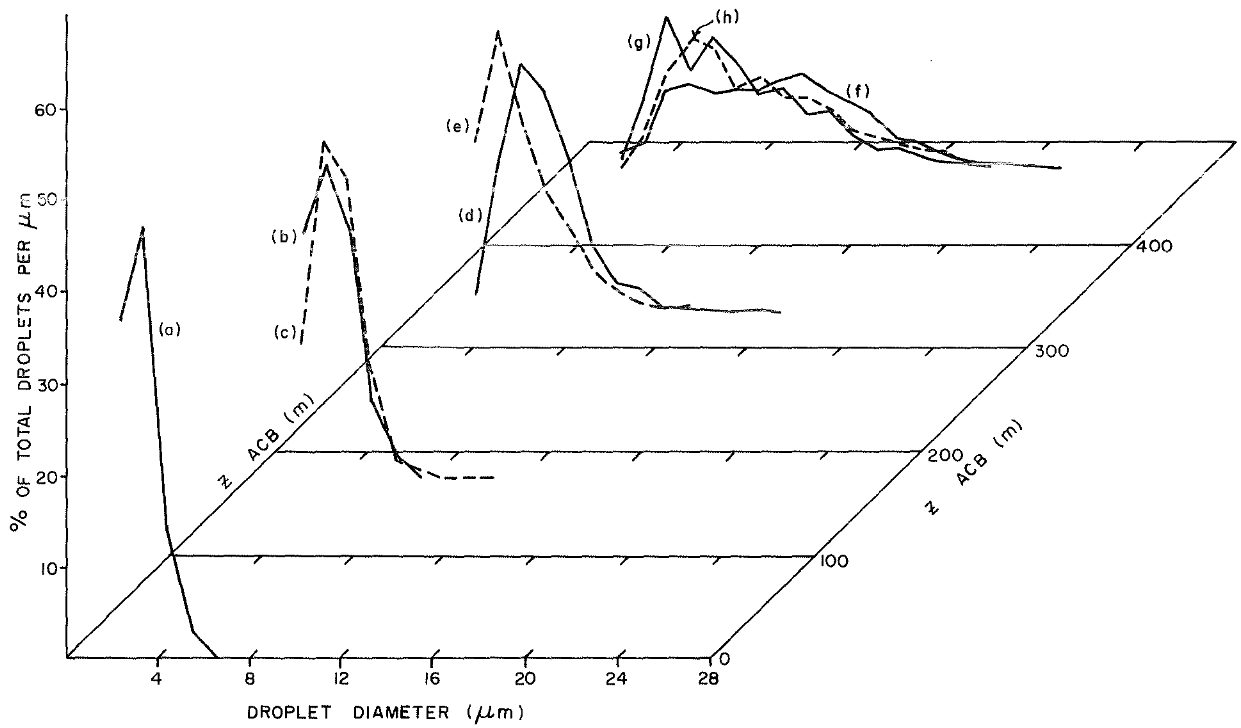

Fig. 2. Composite plot of the droplet spectra measured in Case I. Each spectrum is identified by a letter; they are plotted according to the height above cloud base. The inset table gives the number of droplets in each sample, the mean diameter, and the dispersion.

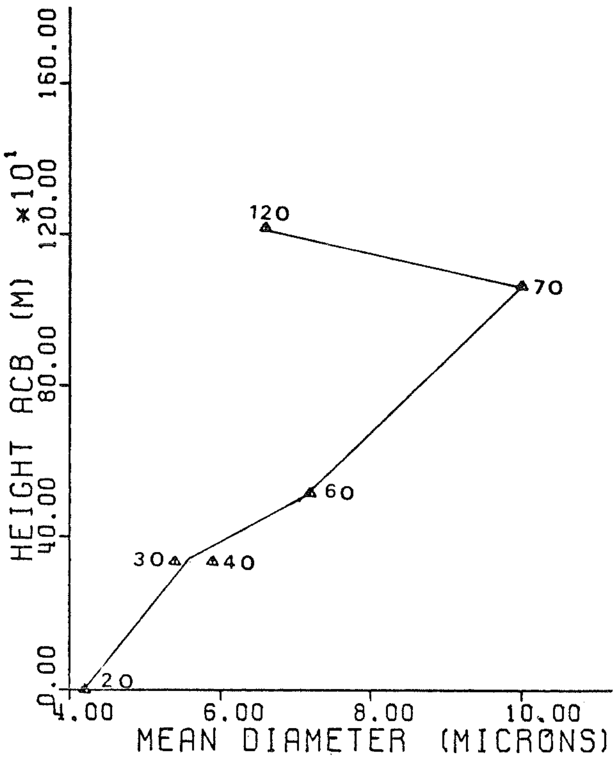

Fig. 3. Mean droplet diameter as a function of height above cloud base for Case II. Each numbered triangle indicates an observation from one slide.

interpretation was made by Warner (1969) in order to estimate supersaturations existing in cloud and will be used later in this paper for the same purpose.

Fig. 3 shows that a sizable fraction of the slides, usually one of a pair, did not capture droplets. Almost all of the blank slides on this day resulted from incorrect loading, an aggravatingly easy mistake to make.

In spite of the somewhat different weather situation and storm type in this case, the measured droplets are in the same size range as in Case I. The one distinguishing feature of this case is the sudden decrease in mean droplet size between the last two levels. The dispersions showed the same pattern, increasing from 0.30 on slide 2 0 to 0.38 on slide 7 0, then decreasing to 0.31 on slide 12 0. It is possible, based on the observed radar structure and the behaviour of the encountered updraft speeds, that the last penetration (resulting in slide 12 0) was through a newly developing cell of the same storm. This might explain the discontinuity of droplet size evolution.

6. Case III: August 10, 1975

The airmass over Alberta on this date was virtually identical in stability and moisture characteristics to that of August 2. The storm studied was similar to the previous one, with high cloud base (2743 m above sea level). Like Case II, it was also embedded in a long line of storms. Updraft speeds were weaker in this case, however, with a maximum of 5.1 m s^{-1} as opposed to 10.0 m s^{-1} in the August 2 storm.

The Case III storm also had quite high values of measured liquid water content. Values up to 1.7 g m^{-3} were found. Possibly as a result of this, the slides showed many overlapping replicas resulting from multiple impacts or coalescences on the slide. Nevertheless, on most slides a sufficiently large number of droplets were measured, providing what is hoped to be a representative sample.

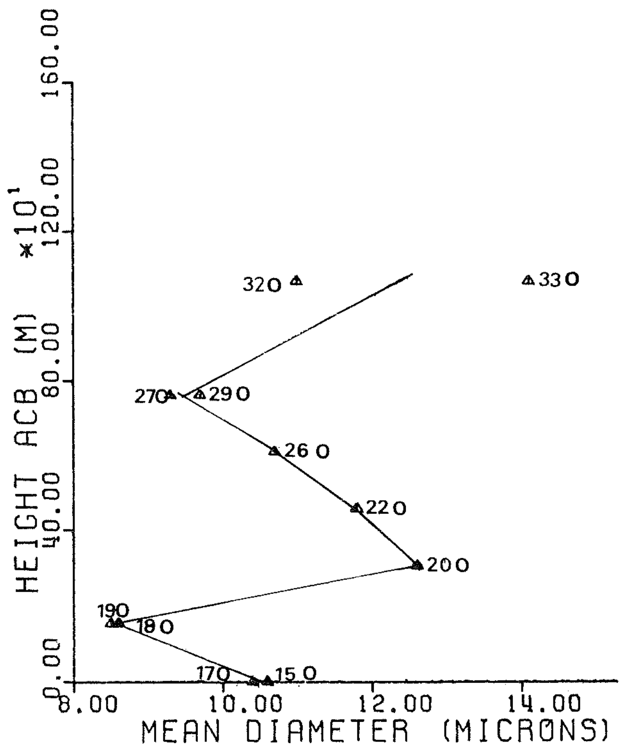

Fig. 4. As Fig. 3, except for Case III.

Fig. 4 shows the mean droplet diameter as a function of altitude. These sizes are generally larger than in the previous two cases, ranging from 8.5 μm to 14.1 μm and with no systematic tendency to increase with height. Slides 27 0 and 29 0 showed the only truly bimodal spectra in any sample. Modal diameters are near 4 μm and 11 μm. This exposure corresponded to the lowest measured liquid water content of Case III, possibly indicating that this exposure occurred near the updraft edge, where mixing may have been significant.

7. Derived Properties

7.1 Supersaturation

Assuming that the data may be interpreted as indicating droplet growth with time of ascent, it is possible to estimate an effective value of supersaturation over the time of growth. The diffusional growth equation may be written

$$(S-1) = (F_k + F_d)\ (r_f^{\,2} - r_i^{\,2})\ /2t$$

where $S-1$ = supersaturation (assumed constant)

F_k, F_d = thermodynamic factors dependent upon the conduction and diffusion coefficients

r_f, r_i = final and initial droplet radii

t = time of growth from r_i to r_f.

This equation was applied to the data by using the mean radii for r_f and r_i, and by determining t from the updraft velocity.

For Case I, the overall effective supersaturation for the layer sampled was found to be 0.13%. On the basis of the first four exposure levels in Case II, a value for (S-1) of 0.12% was found. When a more exact form of the diffusional growth equation was used, one that includes kinetic corrections of Fukuta and Walter (1970) and also the effects of surface tension and solution on the equilibrium vapor pressure, a supersaturation of 0.09% was found for Case II. It therefore seems that supersaturations in the order of 0.1% were present in these clouds.

The behaviour of mean droplet size in Case III was too irregular to allow an estimate of the supersaturation.

7.2 Droplet Concentrations

Droplet concentrations may be estimated from the measured number of droplets that are collected and the effective cloud volume which is sampled. The cloud volume depends upon air speed, exposure time, and the area of the slide photographed. There is some uncertainty in this volume because the exposure time is not known exactly. For essentially the same kind of sampler, G. Isaac (unpublished) found the exposure time to be approximately 0.02 sec. This value was used in the present study.

In Case I, the concentrations were found to range from 231 to 680 cm^{-3}. The range in Case II was broader, from 79 to 729 cm^{-3}, and with a tendency to decrease with height. These estimates are thought to be accurate to within a factor two, and are consistent with observations by others in continental cumulus.

It was not feasible for Case III to estimate the concentrations, because of the large number of overlapping replicas.

7.3 Liquid Water Content

Liquid water contents calculated from the droplet spectra turned out to be very small. There were only three exposures for which the calculated values could be compared with those measured by the Johnson-Williams instrument. In two of these the agreement was good. The calculated values in Case I ranged from 0.006 $g\ m^{-3}$ to 0.21 $g\ m^{-3}$. Case II values were quite constant, ranging from 0.02 to 0.06 $g\ m^{-3}$. It was not possible to calculate liquid water contents for Case III, because the concentrations were unknown.

8. Spectral Broadening

The droplet spectra in Case I and for the first four levels in Case II were found to broaden with height. It is generally assumed that a population of droplets growing by condensation alone will experience spectral narrowing. This is true if all the condensation nuclei on which the droplets have formed have been activated -- that is, if the droplets are larger than the critical radii for their particular condensation nuclei. On the basis of available information on the typical sizes of condensation nuclei, it seems quite likely that some of the very small droplets in these samples had not yet exceeded the critical radii and were thus still haze droplets. These droplets grow only in response to increasing ambient supersaturation, and are therefore limited in size unless their critical supersaturation is exceeded. In a mixed population of droplets, some of which have not yet exceeded their critical size, diffusional growth can lead to a distribution that spreads briefly before assuming a bimodal character.

Calculations were made to investigate whether this effect could account for the observations. A group of five droplets ranging in 1 μm steps from 0.5 to 4.5 μm, each on a plausibly-sized condensation nucleus, was allowed to grow under various conditions of ambient supersaturation. For a constant supersaturation of 0.1%, corresponding to that inferred for Case I, the smaller droplets were limited in growth and there was a broadening of the range of droplet sizes with time. Eventually, a bimodal spectrum with two narrow peaks would emerge. A more convincing simulation assumed that the supersaturation varied randomly between +1% and -1%. This resulted in a spreading of droplet sizes similar to what was observed (see Fig. 5).

9. Acknowledgments

This report is a summary of the author's M.Sc. thesis. I wish to thank Dr. R.R. Rogers for his interest and supervision during the preparation of the thesis and this paper. Financial support was provided by the Atmospheric Environment Service of Canada and the Research Council of Alberta. Assistance during the field program by personnel of the Research Council, the AES, and the Alberta Weather Modification Board is gratefully acknowledged. Dr. J.E. Jiusto, State University of New York at Albany, provided helpful advice on the use and interpretation of gelatin-coated slides.

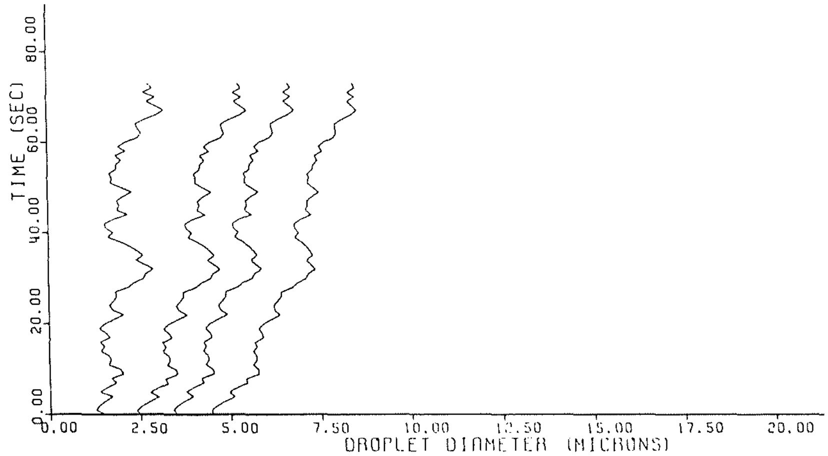

Fig. 5 Droplet population growth according to modified Fukuta and Walter diffusional growth equation. Supersaturation varying randomly between -1% and + 1% at intervals of 1 sec (≃ 5 m).

10. References

Fukuta, N., and L.A. Walter, 1970: Kinetics of hydrometeor growth from a vapor-spherical model. J. Atmos. Sci., 27, 1160-1172.

Jiusto, James E., 1965: Cloud particle sampling. Dept. No. 6, Dept. of Meteorology, The Pennsylvania State University.

Kumai, M., 1973: Arctic fog droplet size distribution and its effect on light attenuation. J. Atmos. Sci., 30, 635-643.

Warner, J., 1969: The microstructure of cumulus cloud. Part I. General features of the droplet spectrum. J. Atmos. Sci., 26, 1049-1059.

4.2.6

SINGLE-LEVEL MICROPHYSICAL STRUCTURE OF FLORIDA CUMULI: SELECTED CASE STUDIES

Robert I. Sax, Jane C. Eden and Paul T. Willis

NOAA, National Hurricane and Experimental Meteorology Laboratory
Coral Gables, Florida 33124

1. MOTIVATION AND METHODOLOGY

The Florida Area Cumulus Experiment (FACE), conducted by the Cumulus Group of NOAA's National Hurricane and Experimental Meteorology Laboratory, has as its principal objective, the determination of whether or not rainfall can be increased on an areal basis through the "dynamic" seeding of supercooled Florida cumuli. The success of the program depends hypothetically upon a number of sequential microphysical and dynamical events, one of the first of which is the conversion of a significant quantity of supercooled water to ice through the action of silver iodide nucleant. Experience has indicated, however, that rapid glaciation of Florida cumuli can occur under natural conditions, even in cloud towers with tops no colder than about the -12°C isotherm level. Sax and Willis (1974) have documented the evolution of ice in a growing Florida cumulus bubble penetrated at three different altitudes in a quasi-Lagrangian manner. Koenig (1963) found rapid glaciation in cumuli developing over Missouri, though he did not attempt to distinguish exactly where in the cloud envelope ice was occurring. Sax (1969) inferred from their dynamical response to seeding that maritime cumuli growing in the Caribbean contained essentially ice-free updraft cores while glaciation possibly proceeded around the periphery. Several investigators (Koenig, 1963; Mossop et al., 1970) have linked glaciating behavior with the presence of raindrops and/or a broad cloud droplet size distribution. An understanding of the conditions under which ice can be expected to form naturally in relatively warm supercooled convective clouds, is one of the most fundamental problems confronting cloud physicists today. The manner in which the various in-cloud microphysical parameters are interrelated undoubtedly holds a clue to the successful prediction of where and when rapid ice formation might likely occur within convective towers.

The 1975 FACE program provided a unique opportunity for a detailed investigation into the characteristics of the microstructure of Florida cumuli, particularly with regard to the partitioning of cloud condensate as a function of the updraft profile. The NOAA DC-6 aircraft was specially equipped with microphysical instrumentation capable of providing continuous information relating to mass of water contained in cloud droplet (Johnson-Williams) and hydrometeor (foil impactor) sizes, concentration of raindrops (foil impactor), concentration of ice particles (Mee and University of Washington optical counters), and mass of total water condensate (lyman-alpha evaporator). A Desert Research Institute formvar replicator and a 2-D Knollenberg particle spectrometer system were operative on some flights and provided data bearing on the sizes, concentrations, and habits of ice crystals and the size distribution of cloud droplets. Vertical velocity was computed using the measured aircraft pitch and attack angles combined with filtered values of radar altitude changes. Spatial resolution of electronically-recorded data was of the order 100 m with the aircraft data system accessed once per second.

Since the cloud physics sub-program of FACE was conducted in consort with, and in support of, the area-wide randomized (by day) "Core" seeding experiment, the usual flight procedure was to penetrate as many clouds as possible in the shortest time. However, there were several occasions when the DC-6 was operated in an "Intensive Phase" mode to carry out special penetrations into clouds of interest and to repenetrate cumulus towers to obtain data relevant to the evolution of their microstructure. The flight altitude typically was at the -8°C to -10°C isotherm level (5.8 km) but a large number of penetrations were also conducted routinely at the -4°C to -6°C isotherm level (5.2 km). It should be emphasized that all microphysical data were collected at a single level within a particular tower. The aircraft was operating near its ceiling altitude and did not have the performance capabilities to enable multi-level penetrations within the same cloud.

The DC-6 cloud physics program was carried out during the month of July within the 13000 km^2 FACE target area of the south Florida peninsula. The aircraft normally began making cloud penetrations at the 5.2 km level during early afternoon (1400 local time) and at the 5.8 km level by mid afternoon (1500 local time). On most days this was the time period that convection over the south Florida peninsula was becoming organized well enough to produce a moderate number of cumulus towers growing through the respective flight altitudes. As a general rule, the aircraft penetrated towers within 0.5 km of their tops, although a few, especially those which were repenetrated, had grown 1 to 2 km above flight altitude. Towers in an active stage of development not associated with larger convective systems were selected preferentially for initial penetrations, particularly when the DC-6 was used as a platform for seeding. A wide variety of cumulus diameters were encountered, ranging from a few hundred meters, when traversed close to the tower top, to as much as three or four kilometers when traversed closer to the bottom of the rising bubble cap. Cloud bases on all days were at altitudes within the range 0.7 to 1.0 km (approximately 20°C to 22°C). A detailed description of flight procedures, the target area, and the experimental design of FACE is available elsewhere (Woodley and Sax, 1976).

This paper concerns itself with the interrelationship and interpretation of a common set of data obtained with the Johnson-Williams, foil impactor, lyman-alpha, vertical velocity, and Mee ice particle instrumentation. These microphysical devices were totally operative for each of the case study clouds selected, and therefore can provide a data base which is mutually consistent for all penetrations. Turner et al. (1976) and Sax (1976) have intercompared ice particle data obtained during FACE 75 from the Mee and University of Washington optical counters and the formvar replicator. Although further studies are in progress, it appears that the ice particle data from all three sensors were in broad general agreement provided the Mee channel selected for analysis had a signal threshold of 300 mv and provided that small (<200μm major axis length) vapor-grown columnar crystals were not present in large concentrations.

2. RESULTS

Four clouds, each penetrated three times, have been selected as case studies. None of the four clouds were seeded at any time during their life history, nor had any seeding activity occurred anywhere within the target area for at least 23 hours (and in most cases several days) prior to these series of case-study penetrations. These were the only non-seeded cloud towers to be penetrated more than twice by the DC-6 aircraft. Each cloud was in an actively-growing stage of development when first penetrated, and each cumulus tower was relatively isolated (not flanking a larger convective complex) with its top no more than 0.5 km above the aircraft flight level during the initial traverse. It is estimated from nose camera photography that none of these selected clouds grew more than about 1 km following the first penetration. The visual appearance of each of these clouds changed from moderately "hard" prior to the initial penetration to obviously "soft" by the time of the third penetration. The clouds were repenetrated on reciprocal headings with the exception of 8 July C #2 which was a repenetration of C #1 on a perpendicular heading.

Figure 1 shows the microphysical data for three penetrations into a cumulus tower on July 4th. The mean temperature during each traverse was about -7°C. The initial penetration was carried out very close to the top of the largest turret. The cloud did not appear to be growing vigorously, but still possessed very sharp edges indicative of a composition of mainly supercooled water. By the time of the second penetration, the cloud still appeared "hard" in the center and growing slowly, but its edges had become somewhat diffuse. The tower very obviously was in a dissipating state by the time of the third penetration and had become diffuse throughout. It can be seen that during the first traverse (Figure 1a) neither ice nor hydrometeor water[1] is present. The vertical velocity is relatively low, peaking at 5 m sec^{-1}, but the cloud water content (max 1.5 gm m^{-3}) is appreciable. The discrepancy between total water condensate[2] (peak 2.5 gm m^{-3}) and the cloud water content is probably due to the existence of a sizable concentration of drops in the size range 50-500μm diameter. By the time of the second penetration three minutes later (Figure 1b) it can be seen that some rainwater and ice have developed across the cloud tower. The vertical velocity maximum is still 5 m sec^{-1}, but the cloud water content is only about one half that of the previous penetration. The total water condensate is not greatly different from the first pass, but now is comprised of some water in hydrometeor sizes. A dramatic change in the microstructure occurs during the 3-1/2 minutes between the second and third passes. The third penetration (Figure 1c) now shows a large concentration of ice particles (10 to 30 ℓ^{-1}) and an almost complete absence of upward vertical motion and cloud water. The total water condensate is reduced from the previous two passes and is largely comprised of hydrometeor drops. The inference, therefore, might be that the ice particles are probably of small size and contribute little to the mass of condensate. It should be pointed out, however, that the lyman-alpha probe has a small sampling volume (≃7 ℓ sec^{-1} at the DC-6 air speed) and thus may seriously underestimate the mass contribution of large drops. It is therefore conceivable that the instrument may be responding more to the presence of ice than to precipitation. The main feature of this case study is the sudden onset of glaciation following the occurrence of precipitation-sized drops, coincident with the decay of the updraft and the disappearance of cloud water.

The case study cloud on 8 July (Figure 2) shows the same feature even more dramatically. The mean temperature during these penetrations was about -9°C, and the cloud top may possibly have reached the -12°C isotherm level during its life history. The cloud appeared to be growing vigorously prior to the initial traverse. The first penetration (Figure 2a) showed strong updrafts (peak 20 m sec^{-1}) throughout the tower with a broad region of cloud water content in excess of 1 gm m^{-3}. An insignificant amount of water was contained in hydrometeor-sized drops, and no ice was found to be present. The second penetration less than three minutes later (Figure 2b) also showed an absence of ice, but the concentration of hydrometeor-sized drops and water content had increased substantially. The vertical velocity profile remained strong and the cloud water content still peaked near 1.25 gm m^{-3}. By this time the cloud had grown by about 500 m and, though still active, was somewhat "softer" in appearance and was not nearly as vigorous. Within the next 4-1/2 minutes, the microstructure and physical appearance of the cloud changed considerably. The cloud had stopped growing and appeared diffuse near the edges. The tremendous increase in ice particle concentration, coincident with the decay of the updraft profile and the almost total absence of cloud water, is readily apparent in Figure 2c. It should also be noted that the concentration of raindrops >0.5 mm diameter measures less

[1]here defined as water contained in raindrops >0.5 mm diameter.

[2]contribution of vapor phase subtracted from the total water content measured with the lyman-alpha evaporator.

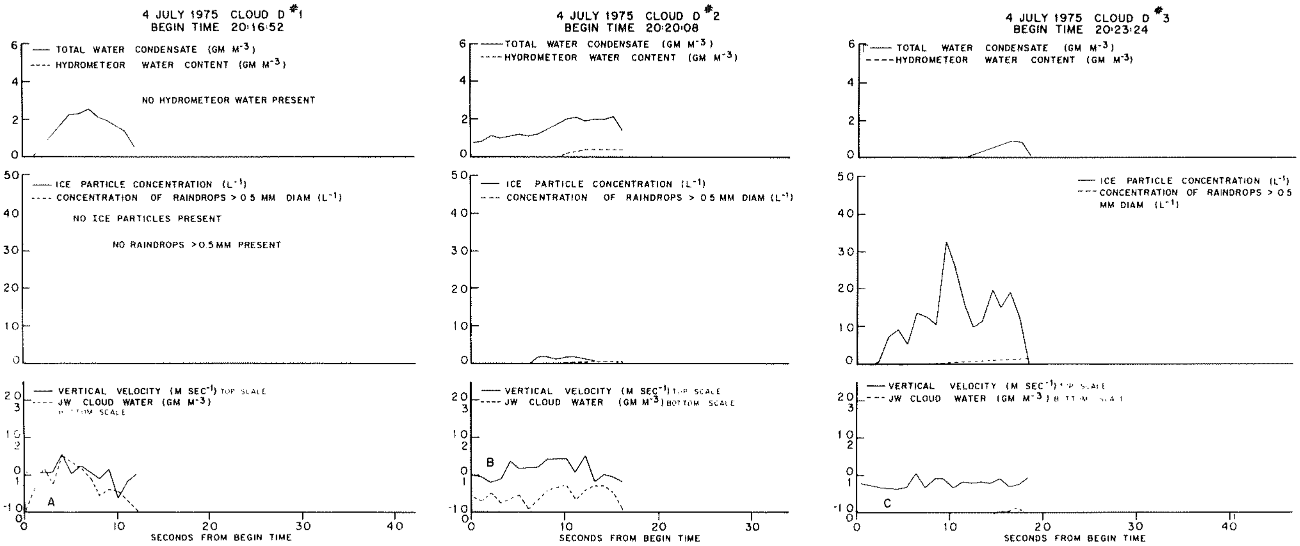

Figure 1. Evolution of the internal microphysical structure for non-seeded cloud penetrated three times on July 4th. The lower panel shows the profiles of the computed vertical velocity (top scale in m sec^{-1}) and the cloud water content as measured by the Johnson-Williams probe (bottom scale in gm m^{-3}). The middle panel shows the ice particle concentration (ℓ^{-1}) as measured by the 300 mv channel of the Mee optical ice particle counter and the concentration of raindrops (ℓ^{-1}) > 0.5 mm diameter as determined from analysis of data collected with the foil impactor. The top panel shows the total water condensate (gm m^{-3}) as determined from the lyman-alpha data with the vapor contribution removed, and the hydrometeor water content (gm m^{-3}) as analyzed from foil data. The horizontal scale is in seconds from the begin time indicated at the top of each group. One second in time corresponds approximately to 100 m in spatial scale.

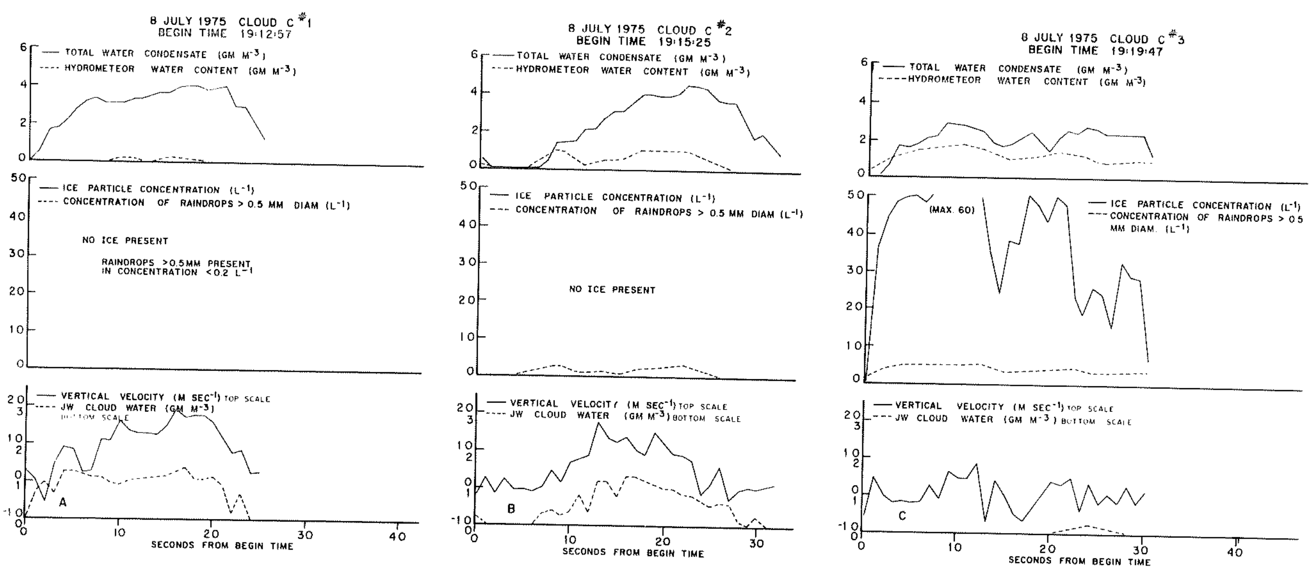

Figure 2. Evolution of the internal microphysical structure for a non-seeded cloud penetrated three times on July 8th. See Figure 1 caption for details.

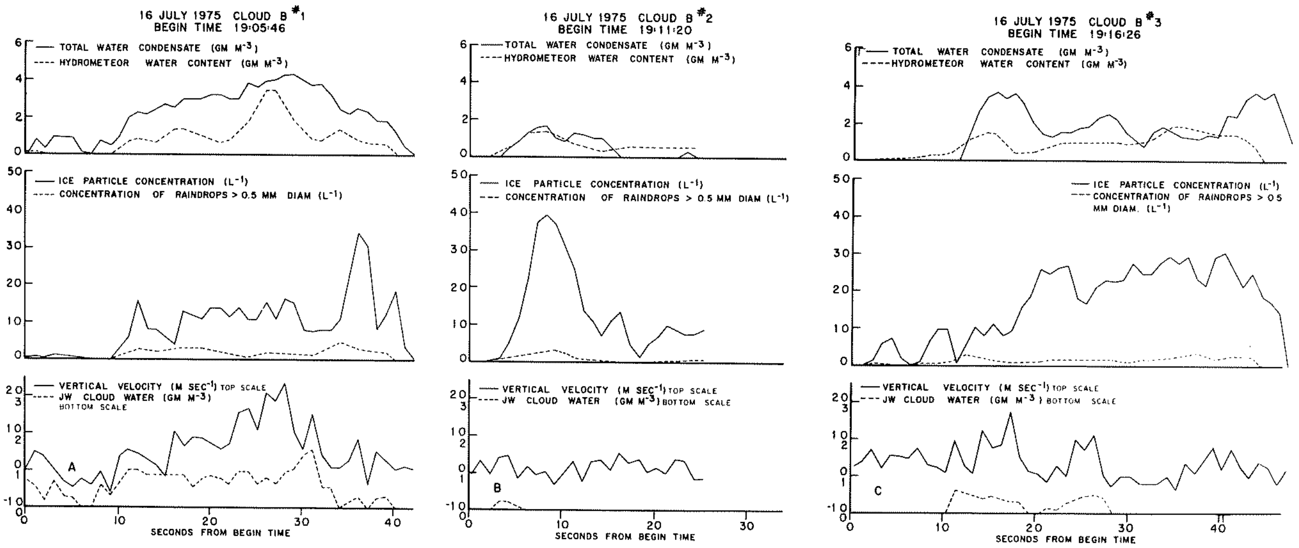

Figure 3. Evolution of the internal microphysical structure for non-seeded cloud penetrated three times on July 16th. The lower panel shows the profiles of the computed vertical velocity (top scale in m sec^{-1}) and the cloud water content as measured by the Johnson-Williams probe (bottom scale in gm m^{-3}). The middle panel shows the ice particle concentration (ℓ^{-1}) as measured by the 300 mv channel of the Mee optical ice particle counter and the concentration of raindrops (ℓ^{-1}) > 0.5 mm diameter as determined from analysis of data collected with the foil impactor. The top panel shows the total water condensate (gm m^{-3}) as determined from the lyman-alpha data with the vapor contribution removed, and the hydrometeor water content (gm m^{-3}) as analyzed from foil data. The horizontal scale is in seconds from the begin time indicated at the top of each group. One second in time corresponds approximately to 100 m in spatial scale.

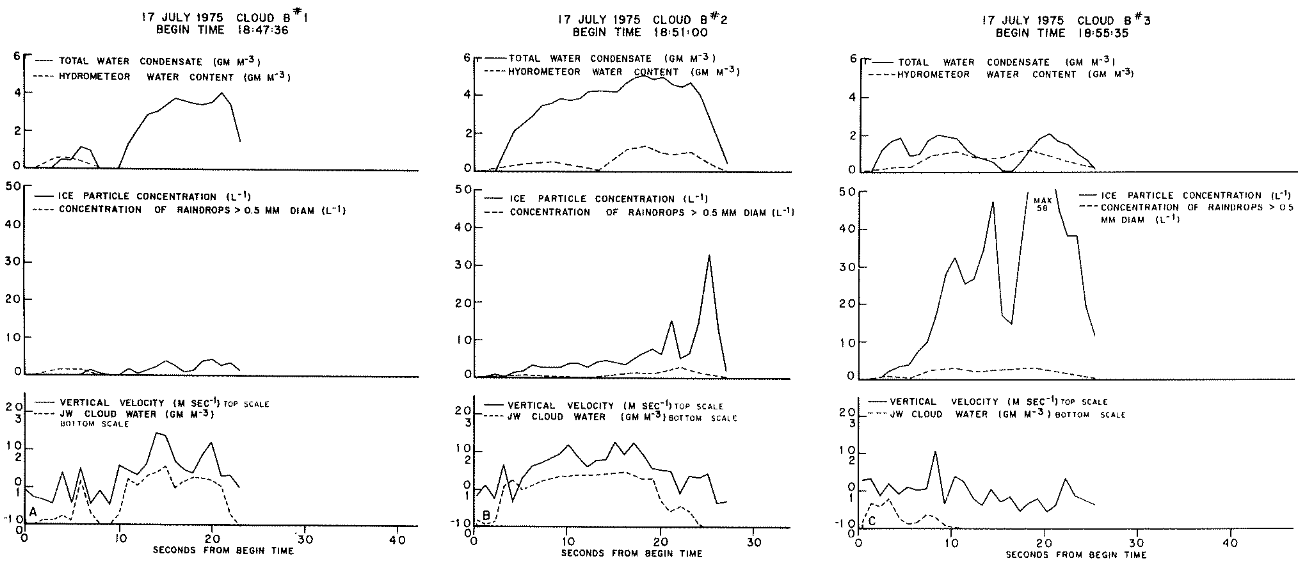

Figure 4. Evolution of the internal microphysical structure for a non-seeded cloud penetrated three times on July 17th. See Figure 3 caption for details.

than 10 percent of the ice particle concentration as determined from the Mee counter, so ambiguity due to the possible failure of the instrument to totally discriminate between water and ice should not be of importance in the interpretation of these data. A signature of rapid glaciation following the onset of precipitation-sized drops is very much evident in this cloud.

Figure 3 shows three penetrations into a cloud growing on July 16th. The penetration isotherm level was -9°C. It is doubtful if the cloud top temperature was any colder than -13°C during the tower's lifetime. The first penetration (Figure 3a) was properly carried out into the center of the rising tower, and it can be seen that ice concentrations of 10-20 ℓ^{-1} are present throughout the cloud. A substantial amount of hydrometeor water is also present which indicates that the cloud is already well advanced into its microphysical life cycle at this altitude. However, a strong updraft with a broad region of moderate cloud water content is evident. The highest concentration of ice (exceeding 30 ℓ^{-1}) coincides with a region of relatively low updraft and very little cloud water apparently located on the periphery of the main core. The second penetration (Figure 3b) was incorrectly carried out to the right of the main updraft core and thus the peripheral region was sampled (note the shortness of the second penetration relative to the first and third). It can be seen that the updraft velocity oscillated around 0 m sec^{-1} with only a hint of cloud water in a small region near the penetration entry point. A rather broadly-peaked high concentration of ice particles can be seen, and here again, the total water condensate profile seems to be correlated with hydrometeor water, thereby suggesting (probably falsely) only a small mass contribution by the ice particles. The third penetration (Figure 3c) was correctly carried out into the core region of the tower (with the same aircraft heading as pass 1), and it can be seen that, relative to pass 1, the ice concentration has increased by a factor of two over a broad region, while the updraft velocity and cloud water content have generally decreased. It should be noted that nearly 12 minutes have elapsed between the first and third penetrations. It is not entirely clear whether the two vertical velocity and cloud water peaks during the third pass are remnants of the original tower or else represent new bubbles growing through the original mass. In the latter situation, it is easy to see how ice debris from older clouds can serve as "proto ice" in young towers as speculated by Hallett et al. (1976).

The final case study (Figure 4) shows three penetrations into a cloud on July 17th with a temperature at flight level of about -5°C. The top of this cloud almost certainly never was colder than -11°C during its lifetime. At the time of the initial penetration the cloud was growing vigorously with a "hard" visual appearance and the tower top was no colder than -8°C, yet some ice is already in evidence through a portion of the pass (Figure 4a). Some precipitation-sized drops are also present, but in a different portion of the cloud. Strong upward motion coincident with high values of cloud water occur in the region of the tower without hydrometeor water. The tower was isolated and appeared to be growing into clear air which was visibly free of any cloud debris. By the time of the second penetration 4 minutes later the tower had grown nearly 1 km and retained a "hard" visual appearance in its center. The region of the cloud which had hydrometeor water now has a substantial quantity of ice (Figure 4b), while the region of the cloud previously devoid of hydrometeor water now shows evidence of some large drops. The ice particle concentration in the region of cloud with strong updraft and high cloud water content has not increased from pass 1 to pass 2, nor has the character of the velocity and cloud water profiles been significantly altered. However, by the time of pass 3 (Figure 4c) four minutes later, large concentrations of ice are now present throughout most of the cloud, with cloud water content confined to a very small region near the penetration entry point. With the exception of a one-second peak of 10 m sec^{-1}, the updraft velocity has decayed to oscillating around the 0 m sec^{-1} value. Visually, the tower had softened considerably and its height to width ratio had narrowed to the point where it appeared shaped like a finger. The main feature documented by this case study is once again the sudden increase in ice associated with the occurrence of hydrometeor water. It would appear from Figure 4c that the total water condensate profile is responsive to changes in ice particle concentration and is failing to account for all of the hydrometeor water present.

3. DISCUSSION

The four case studies graphically illustrate that the time window in which supercooled Florida cumuli with tops no colder than -12°C are free of ice can be extremely short. It should not be implied from this study that glaciation proceeds rapidly on all days, but the data accumulated during July of 1975 indicates that a sudden onset of ice is the rule rather than the exception. Furthermore, the data suggest that rapid ice formation can be expected if the cloud is found to have a "noticeable" concentration of large (>0.5 mm diameter) drops, even though the vertical velocity and cloud water profiles might still be indicative of a tower in an active stage of development. This is particularly well illustrated by the case study on July 8th. The dramatic buildup of ice within 4-1/2 minutes is difficult to explain unless it can be assumed that nearly all of the large drops (>0.5 mm diameter) froze by some unknown mechanism and acted as a source of primary ice to initiate a secondary crystal production mechanism (Hallett et al., 1976). Admittedly, this explanation is not very satisfactory.

The concentration of ice nuclei as measured by an acoustical counter at low altitudes (600 m) was very high (≈10 ℓ^{-1} active at -20°C) on July 8th, a day which was polluted by an outbreak of Saharan dust loading (Allee et al., 1976). The concentration of ice nuclei was also high (≈5 ℓ^{-1} active at -20°C) on the 4th, but was "normal" (≈1 ℓ^{-1} active at -20°C)on the 16th and 17th. The concentration of CCN active at 0.75 percent supersaturation varied from about 250 cm^{-3} on July 8th to about 1000 cm^{-3} on July 16th. A more detailed analysis of the relationship between low-level aerosol characteristics and upper-level cloud microstructure is currently underway, but no clear-cut trends appear to be developing in relation to the case studies presented here.

Caution is advised against accepting the data in an absolute quantitative sense. Relative values of the microphysical parameters from pass to pass on the same day, and from case study to case study on different days, should be meaningful. It is not known with certainty how the Mee ice particle data from a given signal threshold level relate to the absolute concentration of ice in clouds, though evidence (Sax, 1976) suggests that data from the Mee counter as configured for the FACE 75 program compared fairly well (to within about a factor of two) to data obtained with a formvar replicator in clouds containing primarily graupel ice. The vertical velocity data are known to contain an occasional bias of ±2-3 m sec^{-1} and should certainly not be considered to any greater accuracy. The hydrometeor images on the foil impactor were analyzed in groups of five frames of data (elapsed time approximately five seconds) and then linearly interpolated to derive one-second values of concentration and mass. This analysis method, of course, serves to smooth out rapid fluctuations due to sampling volume problems while at the same time forcing a short-time response which may not be representative of the real data. None of the reasonable uncertainties in the absolute magnitudes of the microphysical data, however, should affect the validity of the points raised in this paper.

4. CONCLUSION

The case studies document an association between the presence of drops > 0.5 mm diameter and the onset of rapid glaciation in Florida cumuli. The formation of ice also seems to be associated with a significant decay of updraft strength and the nearly total disappearance of cloud-sized water droplets. There is also evidence suggesting that ice initially forms in peripheral regions of the updraft core. It is evident from the data that new towers growing through old cloud debris on a time scale of the order 10 minutes would be provided with an endowment of ice particles.

5. REFERENCES

Allee, Paul, Robert I. Sax and Emil Delgado, 1976: Distribution and interrelationship of CCN, IN, and Aitken aerosol over selected oceanic and continental sites. Proc. Int. Conf. on Cloud Physics, Boulder, CO. To be published.

Hallett, John , Dennis Lamb, A.S. Ramachandra Murty and Robert I. Sax, 1976: Aircraft measurements relating to secondary ice crystal production in Florida cumuli. Proc. Int. Conf. on Cloud Physics, Boulder, CO. To be published.

Koenig, L.R., 1963: The glaciating behavior of small cumulonimbus clouds. J. Atmos. Sci., 20, 29-47.

Mossop, S.C., A. Ono and E.R. Wishart, 1970: Ice particles in maritime clouds near Tasmania. Quart. J. Roy. Meteor. Soc., 96, 487-508.

Sax, Robert I., 1969: The importance of natural glaciation on the modification of tropical maritime cumuli by silver iodide seeding. J. Appl. Meteor., 8, 92-104.

Sax, Robert I., 1976: Microphysical response of Florida cumuli to AgI seeding. Proc. WMO Int. Conf. Wea. Mod., Boulder, CO. To be published.

Sax, Robert I. and Paul T. Willis. 1974: Natural glaciation characteristics of an ensemble of Florida cumulus clouds. Proc. AMS Conf. on Cloud Physics, Tucson, AZ, 152-157.

Turner, F.M., A.S. Ramachandra Murty, R.I. Sax and L.R. Radke, 1976: Field measurements obtained with two optical ice particle counters in cumulus clouds over Florida. Proc. Int. Conf. on Cloud Physics, Boulder, CO. To be published.

Woodley, William L. and Robert I. Sax, 1976: Florida Area Cumulus Experiment (FACE). NOAA Technical Memorandum ERL-WMPO 6, National Hurricane and Experimental Meteorology Laboratory, Coral Gables, FL, 204 pp.

6. ACKNOWLEDGEMENTS

The expertise and dedication of personnel at NOAA's Research Facilities Center is gratefully acknowledged. Mr. Fred Toepfer, Mr. Jorge Viscaino, and Mr. Jose Gutman of the NHEML Cumulus Group each contributed greatly to the data analyses.

4.2.7

WATER CONTENT AND ENTRAINMENT OF SELECTED CONVECTIVE CLOUDS

Kathy Doster and Paul T. Willis

National Hurricane and Experimental Meteorology Laboratory
Weather Modification Program Office
Environmental Research Laboratories
National Oceanic and Atmospheric Administration
Miami, Florida

1. INTRODUCTION

To link larger scale, dynamical processes with the microphysical, meteorological observations must be made and then placed in a format that permits model parameterization and verification. In the words of Mason (1969): "Although important microphysical problems remain to be solved, this aspect of the subject has advanced quite rapidly relative to our knowledge of the air motions. Indeed, it may be difficult to identify the important gaps in our current understanding of the microphysical events until this has been formulated in a dynamical context and tested against the results of observation, measurement, and prediction."

Since the main driving mechanism of a cumulus is the condensation of water vapor, a microphysical process, it is not surprising that there is a close interaction of a cloud's microphysics with its dynamical life. Alternately, the elementary micro-processes taking place in clouds are, in turn, affected by the dynamics fields. Droplet growth rates and size distributions are undoubtedly affected by external variables, such as the vertical wind and the wind shear.

In addition, cumulus entrainment and cloud erosion together form one of the central problems in understanding the behavior of cumulus clouds and convective cloud systems. Stommel (1947), and many others following, have shown that a cumulus cloud's interaction with its environment has strong influence on its life cycle. Convective modelers have used, almost exclusively, expressions for entrainment that treat the entrainment rate as an inverse function of the cloud radius. Sloss (1967) and McCarthy (1971) have attempted to verify the E-R relationship; only the latter has had any degree of success (and that was limited) on a small, very specialized, sample of clouds.

The purpose of this study is to contribute to the central objective of GATE (increased understanding of cloud clusters and their relationship to tropical disturbances) by 1) examining the water content of tropical maritime and hurricane cumuli in conjunction with measured draft scale vertical winds, and 2) by computing entrainment rates for selected updrafts isolated through direct measurements of vertical wind.

2. EXPERIMENTAL DATA AND PROCEDURES

All microphysical measurements involved in this study were collected aboard NOAA's C-130 aircraft. The water content parameters were obtained with a Lyman-alpha total water content instrument and a Johnson-Williams hot wire cloud droplet liquid water content instrument. Both instruments are described in detail by Willis (1972). The temperatures in the entrainment calculations were measured with a Rosemount total temperature probe. The vertical winds were computed from measurements from a heated angle of attack (α) sensor, (and sideslip angle sensor (β)), and from parameters from a high quality inertial navigation system. The primary parameters from the inertial system were the pitch angle (θ), the vertical motion of the aircraft (V_w) determined by integration of the vertical accelerometer output, the roll angle (r), and the true airspeed calculated as part of the navigation routine (U). The vertical air velocity, or vertical wind (w), was calculated with the following relationship:

$$w = -U \sin\theta + U \tan\alpha \cos\theta \cos r - U \tan\beta \cos\theta \cos r + V_z \qquad (1)$$

Most GATE data used in this analysis were taken in the east central portion of the B-scale array (around 9° N 23° W), while the hurricane data were taken from Hurricane Gladys (1975) on 1 October when it was located near 30° N 72°W. The GATE convective cloud penetration passes selected for analysis, and those presented, represent typical clouds with fairly typical distributions of water content and vertical winds. The data analysis is primarily accomplished with two computer programs. One computes 3-second running means from 1-second mean values of vertical wind and water contents, and sorts the water content values into class intervals according to mean vertical wind. Then, for each class interval of vertical wind, this program computes 1) the mean total condensate content, 2) the mean cloud droplet liquid water content, and 3) the correlation coefficient between cloud droplet liquid water content and vertical wind.

The second program computes the thermal and the water entrainments. The total water content values have had the vapor baseline subtracted from the data, and thus are values of the total condensate. Correlations are computed between total condensate content and vertical air

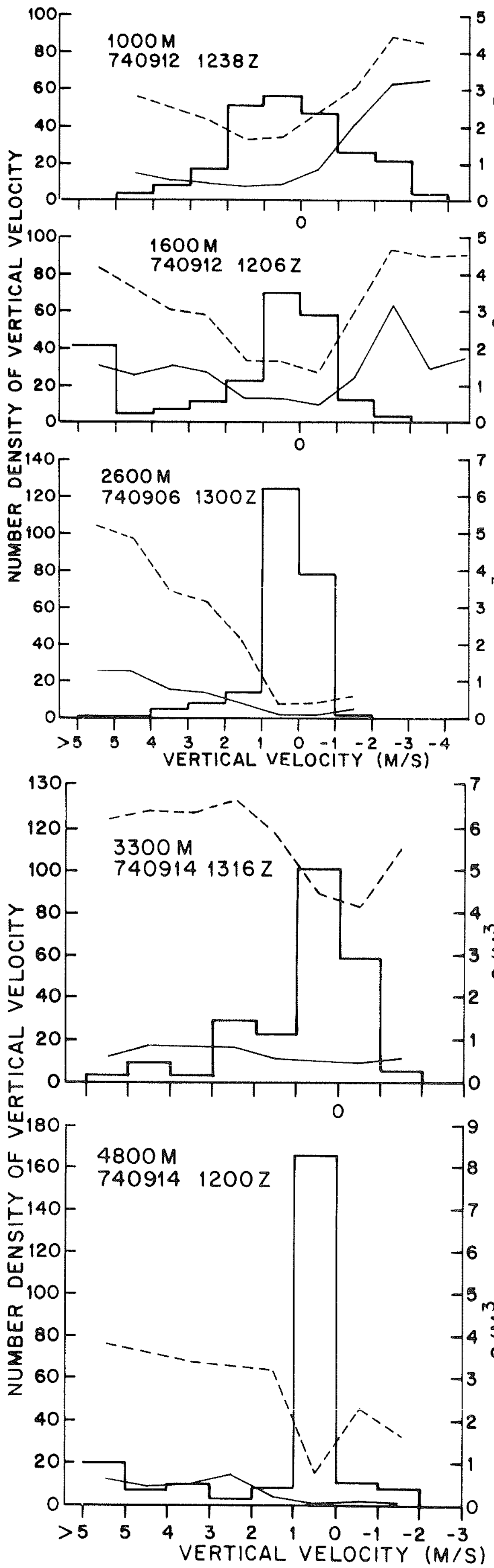

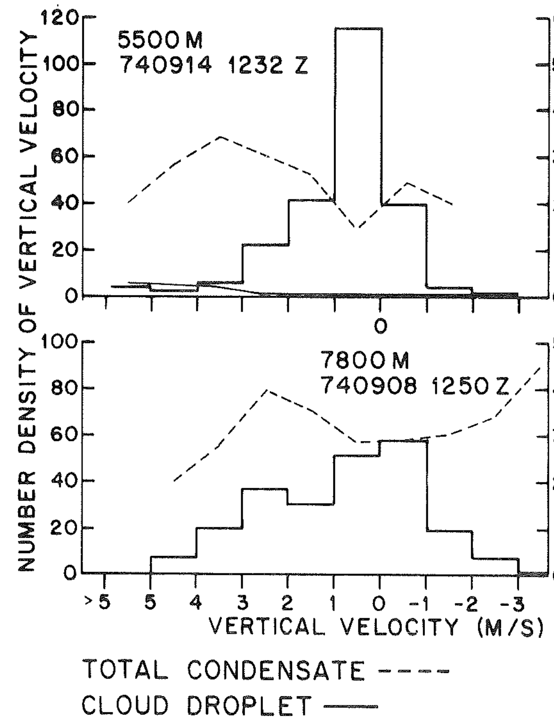

Figure 1. Observed vertical air velocity distributions (bar graph) and mean cloud droplet liquid water content (-) and mean total condensate content (---) for typical GATE cloud passes.

velocity as well, but are not presented because the correlation coefficients are generally smaller. The passes at 3300 m contain too few correlations to plot.

3. RESULTS

Figure 1 presents the vertical velocity distributions and the mean water content (cloud droplet and total condensate) in clouds at levels from 1000 m to 7800 m. The measurements in all of these clouds were taken at about 1230Z in the east central portion of the B-scale array. The levels given are radar altitudes above mean sea level. In all passes the sample length is 232 seconds. The total condensate content maximum seems to increase slightly with height up to 3300 m where it begins a gradual decrease. Suprisingly, the small droplet content at 1000 m and 1600 m is greater in the downdrafts than in the updrafts. There is no appreciable small droplet content at 7800 m.

In Figure 2, correlation coefficients between cloud liquid water content and vertical air velocity, and between cloud droplet content, and vertical velocity are plotted versus category of vertical velocity. The passes at each level do not necessarily correspond to the passes in Figure 1. A student's "t" test was performed on the correlation data and only those found to be within the 90% confidence level are presented here. In general, the correlation coefficients tend to be positive and high in moderate updrafts, very small in inactive cloud regions (-1 to +1 vertical wind), and fairly high and negative in weak downdraft regions (-1 to -4).

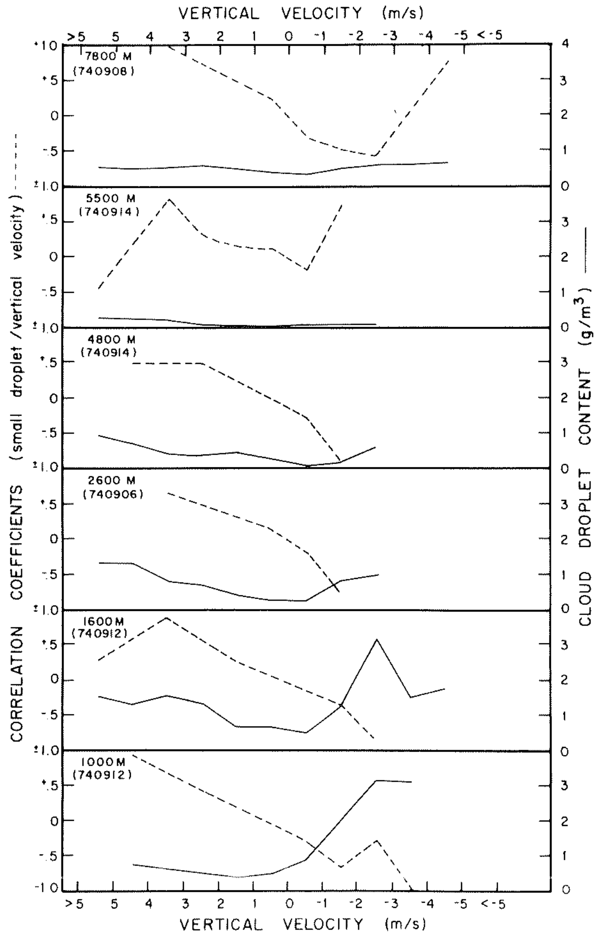

Figure 2. Correlation of vertical air velocity and cloud droplet liquid water content (J-W) and mean cloud droplet liquid water content for typical GATE cloud passes of sample size 232 seconds.

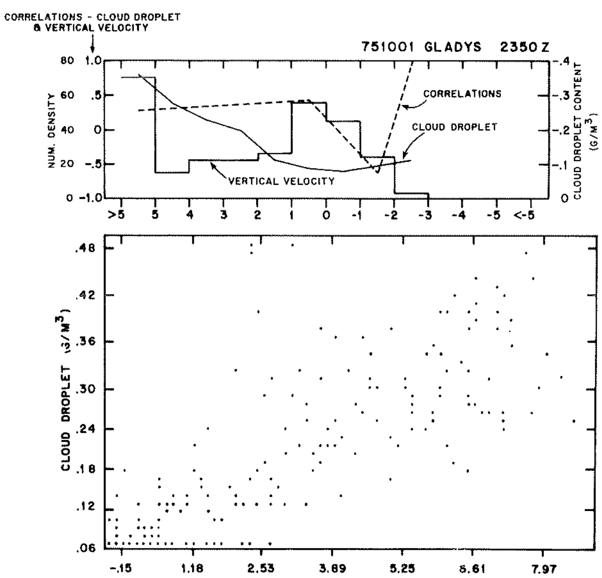

Figure 3. Upper frame - vertical air velocity distribution and correlation between vertical air velocity and cloud droplet liquid water content (283 sec sample size). Lower frame - vertical air velocity versus cloud droplet liquid water content. Both from Hurricane Gladys, 1 October 1975, 2350Z.

Figure 3 exhibits the vertical velocity distribution within the eyewall of Hurricane Gladys at 3111 m above mean sea level from a 283-second sample, along with the cloud droplet liquid water content (notice change of scale), and the correlation between the two. The lower graph is a plot of vertical velocity versus cloud water content. The correlation coefficients are smaller for the moderate updrafts than for the GATE clouds. Although the sample size is small, it appears that the cloud droplet liquid water concentration becomes very low in the -2 to -3 m/sec downdraft category. Passes through the hurricane eyewall at higher altitudes demonstrated even lower correlations, even though a broader range of updrafts and downdrafts was experienced.

For the examination of entrainment, only sections of passes characterized by continuous updrafts were computed by multiplying the measured true air speed by the seconds the aircraft was within a continuous updraft. Figure 4a

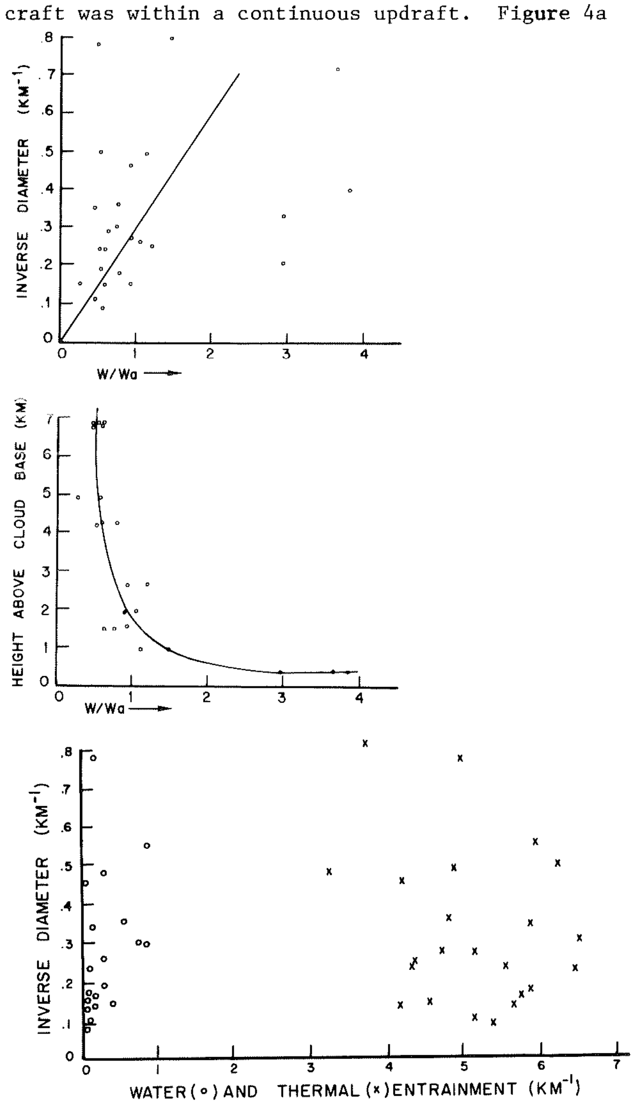

Figure 4a. The ratio 3-second running mean updraft maximum total condensate to adiabatic liquid water content (abscissa) versus inverse updraft diameter (ordinate) for selected GATE clouds. 4b. Same abscissa as 4a versus height above cloud base (ordinate) for the same data set. 4c. Water and thermal entrainments versus inverse updraft diameter for the same data set.

is a graph of inverse updraft diameter versus the ratio of condensate content to adiabatic water content. The condensate content is the 3-second running mean maximum for the plume. The cloud base values used for the computation of adiabatic water content were obtained from ship tether balloon data. Remember that total condensate content is being used in these comparisons rather than cloud droplet liquid water content. These updrafts are embedded within cloud systems that have complex mixing and precipitation mechanisms, and are not completely isolated clouds. Figure 4b is a plot of the same water content ratios to the height above cloud base. Note that, in general, the ratio of total condensate to the adiabatic value does tend to decrease with height above cloud base. The high values just above cloud base are probably dominated by hydrometeors in these updrafts.

The thermal entrainment (E_t) was computed according to the equation:

$$E_t = \frac{\frac{\Delta Q}{\Delta p} + \frac{C_p}{L}\frac{\Delta T}{\Delta p} + \frac{RT}{Lp}}{\frac{C_p}{L}(T-T') - (Q-Q')}$$

The terms are defined in the Appendix. The entrainment parameters were converted to km^{-1} from mb^{-1} using an approximation to the hydrostatic relationship. The cloud environment sounding, which was developed as a mean GATE Phase III sounding, was used (Antipovich, 1975).

Water entrainment (E_w) was computed according to the equation:

$$E_w = \frac{\frac{\Delta W}{\Delta P} + \frac{\Delta Q}{\Delta P}}{Q' - Q - W}$$

The variables are defined in the Appendix. Figure 4c represents the results of the application of the two preceding equations to the GATE data. Table 1 is a list of the specific values plotted and other related parameters.

Table 1. Synopsis of entrainment calculation input and results.

DATE	BEGIN TIME	END TIME	MAX TOTAL CONDENSATE	MAX VV	ELEVATION	DIAMETER	$E_t (KM^{-1})$	$E_w (KM^{-1})$
740905	130059	130231	4.61 g/m^3	8.9 m/s	1763 m	3652 m	5.24	.88
P_{cb} = 980 mb	132518	132550	3.55	5.9	1712	3311	6.61	.74
T_{cb} = 24.2°C	133750	133823	2.97	5.4	1705	3441	4.77	.88
	150040	150105	3.58	6.8	1673	2750	4.87	.62
Q_{cb} = 18.9 g/kg								
740906	130002	130038	5.14 g/m^3	3.9 m/s	2630 m	3814 m	4.53	.04
P_{cb} = 930 mb	133058	133109	3.74	3.5	1651	1231	3.78	-.37
T_{cb} = 18.9°C	133144	133202	2.93	5.9	1672	2043	3.30	-.14
	135348	135448	4.48	5.5	2628	6894	4.22	.12
Q_{cb} = 15.0 g/kg								
740908								
P_{cb} = 898 mb	130309	130328	4.24 g/m^3	5.2 m/s	7792 m	2820 m	5.91	.20
T_{cb} = 16.1°C	130331	130446	5.24	3.8	7790	10874	5.47	.14
Q_{cb} = 13.1 g/kg	130452	130553	4.30	4.3	7802	8981	5.19	.19
	132705	132718	5.02	6.2	7830	2014	6.32	.15
	140754	140821	5.45	5.1	7846	4128	5.63	.12
	141741	141809	5.21	2.3	7824	4175	6.57	.14
	141907	141915	4.58	5.6	7832	1287	5.00	.17
740914	110919	111014	5.48 g/m^3	8.1 m/s	4866 m	6632 m	4.63	.21
P_{cb} = 938 mb	114038	114124	7.43	9.7	4842	5685	5.98	.11
T_{cb} = 19.8°C	120219	220302	4.92	7.1	4829	5245	9.07	.28
Q_{cb} = 15.9 g/kg	125410	125459	5.55	5.3	5505	6433	5.73	.21
	131811	131846	8.09	5.3	3253	4066	4.38	-.01
	131854	131912	6.35	5.7	3239	2174	4.27	.09
	145220	145313	3.48	5.0	5486	6613	5.82	.43

4. DISCUSSIONS AND CONCLUSIONS

This paper describes an attempt to analyze the Phase III GATE data, and some 1975 hurricane data, so as to exhibit some pertinent features of convection in tropical cloud systems. The distributions of measured vertical air velocities are presented, and it is clear that strong updraft or downdraft does not, at any given instant, span a large fraction of the area covered by visible cloud. In the GATE clouds, the correlation of vertical velocity and cloud droplet liquid water content indicates that values tend to be high in updrafts, as expected, but it is also seen that fairly weak downdrafts are characterized by high, small cloud droplet liquid water content.

Entrainment calculations were limited to only sections of cloud passes with measured active continuous updrafts, first by the use of an equation for thermal entrainment, and then by use of an equation for water entrainment. It was found that in the clouds selected for study according to certain boundary conditions and selected criteria, there was no apparent relationship between inverse diameter of the updraft plume and thermal or water entrainment rates. This is not to say that there is no relationship, but only that a greater degree of stratification is required, or a different method of looking at the entrainment parameter is needed to establish a more definite correspondence.

It was thought that since the calculation of entrainment was limited to only active continuous updrafts, and since total condensate content was used, the calculations would be useful. There are several reasons that a dependence on inverse diameter, assuming it is operative, was not shown by these calculations: 1) when actual updrafts embedded in a typical larger convective cloud system are considered, it is probably impossible to adequately describe the characteristics of the air actually being entrained with any environmental sounding: and 2) a single interval from cloud base to the measurement level was utilized in the calculation of the entrainment. The difference in magnitude between the thermal and water entrainments is probably due to this single interval method. It is clear from an analysis of the structure of these clouds that they bear little resemblence to the isolated steady state cloud represented by one dimensional cumulus models. Further studies in this area are necessary.

5. ACKNOWLEDGMENTS

Thanks are due to many people who assisted in the preparation of this paper. A great amount of programming logical assistance was given by Keith Moh, Dick Darby allowed us to use his routine to read and deblock the AWRS data tape, Bill Jenrette shared his printer-plotter program with us, Eddie Brunson added in the initial program debugging. Dale Martin and Tony Mijares drafted the figures, and Cathy Delgado typed the manuscript. Charles True handled the photography. David Emmitt kindly gave us his tether balloon measurements taken during GATE.

6. REFERENCES

Antispovich, V.A., Snitkovsky, A.I. and Falkovich, A.I., 1975: On the orders of the values of the meteorological elements obtained in the A/B array in the period of GATE. GATE Report No. 14, (II), 99-116.

Axford, D.N., 1968: On the accuracy of wind measurements using an inertial platform in an aircraft, and an example of measurement of the vertical mesostructure of the atmosphere. J. App. Meteor., 7, 645-666.

Mason, B.J., 1969: Some outstanding problems in cloud physics - the interaction of microphysical and dynamical processes. Quart. J. Roy Meteor. Soc., 95, 449 - 485.

McCarthy, J., 1974: Field verification of the relationship between entrainment rate and cumulus cloud diameter. J. Atmos. Sci., 31, 1628-1639.

Sax, R.I., and Willis, P.T., 1974: Natural glaciation characteristics of an ensemble of Florida Cumulus Clouds. Preprints, Conf. on Cloud Phys., Tucson, Ariz., Amer. Meteor. Soc., 152-157.

Stommel, H., 1947: Entrainment of air into a cumulus cloud. J. Meteor., 4, 91-94.

Warner, J., 1975: Comments on "Field verification of the relationship between entrainment rate and cumulus cloud diameter." J. Atmos. Sci., 32, 995-997.

Willis, P.T., 1972: The morphology of tropical cumulus. Project STORMFURY Annual Report - 1972, U.S. Dept. of Commerce, NHEML, Coral Gables, Fla., 61-89.

7. APPENDIX

Terms in thermal and water entrainment equations are:

Q = mixing ratio (g/kg)
P = pressure (mb)
C_p = specific heat capacity at constant pressure = .24 cal/g-^{o}K
L = latent heat of condensation = 597.3 cal/g
R = gas constant for moist air =.117 cal/g-^{o}K
T = temperature (^{o}K)
T' = temperature out of cloud (^{o}K)
Q' = mixing ratio out of cloud (g/kg)
ΔQ = Q at cloud base - Q in cloud at altitude
ΔT = T at cloud base - T in cloud at altitude
ΔP = P at cloud base - P in cloud at altitude
W = total condensate content (g/m^3)
ΔW = W at cloud base (taken to be zero) - W in cloud at altitude (g/m^3)

4.3.1

COMPARISONS OF CLOUD MODEL PREDICTIONS: A CASE STUDY ANALYSIS OF ONE- AND TWO-DIMENSIONAL MODELS

By

B. A. Silverman, D. A. Matthews, L. D. Nelson
Bureau of Reclamation
Division of Atmospheric Water Resources Management
Denver, Colorado

And

H. D. Orville, F. J. Kopp, R. D. Farley
South Dakota School of Mines and Technology
Rapid City, South Dakota

1. INTRODUCTION

One measure of our understanding of cloud and precipitation processes is our ability to simulate the essential features of their behavior through numerical cloud models. Model development will progress most rapidly when modelers and observationalists interact iteratively with feedback from one to the other in a mutually supportive fashion. Unfortunately, this approach has been only seldom followed.

A convective cloud modeling workshop was convened by the Bureau of Reclamation's Division of Atmospheric Water Resources Management in Denver, Colorado, on June 11-13, 1975. The main objective of this workshop was to design a specific and continuing effort to close the gap between models and observations and thereby maximize the utility of models to contribute to our understanding of natural and artificially modified convective clouds. The workshop focused its discussions on (1) model initialization data requirements; (2) model verification data requirements, including the method or methods by which model predictions can be time-synchronized with observations of cloud development; and (3) objective model verification criteria.

To lay the foundation for these discussions, each participating modeler presented the results of his model for two standard input data sets, which were sent to him beforehand. The models were compared first to each other and then against such verification data as were available, which were first presented to the modelers at the workshop.

Twenty-two scientists representing several universities, Government agencies, and industrial groups participated in the workshop. Results from three one-dimensional, steady-state models (1D, SS), five one-dimensional, time-dependent models (1D, TD), four two-dimensional, time-dependent, axi-symmetric models (2D, TD, Axi), and two two-dimensional, time-dependent, slab-symmetric models (2D, TD, SLAB) were presented.

The purpose of this paper is to summarize the results of this workshop and indicate what follow-on work is planned or in progress.

2. MODEL PREDICTIONS AND OBSERVATIONS

Data used in the workshop were collected on August 10 and 17, 1973, in the vicinity of St. Louis as part of Project Metromex. They were graciously provided by Dr. Bernice Ackerman of the Illinois State Water Survey, who also participated in the workshop. Input rawinsonde soundings and supporting data that were used to initialize the models are shown in figures 1 and 2 and table 1, respectively.

It can be seen from figures 1 and 2 that the sounding for August 10 was quite unstable while that for August 17 was not so unstable. This resulted, as we shall see later, in the development of clouds with different growth and precipitation characteristics, which is the reason why these 2 days were selected for the workshop cases. Since the input and verification data sets were limited, we were anxious to see if the model predictions could at least distinguish the nature of the convective activity on these 2 days.

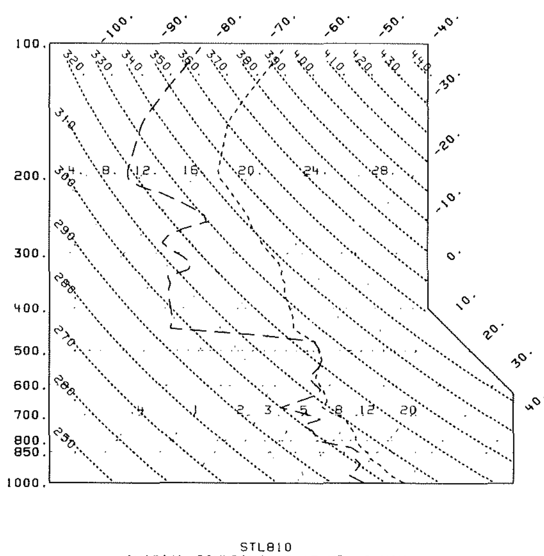

Figure 1. Skew-T, Log-P thermodynamic diagram showing initial sounding temperature and dewpoint profiles for St. Louis, Mo., on August 10, 1973, at 1300 L.S.T.

Before discussing the results of the model comparison with observations, several points concerning this phase of the workshop need to be emphasized. First, it should be recognized that the data sets were not collected for this purpose and are, therefore, not as appropriate as they might need to be. The second point is that model runs were necessarily limited by the available input data and program run costs, an expense which was borne by the sponsors of the participating modelers. Considering the sensitivity of model results to input conditions, this is an important point to remember when examining the comparative predictions. Lastly, it should be remembered that a major purpose of this model comparison was to lay the foundation for designing a more explicit and meaningful model-observation experiment that would be conducted in the future.

Tables 2 and 3 give results of the various model runs for clouds which fit into approximately the size of the observed clouds for that day, except for the slab-symmetric models which predict their own size clouds. Table 2 is for August 10 and table 3 is for August 17. In general, the one-dimensional, steady-state models or single parcel Lagrangian models, which are models 1 through 3, predict the taller clouds observed on the days. Their maximum vertical velocities ranged from 15 to 25 m sec^{-1}. Note the different results for model 1 (1a and 1b of tables 2 and 3). These two sets of results show the model's sensitivity to different initiating impulses of 2 and 1 m sec^{-1}, respectively. This further illustrates the importance of proper model initialization. In general, all of the parameters for each of the three models showed the proper tendency when compared with observations. That is, the parameter differences tended to be of the same sign, though not necessarily of the same magnitude, as the observed differences between August 10 and 17. The rainfall accumulations from these 1D, SS models were not considered to be a realistic prediction and were not taken very seriously by the modelers at the conference.

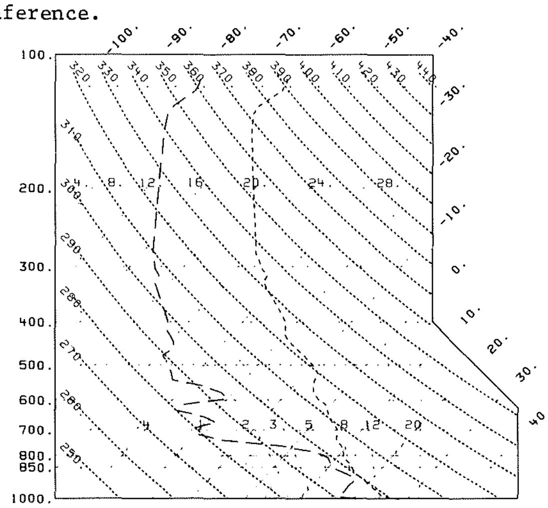

Figure 2. Skew-T analysis showing temperature and dewpoint profiles for St. Louis, Mo., on August 17, 1973, at 1300 L.S.T.

The one-dimensional, time-dependent (1D, TD) models numbered for the 10th, of which three gave fairly realistic results. For August 17, there were five runs made with one-dimensional, time-dependent models. In general, the one-dimensional, time-dependent models gave lower cloud tops than the steady-state models. The bases were predicted by these models and, in some cases, checked out fairly well, and in all cases within one grid interval of observed cloud base. Maximum vertical velocities for these models on August 10 ranged from 16 to 19.8 m sec^{-1} and on August 17 from 11.4 to 21.5 m sec^{-1}. The rain rates on August 10 were up to 54 mm hr^{-1}, which agreed well with the observations for that size cloud. Rainfall accumulated on the ground in these models was, in general, less than observed. Two of these models did predict hail at the ground, which was observed, and most of the models predicted the right tendency, at least partly.

The two-dimensional, time-dependent (2D, TD) slab models predicted a field of clouds and were successful in predicting the proper tendency from the 10th to the 17th. In addition, the cloud tops, vertical velocity maximum, maximum rain rate, and maximum accumulated rainfall were within the range of the observations. Neither of these models predicted significant hail at the ground, although one of them does include a hail process.

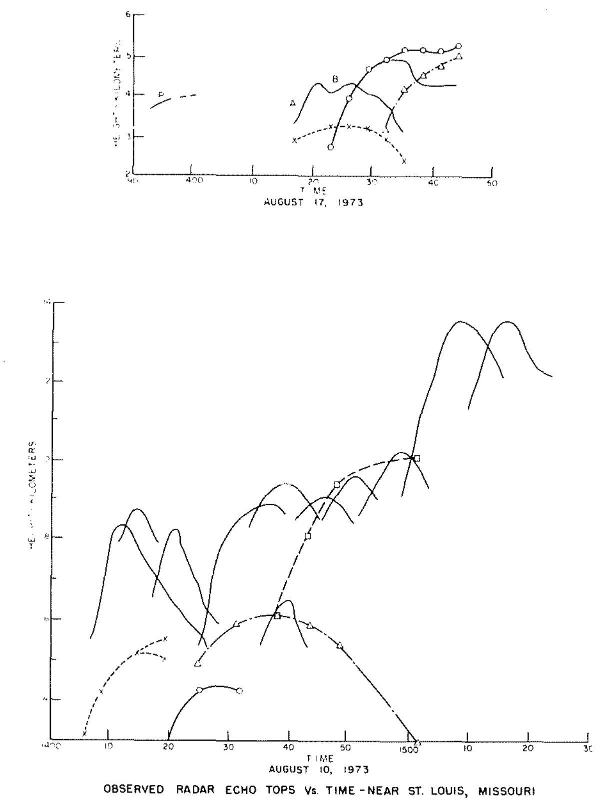

Figure 3. Comparison between observed radar echo-top height (solid lines) and predicted time-height cross section (dashed) from three models for August 10 and 17, 1973. Note the similar characteristics of models and observations.

Table 1. MODEL WORKSHOP INITIALIZATION DATA

	August 10, 1973	August 17, 1973
Cloud properties		
Updraft radius (km)	1.0, 2.0*	1.0, 2.0*
Base height (km)	1.2	1.4
CCN (C, K)**	4493.7, 0.29	1597.8, 0.37
Ice Nuclei (No./l at -16° C)	0.1-0.15	0.1-0.15
Environmental properties		
Surface maximum temperature (° C)	30.3	29.4
Corresponding dew point (° C)	19.7	21.4
Average sub-cloud convergence (sec^{-1})	-1.0×10^{-4}	-5×10^{-5}

* Use these as standards of comparisons, other radii optional
**$N(cm^{-3}) = CS^K$, where S is supersaturation

The two-dimensional, time-dependent, axi-symmetric models predicted tops within the range of the observations and, in general, had good predictions of cloud base. Their maximum vertical velocities were larger, ranging from 20 to 29 sec^{-1} on August 10 and from 8 to 13 m sec^{-1} on the 17th. In general, their clouds were larger than the slab model clouds. Except for one model, their maximum rain rates were in the proper range and where they were run on both cases they caught the proper tendency from the 10th to the 17th. Also, two of the two-dimensional, time-dependent, axi-symmetric models predicted hail on the 10th and not on the 17th.

It should be noted that the two-dimensional models predict a considerable amount of additional information that is worthy of comparison but could not be used because of the limited observations.

In general then, the models predicted the characteristics of convection on these 2 days and gave quantitative information about rainfall rates and quantities of rain from individual cells in most cases and from the whole field of convective clouds in two cases. The factor of three difference in rainfall rate in the observations was predicted in some of the models. The vertical velocity of the observations came from the rise of echo heights, which is probably an underestimate of the vertical velocity.

The time for integration is indicated in the last row of tables 1 and 2. It is seen that the time range from a few seconds to 2 hours for the one-dimensional models and up to 4 hours for the two-dimensional, time-dependent models. The axi-symmetrical models treat a single cloud, whereas the slab models treat a field of clouds, and their integration can then continue for longer times. One of the axi-symmetric models has quite detailed microphysics, including the ice stage, and its time required was not greater than the field-of-motion model.

Dr. Ackerman stressed the fact that convection on both of these days was characterized by a series of pulses, as is convection on most days. However, the data requested from the modelers did not include time-height histories, although some of the presentations indicated a spectrum of clouds. One field-of-motion model predicted the evolution of the cloud-size scales quite accurately. The other field-of-motion model gave radar echoes, and those data (dashed lines) have been plotted on figure 3, which also shows the observed rise of echoes (solid lines) on August 10 and August 17. The echo data from the model were analyzed after the fact, being initialized from the time of observed first echo. Again, the general characteristics of the convection are captured by the numerical simulations.

3. INITIALIZATION AND VERIFICATION DATA REQUIREMENTS

Specific observations required to initialize and verify a model will vary according to the complexity of the model. The following observations, listed in general order of priority, were considered important for initializing models:

a. "Representative" rawinsondes close in time and space to the appearance of the first cloud, and serial releases every 2 hours thereafter.

b. Mesoscale Beta (50-150 km) divergence measurements every 2 km up to 20 km.

c. Cloud condensation nuclei activity spectra at cloud base and 5 km.

d. Cloud base temperature and size and magnitude of updraft velocity at cloud base during developing stage.

e. Surface observations of temperature, humidity, and winds from mesoscale Alpha (10-50 km) network.

f. Ice nuclei activation spectra at cloud base as a function of supersaturation and temperature.

g. Giant nuclei (5-20 μm) number density at cloud base.

h. Cloud cover.

Table 2. AUGUST 10, 1973 - CLOUD MODEL RESULTS

	1D, SS				1D, TD				2D, TD, SLAB		2D, TD, Axi				Observations
Model	1a	Δ1b	2	3	4	5	6	+8	9	10	11	12	13	***14	
Parameters															
Radius (km)	2	2	2	2	1	2	2	1	#1.5-5.0	1-2	2.0	2.5	1.5	1.5	2.0
Top (km)	13.7	11.4	11.4	14	10.6	9.6	8.4	3.0	*9.0	10	9.6	10	9	9.8	9-10.3-14.5
Base (km)	1.2	1.2	1.2	1.2	1.0	1.5	1.4	1.4	1.4	1	1.2	1.5	1	1.2	1.2
Max W (m/sec)	17.7	14.7	24	25	19.8	17.4	16	2.1	10.6	16.7	29	23	20	20	14-15
Max rain rate (mm/hr)	-	-	-	-	-	54	47.9	-	-	**50	12	53	34	130	21.8-68-40
Rainfall depth (mm)	40	27	8	13.4	2.5	8.4	3.7	0	-	11.7	-	10.8	3.4	3.0	2.8-14-13
Hail at ground	-	-	-	-	Yes	Yes	N/A	N/A	N/A	No	Yes	N/A	N/A	Yes	Yes
Proper tendency August 10 to August 17	Yes	Yes	Yes	Yes	Partly	Partly	Partly	No	Yes	Yes	Yes	Yes	-	-	
Computer time (sec) (CDC 660)	13	-	5	-	2,200	7,200	-	910	-	14,000	9,600	-	-		

Table 3. AUGUST 17, 1973 - CLOUD MODEL RESULTS

	1D, SS				1D, TD					2D, TD, SLAB		2D, TD, Axi			Observations	
															Single cloud	Cloud complex
Model	1a	Δ1b	2	3	4	5	6	7	8	9	10	11	12	†14		
Parameters																
Radius (dm)	2	2	2	2	2	2	2	2	1	1.3	1-2	2.0	2.5	1.5	1.2	2.0
Top (km)	9.1	6.1	8	10.2	9.8	6.3	5.7	5.7	3.0	7.5	7.0	5.6	4.5	5.1	4.5-5	7.5
Base (km)	1.2	1.5	1.4	1.2	1.0	1.2	1.4	1.2	1.5	1.2	1.0	1.2	1.0	1.3	1.4	1.4
W max (m/sec)	14.6	9.2	14	16.5	21.5	14	11.4	13	2.1	6.1	13.8	13.2	9.6	8.0	-	12
Max rain rate (mm/hr)	-	-	-	-	-	78	36.4	37	None	-	**16	0.4	18	215	6.6	18
Rainfall (mm)	22.6	4.3	4.0	12.6	1.6	9.5	4.7	3.8	None	-	2	-	2.9	5.0	0.5-0.7	7.4
Hail at ground	-	-	-	-	Yes	No	N/A	N/A	N/A	N/A	No	No	N/A	No	No	No
Computer time (sec) (CDC 6600)	10	-	5	86	2,100	4,600	-	60	-	-	6,400	4,500	-			

*Cloud Growth to Model Domain Top.
**Cumulative rain plots at different times used to give rain rates after the fact.
***Results completed after the workshop.
#Initial and fully developed cloud radii.
+Model 8 omitted due to inapplicability of warm cloud simulations to this case.
ΔSame model, different initial conditions: initiating impulse 2.0 and 1.0 m sec^{-1} for 1a and 1b, respectively.
†Model 13 omitted due to insufficient computer resources.

Verification data requirements, listed in general order of priority are:

a. Radar (preferably 10 cm) - Life history for as many clouds as possible for each experimental day.

(1) First echo height, base and top defined by 10-20 dBz contour.

(2) Time - height (h) plot of average and variance of reflectivity (Z) over each cell, where a cell is defined by about the 10-20 dBz contour. (Exact contour to be determined in preliminary analysis.)

(3) x-h cross-section versus time through maximum reflectivity, preferably in plane (x) of wind or direction of echo movement.

(4) Maximum Z versus time.

(5) Maximum reflectivity for cell: time, x, and h position.

(6) Areal distribution (x, y) of maximum height of echo above 10-20 dBz (contoured) and maximum echo reflectivity every 30 minutes.

b. Aircraft

(1) Drop-size distribution at cloud base in updraft during developing stage.

(2) Partitioning of water substance into liquid and ice, averaged over the updraft, for cloud-size particles ($r<100$ μm) and precipitation-size particles ($r\geq 100$ μm) at the height of maximum reflectivity of the first radar echo.

(3) Temperature, rate of climb, and vapor in updraft and downdraft.

(4) Average cloud drop distribution over updraft and downdraft.

(5) Precipitation distribution at cloud base.

c. Surface rainfall and hail, maximum rain rate over 5 minutes and total precipitation from cell.

d. Rawinsonde, continued serial ascents, monitoring the changes in environment.

e. Visual cloud characteristics:

(1) Time lapse.

(2) Satellite - areal distribution.

(3) Human observation.

NOTE: Appearance of first echo (10-20 dBz) is the synchronization time between models and observations.

4. OBJECTIVE MODEL VERIFICATION CRITERIA

It was suggested that the verification of models must be objective and allow for natural variability between clouds on a given day, thus leading to careful verification of intermediate stages leading to precipitation. The sequence of verifiable events must be identified for each model. A figure-of-merit (FOM) test statistic was recommended for model verification between predicted (P_i) and observed (O_i) parameters,

$$\text{FOM} = \frac{\sum_i w_i \left[\dfrac{P_i - O_i}{\text{Max}(P_i/O_i)}\right]^2}{N}$$

where w_i is a weighting factor that is proportional to the parameters' certainty and/or importance and N is the number of parameters considered. A summation value of zero is a perfect score and one is a perfect bust.

It was recognized that even if precise initial conditions were known, the assumptions required to make models physically and computationally reasonable would preclude the exact duplication of the real cloud. However, a model can provide insight into the characteristic nature and time scale of clouds and precipitation that develop in the air mass represented by the given sounding. By making several runs with reasonable variations in initial conditions, as indicated by observations, it should be possible to describe the range of cloud types that could be expected.

5. CONCLUSIONS

The modeling workshop was an extremely useful first step in narrowing the gap between models and observations. It provided encouragement to the modelers by showing the ability of most models to properly characterize cloud development on the two test days. In no case were modelers trying to predict the actions of a particular cloud. They did, however, try to predict important precipitation mechanisms, types, and regions, and the detection in quantitative terms of the importance of the ice process on August 10 and its unimportance on August 17 is significant.

The workshop produced a list of observations for initializing and verifying models and suggested objective verification criteria. In the future, another workshop may be called to consider a more complete data set which is being collected primarily for this purpose as part of Project HIPLEX.

Computer-manpower resources expended in conducting this workshop were considerable. The value gained in building confidence in models, defining problems, and discussing observations made the effort worthwhile.

ACKNOWLEDGEMENTS

Those present or represented were Mr. Donald Perkey of NCAR and Drexel University; Dr. William Cotton of Colorado State University; Dr. Rainer Bleck of the National Center for Atmospheric Research; Dr. Geoffrey Hill of Utah State University; Dr. Frank Murray of Rand Corporation; Dr. Terry Clark of the Atmospheric Environment Service of Canada; Dr. Peter Hobbs of the University of Washington (absent but data presented by Bureau of Reclamation personnel); Dr. S. Soong and Dr. Robert Wilhemmson of the University of Illinois; Dr. Kenneth Young of the University of Arizona; Mr. Morton Glass of the Air Force Cambridge Research Laboratory; Mr. Richard Farley, Mr. Fred Kopp, and Dr. Harold Orville of the South Dakota School of Mines and Technology; and Dr. Bernard Silverman, Mr. Loren Nelson, and Mr. David Matthews of the Bureau of Reclamation.

All that is described in this paper resulted from the hard work and stimulating constructive discussions by the participants of the workshop. Credit for all the material comprising this summary goes to all participants. The Division of Atmospheric Water Resources Management is grateful to all participants for giving so generously of their computer resources and their time and effort expended in analyzing and presenting their model results.

THE NUMERICAL SIMULATION OF A HAILSTORM

H. D. Orville and F. J. Kopp

Institute of Atmospheric Sciences
South Dakota School of Mines and Technology
Rapid City, South Dakota 57701

1. INTRODUCTION

A hailstorm called the Fleming storm occurred on 21 June 1972 in the National Hail Research Experiment (NHRE) project area. Many observations were taken of the storm and a paper has been written by Browning and Foote (1976) concerning the storm. A numerical simulation using an atmospheric sounding from that particular day taken at Sterling, Colorado, has been employed as initial conditions for our two-dimensional, time-dependent cloud model. Several points of similarity occurred in the numerical simulation and the conceptual (largely observational) two-dimensional flow field that Browning and Foote developed for that storm (Fig. 1). Although in general we do not claim that two-dimensional, time-dependent models can simulate the details of a particular storm, still there were enough similarities on this day between the observations and the model results to probe the numerical results a little more thoroughly and relate them to the observed features of the storm for that day.

2. CLOUD MODEL

A two-dimensional, time-dependent cloud model, developed from the work of Orville (1965), Liu and Orville (1969), and Wisner et al. (1972), was used to integrate the equations on a 20 km square grid in the x-z plane with 200 m spacing. A density-weighted stream function has been used to extend the model to deep convection. Atmospheric motion, potential temperature, water vapor, cloud liquid, rain, cloud ice, and precipitating ice (graupel and small hail) are the primary dependent variables in the set of nonlinear partial differential equations which constitute the model. Production of cloud water and ice, rain and precipitating ice are simulated in the water conservation equations. Ideas from Kessler (1969) and Berry (1968) are used in the equations for production of rain from cloud water. Precipitating ice is formed by freezing rain by means of an equation due to Bigg (1953), and through an approximation to the Bergeron-Findeisen process (Orville and Kopp, 1974) with an equation that

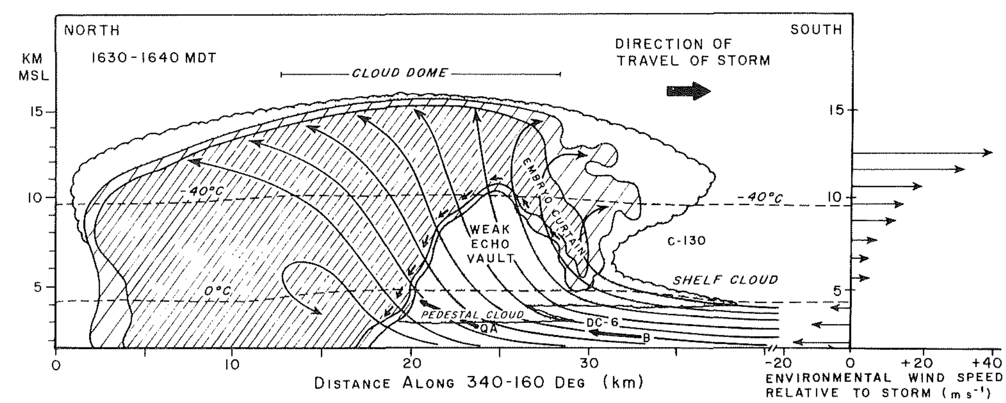

Fig. 1. Vertical section showing features of the visual cloud boundaries of the Fleming storm at 1630-1640 MDT superimposed on the pattern of radar echo. The section is oriented in the direction of travel of the storm. Two levels of radar reflectivity are represented by different densities of hatched shading. Areas of cloud devoid of detectable echo are shown stippled. Short, thin arrows skirting the boundary of the vault represent a hailstones trajectory. The thin lines are streamlines of airflow relative to the storm drawn to be consistent with the other observations. To the right of the diagram is a profile of the wind component along the storm's direction of travel, derived from a Sterling sounding 50 km south of the storm. [Figure taken from Browning and Foote (1976)]

transforms cloud liquid to precipitating ice. Accretion of cloud water by rain, cloud water and cloud ice by hail, and rain by hail is modeled. Wet and dry growth of hail and the shedding of rain from hail are simulated. An exponential size distribution is assumed for rain (Marshall-Palmer, 1948), and for hail, which is consistent with observations by Douglas (1960), and Federer and Waldvogel (1975). Cloud water freezes to cloud ice isobarically (Saunders, 1957) at a preselected temperature. Cloud liquid and ice travel with the airflow, while rain and precipitating ice fall out with terminal velocities related to the mass-weighted diameter of the precipitation. Evaporation of all forms of cloud particles can occur, and melting of frozen particles is simulated.

On the left and right boundaries, the horizontal gradients of each variable are assumed to be zero. At the top boundary all variables are held constant. Temperature and water vapor vary at the lower boundary, the earth's surface, to simulate heating and evaporation and cloud shadow effects, while the stream function is held constant. Rain and precipitating ice are permitted to fall onto the surface.

3. RESULTS

Conditions for this day are given in the Browning and Foote (1976) paper and are shown in Fig. 2 here. Light surface winds from the south less than 10 m sec^{-1} were overlain by strong upper level winds from the west-northwest greater than 50 m sec^{-1}. The model simulation used initial winds of about 2 m sec^{-1} from right to left in the lower levels below 1 km, and only 10 m sec^{-1} from left to right in the upper level. Our general experience in simulating actual observations in 2-D models is to use only a fraction of the actual winds, particularly in mid-levels, or else the convection will be inhibited and clouds advected rapidly off the grid.

The times of most intense convection in this particular simulation are shown in Figs. 3a-h. These are "snapshots" of the storm taken at 3-min intervals, starting at 99 minutes of simulated real time. Features that can be compared with the Browning-Foote cross section (Fig. 1) are the presence of pedestal and shelf clouds, evident particularly in the first few graphs, the rounded dome of the main cloud top, and the associated diverging streamline flow at about 10 to 12 km above ground level (AGL), and the general flow pattern of sloping updraft and strong inflow from the right. Keep in mind that Fig. 1 shows relative storm motions and Fig. 3 actual storm motions and streamlines.

The circulation illustrated by the streamlines is of the classical two-cell type at the early stages of the numerical integration. Figure 3a shows mid-level flow coming in from the rear of the storm; that is, from the left, turning into a downdraft in the main precipitation region slightly to the left of the mountain ridge and then reverse flow back out to the left of the domain, the first of the cells. At the same time there is low-level inflow from the right (Fig. 3a) that feeds a sloping updraft upshear with upper level outflow toward the right to complete the large-scale cell on the right of the grid. As

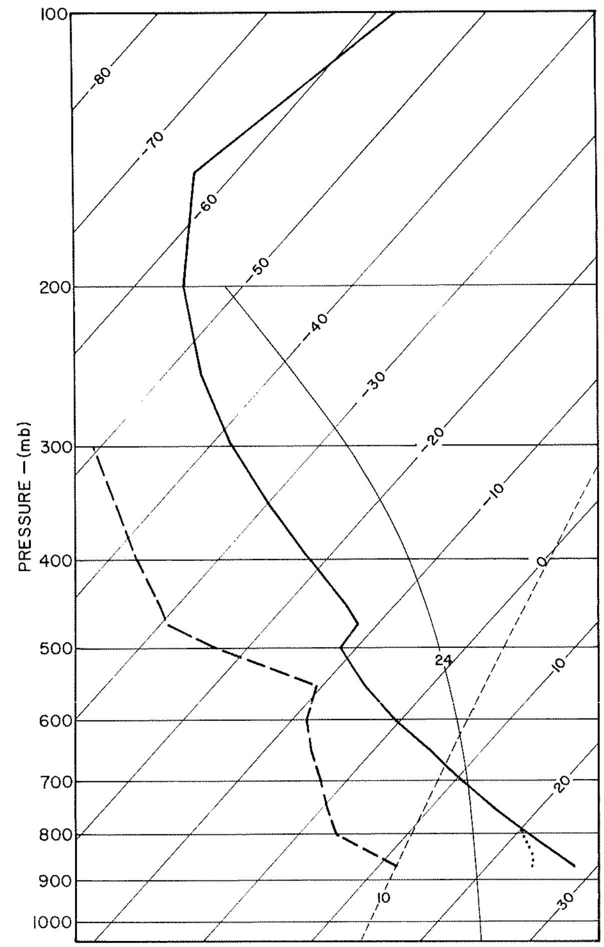

Fig. 2. An atmospheric sounding taken from Sterling, Colorado on 21 June 1972 at 1541 local time. Dashed line is dew point; solid line, the temperature; and dotted line is the observed temperature values appropriate to the environment encountered by the storm.

the precipitation impinges on the mountain ridge in Figs. 3b and 3c, no reverse flow is possible and motion down the mountain slope is then obvious. A gust front is evident in these first few panels (Figs. 3a to 3e), accelerating from speeds of 12 km hr^{-1} to 24 km hr^{-1}. An arrow indicates the streamline separating inflow from the front and inflow from the back. After this gust front moves off the grid in Fig. 3f at 114 min, the storm loses its intensity and dissipates shortly thereafter. Inflow from the right boundary is forced higher and higher; inflow from the first km is completely shut off in Fig. 3h (120 min). The updraft slope allows the main precipitation to fall out to the left, or the upshear, portion of the updraft with smaller amounts of precipitation being stripped off the upper parts of the updraft and advected to the right of the domain. This results in the appendages of the precipitating ice field shown in Figs. 3b and 3c.

The precipitation fields (only values greater than 1 gm kg^{-1} illustrated) show hail in the upper levels melting to rain in the lower levels (Figs. 3a, b, c). The rain spreads out over the mountain ridge (Figs. 3c, d). Some of the rain is recycled into the updraft, evident in Figs. 3f, g, and h. Figures 3f and 3g show that the hail rapidly consumes any rain present at temperatures below 0C so that only a small amount of rain is left at the 3 km level (AGL) in Fig. 3g. This occurs because of the accretion of the rain by the hail. Maximum depth of hail and rain on the ground was 2.8 cm and 3.0 cm, respectively, which is the greatest amount of hail in any of our numerical simulations.

The radar echoes are shown in Figs. 4a-4d at 6 min intervals starting at 99 minutes of simulated real time. They correspond to Figs. 3a, 3c, 3e, and 3g. These figures show that the radar echo is much more extensive than the precipitation fields illustrated in Fig. 3 (limited to 1 gm kg^{-1} or greater values). The overhang evident in these radar echo patterns is caused by the precipitation that has been stripped off the upper part of the sloping updraft and recycled to the right of the domain. The overhang is caused primarily by small amounts of precipitating ice, which in the modified Marshall-Palmer distribution would be primarily the graupel and small hail particles. The radar reflectivity factor patterns show the precipitation cascade where radar reflectivity factors approach 66 - 67 dBz over an extended depth in the atmosphere. The patterns are more important than the maximum values, because the ice parameterization overestimates the dBz values. The movement of the gust front and the reverse flow aloft are crucial to the maintenance of the radar overhang as it then moves to the right with the gust front. The particles in the overhang have terminal velocities about equal to the air vertical velocity and so do not fall out until passed to the downdraft portion of the circulation, or at least to weaker updrafts.

Figures 5a-e and 6a-g show the vertical velocity and buoyancy fields at 3 min intervals. Comparison of these fields at 105 and 108 minutes (Figs. 5a, b; 6c, d) shows that the buoyancy maximum is well correlated with an accelerating updraft, which has at 108 min (Fig. 5b) reached 26 m sec^{-1}. By 111 minutes the velocity maximum has reached the diverging portion of the streamlines and the buoyancy maximum splits into two parts at the 8 km level (AGL), (Figs. 6d, e). At this time the vertical velocity field and the buoyancy field are decoupled and the vertical velocity bubble at 8 - 10 km height then weakens noticeably. However, the accelerating updraft at 108 minutes (Fig. 5b) has caused a convergence of the streamlines in that region (4 to 6 km AGL and over the mountain ridge in Fig. 3d), and the effect of the compensation for $\partial\rho w/\partial z$ by $\partial\rho u/\partial x$ means that a bubble in both vertical velocity and buoyancy is left behind. These bubbles in velocity and temperature excess form a second convective cell to continue up the primary sloping updraft path and <u>leads to the concept of a large circulation cell upon which is superimposed smaller perturbations</u>.

The two-dimensionality of the model does accentuate this process, but we suspect that three-dimensional simulations will show similar constrictions connected with accelerating updrafts. The constrictions seen in rapidly growing cloud turrets may be a manifestation of an accelerating updraft.

This second buoyant cell is obvious in Figs. 5c, d; 6e, f. The cell, with a maximum vertical velocity of 16 m sec^{-1} at 111 min, accelerates to a vertical velocity of 29 m sec^{-1} at 114 minutes. The buoyancy bubble at the same time is advected upwards in the atmosphere and from 114 to 117 min (Figs. 6f, g) splits into two just as the previous cell had done. The warm bubbles caused by this splitting of the buoyant cell at about 10 km (AGL) are advected both to the right and to the left of the main updraft region. The advection speed is about 15 to 20 m sec^{-1} in agreement with the horizontal winds at these levels.

These buoyancy patterns have indicated two main cells forming the primary cloud, each cell of 10 to 15 minutes duration, but they overlap slightly so that the primary storm lifetime is approximately 20 minutes. The pedestal cloud can be identified with the buoyancy bubbles in their early stages (Figs. 6b and 3b; Figs. 6d and 3d).

The large negative temperature deviations in Figs. 6e-g are due to the overshoot into the stable stratospheric regions. The negative buoyancy in the sub-cloud layer can be traced backwards to the first fallout of rain and the evaporative cooling caused by the rain. This cool region is then advected over the mountain ridge and into the updraft region in Figs. 6e, f, and g at 111, 114, and 117 min, respectively.

4. SUMMARY

The importance of the sloping updraft is evident in the results. The upshear slope of the updraft means that the precipitation can fall into the lower atmosphere and with only minor recycling not affect the continuance of the updraft by loading. The diverging flow aloft strips off smaller amounts of precipitation and creates the radar overhang.

The radar overhang is intimately connected with the accelerating gust front, which is also an important feature of this simulation. The gust front movement towards moist air means that a greater percentage of the air flows into the storm from the front than from the back, although inflow is from both directions. The movement of the gust front off the grid to the right of the domain signifies the death of this particular model storm, cutting off flow from the lower surface layers. A wider domain would, we believe, lead to an even longer lasting storm.

The accelerating updrafts associated with warm buoyant bubbles in the atmosphere lead to cellular patterns and a general picture in which the larger storm scale circulation has superimposed on it smaller perturbations which travel up the main sloping updraft and intensify the storm periodically.

The vertical velocity and buoyancy fields are correlated in the accelerating stage of the updraft and are decoupled in the decelerating stage where the streamline flow is diverging sharply. The buoyancy bubbles separate at the inversion levels and the centers advect downwind; that is, both to the right and to the left of the main updraft region. Although not shown in these graphs because of shortage of space, the base of the shelf cloud region is at an inversion level 5 km (AGL), (the shelf cloud is indeed a manifestation of the inversion level), and it was obvious in the early stages of the integration that buoyant bubbles were splitting at that inversion level and spreading in the horizontal, just as the main cells did at the tropopause later.

Cool updrafts are indicated in the subcloud region, which in this simulation have their source from evaporating rain at an earlier stage. Slight recycling of rain occurs in the updraft, but not enough to significantly load or kill the updraft. Formation of pedestal clouds, shelf clouds, rounded dome topping off at about 13.7 km (msl), the sloping updrafts, and some features of the radar pattern are all characteristic features of the observations for that day. The flow from the rear into the gust front, the lack of any weak echo vault in the model simulations, and the mismatch of the height of the shelf cloud are obvious disagreements with the observations.

These results, combined with several other model simulations using real data, have led us to be encouraged that the general convective characteristics and primary precipitation processes on a particular day may be detected via the use of numerical simulations. Consequently, models of this complexity might be an aid in evaluating field projects and possibly might even be used for predictions with the next generation computers. The main improvement to the model needs to be made in the simulation of hail (via modeling of discrete size intervals) and is being accomplished at this time.

Acknowledgments. This research was performed as part of the National Hail Research Experiment, managed by the National Center for Atmospheric Research, under Grant No. DES73-03882 and under National Science Foundation Contract No. C760, Subcontract NCAR S5011.

The National Center for Atmospheric Research, which is sponsored by the National Science Foundation, provided computer time for this research.

REFERENCES

Berry, E. X., 1968: Modification of the warm rain process. Preprints 1st Natl. Conf. Wea. Modif., Albany, New York, Amer. Meteor. Soc., 81-88.

Bigg, E. K., 1953: The supercooling of water. Proc. Phys. Soc. B, 66, 668-694.

Browning, K. A., and G. B. Foote, 1976: Airflow and hail growth in supercell storms and some implications for hail suppression. Quart. J. Roy. Meteor. Soc., (in press).

Douglas, R. H., 1960: Size distributions, ice contents and radar reflectivities of hail in Alberta. Nubila, 3, 5-11.

Federer, B., and A. Waldvogel, 1975: Hail and raindrop size distribution from a Swiss multicell storm. J. Appl. Meteor., 15, 91-97.

Kessler, E., III, 1969: On the distribution and continuity of water substance in atmospheric circulations. Meteor. Monogr., 10, No. 32, 84 pp.

Liu, J. Y., and H. D. Orville, 1969: Numerical modeling of precipitation and cloud shadow effects on mountain-induced cumuli. J. Atmos. Sci., 26, 1283-1298.

Marshall, J. S., and W. McK. Palmer, 1948: The distribution of raindrops with size. J. Meteor., 5, 165-166.

Orville, H. D., 1965: A numerical study of the initiation of cumulus clouds over mountainous terrain. J. Atmos. Sci., 22, 684-699.

________, and F. J. Kopp, 1974: Numerical simulation of cloud seeding experiments. Preprints 4th Conf. Wea. Modif., Ft. Lauderdale, Florida, Amer. Meteor. Soc., 28-35.

Saunders, P. M., 1957: The thermodynamics of saturated air: a contribution to the classical theory. Quart. J. Roy. Meteor. Soc., 83, 342-350.

Wisner, C. E., H. D. Orville, and C. G. Myers, 1972: A numerical model of a hail-bearing cloud. J. Atmos. Sci., 29, 1160-1181.

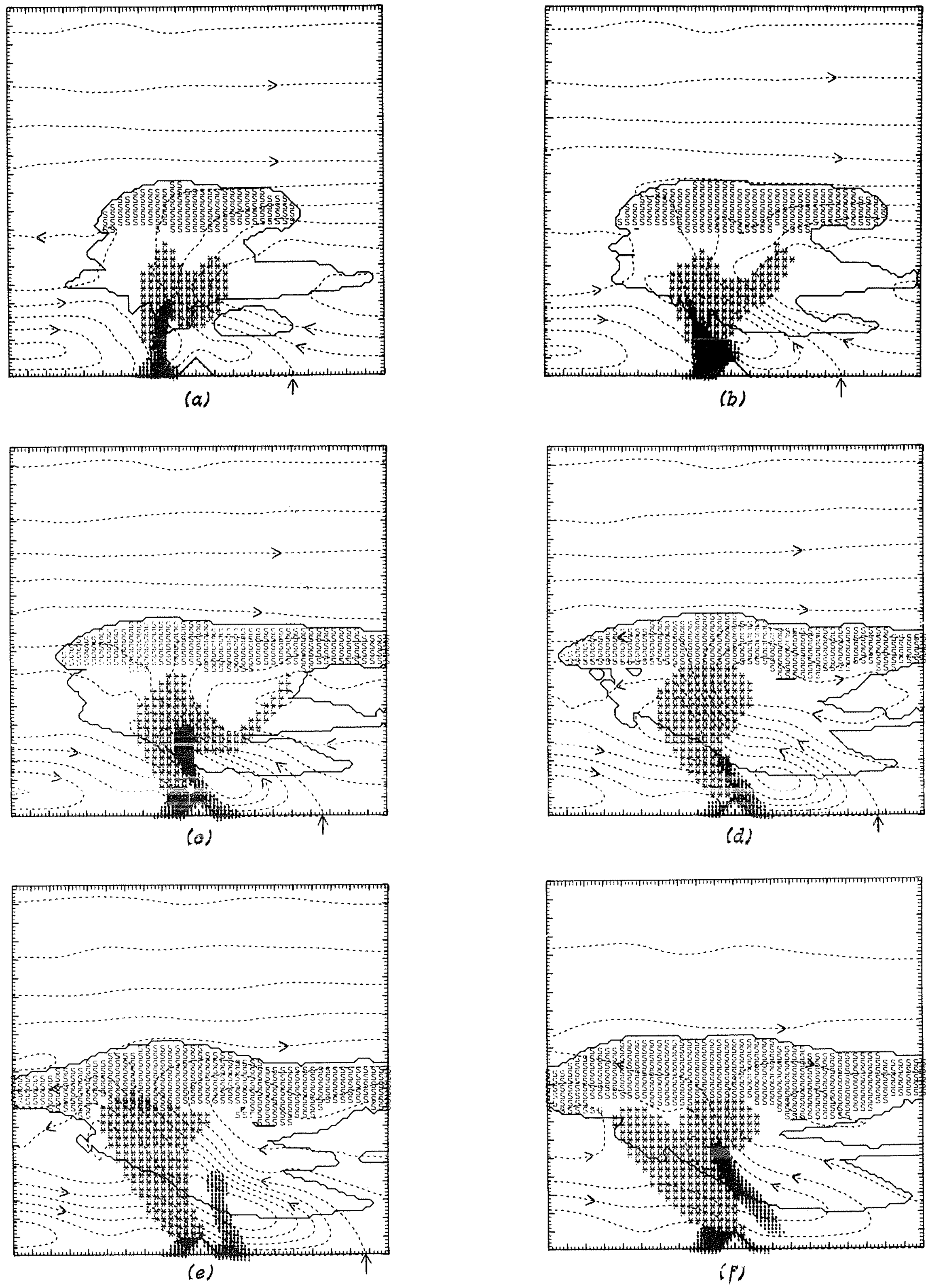

Fig. 3a-h. Numerical simulation of cloud and precipitation evolution in a vertical cross section of the atmosphere, 20 km on a side. A mountain ridge 1 km high is centered on the lower boundary. Cloud areas (100% relative humidity) are outlined by the solid lines; the stream function illustrates the airflow and is given by the dashed lines (contour interval 5×10^3 kg m^{-1} s^{-1} except in (f) and (h) where the interval is 1×10^4 kg m^{-1} s^{-1}). The symbols • and * denote rainwater and graupel or hail contents greater than 1 gm kg^{-1}, respectively, and the S denotes cloud ice regions. Figure 3a is for 99 min of simulated real time, the other figures follow at 3 min intervals, the last being for 120 min. The arrow on the lower border denotes the gust front. Major tick marks are 1 km apart.

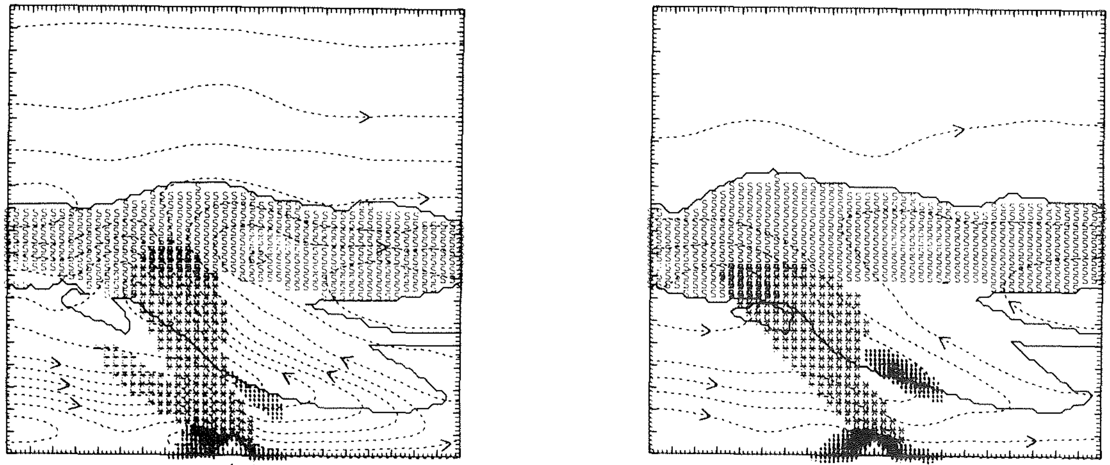

(g) (h)

(Figure 3 continued.)

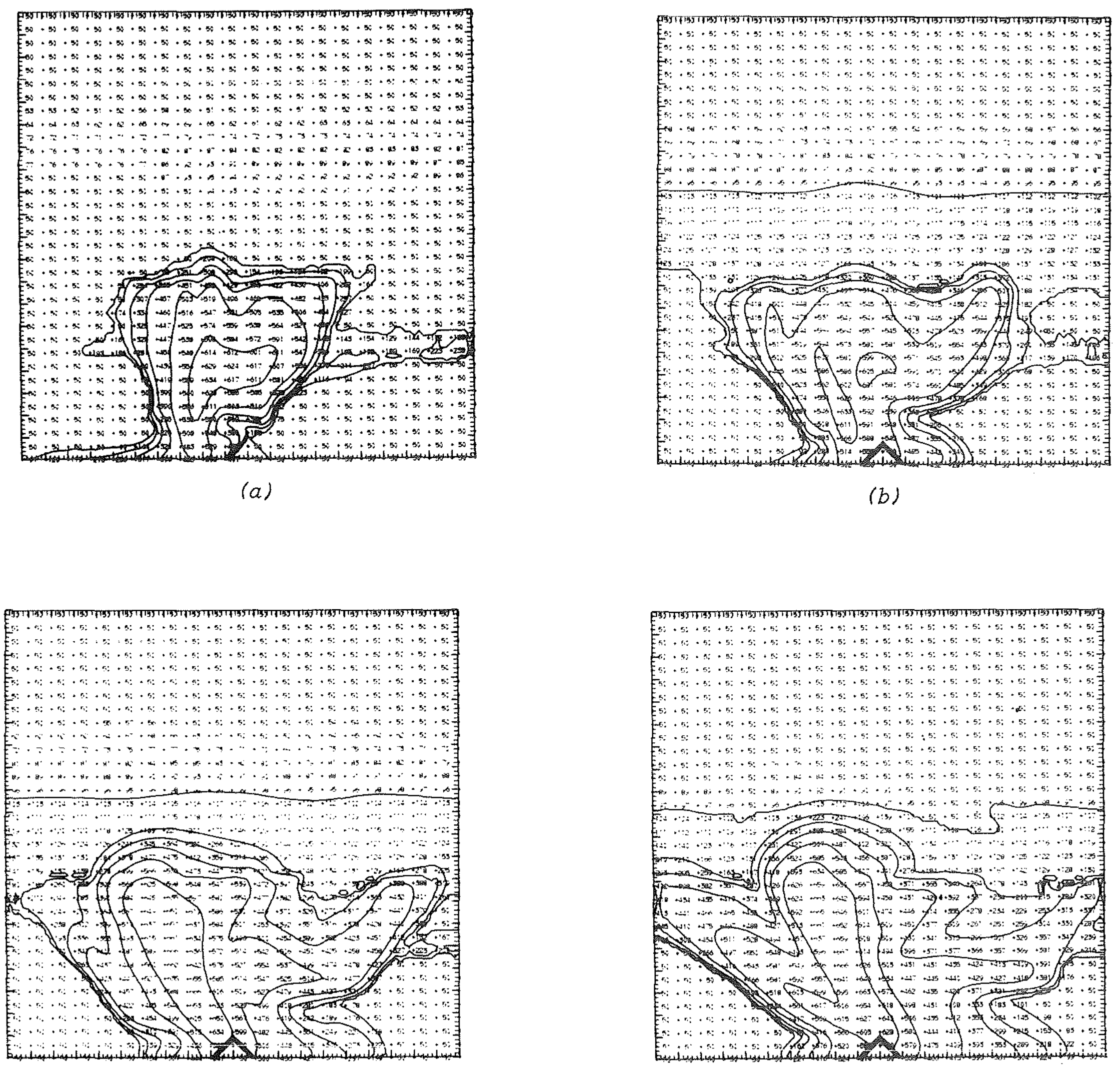

(a) (b) (c) (d)

Fig. 4a-d. Radar reflectivity factor patterns at (a) 99 min, (b) 105 min, (c) 111 min, and (d) 117 min. The contours are for every 10 dBz starting at 10 dBz.

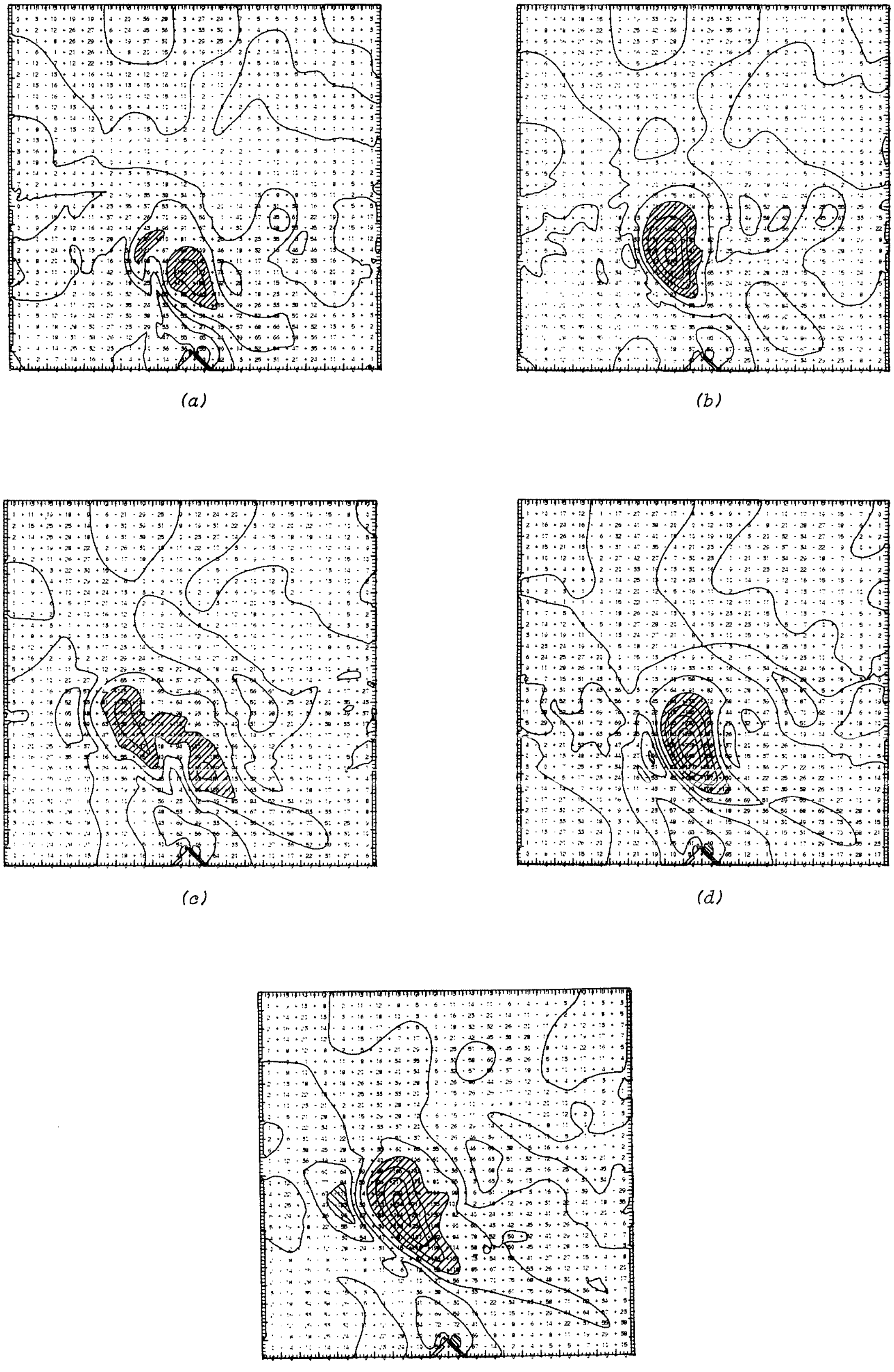

Fig. 5a-e. The vertical velocity fields at (2) 105 min, (b) 108 min, (c) 111 min, (d) 114 min, and (e) 117 min. Contour interval is 5 m s^{-1}, the values greater than 10 m s^{-1} are shaded (negative values less than -10 m s^{-1} have opposite slant).

a) 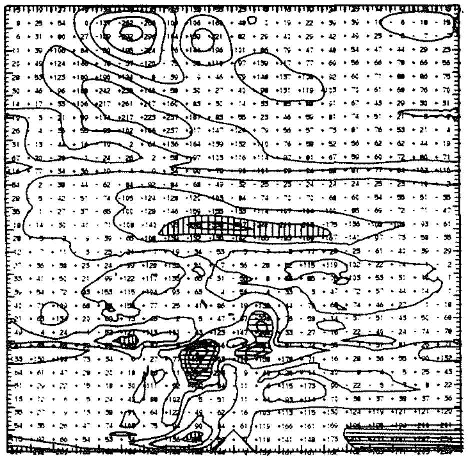

b) 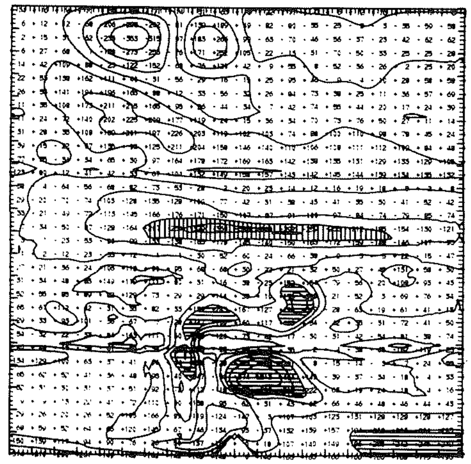

c) 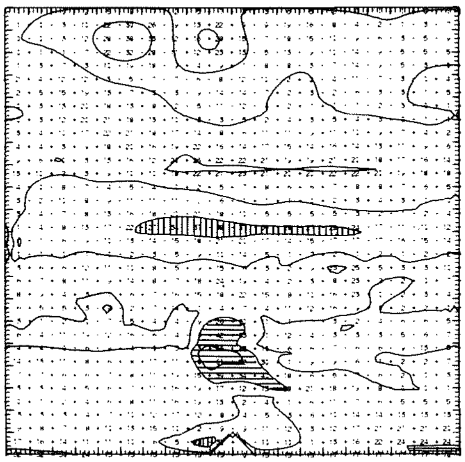

d) 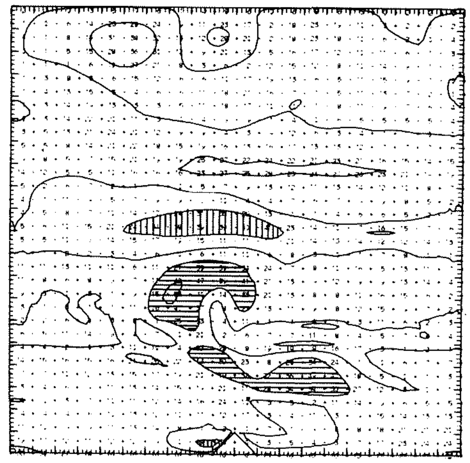

e) 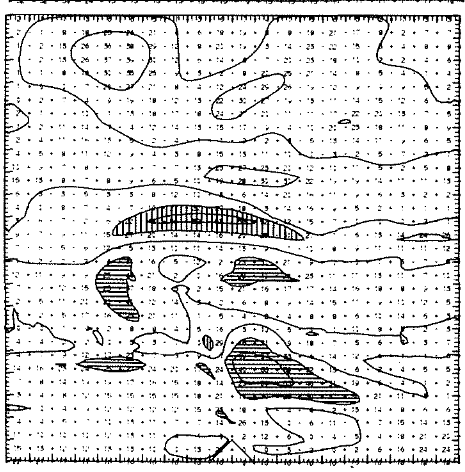

f) 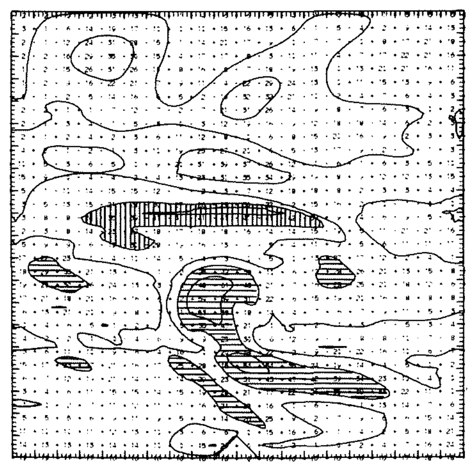

g) 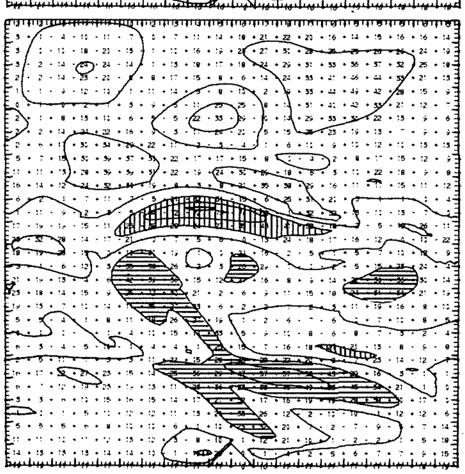

Fig. 6a-g. The temperature deviation from the initial conditions (°C) for (a) 99 min, (b) 102 min, (c) 105 min, (d) 108 min, (e) 111 min, (f) 114 min, and (g) 117 min. Areas with temperature changes greater than absolute value of 2C are shaded in (a) and (b) where contour intervals are for every °C, and for values greater than absolute value of 2.5C in (c) through (g) where the interval is 2.5C. Vertical shading denotes cool regions; horizontal shading is warm regions.

4.3.3

COLD DOWNDRAFTS IN CUMULONIMBUS CLOUDS; A NUMERICAL EXPERIMENT

Krzysztof E. Haman and Michal Niewiadomski

Institute of Geophysics, University of Warsaw
Warsaw, Poland

1. INTRODUCTION

The mechanism of cold, negatively buoyant downdrafts in Cumulonimbus clouds is a not completely clear phenomenon. Byers and Braham (1949) in "The Thunderstorm" attributed it to the precipitation, which initiates the downdraft by the drag and cools it by evaporation. Most of the numerical cloud models adopted this point of view, assuming, that in the presence of any liquid water, the air is saturated. However, Kamburova and Ludlam (1966) have proved, that typical raindrops evaporate so slowly, that for reasonable rainfall intensity they can provide negative buoyancy only at very low downward velocities, or at very low hydrostatic stability of the ambient air. Recently Girard and List (1975) took this fact into account in fairly sophisticated Cb model, showing that the rainfall can induce a cold downdraft but only of short duration. Thus the mechanism of quasisteady cold downdrafts which is an essential feature of squall lines or supercell storms is still unclear.

Haman (1973) suggested that entrainment of air from the neighbouring updraft which is rich in small, fast evaporating droplets may explain this phenomenon. However effect of entrainment of liquid water which chills the updraft by evaporation, is in this mechanism partly compensated by paralell entrainment of positive buoyancy and opposite vertical momentum. This suggested, that there might be only a limited range of conditions under which such mechanism of chilling and maintaining the downdraft would work. A qualitative analysis performed in mentioned paper by Haman (1973) confirmed this supposition, but a numerical experiment was necessary for more quantitative information. Performing this experiment was the primary goal of the present work, described shortly in the sections 2 and 3.

However, in course of computations, it was found, that the effect of entrainment from the neighbouring updraft for realistic values of entrainment rates and stratifications, is less effective than it had been formerly expected, particularily in the lower portions of the cloud. Search for another mechanism brought the authors to a hypothesis, that if the updraft-downdraft interface is slanted, the precipitation falling from the updraft may supply additional amount of fast evaporating water. It seems, that the fraction of updraft's liquid water contained in droplets with diameter within the range 0.3 - 0.7 mm, can be effective in driving the downdraft below the cloud base.

2. THE MODEL

2.1 Description

The model used in the present paper consists of one-dimensional, purely buoyant (no perturbation pressure forces) updraft, and also one-dimensional, purely buoyant downdraft, in form of steady jets with top hat profiles of all variables. The updraft entraines the air from ambient environment; the downdraft - from the updraft and eventually from the environment as well (Fig.1). A monodispersive rain is allowed to fall through the downdraft, interacting with small droplet fraction and water vapour, by condensation-evaporation and coalescence. Small droplet fraction is assumed to have zero free-fall velocity and to evaporate instantly in unsaturated air. Intensity of the rainfall is predetermined at the top of the downdraft. Entrainment into the updraft is assumed constant; for the downdraft, it has been parametrized in various ways. For the updraft the initial conditions with respect to altitude (Cauchy type), are determined at the assumed cloud base; for the downdraft - at certain pre-determined level ("computational top"), at which the downdraft is assumed to have already a non-zero velocity. The computations are started from calculation of the vertical profile of the updraft, from the cloud base to the "computational top" of the downdraft. Then initial conditions for the downdraft, consistent with the updraft properties, are formulated and vertical profile for the downdraft computed. Let us notice, that in this way only the influence of the updraft upon the downdraft is taken into account. Consideration of mutual interaction is very complex from mathematical point of view and presumably would not help much in understanding the physics of the problem.

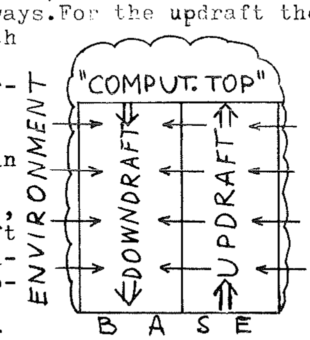

Fig.1

2.2 Equations

Equations are essentially the same as used by Haman (1973), except that the thermodynamics is less simplified and contains the effects of rainfall. Below only equations for downdraft are given; those for updraft differ from them only formally.

The following symbolics is used: B - ventilation factor; c_p - specific heat of air at constant pressure; c_w - specific heat of water(liquid); E - coalescence effitiency for rain and small droplet fraction (SDF), in computations assumed 0.6; g - gravity acceleration; L - latent heat of water condensation; m - raindrop mass; N - number of raindrops in unit volume; q - specific humidity; Q(p,T) - saturation specific humidity; p - hydrostatic pressure in ambient air; r - raindrop radius; R - linear scale of the downdraft or updraft (for instance radius); S - downdraft or udraft cross-section area; T - temperature(Kelvins); U - horizontal velocity; V - SDF specific liquid water content; w - vertical velocity (positive upwards); z - vertical coordinate (positive upwards); - udraft-downdraft inclination angle; ϱ - density; μ - entrainment coefficient; $\mu_e^{\downarrow}$ - partial entrainment coefficient (ambient air into downdraft); $\mu_u^{\downarrow}$ - partial entrainment coefficient (updraft air into downdraft);

Indices: "$_o$" - refers to the ambient air; "$\uparrow$" - refers to the updraft; "$\downarrow$" - refers to the downdraft; "r" - refers to the raindrops with radius r (w_r - free-fall velocity of raindrops with radius r); "$_w$" - refers to the liquid water.

Few other symbols are explained in the text. All units in SI, if not otherwise stated.

Equations:

$$\mu = \frac{1}{\varrho S w}\frac{d(\varrho S w)}{dz} \; ; \quad \mu^{\downarrow} = \mu_e^{\downarrow} + \mu_u^{\downarrow} \quad \ldots\ldots(1)$$

$$w^{\downarrow}\frac{dw^{\downarrow}}{dz} = \left(\frac{\varrho_o - \varrho^{\downarrow}}{\varrho^{\downarrow}} - V^{\downarrow} - \frac{Nm}{\varrho^{\downarrow}}\right)g - \mu_e^{\downarrow}w^{\downarrow 2} + - \mu_u^{\downarrow}w^{\downarrow}(w^{\downarrow} - w^{\uparrow}) \quad \ldots\ldots(2)$$

$$\frac{d(q^{\downarrow} + V^{\downarrow})}{dz} = \mu_e^{\downarrow}(q_o - q^{\downarrow} - V^{\downarrow}) + \mu_u^{\downarrow}(q^{\uparrow} + V^{\uparrow} - q^{\downarrow} - V^{\downarrow}) - \frac{N(w^{\downarrow} - w_r)}{\varrho^{\downarrow} w^{\downarrow}}\frac{dm}{dz} \quad (3)$$

If $q + V \geqslant Q(p,T)$ then $q = Q(p,T)$ ....(4)

If $q + V < Q(p,T)$ then $V = 0$.............(5)

$$c_p\frac{dT^{\downarrow}}{dz} = \frac{1}{\varrho^{\downarrow}}\frac{dp}{dz} + \mu_e^{\downarrow}c_p(T_o - T^{\downarrow}) + \mu_u^{\downarrow}\left[c_p(T^{\uparrow} - T^{\downarrow}) + - LV^{\uparrow}\right] + L\frac{N(w^{\downarrow} - w_r)}{\varrho^{\downarrow} w^{\downarrow}}\frac{dm}{dz} \; ;(\text{for } V^{\downarrow} = 0) \ldots(6)$$

$$\left(c_p + L\frac{\partial Q}{\partial T}\right)\frac{dT}{dz} = \left(\frac{1}{\varrho^{\downarrow}} - L\frac{\partial Q}{\partial p}\right)\frac{dp}{dz} + \mu_e^{\downarrow}\left[c_p(T_o - T^{\downarrow}) + L(q_o + Q^{\downarrow})\right] + \mu_u^{\downarrow}\left[c_p(T^{\uparrow} - T^{\downarrow}) + L(q^{\uparrow} - q^{\downarrow})\right] \quad (\text{for } V > 0) \ldots(7)$$

$$\frac{dN}{dz} = -\frac{N}{w^{\downarrow} - w_r}\left(\frac{dw^{\downarrow}}{dz} - \frac{dw_r}{dz}\right) \ldots(8)$$

$$\frac{dm}{dz} = \frac{\pi r^2 E\varrho^{\downarrow}V^{\downarrow}w_r}{w^{\downarrow} - w_r} + \frac{4\pi r\varrho^{\downarrow}BD(q^{\downarrow} - Q_r)}{w^{\downarrow} - w_r} \ldots(9)$$

$$\frac{dT_r}{dz} = \frac{3E\varrho^{\downarrow}V^{\downarrow}w_r(T^{\downarrow} - T_r)}{4\varrho_w r(w^{\downarrow} - w_r)} + \frac{3\varrho^{\downarrow}BD\left[(q^{\downarrow} - Q_r)L + c_p(T^{\downarrow} - T_r)\right]}{c_w\varrho_w r^2(w^{\downarrow} - w_r)} \ldots(10)$$

The following parametrizations of $\mu^{\downarrow}$ were used:

$$\mu_e^{\downarrow} = \text{const}; \quad \mu_u^{\downarrow} = \text{const}; \ldots(11)$$

$$\mu_e^{\downarrow} = \frac{\text{const}}{R} \; ; \quad \mu_u^{\downarrow} = \frac{\text{const}(w^{\uparrow} - w^{\downarrow})}{R\, w^{\downarrow}} \ldots(12)$$

$$\mu_e^{\downarrow} = 0 \; ; \quad \mu_u^{\downarrow} = \frac{1}{\varrho^{\downarrow}}\frac{d\varrho^{\downarrow}}{dz} - \frac{2\,U\,w_r}{\pi R\,(w^{\downarrow} - w_r)w^{\downarrow}} (13)$$

$$\mu^{\downarrow} = F \text{ if } F < 0; \quad \mu^{\downarrow} = 0 \text{ if } F \geqslant 0, \text{where}$$

$$F = \frac{w_r}{w^{\downarrow} - w_r}\left(\frac{1}{\varrho^{\downarrow}}\frac{d\varrho^{\downarrow}}{dz} + \frac{1}{w^{\downarrow}}\frac{dw^{\downarrow}}{dz}\right) \ldots(14)$$

3. RESULTS

The number of variants analysed within the present experiment is too large to permitt full discussion within a paper of so limited volume; some parts of the experiment are still being continued; thus, only general conclusions illustrated by few examples (Fig.2-4) are given here. In their interpretation one should remember, that the model is based on physically clear, but often unrealistic assumptions (for instance - monodispersive rain), and adoption of the presented conclusions to the real clouds must be made with sort of inter- or extrapolation. All downdrafts used as illustrations in this paper has been calculated for stratifications and updraft profiles given on the Fig.2. Downdrafts were started at 7000m ("computational top"). Downdraft computations were terminated if $|w^{\downarrow}|$ became smaller than 0.1m/s. The downdrafts were tested for their sensitivity to initial conditions, ambient stratification and entrainment parametrization.

The general conclusions are as follows:

Entrainment of upward momentum and positive buoyancy might have an essential restraining effect on the downdraft in its most upper portion (below the "computational top"). Presence of rainfall drag and negative buoyancy at "computational top" help sometimes to overcome this effect. Initial values of $w^{\downarrow}$ and $V^{\downarrow}$ are of secondary importance. In central and lower parts of the downdraft the role of rain is negligible or even negative (washout of small droplet fraction). This suggests that the mechanism proposed by Byers and Braham (1949), being probably essential at the initial stage of the downdraft, is not responsible for its further behaviour. It is worth of noting, that downdraft with no entrainment, penetrates fairly deeply downwards as warm downdraft, mainly due to downwards momentum acquired in its upper part and not diluted below.

The downdraft behaviour depends essentially on the value of $\mu^{\downarrow}$ but any reasonable parametrization of $\mu^{\downarrow}$ brings to fairly similar results as $\mu^{\downarrow}$= const; the feedbacks present in the assumed parametrization schemes tend to stabilize $\mu^{\downarrow}$ along considerable portions of the downdraft. Additional entrainment od ambient, cloudless air invigorates in certain cases the downdraft by more intense evaporation in the saturated part, but the downdraft earlier shifts from saturated to unsaturated regime of motion. Let us notice that in most cases corresponding to realistic stratifications and values of $\mu^{\downarrow}$, this change results in fast loss of negative buoyancy.

No reasonable choice of the parameters of the model and environmental stratification has been found til now, which would give downdrafts terminating lower than ca 1000 m above the cloud base. Thus another mechanism seems to be necessary for an explanation of the existence of fairly steady, cold downdrafts reaching the surface.

4. NEW HYPOTHESIS

The results presented in the previous section show, that the entrainment of cloudy air from the updraft, though fairly effective in upper and central parts of the cloud, is not likely to drive the cold downdraft to the ground, or even to the cloud base.

Let us now suppose that the updraft is slanted and placed above the downdraft (Fig.5). Since the cloud and precipitation droplets in the updraft have certain gravitational sedimentation speed w_g, they will moove across the updraft-downdraft interface (provided that the turbulence is unable to obscure this process). If the droplets are small enough, that they can be assumed to evaporate instantly in unsaturated air (as SDF in previous model), keeping the downdraft nearly saturated in a belt of width $R^{\downarrow}$, the effect of their transfer will be equivalent to adding to the term $\mu_u^{\downarrow}V^{\uparrow}$ in Eqs.(3) and (6) a new one:

$$\mu_g^{\downarrow}V_g^{\uparrow} = V_g^{\uparrow}\frac{w_g \ \mathrm{ctg}\alpha}{w^{\downarrow}R^{\downarrow}} \ \ldots\ldots\ldots\ldots (15)$$

where index "g" refers to the average properties of the part of $V^{\uparrow}$ which participates in the considered process.

If radii of droplets are so large, that assumption of instantaneous evaporation becomes too crude, their effect can be calculated as for rainfall, and for droplets with radius r, introduced as an additional expression in Eqs.(3) and (6):

$$N_r^{\downarrow} \frac{4\pi BDr(q^{\downarrow}-Q_r)}{w^{\downarrow}} = V_r^{\downarrow}\frac{3BD(q^{\downarrow}-Q_r)}{w^{\downarrow}r^2} \ \ldots (16)$$

where $N_r^{\downarrow}$ and $V_r^{\downarrow}$ correspond to the fraction of $V^{\downarrow}$ with radius r.

Simple considerations upon the kinematics of droplets motion close to the updraft-downdraft interface show, that the concentration of droplets on both sides of the interface should be the same. Thus the expression:

$$\mu_r^{\downarrow}V_r^{\uparrow} = V_r^{\uparrow}\frac{3BD(q^{\downarrow} - Q_r)}{w^{\downarrow}r^2} \ \ldots\ldots\ldots\ldots (17)$$

should be an overestimate of (16); note that r refers now to the droplets in the updraft, so, that the evaporating surface of droplets is overestimated by that at the beginning.

Let us notice, that while (15) is too crude as an overestimate of evaporation of too large droplets, (17) is too crude for too small ones and while the first one depends on the size of the downdraft, the second one does not. Substituting: $R^{\downarrow} \approx 1000$; $w^{\downarrow} \approx -5$; $\mathrm{ctg}\alpha = 1$; $w_g \approx 1$ (droplets about 0.2mm in diameter) we find $-\mu_g^{\downarrow} \approx 2.10^{-4}$, what is close to the lower limit of $\mu^{\downarrow}$ significant to the downdraft maintenance. The same value 2.10^{-4} we find for $\mu_r^{\downarrow}$ in (17) substituting: $w^{\downarrow} \approx -5$; $D \approx 2.10^{-5}$; $B \approx 3$; $\rho_w \approx 10^3$; $q - Q_r \approx 10^{-3}$ $r \approx 0.5$ mm. This means, that with the accuracy to the particular choice of data in the above examples (which seems to be fairly reasonable), droplets with diameters smaller than 0.2 mm, or larger than 1 mm, would be hardly effective in maintaining cold downdrafts of reasonable size. Since the two overestimates (15) and (17) intersect for droplet diameter somewhere about 0.5 mm, the interval of droplet diameters 0.3 - 0.7 mm is probably optimal for downdraft cooling by the mechanism now under consideration.

The essential feature of this mechanism is the increase of the entrainment coefficient for $V^{\uparrow}$ with respect to those for opposite buoyancy and momentum. This is equivalent to adding to the term $\mu_u^{\downarrow}V^{\uparrow}$ in (3) and (6) a new term of the form:

$$\mu^{*}V^{\uparrow} = \frac{\beta}{w^{\downarrow}} \ V^{\uparrow} \ldots\ldots\ldots\ldots\ldots\ldots (18)$$

where β depends on the angle of downdraft inclination, downdraft size and shape, and droplet spectrum of the updraft liquid water content, becoming small if this spectrum is strongly shifted towards large or very small droplets. Some experiments performed with $\beta =$ const (Figs.6 and 7) seem to confirm, that this mechanism can lead to a cold downdraft of reasonable size and intensity, down to the cloud base.

5. CONCLUSIONS

The numerical experiments performed with the one dimensional model of updraft-downdraft interaction confirmed, that rainfall of realistic intensity is not likely maintain a steady, cold downdraft down to the ground, unless the hydrostatic stability of the environmental air is very low. Entrainment of the cloudy air from the neibouring updraft can maintain such downdraft in the upper and central parts of the cloud, nevertheless such downdraft is not likely to reach the ground, nor even the cloud base. Fairly realistic cold downdrafts, able to reach the surface form, if additional supply of easily evaporable water is allowed. A source of such a supply can be attributed to the updraft, provided, that the updraft-downdraft interface is slanted and that the updraft (overlaying the downdraft) contains sufficient amount of liquid water in small, but not too small, droplets.

6. REFERENCES

H.R.Byers and R.R.Braham, Jr., 1949: The Thunderstorm, Report on The Thunderstorm Project, U.S.Weather Bureau, Washington D.C., pp.31-38.

C.Girard anf R.List, 1975: Thermodynamics of falling precipitation zones, Pageoph, Vol.113, pp.1035-1053.

K.Haman, 1973: On the updraft-downdraft interaction in convective clouds, Acta Geoph.Pol. Vol.XXI, pp.215-233.

P.L.Kamburova, F.H.Ludlam, 1966: Rainfall evaporation in thunderstorm downdroughts, Quart.J. Roy.Met.Soc., 92, pp.510-518.

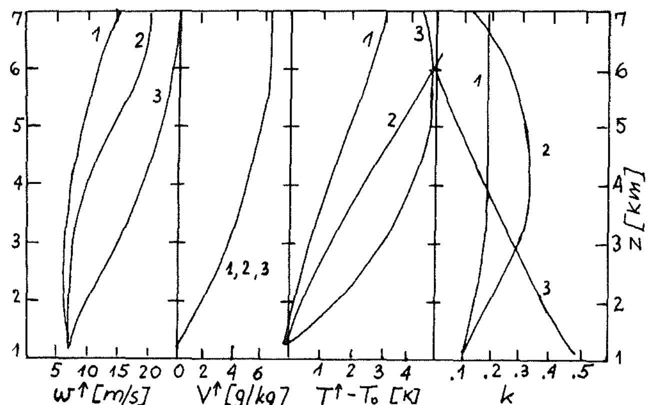

Fig.2. Stratification and updraft profiles. $k=(\gamma - \Gamma_w)/(\Gamma_d - \Gamma_w)$ where Γ_d, Γ_w, γ : dry-adiabatic, wet-adiabatic and environmental lapse rates; z-independent rel.humidity 85% $\mu^{\uparrow}$ =.00015; at cloud base z=1200m, p=880mb, T_0=18°C.

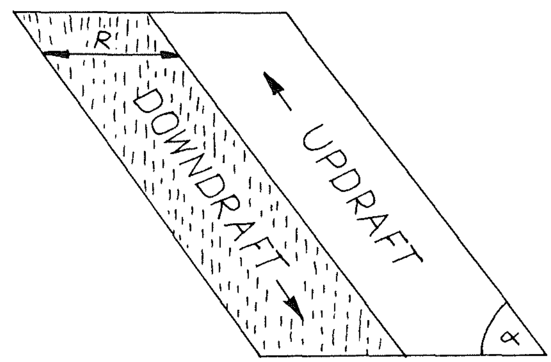

Fig.5. Updraft-downdraft configuration. See section 4.

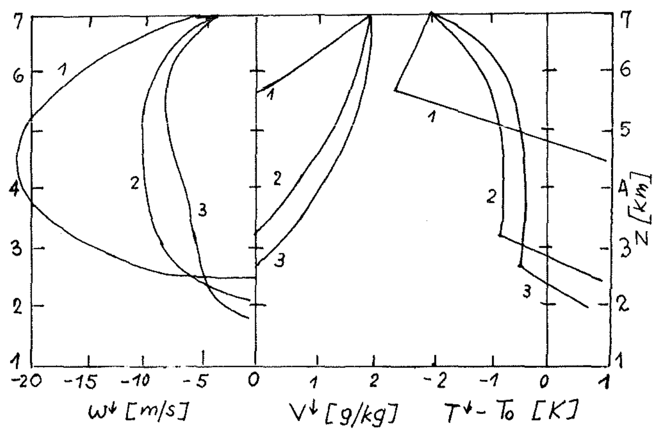

Fig.3. Downdraft profiles. See section 3. $\mu_e^{\downarrow}$=0; updraft as "1" on Fig.2. 1: $\mu_u^{\downarrow}$ =0; 2: $\mu_u^{\downarrow}$=-.0003; 3: $\mu_u^{\downarrow}$ =-.0004.

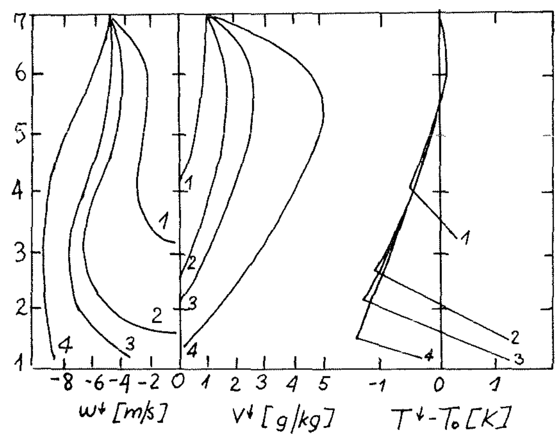

Fig.6. Downdraft profiles. See section 4. $\mu_u^{\downarrow} = \mu_e^{\downarrow}$ =-.0003; updraft as "1" on Fig.2. 1: β=0; 2: β=.001; 3: β=.002; 4: β=.005.

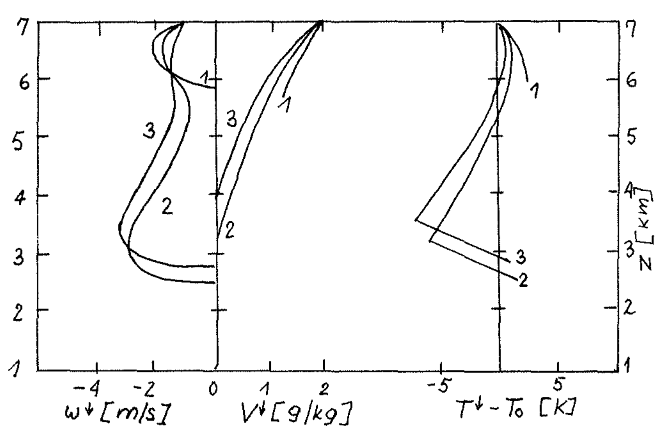

Fig.4. Downdraft profiles. See section 3. $\mu_u^{\downarrow}$ =-.0004; updraft as "1" on Fig.2. 1: $\mu_e^{\downarrow}$ =-.0003; 2: $\mu_e^{\downarrow}$ =-.0004; 3: $\mu_e^{\downarrow}$ =-.0007.

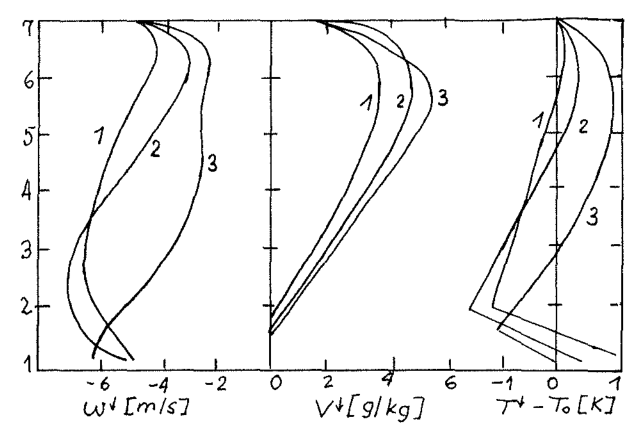

Fig.7. Downdraft profiles. See section 4. $\mu_u^{\downarrow}$ =-.0003; $\mu_e^{\downarrow}$ =-.0006; β =.003; updrafts as on Fig.2.

4.3.4

NUMERICAL SIMULATION OF CUMULONIMBUS CONVECTION IN TEMPERATE ATMOSPHERES

D. A. Bennetts

Meteorological Office,
Bracknell, England.

1. INTRODUCTION

Recently the three-dimensional numerical model, developed by Miller and Pearce (1974) to study deep tropical convection, has been extended to cover conditions appropriate to temperate latitudes. The mode of initiation and early development was found to differ significantly from the tropical cloud. In particular, the model built up the main convective cell from smaller cells. This is relevant to the ideas of bubble or successive thermal theories of convection discussed notably by Scorer and Ludlam (1953) and used recently by Mason and Jonas (1974) in an attempt to account for the drop size distribution in cumulus.

The model is three-dimensional with 15 x 15 x 19 grid points; 15 x 15 in the horizontal at 1 km intervals and 19 levels in the vertical. The vertical resolution is 50 mb.

2. INITIATION AND SUCCESSIVE THERMAL DEVELOPMENT

Three types of initiation have been used. Firstly heat and/or moisture bubbles (e.g. Takeda 1971); secondly continuous heating, with corresponding moisture increase, to put in 0.5 to 3°C excess temperature in a short time ($\sim$ 4 mins), as used by Miller and Pearce; and thirdly, the computationally wasteful but more realistic continuous heating at about 2°C hr^{-1} of the lowest layers of the atmosphere.

These have been used to initiate convection in various temperate and tropical atmospheric soundings, some with light vertical wind shear and some with an initially stagnant atmosphere. The conclusions of this section are based on a total of about 25 integrations.

2.1 General findings of the model

It appears that the convective bubbles developed by the model may be explained in terms of 'gravity' or 'buoyancy' waves, two modes being excited. The low wave number ($\sim$ 0.15 km^{-1}) represents the cloud as a whole and extends throughout the depth possible for convection; the high wave number (.3 to .5 km^{-1}), gives rise to the smaller cells. The two waves will be referred to as the $\mathcal{L}$ (large) and ℓ (small) cells respectively. Successive ℓ cells will be referred to as ℓ_1, ℓ_2 etc, and the reader is directed to Fig 1 where these can readily be seen.

The scale and amplitude of the $\mathcal{L}$ cell is determined by the vertical extent of the available potential energy while the ℓ cells are, in the model, controlled by the initiation process. The input heat determines their amplitude but, because of the discontinuous transition from dry to moist convection, their scale is related to the height of the condensation level above the ground. There is a complex link between the $\mathcal{L}$ and ℓ cells but the variation of the ratio of their amplitude gives rise to distinct types of clouds as the following three selected examples demonstrate.

a) A mid-latitude sounding taken about 1 hour before the onset of convection. Initiation is by a heat bubble excess 2°C put into the lowest two levels of the model in the centre kilometre square.

b) The same sounding but with uniform heating at 1.5°C hr^{-1} in the lowest level (975 mb) and 0.75°C hr^{-1} at the next level (925 mb). Convection is initiated in the required spot by heating 4 grid points at an additional 0.5 and 0.25°C hr^{-1} at the respective levels. Heating is terminated when cloud cover forms at about 50 mins.

c) A moist tropical sounding initiated as (b).

Integration of case (a) shows the bubble has enough energy to rise through the condensation level but the surrounding air is stable and prevents any general release of potential instability. Consequently the cloud retains its initial form as it rises through the atmosphere, being composed of a ℓ cell only. This is meteorologically unrealistic but might be representative of an intense local heat source, for example a fairly large explosion in the 1 kiloton of T.N.T. range.

Case (b) represents the more natural process where the heat is put in gradually. The model forms the ℓ_1 cell from the input heat and as it moves away from the boundary layer the convergence zone below it amplifies the ℓ_2 cell, the potential energy of the ascent is released, and the cloud forms as a $\mathcal{L}$ cell with three, and the beginning of a fourth, ℓ cell. However the cells would be obscured and to an observer the cloud would appear single celled with development taking place in pulses as the successive ℓ cells reach the top and dissipated. This example is presented in more detail later. (Fig 1).

Finally in case (c), that of a tropical cloud, the initial perturbation grows vigorously and easily releases the available potential instability. This gives rise to smaller amplitude and shorter wavelength ℓ cells which more easily merge with the $\mathcal{L}$ cell leading to a smoother development.

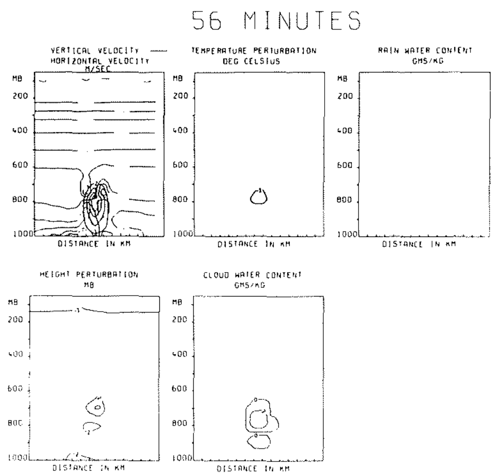

Fig. 1a

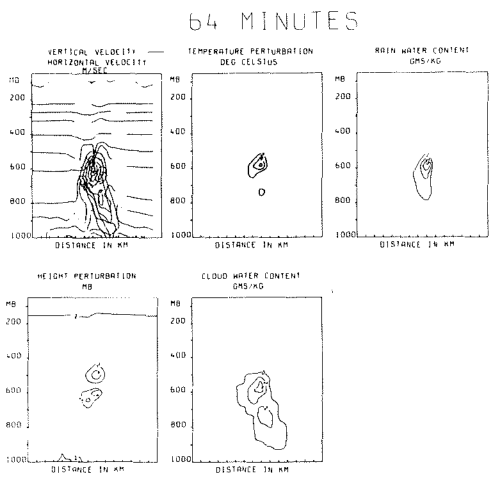

Fig. 1b

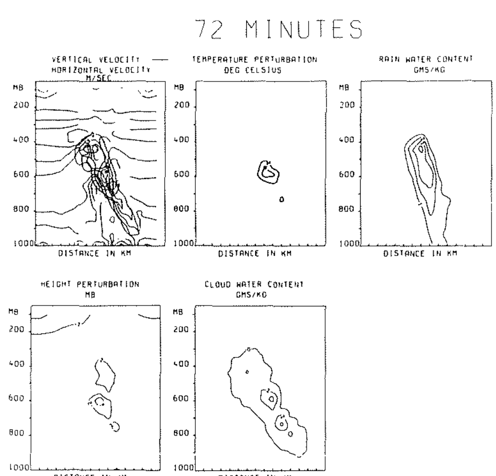

Fig. 1c

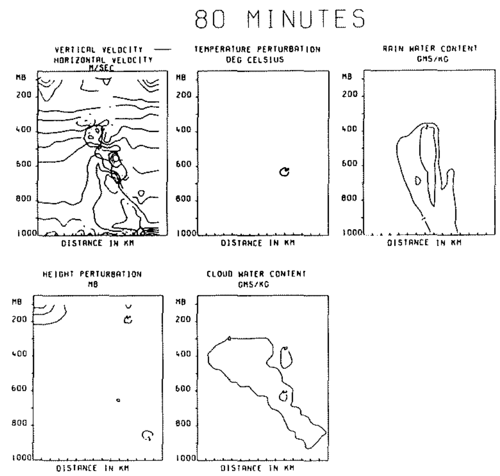

Fig. 1d

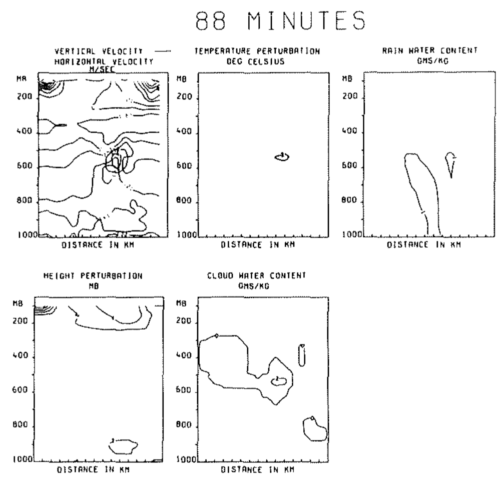

Fig. 1e

Fig. 1. The results of the numerical integration of case b. Uniform wind shear was applied in the x-direction; 6 ms^{-1} at 975 mb to -7 ms^{-1} at 300 mb and reducing again to zero at the tropopause (225 mb). The figures show a vertical cross-section through the middle of the cloud parallel to the shear. The horizontal and vertical velocities are superimposed to give an indication of the circulation through the cloud. Contour intervals in all except the rain water content are in units of 2. Rain water contours are in units of 1. No ice phase is included.

Grid size 1 km x 1 km x 50 mb.

2.2 Details of one integration

Fig 1 shows the results of an integration with a temperate latitude sounding. There is vertical wind shear only in the x-direction, with u proportional to the pressure, ranging from 6 ms^{-1} at 975 mb to -7 ms^{-1} at 300 mb and falling to zero at the tropopause (225 mb). Convection is started by heating the whole grid as for case (b) and initiated in the centre by adjusting the extra heating of the four grid points so that they move with the wind and arrive in the centre of the grid when the cloud first forms, at about 50 mins. Fig 1 shows a vertical cross-section through the centre of the cloud with the horizontal direction parallel to the shear. The cloud also has structure at right angles to this cross-section with similar dimensions but, in the absence of y-directional shear, it is symmetrical.

Fig 1a shows the cloud soon after condensation first occurs. The break in the cloud is simply a product of the contouring routine. It must be stressed at this stage that in the integration the cloud has been treated as a warm cloud. Crudely the effect of the release of the latent heat of fusion would give a more vigorous development at the top of the cloud but, as a preliminary investigation with the inclusion of the ice phase has confirmed, this does not significantly alter the general mode of development. Figs 1c, d and e show the continuing development of the cloud by ℓ_3 and ℓ_4 cells, convection finally ceasing as the cloud base nears the edge of the integration area. This is arranged to prevent computational boundary problems.

2.3 Comparison between a sheared and stagnant atmosphere

The integration in Fig 1 was first performed for an initially stagnant atmosphere. Then the ℓ_1 cell rose in a similar manner, but vertically, with the ℓ_2 cell following, the final form being very similar to Fig 1b. After that however the rain, that can be seen forming in the ℓ_1 cell, fell through the ℓ_2 cell, not to the side as in the sheared case (Fig 1c). The increased weight of liquid water modified the subsequent development preventing any ℓ_3 or later cells forming. The other major difference was that in the non-sheared flow the rain fell most of the way in the cloud, i.e. in a saturated region. This gave an unrealistically high precipitation rate of 153 mm hr^{-1}. However with shear, the rain fell outside the cloud and could evaporate, bringing the maximum precipitation rate down to 35 mm hr^{-1}. Without shear 75% of condensed water fell as precipitation, with the shear used in the above example this dropped to about 25% and the maximum to fall at any point on the ground was 3.3 cm and 2.1 cm respectively.

3. CONCLUSIONS

It has been shown that a three-dimensional numerical model of mid-latitude cumulonimbus predicts that the growth of the cloud will be by successive thermals in contrast to the tropical cumulonimbus which appears to have a much smoother development. The initiation generates gravity waves whose growth is affected by the basic sounding and it is the ratio of the amplitude of the two largest gravity waves that determines the mode of development. In a tropical cloud the ℓ_1 cell dominates whereas in the mid-latitude cumulonimbus they have similar amplitudes.

3.1 Acknowledgements

I would like to thank Dr M J Miller for the use of his computer programme, Dr W T Roach and Dr P R Jonas for many useful discussions and Mr P Goldsmith who suggested this problem.

4. References

MASON, B J and JONAS, P R 1974 The evolution of droplet spectra and large droplets by condensation in cumulus clouds. Quart. J. R. Met. Soc., 100, pp 117-135.

MILLER, M J and PEARCE, R P 1974 A three-dimensional primitive equation model of cumulonimbus convection. Quart. J. R. Met. Soc., 100, pp 133-154.

SCORER, R S and LUDLAM, F H 1953 Bubble theory of penetrative convection. Quart. J. R. Met. Soc., 79, pp 94-103.

TAKEDA, T 1971 Numerical simulation of a precipitating convective cloud; the formation of a 'long-lasting' cloud. J. Atmos. Sci. 30, pp 350-376.

4.3.5

A NUMERICAL MODEL OF THE SYSTEM OF CONVECTIVE CLOUDS AND SHOWERS FOR WIND CHANGE WITH HEIGHT

S. L. Lebedev

All- Union Research Institute
of Hydrometeorological
Information - World Data Centre
Hydrometeorological Service of the USSR
Obninsk, Kaluga

In mathematical modeling of an individual convective cloud which is the only one in infinitely large space the buoyancy force can be regarded as proportional to the deviation of virtual temperature from its initial values. On the lateral boundaries of the solution region which is large enough the state of air can be assumed not to differ from the initial one. The convection with a single cloud development described by such model is rather uncommon in real atmosphere. Usually air mass convection is followed by the development of the system of clouds which recur periodically in horisontal direction. As this takes place the variables characterizing air vary with time both inside the clouds and between them. This feature should be taken into account in calculating the buoyancy force and in prescribing the conditions on the lateral boundaries of a convective cell. If on these boundaries the derivatives of the desired functions with respect to the boundary normal are taken to equal zero then, provided the buoyancy force is calculated properly, the solution will reflect the cloud system evolution in the air mass in which the ambient wind does not vary with height. When the wind varies with height the boumdary conditions spoken above do not reflect reality on the lateral boundaries of a cell which are not parallel to the wind.

The peculiarities mentioned above as well as some other specific features of the problem have been taken into account in the calculations given below. The model obtained differs significantly from other three- dimensional non-stationary models of convection under wind variation with height (see Pastushkov, I972; Steiner, I973; Miller and Pearce, I974; Wilhelmson, I974). One of the distinguishing features of the model obtained is that it describes simultaneously both the system of the clouds with any length of its lifetime and the precipitation occurence. The calculations are based on the set of equations, derived by the author (I966) while designing the first three- dimensional non - stationary model of convection with precipitating cloud development. The ambient wind velocity changing in modulus with height and constant in direction (parallel to the x- axis) is incorporated into this set of equations. Then the set takes the form

$$\frac{\partial w}{\partial t} = F - \bar{F} ,$$

$$\frac{\partial Q}{\partial t} = -(\mathcal{U} + u)\frac{\partial Q}{\partial x} - v\frac{\partial Q}{\partial y} - w\frac{\partial Q}{\partial z} + \frac{1}{\rho}\frac{\partial(\eta \rho m)}{\partial z} + \nu \Delta Q ,$$

$$\frac{\partial T}{\partial t} = -(\mathcal{U} + u)\frac{\partial T}{\partial x} - v\frac{\partial T}{\partial y} - w\frac{\partial T}{\partial z} + \left(C_p + 0{,}622\frac{\sigma L}{p}\frac{\partial E}{\partial T}\right)^{-1}\Big[-g w \times \left(1 + 0{,}622\frac{\sigma L \rho E}{p^2}\right) + \nu C_p \Delta T + 0{,}622\,\sigma L \nu \Delta\left(\frac{E}{p}\right) - L\delta\nu\left(\frac{\partial Q}{\partial x}\frac{\partial m}{\partial x} + \frac{\partial Q}{\partial y}\frac{\partial m}{\partial y} + \frac{\partial Q}{\partial z}\frac{\partial m}{\partial z}\right)\Big],$$

$$\frac{\partial^2 \varphi}{\partial x^2} + \frac{\partial^2 \varphi}{\partial y^2} = -\frac{1}{\rho}\frac{\partial(\rho w)}{\partial z} ,$$

$$F = g\left(\frac{T_6}{\bar{T}_6} - 1\right) - \sigma g m - (\mathcal{U} + u)\frac{\partial w}{\partial x} - v\frac{\partial w}{\partial y} - w\frac{\partial w}{\partial z} + \nu \Delta w ,$$

$$u = \frac{\partial \varphi}{\partial x} , \quad v = \frac{\partial \varphi}{\partial y} ,$$

$$E = E_0 \exp\left(\frac{\alpha_1 T - \alpha_2}{T - \alpha_3}\right) ,$$

$$\eta = \sigma B\left[1 - \exp(-a\rho m)\right] ,$$

$$T_в = [1 + 0{,}608(Q - \sigma m)]T,$$

$$m = Q - 0{,}622\frac{E}{P}, \quad \bar{F} = \frac{1}{S}\iint_S F\,dx\,dy,$$

$$\bar{T}_в = \frac{1}{S}\iint_S T_в\,dx\,dy,$$

$$\sigma = \begin{cases} 1, & \text{if } m > 0 \\ 0, & \text{if } m \le 0 \end{cases}, \quad \delta = \delta(m),$$

where x, y, z are rectangular Cartesian coordinates (the z -axis is directed vertically upward), t is the time,

$$\Delta = \frac{\partial^2}{\partial x^2} + \frac{\partial^2}{\partial y^2} + \frac{\partial^2}{\partial z^2}.$$

The prescribed constants are: C_p the specific heat of air at constant pressure, L the latent heat of condensation of water vapor, g the acceleration of gravity, ν the turbulent diffusion coefficient, S the horisontal section area of the solution region; B, a, E_0, d_1, d_2, d_3 are the constants determined empirically; the prescribed functions of z are: P the atmospheric pressure, ρ the air density, U the ambient wind velocity. The main values sought are: u, v, w velocity components of the air movement called convection, Q the total water content per unit mass, T the air temperature ($^\circ K$), m the liquid water content per unit mass (the notion of the liquid water content involves negative values also). To obtain these variables it is necessary to calculate the horisontal velocity potential φ, the saturation vapor pressure E, the virtual temperature $T_в$, the mean weighted velocity of raindrops fall as related to the air η, the delta function δ; $\sigma, \bar{T}_в, F, \bar{F}$ are the variables determined by the expressions of the set of equations.

The solution is sought in the inside region limited by the planes $x=-A$, $x=A$, $y=0$, $y=A$, $z=0$, and $z=H$, where A, H are the prescribed constants. The periodicity of the process in wind direction is given by the expressions, which were used by the author earlier (I973) and connect both the desired functions on the opposite boundaries, perpendicular to the wind and the derivatives of these functions

$$w(-A, y, z, t) = w(A, y, z, t),$$

$$\frac{\partial w}{\partial x}(-A, y, z, t) = \frac{\partial w}{\partial x}(A, y, z, t).$$

The boundary conditions for Q, T, φ are the same here. While providing a unique solution these boundary conditions along with others do not prevent varying with time of the derivatives of the desired functions with respect to x on the boundaries $x=-A$, $x=A$. On the vertical boundaries parallel to wind the derivatives of w, Q, T, φ with respect to y are equal to zero. On the lower boundary $w=0$, Q is the prescribed constant, T is the prescribed function of t; on the upper boundary $w=0$, Q, T are the prescribed constants.

The problem considered was solved for four wind profiles under the same initial conditions (see the Table). Some results of the solution are presented in Figures I,2,3. They show the atmosphere sections under wind profiles a, b, c, d. The sections were made by the vertical plane, that is parallel to the wind and passes through the point at

Table

Height (m)	Pressure (mb)	Temperature (°C)	Dew Point (°C)	Wind (m/sec) a	b	c	d
0	I000	27,0	I8,2	0	0	0	0
750	9I7	I9,5	I5,0	0	2,0	4,0	8,0
I500	839	I2,0	I0,0	0	3,0	7,0	I4,0
2250	766	8,0	5,5	0	3,5	9,0	I8,0
3000	698	4,0	I,0	0	3,9	I0,5	2I,0
3750	635	0,0	-3,5	0	4,2	II,5	23,0
4500	578	-4,0	-8,0	0	4,4	I2,3	24,6
5250	525	-8,5	-I2,5	0	4,6	I2,8	25,6
6000	476	-I3,0	-I7,0	0	4,7	I3,2	26,4
6750	43I	-I6,5	-2I,5	0	4,8	I3,5	27,0
7500	389	-I9,0	-26,0	0	4,9	I3,7	27,4
8250	350	-20,5	-30,5	0	5,0	I3,8	27,6
9000	3I5	-22,0	-35,0	0	5,0	I3,9	27,8
9750	283	-23,0	-39,5	0	5,0	I3,9	27,8

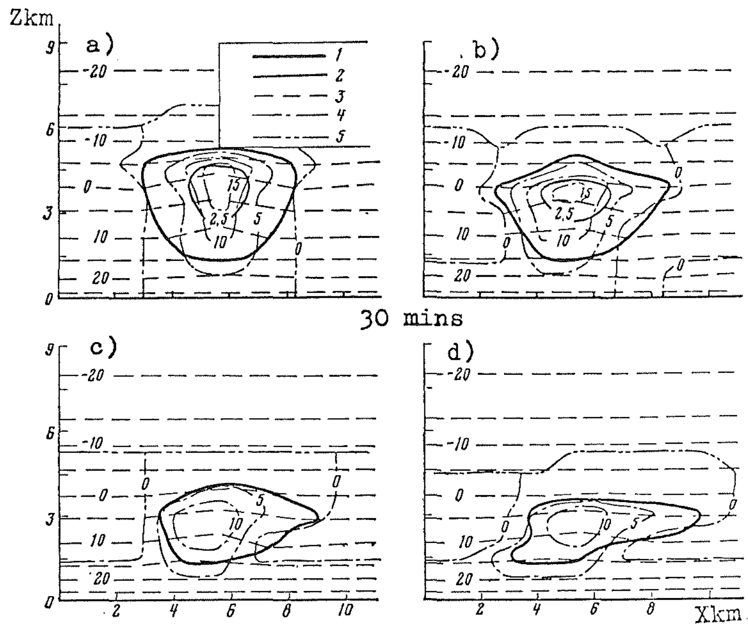

Fig. I. Vertical sections of the atmosphere 30 minutes after the convection started under different (a,b,c,d) wind profiles.

I - cloud boundaries, 2 - the isolines of liquid water content (gr/m^3), 3 - the isotherms (°C), 4 - the isolines of vertical velocity (m/sec), 5 - the upper boundary of convection influence.

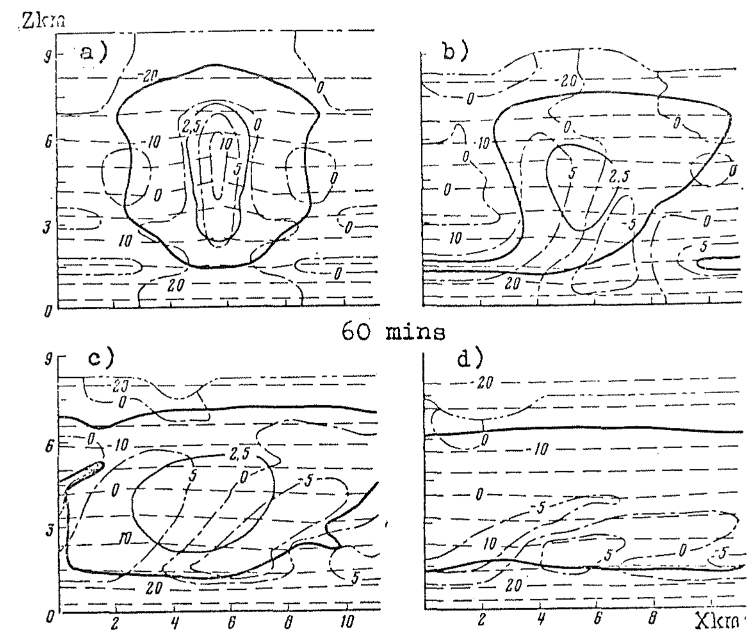

Fig. 2. Vertical sections of the atmosphere one hour after the convection started (for the legend see Fig. I).

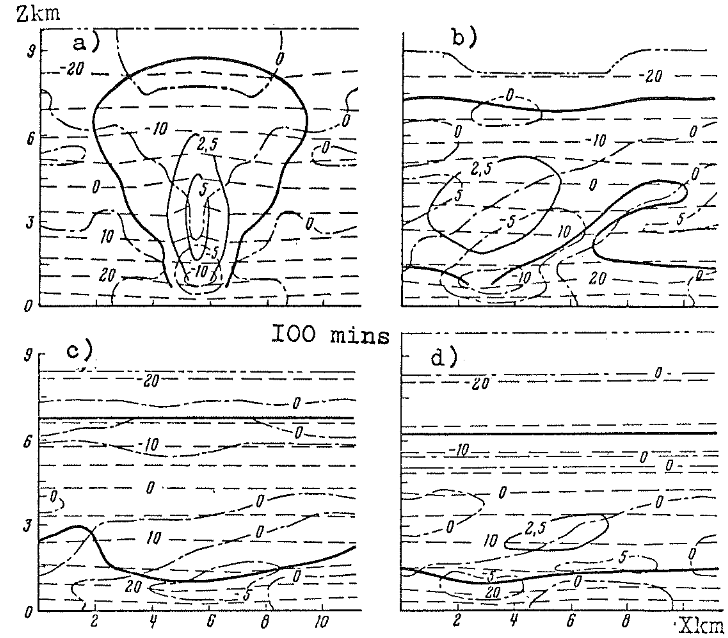

Fig. 3. Vertical sections of the atmosphere one hour and 40 minutes after the convection started (for the legend see Fig. I).

which the initial temperature impulse was prescribed. The pattern recurs periodically as the x-axis is extended. In the direction perpendicular to the wind the solution is also periodical (not illustrated). For the no-wind case (a) the two perpendicular sections which pass through the point of prescribing the temperature impulse are identical. When the wind changes with height (b, c, d cases) the clouds in all the cells stretch in the wind direction as time passes and merge with neighbouring clouds into billows. After some period of time these billows stop increasing in diameter: cloudiness alternates with cloudlessness in the perpendicular to the wind direction. Heavy lasting rain fell out in no-wind case (Fig. 3a); slight short-period rainfall - in (b) case (Fig. 3b) and in (c) case (rain lasted less than I hour 40 minutes); and there was no rain in the case of maximum wind variation with height (d). From one profile to another the intensity of the processes decreases as the derivative of wind velocity with respect to the height increases.

REFERENCES

Lebedev,S.L.,I966:Three-dimensional non-stationary model of an atmospheric convective cell with a cloud.Izv.Akad. Nauk, SSSR,Fiz.Atm.Oke.,v.II,NI,I4-27.

---,I973:On numerical simulation of the processes in the unsteady atmosphere and in convective clouds with wind changing with height.Meteor.Hidrol., N8,3-II.

Miller,M.J.,and Pearce,R.P.,I974:A three-dimensional primitive equation model of cumulonimbus convection.Quart.J. Royal Met.Soc.,I00,424,I33-I54.

Pastushkov,R.S.,I972:Numerical simulation of interaction of convective clouds with ambient atmosphere.Trudy ZAO, v.I08,pp.I28.

Steiner,J.T.,I973:A three-dimensional model of cumulus cloud development. J.Atm.Sci.,30,4I4-435.

Wilhelmson,R.,I974:The life cycle of a thunderstorm in three dimensions. J.Atm.Sci.,3I,I629-I65I.

4.3.6

ON SPREADING AND WASHOUT OF ADMIXTURES IN CUMULI RAIN CLOUDS

B.J.Styra, S.S.Shalavėjus, L.J.Morkeliūnas
B.K.Vėbrienė, N.K.Shpirkauskaitė

Institute of Physics and Mathematics of the
Academy of Sciences of the Lithuanian SSR,
Vilnius, U.S.S.R.

1. INTRODUCTION

The study of physical processes taking place in cumuli rain clouds appears to be the most actual problem both of the modern Cloud Physics and of the active influences on these processes. Since air-plane sounding or the study of such clouds with the help of mechanical devices is very difficult so the injection of radioactive or radioactivated tracers into them appears to be almost the only method of investigation of the processes occuring inside the cloud and of the behaviour of aerosols having entered it.

Tracer investigations of clouds were carried out in a number of works presented in the list of references of this paper. It was shown that the tracer injected into Cb was spreading in all directions and wasn't associated with the transition of the cloud system. Velocities of such transitions were shown to be very high and the washout of aerosol tracers was going on rather effectively.

2. EXPERIMENT

While continuing such tracer investigations in the run of I972 and I974 we carried out 11 natural experiments on the proving ground in the Moldavian SSR. In these experiments radioactive Po^{210}, P^{32} or simultaneously Po^{210} and heavy water D_2O were injected into the fixed point of the powerful clouds Cb with the help of rockets. Sampling was performed on the proving ground in the radius of 20 km and the highest density of sampling devices was concentrated in the circle of 10 km radius.

All in all almost I80 sampling devices representing polyethylene cones were exposed with the sampling area of about 0.3 m^2. Precipitation gathered from one Cb was brought for analysis to the laboratory by automobiles and a helicopter. During the experiment beside the exposed sampling devices mobile points were located in various directions from the base. Samples were being gathered at the interval of 2 min. both into the vessels and on the plotting boards where separate drops were captured. The precipitation gathered was concentrated and Po^{210} was separated with a subsequent deposition by the natural electrolysis on the copper plate in the electrolyzer heated up to the temperature of $\sim 80^{\circ}C$. Then radioactivity of Po^{210} was measured. Chemical yield of Po^{210} was determined by Po^{208}. Plotting-boards with separate drops were put into contact with nuclear emulsion of the type A-2 sensitive to α-particles. After photoexposition and developing α-tracks were studied and their calculation was performed on the area which was in contact with the track of the drop. The background was studied by the control plates. These measurements enabled us to determine the time of arrival of first portions of the isotopes injected and at the same time gave a possibility to determine velocity of isotopes spreading in various directions from the injection point.

The amount of deuterium in the samples was measured with the help of a mass-spectrometer by the ratio to the standard. Radar data were widely used in these experiments.

3. RESULTS OF THE EXPERIMENT

An example of spreading of Po^{210} and deuterium field during the experiment of the 20th of July, I974 is presented in Fig.1. Isolines restrict the field of their spreading to the values which may be well ascribed to the tracer injected and which exceed the background values. As we see the area of spreading of Po^{210} aerosols considerably exceeds the spreading area of deuterium. In Fig.2 an example of the scheme of situation of the mobile points is given where the moment of appearance of the tracer at the fixed point was determined by the measured radioactivity of separate drops and the velocity of spreading of admixture injected into the frontal part of the large-drop zone was estimated. The evolution of a projection of the large-drop zone of the cloud in time is presented by closed curves. Velocity of admixture spreading from the injection point is indicated by arrows. The maximum velocity is directed to the opposite side of the cloud transfer.

The data on concentration variation of deuterium and Po^{210} in precipitation during their falling in different points of the proving ground are presented in Fig.3 .

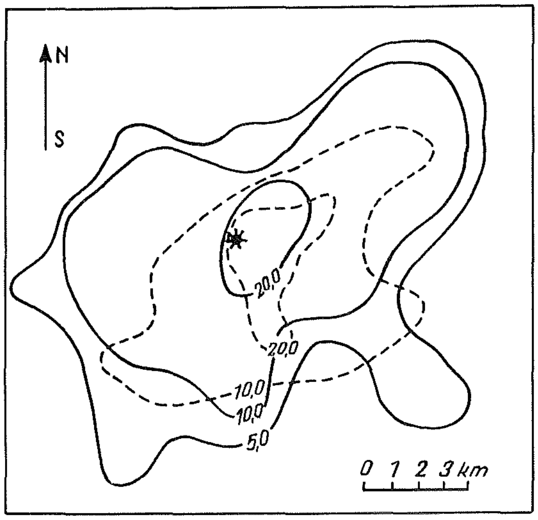

Figure 1. The field of fallout of Po^{210} (continuous lines) and deuterium (dotted lines) on the proving ground. The projection of the explosion point is marked by the asterisk.

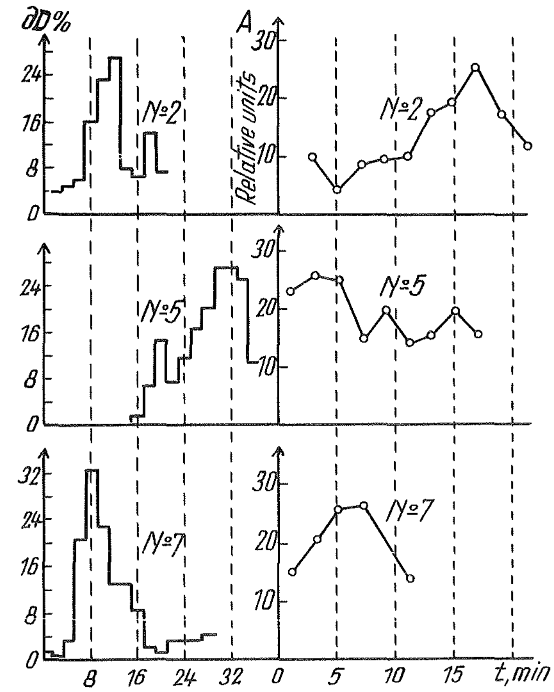

Figure 3. Variation of deuterium concentration (on the left) in ∂D % units and polonium (on the right) in relative units during the falling of precipitation after the injection of admixture. The beginning of coordinates corresponds to the moment of injection; the points of measurement are marked with figures.

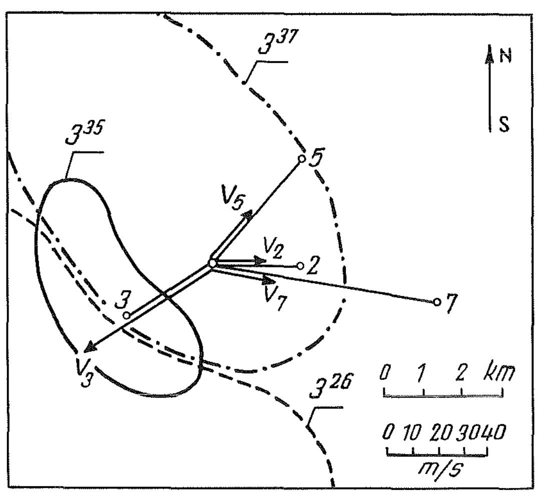

Figure 2. Velocities and direction of Po^{210} spreading from the injection point. The lines determine radar projections of a large-drop zone; figures beside them denote the time of the day; mobile points are marked with synonymous figures.

These data show the high velocity of spreading of polonium aerosols. From the analysis of the data obtained from 11 experiments we may draw the following conclusions:

1) When injecting the tracer into the frontal part of the developing large-drop center regardless of the height of the injection point it is transfered to the rear part of the cloud where the maximum density of the fallout is marked. Here the intensive process of washout takes place. The occurence of the tracer in the front of displacement of the cloud coincides in time and in trajectory of the transfer of the rear part of the large-drop zone.

2) At the presence of several large-drop zones in the cloud the tracer is spreading mainly in that zone in which it has been injected. Evidently, separate large-drop centers represent independent cells of the storm-cloud and possess a certain autonomy.

3) When injecting Po^{210} and deuterium into the frontal part of the large-drop center the admixture is washed out on the large area. According to aproximate evaluations the highest velocities of admixture transfer are observed in the opposite side from the general air mass transfer and the displacement of the large-drop zone and are of 50÷60 m/s . Velocities in other directions are of 20÷24 m/s . This proves to the fact that in the frontal part of the large-drop zone there are convective streams which transfer the admixture into the rear part of the cloud with high velocities. As a result of strong turbulence in clouds the tracers quickly mix up in them.

4) When injecting the tracer into the central part of the large-drop zone the admixture is spreading in all directions from the injection point and practically is independent of the air stream direction at the height of the cloud. The velocity of admixture spreading is considerably higher than that of wind. When the admixture is injected during the stage of the cloud's growth the fallout bears a scrap-form character while the spreading velocity of admixture in different directions varies 6÷60 m/s .

5) While injecting the isotope into the large-drop zone, being in the decay state, the density maximum of tracer fallout is observed below the epicenter of its injection.

6) In some cases in the zone of maximum concentration of tracer fallout the effect of its dilution by a less active precipitation is observed.

7) By introducing the admixture into the rear part of the cloud the character of the fallout distributuon depends upon the height of the injection point. In the case when Po^{210} was injected into the rear part of the large-drop zone at the height of 1000 m and deuterium at the height of 5000 m the maximum fallout was observed at some distance in the direction of transition of that zone: the admixture was transfered to the frontal part of the large-drop zone at velocities of 19÷26 m/s and was washed out in the direction of the displacement of the cloud.

When injecting the admixture into the rear of the large-drop zone, located in the rear part of the cloud, the density maximum of the fallout was observed below the epicenter of the injection point of the tracer. The spreading velocity of admixture was 9÷17 m/s .

8) Radioisotope Po^{210} is washed out in the area of 2-3 times larger than that of deuterium.

9) Investigations showed that coagulation of aerosol particles carrying Po^{210} was going on very quickly and that it was washed out with raindrops of a mass varying from 1 to 3 mg (radius - 600÷1000 μm). The drops of such size during the intensive washout bear maximum radioactivity.

10) When studying spreading fields of Po^{210} and deuterium, Po^{210} was found to spread in a larger area. This may testify to the presence of different mechanisms of spreading. Heavy water after breaking up the head of the rocket evaporates with a subsequent condensation on the drops. Deuterium is spreading together with the drops. Po^{210} can also coagulate with drops and together with them can spread in the cloud. Nevertheless, having in mind a large spreading area of Po^{210}, it is possible to assume that Po^{210} being in the state of aerosols and possessing high electrical mobility can be transfered simultaneously with turbulent whirlwinds under the influence of electric fields and coagulate with drops only at some distance from the explosion point.

All the conclusions given are experimentally confirmed and because of the limited volume of the paper it was impossible to give a full proof of these statements.

The results presented are of great interest both for the theory of Cb and for the practice of active influences on cloud systems.

REFERENCES

Batoni, V.V., Eh.Ya.Begun, A.Sh.Bibilashvili, I.I.Burtsev, T.I.Zhigalovskaya, L.V.Kirilenko, S.V.Shvedov, I.A.Shilina and A.A.Seredkin, 1971: On the use of artificial tracers in investigation of local atmospheric processes. Trudy VGI, 19.

Burtsev, I.I. and L.V.Burtseva, 1968: On washout of radioactive aerosol P^{32} by the cloud drops according to the chamber test data. Trudy VGI, 8, 25-31.

Burtsev, I.I., L.V.Burtseva and S.G.Malakhov, 1968: Characteristics of the washout of aerosol P^{32} injected into the cloud. In: Issledovanie protsessov samoochishcheniya atmosfery ot radioaktivnykh izotopov. Vilnius, "Mintis".

Burtseva, L.V., I.I.Burtsev and Eh.Ya. Begun, 1970: Investigation of spreading characteristics of aerosol dispersed by the explosion of the hail-preventing shell "Ehl'brus-2" in the free atmosphere. Trudy VGI, 17.

Dingle, A.N., 1973: Rain scavenging studies. Progress Report N9, US Atomic Energy Commission Contract N AT(11-1)-1407, Argonne, Illinois.

Dingle, A.N., I971: Tracer experiments on convective streams in scientific research on nucleation. Supplement volume of proceedings of the 7th International conference on condensation and ice nuclei. Sept. I8-24, I969, Prague and Vienna.

Styra, B.J., V.J.Lujanas and K.K.Shopauskas, I975: Radioaktivnost' i meteorologiya. Vilnius, "Mintis".

Shalavėjus, S.S., E.J.Vėbra, L.A.Dinevich, E.I.Potapov, B.J.Styra, I.I. Gajvoronskij, I.A.Khrustitskaya and B.K.Vėbrienė, I974: Investigation of spreading and washout character of polonium-210 injected into the local space of the cumulonimbus cloud. In: Tezisy dokladov, Fizicheskie aspekty zagryazneniya atmosfery. Vilnius.

Shopauskas, K.K., I.I.Gajvoronskij, B.J.Styra, E.J.Vėbra, S.S.Shalavėjus and D.A.Shopauskienė, I968: On methodic of investigation of spreading of passive admixture in the clouds with the help of radioactive isotopes. Fizika atmosfery i okeana. t.4, N7, 792-796.

Shopauskas, K.K., B.J.Styra, E.J.Vėbra, B.K.Vėbrienė, S.S.Shalavėjus and D.A.Shopauskienė, I968: On washout of radioactive isotopes artificially injected into the cloud according to the data of observational ground-stations. In: Issledovanie protsessov samoochishcheniya atmosfery ot radioaktivnykh izotopov. Vilnius, "Mintis", 323-333.

Shopauskas, K.K., B.J.Styra, E.J.Vėbra, B.K.Vėbrienė, A.A.Kirkaitė, R.A. Minkevichius, S.S.Shalavėjus and D.A.Shopauskienė, I969: On the wash-out of radioisotopes injected into the cloud. In: Tezisy dokladov Vsesoyuznoj konferentsii po yadernoj meteorologii. Obninsk, I.Eh.M. GUGMS SSSR.

Shopauskas, K.K., B.J.Styra and E.J. Vėbra, I971: Spreading and rainout of passive admixture injected into the cloud. Supplement volume of proceedings of the 7th International conference on condensation and ice nuclei. Sept. I8-24, I969, Prague and Vienna, 340-346.

Vėbra, E.J., B.A.Mishveladze, K.K.Shopauskas and V.M.Mal'bakhov, I975: On admixture spreading in the clouds. In: Fizicheskie aspekty zagryazneniya atmosfery, Fizika atmosfery, N2, Vilnius, "Mintis".

Vėbrienė, B.K., B.J.Styra, L.A.Dinevich, E.I.Potapov, S.S.Shalavėjus, E.J. Vėbra and I.A.Khrustitskaya, I974: On radioactivity washout by raindrops of various size. In: Tezisy dokladov, Fizicheskie aspekty zagryazneniya atmosfery. Vilnius.

4.3.7

NUMERICAL SIMULATION OF MICROPHYSICAL PROCESSES AND THEIR INFLUENCE UPON THE DYNAMICS OF A CONVECTIVE CLOUD

by
V.P. Lominadze, I.T. Bartishvili, N.A. Begalishvili, N.D. Japaridze, B.A. Mishveladze, G.A. Nadibaidze
Transcaucasian Hydrometeorological Research Institute
Tbilisi
U.S.S.R.

Theoretical study of microphysical processes in a convective cloud and their interaction with cloud dynamics are of considerable interest for understanding physics of natural and artificial precipitation initiation.

In the first section of the work one dimensional nonstationary model of precipitation forming kinetics in a mixed convective cloud is developed. A system of linearized kinetic equations of coagulation, describing convective transfer and sedimentation of large cloud particles (droplets, crystals), their gravitational coagulation with small droplets, large droplet breakup and freezing is expressed as

$$\frac{\partial n_1(m,z,t)}{\partial t}+\frac{\partial}{\partial z}\left[\omega(m,z)n_1(m,z,t)\right]=-n_1(m,z,t)\int_0^\infty\sigma_{10}(m,m_1)n_0(m_1)dm_1+$$
$$+\int_0^m\sigma_{10}(m-m_1,m_1)n_1(m-m_1,z,t)n_0(m_1)dm_1-n_1(m,z,t)P_1(m)+$$
$$+\int_m^\infty n_1(m_1,z,t)Q_1(m_1,m)P_1(m_1)dm_1-n_1(m,z,t)P_2(m,z), \quad (1)$$
$$\frac{\partial n_2(m,z,t)}{\partial t}+\frac{\partial}{\partial z}\left[\omega(m,z)n_2(m,z,t)\right]=-n_2(m,z,t)\int_0^\infty\sigma_{20}(m,m_1)n_0(m_1)dm_1+$$
$$+\int_0^m\sigma_{20}(m-m_1,m_1)n_2(m-m_1,z,t)n_0(m_1)dm_1+n_1(m,z,t)P_2(m,z). \quad (2)$$

With initial and boundary conditions when $t=0$ and $z=0$ (cloud base)

$$n_1(m,z,t)=n_1(m), \quad n_2(m,z,t)=0. \quad (3)$$

Here $n_1(m,z,t)$ and $n_2(m,z,t)$ are the functions of m mass distribution at the space point with vertical coordinate z at time moment t of large droplets and ice particles respectively; $n_0(m_1)$ is a function of small droplet mass distribution which was given in an exponential form. Initial spectrum of large droplets at cloud base was accepted monodisperse as well as exponential. $\sigma_{10}(m,m_1)$ is the probability of a large m mass droplet coagulation with a small m_1 mass droplet; σ_{20} is the probability of coagulation between an ice particle and a small droplet. To compute $\sigma_{10}(m,m_1)$ and $\sigma_{20}(m,m_1)$ expression of gravitational coagulation was used. Rate of cloud particle motion was accepted equal to

$$\omega(m,z)=W(z)-V_m$$

while the dynamics of updraft was given stationary in a form of certain profile of convective flow rate with the height $W(z)$; V_m is the final (established) velocity of fall as a function of particle size. $P_1(m)$ and $P_2(m,z)$ are droplet breakup and freezing probabilities respectively (Srivastava, 1971; Mazin, 1974). $Q_1(m,m_1)$ is m_1 mass droplet distribution produced while m mass droplet breakup (Srivastava, 1971).

The system (1), (2) was numerically solved by the Monte Carlo method (Enucashvili and Begalishvili, 1973; Enucashvili et al., 1974). Probability nature of coagulation, breakup and freezing allowed to carry out numerical simulation of these processes. During the time step a history of each large cloud particle was performed. Unknown functions of distribution were determined by numbers of filling cells of phase space in each time step.

From results of numerical experiments carried out following conclusions may be drawn:

1. One-fold rize and lowering of particles in a convective cloud model (with concentration and water content of small droplets equal to $N_0=300 cm^{-3}$ and $V_0=10^{-6} g cm^{-3}$) resulted in formation of large ice particles with sizes of 1 cm order radius during an hour of physical time. In this case it is necessary that at the beginning of the process at cloud base large droplets of mean sizes with radii of 5×10^{-3} cm should be present.

2. Process of crystallization began in the model on higher levels of relatively small droplet freezing and expanded downward while droplets of larger sizes were freezing. Time of crystallization was in a satisfactory agreement with real times of crystallization in a cloud.

3. Process of large droplet breakup resulted in formation of small thickness chain process layer at cloud base and did not influence upon formation of precipitation droplet spectrum and characteristics of liquid precipitation fallout as well.

4. Formation of liquid accumulative zones above the level of maximum rate of flow was not observed in the model, since accepted thermal stratification consistent with temperate latitudes favoured large droplet crystallization above the level of maximum rate of flow.

In the second section of the work numerical simulation of warm convective cloud life cycle is carried out within the framework of space axisymmetric model and with allowance for main micro- and macrophysical processes. At a certain stage of cloud evolution instantaneous formation of large droplets in the local region of a cloud is simulated. Later on while studing the evolution of large droplet spectrum the following processes are considered: convective transfer of large droplets, turbulent mixing, sedimentation, condensation (evaporation), gravitational coagulation with small droplets in terms of the continuous growth mechanism and the breakup of large droplets. To control the influence of large droplet evolution upon the macrocharacteristics of a cloud following processes are considered: entrainment of cloud air by moving large droplets, latent heat liberation (absorption) during large droplet condensation (evaporation) and small cloud droplet absorption by large ones. A joint system of hydrothermodynamic and kinetic equations in a cylindrical system of coordinates is expressed as

$$\frac{dW}{dt}=\lambda\vartheta-F+\hat{F}W;\quad \frac{d\vartheta}{dt}=(\gamma-\gamma_a)W+\frac{L}{c_p}(\Phi_1+\Phi_2)+\hat{F}\vartheta;$$

$$\frac{dq}{dt}=\gamma_q W-\Phi_1-\Phi_2+\hat{F}q;\quad \frac{dV}{dt}=\Phi_1-\left(\frac{\partial V}{\partial t}\right)_K+\hat{F}V;$$

$$\frac{\partial n_1}{\partial t}+u\frac{\partial n_1}{\partial r}+(W-V_m)\frac{\partial n_1}{\partial z}+\frac{\partial}{\partial m}\left[(\dot{m}+\dot{m}_K)n_1\right]=$$

$$=-n_1(m)P_1(m)+K^2 n_1(Km)P_1(Km)+\hat{F}n_1;$$

$$\frac{\partial ur}{\partial r}+\frac{\partial Wr}{\partial z}=0.$$

The operators $\frac{d}{dt}$ and $\hat{F}$ are expressed as $\frac{d}{dt}=\frac{\partial}{\partial t}+u\frac{\partial}{\partial r}+W\frac{\partial}{\partial z}$; $\hat{F}=\frac{1}{r}\frac{\partial}{\partial r}\nu r\frac{\partial}{\partial r}+\frac{\partial}{\partial z}\nu\frac{\partial}{\partial z}$, where ν is a turbulent coefficient. Here u, W are the radial and vertical components of air motion rate, r, z-radial and vertical coordinates (axis z is directed upward), ϑ, q -temperature and humidity deveations from their values $\Theta(z)$ and $Q(z)$ in nondisturbed atmosphere, V -cloud water content, γ, γ_a -vertical and dry-adiabatic temperature gradient, L -latent heat of condensation, $\lambda=g/\Theta(z)$; g-gravitational acceleration, c_p-specific air heat with the constant pressure, γ_q -the vertical gradient of specific humidity, Φ_1 and Φ_2 -rates of condensation (evaporation) of cloud (small) and large droplets respectively, $\dot{m}, \dot{m}_K$ -rates of condensation and coagulation growth of a single large droplet, F -large droplet force of pressure upon the cloud air mass

$$F=\int_0^\infty f(m)\,n_1(m,r,z,t)\,dm$$

where $f(m)$ is the large droplet force entraining air. Term $(\partial V/\partial t)_K$ describes small cloud droplet absorption by large ones,

$$\left(\frac{\partial V}{\partial t}\right)_K=cV\int_0^\infty m^{2/3}V_m\,n_1(m)\,dm$$

K is number of droplets produced during large droplet breakup. Describing the mechanism of large droplet breakup it has been assumed that a drop broke up into droplets of equal sizes. This circumstance allowed to oversimplify the mathematical description of breakup mechanism.

Initial and boundary conditions for given problem are expressed as

with $z=0$ $\quad W=\frac{\partial\vartheta}{\partial z}=\frac{\partial q}{\partial z}=\frac{\partial V}{\partial z}=\frac{\partial n_1}{\partial z}=0$;

with $r=0$ $\quad u=\frac{\partial W}{\partial r}=\frac{\partial\vartheta}{\partial r}=\frac{\partial q}{\partial r}=\frac{\partial V}{\partial r}=\frac{\partial n_1}{\partial r}=0$;

with $r,z=\infty$ $\quad W=q=\vartheta=V=n_1=0$;

with $m=0,\infty$ $\quad n_1=0$;

with $t=0$ $\quad W=q=V=0$, $\vartheta=\vartheta_0(r,z)$;

with $t=t_1>0$ $\quad n_1=n_1(m,r,z)$.

To solve the problem an explicit numerical scheme was used satisfying conservation laws. The kinetic equation was solved by means of non-linear monotone numerical scheme (Mishveladze, Malbakhov, 1976).

Results of estimations gave possibility to follow a single warm convective cell evolution since its initiation up to precipitation fallout and the further dissipation of the cell. Integrated characteristics of rain spectrum (intensity, duration, total mass of precipitation, etc.) are estimated. It proved to be that total mass of precipitation was determined mainly by the location of large droplet initiation zone in a cloud. In a number of cases cloud "self-seeding" by large droplets took place which appeared to be reinvolved in the process of precipitation formation inside the cloud. In addition, precipitation formation and its droplet fallout resulted in a significant transformation of a cloud. In this case cloud lower part washout by the flow of falling large droplets was observed resulting in the formation of downdraft under the cloud, and its further dissipation.

REFERENCES

Enucashvili I.M., Begalishvili N.A., 1973: Numerical solution of the linearized kinetic equation of cloud droplet coalescence by the Monte Carlo method. Izv. Acad. Nauk SSSR, ser.FAiO, 9, No7, pp.737-747.

Enucashvili I.M., 1974: On the numerical modeling of the Langmur chain reaction in cumulus clouds by the Monte Carlo method. Soobsh. Akad. Nauk GSSR, 76, No1, pp.73-76.

Mazin I.P., 1974: On parametrization of the processes of ice phase formation in clouds. Trudy CAO, No106, pp.67-76.

Srivastava R.C., 1971: Size distribution of raindrops generated by their breakup and coalescence. J.Atm.Sci., 28, No3, pp. 410-415.

Mishveladze B.A., Malbakhov V.M. 1976: Numerical modeling of convective cloud modification with the purpose of precipitation stimulation by large droplets. Trudy ZakNIGMI, No 64(70).

THE EFFECTS OF PRESSURE PERTURBATION ON PRECIPITATING CLOUDS

Chang-Shin Chen

Institute of Atmospheric Sciences
South Dakota School of Mines and Technology
Rapid City, South Dakota 57701

1. INTRODUCTION

In most of the one-dimensional cloud model simulations, the vertical pressure distribution is often assumed hydrostatic and pressures inside and outside the cloud regions are equal. However, the studies of two-dimensional cloud simulations by Wilhelmson and Ogura (1972) show that the pressure difference inside and outside the cloud regions is not small; thus the perturbation pressure gradient force in the vertical direction cannot be ignored as it has some contribution to the vertical motion. Holton (1973) developed a diagnostic equation for the pressure perturbation field in the cloud region. He found that the vertical velocity profile is improved from a sharp decreasing velocity profile above the level of maximum vertical velocity to a near parabolic velocity distribution in a shallow, convective, non-precipitating, steady-state cloud.

In the present study, the anelastic approximation is used to develop the diagnostic equation to account for the deep convective cloud dynamics. The present model simulates more cloud microphysical processes than Holton, including condensation/evaporation, water and ice phase precipitation mechanisms. The cases are run on a real sounding. The comparison of case studies is made in order to study the effects of pressure perturbation on the dynamics and microphysics of clouds.

2. MODEL

In this model, the Asai-Kasahara (1967) dynamic framework is adopted, which consists of two concentric air columns: an inner column corresponding to the cloud region and an outer concentric annular column corresponding to the environment. The physical quantities are averaged in the cloud and the environmental regions. The mixing of the cloud and the environment is simulated by using mixing length theory. The mixing consists of two parts: the lateral eddy mixing term, which is proportional to the vertical gradient of the physical quantity, and the dynamic entrainment term, which is proportional to the horizontal gradient scaled by the cloud radius. The microphysical processes are adopted from the model developed by Wisner et al. (1972). The interactions and formation of water substances, i.e., water vapor, cloud water, rainwater, and hail are simulated by the bulk parameterization. The development of the governing equation is discussed briefly with all symbols defined in the appendix.

The motion is assumed to be axisymmetrical. The equations of motion in the horizontal and vertical directions are

$$\frac{\partial}{\partial t}(\rho_o u) + \frac{1}{r}\frac{\partial}{\partial r}(r\rho_o uu) + \frac{\partial}{\partial z}(\rho_o uw) = -\frac{\partial(\Delta p)}{\partial r} \quad (1)$$

$$\frac{\partial}{\partial t}(\rho_o w) + \frac{1}{r}\frac{\partial}{\partial r}(r\rho_o uw) + \frac{\partial}{\partial z}(\rho_o ww) = -\frac{\partial(\Delta p)}{\partial z} + \rho_o\left[g\left(\frac{\Delta T_v}{\bar{\bar{T}}_v}\right) - \tau_p\right] \quad (2)$$

The continuity equation in the locally incompressible flow is

$$\frac{1}{r}\frac{\partial}{\partial r}(r\rho_o u) + \frac{\partial}{\partial z}(\rho_o w) = 0$$

where a mass-weighted divergence δ can be defined as

$$\delta = \frac{1}{r}\frac{\partial}{\partial r}(r\rho_o u) = -\frac{\partial}{\partial z}(\rho_o w) \quad .$$

Differentiating (1) with respect to r and adding (1)/r, we get a horizontal divergence equation. We can also get a divergence equation by differentiating (2) with respect to z. We use these two equations to eliminate the time-dependent term. The equation of continuity is used to manipulate terms; thus we get the diagnostic equation for the pressure perturbation

$$\left(\nabla_h^2 + \frac{\partial^2}{\partial z^2}\right)\Delta p = \frac{\partial}{\partial z}\left(\rho_o g\left(\frac{\Delta T_v}{\bar{\bar{T}}_v} - \tau_p\right)\right) - \frac{1}{r}\left\{\frac{\partial}{\partial r}(ru\delta) - \frac{\partial}{\partial r}(\rho_o uu) + \frac{\partial}{\partial r}\left(r\rho_o w\frac{\partial u}{\partial z}\right) + \frac{\partial^2}{\partial z\partial r}(r\rho_o uw)\right\} - \frac{\partial^2}{\partial z^2}(\rho_o ww) \quad (3)$$

In the following discussion the variables with subscript a and b represent the cloud and environment values, respectively. The perturbation method and the averaging method used by Asai-Kasahara are applied here for developing the averaged equations. The ― notation is neglected for simplicity. The assumption used by Holton $\nabla_h (\Delta p) = - k^2 (\Delta p)$, gives the averaged diagnostic equation

$$
\begin{aligned}
\left(\frac{\partial^2}{\partial z^2} - k^2\right) (\Delta p)_a &= \frac{\partial}{\partial z} \left(\rho_o g\left(\frac{\Delta T_v}{\bar{T}_v} - \tau_p\right)\right) \\
&+ (w_a - \tilde{w}_a) \frac{\partial \delta_a}{\partial z} - \frac{\partial}{\partial z} (\tilde{w}_a \delta_a) - \frac{\delta_a}{\rho_o} \left[\frac{3}{2} \delta_a + \tilde{\delta}_a \right. \\
&\left. + (2 w_a - \tilde{w}_a) \frac{\partial \rho_o}{\partial z}\right] - \rho_o w_a \frac{\partial^2 w_a}{\partial z^2} + \frac{\nu}{a^2} \frac{\delta_a}{1-\sigma^2} \\
&- \frac{4\rho_o}{a^2} \frac{w_a}{1-\sigma^2} \frac{\partial \nu}{\partial z} + \frac{\partial^2}{\partial z^2} \left(\nu_z \frac{\partial}{\partial z} (\rho_o w_a)\right)
\end{aligned}
\tag{4}
$$

The averaged prognostic equations in the cloud region are written in short form as follows

$$
\begin{aligned}
\frac{\partial A_a}{\partial t} &= - w_a \frac{\partial A_a}{\partial z} + \frac{2\tilde{u}_a}{a} (A_a - \tilde{A}_a) + \frac{2\nu}{a^2} (A_b - A_a) \\
&+ \frac{1}{\rho_o} \frac{\partial}{\partial z} \left(\nu_z \frac{\partial}{\partial z} (\rho_o A_a)\right) + S_a
\end{aligned}
\tag{5}
$$

where A_a can be w_a, T_a, $(X_V+X_W)_a$, $(X_R)_a$, or $(X_I)_a$; and the source terms for different variables are

$$
S_a = \left\{
\begin{array}{l}
g \left(\frac{\Delta T_v}{\bar{T}_v} - \tau_p\right) - \frac{1}{\rho_o} \frac{\partial}{\partial z} (\Delta p)_a \\
- \frac{g}{C_p} w_a + \frac{1}{\rho_a C_p} [(L_f P_I + L_v P_C) \\
\qquad + (T_a - T_o) C_w P_I (1-\varepsilon) + L_v P_{RE}] \\
\qquad - \frac{1}{C_p} [(w_a - v_R) X_R C_w + w_a X_w C_w \\
\qquad + (w_a - v_h) X_I C_I \varepsilon] \frac{\partial T_a}{\partial z} \\
P_c/\rho_a \\
P_R/\rho_a \\
P_I/\rho_a
\end{array}
\right\}
$$

The horizontal velocity is diagnosed from the following equation

$$
\frac{2}{a} \tilde{u}_a + \frac{1}{\rho_o} \frac{\partial}{\partial z} (\rho_o w_a) = 0 \tag{6}
$$

The environmental conditions are simpler, no cloud water, rainwater, or hail being considered. The governing prognostic equations are

$$
\begin{aligned}
\frac{\partial A_b}{\partial t} &= - w_b \frac{\partial A_b}{\partial z} - \frac{2\sigma^2 \tilde{u}_a}{a(1-\sigma^2)} (A_b - \tilde{A}_a) \\
&- \frac{2\sigma^2 \nu}{a^2(1-\sigma^2)} (A_b - A_a) \\
&+ \frac{1}{\rho_o} \frac{\partial}{\partial z} \left(\nu_z \frac{\partial}{\partial z} (\rho_o A_b)\right) + S_b
\end{aligned}
\tag{7}
$$

where

$$
A_b = \left\{ \begin{array}{c} T_b \\ (X_v)_b \end{array} \right\} \quad ; \quad S_b = \left\{ \begin{array}{c} - \frac{g}{C_p} w_b \\ 0 \end{array} \right\}
$$

The vertical motion is diagnosed from the following equation

$$
w_b = - \left(\frac{\sigma^2}{1-\sigma^2}\right) w_a \tag{8}
$$

In equations (4), (5), and (7), the ∿ quantity is evaluated according to the sign of lateral flow $\tilde{u}_a$. In the inflow situation $\tilde{u}_a < 0$, ∿ quantity takes the environmental value and in the outflow situation $\tilde{u}_a > 0$, the cloud value is used. The complete set of equations consists of equations (4) to (8).

3. INITIAL AND BOUNDARY CONDITIONS

The initial environmental sounding shown in Fig. 1 is taken from a sounding for August 10, 1973, in St. Louis. At each height level, the initial velocities are zero, the temperatures inside and outside the cloud region are equal, and the vapor contents are equal in and outside the cloud regions above the pre-calculated cloud base (LCL). The cloud is started by imposing a vapor excess below LCL; i.e., the relative humidity is 85% at the ground and increases linearly at the rate of 5% per km. The initial dew point distribution in the center core is shown in Fig. 1. This condition insures the positive virtual temperature excess which induces the vertical motion. The pressure deviation is zero at the initial time.

The boundary conditions at the ground in the central region are as follows: the vertical velocity is zero, and the temperature and vapor content are fixed until precipitation reaches the boundary. At the upper boundary, vertical outflow is permitted, but no inflow is permitted. The technique of handling this boundary condition is mentioned in Wisner et al. (1972). However, the flow at the top boundary is so weak that it can be considered as a fixed boundary.

The boundary conditions for the pressure diagnostic equation are

$$
\frac{\partial (\Delta p)_a}{\partial z} = 0 \qquad (z = z_{top}) \tag{9}
$$

$$\frac{\partial(\Delta p)_a}{\partial z} = \rho_o g \left(\frac{\Delta T_v}{\bar{T}_v} - \tau_p\right) \quad (z = 0) \tag{10}$$

These conditions are derived from the first equation of (5) with the assumption that $w_a = 0$ at both boundaries, and the mixing and source terms are zero. The lower boundary condition is dissimilar to that of Holton, but similar to that of Wilhelmson and Ogura (1972) and Arnason and Greenfield (1972). The effect of boundary conditions will be discussed later.

4. COMPUTATIONAL METHOD

The upstream differencing method is used for the integration of the vertical advection term. This method and the calculations of water substance productions are discussed at length in Wisner et al. Since implicit diffusion is included in this numerical technique, the sub-grid ν_z-type diffusion term mentioned in Holton (1973) is purposely neglected.

The pressure diagnostic equation is solved by the one-dimensional successive relaxation (Liebmann) method with 10^{-6} dyne cm^{-2} for the convergence limit. The diagnostic equations are solved at each time step.

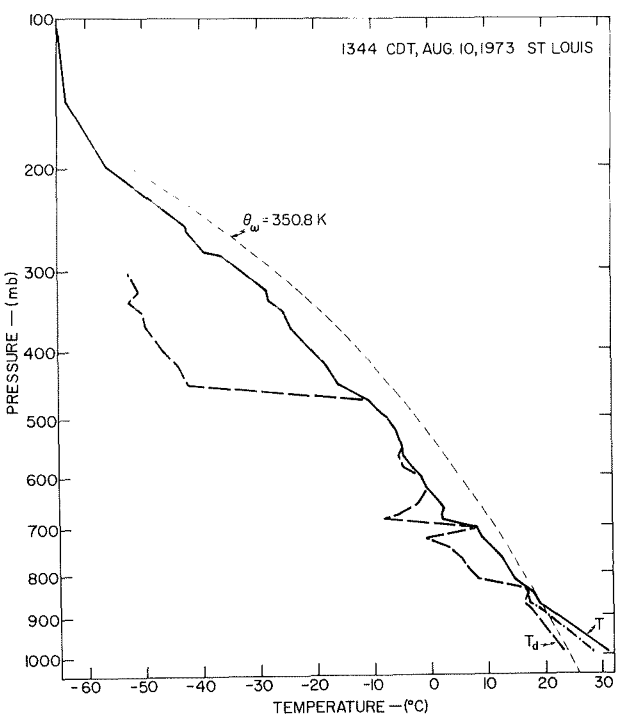

Fig. 1. Environmental sounding, August 10, 1973, St. Louis. The solid line is environmental temperature; the dash line is dew point; and the dash-dot line is initial cloud region dew point. (See text for explanation.)

5. RESULTS AND DISCUSSION

Two cases are studied. In Case 1 no pressure perturbation is included, while in Case 2 pressure perturbations are included. The results are presented in Figs. 2 - 8.

In Figs. 2 and 3, the vertical velocity profiles for Cases 1 and 2 are given. Before the cloud grows to the maximum height in the region above the maximum velocity level, the velocity contours in Case 1 are clustered together, while in Case 2 wider spacing between the contours is observed. The rate of rise of the cloud top of Case 2 is larger than that of Case 1. This is due to a maximum positive pressure deviation and a positive pressure gradient force present near the cloud top where an additional force enhances the vertical motion (Fig. 6).

The virtual temperature excess fields of the two cases are shown in Figs. 4 and 5. The patterns are similar. The double maxima of virtual temperature excess fields reflect the double maxima of velocity distribution in both cases. The perturbation pressure gradient force distribution is shown in Fig. 6. Comparing Figs. 5 and 6 shows that the virtual temperature excess (or, more precisely, buoyancy force) is generally opposite in sign to the pressure gradient force. In the positive (negative) virtual temperature excess region, there is a negative (positive) pressure gradient force. This compensating effect is also observed in the studies of Wilhelmson and Ogura (1972) and Soong and Ogura (1973).

The maximum vertical velocity of Case 2 is 15 m sec^{-1}, which is less than that of Case 1 (17 m sec^{-1}). From the smaller maximum vertical velocity in Case 2 (compared to that in Case 1), it can be reasoned that the negative pressure gradient reduces the vertical upward motion. Soong and Ogura defined a region roughly between the maximum velocity level and the cloud top, which characterized the path of the initial buoyant element in which the ratio of absolute values of buoyancy and pressure gradient forces is 3:1. The pressure gradient force is predominantly negative in this region. The present study shows the same distribution of pressure gradient force is observed. The ratio of the two forces is also about 3:1. A similar conclusion was drawn by Schlesinger (1972).

Before the precipitation reaches ground, in the sub-cloud region a weak positive pressure perturbation gradient force near the ground is observed (Fig. 6). In the other case studied (shown in Fig. 9), a rather strong negative pressure perturbation gradient force is found. In the results of Arnason and Greenfield (1972) and Holton (1973) a small positive gradient is observed, while in Wilhelmson and Ogura (1972) a large negative gradient force is observed. It is speculated that the difference in pressure distribution is caused by the different soundings.

Holton's boundary condition for the pressure deviation is zero pressure gradient at the lower boundary, thus affecting the solution of the diagnosed pressure deviation. A preliminary study that I carried out based on Holton's boundary condition, shows that a large positive gradient force is present in the sub-cloud region, prolonging the steady-state and preventing the cloud from breaking down. This unrealistic feature is eliminated by using the correct boundary condition (10), which includes buoyancy and water loading effects.

The distribution of hydrometeors of Cases 1 and 2 are shown in Figs. 7 and 8. The evolutions of clouds in the two cases are qualitatively similar; however, the the time-space distributions of rain and hail contents are different. The maximum updraft velocity of Case 2, which is affected by the pressure distribution, is less than that of Case 1; thus, the fallout of precipitation is more efficient than in Case 1, as can be seen from comparing contour maxima in Figs. 7 and 8.

The pressure gradient force causes the earlier breakdown of the steady-state in the precipitating stage. In this stage the water load effect on the vertical motion is important, and since the pressure term and the buoyancy term act against each other, the downward motion is easier to form than in the case without pressure effect. The present study shows that the formation of downward motion in Case 1 lags Case 2 by about 10.5 minutes. However, when the downdraft reaches the ground, a substantial positive pressure gradient force is formed near the ground, delaying the total collapse of the cloud (refer to .5C contour between 45 to 60 min in Fig. 6). Thus the precipitation time in Case 2 is slightly longer than in Case 1, and the cumulative precipitation of Case 2 (.685 cm) is larger than that of Case 1 (.50 cm).

A rough comparison of the model output and the observation data are listed in Table 1. The clouds on that day showed multiple-cell development; therefore several values of a parameter are listed. The present case study simulates a single cell; therefore the comparison can only be partial. It appears Case 2 shows better simulation in terms of vertical velocity and rainfall depth, while Case 1 over-predicts vertical velocity and under-predicts rainfall.

6. CONCLUSION

Inclusion of the pressure perturbations and the compensating environmental motion in the one-dimensional cloud model makes the dynamic features similar to those of the two-dimensional axisymmetric cloud models. The present case studies show that the effects of pressure perturbation in one-dimensional clouds are:

1) A redistribution of velocity, temperature, and water substances is observed.
2) More precipitation is observed on the ground even with a shorter cloud lifetime.

Acknowledgment. The author appreciates Mrs. Chin-Ho (Lin) Moeng's and Dr. H. D. Orville's helpful discussions.

This research was sponsored by the Atmospheric Sciences Section, National Science Foundation, under Grant No. DES75-03882. The computations were done partly at the Computer Center of the South Dakota School of Mines and Technology. The major portion of the computations were done at the National Center for Atmospheric Research, which is sponsored by the National Science Foundation.

REFERENCES

Arnason, G., and R. S. Greenfield, 1972: Micro- and macrostructures of numerically simulated convective clouds. J. Atmos. Sci., 29, 342-367.

Asai, T., and A. Kasahara, 1967: A theoretical study of the compensating downward motions associated with cumulus clouds. J. Atmos. Sci., 24, 487-496.

Holton, J. R., 1973: A one-dimensional cumulus model including pressure perturbations. Mon. Wea. Rev., 101, 201-205.

Schlesinger, R. E., 1972: A numerical model of deep moist convection: the influence of ambient conditions and internal physical mechanisms. Studies of the atmosphere using aerospace probings, space science and engineering center, University of Wisconsin, April 1972, 149-356.

Soong, S. T., and Y. Ogura, 1973: A comparison between axisymmetric and slab-symmetric cumulus cloud models. J. Atmos. Sci., 30, 879-893.

Wilhelmson, R., and Y. Ogura, 1972: The pressure perturbation and the numerical modeling of a cloud. J. Atmos. Sci., 29, 1295-1307.

Wisner, C., H. D. Orville, and C. Myers, 1972: A numerical model of a hail-bearing cloud. J. Atmos. Sci., 29, 1160-1181.

TABLE 1

Comparison Between the Model Output and the Observation

	Cloud Radius (km)	Base (km)	Top (km)	W_{max} ($msec^{-1}$)	Rainfall (mm)
Case 1 (no Δp)	1.5*	1.2	9.2	17	5.00
Case 2 (with Δp)	1.5*	1.2	9.2	15	6.85
Observation	2.0	1.2	9,10,14.5	14, 15	2.8,14,13

*Input value.

APPENDIX: List of Symbols

Notation	Description	Value	Unit
A	A physical quantity; the cloud value with subscript a; the environmental value with subscript b		
$\overline{A}$	Area mean of A		
$\tilde{A}$	Radial mean of A		
a	Radius of a cloud	1.5×10^5	cm
C_I	Specific heat of ice	2.093×10^7	erg gm^{-1} K^{-1}
C_p	Specific heat of air at constant pressure	1.005×10^7	erg gm^{-1} K^{-1}
C_w	Specific heat of water	4.816×10^7	erg gm^{-1} K^{-1}
g	Gravitational acceleration	980.5	cm sec^{-2}
k	A coefficient in the pressure diagnostic equation	2.4/a	cm^{-1}
L_f	Latent heat of fusion		erg gm^{-1}
L_v	Latent heat of evaporation		erg gm^{-1}
P_C	Production rate of cloud water		gm cm^{-3} sec^{-1}
P_I	Production rate of hail		gm cm^{-3} sec^{-1}
P_R	Production rate of rain		gm cm^{-3} sec^{-1}
P_{RE}	Evaporation rate of rain		gm cm^{-3} sec^{-1}
p	Pressure		dyne cm^{-2}
r	Radial coordinate		cm
S_a	Source term in the core region		
S_b	Source term in the environment		
T_a, T_b	Temperatures of the cloud and the environment		K
T_o	Freezing temperature	273.16	K
$\overline{T}_v$	Mean virtual temperature		K
$\tilde{u}_a$	Mean radial velocity at the cloud boundary		cm sec^{-1}
v_h	Mean terminal velocity of hail		cm sec^{-1}
v_R	Mean terminal velocity of the rainwater		cm sec^{-1}
w_a	Average vertical velocity in the core region		cm sec^{-1}
w_b	Average vertical velocity in the environment		cm sec^{-1}
X_I	Mixing ratio of hail		gm gm^{-1}
X_R	Mixing ratio of rain		gm gm^{-1}
X_V	Mixing ratio of water vapor		gm gm^{-1}
X_W	Mixing ratio of cloud water		gm gm^{-1}
z	Vertical coordinate		cm
z_{top}	The height of upper boundary	1.6×10^6	cm
α^2	Mixing coefficient	0.1	
δ	Mass weighted divergence		gm cm^{-3} sec^{-1}
ε	$\varepsilon = 1$, if temperature larger than 0C; otherwise 0		
ν	Eddy diffusion coefficient	$\alpha^2 a \lvert w_a \rvert/(1-\sigma^2)$	cm^2 sec^{-1}
ν_z	Sub-grid eddy diffusion coefficient		cm^2 sec^{-1}
Δp	Pressure deviation; the departure from hydrostatic pressure		dyne cm^{-2}
ΔT_v	Virtual temperature difference between the cloud and the environment		K
σ^2	Area ratio of cloud region and cloud free region	0.023	
ρ	Density of air		gm cm^{-3}
ρ_o	Reference air density		gm cm^{-3}
τ_p	Total hydrometeor mixing ratio; total content of cloud water, rainwater, and hail		gm gm^{-1}
∇_h^2	Horizontal Laplacian operator in cylindrical coordinate		cm^{-2}

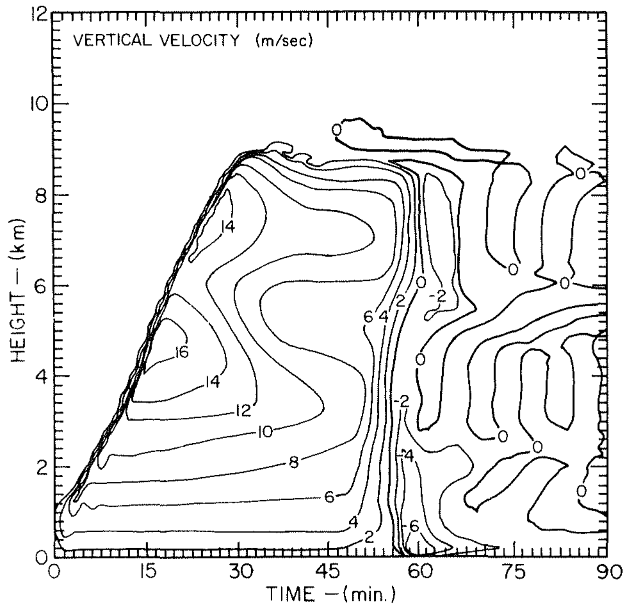

Fig. 2. Vertical velocity profile for Case 1. The contour interval is 2 m sec^{-1}.

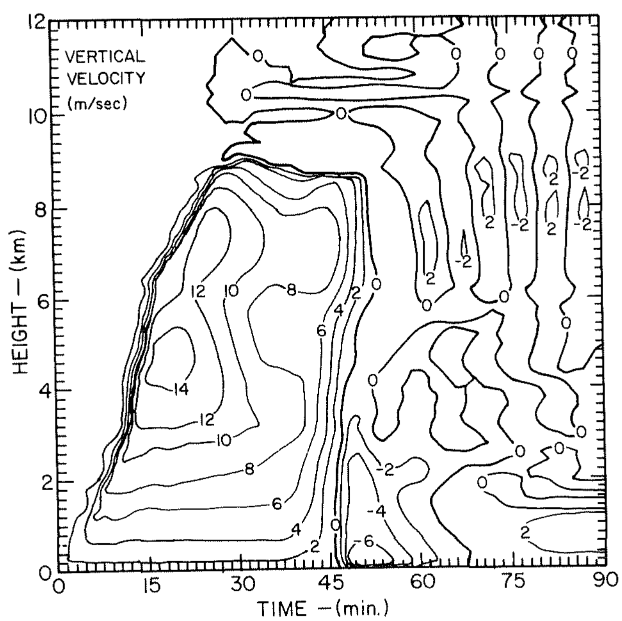

Fig. 3. Vertical velocity profile for Case 2. The contour interval is 2 m sec^{-1}.

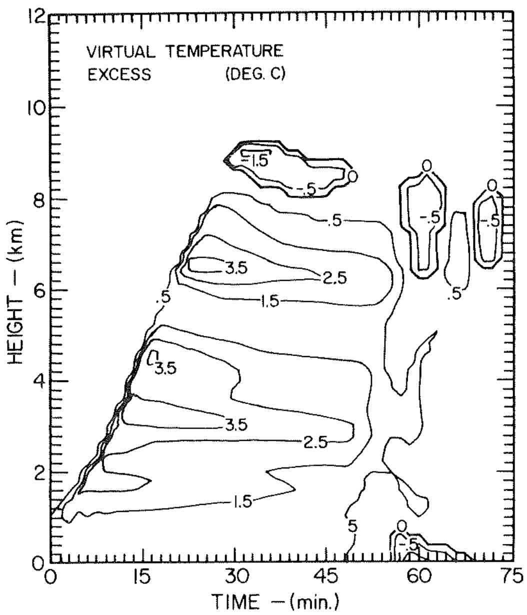

Fig. 4. Virtual temperature excess distribution for Case 1. The contour interval is 1.0C.

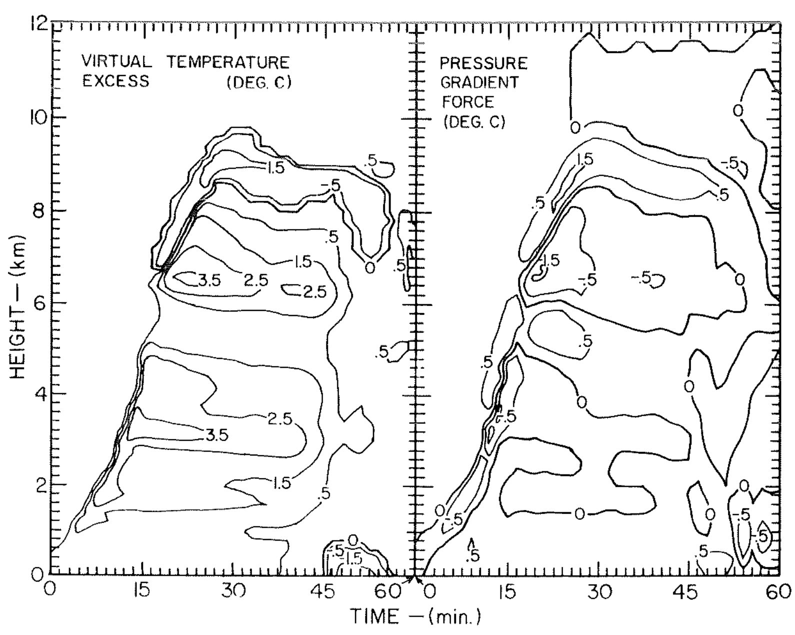

Fig. 5. Virtual temperature excess distribution for Case 2. The contour interval is 1.0C.

Fig. 6. Perturbation pressure gradient force distribution for Case 2. The value is expressed in equivalent temperature. The contour interval is 0.5C.

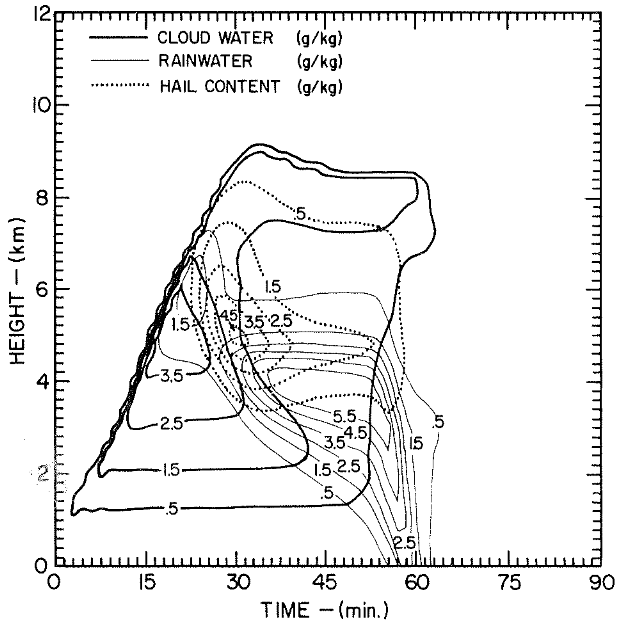

Fig. 7. Hydrometeor distributions for Case 1. The bold solid line is for cloud water, the thin solid line is for rain, and the dot line for hail. The counter interval is 1 gm kg^{-1}.

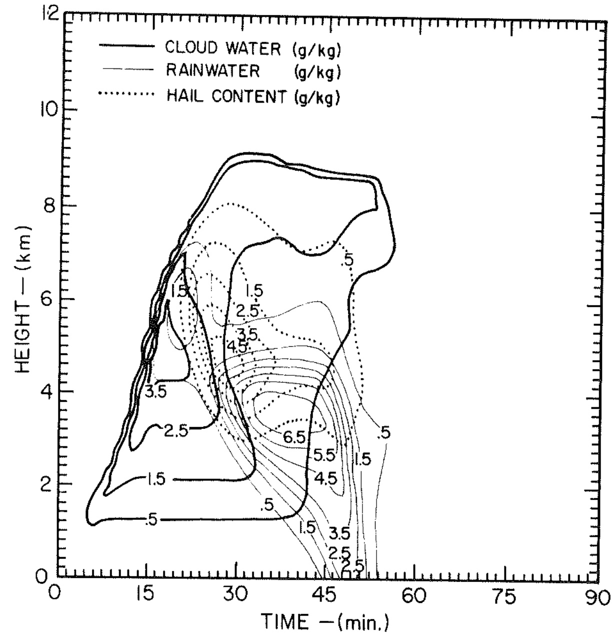

Fig. 8. Hydrometeor distributions for Case 2. The bold solid line is for cloud water, the thin solid line is for rain, and the dot line for hail. The counter interval is 1 gm kg^{-1}.

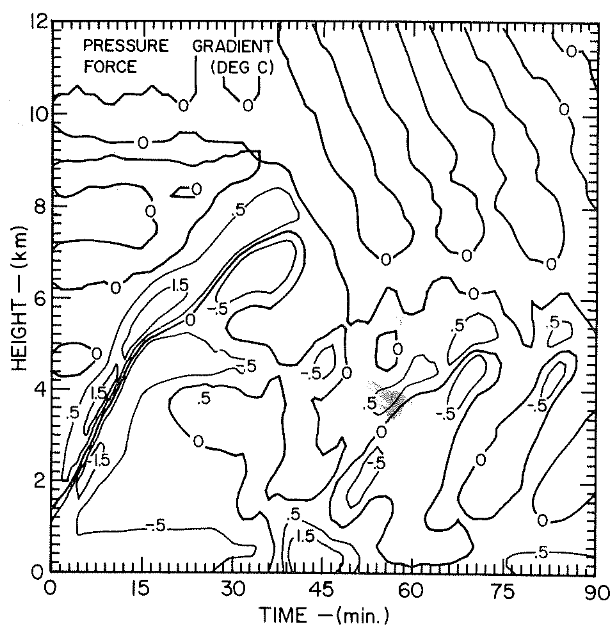

Fig. 9. Pressure gradient force distribution for a case based on 1335 CDT, August 17, 1973, St. Louis sounding.

RADIATIVE-DIFFUSE MODELS OF ARCTIC STRATUS CLOUDS

Gerald Herman

Space Science and Engineering Center
University of Wisconsin

and

Richard Goody

Harvard University

1. INTRODUCTION

Persistent and extensive layers of fog, and stratus and stratocumulus type clouds occur over the Arctic basin, particularly during the melting season. These cloud layers, which we refer to as *Arctic stratus*, are an important element of the climate of the Arctic Basin since they profoundly influence the radiation budgets of the free atmosphere and the surface.

According to the analysis of Vowinckel and Orvig (1970), the mean cloud amount during July exceeds ninety percent over the polar oceans, while the frequency of stratiform clouds during this period exceeds seventy percent. That analysis also illustrates the apparently radical temporal behavior of Arctic stratus clouds: cloud amounts increase from their wintertime values of 40-60 percent to their high summertime values of 70-90 percent over a relatively short period of about four weeks. Arctic stratus clouds tend to occur in well-defined layers separated by clear interstices (Jayaweera and Ohtake, 1973) with individual cloud layers 300-500 m thick, and liquid water mixing ratios of $0.5\text{-}1.0 \times 10^{-4}$. A complete review of observational data on Arctic Stratus is given elsewhere (Herman, 1975).

This paper describes several aspects of an internally consistent radiative diffusive model that was developed to illustrate and explain many of the observed properties of summertime Arctic stratus. Our model treats the modification of continental polar air due to radiative transfer and turbulent exchange as it streams over the pack ice. Following observations, we assume that during the summer the surface of the ice-covered basin is melting ice and that surface temperature is 0°C. We assume that the thermodynamics of the boundary layer is decoupled from the thermodynamics of the large-scale flow, and that we can parameterize the effect of large-scale subsidence. Moreover we assume that the air parcels follow a trajectory which allows them to remain over the ice long enough for near-steady conditions to be established.

2. DESCRIPTION OF THE MODEL

The steady state distribution of equivalent potential temperature θ_E and total water r in a moist Boussinesq atmosphere is given by

$$U_o \frac{\partial \theta_E}{\partial x} = \frac{\theta_E}{\rho C_p T} H_{rad} - \frac{\partial}{\partial z} (\overline{w'\theta_E'}) \qquad (1)$$

$$U_o \frac{\partial r}{\partial x} = - \frac{\partial}{\partial z} (\overline{w'r'}) - w_f \frac{\partial r_\ell}{\partial z} \qquad (2)$$

Here the advective terms are linearized about a constant geostrophic current U_o, H_{rad} is the volume rate of radiative heating, w_f is the fall velocity computed from Stokes' law, r_ℓ is the mass mixing ratio of liquid water, and $(\overline{w'\theta_E'})$ and $(\overline{w'r'})$ are the turbulent fluxes of equivalent potential temperature and total water, respectively. The specific heat at constant pressure is C_p, ρ is the density and T the temperature. We assume that the distribution of both liquid water r_ℓ and water vapor r_v can be described with a single equation for the total water content, r.

We include the momentum equations

$$U_o \frac{\partial u}{\partial x} = fv - \frac{\partial}{\partial z} (\overline{w'u'}) \qquad (3)$$

$$U_o \frac{\partial v}{\partial x} = - fu - \frac{\partial}{\partial z} (\overline{w'v'}) \qquad (4)$$

where f is the Coriolis parameter and u and v are departures from the invariant geostrophic winds U_o and V_o ($V_o = 0$). The terms $(\overline{w'u'})$ and $(\overline{w'v'})$ represent the vertical turbulent transports of x-momentum and y-momentum respectively. Equations (3) and (4) are coupled to (1) and (2) only through our parameterizations of turbulence in the surface and Ekman layers. In both regions the transports are functions of the velocity gradients $\partial u/\partial z$ and $\partial v/\partial z$, as well as the gradients $\partial\theta_E/\partial z$ and $\partial r/\partial z$. We solve the system (1)-(4) as a time-marching problem with the substitution (Deardorff, 1967)

$$U_o \frac{\partial}{\partial x} [\qquad] = \frac{\delta}{\delta t} [\qquad] \qquad (5)$$

where the downstream derivative $\delta/\delta t$ relates the change in time t to the change experienced over the corresponding travel distance x moving with the velocity U_o. We solve (1)-(4) numerically in the domain $t = 0$ to $t = t^*$ and from $z = 0$ to $z = 2050$ m, where the upper limit of z is slightly greater than the characteristic vertical scale of Arctic stratus.

Our parameterization of the surface layer closely parallels that of Deardorff (1972). We consider Paulson's (1970) integration of the Monin-Obukhov universal functions derived by Businger (1973). Denoting the integrals for heat and momentum by I_h and I_m, respectively, we define a bulk Richardson number

$$Ri_B = (z/L)I_h(z/L)I_m^{-2}(z/L) \tag{6}$$

where L is the Obukhov stability parameter defined in terms of the virtual potential temperature. We use (6) to obtain unique values of z/L given the wind speed at the top of the surface layer, U, and virtual potential temperature difference across the surface layer, $\Delta\theta_v$, by defining drag laws that yield surface fluxes of momentum, virtual potential temperature, and specific humidity. Above the surface layer we use the simplest parameterizations which give a closed physical model. All parameterizations are based upon an eddy diffusion coefficient K(z) which is the same for heat, momentum and moisture. In the case of unstable atmosphere we do not attempt the difficult task of calculating the time evolution of the profiles of θ_E. Instead, we use the principle of convective adjustment, as employed by Manabe and Strickler (1964) and Gierasch and Goody (1970), whereby entropy, momentum and total water are conserved in a rapid mixing process.

Our treatment of radiative transfer closely follows that of Gierasch and Goody (1970) for the clouds of Venus. The absorption optical depth is

$$\tau(\nu) = \int_z^\infty [k_c(\nu) + k_g(\nu)]dz \tag{7}$$

where $k_c(\nu)$ and $k_g(\nu)$ are the volume absorption coefficients for the cloud and gas, respectively. In the first approximation (Chandrasekhar, 1960) we obtain a linear homogeneous second order differential equation for the net solar flux F_S,

$$\frac{d^2F_S}{d\tau^2} - \beta^2F_S = 0 \tag{8}$$

where the scattering parameter is

$$\beta^2 = \frac{3(1 - \tilde{\omega}_o\langle\cos\theta\rangle)}{(1 - \tilde{\omega}_o)} \tag{9}$$

and where the single scattering albedo is

$$\tilde{\omega}_o = \frac{s(\nu)}{s(\nu) + k_c(\nu) + k_g(\nu)} \tag{10}$$

The asymmetry factor is $\langle\cos\theta\rangle$. The boundary conditions are

$$\frac{dF_S}{d\tau} + \sqrt{3}\left(\frac{1 + \alpha}{1 - \alpha}\right)F_S = 0 \qquad \tau = \tau^* \tag{11}$$

$$\frac{dF_S}{d\tau} - \sqrt{3}F_S = 2\sqrt{3}\,\mu_o f(\nu) \qquad \tau = 0 \tag{12}$$

where α is the surface reflectivity, μ_o is the cosine of the solar zenith angle, $f(\nu)$, the solar irradiation at $\tau = 0$, and where the asterisk denotes the value of a quantity at the surface.

For a single frequency (8) is solved by dividing the atmosphere into N discrete homogeneous layers. In each of the N homogeneous regions the solutions are exponential

$$F_S(\tau_N) = C_{1,N}\, e^{\beta_N\tau_N} + C_{2,N}\, e^{-\beta_N\tau_N}$$

the coefficients $C_{1,N}$ and $C_{2,N}$ are a set of 2N constants. Two of the constants are provided by the boundary conditions (11) and (12), while the remaining 2N - 2 conditions are provided by requiring the continuity of F_S and $dF_S/d\tau$ at the N - 1 interfaces.

Our concern is with the integrated solar flux, i.e., integrated over all frequencies and this can involve a variety of gases each with many bands. We consider only water vapor absorption. This is a complicated spectrum and we adopt the frequently used approach (Lacis and Hansen, 1974) of dividing the spectrum into regions with an absorption coefficient k_i covering a noncontiguous fraction a_i. Then the mean transmission is

$$\overline{T} = \sum_i a_i\, e^{-k_i u} \tag{13}$$

Over the range of water vapor densities, ρ_w, encountered in the Arctic we find an adequate fit to the transmission with two regions only: a transparent region with $a_1 = 0.91$ and $k_1 = 1.1\rho_w$ (m^{-1}) and an opaque region, with $a_2 = 0.08$ and $k_2 = 255\rho_w$ (m^{-1}).

We treat the cloud as a grey absorber and scatterer for solar radiation by employing Planck mean efficiencies ($\overline{Q_a^S}$ and $\overline{Q_s^S}$, respectively), based on a 6000 K thermal source function:

$$\overline{s} = \overline{Q_s^S}(a)\; N_o\pi a^2 \tag{14}$$

$$\overline{k_c} = \overline{Q_a^S}(a)\; N_o\pi a^2 \tag{15}$$

where N_o is the number density of cloud droplets and a is the radius. The term $\langle\cos\theta\rangle$ does not vary greatly for water droplets in the range 3-10 μm and we use a single value of 0.85.

We employed the asymptotic form of van de Hulst (1957, Ch. 11) for large droplets to compute $\overline{Q_a^S}$ and $\overline{Q_s^S}$ as a function of a, using the spectral data of Ivine and Pollack (1968).

For thermal radiation the differential equation governing the flux (F_T) contains an additional thermal source function. Boundary conditions imposed are that the upward intensity at the ground is equal to the Planck function corresponding to the surface temperature and that the downward radiation is zero above the atmosphere. We employ Planck mean coefficients defined on the basis of a 273 K thermal source function.

Neglecting scattering, the integrated net flux is expressed in the form with B and B^* denoting the Planck function corresponding to the ambient and surface temperatures respectively,

$$F_T = - \int_0^z \pi B(z')d\varepsilon[3^{1/2} m(z,z');3^{1/2} u(z,z')]$$
$$+ \pi B^*[1 - \varepsilon(3^{1/2}m(z,0);3^{1/2}u(z,0)]$$
$$- \int_z^\infty B(z')d\varepsilon[3^{1/2}m(z,z');3^{1/2}u(z,z')] \quad (16)$$

where

$$u(z,z') = \left| \int_z^{z'} \rho_w(z'')dz'' \right| \quad \text{kg m}^{-2} \quad (17)$$

$$m(z,z') = \left| \int_z^{z'} N_o(z'')dz'' \right| \quad \text{m}^{-2} \quad (18)$$

If the absorption spectra of cloud and water vapor are uncorrelated, or if the emissivity of either is small, the emissivity of the gas-cloud mixture can be written

$$1 - \varepsilon_M(m;u) = [1 - \varepsilon_g(u)] \times [1 - \varepsilon_c(m)] \quad (19)$$

where ε_g and ε_c are the gas and cloud emissivities, respectively. We take

$$\varepsilon_c(m) = 1 - \exp(-3^{1/2} \pi a^2 m\overline{Q_a^T}) \quad (20)$$

where $\overline{Q_a^T}$ is the thermal absorption efficiency. For gaseous emissivities we follow Rodgers (1967).

3. RESULTS

We present results from sample calculations that illustrate the dependency of cloud heating rates on the volume absorption coefficients for thermal radiation, k_T, and for solar radiation k_S. In our notation $k_T = N_o\chi_a^T$, where the thermal absorption cross section is $\chi_a^T = \overline{Q_a^T}\pi a^2$, and $k_S = N_o\chi_a^S$, where $\chi_a^S = Q_a^S\pi a^2$.

Calculations for thermal radiation are shown in Fig. 1, which we have plotted on an arctangent scale to accommodate the large positive and negative values of the heating rate. We assume a homogeneous cloud layer between 500 and 1000 m overlying a 273 K surface in an adiabatic atmosphere. The clear atmosphere ($k_T = 0$) cooling is about one degree per day. An opaque cloud ($k_T = 5 \times 10^{-4}$ cm^{-1}) cools intensively at the top and is warmed at the base, while the size of the heating and cooling is less in a tenuous cloud ($k_T = 5 \times 10^{-6}$ cm^{-1}) and is more evenly distributed throughout the depth of the cloud. Under typical Arctic stratus conditions ($k_T \sim 5 \times 10^{-5}$ cm^{-1}) cloud tops cool at about 10°C per day, with some warming occurring at the base.

Strong cooling at stratus cloud tops has been verified experimentally: Markosova and Shlyakov (1972) have determined cooling rates of 1.0 ± 0.5°C hr^{-1} at the top of Sc and St type clouds.

Sample heating rates are illustrated in Fig. 2 for a 500 m cloud embedded in a boundary layer with 3 g kg^{-1} of water vapor. Solar heating of 3°C per day occur under typical Arctic stratus conditions ($k_S = 5 \times 10^{-5}$ cm^{-1}) and increases

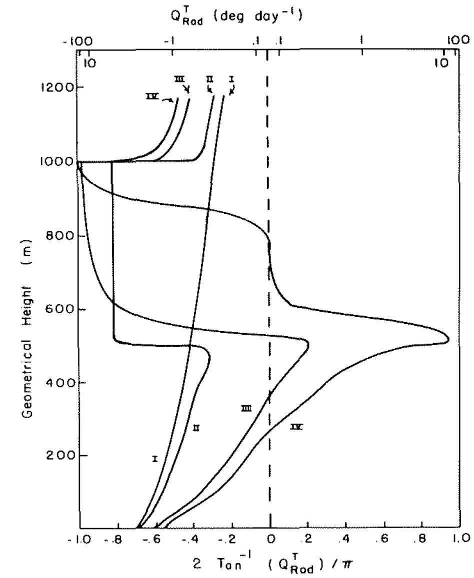

Fig. 1. Longwave heating rate profiles in a 500 m cloud layer over a 273 K surface. Cases I through IV represent $N_o\chi_a^T = 0$, 5×10^{-6}, 5×10^{-5}, and 5×10^{-4} cm^{-1}, respectively.

of k_S slightly alter the heating in the sub- and supra-cloud regions, while causing order of magnitude changes within the cloud layer itself. The results of other calculations, not shown here, suggest that solar heating in a cloud layer over a highly reflective surface ($\alpha = .80$) is twice as large as the solar heating in a cloud over a dark surface ($\alpha = 0$).

These results have important implications for the dynamics of stratus clouds. With an absorption coefficient k_T of 5×10^{-5} cm^{-1} a cloud will undergo substantial cooling over a depth of $(\sqrt{3}k_T)^{-1}$, or about 100 m. Solar heating

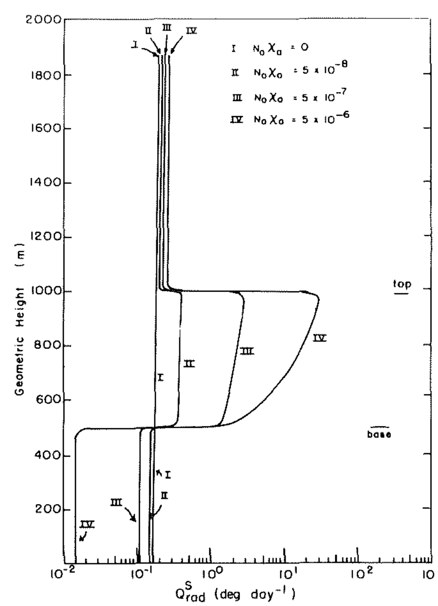

Fig. 2. Sample solar heating rates for a 500 m cloud layer for selected values of the parameter $k_S = N_o\chi_a^S$.

will be largest over a depth of $(\beta k_S)^{-1}$ or about 700 m. Cloud top cooling combined with interior heating is likely to induce mixing in the absence of other processes, as Fritz (1958) has suggested.

The conditions in the basic models are the following:

Boundary conditions. The temperature at the lower boundary (z = 0) remains constant at the equilibrium temperature of melting fresh-water ice, 273 K. The surface is saturated with respect to liquid water at this temperature. The surface reflectivity α is 0.40, which is typical of a melting ice surface with crusted snow and meltwater ponds. A mean surface roughness z_o of 1 mm is assumed. At the top of the boundary layer ($z = z_T$) we assumed zero flux conditions, i.e. $\partial\theta_E/\partial z = 0$, $\partial r/\partial z = 0$, with u = 0 and v = 0. At the lower boundary, $\theta_E = \theta_E(0)$, $r = r_s(0)$, $u + U_o = 0$, and v = 0.

Following Lilly (1968) we add to (6) a term of the form $w\partial\theta_E/\partial z$ to represent heating due to subsidence, where w is a mean vertical velocity. We assume w = Az, where $A = -1.4 \times 10^{-7}$ sec^{-1}.

Initial conditions. We assumed $\theta(0)$ = 277K and $\partial\theta_E/\partial z = +1°C\ km^{-1}$, which corresponds to a stable column of air initially 4°C warmer than the surface. The initial relative humidity was 90% throughout the depth of the boundary layer, and the initial wind profile was a balanced Ekman spiral corresponding to a constant eddy diffusivity of 2.5 $m^2\ sec^{-1}$.

Radiative conditions. The diurnal cycle of solar radiation was not included in the basic state and a mean solar zenith angle of 74° was used. Following the observations of Jayaweera and Ohtake (1973), all extinction parameters were computed on the basis of a droplet radius of 6.5 μm. We use $Q_a^T = 0.690$, $Q_s^S = 2.004$, and $Q_a^S = 0.016$. The superincumbent water vapor u_o remained fixed at 5 km m^{-2}.

Other conditions. The eddy diffusivity K(z) was computed from the unmodified mixing-length of Blackadar (1962). The fall velocity

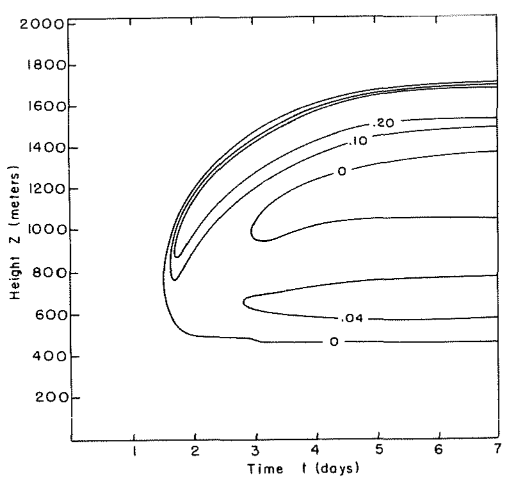

Fig. 3. Liquid water distribution for air initially 4°C warmer than ice and relative humidity of 90%. Isolines are g kg^{-1}.

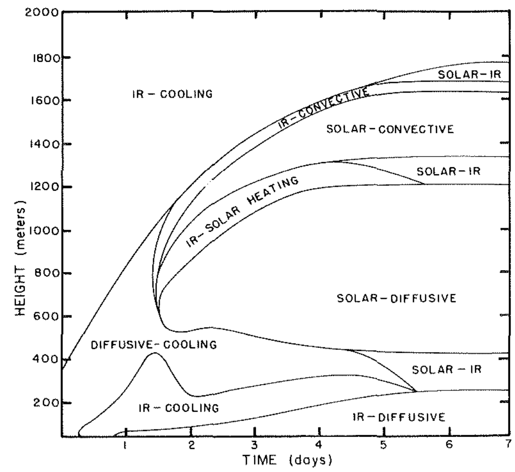

Fig. 4. Components of the radiative and turbulent regimes.

w_f for a 6.5 m drop computed according to Stokes Law is 5 mm sec^{-1}.

The results of a seven-day integration are shown in Fig. 3, where the liquid water content of the boundary layer is shown as a function of height and time.

Condensation initially occurred after 34 hours at a height of 500 m. The base of the cloud remained at a nearly constant height throughout the integration, while the top rose slowly and appeared to level out in about five days. After 66 hours the cloudy region divided into two well-defined cloud layers separated by a distinct interstice. The bases and tops of both layers approached stationarity in about five days. The upper layer is the more dense with a maximum water mixing ratio of 3.4 x 10^{-4} at the top (about 3.7 x 10^{-4} kg m^{-3}). The lower layer is more tenuous, and has a maximum mixing ratio of 4 x 10^{-5} (about 5 x 10^{-5} kg m^{-3}). At equilibrium the base and top of the lower layer were located at 500 m and 1050 m, and the base and top of the upper layer were located at 1450 m and 1700 m. The interstice was 400 m deep.

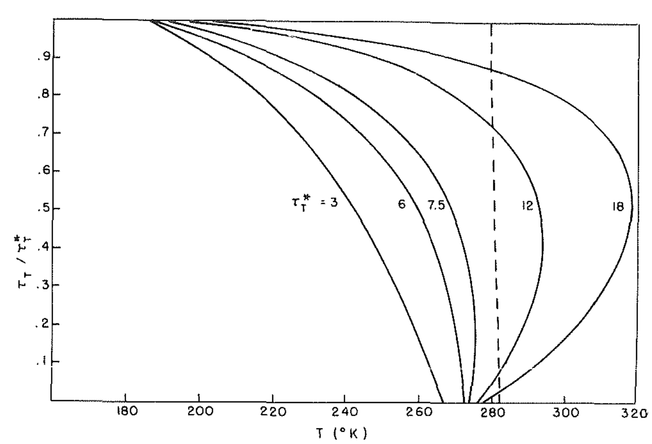

Fig. 5. Radiative equilibrium temperature profiles.

The radiative and turbulent processes within the cloud layers are illustrated schematically in Fig. 4. Here the terms *heating* and *cooling* refer to the sign of the local time rate of change of equivalent potential temperature; *diffusive* refers to the divergence of the turbulent flux under stable conditions, while *convective* refers to the divergence of the turbulent flux under unstable conditions. The terms *solar* and *IR* refer to the divergences of the net solar flux F_S and the net thermal flux F_T.

The IR-cooling zone of the upper left hand corner is the cooling of the upper regions of the boundary layer by direct longwave exchange with space. Diffusive-cooling and IR-cooling lower the boundary layer temperature to condensation in slightly more than a day, and a zone of near-equilibrium between IR boundary exchange and diffusion is rapidly established close to the surface.

Once the condensate has formed the radiative regime is greatly altered by the absorptive properties of the droplets. The upper cloud layer becomes unstable due to the intense longwave loss from the top of the cloud. A radiative-convective balance is established in the cloud layer, with convective warming approximately equal to radiative cooling at the top, while the convective cooling balances the heating due to solar absorption in the interior. A region of intense radiative heating forms within the cloud interior by a greenhouse mechanism. After approximately three days the heating and cooling terms become small, and several steady state zones are established. Note also that two radiative equilibrium zones are located between radiative-convective and radiative-diffusive zones. The clear interstice is a region in which the ambient temperature exceeds the dew point temperature corresponding to the local specific humidity. This structure is partially due to the differing optical properties of the cloud in the solar and terrestrial portions of the spectrum, and partially due to the 0°C surface temperature constraint. Radiative equilibrium temperature profiles are shown in Fig. 5 for several values of the total thermal optical depth τ_T^* for an atmosphere in which the lower boundary temperature is 273 K and in which $\beta\tau/\sqrt{3}\tau_T = 0.07$.

The upper part of the cloud becomes warmer with increasing optical depth as less longwave radiation escapes to space. For $\tau_T^* \gtrsim 7.5$ the temperature decreases with increasing optical depth and becomes very close to T^* at $\tau = \tau_T^*$. If the interior is so warm that $T(\tau_T) > T_d(\tau_T)$, where T_d is the dew point temperature, that portion of the cloud must evaporate. The broken line in Fig. 5 runs parallel to the lapse rate of T_d in an atmosphere with a constant mixing ratio of $r_v = 0.003$. The intersection of this line with the temperature curves defines to a first approximation the clear interstice of the stratus cloud.

ACKNOWLEDGEMENTS

Gerald Herman has been supported by ERDA grant AT(11-1)-2195 at MIT. Richard Goody is partially supported by NSF grant DES-72-01472 A03.

REFERENCES

Blackadar, A. K. (1962), "The Vertical Distribution of Wind and Turbulent Exchange in a Neutral Atmosphere," J. Geophys. Res., 67, 3095-3102.

Businger, J. A. (1973), "Turbulent Transfer in the Atmospheric Surface Layer," in Workshop on Micrometeorology, D. Haugen (ed.), Boston: American Met. Soc., 392 pp.

Chandrasekhar, S. (1960), Radiative Transfer, New York, Dover Publications, 393 pp.

Deardorff, J. W. (1967), "Empirical Dependence of the Eddy Coefficient for Heat upon Stability Above the Lowest 50 m," J. Appl. Met., 6, 631-643.

______ (1972), "Parameterization of the Planetary Boundary Layer for Use in General Circulation Models," Mon. Wea. Rev., 100, 93-106.

Fritz, S. (1958), "Absorption and Scattering of Solar Energy in Clouds of 'Large Water Drops'-II," J. Met., 15, 51-58.

Gierasch, P. and R. Goody (1970), "Models of the Venus Clouds," J. Atmos. Sci., 27, 224-245.

Herman, G. F. (1975), "Radiative Diffusive Models of the Arctic Boundary Layer," Scientific Report No. 3, MIT Meteorology Dept. (COO-2195-21), 171 pp. Available from NTIS.

Irvine, W. M. and J. B. Pollack (1968), "Infrared Optical Properties of Water and Ice Spheres," Icarus, 8, 324-360.

Jayaweera, K. O. L. F. and T. Ohtake (1973), "Concentration of Ice Crystals in Arctic Stratus Clouds," J. Rech. Atmos., 7, 199-207.

Lacis, A. A. and J. E. Hansen (1974), "A Parameterization for the Absorption of Solar Radiation in the Earth's Atmosphere," J. Atmos. Sci., 31, 118-133.

Manabe, S. and R. F. Strickler (1964), "On the Thermal Equilibrium of the Atmosphere with a Convective Adjustment," J. Atmos. Sci., 21 (4), 361-385.

Markosova, L. I. and V. I. Shlyakov (1972), "Problem of Radiation Properties of Clouds in the Middle and Upper Levels and with Vertical Development," Meteorologiya i Gidrologiya, 5, 89-93.

Paulson, C. A. (1970), "The Mathematical Representation of Wind Speed and Temperature Profiles in the Unstable Atmospheric Surface Layer," J. Appl. Met., 9, 857-861.

Rodgers, C. D. (1967), "The Use of Emissivity in Atmospheric Radiation Calculations," Quart. J. R. Met. Soc., 93, 43-54.

Van de Hulst, H. C. (1957), Light Scattering by Small Particles, New York: Wiley, 470 pp.

Vowinckel, E. and S. Orvig (1970), "The Climate of the North Polar Basin," in World Survey of Climatology Vol. 14, Climates of Polar Regions, S. Orvig (ed.) New York: Elsevier, 370 pp.

4.4.2

ALBEDO REDUCTION AND RADIATIONAL HEATING OF WATER CLOUDS BY ABSORBING AEROSOL PARTICLES

Hartmut Grassl

University of Mainz, West Germany

1. INTRODUCTION

The size distribution of cloud droplets strongly depends on the size distribution and chemical structure of the aerosol particles. The smaller the vertical velocity, the stronger this dependence will be, thus chemical structure and aerosol size distribution have maximal influence on droplet sizes in stratus cloud decks. Clouds with the same liquid water content and geometrical thickness however different scattering or phase functions depending on droplet size distribution differ in albedo, one of the main parameters affecting the climate of the globe.

Another effect on the albedo nearly completely neglected up to now (TWOMEY (1972) and GRASSL (1975)) can be caused by absorbing aerosol particles. This absorption in the solar part of the spectrum measured by FISCHER (1970, 1973) and LAUDE, LINDBERG (1974) is important in the range of extremely weak absorption by liquid water and water vapour. Due to the coincidence of wavelength of maximum solar radiation and minimum absorption by liquid water and water vapour, absorbing aerosol particles get an extreme influence with respect to their mass in the visible part of the spectrum. Since scattering events of a photon are multiplied within optically thick water clouds only a slight deviation of the single scattering albedo ω_0 from the value 1.0 standing for conservative scattering causes strong absorption and thus heating of the cloud simultaneously reducing its albedo. The single scattering albedo of an ensemble of particles is defined as the ratio between scattering and extinction coefficient.

In this paper the single scattering albedo ω_0 and the radiative flux divergence inside clouds and cloud albedo will be presented using one of the socalled 'exact' radiative transfer models, the Matrix-Operator-Theory (MOT) as summarized by PLASS (1973).

THE SINGLE SCATTERING ALBEDO OF CLOUD AIR

The main problem in estimating the proper values of ω_0 of cloud air combining droplets and those aerosol particles not used as condensation nuclei is to find where the absorption measured with dry aerosol particles will be after the development of a droplet size distribution. In a former paper (GRASSL 1975) the possibilities were discussed. Since we have up to now no particle size dependent absorption values this possible uncertainly cannot be removed. The following table 1 was attained by assuming CCN soluble particles per unit of volume serving as cloud condensation nuclei and by fixing the ratio CCN/N (N is the total number density of all particles), which is a measure of supersaturation in a cloud. The wavelength dependence of the absorption coefficient of dry aerosol particles was taken from FISCHER (1973) (measured Nov. 28, 1972 at Mainz, West Germany) and the growth of particles with relative humidity of an aerosol size distribution $n(r) = 4.9757 \cdot 10^6\, r^2\, e^{-15.1186 \sqrt{r}}$ in $cm^{-3}\, \mu m^{-1}$ (Haze L after DEIRMENDJIAN (1969)) follows HÄNEL (1975). Thereby assuming that all particles of radius $r \geqslant r_2'$, if r_2' is calculated from $CCN/N = \int_{r_2'}^{r_2} n^*(r)dr / \int_{r_1}^{r_2} n(r)dr$, resulted in a cloud drop size distribution C 1 with $n^*(r) = 2.373 \cdot r^6 e^{-1.5r}$ as given by DEIRMENDJIAN (1969). All ω_0 values were calculated using Mie-theory which is surely applicable to spherical water droplets and smaller aerosol particles at water vapour saturation level.

Table 1
ω_0 depending on wavelength λ and fraction CCN/N of particles used as condensation nuclei.

λ \ CCN/N	0.1	0.3	0.5	0.8
0.35	0.9943	0.9967	0.9980	0.9987
0.45	0.9949	0.9972	0.9983	0.9989
0.55	0.9950	0.9970	0.9932	0.9989
0.65	0.9952	0.9972	0.9983	0.9989
0.76	0.9953	0.9973	0.9984	0.9990
0.55	0.9967		0.9989	

Neglection of the aerosol particles grown with relative humidity but not big enough to be incorporated in the cloud drop size distribution leads to the lowest line in table 1 and means a considerable loss of possible absorption since 1- ω_0 is proportional to the amount of absorption per scattering event.

RADIATIVE TRANSFER MODEL ASSUMPTIONS

MOT has to assume a plane-parallel atmosphere. The cloud is homogenous as to the particle and liquid water content, can have a temperature gradient and therefore a gradient in water vapour density. The restriction to plane-parallel layer clouds can be removed by the knowledge of the deviation of undulating and broken cloud fields from the layer cloud with the same mean optical thickness (WENDLING 1976). The gaseous absorption was handled in expanding the transmission in a six-term series of exponentials using measured data given by MOSKALENKO (1969).

ABSORPTION OF SHORTWAVE RADIATION IN WATER CLOUDS

All results concerning aerosol absorption effects have to be compared to the absorption by atmospheric gases and droplets consisting of pure water. The values ω_0 given in table 1 are only valid for a particular aerosol type measured in Mainz, West Germany, in a polluted area. The possible variations of ω_0 in different climates are surely covered in fig. 1 showing the absorption in percent of the incoming radiation at o.55 μm wavelength. Measurements of aerosol absorption in different climates (FISCHER 1973) show that even in remote areas like the bushland region of South-West Africa the absorption of dry aerosol particles can be as high as in the heavily polluted industrial area near Mainz, West Germany. The general trend however is lower values in remote continental locations and strongly lower values in marine environments. Therefore in general the more polluted the area the stronger the heating will be, since both effects the higher absorption and the higher particle mass loading cause additional heating. Because of the very small deviations of ω_0 from the value 1.o the linear relationship between (1- ω_0) and the total amount of absorption holds and heating rates at different ω_0 can easily be calculated.

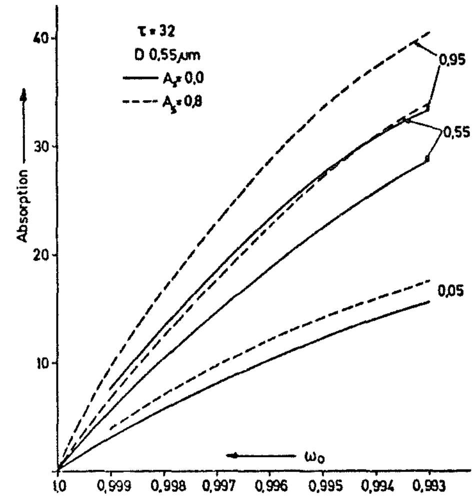

fig 1: Absorption in percent of the incoming radiation depending on ω_0 for different angles of incidence cos φ = o.95, o.55, o.o5 and surface albedo A_s at o.55 μm wavelength and an optical depth $\tau_{0.55}$ = 32 corresponding to a cloud height of 2ooo m at a liquid water content of o.o6255 g m^{-3}.

In a next step the wavelength integration leads to the total heating rates in the solar part of the spectrum from o.3 to 2.5 μm wavelength taking into account molecular scattering, ozone and water vapour absorption above the cloud. The results displayed in fig 2 for the same cloud as in fig 1 and CCN/N = o.5 indicate the substantial contribution of absorbing aerosols as compared to the heating rates due to gaseous absorption within the cloud and the absorption by pure water droplets. The given heating rates in K /day only describe a possible change of a stable cloud. Under real conditions accounting for radiational effects means calculation of heating rates in time steps of minutes and changing the cloud parameters according to lapse rate changes introduced by the radiational heating.

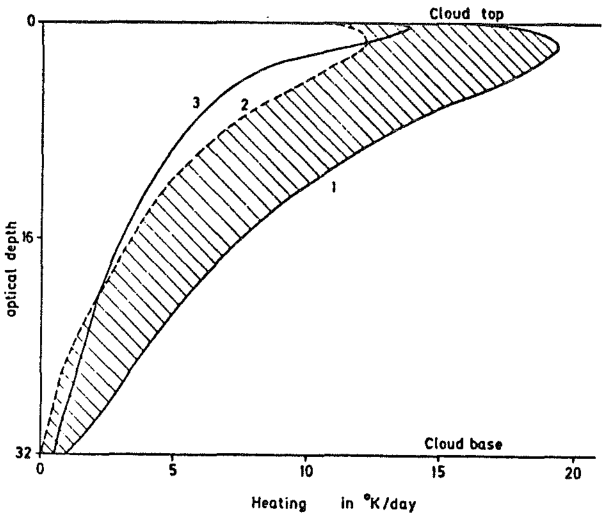

fig 2: Heating rates in a thick cloud with total optical depth $\tau_{0,55} = 32$ with (1) and without (2) absorbing aerosol particles for cos φ = 0.833 (φ = zenit angle of solar radiation) and cos φ = 0.5 (3). The water vapour amount above the cloud is 0.3 g cm^{-2}.

In a further step the cooling or heating due to the terrestrial radiation from 5 - 100 µm is included. From fig. 3 the strong cooling at the uppermost parts of the cloud dominates heating even at nearly vertical incidence (cos φ = 0.9). For very slant paths the heating strongly declines. For steep incidence of solar radiation big parts of a cloud will be warmed tending to dissolve the clouds. However in all existing cloud decks the infrared cooling near to the top causes buoyancy in coincidence to the observation.

A comparison to cloudfree regions with the same amount of particulate matter shows an increase in absorption in clouds at high solar elevation and a decrease at low solar elevation in agreement to TWOMEY (1972).

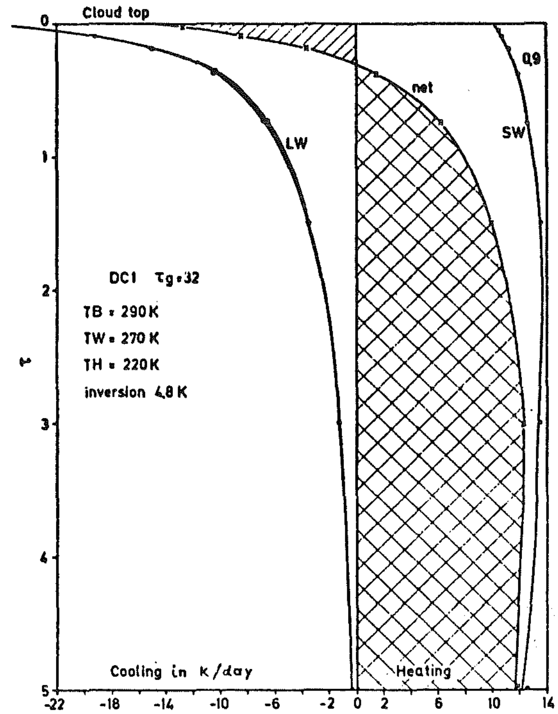

fig 3: Infrared cooling (LW) with and without a temperature inversion at the top, solar heating (SW) with cos φ = 0.9 and the net effect (net) for the upper part (0 - 5 optical depth) of the same cloud as in fig 2. Mean cloud temperature TW = 270 K, ground temperature TB = 290 K and clear sky emission temperature 220 K. Cloud layer from 2 - 4 km.

ALBEDO REDUCTION

All measurements of the albedo A_c of very thick clouds have shown $A_c \leq 0.8$. However A_c is close to 1.0 if the single scattering albedo of pure water is used. This discrepancy points to an additional absorber. Absorbing particulate matter inside cloud droplets (mainly soluble) and very small aerosol particles with water shells in cloud air can lead to a substantial reduction in cloud albedo. Results in table 2 show this reduction for 0.55 µm wavelength. If this reduction is caused by increasing absorption at stable particle numbers and cloud drop size distribution the planet earth would gain energy. This statement can not be confirmed, since additional absorption in polluted areas is accompanied by increasing particle numbers and change of chemical structure and therefore by variations of cloud droplet spectra which have a strong influence on cloud albedo. A judgement whether additional absorption accompanied by particle number increase and change in chemical composition leads to decreasing or increasing cloud albedo is not possible with the present knowledge.

Table 2: Albedo A_c of the same cloud as in fig 2 and 3 at 0.55 µm wavelength depending on angle of incident radiation and single scattering albedo ω_0 for two different surface albedo values A_s

$A_s = 0$

ω_0 \ $\cos\varphi$	0.95	0.55	0.15
1.000	0.730	0.804	0.888
0.999	0.690	0.769	0.865
0.998	0.655	0.739	0.845
0.996	0.596	0.687	0.809

$A_s = 0.8$

ω_0 \ $\cos\varphi$	0.95	0.55	0.15
1.000	0.860	0.899	0.943
0.999	0.786	0.839	0.905
0.998	0.727	0.791	0.874
0.996	0.639	0.718	0.827

REFERENCES

DEIRMENDJIAN, D., 1969: Electromagnetic scattering on spherical polydispersions. Elsevier New York

FISCHER, K., 1970: Measurement of absorption of visible radiation by aeorol particles. Contr.Atm.Phys. 43, 244

FISCHER, K., 1973: Mass absorption coefficient of natural aerosol particles in the 0.4-2.4 µm wavelength interval. Contr.Atm.Phys. 46, 89

GRASSL, H., 1975: Albedo reduction and heating of clouds by absorbing aerosol particles. Contr.Atm.Phys. 48, 199-210

HÄNEL, G., 1975: The properties of atmospheric aerosol particles as functions of the relative humidity at thermodynamic equilibrium with the surrounding moist air. Adv. in Geophysics 19, 73-188

LAUDE, L.S., LINDBERG, J.D., 1974: A Measurement of the absorption coefficient of atmospheric dust. Appl. Opt. 13, 1923-1927

MOSKALENKO, N. I. 1969: The spectral transmission function in the bands of the water vapour, O_3, N_2O, and N_2 atmospheric components. Izv. Atmosph. and Oceanic Phys. 5, 1179-1190

PLASS, G.N., KATTAWAR, G.E., CATCHINGS, G.E., 1973: Matrix Operator Theory of Radiative Transfer. Appl. Opt. 12, 314-329

TWOMEY, S., 1972: The effect of cloud scattering on the absorption of solar radiation by atmospheric dust. JAS 29, 1156-1159

WENDLING, P., 1976: private communication

4.4.3

NUMERICAL MODEL OF RADIATION FOG AND STRATUS FORMATION TAKING INTO ACCOUNT INTERACTIONS AMONG DYNAMICAL, RADIATIVE AND MICROPHYSICAL PROCESSES

M.V. Buikov and V.I. Khvorostianov

Ukrainian Hydrometeorological Research Institute

Kiev, U.S.S.R.

1. INTRODUCTION

The most important and interesting problems of theoretical cloud physics are those which permit to formulate the closed system of equations for all main cloud and atmospheric characteristics under minimal number of hypothesis and suggestions;such approach facilitates comparing theory with experimental data.For example to describe consistently the development of a cumulus it is necessary to take into account dynamical,thermodynamical and microphysical processes.The formation and evolution of radiation fog and stratus in the boundary layer of the atmosphere belongs to the same class of problems.Many papers are devoted to theory of radiation fog and stratus (Loushev,Matveev(1967),Feigelson (1970), Zdunkowski and Barr(1972),Zakharova (1975)),but size distribution of droplets was never calculated.In this paper the simulation of fog will be carried ont taking account for dynamics and thermodynamics of wet air,long-wave radiation transfer and evolution of droplet spectrum.

2. BASIC EQUATIONS

2.1 To describe the boundary layers dynamics are used the:equations of air motions;equation of the balance of turbulent kinetic energy;Kolmogorov's similarity relations connecting the turbulent diffusion coefficient k with the rate of the turbulent energy dissipation and the mixing-length;Laikhtman-Zilitinkevich's suggestion for mixing-length(Lykosov,Gutman(1970)).

2.2 To describe heat and water vapor transport processes the following equations for the temperature T and specific humidity q are used:

$$\frac{\partial T}{\partial t}-\frac{\partial}{\partial z}\kappa\left(\frac{\partial T}{\partial z}+\gamma_a\right)=\frac{L}{c_p}\mathcal{E}_c+M_{rad}\,; \qquad (1)$$

$$\frac{\partial q}{\partial t}-\frac{\partial}{\partial z}\kappa\frac{\partial q}{\partial z}=-\mathcal{E}_c\,. \qquad (2)$$

2.3 Fog microstructure can be found as the solution of kinetic equation for the droplet size distribution:

$$\frac{\partial f}{\partial t}-\frac{\partial}{\partial z}\kappa\frac{\partial f}{\partial z}-cr^2\frac{\partial f}{\partial z}=-\frac{\partial}{\partial r}(\dot{r}f), \qquad (3)$$

where c is Stokes' parameter.Droplet growth rate is defined by Maxwell's formula.

$$\mathcal{E}_c=4\pi\rho\int_0^\infty dr\,\dot{r}r^2f(r,z,t). \qquad (4)$$

2.4 The radiation transfer is described by the equations for up and down spectral fluxes.Computations are carried out for 32 wavelengths over 5,5÷35 μm which includes about 90% of infrared energy.Droplet water monochromatic absorbtion coefficient $\alpha_{\lambda L}$ can be evaluated as follows(Feigelson(1970)):

$$\alpha_{\lambda L}(z,t)=\rho_a\int_0^\infty dr\,\sigma_\lambda(r)f(r,z,t), \qquad (5)$$

where ρ_a is the air density.The absorbtion cross sections $\sigma_\lambda(r)$ are calculated using the exact Mie's expression and approximate Shifrin's formula(Buikov,Khvorostianov(1976)).

2.5 Wind,temperature,specific humidity are given, fog is absent at the initial moment of time.Boundary conditions for wind,turbulence,temperature,radiative fluxes are of usual type.The following boundary condition on the underlying surface for specific humidity is used:

$$-\kappa\frac{\partial q}{\partial z}=\frac{\alpha_{ef}\cdot\bar{v}}{4}(q-q_m), \qquad (6)$$

where v is heat velocity of vapor molecules, q_m is saturation humidity, α_{ef} - effective condensation coefficient which depends on soil properties.It was assumed that the activation and transformation into droplets of N_m condensation nuclei takes place when saturation is achieved on the given heigth.

The system of the equations formulated contains only three physical parameters(geostrophic wind G,the number of activated nuclei N_m ,condensation coefficient α_{ef})except of some number of material constants and initial values.

3. COMPUTATIONAL RESULTS

The system of equations formulated was solved with the purpose:1)to describe the formation and evolution of fog under typical atmosperic conditions; 2)to investigate the contributions of different processes to the energetics of fog;3)to find out the influence of the phase transition in the boundary layer on its dynamics;4) to establish the criteria of the transformation of fog into stratus and vice versa in the connection with soil characteristics;5)to investigate the droplet spectrum and radiation properties of fog.

3.1 Let us consider evolution of the boundary layer over the dry underlying surface (α_{ef} =0) with the following set of parameters,which will be called so far "the basic set":G=10m/s,q_{ro}=90%; T_o=10°C,N_m=0,5·$10^6$1/g.At the initial moment of time temperature is linearly decreasing with height,lapse rate is -0,6 deg/100m,k is increasing with height,achieves maximum value 11m/s on the level 90m and then falls.The boundary layer thikness,defined by the equality k to zero is 690m.

After 1,5h of development the condensation of vapor and the formation of fog beginsdue to radiative cooling. The cross section of fog is shown on Fig.1.

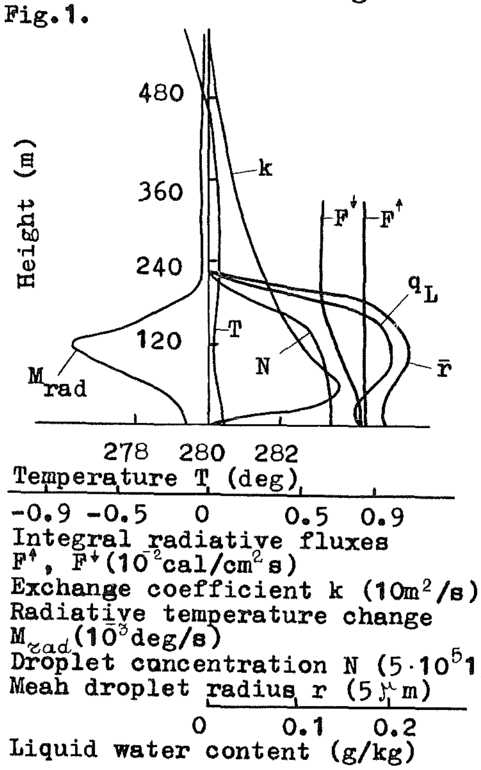

Figure 1. Dependence of boundary layer and fog characteristics on height at t=2h for the basic set of parameters:G=10m/s,N_m=0,5·10 1/g, T_o=10°C,q_{ro}=90%(the basic set of parameters)over dry soil

The thickness of the fog is 220m,radiative cooling maximum moved from the ground to the middle of the fog ($(\partial T/\partial t)_{rad}$=-2,52deg/h),the maximum value of L.W.C. is also at this height.The shift of radiative cooling upward and heating from the soil results in displacing of temperature inversion into the upper fog layers and in restoring of normal temperature fall near the ground.Maximum value of k is half as mush and it is now nearer to the ground.

3.2

Table 1.Contributions of different partial temperature rates of change(deg/h) to fog energetics

z,m	60	150	300	360
		t=2h		
$(\partial T/\partial t)_{turb}$	-0.108	-0,036		
$(\partial T/\partial t)_{rad}$	-0.7	-1,21		
$(\partial T/\partial t)_{cond}$	+0.36	+0,644		
$(\partial T/\partial t)_{tot}$	-0.448	-0,612		
$(T^{\delta+1}-T^{\delta})/\Delta t$	-0.432	-0,601		
		t=3h 40min		
$(\partial T/\partial t)_{turb}$	+2,06	+1.559	-0,265	-0,691
$(\partial T/\partial t)_{rad}$	-0,019	+0.01	-0,907	-2,04
$(\partial T/\partial t)_{cond}$	-1,71	-0.159	+0,835	+1,336
$(\partial T/\partial t)_{tot}$	-0,33	+1.39	-0,339	-1.395
$(T^{\delta+1}-T^{\delta})/\Delta t$	-0,295	+1.31	-0,336	-1,285

At t=2h there is an intensive radiative cooling near the upper boundary only one half of which is compensated by the phase transition heat.Turbulent transfer results in cooling too but it is small.At t=3h40min there is strong turbulent heating at low levels due to heat influx from the soil,about 83% of this influx is spent for drop evaporation.Radiative temperature rate of change is small(1% of turbulent one)because of the large optical path length inside the fog.In upper layers of the fog intensive condensation continues due to radiative cooling.

3.3 If soil is dry heating in lower layers may lead to the fog separation from the ground and its transformation into low stratus cloud.The cross-section of the cloud formed after fog separation from the ground at t=8h is shown in Fig. 2.Lower and upper cloud boundaries are correspondingly at the heights 90 and 670 m. The LWC maximum(0,5 g/kg) is near the upper boundary.The mean droplet radius is almost constant through all the cloud and is equal to 8 - 9μm.The radiative cooling peak and temperature invesion are in the upper layers.There is a slight radiative warming in the lower layers where lapse rate is greater than initial one.

It can be shown that for dry soil there is some critical value of geostrophic wind G_{cr} so that for $G < G_{cr}$ fog never turns into cloud,but always for $G > G_{cr}$. For the basic set of parameters G_{cr}=4m/s

The cloud formed over wet soil and characterized by the basic set of parameters spreads downward and join up

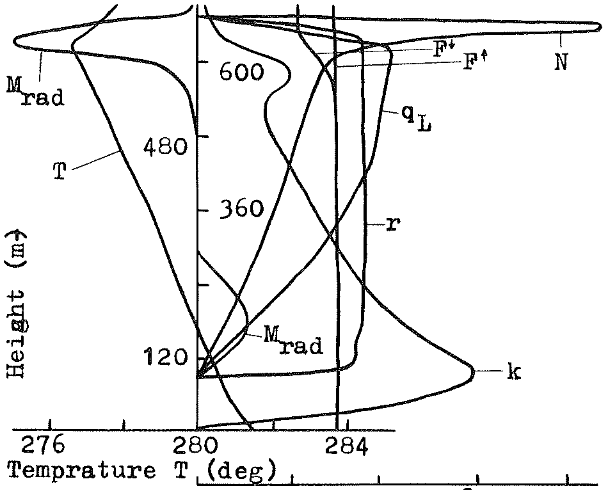

Liquid water content q_L (0,25 g/kg)
Droplet concentration N (10^5 1/g)
Integral radiative fluxes
$F^{\uparrow}$, $F^{\downarrow}$ ($0{,}5 \cdot 10^{-3}$ cal/cm^{2}s)
Exchange coefficient k (5 m^2/s)
Mean droplet radius r (5 μm)
Radiative temperature change M_{rad}
($0.5 \cdot 10^{-3}$ deg/s-warm., $0.5 \cdot 10^{-2}$ deg/s-cool.)

Figure 2. The same as in Fig. 1, t=8h

the haze which appeared near the ground But for G=20 m/s when turbulence is high enough and if soil heat conductivity coefficient is three times larger than for the basic set the cloud develops downward only slightly and does not turns into fog.

The variations of α_{ef} allow to describe all the types of soils from dry to wet.

3.4 Before the beginning of condensation the cross-isobar angle increases by one half from 20° to30° for the basis set of parameters due to damping of turbulent exchange. When fog or cloud reaches steady-state cross-isobar angle approaches the initial value but the wind velocity profile differs greatly from the initial one. At all moments of time rather thick layer exists where wind velocity exeeds geostrophic wind by 10-15%(low level jet). When fog is in steady-state the jet localizes at the fog top. The main rotation of the wind occurs just within the jet.

3.5 There are some differences in the mechanism of fog or cloud formation over dry and moist soils. The equation for the supersaturation $\Delta = q - q_m$ when the second derivatives on heihgt are neglected is as follows

$$\frac{\partial \Delta}{\partial t} = \frac{\partial}{\partial z} K \frac{\partial \Delta}{\partial z} - \gamma_a \frac{\partial q_m}{\partial T} \frac{\partial K}{\partial z} . \quad (7)$$

The second term of the right-side of(7) gives the maximum positive contribution in the region of decreasing of k. For dry soil when turbulent flux of vapor at the ground is equal to zero the maximum of humidity and radiative cooling are near the ground where condensation begins first of all. But for wet soil when the formation of dew is possible (turbulent flux of vapor is not equal to zero at the ground) the lowest layer of air becomes relativly more dry than the upper one and this leads to the first portion of fog in the region where $\partial K/\partial z < 0$ and it has the maximum value.

3.6 The time and space change of droplet size distribution can be found as the solution of the kinetic equation (3). Fig. 3 represents droplet size distribution function for the case of wet soil and the basic set of parameters.

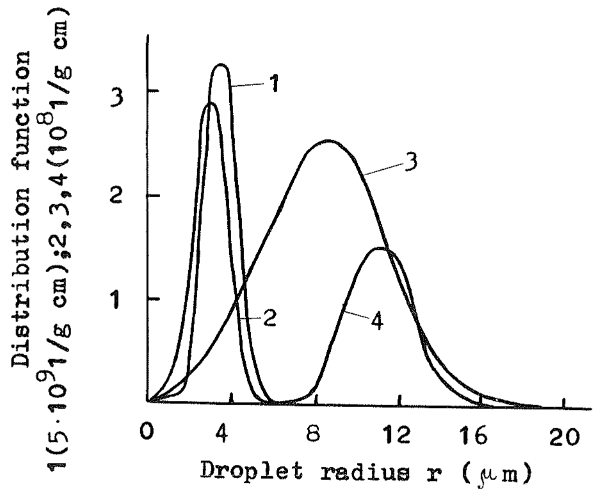

Figure 3. Droplet size distribution function in fog formed over wet soil for the basic set of parameters.
Curve 1 - t= 3h10min, z=150m, r=2.76 m
Curve 2 - t= 3h10min, z=0, n=26, r=3.57
Curve 3 - t= 10h, z=150m, n=7.9, r=8.5 m
Curve 4 - t=, 10h, z=780m, n=52, r=11.2 m
Where n is the parameter of γ-distribution.

The curves 1,2 are typical for a "young" cloud after 20 min of cloud development. The spectra are not broad and the mean droplet radius is small. In the main bulk of steady-state fog(curve 3) the spectrum grows broader, near the fog top it remains narrow, but the mean droplet radius increases. Almost all calculated droplet spectra may be approximated by γ-distributions.

3.7 The existence of sharp radiative cooling near the cloud or fog top is accounted for by the fact that the downward radiation flux in this layer approaches quickly the upward flux. This is demonstrated by Fig. 4 which represents the dependence of the spectral downward flux on height(dry soil, G=12 m/s, q_{r0}=0.8). The rate of change of the spectral downward flux is strong within the atmospheric window but very weak out of it. The radiative warming in the part of cloud is caused by the absence of radiative equilibrium in this layer: the radiative flux coming from the soil exeeds the black body flux at this level.

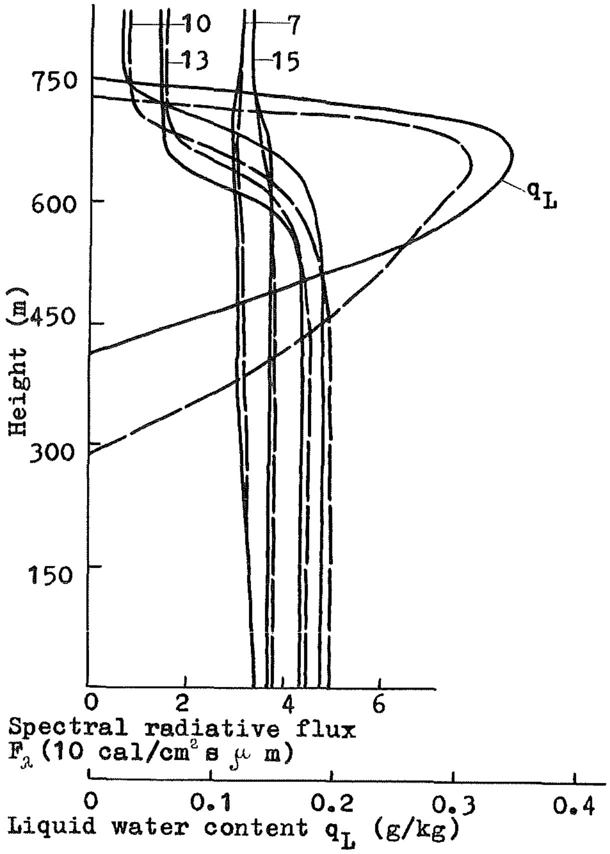

Figure 4. The radiative spectral fluxes calculated using the exact Mie's formula(solid lines) and the approximate Shifrin's formula for absorption cross-section(dashed lines).Numbers at the curves mean wavelengths in μm

The dependence of droplet water spectral absorption coefficient $\alpha_{\lambda L}$ for the calculated droplet size distribution on wavelength is strong for narrow spectra and it weakens when spectrum grows broader.The main part of radiative cooling is caused by the radiation transfer within the atmospheric window where the coefficient $\alpha_{\lambda L}$ varies slightly with time and wavelength and is approximately equal to 450--550 cm/g.

3.8 It should be noted that the characteristics of the theoretical cloud with the basic set of parameters are very similar to that of the statistically averaged experimental cloud described by Feigelson(1970).

Table 2

	Experimental	Calculated
Upper boundary,m	430	400
Lower boundary,m	830	760
Thickness,m	400	360
Maximum of LWC,g/kg	0.3	0.34
Maximum of radiative colling rate,deg/h	-3.55	-3.34
Maximum warming,deg/h	0.1-0.2	0.21

4. Conclusion

The simulation fog or cloud formation using more complete description than earlier(the main feature is the calculation of droplet spectrum and spectral radiation fluxes) allowed to obtain some theoretical results which can be verified by comparing with observations.It would be worthwhile to note that the experimental model of stratus cloud was obtained with no use of empirical information about cloud.The existence of the second maximum of turbulent exchange and the localization of low level jet near the top of steady-state cloud or fog are also in accordance with observations.It seems to be of some physical interest the time evolution of turbulent exchange and cross-isobar angle within boundary layer during fog formation. and the dependence of the conditions of turning fog into cloud or vice versa on geostrophic wind value and soil properties.Especially it is important to underline that the thick lower part of cloud exists during long time in unsaturated air.This result could not be obtained without detailed description cloud microstructure.

References

Buikov,M.V.,Pirnach,A.M.,1973:A numerical model of two-phase layered cloud taking into account its microstructure. Proc.(Izv.)Acad.Sci.USSR,Atm.Ocean Phys v.9,No 5,pp.486-499.

Buikov,M.V.,Khvorostianov,V.I.,1976: Numerical simulation of fog and stratus formation in the atmospheric boundary layer over dry underlying surface taking into account microphysical processes Trudy UkrNIGMI,No146.

Buikov,M.V.,Khvorostianov,V.I.,1976: Numerical simulation of radiation fog and stratus over wet underlying surface taking into account microstructure.Trudy UkrNIGMI,No152.

Feigelson,E.M.,1970:Radiative heat exchange and clouds.Hydromet.Press,Leningrad,p.231.

Loushev,Yu.G.,Matveev,L.T.,1967:The pecularities of the formation and structure of radiation fogs(a numerical experiment).Proc.(Izv.)Acad.Sci.USSR,Atm.Ocean Phys.,v.3,No5,pp.459-472.

Lykosov,V.N.,Gutman,L.N.,1970:A stationary problem of the turbulence in the planetary boundary layer of the earth. Proc.(Izv.) Acad.Sci. USSR,Atm.Ocean Phys.,v.6,No12,pp.1238-1254.

Zakharova,I.M.,1975:Numerical modelling of radiation fog formation and development.Trudy IEM,No9(52),pp.124-136.

Zdunkovski,W.G.,Barr,A.B.,1972:A radiative-conductive model for prediction of radiative fog.Boundary layer meteorogy,v.3,No2,pp.152-177.

4.4.5

REFLECTION OF HORIZONTALLY INHOMOGENEOUS CLOUDS

Peter Wendling

Meteorologisches Institut der
Universitaet Muenchen *

1. INTRODUCTION

The accurate determination of the radiation balance of the earth-atmosphere system requires detailed knowledge of the radiation reflected and emitted by clouds. All the efforts until now to include the radiative effects into the determination of the albedo of the earth-atmosphere system have been limited to the effects of plane parallel cloud layers. Real clouds, however, are often formed by convection and show irregular surfaces or occur in discrete cloud cells.

In this study calculations of the albedo and reflected radiance of clouds with horizontal inhomogeneities are presented. The Monte Carlo method has been applied to clouds with a periodic horizontal structure of the type first discussed by Van Blerkom (1971). Two different anisotropic scattering functions have been employed based on aircraft measurements of cloud drop size distributions.

2. COMPUTATION METHOD AND CLOUD MODEL

As to the author's knowledge, the Monte Carlo method is best applicable to the radiative transfer of clouds with arbitrary shape. The application of the Monte Carlo method for solving radiative transfer problems has been described in detail by Collins and Wells (1965) and by House and Avery (1969). Following this method, the radiation transfer calculations are mainly a computer simulation of the radiative transfer processes which are based upon the physical laws of interaction between photons and a prescribed medium. The photons are followed until they escape from the medium, desired quantities as the direction and the state of polarization being recorded.

The assumed cloud model is shown in Fig. 1. The cloud shows a regular pattern of striations in the surface running from $y=-\infty$ to $y=+\infty$. The length of one period of striations is $\Delta x_1 + \Delta x_2$.

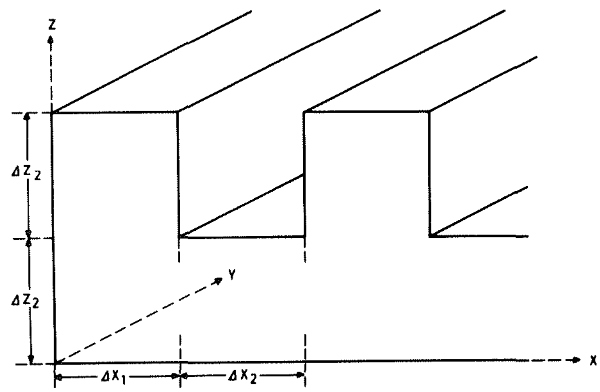

Fig.1 Cloud model

Because of the structural regularity, the transfer of radiation of the cloud as a whole can be determined by following photons through only one period of the striations, so for example, a photon striking the boundary $x=\Delta x_1 + \Delta x_2$ is replaced by a photon entering at $x=0$ with the same direction. Two different cloud drop size distributions as measured by Diem (1942) and Pedersen and Todsen (1960) are used. The two distributions are quite different both in the absolute number of drops per cm^3 and in the position of their maximum. Both distributions have been normalized to a liquid water content of 0.1 g/m^3. All calculations have been done for a wavelength of 0.55 μm. By applying classical Mie theory for the scattering on water drops the scattering functions are calculated for both size distributions. The size distribution of Diem has more large particles which results in an increased forward scattering compared to the size distribution of Pedersen as is indicated in Fig. 2. The computations have been done for three types of striated clouds called in the following A, B, and C and which have, when averaged over one period of the striations, all the same optical thickness equal to 3/4 of the optical thickness of the plane parallel cloud. The thickness of the full plane parallel cloud is assumed to be 1 km. The striated cloud is illuminated by the sun in the (x-z)-plane.

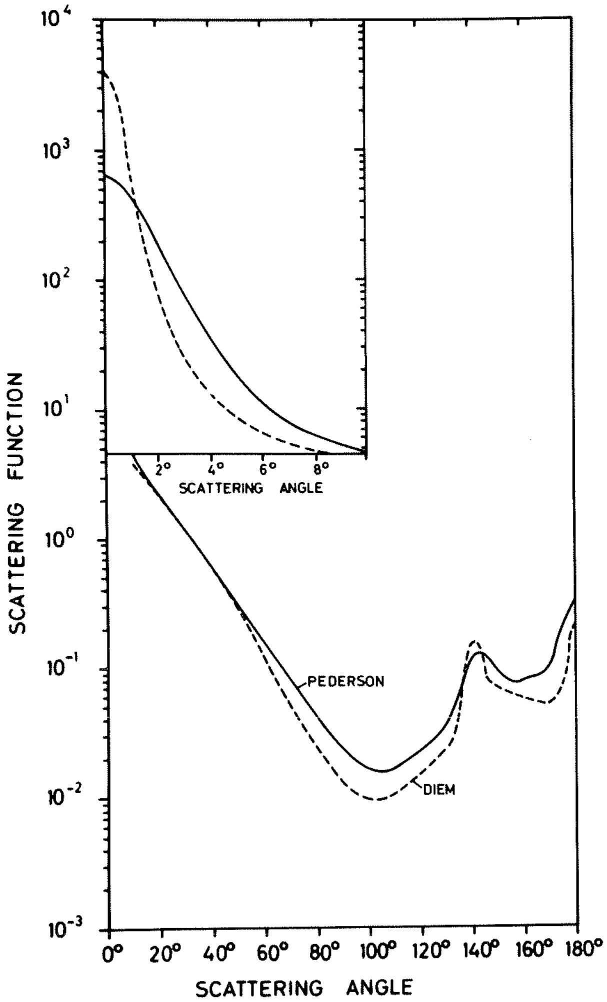

Fig. 2 Scattering functions for the two size distributions

Albedo of striated clouds with different column heights and widths but constant mean optical thickness (period of striations = 1 km, droplet spectrum: PEDERSEN, σ_E = 20.5 km^{-1})

sun zenith angle	cloud albedo			
	striated cloud type A	striated cloud type B	striated cloud type C	plane parallel cloud ΔZ = 0.75 km
μ_o = -1.0	0.519	0.488	0.445	0.562
μ_o = -0.7	0.646	0.647	0.637	0.646
cloud type				

Table I Albedo of striated clouds with different column heights and widths but constant mean optical thickness (period of striations = 1 km, droplet spectrum: Pedersen, σ_E= 20.5 km^{-1})

3. RESULTS AND DISCUSSION

The results for the cloud albedo as function of the zenith angle of the sun and of the type of striation are shown in Table I. At a first look one might think that the cloud with the smallest width of the striations has the highest albedo. But as the average optical thickness remains constant this cloud type has the deepest striations. That means the striations act as a light trap, photons going downward very easily penetrate the remaining thickness and are lost for reflection. Photons going upwards must move within a very narrow angular cone so as to be able to leave the striations without any further collisions. This is not the case for the clouds of type A and B. The differences between the striated clouds and the plane parallel cloud of the same mean optical thickness get larger when the zenith angle of the sun decreases. The differences reach up to 20% for the cloud of type C, the accuracy of the Monte Carlo results being better than 0.5%.

What happens when the drop size distribution is changed is shown in Table II. Considering only a striated cloud of type A, the calculations have been done for two optical thicknesses given in terms of the extinction coefficient σ_E. The cloud with a drop size distribution according to Diem shows always a lower albedo because of the enhanced forward scattering compared to the Pedersen distribution. The differences decrease with increasing optical thickness which means that we have more scattering events and thus differences in the scattering functions are smeared out. If we consider only the cloud with an extinction coefficient of σ_E= 20.5 km^{-1} and a sun zenith angle of μ_o = -1.0 we get differences in the albedo by changing the scattering function in the same order as if we would change the cloud surface structure from type A nearly to type B.

Albedo of striated clouds (type A) as function of droplet spectrum and optical thickness

sun zenith angle	cloud albedo	
	σ_E = 7.8 km^{-1}	
	droplet spectrum: PEDERSEN	droplet spectrum: DIEM
μ_o = - 1.0	0.281	0.236
μ_o = - 0.2	0.671	0.649
	σ_E = 20.5 km^{-1}	
μ_o = -1.0	0.519	0.471
μ_o = -0.2	0.808	0.790

Table II Albedo of striated clouds (type A) as function of droplet spectrum and optical thickness (period of striations = 1km)

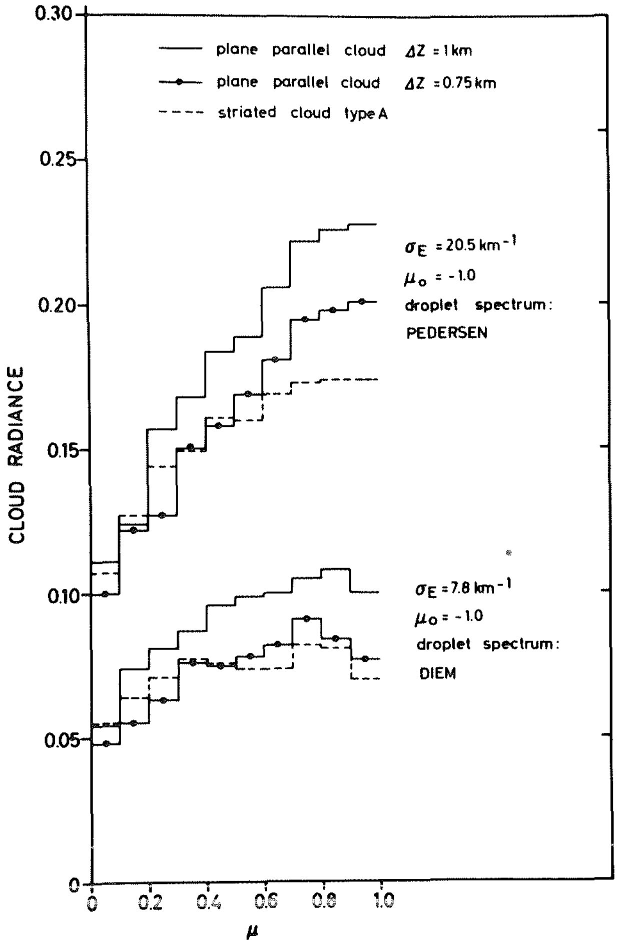

Fig. 3 Cloud radiance as function of zenith angle

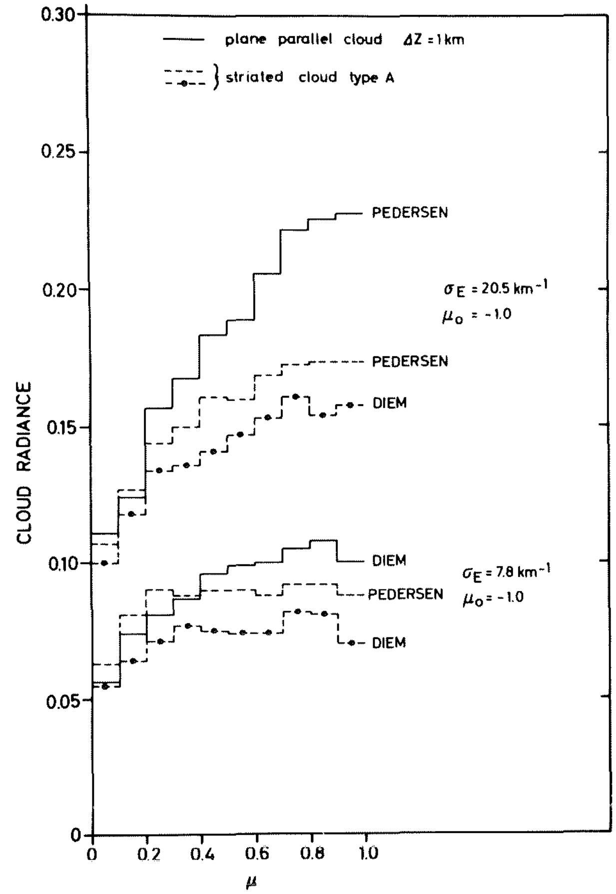

Fig. 4 Cloud radiance as function of zenith angle

Nearly all radiation measurements from satellites are basically radiance measurements. It is therefore important to know how cloud radiance measurements are influenced by cloud surface structures. The largest differences between the reflected radiance of a striated cloud and that of a plane parallel cloud of the same mean optical thickness occur for a vertically incident sun and for the emerging radiance in the zenith as is shown in Fig. 3. The reflected radiances fall off to a minimum near the horizon where the effect of the striations nearly disappears. As can be seen in the lower part of Fig. 3, the reflected radiance of a striated cloud of low optical thickness may be well represented by that of a plane parallel cloud of the same mean optical thickness. With increasing optical thickness this approximation fails, especially for the vertically emerging radiance (upper part of Fig. 3).

Changing the cloud drop size distribution shows differences in the reflected radiances which are of the same order as if the cloud surface structure would be changed. This shows a comparison between the results of Fig. 4 and Fig. 5. As shows Fig. 5, the radiances reflected by a striated cloud of type C have always smaller values than those reflected by striated clouds of type A and B. This is due to the deepness of the striations of type C which causes many photons to be lost for reflection.

4. CONCLUSION

The Monte Carlo method has been applied to the transfer of solar radiation through clouds with horizontal inhomogeneities. The inhomogeneities are represented by horizontally periodic striations in the surface of the cloud. At a wavelength of 0.55 μm, the albedo and reflected cloud radiance are calculated for two different drop size distributions as function of optical thickness, solar geometry, and type of striation. The comparison between the radiative effects of striated clouds and clouds of the same mean optical thickness indicates that the albedo of clouds with

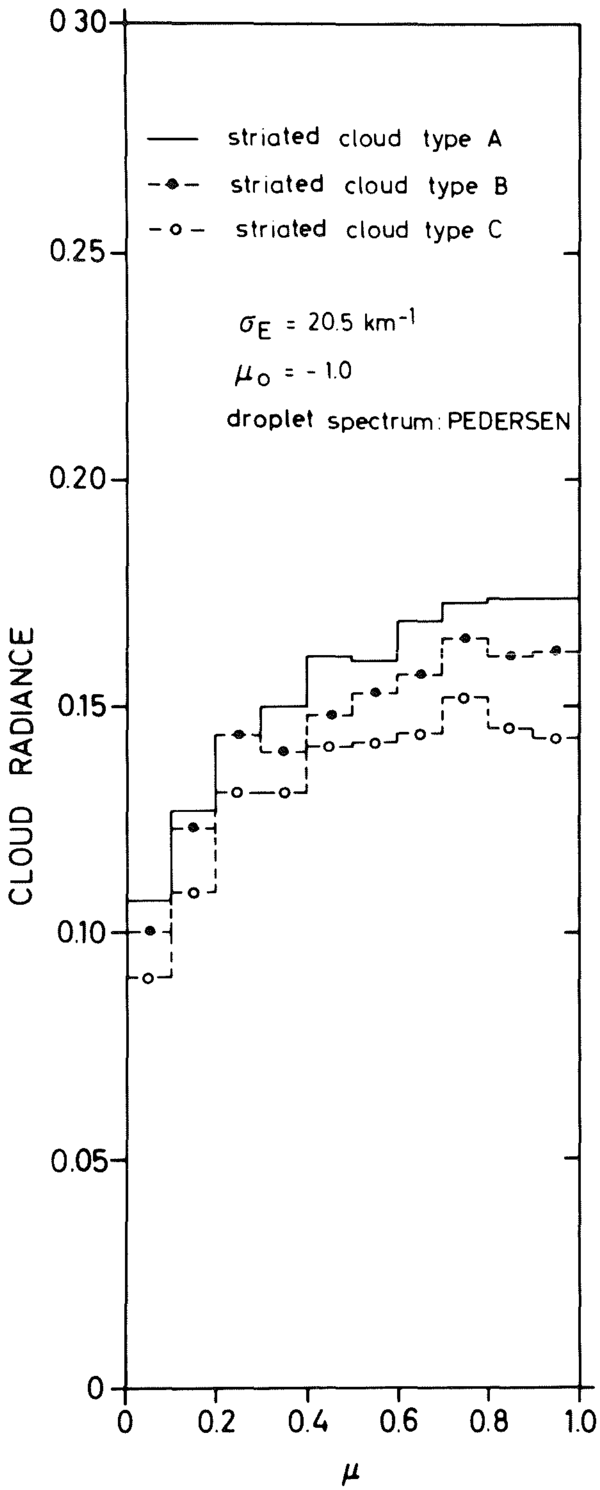

Fig. 5 Cloud radiance as function of zenith angle

horizontal inhomogeneities is always lower than the albedo of the plane parallel cloud with the same mean optical thickness. This plane parallel cloud is only a good approximation for the cloud albedo when the striations are not too deep. With regard to the cloud albedo, the effect of changing the cloud drop size distribution can be of the same magnitude as the effect caused by changing the cloud surface structure, the mean optical thickness remaining constant. The reflected cloud radiance is well approximated by that reflected of the plane parallel cloud of the mean optical thickness only in the case of low optical thickness.

REFERENCES

Collins, D.G. and M.B. Wells. Radiation Research Associates, Inc. Report ECOM-00240-F, August (1965).

Diem, M. Annln. Hydogr. Berl., 70, 142. (1942).

House, L.L. and L.W. Avery. J. Quant. Spectrosc. Transfer, 9, 1579 (1969).

Pedersen, K. and M. Todsen. Geophysica Norvegica, 21, 1 (1960).

Van Blerkom, D.J. Astrophys. J., 166,235 (1971).

*present affiliation: NOAA, Environmental Research Laboratories, Atmospheric Physics and Chemistry Laboratory Boulder, Colorado as a Research Associate of the Cooperative Institute of Research in Environmental Sciences (CIRES).

MICROPHYSICS OF POST SANTA ANA FOGS

J. G. Hudson and P. Squires

Desert Research Institute
University of Nevada System
Reno, Nevada

1. INTRODUCTION

Sea fogs are usually divided into two main types - steam fogs, in which relatively cold air is being rapidly heated and moistened in contact with warmer water, and advection fogs, which occur over relatively cool waters. The former type was studied by Saunders (1964), near Cape Cod, and indeed is more or less characteristic of the east coasts of continents in mid-latitudes. Off west coasts, advection fog is the common type.

Near the southern California coast, it is possible to recognize two major fog types, one of which occurs characteristically in winter, and the other in summer. In both, warm dry air overlies a shallow "marine" layer, which is both cooler and moister. The marine layer, trapped below the inversion, sometimes contains cloud, and sometimes fog.

The synoptic situations which give rise to these conditions are, however, quite different. In winter, the stage is set when an easterly Santa Ana flow occurs over southern California which transports dry, warm continental air out over the relatively cool coastal waters. The lowest layers are rapidly cooled and moistened, so that a strong inversion is formed at a low elevation. Leipper (1948) has described this sequence of events, and how subsequently with clear skies and dry air aloft, radiative cooling can result in the trapped marine layer becoming even cooler than the sea below, and eventually, in the formation of fog. When the easterly flow weakens and reverses, the fog filled layer moves inshore and arrives at the coast as a shallow, but optically dense, fog. The whole cycle of events characteristically occurs over a period of the order of five days.

In summer, the low level flow over the eastern Pacific is dominated by the strong and persistent North Pacific subtropical high, centered in July at about 150° W, 38° N. Over the coastal waters, a persistent north to northwesterly flow moves southward to the tropics where it turns eastward and forms the roots of the northeast trade. A strong subsidence inversion exists at elevations of a few hundred meters near the coast, sloping upwards towards the west. Below this inversion, a "marine" layer is found, which is frequently capped by an extensive sheet of strato-cumulus. In areas where the inversion is particularly low, the cloud base sometimes lowers to the sea surface, resulting in fog.

2. THE MICROSTRUCTURE OF MARINE FOGS

A. Fogs in General

Fogs, in general, vary greatly in their microstructure; for example, in the polluted air of a city, their droplet concentrations and optical density can be relatively quite high. Pilié (1969) has given a table of typical fog properties, distinguishing between inland radiation fogs and coastal advection fogs, as follows:

TABLE 1

Typical Fog Properties (from Pilié)

Fog Parameter	Inland Radiation	Coastal Advection
$\bar{d}$ (μm)	10	20
Range of d (μm)	5-35	7-65
w (g m^{-3})	0.11	0.17
n (cm^{-3})	200	40
Vis (m)	100	300

The contrast in microstructure shown above was attributed by Pilié to the difference between the inland and coastal aerosols.

B. Summer Fogs off California

The summer fogs off the west coast are a relatively homogeneous group, forming as they do in unmodified maritime air. From a series of measurements on these fogs, Mack et al. (1974) give the following mean properties of fogs at sea, at an elevation of 3 m: $\bar{r}$ = 6.5 to 9.3 μm, $\bar{n}$ = 5 to 29 cm^{-3}, $\bar{w}$ = 0.04 g m^{-3}, $\bar{V}$ = 300 to 1000 m.

C. Winter (Post-Santa Ana) Fogs off California

Because of the continental origin of the air in which these fogs form, it might be expected that their microstructure would differ from that of summer fogs; in the clear weather situations accompanying and following a Santa Ana event, the major mechanism of atmospheric scavenging (precipitation) is absent. Over periods of a few days, particle fall-out and Brownian diffusion to the sea surface are likely to have only a small effect on the aerosol spectrum in the newly formed marine layer. The depletion of the continental aerosol to the concentrations typically found over the sea may therefore proceed quite slowly. In these situations it would be expected that this depletion would require a longer period than the three days which Twomey and Wojciechowski (1969) found to be a characteristic transition time. An additional clue pointing in the same direction is given by the fact that the visibility in wintertime fogs is distinctly less than in summer fogs.

3. INITIAL FOG DROP MEASUREMENTS

Some measurements of marine fog microstructure were therefore made on the coast at San Diego in December 1974, using an optical particle counter (Royco Model 225 main frame with a Model 241 optical bench, equipped with a Model 508 counting module), which yielded the cumulative count of droplets with diameters larger than five threshold values. These measurements indicated that these wintertime post Santa Ana fogs contained about 10^3 cm^{-3} droplets larger than $r = 0.3$ μ m, of which about 1% were larger than $r = 4$ μm. These spectra were used to compute visibility, which agreed fairly well with the values recorded by a nearby M.R.I. Visiometer. Because of this agreement, and because the measured spectra implied plausible liquid water contents ($\sim$ 0.1 g m^{-3}), it was felt that these results had not been too seriously affected by the calibration problems of the optical counter, impaction and splashing of droplets in the intake, or evaporation of droplets. Measurements of such high fog droplet concentrations have also been made by May (1961).

Such high drop concentrations pointed to one of two conclusions, 1) relatively high supersaturations in the fog, or 2) very high CCN concentrations.

4. CCN MEASUREMENTS

To resolve this dilemma CCN measurements were made at the San Diego site during November and December of 1975. Data were collected on 15 days during the six week period. The CCN counter or counters ran continuously when they operated which was often for more than 24 hours at a time. Several post Santa Ana fogs occurred while these CCN concentration measurements were made. The concentration of CCN active at 0.14% supersaturation (that is those with critical supersaturations, S_c, less than 0.14%) was almost never less than 800 cm^{-3}. Sometimes these concentrations were as high as 4000 cm^{-2} but they were usually about 2000 cm^{-3}.

Very low CCN concentrations which approached that of a marine aerosol ($\lesssim$ 200 cm^{-3} for $S_c \lesssim$ 0.14%) were recorded on only one occasion. This occurred several hours after a rather strong front passed through the area. This low concentration was not reached until there had been at least 18 hours of rather strong westerly winds and a few hours of moderately heavy rain. On several other occasions there was considerable cloudiness and even precipitation which did not have much effect on the CCN concentrations. Fog occurrences also had little effect on CCN concentrations. In fact, the CCN concentrations were perhaps a bit higher than usual during periods when fogs occurred. Measurements of persistently high CCN concentrations, especially when measured in fogs, made it clear that it is the high CCN concentrations and not high supersaturations which are responsible for the high drop concentrations in wintertime southern California fogs. These CCN measurements and the measurements of drop concentrations in the fog also made it clear that, as is usually thought to be the case with most fogs, only those nuclei with very low critical supersaturations, S_c, are important in the formation of post Santa Ana fogs.

5. MEASURING CCN WITH VERY LOW S_c's

Horizontal plate thermal diffusion cloud chambers cannot accurately measure CCN below 0.2% supersaturation (Twomey, 1967; Sinnarwalla and Alofs, 1973; Hudson and Squires, 1976). Vertical plate thermal gradient diffusion cloud chambers (Sinnarwalla and Alofs, 1973; Hudson and Squires, 1976) can accurately measure CCN at supersaturations as low as 0.1%. Laktionov (1972) presented a method of extending the range of useful measurements below 0.1% supersaturation by using the equilibrium haze droplet size at zero supersaturation, S, to determine the S_c of the CCN. This method has been usefully analyzed by Podzimek and Alofs (1974) and experimentally demonstrated in another paper in these proceedings (Hudson, 1976). The success in matching the Laktionov method (using an isothermal diffusion chamber) with a vertical plate diffusion chamber in the supersaturation range between 0.1% and 0.2% has given some confidence in applying the method to lower values of S_c. As was shown in Hudson (1976) the haze droplets must be allowed sufficient time to grow to their equilibrium size at $S = 0$. However, they must not be allowed so much time that they fall to the floor of the cloud chamber or evaporate in moving from the cloud chamber to the optical counter. Again the existence of a plateau in droplet concentration when plotted against the rate of flow, F, of air through the cloud chamber should indicate that these problems do not exist. Figure 1 demonstrates that such a plateau can be obtained in the isothermal chamber for droplets which correspond to S_c's as low as 0.03%. This figure also illustrates the fact that these larger droplets require longer growth times to achieve their equilibrium sizes. The manufacturer's calibration curve must be used to determine drop sizes for S_c's below 0.1%, but the results of the test of Laktionov's method (Hudson, 1976) offer justification for doing this.

Figure 2 shows some typical spectra which were obtained with the Laktionov technique and with the thermal gradient diffusion chamber. In each curve the two measurements below 0.1% supersaturation were taken simultaneously with one of those taken above 0.1%. The other measurements were taken at points very close in time. The logarithmic slope of the curve, K (from $N = CS_c^K$ where N is CCN concentration and C is the concen-

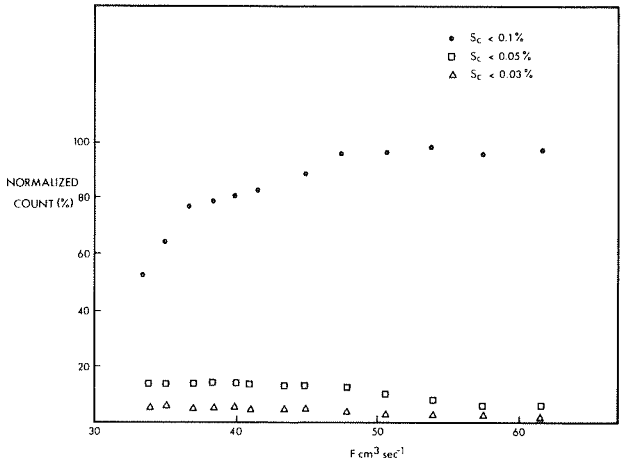

Figure 1. The concentration of drops greater than particular threshold sizes in the isothermal chamber normalized to the concentration of CCN active at 0.1% in the other cloud chamber operating at 0.1%. These threshold sizes correspond to the maximum critical supersaturation of the CCN given in the figure. The relationship between the droplet radius, r_o, at supersaturation, S, equal to 0, and S_c is $r_o = 4.1x10^{-6}/S_c$ (Hudson, 1976).

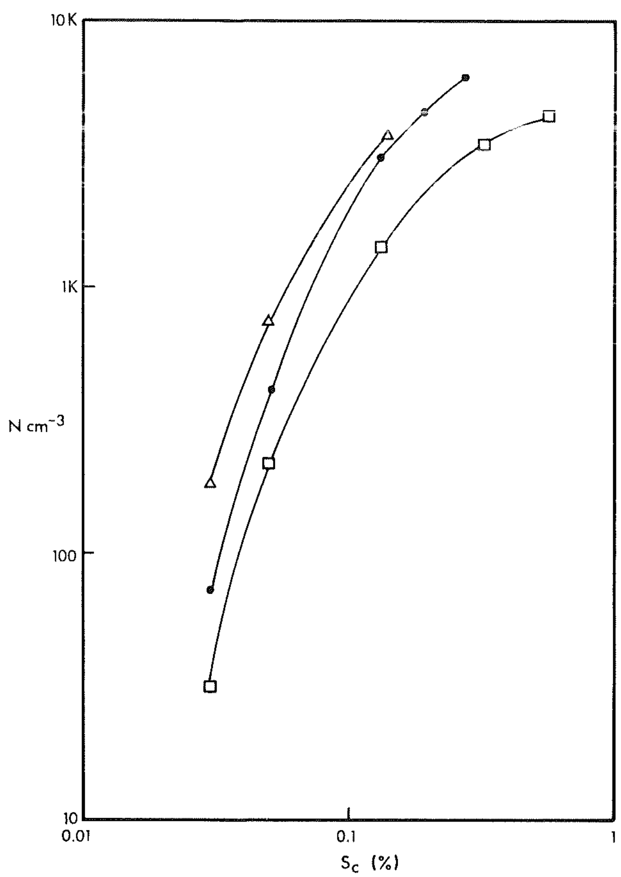

Figure 2. Typical CCN spectra taken at San Diego in December, 1975.

tration at 1% supersaturation), increases with decreasing S_c to a value of about 2 at the lowest supersaturations. The shapes of these curves are very much in keeping with CCN spectra measured at other sites with the same apparatus. Numerous CCN spectra above 0.2% supersaturation were measured with the same apparatus at an unpolluted continental site (Fallon, Nevada) from August to October of 1975. The values of K in the region of overlap (0.2% to 1%) were very similar at the two sites ($k \sim 0.4$). Also, the ratio of the Aitken concentrations, measured at both sites with the same Gardener Counter, to the CCN concentrations was very similar at the two sites. Even though the concentrations were several times higher at San Diego ($N \approx 400$ for $S_c = 0.2\%$ and $N \approx 1000$ for $S_c = 1.0\%$ at Fallon) the above facts indicate that this polluted aerosol has aged to a near equilibrium size distribution. This would imply that these CCN measurements are a good representation of the ambient aerosol in the region and are not due to local pollution effects which often tend to produce an aerosol with a very high K. Incidentally there were no large scale pollution sources within several kilometers of the site as it is located on a peninsula which is made up of a naval research base and a residential area. Figure 3 shows an example of CCN concentrations at three supersaturations measured over several hours. As this figure indicates, there did not seem to be much of a diurnal trend to the CCN concentrations. The facts presented in this paragraph and in section four seem to be in keeping with the theory of the formation of post Santa Ana fogs presented in section one. In particular, it seems quite possible that the aerosol is carried out to sea for great distances (of order 100 Km).

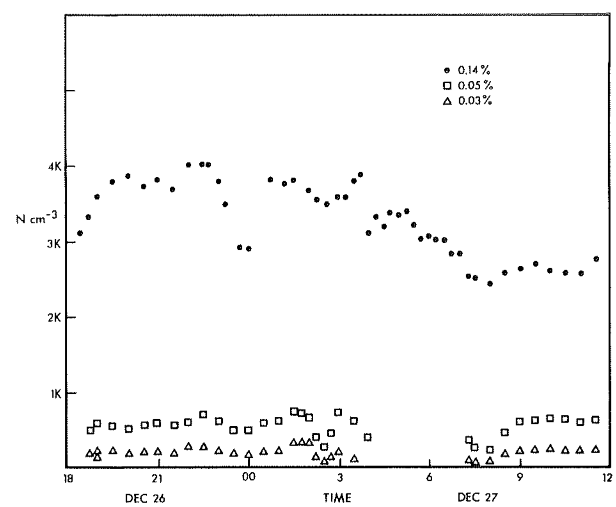

Figure 3. CCN concentrations at three supersaturations using the isothermal chamber and a cloud chamber operating at 0.14% at the San Diego site. This figure shows temporal variation with Pacific Standard Time. Dense fog occurred from 22:00 until 22:15 and for most of the period between 1:30 and 8:00.

6. FURTHER DROP MEASUREMENTS

Again in 1975 extremely high drop concentrations were recorded in post Santa Ana fogs at San Diego. Before the second fog season the optical counter was modified to collect counts for six second intervals instead of one minute intervals. This allowed a complete simultaneous readout in all five size channels even in the most dense fogs. This had not been possible during the previous season because the capacity of some of the channels was exceeded. The improved data revealed that the drop concentration was sometimes near or beyond the acceptable count rate of the optical counter. Concentrations above 1000 cm^{-3} actually "saturated" the optics and/or electronics. This fact in no way negated the very high drop concentrations in the fog since it means that the actual concentrations may have been even higher than that which could be measured. It is now clear that either a smaller sample flow or a dilution technique must be used in the unusually dense fogs. It should be made clear that many less dense fogs were measured which had drop concentrations which were definitely within the capabilities of the optical counter. In fact, some concentrations measured in fog were an order of magnitude lower than in the very dense fogs.

Visibility can be calculated using Koschmieder's formula

$$V = \frac{3.91}{\sigma}$$

where $\sigma = \sum_i K_s N_i \; 2 \; \pi r_i^2$ where N is drop concentration, r is drop radius, and K_s is the total scattering coefficient which depends on the ratio of the drop radius to the wavelength of the light. When the visibility is calculated using measured drop size distributions it shows very good agreement with simultaneous measurements of visibility using an M.R.I. visiometer. The two methods agreed to within 50% over a range of visibilities between 150 meters and 1000 meters. Although this may be fortuitous the essential point is that the concentration of small drops (< 5μ m radius) was so high that they alone could reduce the visibility below a kilometer.

7. DISCUSSION

The very high CCN concentrations and the very high concentrations of small drops suggest the possibility that unactivated haze droplets are responsible for much of the visibility degradation. In fact, if the aerosol is exposed to 100% relative humidity, R.H., (S = 0) and equilibrium haze droplets grow on all of the CCN then their sizes would be

$$r_o \, (S=0) = \frac{4.1 \times 10^{-6}}{S_c} \quad \text{(Hudson, 1976).}$$

A drop size distribution based on the above equation and actual CCN measurements at the time of fog occurrences shows a remarkable similarity in shape and magnitude to the actual drop size distributions which were measured in fogs. Put another way, the drop distributions and concentrations in the isothermal cloud chamber using ambient aerosol were very similar to the drop distributions and concentrations which were measured in the fog. The cloud chambers were mounted inside a trailer which was at least 10°C warmer than the outside during all fog occurrences. Since the aerosol spent several seconds in tubing inside the trailer before entering the saturated volume of the cloud chamber, all drops or droplets had plenty of time to evaporate down to nearly dry particles before droplets were artificially grown on them in the cloud chamber. The fact that the aerosol showed no noticeable change in concentration with the onset of fog further substantiates that the "fog" was completely reformed in the cloud chamber. Furthermore, visibility calculations based on distributions of droplets at S = 0 for the measured CCN concentrations shows good agreement with the M.R.I. visiometer. Thus ambient CCN concentrations seem to be capable of producing visibilities of less than one kilometer (<200 meters in some cases) when haze drops in equilibrium at S = 0 grow on them. However, even the highest CCN concentrations can not produce a visibility of less than 2Km (assuming that the nuclei behave like NaCl) if the R.H. reaches only 99%. Visibility calculations for 100% R.H. applied to a typical marine aerosol (Twomey and Wojciechowski, 1969) yielded a visibility of about 8 Km. This is, in fact, probably an underestimate of this visibility because the CCN concentrations had to be extrapolated for S_c's below 0.2%. For the purposes of this calculation a straight line extrapolation on the log-log plot of N vs. S_c was used but as section four and figure three indicate, this is probably an overestimate of CCN concentrations at low S_c's. Visibility calculations based on a natural continental aerosol were not attempted because of the uncertainty of extrapolating concentrations to low S_c's. Since measurements of the natural continental CCN concentrations below 0.2% are not available, and since these corresponding larger haze droplets are so important in determining the visibility, it is not proper to make such conjectures. It is possible, though very improbably, that the natural continental concentrations of CCN below 0.1% are nearly the same as those which were measured at San Diego. If this were the case then the fog visibilities would not differ by a great deal in the two cases.

8. CONCLUSIONS

Low visibility fogs near the southern California coast in winter do indeed seem to be made up of very high concentrations of very small drops. These numerous small drops seem to account for the low visibilities in these particular fogs. The observed drop distributions seem to be due to very high CCN concentrations which are an order of magnitude higher than a marine aerosol and several times higher than a natural continental aerosol. Extensive CCN measurements indicate that this aerosol is persistent, well-aged, and probably widespread. This seems to support the hypothesis that continental aerosol (and probably polluted aerosol) can affect fog visibilities for some distance out to sea.

The CCN concentrations, in fact, seem to be so high that a relative humidity of 100% ($S = 0$) is sufficient to produce a drop size distribution which yields visibilities which are characteristic of fog ($V < 1000$ meters). In fact the analysis implies that even very low visibilities ($V < 200$ meters) can occur in what is technically a haze (R.H. $\leq$ 100%) rather than a fog ($S > 0$). This is not to say that these fogs are not supersaturated. However, even when slightly supersaturated the unactivated haze droplets still make a major contribution to visibility reduction. Certainly some "fogs" ($V < 1$ Km) do form in unsaturated air when there are so many CCN and in some cases the visibility cannot get much worse than it is at saturation. The analysis shows that the relative humidity must be well above 99% and close to 100% in the most polluted air to produce a "fog" if the nuclei are in equilibrium. It could very well be that stratus clouds sometimes exhibit some of the phenomena which have been described in this paper.

9. ACKNOWLEDGEMENTS

This research was supported by the Office of Naval Research under contract N-00014-75-C-0527 using equipment which was obtained with funds from the National Science Foundation under grant DES-73-0631. The cloud chambers were constructed and along with associated equipment were installed in the field trailer by Mr. Robert Laird. The authors would like to thank Jurgen Richter, V.R. Noonkester, and Doug Jensen of the Naval Electronics Laboratory Center in San Diego for supplying the visiometer data and other meteorological data which was useful for the analysis. We would also like to thank them for their cooperation in getting our trailer located and for their cooperation, suggestions and help in carrying out this research. We would also like to thank the naval weather forecasters at North Island for help in planning for the measurements.

10. REFERENCES

Hudson, J.G. and P. Squires, 1976: An improved continuous flow diffusion cloud chamber. J. Appl. Meteorl., submitted August, 1975.

Hudson, J.G., 1976: A CCN spectrometer. International Cloud Physics Conference Proceedings, Boulder, Colorado, July 1976 (this volume).

Laktionov, A.G., 1972: Isothermal method for the determination of cloud condensation nuclei concentration. Izv. Akad. Nauk. S.S.S.R., Fiz. Atmos. Okeana, 8, 672-677.

Leipper, D.F., 1948: Fog development at San Diego, California. Journal of Marine Research, 7, 337-346.

Mack, E.J., V. Katz, C.W. Rogers, and R.J. Pilié, 1974: The microstructure of California coastal stratus and fog at sea. Calspan Report No. CH-5404-M-1, Calspan Corp., Buffalo, New York.

May, K.R., 1961: Fog-droplet sampling using a modified impactor technique. Quart. J. Roy. Meteorl. Soc., 87, 535-548.

Pilié, F.J., 1969: A review of project fog drops "Progress of NASA Research on Warm Fog Properties and Modification Concepts", NASA, SP-212.

Podzimek, J. and D.J. Alofs, 1974: A review of Laktionov's isothermal cloud nucleus counter. J. Appl. Meteorl., 13, 511-512.

Saunders, P.M., 1964: Sea smoke and steam fog. Q.J. Roy Met. Soc., 90, 156-165.

Sinnarwalla, A.M. and D.J. Alofs, 1973: A cloud nucleus counter with long available growth time. J. Appl. Meteorl., 12, 831-835.

Twomey, S., 1959: The nuclei of natural cloud formation - Part II. Geofisica pura e applicata, 43, 243-249.

Twomey, S., 1967: Remarks on the photographic counting of cloud nuclei. J. Rech. Atmos., 3, 85-90.

Twomey, S., and T.A. Wojciechowski, 1969: Observations of the geophysical variation of cloud nuclei. J.A. Sci., 26, 684-688.

5.1.1

SOME RESULTS FROM A SKYLAB CLOUD PHYSICAL PROPERTIES INVESTIGATION

John C. Alishouse

National Oceanic and Atmospheric Administration
National Environmental Satellite Service
Washington, D. C.

1. INTRODUCTION

It was proposed by Hanel (1961) that absorption in the 2.0 μm band of CO_2 could be used to infer cloud top pressure altitude from an earth-orbiting satellite. Yamamoto and Wark (1961) suggested that the oxygen "A" band at .76 μm could be used for this purpose. Independently, Chapman (1962) also proposed using the "A" band to determine cloud top altitude.

The purpose of the Skylab Cloud Physics Investigation was to assess the feasibility of inferring certain cloud physical properties by remotely sensing reflected sunlight in selected spectral intervals. These properties are: cloud top pressure level, thermodynamic phase of the cloud particles, optical thickness, a particle size parameter, and the density of the particles. The spectral intervals proposed were in and just out of the oxygen A band at .763 and .754 μm respectively; in and just out of 2.0 μm CO_2 band at 2.06 and 2.12 μm respectively; and 1.61 μm.

2. EXPERIMENTAL DATA

It was our plan to compute transmittances for the A band and CO_2 band and the ratios of the three out-of-band channels. Due to a variety of hardware and software difficulties, A band transmittances have not been obtained.

2.1 2.0 μm Transmittance Data

The main purpose of the 2.0 μm data was to provide a correction to the A band transmittance data due to penetration of the solar beam into the cloud. Values were obtained for snow, cirrus, coastal stratus, and clouds associated with fronts. These values have been reported in detail in Alishouse (1976). The transmittances reported in Alishouse (1976) have not been corrected for cloud penetration or for the fact that snow seems to have less reflectance at 2.06 μm than at 2.12 μm, O'Brien and Munis (1975). The values in general seem to be significantly lower than expected and often exhibit standard deviations of 10% or greater.

2.2 The Ratio I(1.61 μm)/I(2.125 μm)

As the experiment was originally conceived this ratio was to be used to determine the thermodynamic phase (i.e., whether the cloud particles are liquid or ice); however computations utilizing techniques described in Twomey, Jacobowitz, and Howell (1966, 1967) and presented in Alishouse (1976) indicate that this ratio will not permit discrimination between liquid water and ice clouds.

The experimental results confirm the theoretical predictions. Twelve sets of snow data yield a range in this ratio from 3.04 to 3.66. Four sets of coastal stratus (liquid water clouds) give a range from 2.80 to 3.68. Three sets of cirrus data yield a range from 3.17 to 3.24. Thus it is necessary to look to other spectral regions for this discrimination.

2.3 The Ratio I(.754)/I(1.61)

This ratio offers promise, both theoretically and experimentally, of being able to provide the desired discrimination.

Table 1 summarizes the experimental SKYLAB results for I(.754/I(1.61) and I(.754)/I(2.125).

Table 1

Date	Range of Air Mass	I(.754)/ I(2.125)	I(.754)/ I(1.61)
	Snow Data		
Jan. 11	3.4-3.5	117.2 ± 15.6	33.6 ± 5.9
Jan. 12	3.4-3.5	174.5 ± 15.3	49.1 ± 5.2
Jan. 20	∿4.2	168.5 ± 38.4	59.9 ± 9.3
Jan. 20	∿4.1	185.9 ± 35.8	61.2 ± 9.7
Jan. 22	3.5-3.6	82.3 ± 8.3	25.8 ± 1.3
Jan. 22	3.4-3.5	87.2 ± 3.8	27.6 ± 1.2
Jan. 22	3.2-3.3	115.2 ± 11.7	33.5 ± 2.7
Jan. 24	3.7	140.8 ± 41.5	40.3 ± 7.2
Jan. 24	3.4-3.5	165.1 ± 16.8	42.5 ± 3.9
Jan. 24	3.2-3.4	185.4 ± 22.6	49.8 ± 5.8
	Cirrus Data		
Jan. 18	3.8	56.0 ± 17.6	18.3 ± 4.8
	Coastal Stratus Data		
Aug. 8	3.2-3.3	31.9 ± 2.7	8.5 ± 0.4
Sept. 10 est	2.1-2.5	27.8 ± 2.3	7.7 ± 0.4
Sept. 15	∿2.6	18.5 ± 2.8	6.8 ± 1.0
Sept. 15	2.5-2.6	22.0 ± 3.1	7.1 ± 0.8
	Frontal Cloud Data		
Aug. 9	2.9-3.1	48.7 ± 18.2	14.5 ± 6.5
Jan. 25	2.8-2.9	26.0 ± 6.2	7.2 ± 1.3
Jan. 25	2.7-2.8	29.6 ± 7.7	9.1 ± 2.2
Jan. 25	2.6-2.7	67.2 ± 6.2	24.0 ± 4.8

The ratio, I(.754)/I(1.61), ranges from 25.8 to 61.2 for the snow data. We note that the three lowest values occurred on the same day. The imagery taken in conjunction with the radiometric data for this day strongly suggest the presence of a thin layer of cirrus.

Unfortunately there is only one unambiguous set of data for cirrus clouds. Two days of cirrus data were eliminated because of anamolous values at .754 μm. The Aug. 9 data probably are Ci, but will be discussed later. Nevertheless based on a sample of one (or two) we see that the ratio I(.754)/I(1.61) is significantly different from that for snow. There are four sets of coastal stratus data in which the ratio I(.754)/I(1.61) varies between 6.8 and 8.5. Thus it appears that the ratio I(.754)/I(1.61) can be used for discriminating among snow cover, clouds composed of ice particles, and clouds composed of water droplets.

The imagery taken during the August 9th pass indicate the clouds are cirrus with small breaks in them. The radiances at both .754 μm and 1.61 μm show wide amplitude fluctuations indicating a considerable range of thickness. This probably accounts for the rather large standard deviations in this day's data.

The first two data sets for Jan. 25 appear not to fit into the classification scheme just presented. The ratios are clearly in the liquid water range yet a NASA aircraft flew along the satellite ground track and reported Ci whose tops were between 30,000 and 40,000 feet. It must be noted that the aircraft flight occurred between one-half and one and one-half hours after the satellite pass. The spacecraft imagery indicate initially the presence of two layers of clouds and then only a single layer is apparent. A detailed analysis of the meteorological situation is being carried out. The third data set, taken beyond the range of the aircraft flights, seem to be cirrus (ice) clouds from both the ratios and the imagery.

2.4 The Ratio I(.754)/I(2.125)

This ratio is designed to give particle size information although as can be seen from the results in Table 2 it appears to be as effective as the ratio I(.754)/I(1.61) as a phase discriminator. It is worth noting that this ratio is in the water or small particle region for the first two data sets of January 25. Unfortunately no independent measurements of cloud particle size distributions were made for the SKYLAB missions. Theoretically it may be difficult to distinguish thin ($\tau < 1$) ice clouds from liquid water clouds.

3.0 SUMMARY OF RESULTS

The results from the S-191 radiometer on SKYLAB were, in general, rather disappointing in terms of what we hoped to achieve. These were five parameters which it was hoped to infer from the measurements. Only one, the thermodynamic phase, could be considered in any detail. The remaining four; optical thickness, cloud top pressure, particle size and particle density could not be inferred because of either instrumental inadequacies such as wavelength calibration or low spectral resolution or there was no independent determination of the parameter.

On the brighter side, the A band technique works a great deal of time, Wark (1968), and the ratios presented in Table 1 look promising at least for thermodynamic phase discrimination. One earlier concept has been shown to be erroneous from both more sophisticated theoretical analysis and experimental data.

Finally a theoretical basis and capability have been established to refine the experiment and aid in the analysis of future data.

REFERENCES

Alishouse, J. C., 1976: A cloud physics investigation utilizing Skylab data. Final Report for EREP 9611, NOAA/NESS 36 pp. (available from author, NOAA/NESS, Washington, D. C. or NTIS, Springfield, Va.).

Chapman, R. M., 1962: Cloud distributions and altitude profiles from a satellite. Planet. Space Sci., 9, 70-71.

Hanel, R. A., 1961: Determination of cloud altitude from a satellite. J. Geophys. Res. 66, 1300.

O'Brien, H. W., and R. H. Munis, 1975: Red and near-infrared spectral reflectance of snow. Research Report 332 Cold Regions Research and Engineering Laboratory, Hanover, N. H.

Twomey, S., H. Jacobowitz, and H. Howell, 1966: Matrix methods for multiple scattering problems. J. Atmos. Sci., 23, 289-296.

----------, -------------, and ---------, 1967: Light scattering by cloud layers. J. Atmos. Sci., 24, 70-79.

Wark, D. Q., 1968: Indirect measurements of cloud-top altitudes. IUGG/WMO Symposium on Radiation, August, 1968, Bergen, Norway. (Summaries published by WMO.)

Yamamoto, G., and D. Q. Wark, 1961: Discussion of the letter by R. A. Hanel, 'Determination of cloud altitude from a satellite'. J. Geophys. Res., 66, 3596.

ESTIMATES FROM SATELLITES OF TOTAL ICE AND WATER CONTENT OF CLOUDS

James T. Bunting and John H. Conover

Air Force Geophysics Laboratory
Bedford, Massachusetts

1. INTRODUCTION

1.1 Objectives

The performance of high speed vehicles such as supersonic aircraft and rockets can be seriously impaired by erosive wear of exposed materials impacted by water or ice particles of clouds. Engineering tests of various materials suggest that the mass density of hydrometeors is the most significant meteorological parameter related to erosion. Since cloud mass density is not measured so routinely as other meteorological parameters such as temperature or humidity, a program to estimate cloud ice and water contents from satellites has been established. Since it is difficult to model the radiative properties observable by satellites for ice particles with varying shape, size and number concentration, data from satellites have been compared to cloud measurements by simultaneous aircraft underflights. A variety of cloud conditions including nimbostratus, stratocumulus and cirrus have been sampled over mid-latitudes of the USA during winter and spring months. In this paper, aircraft measurements of total ice and water contents of clouds are related to simultaneous infrared (IR) and visible measurements from NOAA satellites. The methods presented may also be used to improve the detection of heavy weather over data sparse regions and to verify the ability of numerical weather prediction models to forecast clouds and rain.

1.2 Previous Research

A number of studies have related cloud properties to satellite measurements of radiation in the visible and IR window regions. None of these studies has dealt directly with cloud mass; however, their conclusions suggest the outcome of a cloud mass approach. Booth (1973) and Shenk, Holub, and Neff (1976) have considered cloud typing from visible and IR measurements. Published mass density data for various cloud types could be applied to cloud type estimates from satellites. The total cloud mass is the product of the mass density, which is known to vary with temperature, and the cloud thickness. That approach has the disadvantage of assigning the same total mass to all clouds of the same type unless the cloud thickness is independently known.

Satellite estimates of geometric thickness are difficult to obtain from passive sensors. Measurements of the IR window are customarily converted to temperatures of a blackbody, weighted over the spectral inverval of the instrument. The temperature, along with a temperature altitude relation, allows an estimate of cloud altitude. The IR altitude is useful for estimating cloud thickness for some clouds, e.g., convective clouds in the tropics, but not for other clouds, e.g., cirriform clouds.

Reynolds and Vonder Haar (1973), Griffith and Woodley (1973), and Park, Sikdar, and Suomi (1974) have related the visible reflectance of clouds to cloud thickness, the thickest clouds appearing the brightest. The studies considered only convective clouds. Stratiform clouds or clouds without radar echoes may not follow these published relations. Considerable scatter about the lines of best fit relating visible measurements to cloud thickness was evident. The primary explanation for the observed relations was that thicker clouds should have more particles to scatter sunlight back to the satellite and thus appear brighter. Following this reasoning, thicker clouds are also expected to have a higher mass.

Woodley and Sancho (1971) and others have related rainfall from convective clouds to satellite measurements in the visible. Higher rainfall, like thicker clouds, is associated with heavier cloud mass. However, considerable variability is both observed and expected since a number of complicated processes of cloud particle physics determine the true relation between mass density within a cloud and rainfall beneath it.

Theoretical studies have simulated the radiative properties of clouds at IR and visible regions. Extensive calculations have been made for many spectral regions, primarily using Mie theory to calculate scattering, absorption, and emission for spherical cloud particles. Summaries of results are available (Deirmendjian, 1969), (Mosher, 1974). The form of results is instructive. For instance, calculations for IR show that water clouds, with many small particles, are effective absorbers of infrared radiation while thin cirrus clouds are semitransparent. Calculations in the visible by Twomey, Jacobowitz, and Howell (1967) and others show that cloud reflectance increases with increasing cloud depth, rapidly for thin clouds but more slowly for thicker clouds, approaching an asymptotic limit at less than 100 percent reflectance.

Although theoretical calculations of sunlight scattered by clouds suggest the general form of relationships between cloud mass and reflectivity in the visible, it was decided that direct observations were necessary due to the following limitations in the calculations: (1) scattering models generally use a uniform distribution of cloud particles throughout the cloud, and vary the thickness of the cloud. The assumption is probably reasonable for thin clouds such as stratocumulus or cirrostratus, but is not consistent with cloud particle measurements in deep, precipitating clouds; (2) scattering models assume that all particles have a simple shape, usually spherical or perhaps cylindrical (Liou, 1972). Again, this assumption is probably valid for some thin clouds, but is incorrect for deep clouds containing ice crystals, which may contain ice fragments, aggregates, graupel, rimed particles, dendrites or other irregularly shaped particles. These uncertainties of shape make it difficult to calculate phase functions for single scattering, let alone multiple scattering; (3) scattering models must account for a small amount of absorption of visible light by cloud particles and gases; (4) the spacecraft sensor must be calibrated to absolute physical standards; and (5) the reflecting properties of the underlying surface must be known. The most serious difficulty in a theoretical approach is the need to guess at the particle size distribution of the cloud and consider major variations with altitude.

2. OBSERVATIONS

2.1 Satellite Data

The satellite instruments used in this study are the scanning radiometers onboard the NOAA ITOS series of satellites. The NOAA radiometers are broadband sensors which simultaneously detect both visible (.52 to .72 μm) and IR window (10.4 to 12.5 μm) radiation. Horizontal resolution of the original satellite data is roughly 3 km for the visible channel and about 6 km for the IR channel near the satellite subpoint.

The NOAA spacecraft are sun-synchronous polar-orbiting satellites. Simultaneous IR and visible measurements are available once per day at 0900 to 1000 local time for mid-latitudes in the Northern Hemisphere. Details of the scanning radiometer data archive have been described by Conlan (1973). Data from 12 or 13 consecutive orbits are archived each day in the form of 2048 x 2048 arrays for each hemisphere. The arrays of visible and IR data are aligned with the conventional numerical weather prediction grid, so that the arrays are equally spaced on a polar sterographic projection. The spacing of adjacent grid points on the surface of the Earth increases from about 6 km at the Equator to about 13 km at the poles. The grid is in some instances larger and in other instances smaller than the horizontal resolution of the original radiometer data, depending on whether the data are visible or IR, on the zenith angle of observation by the satellite, and the latitude of the grid point. When the original radiometer data are of finer resolution than the array, for example, when the radiometers are looking straight down, no attempt is made to average values close to the array point - only the last value processed is retained. The visible and IR values for comparison to aircraft measurements were averaged over about 50 array grid points, which represent an area of about 70 x 70 km.

The archives of visible data are received normalized for solar zenith angle. However, inconsistencies in brightness are often noted at the swath edges between satellite passes. An attempt was made to reduce these irregularities by implementing the bi-directional reflectance model of Sikula and Vonder Haar (1972). Further details of the application are described in a technical report (Bunting and Conover, 1976). Observations in the IR array are less sensitive to viewing geometry and have not been normalized by us. The archive for IR includes a small correction for limb darkening due to water vapor absorption.

2.2 Aircraft Data

A series of simultaneous measurements of clouds by satellites and aircraft began in January 1974. At the approximate time of the satellite pass, an aircraft equipped with cloud physics instrumentation would descend from 10 km altitude in a spiral of diameter 35 km at a descent rate of 0.3 km min^{-1} (1000 ft min^{-1}) to 0.3 km or as low as air traffic control would permit. A variety of probes was available, including a "snow stick" for visual identification of crystal habit and size, J-W liquid water sensor, continuous formvar replicator, cloud scene cameras, and Particle Measuring System 1-D spectrometers. A flight director would observe the altitudes of cloud tops and bases, estimate cloud tops when clouds were above the maximum ceiling of the aircraft, estimate the fractional coverage of cloud layers, note optical effects such as halos, and describe particles intercepted by the snow stick. Supporting data consisting of raingage records, radar PPI scope photographs, GEOS satellite imagery, and temperatures from nearby radiosondes were also collected.

The aircraft information was used to estimate cloud mass as a function of altitude averaged over a horizontal area of about 70x70 km. The horizontal area for cloud mass estimate was matched to a set of Vertical Temperature Profile Radiometer (VTPR) measurements made over a square of that size. Estimates of the altitudes, transmissivities, and ice contents of cirrus clouds using VTPR radiances is discussed in an earlier report (Bunting and Conover, 1974).

The particles sampled directly by the aircraft were generally too few for a representative estimate of cloud mass over a horizontal scale of 70 x 70 km, particularly in the case of scattered or broken layers. Furthermore, the problem of matching satellite measurements to aircraft measurements is compounded by the fact that the satellite measurements are sensitive to clouds at all altitudes, but are recorded over a large horizontal scale in only 10 seconds or less. If the aircraft loiters at one altitude to get a better estimate of cloud mass, clouds at a lower altitude may advect or change before the aircraft descends to sample them.

The following approach to cloud mass estimates was therefore followed. Cloud probes were used to determine cloud particle types. Climatological values were used instead of microscale estimates of mass density. More specifically, mass density was expressed as a function of cloud type and cloud temperature. Clouds which appeared thin were assigned an arbitrary lower mass density. The appropriate cloud mass density was simply multiplied by the vertical depth of the cloud and by the fractional coverage of the cloud layer.

Precipitation from clouds was treated differently. An average precipitation rate at ground level was estimated from raingage and radar data supplemented by measurements from the Knollenberg 1-D system. The precipitation rate was converted to mass density by logarithmic relationships for rain, small snow, and large snow. The estimated mass density for precipitation was simply extrapolated upward to the generating altitudes of the clouds. The mass density estimated for rain was increased to a consistent value for snow above the melting level.

A total of 37 cases had been analyzed at the writing of this report. The following sections present results of this method of inferring the hydrometeor environment underneath satellite measurements. The results are remarkably good in light of the many assumptions which have been made. It should, however, be noted that these cases were primarily of stratiform cloud systems, with occasional embedded convection, during winter and spring months over temperature latitudes.

3. CORRELATION OF CLOUD MEASUREMENTS FROM SATELLITES AND AIRCRAFT

Figure 1 relates total cloud mass, the integral of cloud mass density over all altitudes, to visible and IR satellite measurements. Total cloud mass is given for each case in units of gm^{-2}. Only the first two digits of total cloud mass are significant.

The scale of normalized visible measurements ($\bar{B}_N$) ranges from 50 to 254, and is directly proportional to illuminance in foot lamberts (Conlan, 1973). Infrared measurements ($\overline{IR}$) are given as degrees Kelvin over a range of 200 to 300. The visible, IR, and cloud mass data are all averaged over a horizontal scale of about 70x70 km. Figure 1 demonstrates that simultaneous measurements were obtained for a considerable range of both satellite and aircraft data.

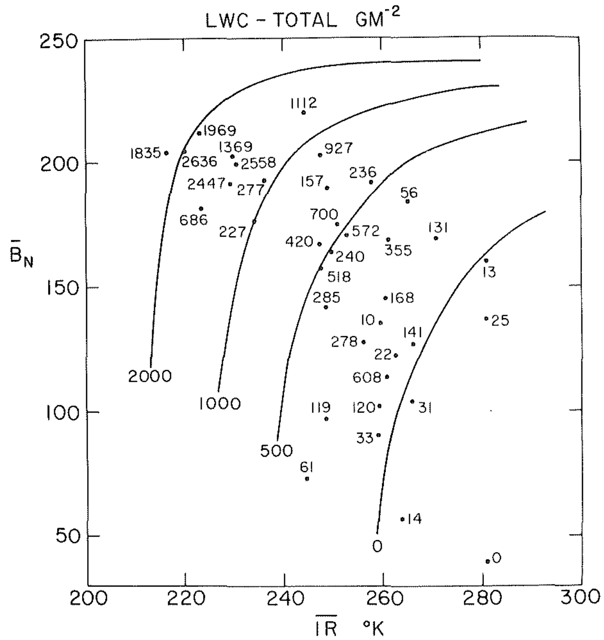

Fig. 1 Simultaneous observations of cloud mass (LWC) by aircraft, and cloud visible and IR radiation from satellite measurements. The cloud mass is the total of both liquid and ice content integrated over altitude. The solid curves are solutions of Eq. (1).

The curves on Figure 1 are solutions of the following equation.

$$LWC = 91735\left(\frac{1}{\overline{IR}-184}\right) + 54886\left(\frac{1}{254-\bar{B}_N+10.1}\right) - 1485 \quad (1)$$

The constants were determined by first linearizing both IR and visible measurements separately with respect to LWC and then applying multiple regression to the linearized quantities. The standard error of estimate for the 37 cases is 410 gm^{-2}; and the correlation coefficient is 0.84. When predictions of total water content are less than zero they are arbitrarily increased to zero.

The observations of Figure 1 clearly confirm a very simple but most reasonable physical hypothesis: clouds which are brightest in the visible and coldest in the IR have the greatest total mass.

4. APPLICATION TO A CASE STUDY

The cloud system of 23 April 1975 over the central US was chosen to illustrate widespread LWC which reached a maximum of about 12,000 gm^{-2}.

Figures 2-5 are photographs of the CRT display of a Man-computer Interactive Data Access System (McIDAS) at the AF Geophysics Laboratory.

Bright dots for coastlines and state boundaries were added by a McIDAS subroutine and do not appear in the data archive. In Figure 2 the surface synoptic situation has been sketched on the McIDAS base map. It shows a developing cyclonic storm over Wisconsin and trailing wave over Kansas and Nebraska. Visible data from the scanning radiometer archive for the NOAA-4

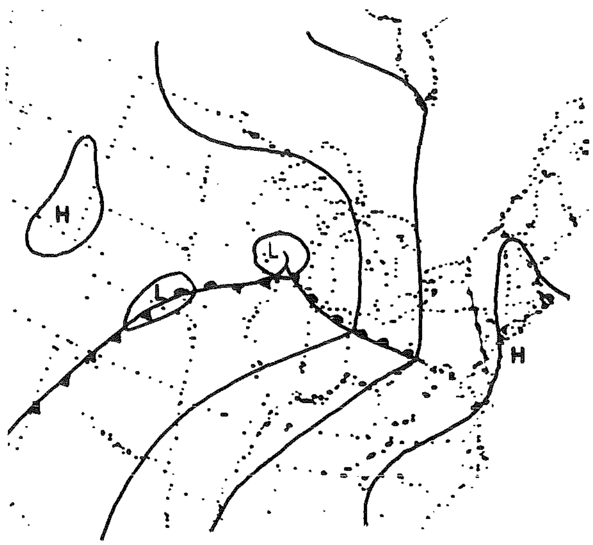

Fig. 2 Surface weather features for 15Z, 23 Apr 1975

satellite are displayed in Fig. 3. The dark rectangle over Indiana marks the approximate location of one of the C-130 aircraft cloud sounding flights. A discontinuity between orbits is evident from western Texas to James Bay, Canada. The data on the eastern side were

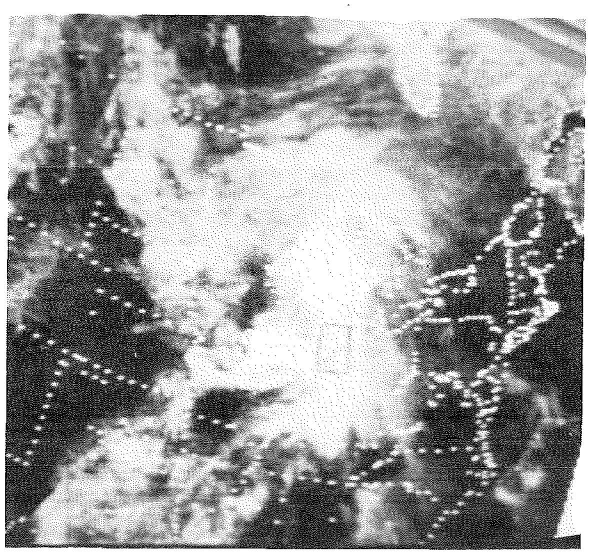

Fig. 3 McIDAS CRT display of NOAA-4 visible data archived for 23 April 1975.

taken at approximately 1530 GMT while the data on the western wide were recorded two hours later. Extensive cloudiness over central USA and Canada is evident. Snow cover over eastern Canada and ice on Lake Winnepeg and Hudson Bay are also evident. The snow and ice appear as bright as the extensive cirrostratus over the Great Lakes. The bars near the upper right correspond to noise in scans by the radiometer or during readout. Figure 4 is an equivalent display for IR temperatures observed by the radiometer. Snow and ice are no longer obvious since

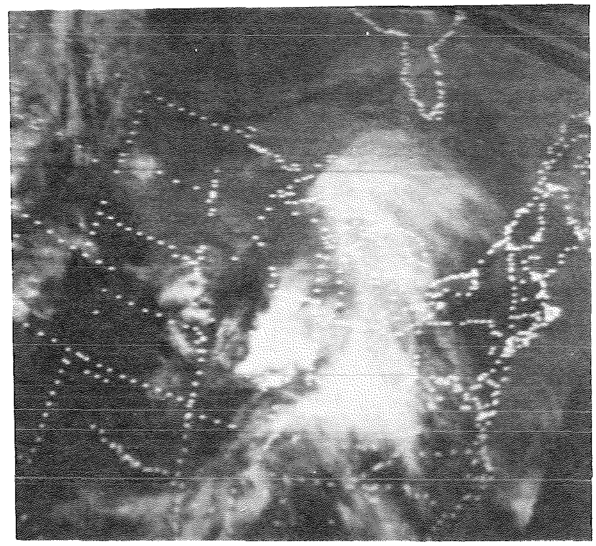

Fig. 4 McIDAS CRT display of NOAA-4 infrared temperatures archived for 23 April 1975.

their temperatures are not so cold as the cloud temperatures of the cyclonic storm; however, the extensive cirrostratus shield over the Great Lakes appears nearly as cold as the more dense clouds to the south.

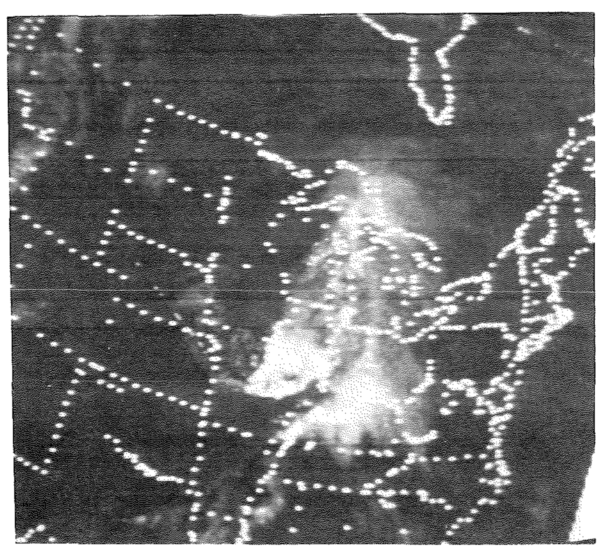

Fig. 5 McIDAS CRT display of total cloud mass for 23 April 1975. Equation (1) has been applied to the visible and infrared data displayed in Figs. 3 and 4.

An application of equation (1) to the

joint measurements of visible and IR is displayed in Figure 5. The darkest shade represents no cloud mass while the brightest shade represents 6400 gm^{-2} or greater. Only a few 10x10 km spots exceeded 6400 gm^{-2}. Bright shades are evident in central Illinois and also in the border regions of Indiana, Ohio, and Kentucky. Snow and ice are not evident, as in the visible display. The extensive shield of cirrostratus is detectable but has less cloud mass than the precipitating clouds over Illinois, Indiana, and Ohio.

It is of interest to compare the LWC display with the National Radar Summary which has been sketched in Figure 6. The areas of high LWC are also areas of precipitation. However areas of relatively low LWC may or may not be areas of precipitation as noted over Lake

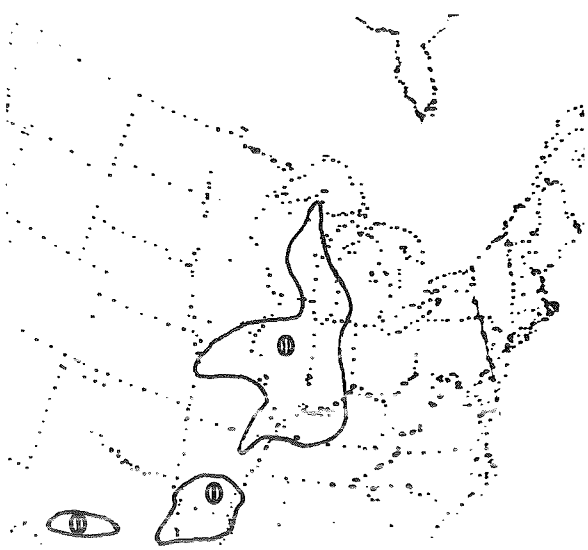

Fig. 6 National Weather Service radar summary for 1435Z, 23 April 1975. Areas of broken and scattered radar echoes are identified.

Michigan and the State of Michigan.

These illustrations show that the LWC display in Figure 5 is unique - it is not equivalent to either cloud brightness or precipitation areas as detected by radar, or cloud temperature.

5. FUTURE WORK

There is room for improvement in several areas. First of all, models for normalization of reflected sunlight to standard viewing geometry are expected to improve in the near future as results become available from the Earth Radiation Budget Experiment on the Nimbus 6 satellite. Secondly, methods to estimate average cloud mass density over areas from aircraft, radars, and lidars are also expected to undergo gradual improvement. Thirdly, we are seeking to expand our own data bank to include cases of heavier weather in convective systems and anvil cirrus. Our highest cases of cloud mass were 2600 gm^{-2}. Considerably higher values for total cloud mass are expected in tropical or temperature latitude summer weather. Data published here were recorded in stratiform cloud systems during winter and spring. Finally, areas with snow cover may appear sufficiently bright in the visible and cold in the IR to be misinterpreted as areas of cloud cover. These "false alarms" can be reduced by converting temperature to altitude and using a new regression estimate for LWC. Ratios of narrow band measurements of reflected sunlight at .76, 1.6, and 2.1 μm may not only correct this snow problem for future satellite instruments, but also distinguish among ice clouds, water clouds, and snow (Alishouse, 1976).

Clouds which are brightest in the visible and coldest in the IR have the highest total mass. Cold IR temperatures correlate with bright visible reflectances. Either predictor explains a significant fraction of observed cloud mass in the dependent data sample for simple linear regression. However, for single regression, IR measurements explained more variance of the observed cloud mass. The IR - cloud mass correlation was 0.80. Although estimates based on IR data alone are not so good as those from IR and visible, they can be made from nighttime satellite passes.

Sun-synchronous passes by satellites provide data at a given location only twice per day; however, there is no reason why the technique discussed in this paper could not be applied to geostationary satellites thereby permitting hourly estimates of LWC.

6. ACKNOWLEDGMENTS

The following report relies on measurements from complicated satellite and aircraft systems. Data reduction would not have been possible without the assistance of many members of the Convective Cloud Physics Branch, AFGL, who recorded and reduced aircraft measurements of cloud particles. Capt. Doug Brooks was flight director and observer for a majority of the research flights. The aircraft were operated by the Air Force Special Weapons Center for AFGL, and by Meteorology Research, Inc., under DNA sponsorship. Assistance with satellite data was given by Miss Patricia Bench and Mr. Leonard Abreu of the Satellite Meteorology Branch, AFGL, and Mr. Edward Conlan, Mr. Frank Porto, Mr. Eugene Hoppe and others of the National Environmental Satellite Service and the National Climatic Center, NOAA.

7. REFERENCES

Alishouse, J. C., 1976: Some results from a Skylab cloud physical properties investigation. Proceedings of the International Cloud Physics Conf., Boulder CO

Booth, A. L., 1973: Objective cloud type classification using visual and infrared satellite data. Proceedings of the 3rd Conf. on Probability and Statistics in Atmospheric Science, 220-227

Bunting, J. T. and J. H. Conover, 1974: Progress on derivation of cloud water content from satellites. Proceedings of the 6th Conf. on Aerospace and Aeronautical Meteorology, 205-207

________, and J. H. Conover, 1976: The Use of Satellite Data to Map Excessive Cloud Mass. AFCRL Technical Report 76-0004.

Conlan, E. F., 1973: Operational Products from ITOS Scanning Radiometer Data. NOAA Technical Memorandum NESS 52.

Deirmendjian, D., 1969: Electromagnetic Scattering on Spherical Polydispersions. American Elsevier Publishing Co. Inc.

Griffith, C. G., and W. L. Woodley, 1973: On the variation with height of the top brightness of precipitating convective clouds. J. Appl. Meteor., 12, 1086-1089.

Liou, K., 1972: Light scattering by ice clouds in the visible and infrared: a theoretical study. J. Atmos. Sci., 29, 524-536.

Mosher, F. R., 1974: Cloud brightness contrast as viewed by a satellite. Measurements from Satellite Systems, Univ. of Wisconsin Press, 61-100.

Park, S., D. N. Sikdar, and V. E. Suomi, 1974: Correlation between cloud thickness and brightness using Nimbus 4 THIR data (11.5 μm Channel) and ATS 3 digital data. J. Appl. Meteor., 13, 402-410.

Reynolds, P. and T. H. Vonder Haar, 1973: A comparison of radar-determined cloud height and reflected solar radiance measured from the geosynchronous satellite ATS-3. J. Appl. Meteor., 12, 1082-1085.

Shenk, W. E., R. J. Holub, and R. A. Neff, 1976: A multispectral cloud type identification method developed for tropical ocean areas with Nimbus-3 MRIR measurements. Mo. Wea. Rev., 104, 284-291.

Sikula, G. J., and T. H. Vonder Haar, 1972: Very Short Range Local Area Weather Forecasting Using Measurements from Geosynchronous Meteorological Satellites. Final Report for Contract F19628-71-C-0073, AFCRL-72-0260.

Twomey, S., H. Jacobowitz, and H. B. Howell, 1967: Light scattering by cloud layers. J. Atmos. Sci., 24, 70-79.

Woodley, W. L., and B. Sancho, 1971: A first step towards rainfall estimation from satellite cloud photographs. Weather, 26, 279-289.

5.1.3

EFFECTS OF CLOUD SIZE AND CLOUD PARTICLES ON SATELLITE OBSERVED REFLECTED BRIGHTNESS

David W. Reynolds, T. B. McKee and K. S. Danielson

Department of Atmospheric Science
Colorado State University
Fort Collins, Colorado

1. INTRODUCTION

Modeling of the visible radiation scattered from semi-infinite to finite size clouds has been attempted for several years. Hansen (1969) and Twomey, Jacobowitz and Howell (1967) resolved that for a plane parallel atmosphere with semi-infinite clouds having optical depths near 100 (cloud 1 - 1.5 km deep and having liquid water contents of .2 gm/m^3) that these clouds would be at their maximum brightness. These results showed that remote sensing of clouds in the mid-visible wavelengths would be of little value for clouds of any real vertical extent, and it would be impossible to determine anything about the clouds microphysical properties. However, observational measurements from satellites of convective clouds of significant vertical extent, (>>2 km), have shown increasing brightness with increasing height, Griffith & Woodley (1973), Reynolds & Vonder Haar, (1973), Griffith et. al., (1976). Recent work by Busygin et. al., (1973) and McKee and Cox (1973, 1975) have shown that the finite cloud poses a particular problem for monitoring its brightness due to energy passing through the vertical sides of the cloud. Thus their reasoning for this observed brightness-height change is related to the fact that as the cloud grows it becomes wider as well as thicker making side effects less important and allowing more light to be reflected off the top. However, even this theory does not account for some of the observed change in brightness for semi-infinite clouds which will be reported in this article.

During this past summer, a unique data set was obtained during the South Park Cumulus Experiement (SPACE). Data on cloud dimensions and cloud position were collected through the use of two cameras which simultaneously photographed the experimental area. Since these stereo photographs were taken in a time lapse mode, the growth characteristics of the clouds could also be deduced. Cloud microphysical data for the experiment were collected by aircraft, radar, and surface observations. Three aircraft were used to penetrate the cumulus clouds. The CSU Areocommander and the University of Wyoming Queenaire both are instrumented to study cloud microphysical processes. Emphasis is placed on collecting data pertaining to cloud particle distributions, IN and CCN concentrations, and liquid water contents as well as the state parameters. The NOAA/NCAR Explorer sailplane, because of its ability to remain in the clouds for extended periods of time while collecting microphysical data, was a particularly unique data gathering system which was utilized extensively in SPACE. The Limon WSR-57 10 cm radar and the CSU M-33 10 cm radar provides data on position, intensity and motions of clouds with precipitation sized particles. The CHILL dual 10 cm and 3 cm wavelength radar with doppler capabilities was used to determine position and intensity of natural clouds and was also used in radar chaff tracer experiments which have yielded substantial data on cumulus cloud microphysical processes and on cloud morphology. A surface meso-net collected data on low level fluxes of heat and moisture. A surface chase vehicle provided data on precipitation type and size distribution. Several daily air mass soundings were taken to provide data on the changes experienced by the non-cloud air mass and provided a reference for satellite derived cloud-top temperatures. All these data complement, support, and strengthen observations made by the satellites of the South Park region.

Along with this data, digital SMS-2 (Synchronous Meteorological Satellite) visible (.5 - .7 μm) (.9 km resolution at SSP) and infrared (10.5 - 12.5 μm) (9 km resolution at SSP) radiance data were received for this area through the Direct Readout Ground Station at White Sands Missile Range. This allowed us to observe reflectance patterns of the clouds as well as estimate their top heights.

Using the Monte Carlo cloud model for finite clouds developed by McKee and Cox, (1973) we used different distributions of drop sizes and numbers (Deirmendjian, 1969) along with varying cloud depths and widths to determine how theory would predict what the satellite would view from its given location in space. Results of these runs along with satellite observed reflectance will be presented in the following sections.

2. MODEL CALCULATIONS

Fig. 1 shows the two drop size distributions used in the model (C.1, C.3), along with the average distribution observed during the last 3 days of SPACE. Note that the two distributions used bounded that observed during this period so that C.2 results would fall between the curves shown in Fig. 2. From Deirmendjian (1969), we obtained the 2 phase functions and volume scattering coefficients for a water cloud at a wavelength of .7 μm. The phase function labeled C.1 is characterized by a very strong forward scattering peak while C.3 is not nearly as strongly peaked. Accuracy of the computations depends on the number of photons processed through the computer program.

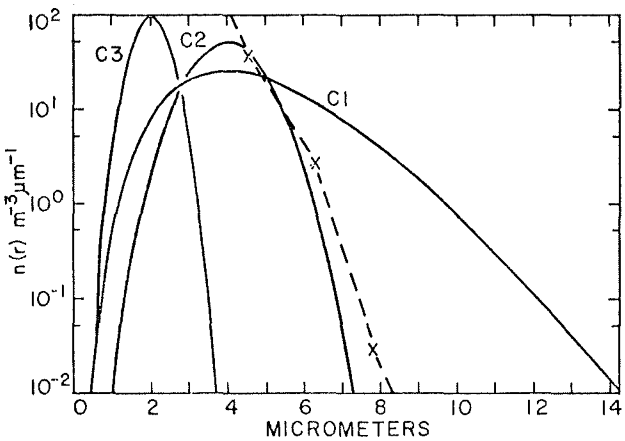

Fig. 1. Particle size and number distributions available for model input (Deirmendjian, 1969). South Park observed distributions are shown as the dashed line. Note curve continues upward showing large number of small particles.

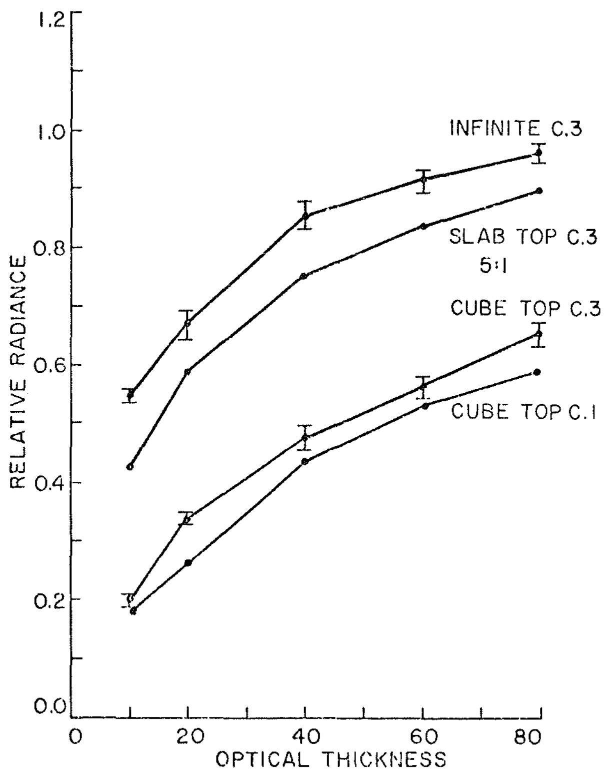

Fig. 2. Model results showing small variation in relative radiance for C.1, C.3 drop size distributions over the optical depths shown. Note also that a cloud slab having a width to depth ratio of 5:1 by optical depth 80 is very nearly equal in brightness to an infinite layer.

The accuracy of the relative radiance for a semi-infinite cloud and the top of a cubic cloud is indicated by error bars.

Fig. 2 shows the results from this computational study. The first test was to determine what effect the two drop size distributions would have on the reflected brightness for the top of a cubic cloud. To orient the reader, for a cloud having a C.2 particle distribution and a τ = 80, its' vertical depth would be 1.5 km and have a liquid water content of .15 gm/m^3. The two curves show that over a wide range of optical depths, there appears to be a small effect due to phase functions which were determined from the drop size distributions. This confirms the early work by Twomey, Jacobowitz and Howell that remotely sensing clouds in the mid-visible wavelengths for determining their microphysical structure seems unlikely.

The second study carried out was to determine the differences in reflectance between infinite and cubic clouds. Fig. 2 indicates the relative radiance for the semi-infinite cloud is about 50% greater than for the top of the cube at optical depth of 80. The relative difference increases for smaller optical depths. The semi-infinite cloud is near a theoretical limit for optically thick clouds as the slope of the curve is nearing horizontal. The cubic clouds have a theoretical limit identical to the semi-infinite cloud but require a much larger optical thickness to approach this limit. Consequently, the cubic cloud would continue to get brighter for increasing optical thickness.

A third feature is indicated by calculating the relative radiance for a cloud with a width to depth ratio of 5 to 1 while maintaining a square top. Theory indicates the radiances are closer to the semi-infinite layer than to the cube. Observations illustrated in Fig. 4 indicate a ratio of 10 to 1 needed to approach a maximum brightness. Real clouds do not have flat tops as is the condition of the cube. Irregular structure is likely to slow the transition to a semi-infinite layer, since small irregularities will retain characteristics of smaller clouds.

3. SATELLITE OBSERVED REFLECTED BRIGHTNESS

Digital SMS-2 VISSIR (Visible and Infrared Spin Scan Radiometer) data was obtained for August 6, 7, and 8th during the initial stages of convection over South Park, Colorado. The SMS-2 satellite was positioned at 115°W during this period giving it a nadir angle of the South Park area of 46° and 17° west of a due south view. This gives SMS a ground resolution in this area of 1.2 km in the visible. The infrared sensor on board allowed cloud top temperature/heights to be determined for clouds with horizontal dimensions greater than 12 km. Thus only large clouds could be viewed. For those clouds where heights could be determined, the maximum heights ranged to 1.5 to 2 km. Fig. 3 is an SMS-2 view of the South Park region showing the range of cloud sizes observed on August 6 which was fairly typical of the clouds observed on the following two days although this day may have been a little more active. A comparison was first made of satellite measured visible radiance versus satellite derived cloud top temperature for co-located SMS visible - IR digital sectors. Nine separate sectors were compared for the three days, all within 1 hour of local noon. Approximately 250 data points per picture were correlated. From this, correlation coefficients ranged from -.3 to -.65. These were fairly low correlations and seemed to show that visible radiance was not well related to top temperature/height. The relationship between visible radiance and cloud horizontal dimensions was also

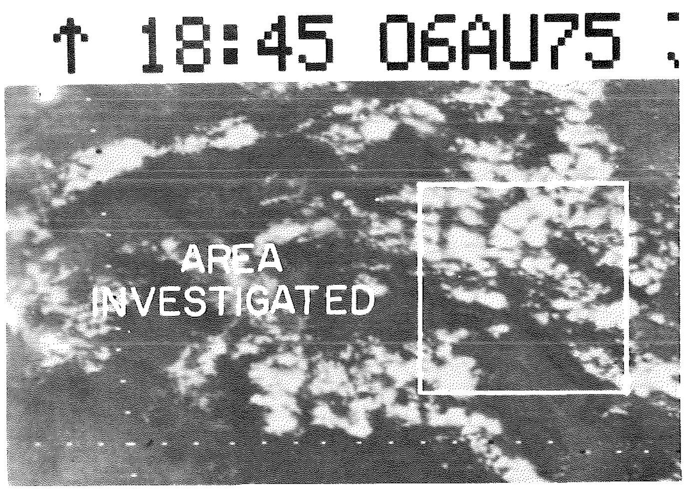

Fig. 3. SMS-2 .9 km visible image for 1845Z 6 August 1975. Area of interest is shown. Scale: 1mm = 6.2 km

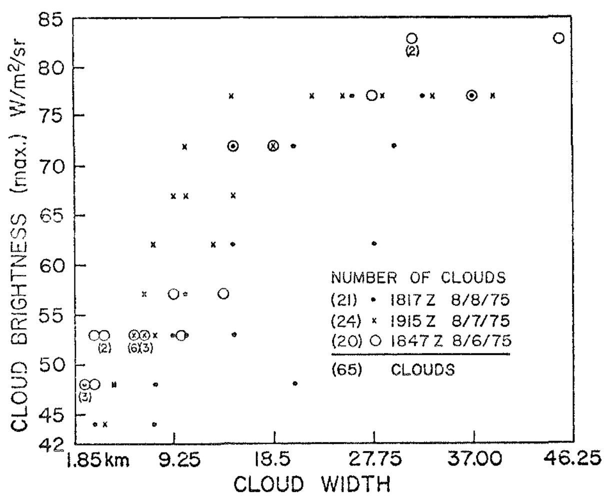

Fig. 4. Satellite derived maximum cloud brightness versus horizontal width for 65 clouds investigated during this three day period. Numbers under points represent multiple data points at this location.

investigated. Clouds were chosen from the three days at three different times around local noon and their horizontal dimension and maximum brightness were determined. Fig. 4 shows the results of this study which indicate that the brightness does not level off until the width approaches 20 km. For clouds approaching the 2 km height the ratio of width to depth is 10 to 1. This is well past the 5 to 1 ratio suggested by McKee and Cox where the brightness changes should level off. This curve may be demonstrating a lack in the model in its handling of the cloud top surface features. As was mentioned earlier, the model handles only flat tops of clouds, while we know that growing cumulus are distorted, rough turrets. It is felt that due to this cloud top configuration, that a cloud may not approach the infinite stage until much further in its life cycle when the top begins to flatten and glaciate. We should add here that many of the larger clouds viewed were conglomerates of clouds spaced closer together than 1.2 km so were averaged by the sensor into a large cloud. There may be some interaction between the cloud sides that we see but this is assumed to be small compared to cloud top reflectance properties. Ranges of visible radiance measured for these clouds for the wavelength interval used agrees well with what theory predicts. The discrepancy occurs in the sizes of clouds over which this range should exist.

4. CONCLUSIONS

Several results have been obtained through looking at theoretical and observational cloud reflectance properties:

1) Cannot remotely sense the microphysical structure and change taking place in cumulus clouds in the mid-visible spectral region for clouds greater than 1.5 km in depth.

2) Can predict that geometrical factors will strongly affect the cloud brightness and far outweigh microphysical changes but have not predicted these changes for clouds of width to depth ratios as large as that observed from satellites (10:1).

3) The theory used can predict the range of brightness that should be observed, but does specify the width to depth ratios in accord with observations.

4) Discrepencies from theory and observations may be due to theory not adequately representing the non-uniformity of the cloud top which we feel strongly controls the brightness observed from satellites.

Work is progressing on modifying this program to handle more of the shape factors involved with clouds as well as streamlining the computational scheme to reduce the noise problem. It appears that some reflection is needed on previous work which has compared satellite brightness to cloud heights and rainfall rates and liquid water contents. We may better appreciate what these apparent brightness changes in observed clouds are actually telling us through both theoretical modeling and comparison from ground and aircraft observed cloud structure, as well as satellite observations.

5. REFERENCES

Busygin, V. P., N. A. Yevstratov and Ye. M. Feygel'son (1973): Optical Properties of Cumulus Clouds and Radiant Fluxes for Cumulus Cloud Cover, Atmos. and Oceanic Physics, Vol. 9, No. 11, pp. 1142-1151.

Deirmendjian, D. (1969): Electromagnetic Scattering on Spherical Polydispersion. The Rand Corp., Santa Monica, California, Published by American

Elsevier Publishing Co., Inc., New York, 290pp.

Griffith, C. G., and W. L. Woodley (1973): On the Variation with height of the top brightness of precipitating convective clouds. J. Appl. Meteor., 12, 1086-1089.

Griffith, C. G., W. L. Woodley, S. Browner, J. Teijero, M. Maier, D. W. Martin, J. Stout, D. Sikdar (1976): Rainfall Estimation from Geosynchronous Satellite Imagery During the Daylight Hours. NOAA Tech. Rep. ERL 356-WMP07. U. S. Dept. of Commerce.

Hansen, J. E. (1969): Exact and Approximate Solutions for Multiple Scattering by Cloudy and Hazy Planetary Atmospheres. J. Atmos. Sci., 26, No. 3, pp. 478-487.

McKee, T. B. and S. K. Cox, (1974): Scattering of Visible Radiation by Finite Clouds. J. Atmos. Sci., 31, No. 7, pp. 1885-1892.

McKee, T. B. and S. K. Cox (1975): Simulated Radiance Patterns for Finite Cubic Clouds. Submitted to J. Atmos. Sci.

Reynolds, D. W. and T. H. Vonder Haar, (1973): A Comparison of Radar Determined Cloud Height and Reflected Solar Radiance Measured from the Geosynchronous Satellite ATS-3. J. Appl. Meteor., 12, 1082-1084.

5.1.4 PHYSICAL AND RADIATIVE PROPERTIES OF SUMMER CLOUDS IN ALASKA FROM SATELLITE IMAGERY

A. K. Biswas and K.O.L.F. Jayaweera

Geophysical Institute
University of Alaska
Fairbanks, Alaska 99701

1. INTRODUCTION

The National Weather Service recognizes four major climatic zones in Alaska. They are Arctic, Continental, Transition and Maritime (see Fig. 1). These climatic divisions are based on annual temperature and precipitation. The transition zone is intended to show the gradual change from the Maritime climate along the Gulf of Alaska and southwest Bering Sea to the Continental climate of the interior. But the overall climate of this zone is very close to that of the continental zone. Thus, for most practical purposes there are three climatic zones in Alaska separated by its two mountain ranges. The Brooks Range in the north separates the Arctic from the Continental zone and the Alaska-Aleutian range separates the Maritime from the Continental zone.

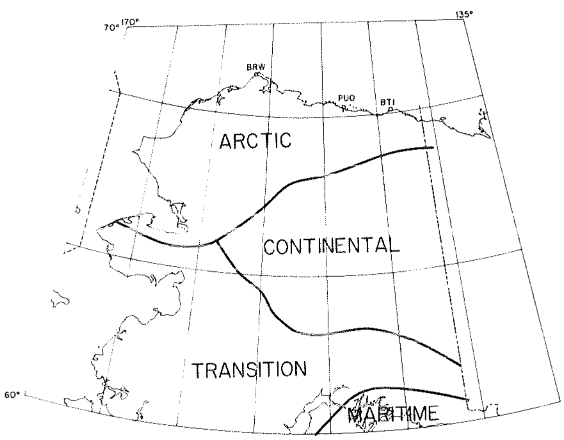

Figure 1. The climatic zones of Alaska as recognized by the National Weather Service.

The weather in the Maritime zone is dominated by the passage of fronts originating in the northmost Pacific. The warm, moist air associated with these weather systems account for a large amount of precipitation in this sector of Alaska.

In contrast, the Arctic region has very little precipitation, and during the summer months (May to October) low stratus clouds cover this area almost continuously. This persistent cloudiness in the summer appears to be a permanent climatological feature.

The continental interior is the region of extreme seasonal temperature contrast. The hot summers of the interior of Alaska are conducive to the formation of thunderstorms. During the course of a typical summer day, convective clouds appear to form in certain areas and continue to develop until late afternoon. The period of activity begins about 1000 hours and ends around 1900 hours local time. Burns (1974), in his analysis of data for northwest Canada, found that there is a diurnal variation in thunderstorm activity with two peaks, one in the late morning around noon (local time) and the other in the late afternoon around 1700 (local time). These thunderstorms account for most of the summer precipitation.

Due to the sparse network of weather observing stations, climatology of clouds in Alaska is poorly documented. Furthermore, only recently has there been sufficient interest to attempt documentation of cloud conditions. Although weather satellites have improved tremendously the data collection of cloud condition in the temperate and equatorial zones, very few reports exist on the use of polar orbiting satellites in such studies in the Arctic. In this paper we intend to show the advantages of satellite imagery for cloud climatology and measurement of the cloud top temperatures. Such information is essential in the calculation of radiative fields in the Arctic.

2. PREVIOUS STUDIES

Long-term cloud statistics do not exist for interior and Arctic Alaska. Some idea of the cloud conditions for the Arctic region may be obtained from the studies of Huschke (1969). The Arctic cloud statistics compiled by Huschke using 63 months of surface synoptic weather data and the analysis of weather reconnaissance flights of the U.S. Air Force by Henderson (1967) give an accurate picture of the monthly variation of spatially averaged cloud conditions. The important finding of these studies is that the amount of cloudiness and their frequency of occurrence are essentially a step function of time (Fig. 2a) and that the increase of cloudiness during the summer is due to the presence of low level stratus clouds (Fig. 2b). It must be mentioned, however, that these results are applicable more over the central Arctic Ocean rather than to the Alaska North Slope and Beaufort Sea.

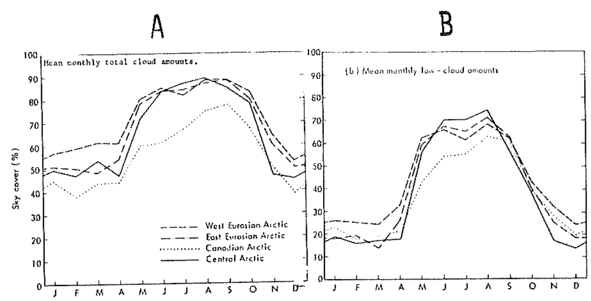

Figure 2. (a) The mean monthly total cloud amounts, and (b) mean monthly low cloud amounts after Huschke (1969).

One of the interesting features of the Arctic stratus is layering. Although observed by many aviators in the Arctic, this feature of the stratus clouds occurring in distinct layers of two or three has only recently been mentioned in the meteorological literature by Jayaweera and Ohtake (1973). The few observations mentioned in this work cannot give a cohesive explanation for the layered nature of these clouds. A theoretical description of layering is given by Herman (1975). He developed a self-consistent radiative diffusive model to predict the observed layers. Herman's model attributes the layering to a greenhouse mechanism whereby solar radiation penetrates to the interior of the cloud and causes evaporation there, while at the same time the top remains cold due to emissions to space and the lowest layer reamins cold since the surface temperature is fixed at 0°C. Although this model explains the occurrence of two layers, it is not detailed enough to account for multilayers.

Apart from these observational and theoretical studies, we know very little about the extent or duration of the individual stratus decks which comprise the long term means. There are no data pertaining to the horizontal variation of the stratus base and top heights.

The few invesigations on the summer climatology of interior Alaska resulted from the importance of thunderstorms in Alaskan forest fires. Thus, all the previous studies were a part of the Bureau of Land Management fire control efforts. These studies, notably by Sullivan (1963) and Comiskey (1966) were based on sparse observational data, hence some of their inferences as to the geographical distribution and the meteorological conditions for the formation of thunderstorms are questionable. Existence of preferred zones for convective activity in Alaska has been suspected for a long time but only recently confirmed by Jayaweera and Ahlnas (1974) and Biswas and Jayaweera (1976) through the analysis of NOAA-2 and -3 satellite imagery.

Due to the lack of large scale horizontal convergence such as cyclones, frontal over-running in interior Alaska, many meteorologists were led to propose that the thunderstorms in Alaska are primarily air-mass type. Thus undue emphasis has been given to insolation in the various indices that have been devised for forecasting thunderstorm development. The recent studies with satellite imagery have shown that moisture advection is very important and that tracks of moisture could be traced from the cloud patterns visible in the imagery. It is anticipated that the availability of high resolution satellite imagery will shed more light on the understanding of thunderstorm formation in Alaska by providing better climatology of convective clouds than is presently available.

3. NOAA-2, -3 and -4 SATELLITE CHARACTERISTICS

The orbital and the very high resolution sensor characteristics of the NOAA-2, -3 and -4 environmental satellites are given in Table 1. Of these three satellites, NOAA-4 is the prime satellite at present with NOAA-3 acting as a back-up. The NOAA-2 has been switched off. The coverage of these satellites is such that any point on the equator will be seen by the VHRR sensor once a day during the ascending mode and the descending mode. Over the higher latitudes, all polar orbiting satellites have a greater coverage. As such, interior Alaska and the adjoining Arctic Ocean are covered at least for three passes a day. During the descending mode most of this region is visible at near 1100 and 1300 local time, and during the ascending mode near 1700 local time. Fortunately, these times are very convenient for studies in thunderstorm development as they are within the periods of maximum activity of thunderstorms.

Table 1

NOAA 2, 3, and 4 Satellites

ORBIT CHARACTERISTICS:	NOAA 2 *	NOAA 3	NOAA 4
ALTITUDE: APOGEE	1453.98 km	1509.22 km	1457.73 km
PERIGEE	1448.10 km	1500.07 km	1443.88 km
INCLINATION (ASCENDING)	101.771^0	102.032^0	101.732^0
PERIOD	115.00767 min.	116.08574 min.	114.89850 min.
EQUATOR CROSSING (DESCENDING)	08:52 A.M.	08:30 A.M.	08:30 A.M.
RATE OF PRECESSION OF ORBIT PLANE	.9874 DEG/DAY	.9894 DEG/DAY	.9887 DEG/DAY
ON BOARD SENSORS:	VERY HIGH RESOLUTION RADIOMETER (VHRR) SCANNING RADIOMETER (SR) VERTICAL TEMPERATURE PROFILE RADIOMETER (VTPR)		
VHRR CHARACTERISTICS			
VISIBLE CHANNEL:	0.6-0.7 μm		
INFRARED CHANNEL:	10.5-12.5 um		
BRIGHTNESS RANGE (VIS):	65 to 10^4 FOOT-LAMBERTS		
SCENE TEMPERATURE RANGE (IR):	180^0-315^0K		
SPATIAL RESOLUTION:	0.9 km		

* (NOAA 2 is not being tracked presently)

Of the sensors aboard these satellites the very high resolution radiometers are the most useful in the present study. The visible and the thermal infrared imagery from these sensors are obtained essentially in a direct read-out mode. The tape recording capability is limited only to 8 minutes. For the region of our interest, data is obtained from Gilmore Tracking Station, Alaska. This station, located in the vicinity of Fairbanks, can receive data from approximately within the area shown in Figure 3. This information from almost the entire western half of the Arctic Ocean and North America is available from this tracking station.

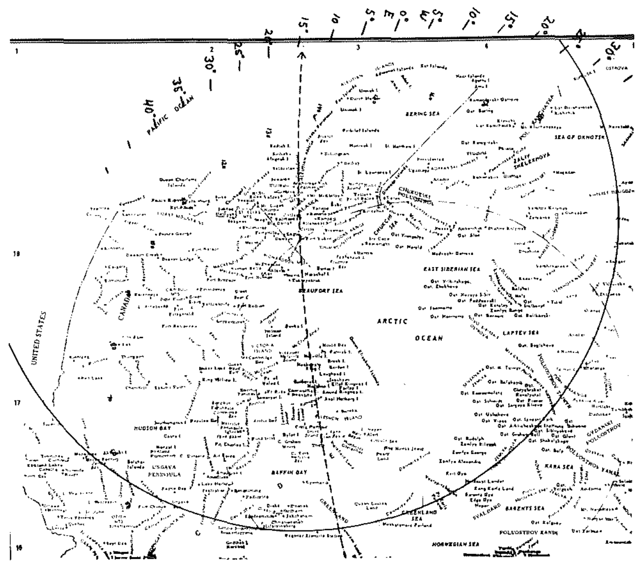

Figure 3. The maximum area that can be tracked from the Gilmore Tracking Station, Alaska.

The satellite data are available in analog, digital or photographic form. The latter mode being the most convenient for use and readily give a 'picture' of the cloud cover situation. The gray scale for these images are chosen so that the photographic image will yield a wide range of information of general interest to many users. This 'first look' product is of sufficient value to decide on making special products for particular applications. In these special products the gray scale could be chosen to bring out features that are of special interest. For example, in the infrared, small temperature differences or particular temperature could be shown. In the present study, infrared enhancements were used to identify thunderstorms from other convective clouds and the cloud top temperatures of stratus cloud layers.

4. PROPERTIES OF ARCTIC STRATUS CLOUDS

Although arctic stratus clouds have come to the attention of polar meteorologists, hitherto no attempts have been made to use satellite imagery to compile cloud distributions. One of the problems encountered in interpretation of cloud cover in the Arctic is to distinguish clouds from the underlying ice surface. Because of similar albedos from ice and clouds, and the possibility of clouds warmer than the pack ice, it is necessary to use techniques different from those used at lower latitudes to distinguish Arctic clouds.

The boundaries of the stratus clouds are inferred from the visible imagery of the VHRR by recognizing the existence of highlights and shadows cast by the sun. These features appear on the cloud boundaries due to the low sun angle in these latitudes. Thus higher layers of clouds are readily seen from the lower clouds or the ice surface (Fig. 4). The infrared imagery is then used to determine the cloud top temperatures (Fig. 5). Notice that cirrus clouds which are not obvious in the visible come out clearly in the infrared because of their low temperatures. The special enhancements of the infrared imagery specify the gray tone to the radiative temperature of the cloud. Therefore the temperature measured by the satellite is not the cloud top temperature but its radiative temperature. Arctic stratus clouds have mean thicknesses in excess of 200 m. The emissivities in the atmospheric window band (11-13 μ) for stratus clouds of this thickness is in excess of 0.8 (Hunt, 1973). Thus the radiative temperature of these clouds is nearly 95% of the top temperature. Thus we may reasonably assume that the satellite measured temperature is essentially that of the top of the stratus cloud.

In the present investigation we have confined ourselves only to the Arctic climatic region of Alaska and that of the adjoining Arctic Ocean. This region is shown in Figure 6. Although, as mentioned earlier, satellite information is available for the western half of the Arctic Ocean, we confined ourselves to this region because this investigation is primarily designed to test the use of satellite imagery for cloud cover observations in the Arctic rather than to obtain cloud cover statistics. The results were based on the satellite imagery for the summer of 1975.

The amount of stratus cloud cover over this area for the summer of 1975 is shown in Figure 7a. The amount of cloudiness does confirm the high cloudiness observed over the Arctic in the early part of summer. But the extremely low cloudiness during mid-summer is quite unusual. Although we cannot draw any real conclusions from a single year's data, the nearly total lack of cloudiness for almost a two week period in midsummer is not documented anywhere. Huschke (1969) does mention a slight drop in the cloudiness dur-

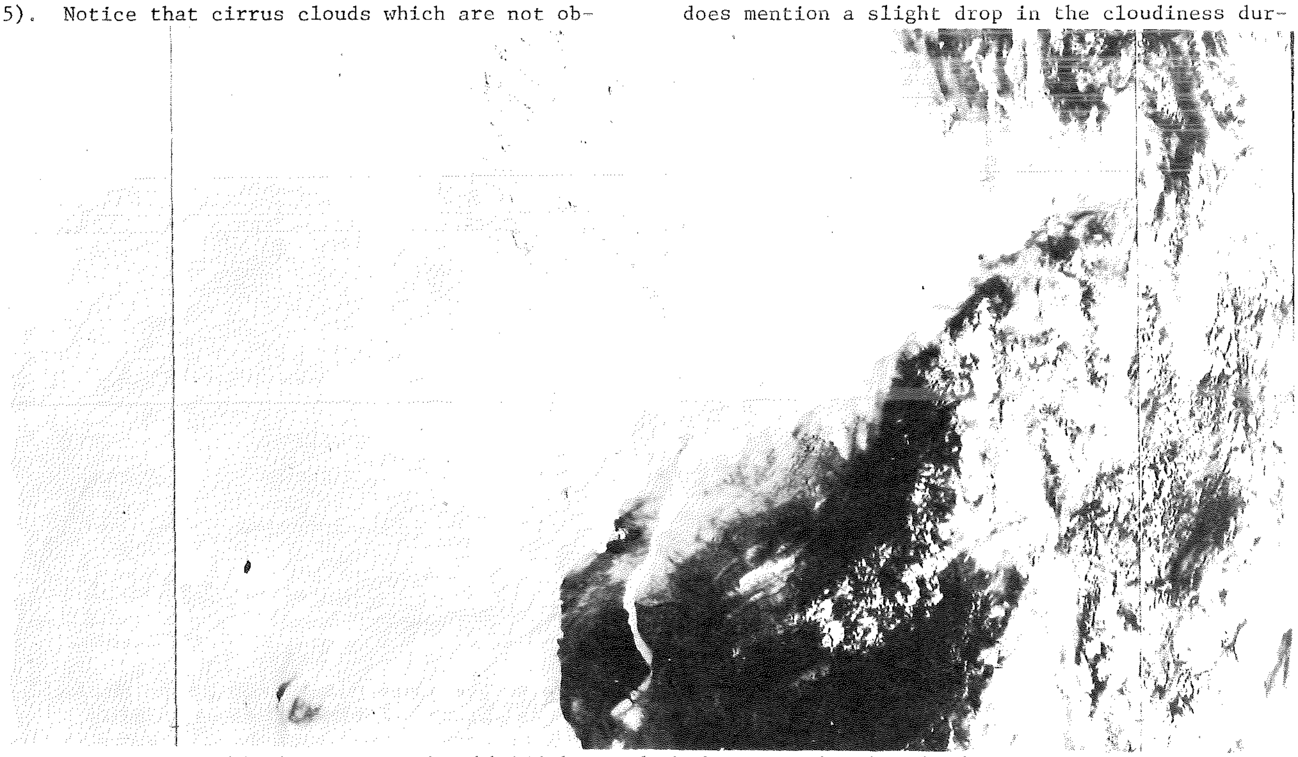

Figure 4. The visible imagery showing highlights and shadows cast by the clouds.

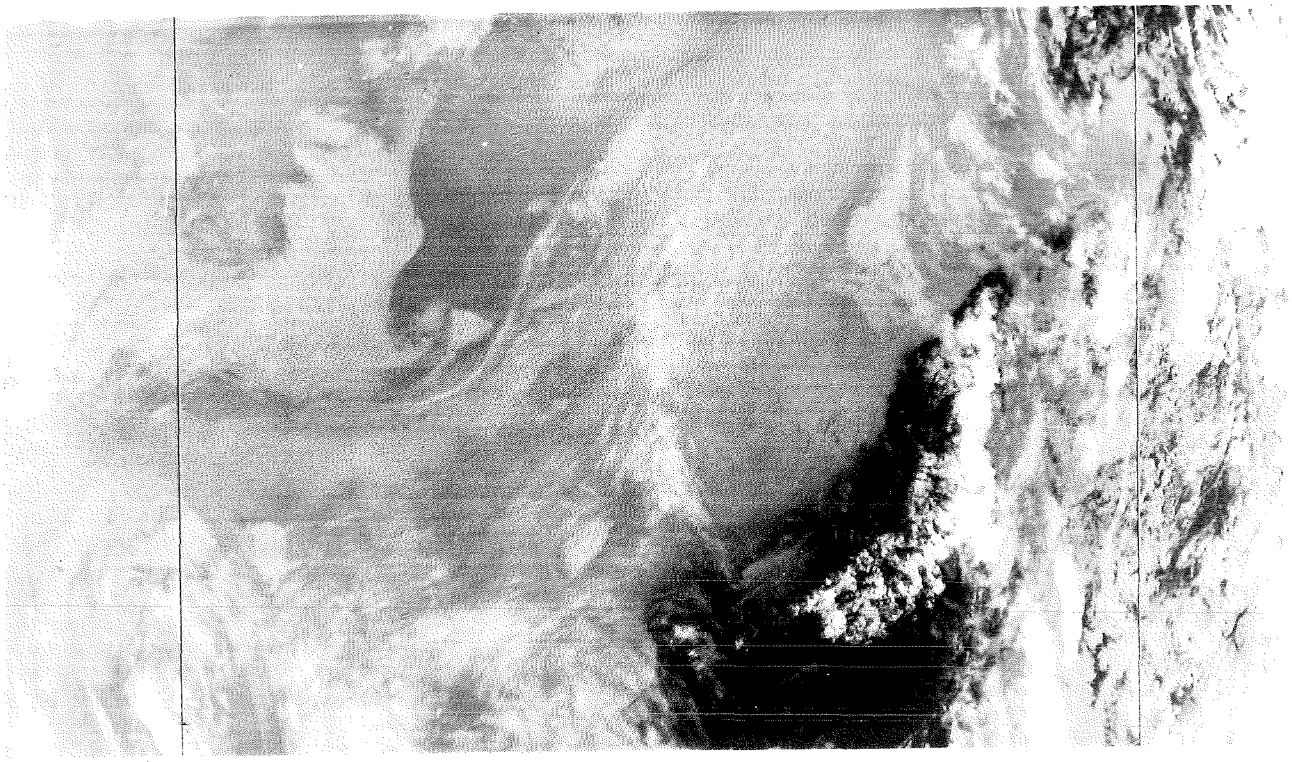

Figure 5. Infrared imagery showing the cloud top temperature.

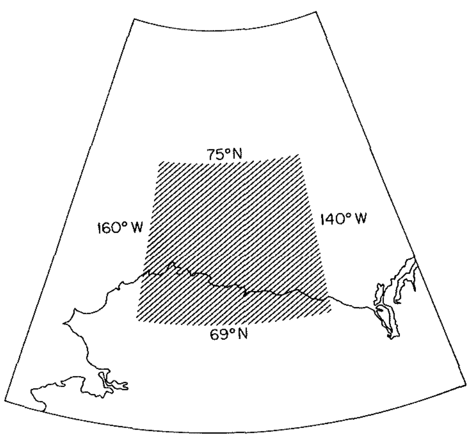

Figure 6. The region of investigation.

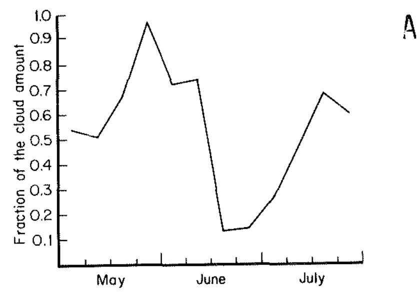

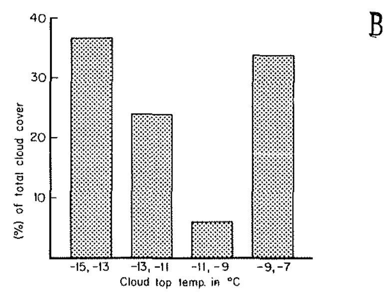

Figure 7. (a) The amount of cloud cover, and (b) the distribution of cloud top temperature of the stratus clouds over the region shown in Fig. 6 during the summer 1975.

ing this time for each of the four regions considered, but this drop is far smaller than our observations show.

The formation of stratus clouds is generally believed to be controlled by the amount of sensible, latent and radiative fluxes. The low amount of mid-summer cloudiness is attributed by Herman (1975) to a minimum in the sensible and latent heat fluxes during this time. Because the region investigated in this study was not included in Huschke's analysis, the small amount of mid-summer cloud cover, if it is a real effect, will have important implications on the variations of sensible and latent heat fluxes during the summer.

From the infrared imagery, the temperature of the tops of stratus clouds could be determined. In Figure 7b the distribution of the cloud top temperature is shown. This distribution could be used to determine the effect of the stratus clouds on the long-wave radiation emitted to space.

For Summer 1975, the average cloud cover over the region investigated is 53%. Assuming that the clouds radiate as black bodies at their top temperatures and the underlying ice surface as a black body at -2°C (freezing point of sea water), the contributions by the clouds and the ice to the total outgoing radiation are 14.3

and 14.0 mw cm^{-2}, respectively. Thus for this period the distribution of clouds was such that the two components are equal.

5. PROPERTIES OF CONVECTIVE CLOUDS

Convective clouds could be easily distinguished from either visible or infrared satellite imagery. In the interior of Alaska, build up of convective clouds begins about 1000 local time, and under certain conditions these clouds turn into thunderstorms. Our interest in this study was to investigate the occurrence of thunderstorms.

Thunderstorms were distinguished from other convective clouds using both the visible and infrared as suggested by Jayaweera and Ahlnas (1974) and assuming that convective clouds with tops colder than -28°C are thunderstorms as discussed by Biswas and Jayaweera (1976). By analyzing the satellite imagery for the summers of 1974 and 1975, we find although there are perferred zones for thunderstorm formation, there is no definite period common to both seasons where maximum activity was observed. However, the temporal distribution did show sharp contrasts in activity over the season (Figs. 8a, b). Analysis for the thunderstorm activity from the morning and afternoon satellite passes shows that the distribution follows the same pattern for each season. Furthermore, comparison of these events for 1974 and 1975 (Figures 9a,b) suggests that there is no reason to believe that a consistent difference exists between the morning and afternoon.

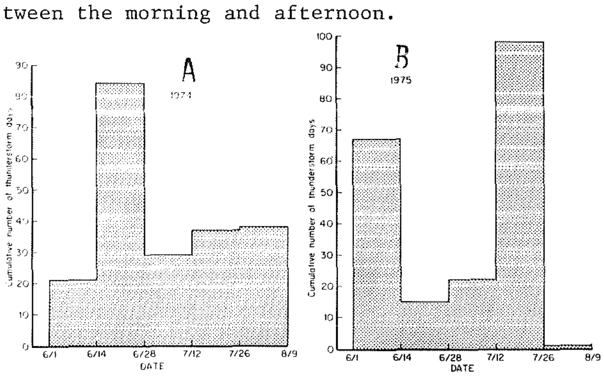

Figure 8. The temporal distribution of thunderstorms days for (a) 1974 and (b) 1975.

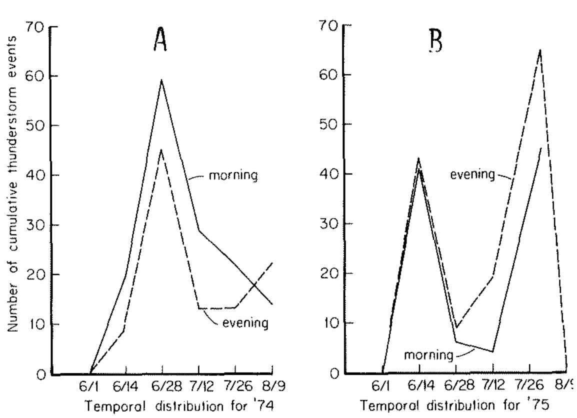

Figure 9. The number of thunderstorm events in the morning and afternoon for (a) 1974 and (b) 1975.

The variation of thunderstorm activity during the summer and the preferential zones for its formation suggest that indeed certain areas of the State are conducive to thunderstorm formation. However, there is no evidence that insolation is the primary cause for thunderstorm formation. This is in contrast to the present beliefs about thunderstorm formation in Alaska (Grice and Comisky, 1976).

The occurrence of preferred zones suggests that convective activity in the initial stages occurs as a result of the interaction between solar heating and terrain. Certain changes in the wind direction in these preferred zones are noticeable during the afternoon, presumably as a result of the solar heating on mountain slopes. But the moisture and energy to convert these convective clouds to thunderstorms must come from large scale weather systems.

Satellite imagery also proves useful in delineating such systems. Using this imagery and the weather maps we have been able to differentiate four particular weather patterns conducive to the formation of thunderstorms. These are:

(1) Easterly flow aloft with low level moisture coming in from the southeast. A deep vertical low over the Gulf of Alaska was the most significant feature of this pattern. This pattern gives rise to thunderstorm activity over the central and east-central part of the State.

(2) North-westerly flow aloft with moisture coming in from southeastern Bering Sea. This type of flow results from a stagnant cold front over western part of the State. This pattern gives rise to thunderstorm activity over west-central sector of the State.

(3) A quasi-stationary Arctic front from north-northeast on the surface with a distinct dry line along the Brooks Range. This type of pattern gives rise to thunderstorms oriented along the mountain range.

(4) Similar to the previous system, except for a closed low over the central interior. This pattern gives rise to scattered thunderstorms instead of a line formation.

Our studies so far indicate that all thunderstorm activity in the State fall into these four weather patterns. The ability to clarify thunderstorms thus shows that major weather systems are an essential feature for the formation of thunderstorms in Alaska. The solar insolation may only be the initial cause of convection.

We have attempted in this paper to demonstrate the ability of very high resolution satellite imagery to furnish useful information for cloud climatology studies. Admittedly these are only preliminary attempts and our conclusions are based on few years data. However, the results to date suggest that for areas lacking in observational stations, satellite imagery will both supplement and complement the existing information on weather.

6. ACKNOWLEDGMENTS

This work was supported by the Office of Naval Research, Arctic Program, grant number N00014-76-C-0443 and by State of Alaska funds.

7. REFERENCES

Biswas, A. K. and K.O.L.F. Jayaweera, NOAA-3 satellite observations of thunderstorms in Alaska, Mon. Wea. Rev. (in press) 1976.

Burns, B. M., The climate of the Mackenzie Valley-Beaufort Sea, Environment Canada, 2, 9, 1974.

Comisky, A. L. The insolation index and its use for forecasting thunderstorms in Alaska, Proceedings Western Region Fire Weather Conference, March 23-25, Portland, Oregon, 1966.

Grice, G. K. and A. L. Comisky, Thunderstorm climatology of Alaska, NOAA Tech. Memo NWS AR-14, NOAA/NWS, 36, 1976.

Henderson, P. M., Cloud conditions over the Beaufort Sea, Publications in Meteorology, 86, McGill University, Montreal, Canada, 1967.

Herman, G. F., Radiative-diffusive models of the arctic boundary layer, Scientific Report No. 3, Dept. of Meteorology, Massachusetts Institute of Technology, Cambridge, Mass., 1975.

Huschke, R. E., Arctic cloud statistics from "air-calibrated" surface weather observations, RAND Corporation Memorandum RM-6173-PR, 1969.

Hunt, G. E., Radiative properties of terrestrial clouds at visible and infrared thermal window wavelengths, Q. J. Roy. Met. Soc., 99, 337-345, 1973.

Jayaweera, K.O.L.F. and T. Ohtake, Concentration of ice crystals in arctic stratus clouds, J. Res. Atm., 7, 199-207, 1973.

Jayaweera, K.O.L.F. and K. Ahlnas, Detection of thunderstorms from satellite imagery for forest fire control, J. Forestry, 72, 677-690, 1974.

Sullivan, W.G., Jr., Low-level convergence and thunderstorms in Alaska, Mon. Wea. Rev., 91, 89-92, 1963.

5.1.5

SATELLITE CLOUD CLIMATOLOGY OF SUMMERTIME CUMULUS RESEARCH AREAS

Richard W. Stodt and Lewis O. Grant
Department of Atmospheric Science
Colorado State University
Fort Collins, Colorado

1. INTRODUCTION

Satellite imagery produced by the Defense Meteorological Satellite Program (DMSP) has provided very high resolution visual images of the western United States once daily during daylight hours from each satellite. This study utilizes DMSP data available for the summer of 1974 to construct a cloud climatology of areas where weather modification or cloud physics experiments are currently being conducted or planned. These areas include the three High Plains Experiment (HIPLEX) sites at Colby, Kansas (CBY), Big Springs, Texas (BGS), and Miles City, Montana (MLS); South Park, Colorado (SPK), where the South Park Area Cumulus Experiment (SPACE) is being conducted; and the National Hail Research Experiment (NHRE) area in northeastern Colorado. The Palmer Lake Divide region (PLD) located between Denver and Colorado Springs, Colorado, and the upper Arkansas River Valley (ARK) between Buena Vista and Leadville, Colorado, were chosen for thier proximity to current weather modification projects and their potential as sites for new weather modification studies.

The satellite used in this study is sun-dynchronous polar orbiter passing over the study areas at approximately 1200 local time. Digital data tapes were produced from the transparencies and a computer analysis was accomplished, producing areas and numbers of clouds for each area and day as well as providing data for cumulative averages over selected time periods for each study area. Cloud locations and sizes were stratified with respect to a subjective cloud classification scheme as well as with respect to synoptic weather conditions. The relationship between cloudiness and topographic features was also examined.

2. DELINEATION OF STUDY AREAS

Figure 1 shows the location and shape of each of the areas analyzed in this study. The three HIPLEX sites are circles with a 112 km (60 n.m) radius from MLS, CBY, and BGS. These sites are included even though a similar study has already been performed for the summers of 1972-74 using data from the ATS-III satellite (Reynolds and Vonder Haar, 1975) since the DMSP satellite data has better resolution. The NHRE area was described for analysis purposes by using the 1973 borders of the NHRE study area (NCAR, 1974). The PLD area was chosen with the western border at the edge of the Front Range of the Colorado Rockies. The eastern border is the most easterly extent of the divide itself, about 130 km (70 n.m) east of the mountains. The north-south extent of the study area is equal to the width of the divide. from the south edge of Denver to the north edge of Colorado Springs, a distance of about 90 km (50 n.m). The western boundary of this area was determined to have "hot spots" that favored thunderstorm formation (Henz, 1973). The South Park study area (SPK) was chosen to provide satellite data coverage of the geographical area of interest in the South Park Area Cumulus Experiment (SPACE) presently being conducted by Colorado State University. The area was designed to include all of the topographical features known as South Park as well as to have a rectangular shape for ease in computer processing of data. The area for which satellite data is analyzed is bounded by the crest of the Mosquito Range to the west, the Kenosha and Tarryall Ranges to the east, a latitude line through Buena Vista on the south, and the Continental Divide to the north. The area is approximately 45 km (23 n.m) east-west and 65 km (35 n.m) north-south. The seventh area encompasses the upper

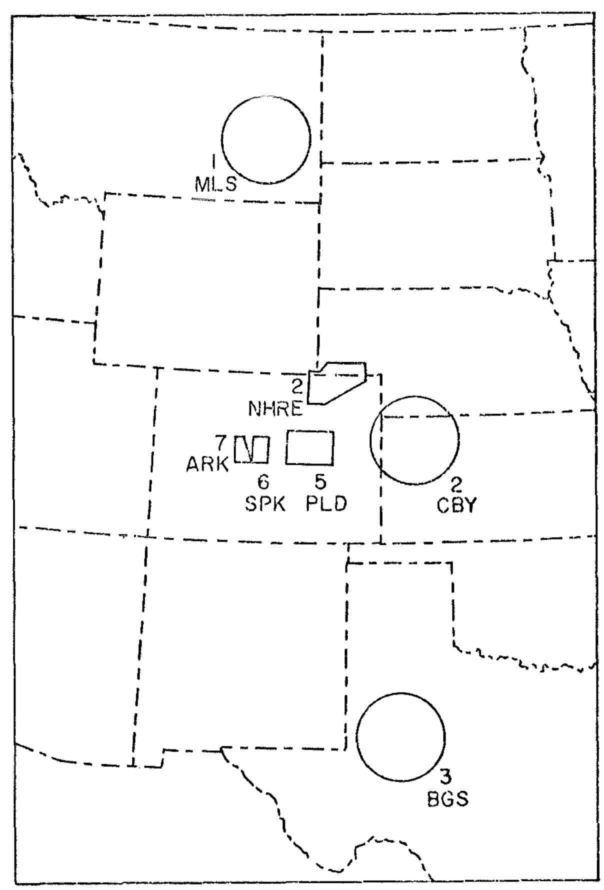

Figure 1. Study and analysis areas.

Arkansas River valley bounded roughly by the Continental Divide north of Leadville, on the north, the latitude of Buena Vista on the South, the Sawatch range to the west and the Mosquito range to the east. The area of study becomes narrower to the north as the river valley narrows. The approximate size is 65 km (35 n.m) north-south and averages 30 km (16 n.m) east-west. This area was chosen for study because of its proximity to SPACE.

3. SATELLITE SENSOR DATA

The DMSP satellite that produced the data used in this study is a polar orbiter with an average spacecraft height of 833 km (450 n.m). The orbit is circular with an angle of inclimation of 98.7°. This inclination angle was selected to insure the satellite orbit would be sun-synchronous at this altitude. (Dickinson et al, 1974) The nodal period of this sun-synchronous orbit is 101.56. Since the earth revolves under the orbit to the east, and the orbit precesses slightly to the east, each nodal crossing is approximately 25.4 degrees west of the previous crossing. The sensor scans 26.6 degrees of latitude across the subtrack. The very high resolution visual radiometer that provided the data for this study has a spectral range of 0.4 to 1.1 micrometers. The resolution of the imagery is nominally 0.6 km (.33 n.m) at the satellite subtrack. This degrades slowly to about 3.7 km (2 n.m) at the edge of the data due to foreshortening. It is interesting to note that while each nodal crossing is 25.4 degrees west of the previous crossing, the width of the scan track is 26.6 degrees of latitude. This causes a 1.2 degree overlap at the equator between successive passes which becomes progressively larger as the satellite approaches either pole. Although the resolution at the edge of the scan is degraded by foreshortening, if the area of interest falls near the edge of two successive passes, data can be obtained on cloud movement and cloud growth occurring during the 101.56 minute orbital period. The satellite used for this study (DSMP 8531) has a noontime sun-synchronous orbit. For the area of interest in this paper, a latitude range from 32 degrees to 47 degrees north, the longitude of the ascending node of the satellite is about 7 to 13 degrees east of the longitude of the satellite subtrack. Since best resolution is obtained when the satellite subtrack passes over or very close to the area of interest, the local solar time of satellite passover varies from about 20 minutes before local noon at BGS to about 35 minutes before local noon at MLS.

4. SITE IDENTIFICATION

The method chosen for accurately locating the study areas on the satellite imagery involved producing an overlay containing several properly located geographical reference points large enough to be easily visible on the imagery. The study areas were then accurately positioned on the overlay with respect to these landmarks. Since most days during the summer had large areas of clear skies, the method worked well. On days when landmarks were obscured by cloud, the study area overlay was accurately positioned using the grid supplied with the satellite imagery. It has been estimated that land or cloud features can be located to within 2.8 km (1.5 n.m) across track and 5.6 km (3.0 n.m) on the center line using the grid (Dickinson et al, 1974). The landmark method appeared to work equally well.

5. SYNOPTIC WEATHER PATTERN

In order to provide a better background for the cloud climatology data, a brief summary of significant weather patterns for Summer 1974 is included here. The weather of June 1974 was characterized by a well developed broad ridge over the western states which was accompanied by persistent clear skies, warmer than normal maximum temperatures, and generally below normal precipitation except for portions of western Kansas and eastern Colorado. The first week of June was cool and wet with snow falling in the Colorado mountains June 8 and 9. The warm and dry pattern became established the second week of June and maintained itself for the rest of the month (Taubensee, 1974). The mean 700 mb ridge migrated slightly eastward during July and became established over the Central Plains. The HIPLEX areas were warmer and drier than normal with the greatest precipitation deficiency being observed in the CBY and BGS areas. The Colorado mountain and plains areas generally reported near normal temperatures in the mountains (Wagner, 1974). There were marked circulation changes from July to August over the western states and Great Plains area. Troughing at 700 mb replaced the mean ridge over the central plains resulting in cooler than normal temperatures over the entire region. Precipitation was generally above normal in the southern and central plains, near normal in eastern Montana, with all the areas in Colorado involved in this study receiving less than normal precipitation (Dickson, 1974).

In Colorado during the summer months, storms typically form over the mountains, translate and propagate eastward onto the High Plains during the afternoon and evening. The mechanism for storm formation is a combination of diurnal heating and local mountain-valley breeze circulation. The propagation seems to be controlled by low level fluxes of heat and moisture, the stability, and the atmospheric wind structure (Erbes, 1976). Since this study is a climatology representing only one point in time during the day, this effect is reflected in the size and number of clouds observed in the areas.

6. DATA ACQUISITION

Very high resolution visual data for the months of June, July and August, 1974 were obtained from DMSP archives maintained by the University of Wisconsin, in the form of transparencies produced from original satellite analog data. Eighty-eight days of very high resolution (0.6 km) data were available and four days of high resolution (3.7 km) data making a complete set of 92 days of satellite imagery near local noon available for analysis. The scale of the 0.6 km data is 1:7,500,000 and the scale of the 3.7 km is 1:15,000,000. Two data reduction methods were employed. The first involved subjective classifications of clouds in

Table 1

This table shows the percentage of days of each type of major synoptic classification. Figures in parantheses indicate the percentage of occurrence of each cloud category within the mesoscale classification.

	EXPERIMENT SITES						
	1	2	3	4	5	6	7
CLOUD CLASSIFICATION	MLS	CBY	BGS	NHRE	PLD	SPK	ARK
COLD FRONT (Synoptic Scale)	19%	18%	7%	4%	2%	3%	3%
UPSLOPE	5%	5%	0	7%	6%	1%	1%
MESOSCALE	76%	77%	93%	89%	92%	96%	96%
SMALL CUMULUS < 2 km dia.	(31%)	(41%)	(36%)	(52%)	(25%)	(27%)	(29%)
ISOLATED CB	(33%)	(41%)	(27%)	(34%)	(65%)	(49%)	(44%)
CLOUD CLUSTER	(4%)	(14%)	(24%)	(2%)	(6%)	(20%)	(25%)
CLOUD LINE	(23%)	(2%)	(4%)	(10%)	(2%)	(2%)	(2%)
EMBEDDED CB	(9%)	(2%)	(9%)	(2%)	(2%)	(2%)	(2%)
TOTAL SAMPLE SIZE (days)	92	92	92	92	92	92	92
NO. OF DAYS WITH CLOUDS	59	61	59	46	65	76	75
% DAYS WITH CLOUDS	64%	66%	64%	50%	71%	83%	82%

the project areas by cloud type and cloud amount. The second method involved digitizing the images of project areas on the Optical Data Digitizer and Display System (OD^3) at Colorado State University. The components of the OD^3 system are a videcon camera, a television screen, a small computer, and a typewriter for transmitting instructions to the system. The computer was programmed to sense brightness levels from the screen and convert these into digital data. The data is stored on magnetic tape for later processing. For the digitizing process, one pixel or one data bit was equated to the resolution of the imagery such that the area represented by one pixel was equal to the highest resolution of the sensor.

7. DATA CLASSIFICATION

Subjective classification of the data with respect to synoptic and mesoscale influences was performed by inspection of the satellite imagery. Table 1 shows the categories used and the percentage of days during the summer that each of these cloud types and weather types was present. Three major categories , cold front, upslope, and mesoscale, were considered. Mesoscale systems were further divided and values in parentheses show the percentage of mesoscale days affected by the respective cloud types. These divisions were patterned after a cloud study of the HIPLEX areas by Reynolds and Vonder Haar (1975). The small cumulus category was added because of the increased resolving power available from the DMSP sensor. Mesoscale processes dominated the weather pattern over the region for most of the summer. The two most common mesoscale cloud types observed on the noontime imagery at all areas were the small cumulus, and the isolated cumulonimbus. From Table 1 it is seen that imbedded cumulonimbi account for 9% of the mesoscale occurrences at MLS, 2% at CBY, and 9% BGS. If the small cumulus category is removed to make the data more comparable with the Reynolds and Vonder Haar study and the mesoscale percentages are recalculated, imbedded cumulonimbi then account for 13% of the mesoscale weather occurrences at MLS, 3% at CBY, and 14% at BGS. These percentages are larger than those determined by the previously mentioned study, no doubt due in part to the better resolution of the DMSP data. Frontal activity was more apparent at MLS and CBY than at any of the other areas. In both cases, most of this activity was observed during the month of August. Surface frontal systems did not appear to penetrate as far south as BGS until the last few days of August. A large number of days when no clouds could be seen occurred at every area except SPK and ARK. The fewer number of clear days at these stations can be considered an indication of the effectiveness of the surface heating, mountain-valley circulation regime in producing cumulus clouds. These statistics, though in similar format to Reynolds and Vonder Haar (1975), are not directly comparable due to the inclusion of 1972 and 1973 data in the previous study.

8. DATA ANALYSIS

The digitized data discussed in Section 6 has been subjected to a number of tests. The first involved determining cloud sizes and cloud numbers for each of the areas for the summer of 1974. This is done by selecting a brightness threshold for the cloud border and summing all of the pixels within that border to determine the total area of the clouds.

The cloud brightness threshold was chosen by comparison of printouts of cloud pictures with printouts of actual digitized brightness values for each file. The computer senses each closed threshold brightness value contour as a cloud. The total number of clouds per site, the total cloud coverage for the day studied, and the average size of the clouds within the site area were calculated. Table 2 presents a summary of this output for the month of July 1974. Three tabulations are presented, the average percent of cloud cover, the average number of clouds normalized to an area of 10,000 km^2, and the average size of the cloud in km^2 for each study area. At both MLS and CBY the average cloud size was relatively large but the number of clouds per 10,000 km^2 was low. These data would seem to indicate that when convective activity was present at noon it was already well developed. The data for BGS in conjunction with Table 1, showed that large numbers of small cumulus clouds predominated at noon but that the few cases when larger cumulonimbi were present increased the average individual cloud area. NHRE, PLD, SPK, and ARK, when considered together, corroborate the description of a typical weather day over the mountains and high plains of Colorado. Since SPK and ARK are both located in the mountains, a noontime climatology should show a relatively high amount of clouds in these areas. This was, in fact, the case with SPK and ARK having an average cloud cover of 20.3% and 27% respectively. There were a large number of clouds present with individual clouds having relatively large sizes. PLD, located adjacent to a "hot spot" for thunderstorm development had less average cloud cover than the mountain areas and fewer clouds. Since all of the activity analyzed at PLD for this month was convective, the clouds that were present at this time were already well developed and they tended to be positioned at the western edge of the area. NHRE, being further away from the mountains had a low average percent cloud cover, few clouds, and a small average cloud size. On most days during the month the mountain thunderstorm cycle did not begin early enough for large cells to reach NHRE by pass time. Although not applicable to these data sets, cloudiness should have increased in the NHRE, MLS, CBY, BGS, and PLD areas later in the afternoon due to eastward translation and propagation of mountain induced thunderstorms, with a corresponding decrease in mountain cloudiness.

9. SUMMARY

Mesoscale processes dominated the weather pattern over the entire study region, more so over the mountains than over the plains areas. The smallest and least developed clouds were observed at NHRE. More developed, larger clouds were observed at the three HIPLEX areas, more so in the northern and central plains, probably due to a greater frequency of synoptic scale effects. PLD, SPK, and ARK were all similar in cloud size. The least number of clouds present were on the central northern plains averaging 4 to 6 per 10,000 km^2. More clouds were present at BGS and PLD, but, by far, the greatest number of clouds were present over the mountain areas. Average coverage was sparse everywhere east of the mountains at this time with the greatest percent cloud cover over the mountain sites. This compares well with the typical diurnal summertime cloud regime over Colorado. These satellite data are a valuable tool for determining cloud popolations and with the advent of geosynchronous satellite data. Cloud systems can be followed from development to dissipation at half hour time increments.

10. ACKNOWLEDGEMENTS

This research was supported in part by the National Aeronautics and Space Administration under Grant NSG-5011 and by the National Science Foundation under Grant ERT 71-01885-A03.

11. REFERENCES

Dickinson, L.G., S.E. Boselly, III, and W.W. Burgmann, 1974: Defense Meteorological Satellite Program (DMSP) User's Guide. AWS-Tech. Report 74-250, 98 pp.

Dickson, R. R., 1974: Weather and Circulation of August 1974 - Relief from Heat and Drought in the Central United States. Mon. Wea. Rev., 102., 807-811.

Erbes, R. E., and L.O. Grant, 1976: A Kinematic Description of some Colorado Thunderstorms. Preprints of Int'l Cloud Physics Conf., Boulder, Colorado.

Henz, J. F., 1973: Characteristics of Severe Convective Storms on Colorado's High Plains. Proc. 8th Conf. on Severe Local Storms, Amer. Meteor. Soc., 96-103.

NCAR, 1974: Calendar of Events During 1973 Field Operations of the National Hail Research Experiment. NHRE Data Report No. 73/1, 62 pp.

Reynolds, D.W., and T. H. Vonder Haar, 1975: Satellite Support to the HIPLEX Activities for 1974. Final Report to Bureau of Reclamation, Contract No. 14-06-D-7630, 137 pp.

Taubensee, R. E., 1974: Weather and Circulation of June 1974 - Increasing Drought in the Northwest. Mon. Wea. Rev., 102, 662-666.

Wagner, A.J., 1974: Weather and Circulation of July 1974 - Heat Wave and Drought Over the Middle Third of the Country. Mon. Wea. Rev., 102, 736-742.

Table 2

Mean values for days with clouds, July 1974

	MLS	CBY	BGS	NHRE	PLD	SPK	ARK
Average Cloud Cover (Percent)	4.9	10.1	8.3	4.4	11.1	20.3	27.0
Average Number of Clouds/10,000 km^2	4	6	9	8	7	18	19
Average Size of Cloud km^2	144.1	172.1	87.3	54.7	158.1	115.2	140.5

5.2.1

EFFECTS OF THE LIFE-CYCLES OF CUMULUS CLOUDS ON THE LARGE-SCALE HEAT AND MOISTURE BUDGETS

Han-Ru Cho

Department of Physics
University of Toronto
Toronto, Ontario, Canada

1. INTRODUCTION

Two heating mechanisms of cumulus clouds on large-scale weather systems have been proposed in the past. Kuo (1965) proposed that the heating of the atmosphere by cumulus clouds is accomplished by the mixing of the warmer cloud air with the environmental air. Ooyama (1971) and Arakawa and Schubert (1974) proposed that the cloud induced subsidence in the cloud environment is the main heating mechanism. In Ooyama's formulation, cumulus clouds are represented by an ensemble of rising bubbles of various sizes generated in the sub-cloud layer. In Arakawa and Schubert's formulation, a simple one-dimensional steady state plume model is used to represent the behaviour of cumulus clouds. Fraedrich (1973) has shown that both heating mechanisms discussed above can be formulated into the cloud-environment interaction equations if finite life-cycles of cumulus clouds are taken into account. The reason that the mechanism proposed by Kuo does not appear in Arakawa and Schubert's formulation is because in their derivation a steady state cloud model is used. The purpose of this paper is to derive the effects of life cycles of cumulus clouds on large-scale heat and moisture equations by introducing a cloud distribution function which is a function of cloud top height as well as cloud age. The cloud time scale is carefully separated from the time scale of large-scale processes. As a result, the derivation and the results are somewhat different from Fraedrich's formulation. The effects of cloud life-cycles are represented in terms of a recycling rate of the atmospheric air by cumulus clouds as a function of height. The formulation is then applied to a typical trade wind weather situation observed during Phase III of BOMEX to identify the cloud life-cycle effects. Both the total cloud mass flux and the effective recycling rate as functions of height are determined.

2. FORMULATION

The large-scale heat and moisture equations, when including the effects of cumulus clouds, have the following forms:

$$Q_1 = \frac{\partial \bar{s}}{\partial t} + \nabla\cdot\bar{v}\bar{s} + \frac{\partial \bar{\omega}\bar{s}}{\partial p} = L(\bar{c}-\bar{e}) - \frac{\partial \overline{\omega' s'}}{\partial p} + Q_R \qquad (1)$$

$$Q_2 = -L\left(\frac{\partial \bar{q}}{\partial p} + \nabla\cdot\bar{v}\bar{q} + \frac{\partial \bar{\omega}\bar{q}}{\partial p}\right) = L(\bar{c}-\bar{e}) + L\,\frac{\partial \overline{\omega' q'}}{\partial p} \qquad (2)$$

Here s is the dry static energy, q the water vapour mixing ratio, c the rate of condensation of water vapour, e the rate of evaporation of liquid water, L is the latent heat, Q_R is the radiative heating rate. The overbar has been used to denote the average over an area A which is large enough to contain a large number of cumulus clouds, yet small enough to be considered as a small fraction of the large-scale weather systems. Q_1 and Q_2 are customarily referred to as the apparent heat source and apparent moisture sink, respectively.

Let us first classify various types of cumulus clouds according to the maximum cloud top height reached by a cloud. We shall assume that clouds with the same maximum cloud top height have the same properties and go through the same life cycle. Let τ be used to denote the age of a cumulus cloud and τ_p be the life span of cumulus clouds with maximum cloud top height p. We shall define a cloud distribution function $f(\tau,p,t)$ as the fractional area density function at time t for clouds with maximum cloud top height p and age τ. $f(\tau,p,t)\,\Delta p\Delta\tau$ gives the total fractional area covered by clouds with the maximum cloud top height $p - \Delta p/2 < p < p + \Delta p/2$ and age $\tau - \Delta\tau/2 < \tau < \tau + \Delta\tau/2$. The fractional coverage density function $\sigma(p,t)$ which has been used by previous investigators can be defined as

$$\sigma\,(p,t) = \int_o^{\tau_p} f(\tau,p,t)d\tau \qquad (3)$$

Let T_c be the maximum life span of all types of clouds, and T_L be the time scale for the large-scale process. Typical magnitudes of T_c and T_L are of the order of 10^3 and 10^5 seconds, respectively. We note that $f(o,p,t)$ gives the rate of generation of clouds with maximum cloud top height p at time t. At time t, clouds of age τ were generated at time $t - \tau$. It follows then that $f(\tau,p,t) = f(o,p,t-\tau)$. Since f is a large-scale variable and $\tau < T_c << T_L$, we can show by Taylor series expansion that, within an error of the order of T_c/T_L, $f(\tau,p,t)$ is constant in τ. The number of clouds is uniformly distributed among all stages of development and

$$f(\tau,p,t) = \frac{\sigma(p,t)}{\tau_p}\left[1 + 0\,(T_c/T_L)\right] \qquad (4)$$

The sensible and latent heat fluxes due to cumulus clouds can be expressed in terms of the cloud distribution function:

$$\overline{\omega' s'} = \int_{p_T}^{p} \int_{o}^{\tau_{p'}} f(\tau,p',t)\omega_c(t,p;\tau,p')\left[s_c(t,p;\tau,p') - \bar{s}\right]d\tau dp' \quad (5)$$

and

$$\overline{\omega' q'} = \int_{p_T}^{p} \int_{o}^{\tau_{p'}} f(\tau,p',t)\omega_c(t,p;\tau,p')\left[q_c(t,p;\tau,p') - \bar{q}\right]d\tau dp' \quad (6)$$

Here, the subscript c is used to denote cloud variables. If x_c is a cloud variable, $x_c(\tau,p;\tau,p')$ denotes the value of x_c at time t and height p for clouds with maximum cloud top height p' and age τ. The cloud properties s_c and q_c should be determined from the governing equations for cumulus clouds. Let us consider a cloud generated at time t_o. At time $t < t_o + \tau_{p'}$, the age of the cloud is $\tau = t-t_o$. The equations governing s_c and q_c can be written as

$$\frac{\partial}{\partial t} s_c(t,p;t-t_o,p') + \nabla\cdot V_c s_c + \frac{\partial \omega_c s_c}{\partial p} = L(c-e) \quad (7)$$

$$\frac{\partial}{\partial t} q_c(t,p;t-t_o,p') + \nabla\cdot V_c q_c + \frac{\partial \omega_c q_c}{\partial p} = e-c \quad (8)$$

Multiply these equations by $f(t-t_o,p',t)$, one obtains the following equations:

$$\frac{\partial}{\partial t}\left[f(t-t_o,p',t)s_c(t,p;t-t_o,p')\right] + f\nabla\cdot V_c s_c + \frac{\partial f\omega_c s_c}{\partial p} - s_c\frac{\partial f}{\partial t} = L\ f\ (c-e) \quad (9)$$

$$\frac{\partial}{\partial t}\left[f(t-t_o,p',t)q_c(t,p;t-t_o,p')\right] + f\nabla\cdot V_c q_c + \frac{\partial f\omega_c s_c}{\partial p} - q_c\frac{\partial f}{\partial t} = f\ (e-c) \quad (10)$$

Since f is a large-scale variable, the last terms of the left-hand sides of equations (9) and (10) are at most of the order of $s_c f/T_L$ and $q_c f/T_L$. On the other hand, since q_c and s_c are cloud variables, the magnitudes of the first terms on the left-hand sides of the equations are of the order of $fs_c/\tau_{p'}$ and $fq_c/\tau_{p'}$. We conclude therefore that the terms $s_c\ \partial f/\partial t$ and $q_c\ \partial f/\partial t$ can be neglected in the above equations with an error of the order of $\tau_{p'}/T_L$. We note that if x_c is a cloud variable,

$$\int_{p_T}^{p} \int_{o}^{\tau_{p'}} \frac{\partial}{\partial t}\left[f(\tau,p',t)x_c(t,p;\tau,p')\right]d\tau dp'$$

$$= \frac{\partial}{\partial t}\int_{p_T}^{p} \int_{t-\tau_{p'}}^{t}\left[f(t-t_o,p',t)x_c(t,p;t-t_o,p')\right]dt_o dp'$$

$$- \int_{p_T}^{p}\left[f(o,p',t)x_c(t,p;o,p') - f(\tau_{p'},p',t)\, x_c(t,p;\tau_{p'},p')\right]dp' \quad (11)$$

Here, p_T is the height of the tropopause. Since the ensemble average of a cloud property is a large-scale variable, it should vary according to the time scale of the large-scale process therefore, the first term on the right-hand side of the above equation is only of the order of $\int_{p_T}^{p} f\ x_c\ T_c/T_L\ dp'$. It can be neglected when compared with the second term. Substituting equations (4) through (11) into equations (1) and (2), one obtains

$$Q_1 - Q_R = L(\bar{c}-\bar{e}) - L\int_{p_T}^{p}\int_{o}^{\tau_{p'}} f(c-e)d\tau dp' + \int_{p_T}^{p}\frac{\sigma(p')}{\tau_{p'}}\left[s_c(\tau_{p'}) - s_c(o)\right]dp' + \int_{p_T}^{p}\int_{o}^{\tau_{p'}} f\left[\nabla\cdot V_c s_c + \bar{s}\frac{\partial\omega_c}{\partial p}\right]d\tau dp' + \left[\int_{p_T}^{p}\int_{o}^{\tau_{p'}} f\ \omega_c\ d\tau dp'\right]\frac{\partial\bar{s}}{\partial p} \quad (12)$$

$$Q_2 = L(\bar{c}-\bar{e}) - L\int_{p_T}^{p}\int_{o}^{\tau_{p'}} f(c-e)d\tau dp' - L\int_{p_T}^{p}\frac{\sigma(p')}{\tau_{p'}}\left[q_c(\tau_{p'}) - q_c(o)\right]dp' - L\int_{p_T}^{p}\int_{o}^{\tau_{p'}} f\left[\nabla\cdot V_c q_c + \bar{q}\frac{\partial\omega_c}{\partial p}\right]d\tau dp' - L\left[\int_{p_T}^{p}\int_{o}^{\tau_{p'}} f\ \omega_c\ d\tau dp'\right]\frac{\partial\bar{q}}{\partial p} \quad (13)$$

In defining the cloud distribution function, it is necessary to distinguish between areas occupied by clouds and the clear air. In Arakawa and Schubert's formulation as well as in recent diagnostic studies by Yanai, et. al. (1973), and Ogura and Cho (1973) cloud areas are identified as the regions occupied by condensation induced updrafts. The compensating downward motion induced by cumulus clouds is assumed to spread uniformly in the area surrounding the clouds. One apparent defect of this simple cloud picture is that it does not take into account the fact that strong downdraft is usually observed in the immediate surrounding area of the updraft region. These strong downdrafts are generally believed to be induced by the evaporation of cloud liquid water when the cloud air mixes with the unsaturated environmental air. In order to take this into account, we shall define an area occupied by a cloud as the region of the air above the cloud base level that is not in hydrostatic balance with the large-scale environment. This definition is essentially the same as that given by Fraser (1968). For simplicity, we shall neglect the virtual temperature effect and assume that the cloud air comes into hydrostatic equilibrium with the environment if and only if the cloud air temperature equals the environment air temperature.

According to this definition, the area covered by a cloud is somewhat larger than the area covered by the updraft of the cloud, which will be referred to as the core region of the cloud. The region of the cloud outside the core region will be referred to as the outer region. In the outer region of a cloud, air from the environment mixes with the air from the core region. The thermodynamics of mixing in this outer region has been studied by Fraser (1968). Generally speaking, the air temperature in the outer region decreases from the boundary of the core region and reaches a minimum at the visible edge of a cumulus cloud where the liquid water content vanishes. At the visible edge of a cloud, the cloud temperature is lower than the environmental temperature. The cloud air temperature increases gradually from the visible edge of the cloud to the environmental air temperature at the outer boundary of the cloud. The water vapour mixing ratio decreases monotonically to the value of the environmental air from the boundary of the core region to the outer boundary of the cloud. Since the cloud temperature and water vapour mixing ratio equal those of the environment at the outer boundary, the heat and moisture fluxes going into and out of a cloud at the cloud boundary due to air convergence or divergence can be expressed as

$$\int_{a_c} \nabla\cdot V_c s_c da = \oint V_n \bar{s} d\ell \quad \text{and}$$

$$\int_{a_c} \nabla\cdot V_c q_c da = \oint V_n \bar{q} d\ell \tag{14}$$

Here, the line integrals are carried around the cloud boundary. V_n is the component of the horizontal wind velocity perpendicular to the boundary of the cloud. a_c is the horizontal cross-sectional area of the cloud. We shall assume that condensation of water vapour is realized mostly within cumulus clouds:

$$\bar{c} = \int_{p_T}^{p} \int_{o}^{\tau_{p'}} f\ c\ d\tau\ dp' \tag{15}$$

Since the evaporation of cloud liquid water produces cooling effect and leads to negative buoyancy, it must happen mostly within the cloud areas. We may also assume that

$$\bar{e} = \int_{p_T}^{p} \int_{o}^{\tau_{p'}} f\ e\ d\tau\ dp' \tag{16}$$

Before a cumulus cloud is initiated, the air in a cloud region is the same as the environmental air. This implies that

$$s_c(\tau=0) = \bar{s} \quad \text{and} \quad q_c(\tau=0) = \bar{q} \tag{17}$$

Incorporating equations (14) through (17), equations (12) and (13) can be simplified to become

$$Q_1 - Q_R = \int_{p_T}^{p} \frac{\sigma(p')}{\tau_{p'}} \left[s_c(\tau_{p'})-\bar{s}\right]dp' - M_c \frac{\partial\bar{s}}{\partial p} \tag{18}$$

$$Q_2 = -L \int_{p_T}^{p} \frac{\sigma(p')}{\tau_{p'}} \left[q_c(\tau_{p'})-\bar{q}\right]dp' + L\ M_c \frac{\partial\bar{q}}{\partial p} \tag{19}$$

Here, M_c defined by

$$M_c = -\int_{p_T}^{p} \int_{o}^{\tau_{p'}} f\ \omega_c\ d\tau dp'$$

is the total cloud mass flux. The end of a cloud life-cycle shall be defined at the stage of cloud development when the cloud area reaches hydrostatic balance again with the large-scale environment. At this stage, the cloud vertical circulations cease to operate and $s_c(\tau_{p'}) = \bar{s}$ if the virtual temperature effect is neglected. Equation (18) can be further reduced to become

$$Q_1 - Q_R = -M_c \frac{\partial\bar{s}}{\partial p} \tag{20}$$

The first terms on the right-hand sides of equations (18) and (19) represent the effects of cloud life-cycles. These effects were first discussed by Fraedrich (1973). Through his analysis, he found that the half-lifetimes of the clouds, instead of the lifetime $\tau_{p'}$, should be used in the denominators of these terms. Furthermore, instead of $s_c(\tau_{p'})$ and $q_c(\tau_{p'})$, the values of s_c and q_c at the mature stages of the clouds were used. The other terms in equations (18), (19) and (20) are essentially the same as those derived by Ooyama, and Arakawa and Schubert, except that average over cloud life cycles is introduced in defining M_c.

3. APPLICATION

The meteorological data selected for this study to estimate the cloud life-cycle effects were collected during Phase 3 of the Barbados Oceanographic and Meteorological Experiment (BOMEX). The large-scale heat and moisture budgets for the period of Phase 3 of the BOMEX have been analyzed by Nitta and Esbensen (1974). During an undisturbed period (22-26 June, 1969) of Phase 3 of BOMEX, mean thermodynamic profiles show a typical trade wind inversion layer lying between 840 mb and 780 mb level. Within this layer, dry static energy increases rapidly and water vapour mixing ratio decreases rapidly. Q_1 and Q_2 profiles show a large apparent heat sink and a large apparent moisture source near the top of the trade inversion layer. Both Q_1 and Q_2 values decrease rapidly to zero above the inversion layer, indicating that few clouds have penetrated above the 700 mb level.

Based upon Nitta's mean Q_1 and Q_R profiles, the vertical profile for the total cloud mass flux M_c has been computed and is presented in Figure 1. In the figure, $\bar{M} = -\bar{\omega}$ is the mean large-scale vertical flux. $\tilde{M}$ is the vertical mass flux in the clear area between the clouds. The value of M_c is negative between 700 mb and 850 mb levels, and is positive between 850 mb and the cloud base level. The negative values of M_c between 700 and 850 mb are caused by the downdrafts induced by the evaporative cooling effects of cloud liquid droplets. Within the inversion layer, because of the strong static stability, cloud air diverges from the stunted cumulus clouds and mixes with the environmental air. This produces a large amount of evaporation of cloud liquid water and accounts for the large apparent moisture source, the large apparent heat sink, and the negative cloud mass flux within the inversion layer.

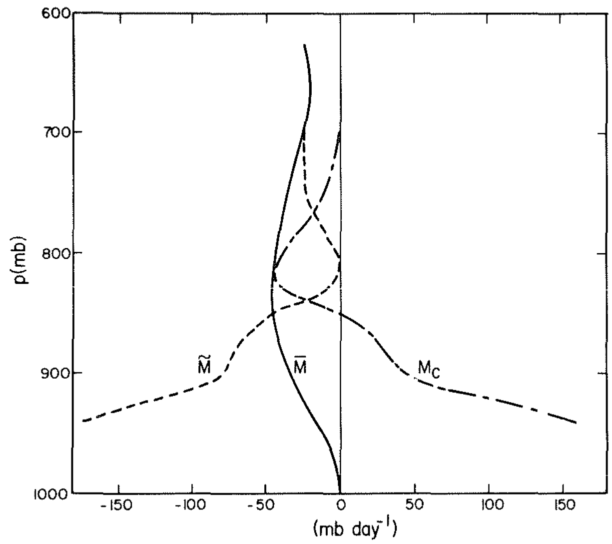

Figure 1. Vertical distributions of the large-scale mean vertical mass flux $\bar{M}$, the total cloud mass flux M_c, and the vertical mass flux in the environment of clouds $\tilde{M}$.

The total cloud mass flux and the cloud spectrum distribution for the same case studied here have also been determined by Nitta (1975). In his study, a steady state entraining plume model was used as the cloud model. Since the evaporation induced downdraft is not counted as part of the cloud mass flux in this model, M_c values determined by Nitta are positive everywhere. The values of M_c and $\tilde{M}$ at the cloud base level were found to be about 273 and -289 mb day^{-1}, respectively. The values of M_c and $\tilde{M}$ determined according to the present formulation are about 160 and -173 mb day^{-1}. The differences could have been caused by several factors. Besides the effect of the evaporation induced downdrafts, Nitta's values of M_c and $\tilde{M}$ are rather sensitive to the assumptions of cloud base conditions. By considering the sub-cloud layer budgets, Sarachik (1974) concluded that Nitta's value of $\tilde{M}$ (and therefore M_c) has been overestimated by about a factor of two. In order to fit the observational data, Sarachik found that the $\tilde{M}$ value at the cloud base level should be about -154 mb day^{-1}. This value agrees fairly well with the value determined by the present formulation.

Figure 2 shows the balance of the moisture budget equation. In the trade inversion

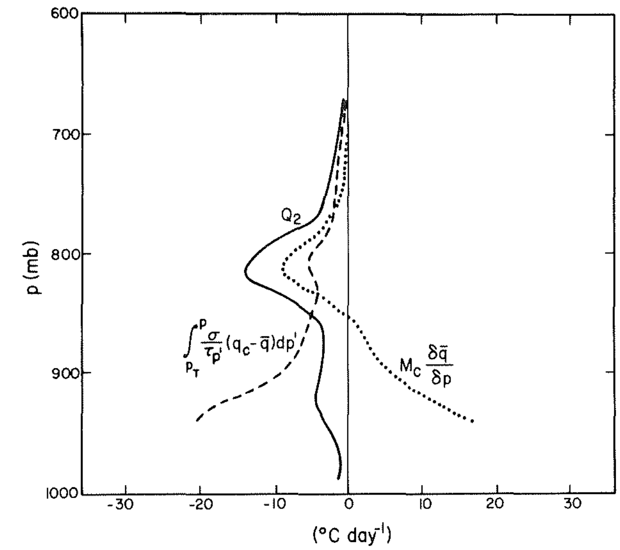

Figure 2. Vertical distributions of the contributions of various physical processes to the large-scale moisture balance.

layer, both the cloud life-cycle and the cloud induced circulation have moistening effect. Below the inversion layer, the cloud induced circulations have a drying effect, while the cloud life cycles have a moistening effect. The cloud life-cycle effect on the moisture budget equation can be used to determine the $\sigma(p')/\tau_{p'}$ distribution as a function of p'. To do this, one needs to know the cloud moisture distributions $q_c(p)$ at the ends of cloud life-cycles. Since it seems reasonable to assume that $q_c(t,p;\tau_{p'},p')$ is not far from the saturation mixing ratio $\bar{q}^*$, we shall define the effective fractional cloud coverage $\sigma^*(p')$ by the equation

$$(\bar{q}^*(p)-\bar{q})\int_{p_T}^{p} \frac{\sigma^*(p')}{\tau_{p'}}\,dp' = \int_{p_T}^{p} \frac{\sigma(p')}{\tau_{p'}}\,(q_c(\tau_{p'})-\bar{q})dp'$$

The quantity $\int_{p_T}^{p} \frac{\sigma^*(p')}{\tau_{p'}}\,dp'$ can be interpreted as

the effective recycling rate of the atmospheric air by cumulus clouds at level p. The vertical distribution of this effective recycling rate has been computed and is presented in Figure 3. It is a monotonically increasing function of p as it should be since $\sigma(p')$ and, therefore, $\sigma^*(p')$ are positive quantities. The recycling rate at the cloud base level is about 2.7 day^{-1}. It implies that the entire layer of atmospheric air at the cloud base level is processed by cumulus clouds about 2.7 times a day. The recycling rate is about 0.5 day^{-1} near the base of the inversion layer, and becomes zero near the top of the inversion layer.

The total cloud mass flux at the cloud base level, M_{cB}, can be expressed in terms of the total cloud fractional coverage and the average cloud base vertical velocity ω_{cB}:

$$M_{cB} = -\int_{p_T}^{p_B}\int_{o}^{\tau_{p'}} f\ \omega_c(p_B)d\tau dp' = -\ \omega_{cB}\int_{p_T}^{p_B} \sigma(p')dp'$$

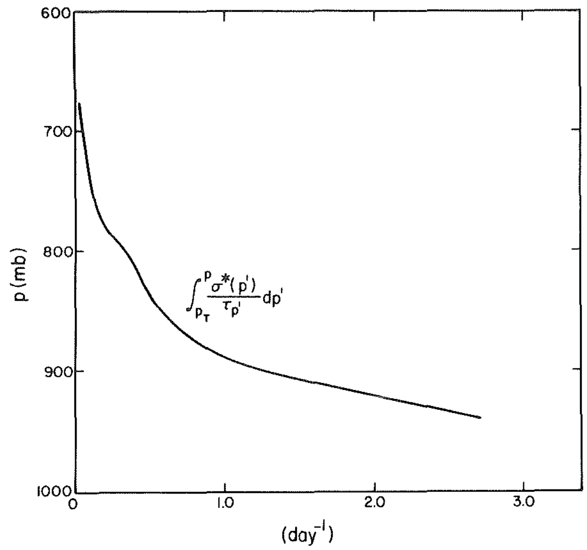

Figure 3. Vertical distribution of the effective recycling rate of atmospheric air by cumulus clouds.

On the other hand, the recycling rate at the cloud base level can be expressed in terms of the total fractional cloud coverage and a weighted mean life span of the cloud population τ^*:

$$\int_{p_T}^{p_B} \frac{\sigma(p')}{\tau_{p'}} dp' = \frac{1}{\tau^*} \int_{p_T}^{p_B} \sigma(p')dp'$$

If one assumes that the value of ω_{cB} is of the order of 1 m sec^{-1}, the value of the fractional cloud coverage estimated from M_{cB} will be about 1.7%. Since σ and σ^* should be at least of the same order of magnitude, the mean life span τ^* estimated from the effective recycling rate will be of the order of 9 minutes. These values completely depend on our assumption about the value of ω_{cB}. If the value of ω_{cB} is 0.5 m sec^{-1}, the values for σ and τ^* should be 3.4% and 18 minutes, respectively.

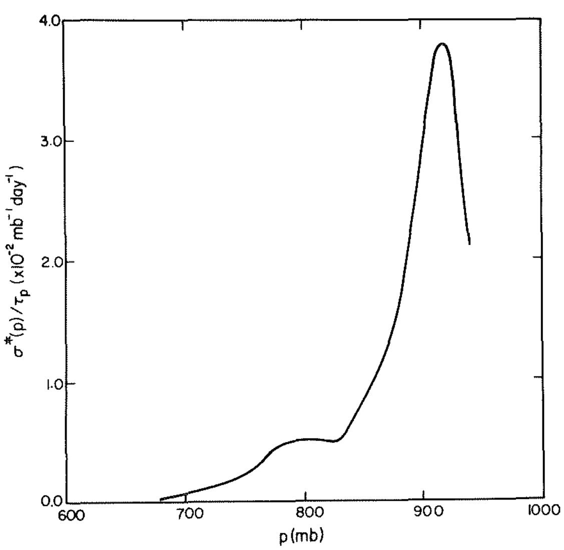

Figure 4. Vertical distribution of $\sigma^*(p)/\tau_p$.

The $\sigma^*(p)/\tau_p$ distribution as a function of cloud top height p is plotted in Figure 4. Its value reaches a maximum at the 920 mb level, then decreases to about 2.1 x 10^{-2} mb^{-1} day^{-1} at the cloud base. The $\sigma^*(p)$ distribution can not be determined because of the lack of information about τ_p. If we assume that the value of τ_p decreases monotonically with p, and approaches zero as p goes to p_B, $\sigma(p)$ should approach zero at the cloud base level. This implies that the cloud spectrum distribution $m_B(p)$ defined by

$$m_B(p) = - \sigma(p)\ \omega_{cB}$$

should also go to zero at $p = p_B$. These results seem to disagree with the results of previous diagnostic studies using a time independent cloud model (e.g., Nitta, 1975) where it is found that $m_B(p)$ reaches a maximum at the cloud base.

4. CONCLUSIONS

The effects of the life cycles of cumulus clouds on large-scale heat and moisture budgets are derived in this paper by introducing a cloud distribution function which is a function of both the maximum cloud top height as well as the cloud age. These effects are found to be proportional to the fractional cloud coverage and the differences between cloud thermodynamic properties at the ends of cloud life cycles and the large-scale mean thermodynamic properties, and inversely proportional to the life spans of clouds. The formulation has been applied to a typical trade wind weather situation observed during Phase 3 of BOMEX. Both the total cloud mass flux and the effective recycling rate of atmospheric air by cumulus clouds are determined. The cloud life cycles are found to have a very significant effect on the balance of the large-scale moisture budget in the trade wind weather situation.

Recently, Soong and Ogura (1976) have used an axisymmetric numerical cloud model to determine the cloud population associated with an undisturbed period (June 22-23) of BOMEX Phase 3. Using the observed temperature and humidity profiles as the environmental conditions, a total of six classes of clouds, labelled A through F were simulated by varying several cloud parameters. To fit the large-scale heat and moisture budgets, they found that only three types of clouds, namely, cloud types A, D and E are needed. Cloud types A and D are shallow clouds with maximum cloud top height below the trade wind inversion layer. Cloud type E penetrates into the inversion layer. The variations of cloud variables as functions of radius at a mature stage of cloud type E have been presented by Soong and Ogura at the cloud base height and at a height near the base of the trade inversion layer. Their results show that the cloud core region, that is, the region where cloud temperature is warmer than that of the environment, has a radius of about 150 m. In this region, the vertical velocity is upward at both heights. Between radii 150 m and 400 m, cloud vertical velocity is downward at the base of the inversion layer. The total vertical cloud mass flux at the cloud base is of the order of 1.30 x 10^8 gm/sec at this mature stage. At the inversion base level, the upward mass flux in the core region is of the order of 3.04 x 10^8 gm/sec. The downward mass flux in the outer region is of the order of 5.48 x 10^8 gm/sec. Combined they give a net downward mass flux of the order of 2.44 x 10^8 gm/sec at the base of the inversion layer. Therefore at the mature stage of cloud type E, one unit of upward mass flux at the cloud base induces about two units of downward mass flux at the base of the inversion layer. How this ratio will be modified if the cloud mass fluxes are averaged over the life-cycle of the cloud cannot be determined exactly from the data presented by Soong and Ogura. The mature stage of cloud type E lasts about 20 minutes. It is preceded by 15 minutes of developing stage and followed by 15 minutes of decaying stage. Based upon the time-height cross section of vertical velocities at the cloud central axis presented in their paper, it seems that this ratio between the total mass flux at the inversion base and the total mass flux at the cloud base, averaged over the cloud life cycle, should not be too much different from two. Soong and Ogura have found that cloud type E contributes about 18% of the total cloud mass flux at the cloud base level. We may therefore conclude that the total cloud mass flux associated with the cloud population determined by Soong and Ogura should be downward at the base of the inversion layer, and its value should be about 36% of the total cloud mass flux at the cloud base height. Results of this study show that the M_c value at inversion base level is about -50 mb day^{-1}, which is about one third of the M_c value at the cloud base. This value, although rather large, may not be unreasonable when compared with Soong and Ogura's results. The M_c value at the cloud base determined by Soong and Ogura is about 395 mb day^{-1}, which is much larger than the value determined in this study. This difference may have been caused partly by the different interpretations of cloud mass flux, and partly by the different observation periods used for the studies.

Although the results of this study are gratifying, not all of the properties of the cloud population have been resolved. Because of the lack of a numerical cloud model, we have not been able to determine the cloud spectrum distribution function. We have no information about the life spans for different types of cloud, and consequently, have not been able to resolve the fractional coverage distribution. All of these may be resolved in future studies by combining a proper numerical cloud model with the formulation presented in this paper.

Acknowledgements. This work was supported by the Negotiated Development Grant D-54 from the National Research Council of Canada. The author would like to express his appreciation to Miss. O. Kowalishen for her help in preparing the manuscript.

REFERENCES

Arakawa, A. and W.H. Schubert, 1974: Interaction of a cumulus cloud ensemble with the large-scale environment, Part I, J. Atmos. Sciences, 31, pp. 674-701.

Fraedrich, K., 1973: On the parameterization of cumulus convection by lateral mixing and compensating subsidence. Part I, J. Atmos. Sciences, 30, pp. 408-413.

Fraser, A.B., 1968: The white box: the mean mechanics of the cumulus cycle. Quart. J. Roy. Meteor. Soc., 94, pp. 71-87.

Kuo, H.L., 1965: On formation and intensification of tropical cyclones through latent heat release by cumulus convection. J. Atmos. Sciences, 22, pp. 40-63.

Nitta, T., 1975: Observational determination of cloud mass flux distribution. J. Atmos. Sciences, 32, pp. 73-91.

Nitta, T. and S. Esbensen, 1974: Heat and moisture budget analysis using BOMEX data. Mon. Wea. Rev., 102, pp. 17-28.

Ogura, Y. and H.R. Cho, 1973: Diagnostic determination of cumulus cloud populations from observed large-scale variables. J. Atmos. Sciences, 30, pp. 1276-1286.

Ooyama, K., 1971: A theory of parameterization of cumulus convection. J. Meteor. Soc., Japan, 49, pp. 744-756.

Sarachik, E.S., 1974: The tropical mixed layer and cumulus parameterization. J. Atmos. Sciences, 31, pp. 2225-2230.

Soong, S.T. and Y. Ogura, 1976: A determination of the trade wind cumuli population using BOMEX data and an axisymmetric cloud model. To appear in the J. Atmos. Sciences.

Yanai, M., S. Esbensen and J. Chu, 1973: Determination of average bulk properties of tropical cloud clusters from large-scale heat and moisture budgets. J. Atmos. Sciences, 30, pp. 611-627.

5.2.3

AIRCRAFT AND DOPPLER RADAR MEASUREMENTS OF THE MICROPHYSICS AND DYNAMICS OF LONGITUDINAL ROLLS ASSOCIATED WITH DEEP ICE CLOUDS

Andrew J. Heymsfield
National Center for Atmospheric Research*
Boulder, Colorado

Richard E. Carbone
Meteorology Research Incorporated
Altadena, California

Peter V. Hobbs
University of Washington
Seattle, Washington

1. INTRODUCTION

Ice particle growth in compact convective cells in the middle and upper troposphere has been a topic of considerable attention among cloud physicists and radar meteorologists during the past 20 years. Early radar measurements were limited to identifying generating regions and the resulting precipitation trails (Marshall, 1953; Wexler, 1955; Langleben, 1956; Douglas et al., 1957). Generating cells were found to range between 1 and 3 km in diameter and to average 1 km deep. Particle terminal velocities were estimated from trail patterns to be 1.0 to 1.5 m sec^{-1}. Updraft velocities were deduced through mass-vapor flux considerations to be 0.2 to 1.1 m sec^{-1} (Wexler and Atlas, 1959) and from latent heat and thermal stability considerations to be 1.0 to 3.0 m sec^{-1} (Douglas et al., 1957).

More recently, the particle characteristics and updraft velocities have been interpreted through use of aircraft and Doppler radar measurements. High ice particle concentrations and large particle sizes were measured within and below the generating regions through use of airborne particle size spectrometers (Heymsfield, 1975A). Vertical velocity magnitudes ranging between 0.5 and 1.5 m sec^{-1} in convective cells and 0.5 m sec^{-1} in a generating region below were deduced from Doppler radar measurements (Heymsfield, 1975B; Carbone and Bohne, 1975).

While the above mentioned radar and aircraft studies were primarily related to cellular convection with scales of 1 to 5 km, observational studies of cloud bands or rolls at mid and upper levels indicate motions exist with scales of 10 to 500 km. Characteristics of cloud bands found in the jet stream were deduced utilizing photogrammetric techniques (Conover, 1958; Reuss, 1963). Conover found that cirrus bands tend to parallel the jet stream and were formed by roll-like motions. Within these bands, cellular structures were frequently found with cell spacings averaging 1.3 km. Theoretical studies of longitudinal rolls (Kuo, 1963; Kuettner, 1971; LeMone, 1973) have defined the mechanisms responsible for roll formation and have supported many of the previous observations.

While photogrammetric observations have shown that cloud bands are common structures at mid and upper altitudes and radar observations indicate that generating cells are common features in precipitating ice clouds, there has been no attempt to relate these dynamical structures. In the present study, aircraft and Doppler radar observations were utilized to link these dynamical structures in deep precipitating ice clouds and to define their importance in precipitation formation.

2. DATA COLLECTION AND CALCULATIONS

Data was collected at Seattle, Washington during the period December 1974-January 1975 and at Champaign-Urbana during March 1974 with meteorological aircraft and Doppler radar. Measurements taken on 13 January 1975 at Seattle (Case A) and 15 March 1974 at Champaign-Urbana (Case B) will be discussed in detail in this paper. Aircraft sampling at Seattle was with the National Center for Atmospheric Research (NCAR) Sabreliner[1] and the University of Washington B-23 and at Champaign-Urbana was with a WB57F. Instrumentation on the Sabreliner included a Particle Measuring Systems (PMS, Knollenberg) Particle Size Spectrometer, sizing in the range 70-1050 μm in 70 μm intervals, state parameter and dew point measurements, and an Inertial Navigational System for wind speed and direction determination. The Sabreliner measurements were supported with nearly simultaneous state parameter measurements and replicator data for ice crystal habit determination from the B-23. The aircraft state parameter measurements were supported with radiosonde ascents from a ground-based site. The Doppler radar utilized in the Seattle study was the NCAR CP-3, operated with the antenna primarily in the vertically pointing mode, which resulted in the measurement of only the falling component of the particle velocity. The WB57F contained 3 PMS probes sizing in the range 2-2000 μm, a formvar replicator and an Inertial Navigational System. The Doppler radar used in this study was the University of Chicago-Illinois Water Survey (CHILL) FPS-18[2].

*The National Center for Atmospheric Research is sponsored by the National Science Foundation.

[1]Project Cycles, under the direction of P. V. Hobbs.

[2]For a more complete discussion of instrumentation, see Heymsfield (1975C), and Carbone and Srivastava (1975B).

Aircraft sampling patterns were centered over the Doppler radars at altitudes to collect representative data on the vertical distribution of the cloud microphysics. Aircraft sampling patterns consisted of a 0.6 km step-down from the cloud top at 7.5 km to below the cloud base at 1.4 km during Case A and a 1.2 km step-down from 10.4 to 4.4 km and a descent to 2.6 km during Case B. Sampling passes were in a direction parallel to the wind. Measurements were averaged over 2 minute intervals centered over the radar. Doppler spectral information from the CP-3 radar was recorded in 16 range gates enabling 0.4 km resolution, and Doppler velocities used for comparison were averaged over one revolution of the antenna (67 sec).

The aircraft particle size spectra measurements and ice crystal habit information for each constant altitude pass permitted calculation of the cloud ice water content (IWC), radar reflectivity factor (Z) and mean Doppler fall speed ($\bar{v}$) (see Heymsfield, 1976A). The derived values of Z were used to assess the accuracy of the calculations and Z and $\bar{v}$ were used to interpret Doppler radar data. The values of Z were generally within ± 2 dBZ of the radar derived values. Combining $\bar{v}$ and Z in the form $\bar{v}_E = AZ^B$ through a curve fitting technique enabled calculation of the updraft velocity (u_p) by subtracting the measured mean Doppler velocity ($\bar{v}_m$) from the expected Doppler velocity $\bar{v}_E$:

$$u_p = \bar{v}_E - \left| \bar{v}_m \right| .$$

3. SYNOPTIC ANALYSIS

The synoptic situation characterizing Case A was a stationary E-W front located approximately 100 miles south of the radar with a strong jet stream aloft. Overrunning was primarily responsible for cloud formation, and a homogeneous cloud layer was observed between 0.6 and 6.9 km with continuous precipitation averaging 1.6 mm hr^{-1} reaching the ground. Case B differed in that a warm front was located about 100 miles south of the radar, but strong jet stream winds were observed aloft. On the basis of the surface condition and the upper level support, this system would be classified as a weak to moderate cyclonic system. Steady light rain, with an average precipitation rate of 0.8 mm hr^{-1}, was reported throughout the area during the measurement period.

Soundings obtained from nearly coincident radiosonde and aircraft data during Case A indicated several important features of the atmospheric stability (see Fig. 1). A conditionally unstable lapse rate existed between 5.7 and 6.9 km in a layer containing little directional shear and light positive vertical shear, and a dry adiabatic layer was situated between 4.8 and 5.7 km. A stable lapse rate was noted below 4.5 km, with an overrunning surface at about 3.3 km. Radiosonde data taken four hours prior to sampling at Peoria, Illinois, located 100 miles west of the sampling point, was used to interpret the thermal and wind structure during Case B. Strong jet winds were found above 8.0 km. A conditionally unstable layer was found between 5.6 and 8.0 km, and the frontal overrunning surface was centered in the layer between 5.6 and 8.0 km.

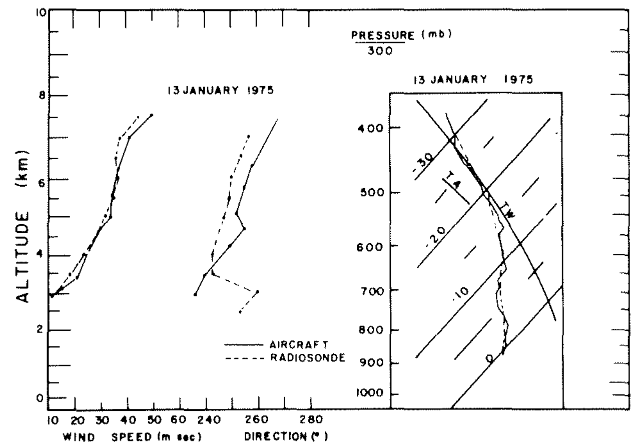

Fig. 1. Aircraft and simultaneous radiosonde and wind and temperature sounding on 13 January 1975 (Case A), T_A and T_W are dry and moist adiabatic lapse rates, respectively.

4. PLAN PATTERNS OF LONGITUDINAL ROLLS AND PRECIPITATION SHEATHS

Previous observations of longitudinal rolls in the middle and upper troposphere have been limited to defining their characteristics in otherwise clear air. As complete evaporation of particles below the roll prevented the development of long precipitation trails, there have been no measurements of longitudinal rolls and resulting streamers where particles continued to grow to the surface. In order to interpret observations discussed later in this paper of longitudinal rolls embedded within a deep cloud layer where evaporation is not occurring below the roll, the plan and vertical patterns of longitudinal rolls and resulting streamers were calculated.

Observations of jet stream bands indicate an orientation from the mean wind at the roll layer ranging between 2 and 15°. Illustrations of longitudinal rolls oriented at 8° to the right of the wind in which ice particle generation is occurring continuously along the lifting region of the roll appears in Fig. 2A and in which cellular convection is occurring along the lifting line appears in Fig. 2B. The plan pattern presented in Fig. 2A depicts the sheath of particles in space generated from a roll, assuming ice particles falling at 0.8 m sec^{-1}, no directional shear, and a linear wind shear increasing to 50 m sec^{-1} at the generation region. As indicated in the figure, the roll oriented to the right of the wind produces a trail which slopes toward the left in space. If this same roll was oriented to the left of the mean wind, the trail would slope toward the right. From the situation described in Fig. 1A, a mean wind direction below the roll layer to the left of the mean wind direction in the roll layer will extend the length of the sheath in space. A mean wind direction below the roll to the right will shorten the length of the sheath in space and perhaps pro-

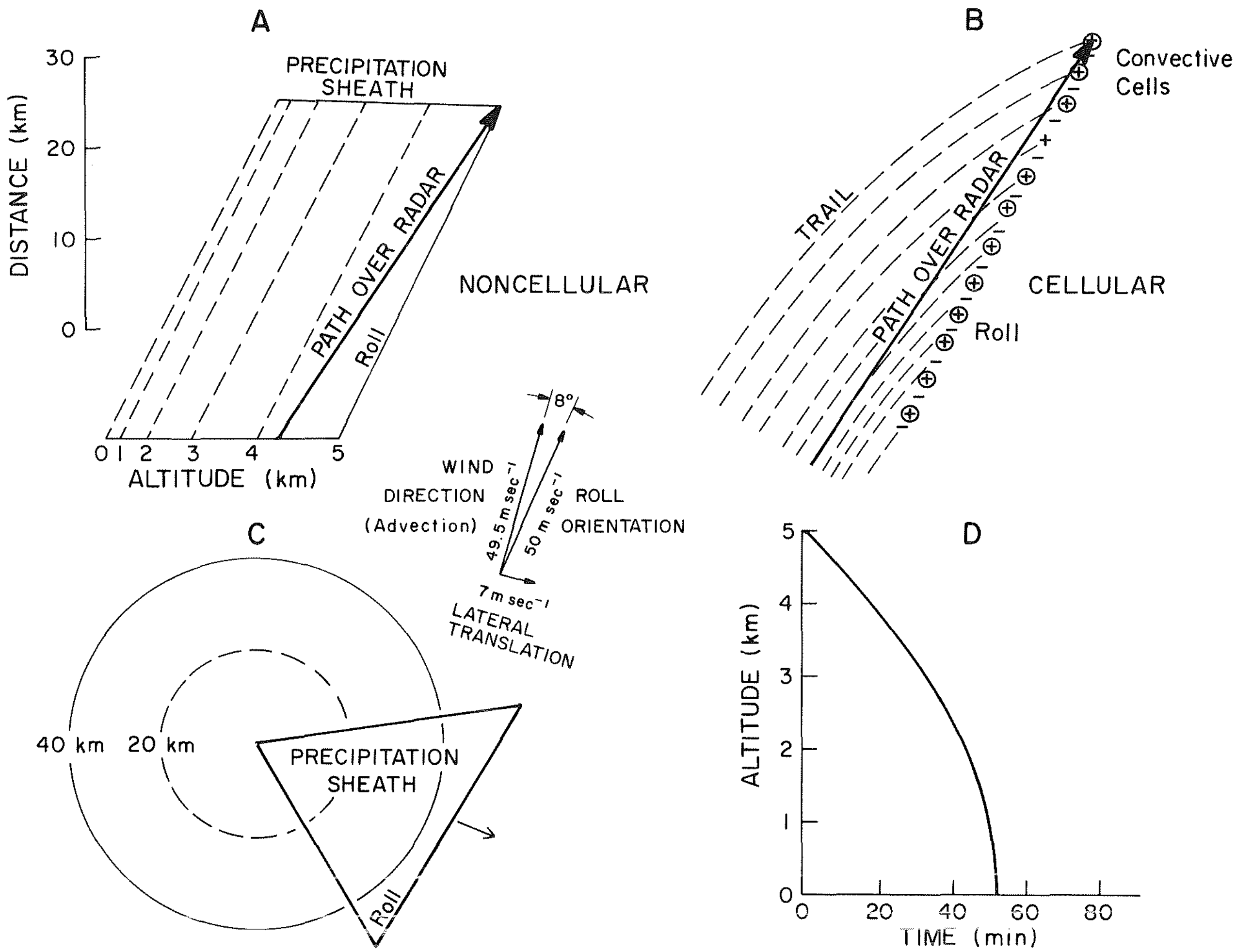

Fig. 2. Pattern of longitudinal rolls with no directional shear below roll layer. A: Uniform lifting along roll line with roll oriented 8° to right of mean wind. B: Similar to (A) with convective cells forming along lifting line. C: PPI view of (A). D: Pattern with vertically pointing radar measurements of (A).

duce a bending back effect in which a lower segment would fold under an upper segment.

Viewing the roll on a Plan Position Indicator (PPI) display will produce a banded pattern with inflections characteristic of the orientation of the band with respect to the wind. When a band is directly over a radar and its orientation with respect to the wind is similar to that of Fig. 2A, an inverted V pattern will be produced similar to that indicated in Fig. 2C. When the direction of the band is to the left of the wind, the inflection will be a V-shaped pattern. If the wind direction below the roll is different from the mean wind direction in the roll layer, another inflection at ranges closer in will be produced. If the wind direction is to the left of the mean wind in the roll layer, a V pattern will be produced, and if to the right, an inverted V pattern will occur. In any case, the band orientation can be found to be that angle connecting two portions of the same precipitation sheath falling equidistant from the radar.

An observation of a roll-sheath pattern with a vertically pointing radar will produce somewhat predictable results. If the sheath depicted in Fig. 2A passes over the radar, a pattern similar to Fig. 2D will be produced. With the lateral speed of 7.0 m sec^{-1} as indicated in Fig. 2A, the passage time of the roll-sheath combination over the radar will be nearly one hour. If the updraft in the roll layer is seen first, the sheath will pass below the downdraft region, while if seen last, the sheath will emanate from the updraft region. Directional shear to the left of the wind will increase the trail length while to the right may produce a bending over effect. If the roll is to the left of the wind, a nearly identical pattern with a vertically pointing radar will be produced. If the directional shear below the roll is to the right of the wind, the trail will appear to lengthen; if the directional shear is to the left, the trail pattern may appear to be doubling over. From the above discussion, it can be inferred that the location of the updraft region, trail length and wind direction below the generating level permit interpretation of the roll orientation from a vertically pointing radar.

Patterns produced from continuously generating convective cells as indicated in Fig. 2B will generally be similar to those obtained from a continuous line generator when observed on plan view. When observed on a vertically pointing radar, however, a number of short segments of trails rather than a continuous trail pattern is produced.

5. THE OBSERVATIONS

a. The Vertical Pattern and Vertical Velocities of Longitudinal Rolls

Data from the Doppler radar with the antenna vertically pointing obtained over a five hour period during Case A indicated precipitation streamers emanating from updraft regions at upper levels and extending continuously to lower levels. Regions of low reflectivity were correlated with downdraft regions and of high reflectivity with updraft regions. The frequency of passage of one discern ble structure was approximately one per half hour. Data from the time interval between 0950 and 1040 PST, appearing in Figure 3, illustrates several of these regions. Noted in the upper portion of Figure 3 between 5.0 and 7.0 km in the region of a conditionally unstable lapse rate (see Fig. 1) are two regions of a minimum in dBZ value, each followed by a maximum. These maxima were continuous to below 2.0 km and, therefore, can be though of as a "sheath" of particles. The outline of these higher reflectivity regions arc indicated in the lower part of the figure, along with the computed vertical velocity magnitudes. As indicated by the vertical velocity values between 5.7 and 7.0 km, well defined regions exist with velocities of -40 cm sec^{-1} in the low reflectivity regions and +40 to +50 cm sec^{-1} in the high reflectivity regions. Time scales of 20 minutes for the passage of the downward and upward moving regions of each structure and 50 minutes for the entire sheath are similar to those found for the roll sheath pattern in Section 4, Fig. 3a where passage time was 50 minutes over a comparable altitude range. These time scales are much too long for the structure to be a convective cell. Also noted in the figure is a layer between 4.5 and 5.7 km of high vertical velocities that appear to be coupled in some way to the roll structures. These values were continuous for a period of over 5 hours.

The interpretation of the above patterns was aided by the discussion of roll patterns in Section 4. The wind direction during Case A at layers below the roll were to the left of the mean wind in the roll layer; thus, the trail would be extended in space if the roll was to the right of the mean wind and perhaps create a folding over effect if to the left of the mean wind. The continuous trails illustrated in Figure 3 indicate that the roll was to the right of the mean wine. Detailed calculations of the roll-sheath pattern in space derived from values of the wind magnitude and direction and from the mean particle fall speed were compared to the observed pattern in Fig. 3. From this analysis, it was deduced that the roll was oriented at 9° to the right of the mean wind.

Data from the CHILL Doppler radar with the antenna vertically pointing obtained during Case B provided an example of convective cells which were apparently forming along the lifting portion of a roll. Measured dBZ values between 1147 and 1152 CDT as shown in Fig. 4A indicate that a nearly uniform structure existed during that time period.

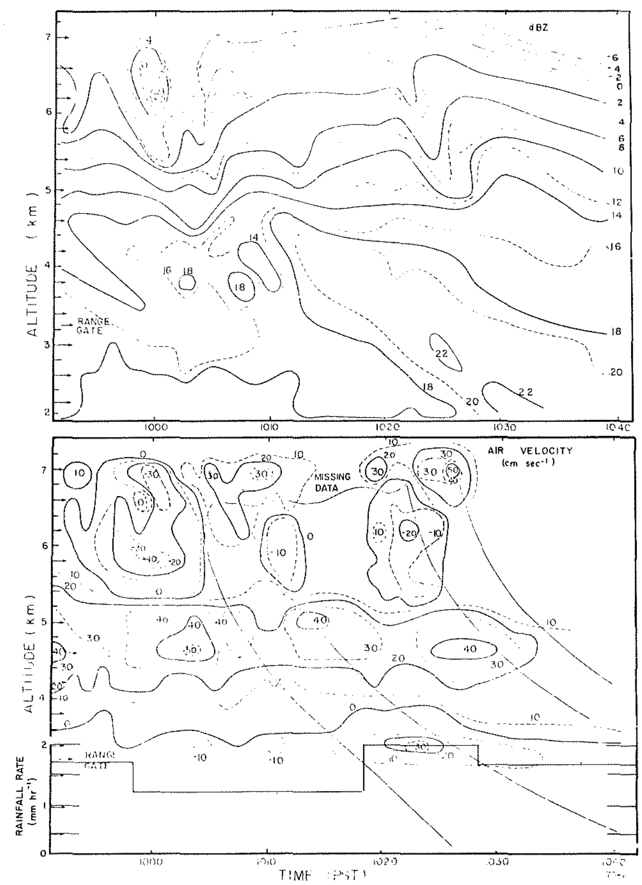

Fig. 3. Time section of radar reflectivity factor (dBZ) and derived air velocities on 13 January 1975 (Case A). Trails are denoted by nearly vertical solid lines. Each data point was 67 second average. Precipitation rate noted on bottom.

However, a relatively high reflectivity region existed between 5.6 and 9.0 km at 1147:30 and from 1149 to 1152 CST, as exemplified by the 10 dBZ contour 1 km higher at these times than at other times.

The measured mean Doppler velocities and derived air velocities appear in Figs. 4B and 4C, respectively. Figure 4C indicates three cellular structures between 5.6 and 8.0 km with velocities of + and -50 cm sec^{-1} nearly identical in form and coincident in time with the higher reflectivity regions. In addition, a very similar form to those described above existed at 1147:30 with velocities of + and -30 cm sec^{-1}. A thin layer existed at 5.6 km with downward velocities of -25 cm sec^{-1} for nearly the entire time period; during the last minute, upward velocities of +30 cm sec^{-1} were found in the layer.

The regular succession of cells along the lifting line coincident with regions of higher reflectivity are similar in form to those discussed in Section 4 and displayed pictorially in Figure 2B. These cells originate slightly above the base of an unstable layer. The cells were deduced to be approximately 1.0 km across, assuming the cells are moving with the wind and using the measured wind velocities close to the sampling location. This value is close

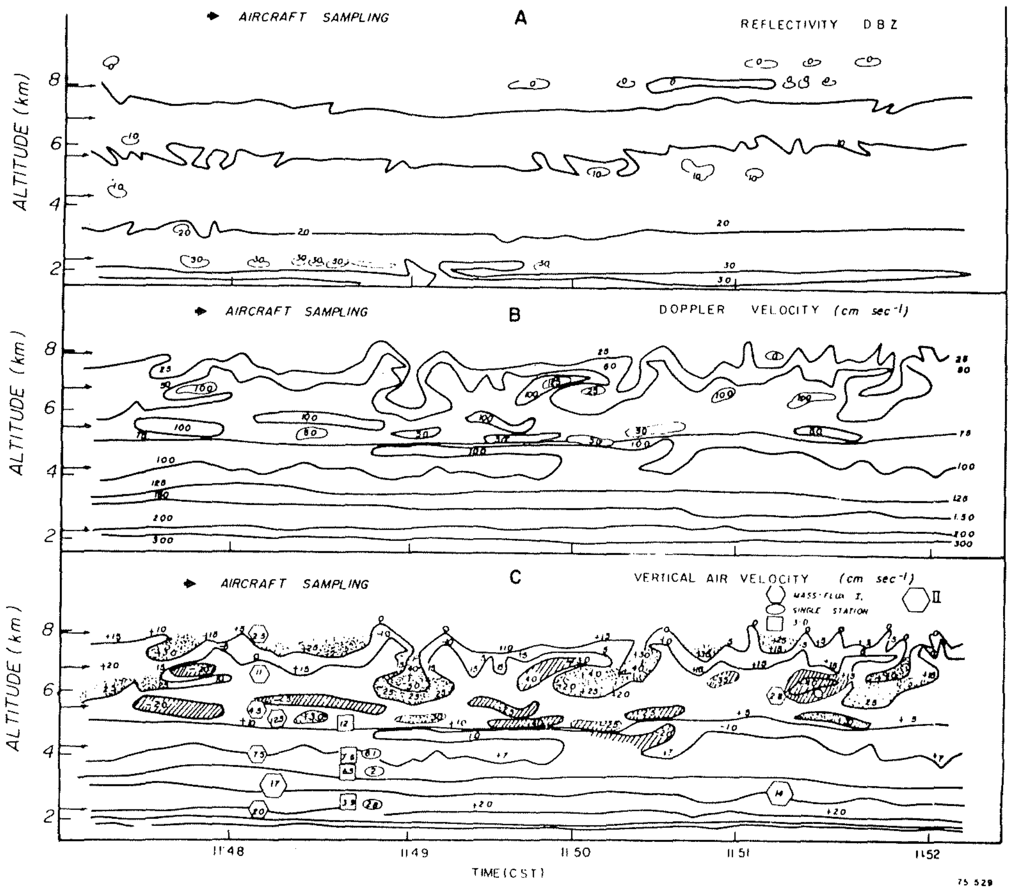

Fig. 4. Radar measurements on 15 March 1975 (Case B). A: Radar reflectivity factor (dBZ). B: Doppler fall speeds (positive value falling toward ground). C: Derived air velocities. Stippled lines: Downward moving air. Hashed lines: Velocities higher than 25 cm sec^{-1}. Boxes and triangles: Vertical velocities calculated through mass-flux and synoptic techniques.

to that of 1.3 km obtained by Conover (1958) for cells forming along jet stream bands. Cells forming in lines oriented with the wind were also found by Wexler (1955) and Langleben (1956) from PPI scans. Cells forming in lines observed with vertically pointing Doppler radar were found by Heymsfield (1975) and Carbone and Bohne (1975). In the latter observations, a thin layer with an updraft velocity of +0.5 m sec^{-1} was found directly below the cell layer. It is suggested that in the present case cells are formed along the upward moving portion of a roll that is tilted in space. With this configuration, a downward velocity would be measured at the base of the roll layer, followed by an upward velocity. This pattern conforms to the present observations.

An additional case study in which synoptic conditions were nearly identical to those in Case A indicated up-and downward velocities and trail sheaths similar to those discussed for Case A. However, complete evaporation was occurring near the surface, thus preventing any precipitation from reaching the ground. The length of the trail was extended by approximately 0.6 km below the continuous cloud layer, as shown pictorially in Figure 5. It was clear from the data that particles falling in the precipitation sheath survived considerably further distances in the evaporative layer than outside.

b. Plan Pattern of Longitudinal Rolls

PPI data for Case A taken in 30 minute intervals between 0915 and 1045 PST at 1, 10, and 20 degree elevation angles comfirmed the analysis of banded structures with well-defined precipitation sheaths discussed in Sections 4 and 5A. The precipitation sheaths were most apparent at 1015 PST. Echo maxima were typically 3 to 5 dBZ greater than intervening minima, corresponding roughly to a factor of two in precipitation rate. Observable length varied from 15 to 40 km and spacing from 2 to 8 km. Bands were oriented predominantly at 260° or 8° to the right of the mean wind in the layer, and an inverted V pattern was observed when a sheath was directly over the radar. This was consistent with the calculations discussed in Sections 4 and 5A.

PPI observation of the active roll region between 5.5 and 7.0 km was not possible due to limited radar display sensitivity. Furthermore, the projection of precipitation sheaths on a conical surface made interpretation difficult and sometimes ambiguous. Given this potential ambiguity, it was deduced that band migration was southward with respect to the mean wind between 5.8 and 6.7 km and approximately parallel to the horizontal shear vector across the layer. The trails extended northward and westward in the layer below, frequently enhancing the bright band reflectivity factor at 1.2 km.

A PPI photograph of the NCAR Doppler Radar Display showing range normalized radar reflectivity factor (dBZ) taken during a meteorological situation similar to Case A appears in Figure 6. Increased radar display sensitivity over that during Case A permitted a better definition of the active roll region. The elevation angle in the figure was 7° and outside range marker was 40 km. The color coding for reflectivity factor values (dBZ) are listed below R/S to the right of the figure. The

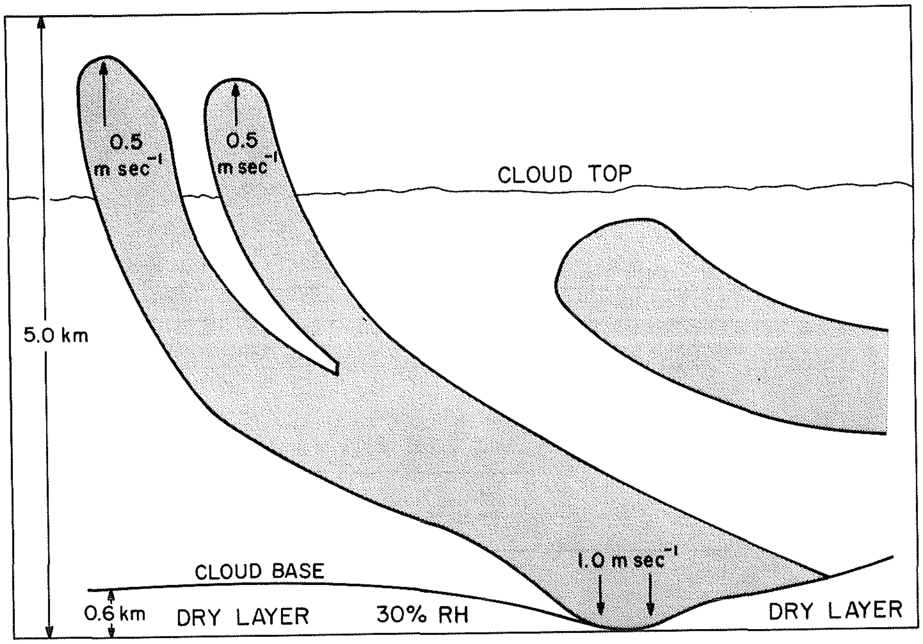

Fig. 5. Schematic representation of observed precipitation sheath embedded within a deep cloud layer and precipitating into an evaporative layer.

values noted with each color represent approximately 10(dBZ-22). Therefore, the gold color noted as 425 is approximately 22.5 dBZ. Indicated to the right of the center of the PPI display were continuous bands of high radar reflectivity. These sheaths extended from 40 km, corresponding to an altitude of 5.0 km, inward to 10 km, where they enhanced the bright band. Rapid evaporation was taking place at low levels to the right of the center and to the left of the PPI photograph, making it impossible to see a continuous band from the right to the left of the photograph. However, the roll region was still active to the left of the figure, as indicated by two brown and white patches at 20 to 25 km and 260 to 270°. These active roll regions were found to be continuous with the bands to the right of the display crossing the 20 km marker at 70 to 90°.

c. Particle Characteristics and Surface Precipitation Rate

Liquid water was noted within the roll layer during Cases A and B. In Case A, icing of the leading edge of the Saberliner and replication of small droplets with the B-23 was noted between 5.7 and 6.3 km. The Sabreliner observations were coincident with the location of a band, as determined from the PPI display. The B-23 measurements indicated a maximum liquid water content of 0.05 to 0.10 g m^{-3} existed within the layer. The collection of bullet rosettes and other spatial forms, indicative of nucleation through droplet freezing, and the presence of moderate riming of these ice crystals confirmed the presence of liquid water in this layer. In Case B, droplets in concentrations of 10 cm^{-3} were noted at 5.6 km, coincident with icing observations with WB57F. The maximum liquid water content calculated from particle size spectra measurements in the layer was 0.02 g m^{-3}.

Rainfall amounts in 10 minute intervals during Case A were collected from a location 12 km south of the radar. These measured amounts were shifted back in time to the radar location according to the approximate translational speed of the bands (9° calculated band orientation). The precipitation rate averaged 1.57 ± 0.53 mm hr^{-1} during an 8 hour period, with increases from the average of up to 1.0 mm hr^{-1} during precipitation sheath passage, followed by decreases from the average of a comparable amount. One period of comparison appears in Fig. 3. In this figure, the measured precipitation rate has also been shifted back in time to account for the fall time from 2 km to the surface. Note the close correspondence between the increase in precipitation rate at the ground and passage of a longitudinal roll, demonstrating a continuity of the precipitation sheath in time and space.

6. SUMMARY AND CONCLUSIONS

Well defined precipitation sheaths embedded within stratiform ice clouds were observed through use of aircraft and Doppler radar measurements to emanate from longitudinal rolls situated in the mid and upper troposphere. Vertical velocities of + and -50 cm sec^{-1} were measured within the up-and downward moving regions of a roll, respectively. Liquid water and rimed spatial ice crystal forms were observed within the upward moving region at temperatures between -20 and -25C. Cases displaying uniform lifting and cellular convection along the lifting region, observed between 5.5 and 7.0 km and associated with the jet stream, apparently differed because of the stability of the layer. The bands were found to be oriented along the shear vector. A consistency was found to exist between calculated and measured trail patterns and band orientation.

Precipitation sheaths were found to emanate from the upward moving region of the roll and fall to the ground when a sufficient water vapor density was available for ice particle growth. Ice crystal survival distances within sheaths were found to be markedly increased over non-sheath regions in evaporative layers. Precipitation rates at the ground during Case A were found to increase from an 8 hour mean of 1.57 ± 0.53 hr^{-1} to 0.4 to 1.1 mm hr^{-1} in sheath regions and to decrease by 0.2 to

0.8 mm hr^{-1} from the average between bands. The overall enhancement in the precipitation rate at the ground from an active roll can be estimated from a recent study by Heymsfield (1976B). For convective cells situated between -20 and -30C, an upward velocity of +40 cm sec^{-1} will increase the precipitation rate at the ground by 0.63 mm hr^{-1} at 50 cm sec^{-1} by 0.76 mm hr^{-1}, at 100 cm sec^{-1} by 1.49 mm hr^{-1}, and at 150 cm sec^{-1} by 1.96 mm hr^{-1}. The range of precipitation rate increases given above are consistent with precipitation rates measured at the ground where generating cells were very numerous (Douglas et al., 1957). The range of vertical velocities given above of 40-150 cm sec^{-1} are the likely magnitudes expected for these banded structures which imply precipitation rate increases of 0.6 - 20 mm hr^{-1} at the ground.

Longitudinal rolls provide an explanation for the presence of continuously generating convective structures forming in lines at mid and upper levels as observed in previous studies. Langleben (1956) found that generating cells were oriented in lines at angles ranging between 15 and 75° from the wind direction in 5 out of the 7 cases he investigated. Carbone and Bohne (1975) observing a line of convective cells, deduced an orientation of 10 to 15° with respect to the mean wind in the convective layer. These present observations explain observations by Wexler and Atlas of a group of cells 8.0 to 11.0 km across. Langleben found that individual cells he observed had lifetimes as long as 2 hours. Heymsfield (1975) calculated cell lifetimes of over 2 hours in the case he investigated.

ACKNOWLEDGMENTS

The authors wish to thank the Field Observing Facility, particularly C. Frush, and the Research Aviation Facility at NCAR, for their support in this study. We wish to thank all members of the University of Washington's Cloud Physics Group, particularly Mr. P. Herzegh who helped in this study. The manuscript was reviewed by Ms. M. Heymsfield and typed by Ms. C. Brown. This research was supported by the National Science Foundation under Grant ATM-74-14726-A02 from the Atmospheric Research Section (Meteorology of the National Science Foundation) and Air Force Cambridge Research Laboratories.

REFERENCES

Carbone, R. E. and A. R. Bohne, 1975: Cellular snow generation - A Doppler radar study. J. Atmos. Sci., 32, 1384-1394.

_______, and R. C. Srivastava, 1975: Simultaneous aircraft and Doppler radar observations of a deep stratiform layer. Part II - Radar measurements and derived air motions. Proc. 16th Radar Meteor. Conf., 441-446.

Conover, J., 1960: Cirrus patterns and related air motions near the jet stream as derived by photography. J. Meteor., 17, 532-546.

Douglas, R. H., K. L. S. Gunn and J. S. Marshall, 1957: Pattern in the vertical of snow generation. J. Meteor., 14, 95-114.

Heymsfield, A. J., 1975: Cirrus uncinus generating cells and the evolution of cirriform clouds. Part I: Aircraft measurements and observations. J. Atmos. Sci., 32, 799-808.

_______, Part II: The structure and circulations of the cirrus uncinus generating head. J. Atmos. Sci., 32, 809-819.

_______, 1975: Simultaneous aircraft and Doppler radar measurements of a deep stratiform layer. Part I: Aircraft measurements and microphysical calculations. Proc. 16th Conf. Radar Meteor., 433-440.

_______, 1976: Precipitation development in stratiform ice clouds: A microphysical and dynamical study. Accepted for publication in J. Atmos. Sci.

_______, 1976: A technique for computing the cloud ice water content and precipitation rate from radiosonde data. Proc. Sixth Conf. Weather Forecasting and Analysis, 92-97.

Kuettner, J., 1971: Cloud bands in the earth's atmosphere: Observations and theory. Tellus, 23, 404-425.

Kuo, J., 1963: Perturbations of plane Cotte flow and the origin of cloud streets. Phys. Fluids, 6, 195-201 .

Langleben, M. P., 1956: The plan pattern of snow echoes at the generating level. J. Meteor., 13, 554-560.

LeMone, M. A., 1973: The structure and dynamics of horizontal roll vortices in the planetary boundary layer. J. Atmos. Sci., 30, 1077-1091.

Marshall, J. S., 1953: Precipitation trajectories and patterns. J. Meteor., 10, 25-29.

Reuss, J. H., 1967: Wolken-Stereomessbildreichen, II; Grossraumige cirrus bandes als merkale von Luftmassengrenzen der hohes troposphäre und ihrer Eigenshaften. Phy. der Atmos., 7-15.

Wexler, R., 1955: Radar analysis of precipitation streamers observed on 25 February 1954. J. Meteor., 12, 391-393.

_______, and D. Atlas, 1959: Precipitation generating cells. J. Meteor., 16, 327-332.

Figure 6. This photograph is an illustrative example of precipitation sheaths which emanate from cloud bands, presumably longitudinal rolls, embedded within deep stratiform ice clouds. The range normalized display represents horizontal projection of a conical surface scanned by the NCAR CP 3 radar at 7° elevation. The color codes of equivalent radar reflectivity factor and Doppler velocity are located to the right of the reflectivity display together with pertinent housekeeping information. The outer range ring is at 40 km slant range corresponding to a maximum altitude of 5.2 km MSL. The radar is at 0.15 km MSL. The reflectivity color code headed by the column marked R/S may be obtained from displayed numbers through a division by 10 and a subtraction of 20. It follows that the range of values shown is from 32.5 to 0.0 dBZ, where the units of Z are $mm^6\ m^{-3}$. The 20 dBZ level is highlighted in white to show maxima in the precipitation sheaths. The combination of directional wind shear with altitude and conical surface displayed, results in V shaped pattern, where individual sheaths are observed from east to west of the radar. The intense reflectivity ring at 13 km range is the O°C melting level, commonly referred to as the bright band. Photograph by Dr. Howard Baynton, NCAR.

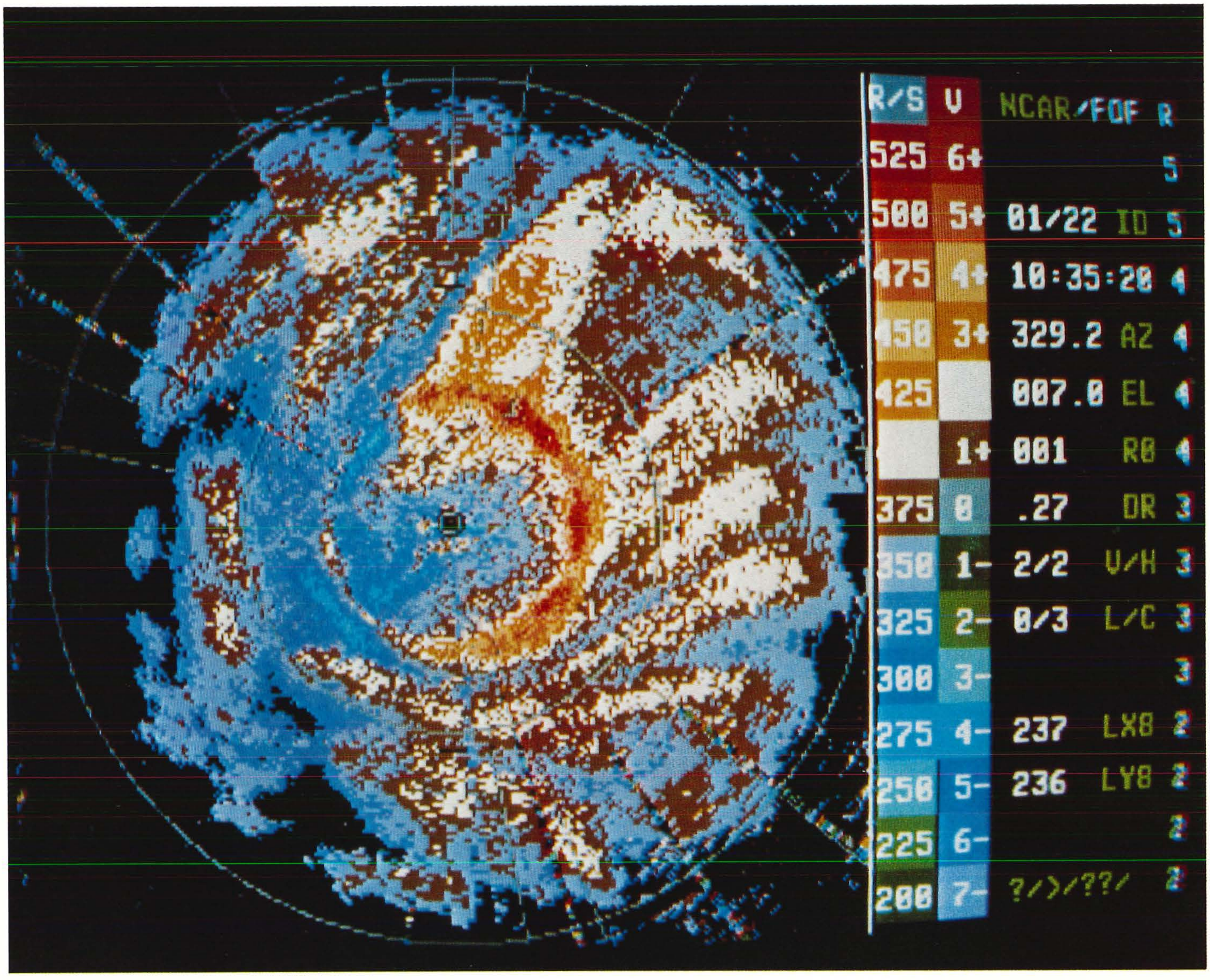

5.2.4

CLOUD DROPLET SPECTRA, AEROSOL CONCENTRATIONS AND RAIN-ACTIVITY IN MARITIME, MODIFIED MARITIME AND CONTINENTAL REGIONS

...

R. K. Kapoor, S.K.Paul, L.T.Khemani, S.K.Sharma, A.S.R.Murty, K. Krishna and Bh.V.Ramana Murty

Indian Institute of Tropical Meteorology
Poona 411 005 - INDIA.

1. INTRODUCTION

The characteristics of cloud droplet spectra depend upon the basic population of nuclei present in the atmosphere and the processes of condensation and coalescence taking place as the cloud develops, Rosinski (1974). The clouds in a continental region are colloidally stable compared to those in a maritime region which relatively precipitate with ease, Twomey and Squires (1959) and Twomey and Warner (1967). A study of droplet spectra of clouds and the associated aerosol state in different regions is, therefore, of importance for understanding the inter-relationships between aerosol concentrations, cloud droplet spectra and rain activity.

Droplet size distributions were obtained in three meteorologically different regions during the summer monsoon period, June to September, of 1973 and 1974. Measurements of giant hygroscopic aerosols were also made at cloud base level during the period. The results are presented along with the rain activity reported in the regions.

2. REGIONS AND PERIODS OF MEASUREMENT

The three regions where measurements were made are Bombay (18° 51' N, 72° 49'E, 11 m MSL), Poona (18° 32'N, 73° 51'E, 559 m MSL) and Rihand (24°12'N, 83° 03'E, 310.5 m MSL).

Bombay is located on the west coast and measurements were made at locations 25 km off coast. The period of measurement was at the end of the monsoon in 1973 i.e. from 29 September to 3 October; and while the monsoon was still active in 1974 i.e. from 11 to 30 September. The clouds in the region are maritime.

Poona is about 100 km inland from the west coast and is directly in the path of the monsoon westerlies. It is situated on the lee side of the Western Ghats. Measurements were made at locations 40 km east of Poona. The period of measurements was from June to September. The clouds in the region are modified maritime.

Rihand is well inland and is situated in northeast India. It is about 500 km from the coast. Measurements were made over the catchment area of the Rihand reservoir. The catchment area lies in the monsoon trough zone. The period of measurements was August to September in 1973 and July to September in 1974. The clouds in the region are continental.

The level of the 0°C isotherm is around 5 km at Bombay and Poona and 6 km at Rihand during the monsoon.

3. MEASUREMENTS

3.1 Droplet spectra

A spring loaded sampler was used for collection of droplets on magnesium oxide coated slides, Kapoor et al., (1975). Each slide was exposed to the cloud for a period of 200 milliseconds through a window of DC-3 aircraft. Samples were collected inside the cloud at a height of a few tens to a few hundred metres from the base by traversing through the cloud.

The limitations of the sampler for collection of droplets of various sizes, and the procedure adopted for obtaining actual sizes and true concentrations were reported, Kapoor et al.,(1976).

Measurements were made in 18 cloud cases off Bombay coast, 7 on 3 days during 1973 and 11 on 6 days during 1974; 153 cloud cases at Poona, 57 on 16 days during 1973 and 96 on 22 days during 1974; 143 cloud cases at Rihand, 62 on 16 days during 1973 and 86 on 32 days during 1974.

3.2 Aerosol concentrations

Aerosol samples were obtained with the help of Cascade Impactor, May (1945). It was operated through an opening provided in the body of the aircraft in the cockpit. The sampling was made in cloud-free air at a height corresponding to cloud base level which was between 1.5 to 2.0 km above msl during the season at Poona and Rihand. At Bombay, the sampling level varied between 0.6 to 1.2 km above msl. All the four slides of the Impactor, which provide a spectrum of large and giant size aerosols, were examined. The concentration of hygroscopic aerosols of radius 3 μm and above was considered in the present study.

Aerosol measurements were made on 11 occasions off Bombay coast, 4 in 1973 and 7 in 1974; on 42 occasions at Poona, 13 in 1973 and 29 in 1974; and on 36 occasions at Rihand, 12 in 1973 and 24 in 1974.

4. RESULTS

4.1 Droplet size distribution

Mean droplet size distributions were evaluated region-wise and yearwise. These distributions were expressed in 7 size classes. The mean concentrations under the different classes, and the mean total concentrations are listed in Table 1.

Table 1 : Mean droplet concentration (cm^{-3}) in different size classes (μm), mean total concentration (cm^{-3}), and computed liquid water content (LWC) in gm m^{-3} and median colume radius (MVR) in μm.

Size Class 2-15	15-30	30-40	40-50	50-70	70-110	>110	Total concentration	LWC	MVR
Bombay (Maritime)				1973					
20.0	3.07	0.57	0.00	0.06	0.000	0.000	23.7	0.035	7.05
				1974					
46.9	9.57	1.61	0.39	0.31	0.194	0.026	59.0	0.240	9.90
Poona (Modified Maritime)				1973					
22.7	6.19	1.79	0.41	0.81	0.550	0.150	32.6	0.659	16.90
				1974					
42.2	10.35	1.06	0.25	0.13	0.145	0.065	54.2	0.269	10.59
Rihand (Continental)				1973					
21.6	5.79	0.62	0.36	0.22	0.094	0.016	28.7	0.148	10.72
				1974					
26.7	12.56	1.15	0.34	0.12	0.023	0.007	40.9	0.152	9.57

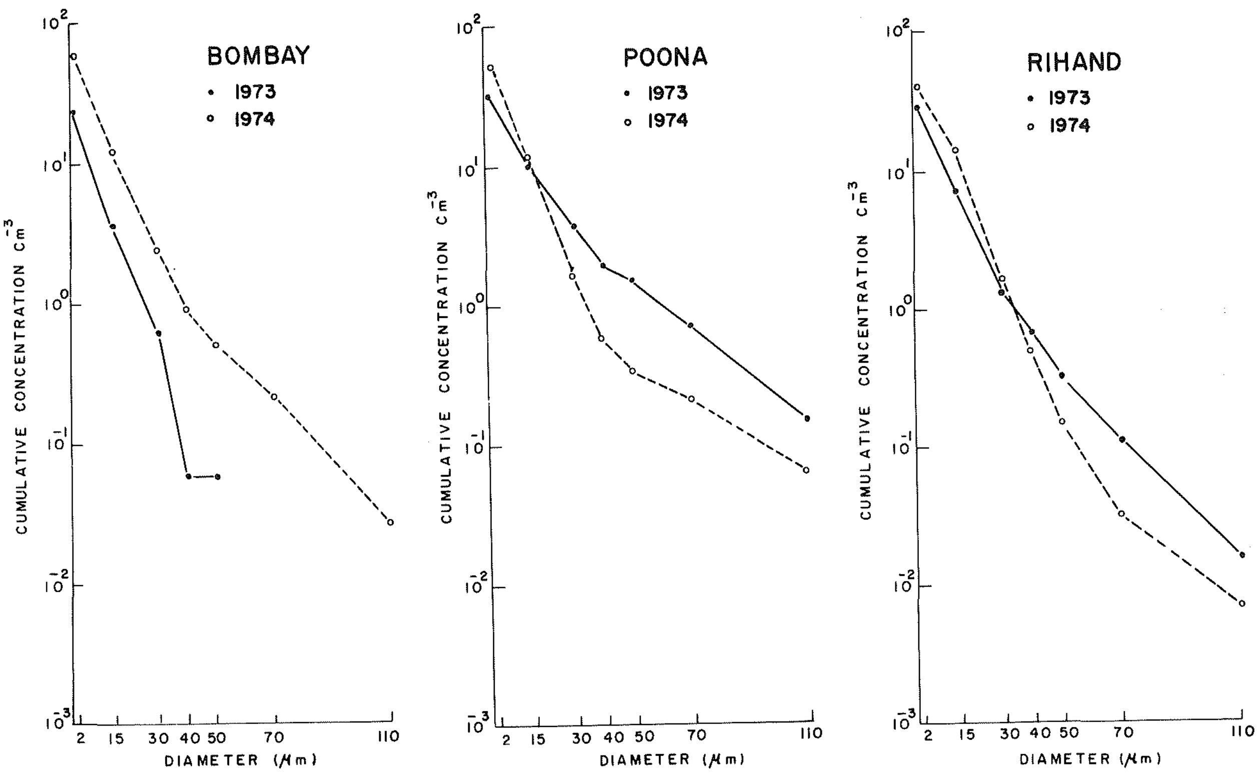

Figure 1 : Cumulative mean droplet concentrations above indicated sizes at Bombay, Poona and Rihand during the summer monsoon seasons of 1973 and 1974.

The median volume radius (MVR) and the computed liquid water content (LWC) are given in the same table. The cumulative concentrations are shown in Figure 1 for Bombay, Poona and Rihand.

The values of the mean total concentration in the three regions did not differ widely. They varied between 23.7 and 32.6 per cc in 1973, and between 40.9 and 59.0 per cc in 1974. Class-wise, the concentrations were higher in all the classes in 1974 at Bombay. Also, in 1974, the droplet spectra at Bombay extended well beyond 60 μm. At both Poona and Rihand, the concentrations were less in large-size classes, (above 40 μm), in 1974. Between Poona and Rihand, they were higher (6 to 9 times) at the former in both the years.

The values of liquid water content and median volume radius were higher at Poona than at Rihand in both the years. At Poona, the values were less in 1974, whereas at Rihand they were nearly the same in both the years.

4.2 Aerosol concentrations

The mean concentrations, year-wise and region-wise, are given in Table 2.

Table 2 : Mean concentration per litre of giant hygroscopic aerosols and values of seasonal rainfall in mm.

Year	Place	Hygroscopic aerosols	Rainfall
1973	Bombay	14.9	1783.8
	Poona	15.8	639.2
	Rihand	0.5	1120.4
1974	Bombay	1.7	2306.3
	Poona	1.7	489.4
	Rihand	0.3	880.7

The concentrations in the two years differed significantly in all the regions. They were higher (2 to 9 times) in 1973. In both the years, the concentration was lowest at Rihand, being 6 to 30 times less than at Bombay and Poona.

4.3 Rain activities

The values of rainfall reported for the three places during the monsoon period were considered to represent the rain activities in the regions during the periods of measurement. These values, for the two years, are given in column 4 of Table 2. The rain activity at Bombay was less in 1973 than in 1974. It was in the reverse direction at Poona and Rihand.

5. DISCUSSION

Of the three regions, maritime (Bombay), modified maritime (Poona) and continental (Rihand), extensive measurements were available in the case of the latter two. The analysis of the measurements made in these regions pointed out close association between the cloud microstructure, aerosol state of the air and rain activity.

The droplet size distribution in the modified maritime and continental clouds showed that in 1973, when the rain activities at Poona and Rihand were more intense, the size spectra contained remarkably higher number of bigger size ($\geq$ 40 μm) droplets, vide Table 1 and Figure 1. Further, in that year, the cloud forming air over both the regions contained remarkably higher concentrations of giant size hygroscopic particles (vide Table 2). If the day-to-day concentrations of giant size aerosols (these are not presented in the text for the sake of brevity) are considered in the two years, it is seen that the number of days associated with zero concentration totalled to 11 in 29 cases at Poona and to 18 in 24 cases at Rihand in 1974. The number of days associated with such deficient aerosol state was fewer in 1973 at both the places, nil out of 13 cases at Poona and 2 out of 12 cases at Rihand. These features suggest the importance of the aerosol state of the air and the microstructure of the clouds in facilitating rainfall in the Poona and Rihand regions by the warm process.

In so far as the measurements in maritime clouds (Bombay) are concerned, the droplet spectra contained remarkably higher number of bigger size ($\geq$ 40 μm) droplets and also extended well beyond 40 μm in 1974 when the rain activity was more (vide Figure 1). These features were conspicuously absent in the clouds sampled in 1973, suggesting close association, similar to what was noticed at Poona and Rihand, between cloud microstructure and rain activity in the Bombay region also. However, aerosol observations in this region pointed out conspicuously smaller number of giant size hygroscopic particles in the year of higher rain activity (1974), indicating a trend which was the reverse of what was noticed at Poona and Rihand (vide Table 2). The authors have no explanation to offer for this observed feature. It is considered that more extensive observations are required in the Bombay region before a definite conclusion becomes possible in the case of maritime clouds.

Also, the concentrations observed in the continental clouds (Rihand) were small, being only a few tens per cc as against a few hundred per cc reported by various investigators for continental clouds in the other parts of the globe. The reason for this observed feature in the present study is not clear.

6. CONCLUSION

The study pointed out that there is close association between cloud microstructure, aerosol state of the air and rain activity in modified maritime and continental clouds. In so far as maritime clouds are concerned such association has not been clear.

Acknowledgement

The authors are thankful to Messrs K.V. Sethu Madhavan and A.Girija vallabhan for typing the manuscript of this paper.

REFERENCES

Kapoor, R.K., S.K.Paul, A.S.Ramachandra Murty, K.Krishna and Bh.V.Ramana Murty, 1975 : Study of dropsize distribution in warm clouds subjected to repeated seeding. J. Weather Modification, Vol.7, No.1, 116-126.

Kapoor, R.K., S.K.Paul, A.S.Ramachandra Murty, K.Krishna, S.K.Sharma, and Bh.V.Ramana Murty, 1976 : Measurements of cloud droplet size distribution in seeded warm cumulus clouds. J.Pure and Applied Geophysics, (PAGEOPH), Vol.114.

May, K.R., 1945 : The Cascade Impactor, An Instrument for sampling coarse aerosols. J.Sci. Instrum., 22, 187-195.

Rosinski, J., 1974 : Role of aerosol particles in formation of precipitation. Reviews of Geophysics and Space Physics, 12,129-134.

Twomey, S., and P.Squires, 1959 : The influence of cloud nucleus population on the microstructure and stability of convective clouds. Tellus, 11, 408-411.

Twomey, S., and J.Warner, 1967 : Comparison of measurements of cloud droplets and cloud nuclei. J. Atmos. Sci., 24, 702-703.

5.2.5

A KINEMATIC DESCRIPTION OF SOME COLORADO THUNDERSTORMS

R. E. Erbes and L. O. Grant
Department of Atmospheric Science
Colorado State University
Fort Collins, Colorado

1. INTRODUCTION

Much of the summertime precipitation in Colorado is due to orographically induced convective storm systems that initially form over the mountains and later move across the plains. It is the general purpose of this study to describe some of the physical kinematic structure of these storms. Three storm systems were studied using radar data obtained from the M-33 radar operated by Colorado State University during the South Park Area Cumulus Experiment (SPACE) of 1974 and the WSR-57 radar operated by the U.S. Weather Bureau and located at Limon, Colorado. The radar data were studied to (a) qualitatively describe the kinematic structure of orographically initiated convective storm systems; (b) describe changes in structure as the storm system translates and propagates eastward across the Colorado plains; and (c) describe the general environmental conditions that favor long lived, long moving convective systems.

2. PROCEDURE

2.1 Geographic Location

The Tarryall Range is located approximately 75 km southwest of Denver, Colorado. East of the Tarryalls the terrain is a relatively flat plain of about 1500 meter mean sea level (MSL) elevation. Just west of the Tarryalls is an oval shaped flat valley, South Park, with overall dimensions of 30 km east-west by 45 km north-south and at an elevation of about 2.8 km MSL. The town of Fairplay is located in the northwest corner of South Park. During 1974 the SPACE project operated a modified M-33 acquisition radar located at Kenosha Pass (elevation 3.1 km MSL) near the northern end of the Tarryall Range. The M-33 radar was positioned so that the radar operator could initially observe thunderstorms that formed over the mountains which surround South Park and then observe the storms as they moved eastward across the plains. The WSR-57 radar was located about 180 km nearly due east of the M-33 radar.

2.2 Storm Environment

The synoptic environment of the convective systems was determined by examining the daily U.S. Weather Bureau weather maps. The wind and thermal environment of the storm was determined from the standard U.S. Weather Bureau rawinsondes taken at Denver at 0600 and 1800 MDT and radiosondes that were launched from a site near Fairplay for the SPACE project. (All times in this paper will be presented as Mountain Daylight Time - MDT. Greenwich Mean Time is six hours later than MDT) The South Park radiosondes were launched each day at about 0600 and often followed by other launches at 0800 and 1200. The radiosondes were also tracked with an M-33 tracking radar so that upper level winds could be determined.

2.3 Radar Analysis

Both the WSR-57 and M-33 radars are 10 cm wavelength radars operating mainly in a PPI mode. Data was recorded from both radars by taking single frame pictures of the PPI scope presentation. WSR-57 pictures were taken once every five minutes while a beam elevation of 1/2° was maintained, but the M-33 was spiral scanned from 0° elevation to echo top (usually about 16° elevation). M-33 non-range normalized echo intensity was determined by reducing receiver gain by 10 dB after the PPI sweep was photographed. This necessitated 3 to 4 sweeps at one elevation angle before the antenna was raised 2° in the spiral scan sequence. Accordingly, a spiral scan with intensity data required 5 to 7 minutes to complete. WSR-57 echo intensity data was automatically range normalized and displayed in alternating grey, white, and black shades on a single scope photograph.

In order to select storm systems for study, the photographic data from both radars were examined to find storms that (a) were initially detected by the M-33; (b) detected at some time by both radars simultaneously; (c) radar detectable for more than one hour; and (d) relatively isolated systems, i.e., not part of a line. Once promising storms were selected, the PPI echoes of both radars were traced onto a common grid so that individual echoes could be tracked. In addition, synthetic RHI profiles were constructed from the M-33 spiral scans. The WSR-57 echoes were analyzed by manually determining the area of each echo intensity level and then applying Danielson's (1975) Z-R relation of $Z=800R^{1.44}$ to estimate the volume rainrate of the storm (volume rainrate equals rainrate multiplied by the echo area).

2.4 Data Limitations

Time and space resolution limitations present important analysis problems. Time resolution with the WSR-57 is approximately 5 minutes. The M-33 radar takes 7-15 minutes to complete a spiral scan sequence. The spatial resolution of the WSR-57 is limited by the 2° beam width and the .8 km pulse length. The storms observed in this study were initially about 130 km from the WSR-57. At this distance, the radar was sampling a horizontal area of 4.5 km by 1.8 km. The bottom of the radar beam was at ground level,

TABLE 1

Summary of Selected Storm Systems

Synoptic Situation	Western U. S. under vast upper level high. Weak stationary surface front in eastern Colo.	Upper level flow zonal Weak cold front moved through Colo. during the day.	Upper level flow zonal Significant moisture at 500 mb. Surface cold front remained stationary in eastern Colorado
Thermal instability at 500 mb	+2 C	+2 C	+5 C
Average cloud layer Wind	205/3 ms^{-1}	260/8 ms^{-1}	265/19 ms^{-1}
Average sub-cloud Wind	L/V	270/3 ms^{-1}	100/5 ms^{-1}
Total number of cells identified	4	8	13
Duration of cells Average/Deviation	30/22	43/30	44/24
Total duration of system	62 min.	131 min.	219 min.
Distance traveled by system	5 km	73 km	134 km

while the top of the beam extended to a height of 7 km MSL. The M-33 space resolution was limited by the 2° beam width and 0.4 km pulse length. At a range of 65 km the horizontal area sampled by the M-33 radar was 2.2 km by 4 km.

2.5 Terminology

Byers and Braham (1949) define a thunderstorm cell as a localized region of convective activity. In this paper the word cell will be defined as a radar echo with a single intensity core. The two definitions are not in disagreement unless two localized regions of convective activity have the same echo intensity and are separated by less than 4.5 km. Regions of this type will appear as a single WSR-57 radar echo with a single intensity core and for this paper will be termed a single cell. The word storm system is defined in this paper to mean the entire group of cells whose echo boundaries appear in the PPI scope photos to be within about 3 km of each other.

3. RESULTS

3.1 Storm System Summary

Three storm systems on three different days were selected for study. The systems studied occurred on 13 July 1974, 7 August 1974, and 15 August 1974. The synoptic, thermal, and wind environments, and the overall characteristics of each storm system are presented in Table 1. Figure 1 shows only the WSR-57 echoes of the 15 August storm system, while Figure 2 shows only the M-33 echoes of the 13 July system. Note that the storm system of 15 August, shown in Figure 1 was actually detected by the M-33 radar before any echoes appeared on the WSR-57. However, only the WSR-57 echoes are shown in the figure. Since the 7 August system behaved and appeared very similar to the 15 August system, the 7 August echoes are not shown.

3.2 Multicellular Structure

It is clear from examining Figure 1 that, at any given time, the 15 August storm system consisted of more than one active cell. There is a discrete type of propagation apparent near the leading (eastern) edge of the storm. This discrete propagation allows one to classify this storm as a multicell. There is other evidence also supporting the multicell classification. Supercell and severely sheared single cell storms have been characterized by a consistent and unique RHI profile. Foote and Fankhauser (1973) have shown an RHI profile of a supercellstorm that did not change appearance for 73 minutes. The available RHI profiles of the 15 August storm system were not at all consistent. In fact, the profiles changed so much in 10 to 15 minutes that it was even difficult to identify individual cells from one profile to the next. Also, none of the other supercell RHI characteristics, e.g., precipitation wall, echo free vault, or echo overhand, were apparent on the 15 August RHI profiles. It is also important to note that the storm system began as a multicell storm while over the mountains, and remained a multicell as the system progressed eastward. All three systems exhibited characteristics similar to the 15 August system and, accordingly, all three systems are classified as multicell.

Even though the three storm systems are all multicell systems, there are some significant differences. Note, from Table 1, that although the thermal instability and low level moisture on both 13 July and 7 August were the same, the storm system of 7 August lasted twice as long as the 13 July storm. The main identifiable difference between the two days was the considerably stronger winds. Correspondingly, the 7 August storm tended to be better organized. This system organization forced new cells to form in a preferred location, such that two cells were not competing for the same low level moisture at the same time. An examination of the PPI echoes from both systems

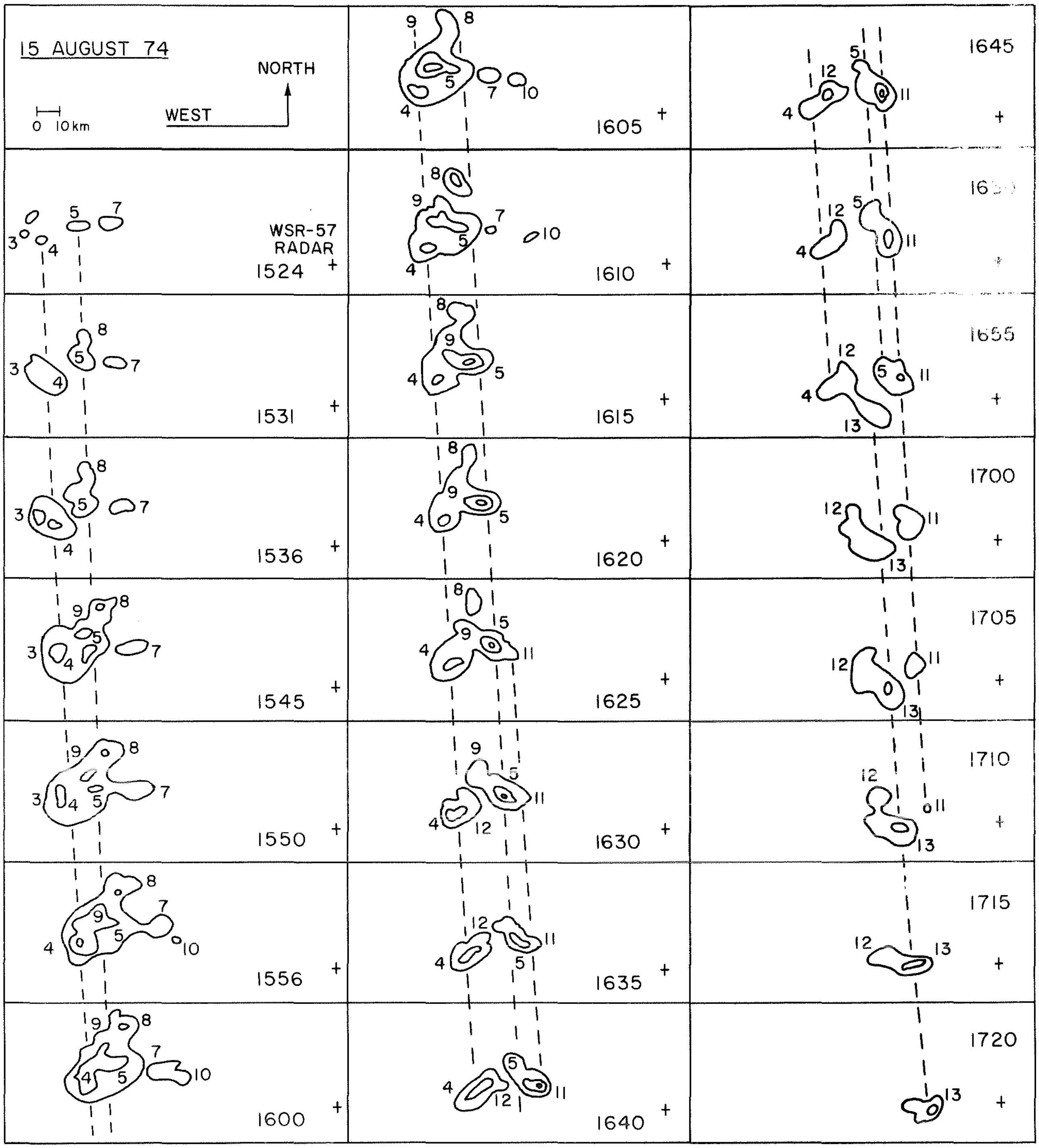

Figure 1. Echoes of 15 August 1975 storm system. The small (+) indicates location of the WSR-57 relative to the echo for each time period identified. The small numbers near the echoes indicate cell identifications. (Cells 1 through 7 had already been identified before 1524 by using M-33 echoes not shown.) The echo contours correspond to 18, 31, and 41 dBz.

shows that the new cells on 7 August always formed on the eastern edge of the system, while the new cells of 13 July formed on both the northern and western edges of the system at the same time. Support for this explanation is also provided by the behavior of the 15 August system. This system was the longest lived system of the data set and, although stability might affect the system duration, it is apparent from Figure 1 that new cells always formed on the eastern edge of the system - a prefered location. The longest lived multicell systems should require an environment of not only adequate moisture and instability, but also moderately strong low and upper level winds. Other research tends to support this conclusion. Miller and Frank (1975) describe a multicell storm on 31 July 73 that occurred on a day of +6°C thermal instability buy sub-cloud winds of less than 3 ms^{-1}.

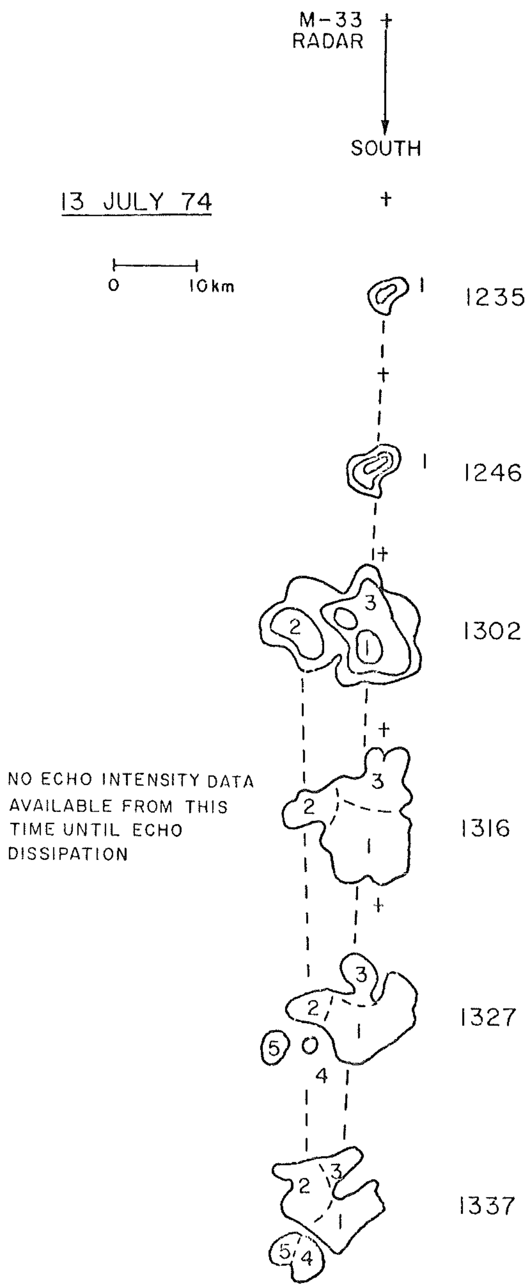

Figure 2. Echoes of the 13 July 1974 storm systems. The small (+) indicates the location of the M-33 radar relative to the echo for each time period. The small numbers inside the echoes indicate cell identifications. The large numbers indicate the time of the specific PPI scan. The echo contours correspond to reflectivities of 19, 29, and 39 Dbz. The dashed lines in the interior of the echoes indicate hypothesized cell locations.

This multicell system lasted about 90 minutes. Kropfli and Miller (1975) describe a multicell storm system of 138 minutes duration that occurred on a day of moderate instability, low level winds of 6-8 ms^{-1}, and cloud layer winds of 15-17 ms^{-1}.

3.3 Pattern of Cell Devlopment

Table 2 lists the time of initial radar detection, time of final radar detection, and minimum duration of each of the cells of the 7 and 15 August systems. (The cell duration presented in Table 2 is listed as "minimum" because the WSR-57 PPI scans are taken only once every five minutes and the actual cell duration could be nearly 10 minutes longer than indicated on radar.) Figures 3 and 4 show the time variation of the volume rainrate of the same two storm systems. By comparing Figure 3 and Table 2 for the 15 August system, one notices that by time 1550 only 18% of the total rainfall of the storm had been detected , but nearly 70% of all cells in the system had been identified. Also note that during the time from 1550 to 1620, the time of most intense rainfall, only one new cell developed, and this one cell, cell 6, was of low intensity and only lived for 14 minutes. In addition, nearly 50% of the cells that formed during the first part of the storm system's lifetime (cells 3 through 9) lasted for more than 50 minutes. During the time period 1441 to 1550 there was an average rate of cell formation of one new cell every 8 minutes, but from 1550 to 1610 only one new cell formed every 20 minutes, and from 1610 to 1720 only one every 23 minutes. The 7 August storm system exhibits similar characteristics. For example, from 1420 to 1517 nearly 70% of all system cells had been detected, but only 38% of the total rain had fallen. However, Figure 4 also shows a nearly 20% decrease of volume rainrate of the 7 August storm system at 1517. This decrease coincides with the time of initial

Table 2

Cell characteristics of 7 August and 15 August 1974 storm systems

Cell Number	Initial Detection Time	Final Detection Time	Minimum Duration (min.)
7 August 1974			
1	1421	1523	62
2	1432	1454	22
3	1446	1615	89
4	1517	1615	58
5	1517	1627	70
6	1539	1555	16
7	1600	1605	5
•8	1610	1632	22
15 August 1974			
1	?	1523	?
2	?	1454	?
3	1521	1550	29
4	1531	1655	84
5	1531	1655	84
6	1531	1542	11
7	1524	1610	46
8	1531	1625	54
9	1545	1630	45
10	1556	1610	14
11	1625	1710	45
12	1630	1715	45
13	1655	1720	25

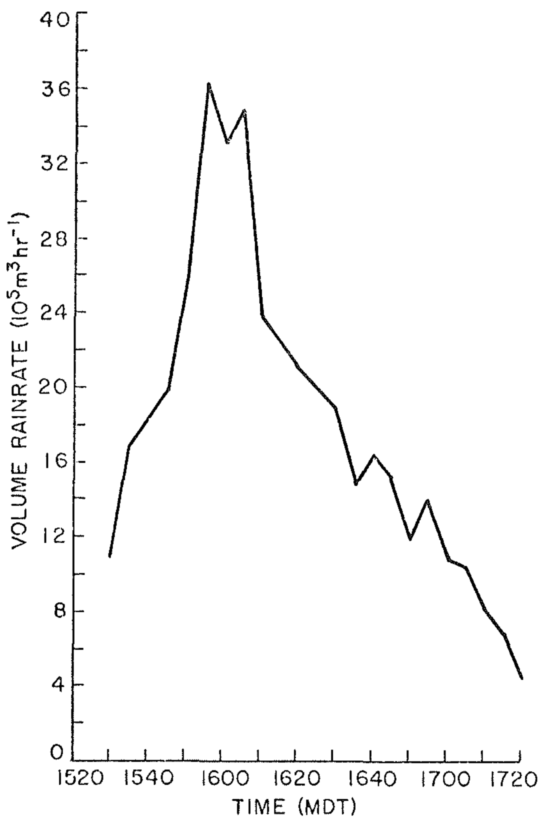

Figure 3. Volume rainrate of 15 August 1974 storm System.

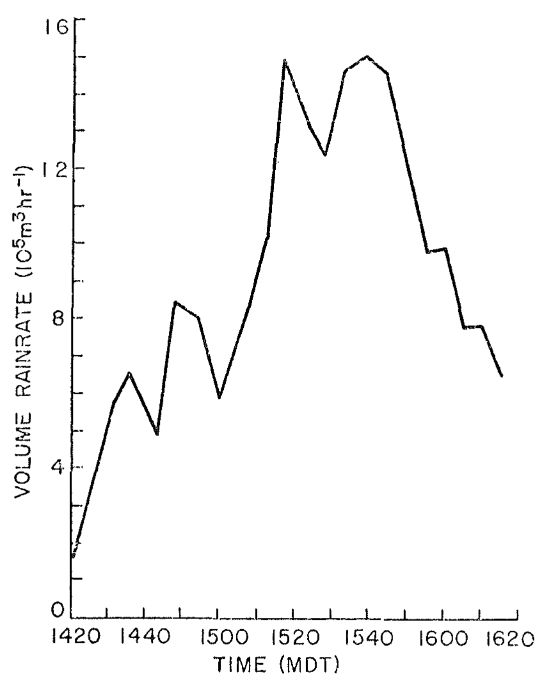

Figure 4. Volume rainrate of 7 August 1974 storm system.

detection of two new cells, both of which formed east (ahead) of the older cells in the storm system, and formed just at the time when the storm system had reached a maximum volume rainrate. No 20% decrease followed by an increase in volume rainrate was observed for the 15 August system (Figure 3), and during the most intense part of this storm only one small cell formed ahead of the storm system.

It appears from the above data that multicell storm systems begin over the mountains as a group of numerous cells all competing for the available moisture. As the system grows, becomes more intense, and moves over the plains, a point is reached where new discrete cell initiation is inhibited. Not until the system volume rainrate begins to diminish are new cells allowed to form. These later cells are not as intense nor as long lived as the earlier cells. If new cells do form during the intense stage of the storm system (as in the 7 August system at 1517), the system volume rainrate is sharply decreased until the new cells can grow large enough to add to the total system rainfall. It also seems significant that even during the most intense stage of the system development there are still several cells (six cells on 15 August and 4 cells on 7 August) active at the same time.

3.4 Cell Duration

The convective cells as identified in this study had an average radar detectable lifetime of 41 minutes, and four cells lasted for more than one hour. The cell duration of 41 minutes is longer than most of the cell durations reported in the literature. Kropfli and Miller (1975) found an average cell duration of 30 minutes in a northeast Colorado hailstorm. Their use of a very high resolution radar increased their ability to monitor individual cells. The resolution of the WSR-57 used in the present study leaves the possibility that new cells were forming in a location such that they would not be detected as separate echoes. In fact, the 13 July 74 system that appears as several cells on the M-33 radar (Figure 2) actually only appeared as a single cell on the WSR-57 radar since that storm system was much closer to the M-33 than the WSR-57.

It is interesting to compare the average cell durations of the cells that form early in a system's lifetime to those cells that form late. From Table 2 it is seen that the average duration of cells forming early in the lifetime of the 15 August system (prior to 1550) was 50 minutes, while the average duration of the cells that formed after the system had reached maximum intensity was 32 minutes. Similarly, for the 7 August storm system, the early cells lasted an average of 60 minutes, while the late developing cells only lasted 14 minutes. This observation of cell duration tends to support the description of multicell storm system development presented in the previous section.

4. CONCLUSIONS

Three different storm systems that occurred on three different days were examined by two PPI radars. The main conclusions from this study are (a) storm systems that initially form over the mountains of Colorado begin as multicell systems and remain multicell systems as they move onto the High Plains; (b) the longest lived and longest traveling multicell systems occur on days of moderate instability and strong winds (19 ms^{-1} average cloud layer wind and 5 ms^{-1} average subcloud wind); (c) numerous convective cells form early in the development of the multicell system, but as the system reaches its most intense stage, very few, if any, new cells form; and (d) cells that form before the storm system reaches maximum volume rainrate tend to last 18 to 42 minutes longer than those cells that form late in the storm system's lifetime. The average duration of all storm system cells is 41 minutes.

5. ACKNOWLEDGEMENTS

This work was partially supported by National Science Foundation Grants ERT 71-01885 and DES 75-17313, and by the state of Colorado.

6. REFERENCES

Byers, H. R., and R. R. Braham, 1949: The Thunderstorm. U.S. Government Printing Office, Washington, D. C., 287 pp.

Danielson, K. S., 1975: Continental Mountain Cumulus Clouds. M.S. Thesis, Colorado State University, Fort Collins, Colorado, 172 pp.

Foote, G. B., and J. C. Fankhauser, 1973: Airflow and Moisture Budget Beneath a Northeast Colorado Hailstorm. Journal of Applied Meteorology, 12, 1330-1340.

Kropfli, R. A., and L. J. Miller, 1975: Dual Doppler Radar Measurements within a Hail Producing Storm in Norhteast Colorado. Preprints of 16th Radar Meteorology Conference, American Meteorological Society, 227-282.

Miller, L. J., and H. W. Frank, 1975: Three-Dimensional Air Moition within a Northeast Colorado Hailstorm. Preprints of 16th Radar Meteorology Conference, American Meteorological Society, 321-327.

5.2.6

SIGNIFICANT DIFFERENCES AMONG FOUR SIMULTANEOUS MESOSCALE RAWINSONDE OBSERVATIONS: IMPORTANT EFFECTS ON CLOUD MODEL PREDICTIONS

David A. Matthews and Richard L. Eddy

Bureau of Reclamation
Division of Atmospheric Water Resources Management
Denver, Colorado

1. INTRODUCTION

The purpose of this paper is to determine (1) if significant variations in the thermodynamic structure exist on the mesoscale (50-100 km) and (2) if these variations are important to cumulus development, as objectively determined by cloud model predictions and as observed by geosynchronous satellite.

Atmospheric thermodynamic structure is important in determining the convective potential for clouds through the buoyancy generation term in the vertical equation of motion. This, in turn, is important to the cloud physicist because it determines the internal cloud dynamics that are simulated by numerical cloud models. If these models are to be compared with observed clouds for verification of their ability to simulate nature, they must be initialized with soundings representative of the natural phenomena they are simulating. This paper addresses the problem of spatial and temporal observation scales required to adequately represent important features in the convective environment.

2. HIPLEX MESOSCALE SOUNDING DATA

During the period from June through August, 1975, a mesoscale rawinsonde (raob) network was operated in eastern Montana at the stations shown in figure 1. Note the large difference in distances between the synoptic-scale National Weather Service (NWS) stations and the High Plains Cooperative Program (HIPLEX, see Kahan, 1976a) mesonet shown in the insert. The distance between NWS stations ranges from 571 to 357 km in comparison to 105 and 81 km between the mesonet stations. These four stations routinely took 0000 GMT and 1200 GMT rawinsondes and observed special three-hourly sequences from time of first convective cloud development on thirty-eight operational days. Much care was taken in hydrostatic checking of soundings for internal consistency, and the data were archived for rapid computer processing (see Kahan, 1976b).

In June a RD-65 was operated at Miles City, while GMD equipment was used at all other sites. The RD-65 was replaced by a GMD in early July. All rawinsondes were released simultaneously at each observation time selected for this analysis.

3. ANALYSIS OF RAWINSONDE DATA

Data were processed for all times having four simultaneous releases in three basic data sets: 1200 GMT, (74 cases - 296 raobs), 000 GMT (68 cases - 272 raobs), and special convective events (38 cases - 152 raobs). These 720 raobs were plotted on "Skew-T" thermodynamic diagrams, individually and in sets of four. From these diagrams basic thermodynamic differences were observed. The most obvious variation between soundings was that of moisture, particularly that in the boundary layer. This boundary layer variation, illustrated in figure 2, is critical to cloud base height determination.

The next most critical variation between simultaneous raobs was the variation in low-level stability. On some days this was sufficient to cause wide variation in releasible instability and convective cloud development predicted by cloud models (see section 4). In general, upper-level lapse rates were nearly identical, with small variation only in reference temperature (see figure 3).

4. MODEL ANALYSIS OF RAOB VARIATIONS

Two fast one-dimensional steady-state cloud models were used to analyze convective potential. The Great Plains Cloud Model (GPCM) is a Lagrangian parcel model developed by Hirsch (1971) that calculates a number of cloud variables for each of six cloud radii. Three sets of soundings were analyzed by the model, which used the convective condensation level (CCL) for cloud base height. The CCL was based on an assumed 50-mb mixing layer. Preliminary analyses of these data indicate that significant variations among predicted clouds occurred on many days. A complete statistical analysis will be available before the conference.

Twenty-eight cases (each composed of four simultaneous sounding releases) were analyzed by MESOCU - a cloud environment interaction model developed by Perkey and Kreitzberg (1974, 1976). This model simulates the effect of mesosynoptic scale lifting, subsidence induced by convective clouds, mixing of cloud and environment, subcloud evaporation of precipitation, surface eddy mixing, and solar heating. The ability of MESOCU to predict convective development in the High Plains has been demonstrated using Colorado soundings from the National Hail Research Experiment (see Matthews and Henz, 1975). Similar experiments showing the model's ability to predict the evolving convective environment have shown that the model is a reasonably good predictor of local convective environment interaction; however, it does not predict development well in cases of advection (see Matthews and Henz, 1975b). The

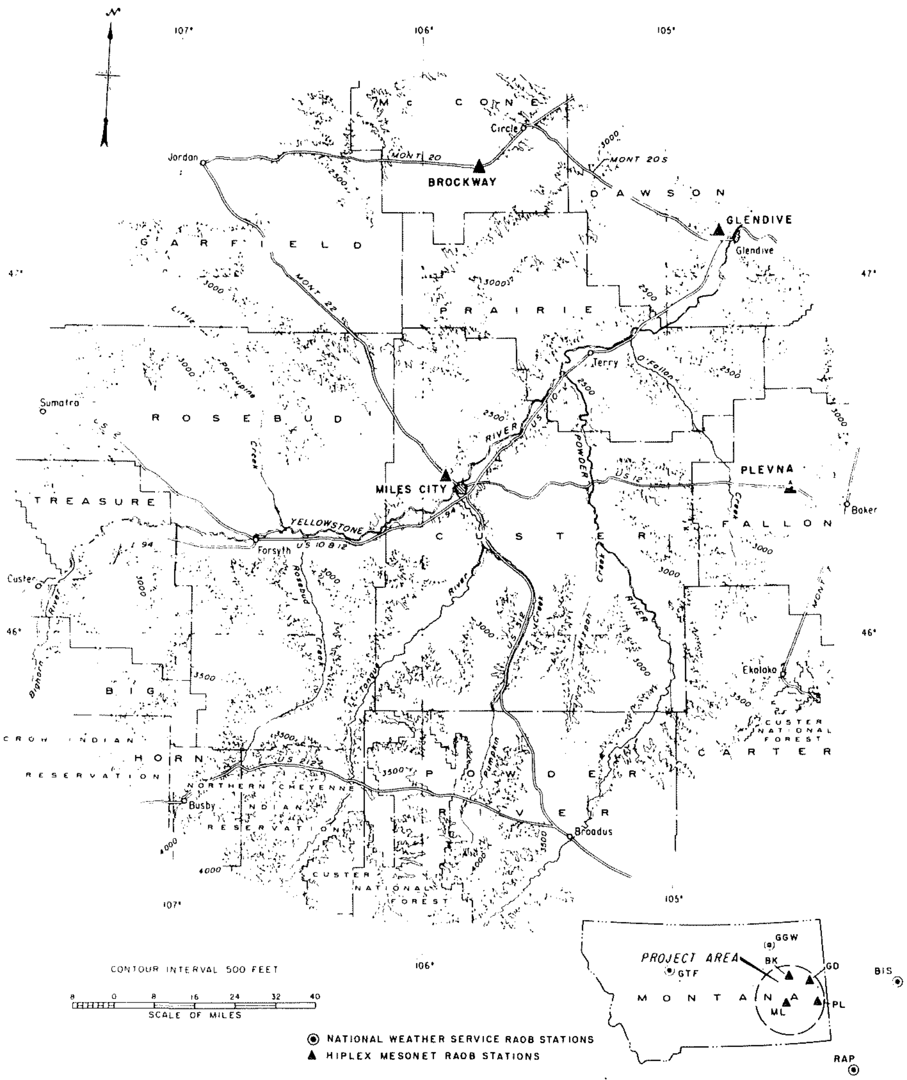

Figure 1. Map of HIPLEX field site at Miles City, Montana, showing four rawinsonde stations: Miles City (ML), Brockway (BK), Glendive (GD), and Plevna (PL), and National Weather Service raob stations (GTF, GGW, BIS, RAP).

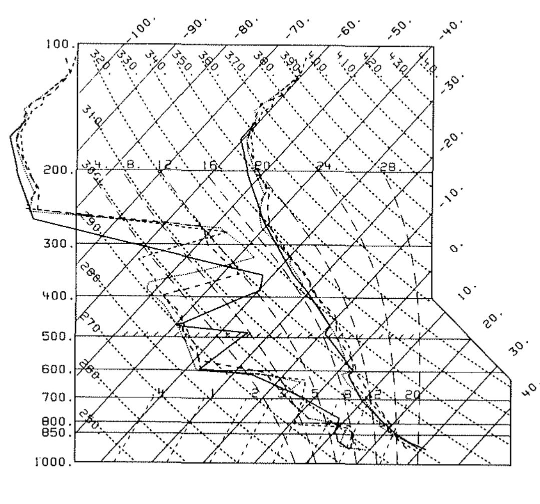

Figure 2. Skew-T thermodynamic diagram showing typical variation in temperature and moisture of simultaneous soundings taken at 0000 GMT on July 7, 1975. Station code: ML —, BK ···, GD ---, PL — — —.

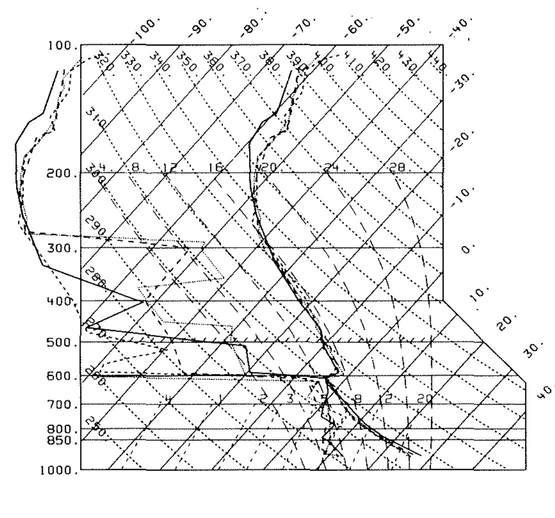

Figure 3. Skew-T analysis showing typical variation in low-level stability and moisture and small variations in upper-level lapse rates for 0000 GMT on July 10, 1975.

Table 1. - Statistical Summary of All Model Predictions.

Parameter	Time (LST)					
	1800			1900		
	Mean	Standard deviation	Standard error	Mean	Standard deviation	Standard error
Cloud base height (km)	1.624	1.057	0.200	1.394	1.020	0.193
Cloud top height (km)	3.870	3.196	0.604	2.755	2.217	0.419
Cloud depth (km)	2.246	2.595	0.490	1.361	1.778	0.336
Thermal depth (km)	3.196	2.868	0.542	2.090	1.896	0.358
Sample size:		28 cases 112 raobs			28 cases 112 raobs	

Table 2. - Statistical Summary of Model Predicted Clouds.

Parameter	Time (LST)					
	1800			1900		
	Mean	Standard deviation	Standard error	Mean	Standard deviation	Standard error
Cloud base height (km)	3.230	1.176	0.277	3.001	1.181	0.295
Cloud top height (km)	7.671	3.556	0.838	6.064	3.033	0.758
Cloud depth (km)	4.441	3.407	0.803	3.063	2.896	0.724
Parcel depth (km)	6.247	3.292	0.776	4.518	2.726	0.681
Sample size:		18 cases 49 raobs			16 cases 42 raobs	

Table 3. - Statistical Summary of Standard Deviation of Predicted Parameters for Simultaneous Sounding Cases with Two or More Clouds.

Parameter	Time (LST)					
	1800			1900		
	Mean	Standard deviation	Standard error	Mean	Standard deviation	Standard error
Cloud base height (km)	0.417	0.593	0.10	0.347	0.467	0.08
Cloud top height (km)	1.274	1.343	0.23	1.466	1.399	0.25
Cloud depth (km)	1.549	1.454	0.24	1.620	1.538	0.27
Parcel depth (km)	1.597	1.501	0.25	1.597	1.584	0.28
Sample size:		18 cases 49 raobs			16 cases 42 raobs	

results of these cases indicate that significant initial sounding variations exist on the mesoscale. In addition, model results for one hour of cloud-environment interaction indicate that there is a significant difference in predicted development among the four raobs. Statistics showing this variance are given in Table 1. Statistics are compiled for the initial sounding 1800 LST (0000 GMT) and the predictions for 1900 LST which result from model prediction of cloud-environment interaction from 1800 to 1900 LST. Here the mean standard deviation and standard error of each case of MESOCU predictions for four simultaneous soundings are summarized for all twenty-eight cases. Results in Table 1 summarize all model predictions, including events where no clouds were predicted for a particular sounding. The emphasis here is on the standard deviation of the parameters. This provides an objective measure of the model responses to thermodynamic differences among each of the four soundings. There are significant variations of all parameters, particularly cloud base height and cloud tops. The wide variation in cloud base height is a direct response to boundary layer moisture and instability, both of which showed considerable variation in Skew-T plots discussed in section 3. In seven cases only one cloud was predicted from the set of four rawinsondes, and in seven other cases only two of the four raobs resulted in clouds predicted by the model. These pairs of raobs that predicted cloud development showed strong geographic consistency between the prediction of cloud and no cloud. Either the two western-most, southern-most, or northern-most raobs predicted cloud development, while the other two did not, thus suggesting spatial continuity. In 90% of the

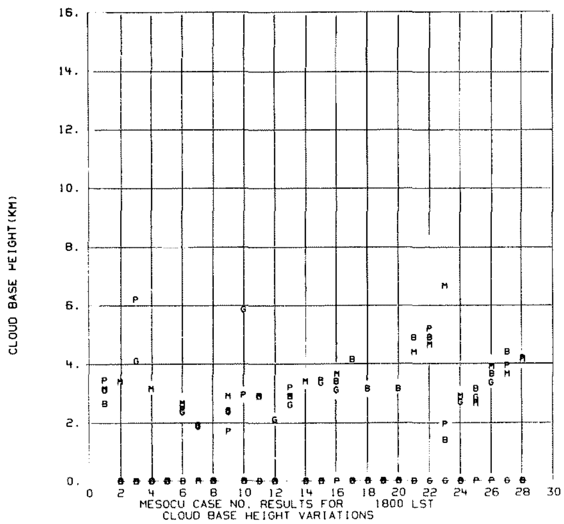

Figure 4. Cloud Base Height variations for all 28 cases of simultaneous 0000 GMT (1800 LST) rawinsondes. Labels according to station name ML(M), BK(B), GD(G), PL(P).

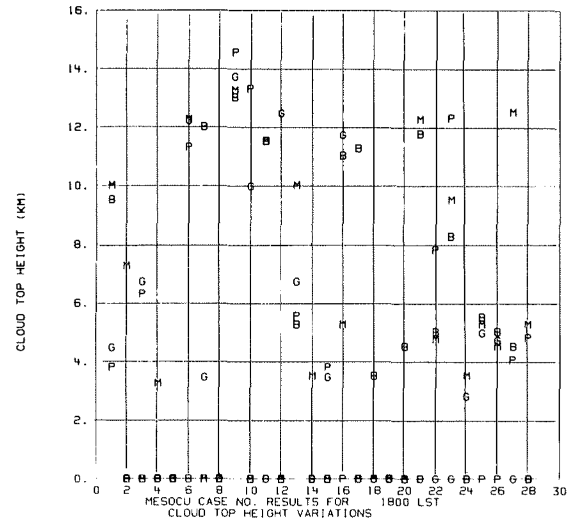

Figure 5. Cloud Top Height variation for all 28 cases of simultaneous 0000 GMT raobs. Labels as in Figure 4.

cases this appears consistent with cloud development observed by satellite as described in section 5. (Further comparison with radar and satellite observations will be performed.)

There is a large daily variation in the model-predicted cloud properties as shown in Tables 1 and 2. These results show the wide variation in predicted parameters. The large standard deviations indicate important ranges of parameters that are physically significant to the cloud dynamics predicted by more sophisticated numerical cloud models. Table 2 summarizes the statistics for all clouds predicted by the model. This shows the mean and standard deviation of each parameter for all sets of simultaneous soundings. The large natural variation from day to day is reflected in these statistics.

In contrast, the variation among simultaneous releases is summarized by Table 3. Here the mean standard deviations of each parameter and their standard deviation and standard errors are presented. The large standard deviation of the mean standard deviations (for 19 cases of raobs at two or more sites) in cloud base height (584 meters) represents variations in cloud base height as large as 5200 meters (for case number 23 shown in figure 4) among four simultaneous raobs. Similar statistics for cloud top height reflect the large variations shown in figure 5. Large variations of this magnitude are highly significant to the physical development predicted by cloud models.

Similarly, large mean standard deviations are reflected in the statistics for cloud depth and thermal depth (the sum of dry and moist adiabatic ascent) predicted by MESOCU.

5. SATELLITE OBSERVATIONS

Typical variations of clouds in the mesonet are illustrated by satellite observations of conditions on July 9 and 28 (see figures 6 and 7). The encircled region of each photograph shows clouds in the vicinity of the mesonet. The circle diameter is 220 km. Within this region on July 9, 1975, there were two bands of convective clouds on the north and south sides of the circle, respectively, which correspond to model predictions shown in Table 4. These bands were composed of cumulus congestus, cumulonimbus, and middle level clouds oriented with the 500 mb flow. Note the thin convective lines in west central South Dakota (see arrow in figure 6) which have very pronounced spatial variations within a 70-km-wide band composed of three thin lines of cumulus 14 km wide and 250-300 km long. This structure illustrates the typical spatial variations in cloud patterns in the convective environment on the meso-β scale.

On July 28th more distinct convective cloud development occurred in a narrow band 55 km wide extending northeastward from Miles City toward Brockway and Glendive (see figure 7). In this case large convective clouds were predicted by MESOCU for Miles City and Brockway, and none for Plevna and Glendive (see Table 4).

Widespread convective development in Montana, Wyoming, and Colorado on this day shows the typical extent and spatial variation found in major cumulonimbus development. Note the three major thunderstorm clusters west of the mesonet, each of which has anvils of cirrus canopies extending more than 200 km. These mesoscale systems illustrate the wide range of important spatial variations in convective development.

Model predictions corresponding to cloud conditions observed in the mesonet on July 9 and 28 show the quantitative spatial variations that are typical of soundings used in this study (see Table 4). These variations show that important thermodynamic differences do exist on the mesoscale. Satellite observations of clouds in the vicinity of each sounding are also rated. These observations tended to show the same spatial

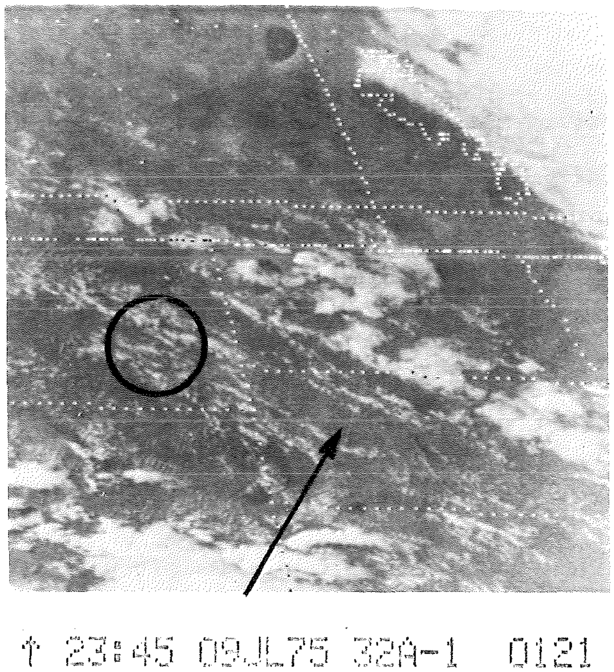

Figure 6. Geosynchronous satellite (SMS-2) visible imagery over Northern High Plains taken on July 9, 1975, at 2345 GMT. Circle shows Miles City, Montana. HIPLEX mesonet area. Arrow illustrates scale for thin lines of cumulus (see text).

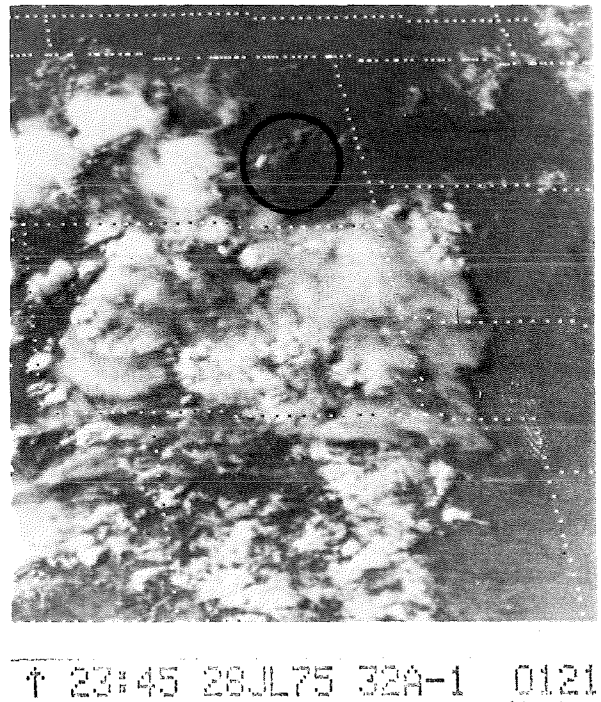

Figure 7. SMS-2 visible imagery over the Northern High Plains showing typical mesoscale convection within the HIPLEX mesonet (circle) taken on July 28, 1975, at 2345 GMT.

Table 4. Comparison of Model-predicted Cloud Characteristics and Satellite-observed Cloud Types.

Date	Station	Model prediction (0000 GMT)			Satellite (2345 GMT) observation
		Base (km)	Top (km)	Depth (km)	
July 9	ML	2.901	10.026	7.125	Cb
	BK	2.902	5.277	2.375	Cu+
	GD	2.605	6.730	4.125	Cu+
	PL	3.193	5.568	2.375	Cu+
July 28	ML	4.401	12.276	7.875	Cb
	BK	4.901	11.776	6.875	Cu+
	GD	0	0	0	CLR
	PL	0	0	0	CLR

ML - Miles City
BK - Brockway
GD - Glendive
PL - Plevna

Cb - Cumulonimbus
Cu+ - Towering cumulus
CLR - Clear

variations as predicted by the model. However, a more rigorous analysis of digital imagery is required to quantify relationships between radiance and model predictions.

6. CONCLUSIONS AND FUTURE ANALYSIS

Definite variations in the atmospheric thermodynamic structures occur on the meso-β scale. These spatial variations in stability and moisture produce significant differences in simple numerical cloud-model predictions of cloud base height, cloud top height, cloud depth, and thermal depth. These variations in four simultaneous soundings indicate the need for soundings that are representative of the cloud environment. The fact that large variations exist on the mesoscale, within distances of 50 to 100 km, indicates the need for soundings near the immediate cloud that is to be simulated. The verification of spatial variations in cloud types using satellite observations adds confidence to the model's ability to accurately predict significant thermodynamic variation among soundings. The large range of clouds that may be predicted by models further indicates the need for careful selection of input soundings and examination of basic thermodynamics for representativeness.

Satellite soundings will contribute to detailed mesoscale analyses of horizontal gradients of temperature and moisture. Spatial resolution of 15 to 30 km for these variables will be extremely useful in determining the mesoscale representativeness of soundings and in describing important mesoscale triggering mechanisms. Such satellite sounders are planned for geosynchronous operation in the late 1970's on the Storm Observation Satellite (SOS) (see Shenk, 1975). These data will greatly help resolve the thermodynamic variations on the mesoscale that are important to the fields of weather modification, cloud physics, and severe storm forecasting.

Future studies of the HIPLEX rawinsonde data will examine details of the temporal and spatial variation for all soundings by compiling statistical analysis of one-dimensional model predictions. In addition, detailed case analyses of satellite imagery, radar, and sounding variations will be made to verify the relationship between observed clouds and sounding variations.

7. REFERENCES

Hirsch, J., 1971. Computer Modeling of Cumulus Clouds During Project Cloud Catcher. Report 71-7. USBR Contract No. 14-06-D-6796. South Dakota School of Mines and Technology. p. 61.

Kahan, A. M., 1976a. Project HIPLEX, Plans, Progress, and Approach. Proceedings. International Conference on Weather Modification. Boulder, Colorado.

Kahan, A. M., 1976b. 1975 HIPLEX Data Inventory. Bureau of Reclamation Report. Div. Atmos. Water Res. Mgmt. Denver Federal Center, Denver, Colorado. pp. 5.1-5.5.

Kreitzberg, C. W. and D. J. Perkey, 1974. Mesoscale Modeling, Forecasting, and Remote Sensing Research. Final Report to Project THEMIS. AFCRL No. F19629-69-C-0092. (Available from NTIS, refer to AD760-123.)

Kreitzberg, C. W. and D. J. Perkey, 1976. Release of Potential Instability: Part I. A Sequential Plane Model within a Hydrostatic Primative Equation Model. J. Atmos. Sci. Vol. 33. pp. 456-475.

Matthews, D. A., 1974. Simulation of Cumulus Interaction with the Environment Using a One-Dimensional Quasi-Time-Dependent Model. Proceedings. Cloud Physics Conference. Tucson, Arizona. AMS. pp. 216-222.

Matthews, D. A., and J. Henz, 1975a. Verification of Numerical Model Simulation of Cumulus - Environmental Interaction in the High Plains. Pure and Applied Geophysics. Vol. 113. pp. 803-823.

Matthews, D. A., and J. Henz, 1975b. Temperature and Moisture Changes in the Severe Storm Environment Caused by Cloud-Environment Interaction - A Verification of Model Prediction. Proceedings. Ninth Conference on Severe Local Storms. Norman, Oklahoma. AMS. pp. 238-243.

Shenk, W. E. and E. R. Kreins, 1975. The NASA Storm Research Program. Proceedings. Ninth Conference on Severe Local Storms. Norman, Oklahoma. AMS. pp. 468-473.

6.1.1

AN OBSERVATION OF NATURAL CLOUD SEEDING WITH ACCOMPANYING RELEASE OF PRECIPITATION

Lawrence F. Radke and Paul H. Herzegh

Cloud Physics Group, Atmospheric Sciences Department
University of Washington, Seattle, Washington 98195

1. INTRODUCTION

An important part of the University of Washington's CYCLES (Cyclonic Extratropical Storms) PROJECT (Hobbs and Houze, 1976 and Houze et al., 1976) is the study of the meso- and micro-scale phenomena which lead to the formation of precipitation in frontal systems. An interesting phenomenon observed in CYCLES has been the occurrence of anomalous, glaciated patches within larger areas of unglaciated, slightly supercooled, stratiform clouds. Both the origin and the microphysics of these patches are of interest.

In this paper we describe a well-documented observation of anomalous glaciation, which resulted in the formation of precipitation, which was observed on December 6, 1973. On this occasion, unambiguous measurements of persistent, high ice particle concentrations ($>100\ \ell^{-1}$) were made with the University of Washington's automatic ice particle counter (Turner, Radke and Hobbs, 1976). The size and movement of the precipitation associated with the glaciated patch was provided by simultaneous PPI radar coverage.

2. METEOROLOGICAL CONDITIONS

On December 5, 1973, an intensive CYCLES field study of a cyclonic storm was begun while the associated cold front was still more than 1000 km off the coast of Washington State. This study continued for over 48 hours, terminating well after the frontal passage in Seattle.

The cold front position and humidity data from serial rawinsondes launched in Seattle are shown in a time-height cross-section in Figure 1. Figure 1 shows that the anomalous, glaciated cloud which was observed between 1100 and 1300 hours (Pacific Standard Time) on December 6 was contained within a thin layer of moist air between 750 and 920 mb. This moist layer was bounded by very dry air above and relatively dry air below. Further analysis has shown that the moist layer was potentially unstable. As the core of dry air aloft moved over Seattle, precipitation on the ground ceased and radar echoes aloft, as detected by a vertically-pointing Doppler radar in Seattle, were suppressed (Figure 2).

3. OBSERVATIONS

The University of Washington's B-23 aircraft made two series of observations of the anomalously glaciated cloud patch, spanning a period of 80 min. Simultaneous radar observations linked the glaciated patch to a prominent precipitation echo which was tracked for over 90 min.

3.1 Initial Airborne Observation

Prior to the first observation of the glaciated cloud patch, the B-23 aircraft was flying at 3100 m, well above the top of a uniform, unglaciated stratiform cloud deck. The glaciated region was first revealed by a brilliant display of ice optics. The lower tangent arc to the 22° halo was especially prominent (Figure 3). The aircraft observers were immediately struck by the similarity of this display to that which occurs when stratiform clouds are glaciated by artificial seeding (Hobbs and Radke, 1975).

Since the temperature at the top of the stratiform cloud was everywhere higher than -5°C, it seemed likely that the glaciated area of more than 1000 km^2 was being seeded by altostratus and cirrostratus clouds above, which had previously shown prominent ice falls. At the time of the first airborne observations of the glaciated area there were no visual signs of falling ice, although the automatic ice particle counter did show an average reading of $0.1\ \ell^{-1}$ during a 10 km traverse in apparently clear air 400 m above the glaciated area. In addition, 60 km east of the glaciated area slightly higher concentrations of ice were detected at a height of 3100 m in a visible ice fall from altostratus at 5 km. Thus, if natural seeding was in fact the trigger for glaciation of the stratiform cloud deck, the seeding had largely ceased by the time the airborne observations were made. However, radar observations at that time indicated that the resultant generation of precipitation was just getting under way.

The aircraft made two consecutive orbiting penetrations through the tops of the "hardest" appearing clouds, which were in the center of the glaciated region. These orbits penetrated radar echo "A" in Figure 4 and showed that the echo was composed of at least three cells (Figure 5). The particle concentrations measured within the cells were very high, reaching peak values greater than $110\ \ell^{-1}$. Detailed examination of the radar echoes associated with this glaciated area indicated that they were often comprised of a number of smaller, cell-like units approximately 2-4 km in diameter. This cellular structure, which was also reflected in the aircraft measurements of liquid water content, suggests that there was a region of shallow, convective activity within the glaciated cloud. The decrease in liquid water content in cell III (Figure 5) may be a result of the diminished activity of an ageing convective element.

Formvar replicas of the cloud particles, both in the echo region and in other parts of the glaciated area, showed high concentrations of small ice columns and needles ranging in length from 50 to 500 μm. The presence of columns and needles was expected, both on the basis of the cloud temperature and the lower tangent arc observation. However, there was no evidence of any other types of crystals which might have fallen into the cloud from above.

3.2 Continuous Radar Observations

PPI radar coverage revealed the initial development of two small echoes about 5 min before the B-23 aircraft first penetrated the glaciated zone. During the following 90 min the echoes enlarged slightly, joined, and underwent a series of shape changes, while traveling toward the northeast at a speed of 18 to 22 m s^{-1}. Their speed and direction of motion were coincident with the wind speed and direction at the top of the stratiform cloud deck. The sequence of echo positions recorded during this time is shown in Figure 4. From 1230 to 1250 PST the exact shape and position of the echo became more difficult to determine due to blocking of the radar beam by nearby buildings and terrain. Radar tracking ended at 1250 PST when the echo began to merge with ground clutter echoes from the Cascade Mountains.

3.3 Final Airborne Observation

A final aircraft penetration of the glaciated region was made at 1250 PST, when the aircraft was at position "B" in Figure 4 near the trailing edge of the echo region. During this penetration the aircraft descended through the cloud deck in an 18 km long traverse which started at an altitude of 2900 m (-4°C). Data were taken as low as 2100 m (-1°C). As in the initial penetration 70 min earlier, ice particle concentrations were very high, with many peak values over 100 ℓ^{-1} throughout the depth of the cloud (Figure 6). The liquid water content had a cellular pattern similar to that of the initial penetration. The replicated ice particles were very similar to those found in the earlier penetration, except that their average size was larger and there were more rimed particles.

4. DISCUSSION

We have described a striking example of an anomalously glaciated section of stratiform cloud which contained a core region of shallow convection and precipitated at a moderate rate (a few mm hr^{-1} by radar estimation). It seems likely that the rather large area of glaciation resulted in a reorganization of the dynamics within the stratiform layer. Since the cloud was rather shallow, it produced precipitation rather efficiently. A major factor in this efficiency was probably the high ice particle concentration in the mixed phase of the core region.

The actual cause of glaciation remains unclear. Ice crystal growth upon active nuclei present within the tops of the stratiform layer seems unlikely in view of the factor of 10^5-10^6 discrepancy between ice nucleus concentrations active at -5°C and the ice particle concentrations measured within the cloud. The radar observations establish that the onset of precipitation followed the development of a glaciated region within the stratiform cloud, so it is unlikely that convective activity itself induced glaciation. Some remaining possible causes of glaciation are: seeding by ice crystals from the higher level clouds, ice nuclei preactivation, and ice multiplication.

A combination of ice crystal seeding from above and ice multiplication seems the most likely explanation for the observed glaciation. Prominent ice falls were observed in the vicinity of the glaciated patch, and Braham and Spyers-Duran (1967) have shown that ice from cirrostratus can survive very long falls in dry air. However, probably only a small fraction of the ice crystals sampled in the glaciated cloud originated in the higher cirrostratus since there were no signs of crystal habits appropriate to the low temperatures of the upper clouds in the lower cloud. However, crystal seeding from above may have taken place over a relatively large fraction of the glaciated region, and the high concentrations of crystals could then have been produced by ice multiplication. Hallet and Mossop (1974) have observed in laboratory experiments that ice splinters are produced during riming at temperatures between -3° and -8°C, which are similar to the measured cloud top temperatures of the glaciated area.

We have combined our observations with some speculation in forming the conceptual model shown in Figure 7. Figure 7a shows a light ice fall seeding from above triggering ice multiplication which eventually leads to glaciation. The latent heat released during glaciation provides the stimulus needed to organize the core region into small convective elements (Figure 7b). The appearance of such elements is a common occurrence following artificial seeding of stratiform clouds (Knollenberg, 1970; Hobbs and Radke, 1975). These convective elements, in artificially seeded cases, only appear after the cloud top has nearly completed glaciation. The mature stage is shown in Figure 7c, with horizontal divergence assisting in the spreading of the glaciated region at the cloud top. The mixed phase core provides an ideal region for the rapid growth of ice particles by diffusion, riming and coagulation. Calculations show that the observed precipitation rates can be maintained by updraft velocities of 10 to 15 cm s^{-1}. The sloping boundaries between the glaciated and unglaciated regions are consistent with visual observations of this and other glaciated stratiform clouds. Knollenberg (1970) cites evidence for both the sloping boundary and for subsidence near the boundary region, making the core region kinematically similar to a Bénard cell.

ACKNOWLEDGMENTS: We thank Professor Peter V. Hobbs, Director of the CYCLES PROJECT, for his help in this work. This research was supported by Grant ATM-74-14726-A02 from the Atmospheric Sciences Section (Meteorology) of the National Science Foundation.

5. REFERENCES

Braham, R. R., and P. Spyers-Duran, 1967: Survival of cirrus crystals in clear air. J. Appl. Meteor., 6, 1053-1061.

Hallett, J. and S. C. Mossup, 1974: Production of secondary ice particles during the riming process. Nature, 249, 26-28.

Hobbs, P. V. and L. F. Radke, 1975: The nature of winter clouds and precipitation in the Cascade Mountains and their modification by artificial seeding. Part II: Techniques for the physical evaluation of seeding. J. Appl. Meteor., 14, 805-818.

____________ and R. A. Houze, 1976: Mesoscale rainbands in extratropical cyclones. Proceeding of the International Conference on Cloud Physics, Boulder, Colorado, July 1976.

Houze, R. A., P. V. Hobbs, K. R. Biswas and W. M. Davis, 1976: Mesoscale structure of rainfall in occluded cyclones. Proceedings of AMS Sixth Conference on Weather Forecasting and Analysis, Albany, New York, May 1976.

Knollenberg, R. R., 1970: Some results of measurements of the latent heat released from seeded stratus. Proceedings of the Conference on Cloud Physics, August 24-27, Ft. Collins, Colorado, p. 161-162.

Turner, F. M., L. F. Radke and P. V. Hobbs, 1976: Optical techniques for the counting of ice particles in mixed phase clouds. Atmospheric Technology (in press).

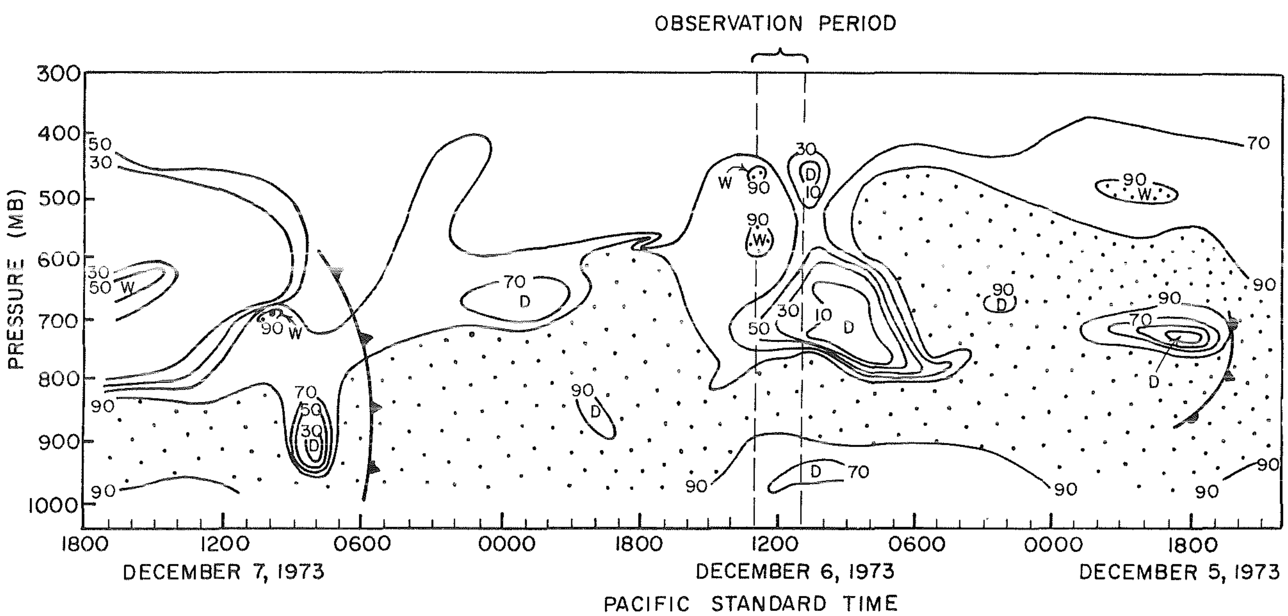

Figure 1. Time-height section of frontal position and relative humidity (in %) in Seattle, Washington. Stippled areas indicate relative humidity over 90%.

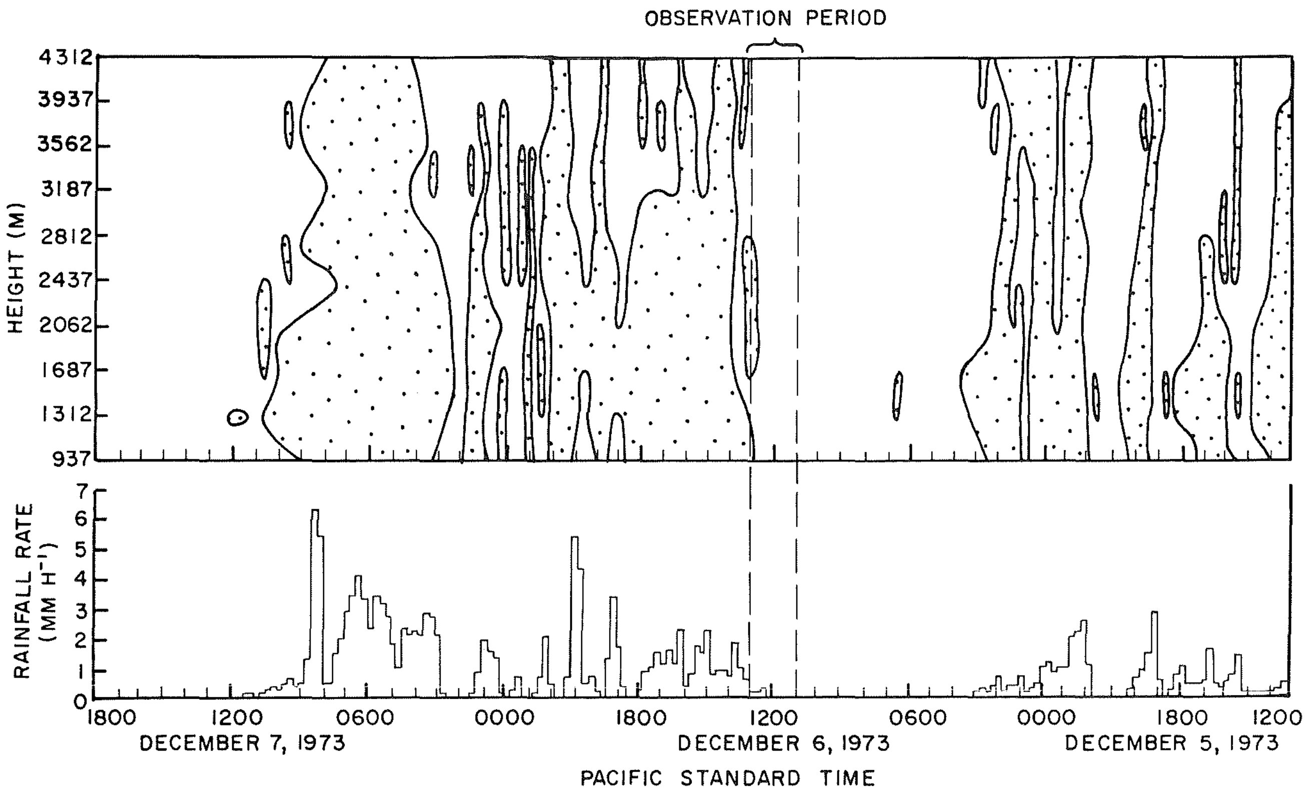

Figure 2. Time-height section of Doppler radar echoes (stippled areas) over Seattle, Washington, and corresponding rainfall rates in Seattle.

Figure 3. A photograph of the glaciated region taken from near cloud top. The centrally-located elipsoidal optical effect is the lower tangent arc to the 22° halo and is caused by columnar ice crystals.

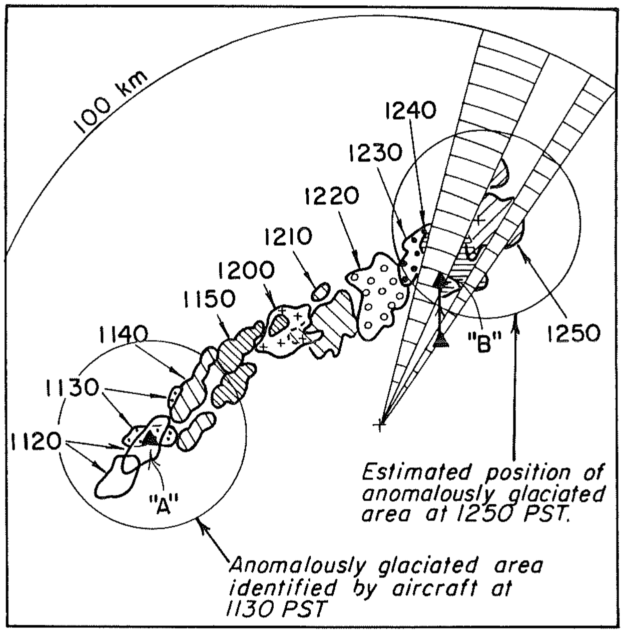

Figure 4. Sequence of radar echo positions near Seattle, Washington at ten-minute intervals from 1120 to 1250 PST on December 6, 1972. Point "A" is B-23 aircraft position at 1130 PST; "B" is position at 1250 PST.

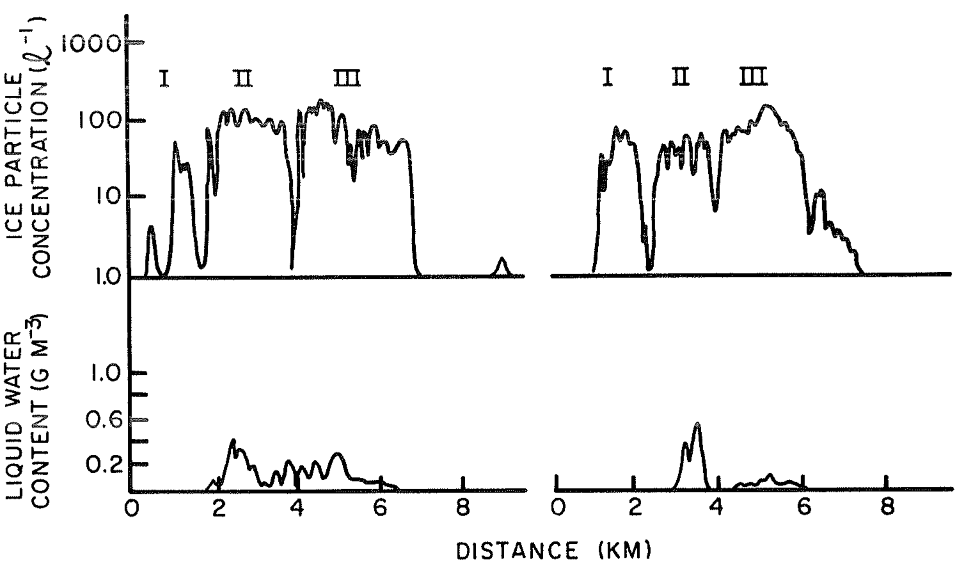

Figure 5. Two consecutive passes near cloud top, through the radar echo marked "A" in Figure 4. Note that in the five minutes between these penetrations, only cell II still contained significant liquid water.

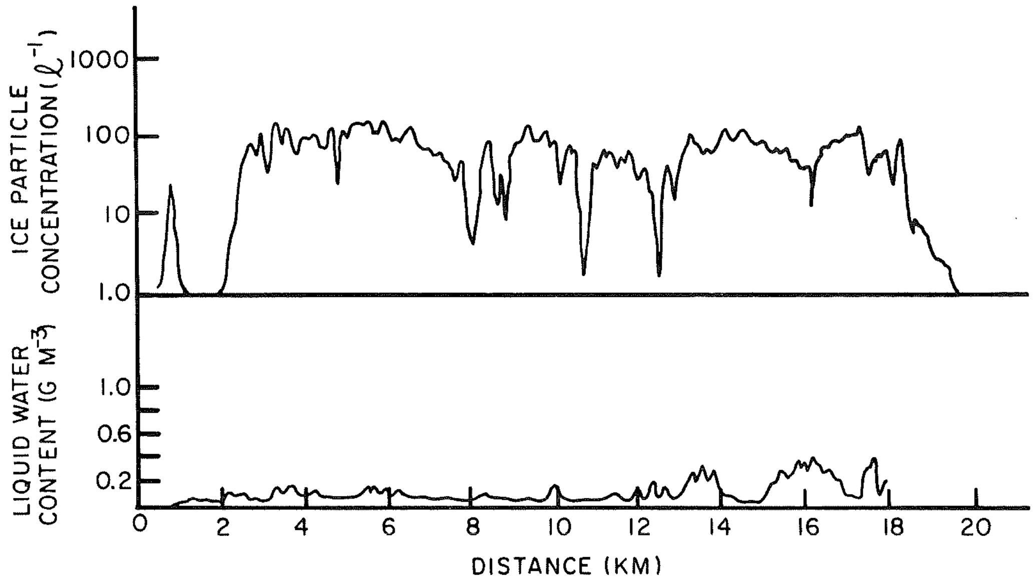

Figure 6. Descent through the glaciated area marked "B" in Figure 4. The cloud was entered at 2800 m (-4°C) and exited at 2100 m (-1°C).

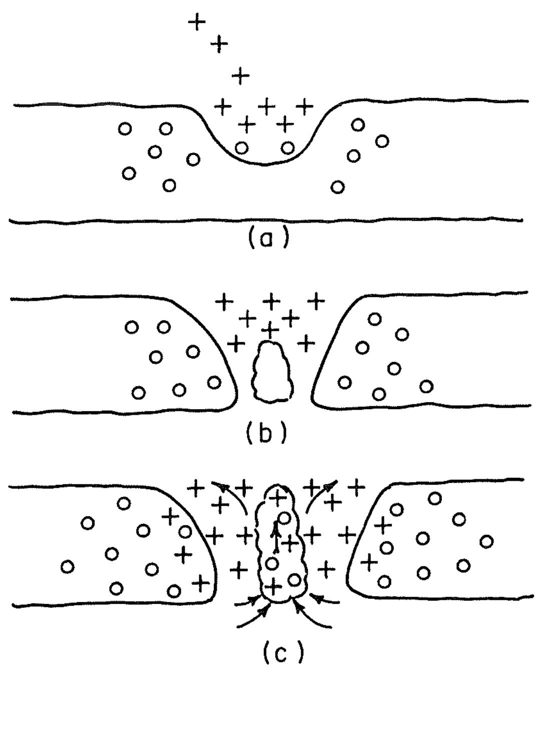

Figure 7. Conceptual model for the anomalous, glaciated area. (a) Anomalous glaciation initiated by seeding from above followed by ice multiplication. (b) Heat released by glaciation provides the stimulus needed to organize the core region into small convective elements. (c) Warm, mixed phase convective core provides an ideal environment for precipitation growth and horizontal divergence at the cloud top aids the spread of glaciation.

6.1.2

ON THE FALL PATTERN OF EARLY SNOW FLAKES

Masahiro Kalikawa

Department of Earth Science, Akita University
Akita, Japan

1. INTRODUCTION

As the basic research for study of growth of snow flakes, it is important to investigate the fall pattern of early snow flakes, which are composed of a few snow crystals.

There are few observations on the characteristics of falling motion of snow flakes, although the laboratory experiment in relation to the fall pattern or formation of snow flakes was performed by many researchers (e.g., Jayaweera and Mason, 1965, 1966; Podzimek, 1968; Sasyo, 1971).

Magono and Oguchi (1955) observed the fall pattern of snow flakes and described the shape of falling state and the characteristics of falling motion. Sasyo (1971) observed the motion of snow particles falling through still air using a stereophotogrammetric method and investigated statistically the feature of motions. However, in his observation the identifying a snow particle to its corresponding trajectory on photographs was not performed. In the observations described above, it is considered that the available data of early snow flakes are not enough for many purposes.

Therefore, the purpose of this observation is to investigate the three-dimensional motion of early snow flakes and the shape of component snow crystals of it, simultaneously, using a stereoscopic camera system with stroboscopic illumination.

The observation was carried out at the Mt. Teine observatory of Hokkaido University, the altitude being 1024 m, during the winter of 1974.

2. APPARATUS AND PROCEDURES

Since the method of measurement is same as in the previous observation (Kajikawa, 1976), the experimental apparatus and procedures will be described briefly.

The apparatus and stereoscopic camera system are shown in Fig.1 and they were

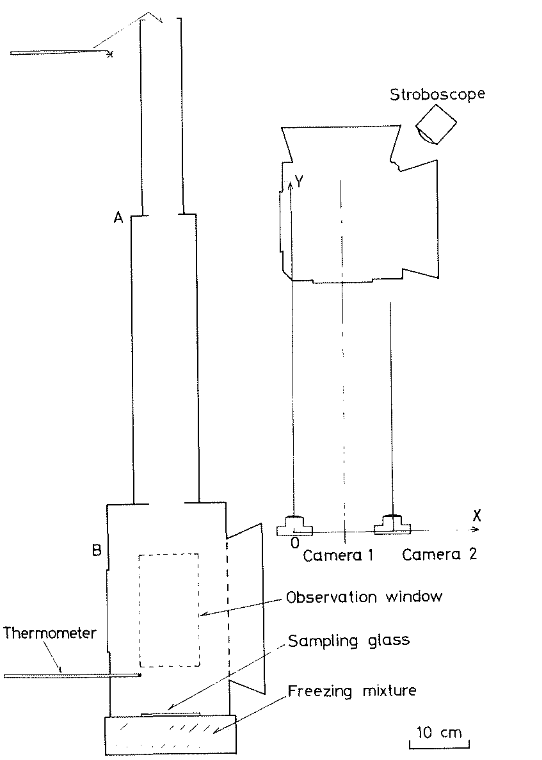

Fig.1. Apparatus and stereoscopic camera system.

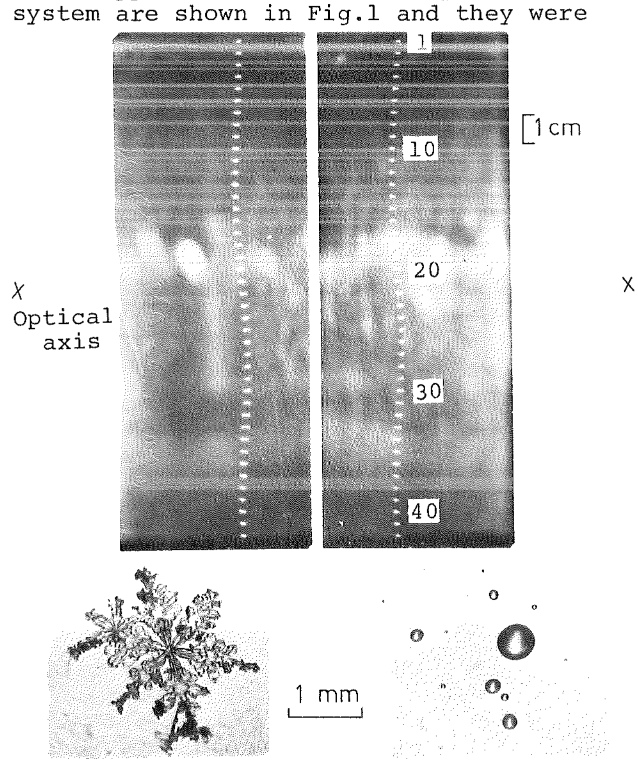

Fig.2. A example of stereoscopic photographs (above) at 1/100 sec intervals. Fallen snow flake composed of three rimed crystals, before melting (below left) and after melting (below right).

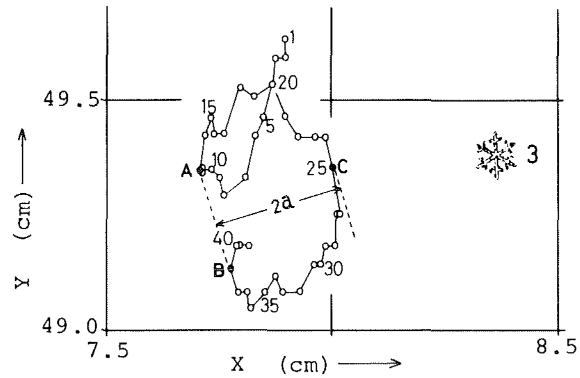

Fig.3. Horizontal movement of the early snow flake of Fig.2.

placed in a cold observation room. This apparatus is made of two parts, a duct (A) for the fall of snow flakes and a wooden box (B) for the observation of motion. One by one, a suitable snow flake was picked up with a piece of wood from many snow particles received on black cloth and it was dropped into the duct gently. For the measurement of three-dimensional motion, the falling snow flake illuminated by stroboscopic light was photographed by means of a stereoscopic camera system with the base line of 16 cm. A example of the pair of photographs is shown in Fig.2.

The fallen snow flake was caught on a sampling glass plate which was covered with white vaseline and it was microphotographed for determing the shape, size and number of component snow crystals. Then the snow flake was melted and the obtained droplets (nearly hemisphere) was microphotographed again, in order to calculate the diameter of melted drop and mass (see Fig.2).

Because the optical axes of two cameras put on horizontal level were parallel, the normal photogrammetry equations were available in the analysis of three-dimensional motion. The optical center of camera 1 was chosen as the origin (O) of rectangular coordinate system (X,Y and Z) in space. The coordinates of center to the circumscribed circle of snow flake were calculated from the corresponding points on the pair of photographs.

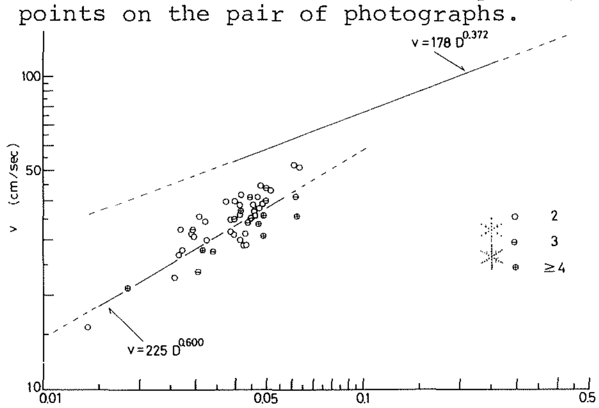

Fig.4. Observed falling velocity of dendritic type snow flakes. 2,3 and 4 indicate the number of component crystals.

Considering possible factors relating to the error of analysis, it may be regarded that the position in space of snow flake is determined within error of ±0.04 cm.

3. RESULTS AND CONSIDERATIONS

The observed snow flakes were classified into several groups according to the type of largest component snow crystals and the number of component crystals.

The falling velocity (mean vertical component of falling motion) of early snow flakes was different from those of usual results. Fig.4 is the present result for the dendritic type snow flakes (the largest component crystal is ordinary dendritic or fernlike crystals). It can be seen from this figure that the falling velocity is similar to that of simple crystals ($v=225\ D^{0.600}$ in Kajikawa, 1975) rather than ordinary snow flakes of dendritic type ($v=178\ D^{0.372}$ in Langleben,1954) , where v is the falling velocity and D the melted diameter. This tendency was also appeared in the case of another type of early snow flakes.

In this observation the classification of snow crystals follows the manner of Magono and Lee (1966).

Whether the early snow flakes, which is composed of two crystals, will fall with unstable motion (rotation and oscillation) or not is determined by Reynolds number ($Re=vd/\nu$, where d is the diameter of circumscribed circle to snow flakes and ν the kinematic viscosity of air) and Sd_2/d_1 , as shown in Fig.5. $S=2\ell/(d_1+d_2)$

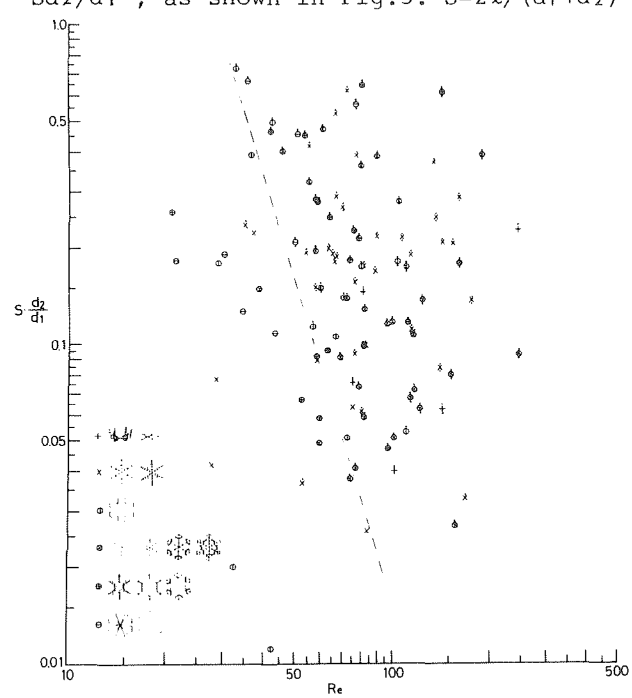

Fig.5. Boundary separating stable and unstable motion for the early snow flakes composed of two crystals.

The upper dots of mark indicate the unstable motion and the lower dots the rimed snow flakes.

is a measure of the combined state of two crystals (Higuchi, 1960), d_1 and d_2 are sizes of two crystals ($d_1 > d_2$) and ℓ is the distance between the center of them.

All of the observed early snow flakes composed more than three crystals exhibited the rotation about vertical axis and the oscillation in horizontal plane, as seen in Fig.2. The horizontal movement (projection of the falling motion on horizontal plane) of the center of snow flake of Fig.2 is shown in Fig.3. In this figure, open circles and number indicate the positions taken in time interval of 1/100 sec, corresponding to the photographs of Fig.2. From this figure and the observation by means of stereoscope, the trajectory of three-dimensional movement of this snow flake seems to be a spiral with slightly inclined axis.

The classification of type of unstable motion and its rate are summarized in Table 1. Although the fall pattern of spiral type was most part of analysed snow flakes, the glide type of unstable motion was observed in the case of early snow flakes composed less than four crystals only.

Nondimensional frequency (nd/v) of spiral movement is in proportion to R_e, as shown in Fig.6, although the data are considerably scattered. n is the frequency of rotation about vertical axis.

Fig.7 is the relation between the angular velocity ($\omega=2\pi/T$) or period (T) of spiral movement and a/d, where a is the amplitude of spiral path (see Fig.3). It can be seen from this figure that the period is in proportion to the nondimensional amplitude of spiral path.

The displacement velocity ($\overline{v}$) of spiral axis increases, as the falling velocity increases, but its value is very small as seen in Fig.8.

According to the analysis mentioned

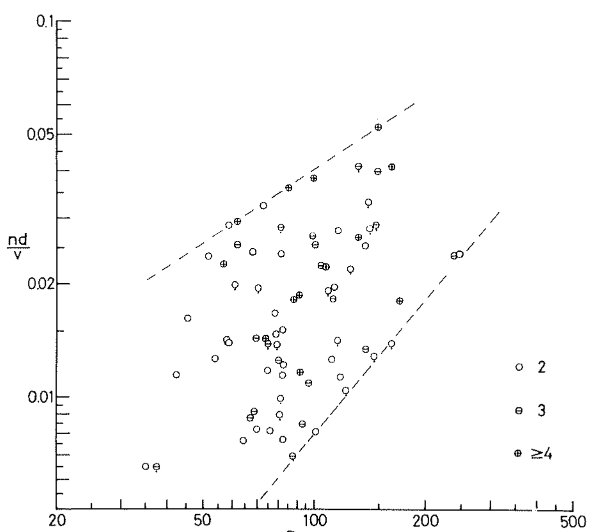

Fig.6. Relation between Re and nondimensional frequency (nd/v) of spiral movement. The early snow flakes of all types are contained in this figure.

Table 1. The classification of unstable motion and the rate of two types.

Number of component crystals	Spiral type	Glide type
2	48	17
3	19	3
4	6	3
5	3	0
6	3	0
7	1	0
8	1	0
Total of analysed early snow flakes and	81	23
rate	77.9 %	22.1 %

above, the spiral movement of early snow flakes in three dimensional space can be expressed as follows,

$$x = \overline{v}_x t + a \cos \omega t$$

$$y = \overline{v}_y t + a \sin \omega t$$

$$z = z_0 + vt$$

$$\overline{v} = \sqrt{\overline{v}_x^2 + \overline{v}_y^2}$$

where $x=y=0$ and $z=z_0$, at time $t=0$.

4. CONCLUDING REMARKS

Fall pattern in still air of early snow flakes was observed by means of the analysis of stereoscopic photographs. In the observation, the trajectory of falling motion has one to one correspondence to

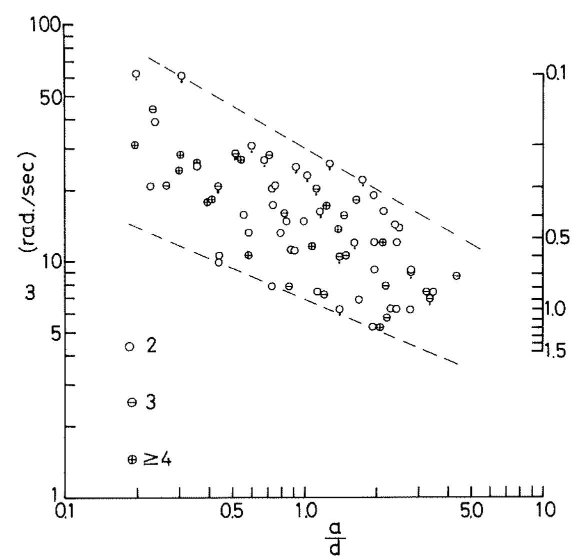

Fig.7. Relation between angular velocity ($\omega=2\pi/T$) or period (T) and a/d of spiral movement.

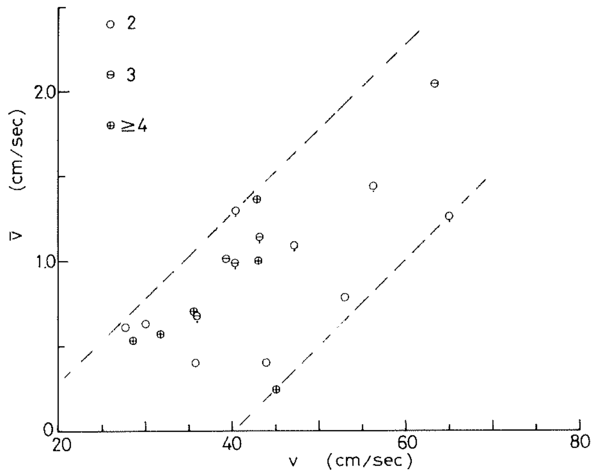

Fig.8. Displacement velocity of spiral axis.

individual snow flakes exactly. Most part of early snow flake, which is composed of more than three crystals, exhibited the spiral motion in space. The elements of this motion, for example amplitude (a), angular velocity (ω) and displacement velocity ($\bar{v}$) were empirically obtained.

Namely, the elements are decided from a following process in dendritic type.

d
↓ Fig.9
D
↓ Fig.4
v
Fig.8 ↙ ↓ Calculation
$\bar{v}$ Re
↓ Fig.6
n
↙ ↘ Calculation
T, ω
↓ Fig.7
a

ACKNOWLEDGEMENTS

The author wishes to thank Prof. C.Magono, Hokkaido University, for making the Mt. Teine observatory available for this study. The expense of this work was defrayed from a fund for scientific research of Education Ministry of Japan.

REFERENCES

Higuchi,K.,1960:On the coalescence between plane snow crystals. J. Meteor.,17,239-243.

Jayaweera,K.O.L.F.and B.J.Mason,1965: The behaviour of freely falling cylinders and cones in a viscous fluid. J.Fluid Mech.,22,709-720.

Jayaweera,K.O.L.F.and B.J.Mason,1966: The

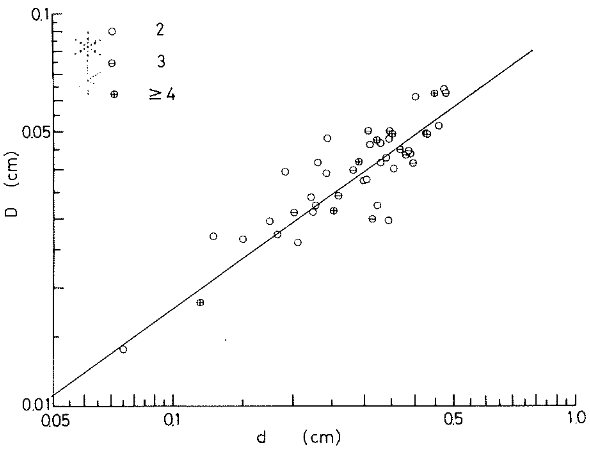

Fig.9. Relation between melted diameter (D) and diameter (d) of nonrimed early snow flakes.

falling motions of loaded cylinders and discs simulating snow crystals. Quart.J.Roy.Meteor.Soc.,92,151-156.

Kajikawa,M.,1975: Experimental formula of snow crystals.J.Meteor.Soc.Japan, 53,267-275.

Kajikawa,M.,1976: Observation of falling motion of columnar snow crystals. J. Meteor.Soc.Japan,(to be published)

Langleben,M.P.,1954: The terminal velocity of snowflakes. Quart.J.Roy.Meteor. Soc.,80,174-181.

Magono,C. and H.Oguchi,1955: Classification of snow flakes and their structures. J.Meteor.Soc.Japan,33,56-67.

Magono,C. and C.W.Lee,1966: Meteorological classification of natural snow crystals. J.Fac.Sci.Hokkaido Univ., Ser.Vll,2,321-335.

Podzimek,J.,1968: Aerodynamic conditions of ice crystal aggregation. Proc.Int. Conf.Cloud Physics,Toronto,26-30 Aug. 1968,295-298.

Sasyo,Y.,1971: Study of the formation of precipitation by the aggregation of snow particles and the accretion of cloud droplets on snowflakes. Pap.Met. Geophys.,22,69-142.

6.1.3

A COMPARISON OF SURFACE AND AIRBORNE ICE CRYSTAL OBSERVATIONS IN OROGRAPHIC CLOUDS

David C. Rogers

Department of Atmospheric Science
University of Wyoming
Laramie, Wyoming

1. INTRODUCTION

The Atmospheric Science Department of the University of Wyoming is involved in a research project to investigate the occurrence of ice crystals in wintertime clouds and to relate ice crystal concentrations to ice nuclei concentrations. As part of this research, field measurements at the surface and aloft have been taken for the past three years in the winter orographic clouds which form over Elk Mountain, Wyoming. The results presented here represent a preliminary summary of one of the interesting aspects this research has produced.

The Elk Mountain Observatory of the Department of Atmospheric Science is located near the summit of Elk Mountain, an isolated, 11,000 ft peak north of the Medicine Bow Range; the mountain rises from the smooth 7,000 ft plains of southeast Wyoming. Elk Mountain is in clouds very often during the winter months, from November to March. Cloud types include large scale traveling cyclones, orographic clouds plus altostratus and cirrus, and the isolated cap cloud which is the simplest case for research. These cap clouds typically have bases at 9,000 to 10,000 ft MSL, and usually have tops around 12,000 to 13,000 ft. Horizontal extent of these clouds in the direction of the winds is typically 8 to 13 km, and because of the large wind speeds usually observed, air parcel residence times inside cloud range from about 500 to 1,000 sec. Because of the small growth times, the crystals which form are usually small and have small settling velocities (less than 0.5 m s^{-1}). The Observatory measurements are thus considered to be in cloud and not in precipitation. These orographic clouds are oftentimes nearly steady-state in their nature (temperature, liquid water, cloud depth, wind speed and direction); this point makes the clouds attractive for cloud physics and dynamics studies.

2. PROCEDURES

For the purposes of this report, the important parameters which were sampled by the research aircraft (10UW) and at the Elk Mountain Observatory (EMO) included dry bulb temperature, dew point, cloud droplet spectra, liquid water content, horizontal wind, and ice crystals. The crystal sampling technique used at EMO involves impaction of crystals onto a glass microscope slide which is coated with oil. This slide is immersed in chilled hexane, and then the sample is photographed. The impaction devices used at the Observatory include a wind tunnel and a rotating arm impactor. Impaction speeds are in the range 10 to 15 m s^{-1}; thus, collection efficiencies do not fall below 50% for unit density particles larger than approximately 15 μm. The ice crystal sampling technique on the research aircraft involves both impaction on oil coated glass slides and in situ imaging using the PMS (Particle Measuring Systems, Inc.) Two-Dimensional Probe. The impaction technique relies on a decelerator which slows the air and crystals by a factor of 11.5; thus, impact speeds are approximately 7 m s^{-1}. Collection efficiencies for this device fall below 50% for unit density spheres smaller than 20 μm diameter. Data reduction is done using a microfilm reader. Only whole or nearly whole crystals are counted, i.e., fragments and blowing snow particles are ignored. The concentrations reported here were derived from both the 2D probe and the impaction slides; these two measurements were usually in agreement.

Cloud droplets are sampled on the aircraft by both the PMS Axially Scattering Spectrometer Probe and by using an impaction device whereby cloud droplets leave crater-like impressions on a soot coated substrate. At EMO, cloud droplets are sampled using a similar impaction device. The collection efficiencies are very nearly unity for droplets larger than 3 μm diameter. Crystal observations are routinely made during the entire day at the Observatory, with sampling frequency greater during 10UW flight periods. The 10UW sampling procedure for isolated cap clouds involves traverses through the cloud from the leading edge to the downwind edge at several different altitudes. During the 1975-76 winter season, two PMS probes similar to those on the aircraft were used on Elk Mountain inside a large wind tunnel; data reduction has not been completed for the latest field season as of this writing.

3. RESULTS

The two case studies which follow present simultaneous crystal observation data taken by 10UW and at EMO during isolated cap cloud conditions. In-cloud temperatures for these two days were nearly the same, -17 to -19C. However, substantial differences in crystal measurements were observed.

3.1 9 January 75 Case Study

Crystal observations on this day indicated a fairly homogeneous cloud, in which crystal habits, sizes and concentrations at the surface were nearly in agreement with those aloft. On this day an isolated cap cloud formed in a postfrontal airmass. The cap cloud contained some small convective elements imbedded in the otherwise stable air. There were some thin, scattered cirrus clouds, but their bases were separated from the top of the cap cloud by nearly 15,000 ft of air of relative humidity less than 50%. The important descriptive parameters for this cloud are given in Table I. Notice that the concentrations of crystals measured aloft and at the surface were approximately equal. The differences in crystal habit and size are consequences of the differences in temperature and growth time. The cloud droplet spectra are fairly typical of most Elk Mountain cap clouds: average droplet diameters are between 5 and 10 μm, maximum diameters rarely attain 25 μm, and liquid water contents (LWC) are usually below 0.1 g m^{-3}.

The steady-state nature of this cap cloud is indicated by the fact that during the two-hour flight the EMO temperature changed by less than 2C, and the winds did not change appreciably. Also, crystal habits and concentrations did not vary significantly except when one of the small convective elements passed over the Observatory. These convective elements were producing dendritic crystals ranging in size from 1 to 3 mm diameter which were in concentrations of approximately 1 $liter^{-1}$ both aloft and at the surface. The aircraft observations indicated that the convective elements formed slightly downwind of the leading edge and were advected through the cloud mass. The 9 January case study indicates that the in situ crystal measurements aloft and at the surface were in substantial agreement. This agreement was not always obtained, as the next case study will show.

Table I. Descriptive parameters for two case study days.

	9 January 1975	18 February 1975
Cloud top/ Temp	11,600'/-19.4C	11,900'/-20.5C
Cloud base/ Temp	8,800'/-12.8C	9,800-10,200'/-17.5C
EMO Temp	-16.0C	-18.0C
Winds aloft	340° 10 m s^{-1}	270° 10 m s^{-1}
Sfc winds	360° 5 m s^{-1}	270° 25 m s^{-1}
Avg droplet diameter	8-10 μm	6-8 μm
Max droplet diameter	22-24 μm	20-22 μm
Max LWC	0.19 g m^{-3}	0.11 g m^{-3}
Ice Crystals:		
10UW		
Conc	0.5-5 $liter^{-1}$	2-7 $liter^{-1}$
Diameter	300-700 μm	60-350 μm
Habit	P1c	C1h, P1c
EMO		
Conc	1-17 $liter^{-1}$	1-10 $liter^{-1}$
Diameter	50-300 μm	120-500 μm
Habit	P1a	C1h
Conc		300-800 $liter^{-1}$
Diameter		40-60 μm
Habit		C1h

3.2 18 February 75 Case Study

An isolated cap cloud formed in strong westerly flow one day after a cold frontal passage. There were no other clouds above or upwind of the cap cloud. (It has been suggested that cirrus clouds may be responsible for higher crystal concentrations by "seeding" lower clouds with crystals.) The important descriptive parameters of this cloud are given in Table I. The steady-state nature of the cloud is indicated by the fact that EMO temperature was -18C and varied by less than 2C during the two hour flight. Figure 1 is a composite chronology of the cloud physical observations from the aircraft and EMO. Crystal concentrations aloft (circles) ranged from extremes of 0.03 to 7 $liter^{-1}$ for both the impaction samples and the 2D measurements. The lowest concentrations were obtained at cloud boundaries. Inside the cloud, concentrations were fairly uniform over the entire volume of the cloud, from the leading edge nearly to the downwind edge; most in-cloud concentrations were between 2 and 7 $liter^{-1}$ (Table I). Thus, it appears that these crystals formed near the leading edge of the cloud and few, if any, additional crystals were formed inside the cloud. This provides some justification for plotting the observations of 10UW in a chronological form in order to facilitate comparison with the EMO measurements in Figure 1. The crystal habits observed by 10UW were skeletal thick plates (C1h) and broad branched crystals (P1c); the crystal classifications are by Magono and Lee (1966). Selected photographs of representative crystal samples from both EMO and 10UW are presented in Figure 2.

Observations at the surface indicated two populations of ice crystals: one population consisted of a small concentration (1 to 10 $liter^{-1}$) of skeletal thick plate crystals, 120 to 500 μm in diameter; the second population consisted of a very large concentration (300 to 800 $liter^{-1}$) of much smaller skeletal thick plate crystals, 40 to 60 μm diameter (this range includes 60% of the crystals). Notice in Table I and Figure 1 that the population of larger crystals was in substantial agreement with the aircraft results, in terms of habit, size and concentration, during the entire flight.

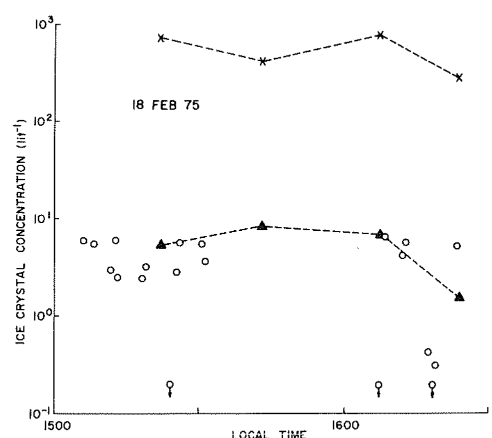

Figure 1. Chronology of crystal concentration measurements for 10UW (circles) and EMO (Δ = crystals larger than 100 μm, X = crystals smaller than 100 μm).

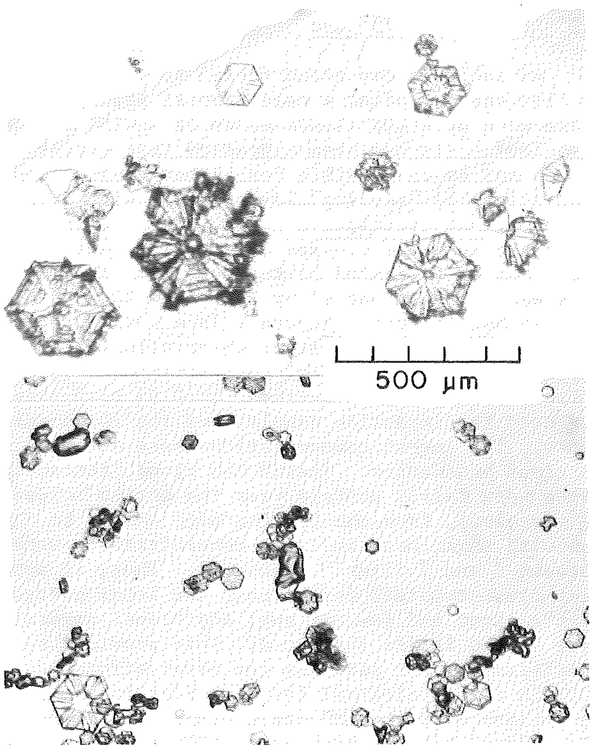

Figure 2. Selected crystal samples of 10UW (above) and EMO (below) for 18 February 75. Sample volumes for these photographs are 1.5 and 0.12 liters, respectively.

Figure 3 is a size distribution above 30 μm of an EMO crystal sample. This distribution appears to be bimodal, a result which was suggested in the sample photograph (Figure 2). Below 100 μm the distribution is nearly log normal, suggesting that the small crystals were forming along the entire trajectory from cloud base to the Observatory. Travel time from cloud base was approximately 60 sec, based on the wind speeds and the upwind distance to cloud base. This growth time for the largest of the small crystal population (60 to 100 μm) is not inconsistent with crystal growth rate equations for this habit and temperature (e.g., Davis and Auer, 1974). Crystal habits

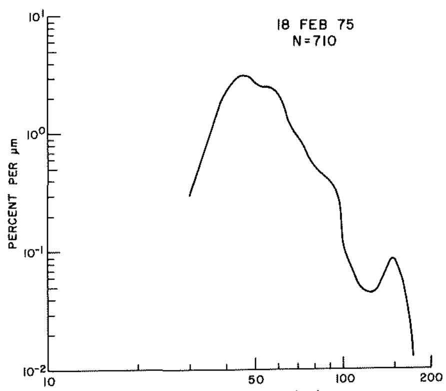

Figure 3. A smoothed histogram of one of the EMO crystal samples taken at 1608.

were the same aloft and at the surface because the cloud was thin and nearly isothermal. Identity of crystal habits aloft and at the surface is not always observed at Elk Mountain, i.e., when the temperatures straddle a habit change.

It is noteworthy that such substantial differences in crystal concentration should be observed on two case study days which are so similar in terms of temperature, cloud depth, droplet spectra and liquid water content. The most significant differences between these case studies are: (1) the 18 February cloud was stably stratified, whereas the 9 January cloud contained convective elements; (2) wind direction and wind speed; and (3) crystal concentrations measured at the surface and aloft. The 18 February 75 case study suggests that the mountain's surface may somehow be providing a region wherein copious numbers of crystals can be produced, in excess of two orders of magnitude above the concentrations aloft. The Hallett and Mossop (1974) multiplication mechanism cannot be invoked to explain these very high concentrations because (1) no droplets were observed to be 25 μm or larger and (2) the warmest temperature in the cloud was -17.5C, which is outside the -3 to -8C range of the mechanism.

3.3 1973-74 General Summary

Figure 4 presents a general summary of crystal concentrations for the first year's observations. The ellipses on this figure indicate the ranges of temperature and crystal concentration for both the aircraft and EMO on sixteen study days. There are several days when either aircraft observations or EMO observations were not made. When the aircraft and EMO measurements are connected by a line, this indicates that the measurements were made during the same time period inside the same cloud. No stratification has been done with regard to cloud types (stratiform or convective), synoptic situation (general snowstorm, cap cloud with higher clouds or isolated cap cloud), or crystal habits. Several features are evident in this figure. Both the surface and aircraft data show increases in concentration with decreases in temperature, as expected. However, the surface concentrations are approximately one order of magnitude greater and show larger scatter than the aircraft data. This figure indicates that crystal concentrations aloft were about one per liter at -5C and increased one order of magnitude for every 10C of cooling. Notice that for all but one of the aircraft-EMO measurements, average concentrations agreed to within a factor of four, although differences in temperature and parcel trajectories were evident; these differences may be expected to affect nucleation rates and crystal habits.

Two EMO measurements stand out in this figure. Concentrations on 14 November and 28 March ranged from 100 to 1,000 liter^{-1} in the temperature range -10 to -15C. Unfortunately, these observations were made at night, and so aircraft measurements were not available for comparison. For these two particular high concentration cases, most of the crystals were nearly identical in habit and size: Plc crystals, generally 50 to 150 μm diameter. Their sizes indicate growth times of one to two minutes, which suggest that they were formed somewhere near the level where cloud base intersects the mountain. Evidently, the conditions necessary

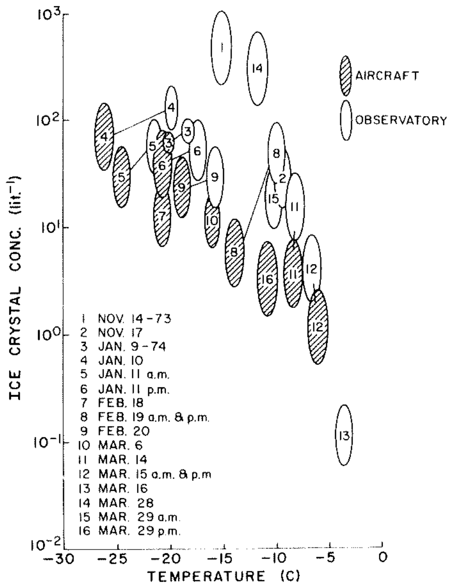

Figure 4. Crystal concentrations in orographic clouds over Elk Mountain for the 1973-74 winter season.

for the formation of an abundance of these small crystals are not commonly present, but occurred only twice out of the thirteen days presented here. The two 1975 case studies reported here complement the earlier years' results. Summary figures for 1974-75 and 1975-76 are being prepared. They indicate a pattern similar to Figure 4.

4. DISCUSSION

These results indicate that simultaneous surface and aircraft crystal measurements are often in good agreement with each other, but occasional periods occur when substantial disagreement is observed. Other case study data support the results presented here and also indicate that crystal concentrations at EMO are rarely less than those aloft. Cases of anomalously high concentrations ("multiplication") have also been observed at the surface over the temperature range -5 to -25C. On all of the "multiplication" days, the very high concentrations resulted from small crystals with narrow size distributions, which suggests a fairly small region of generation. Anomalously high concentrations of crystals are occasionally observed aloft in the plume downwind of Elk Mountain. Other case studies of flights over the Medicine Bow Range whose clouds have much larger dimensions (30 km or 30 minutes traverse time) have shown steady increases in concentration downwind from the leading edge. In view of the Elk Mountain "surface multiplication" observations, these other long fetch cases suggest that the phenomenon may be occurring elsewhere, and that additional time or distance is required for vertical mechanical mixing to transport surface-produced crystals aloft. Low level aircraft samples would help to resolve this phenomenon, but they are difficult and hazardous to obtain. A preliminary analysis suggests that a common feature of these high concentration days is higher wind speeds. There are several possible consequences of high wind speeds that may lead to larger concentrations: (1) blowing snow particles which are broken loose below cloud base and sublimate partially before entering the liquid cloud (however, very few of the small, numerous crystals appear to have blowing snow particles at their centers); (2) very large riming rates on all exposed surfaces in cloud on the surface of the mountain (trees, snow and rime); and (3) higher supersaturations produced by modifications of the airflow in rough terrain (i.e., larger updrafts).

This "multiplication" phenomenon does not appear to conform to the requirements of the Hallett and Mossop (1974) mechanism: maximum cloud droplet diameters are smaller than 25 µm, temperatures range from -5 to -25C, and wind speeds range from near zero to 30 m s^{-1} within the surface layer where riming occurs. On several high concentration days, crystal samples were taken upwind of EMO to ensure that the large concentrations are not caused by the Observatory's generator exhaust or ventilation systems. The upwind samples confirm the Observatory measurements and also suggest crystal formation near the intersection of cloud base with the mountain.

5. CONCLUSION

There are significant advantages in being able to make in situ cloud physical observations from a surface laboratory and compare them with measurements taken aloft. The results to date suggest good agreement (within one order of magnitude) for most of the study days. Occasional "surface multiplication" days are very interesting both from the standpoint of basic cloud physics research and because of the implications this phenomenon has on winter orographic cloud seeding projects: large concentrations of ice crystals may be produced within an orographic cloud, so that seeding effects may be insignificant on certain days.

All of these results should be considered preliminary, but the suggestions and inferences are clear. Case study analyses of the 1974-75 and 1975-76 data are still in progress. It is hoped that the critical factors for this "surface multiplication" phenomenon can be identified and the mechanism explained.

Acknowledgements. This research was sponsored by NSF grant No. ATM75-02515 A01. The financial support of the National Science Foundation and the technical support of the Department of Atmospheric Science, University of Wyoming, are gratefully acknowledged.

REFERENCES

Davis, C. I. and A. H. Auer, Jr., 1974: Use of isolated orographic clouds to establish the accuracy of diffusional ice crystal growth equations. Preprints of the Conference on Cloud Physics, Tucson, Arizona, 141-147.

Hallett, J. and S. C. Mossop, 1974: Production of secondary ice particles during the riming process. Nature, 249, 26-28.

Magono, C. and C. W. Lee, 1966: Meteorological classification of natural snow crystals. J. Fac. Sci., Hokkaido Univ., Ser. VII, 2(4), 321-326.

EVOLUTION OF RAINDROP SIZE DISTRIBUTIONS IN STEADY STATE RAINSHAFTS

J.R. Gillespie and Roland List

Department of Physics, University of Toronto
Toronto, Canada

1. INTRODUCTION

Langmuir (1948) suggested that drop breakup was an essential step in the formation of rain by a "chain reaction" in warm clouds (i.e. clouds containing no ice particles). The growth cycle, according to Langmuir, consists of the accretion of smaller drops by a few large ones, which quickly grow to six millimeter diameters. There aerodynamic instability is supposed to lead to breakup into smaller fragments. These fragments are assumed to be large compared to the cloud droplet population, and thus possess a significant terminal speed, associated with fast growth by accretion. Upon reaching the stability limit they would in turn break up, continuing the cycle.

It has become clear that the supposed stability limit does not control the size of raindrops in nature. One of the authors (R.L.) floated 15 mm diameter drops in the Swiss Hail tunnel in 1960 (unpublished). Experiments by Pruppacher and Pitter (1971) and theoretical work by Klett (1971) show that drops as large as 10 mm equivalent spherical diameter are not disrupted aerodynamically.

Magarvey and Taylor (1956) proposed that the size of raindrops was limited by collision-induced breakup. As shown by the drop mean-free-path calculations by List et al. (1970), coupled with the documented collisions of simulated pairs of raindrops falling at their correct terminal speeds through still air (McTaggart-Cowan and List, 1975), this is the mechanism that acts in nature.

The observed fragment size-distributions produced by McTaggart-Cowan and List (1975) can be used in the construction of a model of raindrop growth by coalescence and size reduction by breakup. It should be noted that the number of coalescences observed in these experiments was very small (less than 3% even for the smallest drop pair collided with diameters of 3.0 and 1.0 mm). Consequently the coalescence efficiency must be much less than unity in the range of sizes observed. This contradicts the assumption of unity by most modellers.

List and Gillespie (1976) describe a spatially homogeneous, time-dependent one-dimensional model in which the raindrops evolve at a constant liquid water content. In contrast to this approach the present investigation is concerned about the raindrop evolution in a rain shaft. Here the precipitation rate is constant and the liquid water content adjusts to the boundary conditions.

2. STEADY-STATE COALESCENCE-BREAKUP MODEL

The physical situation modelled is a wide-spread, 1-dimensional steady-state rainshaft in the absence of any vertical motions. No cumulus-scale cloud dynamics is included. The only microphysical processes allowed are drop coalescence and breakup due to collisions. Sedimentation due to the larger terminal speed of bigger drops is explicitly included, as well as the increase in terminal speed for all drops at higher altitude (lower air density). No evaporation is allowed.

Let $n(m,z,t)dm$ be the number of raindrops per unit volume at time t and altitude z and with mass between m and m + dm. Let $C(m,z,t)$ and $B(m,z,t)$ be the rates respectively, of formation of a drop of mass m by coalescence and loss by breakup (per unit of volume and mass interval). Then

$$\frac{dn(m,z,t)}{dt} = C(m,z,t) - B(m,z,t). \qquad (1)$$

The left side of (1) may be expanded in terms of partial derivatives of $n(m,z,t)$ with respect to m, z and t. In the steady state and with no evaporation or condensation, only the z-term survives:

$$-V_T(m,z)\,\frac{\partial n(m,z,t)}{\partial z} = C(m,z,t) - B(m,z,t), \qquad (2)$$

where V_T = terminal speed.

In the steady state, $n(m,z,t) = n(m,z)$. Also, the right-hand side of (2) may be rewritten as integrals (List and Gillespie, 1976).

The result is

$$\begin{aligned}-V_T(m,z)\frac{\partial n(m,z)}{\partial z} = &\int_0^{m/2} n(\mu,z)\, n(m-\mu,z)\, K(\mu,m-\mu)\,d\mu \\ &-n(m,z)\int_0^{\infty} n(\mu,z)\, K(m,\mu)\, d\mu \\ &+\int_m^{\infty} n(\mu,z)\, W(\mu,m)\, d\mu \\ &-\frac{n(m,z)}{m}\int_0^{m} \mu W(m,\mu)\, d\mu, \end{aligned} \qquad (3)$$

where the coalescence kernel is (4)

$$K(\mu,m) = \pi(r_\mu+r_m)^2 E_1(\mu,m)E_2(\mu,m)\left|V_T(\mu,z)-V_T(m,z)\right|$$

and the breakup function is

$$W(\mu,m) = \pi \int_0^{\mu} n(\mu_1,z)(r_\mu + r_{\mu 1})^2 \, E_1(\mu,\mu_1)$$

$$x[V_T(\mu,z)-V_T(\mu_1,z)] \, P(m; \mu,\mu_1) \quad d\mu_1. \tag{5}$$

r_μ, r_m, $r_{\mu 1}$ are the radii of drops of masses μ, m, and μ_1 respectively, E_1 is the collision efficiency and $P(m; \mu,\mu_1)$ the size distribution of the fragments produced by a breakup involving a drop of mass μ and one of mass μ_1. For a fuller explanation of the meaning of these terms, see List and Gillespie (1976).

By specifying the distribution n(m,z) at the top of the rainshaft, $z = z_o$, equation (3) can be solved as a boundary-value problem.

The coalescence term C(m,z) is evaluated using a fast, approximate method originated by Bleck (1970) and refined in Danielsen, et al. (1972). Bleck's technique is extended to the integration of the breakup term B(m,z) by the authors (List and Gillespie, 1976).

To carry out the solution, certain numerical data are required. The terminal speed $V_T(m,z)$ is obtained from the work of Best (1950):

$$V_T(m,z) = A \exp(bz) \left\{1 - \exp[-(m/a)^p]\right\}, \tag{6}$$

where m is drop mass in milligrams, a = 2.90 mg, p = 0.382, A = 9.32 m s^{-1}, b = 0.0405 km^{-1} and z is altitude in km. This expression is valid for drop masses from 0.014 to 113 mg and altitudes less than 6 km.

Allowing V_T to vary with z introduces an additional complication. For the rainfall rate R to be independent of z (steady-state) as V_T changes, n(m,z) must adjust to keep the flux of rainwater constant. Thus

$$V_T(m,z) \; n(m,z) = F(m)$$

where F(m) is an unknown function of m only. Differentiating with respect to z leads to:

$$\frac{\partial n(m,z)}{\partial z} = - n(m,z) \frac{\partial \ln V_T(m,z)}{\partial z} . \tag{7}$$

For Best's formula the appropriate adjustment is obtained by

$$\frac{\partial n(m,z)}{\partial z} = - bn(m,z) . \tag{8}$$

The collision efficiency E_1 is taken to be unity. For drops of the size of raindrops, inertial forces dominate and prevent approaching drops from being deflected appreciably from their straight-line trajectories. Consequently the geometrical value is correct:

$$E_1(m,\mu) = 1. \tag{9}$$

To represent the coalescence efficiency, the form proposed by Whelpdale and List (1971) was used. This was modified to account for the lack of coalescence with small drops larger than 1 mm diameter according to:

$$E_2(D_s,D_L) = \begin{cases}(1 + D_s/D_L)^{-2} & \text{if } D_s \leq 1 \text{ mm} \\ 0 & \text{if } D_s > 1 \text{ mm}\end{cases} \tag{10}$$

where D_S and D_L are the diameters (in millimeters) of the small and large colliding drops with masses μ_1 and μ respectively. (10) may be rewritten, if desired, in terms of drop masses by using the relationship $m = (\pi/6) \rho_w D^3$, where ρ_w is the density of water.

The data of McTaggart-Cowan and List (1975) were used to determine the fragment probability function $P(m; \mu,\mu_1)$. The observed fragment distributions were bimodal with the peaks described as follows:

The peak at smaller fragment sizes:

$$\text{mean fragment number } \bar{f} = 3.6\sqrt{D_L{}^3 D_s}\,(0.41-0.30D_s/D_L), \tag{11}$$

$$\text{peak value} \quad n_p = 6.0 \; \bar{f} \; / \; D_s. \tag{12}$$

$$\text{Let } k = - 1.0 - 0.0654 \; n_p \bar{f} , \tag{13}$$

$$\text{and } A = n_p \; / \; 0.0654^k. \tag{14}$$

Then the peak at small fragment sizes is

$$P_s(m; \mu,\mu_1) = \begin{cases}Am^k & \text{if } m \geq 1 \text{ mg}, \\ Am^{-2.6} & \text{if } m < 1 \text{ mg}.\end{cases} \tag{15}$$

The peak at large fragment sizes was represented by a Gaussian:

$$\text{peak value } H = 11.84/[D_L{}^4 D_s(0.41-0.30D_s/D_L)], \tag{16}$$

$$\text{standard deviation} \quad \sigma = H^{-1}, \tag{17}$$

$$P_L(m; \mu,\mu_1) = \begin{cases}H \exp[(m-\mu)^2/2\sigma^2] & \text{if } m \leq \mu+\mu_1 \\ 0 & \text{if } m > \mu+\mu_1\end{cases} \tag{18}$$

The overall fragment probability is

$$P(m; \mu,\mu_1) = P_s(m; \mu,\mu_1) + P_L(m; \mu,\mu_1) \tag{19}$$

Note that (19) is determined from observations essentially at sea level. It will be employed at higher altitudes as well, despite the fact that reduced air density may affect the breakup process. No information is available on fragment size distributions at reduced air density. It is only known that the Reynolds number of freely falling precipitation particles varies very little in the atmosphere with height. (List and Dussault, 1967).

3. BEHAVIOUR OF THE MODEL

In general it is found that a drop spectrum initially of the type obtained by Marshall and Palmer (1948) remains essentially so. That is, if a spectrum:

and final line $N_0 = 1.15 \times 10^{-5}$ R have not been examined yet. The true picture may be slightly different for R close to 70 mm h^{-1}.

Figure 7 gives the shape of the approach of N_0 to its final value N_{0f}. For each rainfall rate R, N_0 increases along an S-shaped curve. The approach is more rapid for larger R because of the greater numbers of large drops in the population. The last part of the approach is along an approximately linear, sloped segment which is the same for all R. In this part of the curve, N_0 is increasing just enough to balance the decrease in $V_T(z)$. This apparently linear segment is really a part of the function exp(bz) describing the altitude dependence of the terminal speed, equation (6). For R < 29 mm h^{-1} N_0 essentially does not reach its equilibrium value in 2 km of fall.

Figure 8 illustrates the profile of radar reflectivity vs. altitude obtained in two rainshafts. For the spectrum dominated by breakup, $N_{00} = 8 \times 10^{-6}$ mm^{-4}, there is a monotonic decrease in dBZ = 10log Z (Z in mm^6 m^{-3}). The other spectrum, with $N_{00} = 4.95 \times 10^{-2}$ mm^{-4}, shows a monotonic increase in dBZ as the altitude decreases. Clearly the overshoot in the number of larger drops does not produce a corresponding overshoot in Z. These large drops are so rare that they make no significant contribution to the reflectivity, while the drops that do contribute experience no overshoot. Both spectra tend to the same limiting value of dBZ because their rainfall rates are equal and this determines the equilibrium drop size spectrum.

Figure 9 relates radar reflectivity and liquid water content calculated from the equilibrium spectra. Note the linear relationship

$$Z = 2.26 \times 10^3 \text{ LWC}, \qquad (24)$$

where Z is in mm^6 m^{-3} and LWC is in g m^{-3}. This proportionality is a consequence of the fact that the equilibrium spectra are essentially Marshall-Palmer.

Using $N_0 = 1.15 \times 10^{-5}$R and (24) in Kessler's (1969) relationship between rainfall rate and liquid water content, the reflectivity becomes for the equilibrium spectra

$$Z = 175 \text{ R}. \qquad (25)$$

This formula differs significantly from the Z - R relations observed in natural rain in two ways. First, the exponent on R is unity, compared with the $R^{1.3}$ to $R^{1.5}$ power laws usually found. Second, the proportionality factor 175 is smaller than the usual value. Both facts indicate that the distributions observed in deriving Z - R relations are richer in large drops than the equilibrium spectra found in this study. It is suggested that the usual weather radars, with ranges of approximately 200 km, may not sample raindrop ensembles that have attained equilibrium with respect to coalescence and breakup. Shorter range radar (approximately 10 km or less) may be more appropriate to study localized packets of precipitation near the ground, closer to equilibrium.

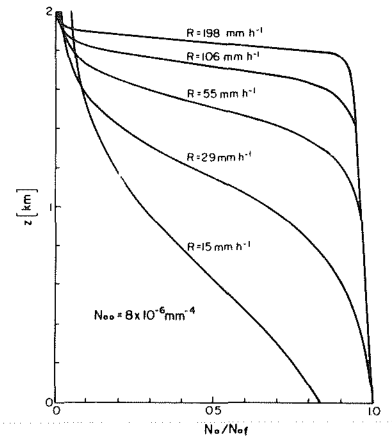

Figure 7. Approach of N_0 to equilibrium during free fall from the z = 2 km level, for various rainfall rates.

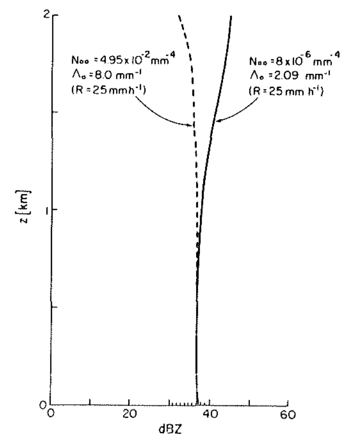

Figure 8. Profiles of radar reflectivity for two distributions with N_0 larger and smaller respectively, than the final equilibrium N_0.

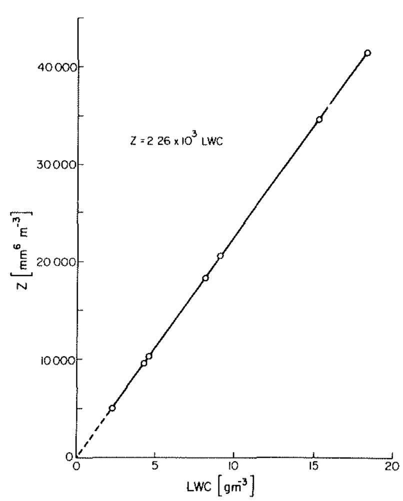

Figure 9. Reflectivity versus liquid water content for equilibrium spectra. Note the linear relationship.

4. CONCLUSIONS

This model of the effects of coalescence and breakup in one-dimensional steady-state rainshafts had led to the following conclusions:

(a) Drop size spectra initially of the Marshall-Palmer type essentially preserve that property in falling to the surface.

(b) Size spectra of falling drop ensembles approach very general equilibrium configurations which depend only on the rainfall rate. For each Marshall-Palmer distribution there is only one equilibrium distribution. For $R \geq 29$ mm h^{-1}, less than 2km of fall are required to approach the asymptotic value.

(c) A spectrum with a lack of large drops tends to overshoot the equilibrium spectrum, producing an oversupply of large drops before settling down. This contrasts with a spectrum having an initial oversupply of large drops where the spectrum approaches equilibrium monotonically.

(d) The equilibrium value of N_o is proportional to the rainfall rate: $N_o = 1.15 \times 10^{-5}$ R mm^{-4} where R is in mm h^{-1}.

(e) The equilibrium value of radar reflectivity is proportional to liquid water content: $Z = 2.26 \times 10^3$ LWC $mm^6\ m^{-3}$, where LWC is in gm^{-3}. In terms of rainfall rate, this becomes Z = 175 R $mm^6\ m^{-3}$.

(f) Equilibrium spectra produced by the model have very low concentrations of large drops compared to observations in temperate regions. They are more characteristic of rain from "warm" clouds with drop growth by coalescence. Coalescence-breakup does not allow growth of larger drops than indicated by the equilibrium spectra - if the model's initial conditions are not grossly violated.

(g) The authors suggest that the large drops observed in "cold" rain - formed in the ice phase and melted before reaching the surface - have not fallen far enough to encounter smaller drops and break up. While frozen, these particles are immune to breakup. Only after melting would they be vulnerable, in the last part of their fall. These ideas are developed in greater detail in List and Gillespie (1976).

While numerical diffusion has not been studied explicitly, it should not be great enough to affect these conclusions. Evidence for this is the fact that spectra with the same R tend to the same equilibrium spectrum, independent of their initial form.

In summary, it can be stated that the modelling of rainshafts throws new light into the microphysics of rain formation. It is clear that the Langmuir chain-process does not occur in nature, and breakup already occurs when particles in the size range 1 to 1.5 mm collide. An exploration of the collision-coalescence-breakup process in more complete, two-dimensional cloud models is needed; the same is true for field testing of the conclusions in respect of radar applications.

ACKNOWLEDGEMENTS

One of the authors (J.R.G.) is indebted to the Atmospheric Environment Service and the National Research Council of Canada for financial support. These two organizations sponsored these investigations together with the National Severe Storms Laboratory in Norman, Oklahoma, of the National Oceanic and Atmospheric Administration, U. S. Department of Commerce.

REFERENCES

Best, A.C., 1950: "Empirical formulae for the terminal velocity of water drops falling through the atmosphere". Quart. J. R. Meteor. Soc., 76, 302-311.

Bleck, R., 1970: "A fast, approximative method for integrating the stochastic coalescence equation". J. Geophys. Res., 75, 5165-5171.

Danielsen, E.F., R. Bleck and D.A. Morris, 1972: "Hail growth by stochastic collection in a cumulus model". J. Atmos. Sci., 29, 135-155.

Kessler, E., 1970: "On the distribution and continuity of water substance in atmospheric circulations". Meteor. Monogr., 10, No. 32, 1-84.

Klett, J.D., 1971: "On the breakup of water drops in air". J. Atmos. Sci., 28, 646-647.

Langmuir, I., 1948: "The production of rain by a chain reaction in cumulus clouds at temperatures above freezing". J. Meteor., 5, 175-192.

List, R., and J.G. Dussault, 1967: "Quasi steady state icing and melting conditions and heat and mass transfer of spherical and spheroidal hailstones". J. Atmos. Sci., 24, 522-529.

------ and J.R. Gillespie, 1976: "Evolution of raindrop spectra with collision-induced breakup". Paper submitted.

------, C.F. MacNeil and J.D. McTaggart-Cowan, 1970: "Laboratory investigations of temporary collisions of raindrops". J. Geophys. Res., 75, 7573-7580.

Magarvey, R.H. and B.W. Taylor, 1956: "Free-fall breakup of large drops". J. Appl. Phys., 27, 1129-1135.

Marshall, J.S. and W. McK. Palmer, 1948: "The distribution of raindrops with size". J. Meteor. 5, 165-166.

McTaggart-Cowan, J.D. and R. List, 1975: "Collision and breakup of water drops at terminal velocity". J. Atmos. Sci., 32, 1401-1411.

Pruppacher, H.R. and R. Pitter, 1971: "A semi-empirical determination of the shape of cloud and rain drops". J. Atmos. Sci., 28, 86-94.

Waldvogel, A., 1974: "The N_o jump of raindrop spectra". J. Atmos. Sci., 31, 1067-1078.

Whelpdale, D.M. and R. List, 1971: "The coalescence process in raindrop growth". J. Geophys. Res., 76, 2836-2856.

6.1.5

OBSERVATIONS OF THE DEVELOPMENT OF PRECIPITATION-SIZED ICE PARTICLES IN NE COLORADO THUNDERSTORMS*

J. E. Dye, C. A. Knight, P. N. Johnson, T. W. Cannon, and V. Toutenhoofd

National Center for Atmospheric Research
Boulder, Colorado 80303

1. INTRODUCTION

The development of precipitation via the ice process in convective clouds is a major concern of cloud physics. Although the general features of the process are well known, the initiation and spread of ice in the early growth stages are still incompletely understood. Recent work conducted by the National Hail Research Experiment in northeastern Colorado has been directed at understanding these processes in thunderstorms because of the potential importance to the formation of hail embryos. These studies have shown that precipitation is formed in the thunderstorms in northeast Colorado predominantly through the ice process. This conclusion is based on three sets of evidence: 1) observations made from the NCAR/NOAA sailplane which show the abundance of ice particles including graupel, the scarcity of liquid water drops (Cannon et al., 1974) and the highly continental nature of the clouds (Dye et al., 1974b); 2) laboratory examination of sailplane collected graupel which all originated through the ice process and of hail collected on the ground which show that 80% of the collected hail originated from graupel and 15% from large frozen water drops; and 3) coordinated microphysical and radar measurements which show that the reflectivities observed in moderate northeast Colorado thunderstorms can be accounted for entirely by observed ice particle sizes and distributions (Dye et al., 1974a).

While the above work demonstrates the dominance of the ice process in the summer convective clouds in northeast Colorado, many questions remain about the graupel formation process. This paper describes observations made within thunderstorms by the NCAR/NOAA sailplane which allow us to draw some generalizations about interactions of the microphysics and dynamics. In particular, they lead to conclusions about the nature of ice particle trajectories within these storms that allow sufficient time for precipitation to form. Combined with radar evidence these observations show that recirculation of particles due to turbulence does commonly occur in the thunderstorms in northeast Colorado and suggests that the resulting complex trajectories may play an important role in precipitation formation.

2. SAILPLANE OBSERVATIONS

During the summers of 1972, 1973, and 1974 the sailplane was used to investigate the early stages of development of thunderstorms in northeast Colorado. Microphysical and vertical velocity measurements were made while the sailplane spiralled up from cloud base in the updrafts of the developing turrets and the weak echo regions of more mature storms. The sailplane measurement systems are discussed by Sartor (1972). The two primary observations used in this study are the microphysical measurements obtained from the Cannon cloud particle camera (Cannon, 1975) and the measurement of vertical velocity of the air. With the camera as it was in 1974 in situ photographs could be taken of all particles larger than about 16 μ diameter; water could be distinguished from ice for particles larger than 200 μ diameter; and estimates of cloud droplet concentrations could be made. The vertical velocity of the air was determined to an accuracy of about 1 m/sec from the equation of motion of the sailplane (Dye and Toutenhoofd, 1973).

a. Ice Initiation

There are two pieces of evidence which suggest that the initial formation of ice is occurring primarily at temperatures of -15°C or colder. First of all the sailplane has often flown in updraft regions at temperatures of -10 to nearly -15°C without detecting ice. (If photographs are taken for one minute at the usual rate of two frames per second the detection limit for 50 and 100 μ diameter particles for this one-minute period is about 0.1 and 0.05 per liter, respectively.) The time periods 131740 to 131800 and 131825 to 131850 MDT in Fig. 1 are two short examples of updraft regions without ice. Crystals nucleated in a 5 m/sec updraft at -5°C would have had sufficient time to grow to 50 or 100 μ at -11 or -13°C (see Knight and Dye, 1976) or if nucleated at -10°C would grow to 50 or 100 μ by -12 or -14°C. (Note as first pointed out by Neumann et al., 1967, that nucleation at temperatures between -5 and -10°C makes little difference in resultant size when the crystals are growing in an updraft.) Since ice crystals of 50 to 100 μ diameter have not been detected at temperatures of -10 to nearly -15°C in 5 m/sec updrafts away from adjacent downdrafts, the concentration of nuclei activated at temperatures of -5 to -10°C in these cases must have been less than about 0.1 liter^{-1}. Although some ice may be nucleated at these temperatures, the concentrations are negligible compared to the typical concentrations of 1-100 liter^{-1} commonly observed in precipitation regions by the sailplane.

A more direct piece of evidence on the temperatures at which ice begins to form in a cloud comes from two case studies (June 15, 1972 and July 26, 1974) in which recently formed ice particles were observed. In both cases ice particles of 50 to 100 μ diameter were observed at temperatures in the range of -15 to -18°C in the presence of some liquid water. Growth times to these sizes in this temperature range should be around 1 minute or less. Thus, the particles must have originated in the near vicinity of the observations. The specific periods during which the above conditions were found and

* This research was performed as part of the National Hail Research Experiment, managed by the National Center for Atmospheric Research and sponsored by the Weather Modification Program, Research Application Directorate, National Science Foundation.

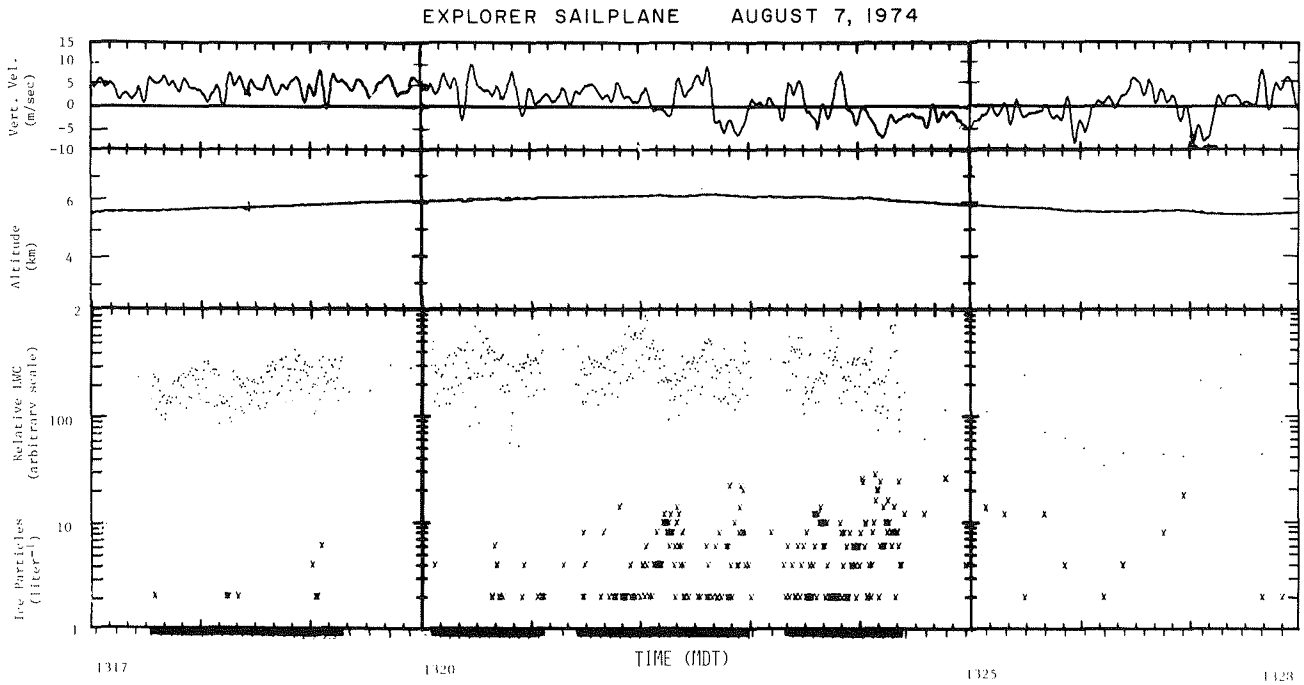

Fig. 1. Vertical velocity of the air, altitude, ice particle concentration (x) and relative liquid water content (.) are plotted as a function of time for data collected on August 7, 1974, at temperatures of approximately -9 to -14°C. The times at which particle camera photographs were taken are shown by tick marks (or solid bars for the 2-frame-per-second mode) at the bottom of the figure.

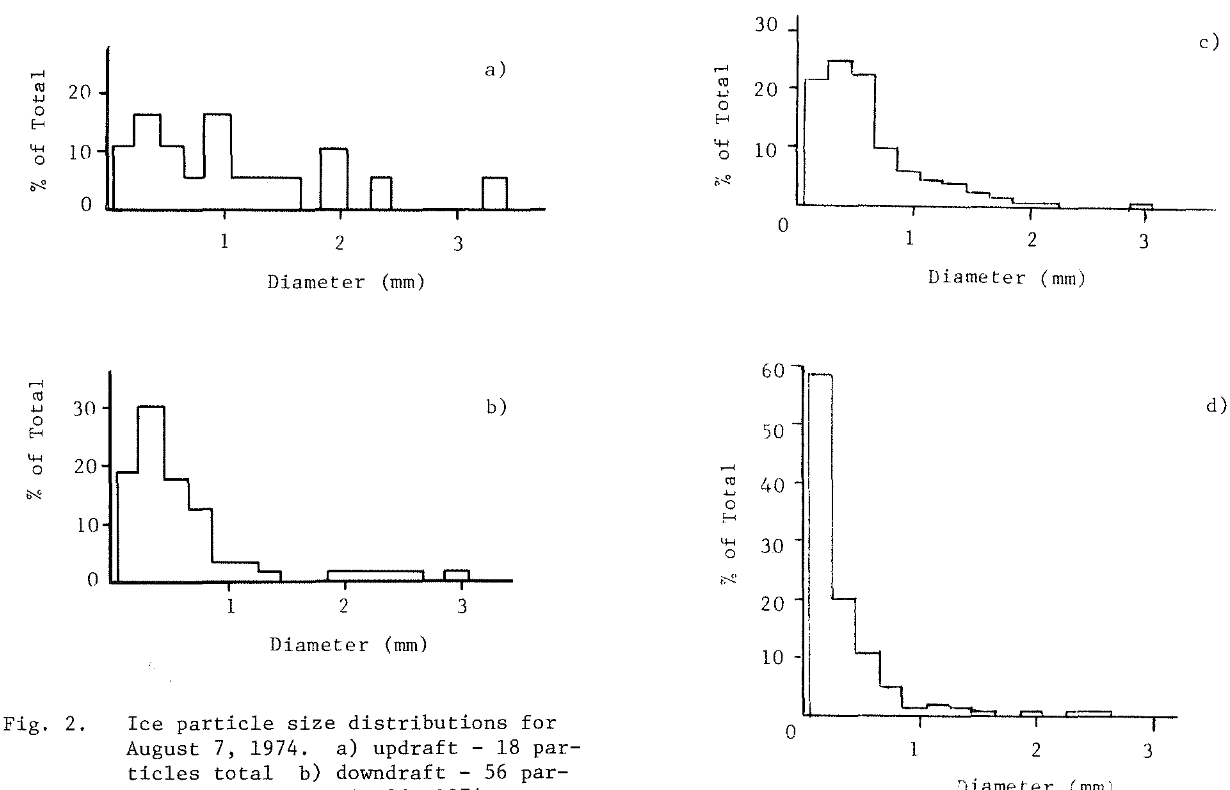

Fig. 2. Ice particle size distributions for August 7, 1974. a) updraft - 18 particles total b) downdraft - 56 particles and for July 26, 1974 c) updraft - 259 particles and d) downdraft - 273 particles.

the observed concentrations of particles of 100 μ diameter or smaller are shown in Table I.

Table I

Concentrations of Recently Nucleated Ice Particles

Time Period	Frames	Particle[1] conc. (l^{-1})	Updraft[2] (m sec^{-1})
June 15, 1972:			
162530-162900	161	∿ 15	
July 26, 1974:			
163824-3842	34	0.1	+3.5
3844-3901	31	0.8	+2
3905-3918	27	0.6	+3.5
4003-4009	13	0.9	+4
4025-4035	21	2.5	+1
3803-3824	30	9.5	-2.5
3918-3936	35	7.5	-1.5
4009-4018	18	4.9	-1

[1] Ice particles ≤ 0.1mm diameter.
[2] Averaged over the time period.

During 1972 the exact times at which photographs were taken were not recorded and it is therefore not possible to positively determine which ice was photographed in updraft and which in downdraft for the June 15, 1972 case. However, there was a rather broad region in which both liquid water and particles of about 100 μ size were photographed. (Since water drops have rarely been observed by the sailplane, the assumption is made that all of these particles are ice.) The concentrations shown in Table I are for that region. For July 26, 1974, the exact photograph times were recorded and particles were seen in both updraft and downdraft. Significantly the concentrations found in the downdraft were approximately an order of magnitude higher than those found in the updraft. It is interesting to note that these observations are qualitatively consistent with the ice nucleation model of Young (1974) which suggests that contact nucleation in the downdraft is a major source of ice nucleation in convective clouds.

b. Spread of Ice in the Cloud

The evidence from the two cases in which recently nucleated ice was found at temperatures of -15 to -18°C as well as the frequent absence of ice in updrafts at warmer temperatures strongly suggests that significant concentrations of ice are not nucleated until about -15°C or colder. Once ice particles have nucleated in the cloud what trajectories do they follow while they are growing to precipitation-sized particles? A number of sailplane observations lead to the conclusion that at least some of these particles gain additional growth time by being recirculated from a downdraft back into an updraft where abundant supercooled water is present. The observations supporting this conclusion are discussed next.

Six out of seven cases of graupel collected on the sailplane and brought back to the laboratory for analysis provide evidence that most of the accretional growth occurred at temperatures warmer than -15°C. Thin sections made from the collected graupel show that the graupel internal structure is composed of the large crystals which are characteristic of growth at temperatures warmer than -15°C (see Knight and Dye, 1976). Since previously discussed observations suggest that most of the ice particles are nucleated at -15°C or colder, the initially formed particles must have a trajectory which takes them from the region of formation to lower altitudes where they can accrete most of the mass at temperatures warmer than -15°C.

One of the most common features of the sailplane measurements is the observation that the presence of ice is roughly correlated with downdrafts and that the highest concentrations normally appear in downdrafts. In some cases this correlation is distinct such as the case shown in Fig. 1. In other cases the correlation is not this distinct but generally the ice particle concentrations are higher when the observed updrafts are less steady and interspersed with regions of downdrafts. While the observation that most of the ice is associated with downdrafts is not surprising since precipitation formed in the cloud falls out in the downdraft, it is a necessary step for recirculation to occur.

Size distributions determined from the photographed ice particles show an interesting difference between the particles in the downdraft and those in the updraft. For the two cases in which the concentration of ice particles were sufficiently high to obtain statistically significant distributions and in which accurate timing of the photographs was possible, the distributions show many more small particles to be present in the downdraft than in the updraft, e.g., Fig. 2. While not conclusive, this evidence tends to support the downward transport of ice nucleated at higher altitudes in the cloud. The size distributions also show that millimetric rimed crystals and graupel are present in both the downdraft and in the adjacent updraft.

From these distributions alone we cannot tell if the millimetric ice found in downdrafts is growing as it falls or simply falling after growing elsewhere. However, measurements from the electrostatic disdrometer (Abbott et al., 1972) before malfunctioning due to icing becomes a problem and from fogging density levels and reticulation on the photographs suggest that usually the liquid water content in the downdraft regions is partially and sometimes totally depleted. While neither of the techniques provides reliable quantitative measurements, there can be little doubt that the liquid water content in downdrafts has been depleted enough to diminsh the length of time and the rate at which precipitation can grow in downdrafts.

The most convincing evidence of particle recirculation is the frequent observation that millimetric rimed ice particles and graupel are present in updrafts at relatively low altitudes at temperatures sometimes as warm as 0 to -5°C. In many cases the updraft is sufficiently strong to be carrying the particles up in the cloud. Since there is insufficient time for particles of this size to have grown during one transit from cloud base (see Knight and Dye, 1976), these particles must have been recirculated from adjacent downdrafts. Several photographs from the most outstanding example, July 29, 1974, are shown in Fig. 3. Measured updrafts for this time period are shown in Fig. 4.

Fig. 3 a) is a 2.5 mm graupel particle while 3 b) is an out-of-focus image of a 1.7 mm diameter particle which must have been mostly water. (See Cannon, 1975, for details about distinguishing water from ice with this camera system.) These particles were within 50 meters of each other at very nearly 0°C in an updraft of roughly 5 m/sec containing abundant liquid water in the form of cloud droplets. Since the updraft changed markedly

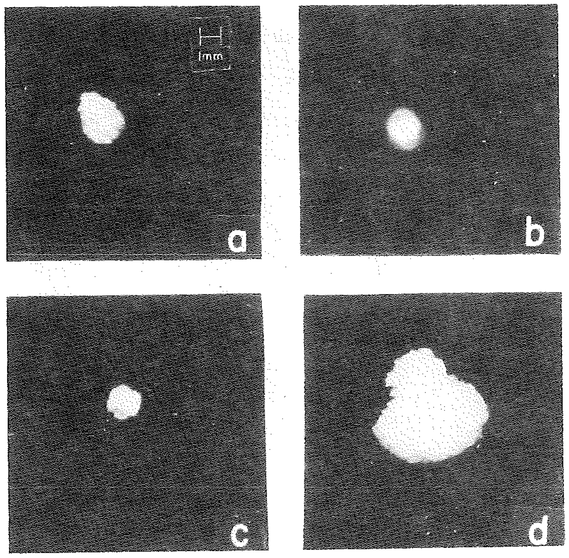

Fig. 3. Particles photographed in updrafts on July 29, 1974. a), b), and c) were photographed at 4.3 to 4.4 km msl about 500 meters above cloud base at a temperature of approximately 0°C. The vertical velocity and liquid water content measured during this period are shown in Fig. 4.
a) is a 2.5 mm graupel particle.
b) appears to be an out-of-focus image of a 1.7 mm diameter distorted water drop or mostly melted graupel particle.
c) is a 0.8 mm rimed particle.
d) is a 5.3 mm conical graupel photographed at 5.3 km at about -6°C in an updraft of 1 to 2 m sec^{-1}.

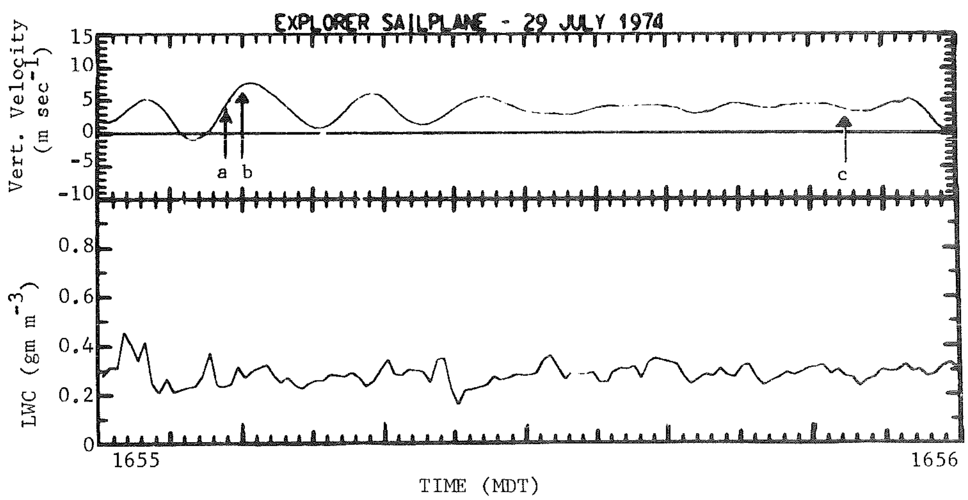

Fig. 4. Vertical velocity and liquid water content measured at 4.3 km (about 0°C) on July 29, 1974. The time at which the particles shown in figures 3. a), b), and c) are indicated by arrows.

along the flight path in this region, we cannot tell if the particles were actually rising or falling, but they were more or less suspended in the updraft and growing. Fig. 3 c) shows a photograph of a 1.6 mm graupel particle which was most likely rising in the updraft while 3 d) is of a 5 mm graupel particle which was probably falling in the updraft. Since the cloud base on this day was only +3°C the particle composed mostly of water and the graupel shown in Fig. 3 a) must have been recirculated from above, with the water particle being circulated low enough to have at least partially melted. In one case in which large water drops were observed higher in the cloud Doppler radar measurements show that the storm organization favored recirculation. The low and middle level winds were oriented so as to direct falling precipitation back into the inflow.

The evidence presented above shows conclusively that some particles are being recirculated into the updraft, but how does this occur? Probably the most outstanding feature of the sailplane observations is the extreme variability of both the microphysical and updraft measurements, particularly in the regions in which mixed up- and downdrafts are found. These large fluctuations are very suggestive of a turbulent mixing process. Radar echo studies presented below provide additional support for this hypothesis.

3. RADAR OBSERVATIONS

While the aircraft observations allow us to study the details of a few cases, the observations are made in a small fraction of the total cloud volume and it is difficult to generalize from these results alone. Radar observation with its broad coverage allows us to examine many more clouds as well as the entire cloud volume, albeit with coarser resolution. In this study the initiation and development of first echoes on 12 different days was examined using the Grover S-band radar data. In most cases the effective lower limit of detection of echoes was 20 dBZ. Preliminary results of the study are shown in Table II and are broken into categories reflecting the maximum reflectivity attained by the cell.

The first conclusion that can be drawn from this study is that the most frequent region of formation of first echoes was at altitudes of about 6 to 8 km msl and temperatures of -15 to -20°C. There was surprizingly little difference between the average temperatures of formation in the 35, 45, and 55 dBZ categories. Perhaps this is related to the fact that the maximum growth rate of ice crystals occurs at -15°C, and that this region therefore is the most likely region to contain ice crystals large enough to start riming.

Table II

First Echo Statistics

Maximum Reflectivity (dbz)	25-35	35-45	45-55	>55
Number of Echoes	22	30	21	14
Midpoint Altitude at First Appearance (km msl)				
Mean	5.5	6.8	7.0	7.2
Standard Deviation	1.3	1.4	1.0	0.8
Range	3.9, 8.8	4.6, 9.3	5.6, 8.8	5.4, 8.4
Midpoint Temperature 1) at First Appearance (°C)				
Mean	-10	-16	-17	-18
Standard Deviation	8.4	8.7	6.1	3
Range	+6, -27	0, -31	-7, -30	-5, -24
Rise Rate of Top 2) (m/sec)				
Mean	-3.7	-0.9	2.2	3.7
Standard Deviation	3.7	2.9	2.7	2.0
Range	-14, +2	-10, +3	-2, +11	1, 9
Fall Rate of Bottom 3) (m/sec)				
Mean	6.3	10.4	9.0	10.6
Standard Deviation	6.0	5.1	2.7	5.6
Range	0, 23.8	5, 16	4, 13	4, 27

1) Based on the environmental temperature from the sounding nearest in time and space.
2) Average rate over first 10 minutes.
3) Average rate until the echo reaches the surface.

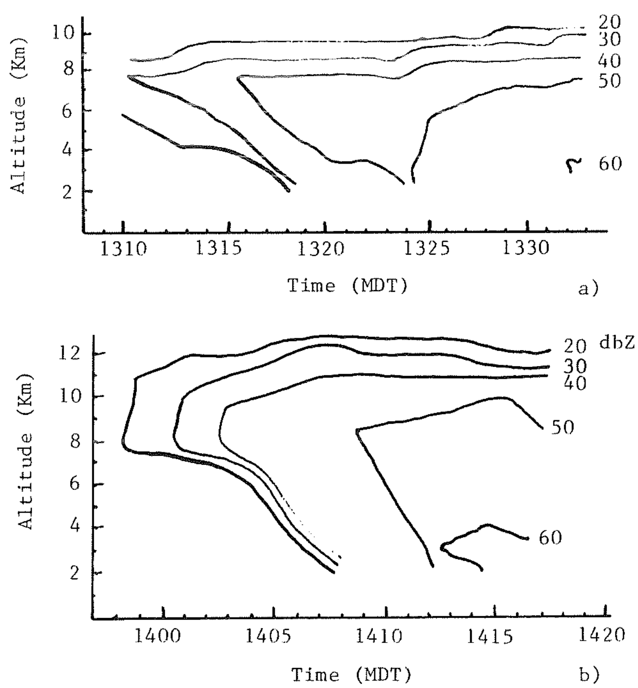

Fig. 5. Time-Altitude profiles of the reflectivity contours of two cells investigated by the sailplane on August 7, 1974. Some of the microphysical observations for cell a) are shown in Fig. 1.

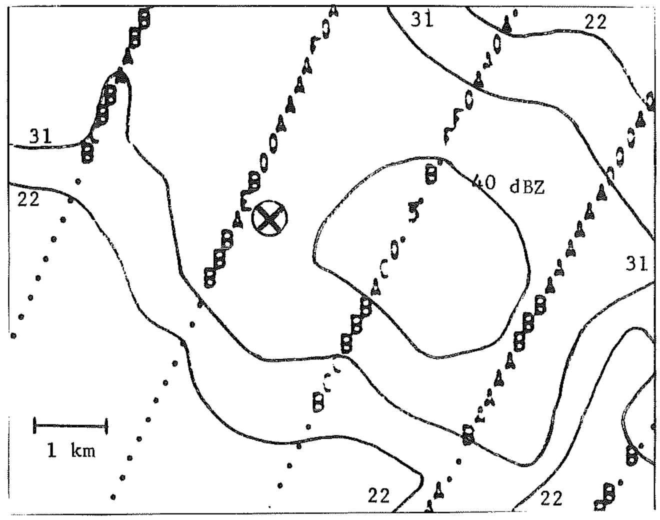

Doppler Velocity Code

Code	Velocity (m/sec)	Code	Velocity (m/sec)
3	-5,-6	B	+ 4,5
2	-3,-4	C	6,7
1	-1,-2	D	8,9
0	0,1	E	10,11
A	+2,3	F	12,13

+ denotes away from the radar

Fig. 6. Coded Doppler velocity measurements superimposed on reflectivity contours for a 3.3° elevation scan (about 5.6 km) taken at 132234 MDT on Aug. 7, 1974. The position of the sailplane which was at about 6.2 km altitude is shown by an ⊗ . The corresponding sailplane observations are shown in Fig. 1.

Another interesting observation of cell growth and one that remains unexplained is that most frequently the altitude of maximum reflectivity remains constant during the early intensification of the cell. Fig. 5 shows two examples of this for August 7, 1974. In order to have this occur it seems likely that the precipitation particles first seen by the radar somehow remain at the same altitude and continue to grow. If so, one possible explanation would be that the particles remain balanced in the updraft as they grow. This requires that as the particles grow the updraft strength increases accordingly to match their increase in fall speed. While this may happen on occasion it seems highly unlikely that the special circumstances required would occur commonly. Mixing and recirculation may play a role but it is not clear how.

The best evidence for a high degree of mixing inside these clouds comes from Doppler radar observations which show great variability even at scales at the limit of resolution of the radar. Fig. 6 shows an example of Doppler data from the Grover radar for August 7, 1974. Differences in average Doppler velocities shown at adjacent points reflect real variations and not statistical fluctuations. This PPI scan at 3.3° elevation was taken through the cell in which the sailplane data shown in Fig. 1 was collected. Note the large measured fluctuations in Doppler velocity in the region in which the sailplane was flying and was observing large variations in the microphysical parameters and vertical velocity. Recent dual-

Doppler measurements made in northeast Colorado have shown extreme values of variance in the shear zone between updraft and downdraft (Strauch and Merrem, 1976). They conclude that the high variances were due to turbulence generated in the shear zone between updraft and downdraft. This is precisely the zone in which the sailplane microphysical observations suggest mixing of particles from the downdraft into the updraft.

4. CONCLUSIONS

Observations made by the NCAR/NOAA sailplane suggest that the nucleation of ice particles in the summer convective clouds in northeast Colorado occurs primarily at temperatures of -15°C or colder while most of the accretional growth of the resulting precipitation, graupel, occurs at temperatures warmer than -15°C. These observations also show millimetric rimed ice particles and graupel to be present and sometimes rising in updrafts at temperatures as warm as 0 to -5°C. Since there is insufficient time for these particles to have grown during one passage from cloud base, they must have formed at higher levels, descended, and then recirculated into updrafts, a conclusion which is consistent with the observed nucleation and growth characteristics.

While the observations do show conclusively that recirculation does occur, it is difficult to determine how important it is for the production of precipitation. However, the qualitative observation that much of the cloud water has been depleted in the downdrafts at temperatures of -15°C and warmer coupled with the observation that most of the accretional growth occurs at temperatures warmer than -15°C strongly suggests that most of the precipitation particle growth occurs in the updraft or at least in the transition zone between updraft and downdraft. Indeed, this shear zone may be of considerable importance to precipitation formation. The turbulent mixing which is observed to occur in this zone can provide the prime ingredients needed for precipitation formation by the ice process in the cold summer clouds of northeast Colorado. The downdraft supplies centers for accretional growth; the updraft provides a continuing supply of supercooled cloud water; and the recirculation and mixing gives the particles the additional time needed to grow to precipitation sizes. Organized dynamic recirculation (e.g., Musil et al., 1976) can also provide the necessary conditions. At this time there are not enough observations to determine the relative importance of these two mechanisms.

These same recirculation processes may be responsible for the production and selection of hail embryos. A few favored particles can be preferentially recirculated or mixed back into an updraft where both supercooled water and stronger updrafts needed for additional growth are found. Again, additional observations are needed before any conclusions can be drawn.

5. REFERENCES

Abbott, C. E., J. E. Dye, and J. D. Sartor, 1972: An electrostatic cloud droplet probe. J. Appl. Meteor., 1, 1092-1100.

Cannon, T. W., J. E. Dye, and V. Toutenhoofd, 1974: The mechanism of precipitation formation in Northeastern Colorado cumulus II. Sailplane measurements. J. Atmos. Sci., 31, 2148-2151.

_____, 1975: A photographic technique for measurements of atmospheric particles in situ from aircraft. J. Appl. Meteor., 14, 1383-1388.

Dye, J. E., and W. Toutenhoofd, 1973: Measurements of the vertical velocity of the air inside cumulus congestus clouds. Preprint Vol. Eighth Conf. on Severe Local Storms, AMS, Boston, Mass.

_____, C. Knight, V. Toutenhoofd, and T. W. Cannon, 1974a: The mechanism of precipitation formation in northeastern Colorado cumulus III. Coordinated microphysical and radar observations and summary. J. Atmos. Sci., 31, 2152-2159.

_____, C. A. Knight, and T. W. Cannon, 1974b: The potential for rainfall modification in some Great Plains cumuli. Preprint, Vol. Fourth Conf. on Weather Modification, Fort Lauderdale, Fla., 13-15.

Knight, C. A., N. C. Knight, J. E. Dye, and V. Toutenhoofd, 1974: The mechanism of precipitation formation in northeastern Colorado cumulus I. Observations of the precipitation itself. J. Atmos. Sci., 31, 2142-2147.

_____, and J. E. Dye, 1976: Seeding "cold cumulus" with ice nuclei to enhance precipitation. Preprint Vo. of Internatl. Conf. on Weather Modification, Boulder, Colorado.

Musil, D. J., C. A. Knight, W. Sand, A. Dennis and I. Paluch, 1976: Radar and related hydrometeor observations inside a multicell hailstorm. Proc. Internatl. Cloud Physics Conf., Boulder, Colorado, 1976.

Neumann, J., K. R. Gabriel, and A. Gagin, 1967: Cloud seeding and cloud physics in Israel: Results and problems. Presented at Internatl. Conf. on Water for Peace, Washington, D. C., May 23-31, 1967, 15 pp.

Sartor, J. D., 1972: Clouds and precipitation. Physics Today, 25, 32-38.

Strauch, R. G. and F. H. Merrem, 1976: Structure of an evolving hailstorm. Part III Internal Structure from Doppler Radar. Accepted for publication, Mon. Wea. Rev.

Young, K. C., 1974: The role of contact nucleation in ice phase initiation in clouds. J. Atmos. Sci., 31, 768-776.

ICE CRYSTALS IN THE ANTARCTIC ATMOSPHERE

Takeshi Ohtake

Geophysical Institute
University of Alaska
Fairbanks, Alaska USA

1. INTRODUCTION

Studies of atmospheric ice crystals from a cloudless sky were carried out in December 1974 at Amundsen-Scott South Pole Station in order to understand their mechanism of production and their influence on the Antarctic climate. Since ice crystal precipitation is the only way to remove water vapor from the atmosphere toward the ground in the polar regions, some knowledge of the formation mechanisms and rates of precipitation is necessary in order to understand the budget of atmospheric water, which in turn affects the infrared radiation balance during the long polar night.

Both nucleation processes and water vapor sources show interesting differences between the Arctic and Antarctic regions. Ice crystals from clear skies in Alaskan cities (Ohtake and Jayaweera, 1971) are formed in a favorable environment in which nuclei and water vapor are provided by power plants, while ice crystals observed at Barrow, Alaska may be from open leads in the Arctic pack ice with abundant water vapor and few local ice nuclei (Ohtake and Holmgren, 1974). In contrast, the environment in which ice crystals form at the South Pole seems to have neither abundant nuclei nor high water vapor availability. This is a report of preliminary observations of ice crystals at the South Pole Station.

2. CONCENTRATION OF ICE CRYSTALS

The concentration of ice crystals was continuously recorded on the ground at the South Pole Station from 14 December, 1974 to 29 January, 1975 by utilizing the acoustic ice crystal counter (Ohtake and Holmgren, 1973 and Langer et al., 1967). The sensor consists of a glass tube that tapers gradually from 2.5 cm diameter to a 6 cm long, 1.5 mm capillary (Fig. 1). This capillary is connected to a vacuum pump which sucks air containing ice crystals through the tube. Ice crystals larger than 30 microns give sharp clicking sounds which are detected by a microphone and counted. Ice crystals smaller than 20 microns, such as fog droplets and air pollution particulates, do not trigger the sensor. A 5 cm long rubber tube is connected to the top of the glass tube to minimize false signals due to whistles caused by wind or blowing snow. The sensor was pointed vertically. The sensor was used at the top of the sky lab building at a height of 18 m, which was high enough to be free from drifting or blowing snow particles from the snow surface. The records of ice crystal concentration were frequently confirmed by visual observations and ice crystal replication records. Unfortunately, these records of ice crystal precipitation did not always agree with National Weather Service observations at the Pole station during the machine observations.

During 31 of the 41 days between 14 December, 1974 and 28 January, 1975, ice crystals including snow crystals were observed. This number of days for ice crystals may be comparable to the annual sum of 317 days for ice crystals reported by Kuhn (1968), if the frequency of ice crystals is much greater in the winter season. The maximum concentration of ice crystals during the period was 87 crystals per liter of air at a ground temperature of -23C.

3. SNOW CRYSTAL REPLICATION

A snow crystal replicator, originally designed by Hindman and Rinker (1967), modified

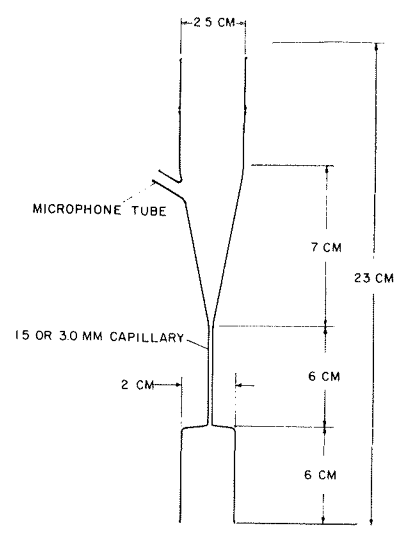

Fig. 1 Acoustic sensor for ice crystal count (Langer et al., 1966). A 5 cm rubber tube is extended from the glass tube to minimize false signals due to whistles caused by wind.

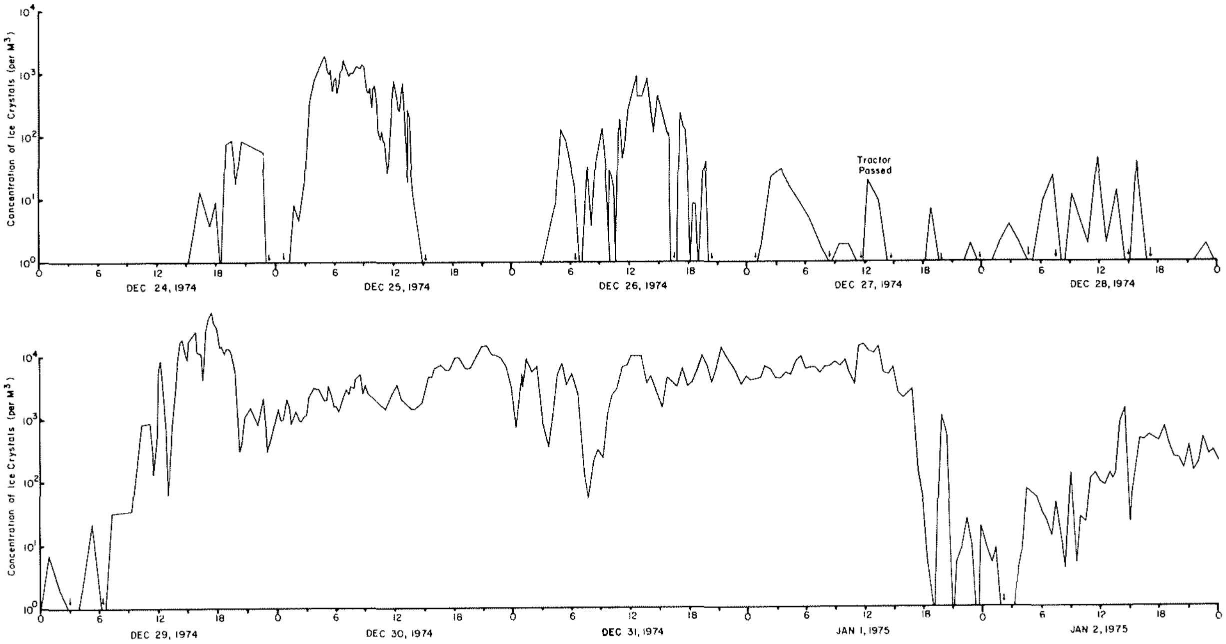

Fig. 2 Ice crystal concentration at the South Pole Station recorded by the acoustic ice crystal sensor.

and manufactured by Western Scientific Services, Inc., was employed to record the shape, size and concentration of ice crystals. The results indicated that: 1) the concentrations of ice crystals obtained from the replication method corresponded to those from the acoustic sensor technique, even at times during which no ice crystals were reported by NWS records, 2) remarkable fluctuations of ice crystal concentrations were noted on 26 December, 1974 and almost constant concentrations were observed in the period from 29 December, 1974 and 1 January, 1975 (see Fig. 2). Diurnal variation of concentrations which was found at Barrow (Ohtake and Holmgren, 1974) was not noticed at the South Pole, which may be due to nearly constant solar elevation all day long at the Pole.

On 17 December, 1974, falling ice crystals had the following forms according to Magono and Lees' classification (1966) of ice crystals: side planes (S1) and combination of side planes, bullets and columns (S3) or radiating assemblage of plates (P7a) fell (Fig. 3). The temperature conditions for the crystals agreed with their proposed conditions for these shapes. Even though we did not have any upper air observations by radiosondes or by our dry ice technique (see section 4) for detection of ice saturation, appearance of As clouds indicated the humidity in the cloud layer was at least water saturation, so that the humidity conditions during the formation of the above crystals also agreed with Magono and Lees'.

Ice crystals falling around noon on 22 December had many small columnar rimings on the mother crystal faces. Most of the mother crystals were about 1 mm long and 0.2 mm diameter columns (R1b) with riming crystals of about 30 microns as can be seen in Fig. 4. Since the crystals precipitated from As (estimated height of 300 m) overcast with possibly Ci and Cs (estimated 4000 m for the cloud observed later), the mother crystals may have formed at a higher layer (possibly 4000 m) than the As clouds and been subjected to slight evaporation below the layer, then got rimings in the As clouds, and the frozen rimed droplets grew to columnar crystals before arriving at the ground.

Another variety of crystals was much smaller. Their diameters averaged about 60 microns and crystals as small as 30 microns in diameter were common. Since they occurred without any visible clouds, these unlike for the former case, should have originated from a source other than cirrus clouds. These small crystals may be insignificant to the Antarctic mass balance, but will have an important consequence on the radiation balance. The study of their origin and the mechanism of formation may be potentially important in regard to the formation of ice clouds in non-polar areas.

4. UPPER CONDITION RELATED TO ONLY A FEW ICE CRYSTALS

Because there were only a few rawinsonde observations during the period of observation, the upper air conditions remained unknown. In order to correlate the crystal observations with humidity, a piece of dry ice was lifted to the sky by a small balloon almost

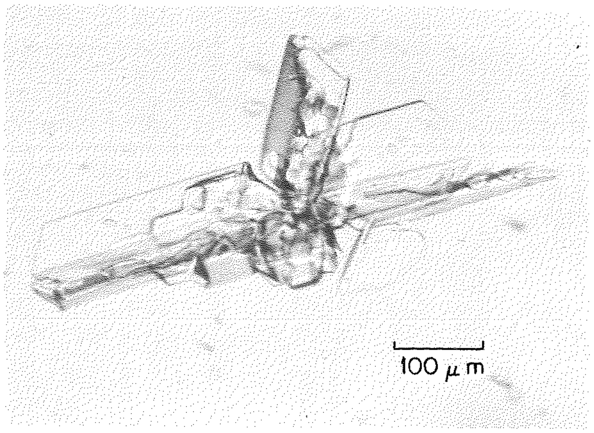

Fig. 3 An ice crystal which fell on 17 December, 1974.

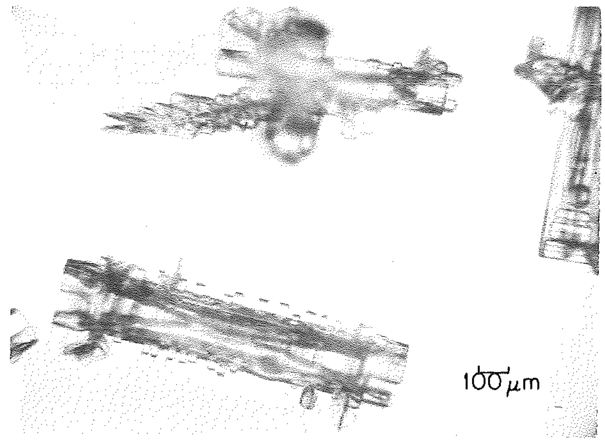

Fig. 4 Ice crystals precipitated on 22 December 1974.

every day to estimate relative humidity in the upper air. Dry ice can create ice crystals in the air by condensation of water droplets and subsequent spontaneous nucleation of the droplets when dry ice contacts the air. The ice crystal clouds will stay in the air if the air is saturated over ice, and then will grow larger in a superstaturated environment, especially at water saturation. If the humidity is below ice saturation, the ice clouds will evaporate and disappear in a short period of time. Since the ascent rate of the balloon was known, the elevation of the dry ice could be fairly well determined with the aid of binoculars and a stopwatch.

We found that falling ice crystals were always associated with a significant thickness of air wetter than ice saturation. The critical thickness for ice crystal precipitation at the ground was about half way from the ground to the level at which we lost track of the balloon which normally occurred about 2000 m from the ground. When crystals with side planes (S1) and combination of bullets (C2a) were observed, the humidity was always high, i.e., the ice cloud formed by the dry ice seeding grew to larger dimensions. In cases of no ice crystals, the ice cloud formed by the dry ice quickly disappeared stayed nominal. So we can conclude that natural atmospheric ice crystals can form only in air with humidities higher than ice saturation.

It was noticed that most of the ice crystals at the Pole station were associated with As or Ac clouds which even in the Antarctic cold environment, normally consist of water cloud droplets. Of course, sometimes Ci or Cs cloud appeared in the sky, but these clouds were not responsible for the ice crystal precipitation. This result is contrary to Hogan (1975) who

Table 1 Chemical elemental compositions (for elements heavier than NE only) of nuclei in individual ice crystals at the South Pole Station.

Collected time	LT	Si	Al	Na	Mg	S	Cl	Ca	K	Others	Shape	Size microns
Dec. 17, '74	17:49	+++	++					0			thin pl	150 dia
	17:49	+++	++								column	175x112
	22:30	++	++	0	0			0	0		thin pl	220 dia
Dec. 18, '74	04:30	++		0							thin pl	470 dia
	14:43			no detectable elements							thin pl	44 dia
Dec. 25, '74	10:10	+++									column	180x120
	10:10	+++	++	++	++	++	++	++	++	0Fe	plate	100 dia
	10:13	++	++	++	++	+	++				column	260x115
	10:17	++	0			+					column	167x110
	12:17			no detectable elements							column	140x97
	13:00					+					column	183x127
	13:00	++	+	++	++	++	+	++	++	+Mn	column	157x90
	13:00	+++	+	++	++	++	++	++	++		irreg	170
Dec. 26, '74	15:58					++	+				thin pl	33
	15:58	++	+	+	0			0	+	+Mn	column	93x40
	15:58	+++	+++	+	+	++	++		+		column	70x40
	15:58			++	+	+				0Fe	plate	70

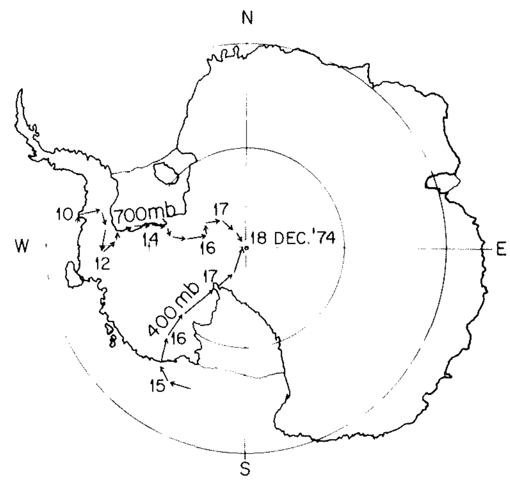

Fig. 5 Air trajectories at both 400 mb and 700 mb levels, arriving at the South Pole at 0000LT 18 December, 1974. Each arrow indicates air flow every 12 hours.

reported that the ice crystal precipitation was only observed at the surface when cirrus bands were present at higher altitudes. On 26 December, 1974, the concentration of ice crystals fluctuated very much both in acoustic sensor technique observations and ice crystal replications. The balloon with the dry ice also indicated quite strong turbulence at the height of 700 m from the ground, which coincides with the level of As clouds reported by NWS. No Ci and Cs clouds was reported. At 14:30 LT, a large amount of moisture was observed between 900 m and 1700 m by the dry ice seeding, even though an extensive dry air layer was noted below the level.

5. SOURCE OF NUCLEI AND WATER VAPOR OF THE ICE CRYSTALS

Nuclei of ice crystals collected at the South Pole Station were examined with a scanning electron microscope and an X-ray energy spectrometer combined to determine the source and chemical composition of the nuclei. Those nuclei were not only at the centers but scattered all through the interior of the crystals. Table 1 gives the elemental composition (for atomic numbers greater than 10) of nuclei in the individual crystals, together with data on the date of collection, shape and size of each crystal. No differentiation was made between centered or randomly located nuclei.

In the table, 12 ice crystals out of 17 contained high contents of Si and 10 crystals included Al, always combined with Si. Two crystals had no detectable amount of chemical elements. Most of the ice crystals on 17 and 18 December, 1974 had primarily Si and Al. In contrast, 7 out of 12 crystals on 25 and 26 December had Na, Mg, Cl, S, K and Ca, which are typical compositions of sea salt, combined with Si and Al.

Air trajectory analyses using 400 mb flow showed that the air arriving at the South Pole normally entered the southwest part of the Antarctic continent (90°W to 170°W) from the Pacific Ocean and traveled about 1700 km in 2 to 4 days from the open ocean. So, it is possible that the ice nuclei such as kaolin particles and clay minerals indicating Si and Al are transported from the desert in Australia or some volcanos. (Incidently, volcanic ash from the recent volcanic eraption of Augustine Island of Alaska showed strong nucleation ability in a Settling Cloud Chamber (Ohtake, 1971) for ice nucleus counting and chemical compositions of Si and Al).

Because of especially stable air condition in the lowest several hundred meters due to the temperature inversion over the Antarctic continent, other trajectory analyses using 700 mb charts were also made. These analyses were intended to estimate the transportation of sea salt particles from the ocean, assuming that the sea salt particles are larger than soil particles and the flow at 700 mb is geostrophic. From the analyses, it was found that the air on 17 and 18 December at the South Pole stayed near the Pole much longer than the air on 25 and 26 December. This comparison of how long the air had stayed inland may explain why the nuclei of the ice crystals on the latter days contained more sea salt mixed with Si and Al.

Acknowledgement: The research presented here has been supported by the National Science Foundation under grant number OPP 74-04037.

REFERENCES

Hindman, E. E., II, and R. L. Rinker, 1967: Continuous snowfall replicator, J. Appl. Meteor., 6, 126-133.

Hogan, A. W., 1975: Summer ice crystal precipitation at the South Pole, J. Appl. Meteor., 14, 246-249.

Kuhn, M., 1968: Ice crystals and solar halo displays at Plateau Station, 1967. ISAGE Symposium, pp. 298-302.

Magono, C. and C. W. Lee, 1966: Meteorological classification of natural snow crystals, J. Faculty of Science, Hokkaido, Univ., Japan, Ser. VII, 2, 321-365.

Langer, G., J., Rosinski and C. P. Edwards, 1967: A continuous ice nucleus counter and its application to tracking in the troposphere, J. Appl. Meteor., 6, 114-125.

Ohtake, T., 1971: Cloud settling chamber for Ice nuclei count, Proc. Intern. Conf. Weather Modification, Sept., 1971, Canberra, 38-41.

Ohtake, T. and B. E. Holmgren, 1974: Ice crystals from a cloudless sky, Proc. Conf. Cloud Physics, 21-24 Oct., 1974, Tucson, 317-320.

Ohtake, T. and K.O.L.F. Jayaweera, 1971: Ice crystal displays from power plants, Weather, 26, 271-277.

6.2.1

MESOSCALE STRUCTURE OF PRECIPITATION IN EXTRATROPICAL CYCLONES

Peter V. Hobbs and Robert A. Houze, Jr.

University of Washington
Seattle, Washington

1. INTRODUCTION

Observational studies with radars, raingauges and aircraft consistently show that precipitation in extratropical cyclones is dominated by mesoscale rainbands which range in length from 100 to 1000 km and in width from 5 to 100 km (Harrold and Austin, 1974; Browning, 1974). In the CYCLES (Cyclonic Extratropical Storms) PROJECT at the University of Washington, we are investigating rainbands in extratropical cyclones, not only in terms of their morphology (which has been the emphasis of most previous studies), but also the physical processes associated with the bands. In this paper, we present examples of the rainbands which we have observed in occluded cyclones and suggest a classification scheme for them. The dynamics and microphysics of the clouds associated with rainbands will be illustrated by reference to a case study of an occluded frontal system.

2. TYPES OF RAINBANDS

We have observed six types of rainbands in the CYCLES PROJECT. These are illustrated in Fig. 1 and can be classified as follows:

Type 1: Warm frontal. Bands typically 50 km in width oriented parallel to warm front and found toward the leading edge of a frontal cloud shield (Band 1 in Fig. 1).

Type 2: Warm sector. Bands typically 50 km in width, found south of the intersection of the surface warm and cold fronts and tending to be parallel to cold fronts (Band 2 in Fig. 1).

Type 3: Cold frontal--wide. Bands approximately 50 km in width oriented parallel to cold front and found toward the trailing edge of a frontal cloud shield (Band 3 in Fig. 1).

Type 4: Cold frontal--narrow. An extremely narrow band (~5 km in width) coinciding with the surface cold front (Band 4 in Fig. 1).

Type 5: Wave. Bands occurring in a very regular pattern similar to waves. Generally smaller than the other types of bands, typically 5 km × 40 km, sometimes as large as 10 km × 100 km (Bands labeled 5 in Fig. 1).

Type 6: Post frontal. Rainbands located in the convective cloud field behind a frontal cloud shield (Bands labeled 6 in Fig. 1).

The storm illustrated in Fig. 1 was somewhat unusual in exhibiting all six types of rainbands. While most of the storms which we have examined show some degree of banded structure, all types do not occur in every storm, nor do they occur in exactly the same arrangement in every case. However, when bands do appear, they are almost always one of the six types mentioned above.

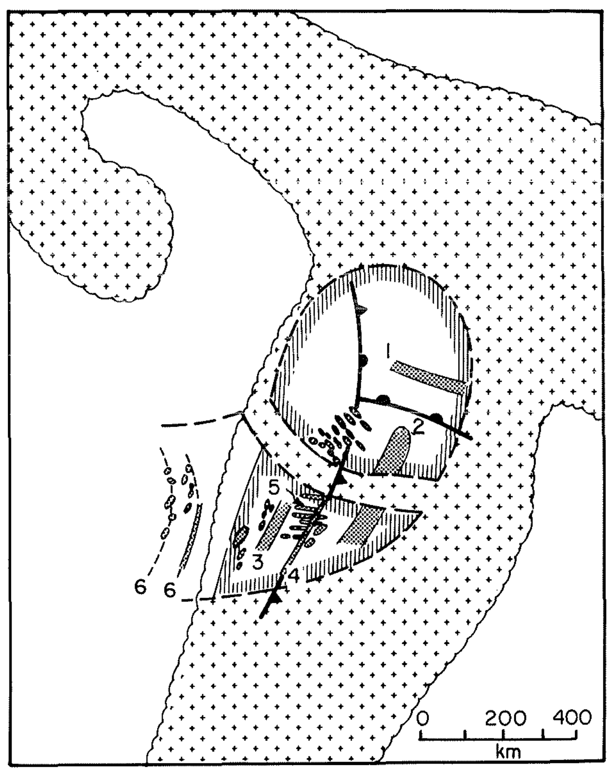

Fig. 1 Schematic presentation of occluded cyclone observed over the Pacific Northwest on 27-28 November 1973. Cloud pattern observed by satellite is shown by (⁺₊⁺₊⁺). Dashed lines enclose portion of cloud shield in which observations were obtained. Hatching (||||||) encloses light rain areas. Heavy rain areas are indicated by (▒▒▒). Numbers refer to types of rainbands discussed in text.

Our classification scheme is consistent with rainbands observed in other parts of the world. Rainbands parallel to and ahead of warm fronts have been observed in open wave cyclones by Browning and Harrold (1969) and Reed (1972). These bands would Type 1 in our classification. Browning and Harrold's observations were over the British Isles, while Reed's were in New England. Similar rainbands, with warm frontal orientation, were found in the leading (eastern) portions of occluded frontal systems described by Nagle and Serebreny (1962) over the eastern Pacific Ocean and by Kreitzberg and Brown (1970) over the northeastern U.S.

In the frontal systems studied by Nagle and Serebreny (1962) and Kreitzberg and Brown (1970), the Type 1 bands in the leading portion of the cloud shield gave way to bands with cold frontal orientations (which would be Type 2 by our classification) in the trailing western portion. In an occluded cyclone over the northeastern Atlantic Ocean, Browning et al. (1973) observed a series of Type 2 bands parallel to multiple cold fronts aloft. Their Type 2 bands, however, were apparently not preceded by a series of warm frontal bands.

Warm sector bands (Type 3 in our classification) were observed frequently in open wave cyclones near Japan by Nozumi and Arakawa (1968). They found that the warm sector bands tended to be parallel to the cold front, often intersection the warm front at right angles. Harrold (1973) also reported that warm sector bands parallel to the cold front occurred frequently in cyclones near the British Isles. Browning and Harrold (1969) found warm-sector rainbands over England which were not parallel to either the cold or warm front in a wave depression; however, the orientation of these bands may have been influenced by the topography of the British Isles. The pre-frontal squall line associated with severe convective storms is a notable special case of Type 3 (warm sector) rainbands.

Type 4 rainbands, that is, long, thin and continuous rainbands coinciding with surface cold fronts, have been observed previously by Kessler and Wexler (1960) in New England and by Browning and Pardoe (1973) in six cases over the British Isles.

Post-frontal convective rainbands (Type 6) were included by Nagle and Serebreny (1962) in their schematic model of radar echoes in occluded cyclones over the eastern Pacific Ocean. The occurrence of mesoscale precipitation bands in cold air masses to the west of surface cyclonic systems is a well known phenomenon during the winter over the Sea of Japan (e.g., Matsumoto et al., 1967).

3. RAINBANDS IN RELATION TO FRONTAL AIR MOTIONS

Besides the morphology of the rainbands, evident in raingauge and radar data, we are employing the CYCLES PROJECT data to investigate the dynamics and microphysics of the clouds associated with the bands. For illustration, we refer to the storm depicted in Fig. 2, which was an occluded frontal system containing

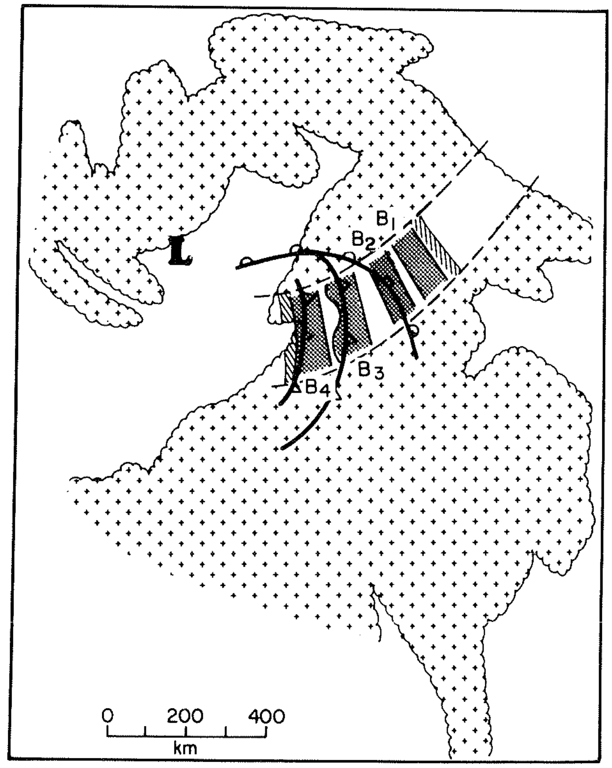

Fig. 2 Schematic representation of storm observed over Washington State on 20 December 1973. Cloud pattern observed by satellite is shown by (+ + +). Dashed lines enclose portion of cloud shield in which observations were obtained. Hatching (||||||) encloses light rain areas. Rainbands are denoted B_1-B_4. Fronts shown are for 720 mb level.

two Type 1 (warm frontal) rainbands (B_1 and B_2 in Fig. 2) and two Type 3 (cold frontal--wide) rainbands (B_3 and B_4 in Fig. 2).

The dynamical framework in which the rainbands existed is illustrated by Figs. 3 and 4. The two-dimensional vertical circulation pattern shown in Fig. 3 was obtained by subtracting the horizontal velocity of the frontal system from the winds observed with serial rawinsondes; it therefore represents the airflow relative to the system. Vertical velocities were computed using the two-dimensionalized mass continuity equation in the plane of the cross section.

The computed flow pattern in Fig. 3 is in good agreement with other data. The region of maximum upward motion in the lower troposphere is centered on the time of the surface trough passage (T in Fig. 3), when the maximum low-level convergence would be expected. The computed upward motion region also coincides exactly with the periods of precipitation and satellite-observed cloudiness at the rawinsonde site. The airflow pattern shown in Fig. 3 is remarkably similar to frontal airflow patterns obtained in previous investigations of Pacific occlusions (Elliott and Hovind, 1965; Hobbs et al., 1975).

The flow of water vapor through the region of upward motion (enclosed by the dashed line in Fig. 3) shows that the primary

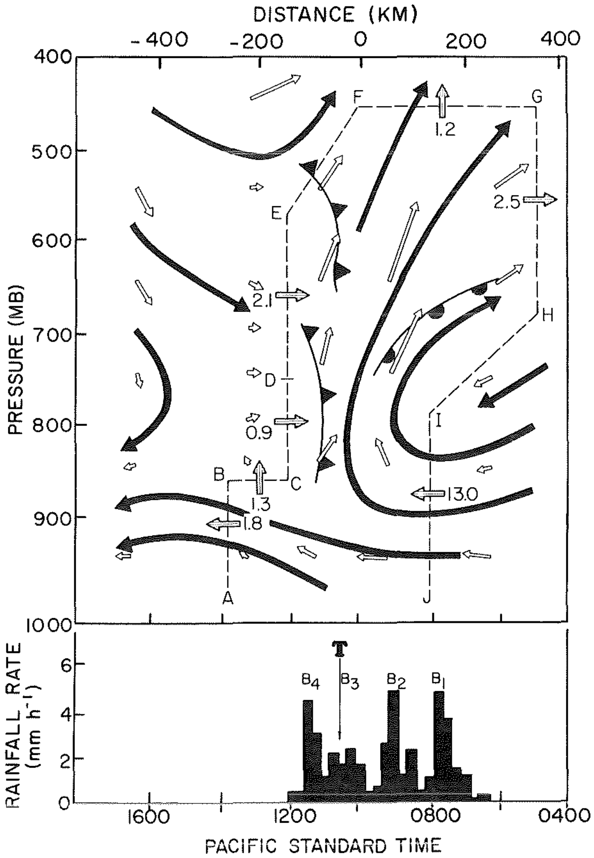

Fig. 3 Two-dimensional airflow in the frontal system of 20 December 1973. Distance scale at top of diagram was obtained by converting time to space on the basis of observed frontal velocities. Streamlines relative to fronts are shown by heavy arrows ( ). Small open arrows ( ) indicate the displacement of a parcel of air in one hour at the computed velocity applying at its origin (vertical component in mb, horizontal component in km). Dashed line surrounds region of upward motion associated with frontal clouds and rainbands (B_1-B_4). Striped arrows crossing dashed line show fluxes of water vapor (with numbers adjacent to arrows indicating magnitudes of fluxes in units of 10^4 g s^{-1} m^{-1}) across boundaries of lifting region. Letters A-J mark points referred to in text. Letter T marks time of surface trough passage.

source of moisture for the region containing the rainbands was the low-level flow through the boundary IJ below the warm front.

The origin of the moist air feeding rainbands B_1-B_4 was investigated by estimating the three-dimensional trajectories of the air flowing through the cross section of Fig. 3. We identified four air parcels in the cross section plane and displaced them backwards in time (in one-hour steps) according to the computed vertical velocity field shown in Fig. 3 and the observed horizontal winds. It was assumed that the airflow in the plane of the cross section of Fig. 3 applied everywhere along a 600 km length of the frontal system. The computed trajectories are shown in Fig. 4. In Fig. 4(a), the frontal motion has been subtracted from the trajectories to show the flow relative to the fronts, while in Fig. 4(b), the trajectories are shown relative to the earth.

From the geographical frame of reference in Fig. 4(b), it is evident that the moisture influx along trajectories W, X, and Y originated from the south to south-southwest of the lifting zone with the moist air moving toward the front in a relative sense at low levels and beginning to rise only as it was overtaken by the approaching frontal system. This trajectory pattern is very similar to that observed by Hobbs et al. (1975) who further showed how such an airflow can be disrupted as it moves over a north-south oriented mountain range.

4. SMALL MESOSCALE AREAS WITHIN RAINBANDS

The mesoscale rainbands in extratropical cyclones typically contain a pattern of small mesoscale (~ 10 km in horizontal dimension) and cumulus-scale (~ 1 km in horizontal dimension) cores of heavy rainfall (Austin and Houze, 1972). Figure 5 shows the track of a typical small mesoscale area which was located in band B_1. This small rain area passed over the University of Washington (UW) radar site during "period 2" of the (UW) raingauge trace seen in Fig. 6. It is seen that the rain during period 2 was generally enhanced and consisted of several peaks of heavy rainfall, each 1 to 3 min in duration, suggesting that the small mesoscale rain area contained cumulus-scale convection.

Figure 6 contains a time cross-section of vertically-pointing pulsed Doppler radar data showing the mean fall speeds of precipitation particles averaged over 3 min periods in band B_1. Since the radar data in Fig. 6 were averaged over 3 min periods, they probably do not fully resolve the embedded convection during period 2; however, the radar data for period 2 do show relatively short periods of enhanced fall speeds which were not present before or after period 2. This is especially notable above the melting layer, where the velocity field was uniform during period 1 but quite variable during period 2.

Serial rawinsonde data collected during the passage of band B_1 showed that the air between 4 and 5 km altitude was potentially unstable and was being brought to saturation by the lifting over the warm front portrayed in Fig. 3. The instability released in the 4-5 km layer aloft apparently accounted for the convective structure seen in the precipitation at lower levels during period 2 of Fig. 6.

5. CLOUD MICROSTRUCTURE ASSOCIATED WITH RAINBANDS

Weiss and Hobbs (1974) have shown that ice particle growth modes can be related to the vertical gradient of the mean particle fall speed. A small gradient ($\lesssim 10^{-4}$ s^{-1} in magnitude) is associated with growth by deposition from the vapor phase while larger gradients

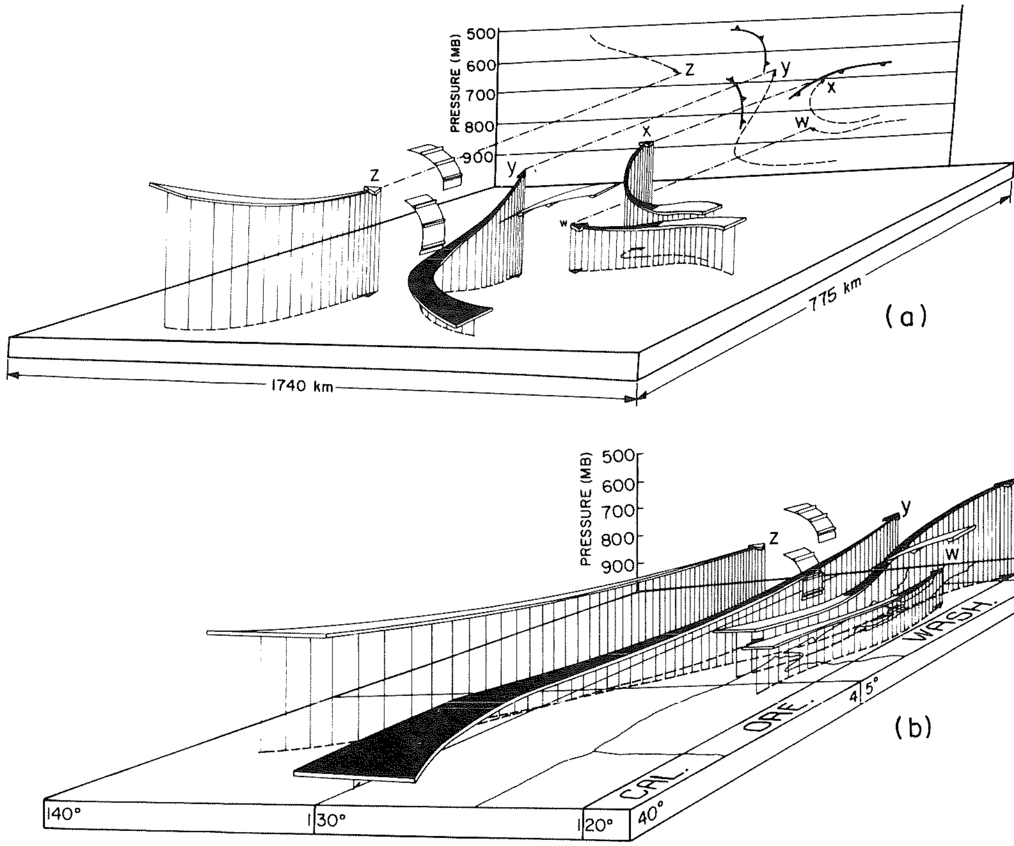

Fig. 4 Three-dimensional trajectories for frontal system of 20 December 1973. Trajectories are for a seven-hour period. In (a) trajectories are shown relative to fronts, while in (b) they are shown relative to the Earth. The background of (a) shows the two-dimensional projections of trajectories W, X, Y and Z in a format similar to that of Fig. 3. Upward moving portions of trajectories are shaded black.

are associated with growth by collection processes (either riming or aggregation). Applying these ideas to Fig. 6, we conclude that the region above about 2.8 km, which was characterized primarily by a very small vertical gradient of fall speed, was dominated by depositional growth. Just below 2.8 km, but above the top of the melting layer, the isotachs of fall speed in Fig. 6 are horizontally oriented and the larger vertical gradient of fall speed ($\sim 10^{-3}$ s^{-1}) indicates that the particles were growing by riming or aggregation in this region.

The cloud microstructure deduced from the Doppler radar was confirmed by direct aircraft sampling (Fig. 7). Ice particles were sampled aboard the University of Washington B-23 research aircraft which flew within the "collectional growth region" deduced from the Doppler radar (Fig. 6). Growth by collectional processes was indicated directly by Formvar and metal foil replication data which showed visual evidence of ice particle aggregation, and the in-cloud temperature, liquid water content, droplet sizes and ice particles sizes which appeared to be favorable for riming.

Ice concentrations measured on board the aircraft in rainbands B_3 and B_4 (Fig. 7) were in the range of 10-200 ℓ^{-1}. This value exceeds the active cloud nucleus concentration to be expected at a cloud top temperature of $-14°C$ (estimated from rawinsonde data) by a factor of $10^{1.5}$ to $10^{3.8}$, indicating that ice enhancement was probably occurring in the rainbands. The ice enhancement could have been produced by ice multiplication during riming, since the conditions at flight level were similar to those which Mossop (1976) observed to produce ice splinters in laboratory experiments.

6. CONCLUDING REMARKS

Morphological studies of rainfall patterns have shown that there are six types of mesoscale rainbands which tend to occur in extratropical cyclones. We have observed these six types of rainbands in extratropical storms in the Pacific Northwest, and comparison with studies of mid-latitude cyclones conducted in other parts of the world indicates that these rainband types occur rather generally in extratropical cyclones.

The dynamics and microphysics of the cloud systems producing the rainbands can be investigated effectively by making simultaneous and well-coordinated rawinsonde, radar, raingauge and aircraft measurements in cyclonic storms. Data collected in this way cover scales ranging from the synoptic scale down to cloud particle scales and permit an examination of both the physical framework within which the rainbands exist and the processes which are at work within them.

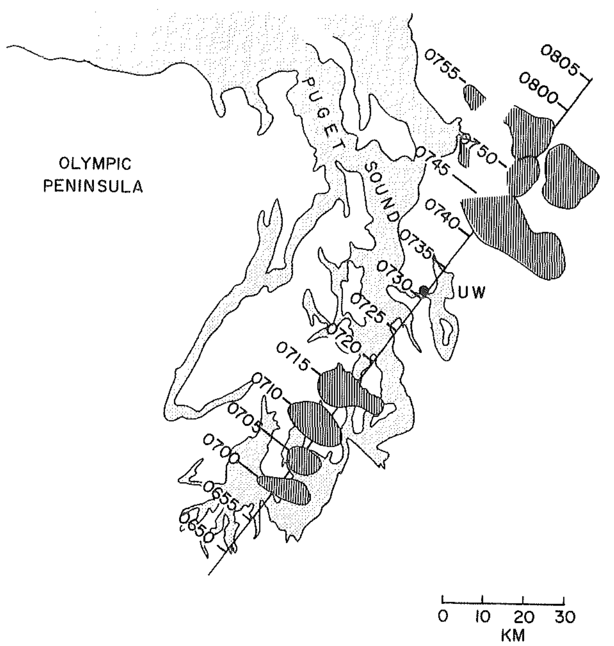

Fig. 5 Path of small mesoscale rain echo (darkest shading) seen on University of Washington (UW) radar PPI on 20 December 1973. Times of interpolated echo positions are shown in the immediate vicinity of UW where the rain echo was obscured by ground clutter echoes.

In a case study from the CYCLES PROJECT, air motions inferred from serial rawinsonde data showed that the rainbands in an occluded frontal system were supplied with moisture flowing into the rainband region from the south to south-southwest at low levels (below 800 mb). This air was swept abruptly upward in the rainbands just ahead of the cold air mass approaching from the west. A small mesoscale area of heavy rain within one of the rainbands in this storm was found to contain cells of cumulus-scale dimension which apparently resulted from the release of potential instability by lifting above the warm front. Vertically-pointing Doppler radar measurements indicated that as ice particles settled below the layer containing the convective cells, they grew first by vapor deposition and then, just above the melting layer, by riming or aggregation. Direct aircraft sampling of ice particles in the rainbands confirmed results inferred from the radar data. Aircraft measurements of ice particle concentrations indicated that ice enhancement was occurring in the clouds associated with the rainbands.

Case studies such as the one described here can be improved greatly by multi-level aircraft sampling in the rainbands. Particle growth modes deduced from radar data can then be checked more effectively by direct particle sampling than is possible with aircraft data from a single level. Weather radars can be used in real time to identify and

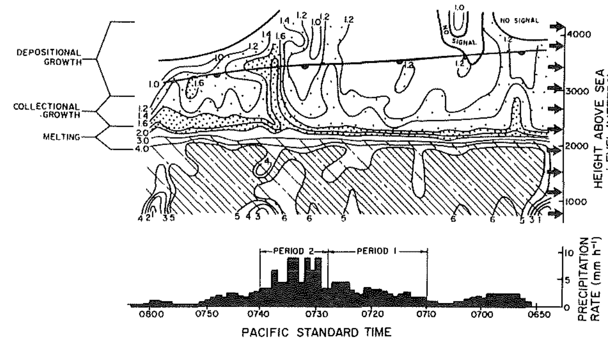

Fig. 6 Vertical cross section showing contours of three-minute average precipitation fall speeds (m s^{-1}) measured with Doppler radar during the passage of rainband B_1. High resolution rai rainfall trace obtained at the radar site is also shown.

monitor the rainbands and direct the research aircraft into different levels in the bands. Studies of this type are now underway as part of the CYCLES PROJECT.

ACKNOWLEDGMENT

This research was supported by the Atmospheric Research Section (Meteorology Program) of the National Science Foundation (Grant ATM74-14726-A02) and by Contract No. F19 628-74-C-0066 from Air Force Cambridge Research Laboratories.

REFERENCES

Austin, P.M. and R.A. Houze, Jr., 1972: Analysis of the structure of precipitation patterns in New England. J. Appl. Meteor., 11, 926-935.

Browning, K.A., 1974: Mesoscale structure of rain systems in the British Isles. J. Meteor. Soc. Japan, 50, 314-327.

________, and T.W. Harrold, 1969: Air motion and precipitation growth in a wave depression. Quart. J. Roy. Meteor. Soc., 95, 288-309.

________, and C.W. Pardoe, 1973: Structure of low level jet streams ahead of mid-latitude cold fronts. Quart. J. Roy. Meteor. Soc., 99, 619-638.

________, M.E. Hardman, T.W. Harrold, and C.W. Pardoe, 1973: The structure of rainbands within a mid-latitude depression. Quart. J. Roy. Meteor. Soc., 99, 215-231.

Elliott, R.D., and E.L. Hovind, 1965: Heat, water and vorticity balance in frontal zones. J. Appl. Meteor., 4, 196-211.

Harrold, T.W., 1973: Mechanisms influencing the distribution of precipitation within baroclinic disturbances. Quart. J. Roy. Meteor. Soc., 99, 232-251.

________, and P.M. Austin, 1974: The structure of precipitation systems - a review. J. de Rech. Atmosph., 8, 41-57.

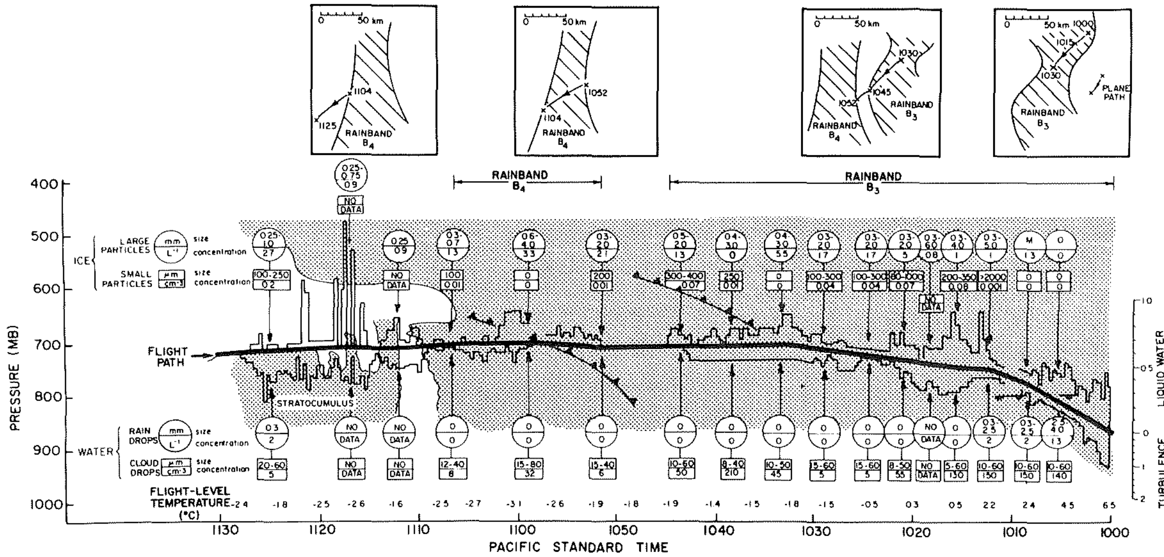

Fig. 7 Vertical cross sections showing aircraft measurements obtained in clouds associated with rainbands B_3 and B_4. The inset drawings show plan views of the aircraft's flight path in relation to rainbands. In the vertical cross section, shaded areas indicate cloudy regions. The origins of the turbulence and liquid water content plots are centered on the flight path line. Whereas, turbulence and liquid water content were measured continually during the flight, ice particle and drop sizes and concentrations (indicated in circles and boxes) were determined only at discrete intervals by replication sampling. The letter M indicates particles were melting and therefore could not be accurately sized.

Hobbs, P.V., R.A. Houze, Jr., and T.J. Matejka, 1975: The dynamical and microphysical structure of an occluded frontal system and its modification by orography. J. Atmos. Sci., 32, 1542-1562.

Kessler, E., and R. Wexler, 1960: Observations of a cold front, 1 October 1958. Bull. Amer. Meteor. Soc., 41, 253-257,

Kreitzberg, C.W., and H.A. Brown, 1970: Mesoscale weather systems within an occlusion. J. Appl. Meteor., 9, 417-432.

Matsumoto, S., K. Ninomiya, and T. Akiyama, 1967: A synoptic and dynamic study on the three-dimensional structure of mesoscale disturbances observed in the vicinity of a cold vortex center. J. Met. Soc. Japan, 45, 64-81.

Mossop, S.C., 1976: Production of secondary ice particles during the growth of graupel by riming. Quart. J. Roy. Meteor. Soc., 102, 45-56.

Nagle, R.E., and S.M. Serebreny, 1962: Radar precipitation echo and satellite observations of a maritime cyclone. J. Appl. Meteor., 1, 279-295.

Nozumi, Y., and H. Arakawa, 1968: Prefrontal rainbands located in the warm sector of subtropical cyclones over the ocean. J. Geophys. Res., 78, 487-492.

Reed, R.W., 1972: Characteristics and development of mesoscale precipitation areas in extratropical cyclones. S.M. Thesis, Dept. of Meteorology, Massachusetts Institute of Technology, 94 pp.

Weiss, R.R., and P.V. Hobbs, 1975: The use of a vertically pointing pulsed Doppler radar in cloud physics and weather modification studies. J. Appl. Meteor., 14, 222-231.

6.2.2 A CLOUD STRUCTURE AND THE RAIN EFFICIENCY AS OBSERVED BY RADARS AND RAINDROP RECORDER

MIYUKI FUJIWARA

METEOROLOGICAL RESEARCH INSTITUTE
TOKYO, JAPAN

1. INTRODUCTION

The Owase area is famous in Japan of heavy rains. Owase weather station recorded annual rain over 6,000 mm in maximum and 4,100 mm in average for past 32 years. In 1968, rain fell 1,434 mm for 2 and a half days. Nevertheless, it has been pointed out that a 5.7-cm weather radar 142 km far from Owase often misses the heaviness of the local rain. This suggests either the height of the raincloud is low, say below 2 km, or the raindrop spectra have special characteristics. Therefore, Japanese cloud physicists have been interested in the rain mechanism (i.e., Isono et al. 1970, Takeda 1974, Yanagisawa 1974). This heavy rain occurs very frequently within a small area of diameter 20-30 km under orographic condition with upper trough and easterly surface wind.

The present field investigation was planned to give an interpretation of the cloud structure capable of heavy rainfall. The instruments used were two X-band radars, one vertically pointing Doppler and one short range search type, one conventional PPI Weather radar and ground raindrop recorders and raingauges. The present paper describes a case study on a rainshower, though not the typical heaviest one.

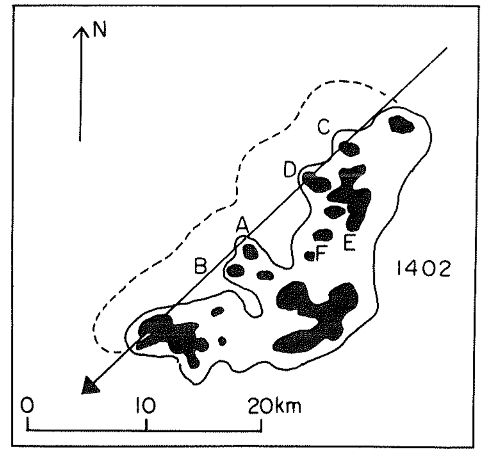

Fig. 2

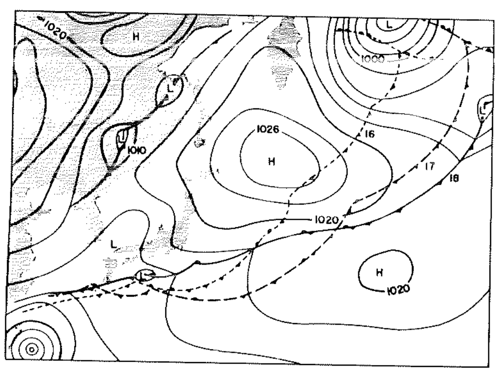

Fig. 1

2. WEATHER SYSTEM

A quasi-stationary front was moving slowly eastwards as shown in Fig. 1, along which considerably heavy showers developed around the Kii-peninsula of Japanese main land Honshu. While the frontal wave crest travelled eastwards, the shower system revealed by Nagoya PPI radar, moved northwestwards with 30 km/hr as shown in Fig. 2; the marginal contour corresponds to 1 mm/hr. Due to the mountain obstacle only the beam at height 1.5-4.7 km was responsible for the PPI observation. Shown by black dots are core echoes stronger than 4.0 mm/hr. Comparing these cores with the field radar data at the spot, it was found that they correspond to precipitation towers illustrated in Fig. 3.

Fig. 3

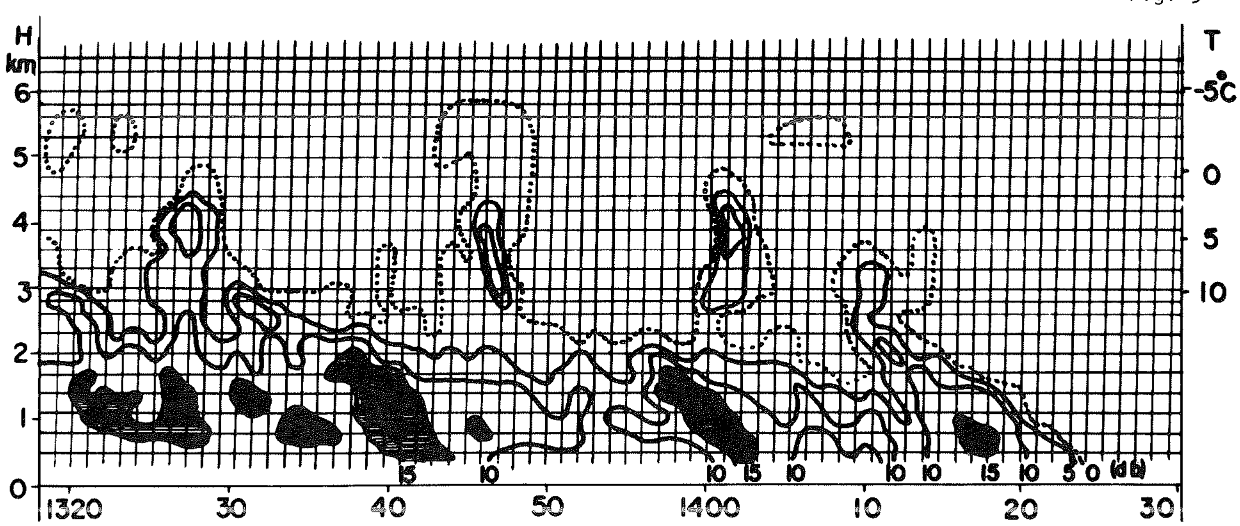

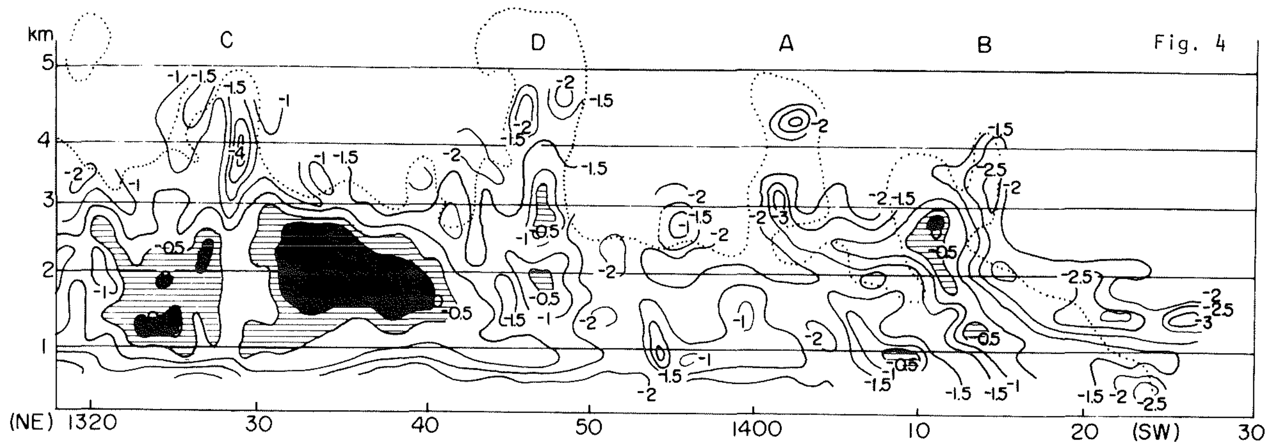

Fig. 4

3. THE SHOWER SYSTEM

Doppler radar with vertical fixed anntena obtained vertical corss section as given in Fig. 3 along the long arrow shown in Fig. 2. Z-pattern, without attenuation correction, exhibits 4 cumulus towers, say C, D, A, and B, with intervals about 10, 7.5, and 5 km. It is noticed that towers are sticking up vertically above 3 km level, with some implication of strong vertical exchange of momentum. Towers C, D, and A do not match well with top of core streaks underneath, but B does. From the nearby sounding data and absence of bright band it is inferred that glaciation was not predominantly associated with this considerable amount of rainfall rate 22 mm/hr in the maximum.

The corresponding cross section of vertical air velocity in cloud is shown in Fig. 4, where Rogers(1964) equation $V_T = 4.0\ Z^{1/14}$ was assumed. Downdraft (shaded area) developed at the heavy Z-streak except one at about 1400. The tower C, D, A, and B involved active updraft cores of 2-4 m/s, Eventually tower B, which has continuous Z ridge from ground to the tower, reveals an evidence that updraft roots reach near ground, that is, towers are not "elevated convections (Douglas et al. 1975)" but protrusions of cumulus convections.

4. UNIT SHOWER CUMULUS

In order to clarify the structure of this meso-scale shower system a kinematical model of the elementary cumulus was built as shown in Fig. 5 in a model picture style. Successive release of buoyant bubbles at a point which travels with the surface wind was assumed for the formation of the updraft street (to be 2.0 m/s in average). Likewise, successive precipitation with average fall speed 2.5-5.0 m/s depending upon the drop size was assumed to be released at the upper part of the cumulus tower. Both the geometries of the updraft street and precipitation streak are obtained by vector sum of vertical movement and a difference of two vectors of horizontal wind and movement of the generating point. Thus, updrafts set up at SSE end, relative to the cloud, turn to W with elevation, and enter the tower center from its N-side. Precipitation falls from the tower turning to NW, to the ground at far W of the cloud, with growth by cloud accretion.

Fig. 5

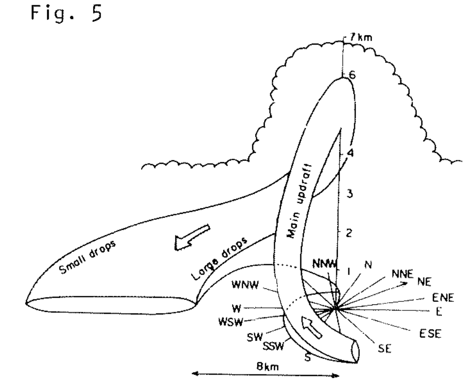

5. STRUCTURE OF THE SHOWER AS CUMULUS COMPLEX

Our search-type short range radar scans VPI mode, vertical cross section changing its azimuth in a rate 360° for 3 min. In Fig. 6a, part of the shower system shown in Fig. 2 is illustrated schematically so composed of cumuli D, A, B, etc. with their individual precipitation spreads. Relative movement of the radar to the system is indicated by arrow SS'. Photo-number represents the frame number in Fig. 6b from top to bottom. In Fig. 6b, 5-vertical cross sections of the VPI video are shown with range markers for every 2 km. The first frame taken at 1352 exhibits two towers, D and A. In between of them streaks probably form towers E and F are seen with slight slit. The second frame 1353 exhibits no tower but only streaks with gentle declination. The third one, 1400, shows a remarkable gap between streaks, probably from tower F, and the shoulder part of cumulus A. In the fourth, 1401, tower A with the upper part of the curving streak appears above F's streak. The tail of A's streak appears again, though faintly, near the left end of the frame. In the last frame, 1401, tower A with its streak is exhibited.

Fig. 6a

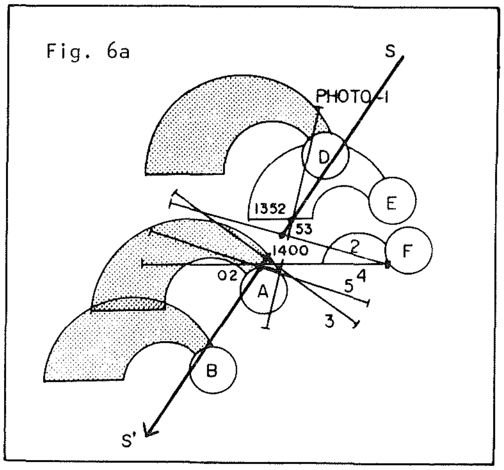

Fig. 6b

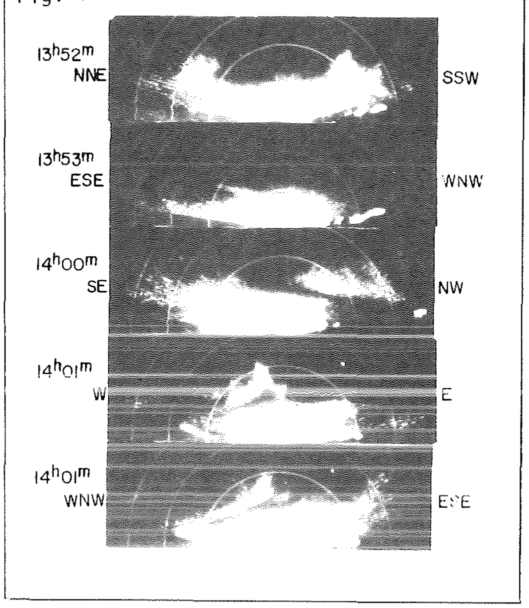

Fig. 7

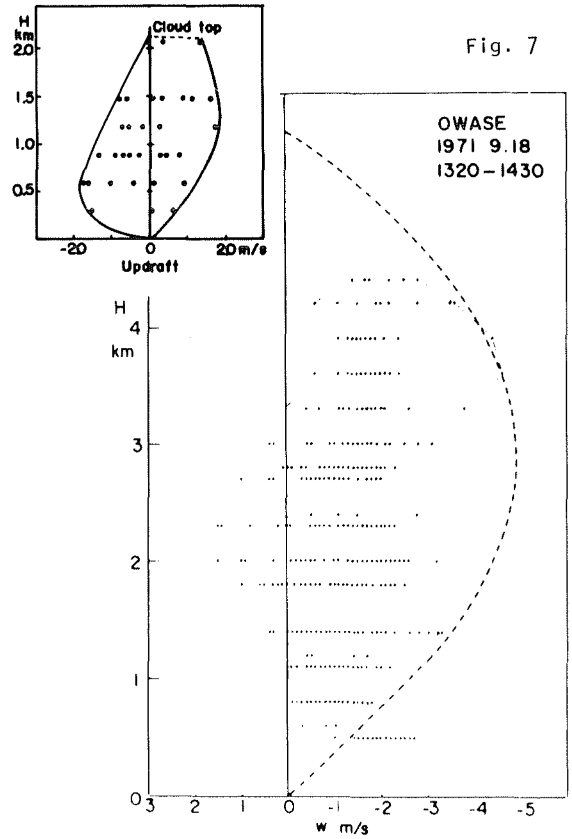

It is very striking that logical coincidence of four radar patterns given in Figs. 2, 3, 4 and 6b seem to increase with the kinematical models as carefully as inspected. Therefore, it is assumed that the structure of shower system with shallow convective rainclouds under a vertical wind shear condition can be modeled in good approximation by kinematical consideration alone.

6. VERTICAL CURRENTS IN THE SHOWER SYSTEM

Although the shower echo structure is constructed with the unit circulations, as given in Fig. 5, it is noticed that the compensating downdraft much less than updraft in between of the cumuli (see Fig. 4). Plotted in Fig. 7 are the data showing the distribution of vertical air currents in the shower system. It is noticed that the average current is of updraft sense very remarkably, and even has a maximum mode about 2 km. (Another mode at the top is of the towering cloud.) For a reference, similar plots, for a snow shower developed under inversion are shown in a suffix of the Figure in which a fairly good balance of up- and down-draft is seen.

It is reported in the sequence of the observation that low level cumuli group generated just out side of the Bay moves into the Bay under the very similar wind situation. Therefore, it is concluded that the present rainshower system had ralatively dense lower cloud as an orographic modification of the assemble of the towering cumuli.

7. R-Dm RELATIONSHIPS AS RAIN EFFICIENCY INDICIES

In Fig. 8, emprical relationship between the biggest drop size sampled from about 1 m^3 spatial volume and the rainfall intensity calculated from the drop data. Regardless of considerable scatteredness, the medium curve will show the efficiency of rainfall rate due to the optimum raindrop growth. It is shown that when the drop diameter, Dm to which the most favorable growth can achive reaches 3 or 5 mm, the instantaneous rainfall rate is expected empirically to be as much as 50 or 100 mm/hr, respectively, in the Owase rain.

This Dm depends not only upon the drop specturm but also sampling volume. The statistically significant cut-off concentration was determined empirically for the biggest drop to be 0.008 in no./litre 0.2 mm. Utilizing this value, a theoretical R-Dm relationships for the exponential size distribution, $N_D = N_0 \exp(-\lambda D)$, are drawn in Fig. 9. Curves for λ = const., pattern A, is much steeper than those of N = const., pattern B. Although other analogous curves can be given by assuming the spectrum equation, these two patterns A and B are regarded as elementary but basic patterns. It is noticed that as R grows

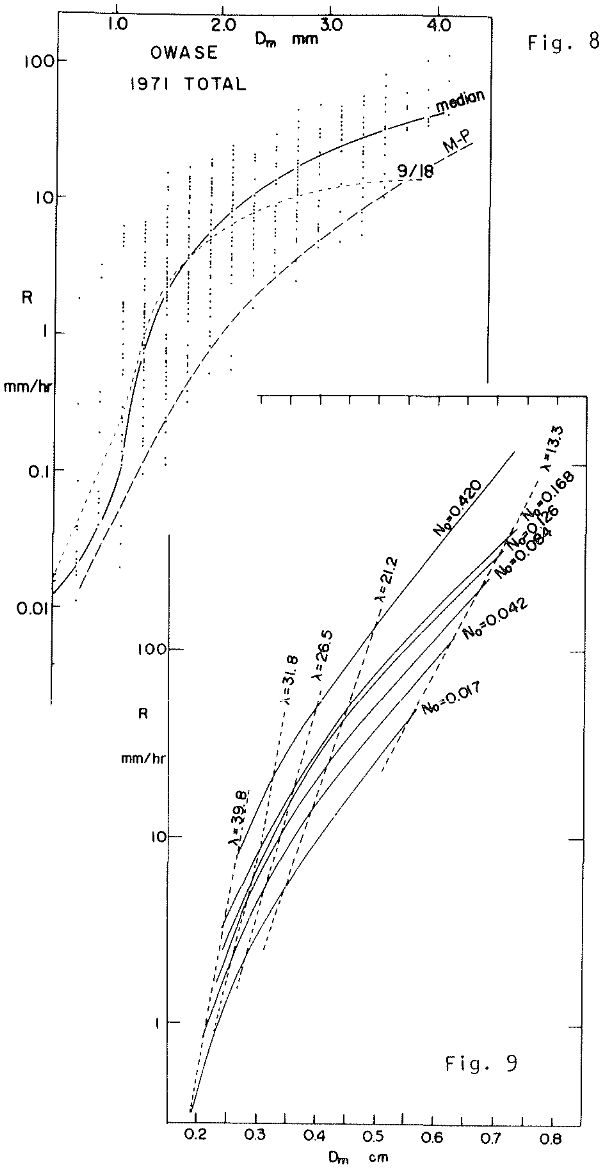

Fig. 8

Fig. 9

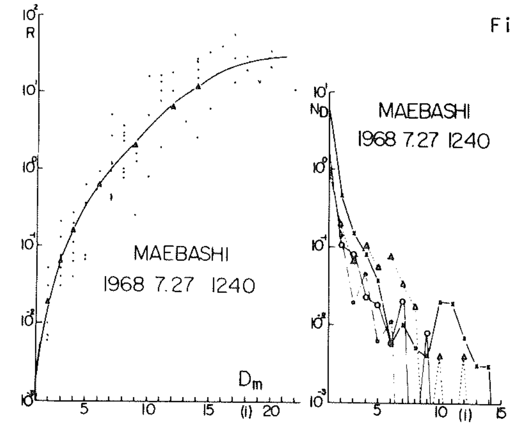

Fig. 10a

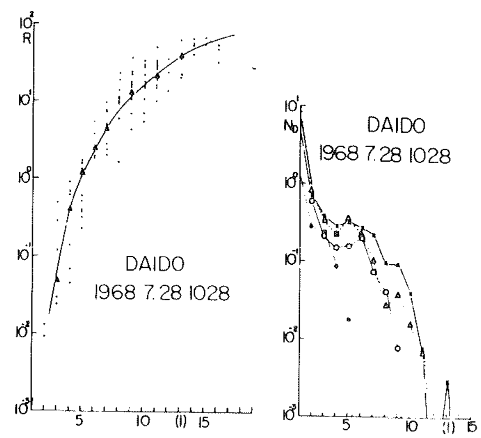

Fig. 10b

the former pattern A turns to the pattern B, (i.e., Fujiwara 1976) and this change concerns the rainfall efficiency. In Fig. 11, two examples of the R-Dm curve are shown; a), thunderstorm, and b), orographic warm rain. The latter shows to have had much more efficient rainfall (curve is steeper) than the case of thunderstorm.

8. N_D-CURVE DEVELOPED BY CLOUD ACCRETION

An application of the R-Dm characteristics to the present case is made as shown in Fig. 11. Five N_D-families, a, b, c, and e are shown from the data a, b, c, d and e indicated in the key Figure (lower right corner), respectively. It is found that, in the family a, rainfall increase is achieved by that of curve height, whereas in C, in which Dm is relatively large, by that of spectrum width. These two growths correspond to the pattern A and B, respectively, as defined above. The family b is of characteristic in between of those a and c.

As shown in Fig. 11c, the typical B-pattern growth of raindrops, that is the spectrum width develops without appreciable increase in the concentration, gives the N_D curves defined as trapezoidal (Fig. 12a) for simplicity. Such type is frequently associated with active rainshowers in subtropical maritime airmass condition (Shiotsuki 1974). In Fig. 11, the equivalent value of Nc in a), thunderstorm case, is read as an order of 10^2 whereas in b), orographic warm rain, about 0.3. It is noticed by a simple culculus of raindrop growth through cloud accretion that the N_D curve develops in a form of quasi-trapezoidal pattern as follows.

$$\partial N_D/\partial h = -\partial[N_D \cdot \tilde{D}]/\partial D,$$

where N_D is the spatial concentration of raindrop, and $\tilde{D}$, continuous growth rate of drop with fall depth by cloud accretion. That is, $\tilde{D} = k \cdot L \cdot h$, where L is cloud water content and k, collection efficiency. Then the solution is

$$N_D = F(x),\ X = D - Dc,\ Dc \equiv k \cdot L \cdot h,$$

where F is given by the initial form of N_D. In other words, among the raindrop growth processes, cloud accretion is only one that shift the N_D value to larger size, resulting in the formation of the trapezoidal curve.

9. RAIN MECHANISM PREDOMINANTLY WORKING IN THE OROGRAPHIC HEAVY RAINFALL

It is concluded, from the analyses so far that the high efficiency of the rainfall in Owase area is attributed to the above two ways well combined with, one is high concentration of

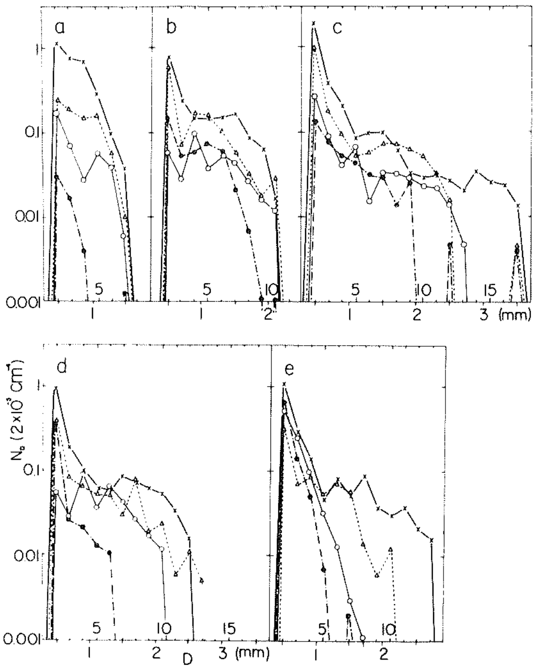

Fig. 11

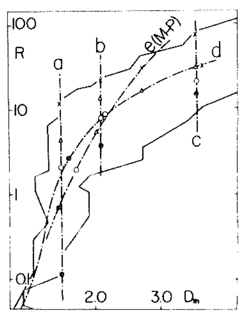

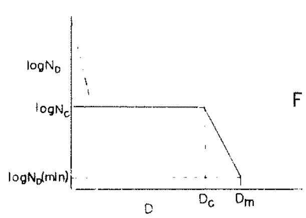

Fig. 12a

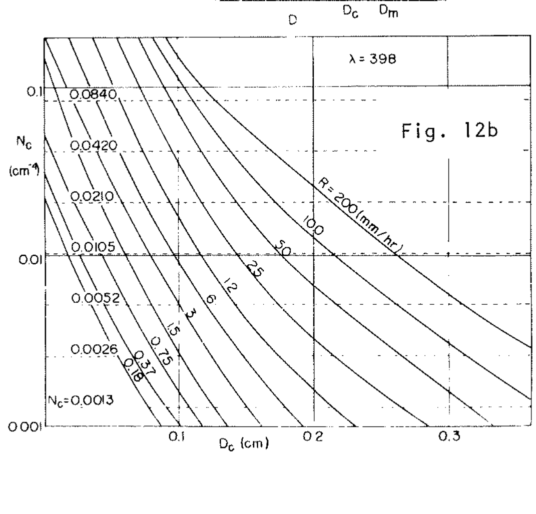

Fig. 12b

initial precipitable drops in the A-pattern, probably chimney-like updraft which brings the precipitable drops of the high concentration, Nc, to the towering cloud top, then seeds over the lower cloud. Nc will increase theoretically proportionally with cloud water contents (Berry 1974) to be released in the chimney. The Nc is estimated as high as 0.1 cm^{-4}. It was also found from the Doppler radar and raindrop recorder that the lower cloud often occurs over the Owase Bay with drizzle rain of high concentration and weak updraft. The other way is the succeeding stage of this. Raindrops develop by accretion resulting into the trapezoidal N_D pattern.

10. POSSIBILITY OF THE HEAVY RAINS BY THIS MECHANISM

With the above model, calculation was made for the growth of rainfall intensity as shown in Figs. 12b and 13. The equations used are simplified employing Spilhaus' equation for V_T,

$$dh/dV_T = (k/L)(W-V_T),$$

$$N_D = Nc\cdot\exp\{-\lambda(D-Dc)\},$$

$$Dm = Dc + 2.30/\lambda\log(Nc/N_{Dmin}),$$

$$N_{Dmin} = 0.34\times10^{-3}\ cm^{-4},$$

$$\lambda = 39.8,$$

$$W = W_{max} - W_{max}/h_m^2(h_m-h)^2,$$

where V_T is the terminal velocity of drop. In the Figure, relationship between the maximum raindrop size and the cloud parameters, cloud water content and updraft parameter (Wmax) of the lower cloud. Ordinates show Wmax and abscissas, cloud water content, L. It is shown that if the initial height of the 100-micron raindrops is low enough (i.e., 500 m) the final drop size attained at the ground does not much differ with L. It is also found if the cloud contains updraft weaker than 4 m/s on an average, and accordingly they will not be responsible for the behavier rainfall than 50 mm/hr, whereas the raindrops precipitated in seeding manner over the cloud top will easily grow to 3 mm in diameter. This is responsible for 50 mm/hr according to Fig. 12b with the probable Nc value.

11. CONCLUSIVE REMARKS

Often the importance of cloud physics in the mechanism of disastrous heavy rainfall is asked. In the present case, the particular cloud system was found to relate with the heavy rain under the orographic influence, and the cloud tectology may principally be interpreted by dynamics of the proper scale. The present cloud system was allotted with two major roles seperately, generation of the initial raindrops of high concentration, Nc, and their accretion growth. Parameters involved in the both processes relate closely to the resulting rainfall rate. However, physics of the former process, which is generation of high Nc, probably under the strong influence of the rate of moisture supply and diffusion, is actually insatisfactory for parameterization. From the empirical analyses of the raindrop spectrum, it is

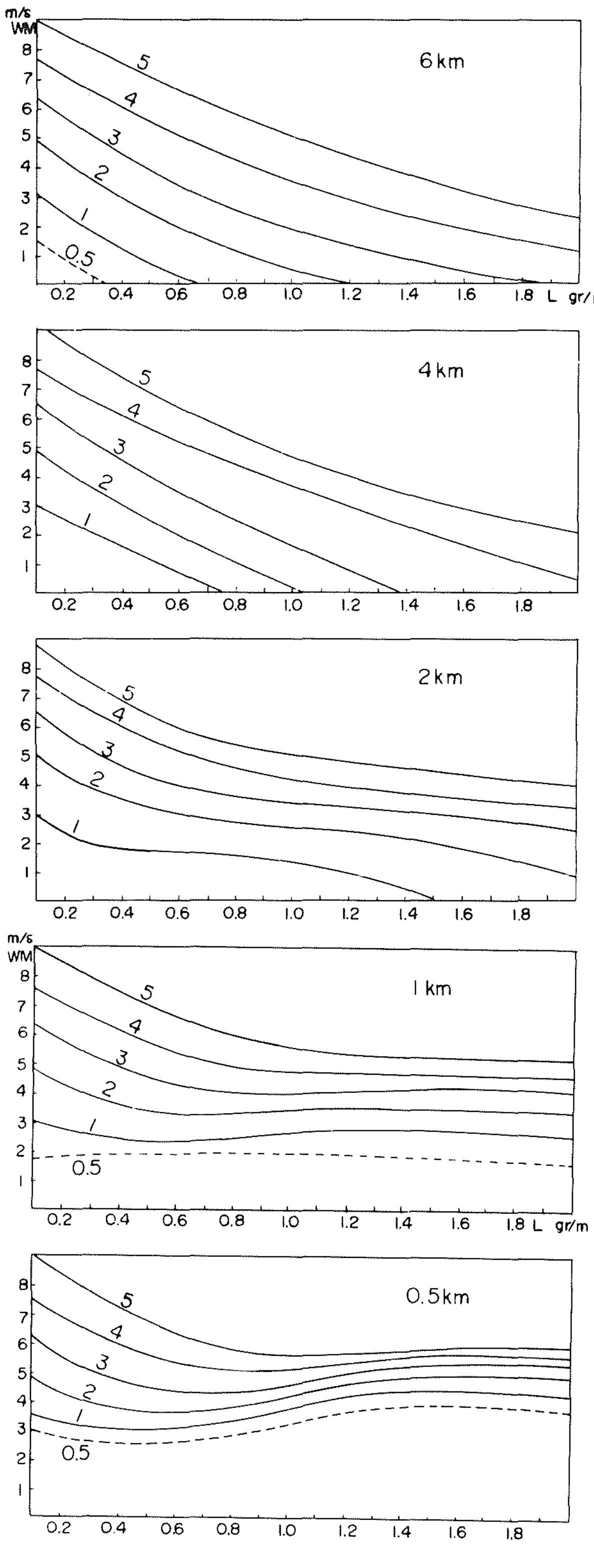

Fig. 13

noticed Nc varies over one decimal order of magnitudes. This is also essential subject of cloud physics.

Fig. 12a: Evaluation of the rainfall rate achieved by the trapezoidal development of log N_D-D spectrum of raindrops.

a) The trapezoid assumed for the calculation. For D<Dc, N_D=Nc; and for D>Dc, N_D= Nc $\exp\{-\lambda(D-Dc)\}$. Also it was assumed, after the test shown by Fig. 11, that $N_{Dmin.}=0.34\times10^{-3}cm^{-4}$.

b) From the diagram it is shown that when the maximum drop diameter Dm increases from 1.8 mm, by about 2.8 mm, the rainfall rate increases from 25 mm/hr to 100 mm/hr, for Nc=0.004 (cm^{-4}), or from 12 mm/hr to 60 mm/hr for Nc=0.002 (cm^{-4}). This range of Nc, from 0.002 to 0.004 (cm^{-4}), was found to be probable in the Owase shower.

12. REFERENCES

Berry, Z. E., 1974: An analysis of cloud drop growth by collection: Part IV. A new parameterization, J. Atmos. Sci., 31, 2127-2128.

Douglas, R.H., K.L.S. Gunn and J.S. Marshall, 1957: Pattern in the vertical snow generation. J. Met., 14, 95-114.

Fujiwara, M., 1967: Raindrop size distribution in warm rain as measured in Hawaii. Tellus, 19, 392-402.

Isono, K., Komabayashi, M., and T. Takahashi, 1964: Study on the heavy rain mechanism of Ohdaigahara and Owase area (I), Report of Basic Study on Local Characteristics of Disaster (in Japanese) 46-49.

Rogers, R.R., 1964: An extension of the Z-R relation for Doppler radar. Proc. 11th Weath. Rad. Conf., 158-161.

Shiotsuki, Y., 1974: On the flat size distribution of drops from convective rainclouds. J. Met. Soc. Japan, 52, 42-60.

Takeda, T., 1974: Characteristic and microphysical process of the concentrated heavy local rainfall. Kishokenkyu-Note, No. 120, 81-95 (in Japanese).

COORDINATED DOPPLER RADAR AND AIRCRAFT OBSERVATIONS OF RIMING AND DROP BREAKUP IN STRATIFORM PRECIPITATION

Richard E. Passarelli, Jr.

University of Chicago
Chicago, Illinois

1. INTRODUCTION

The University of Chicago Laboratories for Cloud Physics and Atmospheric Probing, and the Illinois State Water Survey are conducting coordinated aircraft and Doppler radar experiments to investigate the microphysics of particle growth in winter cyclones in the central United States. The primary goals of these experiments are to develop a detailed, quantitative picture of the microphysical structure and to determine the mechanisms and rates of growth of hydrometeors at different levels and regions of Midwest winter cyclones.

The microphysics of particle growth in the vicinity of the melting layer are an important aspect of winter precipitation since most winter rain in the Midwest is from melted snow. This paper reports aircraft and radar observations of riming growth and drop breakup during the stratiform rain situation of 22 February 1975 at Champaign, Illinois.

2. INSTRUMENTATION

The aircraft used in these experiments was a Lockheed Lodestar leased by the University of Chicago Cloud Physics Laboratory. It is equipped to measure a variety of microphysical parameters. An optical array precipitation spectrometer (Knollenberg, 1970) is used to count and size precipitation particles into 15 equally spaced, 300 μm size categories ranging from 300 to 4500 μm. Cloud and precipitation particles are collected by a continuous Formvar replicator (Spyers-Duran and Braham, 1967) equipped with a deceleration tube to minimize the problem of particle breakup. The primary temperature sensor is a platinum resistance element mounted in a reverse-flow housing. A number of other sensors are also carried, but these are not of primary importance in this study.

The radar used in these experiments is a dual wavelength pulsed radar, 10 and 3 cm, equipped with Doppler processing for the 10 cm band. It is owned by the University of Chicago and the Illinois State Water Survey and operated by the latter. The pulse duration gives 150 m range resolution. The 10 cm Doppler spectra were taken over 512 pulses (512 milliseconds) which gives 10 cm/s velocity resolution. The 32 range gates were set 150 meters apart for maximum range resolution. The data were Fourier analyzed by an on-line CDC processor and stored on magnetic tape.

3. DATA

The stratiform rain which occurred at Champaign, Illinois on 22 February 1975 was associated with overrunning from a weak low to the southwest. The aircraft made passes over the radar at 2.8, 2.2, 1.6, 1.0, and 0.5 km agl while the radar collected vertical incidence data (antenna pointing vertically).

Fig. 1 shows the temperature sounding taken by the aircraft during the steady ascent to 2.8 km agl. Above 2.8 km

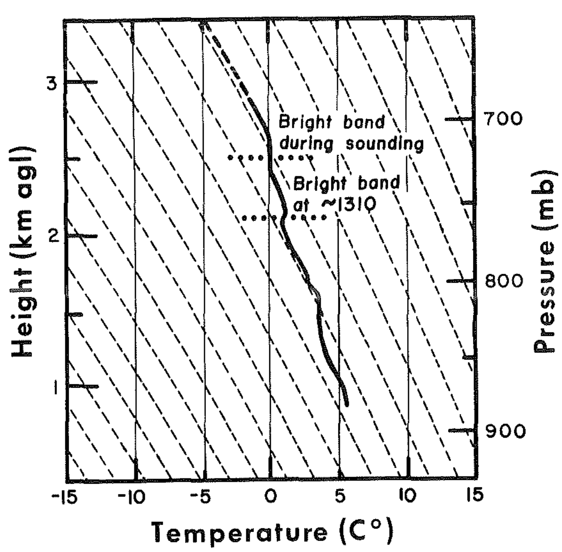

Figure 1. Temperature sounding taken by aircraft. Moist adiabats are dashed. Position of the bright band at the time of the sounding and 30 minutes later is indicated by the dotted lines.

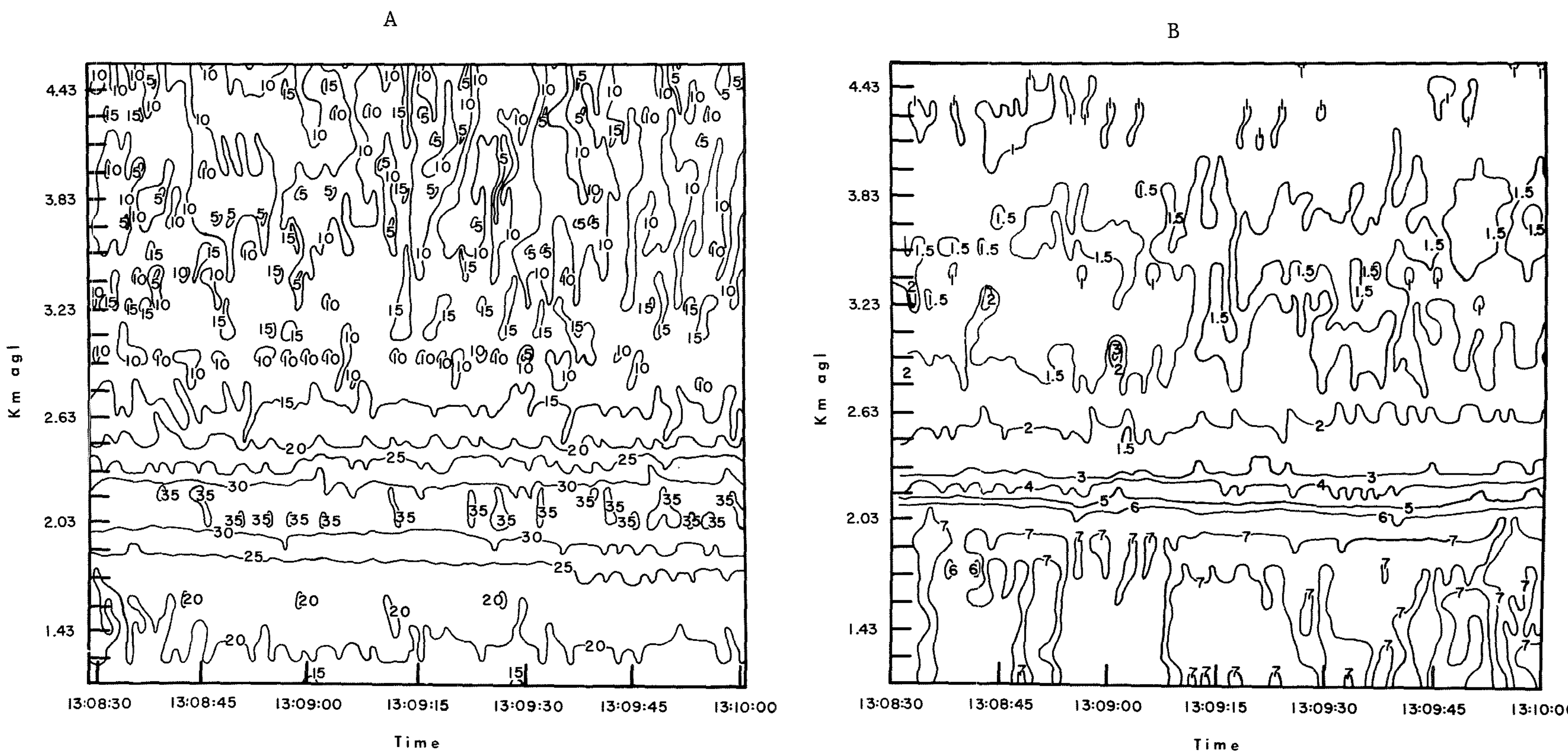

Figure 2. Time-height cross-sections of a)equivalent reflectivity factor in db (mm^6/m^3) and b)mean downward Doppler velocity in m/s.

the 12Z Peoria sounding showed that the atmosphere was moist adiabatic. Between 2.4 and 2.6 km agl is a 0C isothermal layer which is probably due to cooling caused by melting snow (Findeisen, 1940).

The particle replicas which were collected by the aircraft at 2.8 km (above the melting layer) showed a variety of crystal types such as simple plates, needles, and aggregates of plates and needles. However, the most frequently observed large particles were heavily rimed ice crystals and graupel. The particle spectra taken at 2.8 km showed that the concentration of particles greatter than 1 mm in diameter was about 10^{-4} cm^{-3}.

Figure 2 shows time-height cross-sections of vertical incidence mean Doppler velocity and equivalent reflectivity factor. The cross-sections were taken about 30 minutes after the aircraft's 2.8 km pass over the radar. The equivalent reflectivity factor increased from about 7 dBZ_E (mm^6/m^3) at the top of the cross-section to 35 in the bright band, and then fell off to 22 in the region of rain below the bright band.

The bright band dropped 450 m between the time of the aircraft temperature sounding and time of the cross-sections shown in Fig. 2. The two bright band positions are indicated on the temperature sounding of Fig. 1. Calculations by Atlas, et al (1969) show that such a drop in the bright band can be attributed to melting-induced cooling.

The velocity cross-section shows that above the bright band, velocities in excess of 1.5 m/s were common, which is consistent with the aircraft observations of heavily rimed particles. The horizontal uniformity of the velocity contours at the bright band indicates that the vertical air motions in this region were weak. Another important feature of this cross-section is the velocity maximum immediately below the bright band. At the base of this velocity maximum, the Z_E values decrease which suggests that drop breakup was occurring.

4. DISCUSSION

4.1 Riming Growth

Vertical incidence Doppler (VID) spectra contain information on the size distribution of the scatterers. Unfortunately, the standard deviation of the observed Doppler spectra in the snow aloft was typically 20 cm/s. Since the velocity resolution of the CHILL Radar is 10 cm/s, the Doppler spectra are essentially monodispersed so that the radar cannot accurately resolve the particle size distribution.

By considering that the scatterers are monodispersed and falling at the mean Doppler velocity, little information is lost and some important properties of precipitation growth such as particle mass, type, and concentration, dominant growth mechanism and cloud liquid water content can be estimated. The particle mass, M, may be estimated from a mass - fallspeed relation, i.e.,

$$V = aM^b \tag{1}$$

where V is the fallspeed and a and b are constants. The reflectivity factor, Z, assuming Rayleigh scattering, is by definition

$$Z = N\left[\frac{6M}{\pi\rho}\right]^2 \tag{2}$$

where N is the particle concentration and ρ is the density of water. Using Eqs. 1 and 2, the particle concentration is simply

$$N = \frac{ZV^{-2/b}\pi^2\rho^2a^{2/b}}{36} \; . \tag{3}$$

Thus, if the appropriate fallspeed-mass relation were known, the mass and concentration for the monodispersed distribution could be calculated at different heights, and particle growth rates could be estimated.

Whether riming or aggregation growth is dominant in a layer may be determined in steady precipitation by examining the reflectivities and fallspeeds at the layer boundaries. The ratio of the reflectivity factors at any two levels may be written as

$$\frac{Z_2}{Z_1} = \frac{N_2M_2^2}{N_1M_1^2} \; . \tag{4}$$

For steady state riming growth the particle flux through any level can be assumed constant.

$$NV = \text{constant.} \tag{5}$$

Combining Equations 1, 4, and 5, we find that the fallspeed-mass exponent may be estimated from measurable radar quantities

$$b = 2\left[\frac{\log\frac{Z_2}{Z_1}}{\log\frac{V_2}{V_1}} + 1\right]^{-1} \; . \tag{6}$$

Alternatively, if steady aggregation is the dominant particle growth mechanism, then, assuming that the mass flux, VMN, is constant

$$b = \left[\frac{\log \frac{Z_2}{Z_1}}{\log \frac{V_2}{V_1}} + 1 \right]^{-1} . \qquad (7)$$

Values of b have been tabulated (e.g. Locatelli and Hobbs, 1973) for different particle types. Thus if the particle type is known, the dominant growth mechanism may be deduced from vertical incidence radar data. Conversely, if the dominant growth mechanism is known, the particle type can be determined. However, because it is possible to obtain reasonable values of b under either growth mechanism assumption, the method can be ambiguous.

The coefficient, a, in the mass-fallspeed relation, Equation 1, can be estimated by expressing the precipitation rate, R, as a function of V, Z, a, and b, and then solving for a:

$$a = \left\{ \frac{36R}{\rho^2 \pi^2 Z V^{1-1/b}} \right\}^b . \qquad (8)$$

For typical values of b, 0.05-0.30, a is not a strong function of the precipitation rate. For melting layer rain, the precipitation rate may be estimated from the region of rain below the bright band by means of a Z-R relation. This should be about the same rate as in the region immediately above the bright band.

It is unlikely that melting is occurring at 2.63 km agl, 0.5 km above the bright band. Thus the increase in fallspeed from 1.5 m/s at 3.53 km to 1.8 m/s at 2.63 km and the corresponding 10 dbZ increase in equivalent reflectivity factor suggest that particle growth is occurring in this layer. Assuming that aggregation growth is dominating, Eq. 7 yields b = 0.074, while for riming growth Eq. 6 yields b = 0.147 characteristic of rimed particles of the type collected by the aircraft. In view of this and the large fallspeeds, b = 0.147 is probably the better estimate. This supports the hypothesis that riming was the dominant growth mechanism in this layer.

To determine the amount of particle growth, it is necessary to estimate the coefficient a, in the fallspeed relation, Eq. 1. For the region of rain in Fig. 2, the Marshall-Palmer relation ($Z = 200R^{1.6}$) yields a rainfall rate of 1.00 mm/hr. Assuming that this precipitation rate is about the same as that immediately above the bright band, Eq. 8 yields a = 560 cgs units. The complete mass-fallspeed estimate is then

$$V = 560\ M^{0.147} \quad \text{(cgs units)} \qquad (9)$$

which is in good agreement with relations given by Locatelli and Hobbs for densely rimed particles.

Using Eq. 9, the particle mass at 3.53 km is 1.29×10^{-4} g, while at 2.63 the particle mass is 4.46×10^{-4} g. This corresponds to 3.17×10^{-4}g of mass accreted by a particle falling 0.9 km. For a particle density of 0.3 and unit collection efficiency, this requires a mean liquid water content of about 0.2 g/m^3 which is reasonable for stratiform clouds.

The particle concentrations estimated from Eq. 3 are 4.12×10^{-4} and 3.46×10^{-4} cm^{-3} respectively at the top and bottom of the riming growth layer. These are reasonable in light of the aircraft measurements of particle spectra at 2.8 km.

Thus the radar and aircraft data indicate that riming is the dominant growth mechanism in the layer which extends from 2.63-3.53 km agl. In view of the assumptions, the monodispersed model yields reasonable estimates for the fallspeed-mass relation, particle concentration, cloud liquid water content, and particle growth rate. The weak vertical airmotions indicated by the variations in the height of the 1.5 m/s contour in Fig. 2, may be generating liquid water for the observed riming growth.

4.2 Drop Breakup below the Bright Band

The velocity maximum below the bright band in Fig. 2, in conjunction with the 5dbZ drop in reflectivity below the velocity maximum, indicates that drop breakup is occurring after melting. The dropsizes affected by breakup can be better examined by converting Doppler spectra to mass-velocity spectra and plotting mass concentration in a velocity interval as a function of velocity. The first moment of this type of spectrum is the precipitation rate, and the zeroth moment is the precipitation water content. Fig. 3 shows five mass-velocity spectra taken at 1.88 km, within the velocity maximum, and five mass spectra taken at 1.58 km, 300m beneath the velocity maximum. The mass spectra were calculated from Doppler spectra assuming no updraft, Rayleigh scattering and that the drops were falling according to the fallspeed law

$$V = 1090\text{-}1164\exp(-6D) \qquad (10)$$

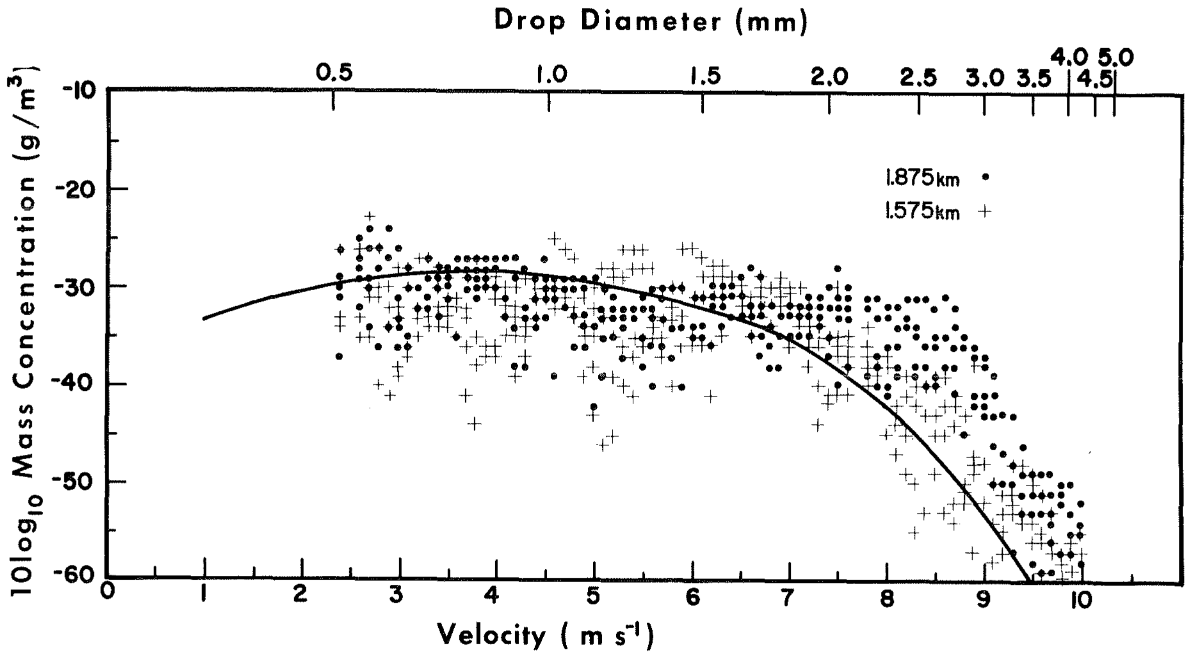

Figure 3. Mass-velocity spectra taken within and below the velocity maximum of Fig. 2.

from Atlas, et al, (1973). This fall-speed law fits the Gunn and Kinzer (1949) data to within 2% for the size range .06 < D < .60 cm and is easily manipulated. The corresponding Marshall-Palmer mass spectrum for 22 dbZ is also drawn in Fig. 3. This figure shows that within the velocity maximum there is considerably more mass in drop sizes greater than 2 mm than in the corresponding drop sizes in the region below. This, of course, means that the concentration of drops greater than 2 mm in diameter is larger within the velocity maximum than below it. The maximum discrepancy occurs at 8.5 m/s (2.6 mm).

Considering the laboratory and theoretical work of Brazier-Smith, et al, (1973) and McTaggart-Cowan and List (1975) it is unlikely that a sufficient number of drop collisions capable of causing breakup could have occurred over a depth of 300 m. The work of Komabayasi, et al (1964) indicates that spontaneous disintegration is unlikely for drops less than about 5 mm in diameter. Thus our current knowledge of spontaneous disintegration and collision-induced breakup cannot explain the observed Doppler spectra.

It is possible that the assumption of complete melting in the high velocity zone is incorrect. If melting were not complete for the largest particles then they may not have achieved the equivalent dropsize terminal velocity. This would lead to undersizing of drops in Fig. 3 and overestimation of the mass concentration in the large drop sizes. Thus it is possible that some of the drops which are sized as 2.6 mm are in reality larger, partially melted particles. These particles could be large enough to disintegrate spontaneously or with a small perturbation (turbulence, small drop collision) after melting is complete. What appears at first glance to be breakup of many medium size drops (2.6 mm) could actually be the breakup of a few very large (> 5 mm) drops. Laboratory studies of the effect of drop collisions on very large metastable drops are difficult to perform due to the transient nature of these drops.

Calculations by Ekpenyong and Srivastava (1970) show that a 5 mm melted diameter snowflake would be about 90% melted after falling 450 m below the 0C isotherm in an atmosphere with lapse rate 6C/km. The aircraft collected replicas of partially melted particles 300 m below the bright band. Thus it is likely that the largest particles were not completely melted in the region of the velocity maximum. The internal ice structure could serve to stabilize large drops which would otherwise disrupt either spontaneously or by means of a small perturbation.

5. SUMMARY

Coordinated Doppler radar and aircraft observations provide a unique look at particle growth processes in the vicinity of the melting layer. The particle measurements which were made by the aircraft were particularly useful in interpreting the Doppler spectra. The data show that riming growth was occurring above the melting layer while drop breakup was occurring immediately below the melting layer.

The riming growth aloft was probably favored by weak vertical air-motions and the small growth rate of particles by diffusion at temperatures close to 0C. The estimated riming growth rate, $\sim 5.8 \times 10^{-7}$ g/s, is about an order of magnitude larger than the growth rate by diffusion growth at -3C and water saturation. By approximating the particle size distribution with a monodispersed distribution it was possible to estimate the dominant mechanism of particle growth, the mean particle mass, large particle concentration, liquid water content, and mass-fallspeed relation from VID measurements of velocity and reflectivity in steady precipitation.

VID profiles of mean velocity and equivalent reflectivity factor indicate that breakup was occurring after melting. The small height over which breakup would have to occur to explain the VID measurements suggests that relatively few, large, unstable drops (> 5mm) are disrupting rather than a large number of intermediate size drops (3 mm). During melting, these otherwise unstable large drops may be stabilized by an internal ice structure.

6. ACKNOWLEDGEMENTS

The author thanks Prof. Roscoe Braham for guidance in this research; T. R. Morris, R. C. Kukuk, and N. C. Carrera for their hard work as crew on the airplane, as well as our fine pilot R. Townsend, the Illinois State Water Survey, E. Mueller and the crew of the CHILL Radar, A. Jameson, A. Bohne, and Prof. R. C. Srivastava of the University of Chicago Laboratory for Atmospheric Probing for their help in the field and subsequent discussions, typist J. Jacobs, NCAR Flight Facility for the loan of equipment and ARIS tape processing, and the NCAR Computer Facility for resources granted for post-flight data reduction. This research was carried out under the sponsorship of the National Science Foundation, Atmospheric Sciences Div., under NSF Grant DES75-14225, and RANN program under NSF Grant AEN72-03399-A03. The National Center for Atmospheric Research is sponsored by the National Science Foundation.

REFERENCES

Atlas, D., R. C. Srivastava, and R. S. Sekhon, 1973: Doppler radar characteristics of precipitation at vertical incidence. Rev. of Geophys. and Space Phys., 11, 1-35.

______, R. Tatehira, R. C. Srivastava, W. Marker, and R. E. Carbone, 1969: Precipitation-induced mesoscale wind perturbations in the melting layer. Quart. J. Roy. Meteorol. Soc., 95, 544-560.

Brazier-Smith, P. R., S. G. Jennings and J. Latham, 1973: Raindrop interactions and rainfall rates within clouds. Quart. J. Roy. Meteor. Soc., 99, 260-272.

Ekpenyong, B., and R. C. Srivastava, 1970: Radar characteristics of the melting layer: A theoretical study. 14th Radar Met. Conf., A.M.S., Nov. 17-20, 1970.

Findeisen, W., 1940: The formation of the 0°C isothermal layer and fractocumulus under nimbostratus. Met. Zeit., 57, 49-54.

Gunn, R., and G. D. Kinzer, 1949: The terminal velocity of fall for water droplets in stagnant air. J. Meteor., 6, 243-248.

Knollenberg, R. G., 1970: The optical array: An alternative to scattering or extinction for airborne particle size determination. J. Appl. Meteor., 9, 86-103.

Locatelli, J. D., and P. V. Hobbs, 1974: Fallspeeds and masses of solid precipitation particles. J. Geophys. Res., 79, 2185-2197.

McTaggart-Cowan, J. D., and R. List, 1975: Collision breakup of water drops at terminal velocity. J. Atmos. Sci., 32, 1401-11.

Spyers-Duran, P. A., and R. R. Braham, Jr., 1967: An airborne continuous cloud particle replicator. J. Appl. Meteor., 6, 1108-1113.

6.2.4

CONDITIONAL SYMMETRIC INSTABILITY

A POSSIBLE EXPLANATION FOR RAINBANDS

D A Bennetts and B J Hoskins
Meteorological Office, Bracknell, England. — Dept of Geophysics, Reading, England.

1. INTRODUCTION

It is well known that warm frontal precipitation is often organized into roughly parallel bands (eg Elliott and Hovind 1964, Browning and Harrold 1969) with a spacing of 100-300 km and an orientation weakly related to the orientation of the surface fronts. Sometimes there is a banded substructure with a spacing of 10-50 km embedded in and aligned with the main structure. The associated motion fields exhibit a roughly band-parallel pattern (Roach and Hardman 1975) suggesting two-dimensional rolls, but with a tendency to resolve into anticyclonic gyres.

This paper describes a theoretical study which suggests that rainbands might be generated by a type of Symmetric Instability modified by latent heat release (eg Hoskins 1974). Consider first a dry uniformly rotating atmosphere with a constant stable vertical temperature gradient and a constant horizontal temperature gradient in geostrophic balance with the vertical wind shear. From a meteorological viewpoint, a perturbation of this basic state can produce two types of instability; Baroclinic Instability (BI) which derives its energy from the available potential energy and Symmetric Instability (SI) which derives its energy from the available kinetic energy of the basic flow. Symmetrically unstable modes are independent of the long-stream coordinate i.e. rolls along the thermal wind, and can therefore be analysed with a two dimensional model; BI requires the third dimension. The fundamental difference between the motions is that in a symmetrically unstable motion fluid particles execute a vertical roll. The gyroscopic torque is weak and this is reflected in the necessary and sufficient condition for SI in this case of no horizontal shear, namely Richardson number $Ri \leqslant 1$ (see Stone 1966). In a baroclinically unstable flow the gyroscopic torque is sufficient to inhibit overturning and non-symmetric motions arise. There are some conditions in which both BI and SI coexist. In such regions SI dominates if $Ri < 0.95$, but for a full review of this and BI the reader is referred to Hide and Mason (1975).

However as Eliassen and Kleinschmidt (1957) showed SI in a dry atmosphere is not applicable to frontal regions and following their suggestion we modify the flow so that particles follow the saturated adiabat for ascent and the dry adiabat for descent. It is this motion that we call <u>Conditional</u> Symmetric Instability (CSI).

Here we outline the linear theory of SI and extend it to cover CSI. However the inclusion of the release of latent heat precludes a full theoretical solution and a non-linear two dimensional model has been developed specifically to investigate CSI. We present the results of the first stage of the investigation which suggests that CSI is a viable explanation of rainbands but much work still remains to be done.

2. THEORETICAL ANALYSIS

For the subsequent analysis we use the Navier-Stokes, the thermodynamic and the continuity equations and apply the Boussinesq approximation. At $z = 0$ we put $u = v = w = 0$, θ specified and at the top boundary $z = H$, $w = 0$, $\frac{\partial u}{\partial z} = \frac{\partial v}{\partial z} = 0$ (stress free) and θ specified.

2.1 Basic State

We assume that $\frac{\partial}{\partial y} \equiv 0$, neglect dissipation and take the thermal wind balance

$$f\frac{\partial v}{\partial z} = \frac{g}{\theta_0}\frac{\partial\theta}{\partial x}, \qquad (2.1.1)$$

where f is the coriolis parameter, θ the potential temperature and v the wind component in the y-direction. Except for a few special cases this is not an exact analytic solution of the primitive equations but it suffices for the purposes of this analysis.

2.2 Perturbation

In the presence of advection, a roll perturbation with zero gradients in one direction can exist only if the basic flow has zero gradients in that direction. Linearizing for a perturbation with $\frac{\partial}{\partial y} \equiv 0$ gives ($u = U + u'$ etc)

$$\nabla_T u' - f v' + \Phi'_x = 0, \qquad (2.2.1)$$

$$\nabla_T w' - \frac{g}{\theta_0}\theta' + \Phi'_z = 0, \qquad (2.2.2)$$

$$\nabla_T v' + \left(f + \frac{\partial V}{\partial x}\right)u' + \frac{\partial V}{\partial z}w' = 0, \qquad (2.2.3)$$

$$\nabla_T \theta' + \theta_x u' + \theta_z w' = 0, \qquad (2.2.4)$$

$$u'_x + w'_z = 0, \qquad (2.2.5)$$

where $\nabla_T \equiv \frac{\partial}{\partial t} - \nu_1\frac{\partial^2}{\partial x^2} - \nu_2\frac{\partial^2}{\partial z^2}$.

Here, advection by and gradients of (U, W) have been neglected. θ_z is understood to have reduced value for saturated ascent.

From continuity, we may introduce a stream function ψ and after elimination we find

$$\nabla_T^2\left(\frac{\partial^2\psi}{\partial x^2} + \frac{\partial^2\psi}{\partial z^2}\right) = \frac{\partial}{\partial z}\left(-F^2\frac{\partial\psi}{\partial z} + S_1^2\frac{\partial\psi}{\partial x}\right) - \frac{\partial}{\partial x}\left(-S_2^2\frac{\partial\psi}{\partial z} + N^2\frac{\partial\psi}{\partial x}\right). \qquad (2.2.6)$$

If $F^2 = f\left(f + \frac{\partial v}{\partial x}\right)$, $N^2 = \frac{g}{\theta_0}\frac{\partial \theta}{\partial z}$,

$$S_1^2 = f\frac{\partial v}{\partial z} = S_2^2 = \frac{g}{\theta_0}\frac{\partial \theta}{\partial x}, \qquad (2.2.7)$$

are treated locally as constant we may look for a solution proportional to $\exp[i(kx + mz + \omega t)]$. The dispersion relationship is

$$\sigma = i\omega = -(\nu_1 k^2 + \nu_2 m^2) \pm$$

$$\left[-N^2 \sin^2\phi + (S_1^2 + S_2^2)\sin\phi\cos\phi - F^2\cos^2\phi\right]^{1/2} \qquad (2.2.8)$$

where ϕ is the disturbance orientation. The maximum instability or minimum frequency is at

$$\tan 2\phi = \frac{S_1^2 + S_2^2}{N^2 - F^2} \quad 0 < \phi < \frac{\pi}{2} \quad (S_1^2 + S_2^2 > 0) \qquad (2.2.9)$$

and there $\sigma = i\omega = -\nu_1 k^2 - \nu_2 m^2 +$

$$\left[-\frac{N^2+F^2}{2} + \left(\left(\frac{N^2+F^2}{2}\right)^2 + \frac{(S_1^2+S_2^2)^2}{4} - N^2F^2\right)^{1/2}\right]^{1/2} \qquad (2.2.10)$$

If $N^2F^2 < \frac{S_1^2+S_2^2}{2}$ there is instability for long enough wavelength.

2.3 Classical Symmetric Instability

The above analysis is of a general nature. In the regime in which we are particularly interested there is thermal wind balance $S_1^2 = S_2^2 = S^2$ say, $N^2 \gg S^2 \gg F^2$ and without loss of generality we may put $\nu_1 = \nu_2 = 0$. Introduce Ertel's potential vorticity $q_v = N^2F^2 - S^4$, a conserved quantity in the absence of friction or diabatic effects, then maximum instability is at $\tan 2\phi = \frac{2S^2}{N^2 - F^2}$,

the slope of the θ surfaces is at $\tan 2\phi$ $= \frac{2S^2}{N^2 - F^2 + q_v/N^2}$, and the slope of the absolute vorticity vector is at $\tan 2\phi = \frac{2S^2}{N^2 - F^2 - q_v/F^2}$.

We can therefore see that the minimum frequency, or maximum instability slope is always between the isentropic surfaces and the absolute vorticity vector, being much closer to the former. There is instability if and only if the isentropic surfaces are more vertical than the absolute vorticity vector, and this is equivalent to q_v negative.

Using the hydrostatic approximation the most unstable mode in a uniform, infinite atmosphere is amenable to a very simple analysis. Then motion along θ surfaces implies zero perturbation pressure gradient. Therefore

$$\frac{\partial u}{\partial t} = fv, \qquad (2.3.1)$$

$$\frac{\partial v}{\partial t} = -u\left(f + \frac{\partial v}{\partial x}\right) - w\frac{\partial v}{\partial z} = -u\zeta_\theta, \qquad (2.3.2)$$

hence $$\frac{\partial^2 u}{\partial t^2} + f\zeta_\theta u = 0, \qquad (2.3.3)$$

where ζ_θ is the absolute vorticity along a θ surface. For a displacement δx, there is a restoring force $f\zeta_\theta\,\delta x$ and instability if this is negative.

2.4 Conditional Symmetric Instability (CSI)

We may expect that a frontal region is stable to symmetric motions (potential vorticity positive) until the rising warm air becomes saturated. At this point the atmosphere is still stable to downward motions, the minimum "restoring force" being $f\zeta_\theta\delta x$ for displacements δx along θ surfaces. For saturated ascent, the minimum restoring force is for displacements δx along the saturated ascent or θ_w surfaces and is of order $f\zeta_{\theta_w}\delta x$. Clearly there is no possibility of instability unless $\zeta_{\theta_w} < 0$. Stability to downward motions and instability to saturated upward motions implies that the θ_w surfaces are more vertical than the absolute vorticity vector which is more vertical than the θ surfaces.

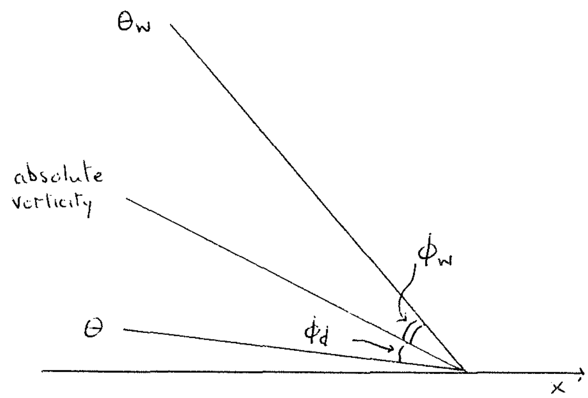

In an infinite atmosphere this would be a sufficient criterion for instability, but boundary conditions have to be satisfied in a finite atmosphere. We may expect the least stable mode to tend to orientate its upward motion along θ_w surfaces and its down motion along θ surfaces. Consider the streamtube shown below

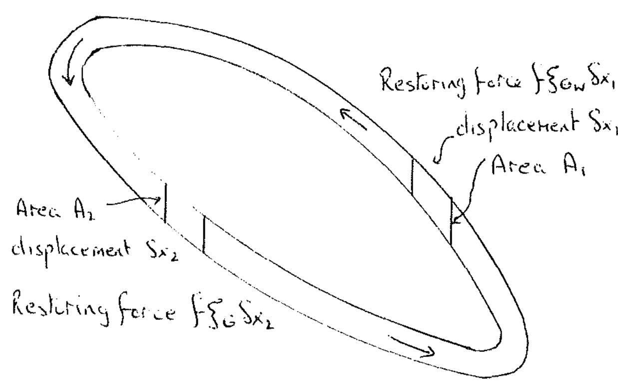

Continuity implies that $A_1\delta x_1 = A_2\delta x_2$ and so the total restoring force is $\sim A\delta x_1 f(\zeta_\theta + \zeta_{\theta_w})$. There will also be contributions from portions not parallel to θ or θ_w but a rough criterion for instability is

$$\alpha\zeta_\theta + \zeta_{\theta_w} < 0, \quad \alpha \sim 1. \qquad (2.4.1)$$

The criterion may be interpreted that the angle between the absolute vorticity vector and the θ_w surface must be greater than α times the angle between the θ surface and the absolute vorticity vector.

$$\phi_w > \alpha' \phi_d , \qquad (2.4.2)$$

with α' describing the efficiency of the motion.

In terms of N^2, S^2 and F^2 the criterion for dry symmetric stability but moist symmetric instability is

$$1 > \frac{S^4}{N^2F^2} > \frac{N^2 - n^2}{N^2 - \frac{\alpha'}{1+\alpha'} n^2} \cdot \qquad (2.4.3)$$

Richardson No

$$Ri = \frac{N^2F^2}{S^4} \quad \text{and} \quad n^2 = \frac{g}{\theta_0}\left(\frac{\partial\theta}{\partial z} - \frac{\partial\theta_w}{\partial z}\right).$$

3. A NUMERICAL EXPERIMENT

In order to determine α' and investigate CSI we have developed a non-linear two dimensional numerical model with 100 x 80 grid points in the horizontal and vertical respectively. Typical grid spacings are 5-10 km in the horizontal and 100 m in the vertical but these can be altered according to the scale of the instability under investigation. A time step of $1\frac{1}{2}$ mins is sufficient for the leap frog integration scheme and the model is stable for integrations up to 30 hrs real time. This takes approximately 20 mins on the IBM 360/195.

The model was checked against the rigorous theoretical solution for Symmetric Instability. The neutral curve was very close to Ri = 1 the discrepancy being due to implicit smoothing in the finite difference scheme.

3.1 The Conditional Symmetric Neutral Curve

For the first experiment the eddy diffusion was set to zero. Several integrations were then performed to find the neutral growth curve for various values of the static stability and this is shown in Fig 1 below. Following McIntyre (1970) in the case of Prandtl number = 1, viscosity will have a damping effect and so the CSI neutral curve will be the upper limit one would expect to find. The CSI curve asymptotes to the SI curve for high static stability as the release of latent heat becomes insignificant. It tends to infinity at $N^2/n^2 \rightarrow 1$ as here the atmosphere becomes unstable to convective motions. (θ_w surfaces vertical).

3.2 The Effect of Eddy Diffusion

In numerical models both SI and CSI tend to organise the motion into a narrow region of strong ascent and a broad region of weak descent. The width of these regions and hence the wavelength of the bands is determined by the eddy diffusion. It is the implicit smoothing in the finite difference scheme that determines the scale of the instability when the eddy diffusion is zero, as in section 3.1, and the bands then tend to be three grid points across. It follows that the results of the integrations with the diffusion set to zero can not, in general, have a meaningful physical interpretation; however supplementary integrations have shown that the onset of instability (neutral curves) is accurately predicted. Fig 2 opposite shows the relationship between the fastest growing wavelength and the horizontal eddy diffusion. (Owing to the steepness of the θ_w curves the vertical diffusion plays a minor role.)

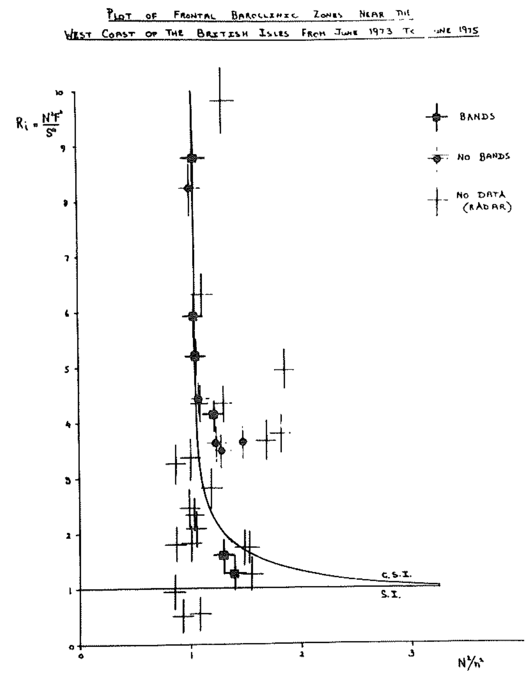

Fig 1. The neutral curves for SI and CSI, at zero viscosity, plotted in a Richardson number - (N^2/n^2) frame. There is instability below and to the left of the curves. The data points marked on the diagram refer to a few examples of atmospheric baroclinic zones, see text 3.4.

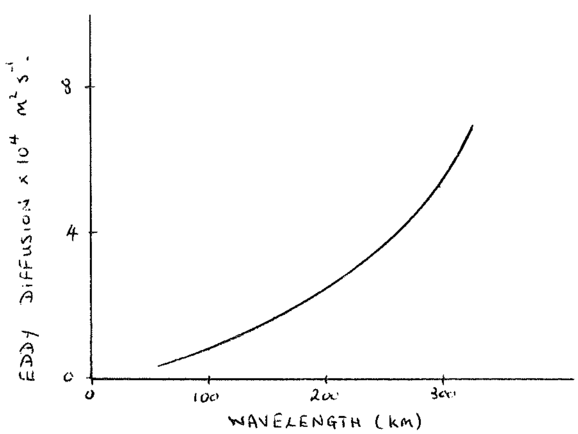

Fig 2. The relationship between the fastest growing wavelength and the horizontal eddy diffusion coefficent.

The simplest criterion by which to determine the above curve would be to introduce a 'white noise' disturbance and look for the fastest growing mode. Unfortunately because of the finite size of the model and the numerical limitations we find that the boundaries are preferred sites for development. Attempts to cure this simply shift the preferred areas elsewhere. The method adopted was to introduce two identical perturbations a fixed distance apart. With all other parameters constant their distance was progressively reduced until the two resulting bands began to interact. This process is complicated by the fact that as the instabilities grow the motions become non-linear. The curves in Fig 2 was therefore determined by finding the minimum spacing between bands so that they grew identically with no interaction up until the time that the θ_W surface began to distort visibly, i.e. up until the time that the flow became non-linear.

3.3 The Structure of the Bands

Fig 3 shows the details of one integration. The basic field was $\frac{\partial\theta}{\partial z} = 3.8^{\circ}C\ km^{-1}$, $\frac{\partial\theta}{\partial x} = \frac{1}{30}{}^{\circ}C\ km^{-1}$, ascent on 10° θ_w surface, $f = 1.2 \times 10^{-4} s^{-1}$, $\Delta x = 10\ km$, $\Delta z = 100\ m$ and horizontal viscosity $= 2 \times 10^{4}\ m^{2} s^{-1}$. Fig 3a shows the initial state with two small perturbations 200 km apart. Fig 3b shows the fully developed bands at 360 minutes. The temperature and θ_ω fields indicate that the bands are beginning to interact, while Fig 3c shows that differential advection has distorted the θ_ω surfaces so much that convective overturning becomes possible and self destruction of the bands has set in. The model is not equipped to deal with this in detail but it is able to crudely show the destruction of the lower band.

3.4 Comparison with the Atmosphere

The results of a pilot study into the applicability of CSI to the atmosphere are shown in Fig 1. In the first instance all strong baroclinic zones that crossed the west coast of the British Isles in a given two year period were analysed from the available information in the Daily Weather Reports and from information stored from the numerical forecasts. No selection, on the basis of precipitation, was made and all the points, with standard error bars, are plotted, with the exception of some with high Richardson numbers. This data was then compared with the radar results from the Meteorological Office Research Unit, Malvern. They only had information on some of the cases and often this was insufficient to determine whether the precipitation was banded or not. The few cases where the distinction was clear cut are indicated by heavy markings. At first glance the agreement is reasonable but it must be remembered that the CSI neutral curve is for zero viscosity and also there are very few cases.

4. CONCLUSIONS

This paper presents a study into the viability of Conditional Symmetric Instability as an explanation for rainbands. The form of the roll instability appears to resemble that shown to exist in rainbands and the CSI neutral curve is not inconsistent with that found in the atmosphere albeit from a very limited survey. The wavelength of the instability is found to depend crucially on the eddy diffusion and varies between 50 and 350 km for diffusion coefficients

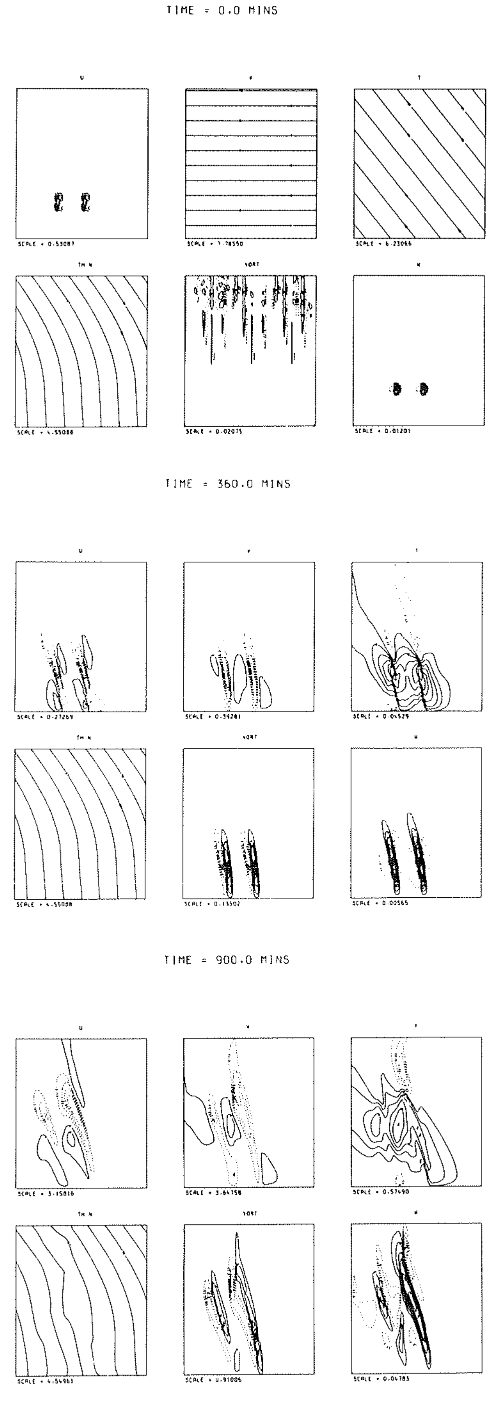

Fig 3. The six boxes in each figure show, reading in the conventional manner, the U-field, V-field, potential temperature, resultant saturated adiabats, the absolute vorticity in units of f, and the vertical motion field. Continuous lines denote positive values and dotted lines negative values. Fig 3a shows the initial V, θ, θ_ω and vorticity (= 1 everywhere) field, Figs 3b and 3c the resultant perturbation on these fields. The horizontal and vertical motion fields are zero in the basic state so the figures show the total field. The contour separation has been printed below each box. To determine the absolute magnitude multiply the contour integer between ± 10, by the scale value. The overall dimensions of each individual box are 8 km by 1000 km.

5×10^3 and 8×10^4 m^2 s^{-1}. This raises important questions as to the suitability of a uniform diffusion coefficient but it does give some sort of comparison with the results of other numerical models. The e-folding times (growth rates) are between 1 and 18 hrs for the above range. Both these facts are not inconsistent with observational evidence. Finally the bands are self destructive, the differential advection produces convective overturning and this provides a mechanism for generating potential instability in frontal regions.

4.1 Acknowledgements

We are grateful to Dr W T Roach who originally drew the rainband observations to our attention and for many subsequent discussions and to Dr M E McIntyre for his help in understanding the relationship between the eddy diffusion and the wavelength.

5. REFERENCES

BROWNING, K A and HARROLD, T W 1969 Air motion and precipitation growth in a wave depression. Quart. J. R. Met. Soc., 95, pp 288-309

ELIASSEN, A and KLEINSCHMIDT. E 1957 Handbuch der Physik, Bk, XLVIII p 71

ELLIOTT, R D and HOVIND, R 1964 On convective bands within Pacific Coast Storms and their relation to storm structure. J. Appl. Met, 3 pp 143-154

HIDE, R and MASON, P J 1975 Sloping convection in rotating fluids. Advances in Physics 24 No 1 pp 47-100

HOSKINS, B J 1974 The role of potential vorticity in symmetric stability and instability. Quart. J. R. Met. Soc. 100 pp 480-482

McINTYRE, M E 1970 Diffusive destabilization of the Baroclinic circular vortex. Geophysical Fluid Dyamics 1 pp 19-57

ROACH, W T and HARDMAN, M E 1975 Mesoscale air motions derived from wind finding drop sonde data: the warm front and rainbands of 18th Jan 1971. Quart. J. R. Met. Soc. 101 pp 437-462

STONE, P H 1966 On non-geostrophic baroclinic stability. J. Atmos. Sci. 23 pp 390-403

6.2.5

RADIATIVE-PRECIPITATIVE EQUILIBRIUM OF THE NORTHERN ATMOSPHERE

Michael Hantel and Herbert Langholz

Meteorologisches Institut der Universität
53 Bonn (W-Germany), Auf dem Hügel 20

1. INTRODUCTION

This is a contribution to quantitative climatology of the free atmosphere. We want to study the two constituents of the diabatic heating, namely, radiation and condensation, by considering both heating terms as divergences of a vertical energy flux. While the radiative flux component will be obtained from a model, the precipitative flux component will be determined from the heat equation. We shall show that the mutual balance of both physically different heat fluxes is almost exact in the global mean but is significantly modified by advection in single latitude belts.

The precipitation flux concept has been introduced recently (Hantel, 1974). It was further discussed from the energy budget and streamfunction viewpoint (Hantel and Peyinghaus, 1976; Hantel et al., 1976). In this study we shall briefly recapitulate the basic concept and then present and discuss monthly patterns of the precipitation flux. Domain is the northern atmosphere in a vertical-meridional section (0-1000 mb, 10°S-90°N, time-scale 1 month).

2. THE PRECIPITATION FLUX CONCEPT

We consider the familiar equations for mechanical and thermal energy:

$$\rho\frac{d}{dt}(k+\Phi) + \vec{\nabla}\cdot(p\vec{v}) = p\vec{\nabla}\cdot\vec{v} \qquad (2.1)$$

$$\rho\frac{d}{dt}(c_v T) - \rho Q = - p\vec{\nabla}\cdot\vec{v} \qquad (2.2)$$

The symbols ρ, t, k, Φ, p, $\vec{v}$, c_v, T, Q, $\vec{\nabla}$ denote, respectively: density, time, kinetic energy, geopotential, pressure, velocity vector, specific heat at constant volume, temperature, diabatic heating, nabla operator. For the sake of simplicity, we have neglected in (2.1), (2.2) viscosity and Reynolds stress terms; this does not affect the points we want to make. For a more complete derivation see Hantel et al. (1976).

If condensation is absent the diabatic heating is caused by radiation and conduction. Van Mieghem (1973) has introduced the notion

$$- \rho Q \equiv \vec{\nabla}\cdot\vec{w} \qquad (2.3)$$

which considers the diabatic heating as the divergence of the radiative (plus conductive) energy flux vector $\vec{w}$. Thus the total energy equation reads:

$$\rho\frac{d}{dt}(k+\Phi+c_v T) + \vec{\nabla}\cdot(p\vec{v}+\vec{w}) = 0 \qquad (2.4)$$

While the parameterization (2.3) is exact in the *dry case* (provided there is no electromagnetic storage of radiation energy), it can be generalized to the case with condensation only in an approximate way because storage of humidity is always present. Nevertheless we adopt (2.3) also for the *moist case* and consider the diabatic heating as the divergence of the generalized heat flux vector (Hantel, 1974):

$$\vec{w} \equiv \{0,0,gH_R-gLH_C\} \quad \left.\begin{array}{l} H_R \text{ (Joule m}^{-2}\text{sec}^{-1}) \\ H_C \text{ (kg m}^{-2}\text{sec}^{-1}) \end{array}\right\} \qquad (2.5)$$

H_R is the vertical radiation flux, H_C the vertical condensation or *precipitation flux*. The gravity g has been introduced for convenient dimensions of H_R, H_C; L is the latent heat of condensation. The conductive heat flux is not included in $\vec{w}$; it is presumably small and will be absorbed into the advective heat flux discussed below. The precipitation flux comprises only the flux of water in *condensed form* but no vapor contribution. The signs in the definition (2.5) are such that H_R, H_C are positive downward. Further, (2.5) considers only the vertical components of radiation and precipitation flux since they are presumably dominant; however, the horizontal components of both could be included in the present framework without difficulty.

The precipitation flux cannot be measured directly. Thus we shall apply (2.5) as a means to determine H_C from the balance condition (2.4). The formula (2.5) reflects a peculiarity of the vertical heat flux: if H_C is downward (positive) it acts as an upward (negative) heat flux, and vice versa. Thus the downward radiation flux and the downward precipitation flux combine in the global mean to an almost zero net heat flux $\vec{w}$.

3. COMPILATION OF THE PRECIPITATION FLUX

The total heat equation (2.4) along with (2.5) is quite general. We shall apply it to the zonally symmetric case. Let us denote the zonal and time mean plus deviation by the familiar symbols (e.g., Oort and Rasmusson, 1971):

$$\text{zonal: } [\ ] + {}^{*}; \quad \text{time: } \overline{} + {}' \tag{3.1}$$

The averaged equation (2.4) reads in pressure coordinates:

$$\frac{\partial}{\partial t}[\overline{\Phi}+c_v\overline{T}] + \frac{\partial[\overline{vs}]\cos\phi}{\partial\eta} + \frac{\partial[\overline{\omega s}+g\overline{H_R}-gL\overline{H_C}]}{\partial p} = 0 \tag{3.2}$$

where we have introduced:

$$\left.\begin{aligned} s &\equiv \Phi + c_pT, \text{ potential heat} \\ \eta &\equiv a\sin\phi, \text{ meridional coordinate} \end{aligned}\right\} \tag{3.3}$$

and have neglected the kinetic energy k since it is small compared to s. We integrate (3.2) with respect to pressure and solve for the precipitation flux. With the abbreviations

$$\left.\begin{aligned} \frac{1}{g}\frac{\partial}{\partial t}\int_0^p[\overline{\Phi}+c_v\overline{T}]dp &\equiv \text{STOR} \\ \frac{1}{g}\frac{\partial}{\partial\eta}\{\cos\phi\int_0^p[\overline{vs}]dp\} + \frac{1}{g}[\overline{\omega s}] &\equiv \text{ADV} \\ [\overline{H_R}] - [\overline{H_R}]_{p=0} &\equiv \text{RAD} \\ L[\overline{H_C}] &\equiv \text{PREC} \end{aligned}\right\} \tag{3.4}$$

we obtain the balance

$$\boxed{\text{STOR} + \text{ADV} + \text{RAD} = \text{PREC}} \tag{3.5}$$

We shall use this formula to determine the unobservable PREC from the sum of the three observable quantities on the left.

For STOR and ADV we employ the zonal mean atmospheric circulation data of the MIT-Library, published by Oort and Rasmusson (1971). The data are monthly averages and are given on 11 pressure surfaces from 50 to 1000 mb with 5° latitude resolution. The horizontal flux of potential heat splits according to

$$[\overline{vs}] = [\overline{v}][\overline{s}] + [\overline{v}^*\overline{s}^*] + [\overline{v's'}] \tag{3.6}$$

(mean, standing eddy, and transient eddy flux). Each of the three splits again into a geopotential and a temperature flux. The resulting 6 components of (3.6) are significant only on the synoptic scale. They are all listed separately in Oort and Rasmusson's tables. Thus the integrals in STOR and ADV could be simply compiled.

Concerning the second component of ADV, it splits in a way similar to (3.6). However, the transient eddy component of $[\overline{\omega s}]$ is subsynoptic and is not listed in Oort and Rasmusson's tables. We have parameterized $[\overline{\omega's'}] \simeq c_p[\overline{\omega'T'}]$ according to Saltzman and Vernekar (1971) with the meridional transient eddy heat flux; the transient potential energy flux $[\overline{\omega'\Phi'}]$ has been neglected in analogy to the meridional fluxes for which $c_p[\overline{v'T'}] \gg [\overline{v'\Phi'}]$. Saltzman and Vernekar's formula is an overestimate in baroclinic zones and an underestimate in the tropics. However, $[\overline{\omega's'}]$ is relatively small (Hantel and Peyinghaus, 1976) so that the parameterization is not crucial. The microturbulent component of $[\overline{\omega's'}]$ is of influence only in the lowest 100 millibars. It was introduced as 'boundary layer flux' by Newell et al. (1969) and was discussed by Thommes (1974) who showed that its influence is relatively minor. In the present study the boundary layer flux has been neglected except at the earth's surface where Budyko's (1963) sensible heat flux values (slightly adjusted) were taken. For technical details of the compilation of STOR and ADV we refer to Langholz (1976).

Concerning RAD, we adopted the monthly radiation flux data from a recent modeling effort (Peyinghaus, 1974; Falconer and Peyinghaus, 1975). The fluxes from this model were compared with observations at the top and bottom of the atmosphere and showed satisfactory agreement (Hantel and Peyinghaus, 1976). However, there do not exist representative radiation flux measurements in any intermediate level. We consider this one principal source of uncertainty in the present results.

4. RESULTS

The 4 terms of eq. (3.5) are portrayed separately in Fig. 1 in vertical-meridional sections for the month of April. The storage term is small over most of the northern atmosphere except in the highest latitudes. We note that STOR was inadvertently calculated with s instead of $\Phi+c_vT$ which does not make much difference; in January and July, STOR is completely negligible. RAD represents a downward heat flux due to net radiation divergence, fairly uniformly distributed throughout the northern atmosphere. ADV represents a downward heat flux in the tropics and midlatitudes and an upward flux in the subtropics and polar latitudes.

VERTICAL HEAT FLUX COMPONENTS (WATT/M²), APRIL

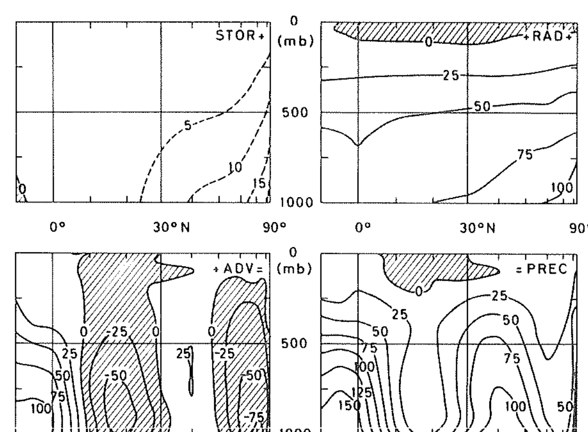

Figure 1. Components of vertical heat flux in northern atmosphere, positive downward, in units Watt/m², valid for April. For STOR, ADV, RAD, PREC, see eqs. (3.4), (3.5).

The resulting pattern of the precipitation flux shows positive values everywhere in the northern atmosphere, not only in April but throughout the year (Fig. 2). This is satisfying since only a net downward precipitation flux makes physical sense and indicates that the data from different sources entering the compilation of PREC fit reasonably together. The small negative patches in the upper atmosphere are presumably below the significance level. Very close to the earth's surface the patterns of Fig. 2 are uncertain due to the neglected boundary layer flux and further due to the non-identity of the earth's surface and the 1000 mb level.

Nevertheless, Fig. 2 reflects the climatological rainbelts in the deep tropics and in midlatitudes, and their seasonal fluctuation. The precipitation flux reaches high up into the upper troposphere with significant values of 25 units even at the 250 mb level, both in the tropics and midlatitudes. The winter midlatitude fluxes seem to be overestimated. This might be qualitatively explained by the known tendency of the radiosonde observing network to underestimate peak wind velocities. Correcting for such a systematic underestimate would increase the meridional potential heat flux in the subtropical jet latitudes which in turn would increase ADV in the subtropics and decrease it in midlatitudes, resulting in a more uniform pattern of PREC between 20^{o}-50^{o}N in winter. However, we have not yet estimated this effect quantitatively.

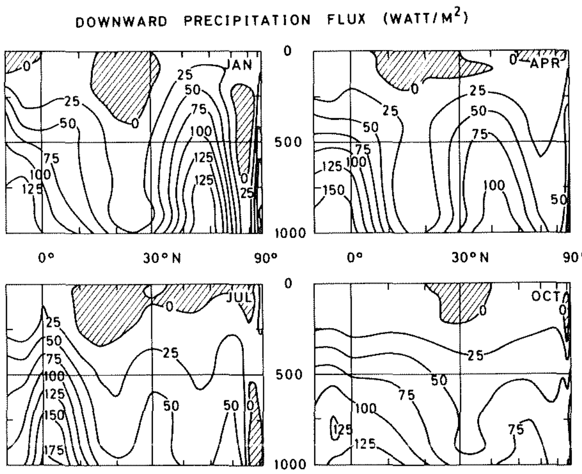

Figure 2. Vertical precipitation flux in northern atmosphere, in units Watt/m^2, for the central months of the seasons.

5. COMPARISON WITH SURFACE PRECIPITATION

The 1000 mb values of Fig. 2, reduced with the surface boundary layer flux, have been converted into rain flux dimensions and are presented in Fig. 3 along with independent estimates of surface precipitation. These are first the classical figures of Möller (1951); further, Rasmusson's (1974) estimates which are based on synoptic-scale data of the water vapor transport and Budyko's (1963) evaporation estimates; finally, Jäger's (1975) zonal averages from a comprehensive global budget of all available precipitation observations with 5^{o} latitude and longitude resolution. In a recent study the overall error of contemporary hemispheric heat budget compilations was estimated and found of the order 10 Watt/m^2 (Hantel, 1976) corresponding to about 1 g cm^{-2}month^{-1}; it has been entered in Fig. 3 as error limits of the fully dotted values.

In general the coincidence in Fig. 3 is fair. The most intriguing discrepancies are visible in the winter midlatitudes where our estimates appear too high and in July in the subtropics where they appear too low. The July discrepancy is difficult

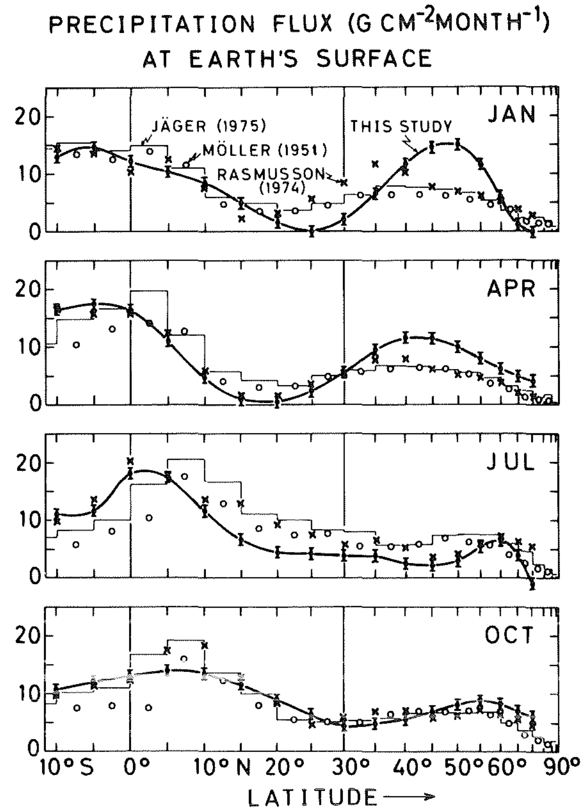

Figure 3. Surface precipitation in units g cm^{-2}month^{-1}. Thick curve connecting full dots with error limits (corresponding to 10 Watt/m^2) from present study, valid for 1000mb. Open circles from Möller (1951). Crosses from Rasmusson(1974). Thin histogram from Jäger (1975). Möller, Rasmusson, and Jäger valid for earth's surface.

to explain. Concerning January, we refer to the above remarks about the tendency of wind measurements to under-represent peak velocities. Further, the 'observed' extratropical precipitation in winter might be too low, due to strong wind influence on rain and snow gauges; this effect can amount up to 30% and more over Canada and Russia (Hare and Hay, 1971).

An interesting analogy between our results and a recent statistical cloud model of Sasamori (1975) might be mentioned. Sasamori computed the surface precipitation for zonal mean global conditions, with the NCAR-GCM data as input. His January curve seems also to overestimate in the 40-50^{o} latitude belt the observed data of Schutz and Gates (1971) by some 100%. Since we consider our Fig. 3 as nothing but a consistency test for the precipitation flux concept, we are satisfied by the moderate fit of our results with independent estimates.

6. SUMMARY AND CONCLUSIONS

We have demonstrated the significance of the vertical precipitation flux PREC by zonal mean cross-sections through the northern atmosphere. They show that PREC is a continuous function of height and latitude. It has sizeable downward directed values across the 250 mb level and increases monotonically towards the earth's surface. Its primary maximum in meridional direction is located in the tropics, a second in midlatitudes. The vertical structure of PREC is largely determined by the radiation term RAD, the meridional structure is governed by the integrated divergence of the zonal mean potential heat flux vector ADV.

The principal errors of the present approach have been as follows:

- Uncertainty of the radiation flux; RAD must be computed from models.
- Uncertainty of the MIT-Library data. Although these data have the highest possible standard, some uncertainty remains, presumably due to wind errors and uneven coverage.
- Uncertainty of the parameterization used for the vertical transient eddy heat flux.
- Uncertainty of the boundary layer flux which cannot be measured.
- Non-identity of earth's surface and 1000 mb level.

Hantel and Peyinghaus (1976) have grouped the various terms of eq. (3.5) in an order different from the present. The vertical flux components $g^{-1}[\overline{\omega s}]$, $[\overline{H_R}]$, and $L[\overline{H_C}]$ were combined into a generalized vertical heat flux F_p. Then F_p could be obtained from the first term of ADV, with $[\overline{H_R}]_{p=0}$ as boundary condition at the top of the atmosphere. The advantage of this approach is that the three components of F_p, which are caused by physically different mechanisms, represent the exact vertical net heat flux across a given atmospheric level. The deficiency of this approach is that F_p turns out to be highly dependent upon a reference constant s_o which represents the mean atmospheric heat content. In the present study this deficiency has been removed: the net advective term ADV is strictly independent of any reference constant.

While RAD is fairly uniformly distributed in meridional direction, PREC shows distinct maxima and minima, due to ADV. The leading term in the definition (3.4) for ADV is the first. However, the horizontal heat flux divergence vanishes when averaged over all latitudes. Thus for the global and annual average, denoted by the tilde $\tilde{}$, (3.5) reduces to the only height-dependent equation

$$\frac{1}{g}\,\widetilde{[\overline{\omega s}]} + \widetilde{\mathrm{RAD}} = \widetilde{\mathrm{PREC}} \qquad (6.1)$$

The first term is small compared to the other two. This is evident at the surface (mean Bowen ratio ≈ 0.35, see Sellers, 1965) and has been shown to apply also for the free atmosphere (Langholz, 1976). Thus it is justified to refer to the global heat budget as an approximate *radiative-precipitative equilibrium*. Recent studies in the tropics (e.g., Betts, 1975) hint toward a similar balance in precipitating mesoscale systems. It is hoped that the current tropical experiments, notably GATE, will further clarify the intriguing role of the atmospheric precipitation flux.

7. REFERENCES

Betts, A.K., 1975: Parametric interpretation of trade-wind cumulus budget studies. *J. Atmos. Sci.*, 32, 1934-1945.

Budyko, M.I., 1963: *Atlas of the Heat Balance of the Earth*. Moscow, Gidrometeoizdat., 69 pp.

Falconer, P.D., and W. Peyinghaus, 1975: Radiative balance in the atmosphere as a function of season, latitude, and height. *Arch. Met. Geoph. Biokl., Ser. B*, 23, 201-223.

Hantel, M., 1974: On the display of the atmospheric circulation with streamfunctions. *Mon. Wea. Rev.*, 102, 649-661.

Hantel, M., 1976: On the vertical eddy transports in the northern atmosphere. I. Vertical eddy heat transport for summer and winter. *J. Geoph. Res.*, in print.

Hantel, M., and W. Peyinghaus, 1976: Vertical heat flux components in the northern atmosphere. *Mon. Wea. Rev.*, in print.

Hantel, M., D. Dedenbach, and H. Hüster, 1976: Energy streamfunctions in the vertical-meridional plane for the northern atmosphere. *J. Atmos. Sci.*, in print.

Hare, F.K., and J.E. Hay, 1971: Anomalies in the large-scale annual water balance over northern north America. *Canad. Geograph.*, 15, 79-94.

Jäger, L., 1975: *Globalbilanzen von Niederschlägen*. PhD-Dissertation, Freiburg, 175 pp.

Langholz, H., 1976: *Der Niederschlagsfluß in der freien Atmosphäre*. Diploma Thesis, Bonn, 66 pp.

Möller, F., 1951: Vierteljahrskarten des Niederschlags für die ganze Erde. *Peterm. Geograph. Mitt.*, 95, 1-7.

Newell, R.E., D.G. Vincent, T.G. Dopplick, D. Ferruzza, and J.W. Kidson, 1969: The energy balance of the global atmosphere. *London Proceedings*, Roy. Met. Soc., 42-90.

Oort, A.H., and E.M. Rasmusson, 1971: *Atmospheric Circulation Statistics*. NOAA Prof. Pap., 5, 323 pp.

Peyinghaus, W., 1974: Eine numerische Berechnung der Strahlungsbilanz und die Strahlungserwärmung der Atmosphäre. *Bonn. Met. Abh.*, 22, 1-63.

Rasmusson, E.M., 1974: Seasonal variation of tropical humidity parameters. In R.E. Newell (Ed.): *The General Circulation of the Tropical Atmosphere, Vol. I*, 193-237.

Sasamori, T., 1975: A statistical model for stationary atmospheric cloudiness, liquid water content, and rate of precipitation. *Mon. Wea. Rev.*, 103, 1037-1049.

Schutz, C., and W.L. Gates, 1971: Global climatic data for surface, 800 mb, 400 mb. January (R-915-ARPA), April (R-1317-ARPA), July (R-1029-ARPA), and October (R-1425-ARPA). Rand Corp., Santa Monica, Calif.

Sellers, W.D., 1965: *Physical Climatology*. The University of Chicago Press, 272 pp.

Thommes, W., 1974: Die Bestimmung der zonal und zeitlich gemittelten Erwärmungsrate durch Kondensation aus dem 1. Hauptsatz. *Annalen d. Meteorol. (Neue Folge)*, 9, 41-43.

Van Mieghem, J., 1973: *Atmospheric Energetics*. Clarendon Press, Oxford, 306 pp.

8. ACKNOWLEDGMENTS

Part of this study has been sponsored by the Ministry of Science and Research, Nordrhein-Westfalen. The figures have been drawn by Miss. B. Eggemann.

6.2.6

FINE STRUCTURE OF RAINFALL SYSTEM FORMED NEAR A CYCLONE

Takao Takeda

Water Research Institute,
Nagoya Univ., Nagoya

1. INTRODUCTION

Case studies of rainfall systems observed in frontal depressions in the British Isles have clarified some structural features of the systems in association with large scale three-dimensional airflow (Browning and Harrold, 1969, 1970: Browning, 1971). It is also well established that layer clouds are often found in cyclonic depressions (Lamb, 1951). Cunningham (1952) obtained the valuable information on precipitation particles in clouds formed around a cyclone by the simultaneous use of an aircraft and a ground radar. In this paper the fine structure of rainfall systems formed near cyclonic depressions, which were observed mainly using a vertically pointing radar, is described. A data processor is connected with the radar so as to study the structure quantitatively. Cases studied here are rainfall systems observed on June 6, June 22, June 28 and July 4 in rainy season ("Baiu") in 1975 at Nagoya University. All of the systems are related to rather similar synoptic situation and they are located in the northeastern part of depressions.

2. BRIEF DESCRIPTION OF RAINFALL SYSTEM OBSERVED ON JULY 4

On July 4 we had rainfall of total amount of 117 mm from 0.00 to 9.00 at Nagoya University. Fig. 1 is the time-height cross section of 10logZe averaged for 5 min, where Ze is an equivalent radar reflectivity factor. The center of the cyclone is about 300 km to the southeastern side of Nagoya at 3.00.

The cross section can be divided into four periods in accordance with characteristic features of radar echoes, atmospheric electric field and rainfall shown in Fig. 3 —— I : 22.00 on July 3 to 0.40 on July 4, II : 0.40 to 2.00, III : 2.00 to 6.20, IV : 6.40 to 8.20. In I period echoes more intensive than 5 db in 10logZe are detected both at levels below 2.0 km and between 5.0 and 8.0 km. In II and III periods echoes are found continuously in the whole layer from the ground to the level higher than 7.5 km and bright band is seen clearly at the level around 4.5 km. Precipitation has a steady and persistent character. In IV period rainfall is very intensive with maximum 10 min amount of 15 mm and atmospheric electric field measured on the ground shows time variation with large amplitude. Rainfall system had large convective activity in the period. It is to be noted that echoes were observed to extend upto 12.0 km level from 2.00 to 8.00 on the A scope of the radar (not shown have).

3. GROWTH OF ICE PARTICLES

Figs. 2 and 4 are time variations of 10logZe averaged for 5 min at levels of 7.4, 5.0, 4.4, 3.6 and 0.8 km and averaged vertical profiles of 10logZe in periods of II, III and IV, respectively. Upper air soundings at Hamamatsu which is 90 km from Nagoya southeastward indicate that the level of $0^{o}C$ is below 5.0 km on July 4 (4.5 km at 9.00). Rapid increase in 10logZe from 5.0 km to 4.4 km in III period can be seen in Figs. 2 and 4. The existence of bright band implies the persistent falling of solid precipitation particles. If it can be assumed that the state is nearly steady and that downward mass fluxes are the same for certain two levels, the difference of 10logZe between these levels is considered to reflect the changesin side distribution of particles and their phase (solid or liquid) in their falling.

It is interesting that 10logZe in III period does not show large increase downwards below melting layer, though slight increase can be found in the layer from 3.5 km to 3.0 km where raindrops would grow due to the coagulation among themselves or the capture of cloud droplets in low-level cloud. This suggests that the growth of precipitation particles is determined definitely before their melting out.

Monotonons increase in 10logZe from 7.5 km to bright band in III period causes us to suppose that precipitation particles found near bright band result from the growth of particles falling from the levels higher than 7.5 km. The increase by about 26 dB in 10logZe from 7.5 km to 4.4 km, which is shown in Fig. 4, means the rapid growth of ice particles due to sublimation, the capture of supercooled droplets and the coagulation among themselves. As discussed by Mason (1971), upcurrents expected in layer cloud associated with warm fronts could not supply water vapor consumed due to the growth of ice particles by sublimation, which leads to the increase more than 6 dB/km in 10logZe and it could not keep the cloud to be steady with the growth of particles. Under the condition that downward mass flux does not vary through the layer of h in height, the aggregation of N ice particles into one particle in falling through the layer causes the increase by 10logN in 10logZe approximately. Thus, it can be concluded that the formation of snowflakes takes place much more efficiently in III period, specially in the layer from 5.0 km to 4.4 km, than in II period. These fasts are depicted in Table 1 and Fig. 5 clearly.

As mentioned above, echoes extended upto 12 km level after 2.00. These high-level echoes were detected in convective rainfall system found during the period of 6.40 to 8.20 too. It would be suggested that many ice particles are supplied from the cloud existing at high levels into the layer cloud which formed in moist air ascending frontal surface and which included much condensed water. Consequently the growth of particles due to sublimation and the aggregation among themselves occurred very efficiently in the layer cloud. Ice particles at high levels might originate from the top of convective cloud found in IV period. We could not verify these processes at present. Precipitation mechanism related to the supply of ice particles from high-level cloud into layer clouds at middle level would be an interesting problem to be studied quantitatively. The efficient formation of snowflakes is suggested in all of layer clouds which were observed on June 6, June 22 and June 28.

4. BREAKING OF MELTING PRECIPITATION PARTICLES

Though breaking processes of precipitation particles in the melting layer have been studied by Ohtake (1969) and Lhermitte and Atlas (1963), it has not been made clear whether or not it occurs in the layer. Present quantitative analyses on radar reflectivity factor indicate that the occurrence of breaking can be inferred from vertical gradients of 10logZe above and below the central level of bright band.

Each point in Fig. 6 means the relationship between vertical gradients along each stresk which has nearly the same echo intensity at the level by 0.2 km higher than the center of bright band. We can see that the relationships have a tendency to be grouped in the area of positive or negative inclination depending upon the period from which streaks are selected. It can be said from simple discussion based on radar equation (not shown here) that in the period including only streaks in which no breaking occurred, points are grouped in the area of positive inclination and in the period in which streaks includig breaking process are also mixed, the group of negative inclination is realized. Further it was inferred that in the latter a melting particle breaks into rather small number of fragments, not many droplets.

References

Browning, K. A., 1971: Radar measurements of air motion near fronts, Part 2: Some categories of frontal air motion. Weather, 26, 320-340.

_______ , and T. W. Harrold, 1969: Air motion and precipitation growth in a wave depression. Quart. J. Roy. Met. Soc., 95, 288-309.

_______ , and _______ , 1970: Air motion and precipitation growth at a cold front. Quart. J. Roy. Met. Soc., 96, 369-389.

Cunningham, R. M., 1952: Distribution and growth of hydrometeors around a deep cyclone. M.I.T. Weather Radar Res. Rep., No. 18, 297-302.

Lamb, H. H., 1951: Essay on frontgeneses and frontlysis. The meteorological Magagine, 80, No. 945, 65-71.

Lhermitte, R., and D. Atlas, 1963: Doppler fall speed and particle growth in stratiform precipitation. Proc. 10th Weather Radar Conf., 297-302.

Mason, B. J., 1971: The Physics of Clouds. 2nd Edition, Clarendon Press, Oxford, 671 pp.

Ohtake, T., 1969: Observations of size distributions of hydrometeors through the melting layer. J. Atmos. Sci., 26, 545-557.

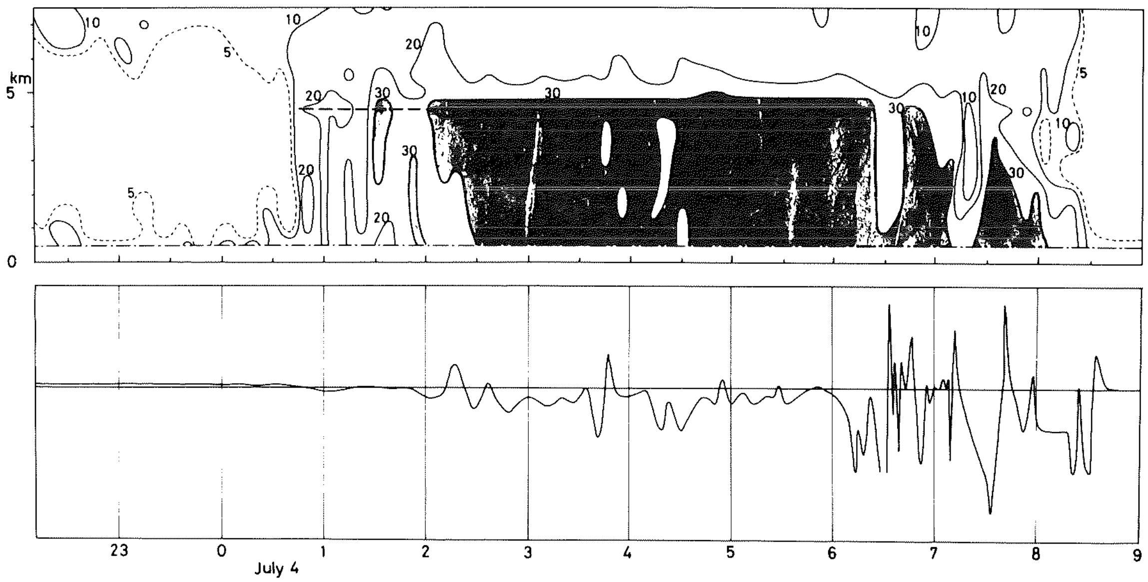

Figure 1 Time-height cross section of 10 log Ze in unit of dB (upper figure) and time variation of atmospheric electric field (lower figure) during the period of 22.00 on July 3 to 9.00 on July 4. Ordinate in the lower figure is drawn in arbitrary unit.

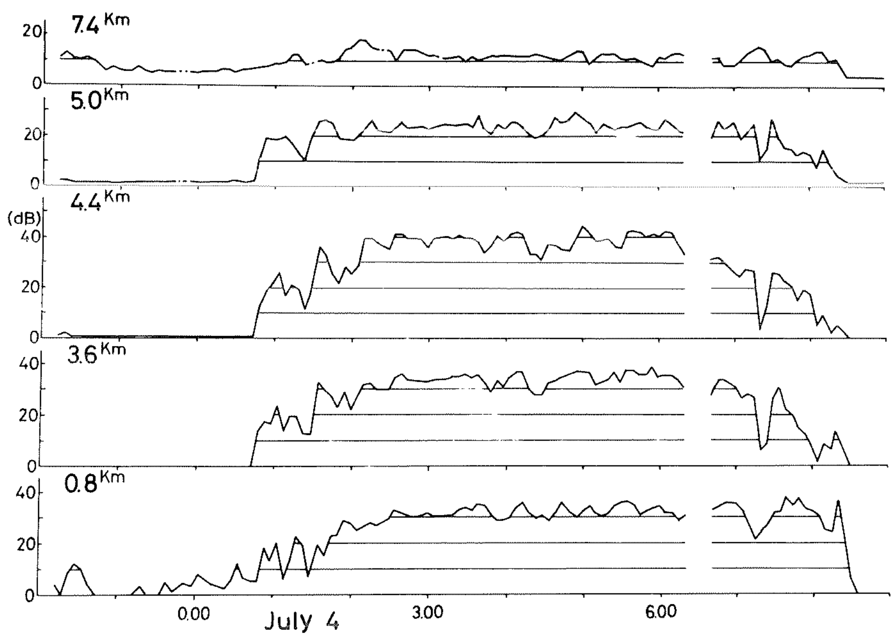

Figure 2 Time variations of 10 log Ze (dB) at levels of 7.4, 5.0, 4.4, 3.6 and 0.8 km.

Table 1 Averaged values of 10 log Ze (dB) at levels of 7.4, 5.0, 3.6 and 0.8 km, and at the central level of bright band in II, III and IV periods.

		7.4	5.0	3.6	0.8	central level of bright band
II	0.40 - 2.00	9.8	17.5	19.4	16.1	24.0
III	2.00 - 6.20	12.7	23.8	33.3	31.4	38.3
IV	6.40 - 8.20	12.0	17.2	19.5	31.0	(20.2)

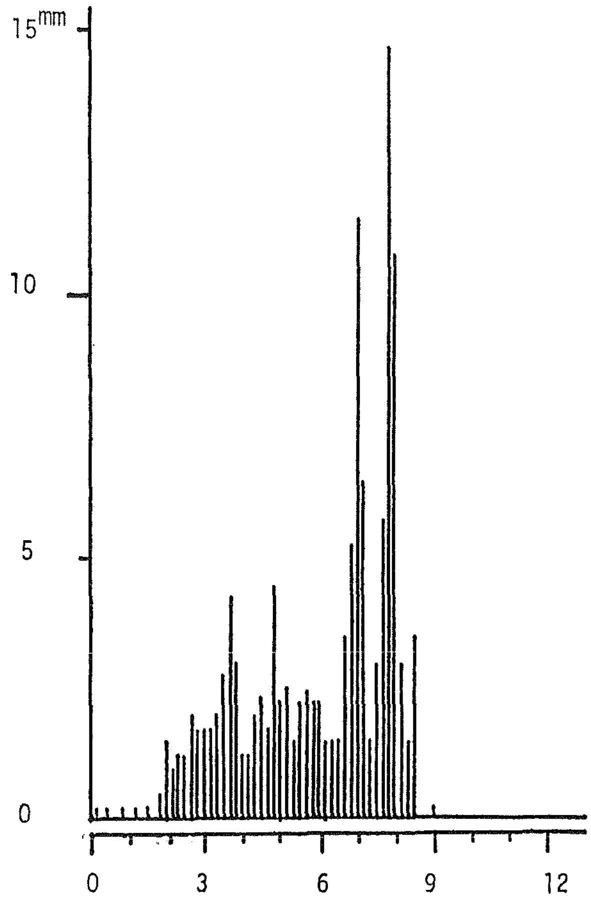

Figure 3 Time variation of 10 min rainfall amount measured at Nagoya University.

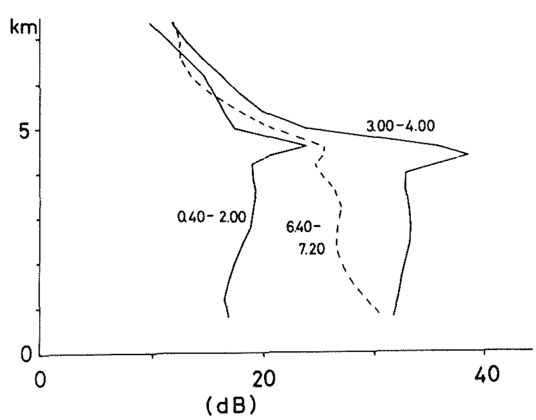

Figure 4 Typical examples of averaged vertical profiles of 10 log Ze (dB) in II, III and IV periods.

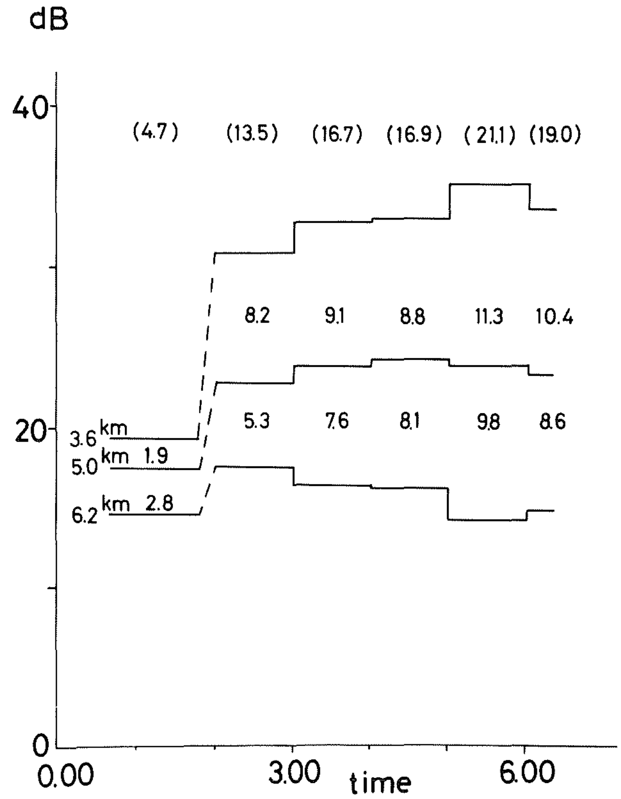

Figure 5 Time variations of 10 log Ze (dB) at levels of 3.6, 5.0 and 6.2 km and the differences between 10 log Ze at these levels in II and III periods.

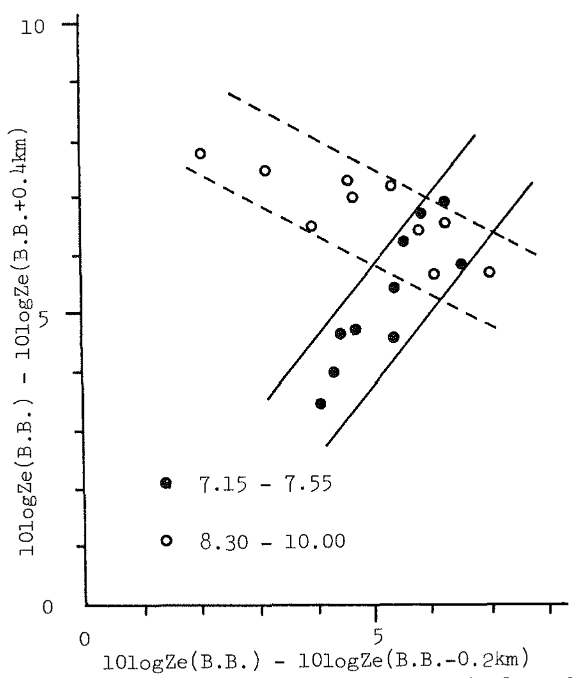

Figure 6 Relationships between vertical gradients of 10 log Ze above and below the central level (drawn B.B.) of bright band on June 28. Abscissa and ordinate are the differences between 10 log Ze at B.B. and at the level higher by 0.2 km than B.B. and between 10 log Ze at B.B. and at the level lower by 0.4 km than B.B. respectively.

6.2.7

INTERPRETATION OF FOIL IMPACTOR IMPRESSIONS OF WATER AND ICE*

C. A. Knight, N. C. Knight, W. W. Grotewold, and T. W. Cannon

National Hail Research Experiment
National Center for Atmospheric Research
Boulder, Colorado 80303

1. INTRODUCTION

Foil impactors, devices by which thin, metal foil is exposed on aircraft to impacts of hydrometeors, have been in use for several years (e. g., Brown, 1958; Duncan, 1966; Cornford, 1966). Several determinations of the functional relation between raindrop size and imprint size have been made, of which the latest is by Shecter and Russ (1970). The use of the foil impactor in the past has been largely limited to clouds containing rain, snow and small graupel, and investigators have expressed confidence that these forms of precipitation can be distinguished by the nature of the impressions produced on the foil (e. g., Miller et al., 1967; Church et al., 1975).

The use of a foil impactor on the South Dakota School of Mines and Technology T-28, an aircraft armored to enable penetration through hailstorms (Sand and Schleusener, 1974), has extended the range of use of the instrument. The T-28 has been used in the National Hail Research Experiment (NHRE), one early objective of which was to evaluate the Soviet accumulation zone model of hail formation (Sulakvelidze et al., 1967). In this model, hail is thought to grow within zones of high concentrations of large, supercooled water drops balanced in fairly strong updrafts. It was therefore very important to make unequivocal determination of the phase of precipitation within hailstorms, and interpretation of impressions on foil was almost the only means available during the early stages of NHRE. Reported data on the T-28 penetrations (May, 1974; Musil et al., 1976) include the results of these interpretations. Liquid water drops of several-millimeter size were reported to exist at -10 to -15°C within the storms, though not in the large concentrations claimed for accumulation zones.

Because of the very great importance of firmly establishing the presence of large, supercooled water drops (their presence or absence might have a large impact upon the possibilities of hail suppression by seeding with ice nuclei), an attempt to "calibrate" the interpretation of the foil impressions has been made.

2. THE INSTRUMENT

The possibility of using a crossbow to achieve the impact velocities needed for calibration arose in discussion between T. Kyle, W. Sand and C. Knight. (We have since learned that crossbows were used at CSIRO in Australia for similar purposes.) The instrument was designed, constructed, and made operational by W. Grotewold and T. Cannon. A crossbow manufactured by "Dave Benedict Crossbows," Chatsworth, California, was used, with a special, 200 lb. pull bow, an extra 4.3 cm. spacer between the bow and the stock, and a specially made, light weight arrow (11.5 grams), to achieve a velocity between 90 and 95 m/sec. Without the spacer and with a 30 gram arrow, speeds of 60 to 65 m/sec. were attained. The arrow is fitted with attachments so that it travels down a "track" consisting of two, tightly strung piano wires. A serious problem was stopping the arrow in a reasonable distance without destroying it. This was accomplished by mounting fairly stiff brushes beneath the track and placing riders on the track itself in the path of the arrow.

A small section of the curved, grooved backing (38 mm radius; 250 microns groove spacing; 14 x 20 mm area) is attached midway along the length of the arrow, extending upwards. The target -- a water drop or ice particle -- is suspended on a thread in such a position that the small section of foil impactor hits it while traveling at its maximum velocity. The velocity is measured by a stroboscopic technique.

3. RESULTS

Two sets of experiments have been done. One, with the early version capable of 60-65 m/sec., was done at the Elk Mountain Laboratory of the University of Wyoming. The other, at 90-95 m/sec., was done at NCAR. A systematic size calibration has not been completed because, as pointed out by Shecter and Russ (1970), the exact calibration probably depends upon the details of the aerodynamics, and these are not precisely duplicated in the experiment. The front of the aircraft version of the foil impactor is

* This research was performed as part of the National Hail Research Experiment, managed by the National Center for Atmospheric Research and sponsored by the Weather Modification Program, Research Applications Directorate, National Science Foundation.

much larger than the 20 x 14 mm section mounted on the arrow. The interpretation of the different kinds of imprints was the major purpose, and the results are as follows:

a) An impact with a particle tends to mold the foil locally into the grooves in the backing plate. Another feature that is sometimes present and sometimes not is a ridge in the foil surrounding the imprinted portion. The presence of such a raised rim has been used as partial evidence of phase, the idea being that liquid spreads out upon impact, pushing up this rim, whereas ice does not. A first result of the present work is to establish that the rim reflects the looseness of the foil over the backing, not the nature of the impacting particle. Such rims never form when the foil is tight, and always form when it is loose. In the experiments the looseness was nearly impossible to control, since it was influenced by aerodynamic and other factors. The looseness usually varied over the foil area, often giving partial rims. Our impression is that the same is true on the airborne foil impactor, though more work needs to be done on that.

b) The types of particles used in the experiments were liquid drops, frozen drops, partially frozen drops, dry rime and compacted snow, soaked rime and compacted snow (slush), and a few natural, small graupel. Types of imprints are shown in the figures. Regarding identification of the nature of the particles, we conclude that distinction between liquid drops, solidly frozen drops, and spherical, very slushy particles (as one gets immediately upon nucleating a drop supercooled to -10°C) is difficult and often impossible. The ice impressions sometimes had a somewhat more ragged edge, but sometimes did not. The molding of the foil into the grooves was uniform and even in all of these cases. Evidently the impact energy is sufficient to crush the solid ice completely, and cause it to behave much like a liquid.

Distinction between rime, including slushy rime, and these above particles is unequivocal, both by imprint shape and by uneven borders and uneven molding of the grooves.

c) A few natural graupel of one to two mm. size were fastened on the thread and impacted against the foil at 60-65 m/sec. Their density was not measured, but they were the heavily rimed but very light graupel found in winter snowstorms. They left virtually no imprint on the foil, though the thread itself made a clear impression.

4. CONCLUSION

We conclude that rime particles may be distinguished from water drops by the nature of the impressions left on the foil, but that solid ice particles may not be distinguished with certainty from liquid drops except when they have distinctly non-spherical shapes. The previous interpretations of foil data within hailstorms are subject to this amount of uncertainty.

5. REFERENCES

Brown, E. N., 1958: A technique for measuring precipitation particles from aircraft. J. Meteor., 15, 5, 462-466.

Church, J. F., K. K. Pocs, and A. A. Spatola, 1975: The continuous aluminum-foil hydrometeor sampler; design, operation, data analysis procedures, and operating instructions. AFCRL-TR-75-0370, Instrumentation Papers, No. 235. Air Force Cambridge Research Laboratories, Hanscom AFB, Mass. 01731, 70 pp.

Cornford, S. G., 1966: A note on some measurements from aircraft of precipitation within frontal clouds. Quart. J. Roy. Meteor. Soc., 92, 105-113.

Duncan, A. D., 1966: The measurement of shower rainfall using an airborne foil impactor. J. Appl. Meteor., 5, 198-204.

May, E. L., 1974: Analysis of foil impactor data from armored aircraft penetration of hailstorm. Report 74-9, Institute of Atmospheric Sciences, South Dakota School of Mines and Technology, Rapid City, S. Dak., 57701, 58 pp.

Miller, A. H. P. B. MacCready, Jr., and D. M. Takeuchi, 1967: Cloud physics observations in South Dakota cumulus clouds. Final Report MRI 67 FR-626. Prepared for the Institute of Atmospheric Sciences by Meteorology Research, Inc., Altadena, California, 59 pp.

Musil, D. J., E. L. May, P. L. Smith, Jr., and W. R. Sand, 1976: Structure of an evolving hailstorm. Part IV: Internal structure from penetrating aircraft. Mon. Weather Rev., in press.

Sand, W. R., and R. A. Schleusener, 1974: Development of an armored T-28 aircraft for probing hailstorms. Bull. Amer. Meteor. Soc., 55, 1115-1122.

Schecter, R. M., and R. G. Russ, 1970: The relationship between imprint size and drop diameter for an airborne drop sampler. J. Appl. Meteor., 9, 123-216.

Sulakvelidze, D. K., N. Sh. Bibilashvili, and V. F. Lapcheva, 1967: Formation of precipitation and modification of hail processes. Israel Program for Scientific Translation, Jerusalem, Israel, 208 pp.

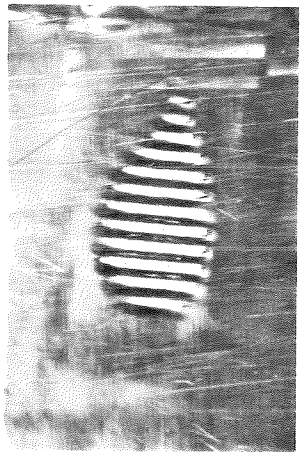

Fig. 1

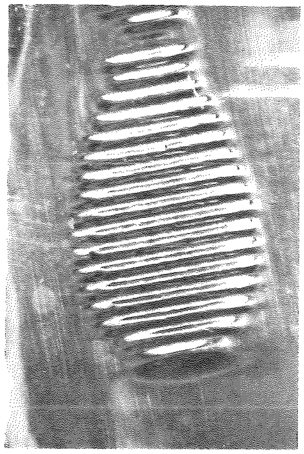

Fig. 2

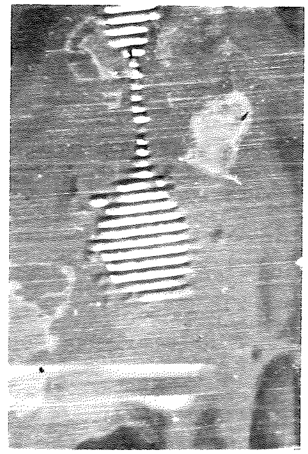

Fig. 3

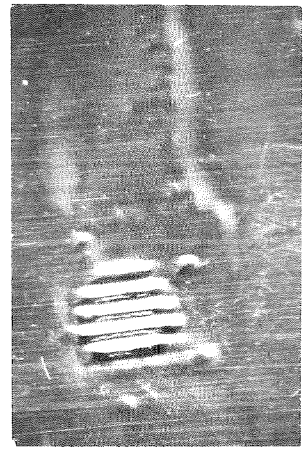

Fig. 4

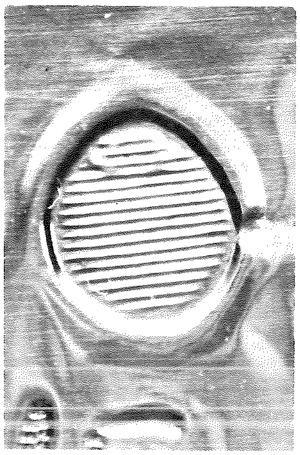

Fig. 5

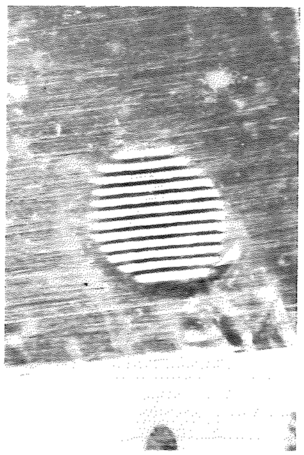

Fig. 6

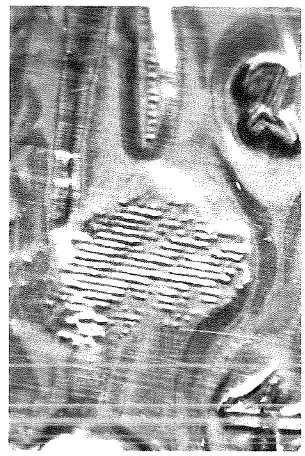

Fig. 7

Fig. 8

FIGURE CAPTIONS: The scale in all figures is given by the 250 micron groove spacing. Figs. 1 and 2 are impressions of a frozen drop and a liquid drop, impacted at between 90 and 95 m/sec. Figs. 3 and 4 show a liquid and a frozen drop impacted at between 60 and 65 m/sec. Figs. 5-8 are all 60-65 m/sec: 5 is a liquid drop impacted on loose foil, 6 on tight foil, showing the influence on the development of a rim; 7 is a piece of rather hard rime, showing the uneven impressions, and 8 is the very slight imprint of a natural, winter graupel. Note the imprint of the thread in several of the photos.

6.2.8

DROP-SIZE DISTRIBUTIONS IN UNICELL, MULTICELL AND SQUALL LINE STORMS

F. PASQUALUCCI

National Institute for Telecommunications Research
of the
Council for Scientific and Industrial Research
Johannesburg, Republic of South Africa

1. INTRODUCTION

Measurements of drop-size distributions in rainfall have been and are being made using various types of instruments. At the beginning screens, filter paper, flour, etc., were used and one of the main disadvantages was the enormous amount of work necessary to measure the large number of raindrop spectra which are required to give a representative sample during a single rainstorm.

To overcome this problem optical and electro-mechanical distrometers have recently been developed and these devices allow the drop-size distributions to be automatically evaluated. A limitation which is common to all the above instruments, is the relatively long integration time (usually one minute or more) which they require to give statistically meaningful drop-size spectra and this is due to the small volume of precipitation they can sample.

The relatively long sampling time can be a severe limitation in certain weather systems like convective thunderstorms, where the short term (of the order of seconds) variation of drop-size distributions could give important clues to the physical processes involved in the formation and evolution of rain.

A Doppler radar pointed vertically is an ideal instrument for drop-size distribution measurements because of its capability of sampling large volumes of precipitation. The main error in radar measurements at vertical incidence arises from the uncertainty in the estimate of the vertical air velocity.

The method which has yielded the greatest success in estimating vertical air velocity is the one suggested by Rogers (1964) and with this method the value of the vertical air velocity has been determined experimentally with a maximum accuracy of $\pm$ 1 m sec $^{-1}$. This uncertainty in the vertical air velocity still leads to intolerably large errors in the estimate of the drop concentration as shown by Atlas and others (1973). To maintain the particle concentration errors within about +100% to -50% over the size range 0,5 mm to 4 mm, the value of the vertical air velocity must be estimated to better than $\pm$ 0,25 m sec $^{-1}$. One way to obtain this accuracy, especially in convective storms, is to make the radar measurements at very low altitudes where, as shown by Pasqualucci (1974), the values of the vertical air velocity do not exceed $\pm$ 0,25 m sec $^{-1}$. Previous radar measurements reported in the literature have been made using pulse Doppler radar systems at altitudes above 300 m and, as a result, the errors in the estimated concentration of raindrops can easily be of the order of -250% to +1000% over the particle size range 0,5 mm to 4 mm.

This paper will discuss drop-size distributions measured in different storm systems with a 35 GHz P-N coded Doppler radar. The three dimensional reflectivity of the analysed storms was monitored with an S-band narrow-beam (1.1°) radar and their structure is representative of most of Transvaal thunderstorms. All the measurements were made at vertical incidence at a mean altitude of 19 m over rainfall rates ranging from 1 mm hr $^{-1}$ to 100 mm hr $^{-1}$. The time interval between the measurements was 10 sec and the integration time was also 10 sec.

To estimate the raindrop concentration the correct Mie backscattering cross-section was used for drops above 0.8 mm diameter because, at the radar operating wavelength of 8.6 mm, the Raileigh scattering approximation is not valid anymore.

2. PARAMETERISATION OF DROP-SIZE DISTRIBUTIONS

Drop-size distributions are usually represented graphically as a histogram of the number of drops N(D) per unit volume and for a certain diameter interval versus the drop diameter D. Some difficulties arise when a large number of drop-size spectra have to be compared, as in the case of the presentation of the time variations of drop-size distributions during a complete storm. One method is to plot successive distributions in a slanting parallel perspective manner to obtain a type of three-dimensional representation in two dimensions. For a more detailed analysis the raindrop concentration N(D) can also be plotted versus time for different drop diameters D. Both these methods have the disadvantage of not giving a simple quantitative description of the drop-size distribution spectra.

In this investigation the measured drop-size distributions will be parameterised using an exponential model of the form:

$$N(D) = No\ e^{-\Lambda D} \tag{2.1}$$

The parameters No and Λ of expression (2.1) are varied so that the water content W, the radar reflectivity factor Z, and the rainfall rate R of the parameterised distribution are least square fitted to W, Z and R calculated from the measured drop-size spectra. The non-linear least square fitting computer program used in this parameterisation is based on a modification by Fletcher (1971) of the Lavenberg-Marquardt technique. Given a set of equations:

$$Fi\ (\underset{\sim}{x}) = 0$$

for

$$i = 1,2,3 \ldots\ldots\ldots\ldots m\ (\geq n) \tag{2.2}$$

$$x = (x_1, x_2, x_3 \ldots\ldots x_n)^T$$

and given the initial values for $\underset{\sim}{x}$, the program attempts to solve the equations to a given accuracy. It does this by adjusting the values of $\underset{\sim}{x}$ so that the following error criterion Φ is a minimum:

$$\Phi = \sum_{i=1}^{m} [Fi\ (\underset{\sim}{x})]^2 \tag{2.3}$$

This is achieved by setting up and solving the so-called normal equations:

$$(J^T J + \lambda I)\, \underset{\sim}{\delta} = -J^T \underset{\sim}{F} \tag{2.4}$$

for the corrections $\underset{\sim}{\delta}$ to $\underset{\sim}{x}$ on an iterative basis. J is the Jacobian matrix and each iteration is described by:

$$J_{iJ} = \frac{\delta F i}{\delta x_i} \tag{2.5}$$

I is the identity matrix and λ is an automatically adjusted constant which controls the convergence of the process. When λ is small, the method approximates the Gaussian-Newton method, and when λ is large the method approximates the steepest descent approach.

Besides certain control parameters, two computer subroutines must be provided. These subroutines calculate respectively:

(a) The $F i\ (\underset{\sim}{x})$ at each stage.

(b) The coefficients of the normal equations, that is $J^T J$ and $-J^T \underset{\sim}{F}$, at each stage.

In the particular application of model fitting, the $F i\ (\underset{\sim}{x})$ would include the residual values which are the difference between calculated and measured values.

The equations used in this parameterisation are derived from the expression which defines the water content W, radar reflectivity factor Z and rainfall rate R for an exponential distribution whose parameters are No and Λ.

The expressions are the following:

$$W = \frac{\pi}{6} \int_0^\infty N_o\, D^3 e^{-\Lambda D}\, dD \tag{2.6}$$

$$Z = \int_0^\infty N_o\, D^6 e^{-\Lambda D}\, d\, D \tag{2.7}$$

$$R = \frac{\pi}{6} \int_0^\infty v(D)\, N_o\, D^3 e^{-\Lambda D}\, dD \tag{2.8}$$

The three quantities W, Z and R can be expressed now as a function of No and Λ. In the case of R the fall speed used is given by expression (2.9):

$$V\ (D) = 10.44 - 11.5\ e^{-0.6 D} \tag{2.9}$$

Equations (2.6), (2.7) and (2.8) can then be solved and written as:

$$W = \frac{\Gamma(4)}{\Lambda^4} \text{No} \frac{\pi}{6} = \text{No} \frac{\pi}{\Lambda^4} \quad (2.10)$$

$$Z = \frac{\Gamma(7)}{\Lambda^7} \text{No} = \text{No} \frac{720}{\Lambda^7} \quad (2.11)$$

$$R = \frac{\pi}{6}\left[\frac{10.44 \text{ No } 3!}{\Lambda^4} - \frac{11.15 \text{ No } 3!}{(\Lambda + 0.6)^4}\right] \quad (2.12)$$

$$= \text{No}\left[\frac{0.1181}{\Lambda^4} - \frac{0.1260}{(\Lambda + 0.6)^4}\right]$$

The units used in equations (2.10), (2.11) and (2.12) are:

W in $mm^3 m^{-3}$, Z in $mm^6 m^{-3}$, R in mm hr^{-1}, No in $m^{-3} mm^{-1}$, Λ in mm^{-1}. It should be noted that the equation for R is valid for the fall speed law given in expression (2.9) which is for an altitude of 2000 m above sea level. Equations (2.10), (2.11) and (2.12) are the ones used in the parameterization program.

3. DROP-SIZE DISTRIBUTION MEASUREMENTS

The radar measurements of drop-size distributions were made in three different storms whose structure is representative of most of Transvaal thunderstorms. The first storm (storm C) was a unicell storm and it developed in the afternoon of the 3rd March 1972. The S-band radar observations showed that this storm was one of two isolated stationary storms. It grew from 70 km^2 to 250 km^2, an increase by a factor of 3.5 which took place in a 20 minute period, ending at 14h26. It shrank back to its original size during the next half an hour and moved about 5 km to the east. The development and the shrinkage seemed to occur concentrically about the original echo and it always remained a monocell storm.

The second storm analysed (storm E) developed on the 22nd March 1972. It started off at 13h00 as several scattered storms 55 to 70 km south of the S-band radar station. The storms were localised along an east-west line of approximately 120 km. While the storm complex moved in a north-northeasterly direction at about 20 km hr^{-1}, new cells formed in between the older ones and merged while others dissipated. It looked like the development of cells took place at the leading edge of the squall line, mainly on the left end of the line and occasionally also on the right end. The squall line reached its maximum east-west extension of about 170 km around 16h30 and at about 17h20 it started to dissipate and split up into individual clusters of relatively light precipitation.

The third storm (storm B) started to develop at about 13h45 on the 2nd March 1973. It moved steadily ESE at about 30 km hr^{-1}, remaining fairly average in size and multicellular. An hour later it started to grow mainly on the right flank by forming new storms there. New cells also formed within the mother complex and along the leading edge which, at certain times, advanced at about 60 km hr^{-1}. In general, cells moved in a ENE direction at 35-40 km hr^{-1}. Storm tops were between 8 km and 10 km, and very seldom they went up to 10.5 km.

The 35 GHz Doppler radar started measuring at vertical incidence at 16h11 in storm B, at 14h20 in storm C and at 16h02 in storm E. For each storm the derived drop-size distributions were used to compute various rainfall parameters like the rainfall rate R, the radar reflectivity factor Z and the median volume diameter Do. The following Z-R and Do-R mean relationships were derived for every storm using a least square fit method:

Storm C	-	$Z = 224 R^{1.27}$	(3.1)
Storm B	-	$Z = 167 R^{1.46}$	(3.2)
Storm E	-	$Z = 215 R^{1.34}$	(3.3)
Storm C	-	$Do = 0.45 R^{0.38}$	(3.4)
Storm B	-	$Do = 0.76 R^{0.24}$	(3.5)
Storm E	-	$Do = 0.71 R^{0.28}$	(3.6)

In the above expressions Do is in mm, R in mm hr^{-1} and Z in $mm^6 m^{-3}$. For each data point the following two quantities are calculated:

$$\Delta R = R - Rc \quad (3.7)$$
$$\Delta Do = Do - Doc \quad (3.8)$$

Where Rc and Doc are derived from the mean relationships using the measured radar reflectivity factor and rainfall rate, and R and Do are the measured rainfall rate and median volume diameter respectively.

The drop-size spectra are parameterised as discussed in paragraph (2) and the two quantities No and Λ are calculated. In order to analyse the time variation of the drop-size distributions, No, Λ and R are plotted versus time and shown in Fig. (3.1), Fig. (3.3) and Fig. (3.5) for storm C, B and E respectively. The quantities ΔR and ΔDo are also plotted versus time to study their correlation and the graphs are shown in Fig. (3.2), Fig. (3.4) and Fig. (3.6).

4. DISCUSSION AND CONCLUSION

The following can be deduced by looking at the data from storms C, B and E:

(a) There is no correlation between No and Λ except for parts of storm B where the highest values of No are correlated with the highest values of Λ.

(b) No shows larger variations in the unicell and multicell storm than in the squall line.

(c) ΔR shows some meaningful correlation with $-\Delta Do$. This correlation is stronger for storms C and B than for storm E.

(d) When ΔR and $-\Delta Do$ are correlated and ΔR is positive and $-\Delta Do$ is negative, No has a high value indicating a high concentration of the population of small drops. When the opposite happens (ΔR negative and $-\Delta Do$ positive), No assumes a low value indicating a low concentration of the population of small drops.

The correlation between ΔR and $-\Delta Do$ indicates that the variation of the small drops population ($D < \sim 1mm$) is a cause of part of the deviation of the data points from the mean Z-R relationship. The high variability of No, especially in storms C and B, could be caused by the bigger drops breaking up or by the drops being sorted either by a time-variable vertical air velocity or by shear. If the break-up mechanism is the main cause, this could indicate the presence of severe turbulence, steep changes of the electric field in the atmosphere, lightning or a combination of these factors. It should be mentioned that, in the case of the squall line storm, a vertical air velocity shear of $9.3\ 10^{-2}\ sec^{-1}$ was indeed observed at an altitude between 300 m and 450 m. This kind of shear, which only lasted for a short time (about two minutes) could easily be the cause of some of the sudden jumps in the value of No which have been observed.

The above discussion clearly shows that a vertically pointing Doppler radar with the capability of observing targets at short range and with high range resolution, can be a very useful experimental tool for thunderstorm research. The possible investigations include drop-size distribution measurements with a good degree of accuracy and the determination of vertical air velocity profiles. This type of experiments should contribute to increase our knowledge of the complex physical processes involved in the formation and evolution of rain.

REFERENCES

ATLAS, D., SRIVASTAVA, R.C., and SEKHON, R.S., 1973. Doppler radar characteristics of precipitation at vertical incidence. Review of Geophysics and Space Physics, Vol. ii, No. 1, 1-35.

LHERMITTE, R.M., 1971. Probing of atmospheric motion by airborne pulse Doppler radar techniques. Journal of Applied Meteorology, Vol. 10, No. 2, 234-236.

PASQUALUCCI, F., 1974. Experimental determination of mean Doppler-reflectivity relationship with a vertically pointing Doppler radar. Geophysical Research Letters, Vol. 1, No. 6, 249-251.

PASQUALUCCI, F., 1975. Low altitude Doppler radar measurements of precipitation at vertical incidence. Proceedings of the 16th Radar Meteorology Conference, American Meteorological Society, Houston, Texas, April, 1975.

ROGERS, R.R., 1964. An extension of the Z-R relationship for Doppler radar. Proceedings 11th Weather Radar Conference, American Meteorological Society, Boulder, Colorado, September, 1964.

FLETCHER, R., 1971. A modified Marquardt subroutine for non-linear least squares. United Kingdom Energy Authority Research Group. Report AERE-R 6799.

CARTE, A.E., and G. HELD, 1973. Thunderstorms in 1971/72. CSIR Research Report 322. Atmospheric Physics Division of the National Physical Research Laboratory, Pretoria, South Africa, 1973.

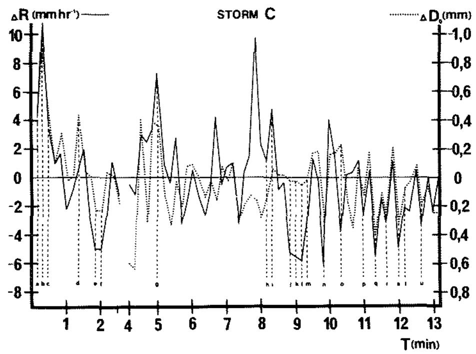

Fig 3.2 ΔR and ΔDo versus time for storm C

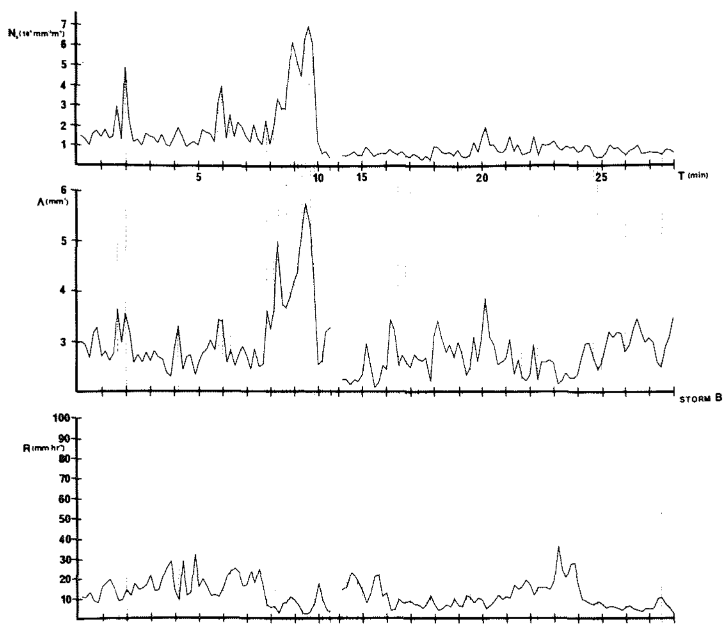

Fig 3.3 No, Λ and R versus time for storm B

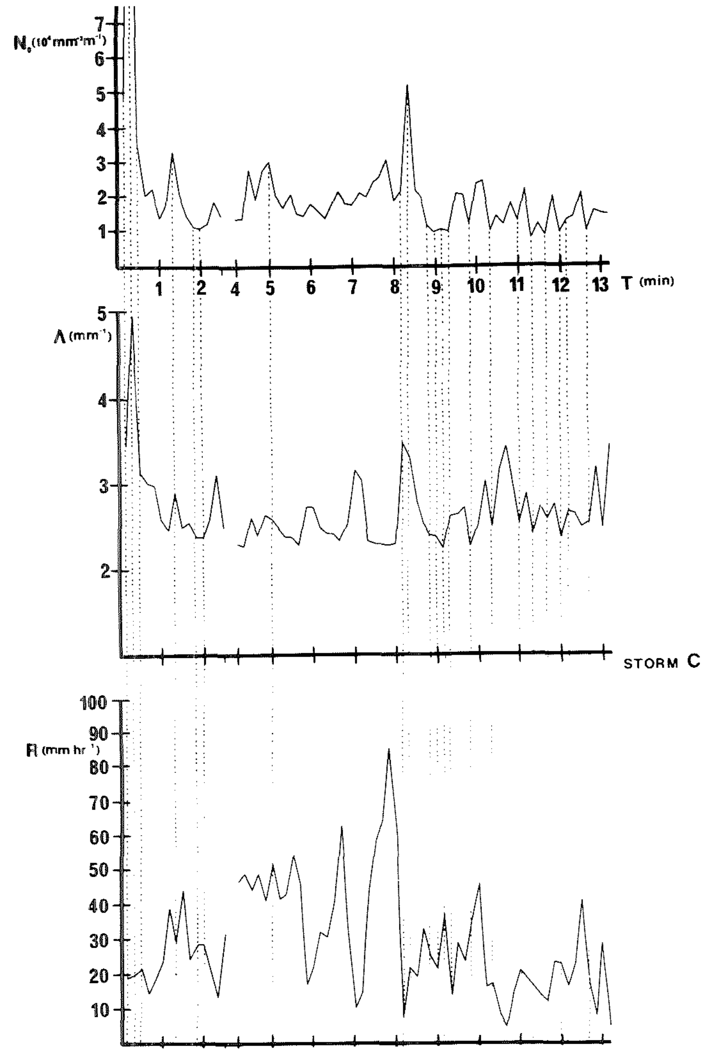

Fig 3.1 No, Λ and R versus time for storm C

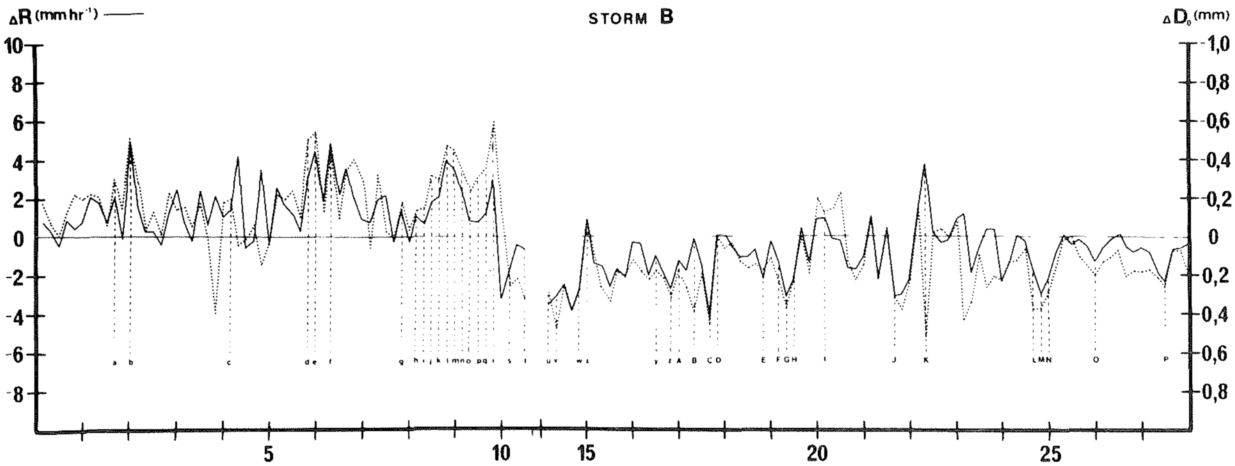

Fig 3.4 ΔR and ΔDo versus time for storm B

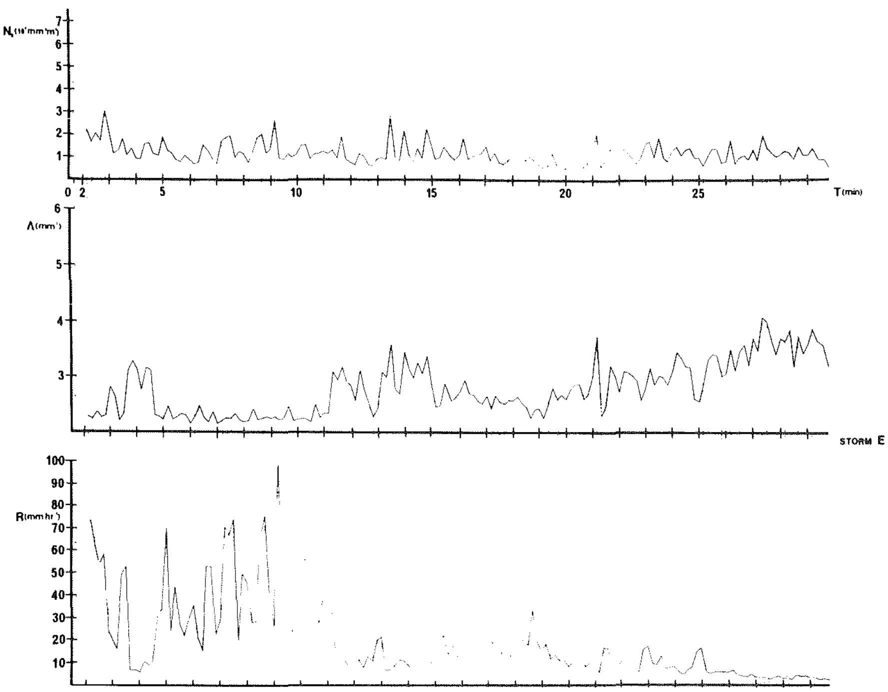

Fig 3.5 No, Λ and R versus time for storm E

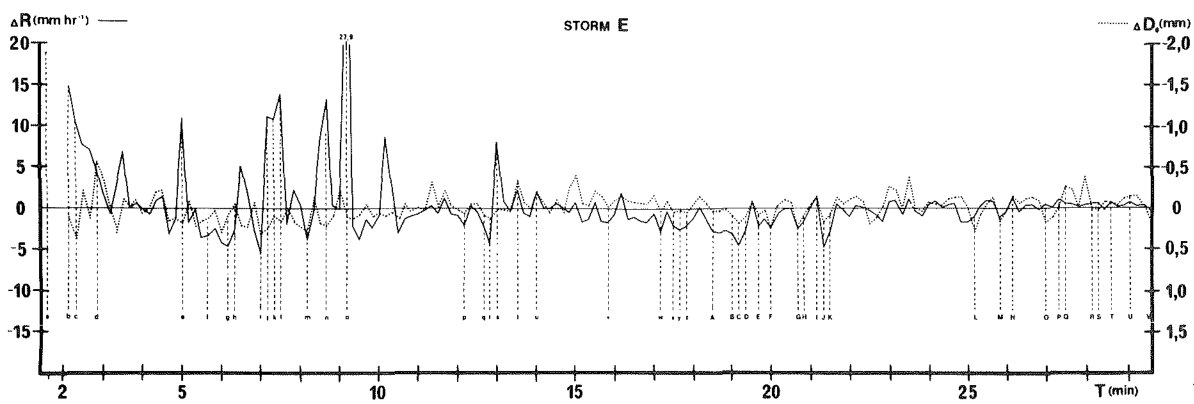

Fig 3.6 ΔR and ΔDo versus time for storm E

6.3.1

NUMERICAL MODELING OF RAIN FORMATION IN A WARM CUMULUS

B. N. Sergueyev

Central Aerological Observatory,
Moscow, USSR

1. INTRODUCTION

The development of rain in warm cumulus clouds is believed to occur due to the condensation and stochastic coalescence of cloud droplets. The characteristics of the drop size distribution which are essential for this process are controlled mainly by vapor condensation. The size distribution and the physico-chemical properties of condensation nuclei may play an essential role in this last process. The sufficiently complete and accurate description of the droplet growth by condensation on hygroscopic nuclei is difficult to incorporate in a cloud model with a sophisticated cloud dynamics. In order to describe adequately the process of rain formation as a whole from the activation of cloud nuclei to the growth of raindrops we have used the simple one-dimensional cloud model with a fixed airflow. The process of rain formation and the dependence of rain characteristics on the nuclei size distribution and on soluble matter content of nuclei are studied within the framework of this model.

2. THE CLOUD MODEL

The cloud formed in a steady updraft with the given vertical velocity profile is considered. The characteristics of the cloud are assumed to be uniform within any horizontal level of the cloud and depend on the vertical coordinate only.

The model incorporates the activation of condensation nuclei, the condensational growth and stochastic coalescence of cloud drops, the breakup of large raindrops, the mixing of the cloud with the surrounding atmosphere and the drop sedimentation. The drop size distribution $\mathcal{F}(r,z)$ formed by all these processes in the cloud was calculated where r is the drop radius, z the vertical coordinate. $\mathcal{F}(r,z)dr$ is equal to the mean number of drops having the radius from r to $r+dr$ in 1 cm^{-3} at the z level.

Firstly the droplet size distribution $\mathcal{F}_0(r,z)$ formed by condensation on hygroscopic nuclei spectrum was calculated using the Lagrangian framework. An ascending uniform cloud volume is considered. It is assumed that the surrounding air containing condensation nuclei is entraind in the cloud volume and uniformly mixed with the cloudy air. The influence of mixing on a droplet size distribution is simulated in such a manner as Mason and Chien (1962) have done. The profiles of the temperature $T(z)$, air density $\rho(z)$, vapor supersaturation $\delta(z)$, and droplet spectrum $\mathcal{F}_0(r,z)$ are calculaded using the balance equations for water vapor and heat, hydrostatic equation and equations for the droplet concentration and radius change rate. The profiles of the vertical velocity u_z, entrainment rate $K_z=(1/M)(dM/dz)$ (M is the air mass in the cloud volume), parameters of the atmosphere and condensation nucleus spectra are assumed to be known values in the calculations. The nuclei size distributions are used in the discrete form. From 30 to 60 nucleus classes are used for the interval $0.016 \leq r_n \leq 10 \mu m$ where r_n is the nucleus radius, and from 10 to 20 classes for giant nuclei ($1 \leq r_n \leq 10 \mu m$).

It should be noted that the techniques employed in the calculation of the condensation droplet growth eliminates numerical spreading of droplet spectra.

Then the drop size distribution $\mathcal{F}(r,z)$ formed by the all abovementioned processes is determined by the stationarization method. The droplet size distribution $\mathcal{F}_0(r,z)$ formed by condensation is used as the initial distribution.

The equation for the change rate of the drop size distribution is expressed in terms of the drop mass distribution $f(x,z,t)$ as (Takahashi, 1973)

$$\frac{\partial f}{\partial t} = -\frac{\partial}{\partial z}[(u_z - V_x)f] + \mathcal{D}\frac{\partial^2 f}{\partial z^2} - K_t f + (f/\rho)\frac{\partial}{\partial z}(\rho u_z) - \frac{\partial}{\partial x}\left(\frac{dx}{dt}f\right) + \int_{x_0}^{x/2} f(x-y)K(x-y,y)f(y)dy - f(x)\int_{x_0}^{x_m} K(x,y)f(y)dy - f(x)P(x) + \int_{x}^{x_m} f(y)Q(y,x)P(y)dy \qquad (1)$$

where t is time, x the drop mass, V_x the terminal fall velocity, $\mathcal{D}$ the turbulent diffusion coefficient, K_t the entrainment rate, $K(x,y)=\pi(r_x+r_y)^2 E\,|V_x - V_y|$, $E(x,y)$ the collision efficiency, x_0 and x_m are the smallest and the largest mass considered respectively, $P(x)$ is the breakup probability of a drop with mass x in 1s, $Q(y,x)$ the mass distribution of drops produced by disintegration of a drop with mass y.

Boundary and initial conditions are expressed as

$$f(x,z,0) = f_0(x,z) \quad (2)$$

$$\left(\frac{\partial f}{\partial z}\right)_{z=0} = 0 \quad (3)$$

$$f(x,z_0,t) = f_0(x,z_0) \quad (4)$$

$$f(x,z_H,t) = 0 \quad (5)$$

where $0 \leq z \leq z_H$, z_0 and z_H are the cloud base and the cloud top levels respectively, $f_0 = \mathcal{F}_0\, dr/dx$. The condition (4) is formulated for the droplets moving upward.

The problem (1)-(5) is solved with the following approximate method. In the course of solution the values of the condensational growth operator G are compared with these of the stochastic coalescence integrals C. The distribution f is equalled to the droplet distribution f_0 formed by condensation for the mass range $x_0 \leq x < x_a(z)$ satisfying $G > C$. The equation (1) is solved without the operator G for the mass range $x_a(z) < x \leq x_m$ satisfying $G < C$.

In this way, the steady-state source of large drops with masses $x > x_a$ is provided. The large drop size distribution formed by stochastic coalescence, drop breakup and drop sedimentation in the updraft is found. It is clear that the techniqes employed underestimates the large drop concentration to the certain extent. However, the influence of the stochastic coalescence on the droplet size distribution in the mass range $x < x_a$ and that of condensation in the range $x > x_a$ were found to be relatively weak for the considered cases of numerical simulation.

The equation (1) was transformed following Berry and Reinhardt (1974). A logarithmic scale with mass in terms of a parameter j is used: $x = x_0 \exp[(j-1)/\ln\sqrt{2}]$ The size distribution f is replaced by the distribution φ using the expression $xf\,dx = \varphi\,dj$. The drop size scale was divided into 61 units and had a minimum radius of 4 μ and a maximum radius of 4 mm.

The values for collision efficiency E were assumed to be equal to ones computed by Klett and Davis (1973) for drop radii $r \leq 70\,\mu$m and equal to 1 for drop radii $r > 70\,\mu$m. The instantaneous breakup was assumed to occur for drops with radii $r \geq 3564$ mm ($j \geq 60$). The $Q(y,x)$ expression was taken according to Srivastava (1971).

The equation (1) was integrated numerically by a finite difference method. The procedure used is based on the conservativ second-order scheme. The stochastic coalescence integrals were calculated by using the Berry and Reinhardt (1974) method. The space increment Δz was 100-200 m, and the time increment Δt was 5s.

3. CLOUD PARAMETERS

The cloud depth H was assumed to be 1.5 km, 2 km and 3 km, and the cloud base level $z_0 = 1$ km. The maximum updraft was assumed to be ranging from 2.5 ms^{-1} to 5 ms^{-1} at the height of $z - z_0 = 0.6H$, and cloud base updraft ranging from 1 ms^{-1} to 2 ms^{-1} for the vertical velocity profiles used. The entrainment rate profiles were calculated using the given liquid water content profiles which were chosen according to the data of observations in cumuli (Войт и Мазин, 1972). The maximum liquid water content values are 1.3 gm^{-3}, 2 gm^{-3}, 2.4 gm^{-3} at the height of $z - z_0 = 0.8H$ for the clouds having depth of 1.5 km, 2 km, 3km respectively. In the model cloud of 3 km depth the entrainment rate K_z computed is 1.4×10^{-3}m^{-1} at the cloud base, it decreases to 1.3×10^{-4}m^{-1} at the level $z - z_0 = 2$ km and increases sharply to 5×10^{-3}m^{-1} near the cloud top. The turbulent diffusion coefficient was assumed to be 250 m^{2}s^{-1}.

The temperature $T(z_0)$ at the cloud base was taken to be 10°C and the atmospheric pressure $p(z_0)$ at this level 900 mb.

The two types of nuclei size distributions were considered. The former is the distribution of a continental type (Андреев, 1970). The latter is the distribution of a maritime type (Warner, 1969). These distributions decreases as $r_n^{-\nu}$ for $r_n > 0.2\,\mu$m where r_n is nucleus radius. The exponent value ν was adopted to be 4 for the maritime distribution and 4 and 5 for the continental distribution. The mass ratio β of soluble (NaCl) and insoluble nucleus parts was assumed to be 0.02, 0.2, 1.0. The nuclei concentration decreased with a height as $n(z) = n(z_0)\exp[-(z - z_0)/h]$ where $h = 2$ km.

4. RESULTS AND DISCUSSION

The average characteristics of the droplet size distributions formed by condensation in the model cloud are reasonably consistent with the data of observations in clouds (e.g.,Боровиков et al., 1961). Indeed,the concentration of droplets is ~ 100 cm^{-3} for the maritime model cloud and ~ 500-700 cm^{-3} for the continental model cloud. The concentration decreases with height in the cloud in the most cases of numerical modeling. However it may increase with height at middle levels of the model cloud because of nuclei activation due to increasing vapor supersaturation in cases of relatively high entrainment rate. The average droplet radius is 5-15 μm in the model cloud. The relative dispersion of droplet size distribution increases from 0.2 at the cloud base to 0.3-0.4 at middle levels of the model cloud.

The results of the calculations show that the size distribution of droplets growing by condensation on nuclei with radii $r_n > 0.5\,\mu m$ may be approximated as

$$\mathcal{F}(r, z_0) \sim r^{-\lambda(\nu-1)-1} \quad (6)$$

at the cloud base. The λ values increase slightly from 1.13 to 1.29 in the ranges $0.1\ ms^{-1} \leq u_0 \leq 10\ ms^{-1}$ and $0.02 \leq \beta \leq 1.0$ where u_0 is the updraft velocity at the cloud base, β mass ratio of soluble and insoluble nucleus parts. In the case of $\beta = 1.0$, it was found $\lambda = 1.29$ irrespective of u_0. The formula (6) is valid for the droplets with radii $r \gtrsim 2\,\mu m$.

At heights of $100\ m \leq z < 1$-1.5 km range above the cloud base the size distribution of droplets growing on giant nuclei (with radii $r_n \geq 1\,\mu m$) are well described with the formula

$$\mathcal{F}(r) \sim r^{-q}, \; q = \frac{5\nu - 2}{3} \quad (7)$$

derived by Smirnov and Sergueyev (Смирнов и Сергеев, 1973). The calculation indicates that this formula can be used in the interval of $15\,\mu m < r < 30$-$50\,\mu m$. for the model cloud considered. The existence of power size distribution of droplets with these radii is consistent with the data of observations (e.g., Okita, 1961, Конышев и Лактионов , 1966)

In $0 < z < 100$ m height range above the cloud base the size distribution of droplets growing on giant nuclei may be approximated by power functions with exponents which have values between those of (6) and (7).

The expressions (6) and (7) may be used for the experimental verification of the role played by giant nuclei in the formation of cloud microstructure.

In order to elucidate the role of giant nuclei in the process of rain development the size distributions of nuclei were taken in the calculations with and without giant nuclei. This role was estimated to be insufficient in the case of the maritime clouds with the droplet concentration $\sim 100\ cm^{-3}$. In this case droplets of 15-20 μm radii which are effective in the process of stochastic coalescence grow on active ($\beta = 1.0$) nuclei with radii $0.5 < r_n < 1.0\,\mu m$ at the relatively high supersaturation ($\delta \sim 0.3\%$). The rain develops only in the presence of giant nuclei in the cases of continental clouds with the concentration of droplets $\gtrsim 400$-$500\ cm^{-3}$ when soluble matter content ($\beta = 0.2$) of nuclei is typical for continental nuclei. The rain initiated by giant nuclei in the continental cloud with the depth of 2-3 km was rather weak (0.1-$6\ mmh^{-1}$). Rain intensities increase with the increase in the cloud depth, giant nuclei concentration and soluble matter content of nuclei. For examle, the rain intensity at the cloud base was $0.12\ mmh^{-1}$, $1.6\ mmh^{-1}$, $4.3\ mmh^{-1}$ for $\beta = 0.02$, 0.2, 1.0 respectively in the 3 km depth continental cloud. The rain does not develop in the continental cloud with the depth of 1.5 km because of insufficient development of the stochastic coalescence.

The size distributions $\mathcal{F}(r, z)$ of large drops decrease monotonously with the drop radius r in the cases of the weak coalescence development in the model cloud when the rain does not form. The distributions $\mathcal{F}(r, z)$ can be approximated with power functions $\mathcal{F} \sim r^{-q}$ for $r > 50\,\mu m$ where $q = 3.7$-10.6, and decreases with z. These results are in agreement with the data of observations of large drop distributions in warm clouds (e.g., Okita, 1961, Боровиков et al., 1965)

In the cases with the rain a secondary mode of the drop size distribution occurs at the middle and lower levels of the cloud in 600-1600 μm radius range due to drop sedimentation. The large drop size distributions can be well approximated with power functions $\mathcal{F} \sim r^{-q}$ ($q = 2.4$-4.48) at the upper levels of these clouds.

The results of calculations show that large drop concentration is of $\sim 50\ m^{-3}$ for drop of radii $r \geq 125\,\mu m$ at the upper levels of the continental cloud with the depth of 2 km. The concentration of such drops reaches $550\ m^{-3}$ in the cloud with the depth of 3 km. Klazura (1971) observed the concentration of large drops ($r \geq 125\,\mu m$) in the upper regions of warm cumuli over southeast Texas. He found that the average concentration was $43\ m^{-3}$ in clouds having the depth of 1.5-2.3 km and $804\ m^{-3}$ in clouds $\gtrsim 3$ km studied during 1969. We see that the calculated concentrations are consistent with these data. The principal characteristic of these latter is a quite pronounced effect of cloud depth on the concentrations of large drops. According to the calculations these concentrations depend sufficiently not only on the cloud depth but on the vertical velocity, the nuclei size spectrum and nuclei activity too.

The preceeding comparisons of the calculation results with the data of observations in clouds demonstrate our model of the rain formation process to be realistic.

In summary, the present study shows that the formation of large drops and raindrops is probably controlled by condensation nuclei within different nuclei size ranges in warm cumuli of different types. The nuclei with radii $r_n < 1\,\mu m$ can play the main role in this process in typical maritime clouds with low concentrations of relatively large cloud droplets On the other hand, in typical continental clouds with numerous small droplets the large drop formation can be controlled by giant nuclei. It is obvious that in intermediate type clouds with small depths the giant nuclei can serve as a large drop source but in such clouds with large depths this role can be played by the smaller nuclei.

The following should be noted. The freezing probability of large drops is more than that of small droplets. If the drop size spectrum does not decrease too rapidly with drop size increase, then the presence of large drops in a cloud can promote the appearance of ice in it. According to the model calculations large drop size distributions depend on nuclei characteristics thereby the latter can play an important role in the ice initiation in cloud, in some situations at least.

Acknowledgment. I wish to thank Dr. V.I. Smirnov for fruitful discussions.

REFERENCES

Андреев, Б.Г., 1970: Полный спектр частиц естественных аэрозолей и оценка доли активных ядер конденсации. Тр. VII Всес. конф. по физ. облаков и актив. возд., Л., ГИМИЗ, 93.

Berry, E.X, and R.L. Reinhardt, 1974: An analysis of cloud drop growth by collection: part I. Double distribution. J. Atmos. Sci., 31, 1814-1825.

Боровиков, А.М., И.И. Гайворонский, Е.Г. Зак, В.В. Костарев, И.П. Мазин, В.Е. Минервин, А.Х. Хргиан и С.М. Шметер, 1961: Физика облаков, Л., ГИМИЗ, 93.

——, И.П. Мазин и А.Н. Невзоров, 1965: Некоторые закономерности распределения крупных частиц в облаках различных форм. Изв. АН СССР, Физ. атмос. и океана, 1, 291-301

Войт, Ф.Я., и И.П. Мазин, 1972: Водность кучевых облаков. Изв. АН СССР, Физ. атмос. и океана, 8, 1166-1176.

Klazura, G.E., 1971: Measurements of precipitation particles in warm cumuli over southeast Texas. J. Appl. Meteor., 10, 739-750.

Klett, J.D., and M.H. Davis, 1973: Theoretical collision efficiences of cloud droplets at small Reynolds numbers. J. Atmos. Sci., 30, 107-117.

Конышев Ю.В., и А.Г. Лактионов, 1966: Самолетный фотоэлектрический измеритель облачных частиц. Изв. АН СССР, Физ. атмосф. и океана, 2, 766-769.

Mason, B.J., and C.W. Chien, 1962: Cloud droplet growth by condensation in cumulus. Quart. J. Roy. Meteor. Soc., 88, 136-142.

Okita, T., 1961: Size distribution of large droplet in precipitating cloud. Tellus, 13, 509-521.

Смирнов, В.И., и Б.Н. Сергеев, 1973: О связи распределений по размерам ядер конденсации и крупных облачных капель. ДАН СССР, 208, 87-90.

Srivastava, R.C., 1971: Size distribution of raindrops generated by breakup and coalescence. J. Atmos. Sci., 28, 410-415.

Takahashi, T., 1973: Numerical simulation of maritime warm cumulus. J. Geoph. Res., 78, 6233-6247.

Warner, J., 1969: The microstructure of cumulus cloud. Pt.2. The effect on droplet size distribution of the cloud nucleus spectrum and updraft velocity. J. Atmos. Sci., 26, 1272-1282.

WARM RAIN UNDER TRADE WIND INVERSION IN HAWAII

Tsutomu Takahashi

Cloud Physics Observatory,
Department of Meteorology,
University of Hawaii,
Hilo, Hawaii 96720

I. INTRODUCTION

Many scientists have been attracted to high rainfall in Hawaii (Fig. 1). In Hawaii, very moist air in the lower layers and the rapid transition from moist to dry air within a few hundred meters at around 2 km characterizes the trade wind humidity profile. In summer time there is no frontal passage from high latitude, but it rains very frequently (Fig. 2) and inversion height which will determine the cloud depth varies day to day.

In this paper, the rainfall in Hilo during August is classified in terms of the character of the inversion. Upper cyclonic cell and vortex are emphasized to modify the character of the inversion in the Pacific.

Rain is typically warm rain type and recent cloud model showed that giant nuclei do not contribute for rain development although they are important for chemical balance. After maximum rainfall intensity versus inversion height is compared with cloud model, discussion extends to the role of ice crystals in precipitation and the intensification of electricity in maritime cloud.

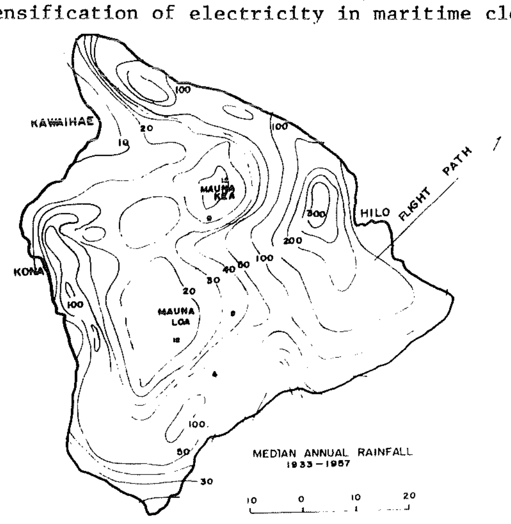

Fig. 1. Annual rainfall (inches) for the Big Island of Hawaii--U.S. Weather Bureau. Flight path for temperature and humidity sounding was also shown.

II. SUMMER RAIN IN HILO, HAWAII

Continuous recordings of rainfall and electric potential gradients in August (1975) as typical of summer rain were shown in Fig. 2.

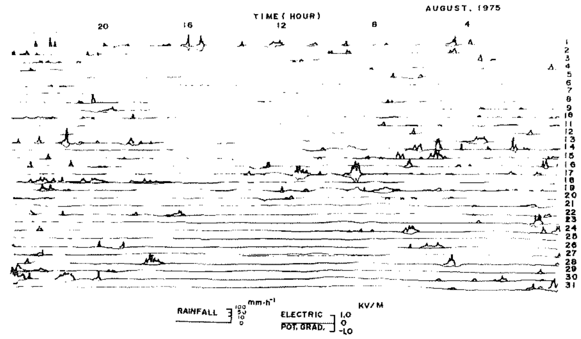

Fig. 2. Rainfall intensity (heavy lines - strain gauge type) and electric potential gradient (thin lines - field mill type) with time in August, 1975, at Hilo, Hawaii. Reader can refer to Takahashi (1975a) for more description of warm rain electricity

It rained almost every day except two days (7th and 25th); rain eased off during the afternoon. Classifications could include morning and evening rain (5th, 8th and 26th), daytime rain (1st, 3rd, 14th, 15th, 16th, 17th, and 20th), night rain (9th, 10th, 21st, 23rd, and 27th), light but long-lasting rain (11th, 18th and 19th).

Since rain development is a strong function of cloud thickness and since cloud height is mainly determined by the inversion height and strength, I attempted to classify rainfall at Hilo in terms of the character of the inversion (Fig. 3).

Temperature profiles obtained at the Hilo Airport Weather Station were shown in Fig. 4a, and humidity profiles in Fig. 4b.

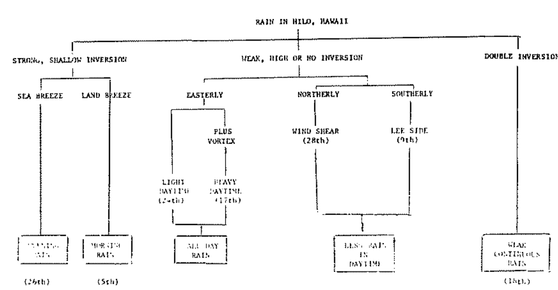

Fig. 3. Classification of rainfall patterns at Hilo, Hawaii.

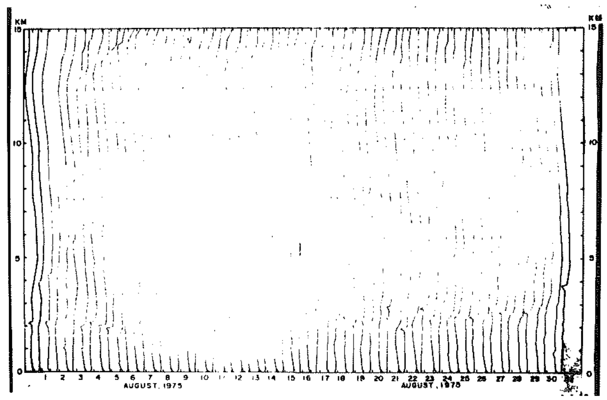

Fig. 4a. Upper temperatures observed by radiosonde at Hilo, Hawaii. Slanted axis is chosen for temperature. Origin of each temperature scale at the ground is 25°C and divisions are at 10°C intervals. When the line is vertical, temperature lapse rate is 6°C km⁻¹.

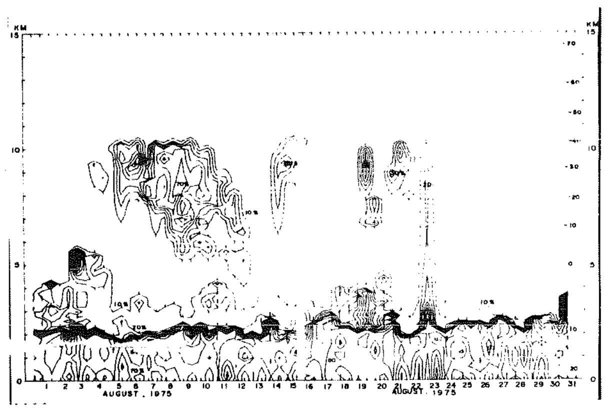

Fig. 4b. Upper relative humidities observed by radiosonde at Hilo (thick solid lines - relative humidity, thin solid lines - temperature).

When the inversion was strong and shallow (1.5 km on the 5th in the afternoon), there was no rain. A shallow inversion around 2 km corresponds to morning rain (5th) and evening rain (26th). When the inversion was higher, light rain also fell in the late morning (24th). Daytime heavy rain occurred when the trade wind cloud deepened. Northerlies and southerlies at cloud level corresponded to less rain, especially during the daytime (28th and 9th), and even when the inversion was weak.

Double inversion corresponded to light but continuous rain (18th). When the inversion is shallow, cloud development is affected by local circulation. In the early morning, cool and dry air is accumulated over the ocean in the lower level to a distance of 15 km from the shore by the land breeze. Cloud develops there and moves successively landward and dissipates shortly after crossing the coast with drizzle (Cessna observation of temperature and humidity, Fig. 5a).

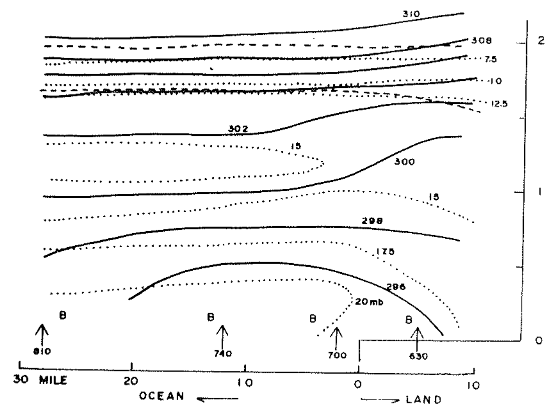

Fig. 5a. Potential temperature (thick line) and water vapor pressure (thin line) in morning. Sounding was done by small spiral climbing of Cessna at positions shown by arrows. Sounding times were shown below each arrow. "B" stands for the location of cloud band. Inversion layer shaded.

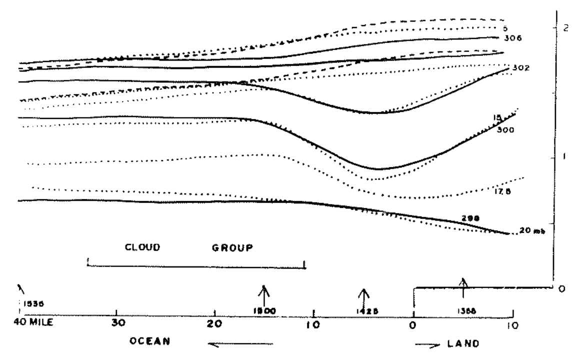

Fig. 5b. Potential temperature (thick line) and water vapor pressure profiles (thin line) in afternoon.

During the daytime (Fig. 5b), sea breeze is intensified by land heating and dry air is introduced from the inversion layer near the coast at a height of 1 km. Less rain during the day might be due to the existence of subsiding dry air near the shore. In the late afternoon, as the land is cooled, this dry air region disappears. Then clouds over the ocean will reach the coast without strong modification, even in the daytime.

Wind direction also affects rainfall in Hilo. Hilo is the lee side when northerly and southerly prevail.

When there is a double inversion, clouds develop at each inversion. Drizzle will be seeded from altocumulus to lower cumulus. The precipitation process will be more efficient and the cumulus will rain out without strong vertical development.

Inversions in summer are affected by two causes. One is by upper cyclonic circulation and the other is by vortex.

Upper wind profile is shown in Fig. 6. Two large upper cyclones moving toward the west hit Hilo on the 3rd and on the 19th (Fig. 7). Weak upper cyclone is also seen on the 13th. All the circulation extended down to 4 km. The upper circulation was preceded and followed by small anticyclonic cells at middle troposphere (3 - 5 km). At each cell passage, winds in the cloud layer change appreciably and the inversion was modified.

Another cause of inversion modification is by vortex. On the 17th, a cyclonic vortex was located south of the island and the easterlies were observed from the surface to 10 km. Cloud developed high and produced heavy rain during daytime in Hilo (Photos 1a and 1b).

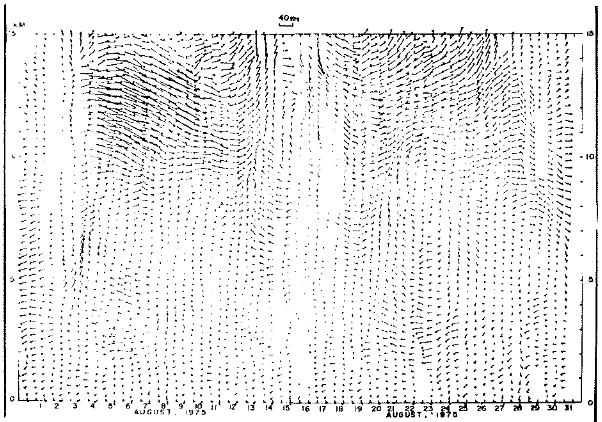

Fig. 6. Upper winds observed by radiosonde at the Airport Weather Station, Hilo, Hawaii.

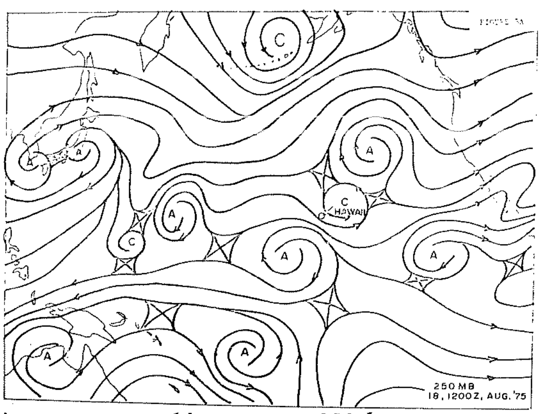

Fig. 7. Streamlines. a: 250mb

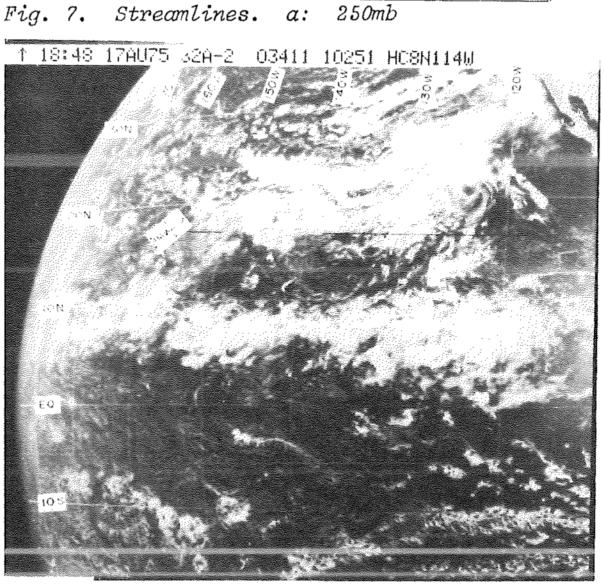

Photo 1a. Satellite picture, 8^h48^m local time (Aug. 17, 1975), by ESSA. Dissipating vortice at 15^oN - 150^oW which travelled from near Panama, originally. New active vortice is seen at 20^oN - 125^oW.

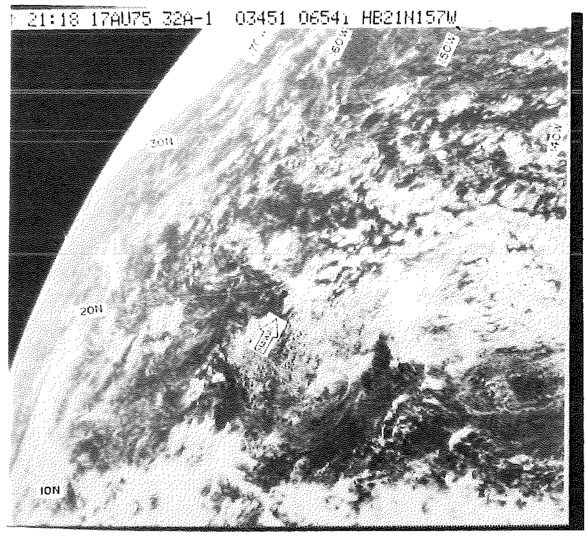

Photo 1b. Satellite picture, 11^h18^m local time (Aug. 17, 1975). Near the island of Hawaii, trade wind clouds are developing at high levels by the effect of the dissipating vortex.

III. WARM RAIN AND CLOUD MODEL

Electric potential gradient changes to negative during the rain and this characterizes the warm rain (Takahashi, 1975a).

Development of warm rain was studied in time dependent cylindrical model (Ogura and Takahashi, 1973), to simulate the raindrop formation from cloud nuclei. The size range of particles is from 0.03 μm to 3.25 mm in radius. The mean salt amount of each drop was kept track of during cloud development and nuclei-drop interactions such as diffusiophoresis, thermophoresis and Brownian motion were included in calculation. Kovetz and Olund's scheme (1969) was used for condensation process (Egan and Mahoney's scheme, 1972, also reached the same conclusion), and Berry's scheme (1967) for collection process. Rain developed within 40 minutes. Drop distribution was shown in Fig. 8a. Drops grow by condensation up to 20 μm in radius and then grow by collection process. In the calculation, giant nuclei ($m>10^{-12}$gm) was removed, but the mode of drop development did not change significantly (Fig. 8b) although mean salt mass of raindrops is one order less than in the case including giant nuclei.

While giant nuclei are important for chemical balance during cloud development (Fig. 9a), they are not important for warm rain development. Instead, cloud droplet concentration seems to be a more critical factor in initiating warm rain (Fig. 9b).

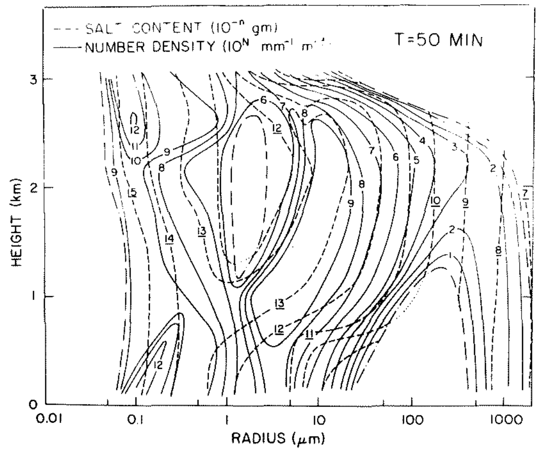

Fig. 8a. Particle and drop density profile (solid line) and salt content of those particles and drops (dashed line) at $T = 50$ min. Number at solid line shows the N when drop density is expressed at $10^N \cdot mm^{-1} \cdot m^{-3}$. Number having underline shows n when salt content is expressed as 10^{-n} g. Maritime case.

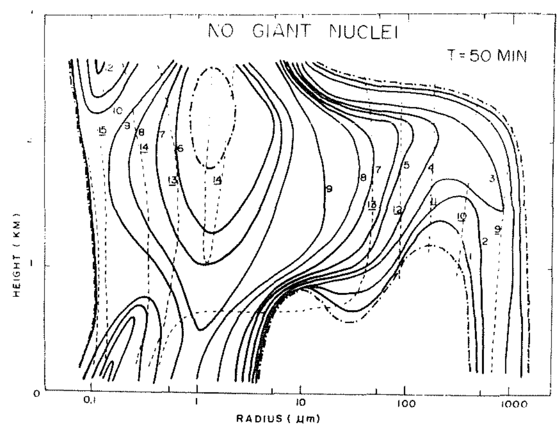

Fig. 8b. Same as Fig. 8a except no giant nuclei.

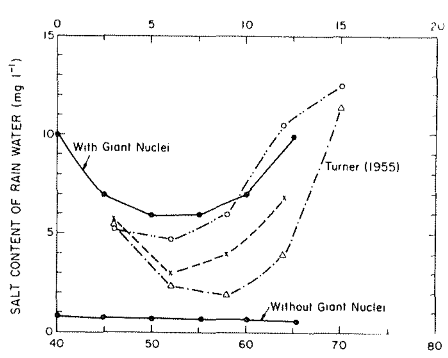

Fig. 9a. Salt content in rain water at the ground, with and without giant nuclei.

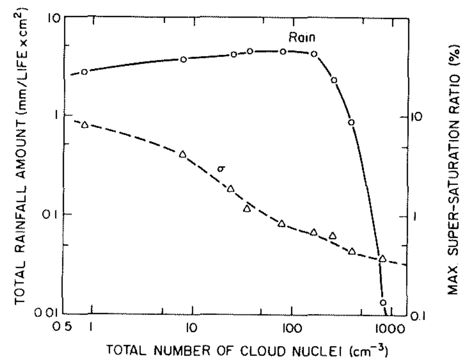

Fig. 9b. Total rainfall as a function of total number of cloud nuclei which have a potential to form cloud droplets (solid line). Dashed line shows the maximum supersaturation ratio in the cloud during entire cloud life.

Maximum rainfall intensity observed in Hilo during the summer of 1975 was analyzed by reference to inversion height (Fig. 10). The large variation of data observed will be due to the large rainfall gradients within showers. An edge of a shower often will hit Hilo. If this is so, only maximum rainfall intensity at each inversion height would be meaningful.

It rains when the inversion is higher than 1.8 km and higher rainfall intensity is observed with higher inversion. When the inversion height is 2.5 km, maximum rainfall is 100 mm per hour.

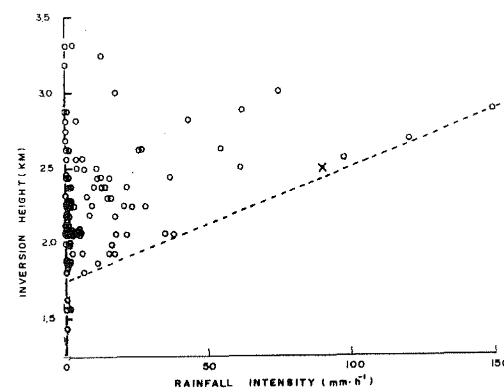

Fig. 10. Maximum rainfall intensity versus inversion height during June, July, August and September, 1975. Cross mark is the maximum rainfall intensity in axi-symmetric cloud model (Takahashi, 1975b).

Warm rain from relatively deep cloud was studied in axi-symmetric cloud model since one-dimensional cloud model fails to include modified environment through cloud development in the deep cloud system (Takahashi, 1975b). Axi-symmetric cloud model using typical sounding could simulate 90 mm per hour rainfall intensity when cloud top height is 25 km (Fig. 11a). Rain falls at cloud boundary initially, and propagates toward the center (Fig. 11b).

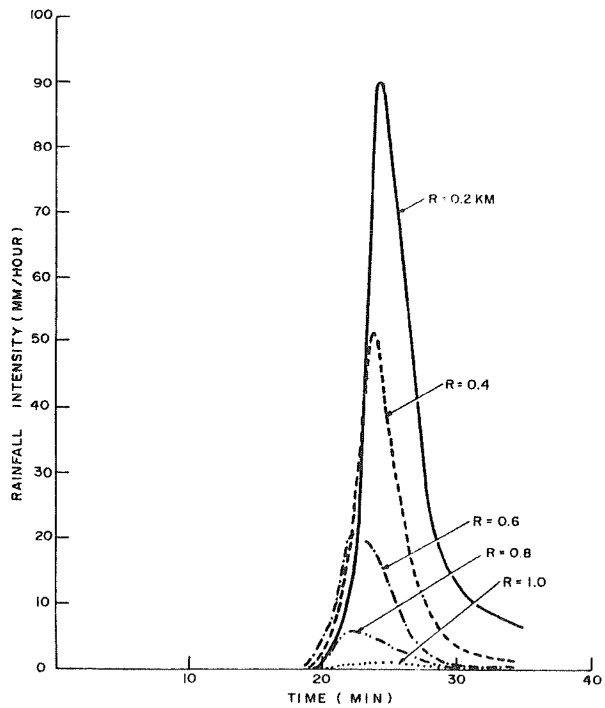

Fig. 11a. Rainfall intensity in the maritime case. Solid line represents rainfall intensity at the cloud center and at the 200 m point along the radial direction, dashed line at 400 m, dash-dotted line at 600 m, dash-double-dotted line at 800 m, and dotted line at 1 km.

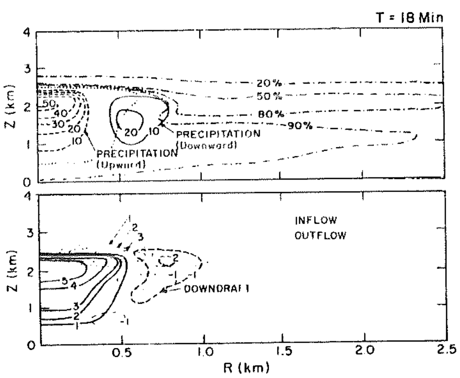

Fig. 11b. As in Fig. 11a, except that T = 18 min and the solid lines (top) are added to indicate downward precipitation particles. Downdraft (thick dashed lines) is seen at the upper side of the cloud boundary (bottom).

IV. COOL RAIN IN THE TROPICS

During the winter time, several thunderstorms hit Hawaii when polar fronts pass the tropics.

Snow falls on Mauna Kea (14,000 ft.) and Mauna Loa (13,600 ft.), and intense rain lasts longer. High positive potential gradient appears and both positive and negative potential gradient increase and often produce lightning (Fig. 12). Those rainfall and electrical character of cool rain has strong contrast with that of warm rain, having intense but short lived shower with weak negative potential gradient.

The existence of ice crystal will be essential to intensify the electricity although the mechanism is not yet known.

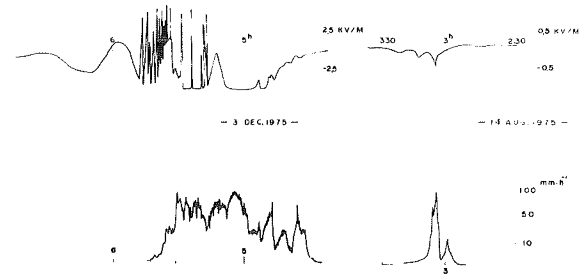

Fig. 12. Electric potential gradient (top) and rainfall intensity (bottom) from warm cloud (August 14, 1975) and from thunderstorm (December 3, 1975).

V. REFERENCES

Berry, E. X. 1967: Cloud droplet growth by collection. J. Atmos. Sciences, 24, 688-701.

Egan, B. A., and J. R. Mahoney, 1972: Numerical model of advection and diffusion of urban area source pollutants. J. Appl. Met., 11, 312-322.

Kovetz, A., and B. Olund, 1969: The effect of coalescence and condensation on rain formation in a cloud of finite vertical extent. J. Atmos. Sciences, 26, 1060-1065.

Ogura, Y., and T. Takahashi, 1973: The development of warm rain in a cumulus model. J. Atmos. Sciences, 30, 262-277.

Takahashi, T., 1975a: Electric charge life cycle in warm clouds. J. Atmos. Sciences, 32, 123-142.

-----, 1975b: Tropical showers in an axisymmetric cloud model. J. Atmos. Sciences, 32, 1318-1330.

-----, 1976: Warm rain, giant nuclei, and chemical balance. (In press J. Atmos. Sciences).

STOCHASTIC VERSUS DETERMINISTIC HAILSTONE SELECTION MECHANISMS

Kenneth C. Young

Institute of Atmospheric Physics
University of Arizona
Tucson AZ 85721

1. INTRODUCTION

We may identify three stages in the history of a hailstone, from its initial growth to precipitation sizes, to its subsequent growth to typical hailstone sizes and its fallout. We often identify each of these stages with a particular region within the cloud although these stages may also be identified in a temporal sequence in the life cycle of a cell. The initial growth of a particle to become a "hail embryo" occurs in the "embryo formation region" (EFR); the growth to hailstone sizes occurs in the "hail growth zone" (HGZ); the fallout occurs in the "hail cascade."

The growth processes in the EFR and HGZ impose certain restrictions on permissible updraft velocities and temperatures within these regions. The necessity of transferring particles from the EFR to the HGZ and finally to the hail cascade requires that these regions be spatially or temporally adjacent. The EFR may be identified as a region of relatively weak updrafts (1-3 m/sec); the HGZ may be identified as a region of quite strong updrafts (> 10 m/sec) and must have an ample supply of supercooled water. Neither region may extend above the -40C level where homogeneous freezing serves to remove the supercooled water.

The EFR serves to supply hail embryos (frozen drops or graupeln) to the HGZ in concentrations on the order of one per liter (e.g., Dye et al, 1974). Yet, English (1973) estimates the concentration of hailstones aloft as 0.01 to 2 per m^3. Clearly, some mechanism must operate within the HGZ to select one in 10^3 to 10^5 of the "potential" hail embryos supplied. The purpose of this paper is to identify and evaluate certain of these selection mechanisms.

2. STOCHASTIC VERSUS DETERMINISTIC SELECTION MECHANISMS

We shall introduce the concepts of a "most favored embryo" and a "most favored trajectory" within the HGZ. The most favored trajectory is that path followed by the most favored embryo during which it encounters undepleted liquid water.

If we consider a vertical plane through the HGZ, the most favored trajectory is also the lowest trajectory. All other trajectories are less favored since they pass through regions of at least partially depleted liquid water.

Given a supply of embryos to the HGZ, we might expect that the most favored embryo will become the largest hailstone (although it will be shown that this is not always true). The problem then is, what mechanisms operate to determine whether or not a particular embryo will follow a favored trajectory?

Clearly, we may expect the size and position (height) of the embryo as it enters the HGZ to influence the trajectory it will follow. The larger the embryo or the lower in the HGZ it is injected, the lower the trajectory it will follow. These selection mechanisms may be termed "deterministic" since, in principle, one may identify particular embryos by their size and location within the EFR that will become hailstones.

However, the path of a growing hailstone through the HGZ is not a smooth trajectory but is affected by turbulence within the updraft (among other effects). Turbulence has the effect of "spreading" like particles which otherwise would follow the same trajectories. Thus, the particular trajectory a particular embryo will follow has a random component due to turbulence. This random component has a feed-back effect in that a random "step" may place the particle in a region of different water content which then alters its growth and affects its fall velocity.

We may envision a large number of initially indistinguishable particles entering the HGZ. Each of these particles follows a unique trajectory, randomly determined. Some of these particles will be fortunate enough to follow trajectories close to the most favored trajectory and will grow to become hailstones. The remainder will not be so fortunate. Thus, the selection is purely random and the mechanism may be termed "stochastic."

3. MONTE CARLO HAIL GROWTH ZONE MODEL

The model used is highly simplified and designed to examine how the deterministic and stochastic selection mechanisms operate rather than to make any quantitative predictions concerning hail production in any particular hailstorm. The insight gained from this simple model however, may be applied to the formation of hail in nature.

The model is a two-dimensional (x,z), kinematic model with a uniform flow field. All cases treated in this paper assume an updraft velocity of 15 m/sec with a horizontal component of 3 m/sec. The model extends 1800 m in the vertical and 1200 m in the horizontal. Each grid square is 60x60 m. Liquid water is carried as a water content and is assumed to be adiabatic at the base of the HGZ (at -20C) from the cloud base (at +5C). Water saturation is assumed and vapor is condensed within the updraft accordingly. Liquid water is depleted by the hailstones, both through diffusion and accretion processes. The ice particles are assumed to be spherical and collect liquid water in a continuous fashion with a collection efficiency assumed to be one. Hailstones are assumed to incorporate unfrozen water until their heat budget allows it to freeze. The liquid water is assumed to be carried with the air; hailstones and embryos fall with a velocity calculated according to McDonald (1960).

The unique feature of this model is that a large number of discrete groups of embryos are injected into the HGZ and the path that each group follows is, in part, randomly determined. The location (x,z) of each group at each time step is known. The growth of particles within a group is determined by the liquid water content (LWC) of the grid square within which the group is residing and the temperature (and pressure) of that level. The group is then translated in space in accordance with the mean flow field, the fall velocity of its particles and a random component (u',w') based on the turbulence. Each random component is determined by random selection from a Gaussian distribution of u' and w' based on aircraft measurements of updraft velocities taken in hailstorms by Sand (University of Wyoming, private communication). The turbulence was assumed to be isotropic and u' and w' were assumed to be uncorrelated. Two intensities of turbulence were used, one corresponding to a quite smooth updraft with $\sigma = 1.17$ m/sec; the second corresponding to a fairly turbulent updraft with $\sigma = 3.71$ m/sec.

Time steps of 4 sec were used, roughly equivalent to the 5 sec averages of the measured updraft velocities. Additional sets of groups were injected every 20 sec. As many as 4000 separate groups were carried simultaneously within the model; the number of particles represented by a group ranged from 7200 to 72,000 (assuming a model thickness of one meter). The order of processing groups was reversed each time step to avoid first-order biasing of the results. The model was run until a quasi-steady-state was reached (after 400 sec) and the spectrum of particles exiting the model was determined.

4. PERFORMANCE OF THE MODEL

The model was run with very low concentrations of particles to illustrate the effect of turbulence on particle trajectories. Figure 1 demonstrates the mixing between particles of the same size (r = 0.025 cm, = 0.5 g/cm^3), injected at three different levels (30,90 and 150 m). The total concentration of particles was 25 per m^3 in groups of 5 per m^3 each at each of the three levels. Although particles injected at the lowest level tend to follow the most favored trajectory, it is clear that particles initially more than 100 m above these, may also attain a most favored trajectory, even under relatively light turbulence.

Figure 2 demonstrates the tendency of particles of different sizes to follow divergent trajectories. Particles of 0.02, 0.025 and 0.03 cm radius were injected at the same three levels as above with three groups in each of the nine categories. The total particle concentration at any one level was 45 per m^3. It is clear that the largest particles tend to follow the most favored trajectories.

5. SELECTION BY LOCATION

In order to assess the effects of initial embryo position on its probability

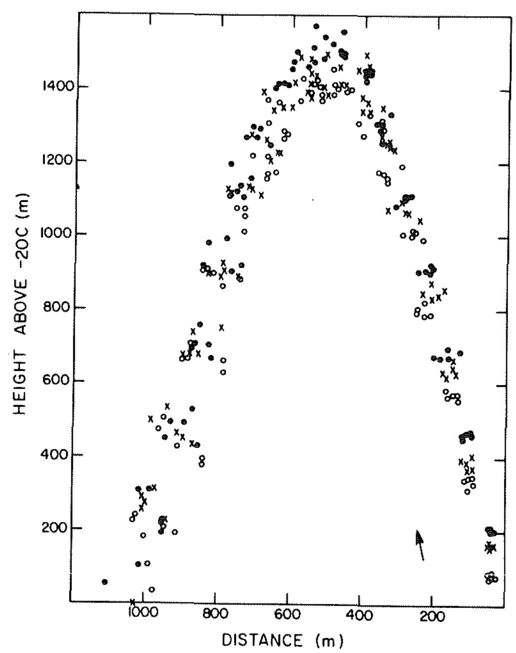

Figure 1. Effect of position and turbulence on group trajectories.

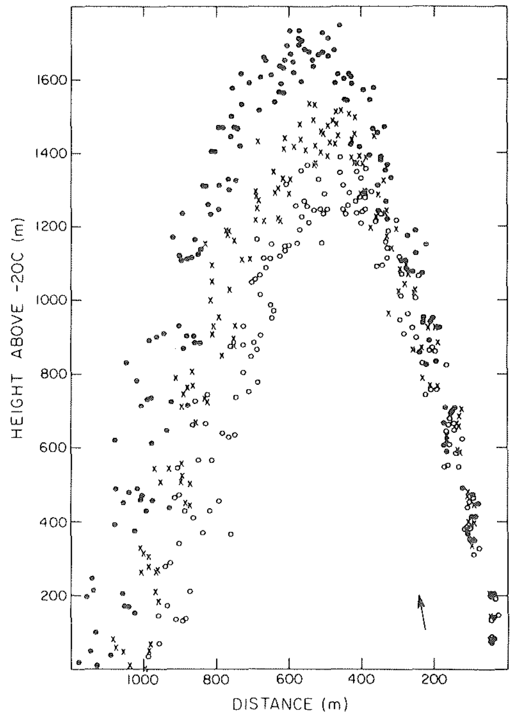

Figure 2. Effect of particle size and turbulence on group trajectories. Smallest particles are indicated by ● ; largest particles are indicated by o .

of being selected to grow to hailstone sizes, embryos of a single size (0.025 cm radius, ρ = 0.5 g/cm^3) were injected at four levels (30,90,150 and 210 m). Two cases having total particle concentrations of 100 and 1000 per m^3 were examined.

The radar reflectivity and LWC fields for the 1000 per m^3 case are shown in Figs. 3 and 4. Note the "radar overhang" in Fig. 3, the strong gradient of reflectivity in the descending echo and values of maximum reflectivity in excess of 50 dBZ. The LWC field exhibits features similar to the reflectivity field with marked depletion of LWC occurring in conjunction with the descending echo. Note that these fields are smoothed since the Monte Carlo simulation produces considerable fluctuations in these quantities.

The spectra of hailstones exiting each grid square at the lower bound of the model are shown in Fig. 5. It is clear that a size-sorting effect is present with the largest hailstones falling out closest to the injection point. The model also produces a fairly broad size spectrum from particles initially all the same size.

Selection by location was most pronounced for the 1000 per m^3 case. No hailstones originated from levels III or IV for the 1000 per m^3 with 97% originating from level I. In contrast, 44% of the hailstones originated from the top

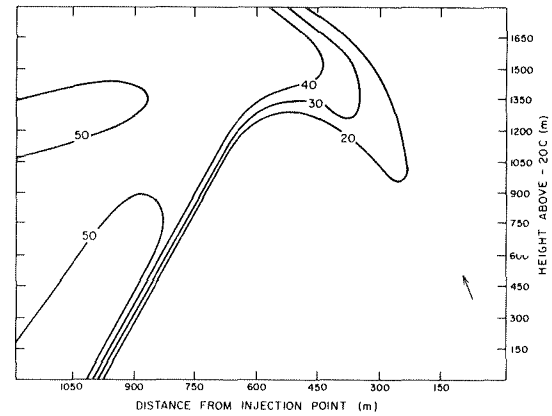

Figure 3. Cross-section of radar reflectivity for uniform size particles injected at 4 levels in a total concentration of 1000 per m^3.

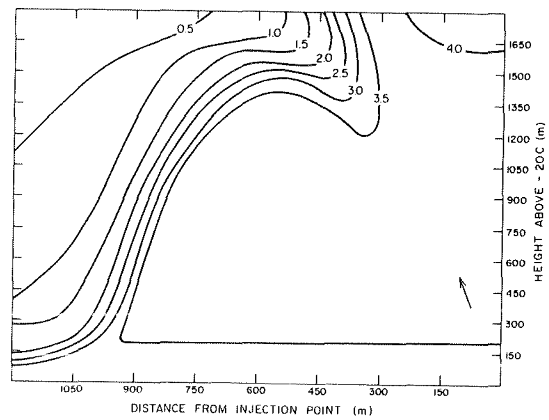

Figure 4. Cross-section of LWC corresponding to Fig. 3.

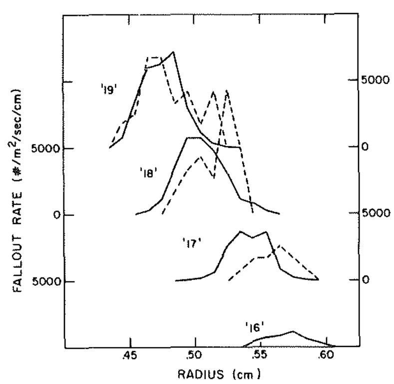

Figure 5. Hail spectra at model base by grid position. Case corresponds to Fig. 3.

two levels for the 100 per m^3 case.

A much larger fraction of the embryos were selected to become hailstones in the 100 per m^3 case. For level I, 96% of the embryos were selected whereas only 31% were selected in the 1000 per m^3 case.

6. SELECTION BY SIZE

In order to assess the effects of initial embryo size on its probability of being selected, the total embryo concentration was divided equally among five size categories. Two cases (100 and 1000 per m^3) were run with radii from 0.025 to 0.029 cm for the 1000 per m^3 case and from 0.02 to 0.032 cm for the 100 per m^3 case.

For the 1000 per m^3 case, embryos from levels III and IV were totally eliminated from the hailfall, regardless of their initial size. The fraction of embryos selected to become hailstones and their average radii are given in Table 1.

Table 1. Fraction of Embryos Selected

	.025	.026	.027	.028	.029	radius
I	0	0	32%	71%	91%	.459
II	0	0	0	5%	30%	.439
III	0	0	0	0	0	-
IV	0	0	0	0	0	-
radius	-	-	.435	.450	.467	

Note that the largest embryos tended to become the largest hailstones. Embryos originating at level II tended to be smaller and fall out further from the injection point than did embryos from level I.

For the 100 per m^3 case, both selection by location and by initial size were less pronounced. Tables 2 and 3 present the fraction of embryos selected and their mean radii (cm) for each of the 20 categories.

Table 2. Fraction of Embryos Selected

	.020	.023	.026	.029	.032	avg
I	17%	62%	97%	100%	100%	76%
II	20%	64%	94%	100%	100%	76%
III	15%	62%	93%	100%	100%	75%
IV	20%	66%	88%	100%	100%	76%
avg	18%	63%	93%	100%	100%	76%

Table 3. Mean Hailstone Radius (cm)

	.020	.023	.026	.029	.032	avg
I	.485	.477	.486	.497	.504	.492
II	.492	.482	.481	.498	.516	.495
III	.496	.488	.485	.497	.517	.498
IV	.504	.493	.492	.502	.509	.500
avg	.494	.485	.486	.499	.511	.496

Although one cannot strictly compare selection by size and by location, it does seem evident that the largest embryos will tend to be selected, regardless of their initial positions, provided the size spectrum of embryos is sufficiently broad.

7. THE EFFECT OF TURBULENCE ON SELECTION

Three intensities of turbulence were examined, the light and heavy turbulence spectra as discussed in section 3 and a zero turbulence case. The latter serves to compare the results of the "stochastic" model with the commonly used "deterministic" model. In each case, total concentrations of 1000 embryos per m^3 were used with particles of uniform size injected into the lowest four levels.

In the case of zero turbulence, the trajectories originating from different levels diverged with no overlap. Hailfall resulted only from the lowest or most favored trajectory. A small amount of numerical spreading resulted in a range of sizes with radii from 0.52 to 0.55 cm. Hailfall occurred only beyond 1080 m of the injection point compared to 950 m and 510 m for the light and heavy turbulence cases respectively. The maximum hailstone size and total number of hailstones were reduced in comparison to the light turbulence case.

Hail spectra for the heavy turbulence case are shown in Fig. 6. Although the size spectra of hailstones falling out at any grid square is much broader than for the light turbulence case, the cumulative distribution of hailstones > 0.5 cm radius is virtually identical.

8. THE BENEFICIAL COMPETITION HYPOTHESIS

The beneficial competition hypothesis for hail suppression states that the mean size of hailstones can be reduced through the introduction of additional embryos

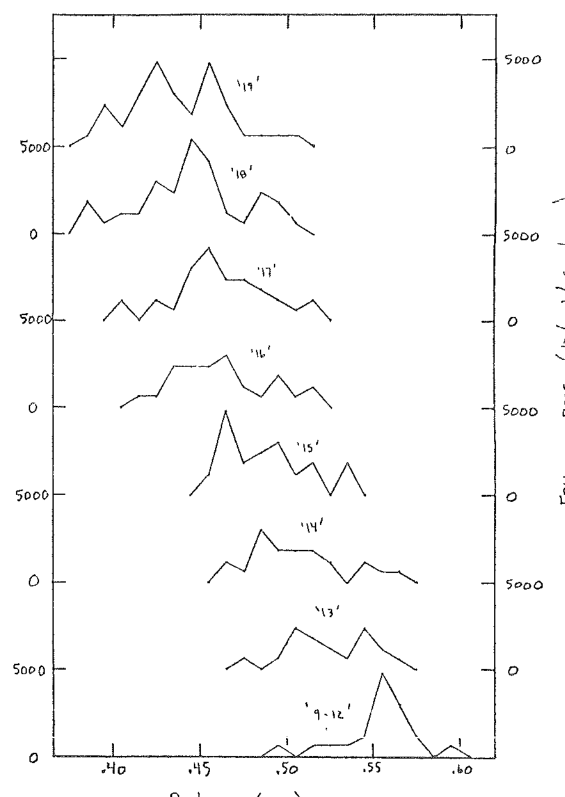

Figure 6. Hail spectra at model base by grid position for heavy turbulence case corresponding to Fig. 3.

which then compete with the naturally occurring embryos for the supercooled water. The hypothesis assumes that the additional embryos follow trajectories similar to those followed by the naturally occurring embryos, i.e., they originate at the same location and have similar sizes. In section 5, embryos of identical sizes were injected into the lowest four levels in concentrations of 100 and 1000 per m^3. The 100 per m^3 case could be considered the "natural" case and the 1000 per m^3 case could be considered the "seeded" case.

The cumulative spectra (Fig. 7) reveal no substantial changes in hailfall between the natural and seeded cases. Closer examination of the results reveals that the fraction of embryos selected in the seeded case is greatly reduced. We may conclude that, provided a sufficient number of embryos are present, i.e., a number such that a noticeable depletion of LWC occurs, the number of favored trajectories is constant, given that the initial embryos sizes are unchanged. The physical reasons behind this conclusion appear to be that each trajectory depletes the LWC by a given amount. The most favored trajectory encounters the largest LWC with successively less favored trajectories encountering less and less liquid water. Once the LWC depletion is such that the trajectory cannot grow a hailstone of given size, the number of favored trajectories is defined. The number of such trajectories is independent of the total number of trajectories.

One may argue that, due to turbulence, a number of different trajectories may be equivalent, i.e., encounter an equivalent amount of liquid water. By increasing the number of embryos, the number of equivalent trajectories could be increased, thereby promoting competition between particles following equivalent trajectories. However, the feed-back nature of the random step process is such that trajectories tend to diverge and equivalent trajectories would not be expected.

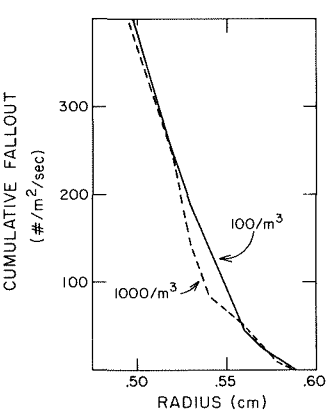

Figure 7. Cumulative hail spectra for uniform size embryos. Natural (100 per m^3)vs. seeded (1000 per m^3).

9. THE TRAJECTORY LOWERING HYPOTHESIS

The trajectory lowering hypothesis for hail suppression states that by increasing the sizes of the largest embryos entering the HGZ or by allowing large particles to enter the HGZ at a lower level, they will follow a lower trajectory through the HGZ. Embryos following lower trajectories will have less time to grow and will be less able to freeze their accreted water and therefore will be smaller when they exit the HGZ and more likely to melt. At the same time, they serve to deplete the liquid water reaching the region of favored trajectories that would have existed in the absence of modification.

In order to test this hypothesis, the "natural" case with 100 embryos per m^3 was modified by the injection of 0.05 cm radius embryos (ρ = 0.9 g/cm^3) in the lowest two levels. Figure 8 compares the cumulative size distributions for the natural case and a case seeded with 100 per m^3 of additional embryos. It is clear that a marked reduction in the numbers of large hailstones has occurred. None of the "additional" embryos grew larger than 0.45 cm radius, i.e., the reduction in hailstone size is due to the depletion of liquid water by the additional embryos. This depletion amounts to more than 1 g/m^3 in some regions.

It should be noted that this reduction in hailstone sizes was effected with a concomitant decrease in the efflux of liquid water, i.e., with an increase in the precipitation efficiency of the system. Of course, this does not consider the survival of these particles as precipitation.

10. DISCUSSION

It is clear that all three selection mechanisms discussed may contribute to

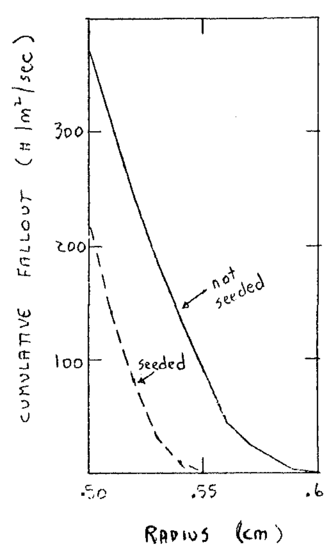

Figure 8. Cumulative hail spectra for natural and hygroscopic seeded cases.

the selection of certain embryos to become hailstones. The initial size and location of the embryo become increasingly more important as the "total concentration" of embryos increases. As the concentration of embryos decreases, the stochastic selection processes become more important.

When we try to apply these results to nature, the definition of "total concentration of embryos" becomes vague. Does this refer to all the ice particles regardless of size or only to those capable of following an up-down trajectory through the HGZ in the absence of other embryos? If we examine these results more closely, we note that the relative dominance of the deterministic or stochastic selection mechanisms is more closely related to the gradient of LWC produced by the falling hailstones. The steeper the gradient becomes, the more dominant the deterministic selection mechanisms are.

These selection mechanisms operate to select a certain number of favored trajectories, regardless of the gradient of LWC (or the "concentration" of embryos). The number of such favored trajectories is governed by the cumulative depletion of LWC that these trajectories represent. Once the LWC is so depleted that an embryo following a given trajectory cannot grow to "hailstone" sizes, the number of favored trajectories is defined. Thus, the addition of more embryos of the same size cannot significantly alter the size distribution of hail resulting from a given HGZ.

This implies that the beneficial competition hypothesis is not viable. To be sure, competition for available liquid water does occur. This competition increases the overall depletion, steepens the gradient of LWC and decreases the fraction of embryos which become hail. Unfortunately, it does not decrease the number of embryos which become hail.

The concept of trajectory lowering for hail suppression is considered a viable option. The necessary requirement of this concept is to introduce significant numbers of particles (> 100 per m^3) that are larger than those occurring naturally. These particles will follow a lower trajectory through the HGZ, spending less time there and consequently will not grow as large as their "natural" counterparts. If present in sufficient concentrations, they may deplete the liquid water and retard the growth of the natural embryos.

Although large particles may be initiated lower in the updraft by seeding with an ice nucleant, it would seem more efficient to employ hygroscopic seeding materials (see Young and Rokicki, 1976). Such hygroscopic seeding may be considered an extension of "natural hail suppression" in clouds having relatively warm bases (see Appleman, 1959). This hail suppression method was proposed by Ludlam (1959) although his chain of reasoning was not well developed.

Certain apparent anomalies should be noted. As was pointed out in section 2, embryos following the lowest or most favored trajectories, do not always grow to the largest sizes. If the concentration of favored trajectories is not large, the increased time available for growth for some less favored trajectories may offset the reduced liquid water. Other apparent anomalies may be accounted for on this basis.

Although this model demonstrates deficiencies in the purely deterministic approach, it still represents only a very crude approximation to the stochastic processes operating within these clouds as they affect hail growth. Even allowing for assumptions such as a uniform mean updraft field, no electrical effects and adiabatic liquid water, the Monte Carlo simulation of the effects of turbulence is highly simplistic. It assumes that hailstones travel as discrete groups, consisting of thousands of individuals. This would correspond to turbulence of a single eddy size (i.e., no spectrum of eddy sizes). It also assumes that there is no correlation between the random components of displacement for nearby groups and no autocorrelation between these components with time. Still, even with these deficiencies, the model does illustrate a number of interesting aspects of hailstone growth.

Acknowledgement. This research was supported by the National Hail Research Experiment under grant SUB NCAR S5004.

REFERENCES

Appleman, H., 1959: An investigation into the formation of hail. Nubila, 2, 28-37.

Dye, J.E., C.A. Knight, V. Toutenhoofd and T.W. Cannon, 1974: The mechanism of precipitation formation in northeastern Colorado cumulus. III. Coordinated microphysical and radar observations and summary. J. Atmos. Sci., 31, 2152-2159.

English, M., 1973: Alberta hailstorms. Part II. Growth of large hail in the storm. Meteor. Monogr., 14, No. 36, 37-98.

Ludlam, F.H., 1959: Hailstorm studies, 1958. Nubila, 2, 7-27.

McDonald, J.E., 1960: An aid to computation of terminal velocity of spheres. J. Meteor., 17, 463-465.

Young, K.C., and M.L. Rokicki, 1976: The formation of precipitation in updrafts. Proc. Intl. Conf. Wea. Modification, Boulder, CO, August 2-6.

6.3.4

A THEORETICAL STUDY OF THE EVOLUTION OF MIXED PHASE CUMULUS CLOUDS

by

Bryan C. Scott and Peter V. Hobbs

University of Washington
Seattle, Washington

1. INTRODUCTION

This paper presents the results of theoretical studies designed to investigate the development of the ice phase in maritime and continental cumulus clouds. The cumulus model of Scott and Hobbs (1976) has been used; this is a one dimensional, time dependent, Eulerian model in which five different ice particle classifications interact among themselves and with cloud droplets. The ice particles include unrimed and rimed plates and columns, graupel and snowflakes. Fig. 1 illustrates the microphysical interactions considered in the model.

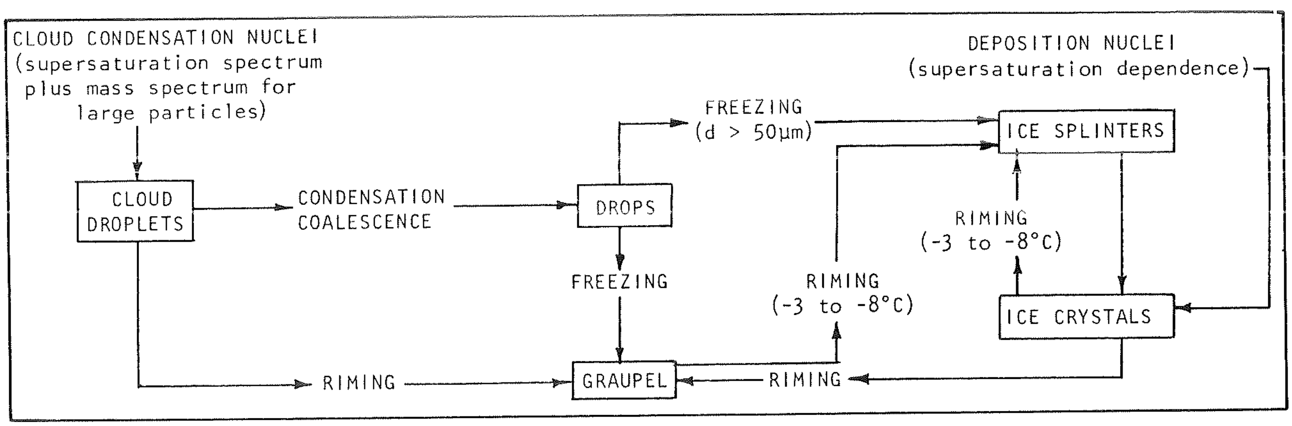

Figure 1. Schematic of microphysical interactions considered in the model.

The effects of possible ice multiplication have been investigated by allowing ice splinters to be produced during riming and during the freezing of isolated drops. The results of Hallet and Mossop (1974) are used for splinter production during riming. For the freezing of isolated drops, either one or four ice splinters are assumed to be ejected from freezing drops $\gtrsim 50$ μm† [Hobbs and Alkezweeny (1968); Pruppacher and Schlamp (1975)]. Results are also presented for "control" clouds in which ice multiplication was not included.

Cloud drops formed on specified numbers of aerosol particles defined in terms of their salt content or supersaturation spectra. Ice particles originated through the activation of deposition nuclei (which were specified by a supersaturation spectra), through the activation of freezing nuclei in supercooled droplets, and through the ice multiplication mechanisms. The same environmental sounding was used in all of the case studies; it produced a cloud base near 0°C and a cloud top near -10°C (thickness 1.5 km). The clouds were initiated with a 2°C temperature perturbation at the surface and were taken to be 0.8 km in radius. The input conditions produced droplet concentrations of about 80 cm^{-3} in the maritime cloud and about 300 cm^{-3} in the continental cloud.

† All dimensions refer to diameters.

2. RESULTS

2.1 Cloud Characteristics

The vertical motions and the total water contents produced for the continental and maritime clouds are shown in Figs. 2 and 3. The cloud tops grow quite rapidly to a height of 2.2 km and remain near this altitude for the duration of the numerical studies (85 min.). During the first 60 min. the vertical velocities slowly decrease from an initial maximum value of 3.6 m s^{-1}. At 60 min. there is a major decrease in vertical velocities, followed by a partial velocity recovery at 70 min. and a subsequent velocity decrease after 80 min. These velocity characteristics are essentially independent of the input aerosol size distributions. The total water distributions for the continental cloud remains virtually unaffected by the velocity fluctuations, however, in the maritime cloud there are large variations in water content due to sedimentation and advection of the cloud drops in the fluctuating velocity field.

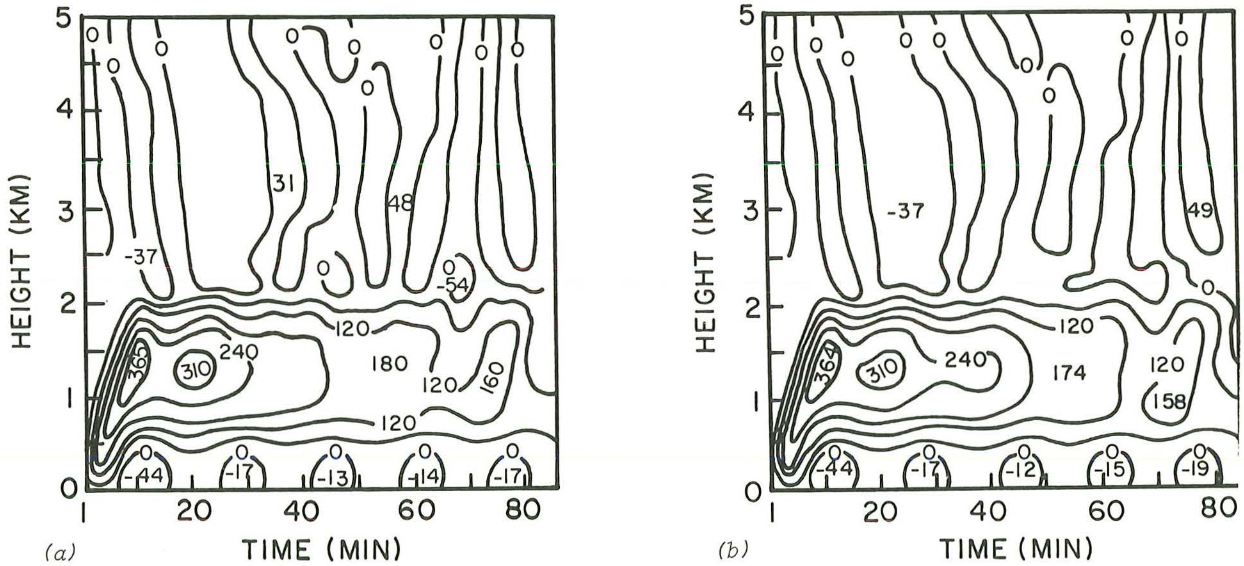

Figure 2. Vertical velocities (in cm s^{-1}) for (a) the maritime cloud and (b) the continental cloud. Contour interval is 60 cm s^{-1}.

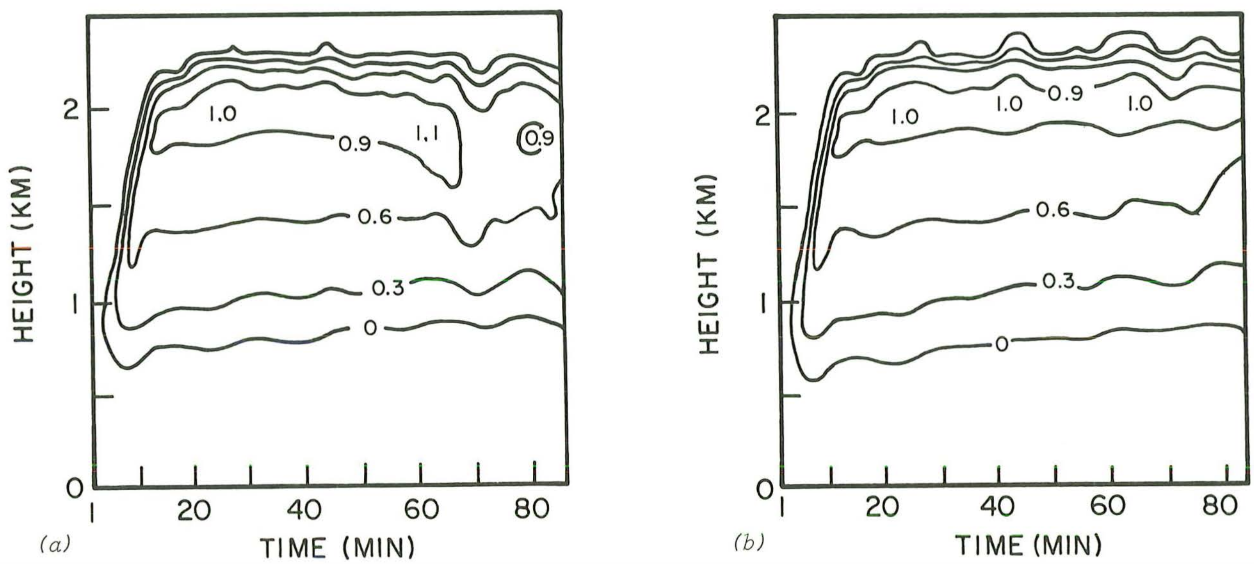

Figure 3. Liquid water content (in g m^{-3}) for (a) the maritime cloud and (b) the continental cloud.

2.2 Drop Characteristics

During the first 60 min., the average cloud drop in both the maritime and continental cloud is generally moving upwards at about 1.5 to 2 m s^{-1} and it has about 10 to 15 min. to participate in the condensation and coalescence growth processes. After 60 min. the lowering updraft speeds allow coalescence to proceed over longer time intervals, and in the maritime cloud drops as large as 1 mm* are produced in concentrations of 0.7 m^{-3} above 1.4 km. The greater drop concentrations in the continental cloud inhibit the growth of drops to sizes large enough to participate in the coalescence process. Consequently the largest drops that develop in the continental cloud in concentrations of 1 m^{-3} are typically about 120 μm.

*The particle size distributions are divided into discrete mass intervals. When a specific dimension and number density is given, it refers to the total number of particles (m^{-3}) in the interval centered on the quoted size. Here we are applying the transformation $n\langle J\rangle dJ = n\langle x\rangle dx$ where $x_J = x_1 2^{J-1}$ and J=1,2,3..., and $n\langle x\rangle dx$ represents the concentration of particles with mass between x and $x+\Delta x$.

2.3 Graupel Sources and Characteristics

Graupel is assumed to originate when drops freeze and when the mass that a crystal acquires by riming exceeds eight times its depositional mass. All graupel is assumed to be spherical. Collisions between small ice crystals and larger cloud drops were the primary source of graupel during the first 10 min. of growth in both the maritime and continental clouds. As the maritime cloud matured, freezing drops continued to be the major source of graupel and eventually produced graupel mass at a rate ten times or more greater than the production rate of graupel mass by rimed crystals. Freezing drops also produced far greater numbers of graupel particles than did rimed crystals in the maritime cloud; the number of graupel produced by rimed crystals being only one tenth the total number of graupel. Activation of freezing nuclei within the larger cloud drops accounted for only about 1% of the total graupel.

Unlike the maritime cloud, a large portion of the graupel in the continental cloud originated from rimed crystals. In the continental "control" cloud the rate of conversion of freezing drops to graupel was three orders of magnitude less than in the maritime "control" cloud. Additionally, in the continental cloud, graupel was produced 5 to 10 times faster by the riming of crystals than by drop freezing.

The differences in graupel sources in the maritime and continental clouds can be attributed to the different drop size distributions. The rate of production of freezing drops depends on the relative sizes of the colliding drops and the ice crystals near cloud top. At -10°C, essentially all collisions between drops and plates produced frozen drops when the drop exceeded 100 μm (200 μm for drop-column collisions). Rimed crystals could have been produced if the plates had been sufficiently large, but the number density of the larger crystals decreased rapidly with size, making frequent collisions unlikely. Also at -10°C, collisions involving crystals and drops less than 60 μm are likely to produce rimed crystals, although frozen drops could be produced in the unlikely event that a small crystal collided with one of these small drops. The concentrations of drops ≤32 μm were about six times greater in the continental cloud than in the maritime cloud. Also, the concentrations of drops >32 μm are one to two orders of magnitude less in the continental cloud than in the maritime cloud. Apparently the greater number of smaller drops in the continental cloud overcame the fact that the collection kernal for the larger drops was twice that of the smaller drops because the mass rate of accretion was larger in the continental cloud than in the maritime cloud. Thus, the production of rimed crystals appears to be strongly dependent upon the concentration of drop <32 μm and the production of frozen drops depends upon the concentration of droplets >100 μm.

Once graupel has formed in the maritime "control" cloud, and in the maritime cloud where ice enhancement is included, it is more effective in converting cloud water to ice than are the other ice particles. At times where the graupel and crystal concentrations are nearly equal, the graupel riming rate is roughly an order of magnitude larger than the crystal riming rate. The graupel originating from large drops can begin to rime immediately after formation, while ice crystals must grow to some minimum size before riming begins. The graupel is generally larger than the ice crystals and would therefore be expected to sweep out larger volumes and to be the more efficient rimer.

The graupel concentrations in the continental cloud are about an order of magnitude less than the total crystal concentrations, but at heights above 1.7 km the crystal riming rates are only twice the graupel riming rates. Here, as in the maritime cloud, the larger graupel accrete drop mass more efficiently than the more numerous but smaller ice crystals.

The mass distributions of graupel near cloud tops in the maritime and continental clouds are compared in Fig. 4. In the maritime cloud the graupel has a fairly smooth, continuous size distribution; the smaller graupel is generally denser than the larger graupel. The continental cloud, by contrast, has a bimodel graupel size distribution with large numbers of small, high density graupel and slightly fewer numbers of larger, low density graupel.

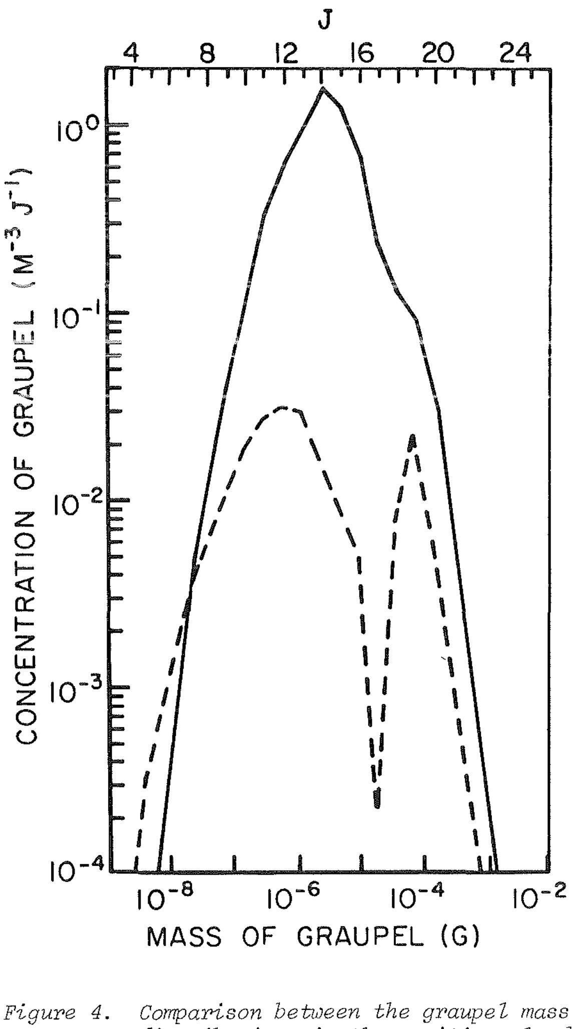

Figure 4. Comparison between the graupel mass distributions in the maritime cloud (———) and the continental cloud (– – –) at 2.0 km and 46 min.

2.4 Ice Particle Concentrations

Hallett and Mossop's (1974) laboratory experiments indicate that ice splinters are only produced by riming between -3 and -8°C. Consequently, the only crystals whose concentrations are significantly affected by ice multiplication from riming are columns. Shown in Fig. 5 are the concentrations of columnar crystals as a function of time in the "control" maritime cloud, and in the maritime cloud in which ice splinters were produced by riming. In the latter case, the concentration of columns begins to increase noticeably at about 65 min. at altitudes of 1.5 km and shortly thereafter at lower altitudes. This increase in column concentrations is directly associated with the arrival of large (1 to 3 mm) graupel at altitudes ≤1.5 km where the temperature is between -3 and -8°C.

Fig. 6 displays the corresponding changes in the concentration of graupel as a function of time for the same two cloud types illustrated in Fig. 5. Prior to 60 min., the updraft speeds were sufficiently strong to prevent the sedimentation of substantial quantities of graupel below 1.5 km. After 60 min. the updraft speed decreased to less than 1.2 m s^{-1} and allowed graupel as small as 700 μm to enter the -3 to -8°C region. In all cases, the onset of ice multiplication is preceded slightly in time by increases in graupel concentrations at the lower levels, indicating the arrival of graupel by sedimentation. It is the sedimentation of the graupel which initiates the chain reaction leading to dramatic ice multiplication. Graupel concentrations increased by 3 orders of magnitude (to 1 ℓ^{-1}) at 1.5 km (-8°C) within 20 min.

Graupel >700 μm in the maritime cloud are the only particles able to acquire sufficient mass to overcome the updraft velocity and to fall relative to the ground. Riming contributed nearly an order of magnitude more mass to these larger particles than did depositional growth and it was primarily responsible for their rapid growth to >700 μm. Indeed, at these high temperatures (-5 to -10°C) and in the short times available (10-15 min.), depositional growth alone would have been unable to produce ice particles massive enough to precipitate in either the maritime or continental cloud.

There appears to be a definite correspondence between the size and the concentration of graupel at the onset of ice multiplication. The concentrations of graupel >1 mm had to be greater than 10^{-2} m^{-3} at two or more levels between -3°C and -8°C before ice multiplication occurred. This critical value is reached only at 1.6 km in the continental cloud: as a consequence the concentration of columns only doubles above 1.6 km due to ice multiplication.

In the maritime cloud, where the majority of graupel originated from frozen drops and was therefore relatively small, the large (>1 mm) graupel accounted for only 3 to 5% of the total concentration of graupel. In the continental cloud, where the majority of graupel originates on rimed crystals, the graupel ≥ 1 mm accounted for up to 70% of the total graupel in the lower portions of the cloud.

There is a strong feedback mechanism between the column concentrations and the production of graupel particles in the maritime

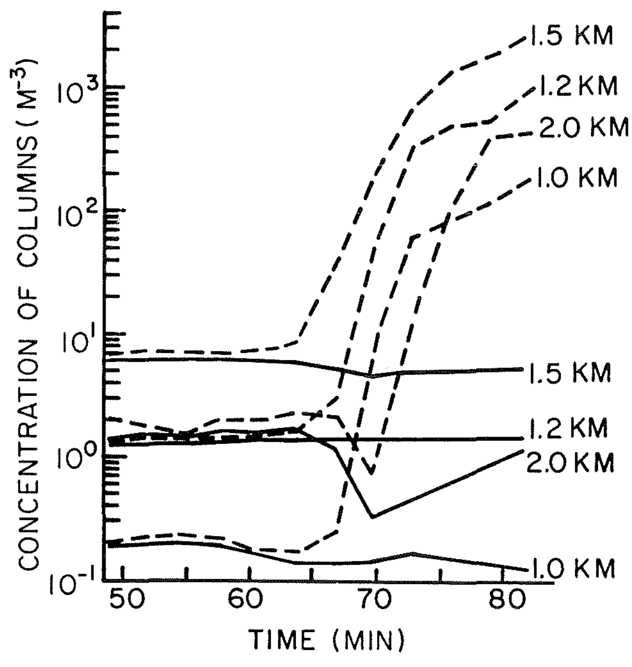

Figure 5. Concentration of columnar crystals at various heights as a function of time in the maritime cloud. The "control" cloud is indicated by (——) and the cloud where ice splinter production due to riming was included is indicated by (— — —).

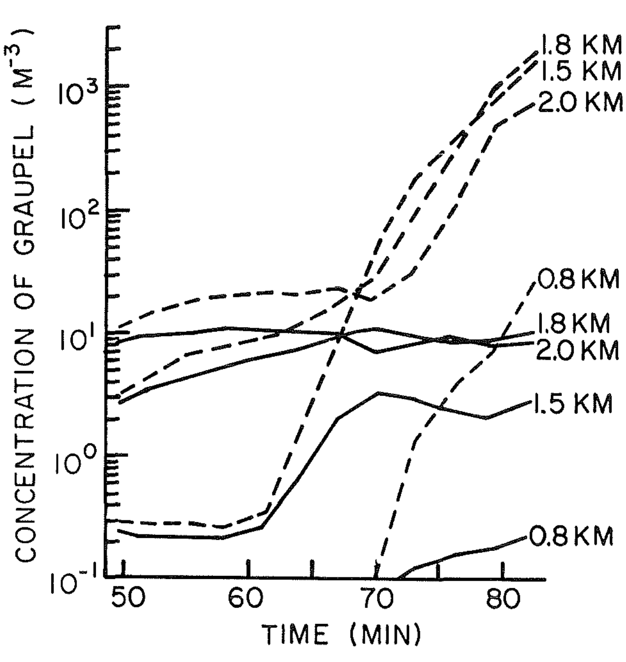

Figure 6. Concentrations of graupel at various heights as a function of time in the cloud. The "control" cloud is indicated by (——) and the cloud in which ice splinters were produced by riming is indicated by (— — —).

cloud. After 65 min., the increase column concentrations result in more frequent column collisions with large cloud drops. The large drops then freeze (they are converted to spherical graupel), advect out of the -3 to -8°C region (riming as they go, and thus ejecting more ice splinters), and move to cloud top where they grow primarily by riming. Once they have accreted sufficient mass, they fall down through the -3 to -8°C region where they continue the ice multiplication process.

In the continental clouds, the total graupel concentrations are some 10 to 50 times less than in the maritime "control" cloud. Consequently when the updraft speed in the continental cloud decrease at 60 min., the concentration of graupel is too low to induce a significant multiplication process. Splintering increases column concentrations only by a factor of two, which is insufficient to enhance the production rate of new graupel through the freezing of larger cloud drops or riming on crystals.

When isolated freezing drops, as well as the riming-splintering mechanism, were allowed to eject ice splinters in the maritime cloud, substantial deviations occurred from the maritime "control" cloud, in the concentrations of graupel well before the extensive updraft reduction at 60 min. When one ice splinter was ejected for every frozen drop ≥ 50 µm, the concentrations of graupel above 1.6 km in the maritime cloud were twice the "control" values by 60 min. With four ice splinters per freezing drop, the concentration of graupel was enhanced throughout the entire maritime cloud. By 60 min. graupel concentrations at cloud top increased to 10 ℓ^{-1} or nearly 100 times the "control" values. At cloud base, graupel concentrations of 0.1 m^{-3} were achieved 3 min. earlier than in the maritime "control" cloud. In the continental cloud, the concentration of drops ≥ 50 µm was too low to produce any significant splinter production from freezing drops. Even when the ice splinter ejection rate was increased to four per drop, graupel concentrations were virtually the same as in the "control" cloud at all levels. These results illustrate the strong dependence of ice splinter production from isolated drop freezing on the drop size distribution. Additionally, they indicate that at least one ice splinter per freezing drop is necessary in these shallow clouds before the freezing of isolated drops can produce significant (factor of 2 or greater) ice enhancements.

3. SUMMARY AND CONCLUSIONS

Our comparative studies of shallow, non precipitating, maritime and continental cumulus clouds have demonstrated the importance of the drop size distribution in determining the dominant mechanism for forming graupel. In the maritime cloud, where there are significant numbers of drops greater than 60 µm, graupel originates on frozen drops produced after collisions with ice crystals. At -10°C freezing nuclei produced only about 1% of the total graupel. In the continental cloud, the greater abundance of small cloud drops (<30 µm) makes the crystal riming process more effective than the drop freezing process, and graupel tends to originate on ice crystal embryos. In both the continental and maritime clouds much of the graupel is of high density (0.6 to 0.8 g cm^{-3}) and is contained in the smaller size catagories (<280 µm); the source is frozen drops. Although our model considers these particles to be spherical, it is possible that naturally occurring drop-crystal collisions produce quite irregularly shaped particles. These particles could be an important source of the numerous irregular ice particles often observed in natural clouds.

The ice splintering studies demonstrate the sensitivity of the ice multiplication process to the presence of large cloud drops. In the continental cloud, the riming mechanism never produced significant increases in ice crystal concentrations, but in the maritime cloud it produced orders of magnitude increases after the updraft velocity had decreased sufficiently to allow the formation and sedimentation of larger drops and graupel. Concentrations as low as 10^{-2} m^{-3} of millimeter-sized graupel were sufficient to initiate a chain reaction leading to ice multiplication in the maritime cloud provided the graupel was present between -3 and -8°C. When each isolated, freezing drop (>50 µm) ejected 4 ice splinters in the maritime cloud, graupel concentrations at cloud top increased to 100 times those in the maritime "control" cloud. When the number of ejected splinters was reduced to 1 per drop in the maritime cloud, the concentrations of graupel differed by only about a factor of two from the "control" cloud. Even the ejection of 4 splinters/freezing drop was insufficient to establish an ice multiplication process in the continental cloud.

Acknowledgements: This research was supported by Grant ATM-74-14726-A02 from the Atmospheric Sciences Section (Meteorology) of the National Science Foundation. The computations were performed on the CDC 7600 at the National Center for Atmospheric Research, which is supported by the National Science Foundation.

REFERENCES

Hallett, J. and S. C. Mossop, 1974: Production of secondary ice particles during the riming process. Nature, 249, 26-28.

Hobbs, P. V. and A. J. Alkezweeny, 1968: The fragmentation of freezing water droplets in free fall. J. Atmos. Sci., 25, 881-888.

Pruppacher, H. R. and R. J. Schlamp, 1975: A wind tunnel investigation on ice multiplication by freezing of water drops falling at terminal velocity in air. J. Geophys. Res., 80, 380-386.

Scott, B. C. and P. V. Hobbs, 1976: A theoretical study of the evolution of a mixed phase cumulus cloud. Part 1: Description of the model. J. Atmos. Sci. (Submitted for publication.)

HAIL IN AN AXISYMMETRIC CLOUD MODEL

Tsutomu Takahashi

Cloud Physics Observatory,
Department of Meteorology,
University of Hawaii,
Hilo, Hawaii 96720

I. INTRODUCTION

A hail formation process was examined in two-dimensional axisymmetric cloud model with detailed microphysics (Fig. 1). Instantaneous formation of the input cloud droplet distribution from cloud nuclei was assumed (process 1 to 2). The cloud droplet distribution calculated at cloud base (Takahashi, 1976a) was used. These cloud droplets grow by condensation (Kovetz and Olund, 1969) and collection (Berry, 1967).

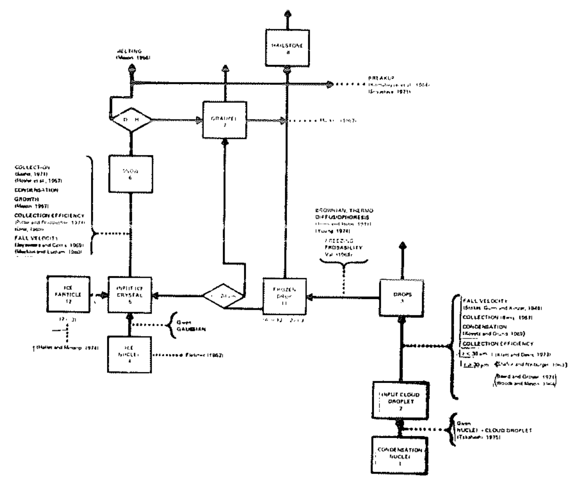

Fig. 1. Microphysical process which may form hail.

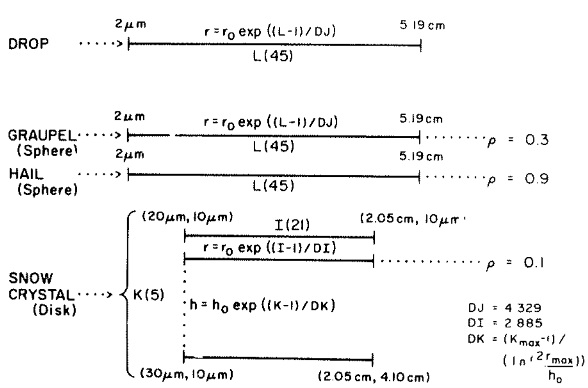

Fig. 2. Classifications of water drops, graupel, hail, and ice crystals.

Concerning collection efficiency, Klett and Davis' (1973) value was used when drop size was less than 30 μm in radius, while Shafrir and Neiburger's (1963) value was used when drop size was larger than 30 μm. The collection efficiency was modified in the case where drop size was almost equal (Woods and Mason, 1964) and where drop sizes were extremely different from each other (Beard and Grover, 1974).

Drops can capture ice nuclei by Brownian motion, thermophoresis and diffusiophoresis (Slinn and Hales, 1971, and Young, 1974). The concentration of ice nuclei in drops was monitored during the condensation and collection processes.

I believe that every ice nucleus has, more or less, a multiple character, playing roles in sublimation, freezing, contact, and condensation-freezing. However, we have not succeeded yet in separating those roles. In this model, Fletcher's (1962) formula was used to determine the activation of natural ice nuclei. Empirically we know that drops collected as rain and hailstones freeze with certain probabilities at different temperatures (Vali, 1968).

Through laboratory work it was shown that ice crystals can grow very rapidly on small frozen drops while the spherical shape is kept for a long time when the frozen drop is large. The critical size was found to be around 20 μm in radius (Takahashi and Kumai, 1976).

Ice crystals are nucleated on ice nuclei. The input ice crystal distribution was given as Gaussian form (modal size is 40 μm in diameter and standard deviation is 3). Ice crystals can also grow in a cloud from small frozen drops, ice particles generated by the ice multiplication process (Hallet and Mossop, 1974), and particles created by collision between graupel and ice crystals.

The shape of the ice crystal was assumed to be a disk and the disk was classified as a function of diameter and thickness (Fig. 2). Riming increases the thickness of an ice crystal; it was assumed that a rimed ice crystal would pass to a graupel class (density = 0.3) when the thickness of the ice crystal was the same as its diameter. When the density during riming is higher than 0.7, graupel moves to hailstone class. Macklin's formula (1962) was used to calculate the density. Nonrimed crystals make snowflakes and the oscillation of these crystals (Sasho, 1971) was considered for the collision process.

A sticking coefficient was calculated by Hosler et al (1957). Condensation growth of ice crystals was calculated by Kovetz and Olund's method.

The collision efficiency was modified by laboratory work and observation (Pitter and Pruppacher, 1974, and Ono, 1969). Fall velocity of ice crystals was derived from Jayaweera and Cottis (1969) and fall velocity of large graupel was modified by reference to Macklin and Ludlam (1960).

Ice crystals and graupel melt when they fall below the melting layer (Mason, 1956) and they break up (Komabayasi et al., 1964, and Srivastava, 1971).

Calculations were done in axi-symmetric model (Takahashi, 1976b). Typical sounding data at Wajima, Japan, during the winter monsoon season were used as environmental conditions.

The total number of cloud nuclei was chosen to be 500 cm^{-3}.

Boundary, environmental, and initial conditions can be referred to Appendix.

II. RESULTS

Vertical Velocity

At 15 min., by latent heat due to condensation, the temperature of the air near the cloud top is 2°C warmer than the base temperature at the same height. Because all of the assumed nuclei were used to form drops, supersaturation over water increases to 4%. The updraft increases to 14 m s^{-1}. The updraft profile becomes asymmetric with respect to height and the maximum downdraft is 2 m s^{-1} at R = 1.4 km from the center (Fig. 3a). Outflow increases to 4 m s^{-1} and inflow to 2 m s^{-1}. The boundary between the inflow and outflow regions increases in height to 2.6 km (Fig. 3b).

At 25 min. the height of the maximum updraft increases further to 3.8 km, while the velocity of the maximum updraft decreases to 8 m s^{-1}, owing to the accumulation of precipitation particles in the cloud and the advection of downward momentum from the cloud boundary. Graupel and small hail fall at 800 m from the cloud center and form a downdraft column in the weak updraft region near the cloud boundary. The downdraft increases to 3 m s^{-1} in a column 500 m to 1.1 km from the center of the cloud (Fig. 4a). Outflow is seen near the upper updraft region; the maximum outflow velocity is 4 m s^{-1}. Weak inflow is seen near the ground (Fig. 4b).

At 35 min. the updraft decreases to 4 m s^{-1}. A strong downdraft is seen near the ground at R = 600 m, owing both to the drag force of graupel and small hail, and to cooling by melting. Air is cooled by 2°C near the ground. The maximum downdraft is 5 m s^{-1} (Fig. 5a). Outflow, corresponding to the upper updraft, decreases to 2 m s^{-1} and a new inflow-outflow area is seen near the ground (Fig. 5b).

The transition from ice crystal to graupel-hail occurs rapidly near cloud top; this graupel-hail fall at R = 600 m and produces a downdraft. Ice crystals become more widely distributed and depending on their size (Fig. 6).

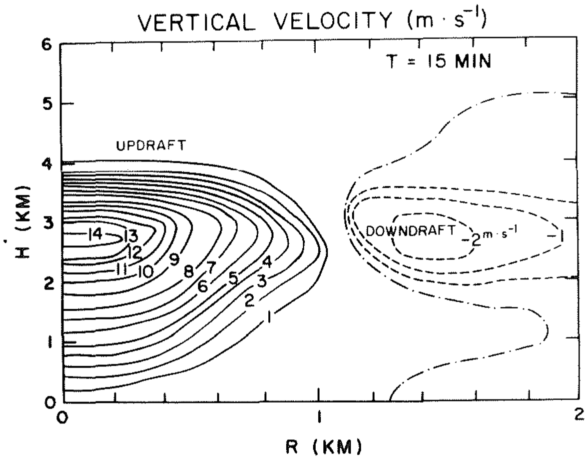

Fig. 3a. Vertical velocity (ms^{-1}) at T = 15 min. Solid lines - updraft and dotted lines - downdraft. Dash-dotted line shows the boundary between updraft and downdraft. Radial distance was cut at 2 km for illustration (boundary of radial direction is 3.2 km).

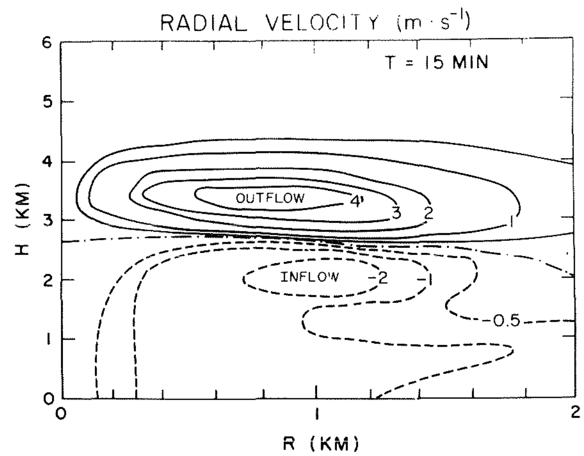

Fig. 3b. Radial velocity (ms^{-1}) at T = 15 min. Solid lines - outflow and dashed lines - inflow. Dash-dotted line shows the boundary between outflow and inflow.

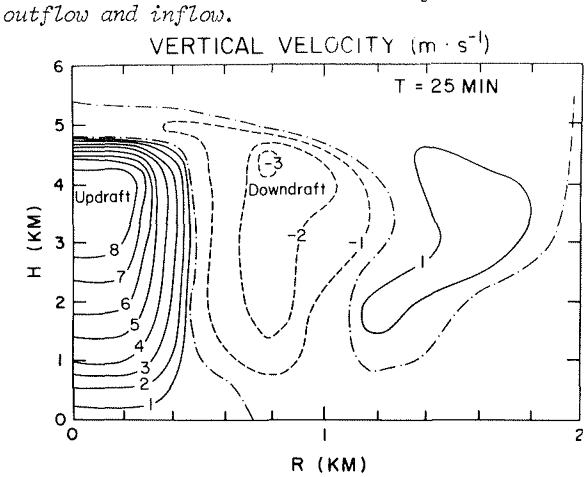

Fig. 4a. Same as Fig. 3a except T = 25 min.

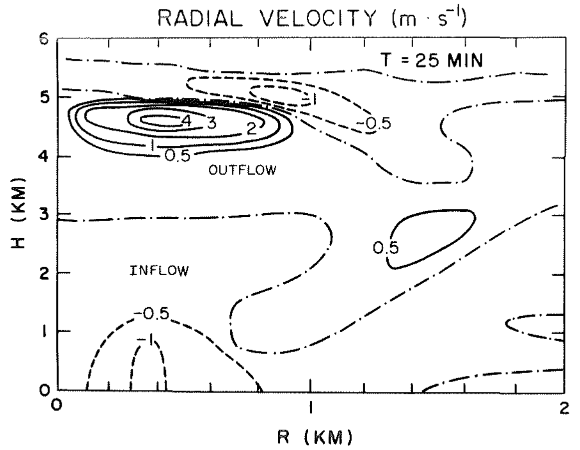

Fig. 4b. Same as Fig. 3b except T = 25 min.

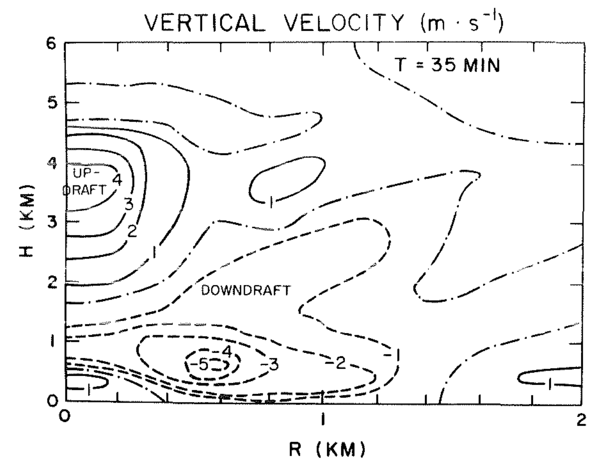

Fig. 5a. Same as Fig. 3a except T = 35 min.

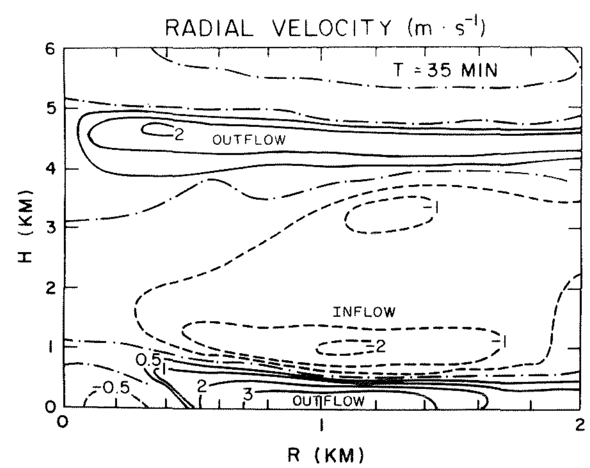

Fig. 5b. Same as Fig. 3b except T = 35 min.

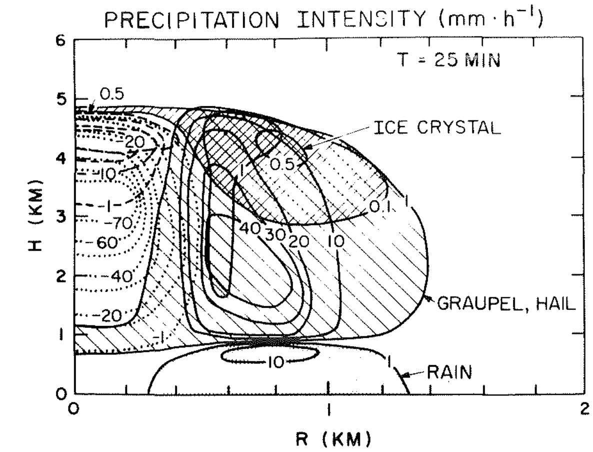

Fig. 6. Precipitation intensity (mm h^{-1}) at T = 15 min. Dotted lines - water drops transported upward, dashed lines - ice crystals transported upward, and dash-dotted lines - hail and graupel. Precipitation of water drops, ice crystals, and hail-graupel is shown by different shaded patterns.

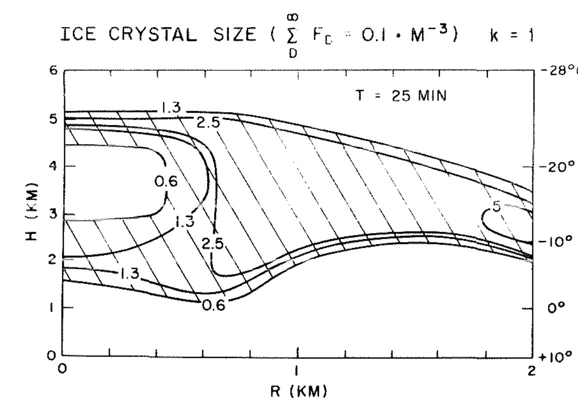

Fig. 7a. Critical unrimed ice crystal size (mm) in diameter where the concentration larger than indicated size is 0.1 m^{-3}. T = 20 min.

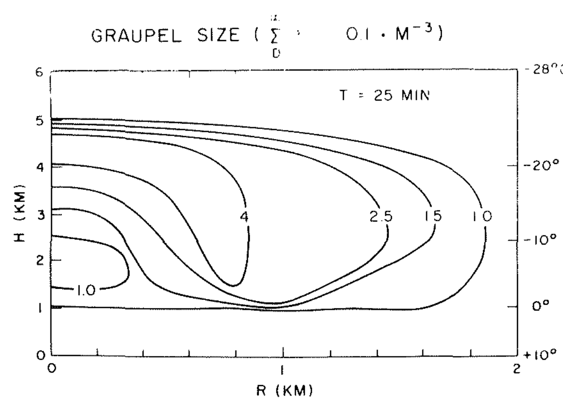

Fig. 7b. Critical size (mm in diameter) where concentration larger than indicated graupel size is 0.1 m^{-3}. T = 15 min. Vertical axis on the right is environmental base temperature.

Ice Crystals and Droplets

At 25 min. unrimed ice crystals are formed near the cloud top (H = 4.8 km) and their size increases during their horizontal movement. Larger ice crystals (D = 5 mm) are seen at R = 2 km. At H = 2.7 km, ice crystals are relatively large (1.3 mm in diameter). Such large crystals must be formed by recirculation (Fig. 7a). Because the high updraft carries the crystals out of the cloud so fast, they cannot grow large enough to initiate riming--unless they are recirculated back into the cloud. During their upward journey the recycled crystals are rimed. Relatively large graupel is formed near cloud top and fall along cloud boundary (Fig. 7b) and they melt and break up.

Broken droplets are carried into the cloud center and form large drops (Fig. 7c). The sudden appearance of large drizzle in the cloud is due to recirculation of broken drops which originated from melting graupel. Relatively large hail near cloud base is observed after the appearance of such large supercooled drops (Fig. 7d).

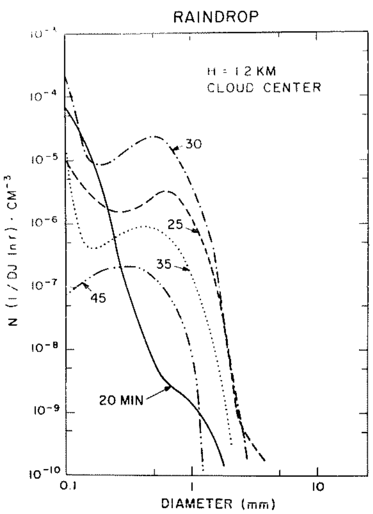

Fig. 7c. Number frequency of drops at H = 1.2 km (cloud center).

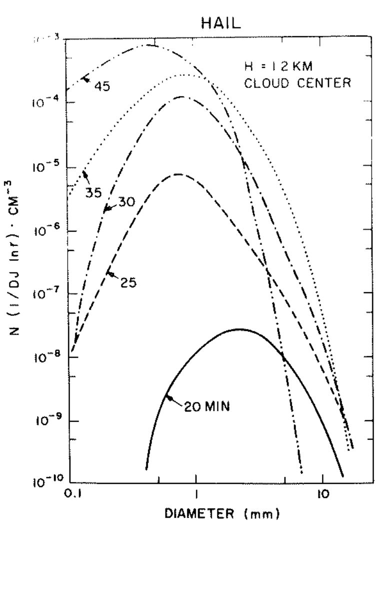

Fig. 7d. Number frequency of hail at H = 1.2 km (cloud center). Solid line (T = 20 min.), Dashed line (T = 25 min.), Dashed-dotted line (T = 30 min.), Dotted line (T = 35 min.), Dash-two dotted lines (T = 45 min.).

III. DISCUSSION

Three different growth stages appear to be needed to form large hail (Fig. 8).

1. Ice crystals are recycled in the developing stages of the cloud.
2. Graupel forms near the cloud boundary, melts below the freezing level, and breaks up. Transportation of small broken drops into the center of the cloud and formation of large drops constitute the mature stage.
3. Graupel and small hail capture the drops and relatively large hail is thus formed, representing the dissipating stage.

Without recirculation, ice crystals nucleated on ice nuclei would not grow large enough to initiate riming effectively because they are carried so quickly out of the cloud by the strong updraft. Because of recirculation, the number concentration of ice crystals increases near the warmer temperature regions and the ice crystal concentration is three orders of magnitude higher than that expected from the ice nucleus concentrations at -5°C. Graupel falls near the cloud boundary and strengthens the downdraft. Those graupel collide with cloud droplets and produce secondary ice particles by the Hallet-Mossup ice multiplication process. (In one case, ice multiplication and Vali's drop freezing were eliminated in the calculation. Although ice crystal concentration decreases without them, hail size did not change significantly).

Riming occurs on large recycled ice crystals and graupel is formed which falls along the cloud boundary. Those graupel melt and break up. The introduction of such broken drops in the cloud accelerates the collection process and form large supercooled drops. Large graupel capture those drops during their fall and form large hail.

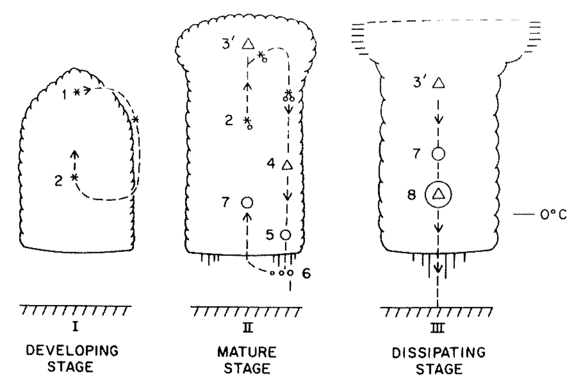

Fig. 8. Model of hail formation process.

Stage I. Ice crystal recycling (1→2)-developing stage (updraft prevails).

Stage II. Graupel formation on recycled ice crystal (2,3). They (4) fall along cloud boundary during growth, melt (5) and breakup (6). Small broken drops are recycled and form large *drops (7) - mature stage (updraft at cloud center and downdraft near cloud boundary).*

Stage III. Graupel and hail (3) fall in cloud center, capture large drops (7) and large hail (8) is formed - dissipating stage (downdraft prevails).

IV. REFERENCES

Beard, K. V., and S. N. Grover, 1974: Numerical collision efficiencies for small raindrops colliding with micron size particles. J. Atmos. Sciences, 31, 543-550.

Berry, E. X., 1967: Cloud droplet growth by collection. J. Atmos. Sciences, 24, 688-701.

Fletcher, N. H., 1962: The Physics of Rainclouds. Cambridge University Press, 386 pp.

Hallett, J., and S. C. Mossup, 1974: Production of secondary ice particles during the riming process. Nature, 249, 26-28.

Hosler, C. L., D. C. Jensen, and P. S. Goldshlak, 1957: On the aggretion of ice crystals to form snow. J. Meteor., 14, 415-420.

Jayaweera, K.O.L.F., and R. E. Cottis, 1969: Fall velocity of plate-like and culumnar ice crystals. Quart. J. R. Met. Soc., 95, 703-709.

Klett, J. D., and M. H. Davis, 1973: Theoretical collision efficiencies of cloud droplets at small Reynolds number. J. Atmos. Sciences, 30, 107-117.

Komabayasi, M., T. Gonda and K. Isono, 1964: Lifetime of water drops before breaking and size distribution of fragment droplets. J. Meteor. Soc. Japan, 42, 330-340.

Kovetz, A., and B. Olund, 1969: The effect of coalescence and condensation of rain formation in a cloud of finite vertical extent. J. Atmos. Sciences, 26, 1060-1065.

Macklin, W. C., 1962: The density and structure of ice formed by accretion. Quart. J. Roy. Meteor. Soc., 88, 30-50.

Macklin, W. C., and F. H. Ludlam, 1960: The fallspeeds of hailstones. Quart. J. Roy. Meteor. Soc., 86, 72-81.

Mason, B. J., 1956: On the melting of hailstones. Quart. J. Roy. Meteor. Soc., 80, 209-216.

Ono, A., 1969: The shape and riming properties of ice crystals in natural clouds. J. Atmos. Sciences, 26, 138-147.

Pitter, R. L., and H. R. Pruppacher, 1974: A numerical investigation of collision efficiencies of simple ice plates colliding with supercooled water drops. J. Atmos. Sciences, 31, 551-599.

Sasho, Y., 1971: Study of the formation of precipitation by the aggregation of snow particles and accretion of cloud droplets on snowflakes. Pap. Meteor. Geophys., 22, 69-142.

Shafrir, O., and M. Neiburger, 1963: Collision efficiencies of two spheres falling in a viscous medium. J. Geophys. Res., 68, 4141-4148.

Slinn, W. C. N., and J. M. Hales, 1971: A reevaluation of the role of theromphoresis as a mechanism in-and below-cloud scavenging. J. Atmos. Sciences, 28, 1465-1471.

Srivastava, R. C., 1971: Size distribution of raindrops generated by their breakup and coalescence. J. Atmos. Sciences, 28, 410-415.

Takahashi, T., 1975: Tropical showers in an axisymmetric cloud model. J. Atmos. Sciences, 32, 1318-1330.

-----, 1976a: Warm rain, giant nuclei and chemical balance. (In press J. Atmos. Sci.)

-----, and M. Kumai, 1976: Growth of ice crystal on frozen drops (to be submitted to J. Atmos. Sciences).

-----, 1976b: Hail in an axisymmetric cloud model. (In press J. Atmos. Sciences).

Vali, G., 1968: Ice nuclei relative to formation of hail. Sci. Rept. MW-58, McGill University Stormy Weather Group, Montreal, Canada, 51 pp.

Woods, J. D., and B. J. Mason, 1964: Experimental determination of collection efficiencies for small water droplets in air. Quart. J. Roy. Meteor. Soc., 90, 373-381.

Young, K. C., 1974: The role of contact nucleation in ice phase initiation in clouds. J. Atmos. Sciences, 31, 768-776.

V. APPENDIX

Boundary, Environmental and Initial Conditions

Temperature and humidity profiles for the model are similar to those which occur in Wajima (Japan) in a typical winter monsoon season. However, temperature at the ground is increased to +10°C so that the cloud base temperature is +5°C, which is that usually observed in hail clouds in Colorado. Temperature is assumed to decrease drop adiabatically up to 1.2 km and then by $6.5^{\circ}C\cdot km^{-1}$ up to 4 km. Above 4 km the temperature decreases by $4.0^{\circ}C\cdot km^{-1}$.

In order to maintain cloud integrity despite its minimal size, a high humidity environment is assumed. Humidity at the ground is 85%; it increases to 95% at 800 m, and is 95% up to 3 km. Humidity then decreases linearly and is 20% at 5.8 km.

Top, bottom, and side boundary conditions were assumed to be free-slip conditions, so that $\zeta = 0$ and $\Psi = 0$ at all boundaries.

Values such as θ and Q_v were fixed at top and bottom boundaries and precipitation particles were set to zero at the bottom boundary. There is no advection from side boundaries.

The advection term was calculated by an upstream scheme to the second order, and other terms were derived by a centered difference scheme. All calculation were done by a forward scheme.

Grid size is 31 in the vertical axis and 17 in the radial axis. The cloud in the axisymmetric model is highly localized so that a small domain in the radial direction will minimize the wall effect. Dynamical terms were calculated by $\Delta t = 5$ s and collection terms by $\Delta = 20$s. Grid size is 200 m for both horizontal and vertical directions. For details on the choice of time intervals, grid sizes or Kovetz and Olund's scheme, the reader is referred to Takahashi (1976).

The initial impulse for Ψ is given in the range from the center to 1.5 km in the R direction, and to 2 km in the Z direction, as

$$\Psi(R,Z) = \Psi_0 \left(\cos \frac{\pi(R - R_0)}{8\Delta R}\right)^2 \left(\cos \frac{\pi(Z - Z_0)}{12\Delta Z}\right)^2$$

where Ψ_0 is 1.8×10^{11}, R_0 and Z_0 are 800 m, and ΔR and ΔZ are 200 m. The initial maximum vertical velocity is 1 m s^{-1}. The area of grid points Z = 400 m to 1.6 km and R = 0 to 800 m is assumed to be saturated in order to initiate the cloud sooner and to save computer time.

Calculation Process

The calculations are performed according to the following steps: (1) Dynamic terms are calculated in fine time steps (Δt = 5 s). (2) After four (or two) repetitions of the cycle, the nucleation and condensation of precipitation particles are calculated and the time steps are increased to 20 s. (3) Riming and freezing rates are calculated. (4) The collection rates for drops and ice crystals are calculated. (5) The melting rates for solid particles are calculated. The rate of temperature change during cloud physical processes and the total liquid water content are derived. Return to step 1. (6) All variables are printed out every 5 min. Radar intensity and precipitation intensity are also calculated every 5 min.

Dynamic equations can be referred to Takahashi (1975).

THREE NEW INSTRUMENTS FOR CLOUD PHYSICS MEASUREMENTS: THE 2-D SPECTROMETER, THE FORWARD SCATTERING SPECTROMETER PROBE, AND THE ACTIVE SCATTERING AEROSOL SPECTROMETER

Robert G. Knollenberg

Particle Measuring Systems, Inc.,
Boulder, CO

1.0 INTRODUCTION

Three instruments have been developed during the past two years at Particle Measuring Systems (PMS) which are becoming widely used by the cloud physics community for airborne particle size measurements. The instruments are 1) The Two Dimensional Optical Array Spectrometer (2-D Probe), 2) The Forward Scattering Spectrometer Probe (FSSP), and 3)The Active Scattering Aerosol Spectrometer (ASAS). The three instruments cover vastly different particle size ranges; however, they have a common technology. The 2-D Probe is a logical extension of the standard Optical Array Spectrometer which sizes in one dimension only. The FSSP and ASAS both use the imaging technology derived from optical array instruments to define their sample volume even though sizing is through pulse height analysis.

2.0 THE 2-D PROBE

The 2-D Probe utilizes a photodiode array and photodetection electronics similar to the standard Optical Array Probes (see Knollenberg, 1970, 1972). However, the 2-D Probe contains a high speed front end memory enabling each photodetector element to encode many bits of shadow information from each particle. The particle's transit scans the array and *image slices* are recorded across the shadow to develop a two-dimensional image. It is thus a true parallel processor of image data as opposed to serial scanning devices common to vidicons, TV and the Reticon array.

The 2-D Probe is packaged in a cylindrical pod (see Fig. 1) and requires a special data acquisition system (DAS) for readout. The particle image data is recorded directly on a computer-compatible tape recorder and simultaneously displayed on a CRT. The probe can collect particle image information at the rate of 128 million bits per second. However, data is recorded only when particles are present resulting in automatic data compression.

Two types of 2-D Probes have been developed covering size ranges of 25-800 μm and 200-6400 μm. The 25 μm resolution instrument employs 32 active photodiode elements in the array and takes image slices at a rate of up to 4 million per second when a particle passes through. At a true air speed of 100 m sec^{-1}, 250 nsec corresponds to 25 μm of distance, which is the effective diameter of each element in the array at 8X magnification (the 200 μm resolution instrument has one-eighth this resolution and image slice rate). At this air speed the size resolution across the array (particle width) is identical to the image slice resolution through the array (particle length) resulting in square raw image data.

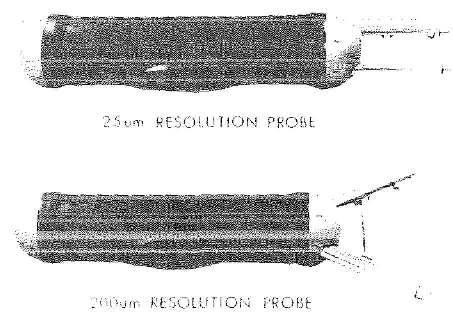

Fig. 1: Photographs of the two 2-D Probes manufactured by PMS.

Data from each image slice is stored in a static MOS shift register which serves as a buffer for writing onto computer-compatible tape via the DAS. Two MOS buffers are employed in a *ping-pong* fashion so one can be available for loading (at a rate determined by incoming particles) while the other is used to unload a previous sampling of particles (at a rate necessary for writing onto tape). As long as unloading is accomplished earlier than loading in each case, no *indigestion* is encountered and the buffer roles can be alternately reversed with no loss of data.

A typical complete DAS employs a standard 9-track 25 ips recorder with 1600 cpi density which limits the average image slice rate to about 7,000 sec^{-1} with a record length of 4096 bytes. With 600 feet of tape available on the 7 inch reel machine, the maximum image slice rate can be maintained for only about 5 minutes on a single reel of tape. However, for average particle rates with reasonable water content values,much longer recording times per reel are typical. By using 2 tape transports, continuous, uninterrupted sampling can be maintained indefinitely.

2.1 The 2-D Probe Optical System

The laser normally used in either 2-D Probes is a 2.0 mW He-Ne unit. The optics seen in

Fig. 2 appear quite different in the two types of probes manufactured; however, they are functionally very similar and only the probe with 25 μm resolution will be described. In this probe, the condensing element is a single f/400 astigmatic cylinder lens. The optical path makes two 90° bends using 45° mirrors on either side of the sample volume. Particles passing through the laser beam, in the vicinity of the object plane, are imaged by a two-stage imaging system onto the photodiode array. A 60 mm f/5.0 coated objective

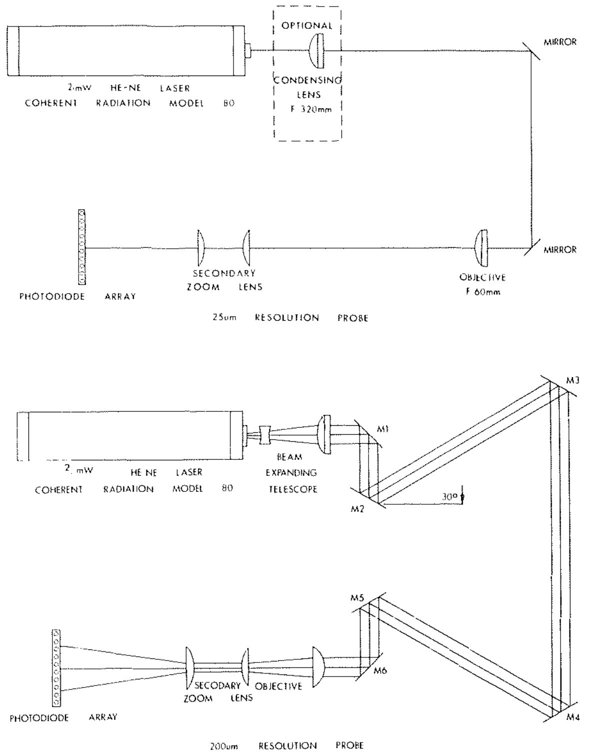

Fig. 2: 2-D Probe optical systems.

provides a magnification of approximately 2.5X. A second-stage lens (microscope zoom eyepiece) provides a variable magnification for setting the desired instrument resolution. Total magnification can be varied from 5X to 10X by setting the zoom. A magnification of 8X provides 25 μm resolution.

2.2 The 2-D Probe Electronics

The photodiode array used is a United Detector Technology PIN device designed especially for the 2-D Probe. The array has 32 circular photodiodes located on 8 mil (200 μm) centers. The photodiode array is back biased such that the photodiode elements are in a photoconductive operating mode. Each array element produces 0.2-0.5 uA photocurrent.

The diode array is mounted on a circuit board which also contains the first stage preamplifiers for each of the elements (see Fig. 3). Following the pre-amp output for each element is a second-stage video amplifier with reference buffer and voltage comparator driving two 1024 bit static MOS shift registers. The second-stage amplifier provides a gain of 10-20 depending on desired output and individual laser power. The output signal of the second-stage amplifier goes directly to one input of the voltage comparator.

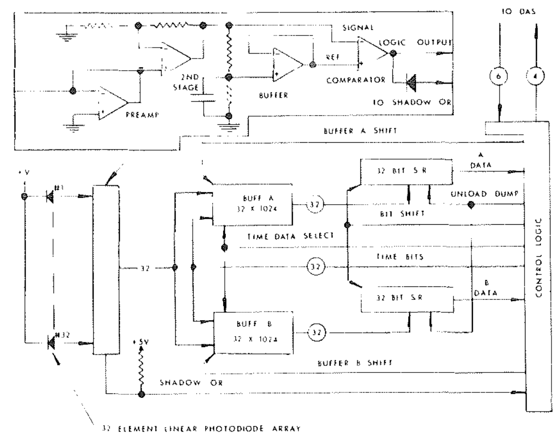

Fig. 3: Simplified 2-D Probe block diagram.

The other input of the voltage comparator is a reference signal derived from passing the signal through a low-pass filter voltage-divider network. The filtered output is buffered by a voltage follower to provide a reference signal of 50% of the quiescent video output signal. When a shadowing event decreases the signal below the reference level, the comparator output changes state and enters shadow bits (zeros) serially into the shift register at a slice rate proportional to true air speed (TAS). When the signal again exceeds the reference, unshadowed bits (ones) are entered. The comparator output of each element is connected through a diode to all other comparator outputs forming a shadow OR such that actual loading of image slices will begin when any one of the 32 elements has been shadowed. Loading is terminated when all elements return to the unshadowed condition. At this time, one slice of time information is loaded which records the precise number of TAS clock periods that elapsed between the particle just loaded and the previous particle. This is followed by an all zeros slice after which the probe is quiescent until the next shadow is encountered. Loading continues in this manner until one buffer is full and then loading is automatically switched to the alternate buffer while a signal to the DAS allows unloading the buffer just filled.

2.3 The 2-D Probe Data Format

Examples of plotted image data are shown in Fig. 4A and 4B generated by a printer/plotter. Shadowed elements are plotted dark (zeros) and unshadowed elements are plotted light (ones) with each particle image separated from adjacent images by a coded time slice and an all zeros slice. In this particular system, the top 8 bits of the time slice and all zeros slice, are fixed alternate bits used for identification purposes. Time progresses from left to right on the plots, with the time slice following each image.

The sample width is 32 elements wide; however, particle images can ordinarily be sized and structure determined even when the image is not completely contained within the sample width.

When computing sample volume, one must use the effective sample width as measured from the center of these shadows. For spherical drops, this poses little difficulty, but for certain structures, care must be taken.

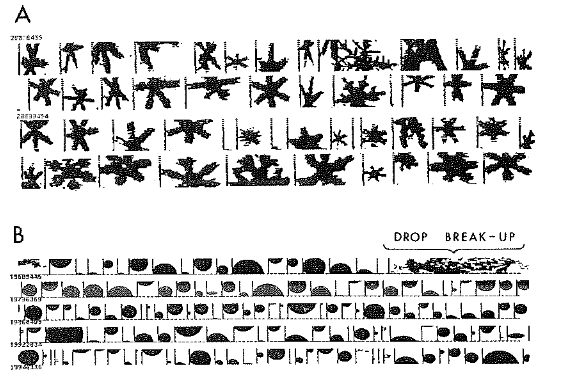

Fig. 4: Flight data samples of 2-D imagery in snow and rain. The snow crystals above are displayed at twice the magnification as the raindrops. Note the plume from a fractured drop in 4B.

2.4 2-D Probe Error Analysis

The data presented in Fig. 4A and 4B are examples of good 2-D Probe imagery. In field use, we have observed fewer problems in precipitation (snow and rain) than clouds. In the above examples, the problems are restricted to the mechanical break-up of drops and snow crystals on the edges of the sampling aperture. Fig. 4B shows the plume from a ruptured raindrop recognizable by its image characteristics. Fractured snow crystals cannot be so easily distinguished unless individual pieces are observed in an image pattern. The frequency of such events is proportional to the ratio of the particle size to sampling aperture width.

The above problem can never be entirely eliminated and is not regarded as serious. Of greater concern has been the effects of the small droplet population in clouds. In high LWC clouds, small droplets collect on the probe tips and the sampling aperture edges and is stripped off by the airflow as large drops. The resulting drops often have a good fraction of the aircraft's velocity and the images are accordingly stretched as shown in Fig. 5. The events are often near depth-of-field limits and the center of such images exhibit

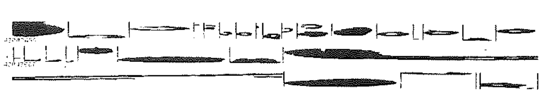

Fig. 5: Images of drops shed from the 2-D Probe tips. Elongation occurs becuase of slow relative velocities.

diffractional filling. This entire activity results from the collection of cloud droplet water and the subsequent shedding of larger drops. While software can be generated to recognize these events, they at times consume considerable recording bandwidth and, in general, detract from otherwise excellent imagery. Part of the problem has been eliminated (~70%) by recent probe tip modifications. Further progress must await the results of aerodynamic studies in the wind tunnel at PMS.

Because of the sophistication of the 2-D Probe, a housekeeping data package is generally used to monitor the instrument's health. One important measurement here is the heated-mirror temperature in the probe tips. The heaters generally produce a 30 - 40°C temperature rise, sufficient to prevent icing and fogging. It is rare that the mirrors become wet in flight. Invariably, the wetting of optics is more probable while the aircraft is on the ground.

In a few of the 2-D Probes with 25 µm resolution we have found alignment problems. In the most severe case (University of Wyoming) a remotely-controlled x-y drive was installed for alignment capability. This instrument has since been modified and alignment is required only on one axis. These effects have been largely traced to material inhomogeneity.

A final temperature-related error was found in the 200 µm resolution instrument. In certain cases, the unheated folding mirrors used in the instrument were observed to distort during cold-soaking. The hard epoxy-bonding cement was replaced by a flexible-bonding agent, eliminating the problem.

The above error sources are believed to be the most important, if not the most common. The 2-D Probe provides its user with a 128 MHz bit rate fully capable of exposing its errors as well as detailing a particle's features in a few microseconds. This has proven to be an invaluable aid for rapid troubleshooting.

3.0 THE FSSP

The FSSP is an improved successor to the Axially Scattering Spectrometer Probe (ASSP), the first light scattering cloud droplet probe manufactured by PMS. The primary improvements are in refinements to its optical and electronic subsystems, rather than in fundamental design changes.

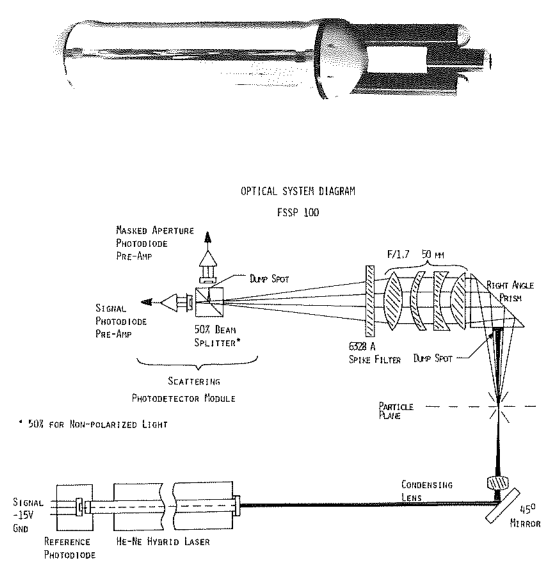

Fig. 6: FSSP Probe and optical system.

Both instruments are truly forward scattering instruments with the FSSP having the wider collecting geometry (4-18° as opposed to 7-16° for the ASSP). However, the physical construction of the FSSP shown in Fig. 6 is entirely different. The physically larger FSSP provided an envelope that not only easily accomodated certain improvements, but also made available space for possible future growth. One proposed use of this unused space is for photomultiplier tube detectors, which will give the FSSP 0.2 μm detectivity at aircraft speed. The pod enclosure is identical in size to the 2-D Probes and they are mechanically interchangeable (requires cable interconnect changes for electrical compatibility).

The FSSP normally has a primary size range of 2-30 μm diameter, resolving particles into 15 size classes. Four switchable size ranges are required to cover 0.5-45 μm. It is normally set up to size particles having velocities from 10-125 m sec^{-1}. The probe electronics are self-contained, the output being the particle size in binary code accompanied by a strobe pulse to increment an appropriately addressed memory channel in a data acquisition system.

3.1 Light Scattering Properties of the FSSP

In the FSSP particles are sized by measuring the amount of light scattered into the collecting optics during particle interaction through a focused laser beam. MIE scattering calibration curves are shown in Fig. 7. Our primary interest here is

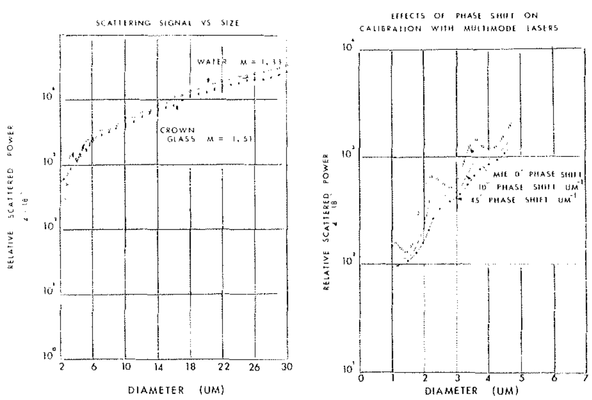

Fig. 7: The figure at left shows a theoretical MIE calibration curve for the 2-30 um primary range of the FSSP. The figure at right illustrates the suppression of resonance effects found in laboratory measurements with multimode lasers. The top curve is the theoretical MIE response. The lower curves show the reduction in resonance amplitude due to variations in phase across the wave front.

to show that the computed resonance behavior between 1-5 μm is experimentally observed to be less pronounced. Laboratory experiments show such resonance to be related to phase front coherence. Fig. 7 (right) illustrates the advantages of multimode lasers where the phase reverses several times in the beam pattern. The resulting smoothed calibration curve substantiates the choice of high order multimode tubes. The resulting errors due to fundamental uncertainties in scattering response are generally less than other experimental errors if the refractive index is known. Even in the 1-5 μm range the uncertainty due to unknown refractive index is less than 1 μm.

3.2 FSSP Laser and Optical System

The laser used in the FSSP is a high order multimode 5 mW He-Ne tube and focused to approximately 200 μm diameter using condensing optics with a 60 mm effective focal length. The point of focus coincides with the center of the sampling aperture. Particles passing through the laser beam in the sampling aperture, scatter energy into the optics. The amount of scattering for a given particle size is a function of the laser mode, as well as the exact chordal transect through the beam. With a high order multimode laser, the probability of intersecting the peak isophote is as high as 90% (typically 80%). Correction for edge effect errors can be accomplished statistically; however, in the FSSP, the particle transit times can be measured precisely, allowing for edge-effect rejection using pulse-width comparison techniques.

The scattered energy is relayed from the object plane by a right angle prism to a 50 mm f/1.7 collecting lens and focused through an interference filter to a masked beam-splitting prism. The transmitted laser beam is dumped at a central stop on the right angle prism. The masking on the prism is a central 1 mm dump spot on the 90° transmitting face creating an annular aperture. This serves to allow only light transmission from particle images when the particles are displaced a certain distance in either direction from the object plane and no transmission when at or very near the object plane.

3.3 FSSP Electronics and Sample Volume Definition

A simplified block diagram of the FSSP electronics is shown in Fig. 8. The FSSP photodiode

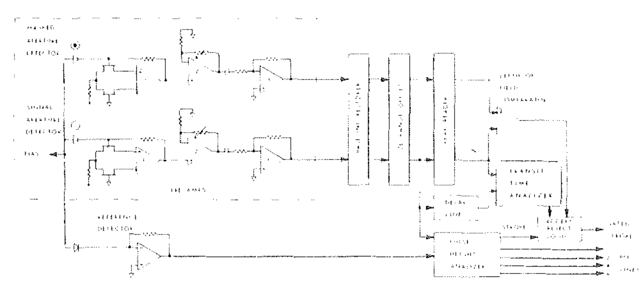

Fig. 8: Simplified FSSP block diagram.

detectors are EG&G SGD-100 devices placed to accept the light directly transmitted through the prism and that reflected 90° through the masked aperture. Two three-stage pre-amps with the above photodiodes amplify the scattering signals passed by the transmitting and masked prism faces. The second stage is a programmable operational amplifier with four internally-multiplexed amplifiers operating at gains compatible with the size ranges selected. This amplifier is remotely controlled by logic lines.

Several measurements are performed on the pulse pairs generated by the two pre-amps. The required circuits are quite complex and will only be described functionally. First, the pulse trains from both signal detectors undergo signal preprocessing. The preprocessing includes baseline restoration, programmed offsets (baseline offset for each range), and peak-reading circuits to momentarily hold the maximum pulse amplitude from both detectors. The simplest pulse measurement is that of the pulse heights of the signal pulses for particle size classification. The scattering-signal pulses are coupled to a pulse height detector comparing their maximum amplitude with a reference voltage derived from a separate measurement of the DC light signal illuminating the particles. This is accomplished with a series of voltage comparators having square weighted voltage thresholds. The outputs are gated to allow only a single size output. It is also necessary to establish whether 1) a particle is within the desired depth-of-field, and 2) if it passes through the central part of the laser beam where the intensity is uniform. Both of these circuit requirements are more demanding. The first requirement uses pulse height comparison of the pulse pairs and will be referred to as depth-of-field truncation. The second requirement uses pulse half-width comparison and is referred to as edge-effect rejection. Both processes provide accept/reject criteria for each pulse height measured, defining the sample volume.

3.3.1 Depth-of-Field Truncation

The total depth-of-field over which a particle is viewed extends over about a 5 mm path. It is necessary to truncate the actual depth-of-field to considerably less than this distance to avoid errors associated with the loss of collecting aperture and scattering signal. This is accomplished by comparing signal levels from the peak readers. Because of the annular aperture in the masked prism face, the light from a particle near the object plane is greatly reduced and is,in general, less because of the loss of collecting aperture. The gain ratio of annulus signal to scattering signal must be greater than unity and is normally 2.5:1. The depth-of-field is defined as that region where the signal pulses are of greater amplitude than the annulus signal pulses. The depth-of-field may be varied by increasing or decreasing the gain in the annulus signal path. The increase in gain decreases depth-of-field while a decrease in gain increases depth-of-field. The instrument is normally set with a depth-of-field between 2 and 3 mm for several reasons. First, the depth-of-field cannot be reduced much below 2 mm because of optical considerations. Secondly, reduction of depth-of-field requires increase of annulus gain and deteriorates annulus S/N. Thirdly, the illumination is uniform enough to allow a 3 mm depth-of-field. The small changes in angular distribution of scattered light with differing drop size have negligible effect on depth-of-field as long as the gain ratio is sufficiently high.

3.3.2 Edge-Effect Rejection Circuitry

In order to reject pulses from particles passing through the edge of the laser beam, the transit time of the particle pulses must be analyzed. The particle transit time varies with particle velocity and the particular chordal transect through the laser beam. When the particle passes through the center of the laser beam, it passes through the widest section and produces the longest transit time. Near the beam edges, the transit times are very short. The beam edges are also regions of weaker intensity, and particles passing through the edges are thus undersized.

In order to avoid pulse amplitude dependency on pulse width, the signal pulse train is first delayed by a delay line for several microseconds. The output of the signal peak reader is divided by a factor of two to derive a comparator threshold at one-half the peak amplitude. The half-width of the delayed pulses are then measured to derive transit time pulses. Particle transit times are measured and compared with stored average values (the average transit time for about 1000 pulses is stored in an up-down counter which maintains a running mean of the average particle transit time). Pulses greater than average in width are accepted.

3.4 FSSP Field Performance

The greater performance of the FSSP, relative to the ASSP, is apparent in field operations using the instrument. The single most important feature of the FSSP increasing its performance is its higher magnification optical system which reduces sample volume to where coincidence errors are less than 10% at concentrations of 10^3 cm^{-3}. Fig. 9A illustrates comparative spectra from flights using the PMS 206 aircraft and a high framing rate data system having one-fifth second resolution. Flying at 60 m sec^{-1}, adjacent spectra show large concentration fluctuations (the concentration fluctuations in clouds ordinarily show peak concentrations several times the mean). The FSSP shows negligible effects of coincidence error on the spectra at the high concentrations relative to lower concentrations. A droplet spectrometer must be able to perform at these high concentrations, which over larger integration times (e.g.,one second) are not often observed. These concentration fluctuations are not the result of sampling statistics but are the real cloud structure.

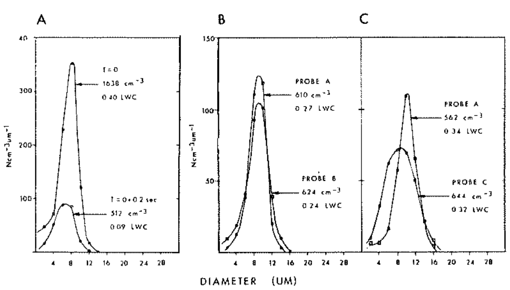

Fig. 9: FSSP flight data samples.

Fig. 9B and 9C illustrate pairs of droplet spectra from three different FSSPs. The first pair in Fig. 9B is typical of the intercomparison of two identical instruments. The second pair in Fig. 9C shows an undersizing effect of an FSSP (C) with a 38 mm condensing lens where the intensity is not sufficiently uniform over the sample volume. The 38 mm lens was initially tried in the FSSP.

The FSSP will probably evolve into an *in situ* aerosol spectrometer. The future use of photomultiplier detectors has already been mentioned. In this regard,the larger collecting angles reduce the effects of refractive index on sizing accuracy. Further increases in magnification may be desirable to handle still higher concentrations. For cloud physics work involving droplet spectra, the FSSP appears to be quite satisfactory. We believe its accuracy is sufficient not to hide the important mechanisms that cloud spectra evidence and that its sampling rate is sufficient to reveal them.

4.0 THE ASAS

The active open cavity of a gas laser provides an intense particle illumination source for light scattering measurements in the submicron range. Work describing single particle extinction within the laser cavity was first described by Schleusener (1969) and later detailed by Schuster and Knollenberg (1972). Instruments using light scattering within the cavity were described by Schehl *et al.* (1973) and Knollenberg (1973). More recently, Knollenberg and Luehr (1975) have described new cavity-scattering instruments providing a detailed noise analysis and theoretical scattering response computations. It is our intention to briefly introduce the ASAS and discuss its application and limitations in fine particle studies.

4.1 General Instrument Description

A typical ASAS is designed with four overlapping size ranges with each size range divided into fifteen linear size intervals. It is packaged in two separate enclosures, housing the probe with its optics and pre-amps, and an electronics console (see Fig. 10).

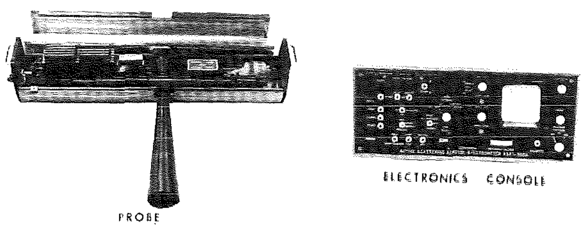

Fig. 10: ASAS Probe and electronics console.

The design of the ASAS Probe utilizes aluminum extrusions for mechanical stability. Laser and detector alignment is achieved with spring-loaded x-y screw adjustments. The ASAS laser is a hybrid He-Ne (6328Å) tube by Coherent Radiation of Palo Alto,California. The tube is specially designed for the ASAS.

A 16 channel pulse height analyzer has its reference voltage derived from the source of illumination providing effective automatic gain control (AGC). A programmable amplifier is used to gain switch and provide the size ranging to accomodate the large dynamic range of the instrument. The primary method of aspiration is unlike any used in conventional aerosol counters. It is in essence a miniature wind tunnel. A 10:1 accelerator produces a flow rate of 6.15 m sec^{-1} intersecting with a 3 cm length of the laser beam. The sample volume is positioned at the center of flow. This system relies entirely upon optical definition of the sample volume. Problems associated with small bore tubing are eliminated. This makes the technique particularly useful for sizing volatile materials such as natural smog.

The data acquisition system within the electronics console has a MOS memory with twenty addresses. Fifteen of the addresses are used for particle size distribution storage. The remaining addresses are normally used for other housekeeping information such as selected size range and time of day. An eight channel subcommutated analog input is also available. A selectable digital display and a graphical CRT display are provided for real-time data monitoring requirements of precise particle counts or distribution functions.

4.2 The Laser and Light Scattering Properties of the ASAS

While there are several advantages of using the laser cavity as a source of particle illumination rather than classical laser scattering approaches, the most important aspect is its unmatched high energy density. The optical diagram of Fig. 11 shows the typical cavity configuration for the ASAS. A hybrid laser is constructed having a plasma tube sealed with a high reflectivity curved mirror and a Brewster's window. An external adjustable high reflectivity mirror completes

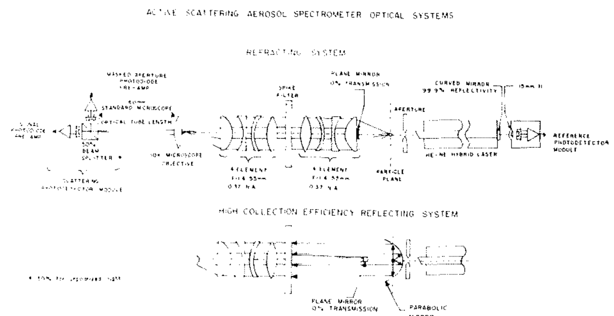

Fig. 11: In the ASAS, the refracting optical system is generally used. The high efficiency reflecting system is reserved for maximum resolution applications.

a hemispherical cavity laser operating in TEM_{00} mode with a beam having a spot diameter of about 300 μm at the plane mirror and 800 μm at the curved mirror. At the sample volume location the laser beam is approximately 500 μm diameter. Assuming a Gaussian intensity distribution, a central brightness in excess of 1000 W/cm^2 is computed. Selected tubes have had measured values as high as 4000 W/cm^2. Since the sealed curved mirror of the laser cavity is a protected surface whose transmission characteristics do not vary with time, the leakage out this mirror is directly proportional to the power illuminating the particles at all times. By measuring the leakage and deriving a voltage reference to a pulse height analyzer, one can compensate for changes in illumination.

Theoretically the particle scattering response in an active laser cavity is closely analogous to electromagnetic scattering in a standing wave. The theoretical solutions we have obtained only approximate the scattering phenomenon because a particle traversing through the beam inside the cavity reduces cavity Q and the laser gain during particle interaction. The effect is nonlinear with much higher extinction relative to scatter. Laboratory measurements of the relative extinction and scattering efficiency factors in current instrument high Q cavities given in Fig. 12 (left) differ by a factor of 10,000. The extinction process is not true extinction at all, but largely cavity detuning and cannot be truly separated from it. The shape of the curves show a characteristics rise in Qsca and Qext with a maximum at about 0.5 μm and with a more rapid decrease than for classical scattering because of laser gain dynamics.

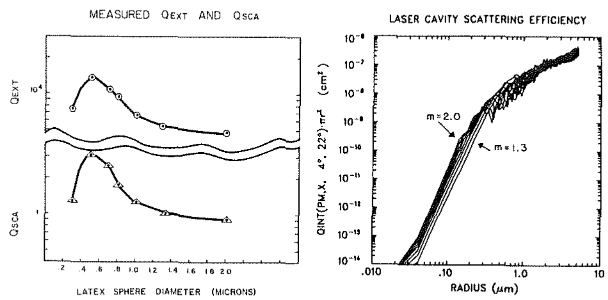

Fig. 12 (left): The above measurements are indicative of the role the cavity "Q" plays in the extinction process. The scattering efficiency factors are reasonably close to computed values.
Fig. 12 (right): Theoretical instrument response (effective cross section) for 4^o-22^o collecting geometry for m=1.3, m=1.4, m=1.5, m=1.6, m=1.7, m=1.8, m=1.9, m=2.0.

Fig. 12 (right) presents theoretical calibration response curves calculated for scattering in a standing wave for the collecting geometry involving collecting angles of $4 - 22^o$ for eight real refractive indices. The results are similar with collecting angles of $5 - 90^o$ but with less variation with refractive index. These results in general show finer structured resonance behavior than the computed response from superimposed MIE solutions for the forward and backward scattered components. Our experimental work shows some differences in the resonance structure,particularly with the resonance amplitudes,but generally support the results. Several factors reduce the observed resonance. The cavity gain dynamics have already been mentioned. In measurements of classical scattering described in Section 3.2, we found ourselves only able to reproduce the full theoretical resonance response if the beam was truly uniphasal which generally necessitated spatial filtering. The lack of spatial filtering or the presence of multimodes always suppressed the predicted resonances. These phenomenon may all be attributed to the lack of phase front coherence implicitly assumed in such calculations. In most cases, the arguments would extend to scattering within a standing wave.

4.3 The ASAS Optical System and Sample Volume Definition

The two variations of optical systems shown in Fig. 11 differ fundamentally in the use of a parabolic mirror instead of refracting lenses in the collecting optics. The reflecting system is used for high efficiency light gathering applications below 0.1 μm. The reflecting system cannot be designed for trajectory analysis at reasonable cost so is used where restricted flow is acceptable. Edge-effect rejection, using transit time analysis similar to that in the FSSP, must be employed. The refracting system is a high resolution system which is used for particle trajectory analysis as well as light gathering (to eliminate problems with particle flow in small bore tubing). Because of its unusual operating mode it will be described in detail.

The high resolution optical system collects the light scattered and reimages at 10X magnification or greater within a dark field. A 50% beam splitter produces two image planes for two detectors. The reflected image prism face is masked with a 0.78 mm diameter vertical slit to block central transmission. The other detector prism face is unmasked. The transmitted laser beam is dumped at a central stop behind the mirror on the first lens element. The masked beam splitter derives two signals, which in conjunction with double pulse height analysis, provide a means of determining if a particle's position is in the desired sample volume. The relative size of the sample volume cross section with respect to the laser beam is depicted in Fig. 13. The sample volume includes only the region near the center of the laser beam. The sample volume cross section is noticeably diamond shaped. The center of

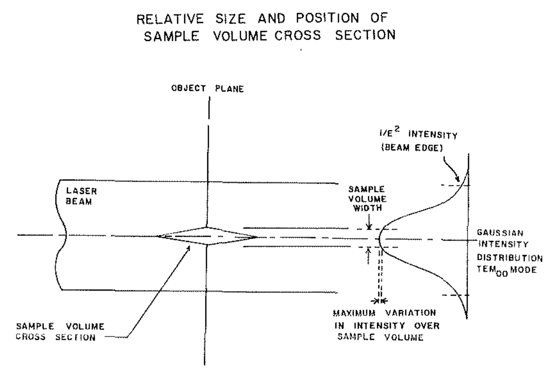

Fig.13: The relative size and position of sample volume cross section.

this diamond cross section coincides with the object plane of the collecting optics. The points of this diamond cross section define the limiting depth-of-field of the ASAS. Both the width of the cross section and the depth-of-field vary inversely with the magnification used in the collecting optics. The diamond shaped sample cross section results from the accept/reject criteria used after

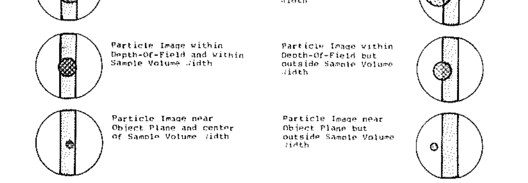

Fig.14: Image sizes and positions on masked aperture detector.

comparing signals at the masked and unmasked detectors. The light transmitted on axis through the beam splitter is the signal used to size the particles. The light reflected at 90^{o} forms its image on a circular aperture with a central opaque vertical slit. Shown in Fig. 14 are the size and positions of images formed by particles at various positions in the illuminated volume. It is important to understand that for small particles (essentially point objects) the image size is only a function of its axial displacement from the object plane. The image size is linearly related to the numerical aperture of the collecting optics and is given approximately by: Image size = N.A. x displacement from object plane. It is apparent that only images that are near the object plane and the center of the sample volume form images with light concentrated on the opaque slit on the masked detector as illustrated in Fig. 14. Thus, such images transmit little signal through the masked aperture. What is normally done in the ASAS is to use a gain ratio of masked aperture detector to signal aperture detector of 4X for best noise immunity. Particles whose pulse amplitudes, as seen by the masked aperture detector, are greater than those seen by the signal aperture detector are rejected. The diamond shaped sample cross section results. The sample cross section is the product of the sample volume width and one-half the depth-of-field.

4.4 ASAS Resolution and Limitations

The ASAS is the best illustration of the power in utilizing a high resolution imaging system when making single particle scattering measurements. The imaging system gives one control of sample volume size, instrument activity and background light. Fig. 15 illustrates the spectral resolution of the ASAS in the submicron range. The resolution is seen to be primarily limited by PHA quantization.

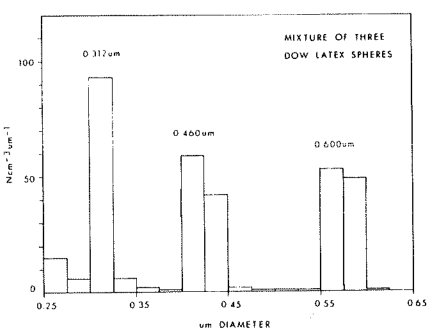

Fig. 15: Particle size spectrum from a mixture of 3 DOW latices showing resolution of ASAS

While the ASAS easily detects very fine particles it has an upper size limit of about 5 µm unless the cavity mirrors are reversed. The light scattered at larger sizes does not continue to increase although the extinction does. In order to extend the instrument beyond 5 µm, the extinction must be measured. Several ASASs using combined scattering/extinction signals have been fabricated extending measurements out to 10 µm. The ASAS will also reach saturation limits when the total particle cross section in the beam results in an equivalent loss to one 5 µm particle. Ordinarily this restricts the instrument to uses where the visibility is greater than 500 meters.

5.0 CONTINUING INSTRUMENT DEVELOPMENT

In the course of development and use of any instrument, one finds ways of making improvements. In most cases, this means increasing the sophistication of the instrument even though one would prefer to simplify it. The current state of development of the 2-D Probe is a good example. We are presently testing a 2-D Probe with 64 elements and a 4 level grey scale. Encoding the grey scale doubles the bit storage requirement for each element. Doubling the number of elements results in a four fold increase in data storage. The grey scale provides sufficient shadow relief to distinguish rimed from pristine crystals. Doubling the array width has obvious advantages. Because of the enormous data rate (512 MHz) we use a microprocessor to preprocess the data. The image quality is far superior to any obtained with current 2-D Probes. However, this instrument may be oversophisticated for cloud physics work. The grey scale is useful in ice crystal work but provides little benefit in droplet work. The 64 element array is highly desirable, even though it involves parallel growth and considerable cost increase. At the present time a good choice would be a 2-D Probe with 64 elements with a programmable threshold rather than continuous grey scale.

We have already mentioned the probable use of photomultiplier tubes in the FSSP to extend its size range to smaller particles. We should also mention that the higher resolution ASAS optical system has been tried in the FSSP. While the accuracy was improved, it resulted in too low a sample volume and the sample volume became size dependent at the larger sizes. Such a modification may still be desirable if the FSSP is restricted to aerosol and small droplet measurements.

In the ASAS, work is still progressing with the parabolic collecting optics in two areas. The first involves a simpler instrument, which collects 2Π steradians and has sensitivity well below 0.1 µm using solid state detectors. The second involves the simultaneous measurement of total scattering and single particle extinction to provide a measure of the imaginary component of refractive index (particle absorption).

REFERENCES

Knollenberg, R.G.1970: The Optical Array: An Alternative to Extinction and Scattering for Particle Size Measurements, *J. Appl. Meteor.*, Vol. 9, No.1

———'1972: Measurements of the Growth of the Ice Budget in a Persisting Contrail, *J. Atmos. Sci.*,Vol.29, No.7, pp 1367-1374

———'1973: An Active Scattering Aerosol Spectrometer, *Atmospheric Technology*,No.2,June 1973

———'and R.E.Luehr 1975: Fine Particles, Aerosol, Generation, Measurement, Sampling, and Analysis, *Academic Press*,Edited by Benjamin Y.H. Liu, pp 669-696

Schehl, R.,S. Ergun and A. Headrick 1973: Size Spectrometry of Aerosols Using Light Scattering from the Cavity of a Gas Laser, *Rev. Sci. Instrum.* Vol. 44, No. 9, p 1193

Schleusener, S.A. 1969: *J. Air Poll. Control Assoc.* 19, p 40

Schuster, B.G., and R. G. Knollenberg 1972: Detection and Sizing of Small Particles in an Open Cavity Gas Laser, *Applied Optics*, Vol. 11, p 1515

CLOUD PHYSICS MEASUREMENTS WITH POLARIZATION DIVERSITY LIDAR

Kenneth Sassen

Department of Atmospheric Science
University of Wyoming
Laramie, Wyoming

1. INTRODUCTION

Laser radar (lidar) systems have in recent years shown increasing applicability for atmospheric science research. As a platform for remotely monitoring atmospheric cloud composition and processes, polarization diversity lidars have indicated great promise following initial measurements which demonstrated water and ice particle cloud discrimination (Schotland et al., 1971). An important development in this area has been the realization that lidar depolarization measurements could be interpreted, with respect to hydrometeor species identification, by means of a "library" of characteristic return signatures compiled with continuous-wave (CW) laser backscattering systems of appropriate design. In view of the present inability to predict ice particle optical scattering behavior through theoretical approaches, such data is essential in assessing the potential of the optical backscatter depolarization technique, and have indicated that several hydrometeor species could be differentiated through polarization measurements. At the same time, their general applicability to lidar data has been shown (Sassen, 1975a). Furthermore, it has been determined through CW laser scattering measurements and verified with lidar observations that melting snowflakes generate increasing amounts of depolarization during the phase transition, as is also experienced at microwave frequencies (Sassen, 1976).

These capabilities of polarization diversity lidar systems suggest that the technique has developed sufficiently to find application in programs of cloud physics and modification research. As examples of such applications, results from two lidar field programs will be considered here. To describe the change in the state of polarization of backscattered energy, linear depolarization ratios (δ, the ratio of returned energies in the planes of polarization orthogonal and parallel to that of the linearly polarized source) are used. The characteristics of the lidar system are given in Table 1.

Table 1. Lidar system specifications.

Transmitter	
Source	Pulsed ruby laser, 6943Å
Power Output	$\sim 10^7$ W
PRF	~ 0.1 sec^{-1}
Pulse duration	$\sim 50 \times 10^{-9}$ sec
Polarization	Vertical, $\delta < 0.1\%$
Beam divergence	10^{-3} rad
Receiver	
Optics	Schmidt-Cassegrainian
Aperture	500 cm^2
Polarization	Glan-air prism (simultaneous)
Field of view	10^{-3} rad
Data Handling	
Recording	CRT photography
Display	Dual-beam oscilloscope
Bandwidth	50 MHz
Operating Characteristics	
Beam alignment	Parallel
Lidar positioning	Searchlight mount
Total weight	~ 400 kg
Environmental	-20 to $+30$°C, >800 mb

2. THUNDERSTORM PRECIPITATION FIELD PROGRAM

a. Theory

To aid in the interpretation of the lidar precipitation profiles of returned energy with height, a numerical simulation of the microphysical aspects and optical scattering behavior of particles within the melting region was performed for ice pellet (e.g., hailstone), graupel and snowflake-initiated rainfall, using the lidar equation (see Schotland et al., 1971). Hydrometeor scattering properties during the phase change were inferred from measurements of relative returned (parallel-polarized) energy values obtained with the CW laser system for the three hydrometeor types at different temperatures (manuscript in preparation). The results of the model for rainfall rates of 1.5, 7.5 and 15 mm hr^{-1} indicated that significant reflectivity bright bands could be expected from melting snowflakes and graupel. However, in contrast to microwave bright bands, the causes of the optical analogs were shown to result primarily from the initial increases in particle and scattering cross sections at the bottom of the melting layer (where particle concentrations changed only slightly with height), followed by strong optical attenuation higher in the melting zone. Fig. 1 shows the results of the calculations for melting snowflakes and graupel at the three rainfall rates, where variations in relative returned energy are shown as functions of height from the freezing level and inferred pseudo-adiabatic temperature.

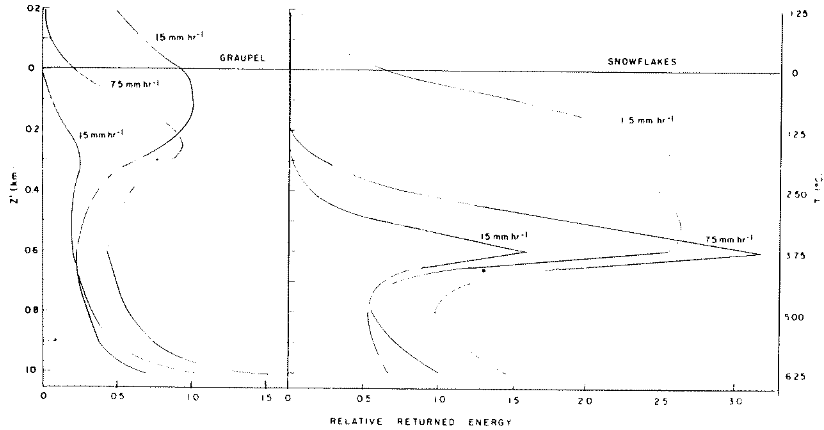

Figure 1. The results of a numerical simulation of the lidar bright band from melting graupel (left) and snowflakes, for three rainfall rates. Profiles of returned (parallel-polarized) energy shown vs. height from freezing level (Z') and pseudo-adiabatic temperature (T).

b. Measurements

In an attempt to characterize the precipitation generating mechanisms acting in high plains thunderstorms at Laramie, Wyoming, lidar observations were carried out on a total of six days during 1975 for which the convective activity could be considered representative of this area. Due to the typically dry surface moisture conditions in the Laramie Basin (∿2.2 km above sea level at the lidar site), convective cloud bases normally occur at heights roughly 2 km above ground level (AGL). Thus, atmospheric freezing levels were usually present a few hundred meters above cloud base, so that the precipitation within the melting region could be viewed by the lidar without the severe signal attenuation losses incurred in dense clouds.

The lidar data collected from thunderstorm precipitation were compared to the simulated returned energy profiles and the measured δ value variations from melting hydrometeors to determine the rainfall mechanisms. The results confirmed the observations in the geographically adjacent clouds in northeast Colorado in that a graupel mechanism predominated during early cumulus cloud development (Dye et al., 1974). However, the presence of a melting snowflake process was indicated by the data obtained during the mature thunderstorm stage, suggesting that the contribution to thunderstorm precipitation from a diffusional ice growth mechanism has been generally underestimated. The lidar data presented below are given as examples to illustrate the agreement of typical lidar profiles to the expected reflectivity and δ profiles.

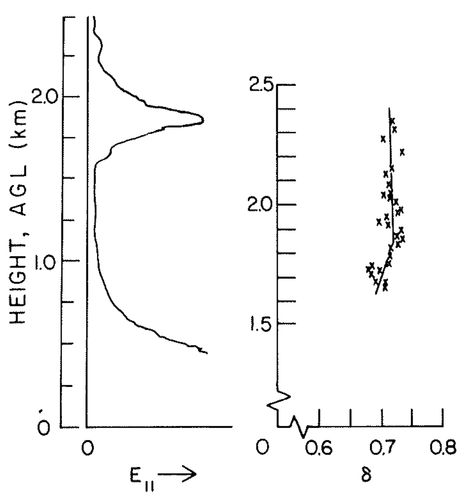

Figure 2. Lidar returned parallel-polarized energy ($E_{||}$) and linear depolarization ratio (δ, in melting region only) profiles vs. height above ground from convective shower precipitation. Environmental freezing level height at 2.6 km AGL.

Shown in Figure 2 are the parallel polarized signal ($E_{||}$) and linear depolarization ratio (δ) profiles from the precipitation beneath a shower cloud, obtained at 1700 MST on 11 August 1975. The form of these profiles clearly indicate that melting graupel were being interrogated. Note that as expected, melting graupel failed to produce a depolarization bright band, but rather maintained a near constant δ value of ∿0.7 throughout much of the melting region (Sassen, 1975b).

Figure 3 gives the profiles obtained from the precipitation beneath a vigorous thunderstorm in its

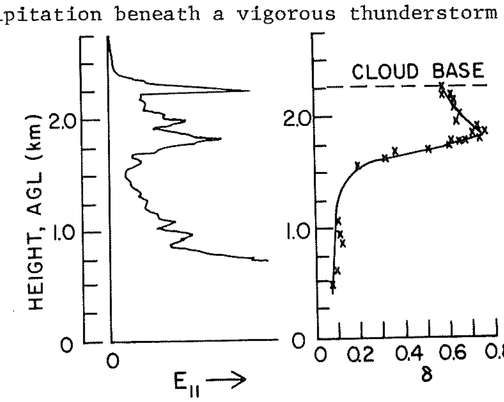

Figure 3. Lidar profiles from precipitation beneath an active thunderstorm vs. height above ground. $E_{||}$ value spike at ∿2.3 km AGL represents entrance of the laser pulse into cloud base. Environmental freezing level at 2.65 km AGL.

mature stage on 26 July 1975, at 1438 MST. In this case, the returned energy and δ profiles resemble more closely those anticipated from melting snowflakes. The abrupt $E_{||}$ signal increase at ∿2.3 km AGL shows that the storm's cloud base was entered at this height, while the vertical depth of the bright band is indicative of a rather light rainfall rate in the area at that time being viewed by the lidar (compare with Figure 1). On this occasion, the temperature at the returned energy maximum of the bright band, as inferred from the 0000Z Denver and Lander soundings, was ∿4°C warmer than the 3.8°C value expected for melting snowflakes, possibly due to the presence of thunderstorm downdrafts. It should be mentioned in this regard that in cases involving weak convective activity and continuous-type precipitation, bright band centers were often noted to correspond to the value predicted by the CW laser measurements.

3. INSTRUMENTED AIRCRAFT SUPPORTED OBSERVATIONS

a. Theory

As shown by Schotland et al. (1971), the linear depolarization ratio can be expressed solely in terms of the volume backscatter coefficients, $\beta'_{||}$ and $\beta'_{\perp}$. These coefficients are subscripted to allow for differences in the values of the terms for backscattering of energy in the planes of polarization parallel ($||$) and orthogonal ($\perp$) to the source, and can be divided into components contributed by liquid and solid phase hydrometeors. Thus, the linear depolarization ratio can be expressed as

$$\delta = \frac{\beta'_{\perp\,(\text{ice})} + \beta'_{\perp\,(\text{water})}}{\beta'_{||\,(\text{ice})} + \beta'_{||\,(\text{water})}} \qquad (1)$$

In attempting to relate (1) with some measure of cloud microphysical content, it can be assumed that $\beta'_{\perp(\text{water})}$ contributes negligibly, and that $\beta'_{\perp(\text{ice})}$ can be expressed in terms of $\beta'_{||(\text{ice})}$ by taking into consideration pure ice δ values (δ_i) representative of the ice species under study. Of course, these simplifications neglect cloud droplet multiple scattering influences, but can be considered valid enough for an approximation when dealing with mixed phase clouds containing significant amounts of ice particles, and when using lidars with narrow beamwidths (see Sassen, 1976). Then, (1) reduces to

$$\delta = \frac{\delta_i\, \beta'_{||(\text{ice})}}{\beta'_{||(\text{ice})} + \beta'_{||(\text{water})}} \qquad (2)$$

The backscatter coefficients are proportional to the sums of cross sectional areas (A) and numbers (N) per unit volume of the hydrometeors in each phase. The backscattering "efficiency" or gain (g) of hydrometeors, depending on scatterer phase and geometry, can be employed to yield the following relation.

$$\beta'_{||(\text{water,ice})} = \Sigma g_{||} AN_{(\text{water,ice})} \qquad (3)$$

Note that the g value, per particle, is equivalent to the normalized backscatter cross section, and is defined in similar terms with respect to the particle's ability to behave as if it were an isotropic scatterer. While $g_{(\text{water})}$ has been shown to be a constant function of spherical droplet scattering properties for drops ∿<4 mm diameter (paper in preparation), $g_{(\text{ice})}$ values may be sensitive to the observation angle if populations of oriented ice crystals are interrogated, and would also likely vary with ice particle species.

Since hydrometeor characteristics enter into (2), a means of expressing some form of microphysical information can be sought. Unfortunately, it is not possible to derive values of N or A from δ values alone without first specifying one of these terms. In dealing with an assembly of scatterers of unknown size and concentration, though, it is possible to specify the quantity $R_{i/w}$, the ratio of the sums of ice particle cross sectional areas to water drop cross sectional areas per unit volume, which relates a measure of cloud microphysical content to its observed scattering properties. That is,

$$R_{i/w} = \frac{\Sigma A_{(\text{ice})} N_{(\text{ice})}}{\Sigma A_{(\text{water})} N_{(\text{water})}} \qquad (4)$$

or, after (3) and (4) are introduced into (2),

$$R_{i/w} = G_{||(w/i)} \left(\frac{\delta}{\delta_i - \delta}\right) \qquad (5)$$

expressed in terms of δ, where $G_{||(w/i)}$ is the ratio of hydrometeor backscattering gains in the parallel polarization plane for particles in the water and ice phases.

The CW laser backscattering measurements can be used to obtain an estimation of the magnitude and possible variability of $G_{||(w/i)}$ values with ice particle type and size. An examination of these data reveal that due to differences in the backscattering efficiencies of various ice species, $G_{||(w/i)}$ values can be expected to vary by a factor of ∿10 with cloud content. An analysis of laboratory mixed phase cloud composition and δ values (using equations 3 and 4) suggests water-ice particle scattering gain ratios of about 10 to 20 for crystal populations <60 μm (modal maximum dimension). On the other hand, direct calculations of g values for raindrops and ice precipitation elements have revealed that $G_{||(w/i)}$ values near unity are more representative of large spatial crystals, crystal aggregates, and graupel particles. Figure 4 shows the $R_{i/w}$ ratios required to generate the range of linear depolarization ratios from 0.1 to 0.45 as functions of several $G_{||(w/i)}$ values typical of the primary ice particle species. Note that because of their greater depolarizing abilities, rimed particles and graupel produce higher δ values for a given $R_{i/w}$ ratio at $G_{||(w/i)} = 1$.

The value of $R_{i/w}$ for cloud microphysical parameterization may seem remote from the more accustomed and specific nomenclature, but yet requires only a measured δ value to be determined once the magnitude of the relative $G_{||(w/i)}$ value has been established. For lidar field measurements, the nature of the ice particles can often be assumed, or, identified through polarization data of any virga or precipitation present to judge δ_i and $G_{||(w/i)}$. And, if information is available describing some of the microphysical character of the cloud system under study, or if knowledgeable criteria are used to limit the range of unknown cloud composition para-

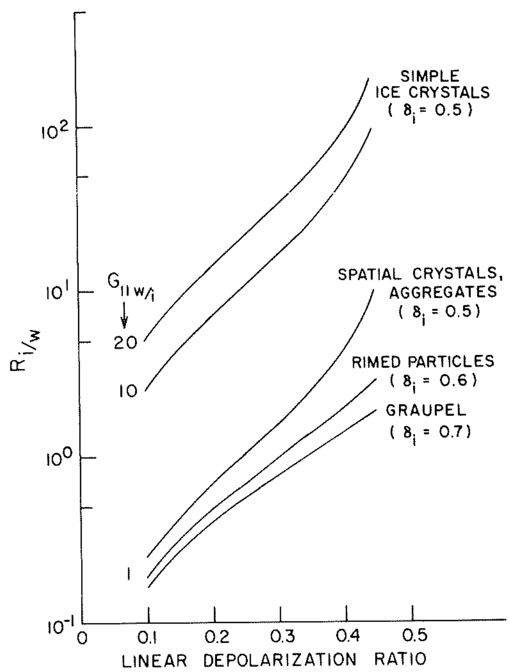

Figure 4. Linear depolarization ratios generated by several ice particle types with the pure-phase δ values (δ_i) and $G_{||(w/i)}$ values shown for $R_{i/w}$, the ratio of the sums of ice to water particle cross sectional areas.

meters, more specific information can be gained. Depolarization measurements, then, can provide by means of this technique an indication of the ice content of clouds. Observations of $R_{i/w}$ values may be particularly useful when employed in a relative comparison among similar cloud types or during single cloud studies.

b. Measurements

As part of winter studies of orographic cloud systems at Elk Mountain (elevation 3.4 km above sea level) in southeastern Wyoming, lidar observations have been taken on several occasions in conjunction with cloud microphysical measurements from an instrumented aircraft platform. The operation of the lidar system at a location 15 km west (2.1 km ASL) of the Elk Mountain Outdoor Laboratory has proved to be a useful supplement to the more conventional data collection methods. Data gathered with the lidar has shown sufficient sensitivity to cloud or precipitation composition to aid in the real-time discrimination of meteorological targets of interest to aircraft penetrations. And, as a stationary ground-based platform, lidar interrogations gathered over long time intervals have provided information concerning spatial variations in conditions not amenable to study with aircraft.

As an example of the lidar monitoring of meteorological processes, a time sequence of data obtained at the Elk Mountain site is presented below. The data were taken over a ∿2 hr time period on 26 January 1976, when considerable cloudiness was present at several atmospheric levels in southeastern Wyoming. The cloud system studied appeared to result from the orographically-induced lifting of moist low level air over the entire Medicine Bow Mountain Range, following the passage of an upper-level trough.

The lidar returns taken during the times shown in Figure 5 are depicted in the parallel polarization channel only, where returned energy increases to the right and the height above ground is given in kilometers. However, features in the returns which possessed δ values <0.5 indicative of mixed phase clouds (Sassen, 1976) are identified in the data sequence by arrows. These regions typically displayed clearly defined cloud bases, as evidenced by abrupt signal increases, while the subsequent rapid decay in returned energy levels indicates strong signal attenuation aloft. Most energy returns at low level (<∿1 km) can be shown on the basis of polarization measurements to result from ice particle virga or precipitation, and could often be noted to descend to the surface prior to the onset of snowfall. At times when snowfall reached the surface (i.e., ending at ∿1505, briefly at ∿1600, and commencing again at ∿1705 MST), energy returns were strong near the ground and higher level features decayed in strength or were absent due to the strong low level attenuation. Linear depolarization ratios for the precipitation and virga were for the most part between 0.6 and 0.65, indicating the presence of rimed ice particles, as a visual inspection of the character of the precipitation elements confirmed. When precipitation or low-lying virga were absent, rather smooth "clear air" returns in the lowest ∿0.5 km were present (e.g., at 1628), yielding δ ∿0.1.

Although the returns shown were taken at a number of different oscilloscope sensitivities (see volts per division scale for each interrogation) to accommodate the prevailing conditions, the changes in the character of the profiles reflect variations in the cloud system. For example, the base of the apparently generating cloud layer at ∿2 km AGL can be seen to undergo an increase in height from about 1617 to 1636, reflecting a general decrease in the presence of ice particles at lower levels. It is also interesting to note that the location of a lower mixed phase cloud at ∿1.2 km AGL (see 1521 interrogation) at later times corresponds to the top of a layer of strong mid-level signal returns displaying typical ice δ values. This feature probably represented a visually observed intermittent stratus cloud layer. At later times, indications were present from an occasional lowering of ice δ values at this height of some continued liquid water showing the then prevailing conditions to be nearly glaciated from the increased presence of ice, or perhaps the scavenging of droplets by ice particles from the higher layer. The correspondence of the aircraft measured temperature of -15°C and precipitation character of dendritic crystals demonstrate that the primary precipitation generating cloud layer was the upper layer at ∿2 km AGL.

Since the aircraft flew through this cloud system from about 1600 to 1715 MST, and made several penetrations in the area being viewed by the lidar, in situ comparisons can be made with some of the features shown in Figure 5. A preliminary assessment of the aircraft data reveals that liquid water was sampled only in the mixed phase cloud layer indicated by the lidar at ∿2 km AGL. Hydrometeor samples obtained on slides typically showed a mixture of rimed and unrimed crystals to be pre-

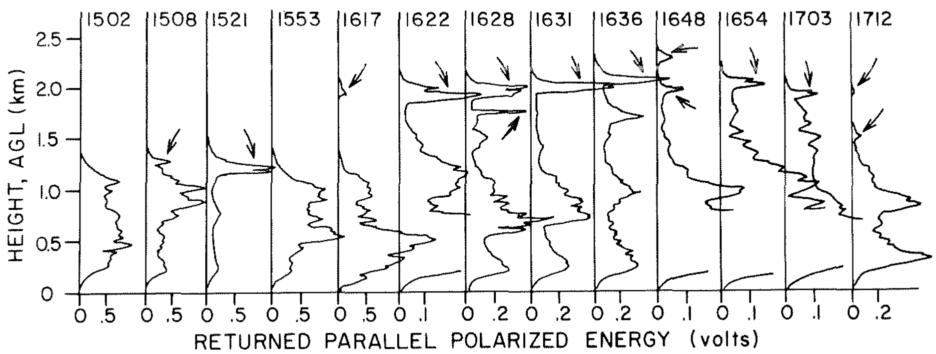

Figure 5. Time sequence of lidar returns obtained on 26 January 1976 with instrumented aircraft supported observations. Arrows indicate features which lidar polarization data indicated as mixed phase clouds.

sent, while the liquid water content was spatially variable, with values (as determined from the ASP) ranging from 0.001 to 0.02 in the approximate areas viewed by the lidar. Although the non-uniformities in the liquid water content and the combination of rimed and unrimed ice particles complicate the parameterization of cloud content, the values of $G_{||}(w/i)$ obtained from (5) with the measured δ values have been found to be within the range expected for the observed mixture of particle types. For example, the cloud layer at 2.1 km AGL at 1654 MST yielded δ values of between 0.29 to 0.34 (as measured at several points in the cloud return and for several sequential returns), while δ_i values of between 0.62 and 0.66 were generated by the virga below. Aircraft-measured ice particle concentrations (from the 2D probe) were relatively constant at 4 ℓ^{-1} in this region of the cloud layer, but liquid water contents varied from averages of 0.002 to 0.09 gm/m^3. Therefore, using the observed cloud droplet spectra and the values given above, $R_{i/w}$ and (coincidentally) $G_{||}(w/i)$ values of about 12 and 3.5 were found for the two values of liquid water content, respectively. These values lie between the expected $G_{||}(w/i)$ values for rimed particles and unrimed simple ice crystals.

It is hoped that as the results of more exact data analyses become available, and as collaborative measurements continue, more quantitative data comparisons will be forthcoming.

4. CONCLUSIONS

Through an assessment of the backscattering behavior of hydrometeors and lidar field programs of cloud studies, the optical backscatter depolarization technique is indicated to display the potential for contributing significantly to the understanding of cloud and precipitation processes. The utilization of the lidar for thunderstorm observations in a manner analogous to radar studies has shown that the dominant precipitation generating mechanisms could be specified according to hydrometeor species. Although the strong attenuation suffered by optical energy in precipitation and dense clouds can severely limit the operational range of lidar measurements in some cases, the information content of depolarization data is indicated to be more sensitive with respect to hydrometeor differentiation than analogous radar techniques. And, the basis for obtaining a quantitative measure of mixed phase cloud ice content has been presented. It is hoped that once a more rigorous demonstration of the validity of this approach has been made through continued data collection and analysis, the value of the $R_{i/w}$ parameter can be examined in terms of its applicability to cloud physics and modification research.

Acknowledgements. This research has been made possible by previous support from the Bureau of Reclamation, Division of Atmospheric Water Resources Management and their continued cooperation, and by the National Science Foundation, Meteorology Program, Atmospheric Science Section (Grant ATM75-02515). The contributions provided by several members of the Department of Atmospheric Science are gratefully acknowledged.

REFERENCES

Dye, J. E., C. A. Knight, V. Toutenhoofd and T. W. Cannon, 1974: The mechanism of precipitation formation in northeast Colorado cumulus III. Coordinated microphysical and radar observations and summary. J. Atmos. Sci., 31, 2152-2159.

Sassen, K., 1975a: A comparison of hydrometeor linear depolarization ratios from CW laser and lidar systems. Conference Abstracts, 7th International Laser Radar Conference, American Meteorological Society, Boston, Massachusetts, 107-108.

_____, 1975b: Laser depolarization bright band from melting snowflakes. Nature, 255, 316-318.

_____, 1976: Polarization diversity lidar returns from virga and precipitation: Anomalies and the bright band analogy. J. Appl. Meteor., 15, 292-300.

Schotland, R. M., K. Sassen and R. Stone, 1971: Observations by lidar of linear depolarization ratios for hydrometeors. J. Appl. Meteor., 10, 1011-1017.

RAIN RESULTING FROM MELTING SNOW*

Louis J. Battan and John B. Theiss

Institute of Atmospheric Physics
University of Arizona
Tucson, Arizona 85721

1. INTRODUCTION

On 20 August 1975 a thunderstorm in an advanced stage of dissipation moved over a zenith-pointing 3.2-cm pulsed-Doppler radar located on the grounds of Tucson International Airport. The radar, described earlier by Battan (1975) has two identical antennas and receiving systems. The antennas are arranged to measure the backscattered signals in orthogonal planes. The unique aspects of this observational system is that it can obtain Doppler spectra in either the plane of transmission or the cross-polarized plane. On 20 August 1975 the radar functioned in the following manner. A sampling gate traveled upwards in steps of about 150 m, dwelling at each altitude for 0.66 sec, during which records were made of the Doppler information in the plane of transmission, while at the same time a recording was made of the integrated backscattered signal in the cross-polarized plane. After repeating this procedure for a second set of observations (called a "frame") between the ground and a preset maximum altitude at 9750 m, the recording mode was changed. Recordings were made of the Doppler spectral data in the cross-polarized plane and the integrated power in the plane of transmission. The recording mode was changed every two frames, i.e., every 86 sec since 43 sec was required for each frame.

As will be seen from an examination of Fig. 1, which is a facsimile recording of two frames, one showing Doppler spectra in the plane of transmission followed by a second showing the data in the cross-polarized plane, there was a radar bright band. It indicated that frozen particles were falling through the freezing level and melting. A great deal has been written about the precipitation mechanisms occurring above

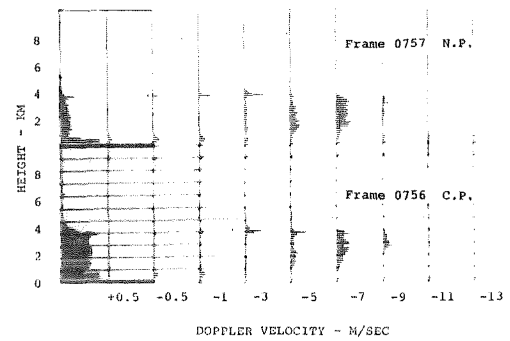

Fig. 1. Doppler spectra (signal voltages) in the plane of transmission (NP) and the cross-polarized plane (CP). The first column displays integrate backscattered signals.

and below the bright band. Disputes about the questions of particle aggregation and breakup have yet to be resolved. Lhermitte and Atlas (1963), Ekpenyoug and Srivastava (1970) and Zwack and Anderson (1970) proposed arguments in favor of the view that there is snow-particle aggregation above the bright band or raindrop breakup below it, or both. On the other hand, duToit (1967), who used Doppler radar data, and Ohtake (1969), who made observations of the hydrometeors up a mountain slope, concluded that aggregation and breakup were not important processes in explaining precipitation falling through a melting layer.

2. OBSERVATIONS

The observations presented in this article cover a period of nine minutes in the life of a decaying thunderstorm. Unlike meteorological circumstances leading to widespread rain from nimbostratus clouds where time and spacial changes sometimes are quite small, in the case of this dissipating shower there is evidence of substantial changes over periods of three minutes.

*This research has been supported by the Atmospheric Sciences Section of the National Science Foundation under Grant ATM 73-06558 A02.

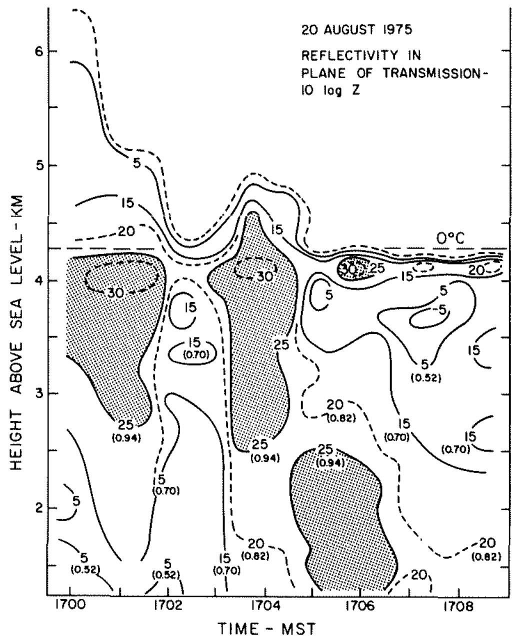

Fig. 2. Reflectivity in plane of transmission.

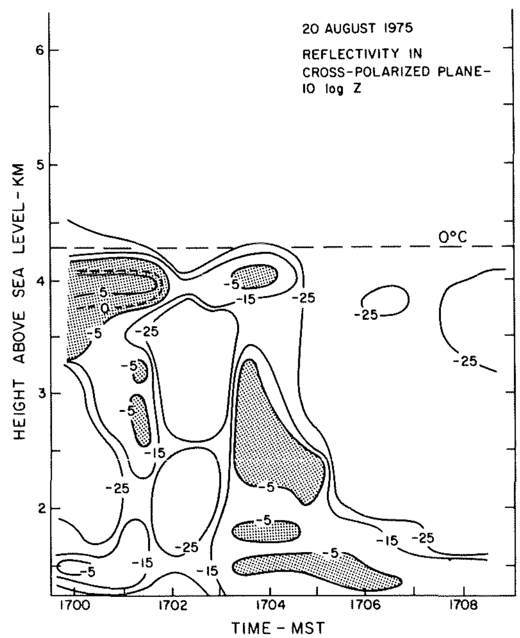

Fig. 3. Reflectivity in cross-polarized plane.

Figures 2, 3, and 4 present measured backscattered powers and depolarization. The first diagram shows that the bright band, exhibiting maxima in reflectivity of just over 30 dBZ, was about 300 m below the 0°C isotherm. Note that at 1702 MST and 1705 MST the reflectivity in the bright band ranged from less than 15 dBZ to more than 30 dBZ. The pattern of echo intensity is indicative of a showery nature in the precipitation. The rainfall intensity at the ground was very light, not measurable with a weighing gauge. On the basis

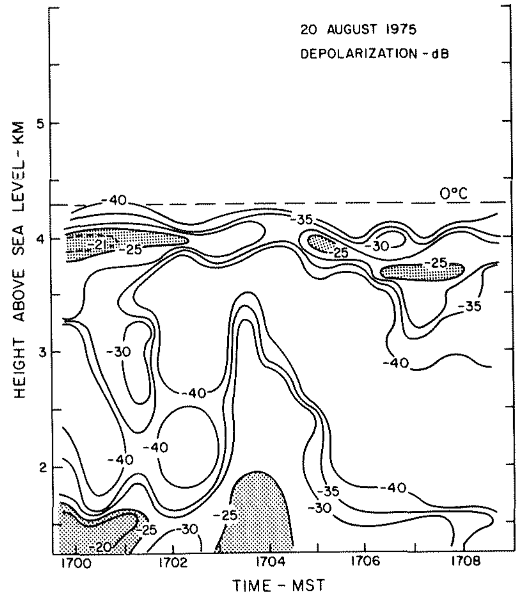

Fig. 4. Depolarization

of $Z = 200\ R^{1.6}$, one obtains maximum values of just over 1 mm hr^{-1} for the period 1703 to 1707 MST.

Before 1705 MST, backscattering in the cross-polarized plane was relatively high, particularly in the bright band layer. During the last half of the period, at altitudes above 2 km, the power in the cross-polarized plane was extremely low or nonexistent.

As would be expected, the pattern of depolarization was similar in most respects to the pattern of power in the cross-polarized plane, except that in and below the bright band after 1704 MST, there is evidence of considerable depolarization. It should be recognized however that the quantities of power in the numerators of the ratios from which depolarization was calculated were quite small, just barely above the noise level of the radar.

During the first two minutes, there was a gradual increase of echo intensity downward from about 5 km to 4.2 km, the center of the bright band. One can visualize as did Lhermitte and Atlas (1963), the aggregation of snow particles above the freezing level, with a more sudden increase of reflectivity as the snow particles fell through the melting region.

From 1703 to 1705 MST, the high reflectivity region extended above the freezing level with a steep gradient of Z at the echo top. It can be visualized that this represents a volume of wet snow or ice pellets. Note that the signals in the cross-polarized plane at 1704 in the bright band were about 10 dB lower than it was at 1701 MST. This would suggest that at 1704 MST, the hydrometeors were more spherical than the hydrometeors accounting from the earlier bright band. After 1704 MST the bright band was narrow and weak, but quite distinct. It is visualized that the hydrometeors were relatively small snow aggregates, which melted fairly rapidly.

In Fig. 2, at heights below 3.5 km, the lines of equal echo intensity are labeled with numbers in parenthesis. They are calculated median volume diameters corresponding to the indicated values of reflectivity. The procedure for obtaining these values assumes that the raindrops conform to the Marshall-Palmer distribution

$$N = N_o e^{-\Lambda D}, \text{ where } \Lambda = 4.1\ R^{-0.21}$$

and

$$Z = 200\ R^{1.6} \qquad (1)$$

Λ and Z are in units of mm^{-1} and $mm^6\ m^{-3}$ respectively when R is in mm hr^{-1}. According to Atlas (1964)

$$\Lambda = 3.67 \frac{D}{D_o}, \qquad (2)$$

where D_o is the median volume diameter. By suitable substitution employing these relations, one obtains

$$D_o = 0.45\ Z^{0.13} \qquad (3)$$

where D_o is in millimeters.

The quantities depicted in Fig. 2 indicate that there were fairly large raindrops under the bright band during the periods 1700-1702 MST and 1703-1704 MST because the median volume diameters were greater than 0.9 mm. On the other hand after 1704 MST, median volume diameters were about 0.5 mm, indicating fairly small raindrops.

If it could be assumed that the precipitation was falling mostly in the plane of observation, it would appear that from about 1701 MST until 1705 MST, there was a net breakup of raindrops because the median volume diameters diminished with altitude. During the period 1705 to 1707 MST, the calculated raindrop sizes near the ground were about the same as they were aloft, indicating little net breakup or coalescence. During the last few minutes of observations there was an apparent increase of raindrop sizes with decreasing altitude, the median volume diameters increasing from 0.5 to about 0.8 mm.

Not surprisingly the trends of changes in raindrop diameters also appear on Fig. 5. It depicts the quantity $\overline{W}_T$ which is a reflectivity-weighted mean Doppler velocity calculated from an equation by Rogers (1964). The numbers in parenthesis are the diameters of raindrops having terminal velocities corresponding to the indicated $\overline{W}_T$. The drop sizes are consistently larger than those in Fig. 2. They are biased to a greater extent by the larger raindrops than are the median volume diameters which are volume weighted rather than reflectivity weighted.

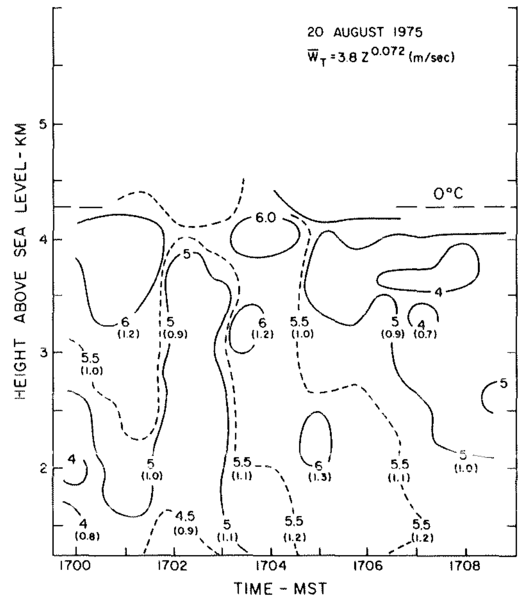

Fig. 5. Mean reflectivity-weighted terminal velocity of raindrops.

The depolarization data tends to confirm the just noted inferences about changes of raindrop sizes with altitude, if one is prepared to accept the notion that the greater the raindrop sizes the greater the depolarization when viewed along the zenith. This seems like a reasonable proposition because the greater the sizes the larger the drop deformation imposed by turbulence and drop collisions.

Additional information about the properties of the air and hydrometeor motions can be obtained by an examination of the Doppler spectrum parameters shown in Figs. 6, 7, and 8. Note that the data at the times indicated by the downward pointing arrows were taken from observations of Doppler spectra of the back-scattered signals in the cross-polarized plane.

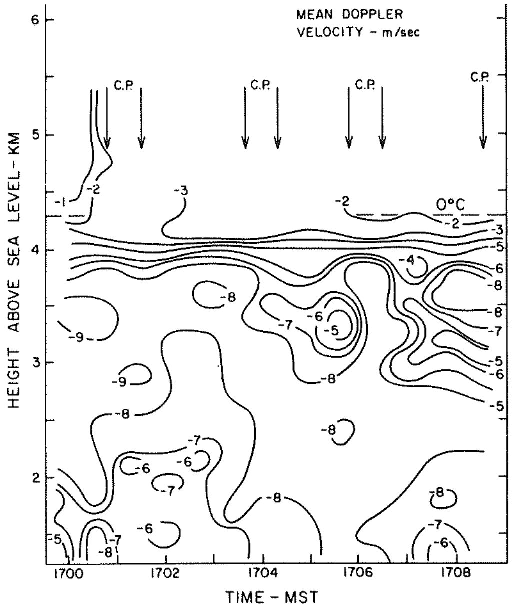

Fig. 6. Mean Doppler velocities. Arrows indicate cross-polarized data (CP).

Figure 6 shows the pronounced downward acceleration, with respect to the ground, of particles falling through the melting level. For the most part their downward velocities were 2 to 3 m sec^{-1} at 4,300 m, the level of the 0°C isotherm and reached 6 m sec^{-1} about 300 m below it. After another 150 m of fall, throughout most of the 9 min. of observations, the particles, presumably raindrops, were falling at about 8 m sec^{-1} except for a few brief periods.

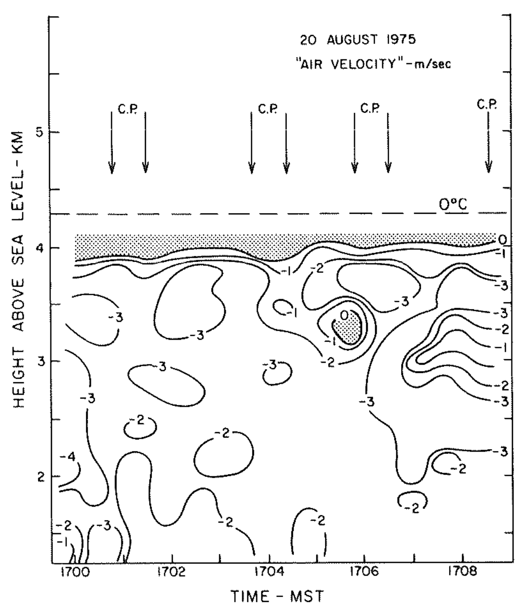

Fig. 7. Calculated "updraft velocity". Negative values indicate downward velocities.

It is seen that over the first three minutes of observations, within the rain region, the mean Doppler velocity decreased from a peak of -9.5 m sec^{-1} at an altitude of 3.5 km to a minimum of -5.5 m sec^{-1} near the ground. An examination of Fig. 7, which displays "updraft velocities" calculated by means of Rogers' (1964) equation (the difference between the data in Fig. 5 and Fig. 4), shows that about 1 to 2 m sec^{-1} of this difference can be explained as a change in downdraft speed. The remaining difference of downward speed can be attributed to changes in the terminal velocity of the raindrops (Fig. 5).

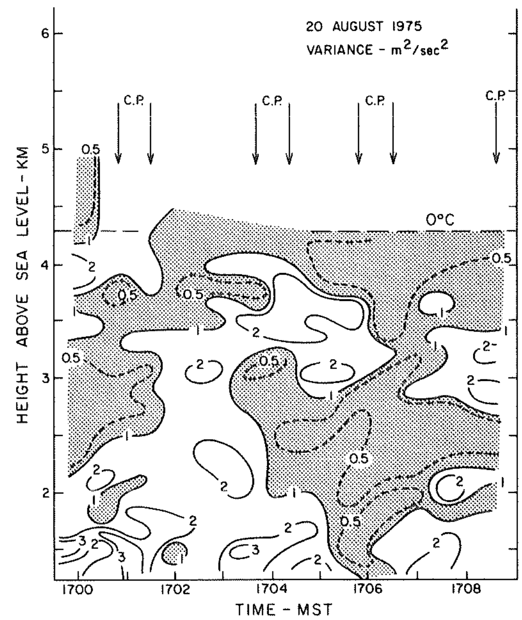

Fig. 8. Variances of Doppler spectra.

During the period between about 1704 and 1707 MST there was relatively little change in the mean Doppler velocity.

The calculated air velocities should be reasonable dependable in the case of rain, but of little value when the hydrometeors are composed of ice crystals or snowflakes, either in the dry or melting states. For this reason, the data in Fig. 7 above about 3.7 km should be ignored. Note that, as was the case in Fig. 6, there is a strong correlation between the velocities measured in the plane of transmission and in the cross-polarized plane less than a minute displaced in time. The most unusual aspect of Fig. 7 is the small region where the air velocity was observed to be upwards at nearly 1 m sec^{-1} surrounded by air descending at about 3 m sec^{-1}. A weak widespread downdraft would be a more likely state of affairs in a dissipating thunderstorm.

Interestingly the highest values of the variance (Fig. 8) of the Doppler spectra occurred in the region of the upwards perturbation of air velocity. Throughout the rain region, variances were mostly less than 1.0 m^2 sec^{-2}, typical values for rain. In the region of the updraft velocity perturbation it was greater than 1.5 m^2 sec^{-2}. It can be speculated that turbulence, generated by horizontal and vertical gradients of vertical velocity, contributed perhaps 1 to 1.5 m^2 sec^{-2} to the variance.

The high value of variance (greater than 2 m^2 sec^{-2}) below 3.5 km at 1703 and throughout most of this record at heights below 1.8 km are difficult to explain in terms of particle size and probably indicate the presence of small scale turbulence. Note that the strongest observed downdraft (5 m sec^{-1}) occurred at about 1701 MST at a height of 1.4 km above sea level, some 600 m above the ground. One has the impression that this feature of the velocity field and the updraft perturbation at 1705 MST indicate that air is moving through the time-height plane of observation at least during some times and at some altitudes.

3. SUMMARY

In summary, it seems to be clear that major changes in precipitation characteristics occurred over short periods of time. The properties of the rain at the ground depend on the properties of the frozen hydrometeors above the 0°C isotherm and on breakup and coalescence processes. In some instances, there may be significant aggregations above the freezing level; at other times little may occur depending on the type, shape, and size of the hydrometeors. In the rain either breakup or coalescence may occur, depending presumably on the initial drop size spectra and possibly on small scale turbulence. Clearly it is important to use this type of radar system for observing rain from a widespread layer of stratiform clouds.

4. REFERENCES

Atlas, D., 1964: Advances in Radar Meteorology. Advances in Geophysics, 10, 318-478.

Battan, L. J., 1975: Doppler spectra of rain in the cross-polarized plane. Bull. Amer. Meteor. Soc., 56, 1271-1272.

duToit, P. S., 1967: Doppler radar observations of drop sizes in continuous rain. J. Appl. Meteor., 6, 1082-1087.

Ekpenyoug, B.E., and R. C. Srivastava, 1970: Radar Characteristics of the Melting Layer. A Theoretical Study. Tech. Note No. 16, Lab. Atmos. Probing, University of Chicago.

Lhermitte, R. M., and D. Atlas, 1963: Doppler fall speed and particle growth in stratiform precipitation. Proc. Tenth Radar Conf., Amer. Meteor. Soc., 297-302.

Ohtake, T., 1968: Change of size distribution of hydrometeors through a melting layer. Proc. Thirteenth Radar Meteor. Conf., Amer. Meteor. Soc., 148-153.

Rogers, R. R., 1964: An extension of the Z-R relationship for Doppler radar. Proc. Eleventh Wea. Radar Conf., Amer. Meteor. Soc., 158-160.

Zwack, P., and C. Anderson, 1970: 25 July 1969: Showers and continuous precipitation. Preprint Vol. Fourteenth Radar Meteor. Conf., Amer. Meteor. Soc., 335-338.

A PARTICLE CAMERA FOR POWERED AIRCRAFT

Theodore W. Cannon

National Center for Atmospheric Research*
Boulder, Colorado 80303

1. INTRODUCTION

A particle camera has been recently developed at the National Center for Atmospheric Research for the South Dakota School of Mines T-28 armored aircraft. This camera is used to photograph cloud and precipitation particles as a data source for the National Hail Research Experiment. The intent is to obtain the following information:

1) Determine if a significant number of water drops larger than about 150 μm diameter exist in hail precursor and hail producing clouds and, if they do, what are the sizes and concentrations in various regions of these clouds.
2) Determine the types, sizes and concentrations of ice particles in various regions of clouds.
3) Make innercomparisons of particle shapes, sizes and/or concentrations measured with other instruments on the aircraft (e.g., foil impactor, PMS 2-D and axially scattering probes, J-W liquid water content meter, Rosemount icing rate probe, and acoustic hail sensor).

The T-28 particle camera is an improved version of the camera used on the NCAR/NOAA sailplane Explorer and described by Cannon (1974). Because power, weight and space restrictions are less severe on powered aircraft, significant improvments possible in the T-28 version were larger sampling volume in each photograph, higher frame rate, and multiple exposure feature.

2. CAMERA DESCRIPTION

The camera consists of two basic units. (1) The 35 mm, double frame film transport, rotating mirror and control electronics unit (FTRM) and (2) the flash system. Figures 1 and 2 show the camera mounted beneath the port wing of the aircraft, with the FTRM housed in the white pod (inboard) and the flash system in the black housing (outboard). Photographs are taken using dark-field illumination; the optical axis is aimed midway between two flash lamps located behind windows on the pod side of the flash system housing. A flat-black area between these windows provides the background for the photographs. Photographed particles are back lighted by the lamps; some fill-in front lighting is provided by light reflected forward by the white portion of the wing and the FTRM pod.

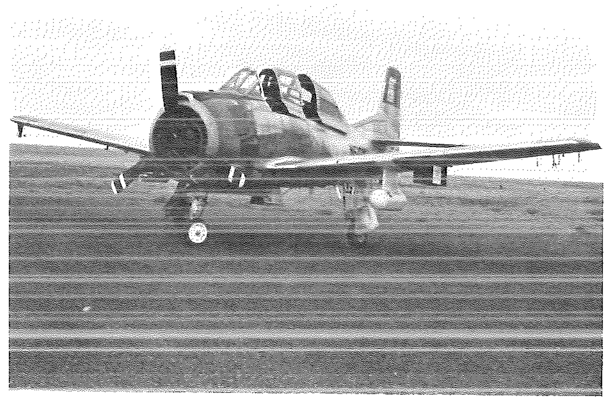

Figure 1. T-28 armored aircraft with camera mounted under port wing.

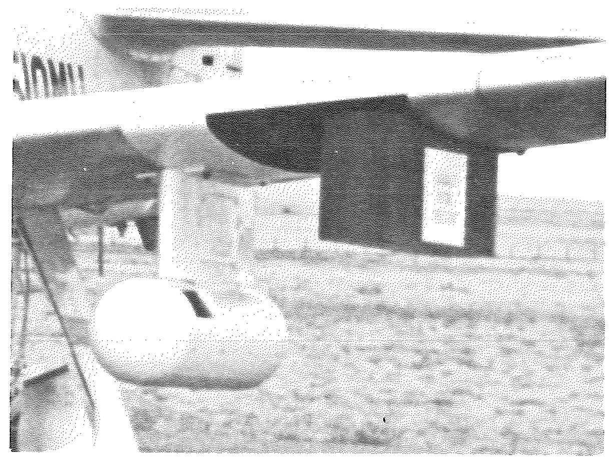

Figure 2. Enlarged photograph of T-28 camera showing film transport and rotating mirror pod (left) and flash housing (right).

*The National Center for Atmospheric Research is sponsored by the National Science Foundation.

The flash system consists of a 28 volt to 1800 volt DC/DC converter, 230 ma capacity, connected to a 4.08 μf capacitor for each of the two Xenon flash lamps, each with reflectors and appropriate triggering circuitry, and cooling fan. The flash duration is about 15 μ sec measured at the one-third of peak light pulse level.

Since the flash duration is too long to adequately stop image motion (airspeed is about 100 meters per second), a motion compensating mirror is located in front of the camera lens. The mirror speed is servoed to be proportional to the output of an electronic true airspeed computer; the constant of proportionately between airspeed and mirror speed is adjustable depending on the lens magnification used.

The servo-motor driven film transport is slaved to the rotating mirror so that, in pulse mode, the shutter is automatically opened during the mirror revolution just prior to exposure and closed during the revolution of the mirror subsequent to exposure. The pilot can adjust a "ratio" control so that exposures are taken at rates from one exposure per 64 mirror rotations to one per two mirror rotations. In cine mode, the camera and mirror servo motors are phase locked together so that the shutter is open at the time the mirror is in proper position for the photograph to be taken. One exposure is taken for every rotation of the mirror in cine mode

An "accumulate" feature allows the pilot to multiple expose up to four flashes per frame at any ratio setting in pulse mode to obtain more data per flight than possible with a single exposure per frame.

The frame rate R for pulse mode at any accumulate value may be calculated using the formula

$$R_F = \frac{R_c}{R+A}$$

where R_c = cine frame rate, R = ratio and A = accumulate. Frame rates at 100 mps true airspeed are shown in Table I.

An additional feature is a film marking LED for flashing the edge of the film at each frame and one to flash the film at the time the "in cloud" button is pressed by the pilot.

3. IMAGING CHARACTERISTICS AND DATA

Use of interchangeable lenses allows the camera to be used with emphasis on small ice and cloud droplets (magnification = 0.60) or precipitation-size particles (magnification = 0.15). Some of the imaging characteristics with two available lenses are shown in Table II.

Distinction between drops and ice is made based on the two dot method described by Cannon (1970). Photographs of airborne falling water drops photographed in the hanger are shown in Figs. 3 and 4. The dot pair images in Fig. 3 are characteristic of smaller drops (in this case 0.2 to 1.3 mm diameter), while the dot quad in

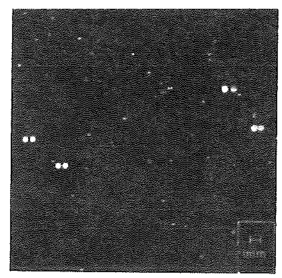

Fig. 3. Airborne droplets from atomizer 0.2 to 1.3 mm diameter imaged in hanger showing dot pair signature characteristic of smaller drops.

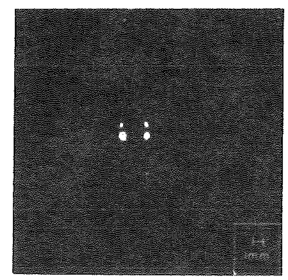

Fig. 4. Freely falling 2.8 mm diameter drop photographed in hanger showing dot quad signature characteristic of larger drops.

Table I. Frame rates at in cine and pulse modes, true airspeed = 100 mps, accumulate = 1.0, magnification = 0.15. Total operating time for maximum (400 foot, 3200 frame) film loading is also shown

Ratio	Frames Sec^{-1}	Sec Frames^{-1}	Total Operating Time
1 Cine	15	0.067	3m 34s
1 Pulse	7.5	0.13	7m 8s
2 "	3.8	0.27	14m 18s
4 "	1.9	0.53	28m 35s
8 "	0.94	1.1	57m 10s
16 "	0.47	2.1	1h 54m 21s
32 "	0.23	4.3	3h 48m 42s
64 "	0.12	8.5	7h 37m 23s

At magnification 0.60 frames sec^{-1} values are 1.3 times and sec frame^{-1} and operating times 0.75 times values in above table.

Table II. Imaging characteristics of T-28 particle camera for various magnifications

(1) Lens Focal Length	(2) Magnification	(3) Diameter of smallest water drop imaged	(4) Diameter of largest particle completely imaged	(5) Diameter of smallest particle with ice/water distinction	(6) Maximum sample volume per frame	(7) In-focus sample volume per frame	(8) Principal Use
58 mm	0.15	50 μm	160 mm	700 μm	6.2 ℓ	1.1 ℓ	Precipitation-size particles
135 mm	0.60	8	40	150	1.4	3 cm^3	Cloud Droplets

Notes

Column (3) Estimated based on calibrations of sailplane particle camera at M = 1.

" (4) Frame height (24 mm) divided by M.

" (5) Estimated based on calibrations of sailplane particle camera at M = 1.

" (6) Total back illuminated volume seen by camera. Very large particles may also be photographed from front illumination over about 22 ℓ at M = 0.15.

Formula $V = \frac{0.288}{u'^2}(u_F{}^3 - u_N{}^3)$ where u' = image distance, u_F = distance from front nodal point of lens to farthest distance within the illuminated volume, u_N = distance from front nodal point of lens to nearest distance within illuminated volume. Formula only applies to double frame 35 mm format (24 mm x 36 mm), all u values in mm and volume in cm^3.

" (7) In-focus sample volume from formula $V = \frac{2CN}{1000} LH \frac{M+1}{M^4}$ where C = diameter of circle of confusion in image space, assumed 0.025 mm, N = f - number of lens, assumed f/11 for M = 0.15 and f/5.6 for M = 0.60, L - length of picture area = 36 mm, H = height of picture area = 24 mm and M = magnification. Values on right-hand side of equation in millimeters give volume in cm^3 using this formula.

Fig. 4 is characteristic of larger drops (in this case 2.8 mm diameter) where both light refracted during passage through the drop and reflected light off the drop surface are evident. The dot pair and dot quad signatures pertain for out-of-focus as well as in-focus images, becoming overlapped disks for the out-of-focus drops. Figure 5 shows the image of a pendant frozen drop photographed with the T-28 camera set up in the laboratory. Absence of the dot quad plus interior structure are indicative of the ice phase.

Photographs taken during an early camera test flight in a snowstorm in the vicinity of Pactola and Deerfield, South Dakota on 5 December 1975 are shown in Fig. 6 and illustrate the quality of imaging. All of these photographs were taken at M = 0.15, ratio = 4 and accumulate = 1, with a TAS of about 80 m sec^{-1}. The photographs illustrate a variety of ice particle forms seen in this particular storm.

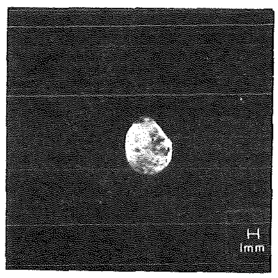

Fig. 5. Pendant 5.7 maximum dimension frozen drop photographed in the laboratory.

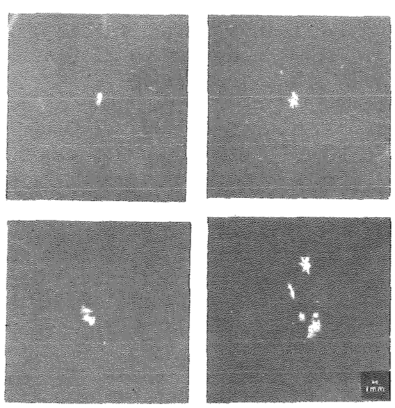

Fig. 6. Snow particles photographed in South Dakota 5 December 1975, M = 0.15, true airspeed about 80 m sec^{-1}. Scale in lower right-hand corner applies to all images.

4. CONCLUSION

By use of the combination short-duration light source (strobe) and rotating mirror it is possible to adequately stop image motion to obtain good quality in situ photographs of cloud and precipitation particles from aircraft. Cameras flown on the sailplane and University of Chicago Lodestar (note paper 3.1.2 by N. J. Carrera) have demonstrated the feasibility of this technique to obtain useful cloud physics information in the past. The T-28 camera should provide valuable data on mature thunderstorms in the coming field seasons of NHRE. Automatic data analysis techniques developed at Colorado State University (note paper 7.1.9 by J. LeCompte et al) will facilitate the heretofore tedious job of reduction of the camera data.

5. REFERENCES

Cannon, T. W., 1970: A camera for photographing airborne atmospheric particles. Image Tech., 12, 37-42.

_____, 1974: A camera for photography of atmospheric particles from aircraft. Rev. Sci. Instr., 45, 1448-1455.

7.1.5

THE MEASUREMENT OF CLOUD DROPLET SPECTRA

P. Ryder

Meteorological Office, Bracknell
Berkshire, U.K.

1. INTRODUCTION

The U.K. Meteorological Office are equipping their Meteorological Research Flight C.130 aircraft for cloud physics research. Aircraft provide good platforms for the exposure of instruments for such research but they have some significant limitations which can be overcome by the use of other platforms, such as tethered balloons, and these additional facilities are also being used in the U.K.

In our view, the current state of cloud physics research places a particular emphasis upon the collection of a range of integrated data on a 'case study' basis. Field studies are seen as providing the data necessary to set up suitable cloud models and to verify, or otherwise, their predictions. The overall aim is to understand, in some detail, the physical processes occurring in and around clouds. The measurement of cloud droplet size distributions is an important part of such a programme, when supported by measurements of the state and motion parameters.

The range of size and number density of cloud hydrometeors to be expected is so large that it is unrealistic to expect any one instrument to make worth-while measurements over the whole range. Any instrument which is likely to resolve particles of 2 to 5 µm diameter at concentrations of several hundred per cc is also likely to have unacceptably long integration times in defining the physically significant, but much lower number density of, either drops in the 20 to 100 µm diameter regime or, ice crystals. This question and the related one of providing real-time or post-experiment data has been discussed previously, Adams (1972). Such considerations have led us to choose the Axially Scattering Spectrometer Probe* (ASSP) and a laser holographic technique as a complementary instrumentation suite for field studies.

The ASSP as delivered in 1974 had some significant problems for use at aircraft velocities and realistic droplet number densities. These are discussed, together with the solutions developed, in the next section.

The use of holography for the determination of the spatial and size distributions of droplets and ice crystals is not new, e.g. Silverman et al (1964), Thompson et al (1966, 1967), Bartlett and Adams (1972) and Thompson (1974). A major disadvantage of the technique arises from the excessive manpower/skill required in the analysis of the reconstructed images. As a result of collaboration in the U.K., between the Chemical Defence Establishment and the Meteorological Office, a major break through has been achieved in devising and implementing an automatic analysis scheme. A full account of this work is being published, Bexon et al (1976), but the salient points are described in section 3. The decision to equip the C.130 aircraft with a holographic disdrometer as outlined in section 4 was based to a significant extent on these findings.

* Manufactured by : Particle Measuring Systems Inc. Boulder, Colorado.

2. THE AXIALLY SCATTERING SPECTROMETER PROBE.

In this probe particles pass through a laser beam perpendicular to the beam axis. Light scattered within 7 to 15° of the beam axis is collected in an annulus co-axial with the beam and focussed onto a photodiode. The intensity of light collected is a function of particle size and its position within the beam. This latter is constrained, for acceptable signals by two electronic systems - 'A' and 'B' - and the peak intensity, as the particle passes through the beam, is measured by a pulse height analyser. After a 'dead-time', a strobe pulse, gated by the 'A' and 'B' circuits, is generated. The presence of this pulse indicates that the particle passed through the beam in a position which allows pulse height to be taken as a measure of particle size. The pulse height analyser generates a signal in one of fifteen channels. With channel number proportional to the square root of pulse size, and hence scattered intensity, Mie theory for spherical particles shows that particle size is approximately proportional to channel number. Experiments with glass spheres and droplets, whose size is also measured by standard magnesium oxide slide techniques, at low number densities and velocities, suggest that the manufacturers calibration is accurate to within ± 2 µm.

The 'A' circuit determines the position of the particle along the axis of the beam. This is necessary because the light intensity scattered into the annular collector depends on the distance of the particle from it and collection optics make the photodetector conjugate with only a very limited region of the beam. The 'A' circuit functions by measuring the output from a second photodetector which has a mask fixed to the centre. A beam splitter directs some of the light incident on the primary photodetector onto the second detector, which only 'leaks' past the mask for out of focus particles.

The 'B' circuit is designed to overcome the problem of undersizing particles passing through the edge of the beam. It functions by comparing each pulse length with a running average. Particles having a less than average pulse length are rejected.

In its original form the probe suffered from several defects. The logic was not designed to cope with more than one particle in any part of the beam 'seen' by the primary photodetector in an interval spanning the time taken for a particle to pass through the beam plus the dead time. The coincidence rate with the original wide beam $\sim 5\%$ at 10 particles/cc and 70 m/sec airspeed. The 'A' circuit was rendered inoperative both by d.c. shifts in the a.c. coupling and noise on the signals. The 'B' circuit was affected by particle coincidences and by the fact that pulse widths are a function of pulse height.

The manufacturer subsequently supplied a laser generating a beam whose diameter is approx -imately half that of the original. (370 to 180 µm). This improved the signal to noise ratio by a factor of four and reduced the co-incidence problem slightly. However, the 'A' and 'B' circuits were still not effective at several hundred drops per cc.

The electronics have been redesigned to minimise the effects of co-incidence by detecting and rejecting such events. Thus, only uncontaminated events are sized by the pulse height analyser and the output is a fair representation of the particle size spectrum shape. However, this has the consequence that the number of particles per unit volume inferred from the flow rate and dimensions of the volume defined by the 'A' and 'B' circuits, is an underestimate. In fact, the integrated water contents for droplet densities in the upper hundreds per cc may be down to a few per cent of their correct values. A statistical program has been devised to obtain a correction based on the measured pulse height analyser spectrum and the raw pulse rate at the main photodetector. Nevertheless, there is a large degree ($\sim 30\%$) of uncertainty in liquid water contents derived from integration of the droplet size spectra and it is likely that the ASSP will not be able to provide reliable absolute measurements of this parameter although relative values are expected to be useful.

D.C. restorers have been incorporated in the analogue signal lines to reduce significantly the effects of d.c. shifts generated when trains of pulses pass through a.c. couplers. The 'B' circuit has been improved in that the running mean pulse length is now only generated from events not contaminated by co-incidence problems. Without this improvement there is a danger that only coincident pulses are accepted at high number densities. There is a further source of error, which in practice tends to reduce the average pulse length, caused by the variation in pulse width with particle size, This has been reduced by measuring pulse width at a level below channel 1 threshold but above noise level and demanding co-incidence between this signal and that of channel one. Without this addition, when large numbers of small particles just exceed the threshold of channel 1, the average pulse width can be reduced to such an extent that the 'B' circuit is effectively inoperative.

With these modifications, and by careful monitoring of probe diagnostics such as the average pulse width for comparison with the expected flow rate and total particle count at the main photodetector, we believe that the ASSP is an excellent tool for measuring average droplet spectra in predominantly water cloud. Hobbs et al (1975) have reported the not surprising conclusion that the ASSP produces an excessive overestimate of ice crystal concentration in all ice clouds because of multiple pulsing from the many faceted scattering particles. Such a phenomenon should, of course, be apparent from the too low average transit time for particles through the beam. It is possible that a bandwidth limiting scheme linked to the expected transit time may allow use of the ASSP as a crude number density counter in all ice cloud but we have not yet attempted this.

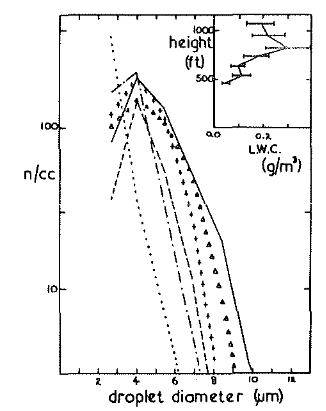

Fig. 1 Droplet Spectra measured in stratocumulus.

Figure 1 shows droplet spectra measured at a range of heights when the ASSP was attached to the cable of a tethered balloon during ascent through non-precipitating stratocumulus. The increase in spectrum width with altitude, followed by a decrease towards the top of cloud, is worthy of note, and appears to be a common feature of this type of cloud. The error bars on the derived liquid water content profile represent estimated systematic, rather than random, errors.

3. THE HOLOGRAPHIC DISDROMETER

As described in section 1 the significant advance with this instrument has been the design and implementation of an automatic analysis scheme.

Laboratory and ground based field studies have used a pulsed ruby laser, operating at a wavelength of 694.3 nm, with an output power in excess of 5 mJ and pulse length of 30 nanoseconds.

The aircraft system uses a frequency doubled Nd Yag laser (section 4). The output is focussed by a lens and diverged through an in-line pinhole to improve beam uniformity. The divergent beam is incident on a hologram plate or film at a distance typically 1 to 2 m from the pinhole, where the interference pattern resulting from interference between light scattered from particles in the beam and that passing unscattered through the object volume, is recorded. The plate or film is developed in high contrast developer but not bleached. Experience has shown that phase holograms produce excessive noise in the reconstruction which has prevented automatic analysis.

The reconstruction system uses a similar in-line configuration of a continuous 5 mW He-Ne laser, lens and pinhole. When illuminated by this source the hologram produces real and virtual images. In the past the real images have been viewed by means of a magnifying system such as a microscope. However, the optical elements in such an arrangement produce noise of similar intensity to that of the 'signal' from the particle images which is not conducive to automatic analysis. Bexon (1973) has reported a method of achieving lensless magnification whose use, we believe, is a key step in the production of high quality magnified images suitable for automatic analysis. He describes, by analogy between a hologram and a lens, how the magnification of a particular recording and reconstruction arrangement may be defined. The overall magnification of the images is a function of the position of the hologram, along the reconstructing laser axis, necessary to achieve focus at a fixed image plane, and of the recording geometry. Linear magnifications of the order of 20 are readily achieved. In practice the system is calibrated by forming a hologram of a graticule of known dimensions in the recording beam. With certain constraints on the recording and reconstructing geometry there are two positions of the hologram which produce real, in-focus, images at the image plane. The ratio of magnifications at, and separation of, these positions along the beam together with the ratio of laser wavelengths in recording and reconstructing allow calculation of the overall magnification. This process is and will remain, essentially, a manual operation. The magnification for any other hologram position can readily be determined from its location relative to either of the above positions. This axial co-ordinate, z, and the relative positions of images (say x and y) in the image plane are also required to obtain the three dimensional distribution of particles generating the hologram.

Thus an automatic analysis scheme must provide the capability of moving the hologram along the reconstruction beam; of detecting focus of images; of detecting and recording an image size (and shape) parameter, the position of the image (x and y) and the position of the hologram at focus relative to some arbitary plane (Z). The major problem has been to devise a reliable in-focus detector.

This has now been achieved, for holograms produced and reconstructed as outlined above, using a commercial image analyser, the Quantimet 720.* A large bibliography exists on this device (see for example, 'Microscope' (1971)) and only the most relevant features are described below. The image detector is either a vidicon or plumbicon. The Quantimet available to us uses a vidicon. This is mounted at the image plane of the reconstruction system. The images formed by the hologram are scanned at a rate of 10.5 frames a second and 720 lines per frame. A feature of the scanner is the precise position and length of each scan line. Each line is resolved into 910 horizontal picture points, whose position is again precisely controlled, so that equal resolution along and across the scan line is achieved. All measurements are made in terms of the number of picture points which make up the image under analysis. The signal from the vidicon passes to a detector module where each of the picture points is assessed and allocated in binary form according to the detected intensity. The module may be set to give three independent fully variable levels providing four output channels with 'above', 'below' and 'between' capability. An internal computer then counts the number of picture points satisfying the criterion set by the operator. For example the number of picture points whose intensity exceeds say level 2 but is less than level 3 may be determined. A sequence of measurements may be obtained by means of a programmer module but greater flexibility has been attained by interfacing a desk calculator/computer to the Quantimet to fulfill this role and provide a suitable data recording medium.

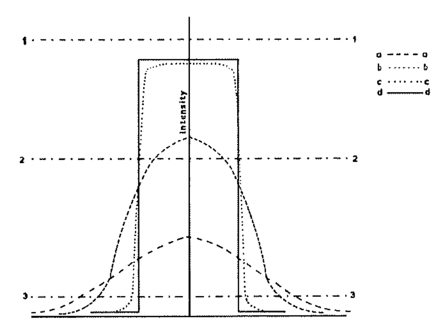

INTENSITY DISTRIBUTION ACROSS A DROPLET IMAGE

Fig 2

In order to understand how a particle may be brought into focus it is necessary to refer to figure 2. Intensity is plotted schematically as a function of distance across a scan line through the centre of a particle image, which is in various degrees of focus. The standard detector levels are set up so that level 3 is above the general background noise level; level 1 is set so that no features are of sufficient intensity to be detected; level 2 is set up approximately midway between these two. A particle which is well out of focus (a - a) will, in general, not generate an intensity greater than level 2. As the

* Manufactured by : Metals Research Ltd., Royston, Cambridge, U.K.

particle is brought closer to focus (b - b) a point is reached in which the central portion of the image exceeds this level. At this stage attention switches to the difference between levels 2 and 3 which is in the form of a halo. The linear dimensions (diameter) of the features at level 2, d_2, and level 3, d_3, are Quantimet output parameters. These change as the image approaches focus but their difference, d_3-d_2, (corresponding to twice the halo thickness) will diminish. Ideally the thickness might be expected to reduce to zero at focus but because of finite resolution and edge effects a situation similar to c - c results. At this stage the halo thickness is a minimum, i.e. the image edges are sharpest.

Several schemes have been attempted which use this concept as a focus criterion but the most useful is as follows : The hologram is mounted on a stepping motor which is driven by the Quantimet so that if there is no feature, greater than a few picture points, above level 2, the motor steps by 1 mm. When such a feature is detected small (0.1 mm) steps are generated. The position of the hologram along the laser axis (Z) is determined from a summation of these large and small steps. Once the small step routine is entered measurements of the area at level 2, (A_2), the area between levels 2 and 3 (A_{23}), the area at level 3 (A_3), the feature perimeter (P), plus z, x and y are made and stored. d_2 and d_3 are calculated from $d_i = \sqrt{\frac{4 A_i}{\pi}}$ as is the z position at which d_2-d_3 is a minimum. A print out of a typical array of these parameters is shown in table 1.

TABLE 1. Image parameters through focus

z	A_{23}	P	A_2	A_3	A_{23}/P	d_2	d_3	d_3-d_2
78	303	229	776	1079	1.32	31.43	37.07	5.64
79	297	226	777	1074	1.31	31.45	36.98	5.53
80	277	218	786	1063	1.27	31.63	36.79	5.16
81	242	218	789	1031	1.11	31.70	36.23	4.53
82	209	218	775	984	0.96	31.41	35.40	3.99
83	187	204	750	937	0.92	30.90	34.54	3.64
84	161	198	724	885	0.81	30.36	33.57	3.21
85	149	196	704	853	0.76	29.94	32.96	3.02
86	141	192	682	823	0.73	29.47	32.37	2.90
87	157	197	674	831	0.80	29.29	32.53	3.24
88	235	207	676	911	1.14	29.34	34.06	4.72
89	288	213	697	985	1.35	29.79	35.41	5.62
90	355	231	709	1064	1.54	30.05	36.81	6.76
91	446	253	713	1159	1.76	30.13	38.41	8.28
92	543	259	691	1234	2.10	29.66	39.64	9.98
93	620	267	668	1288	2.32	29.16	40.50	11.34

The visual focus corresponds exactly with the minimum halo in this case and in 200 cases checked the visual and automatic estimates of focus agree to within one small step. Suggesting a maximum error in area from this source of less than 3%. The parameter A_{23}/P ($= 2\pi r \Delta r / 2\pi r$) is an additional measure of halo thickness which, as it happens, is also minimised at focus in the particular case shown. Parameters such as A_3/P^2 provide form factors which can be used, in principle at least, to distinguish circular drops from non-circular ice crystals but this has not yet been fully tested on the automatic system.

The data shown in figure 3 was produced by sizing glass spheres (8 to 90 μm diameter) on perspex fibres (2 μm diameter) both by the Quantimet/holographic technique and by direct measurement under a microscope. This experiment allows one to one correspondance of the measurements to be made.

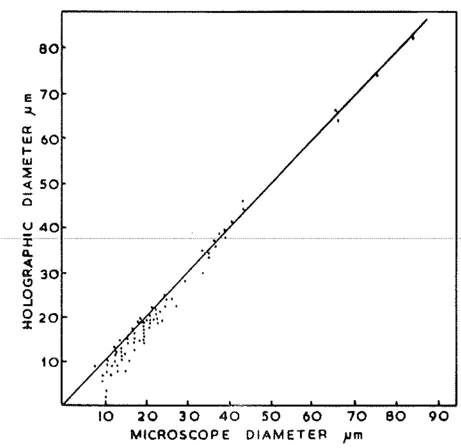

SEMI-AUTOMATIC HOLOGRAPHIC DIAMETER v MICROSCOPE DIAMETER

FIG 3

The area A_2 was used to derive drop diameters and there is evidence from this and similar analyses to suggest that A_3 provides a diameter which is closer to the microscope derived values.

The physical principles of a fully automatic analysis system have been established. The tasks remaining are largely concerned with improving the engineering of the system and transferring a greater level of control from the dedicated hard-wired Quantimet computer to the larger software - controlled desk computer. This will allow solution of the infrequent but finite problem generated when two or more drops are simultaneously close to focus on the vidicon.

4. THE AIRCRAFT INSTRUMENTATION

The ASSP has been fitted to a window blank immediately aft of the forward port side door on the C.130 and a comprehensive data logging system has been built to allow real time display of droplet spectra in histogram form and recording of these on magnetic tape. Spectra averaged over successive 1 second periods (∼ 100 m) can be achieved. Shorter averaging periods are obtainable but the data are then discontinuous along the flight path. The ASSP, in this position on the aircraft, is considered to be a standard facility to be used in conjunction with a liquid water content meter, the gust probe, temperature and humidity measuring instruments and the precipitation radar.

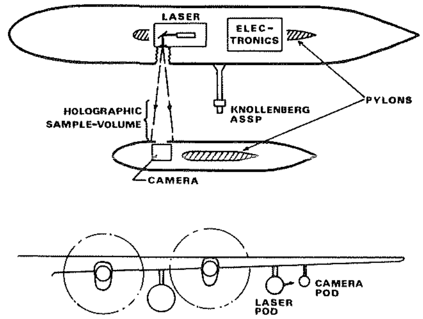

AIRCRAFT INSTALLATION Fig 4

The holographic disdrometer is being mounted beneath the outboard section of the port wing (see figure 4). The laser is a commercially available* Nd YAG type, purpose built for aircraft use. The laser output is frequency doubled to a wavelength of 503 nm and has an output power of 8 mJ at this wavelength, with a pulse length of 20 nanoseconds. The camera is a modified aircraft type fitted with a roller blind shutter and an interference filter centred on the laser wavelength. Experiment has shown that this combination gives negligible fogging of film in all but direct sunlight and produces a small, acceptable degradation of hologram quality. The laser is mounted, within an environmentally controlled housing, in a modified fuel tank. The camera is in a smaller adjacent pod also suspended on a pylon from the wing. The sampling volume is between 0.5 and 1 litre. A second ASSP will be mounted downstream of this volume.

The disdrometer is seen as a non-routine instrument whose use will be restricted to the study of specific phenomena. Thus provision is being made to trigger laser firing at up to 5 times per second under control of, for example, the gust probe, the liquid water content meter or output from any channel or combination of channels of the ASSP. This will allow study of specific features of the particle (ice and water) size and position distribution at cloud boundaries, regions of strong updraught, downdraught or shear, or high and low liquid water content areas.

---

* Manufactured by : Ferranti Ltd., Edinburgh, U.K.

ACKNOWLEDGEMENTS.

The work of both past and present colleagues in the Meteorological Office and Chemical Defence Establishment is gratefully acknowledged.

REFERENCES.

Adams, R.J., 1972 : A holographic system for droplet sizing in clouds and fogs. International Cloud Physics Conference, London.

Bartlett, J. and R.J. Adams, 1972 : Development of a holographic technique for sampling particles in moving aerosols. Microscope, 20, 357-384.

Bexon, R., 1973 : Magnification in aerosol sizing by holography. J. Phys. E; Sci. Instrum., 6, 245-248.

Hobbs, P.V., L.F. Radke and D.G. Atkinson, 1975: Airborne measurements and observations in cirrus cloud. AFCRL - TR - 75 - 0249.

Microscope, 1971 : No. 1, Jan - Apr.

Silverman, B.A., B.J. Thompson and J.H. Ward, 1964 : A laser fog disdrometer. J. Appl. Met, 3, 792 - 801.

Thompson, B.J., G.B. Parrent, J.H. Ward and B. Justh, 1966 : A readout technique for the laser fog disdrometer. J. Appl. Met., 5, 343 - 348.

Thompson, B.J., J.H. Ward and W.R. Zinky, 1967 : Application of hologram techniques for particle size analysis. Appl. Optics., 6, 519 - 526.

Thompson, B.J., 1974 : Holographic particle sizing techniques. J. Phys. E; Sci. Instrum, 7, 781 - 788.

Bexon, R., J. Gibbs and G.D. Bishop, 1976 : Automatic assessment of aerosol holograms. Aerosol Science, (in press).

FIELD MEASUREMENTS OBTAINED WITH TWO OPTICAL ICE PARTICLE COUNTERS IN CUMULUS CLOUDS OVER FLORIDA

by

F. M. Turner†, A. S. Ramachandra Murty*
R. I. Sax‡ and L. F. Radke+

+Cloud Physics Group, Atmospheric Sciences Dept.
University of Washington, Seattle, Washington

*Indian Institute of Tropical Meteorology,
Poona-5, India

‡National Hurricane and Experimental Meteorology
Laboratory, National Oceanic and Atmospheric
Administration, Coral Gables, Florida

1. INTRODUCTION

An intercomparison of airborne instrumentation to measure ice particle concentrations in convective clouds was carried out as a part of NOAA's 1975 Florida Area Cumulus Experiment (Woodley and Sax, 1976). The instruments compared were the automatic ice particle counters (IPC) of the University of Washington (Turner, Radke and Hobbs, 1976) and of Mee Industries (Model 120) and a high-speed Formvar replicator from the University of Nevada's Desert Research Institute.

NOAA's DC-6 was equipped with these three devices as well as a Knollenberg 2-D rain and cloud particle spectrometer system, a foil impactor, a Lyman-alpha total water probe, and a Johnson-Williams cloud droplet sensor. Penetrations were made of cumulus clouds in various stages of development, but with emphasis on those towers which appeared to be actively growing. These penetrations were generally made at the -10°C or -4°C level with occasional penetrations at higher temperatures.

2. DESCRIPTION OF THE INSTRUMENTS

Fig. 1 shows a schematic representation of the University of Washington's automatic optical ice particle counter Mark III (UW-IPC). The instrument utilizes a linearly polarized helium-neon laser which illuminates any particle which passes through the sample port. The primary purpose of the series of collimating disks is to keep outside ambient light from entering the detection system. A polaroid filter is placed at the end of the detection system and set for maximum extinction to the incident linearly-polarized light. The main beam of the laser is absorbed in the light trap so that direct light is not detected by the photomultiplier tube. The forward scattered light which enters the detection system is limited to forward scattering angles from approximately 1/2° to 3-1/2°. An aperture placed on the photomultiplier tube side of the polaroid filter limits the azimuthal angles of the forward scattered light to ±5° on each side of the main planes of the scattering. The light then passes through an interference filter (0.01 μm band-pass at 0.6328 μm wavelength) and is detected by the photomultiplier tube.

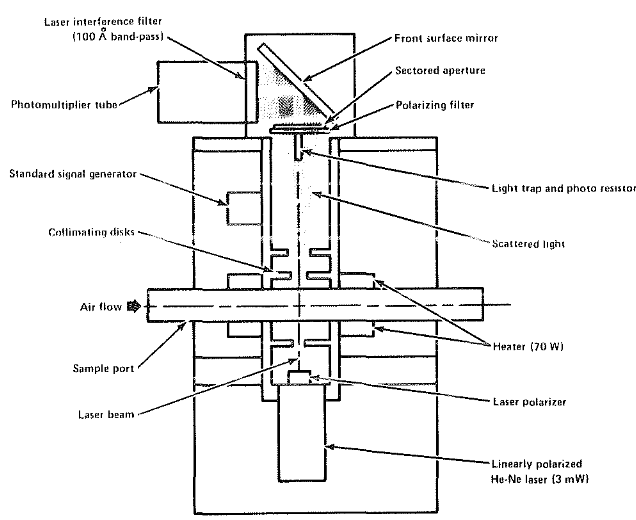

Figure 1. The University of Washington optical ice particle counter (Mark III).

Fig. 2 shows a diagram of the Mee Industries Model 120 ice crystal counter (Mee-IPC). A projection lamp is used as a light source and the light passes through an optical system so that linearly-polarized infrared light is incident on all particles passing through the sample pipe. The light sensor (a solid-state device) detects the infrared light which is scattered at an angle of 90° (actually a cone of light around the 90° scattering angle) after the light passes through an optical system containing a polaroid filter set for maximum extinction.

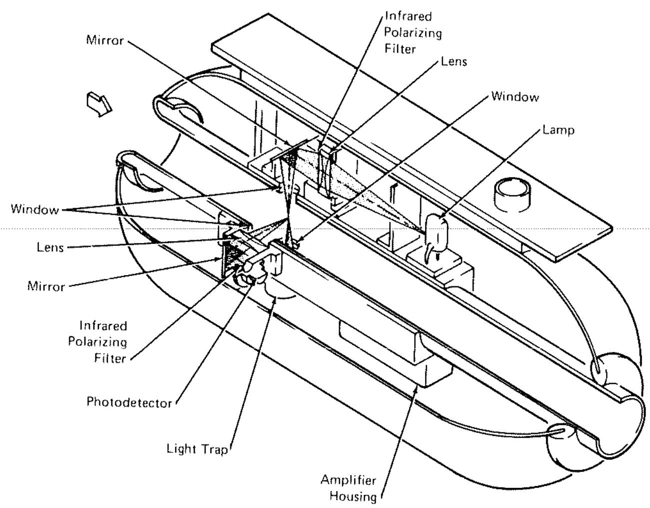

Figure 2. The Mee Industries Model 120 optical ice particle counter.

It can be seen from the description of the two instruments that the UW-IPC detects forward scattered light while the Mee-IPC detects light scattered at an angle of 90°. As we will see below, this difference assumes importance in discussing the possible mechanisms for the detection of ice particles in these two devices.

There is also a difference in the actual volume of air illuminated by the light source in the two instruments. In the UW-IPC the volume of air illuminated is 0.0276 cm^3, with (assuming an even distribution of ice particles in the air) a maximum allowable concentration of ice particles before significant counting errors occur of 36 ice particles per cm^3. In the case of the Mee-IPC, the volume of air illuminated is 0.25 cm^3 with a maximum counting capability of 4 ice particles per cm^3. Since both of these values are well above the generally accepted maximum values of ice particle concentrations in the air there is no problem of coincidence counting errors with either instrument.

The larger sampling volume of the Mee-IPC improves the minimum concentration detection limits but, as will be seen in § 4, it may lead to erroneous counts in high liquid water environments.

3. MECHANISMS FOR ICE PARTICLE DETECTION

There are three possible mechanisms for the detection of ice particles in the instruments previously described (see Turner and Radke, 1973, for a more detailed discussion), namely:

(a) the rotation of the plane of polarization of the light beam, produced by the birefringent property of ice, as it passes through a particle of ice,

(b) the reflection of light from a specular face of an ice crystal and,

(c) light scattered at a preferred angle by ice particles.

The birefringent (or double-refracting) property of ice acts so that linearly-polarized light transmitted through ice will, in general, be rotated so that the light which leaves the crystal will still be linearly polarized, but the plane of polarization will be changed. For example, an ice crystal 226 μm thick which is optimally oriented will rotate incident linearly-polarized light through an angle of 90° (assuming the incident light has a wavelength of 0.6328 μm). The amount of rotation depends on both the thickness and orientation of the ice crystal. It is clear from the geometry of the UW-IPC that the birefringent property of ice provides a direct first order detection mechanism of ice particles.

The reflection of light from specular faces of ice crystals is probably the primary detection method occurring in the Mee-IPC. This detection method relies on the crystal being oriented in such a way that the detector will intercept light reflected from the crystal face. Crystals which do not have regular faces (i.e. rimed or irregular crystals) will not provide as strong a signal to the detector. For both of the detection methods discussed so far the importance of orientation will, of course, rapidly decrease with increasing size and complexity of crystals.

A third possible mechanism for the detection of ice particles (which may improve the sensitivity of the Mee-IPC) is the existence of a preferred scattering angle. Huffman and Thursby (1969) and Huffman (1970) have compared the light scattered from water drops and ice crystals. These measurements show that the difference in relative scattering function is largest (more light scattered from ice crystals) at a scattering angle of about 100°. This difference is probably due to the external reflection mechanism discussed above. For a more detailed discussion of these mechanisms see Turner, Radke and Hobbs (1976) and Turner and Radke (1973).

4. REJECTION OF WATER DROPS

No matter which of the three mechanisms discussed above for detecting ice is effective for a particular counter, water drops may still be detected under some conditions. This is due to practical effects such as imperfect polarizers, stray light, and non-spherical drops. Thus, the criterion in judging the ice particle counters must be their relative ice/water discriminating power, rather than their ability to detect the smallest ice particle.

In the case of the UW-IPC, the instrument was operated in a mode which previous laboratory and field tests had indicated was optimum for ice detection and water rejection. The Mee-IPC, on the other hand, was not felt to be fully optimized and so four different channels of data were recorded (channels 1 to 4 in decreasing order of sensitivity corresponding to threshold signal levels of 100, 300, 500 and 700 mV). Previous tests indicated channel 2 to be nearly optimal.

5. RESULTS

5.1 Ability to Reject Water Drops

Four cases will be discussed: (a) an all water cloud penetrated near its top at about the -1°C level; (b) an all water cloud penetrated near its top at the -9°C level; (c) a totally warm cloud with its top below 0°C and, (d) a rainshaft penetration at the +10°C isotherm.

Fig. 3 shows the results of measurements obtained on July 24, 1975, in a vigorously growing 0°C isotherm and was penetrated near its top at about -1°C. The metal foil sampler showed that practically no precipitation particles were present. The liquid water content (measured by a hot wire technique which detects only small droplets) peaked at 2.1 g m^{-3}. The UW-IPC showed no counts while the Mee-IPC showed a maximum count of $6.6\ell^{-1}$ in channel 1 and a few counts in channel 2.

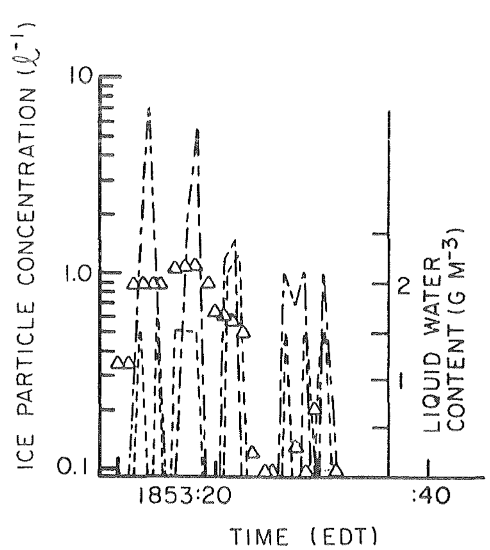

Figure 3. Measurements obtained in an all water cloud on July 24, 1975. (— - —) MEE-IPC-1, (— — — —) MEE-IPC-2, (Δ) Liquid water.

The results of measurements obtained on July 24, 1975, are shown in Fig. 4 for a penetration through a very "hard" appearing cloud. The penetration was made near a cloud top at about -9°C. Although the temperature was well below freezing, the Formvar replicator showed that no ice was present in the cloud. The metal foil sampler further showed that no precipitation size water drops were present in the cloud. As shown in Fig. 4, the Mee-IPC exhibited very high counts in channel 1 while the liquid water content is simultaneously very large, peaking at 2.6 g m^{-3}. The UW-IPC showed no counts in this cloud. The probable reason for the spurious counts registered by the Mee-IPC is that there is an increase in the background noise level due to the large numbers of small water droplets in the sample volume at any instant in time.

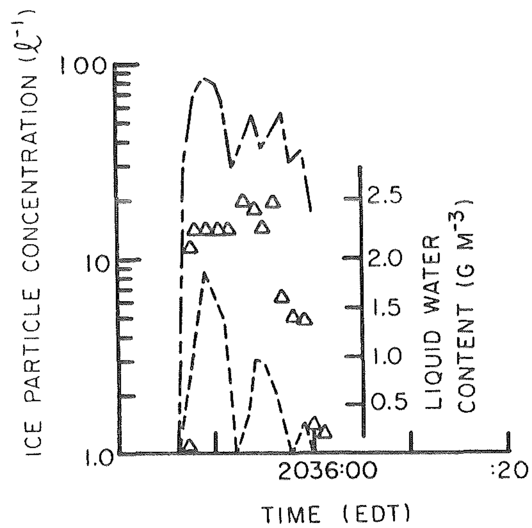

Figure 4. Measurements obtained in an all water cloud on July 24, 1975. (— - —) MEE-IPC-1, (— — — —) MEE-IPC-2, (Δ) Liquid water. UW-IPC was everywhere zero.

Fig. 5 shows measurements obtained in a growing cumulus cell on July 24, 1975. The cloud which was not vigorous, was penetrated at the 3,200 m level about 900 to 1200 m below cloud top.

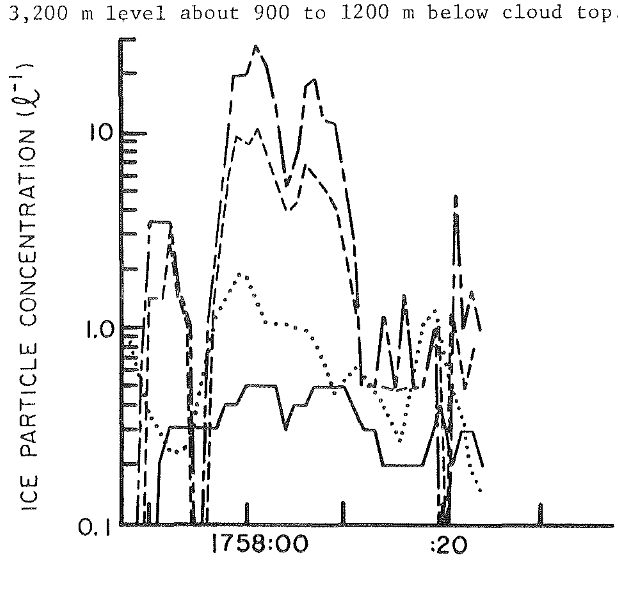

Figure 5. Measurements obtained in a totally warm cloud on July 24, 1975. (———) UW-IPC, (— - —) MEE-IPC-1, (— — — —) MEE-IPC-2, (—·—) Foil sampler.

Thus the entire cloud was warmer than freezing. The liquid water content was fairly low (maximum 0.4 g m^{-3}) while the mass of precipitation sized water drops peaked at 3 g m^{-3}. As can be seen in Fig. 5 the maximum count detected by the UW-IPC was 0.5 ℓ^{-1}, while the Mee-IPC registered a maximum of 28 ℓ^{-1} in the channel 1 and 10 in channel 2. Hence, when precipitation sized water drops are present the Mee-IPC detects them in significant numbers in both channel 1 and channel 2, but in channels 3 and 4 the counts detected are low and similar to those detected by the UW-IPC.

Finally, Fig. 6 shows the results of measurements obtained in a subcloud rainshaft of moderate intensity penetrated at the 10°C level at 2,600 m on July 31, 1975. The results obtained in this penetration are similar to those shown in Fig. 5. The UW-IPC detected a maximum concentration of 0.5 ℓ^{-1} while the Mee-IPC detected a maximum of 28 ℓ^{-1} in channel 1 and 10 ℓ^{-1} in channel 2.

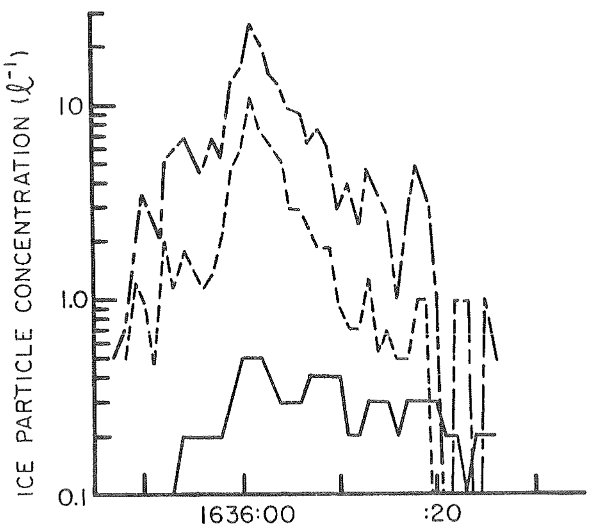

Figure 6. Measurements obtained during the penetration of a rainshaft on July 31, 1975. (———) UW-IPC, (— — —) MEE-IPC-1, (– – – –) MEE-IPC-2.

We conclude from these results that the UW-IPC rejects all but the largest raindrops. Channel 1 of the Mee-IPC is of little value since it counts virtually all precipitation sized drops and in clouds of high liquid water content it suffers from background noise. Channel 2 of the Mee-IPC also appears to count a large fraction of precipitation sized drops (roughly 20 times more than the UW-IPC). However, channels 3 and 4 of Mee-IPC seldom count any significant numbers of precipitation sized drops.

Therefore, in the next section, where we compare the ice counting ability of the two counters, an intermediate channel between 2 and 3 on the Mee-IPC should be compared to the UW-IPC. Since this is unavailable, channel 2 will be used despite possible ambiguity if large drops are present.

5.2 Measurements of Ice Particle Concentrations

The results of measurements obtained on July 14, 1975, are shown in Fig. 7. These measurements were obtained during a -9°C penetration of a long stretch of cirrostratus debris from an old anvil. The liquid water content and mass of hydrometeor water were both negligible during this cloud penetration. As can be seen in Fig. 7 the ice particle concentrations measured by the UW-IPC are generally somewhat lower than those measured in channel 2 of the Mee-IPC. The concentrations deduced from the Formvar replicator (mostly graupel was present) were generally lower than those measured with the two automatic counters (the concentrations of ice crystals deduced from the Formvar replicator were deliberately conservative estimates).

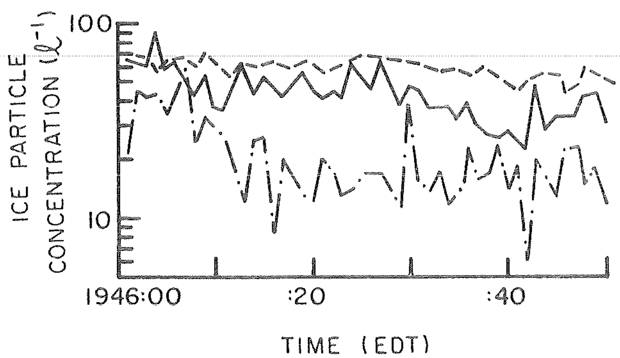

Figure 7. Ice particle concentrations measured on July 14, 1975 in anvil cirrus. (———) UW-IPC, (— — —) MEE-IPC-2, (—·—) Formvar replicator.

Measurements obtained in a cloud which had stopped growing are shown in Fig. 8. The cloud topped more than 1000 m above the aircraft and was penetrated at the -9°C at 5,8000 m. The cloud had a "soft" visual appearance. The liquid water content during this cloud penetration was quite low (peak 0.6 g m^{-3}) and the mass of hydrometeor water peaked at 1.9 g m^{-3}. The concentrations of ice particles obtained with the Formvar replicator (about 60% columns and 40% graupel) were generally higher than those obtained with the two IPC. The concentrations obtained with the two IPC were quite similar with the UW-IPC reading slightly lower than channel 2 of the Mee-IPC. These measurements may indicate low counting efficiency for small columns.

Measurements obtained on July 20, 1975, during the penetration of a "soft" appearing cloud which topped more than 1000 m above the aircraft are shown in Fig. 9. The cloud had stopped growing and was penetrated at about -9°C. The liquid water content in the cloud was very low (peak of 0.1 g m^{-3}). The Formvar replicator showed that only graupel was present in the cloud. The concentrations measured with the UW-IPC was significantly higher than that measured with the Mee-IPC (channel 2) which, in turn, was significantly higher than those measured with the Formvar replicator.

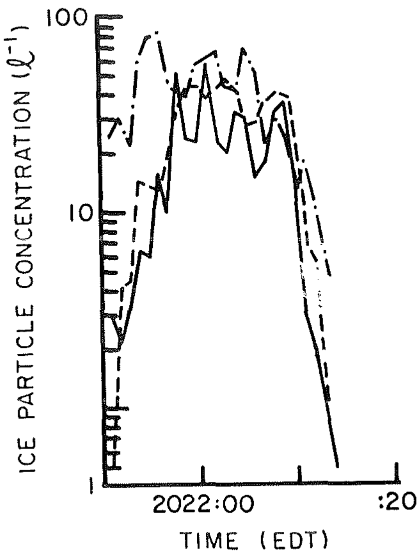

Figure 8. Ice particle concentrations measured on July 24, 1975. (———) UW-IPC, (– – – –) MEE-IPC-2, (— · —) Formvar replicator.

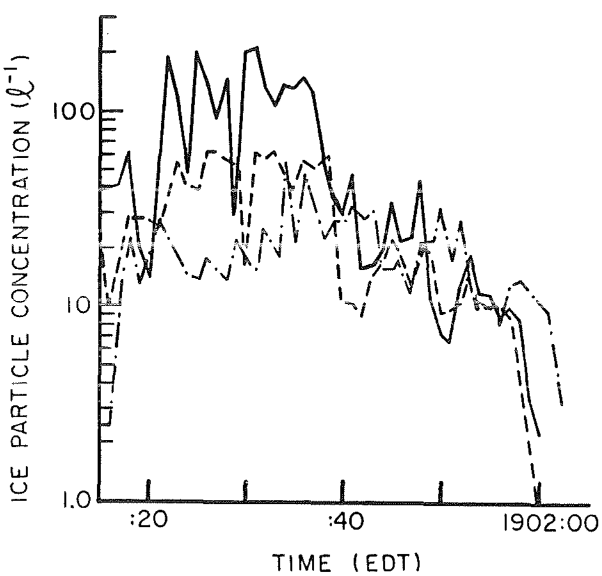

Figure 9. Ice particle concentrations measured on July 20, 1975. (———) UW-IPC, (– – – –) MEE-IPC-2, (— · —) Formvar replicator.

Fig. 10 shows measurements obtained on July 14, 1975, during the penetration of a "soft" appearing cloud at about the -9°C level. The cloud topped more than 1000 m above the aircraft and consisted of several towers. The liquid water content during this penetration was low (peak of 0.5 g m^{-3}) while the mass of hydrometeor water was quite significant, peaking at 4 g m^{-3}. Again the concentrations of ice particles measured with the UW-IPC were significantly higher than those obtained with the Mee-IPC (channel 2). The Formvar data (all graupel) showed very low concentrations, however, the replication was of very poor quality due to liquid water being present over much of the film.

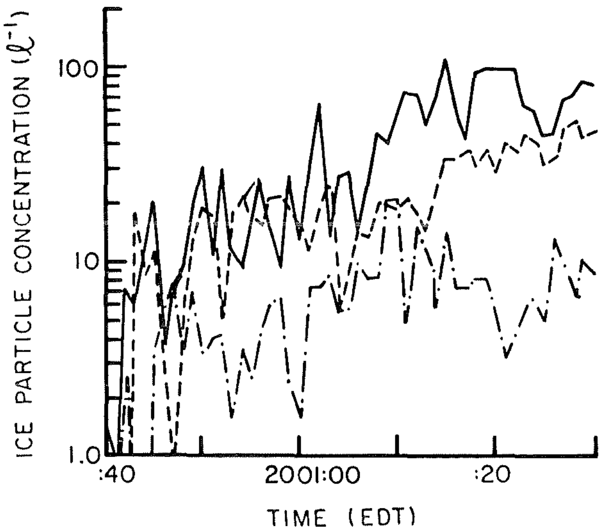

Figure 10. Ice particle concentrations measured on July 15, 1975. Formvar data questionable. (———) UW-IPC, (– – – –) MEE-IPC-2, (— · —) Formvar replicator.

Fig. 11 shows the results of measurements obtained on July 31, 1975, during a cloud penetration at the -10°C level. The cloud, which had nearly stopped growing had a "soft" visual appearance and topped well above the aircraft. There was no significant liquid water present in the cloud (0.2 g m^{-3} peak). The concentration of ice particles measured by the UW-IPC was significantly higher than those measured with the Mee-IPC (channel 2).

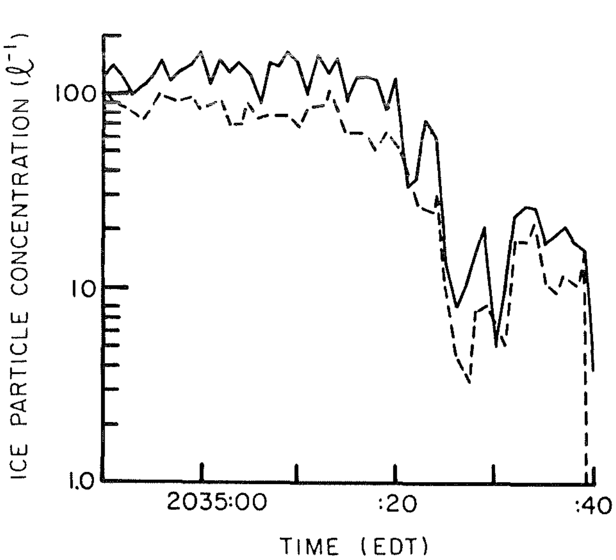

Figure 11. Ice particle concentrations measured on July 31, 1975 in a nearly glaciated cloud. (———) UW-IPC, (– – – –) MEE-IPC-2.

Fig. 12 shows the results of plotting the data shown in Figs. 10 and 11 for the two IPC. It can be seen that the UW-IPC has a somewhat higher counting efficiency than the Mee-IPC (channel 2).

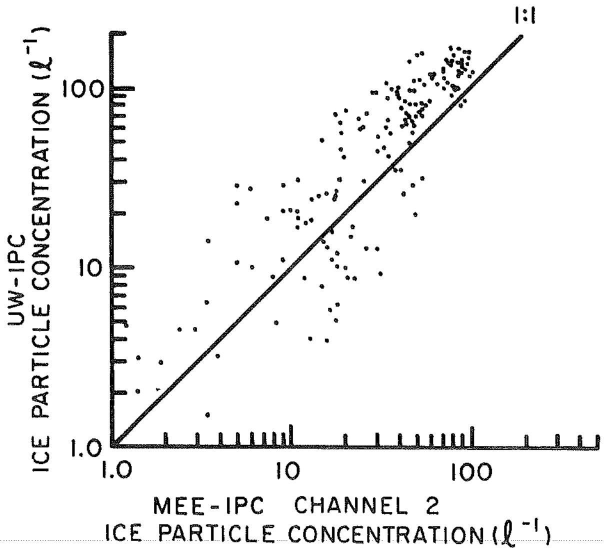

Figure 12. A comparison of the UW-IPC against the MEE-IPC-2 using the data in Figures 10 and 11.

6. CONCLUSIONS

In this paper we have described a first attempt at comparing the measurements obtained with the two automatic ice particle counters. Additional laboratory and field work will be needed before any definitive judgments can be made. However, the preliminary field studies described in this paper indicate that the UW-IPC is slightly superior to the Mee-IPC in its ability to count ice particles while simultaneously rejecting water droplets.

The tests also show that, when operated with care, either of these devices can provide valuable information for airborne cloud physics and weather modification research.

ACKNOWLEDGEMENTS: We would like to thank the NOAA Research Facility Center for aircraft and instrumentation support. Financial support to the University of Washington was from NOAA Grant 01-5-022-1996 and by Grant ATM-74-14726-A02 from the Atmospheric Research Section (Meteorology) of the National Science Foundation.

7. REFERENCES

Huffman P. 1970: Polarization of light scattered by ice crystals. J. Atmos. Sci., 27, 1207-1208.

Huffman P., and W. R. Thursby, 1969: Light scattering by ice crystals. J. Atmos. Sci., 26, 1073-1077

Turner F. M. and L. F. Radke, 1973: The design and evaluation of an airborne optical ice particle counter. J. Appl. Met., 12, 1309-1318.

Turner F. M., L. F. Radke and P. V. Hobbs 1976: Optical techniques for the counting of ice particles in mixed phase clouds. Atmospheric Technology (In press).

Woodley W. L. and R. I. Sax, 1976: The Florida area cumulus experiment: Rationale, design, procedures, results and future course. NOAA Tech. Report ERL 354 WMPO-6, January, p 204.

AN AUTOMATIC SEQUENTIAL RAINFALL SAMPLER FOR ANALYSIS OF CONTAMINANTS AT ABOUT 10^{-6} ppm LEVEL

Jean-Pierre Lacaux and Jean Dessens

Université de Clermont
Centre de Recherches Atmosphériques
65300 Lannemezan, France

1. INTRODUCTION

Analyses of contaminants in rain-water are interesting because their results may be related to the processes of rain formation by condensation nuclei or by ice nuclei, and to rain scavenging of atmospheric aerosols. For example, in experiments on weather modification by seeding with silver iodide, the analysis of silver in precipitation gives some information about the presence of silver iodide nuclei in the cloud droplets (Warburton, 1973 ; Summers, 1972).

Previous measurements using manual or automatic rain samplers have shown that sudden variations in the intensity of convective rain-fall with time often coincide with sharp variations in the concentration of chemical contaminants (Gatz and Dingle, 1971). Whereas there are chemical analysis methods that permit the determination of the concentration of stable elements in water at the 10^{-6} ppm level (neutron activation, atomic absorption spectrometry ...), no rain sampling method is clean enough to be fruitfully associated with them. In particular, one of the most sophisticated systems (Gatz, 1971) does not take into account dry deposition on the collector area, nor the removal of trace substances by the surfaces of the water containers.

This paper describes an automatic sequential rain sampler which collects successive precipitation samples with a high degree of cleanliness. The main characteristics of this sampler are :

- prevention of dry deposition before and after the rain ;
- sequential sampling with constant sample volume and time recording ;
- immediate freezing of the samples in order to prevent changes in chemical composition after sampling.

2. DESCRIPTION OF SAMPLER

The sampler (figure 1) consists mainly of a small pilot rain gauge which controls the operation of a large collecting rain gauge.

Figure 1. The automatic rainfall sampler.

1 *Pilot rain gauge* 4 *Refrigerator*
2 *Electronic device* 5 *Collecting funnel*
3 *Distributing system* 6 *Printer*

2.1. The pilot rain gauge

The pilot rain gauge orders the opening and the shutting of the collecting rain gauge at the beginning and the end of a fall of rain ; this pilot rain gauge also measures the rain volume in order to collect a chosen volume of water in each sample.

The pilot system (figure 2) consists of a small funnel of 250 cm^2 collecting ; the water falls in droplets or in a stream onto two electrodes a and b ; the electrical impulse is processed by an electronic device which orders the opening of the collecting rain gauge and records the time with a one-second resolution. The rain water is then simultaneously but independently collected in the pilot rain gauge and in the collecting rain gauge; when the water in the siphon of the pilot reaches the electrodes c and d (adjustable position corresponding to a chosen rainfall between 0 and 1 mm), the electronic device orders a change of container in the collecting system, records the time, and orders the draining of the siphon.

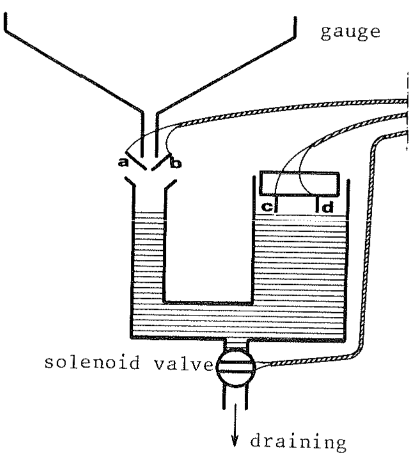

Figure 2. Schema of the pilot rain gauge.

2.2. The collecting rain gauge

The collecting system is composed of a funnel equipped with a removable shutter, a system distributing the water to a maximum of 39 bottles, and a cold-storage compartment for these bottles.

The collecting funnel is a truncated cone made of rigid polyethylene ; with its area of 0.5 m^2, a rainfall of 1 mm gives a sample volume of 500 ml. The funnel moves vertically so that it can be hermetically closed by pressure on an horizontal sheet of polyethylene. When an order to open is given by the pilot rain gauge (figure 3), firstly the collecting funnel descends 3 cm, secondly the shutter uncovers the funnel, and thirdly the funnel ascends again, but by 6 cm this time so that no splash droplets can enter the funnel.

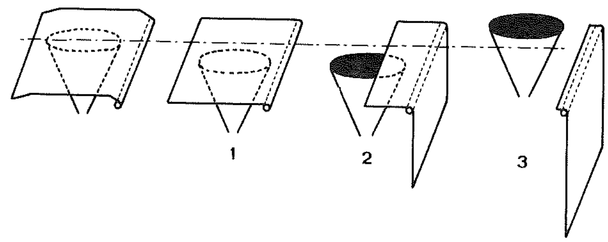

Figure 3. Schematic diagram of the opening of the rain sampler.

1 *The funnel descends ;*
2 *The shutter uncovers ;*
3 *The collecting funnel ascends.*

The distributing system consists of two discs one above the other : there is one hole in the upper disc, and 39 holes in the lower one ; the upper disc rotates with its hole coinciding successively with each the 39 lower holes. A short hose (20 cm) made of polyethylene channels the water from the funnel to the upper hole, and 39 other hoses channel the water from the lower holes into the bottles.

The bottles (capacity : 500 ml) are stored in a refrigerator regulated at -15C. The water samples are frozen within a maximum of 2 hours, and in this manner the removal of contaminants by the surfaces of the bottles is reduced ; for example, in the case of silver analysis, this removal does not exceed 10 to 20 % (figure 4).

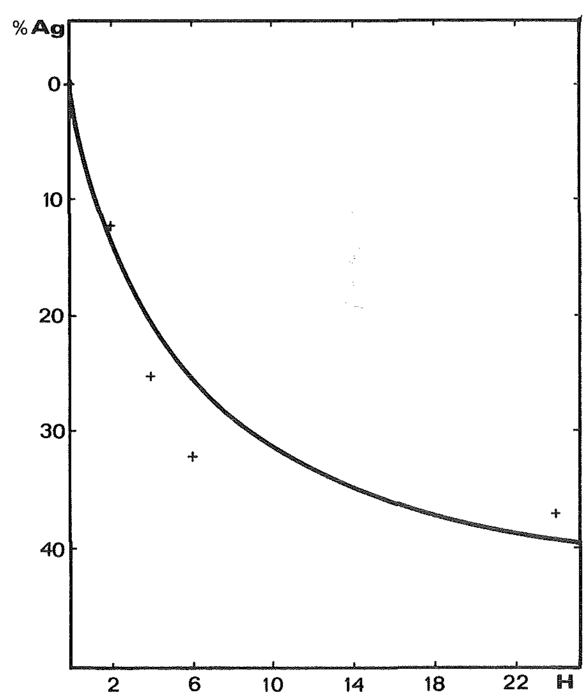

Figure 4. % of silver adsorbed by the walls of a polyethylene bottle (% Ag) versus time in hours (H). Liquid water solution at 10^{-4} ppm.

Table 1 : Automatic sequential collection of 6 rainfall samples,
11 September 1975, Campistrous

	First cell			Second cell		
	Sample n° 5	Sample n° 6	Sample n° 7	Sample n° 8	Sample n° 9	Sample n° 10
Time of sampling						
	from 8.40.54 to 8.57.30	from 8.57.30 to 9.05.30	from 9.05.30 to 9.22.35	from 9.22.35 to 9.25.45	from 9.25.45 to 9.28.30	from 9.28.30 to 9.36.21
Rate of rainfall in mm/h						
	2.2	6.6	1.3	16.3	21.8	3.7
Drop size distributions as % of the total number of raindrops (%N) versus diameter in mm (d)						
Concentration in ppb of the elements analysed by spark source mass spectrometry						
F	2.3	0.9	0.5	0.9	0.9	0.4
Cl	18.1	21.6	12.9	22.1	69	3.3
Br	0.6	0.7	0.5	0.5	0.7	0.04
I	-	0.06	0.03	0.06	0.06	0.03
Li	0.8	0.3	-	3.7	0.36	0.05
Na	91.9	244	132	281	417	53.5
K	670	78.1	487	277	274	132
Ca	250	71.7	179	92	91	43.7
Ba	2.3	26.2	16.4	8.8	2.8	13.4
Ti	0.08	3.5	1.9	3.2	3.2	0.01
Cr	0.07	0.08	0.1	0.06	0.09	0.04
Mn	4.4	2.5	1.6	0.8	2.6	0.38
Fe	20.7	13.1	16.6	10.9	7.8	11.9
Ni	1	0.3	0.25	0.27	0.4	0.06
Cu	7.3	4.2	0.8	1.2	1.3	0.5
Zn	28.2	73.1	29.2	23	34.1	10.4
Pb	-	0.15	0.07	0.13	0.02	-
Al	10.8	12.4	23.2	3	39.1	1.9
Si	23.9	4.2	51.4	19	14.7	7.1
Concentration in ppb of the silver analysed by flameless atomic absorption spectrometry						
Ag	0.015	0.011	0.009	0.006	0.006	0.004

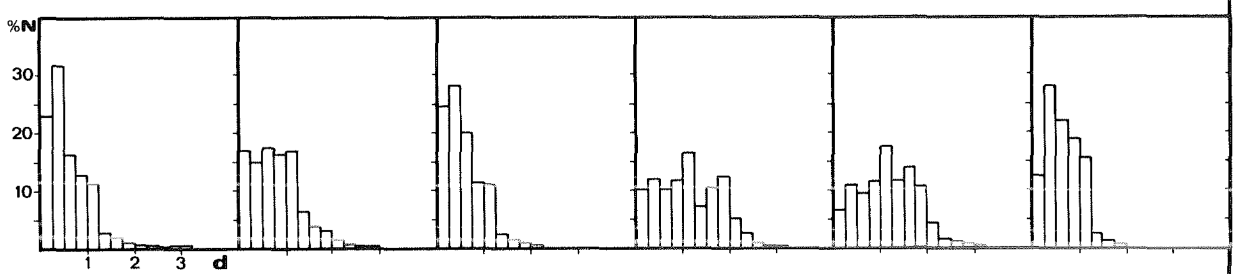

The power requirement for the complete equipment is 220 volts a.c. or 12 volts d.c. (180 watts). The sampler (180 × 110 × 110 cm, 200 kg) can be carried in a small truck.

3. THE ANALYSIS OF SAMPLES

A preliminary study using the sampler was conducted in Lannemezan from July to October 1975 ; the precipitation samples originated in convective clouds. The other equipment used during the study included a 10-cm radar for the survey of the convective cells, a NCAR counter for the measurement of ice nuclei, and a droplet distribution meter (modified Distrometer type Joss). The chemical analyses of the samples were made by spark source mass spectrometry for the elements in general, and by flameless atomic absorption spectrometry for silver (Lacaux, 1972, 1974).

Table 1 gives a summary of the results for the convective rainfalls of 11 September in the morning. The purpose of this paper is only to illustrate the capability of the sampler for chemical analyses, and not to explain the observed relationships between chemical concentrations and rainfall rates. The site is of a rural type, but with three chemical factories 3 km to the south (aluminium, cement and nitrogenized products).

4. ACKNOWLEDGMENTS

This work was supported by the Direction des Recherches et Moyens d'Essais under contract n° 74.018.

5. REFERENCES

Gatz, 1971 : An automatic sequential rain sampler. J. Appl. Meteor., vol. 10, pp 341-344.

Gatz and Dingle, 1971 : Trace substances in rain water : concentration variations during convective rains, and their interpretation. Tellus, 1, pp 14-27.

Lacaux, J.P., 1972 : Dosage de l'argent dans les précipitations par spectrométrie d'absorption atomique sans flamme. J. Rech. Atmosph., vol. 5, pp 329-333.

Lacaux, J.P., 1974 : Contenu en argent des précipitations orageuses dans la région du Languedoc. C. R. Acad. Sc. Paris, t. 278, pp 143-145.

Summers, P.W., 1972 : The silver fallout patterns in precipitation from seeded convective storms. Third National Weather Modification Conference, Rapid City, South Dakota, pp 279-286.

Warburton, J.A., 1973 : The distribution of silver in precipitation from two seeded Alberta hailstorms. J. Appl. Meteor., 12, p. 677.

EFFECTS OF AIRPLANE FLOWFIELDS ON HYDROMETEOR CONCENTRATION MEASUREMENTS

Hillyer G. Norment

Atmospheric Science Associates
P.O. Box 307
Bedford, Massachusetts 01730

1. INTRODUCTION

Hydrometeor concentrations aloft are determined by radar and by airplane-mounted samplers. Radar measurements are strongly biased toward larger particle sizes, and do not discriminate between hydrometeor types. Airplane samples can be used to calibrate the radar measurements, identify hydrometeor types, and fill out the small-particle tails of the size distribution.

There are several difficulties with the airplane sampling techniques. Among these are: restricted spatial and temporal range, small sampling volume, and concentration distortion caused by airflow around the airplane. This paper considers the last of these difficulties.

2. NATURE OF THE PROBLEM

Particle sampling devices of interest here measure particle flux through a small space adjacent to an airplane fuselage. Unless the sampling space is distant enough from the airplane to be in the free-stream, particles of certain sizes will interact with the flow about the fuselage to cause flux distortion. The situation is illustrated in Fig. 1 for 100 μm diameter water drops in airflow about a prolate ellipsoid of fineness ratio 2. Note the impaction on the ellipsoid of the drop closest to the ellipsoid symmetry axis, and note the substantial deflections of the next closest trajectories. Trajectory deflection causes high particle concentrations and high concentration gradients to be observed at a point such as the one marked ⓧ1 in the figure. At point ⓧ2, deflection and impaction combine to produce a region void of particles, a so-called "shadow zone". Smaller drops, with much less inertia, tend to follow the airflow more exactly such that less distortion is observed. Drops large enough to have very high inertia substantially ignore the airflow, and again little distortion is observed. Therefore, distortion is significant over a limited range of particle sizes.

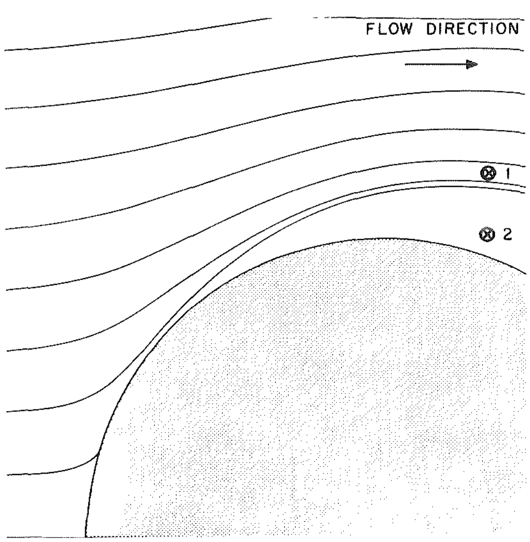

Figure 1. Trajectories of 100 μm diameter water drops in potential airflow about a prolate ellipsoid of fineness ratio 2. (The ordinate scale is expanded by a factor of 2.)

3. CONCENTRATION FACTOR

Principal results of this work are expressed in a quantity called concentration factor. Concentration factor, C_F, is defined as the ratio of particle flux at the sampling or target point, F_t, to the particle flux in the free-stream, F,

$$C_F \equiv \frac{F_t}{F} \quad . \tag{1}$$

The ratio of particle concentration at the target point to free-stream concentration, C_M, is

$$C_M \approx C_F \; V/V_t , \tag{2}$$

where V is free-stream airspeed and V_t is airspeed at the target point. Usually $V/V_t \approx 1$.

Concentration factor is determined by computing particle trajectories from the free-stream (initial plane in Fig. 2) to a small area in the target plane (Fig. 2) that surrounds the target point, such as to define a particle flux tube. Since the particle mass transfer rate through the tube is constant at all cross sections, it is easily shown that

$$C_F \approx \frac{A}{A_t} \quad , \tag{3}$$

where A and A_t are the flux tube cross sectional areas in the free-stream and at the target point. In the limit as A and A_t approach zero, eq. (3) becomes exact.

4. PARTICLE TRAJECTORY CALCULATION

We assume that the bulk air flow is not perturbed by the particles. Moreover, since particle density is large compared to that of air, we can neglect buoyancy and inertial reaction of the fluid to obtain the three-dimensional, normalized equation

$$\frac{d\vec{v}_p}{d\tau} = \frac{1}{F_N}\left\{\frac{1}{v_s}(\vec{v}_a-\vec{v}_p)\frac{B_N R_{N,s}}{B_{N,s}R_N} - \vec{k}\right\} \qquad (4)$$

Non-dimensioned quantities are:

$\vec{v}_p$, $\vec{v}_a$	particle and air velocities
v_s	still-air, terminal settling speed of the particle
$\vec{k}$	unit vector in the z (upward) direction
τ	time
$F_N = V^2/(Lg)$	Froude Number
$R_N = \frac{\rho\delta}{\eta}\left\lvert\vec{v}_a-\vec{v}_p\right\rvert V$	Reynolds Number
$B_N = C_D R_N^{\,2}$	Best Number
C_D	particle drag coefficient

Dimensioned quantities are:

δ	particle dimension
ρ	air density
η	air viscosity
g	gravity acceleration constant
V	free-stream airspeed
L	a characteristic dimension of the fuselage

Here length is normalized by L, velocity by V and time by L/V. $R_{N,s}$ and $B_{N,s}$ are for still air, terminal settling of the particles.

Starting at the initial plane, eq. (4) is integrated with respect to time in three-dimensional space, via the code DVDQ of Krogh (1970). till the target plare is reached. The method used to compute $\vec{v}_a$ at each time step is described next; and drag coefficients are discussed in sec.6.

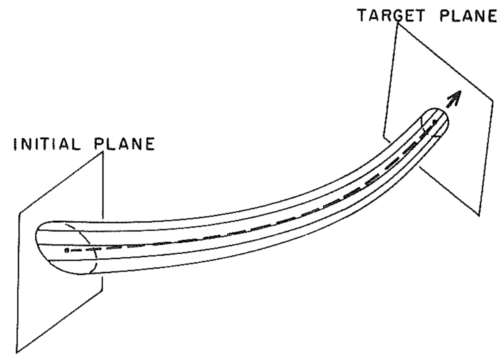

Figure 2. Perspective view of a particle flux tube. The initial plane is in the free-stream. In the target plane the tube cross section is centered at the sampling point.

5. THREE-DIMENSIONAL FLOW CALCULATION

In performing concentration factor calculations for sampling sites on particular airplanes, it is important to use three-dimensional airflow. This is the only way to properly account for: airplane geometry and angle-of-attack, airspeed, altitude, and particle settling.

Cloud physics airplanes are subsonic, sampling runs being made typically between 100-150 kts indicated airspeed (IAS). Particle measurement points are beyond the skin-friction boundary layer, and should be placed to avoid regions of separated flow. Therefore, potential (i.e., frictionless, incompressible, laminar) flow calculations are quite adequate. We use a code developed by Hess and Smith (1962,1967) for calculating potential flow about arbitrary three-dimensional bodies. The Hess-Smith code requires input of a digital description of the fuselage surface. This consists of the coordinates of the corner points of a large number of contiguous, plane, quadrilaterals. An example of the digital description of a fuselage is shown in Fig. 3.

Accuracy of the flow calculations has been checked with excellent results by Hess and Smith (1962) for many bodies for which analytical solutions are available. Norment and Zalosh (1974) have compared computed trajectories around ellipsoids in analytical flow fields with similar trajectories in Hess-Smith flow fields, and they have compared current trajectory results with prior work; agreement is excellent.

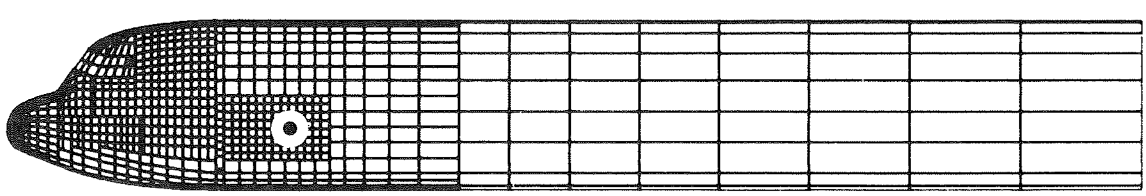

Figure 3. Computer-prepared plot of the digital description of a Lockheed C130E fuselage. The description is provided by 1692 contiguous, plane quadrilaterals. A formvar particle replicator is mounted at the point marked ● (see sec. 7.2).

6. PARTICLE DRAG COEFFICIENT

Davies (1945) shows that still-air terminal settling of spheres can be generalized in terms of the dimensionless numbers $R_{N,s}$ and $B_{N,s}$. Over the range from the smallest spheres, which settle under viscous flow conditions and obey Stokes law, to spheres much larger than of interest here, and for any Newtonian fluid, a reproducible single-valued relationship between $R_{N,s}$ and $B_{N,s}$ exists. Furthermore, $B_{N,s}$ is independent of settling speed, being a function of fluid and sphere properties only; thus for given sphere and fluid, $R_{N,s}$ and hence V_s can be calculated. Polynomials by which $R_{N,s}$ can be computed as a function of $B_{N,s}$ were derived by Davies from a composite of many sets of experimental data.

Since the work of Davies (1945), it has been found repeatedly that this treatment is applicable to particles of other shapes, providing settling is steady and particle orientation is stable.

For the trajectory calculations required here, the problem must be turned around. In addition to gravity settling, there is a particle velocity component (relative to air) caused by the disturbance of the passing airplane. At any time step in the numerical integration of eq. (4), $\vec{v}_a - \vec{v}_p$ (and hence R_N) is known, and B_N must be determined. For viscous motion (i.e., Stokes flow, where $R_N<1$) $B_N = 24\ R_N$ and eq. (4) can be integrated without question. However, for larger R_N the steady-state drag data determined experimentally for terminal settling must be used to compute accelerative particle motion.

Experimental measurements by Keim (1956) and a theoretical analysis by Crowe, et al. (1963) indicate that if the acceleration modulus,

$$A_N = \delta \left| \frac{dV_p}{dt} \right| / V_p^2 \quad ,$$

is smaller than about 10^{-2}, steady-state drag coefficients can be used without significant error to compute accelerative motion. A_N has never been found to exceed 10^{-2} in our trajectory calculations.

For small water drops, which are spherical, the polynomial equations of Davies (1945) are used to compute V_s, while for larger, distorted drops, the equations of Foote and duToit (1969) are used. To compute B_N from R_N, inverse polynomials have been developed, using the data set given by Davies for small drops and Gunn and Kinser (1949) for large drops.

For ice columns, drag data reported by Kajikawa (1971) and Jayaweera and Cottis (1969) for circular cylinders settling with their long axes oriented horizontally were used. Polynomials relating $R_{N,s}$ to $B_{N,s}$ and B_N to R_N were fitted to these data as discussed above. For cylinders, these relations are also functions of the ratio of base diameter to column length. During trajectory calculations we assume that the long axis of a cylinder is oriented perpendicular to the drag vector. Numerous observations confirm that this is the preferred orientation (e.g., see Bragg et al. (1974)). Densities of 700 kg m^{-3} for solid columns and 360 kg m^{-3} for hollow columns were used as reported by Jayaweera and Ryan (1972). Crystal dimensions were computed from the polynomial equations, which relate base diameter to column length, of Auer and Veal (1970).

Though space limitation restricts this discussion to water drops and ice columns, concentration factor calculations have been done for a variety of other ice crystal forms as well.

7. RESULTS

Results for two case studies are briefly described. More details and other studies are presented by Norment and Zalosh (1974) and Norment (1975 a,b).

7.1 Cessna Citation

A Cessna Citation jet (Fig. 4) has been outfitted for cloud physics research. Particle Measuring Systems, Inc (PMS) cloud particle (CPS) and precipitation particle (PPS) spectrometers are mounted on the emergency exit door. The CPS is mounted about 1.5 ft directly above the PPS, fourteen feet aft of the nose, and sampling points of both instruments are 9 inches from the fuselage skin (Fig. 5). Calculations were done for 20 kft altitude at 120 kts IAS (86 m/sec true airspeed)for a 3° angle-of-attack.

Results are shown in Fig. 6. At the PPS, approximately 60% concentration magnification is indicated for drops slightly larger than 100 μm in diameter, with the distortion tapering down gradually as drop diameter increases and decreases. At the CPS a narrow "shadow zone" for drops between ∿ 100-120 μm diameters is indicated. Drops larger and smaller pass through regions of intense concentration magnification (corresponding to point X1 in Fig. 1), and concentration distortion is severe over a wide range of sizes.

The cause of this difference between the two sampling points can be seen in Fig. 7. Drops that are sampled by the PPS, which is mounted at the lower position, must traverse the side of the fuselage nose which tapers aftward gradually. In contrast, particles sampled by the CPS must pass the cockpit window which presents a bluff obstruction to the airstream, and causes greater trajectory deflection at the sampling point.

Results for ice columns are given in Fig. 8. Compared with water drops, concentration factor peaks for ice columns (and other crystal forms as well) are shifted to larger particles and tend to be higher and broader, indicating more severe concentration distortion.

Figure 4. Cessna Citation Executive Jet. Wingspan: 44 ft, overall length: 44 ft, fuselage radius: 2.65 ft. The particle spectrometers are mounted on the emergency exit door, which is directly across the fuselage from the entrance door shown.

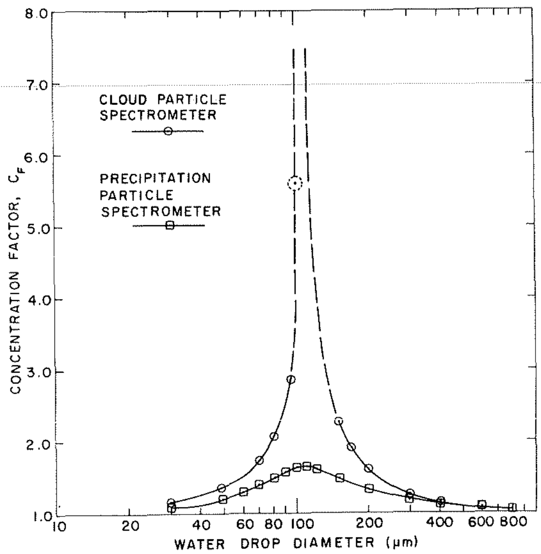

Figure 6. Concentration factor vs. water drop diameter for the PMS particle spectrometers on the Cessna Citation. The point marked ⊙ is hand calculated from a partial result.

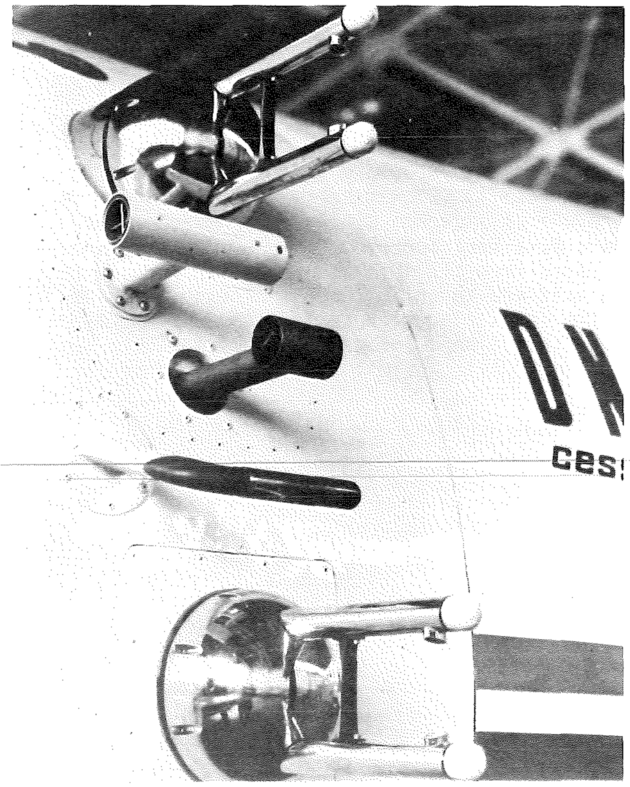

Figure 5. Cloud physics instrumentation on the Cessna Citation. The uppermost and lowermost instruments are the cloud particle and precipitation particle spectrometers, respectively. (Photo courtesy of Meteorology Research, Inc.)

Figure 7. Stereographic plots of flux tubes of 150 μm water drops to the Cessna Citation cloud particle spectrometer (upper, C_F = 2.29) and precipitation particle spectrometer (lower, C_F = 1.48), as viewed from above. Individual trajectories are not resolved.

7.2 Lockheed C130E

The Lockheed C130E is a large propeller driven transport that has been outfitted for cloud physics research by the Air Force Geophysics Laboratory (AFGL). Wingspan is 132 ft, overall length is 95 ft and fuselage radius is about 85 in. Because of competition for space, it was necessary to mount a formvar particle replicator further aft on the fuselage than desirable, in the location shown in Fig. 3.

Calculations were done for 5 kft altitude at 162 kts IAS (91.4 m/sec true airspeed) for a 4° angle of attack. Concentration factor contours as a function of water drop diameter and distance from the fuselage along the replicator arm axis are shown in Fig. 9. The intake slit of the original-design replicator is shown by the dashed line. The calculations indicate that the intake slit would lie in a shadow zone for drops in the diameter range from about 100-300 μm. The nature of the difficulty can be seen in Fig. 10. Defelection and flux distortion are obvious, and these trajectories, which are to a point 10 cm outboard from the intake slit, nearly graze the fuselage. To avoid this problem the replicator arm was lengthened by 8 inches, which places the intake well clear of the shadow zone.

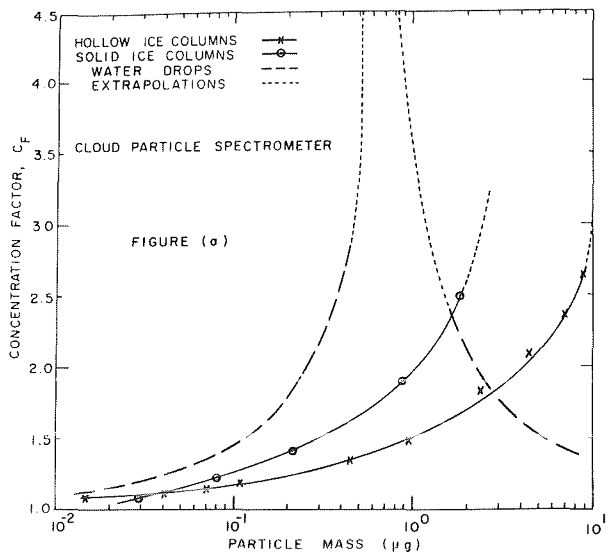

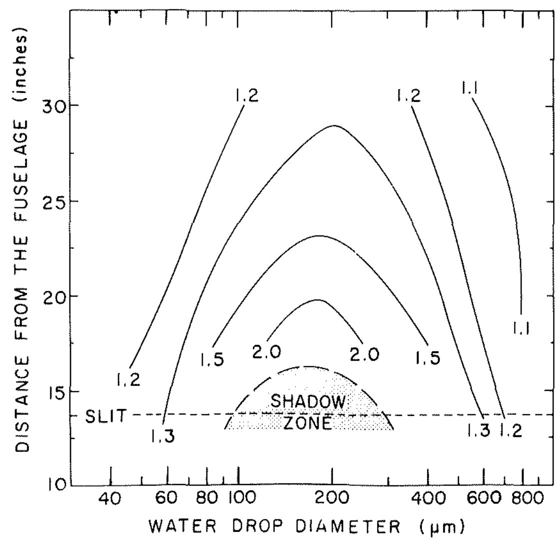

Figure 9. Concentration factor contours as a function of water drop diameter and distance from the fuselage along the formvar replicator arm on the AFGL Lockheed C130E.

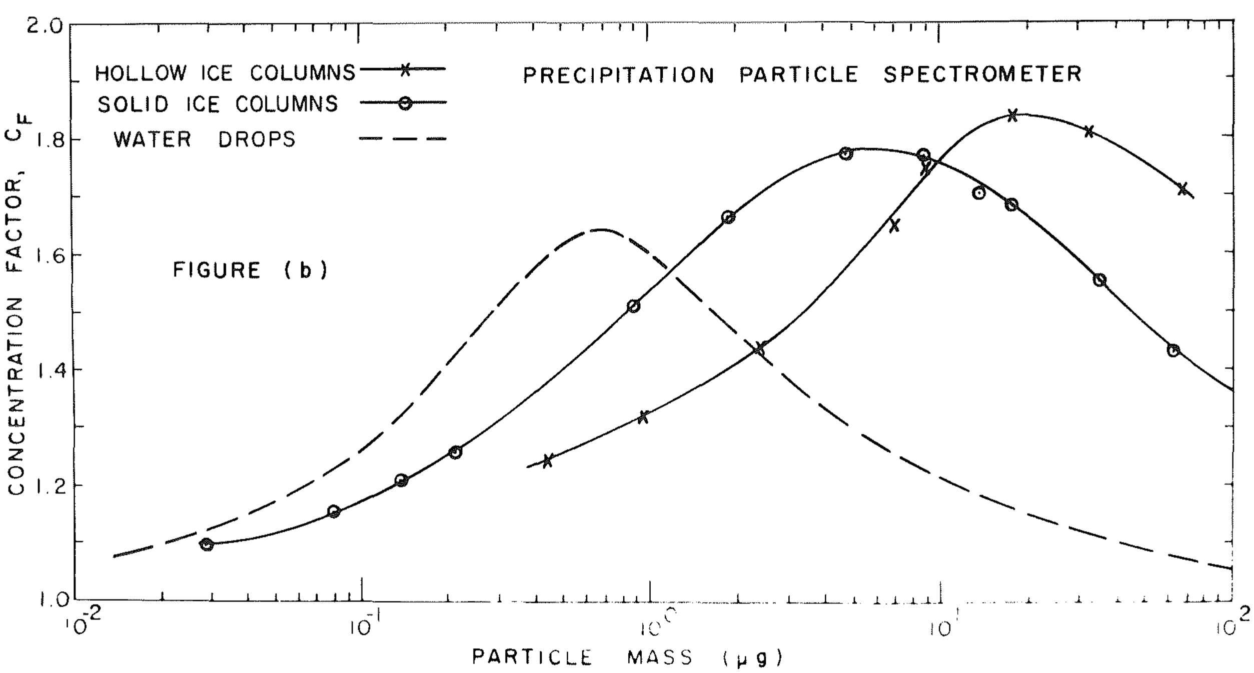

Figure 8. Concentration factor vs. particle mass for solid and hollow ice columns at: (a) the cloud particle spectrometer and (b) the precipitation particle spectrometer on the Cessna Citation.

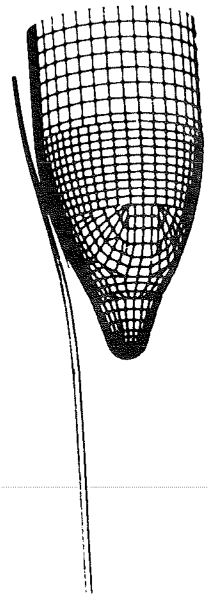

Figure 10. Flux tube of 150 μm diameter water drops to a point 17.7 inches from the Lockheed C130E fuselage along the replicator arm.

8. CONCLUSIONS

A general, three-dimensional computational method is available by which flow-induced concentration distortion of hydrometeors passing fuselage-mounted sampling instruments can be assessed. Results are obtained for particular sampling points on particular airplanes under realistic flight conditions.

Significant concentration distortion has been indicated in all cases studied thus far. In several cases, sampling points are found to be "shaded" for certain ranges of particle sizes such that these particles cannot be sampled by the instruments. In general, locations well aft of the fuselage nose and closer than about 12 inches to the surface can be expected to be shaded against some sizes of some hydrometeor types.

9. ACKNOWLEDGEMENT

This work is supported by the Convective Cloud Physics Branch, Meteorology Division, Air Force Geophysics Laboratory, Hanscom AFB, Bedford, Mass.

10. REFERENCES

Auer, A.H., and D.L. Veal, 1970: The Dimensions of Ice Crystals in Natural Clouds. J. Atmos. Sci., 27, 919-926.

Bragg, G.M., L. van Zuider and C.E. Hermance, 1974: The Free-Fall of Cylinders at Intermediate Reynolds Numbers. Atmos. Environ., 8, 755-764.

Crowe, C.T., J.A. Nicholls and R.B. Morrison, 1963: Drag Coefficients of Inert and Burning Paricles Accelerating in Gas Streams. Ninth Symp. (International) on Combustion, Academic Press, 395-405.

Davies, C.N., 1945: Definitive Equations for the Fluid Resistance of Spheres. Proc. Phys. Soc. (London), 57, 259-270.

Foote, G.B. and P.S. du Toit, 1969: Terminal Velocity of Raindrops Aloft. J. Appl. Meteor., 8, 249-253.

Gunn, R. and G.D. Kinser, 1949: The Terminal Velocity of Fall for Water Droplets in Stagnant Air. J. Meteor., 6, 243-248.

Hess, J.L. and A.M.O. Smith, 1962: Calculation of Non-Lifting Potential Flow About Arbitrary Three-Dimensional Bodies, McDonnel Douglas Report E.S. 40622. AD-282 255.

Hess, J.L. and A.M.O. Smith, 1967: Calculation of Potential Flow About Arbitrary Bodies, Progress in Aeronautical Sciences, Vol. 8, edited by D. Kuchemann, Pergammon Press, New York.

Jayaweera, K.O.L.F. and R.E. Cottis, 1969: Fall Velocities of Plate-Like and Columnar Ice Crystals. Quart. J. Roy. Meteor. Soc., 95, 703-709.

Jayaweera, K.O.L.F. and B.F. Ryan, 1972: Terminal Velocities of Ice Crystals. Quart. J. Roy. Meteor. Soc., 98, 193-197.

Kajikawa, M., 1971: A Model Experimental Study on the Falling Velocity of Ice Crystals. J. Meteor. Soc. Japan, 49, 367-375.

Keim, S.R., 1956: Fluid Resistance to Cylinders in Accelerated Motion. J. Hydraulics Div., Proc. Amer. Soc. Civil Eng., 6, paper 1113.

Krogh, F.T., 1970: Variable Order Integrators for Numerical Solution of Ordinary Differential Equations, Jet Propulsion Lab Technology Utilization Document No. CP-2308.

Norment, H.G. and R.G. Zalosh, 1974: Effects of Airplane Flow Fields On Hydrometeor Concentration Measurements, Mt. Auburn Research Associates, AFCRL-TR-74-0602. AD-A006 690.

Norment, H.G., 1975a: Effects of Airplane Flow Fields on Cloud Water Content Measurements, Mt. Auburn Associates, AFCRL-TR-75-0231. AD- A014 807.

______, 1975b: Effects of Airflow on Sampling of Water Drops by Two Instruments Mounted on the Fuselage of a Lockheed C130B Airplane. Atmospheric Science Associates, final report to Scientific Instrument Group - RFC, NOAA, Miami, Florida.

AUTOMATED ANALYSIS OF CLOUD PARTICLE CAMERA DATA

John LeCompte and Kelvin Danielson
Department of Atmospheric Science
Colorado State University
Fort Collins, Colorado

and

Theodore Cannon
National Center for Atmospheric Research
Boulder, Colorado

1. INTRODUCTION

The concentration, size and shape of cloud particles are data of great importance for the development and verification of numerical and conceptual models of all types of clouds and cloud systems. Extreme interest and effort have culminated in the development of several types of devices to measure cloud particle concentrations, including soot coated slides, impactors, electrostatic disdrometers and optical devices such as the Knollenberg probe and the Cannon in situ cloud particle camera. Advantages of the Cannon camera include the distinguishability of ice particles from cloud water droplets, the possibility of analyzing the data for concentration, size distribution, and shape of the particles, and a sampling volume remote from the aircraft and instrument surfaces. A disadvantage has been that data analysis is not automated and is, therefore, time consuming. An automated analysis system enhancing utilization of the Cannon camera is the focus of this paper.

2. HARDWARE

2.1 The Camera

The Cannon cloud particle camera is flown on the NOAA-NCAR cloud physics research sailplane, Explorer, for the C.S.U. South Park Area Cumulus Experiment, as well as the NHRE study. It is a 35 mm camera with a 135 mm focal length lens focused approximately 34 cm above the top surface of the sailplane canopy and 25 cm below a wing-shaped optical housing which provides a flat-black background toward which the optical axis of the camera is pointed. Illumination is provided by flash lamps located on either side of the lens. The region of space which the camera sees is directly front lighted by the flash lamps; backlighting, necessary because the scattering function of water drops is at a maximum in the forward direction, is provided by corner reflectors mounted on either side of the background, mirroring the light from the flash lamps back through the photographed sample.

In an automatic mode of operation, the camera takes two frames per second with a sampling volume which is particle-size dependent, typically 280 cm^3 for a 1 mm diameter rimed ice particle and 1 liter for rimed ice particles over 5.3 mm diameter at a camera magnification of one-to-one. Cloud water drop images are recorded on 35 mm film as two points of light, both located on a line parallel to the top edge of the frame. The distance separating the two points of light is a function of the diameter of the drop (Cannon, 1970). Ice particle images are two-dimensional images of the illuminated particle. Film recorded images of out-of-focus cloud particles are useful since the actual size and position of the particle is a function of the measured image size and its optical density.

2.2 The Optical Data Digitizer and Display (OD^3)

The OD^3 system located at Colorado State University consists of five basic hardware components: (1) A Spatial Data Systems "Computer Eye" 108 which is a device for digitizing pictures. A digital picture is an array of 8-bit numbers (decimal numbers, 0-255) representing the relative brightness at each X, Y coordinate. There are four parts to the "Computer Eye" 108: (A) A black-and-white vidicon type television camera which scans 512 lines consisting of 480 pixels (picture elements) each. The output of the scanner is an analog signal representing the density or brightness of each pixel as a function of position. A complete scan of the field of view results in an array of 480 by 512 picture elements; (B) A black-and-white television monitor which displays the picture seen by the scanner; (C) A Data Color 401 and color television monitor which receive the analog signal from the scanner and a density range which is specified manually. The analog signal falling within this range is divided into 12 even increments with a color assigned to each increment, resulting in a 12 color contour analysis of the picture; (D) A digitizer which converts the analog signal from each picture element into an 8-bit integer from 0-255 representing the density of the pixel relative to a specified density range. Any portion of the picture may be digitized. (2) A Hewlett-Packard 2100A mini-computer with a 32 K memory and direct memory access; (3) A Hewlett-Packard 79014 disk; (4) A Texas Instruments Silent 700 ASR teletype; (5) A Hewlett-Packard 7970B 7-track Digital Tape Unit which reads and writes at 45 ips and 200, 550, or 800 BPI. The BCD format of this unit is compatible with the CDC 6400 on the C.S.U. campus. Binary formation is different, but software has been written so that tapes created on the H-P 2100A can be read by the CDC 6400 or vice-versa.

2.3 The Film Transport

The film transport with an area for back-lighting the portion of the film which is being viewed by the OD^3, film magazines for film storage, and a constant speed motor to power the film advance, is used to advance the film from one frame to the next. Commands to move and stop the film come from the H-P 2100A mini-computer through an interface board attached to the mini-computer in the form of a three bit integer (0-7, decimal). Each bit of the integer is connected to a relay which in turm controls a grouping of gears. If all bits are at zero logic level, the film is stopped. If one bit, or any combination of bits, is at logic level one, the film is moved forward with the combination of bits at logic level one controlling the speed of the film advance. There are, therefore, seven film speeds forward and a stop.

3. DIGITIZATION ALGORITHM

3.1 Maximization of Range

Camera data is in the form of dark images on a lighter background. The OD^3 interprets film density as a number between 0 and 255, lower numbers representing dark areas and the higher numbers representing light areas. Best resolution of the film density is achieved by setting the 0 value of the OD^3 equal to the darkest area observed on the negatives and the 255 value equal to the lightest area observed. The darkest area on the negatives is a best-focused image. The lightest area on the negatives is the border which separates successive frames. When preparing the system for analysis of data, the light and dark areas described are chosen to define the operating range of the OD^3.

3.2 Standardization of Film Densities

The film density must be an absolute value. Since the OD^3 gives only relative density values, it is necessary to relate OD^3 density values to an absolute scale. The Stouffer scale, a commercially available standardized black-and-white transparency with 21 steps of density, is used to establish the necessary relationship. Two values of the Stouffer scale within the range of densities of interest are measured by the OD^3 and recorded; from this data the absolute density of any value measured by the OD^3 can be calculated.

3.3 Setting a Density Threshold

The sampling volume of the Cannon camera is defined by a film density of six on the Stouffer scale (Cannon, 1974). The OD^3 digital density value which corresponds to the value of six on the Stouffer scale is calculated from data taken in the film density standardization procedure previously described, and is used as a threshold value for deciding which particles are within the sampling volume.

3.3 Setting Resolution

The resolution of the system is dependent on the number of points sampled per frame. If a frame is digitized using one 512 by 480 pixel array then the smallest detectable particle (Cannon camera magnitication of 1/2) would be 140 micrometers in diameter. It is possible to divide a frame into several subunits and digitize each subunit separately with the 480 by 512 pixel array. If the frame is divided into two equal subunits and then is digitized, a particle of 100 micrometer diameter can be detected. This process of subdividing can be used for better resolution until the limit of the film immulsion density is reached. It should be noted that each additional subdivision increases the processing time for the film.

3.5 Digitizing a Frame

A frame of cloud particle camera data is digitized in successive lines from left to right; the density value of each of the 480 picture elements comprising a line is stored sequentially in an array. These numbers are then compared to the threshold value. If a picture element has a density value lower than the threshold, it is considered to contain a cloud particle image or a portion of a cloud particle image within the sample volume of the camera. If the pixel has a value higher than the threshold then it is used to compute an average background. Picture elements of the line which have density values lower than the threshold, and which are adjacent to one another on the line are treated as portions of a single particle image. If a discontinuity exists between picture elements of the line with densities below the threshold, then two or more images are assumed to exist on the line. Each image on the line is assigned a minimum and maximum Y value, each value being a function of the position of the first and last picture elements, respectively, of the image. Thus, digitizing a single line of a frame results in a maximum and minimum Y value for each grouping of densities below the density threshold value.

Maximum and minimum Y values of each image on a line are compared with maximum and minimum Y values of each image on the previous line. If any portion of an image is adjacent, the larger maximum Y value and the lowest minimum Y value of the respective images are stored with the first line on which the image appeared and the last line on which the image appeared. (The X position is a function of the line number of the image.) X and Y image limits are updated as successive lines are digitized. An image is assumed to end when a line has no grouping of densities below the density threshold adjacent to the image on the previous line. The system is programmed so that image integrety is maintained when mergers or separations of images on successive lines of the frame occur.

A set of X and Y limits for each image are obtained from the OD^3 scan of the frame and are used to sepcify areas on the frame which should be redigitized by the OD^3. Since only a portion of the particle may have Stouffer scale values greater than the threshold of six it is necessary to increase the size of the array to assure that the entire particle is digitized. This increase is arbitrarily set at an extra five pixels on each side of the defined array. Rectangular arrays of density values resulting from the redigitization are written on a magnetic tape with corresponding X and Y limits, serving to locate the image within the frame. Frame number, time, date, average background, and other pertinent data are also recorded on the tape for each array. The data can now be analyzed by a larger computer.

3.6 Film Advancement

As the film advances from left to right, a pixel on the middle of the right hand edge of the screen repeatedly digitizes the optical densities of the film passing it, recognizing a series of high numbers as the division between film frames. Density values falling below a preset value signal the driver to stop the film since the right hand edge of a frame has reached the right hand edge of the screen.

4. DATA ANALYSIS

4.1 Distinguishing Ice and Water

Cloud water particles appear as two points of light (dark spots on a film negative) lying on a line parallel to the short dimension of the frame. Therefore, focused cloud water particles will consist of two images on the negative which lie on a line parallel to the top of the frame, separated by a distance proportional to the diameter of the cloud water particle. In order to check all images on a frame using the criteria described above, the center of an image is calculated so that centers can be compared to determine if any two lie on a line parallel to the top of the frame. Sets of images which do are checked for reasonable image shape (circular) and distance of separation. If all tests are passed, the distance separating image centers is calculated. The diameter of the cloud water particle may then be calculated. Out of focus cloud water particles with OD^3 values more dense than Stouffer scale six may appear as a single image on the film with the two density minima (light maxima) parallel to the top of the frame. Film images with distinguishable, properly oriented density minima are considered cloud water particles whose diameters are calculated from the distance between density minima. All images which do not fit into the categoreis described are assumed to be ice particle images.

4.2 Concentrations and Size Distributions

The sampling volume of the Cannon camera is particle size dependent, larger particles having larger sampling volumes (Cannon, 1974). The concentration of particles, therefore, cannot be determined without knowing the size distribution of the sampled particles. The method for calculating cloud water particle diameters has been described. Ice particle size is determined by calculating the major and minor axis for each particle image, the major axis defining the size of the ice particle and the sampling volume associated with the size. The calculation of ice particle size is made by discerning the perimeter of the ice particle through comparison of the particle array with the average background which was calculated when the frame was digitized. Once the perimeter of the particle is determined the distance between all combinations of perimeter points is calculated. The largest distance between any two perimeter points in the array is defined as the major axis. A perpendicular bisector is then constructed, and the distance between the points at which it intersects with the perimeter is calculated and defined as the minor axis.

Several data frames are necessary to obtain a sample large enough to determine a size distribution. The number of particles in a specific size range is assigned the respective size range sampling volume and multiplied by the number of frames of data used, followed by data normalization to yield a size distribution and conentration which is volume dependent.

4.3 Ice Particle Shape

The variety of shapes and orientations which ice crystals may take when photographed makes analysis for shape a difficult procedure. Pattern recognition programs are being studied and developed. An approximation of ice crystal shape currently being used compares the ratio of the major axis to the minor axis of the ice particle images. This method will give a ratio of approximately one for spherical ice particles. The ratio will be largest for needles and columns, and will fall somewhere between these extremes for plates, stellers, dendrites, and similarly shaped ice particles.

4.4 Sample Analysis

Cannon particle camera data taken at a magnification of 1/2 was analyzed by the system described in this paper. Data for 850 frames were analyzed and compared with an observers analysis. Each frame was divided into two subunits which were then digitized. The smallest particle which can be resolved in this analysis is 100 micrometers. Figure 1 shows an ice crystal from one of the frames. Figure 2 shows the digitized output from that crystal. Utilizing digital output similar to that which is displayed in Figure 2, both the concentration and the sizes of particles were calculated. The data analyzed contained no water particles. Neither the automated analysis system or the data analysist observed water particles. The data did have a sufficient number of ice crystals to compare the ability of the two analysis techniques. For ice particles which were definitely in focus the number of particles and the size of the particles observed by the automated system compared very favorably with the observations and measurements of the data analyst. For particles which were slightly out of focus the automated system and the data analysist occasionally disagreed as to whether the particle should be included or excluded from the sampling volume. It is felt that the objective analysis of film density by the automated system is superior to the subjective analysis performed by the data analyst.

Particles which have a velocity through the sampling volume which is not parallel to the direction of mirror rotation result in a dark image with a slightly lighter "streak" adjacent to the particle. In these cases, the automated system assumed that the streak was part of the particle and was included in the size calculation, resulting in too large a particle. Subsequent tests show that by specifying boundary conditions properly, it is possible to eliminate the streak and retain the particle for diameter calculations.

5. CONCLUSIONS

The automated analysis system for Cannon camera data is capable of determining the concentration and size distributions of ice particles. The system appears to have the capability for distinguishing between ice particles and water droplets and for measuring size distributions of water droplets although this capability has not yet been tested. The unit is superior to hand analysis in determining of film density values. The speed of the analysis system is dependent on the desired resolution and the concentration of data on the film. For a single digitization per frame and low concentrations of particles (<2 per frame) the system can analyze data at approximately one frame every 90 seconds. Higher concentrations and better resolution require more time per frame.

6. ACKNOWLEDGEMENTS

This work was partially supported by National Science Foundation Grants ERT 71-01885 and DES 75-17313, and by the state of Colorado.

7. REFERENCES

Cannon, T. W., 1970: A camera for photographing airborne atmospheric particles. Image Technology, April/May.

Cannon, T. W., 1974: A camera for photography of atmospheric particles from aircraft. Review of Scientific Instruments, 45, No. 11 1448-1455.

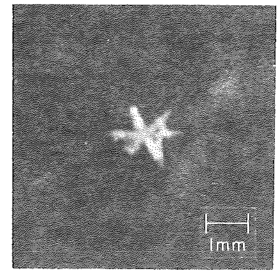

Figure 1. A print of an ice crystal photographed in cloud by the Cannon cloud particle camera.

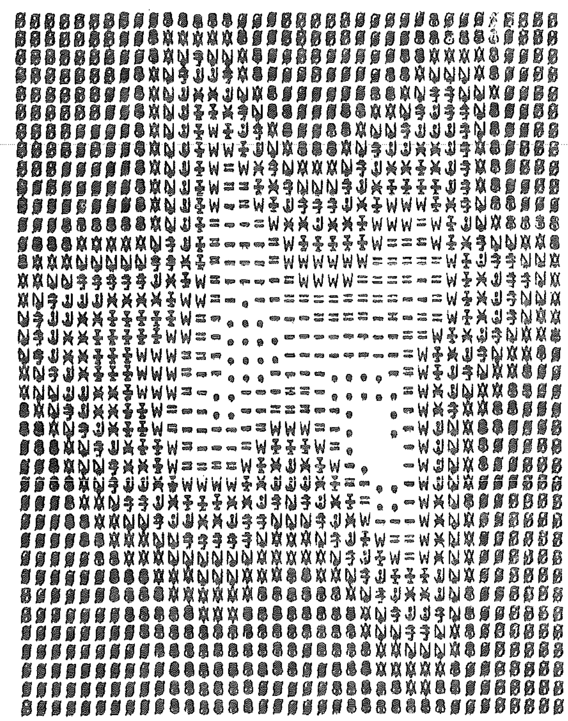

Figure 1a. A character shading print out of the ice crystal in Figure 1.

172	169	166	168	169	170	171	171	168	161	150	140	126	121	122	126	135	143	152	157	161	165	170	173	173	175	174	174	174	175	176	176	176	176
169	162	159	159	159	161	163	164	162	157	147	134	121	113	114	118	126	137	146	152	158	162	166	169	169	171	172	173	173	173	174	175	176	175
168	159	148	146	148	149	153	154	152	149	138	125	113	104	103	107	114	125	137	146	151	158	161	164	166	167	169	169	169	169	168	169	171	171
168	159	146	134	133	133	137	138	138	133	124	112	99	91	88	94	104	115	127	136	145	151	155	157	159	160	161	160	160	159	160	162	164	165
169	159	148	133	119	118	120	121	119	115	104	92	83	76	74	80	91	102	115	125	135	141	144	146	146	147	146	144	145	146	149	149	154	156
170	161	149	133	118	108	107	104	99	94	85	75	67	61	62	67	77	91	103	109	119	123	125	127	125	124	124	123	125	127	129	133	141	143
171	163	153	137	120	107	95	88	83	78	69	62	57	52	53	55	66	75	84	93	97	99	101	101	99	95	95	94	97	101	107	116	124	132
171	164	154	138	121	104	88	82	76	66	60	54	51	47	46	49	55	63	65	71	70	71	69	69	65	63	61	66	71	81	90	104	116	127
166	162	152	138	119	99	83	76	75	67	61	55	51	49	47	46	49	49	49	49	47	42	41	36	39	38	41	51	60	75	90	105	118	129
161	157	149	137	115	94	78	66	67	73	65	60	55	52	49	49	46	44	39	34	31	26	24	24	27	31	41	52	68	84	100	113	126	136
150	147	138	124	104	85	69	60	61	65	72	66	59	55	51	48	43	37	31	28	22	19	17	20	25	35	47	65	83	96	111	124	134	141
145	134	125	112	92	75	62	54	55	60	66	74	65	60	55	49	44	37	33	26	22	18	24	30	37	51	66	85	99	115	126	137	145	150
126	121	113	99	83	67	57	51	51	55	59	65	69	61	57	51	44	41	31	31	28	31	36	46	59	74	89	104	117	129	140	147	151	155
121	113	104	91	76	61	52	47	49	52	55	60	61	63	56	52	46	39	35	34	37	41	53	67	79	93	107	118	129	139	147	153	156	158
122	114	103	88	74	62	53	46	47	49	51	55	57	56	57	52	46	39	41	42	48	57	69	83	97	109	120	130	140	145	150	153	157	158
126	118	107	94	80	67	55	49	46	49	48	49	51	52	52	48	44	42	44	49	58	68	81	95	108	119	130	137	141	149	153	156	158	159
135	126	114	104	91	77	66	55	49	46	43	44	44	46	46	44	41	40	44	51	59	70	83	98	109	122	131	138	143	147	152	154	156	157
143	137	125	115	102	91	75	63	49	44	37	37	41	39	39	42	40	36	43	47	54	63	78	91	104	116	126	136	142	146	149	153	156	156
152	146	137	127	115	103	84	65	49	39	31	33	31	35	41	44	44	43	36	42	46	54	66	79	95	105	118	131	138	144	148	152	154	155
157	152	146	136	125	109	93	71	49	34	28	26	31	34	42	49	51	47	42	37	37	45	55	66	81	95	111	121	130	139	143	148	152	154
161	158	151	145	135	119	97	70	47	31	22	22	28	37	48	58	59	54	46	37	34	37	45	56	68	86	100	116	125	133	140	146	149	151
165	162	158	151	141	123	99	71	42	26	19	18	31	41	57	68	70	63	54	45	37	37	42	51	63	80	96	112	123	133	139	144	148	151
170	166	161	155	144	125	101	69	41	24	17	24	36	53	69	81	83	78	66	55	45	42	44	51	65	80	95	111	123	133	140	144	149	151
173	169	164	157	146	127	101	69	38	24	20	30	46	67	83	95	98	91	79	66	56	51	51	58	71	81	98	114	127	137	142	147	150	153
173	169	166	159	146	125	99	65	39	27	25	37	59	79	97	108	109	104	95	81	68	63	65	71	78	92	108	122	131	140	146	149	152	154
175	171	167	160	147	124	95	63	38	31	35	51	74	93	109	119	122	116	105	95	86	80	80	81	92	106	116	128	136	144	149	153	157	158
174	172	169	161	146	124	95	61	41	41	47	66	89	107	120	130	131	126	118	111	100	96	95	98	108	116	122	135	142	147	151	156	158	159
174	173	169	160	144	123	94	66	51	52	65	85	104	118	130	137	138	136	131	121	116	112	111	114	122	128	135	138	145	151	155	158	160	160
174	173	169	160	145	125	97	71	60	68	83	99	117	129	140	141	143	142	138	130	125	123	123	127	131	136	142	145	151	154	158	159	161	161
175	173	169	159	146	127	101	81	75	84	98	115	129	139	145	149	147	146	144	139	133	133	133	137	140	144	147	151	154	159	160	163	164	163
176	174	168	160	149	129	107	90	90	100	111	126	140	147	150	153	152	149	148	143	140	139	140	142	146	149	151	155	158	160	164	164	165	166
176	175	169	162	149	133	116	104	105	113	124	137	147	153	153	156	154	153	152	148	146	144	144	147	149	153	156	158	159	163	166	167	168	168
176	176	171	164	154	141	124	116	118	126	134	145	151	156	157	158	156	156	154	152	149	148	149	150	152	157	158	160	161	164	165	168	168	169

Figure 2. Digitized data array print out of the ice crystal in Figure 1.

7.2.1

SUPERSATURATION REGIME WITHIN A SETTLING CLOUD CHAMBER: PRELIMINARY RESULTS

Klaus M. Weickmann
Wm. Richard Barchet

University of Wisconsin
Madison, Wisconsin

1. INTRODUCTION

The settling cloud chamber (SCC) is one of a variety of instruments being used to measure ice nucleus concentrations. First developed by Ohtake and Isaha (1961) the SCC has been tested extensively during several international workshops convened to evaluate ice nuclei measurements. One advantage often cited for the SCC is the close simulation of natural cloud conditions provided in the lower portions of the chamber (Bigg, 1971). For a discussion of other advantages and disadvantages as well as recent suggestions for improved operation see Ohtake (1971, 1976).

Actual conditions relevant for the activation of ice nuclei, e.g. saturation ratio (S), liquid water content (LWC), and droplet spectrum and concentration, within the SCC and other instruments used for ice nuclei measurements are usually only described qualitatively; how these parameters differ from device to device is not known. Conclusions from two recent ice nuclei workshops (Bigg, 1971; Vali, 1975; Jiusto and Lavoie, 1975) suggest that the discrepancies between different devices may, in particular, be a result of differences in S achieved - yet few quantitative estimates (Lala and Jiusto, 1972) of S within the instruments are available.

The purpose of this research is to study the initial cloud development process within the SCC with a time dependent, 1-D numerical model and thereby determine the growth environment provided for ice nuclei measurements.

2. THE SETTLING CLOUD CHAMBER

In principle this cloud chamber is a combination of a thermal gradient diffusion chamber in which cloud droplets are formed and a subfreezing, isothermal chamber in which ice nucleation by nearly all mechanisms can occur. The bottom two thirds of the chamber is kept isothermal by a circulating coolant. A strong stable gradient of temperature and moisture is produced above the isothermal layer by a heated, moist top. Prior to the formation of the cloud, the chamber is relatively dry; however after the heated moist top is in place downward diffusion of vapor and heat rapidly supersaturates the upper portion of the chamber. Condensation nuclei in this region absorb water, become haze drops, grow beyond their critical size, and continue growth as cloud droplets. The drops settle at their terminal speed into the cold isothermal portion of the chamber. Evaporation of these droplets in this part of the chamber brings the humidity quickly to satuartion. In a quasi-steady state, downward heat diffusion is balanced by a wall heat sink while downward diffusion of vapor is countered by conversion to cloud water.

3. DESCRIPTION OF MODEL

The physical processes occurring in the SCC are simulated with a 1-D, time dependent numerical model with detailed microphysics of the condensation process; ice nucleation is not modelled. Vertical diffusion of heat and moisture are included in the model, however the heat sink at the walls for the results presented here has been neglected. The initial (pre-cloud) temperature distribution is based on actual measurement in the SCC, while the initial vapor density distribution is assumed to be vertically uniform. Boundary conditions for temperature and vapor density are 42°C and 56.6 gm m^{-3}, respectively, at chamber top and -15.5°C and 1.3 gm m^{-3} at chamber bottom, 30 cm below the top.

The initial condensation nucleus (CN) spectrum, assumed to be pure spherical NaCℓ particles, is discretized into 45 bins which vary logarithmically from 1.67×10^{-20}gm (0.001 µm) to 2.4×10^{-10}gm (3 µm) corresponding to critical saturation ratios (S*) from 1.30 to 1.000001. The number density function (following notation used by Berry, 1970) for the Aitken nuclei (r_s<.03 µm) is given by

$$f\langle r_s\rangle = 2.07 \times 10^8 r_s^{-0.3}$$

or

$$f\langle m_s\rangle = 4.13 \times 10^7 m_s^{-0.767}$$

for particle radius (r_s) in cm and particle mass (m_s) in grams, while nuclei with r_s>.03 µm are assumed to follow a Junge distribution

$$f\langle r_s\rangle = 2.42 \times 10^{-12} r_s^{-3.85}$$

or

$$f\langle m_s\rangle = 6.55 \times 10^{-12} m_s^{-1.95}$$

Initial nuclei number (N) and mass (M) within a bin are obtained by integration over the appropriate bin limits: $N = \int f\langle m_s\rangle dm$ and $M = \int m f\langle m_s\rangle dm$.

Droplets are the only hydrometeors resolved in the model. Howell (1949), Mordy (1959), and Nieburger and Chien (1960) performed a Lagrangian calculation of condensation on an initially discretized CN distribution. In this case, the droplets are allowed to exist at the actual radius calculated after each time step; the number in a given CN interval remains constant.

Alternatively the basis for the condensation calculation can be Eulerian, in which case the size intervals are fixed for all time. This often becomes a necessity as more physical processes, such as nucleation, sedimentation, and collision-coalescence, are considered. The problem now becomes one of transforming the results of an inherently Lagrangian condensation calculation to an Eulerian form after each time step. Various schemes, including, among others, interpolation (Arnason & Greenfield, 1972, and Kovetz & Olund, 1969), moment conservation (Eagan & Mahoney, 1972; Berry & Rheinhardt, 1973), and finite differentiation (Clark, 1973), have been used to achieve this transformation. Droplet growth in the model is treated in an Eulerian framework with 45 logarithmically spaced radius bins ranging from .004 μm to 18 μm.

The vertical transfer of hydrometeors by sedimentation is an important part of the model. The vertical resolution is 1 cm and hydrometeors can fall into any of the lower model layers. Stokes' law is used for computing terminal velocities.

4. MODEL PROCESSES & EQUATIONS

The initial CN are assumed to be uniformly distributed throughout the chamber. Dry CN are transferred to the appropriate cloud drop bin when S exceeds S* within a layer. Nuclei less than 3.0×10^{-15} gm are transferred at their critical radii while larger nuclei are transferred to bins at less than their critical radius because their growth lags the supersaturation (Arnason & Greenfield, 1972). Results from a more complete microphysics model are used to assign the lags.

The growth of droplets by condensation in each layer is computed from

$$\frac{dm}{dt} = 4\pi\, r\, D(\bar{\rho}_\infty - \rho_d) \qquad (1)$$

where r is the drop radius, D is the mass diffusivity, $\bar{\rho}_\infty$ is the mean environmental vapor density and ρ_d is the equilibrium vapor density over the drop. In order to use (1) the drop temperature must be computed explicitly. This is accomplished through use of the following equation:

$$\frac{(\bar{T}_\infty - T_d)}{B^2} = \left(B + \frac{A}{S_d}\right) - \left[\left(B + \frac{A}{S_d}\right)^2 - 2\,\frac{(S_d - S)B^2}{S_d}\right]^{\frac{1}{2}} \qquad (2)$$

$$\text{where} \quad B = R_v \frac{L}{\bar{T}_\infty^2}, \quad A = \frac{k}{DL\rho_s(\bar{T}_\infty)},$$

and, for a dilute solution drop,

$$S_d = e^{\frac{2\sigma}{R_v T \rho r}} .$$

The symbols used in (2) are:

- L - latent heat of vaporization
- R_v - gas constant for water vapor
- $\bar{T}_\infty$ - mean environmental temperature
- k - thermal conductivity
- $\rho_v(\bar{T}_\infty)$ - saturation vapor pressure at $\bar{T}_\infty$
- σ - surface tension of drop
- ρ - density of drop
- S_d - saturation ratio over the hydrometer
- S - mean saturation ratio in the environment

(2) is derived by i) assuming heat storage to be zero in the droplet energy balance, ii) integrating the Clausius-Clapeyron equation with an invariant latent heat, iii) approximating the exponential by a series truncated after the quadratic term, and iv) assuming $\bar{T}_\infty T_d \sim \bar{T}_\infty^2$.

The continuity equations of water vapor and heat within the chamber are given by

$$\frac{\partial \rho_\infty}{\partial t} = \frac{\partial}{\partial z}\left(D\,\frac{\partial \rho_\infty}{\partial z}\right) - \left(\frac{DQ_w}{Dt}\right)_{DROPS} - \left(\frac{DQ_w}{Dt}\right)_{NUC} \qquad (3)$$

$$\frac{\partial T_\infty}{\partial t} = \frac{\partial}{\partial z}\left(K\frac{\partial T_\infty}{\partial z}\right) + \frac{L}{c_p \rho_a}\left(\left(\frac{DQ_w}{Dt}\right)_{DROPS} + \left(\frac{DQ_w}{Dt}\right)_{NUC}\right) \qquad (4)$$

where K is the thermal diffusivity, c_p the specific heat capacity of the air at constant pressure, ρ_a the density of air and

$$\left(\frac{DQ_w}{Dt}\right)_{DROPS} = \sum_{z=1}^{45} N_i \frac{dm_i}{dt} . \qquad (5)$$

N_i is the number of hydrometeors present in the i^{th} drop bin. The term $(DQ_w/Dt)_{NUC}$ is the water mass used to activate dry nuclei to drops.

The local variation of droplet number density can be expressed as

$$\frac{\partial f\langle r\rangle}{\partial t} = -\, v_T \frac{\partial}{\partial z}(f\langle r\rangle) - \frac{\partial}{\partial r}\left(\frac{dr}{dt} f\langle r\rangle\right) + \left(\frac{\delta f\langle r\rangle}{\delta t}\right)_{NUC} \qquad (6)$$

where v_T is the terminal velocity and f<r> is the number density function ($cm^{-3}\Delta r^{-1}$) such that $N_i = \int_{r_1}^{r_2} f\langle r\rangle dr$. The terms on the r.h.s. of (6) represent the change in number density function due to sedimentation, condensation, and nucleation, respectively.

5. NUMERICAL PROCEDURE

The system of equations described in the previous section is essentially a subset of the equations that describe the micro- and macrophysics of the warm rain process. The degree of complexity of these equations has ranged from those describing initial droplet development in closed air parcels, to 1-D numerical simulations of warm rain with very detailed microphysics, to 2-D simulations with some parameterization of the microphysics. The solution to these different models has been approached in slightly different ways by their respective authors. In the present model, techniques developed by Young (1974) are used to solve (3), (4), and (6). The reason for using Young's continuous bin approach to solve (6) is that the results are felt to be more accurate than interpolation schemes or finite difference approaches. Additionally Dr. Young made his model available to the authors and with some modification it was adaptable to the present investigation.

The time derivatives in (1), (3), and (4) are approximated by a simple forward in time finite difference scheme while the spatial derivatives in (3) and (4) are approximated by centered differences. The stability criteria for the diffusional component is $\Delta t < \frac{(\Delta z)^2}{2D} = 1.8$ sec for the choice of $\Delta z = 1$ cm; a $\Delta t = 1$ sec is used here.

6. PRELIMINARY RESULTS

Two experiments are shown in which the initial CN spectra differ; Run A has mostly Aitken nuclei, i.e. $S^* > 1.01$; while Run B has only nuclei with $S^* \leq 1.01$ in a Junge size distribution. Computations extend to 1 1/2 minutes, at which time most of the chamber is saturated for each run.

The primary microphysical data reported here include the saturation ratio, liquid water content, and total droplet concentration. These are presented as time-height cross sections for each parameter; saturation ratio in Fig. 1, liquid water content in Fig. 2, and droplet concentration in Fig. 3. Temperature profile evolution and hydrometeor number density are also determined and will be discussed later.

7. DISCUSSION

Runs A and B appear very similar; a supersaturated region (Fig. 1) quickly develops just beneath the warm moist chamber top while a deep region very near to 100% relative humidity quickly penetrates to the chamber floor. Similar temporal trends are seen in the liquid water (Fig. 2) and drop concentration (Fig. 3). The general trends confirm Ohtake's (1971, 1976) observation that the chamber quickly fills with cloud and rapidly reaches water saturation in the isothermal lower portion of the chamber.

It is in the details that the differences in the two Runs become apparent. The model Runs essentially simulate two extreme conditions: mostly Aitken nuclei and no Aitken nuclei. The first could arise if the air in the chamber is filtered as it enters the chamber; only Aitken nuclei are likely to survive a filtration. The latter case may be approximated by relatively "clean" air which has larger particles but a decidedly reduced Aitken population.

Of special interest is the pulsating structure of all three parameters seen in both Runs. This pulsation appears as sloping bands of alternating high and low saturation ratio, liquid water content, and droplet concentration in Figs. 1, 2 and 3. The amplitude of the pulsation in all parameters is higher in Run A where only Aitken nuclei are available. Pulsations arise as S exceeds S* within a nucleus bin. At the start of a time step the large S causes a great increase in the number of actively growing drops in the layer. The abundant newly-nucleated drops then rapidly grow, depleting the vapor supply, and depressing the S which yields mass and heat balance at the end of later time steps. Sedimentation as these drops grow removes the vapor sink from the layer allowing S to rise until it again exceeds S* for the nuclei that remain in the layer. Pulsations of LWC and drop concentration are out of phase with supersaturation. This is consistent with the growth and sedimentation of drops after a peak in supersaturation occurs.

In Run B with nuclei that have lower S*'s the initial activation of nuclei is rapid. As the resulting drops grow and settle out of the upper portion of the chamber, the supersaturation is governed by heat and moisture diffusion; nucleation ceases to play a role.

The rapid initial growth afforded droplets in Run A by virtue of the high supersaturation also causes the downward penetration of liquid water and drops to be faster than for Run B. Humidification of the lower portion of the chamber in the time period shown depends on the evaporation of drops settling to the bottom.

As nuclei are activated and the drops settle into the chamber a gradual subsidence of the "cloud top" is evident in Figs. 2 and 3. The rate of sinking of this top is less with the Aitken nucleus run since nuclei with high S*'s are available in the upper layers to later times.

The number density function for both runs shows a peak in the vicinity of 5-7 μm radius with slightly more larger drops after 1 1/2 minutes in Run A. This result agrees well with the measurements of drop size made within an SCC by Ohtake (1971).

Perhaps of primary interest is the uniform distribution of relative humidity in the lower model layers, suggesting a good ice nucleation environment as mentioned by Ohtake (1976). The distribution of LWC, however, is quite unsteady in the model, oscillating with S in the upper model levels. The extent to which pulses in LWC and S actually occur in the chamber is difficult to assess. Certainly the discrete numerical approximation to continuous processes must have an impact on these results.

The temperature measurements made in the chamber after cloud formation do not agree with model results, probably due to the exclusion of the wall heat sink. This effect will be parameterized in future runs to assess its impact on the results presented here.

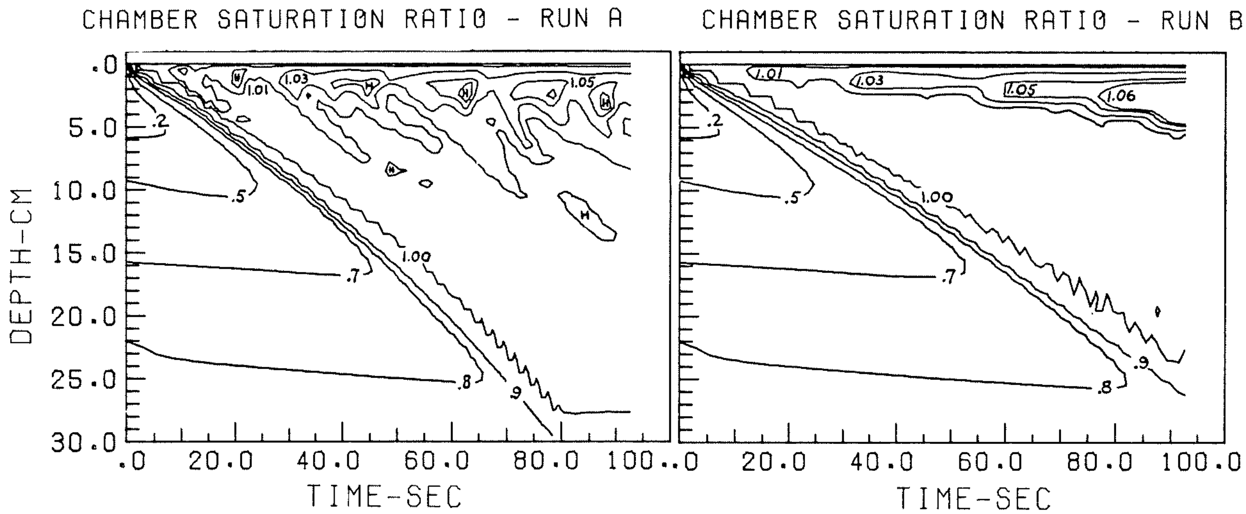

Figure 1. Time-height cross section of model saturation ratio. Contour intervals are: 0.2, 0.5, 0.7, 0.8, 0.9, 1.0, 1.01, 1.03, 1.05 and 1.06.

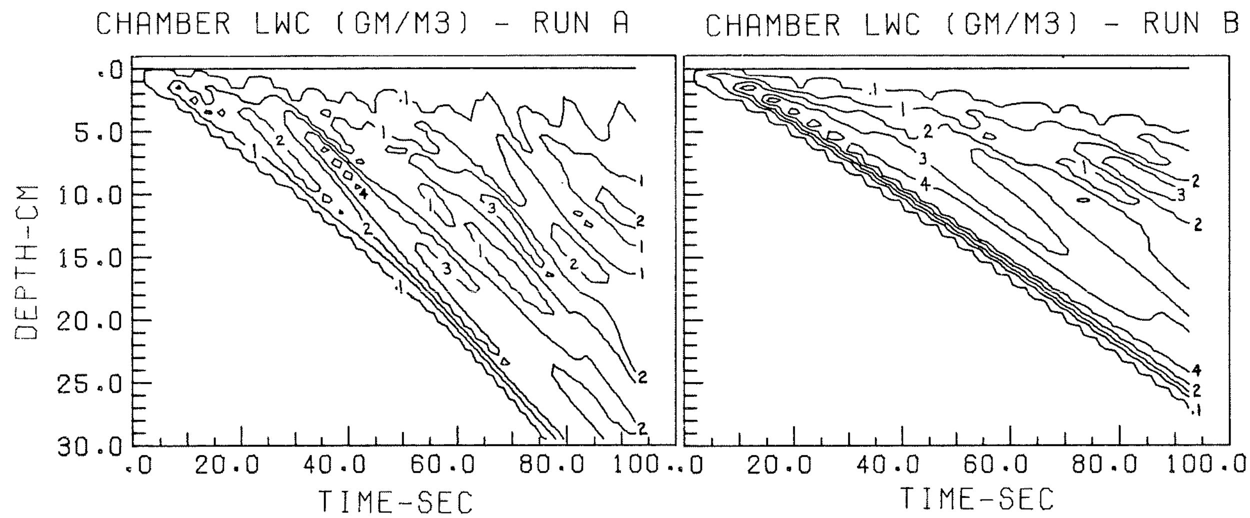

Figure 2. Time-height cross section of model liquid water content. Contour intervals are: 0.0, 0.1, 1.0, 2.0, 3.0 and 4.0.

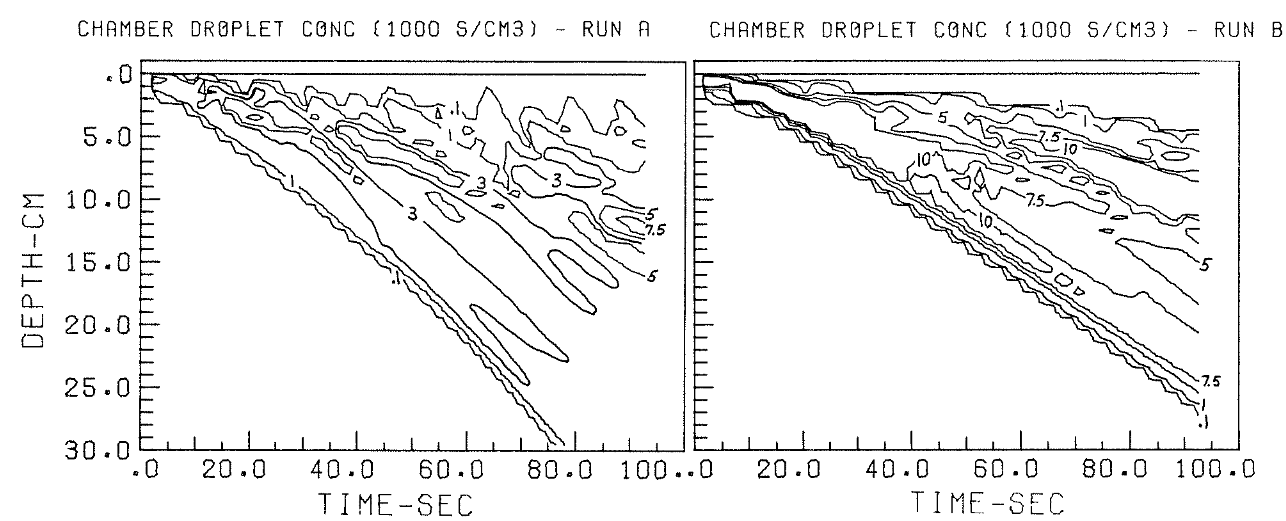

Figure 3. Time-height cross section of model droplet concentration. Contour intervals in 1000's of drops/cm³ are: 0.0, 0.5, 1.0, 5.0, 7.5 and 10.0.

The extent to which actual conditions within the SCC can be inferred from the results must await further experimentation with, and refinements of, the numerical model. However, the model does confirm 1) the importance of sedimentation and evaporation in moistening the lower isothermal region, 2) the uniformly saturated (with respect to water) conditions present in this region, and 3) the importance of the condensation nucleus distribution in determining the evolution and magnitude of the supersaturation in the upper, active portions of the chamber.

In future research the effect of parameterizing nucleation will be investigated by resolving the nucleation into two stages, formation of haze from dry nuclei and growth of haze beyond their critical size. Preliminary results suggest some differences, however the large amount of CPU time used by the more detailed version caused us to restrict runs with it to less than 50 sec.

8. REFERENCES

Árnason, G., and R.S. Greenfield, 1972: Micro- and macro-structures of numerically simulated convective clouds. J. Atmos. Sciences, 29, 342-367.

Berry, E.X., 1967: Cloud droplet growth by collection. J. Atmos. Sciences, 24, 688-701.

_____, and R.L. Rheinhardt, 1973: Modeling of condensation and collection within clouds. Final Report NSF Grant GA-21350, 96 pp.

Bigg, E.K., 1971: Report on the ice nucleus workshop, Fort Collins, August 1970. The Second International Workshop on Condensation and Ice Nuclei, L.O. Grant, Ed., 97-105.

Clark, T.L., 1973: Numerical Modeling of the dynamics and microphysics of warm cumulus convection. J. Atmos. Sciences, 30, 857-878.

Eagan, B.A., and J.R. Mahoney, 1972: Numerical modeling of advection and diffusion of urban area source pollutants. J. Appl. Meteor., 11, 312-321.

Howell, W.E., 1949: The growth of cloud droplets in uniformly cooled air. J. Meteor., 6, 134-149.

Jiusto, J.E., and R.L. Lavoie, 1975: AMS Symposium on the prediction and measurements of ice crystal concentrations in clouds, Laramie, Wyoming, June 1975. Bull. Amer. Meteor. Soc., 56, 1175-1179.

Kovetz, A., and B. Olund, 1969: The effect of coalescence and condensation on rain formation in a cloud of finite vertical extent. J. Atmos. Sciences, 26, 1060-1065.

Lala, G.G., and J.E. Jiusto, 1972: Numerical estimates of humidity in a membrane-filter ice nucleus chamber. J. Appl. Meteor., 11, 674-683.

Mordy, W., 1959: Computations of the growth by condensation of a population of cloud droplets. Tellus, 11, 16-43.

Neiburger, M., and C.W. Chien, 1960: Computations of the growth of cloud drops by condensation using an electronic digital computer. Physics of Precipitation, Washington, D.C., Amer. Geophys. Union, 191-210.

Ohtake, T., 1971: Cloud settling chamber for ice nuclei count. The Second International Workshop on Condensation and Ice Nuclei, L.O. Grant, Ed., 58-60.

_____, 1976: Settling cloud chamber for ice nucleus counting (to be published).

_____, and H. Isaka, 1961: Measurement of effective ice nuclei for weather modification, report on artivicial stimulation of rain, 16, 53-78, May 1961, Tohoken Electric Power Company.

Vali, G., 1975: Ice nucleation workshop, 1975, Laramie, Wyoming, May-June 1975. Bull. Amer. Meteor. Soc., 56, 1180-1184.

Young, K.C., 1974: A numerical simulation of winter time, orographic precipitation: Part I. Description of model microphysics and numerical techniques. J. Atmos. Sciences, 31, 1735-1748.

9. ACKNOWLEDGMENTS

This study was supported by National Science Foundation grants AEN75-03258 and ESR72-03349 (formerly GI-31058).

FIELD APPLICATIONS OF A NEW CLOUD CONDENSATION NUCLEUS SPECTROMETER: INVESTIGATIONS OF CONTINENTAL AND MARITIME AEROSOLS

V. K. Saxena and N. Fukuta
Denver Research Institute, University of Denver
Denver, Colorado 80210

1. INTRODUCTION

Since the introduction of a cloud condensation nucleus (CCN) spectrometer by Fukuta and Saxena (1973), its usefulness has been undisputedly proven both in the laboratory and field studies (Fukuta et al, 1974; Fukuta and Saxena, 1975). Other single supersaturation CCN counters employing a continuous flow thermal diffusion chamber have also become available recently (Hudson and Squires, 1973; Sinnarwalla and Alofs, 1973). Though these counters incorporate some improvements over the previous devices, their usefulness in obtaining the entire activity spectrum of the CCN is limited inasmuch as discrete supersaturations are produced in the chamber at different points in time or a number of chambers are employed at a given point in time in order to obtain the entire activity spectrum. Our CCN Spectrometer, however, simulates the entire range of fog and cloud supersaturations within a single chamber and measures, as well as displays, the entire CCN spectrum in real time with a frequency of 15 sec. These features have rendered it ideally suited for airborne measurements (Veal et al, 1975).

For including the microphysical interactions in cloud and fog models, a knowledge of the CCN spectrum is imperative. The single supersaturation measurements do not produce the required information (Braham, 1974a). Continuous operation and data display by our spectrometer also enable us to track an urban plume, to study the CCN production mechanisms in situ, and to study a number of other phenomena involving CCN as they happen under natural conditions. This helps eliminate doubts regarding the validity of the test sample as repeated checks can be made on the features exhibited by the CCN spectrum in real time. This paper contains the results of field and laboratory studies that demonstrate the importance of real-time CCN spectrum measurements by bringing to light the new information acquired with the help of our spectrometer. The spectrometer was also compared with a conventional Twomey-type chamber and a reasonable agreement was obtained under the available experimental conditions. The counting technique of the spectrometer was cross-checked by using the direct photography of droplets that resulted in a very gratifying agreement, thus enhancing our confidence in the spectrometer performance. These results are also reported here.

2. APPARATUS IMPROVEMENTS

The principle of operation of the spectrometer and its prototype design has been previously reported (Fukuta et al, 1974). The present version of the spectrometer is superior to the prototype one inasmuch as it is more compact, portable, and capable of longer operation without manual attendance. Three modifications were made in the prototype design. First, the main chamber now consists of two parallel 22.9 cm (breadth) x 83.8 cm (length) x 0.64 cm (thickness) copper plates. The plates are separated by two side walls, each 1.9 cm high. One wall is made out of a metal, such as brass or stainless steel depending upon the magnitude of the lowest supersaturation desired to be simulated, while the other wall is made of non-conducting material, such as the phenolic resin. The desired range of temperature differences is created by heating the entire edge of the top plate along the phenolic resin wall and cooling the corresponding edge of the bottom plate. This modification has resulted in linear temperature profiles across the breadth of each chamber plate and across the height of the chamber at each point. The filter paper profiles are adjusted according to the procedure as outlined previously (Fukuta et al, 1974) in order to control droplet growth at different supersaturations.

Second, an automatic feed X-Y chart recorder is used for recording the spectrum instead of a conventional X-Y recorder. This has considerably increased the spectrometer capability of continuously recording the spectrum without manual attendance for longer periods of time. Third, the scanning mechanism for counting the droplets has been made lighter and simpler so as to be compatible with the rough field conditions expected to be encountered aboard a ship or an aircraft. The modified mechanism requires the movement of a very light brass tube (having i.d. of 0.28 cm) along the median plane at the exit end of the chamber. The tube directly feeds the droplets into the optical sensor that are individually counted and recorded by a pulse-rate technique namely, the Climet 201 Particle Analyzer. The field version of the spectrometer is completely automatic.

3. RESULTS AND DISCUSSION

The spectrometer has been compared with a Twomey-type chamber (Fitzgerald et al, 1976) operated by the Naval Research Laboratory (NRL), Washington, D.C. It has also been used in three field studies so far. These results are described below.

3.1 Comparison with a Twomey-Type Chamber

During July-August, 1975, we participated in the Marine Fog Field Expedition of 1975. The opportunity was also utilized to make comparison between the data produced by the two instruments. The comparisons were made aboard the U.S. Naval Ship Hayes by using natural aerosol as the test sample. A total of 12 comparison runs was made. The test aerosol was filled in a 220 liter capacity aluminized mylar bag which supplied the sample to each instrument for comparison purposes. Total time taken by the three instruments for one comparison run was typically less than 20 minutes. In order to avoid biasing the data, the observations of all comparison runs were exchanged on a set date, namely, October 1, 1975, so that the operators of these instruments were unaware of the results produced by the other. These data are reproduced in Table 1.

Table 1
Summary of measurements (Fitzgerald et al, 1976) made aboard HAYES for comparison purposes (Data exchanged on October 1, 1975)

Run No.	S %	NRL cm^{-3}	DU cm^{-3}	Conc-ratio (NRL/DU)
1*	0.3	4520	1060	4.3
2*	0.5	5167	2119	2.4
3	0.3	1421	282	5.0
4	0.75	996	-	-
5	0.4	1146	671	1.7
6	0.5	1347	635	2.1
7†	0.15	114	106	1.1
8	0.15	577	353	1.6
9	0.25	1062	1412	0.8
10	0.25	-	280	-
11	0.5	1135	1766	0.6
12	0.35	1203	530	2.3

*The DU spectrometer was set up to measure a maximum concentration of 3,500 cm^{-3} only. For these two runs, the DU counts are not representative of actual CCN concentration.

†The scatter in the NRL data was of the order of a factor (Max. value/Min. value) of 2.5 that is also the maximum scatter reported in the NRL data.

The NRL counts in Table 1 represent the average of a few runs made at a given supersaturation. Table 2 typically represents the state-of-the-art of intercomparison as of August 1970 when a major comparison program was undertaken at the second IWCIN (International Workshop on Condensation and Ice Nuclei). Experiment #27 is chosen here because it was also selected for the summary (Ruskin and Kicmond, 1971). Without exactly knowing the state-of-the-art, comments for any comparison cannot be put into proper perspective.

Table 2
Concentration measured by the participating static thermal diffusion chambers at the Second IWCIN (August, 1970) Reference: Experiment #27, natural aerosol, S = 0.3%

Run No.	Chamber	Conc., cm^{-3}	Conc. ratio (NRL/Other)
1	NRL (Film)	262	1
2	NRL (TV)	187	1.4
3	CALspan Corp.	128	2.05
4	Univ. of Washington	117	2.2
5	White Sands (U.S. Army)	107	2.4

Considering the above data, the following conclusions seem to be reasonable.

(1) Out of ten comparison runs made with the University of Denver (DU) spectrometer, 80% of the runs agreed with the NRL chamber within a ratio range (NRL/DU) of 0.6 to 2.4 or within an average ratio of 1.58. This ratio is better than the scatter (a factor of 2.5) within the data produced for a single run (e.g., Run #7) by the NRL chamber.

(2) To put the above statement in proper perspective, the results of the second IWCIN (Table 2) show that four participating static thermal diffusion chambers agreed with the NRL chamber within a factor of 2.4. That the NRL counts may be lower than the other chambers was also reported during the second IWCIN. The CAL (Calspan Corp.) chamber counted higher by a factor of 1.54 (or 154%) and the NOAA (formerly ESSA) chamber counted higher by a factor of 1.36 (or 136%).

(3) On the basis of the above statements, it can be said in general, that the agreement between the DU spectrometer and the NRL chamber is about the same as the agreement between the NRL chamber and other static thermal diffusion chambers compared so far.

(4) The ratio of NRL to DU counts exhibits no trend with respect to supersaturation. This is because the scatter within the NRL data is by a factor of 2.5 at 0.15% supersaturation and varies randomly with respect to supersaturation. Since the DU spectrometer is completely automatic, its relative reliability is very high. There is no manual error that affects its interconsistency.

(5) The data of Table 1 are shown plotted in Fig. 1. Runs #1 and 2 are not included in Fig. 1 as the DU Spectrometer was set up to measure concentrations up to 3,500 cm^{-3}. If the concentration exceeds this value, the sample should be diluted in order to get rid of the vapor depletion effect (Squires, 1971). It was not anticipated that the marine aerosol would present CCN beyond 5,000 cm^{-3} at 0.5% supersaturation, and therefore the sample was injected without dilution. For these two runs, the scatter in the NRL data is ~ 20% and this indicates that the actual concentration was ~ 5,000 cm^{-3} and predilution of the sample was needed. Therefore, the values reported by the spectrometer cannot be taken as representative of the actual CCN concentration. It is very gratifying to note from Fig. 1 that for the eight comparison runs, the CCN concentration is within

$\pm$ 23% of the average value.

(6) Run #3 was particularly bad from the viewpoint of the scatter in the data. The NRL reported a scatter of 50% for five measured points and we reported a scatter of 86% for three points. The aerosol was room air and it is suspected that it may not be uniform in concentration throughout the volume of the mylar bag. This is not surprising since no precaution was taken to check the homogeneity of the sample because of the limited time available for comparison purposes.

(7) The comparison presented in Fig. 1 is more representative of a realistic situation than Table 1, as the latter compares the average NRL values with the instantaneous DU values and is, therefore, questionable. If the CCN concentration varied within the test sample, the DU values would show instantaneous concentration (this is inherent of the counting technique used) while the NRL values would give the average over a certain time interval. Thus, for comparisons such as those made above, the scatter in the NRL values should be duly considered. Such consideration leads to the conclusion that the agreement between the NRL chamber and the DU spectrometer lies within the scatter produced by the NRL chamber.

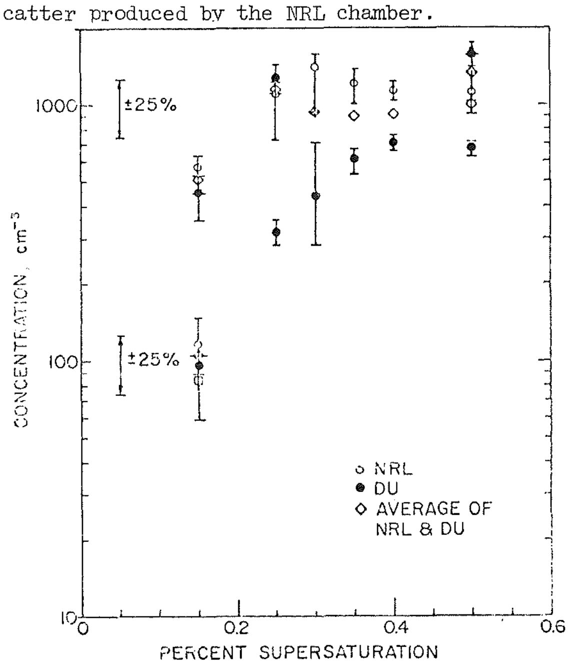

Fig. 1. Plot of CCN concentration (with established scatter) as a function of supersaturation for the 8 comparison runs (run #1 & 2 excluded).

3.2 Cross-Check of the Counting Technique

The preceding discussion makes it obvious that our spectrometer compares well with the Twomey-type device. However, run #1 and 3 in Table 1 warrant further investigations. As pointed out earlier, no check was made on the homogeneity of test samples used for the preceding comparison. This factor may be responsible for the rather large scatter observed in the NRL data and may give rise to spurious disagreement shown by run #1 and 3. In order to confirm this inference, we cross-checked the automatic counting technique with the direct photography method which is used in the NRL chamber. These experiments were done under well controlled laboratory conditions. The results are summarized in Table 3.

Table 3
Comparison of CCN counts obtained by automatic recording and direct photography of droplets

Run No.	% S	Automatic Recording cm^{-3}	Direct Photography cm^{-3}	Deviation %
1	0.30	1483	1339	-10.7
2	0.40	1341	1325	- 1.2
3	0.54	1060	1188	+10.8
4	0.69	741	806	+ 8.1
5	0.89	634	669	+ 5.2
6	1.1	512	410	-24.9
7	1.4	322	382	+15.7
8	1.8	259	219	-18.3
9	2.1	175	178	+ 1.7

For obtaining the above measurements, the test sample was stored in a 1,100 liter capacity mylar bag and a collimated mercury-arc light beam, 6.1 mm in diameter, was passed across the width of the chamber at the exit end. The photographs were taken at right angles to the light beam after stopping the sample flow momentarily. The counts obtained by the two methods agree with an absolute average deviation (treating the direct photography counts as a standard concentration) of 10.7%. This evidence, coupled with the fact that in the normal operation the counts are photoelectronically recorded without any manual interference (such as the counting of droplets on photographic frames), leads us to place a high confidence in the spectrometer performance.

3.3 Measurements on Urban Aerosols

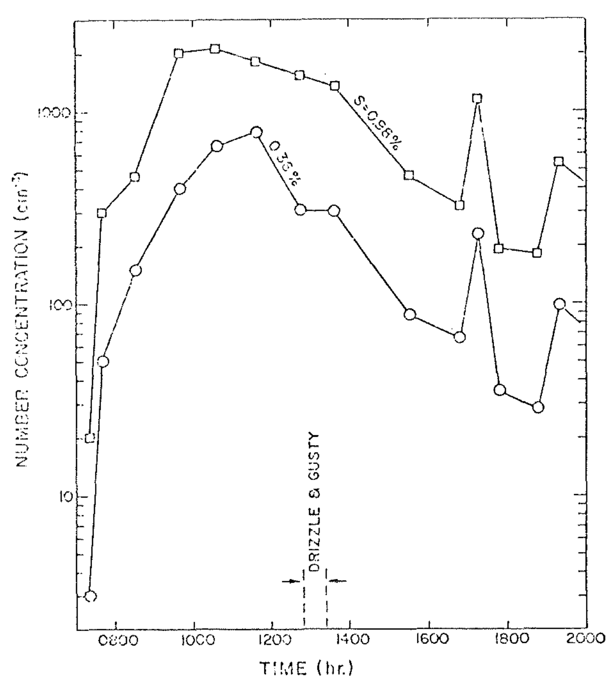

Fig. 2. CCN concentration variation obtained by the spectrometer on August 9, 1974 for the Denver aerosol.

On August 9, 1974, the field measurements of diurnal variations in the CCN spectrum were made. The observation point was established about 18.5 meters above the ground at the southern outskirts of Denver County. Due care was taken to draw the natural atmospheric aerosol. The detected diurnal variations are shown in Figs. 2 and 3. A peak in the CCN concentration representative of an increase in the vehicular traffic during morning and evening hours is obvious (Fig. 2). Figure 3 reveals that the CCN spectrum is concave during morning hours and convex during the afternoon and evening hours. One of the reasons for this change may be the high concentration of the CCN active at low supersaturations during the later period as a result of the coagulation mechanism. The observed effect is, however, a combined result of the CCN generation and the coagulation processes. Sixteen CCN spectra were measured during the day. Each spectrum was fitted to the equation: $N=CS^k$, where C (in cm^{-3}) and k are constants for one spectrum. The least-square-fit values of C and k showed the value of C ranging from 1,988 cm^{-3} at 1035 hr to 16 cm^{-3} at 0720 hr, and of k ranging from 0.6 to 1.8. The k-values are similar to those reported by Braham (1974 b) for the St. Louis aerosol.

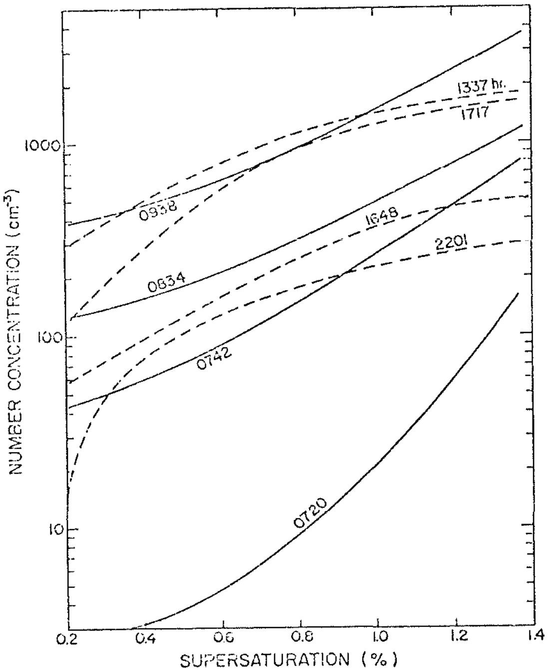

Fig. 3. CCN spectrum recorded at different times of the day on August 9, 1974 for the Denver aerosol.

3.4 DUSTORM Project Measurements

The CCN Spectrometer was flown a total of 36 hours aboard the NCAR (National Center for Atmospheric Research, Boulder, Colorado) Electra aircraft during April and May, 1975. This was done under the project DUSTORM (initiated by Dr. Edwin F. Danielsen at NCAR) in order to unravel the microphysics of the severe storm genesis. The flights were made across the tropopause fold that occurs during dust storms over the U.S. Great Plains in the spring of each year. A sample of results obtained on April 26, 1975 is displayed in Figure 4.

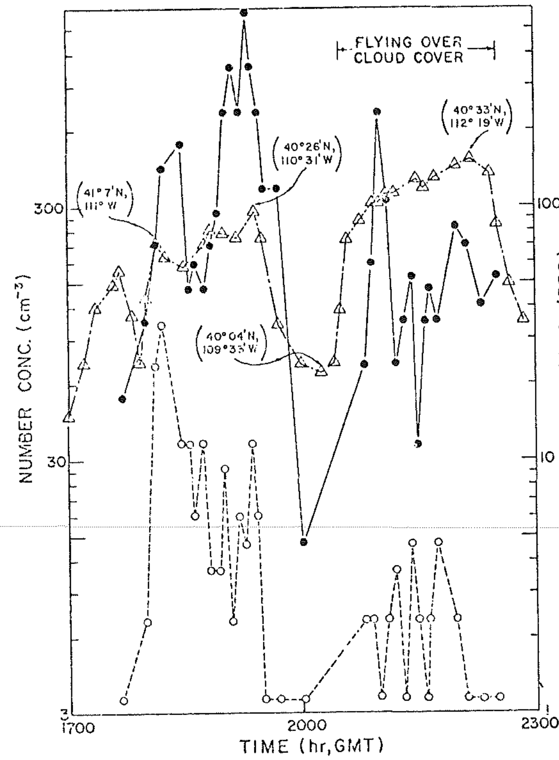

Fig. 4. DUSTORM data: △ - volume conc. of ozone (right-side ordinate); ○, ● - CCN concentration at 0.38% & 1.9% supersaturations (left-side ordinate).

The CCN concentration at 0.38% (open circles) and 1.9% (closed circles) supersaturations is shown plotted as a function of time and so is the ozone concentration in parts per billion (PPB). The boundary of tropopause fold is indicated by a sudden rise in the ozone concentration. Data at supersaturations between 0.38% and 1.9% were also recorded continuously during the flights. Fig. 4 reveals some remarkable features. Before we started flying over clouds (altitude 7,556 meters MSL), the peaks in ozone concentration were well correlated with the peaks in the CCN concentration active at 1.9% supersaturation. A maximum increase by a factor of six was recorded within the fold boundary. Such increases are noted during all the four experimental flights. Is this reflection of in-situ gas-to-particle conversion processes? To answer this question, complete analysis and reduction of the data is needed along with the comprehensive information on the air trajectories involved in the storm. This is being worked out in cooperation with the NCAR scientists.

3.5 Marine Fog Measurements

The measurements taken during the Marine Fog Field Expedition of August, 1975 offer a unique opportunity to comprehensively study some fog episodes since they were extensively monitored by various participants. The spectrometer undoubtedly affords the best time resolution for such studies. This is made evident by the NRL measurements of the CCN spectra as the latter were unable to detect any noticeable change in the fog spectrum during fog episodes. An example of the dramatic variations is presented below.

Let us consider Fog #4 that occurred during the early morning hours (2:00-8:00 A.M.) of August 6, 1975, off the Nova Scotia coast as shown in Fig. 5. The spectrum was monitored during the ship track, A-B-C-D-E. At point D (i.e., at 1:50 A.M.), the true wind direction was 340°. Thus, point D may be regarded as lying at the forming boundary of the fog. At point E, the wind direction was 13°, and it may be considered at the dissipating boundary of the fog. During the episode, the winds were mild to calm, the true wind speed varying from 0.4 (at 3:40 A.M.) to 14.7 knots (at 2:20 A.M.).

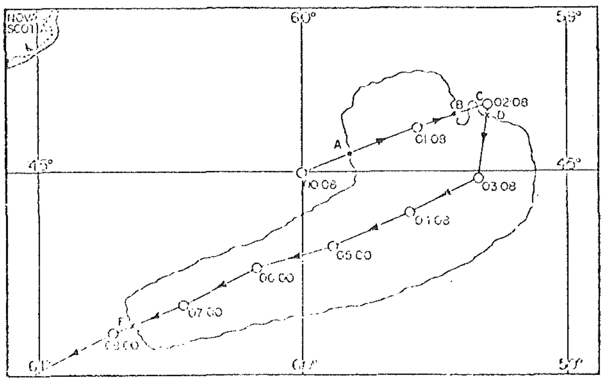

Fig. 5. Track of the U.S. Naval Ship Hayes in fog episode #4 that occurred during the early morning hours (2:00 - 8:00 A.M.) of August 6, 1975.

In Figure 6 the visibility (β) is plotted as a function of time. The plot is based on the data provided by the NRL. To obtain the true value of visibility, the values of Fig. 6 should be divided by 1.65 within the fog. The latter is the calibration factor. However, for our discussion the relative values of visibility will suffice. The fog nuclei spectrum recorded at different times during the episode was reduced to the form CS^k. From Figure 6, the dramatic variations in k, N_1, and N_2 at the fog forming boundary are noteworthy. Just before 2:00 A.M., peaks in visibility (β), k, N_1, and N_2 superimpose on each other. At the fog forming boundary, the nuclei concentration at 0.15% supersaturation drops by a factor of 1.35, while at 1.2%, it drops by a factor of 6.0. The latter indicates a pronounced change that is beyond any kind of experimental error. The mechanism for this dramatic reduction in N_2 may be scavenging. These observations stress the need for monitoring the entire nuclei spectrum at the fog boundaries. Within the fog, the changes in N_1, N_2, and k are not as dramatic but at the fog dissipating boundary, all these parameters show an upward trend and correlate well with the visibility. At the fog forming boundary, the absolute nuclei concentrations (for example, 2,500 cm^{-3} at S = 1.2%) suggest that the aerosol that participated in the fog formation was continental in character.

In Table 4, the values of C and k are listed at different times during the fog episode. For these k-values, the nuclei concentrations in the supersaturation range of 0.15 to 1.2% were considered. In this supersaturation range, all droplets that grew beyond 1.0 μm size were counted. The spectrometer, however, sustained a supersaturation range of 0.06 to 1.2%

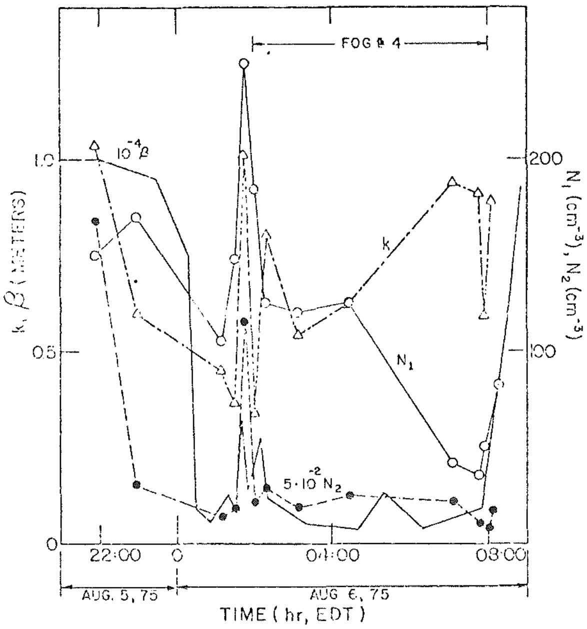

Fig. 6. Plot of visibility (β), nuclei concentrations at 0.15% (N_1) and 1.2% (N_2) supersaturations, and the slope (k) of the nuclei spectrum as a function of time for Fog #4. β is represented by a continuous thick line, k by dash-dot line, N_1 and N_2 by thin continuous line and broken line, respectively.

Table 4
Values of constant (C), slope (k), and nuclei concentrations at 0.15% (N_1) and 1.2% (N_2) supersaturations for Fog #4

Date	Time hr, EDT	C cm^{-3}	k	N_1 cm^{-3}	N_2 cm^{-3}
8/5/75	21:54	2,250	1.36	150	3,350
8/5/75	22:57	530	0.60	170	610
8/6/75	1:09	260	0.45	105	280
8/6/75	1:30	315	0.36	148	330
8/6/75	1:46	2,300	1.13	250	2,500
8/6/75	2:00	330	0.34	185	415
8/6/75	2:17	480	0.80	125	550
8/6/75	3:07	320	0.54	120	350
8/6/75	4:26	370	0.62	125	490
8/6/75	7:06	240	0.94	42	435
8/6/75	7:45	150	0.91	35	185
8/6/75	7:55	145	0.59	51	170
8/6/75	8:02	260	0.89	82	320

and the droplets grown beyond 0.3 μm and 0.5 μm were also recorded. The latter data will be analyzed in the future in order to estimate fog nuclei concentrations active at supersaturations below 0.15%. The nuclei concentrations at 0.15% (N_1) and 1.2% (N_2) supersaturations are also recorded as a function of time in Table 4.

Acknowledgments. The work was supported by the National Science Foundation, Grant NO. DES75-13361, and the Naval Air Systems Command, Department of the Navy, under Contract NO. N00019-75-C-0310. The authors are thankful to Mr. Stuart Gathman and Dr. J.W. Fitzgerald of the Naval Research Laboratory, Washington, D.C., for their cooperation during the Marine Fog Field Expedition of 1975. Valuable guidance received from Dr. Edwin F. Danielsen during the DUSTORM project is gratefully acknowledged.

References

Braham, R.R., Jr., 1974a: Information content of CCN spectra vs. measurements at a single supersaturation. Preprints Conference on Cloud Physics, Tucson, Arizona, 21-24 October, 1974, pp. 9-12.

Braham, R.R., Jr., 1974b: Cloud physics of urban weather modification - A preliminary report. Bull. Am. Meteor. Soc., 55, 100-106.

Fitzgerald, J.W., T.A. Wojciechowski, D.J. Alofs, and V.K. Saxena, 1976: Results of an intercomparison of three thermal diffusion-type cloud condensation nucleus (CCN) counters used in fog research. Presented at the Fourth Annual Marine Fog Investigation Program Review, Reno, Nevada, 6-7 January, 1976.

Fukuta, N., and V.K. Saxena, 1973: Cloud condensation nucleus spectrometer. Bull. Am. Meteor. Soc., 54, 1105.

Fukuta, N., and V.K. Saxena, 1975: Field measurements with a cloud condensation nucleus spectrometer in marine fogs. Annual Project Report on DRI Project #5215, Submitted to the Department of the Navy, Naval Air Systems Command under Contract NO. N00019-75-C-0310, 26 pp. The report is available upon request.

Fukuta, N., V.K. Saxena, and A. Gorove, 1974: Cloud condensation nuclei spectrometer II: Measurements on the natural aerosol. Conference on Cloud Physics, Tucson, Arizona, 21-24 October, 1974, pp. 361-367.

Hudson, J., and P. Squires, 1973: Evaluation of a recording continuous cloud nucleus counter, J. Appl. Meteor., 12, 175-183.

Ruskin, R.E., and W.C. Kocmond, 1971: Summary of condensation nucleus investigations at the 1970 international workshop on condensation and ice nuclei. Proc. Second Intl. Workshop on Condensation and Ice Nuclei, Fort Collins, Colorado, edited by L.O. Grant, pp. 92-96.

Sinnarwalla, A.M., and D.J. Alofs, 1973: A cloud nucleus counter with long available growth time, J. Appl. Meteor., 12, 831-835.

Squires, P., 1971: Diffusion chambers for the measurement of the spectrum of critical supersaturation of cloud nuclei, Proc. Second Intl. Workshop on Condensation and Ice Nuclei, Fort Collins, Colorado State University, pp. 7-10.

Veal, D.L., W.A. Cooper, G. Vali, and J. Marwitz, 1975: A review of the aircraft instrumentation for atmospheric research, Preprints, NHRE Symposium/Workshop on Hail, Estes Park, Colorado, September 21-28, 48 pp.

A CCN SPECTROMETER

J. G. Hudson

Desert Research Institute
University of Nevada System
Reno, Nevada

1. INTRODUCTION

Podzimek and Alofs (1974) have analyzed a device invented by Laktionov (1972) for measuring CCN spectra at low supersaturations. This functions by exposing the aerosol particles to saturated air and measuring the sizes of the haze droplets in equilibrium at zero supersaturation (S = 0). This is a plausible procedure because, for soluble nuclei, if the variation of the van't Hoff factor is ignored, a relationship exists between the critical supersaturation (S_c) of a nucleus and its equilibrium size at 100% relative humidity:

$$r_0 = \frac{4\sigma M_w}{3\sqrt{3}\ \rho RTS_c} \quad (S_c \text{ in absolute units})$$

Substituting numerical values which are appropriate at 20°C,

$$r_0 \simeq \frac{4.1\text{x}10^{-6}}{S_c} \qquad (1)$$

where r_0 is in centimeters, and S_c is expressed in percent.

Thus for $S_c = 0.2\%$, $r_0 = 2 \times 10^{-5}$ cm.

Since optical counters exist which can count and size droplets down to about r = 0.2 μm fairly reliably, Laktinov's method would appear to be usable for values of S_c less than about 0.2%. At lower values of S_c, r_0 is larger, so that the method has a potential utility in the range of values of S_c below 0.1%, where normal supersaturated diffusion chambers are not usable.

The derivation of equation (1) assumes that the van't Hoff factor (i) is the same for the critical droplet as it is for the somewhat more concentrated haze droplet in equilibrium at S = 0. This assumption appears to be moderately accurate for $S_c < 0.2\%$, though it would not be so for much higher supersaturations. If the effective number of moles of solute in a droplet is defined as $(\frac{im}{M})$ where m is the mass of solute and M its molecular weight, the effective molar fraction of the solute in the haze droplet in equilibrium at S = 0 is $(3\sqrt{3}\ S_c/2)$ where S_c is in absolute units, that is, $2.6\text{x}10^{-2}S_c$ where S_c is in percent. Thus for small values of S_c the haze droplet solution is fairly dilute; at $S_c = 0.2\%$, its concentration is $5\text{x}10^{-3}$ effective moles per mole, or 0.3 effective moles per liter. At and beyond this degree of dilution, as may be seen from the tabulations given by Low (1969), i is within 30% of its value at infinite dilution for representative salts such as NaCl and $(NH_4)_2SO_4$. The same will be true, à fortiori, for the more dilute critical droplet. Since equation (1) ignores square roots of i, the error caused there is of order 15% or less for $S_c = 0.2\%$, and smaller for smaller S_c values.

Another possible source of error arises because the original nucleus may have contained an insoluble component. However, measurements of the diffusion coefficient of CCN in the range S_c = 0.3 to 1% (e.g., Twomey, 1972) indicate that they are of such a size that they must in general consist of soluble material to a substantial extent. The effective molecular weights (M/i) of plausible soluble components of CCN center around 30 to 40, that is, about twice the molecular weight of water. On the other hand, the density of dry salts is also about twice that of water. Hence, the original dry soluble component probably had in general a volume of order 10^{-2} of the volume of the haze droplet formed at S = 0 on a nucleus for which $S_c = 0.2\%$. It would appear reasonable to conclude that in general the presence of an insoluble component would have only a slight effect on the accuracy of equation (1).

A further possible source of error arises when the droplet sizes are measured by means of an optical particle counter. Most such counters are calibrated using spheres of polystyrene latex, which have an index of refraction (n) of about 1.6. They cannot be calibrated for water (n = 1.33) because it is too difficult to obtain and keep a monodisperse water droplet aerosol with d < 10 μm. Theoretical predictions are possible (Cooke and Kerker, 1975) but they depend on details of the particular counter in question.

The various possible sources of error in the use of Laktionov's haze droplet method suggest that it would be desirable to check it against another method. Fortunately, its apparent range overlaps slightly with that of the vertical-plate diffusion chamber described by Hudson and Squires (1976), which appears to be capable of an accuracy of 10% or better down to $S_c = 0.1\%$ (Hudson and Squires, 1976). Both methods seem therefore to have a useful accuracy in the range $S_c = 0.1\%$ to 0.2%. The discussion given above concerning the sources of error in equation (1) indicates that if the haze droplet method is satisfactory in this range, it is likely to be even more satisfactory at smaller S_c values, where the haze droplets are larger and more dilute. The results of a comparison of the two methods in the restricted overlap range $0.2\% > S_c > 0.1\%$ are presented below.

2. THE ISOTHERMAL SPECTROMETER

Since the test comparison could not be extended to values of S_c less than 0.1%, the conditions on the Laktionov apparatus were not as demanding as at lower values, where the time required to grow droplets to sizes close to their equilibrium size at S = 0 becomes much longer. It proved to be possible to make the desired test using existing equipment.

Two almost identical continuous flow diffusion chambers, as described in Hudson and Squires (1976), were available. One chamber, running in the vertical mode with 38 cm of wet paper on the cooler plate and 28 cm of wet paper on the warmer plate operated at a low supersaturation such as 0.15% and was adjusted to meet all plateau requirements as described by Hudson and Squires (1976) so that it yielded $N(S_c)$ to ~ 10% accuracy. The other chamber was also operated with its plates vertical, and with the same paper lengths. However, both plates were at the same temperature. Both chambers monitored the same sample at identical flow rates. The Royco Model 225 particle counters with Model 241 optical benches were equipped with 508 modules which have five independently variable size channels, each of which records the number of particles (droplets) which are larger than a particular size corresponding to the particular threshold voltage. By adjusting this threshold voltage properly, one can arrange matters so that the number concentration for a particular channel of the isothermal chamber, $N(r > r_1)$ is equal to the number concentration of activated nuclei in the supersaturated chamber, $N(S_m)$ (where S_m is the operating supersaturation). One can then surmise that all of the haze droplets larger than this particular nominal size are grown on nuclei with critical supersaturations equal to or less than the operating supersaturation of the second chamber. This process was repeated by using various supersaturations in the supersaturated chamber and corresponding voltage thresholds for the counter on the isothermal chamber. Since the particle counter has five channels a different supersaturation can be chosen to correspond to a threshold voltage for each channel. Thus the particle counter monitoring the isothermal chamber yields $N(S_c)$ for several S_c's simultaneously as long as these threshold voltages remain constant.

3. RESULTS WITH THE ISOTHERMAL SPECTROMETER

In order to ensure that the drops in the isothermal chamber had sufficient time to grow close to their equilibrium sizes and did not evaporate before entering the detecting volume of the optical counter, experimental checks were made by changing F, the total flow through the isothermal cloud chamber. The value of F determines the amount of time for which the particles or droplets are exposed to saturated air and also the amount of time which the droplets spend in the space between the saturated volume of the cloud chamber and the

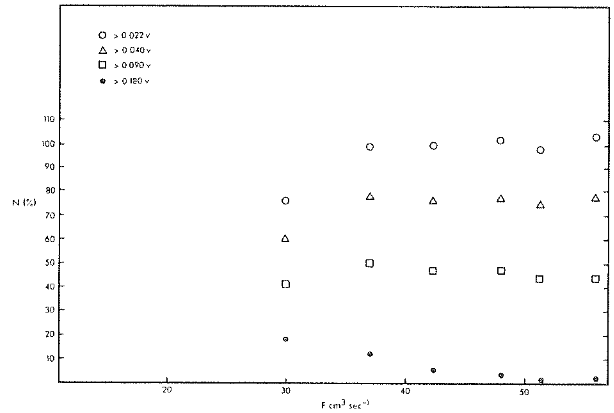

Figure 1. $N(r > r_1)$ (normalized to the other cloud chamber monitoring the same aerosol with all parameters fixed) vs. total flow through the chamber, F, for various nominal droplet radii (isothermal chamber).

detecting volume of the particle counter. This distance consists of only the thickness of the front plate of the cloud chamber, 1.9 cm, and the length of the Royco optical counter inlet spout which was 7.8 cm (the front trunnion described by Hudson and Squires (1976), was removed for the isothermal chamber). Fortunately, there is a range of values of F over which $N(r > r_1)$ for several droplet radii (r_1) is fairly constant (Fig. 1) and the existence of this F-plateau ensures that the drops are at their equilibrium size when they enter the particle counter. As a further check on evaporation effects, a temperature controlling water jacket was placed around the Royco inlet spout, but the only effect this had was to extend the plateau of N vs. F to lower flows, thus indicating that evaporation was a problem only if F was below the previous plateau value.

The experiment then consisted simply of noting the voltage settings on the optical counter connected to the isothermal chamber and the supersaturation in the reference chamber when the two Roycos were counting the same concentration of droplets. From the voltage setting, a nominal droplet radius was deduced using the manufacturer's calibration. The critical supersaturation derived by substituting this radius in equation (1) was then compared with that present in the supersaturated reference chamber. The results were as shown in Tables 1 and 2 for two optical counters, designated as #2 and #3.

Comparison of the values listed in the final two columns of Tables 1 and 2 indicates that the Laktionov method (using a Royco optical particle counter) gives fairly accurate results at supersaturations close to 0.1%, but tends to overestimate the supersaturation (or underestimate concentrations) at values of S_c near 0.2%. It seems possible that this may be in part due to increasing inaccuracy in the Royco calibration at the smallest droplet sizes. The Laktionov method can be used between 0.1% and 0.2% supersaturation with very good accuracy if a calibration curve based on concentration in the two matched cloud chambers (for instance using the first and last columns of Tables 1 or 2) is used.

TABLE 1

Laktionov method using Royco #2

Voltage Threshold for Counter Monitoring Isothermal Cloud Chamber	Royco Radius in μm Corresponding to the First Column Based on Manufacturer's Calibration	S_c for Second Column Based on Equation (1) %	S_m in Reference Chamber %
0.102	0.35	0.12	0.11
0.057	0.26	0.16	0.14
0.022	0.16	0.26	0.17
0.015	0.13	0.32	0.21

TABLE 2

Laktionov method using Royco #3

Voltage Threshold for Counter Monitoring Isothermal Cloud Chamber	Royco Radius in μm Corresponding to the First Column Based on Manufacturer's Calibration	S_c for Second Column Based on Equation (1) %	S_m in Reference Chamber %
0.108	0.34	0.12	0.13
0.077	0.29	0.14	0.14
0.042	0.22	0.19	0.17
0.025	0.18	0.23	0.20

4. DISCUSSION

These results offer encouragement that the Laktionov method may be useful in the range of S_c below 0.1%. One ultimate limitation in attempting to make measurements at very low values of S_c will be that the time taken for haze droplets to reach sizes close to their equilibrium sizes at S = 0 will become longer and longer. In any piece of apparatus designed to use this method, a limit will be reached when the distance fallen by the droplets becomes so large that they reach the chamber floor and are lost.

The isothermal spectrometer can not operate at supersaturations above 0.2% because optical counters can not size such small droplets. However, for many cloud physics applications, it would be desirable to use a much larger range of S_c's.

A possible way of doing this is to operate the spectrometer cloud chamber at a supersaturation above 0% and to again compare its drop size spectrum with the number concentration in the other matched cloud chamber operating at various supersaturations. The spectrometer chamber can operate at a relatively high supersaturation such as 1% so that it can yield $N(S_c)$ over a very wide range of supersaturations.

This increased range is purchased at a considerable price. In the isothermal spectrometer the drops grow to an equilibrium size which is known. In the supersaturated spectrometer the maximum operating supersaturation, S_m, is above the S_c of most CCN so that most drops will grow beyond their critical radius, r_c, and will thus continue to grow with time. Furthermore, it would be very difficult to use droplet growth theory to predict how large they will grow. However, the theory does clearly indicate that those nuclei with lower S_c's are larger to begin with and experience a greater driving force for growth and thus grow faster. Therefore, they will always form larger drops than are formed on nuclei with higher S_c's if the growth times are equal and the condensation coefficient does not vary.

If all nuclei which go through the spectrometer experience the same supersaturation for the same length of time then the size of the drops thus formed will be inversely related to their S_c's. All drops greater than a particular size (r_p) have S_c's less than a particular value so that if a second matched chamber monitors the same air sample at a lower S_m than the spectrometer the S_c for a particular drop size cut-off can be determined when the $N(S_m)$ of the second chamber equals $N(r > r_p)$ in the spectrometer. When the process is repeated for several supersaturations the first chamber can act as a spectrometer.

5. DESCRIPTION OF THE CCN SPECTROMETER

Droplet path lengths are unequal at the end of the cloud chamber where the drops converge into the particle counter so the sample slit width was masked off from 8 cm to 1.5 cm. This meant that the sample flow, f, had to be reduced at least accordingly so that the sample would not be so thick that it would extend over different values of supersaturation which exist in the region between the plates. The necessarily high values of total flow, F, through the chamber also helped to confine the sample to a more narrow region between the plates. Typical values of F and f for the spectrometer, 50 $cm^3\ sec^{-1}$ and 0.1 $cm^3\ sec^{-1}$ respectively, produced a sample 0.04 cm thick with a plate separation of 1.3 cm which means that the sample should experience a supersaturation range much less than 1% of S_m.

In order to eliminate the possibility of any vertical velocities causing varying path lengths by moving some of the sample stream away from the central 1.5 cm (with respect to the sidewalls) the horizontal plate mode of operation was chosen for this spectrometer. Since it operates at a very high supersaturation ($\lesssim$ 1%) it is just about as accurate as the vertical chamber (Hudson and Squires, 1976). The wet surface length on the warm plate must be very short ($\sim$10 cm) not just to prevent drop fallout but also to prevent the drops from growing so large that their size distribution would be out of the range of the particle counter (< 10 μm radius). The spectrometer must be operated on the F-plateau appropriate to its S_m so that one $N(S_c)$ can be obtained directly from the

$N(S_m)$ of the spectrometer. However, it should operate at the high end of the F-plateau so that (as pointed out above) the drop sizes are not out of the range of the particle counter. Also the growth rate of smaller drops will be more dependent upon S_c.

The nuclei do not experience a constant supersaturation as they move through the chamber because the supersaturation rises exponentially from subsaturation to S_m (Hudson and Squires, 1973). This tends to further spread the drops in size according to their S_c's because the nuclei with lower S_c's not only grow faster but also start growing earlier as they are activated earlier and of course are also bigger haze drops to begin with.

As with the isothermal spectrometer the trunnion was removed so that the particle counter could be put right up against the cloud chamber.

6. OPERATION OF THE CCN SPECTROMETER

While the first chamber, which acts as the spectrometer, operates at $S_m \doteqdot 1\%$ as previously stated, the second chamber operates at some lower $S_m = S_{mi}$ between 0.1% and 1.0%. It must satisfy all plateau requirements as stated by Hudson and Squires (1976) and can operate in the horizontal or vertical mode as is appropriate. For $S_m \gtrsim 0.25\%$ it will then yield $N(S_{mi}) = N(S_{ci})$ to about 1% accuracy. With both chambers monitoring the same sample with the same sample flow the drop size discriminator of one of the channels of the particle counter on the spectrometer chamber which has its $S_m = 1\%$ is adjusted until $N(r > r_i) = N(S_{mi})$. Then as long as F, S_m and r_i of the spectrometer remain constant then $N(r > r_i)$ will give $N(S_{mi}) = N(S_{ci})$ as long as the condensation coefficient does not vary. When this process is repeated for several S_{mi}'s and r_i's the first chamber indeed acts as a spectrometer. Since the Royco 508 module has five channels then as many as five S_c's can be monitored simultaneously in the spectrometer.

7. RESULTS WITH THE CCN SPECTROMETER

In order to be a useful tool the spectrometer should be accurate over a wide range of concentrations and values of K (the slope of the log curve of N vs. S_c). It might seem that high concentrations of nuclei could cause enough competition for the water vapor to slow down the growth of droplets enough to thwart the operation of the spectrometer. However, tests with various aerosols with a sample flow of about 0.3 $cm^3 sec^{-1}$ have shown that concentrations from the spectrometer differ from the actual concentration by no more than 25% for as much as an order of magnitude change in concentration. This performance can be improved if the sample flow is reduced by either changing the sample capillary resistor or the pressure deficit in the cloud chamber.

The crucial test of the spectrometer is that it yield accurate measurements over a range of values of K. Moreover, the determination of K is the major purpose of using a CCN spectrometer. It must be clearly demonstrated that the spectrometer is not merely separating fixed percentages of drops into the various size channels which are not dependent upon the critical supersaturation of the nuclei. Figure 2 shows that the ratio of the deduced concentration at a lower supersaturation to $N(S_m)$ in the spectrometer was not fixed but was definitely a function of K. The points in fact lie very close to the curve of the ratio of the actual concentration at the lower supersaturation (as determined by the other cloud chamber which was actually operating at that supersaturation) to $N(S_m)$ of the spectrometer. This figure indicates that the actual readings from the spectrometer are fairly accurate over the natural range of K. Differences from the actual curve are presumably due to slight variations in the path of the growing drops. This could be minimized by further reducing the sample flow and further confining of the sample stream. Moreover, a curve such as Figure 2 could be used to correct the output of the spectrometer to the accurate measurements of $N(S_c)$.

Because of all of the intermediate steps in the calibration, the sensitivity to small fluctuation in F and r and the above considerations, the 1% accuracy of the diffusion chamber cannot be expected for the spectrometer but an accuracy of order 10% seems to be attainable.

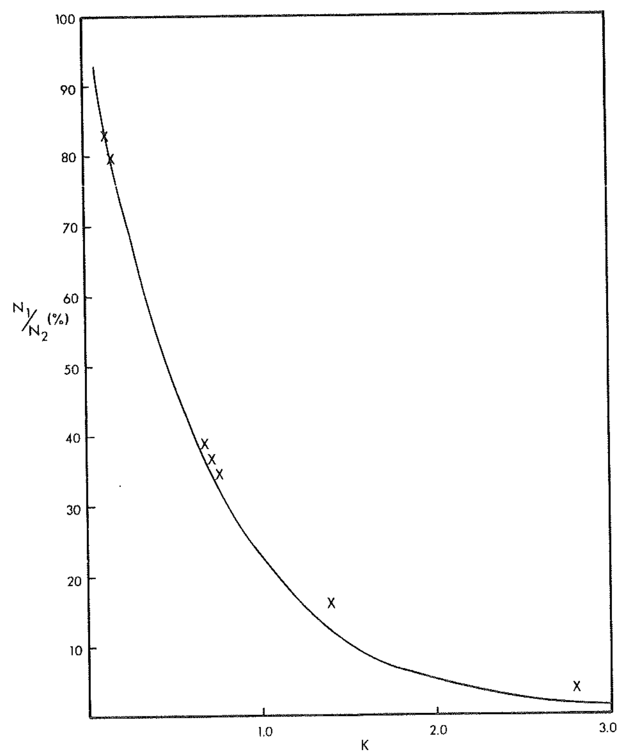

Figure 2. Smooth curve is the ratio of the concentration of nuclei active at 0.26% (determined by a cloud chamber operating at 0.26%) to the concentration of nuclei active at 1.15% (as determined by the spectrometer chamber operating at 1.15%) plotted against K (derived from this data with ($N = cS_c^K$)). The X's represent data taken at the same time with the ratio of the concentration of drops greater than a particular nominal size threshold (in this case r 2.5 μm) from the spectrometer to the concentration of nuclei active at 1.15% determined by the spectrometer plotted against the same K.

8. CONCLUSION

The Laktionov isothermal method of obtaining CCN spectra in the range of supersaturation between 0.1% and 0.2% has been experimentally verified using two well-matched diffusion cloud chambers. A method of using two well-matched CCN counters to obtain $N(S_c)$ for more than two values of S_c over nearly the entire CCN range has also been demonstrated. It operates on a similar principal as was used to check the Laktionov method requiring the two matched chambers for its operation. This method may not work for all aerosols since a different condensation coefficient may affect the rate of drop growth and alter the drop size spectrum in the spectrometer cloud chamber. However, the second cloud chamber which must be used to calibrate this spectrometer can also be used to continuously monitor its performance. Also this apparatus could be used to obtain a qualitative determination of possible variations in the condensation coefficient.

9. ACKNOWLEDGEMENTS

The research described was supported by the National Science Foundation under Grant DES-73-06531 A02 of the Atmospheric Sciences Section. The apparatus was constructed by Mr. Robert Laird whose contribution is gratefully acknowledged.

10. REFERENCES

Cooke, D.D. and M. Kerker, 1975: Response calculations for light-scattering aerosol particle counters. Applied Optics, 14, 734-739.

Hudson, J.G. and P. Squires, 1973: Evaulation of a recording continuous cloud nucleus counter. J. Appl. Meteorl., 12, 175-183.

Hudson, J.G. and P. Squires, 1976: An improved continuous flow diffusion cloud chamber. J. Appl. Meteorl., submitted August, 1975.

Laktionov, A.G., 1972: A constant-temperature method of determining the concentrations of cloud condensation nuclei. Atmos. Oceanic Phys., 8 382-385.

Low, R.D.H., 1969: A generalized equation for the solution effect in droplet growth. J. Atmos. Sci., 26, 608-611.

Podżimek, J. and D.J. Alofs, 1974: A review of Laktionov's isothermal cloud nucleus counter. J. Appl. Meteorl., 13, 511-512.

Twomey, S., 1972: Measurements of the size of natural cloud nuclei by means of nuclepore filters. J. Atmos. Sci., 29, 318-321.

7.2.4

AN AUTOMATIC LIGHT SCATTERING CCN COUNTER

G. G. Lala and J. E. Jiusto

Atmospheric Sciences Research Center
State University of New York, Albany, New York

1. INTRODUCTION

The static thermal diffusion chamber has been used extensively for the measurement of cloud condensation nucleus (CCN) concentrations. This technique offers the capability of accurately prescribing supersaturations which can be varied over the range of values encountered in clouds. In most systems utilizing the static diffusion chamber, the concentration of droplets is measured by photographing a carefully defined illuminated volume and subsequently counting the bright spots on the film. This is not only tedious and time consuming, but limits the amount of information that can be obtained on time and spatial variations of CCN concentrations. The time involved in this procedure precludes real time analysis of CCN variations. One approach to overcoming this problem is the system designed by Radke and Hobbs (1969) in which the number concentration of droplets is determined from a measurement of the extinction coefficient of the droplet cloud when most of the drops have reached a size corresponding to the first Mie peak. A disadvantage of this system is the requirement for a large chamber volume with a corresponding large chamber height which leads to long times to reach equilibrium of the order of two to three minutes. Ideally, one would like to use a chamber of the more common height of one to two centimeters which results in times to reach equilibrium on the order of a few seconds. Twomey and Davidson (1970) have continuously operated a conventional static chamber such that air samples are drawn and photographs automatically taken at approximately hourly intervals. Interesting diurnal and seasonal trends have been indicated, but the subsequent data analysis of such a procedure is formidable.

The method to be described in this paper allows for the determination of the droplet concentration from scattered light measurements while preserving the features of the usual static diffusion chamber design. The instrument has been developed to the state where it can operate unattended for long periods of time providing measurements of CCN supersaturation spectra. (During the period of development of this instrument, an independent development employing the light scattering principle was underway at Mee Industries, Inc., California.)

An expanded version of this paper including system diagrams, model derivations, and complete calibrations has been submitted for publication elsewhere.

2. DESIGN PRINCIPLES

When observing a volume of the chamber illuminated by a tungsten lamp with a photodetector directed in a forward scattering direction, the scattered light signal is observed to rise to a peak and then fall off with time during a sampling sequence. The initial increasing signal is due to the rapid growth of the droplets to near uniform size, and the eventual decline is die to the removal of droplets by sedimentation. The magnitude of this peak scattered light signal is directly proportional to the number concentration of droplets.

The use of a continuous spectrum light source such as a tungsten lamp results in a smoothing of phase effects in the scattered light signal, and the Mie peaks generally are not evident in the signal. This has been verified by recording the scattered light intensity as a function of time for many samples at several supersaturations. The use of a forward scattering angle of 45^{o} with the tungsten illumination insures that the scattering intensity coefficient for the drop sizes involved is reasonably constant (Hodkinson and Greenfield, 1965). The first Mie peak corresponds to a drop radius of approximately 0.5 μm for the light source involved. Most all drops rapidly exceed this size at chamber supersaturations (S) of 0.5% and greater. At lower supersaturations drop sizes become progressively less uniform and smaller such that some variations in drop scattering intensity might be expected. For these reasons, our adopted minimum supersaturation is 0.25%. Conventional static chambers possess a practical lower limit of 0.1-0.2% because of the difficulty in differentiating haze and effective CCN droplets (Twomey, 1967; Squires, 1972).

A simple model for the behavior of the scattered light signal was constructed using the customary r^{-1} dependence for the drop growth rate, Stokes law for the fall speed, and the assumption that the light scattered is proportional to the cross sectional area of a drop. The droplet population was assumed to be monodisperse, and the solution, curvature and kinetic effects were neglected in the drop growth equation following favorable comparison with a more detailed treatment). This system of equations was integrated to give expressions for the time of occurrence t_m of the peak signal and the intensity of the scattered light I_p at the peak, as follows:

$$t_m = \left(\frac{h}{3BGS}\right)^{\frac{1}{2}} \qquad (1)$$

$$I_p = C\frac{4}{3} G \left(\frac{h}{3BG}\right)^{\frac{1}{2}} S^{\frac{1}{2}} N_o \qquad (2)$$

In these equations, N_o is the initial droplet concentration, S is the supersaturation, G is a thermodynamic constant in the drop growth equation, B a constant from Stokes law, h the depth of the scattering volume, and C is a constant related to the incident intensity and the scattering geometry.

The main conclusions from this analysis are that a peak in the scattered light signal occurs at a well defined time dependent only on the supersaturation (equation 1) and the scattered light signal at the peak is directly proportional to the initial droplet concentration and the square root of the supersaturation.

Thus measurement of the peak scattered light from a cloud of droplets can yield the droplet concentration. This is possible because the combined effects of scattering, droplet growth and sedimentation combine to give a definable signal at a fixed time and therefore a fixed particle size. The ratio of the peak scattered light signal to the initial number concentration of CCN is dependent only on the supersaturation.

3. APPARATUS

a. Thermal Diffusion Chamber

The thermal diffusion chamber is a cylindrical volume with an aspect ratio of 9.5 and a height of 0.8 cm. Aluminum plates of 0.7 cm thickness form the top and bottom of the chamber. These plates are covered with blotter paper which is kept wet by a system of holes and channels in each plate which are connected to a water reservoir. The wall of the chamber is a plexiglass ring of 1 cm thickness.

The temperature of the bottom plate is controlled by means of a thermoelectric cooler which forms part of a closed loop temperature regulator. Upper and lower surface temperatures are sensed with linear thermistor composites with differential accuracies of 0.1^o C. The closed loop temperature regulator is capable of maintaining the temperature difference between the upper and lower surfaces to within $\pm$ 0.05^o C of preset values over long periods of time, making it possible to accurately prescribe the supersaturation.

The chamber was originally designed to operate as a conventional system with provision for photographic recording of the droplets. All of the elements of this system have been preserved with the exception of a change in the light source from a 100 watt mercury-arc lamp to a 150 watt tungsten lamp. This change was made necessary by the choice of a silicon photodetector for the scattered light sensor which has much higher sensitivity at longer wave lengths. Also, continuous operation is difficult with the mercury lamp because of its short lifetime and changing characteristics with age. A collimated beam formed by the first lenses in the optical system illuminates a carefully machined slit which is imaged in the center of the chamber by a second lens. The resultant beam of light has a rectangular cross section 0.5 cm high and 0.2 cm wide. A section of the beam of a length of 1.5 cm is sufficiently well defined to prescribe the illuminated volume for photography. This volume is also the sensitive volume for the light scattering measurement. Recording of the droplets is accomplished by photographing the illuminated volume at a right angle with a modified oscilloscope camera using polaroid film.

b. Scattered Light Detector

Components of the scattered light detection system are a simple lens, a slit, and an integrated silicon photodetector-amplifier (Bell & Howell 509-50). The photodetector system looks at the previously described scattering volume from a forward scattering angle of 45^o. A lens serves to provide a large collection aperture and focuses the image of the droplet cloud on a slit carefully machined to eliminate light from sources other than the scattering volume. Located immediately behind the slit is the photodetector which collects the scattered light and provides a voltage output which is a linear function of the incident intensity.

c. Operating Systems

The operating system for controlling the air flow and electro-optics circuits consists of a time sequence generator, peak sample hold circuits, and an output multiplexor. A typical cycle of operation begins with a six second sample period during which the chamber is purged, the lamp intensity is raised from standby to full power and the peak sample hold circuits are reset to the level of the background scattered light as indicated by the photodetector. Following the sampling period is an 18 second interval during which the cloud forms and the scattered light peak is recorded by the peak sample hold. At the end of this cycle, the lamp intensity is reduced to the standby level. During the last part of the cycle, the top plate temperature signal and the temperature difference are transmitted to a digital voltmeter and printer for recording. Following the measurement cycle, the difference between the peak scattered light signal and the previously measured background value is recorded.

A complete four minute sequence consists of measurements at four supersaturations (currently programmed for 0.25, 0.5, 0.75, and 1.0% but readily adjustable to other S values). An internal clock allows spectra to be obtained at any desired intervals from five minutes to several hours. Manual operation for specific experimental purposes is also an option.

4. CALIBRATION

To test the system and determine the gain factors as a function of supersaturation, a calibration was performed against the usual photographic method. Over a period of several days, CCN spectra were measured simultaneously by the photographic method and also the scattered

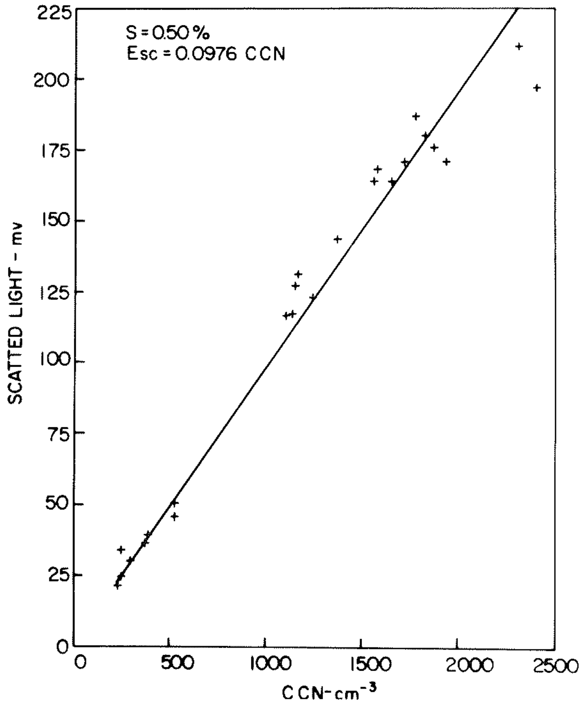

Fig. 1. Calibration curve at 0.5% supersaturation showing scattered light signal vs. photographic count.

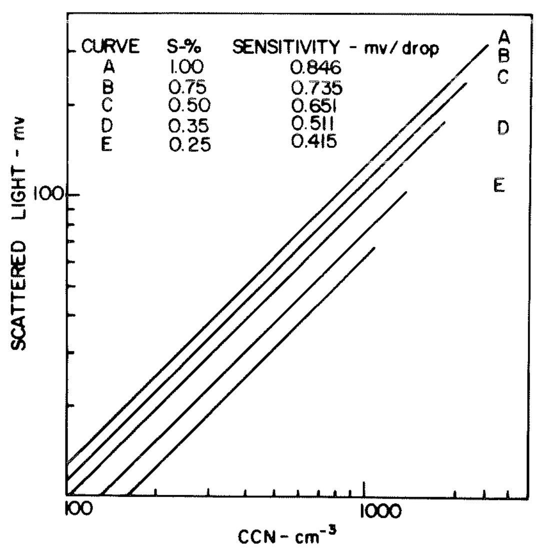

Fig. 2. Composite of calibrations at 5 supersaturations with tabulation of sensitivity vs. supersaturation.

light technique. It is desirable to perform the measurements over a range of conditions that give nucleus counts over concentration limits anticipated. Fig. 1 is a plot of the scattered light signal against the photographic count for 0.5% supersaturation. Also plotted is the least squares fit to the observations. As can be seen from the figure, the scattered light signal is linearly related to the concentration measured by the photographic method. At all supersaturations, virtually all of the observations are within 10% of the best fit straight line. Fig. 2 is a plot of the log of the response versus the log of the CCN concentration at the five supersaturations considered. Also indicated on the figure are the sensitivities (mv/droplet) for each supersaturation. Analysis of the sensitivity factors (F) show them to vary as

$$F = 0.13\ S^{0.504}. \quad (3)$$

This dependence is very clost to that predicted by equation 2.

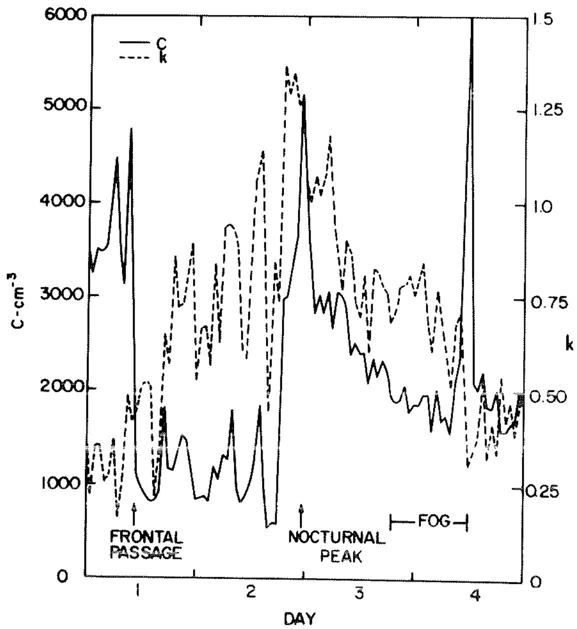

Fig. 3. CCN spectra data from a selected four day period of hourly measurements. Solid curve and left ordinate are the spectrum concentration factor c and the broken curve and right hand ordinate are the spectrum slope parameter k. Local midnights are indicated along the abscissa.

5. SYSTEM APPLICATION

Fig. 3 is a selected four day segment of hourly data taken with the light scattering CCN system showing the time variation of the concentration and slope parameters of the spectra $N = c\ S^k$. (Note that c is equal to the concentration cm^{-3} of CCN at S = 1%.)

On the first day, the passage of a cold front and the associated change of air mass appears as a sharp decrease in the CCN concentration from about 4000 cm^{-3} to 1000 cm^{-3} over a four hour period. The slopes of the spectra, however, show a slight increase during this period. The five days following the front were characterized by clear weather with winds primarily from a southerly direction. The second event of interest is the occurrence of a night peak on the second day of the sequence at about 11:00 P.M. During the five hours preceding the peak, the concentration rises from about 600 cm^{-3} to over 5000 cm^{-3} while the slope changes from 0.4 to 1.3. Lee and Jiusto (1974) in an experiment primarily concerned with the phenomena of the nocturnal peaks noted similar local occurrences in approximately one third of their daily data. The phenomenon was first noted in Australia by Twomey and Davidson (1970). A third major event occurred during days three and four of the sequence. At about 8:00 P.M. on day three a fog formed which lasted through noon of the next day. The interesting segment of data is the strong increase in the CCN concentration during the dissipating stage of the fog (9:00 A.M. to noon on day four). During this time the concentration rapidly increased from 1500 cm^{-3} to over 6000 cm^{-3} while the slope decreased from 0.7 to 0.3. A possible explanation for this result is that the evaporation of the fog drops resulted in the production of cloud nuclei either through some chemical reaction or by some type of nucleus breakup mechanism. The short life of the high concentrations is probably due to mixing by convection following the dissipation of the fog.

As the data clearly show, there are substantial temporal variations in the CCN spectra which would be missed if observations were made at longer time intervals. Clearly, the ability to measure the CCN spectra with good time resolution will be a valuable tool for studying the effect of large scale and local influences on CCN.

6. SUMMARY

The design and principle of operation of a continuous CCN counter have been described. The main features of the system are: 1) the use of a thermal gradient diffusion chamber in which supersaturation is accurately prescribed; 2) a compact shallow chamber with a short time to reach equilibrium at sequential supersaturation; 3) the automatic measurement of the droplet concentration by means of scattered light; 4) the capability of direct calibration by means of the usual photographic method; and 5) the ability to measure and record CCN spectra at fixed time intervals without the presence of an operator.

The instrument has been operated for long periods of time without interruption suggesting that it can be used for routine observations of detailed temporal variations in CCN. One modification planned for the system is a change in the control unit to allow for multiple observations at each supersaturation. This should make possible some smoothing of the data by averaging observations. Extended field studies using the instrument are being planned.

7. ACKNOWLEDGEMENTS

This research was sponsored by the Atmospheric Sciences Section of the National Science Foundation under Grant DES73-00410-A01.

7. REFERENCES

Hodkinson, J. R., and J. R. Greenfield, 1965: Response calculations for light-scattering aerosol counters and photometers. Applied Optics, 4, 1463-1474.

Lee, T. D., and J. E. Jiusto, 1974: Diurnal variations in cloud condensation nuclei. J. Geophys. Res., 79, 5651-5656.

Radke, L., and P. Hobbs, 1969: An automatic CCN counter. J. Appl. Meteor., 8, 105-109.

Squires, P., 1972: Diffusion chamber for measurement of cloud nuclei. J. Rech. Atmos., 6, 565-572.

Twomey, S., 1967: Remarks on the photographic counting of cloud nuclei. J. Rech. Atmos., 3, 85-90.

Twomey, S., and K. A. Davidson, 1970: Automatic observations of cloud nucleus concentrations. J. Atmos. Sci., 27, 1056-1059.

7.2.5

AN ATMOSPHERIC CLOUD PHYSICS LABORATORY FOR THE SPACE LABORATORY

R. Smith, J. Anderson, B. Schrick, C. Ellsworth

Marshall Space Flight Center
Marshall Space Flight Center, Alabama

M. Davis

National Center for Atmospheric Research
Boulder, Colorado

1. INTRODUCTION

An early (1968) NASA study on potential research and applications areas for future manned orbital missions contained a suggestion that atmospheric cloud microphysical phenomena might be a research area which would benefit from the low gravity environment at orbital altitudes. This low gravity environment would reduce convection and also considerably lengthen the time during which water droplets and particles freely suspended in the atmosphere of a cloud chamber could be observed. This would permit experiments closely approximating environmental conditions found in clouds to be performed for periods of time approaching those occurring in nature. Many artifacts introduced into the data obtained in ground based laboratories by
(1) Using higher than normal supersaturations to overcome time limitations due to fall-out, of
(2) Using artificial suspension techniques would be removed. A preliminary assessment of the potential advantages of a low gravity environment to the study of microphysical phenomena indicated that the concept should be studied in more detail; consequently, in 1971 NASA began studying the development of an Atmospheric Cloud Physics Laboratory (ACPL) for flight on the Spacelab/Shuttle. During the early phases of this development effort, members of the scientific community were contacted for suggestions of potential experiments in which the low gravity environment at orbital altitude could be used advantageously in advancing our knowledge of cloud microphysical processes. The experiments suggested by members of the science community were then grouped into 20 experiment classes, Table I, by a group of science advisors. The suggested experiments contained enough details to permit the compilation of a preliminary set of experimental chambers and ancillary equipment, Table II.

2. CURRENT STATUS

Analyses of the above data concluded in October 1974, showed that it was engineeringly and scientifically feasible to develop a multipurpose facility in which atmospheric scientists could perform laboratory experiments on cloud microphysical phenomena. Additional analyses, performed in November 1974 as a result of updated budget projection indicated that under a phased-development approach meaningful scientific experiments could be performed on the early Spacelab/ Shuttle flights with a much smaller complement of equipment if the scope of the research activities was restricted. On the basis of this preliminary decision to focus the research activities during the early flights on warm cloud processes, equipment requirements for the facility for the initial flights were reduced to those shown in Table III. Additional equipment required to conduct extensive experiments in cold cloud processes would be developed and incorporated in the facility on later flights. Engineering studies conducted since that time indicate that it is possible to package this initial facility in a standard Spacelab double rack, Figure 1. A concept for a schematic for this system is shown in Figure 2. In this concept, Spacelab cabin air (after proper conditioning) is used in the experiment chambers. The primary data gathering capabilities are an optical counter and two camera systems, used in conjunction with the continuous flow diffusion chamber and the static diffusion and expansion chambers, respectively.

3. CURRENT DEVELOPMENT ACTIVITIES

3.1 Engineering

At the present time, two distinct development efforts are underway. In the first effort, two aerospace companies are developing preliminary design concepts in parallel study efforts scheduled for completion in January 1977 at which time final design activities will be initiated so that the facility will be ready for flight in 1980.

3.2 Science

The second effort covers the scientific aspects of the Laboratory development program. The current scientific effort is in reality only a more formalized continuation of the assistance and advice provided by the scientific community in their responses to the original solicitation for suggested experiments. In February 1976, NASA sent notices to several thousand scientists soliciting their assistance and advice in the definition and planning of the scientific experiments to be conducted in the Laboratory. From responses to this solicitation, an Advisory Subcommittee of the Applications Steering Committee will be formed which will provide the required scientific support at the NASA Headquarters level.

The Atmospheric Cloud Physics Laboratory development is managed by a Task Team at the Marshall Space Flight Center in Alabama. This Task Team directs the efforts of the aerospace contractors performing the preliminary design work described above. To insure that the design of the facility is truly responsive to the needs of the scientific community and does possess the capabilities required to accomplish meaningful experiments, teams of cloud physicists are being formed by the Universities Space Research Association to: (1) Establish scientific goals for the facility; (2) Define the experiment programs needed to attain those goals; (3) Define specific experiments in detail; and (4) Establish the scientific functional requirements for the Laboratory and its components.

Detailed descriptions of specific experiments established by these teams will be used to specify what the capabilities of the Laboratory and each of its sub-systems and components must be if the experimental results are to be scientifically significant. These capabilities are then given to the aerospace contractors for use in their preliminary design efforts. The scientific functional requirements currently being used by the aerospace contractors are contained in Table IV. Some of these are extremely stringent and will tax the engineering capabilities of the contractors; however, modifications will only be made when the specifications cannot be achieved by acceptable engineering procedures within the current budgetary allocation. Even then, prior approval will be obtained from these science teams before any proposed changes dictated by engineering and/or cost are made. Conversely, should advances in knowledge or operational procedures prompt the science teams to recommend changes in the established requirements, cost impact studies will be performed by the preliminary design contractors to insure once again that the engineering aspects can be accomplished within budgetary limitations.

The lifetime of this facility is expected to be approximately 10 years. Throughout this period, system improvements will be analyzed and incorporated where appropriate. For example, extension of the capabilities to enable experimentation on the role of the ice phase in the atmosphere is clearly a necessary extension; however, scientific functional requirements for the Laboratory to be flown on the first Spacelab mission in 1980 must be firmly established by the end of 1977. For this reason, potential experiments for the early flights must be studied in detail within the next year to insure that the scientific functional requirements used by the engineering contractors truly define the functional capabilities required.

4. FUTURE SCIENCE INVOLVEMENT

In current plans, the Laboratory will be flown two times per year. Approximately two and a half years prior to each mission, NASA will notify the scientific community of the proposed flight date with a solicitation for proposals for experiments to be conducted in the Laboratory. Responses to this solicitation will be evaluated by a team of cloud physicists and experiments will be selected for the specific mission based on scientific merit. Principal Investigators and/or teams will then be funded for the work required to develop the proposed experiment for flight, for the consultation and participation during the flight, and for the post flight analysis of the data. Under this concept, up to four experiment teams may exist at any one time. Each of these teams may be working on a number of different experiments to be performed on a single flight. The exact number will depend on the flight schedule established for the mission based on the time available and the experiments of other disciplinary areas to be conducted on the mission.

5. CONCLUSIONS

Results of research and engineering analyses to date show that it is feasible to develop and fly on the first Spacelab mission a multipurpose laboratory in which experiments can be performed on the microphysical processes in atmospheric clouds.

Scientific functional requirements have been incorporated into the engineering design of the Laboratory to insure that it has the capability to produce data which is scientifically significant.

Procedures have been established which will insure that the Laboratory will be responsive to the needs of the cloud physics scientific community and that members of the cloud physics community will be actually involved during all phases of the program.

Table I. ACPL Experiment Classes

Condensation Nucleation	Saturation Vapor Pressure
Ice Nucleation	Adiabatic Cloud Expansion
Ice Multiplication	Ice Nuclei Memory
Charge Separation	Terrestrial Expansion Chamber Evaluation
Ice Crystal Growth Habits	Condensation Nuclei Memory
Scavenging	Nuclei Multiplication
Riming and Aggregation	Drop Collision Breakup
Droplet Ice Cloud Interactions	Coalescence Efficiencies
Homogeneous Nucleation	Static Diffusion Chamber Evaluation
Collision Induced Freezing	Unventilated Droplet Diffusion Coefficients

Table II. ACPL Preliminary Equipment List

SUPPORT SUBSYSTEMS

Thermal Control/Expendables Storage and Control

Thermal Control
Flow, Humidity, and Pressure Control
Expendable Storage
Cleansing Purge and Vent

Console

Console Support Structure
Power Control and Distribution
Console Panels and Drawers

Data Management

Control Processor Assembly
Tape Recorder Assembly
Master Control Assembly
Signal-Conditioning Electronics Assembly
Instrumentation and Display Assembly

EXPERIMENT-RELATED SUBSYSTEMS

Particle Generators

Wire Probe Retractor, Generator
Water Drop Impeller, Generator
Vibrating Orifice Droplet Generator
Evaporation/Condensation Aerosol Generator
Spray Atomization Nuclei Generator
Powder Dispersion Nuclei Generator
Particle Injector and Size Conditioner

Optical and Imaging Devices

Cine Camera (35mm)
Still Camera (35mm)
Microscope, Trinocular
Video Camera Assembly
Light Source
Anemometer
Stereo Microscope
IR Microscope

Particle Detectors And Characterizers

Optical Particle Counter
Pulse Height Analyzer
Condensation Nucleus Counter
Microporous Filters
Quartz Crystal Mass Monitor
Cascade Impactor
Electrical Aerosol Size Analyzer
Scatterometer
Liquid-Water Content Meter
Droplet Size Distribution Meter
Optical Thermoelectric Dew-Point Hygrometer
Electric Dew-Point Hygrometer

Table III. Initial ACPL - Equipment

SCIENTIFIC EQUIPMENT SUBSYSTEMS

EXPERIMENT CHAMBERS AND AEROSOL RESERVOIR

- EXPANSION CHAMBER
- CONTINUOUS FLOW DIFFUSION CHAMBER
- STATIC DIFFUSION LIQUID CHAMBER
- AEROSOL RESERVOIR

PARTICLE GENERATORS

- VIBRATING ORIFICE GENERATOR
- EVAPORATOR/CONDENSER GENERATOR
- AEROSOL CONDITIONING ASSEMBLY

PARTICLE DETECTORS AND CHARACTERIZERS

- OPTICAL PARTICLE COUNTER (& PHA)
- CONDENSATION NUCLEI COUNTER (AITKEN)
- ELECTROSTATIC AEROSOL SIZE ANALYZER
- MICROPOROUS FILTER

OPTICAL & IMAGING DEVICES

- CAMERA
- OPTICS
- LIGHT SOURCES

FLIGHT SUPPORT SUBSYSTEMS

THERMAL & FLUID CONTROL

- THERMOELECTRIC COOLER ASSEMBLIES
- HEAT EXCHANGER/COLD PLATE
- MOTOR/PUMP
- COOLANT VALVES
- COOLANT FLUID
- EXPANSION CHAMBER/RESERVOIR
- COOLANT LINES
- GAS PRE-CONDITIONING MODULE
- GAS POST-CONDITIONING MODULE
- HUMIDIFIER
- AEROSOL DILUTER
- MIXER
- VACUUM PUMP
- TUBING
- GAS VALVES

DATA MANAGEMENT

- INTERFACE CONTROL UNIT
- DISPLAY AND CONTROLS

POWER CONDITIONING

- DC/AC CONVERTER
- DC/DC CONVERTER
- REGULATOR – DC/DC CONVERTER
- POWER DISTRIBUTION MODULE
- ELECTRICAL LINES

SUPPORT EQUIPMENT

- CONSOLE STRUCTURE
- STORAGE CONTAINERS
- TOOLS/TEST EQUIPMENT

Table IV. Scientific Functional Requirements

1. Expansion Chamber

a. Physical Dimensions

The chamber design must allow the chamber to be opened and reclosed within 1 hour during ground-based testing. In orbit, it must allow for occasional cleaning of the windows and the insertion or extraction of small pieces of hardware or test material. (Examples include film strips or scales for verification of optics alignment, ice crystals of 1cm radius grown on fibers and tubes for extracting drops from the central volume and routing them to an impactor). During experiment operation, condensation on the windows and walls will not be permissible. The sensitive experimental volume in the chamber must be defined by the optics, lighting, and camera in such a way that 3% accuracy can be achieved in counting drops with diameters of $\geq 2\mu m$ at concentrations from 100-1000 cm^{-3}. The volume and thermal characteristics of the walls and ends must be such that the experimental volume discussed above remains adiabatic for up to 200 seconds during expansions with cooling rates of 1°C/min or less. It must remain adiabatic for up to 100 seconds at faster cooling rates.

NASA recognizes the fact that real time measurement of the liquid water content within the expansion chamber is currently beyond the state-of-the-art. Thus, these specifications on the adiabatic condition within the sensitive volume apply only to dry conditions. However, when the system is in use, attempts will be made to follow wet adiabats so the expander, pressure sensor, and control configuration must be designed to facilitate these efforts. This implies that the system must sense the pressure rise induced by condensation and correct for it in the manner dictated by the computer.

b. Operating Range

(1) Initial Conditions

T=constant between 0.5°C and Spacelab ambient minus 1.0°C. T of sensitive volume must be uniform and the experimenter must know what the temperature is to within ±0.014°C.

P=constant between 400 mb and Spacelab ambient. P in sensitive volume must be constant to within ±0.05 mb and measurable to within ±0.05 mg (relative) and ±0.5 mb (absolute). These conditions on temperature and pressure must be maintained for durations in excess of 30 minutes.

For most experimentation, it is expected that the chamber will be flushed until the water vapor content of the air is known to within one part in 10^4 (as calculated from output of the humidifier). The chamber will then be allowed to "settle" until residual air motions have decayed to less than 0.1cm/second.

(2) During Expansion

Pressure changes during single expansions may range from 30 to 350 mb. The difference between the current pressure and the initial pressure must be known to ±0.1mb.

The temperature range and cooling rates over which the chamber must operate are displayed in Table IV-1. The precision with which the experiment computer must specify the temperature curves is also included. An additional requirement which is not included in the table arises because some proposed experiments require cloud formation at temperatures as close as possible to the initial conditions in order to minimize errors. Others require that the cloud be maintained and observed for long periods of time after it has been formed. This implies that the system must be able to reach the maximum cooling rate quickly, i.e., before the temperature runs 0.5°C, and then after about 90 seconds at the maximum rate, it must be able to taper off and hold a low cooling rate (0.5°C/min) for up to 60 minutes.

Table IV-1. Expansion Chamber Operating Range

Case	Slope (°C/Min)	Temp. Range (°C)	Specify Input T(t) Curve (that comes from computer readout)	Duration (min)
A	0	+25 to -25	±.005	90
B	0.5	+25 to -25	±.01	90
C	1.2	+25 to -20	±.01	30
D	6	+25 to -15	±.05	2.5

c. Optics and Lighting System

In addition to the specifications listed above, the system must operate at a maximum rate of 1 frame per second for periods of up to ½hour per experiment. The system cannot introduce either IR or UV radiation into the sample volume.

2. Continuous Flow Diffusion (CFD) Chamber

a. Physical Dimensions

(1) Width of the chamber must be such that the sample never comes within 6h of the "sidewalls", h is the plate separation.

(2) The particle-free and sample air should spend at least five time constants for thermal equilibration, τ_H, between dry plates at the inlet end of the CFD, where,

$$\tau_H = \frac{h^2}{\pi^2 K_H}$$

h is the plate separation, and K_H is the diffusivity of heat in the gas mixture present in the chamber. The relevant velocity to use in fulfilling this criterion is the axial value.

(3) Similarly, the same air should be allowed five time constants for humidity equilibration, τ_w, in the subsequent zone of the CFD, where only the colder plate is wet;

$$\tau_w = \frac{h^2}{\pi^2 K_w}$$

where K_w is the diffusivity of water vapor in the gas mixture present in the chamber.

(4) The same air must spend at least seven τ_w in the final zone of the CFD, where supersaturation equilibration is achieved by having both plates wet.

(5) The sample must spend enough additional time between the wet plates for the nuclei to grow drops to a size sufficiently greater than their critical size so that they can be discriminated from inactivated haze drops. In practice this means that nuclei with critical supersaturations, S_c, of $0.99S_m$ must have enough time to grow above their r_c or to at least be easily distinguishable by the optical counter from those nuclei with $S_c \geqq S_m$. S_m is the maximum supersaturation in the chamber. In cases where r_c is less than the minimum detectable size of the optical counter, the drops must be grown into the size range of the optical counter. Empirical work has indicated that these times should be about 50 seconds at 0.1%, 25 seconds at 0.35%, and 5 seconds at 1%.

(6) The chamber must be able to operate in the 1-g environment in the vertical mode (plates vertical, flow axis horizontal).

(7) It must be possible to clean or replace the wicking surfaces between flights.

b. Thermal, Pressure, and Air Flow

(1) The temperature difference between the plates and the temperature of the plates must be known to an accuracy such that the maximum operating supersaturation of the chamber can be computed to 1% accuracy over the range of supersaturation 0.1% to 3% (ΔT to about 0.1°C, T to about 0.1°C).

(2) The total flow into the particle counter must be sufficient to avoid detection problems due to exceeding the maximum allowable pulse length. For the Royco, this lower limit is $15 cm^3 sec^{-1}$.

(3) All nuclei of interest must be allowed to activate within the humidity contour where supersaturation is $0.99S_m$ or greater. Particularly, phoretic effects, which move the nuclei toward the cold plate at a velocity about $3 \times 10^{-3} \sqrt{S_m\%}$, cm s^{-1}, must not be allowed to violate this condition.

(4) Depletion of the water vapor available for activation and growth must be avoided by restricting the areal number density of droplets (in the plane parallel to the plates) such that

$$\int_{\text{All } r} r\sigma(r)\,dr \leqq \frac{4\times 10^{-3}}{h}$$

until all nuclei of interest have been activated. Regarding the sample lamina as a 2-dimensional surface, $\sigma(r)$ is the number of droplets per square centimeter per radius increment.

(5) The sample flow f can be varied to meet the above requirements but it must always be known to 1% accuracy.

(6) The chamber must be able to handle concentrations ranging from $2000/cm^3$ at the higher supersaturations to as low as $10 cm^{-3}$ at the lower supersaturations. The sample flow should be chosen to meet the above requirements and to maximize the counting efficiency.

(7) The particle-free air must be dry enough to avoid transient supersaturations.

(8) The sample must never experience expansions or temperature differentials which would generate supersaturations greater than or equal to 0.001%.

3. Static Diffusion Chamber (SDL) (Liquid)

a. Physical Dimensions

Where possible, the design of the static diffusion (liquid) chamber should mimic the design of SDL chambers commonly used in earth-based studies. This will facilitate the carry-over of results from the 0-g to the 1-g chambers. The design must allow the wicking surfaces to be cleaned or changed between flights.

b. Thermal and Pressure

The unit must be operable over a range of maximum saturation ratios from 1.0001 to 1.06. The saturation ratio must be known to within ±5% throughout the operating range above 1.001. It must be possible to maintain these conditions for periods of time up to 1200 seconds.

c. Data

The chamber must contain a "sensitive" volume of at least $0.1 cm^3$ which is at 98% of S_m or better. A camera and optics system must be provided which will photograph the volume and allow all drops of radius 1 m to be counted. Maximum framing rate: 16 f/sec.

4. Static Diffusion Ice Chamber

Specifications TBD.

5. Humidifier

a. Physical Dimensions

The physical dimensions must be such that gas leaving the humidifier at rates up to 1 liter per second has a relative humidity of 99.99% at any specified temperature between 0.5°C and Spacelab ambient. It must be constructed so that wicking surfaces can be cleaned or changed on the ground between flights.

b. Thermal and Pressure

These properties must be controlled so that no condensation can occur within the humidifier which would cause water droplets to leave the chamber in the gas, especially during flushing and filling (changing) of the expansion chamber. This implies that the pressure must be stable to within 0.1mb within the unit. If it is decided to mix the aerosol with the air stream before it enters the humidifier, the formation of haze particles (up to $10^3 cm^{-3}$) would, of course, be allowed.

6. Aerosol Characterization Tests

Within the Laboratory, aerosols will be found throughout the size and number density range indicated in Figure IV-1. Instrumentation for characterizing this aerosol must be capable of resolving the diameter to within a quarter decade and the number density to within a factor of 2. Number resolution should be even better for low values of N. In addition, provision must be made for collecting aerosol samples and storing them under an inert gas for later examination by electron microscopy.

7. Particle Generators

The ACPL facility will include two particle generators and a storage/conditioning/mixing capability plus a capability for the addition of an experimenter provided particle generation system. The basic design must be such that it will handle not only the two systems whose scientific functional requirements are listed below, but also a wide range of potential generation systems. More likely, both hydrophobic and hygrophilic aerosols will be required for some experiments, e.g., $(NH_4)_2SO_4$, AgI, latex, and Teflon.

Figure IV-1 shows the range of aerosols that may be required. Since generators often produce more than 10^6 particles per cubic centimeter, a dilution system capable of dilution ratios between 10^6 to 1 and 10^2 to 1 in 3 or 4 steps will be required. In some instances, a fresh aerosol must be generated for each experiment; in others the same aerosol (less than 5% change) must be stored for periods up to 2 hours for use in sequential tests.

a. NaCl Particles

A polydisperse NaCl aerosol is required with a distribution which mimics $N=CS^k$ in such a manner that the integral of dN/dS between S=0 and S=1% has values within the range of 50 to 1000 particles per cubic centimeter. The concentration of particles with diameters larger than 0.05 should not exceed 1 to 10 per cubic centimeter. These particles should not be charged.

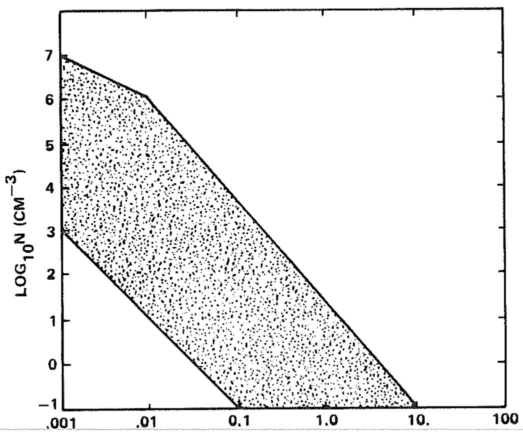

DIAMETER

FIGURE IV–I

b. SO_2 Particles

Some experiments may require particles generated by irradiation of SO_2. Such a system generates large numbers of small particles. Different particle size distributions are obtained through coagulation processes. The system should be capable of providing sets of particles (batches) whose mean diameters range from 0.001 to 1μm. It is expected that this generator will also be used to check air cleanliness in flight. Clean air will be irradiated and allowed to rest in the unit. If trace gases are present which take part in gas-to-particle conversion processes, particles will be produced which will be easily detected in one of the cloud forming chambers.

c. Add-On Generators

It is expected that individual experiments will require specialized aerosols so an interface must be provided for the Principal Investigator to insert his own generator. The interface must be designed to provide maximum flexibility and a complete description provided for the experimenter so he may adequately design his system.

8. General Requirements

No materials or procedures will be used during manufacture and test that will contaminate the experiments.

Surface active materials and gases which take part in gas-to-particle reactions will not be acceptable within the ACPL system.

Design should provide the capability of furnishing aerosol of identical characteristics to each test chamber.

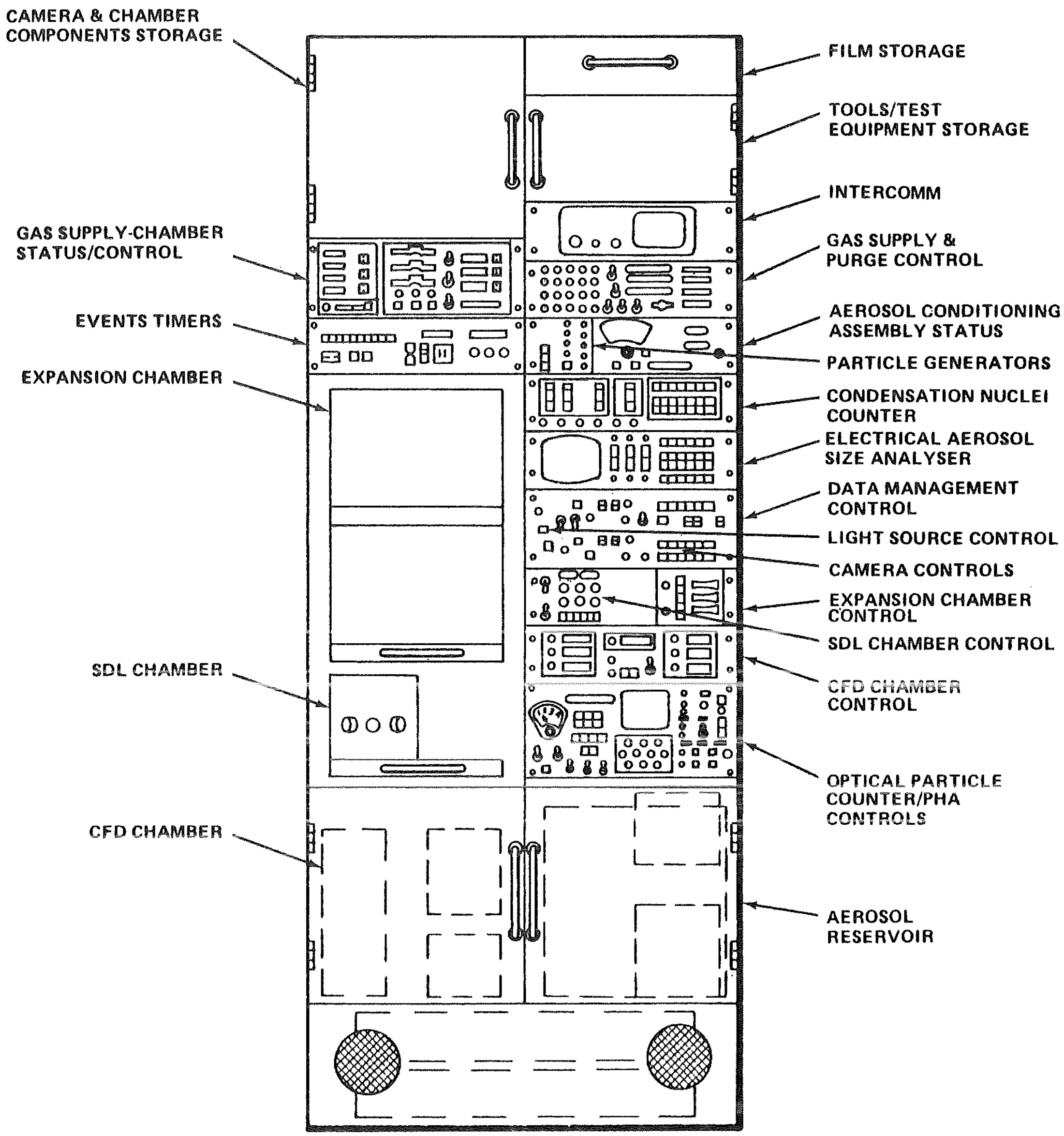

FIGURE 1. INITIAL ACPL CONFIGURATION

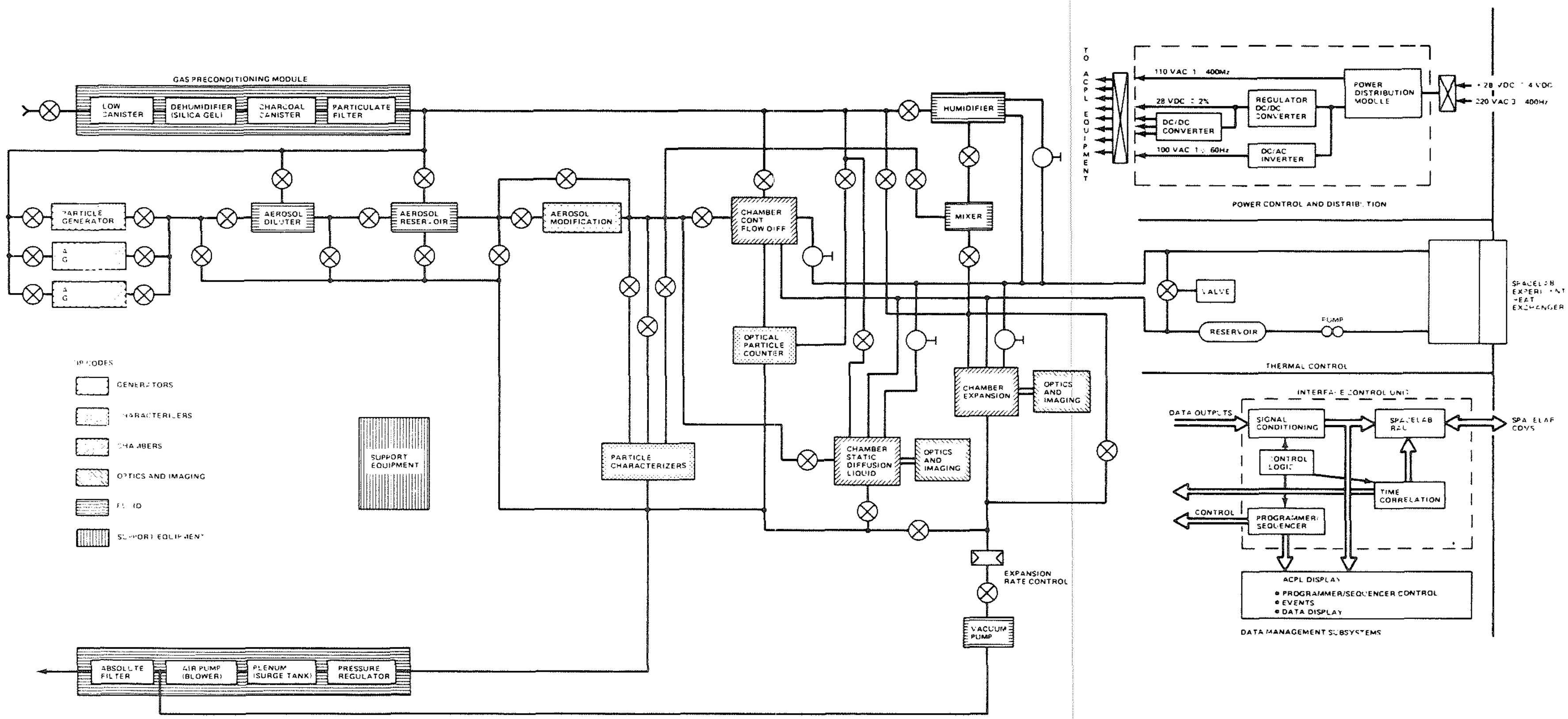

FIGURE 2. ACPL SYSTEMS SCHEMATIC

AIRCRAFT AEROSOL SAMPLING ERRORS

Gerald J. Mulvey and John D. Sheaffer
Department of Atmospheric Science
Colorado State University
Fort Collins, Colorado

1. INTRODUCTION

When one attempts to obtain a representative sample of both natural and artificial aerosols from high speed sampling platforms, size sorting and concentration errors often result. These errors will distort the scientific inferences drawn from the resulting data set. Previous studies of the errors of aerosol sampling nozzles have been confined mainly to air pollution problems, in particular to exhaust dust stack sampling (Hemeon and Haines, 1954; Watson, 1954; Vitols, 1966; Bodzioch, 1959; Dennis et al, 1957; Davies, 1968; and others). Comprehensive reviews of the subject were made by Fuchs (1975) and Belyaev and Levin (1974). As the need for quantative measurements of atmospheric dust loading as well as Aitken, cloud condensation and ice nuclei from aircraft increases the sampling errors induced by probe design alignment and operation must be considered. In this paper we will examine the magnitude of aircraft aerosol sampling errors resulting from the three primary sample distortion mechanisms - anisokinesis; anisoaxiallity; and internal wall deposition. We then address the problem of a realistic design which minimizes these errors.

An inline type of aerosol sampling system is evaluated. This system, the CSU inline aerosol sampling system (IASS) (Mulvey and Sheaffer, 1976) consists of specially constructed intake nozzles, plexiglass filter holder blocks, and mechanisms which raise and lock the sampling blocks into place. The nozzle and filter holder block designs are shown in Figs. 1 and 2.

2. ANISOKINESIS

It has long been recognized that the condition of anisokinesis (a mis-match between the free stream and nozzle entry velocities) cause errors in the representativeness of the aerosol spectra collected. This type of error is accentuated during sampling from a high speed platform. Because regions of local acceleration can occur at various positions within the near

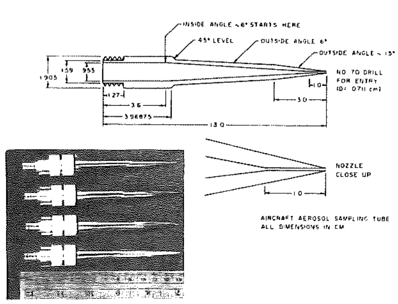

Fig. 1. Inline aerosol sampling system intake probes.

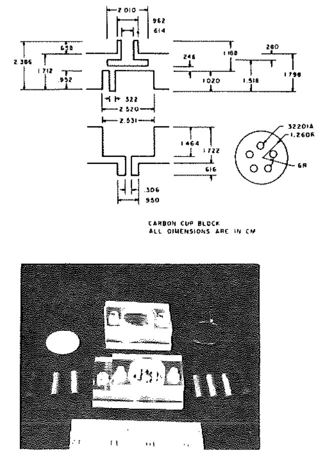

Fig. 2. Carbon cup filters and filter support assembly.

field of the aircraft skin at various flight attitudes and yaws, and because adjustment of the nozzle velocity to the true air speed of the aircraft may be insufficient to achieve true isokinesis, sampling errors can occur. To achieve true isokinesis, a detailed measurement of the flow characteristics in the immediate vicinity of the sampling intake is necessary. Such measurements in the region of the IASS position above the top skin of the Aero Commander 500-B indicated that a local acceleration was increasing the air velocity by some 20-30% above the true airspeed. Errors from this type of anisokinesis can be eliminated by using a small computer or analogue circuitry to control the nozzle flowrate. The controller should take into account the pressure, temperature, indicated airspeed and suitable empirical correction factors to account for the pitot-static probe and intake nozzle position and attitude. If it is not possible or desirable to correct for this error type during sampling, correction factors (aspiration coefficients) may be calculated for various sized particles based on the particle's Stokes Number and the velocity mis-match. The proper method of calculating the aspiration coefficient, however, has not been clearly established.

The semi-empirical formulation of Watson (1954)

$$* \quad A_i = \frac{U_o}{U}\left(1 + f(p)\left[\left(\frac{\overline{U}}{U_o}\right)^{1/2} - 1\right]\right)^2$$

is often given in texts on air pollution as a correction for anisokinessis in stack sampling, e.g., Stern (1968). More recently, Belyaev and Levin (1973) have suggested an alternate formulation for the aspiration coefficient based on theoretical as well as emphirical considerations.

$$A_i = 1 + \left(\frac{U_o}{U} - 1\right)\left(1 - \left(1 + \left(2.0 + 0.617\,\frac{\overline{U}}{U_o}\right) Stk\right)^{-1}\right)$$

*for explanation of the notation see Symbols List

Badziock (1959) also developed an aspiration coefficient formulation

$$A_i\ (U_o/U)\ \alpha + (1 - \alpha)$$

where

$$\alpha = (1 - \exp\ [(6.0\ -1.6D)/V_sU/g)])/\frac{6.0\ -1.6D}{V_sU/\ g}$$

But his coefficients in the micron and sub-micron size ranges are very much smaller than the coefficients for the other authors. Work by Parungo et al (1974) appears to support Watson's formulation, but the controversy is still open. A comparison between the formulation of Watson and that of Belyaev and Levin was obtained by evaluating their respective expressions for typical sampling conditions of the IASS in place on board the 500-B when corrections for local accelerations were not made. The results are shown in Fig. 3 for typical density particles. As can be seen, the differences between the two formulations are maximum in the submicron range (0.3 - 0.7 μm). They both indicate a maximum error of 28%, which is the velocity mismatch, in the larger particle size range. The coefficients also converge with increasing and decreasing particle size.

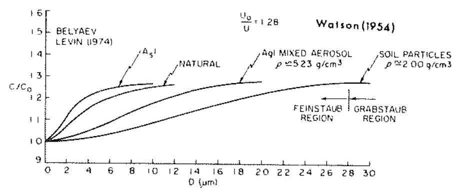

Fig. 3. Anisokinetic sampling errors following Belyaev and Levin (1974) and Watson (1954).

One aspect of anisokinetic sampling errors which is often ignored is the effect of turbulent wind fluctuations. To the author's knowledge, only Belyaev and Levin (1964) attempted to formulate an aspiration coefficient to correct for these errors. The coefficient was derived from the steady state aspiration coefficient formulation.

$$A_i = 1.0 + \frac{\gamma}{2}\ [\frac{1}{1.0 + 2\ Stk_o(1.3 - \gamma)} - \frac{1}{1.0 + 2\ Stk\ (1.3 + \gamma)}]$$

In order for the estimate of the magnitude of these errors to be made, $\gamma = \Delta U/U$ must be known, as well as the Stokes Numbers of the particles being sampled.

3. ANISOAXIALLITY

Anisoaxiallity errors result when the axis of the intake probe is not parallel to the average flow directions. Errors of this class have received the least investigation. Some work has been done in this area by Mayhood and Langstroth. This has been reported by Watson (1954). Fuchs (1975) has also given this problem some attention. He has classified the results given by Watson as unreliable and has proposed his own aspiration coefficient formula for small angles: $A_a = 1.0\text{-}4.0 \sin \theta\ Stk/\pi$.

An alternate approach to the problem is to equate the stopping distance of a particle to the transit time of a particle across the nozzle entry. It should be noted here that the data given by Watson was obtained using a nozzle of unknown entry diameter and the formulation given by Fuchs has no nozzle entry diameter dependence, while the transit time approach is dependent on both the nozzle entry diameter and the particle size. Work by Belyaev and Levin tends to support the work of Mayhood and Langstroth in that their results show an error 3.5% or less is encountered provided the angle of attack does not exceed 15°. Again the particulars of the sampling system and aerosols were not reported. A comparison between the data given by Watson and the proposed formulation of Fuchs is shown in Fig. 4. The results of the transit time approach are shown in Fig. 5 for the intake nozzle of the IASS at typical sampling conditions. A comparison of Figs. 4 and 5 shows a discrepancy at large particle sizes. If we interpret Fig. 5 as the values of θ where $C/C_o = 0$ the agreement between Fuchs's approach and the transit approach is good. Also it is of interest to note that all three methods agree that for small particles the error becomes small.

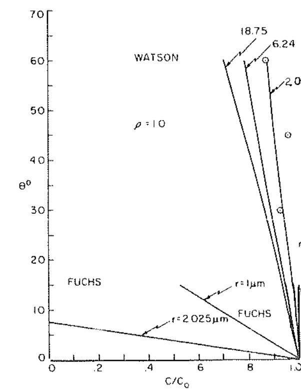

Fig. 4. Anisoaxial sampling errors following Fuchs (1974) and experimental data given by Watson (1954).

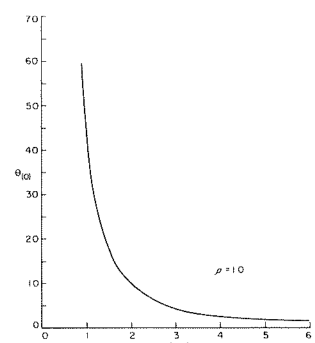

Fig. 5. Critical angle for collection from transit time approach.

4. INTERNAL DEPOSITION ERROR

This type of error results from the impaction and deposition of aerosols on the intake nozzle wall, on the wall of the tubing directing the flow to the collection device and on members supporting the collection device. Experiments to measure depositional losses of aerosol material on the internal walls of the nozzle-filter block assembly were conducted in the CSU Simulation Lab vertical wind tunnel. Although the wind tunnel flow was not laminar or uniform, this test set-up did allow a simulation of high speed sampling conditions using an easily analyzed tracer particle of small size. A CSU Skyfire silver iodide smoke generator (Grant, 1971) was used to produce the test aerosol. For these tests, the sampling system was inserted into a mock housing foil, and sampling rates were monitored using a rotometer. The tunnel was operated at maximum velocity ($U \approx 45$m/sec).

A quantitative determination was made of the AgI deposited in the interior surfaces of the probes and sampling blocks. The deposited AgI was taken up by filling the respective components with an appropriate solvent. High purity three molar nitric acid was adequate for this purpose in the plexiglass cup holders, whereas acetone was more suitable for the stainless steel probes. The silver content of these solution extracts was measured by flameless atomic absorption spectroscopy (precision $\pm$ 5%). By normalizing the measured silver concentration with the volume of solvent used to fill and rinse the various components, the amount of silver deposited in each was computed. Tests showed that the silver blank levels of the surfaces and solvent used were negligible. The tests also showed that the removal of silver by the above method was essentially complete.

The amount of Ag collected in the porous graphite filtration cups was determined in a similar manner. The Ag in the filters was removed by extended (4 hour) soaking in hot concentrated high purity nitric acid in teflon breakers. This extract was also analyzed for silver using flameless atomic absorption spectroscopy. A complete description giving details and establishing the analytical validity of the above techniques is given in Sheaffer and Mulvey (1976).

A summary of these investigations is shown in Table 1. Results show that the major losses usually occur in the probe nozzle and that the percent lost increases with increasing velocity. This is compatible with physical reasoning since the major velocity changes are restricted to the nozzle tip. Also the internal boundary layer thickness is considerably thinned by nozzle velocity increases. The intensity of internal deposition near the nozzle entrance was pointed out by Belyaev and Levin (1974) from their 1970 paper. They recommend that a nozzle entrance diameter be greater than 10 mm to avoid entrance blockage. This is not always practical for aircraft aerosol sampling as this would require a large flow rate which may be beyond the capability of the aircraft vacuum system.

A theoretical estimate of internal wall deposition was made by considering a uniform aerosol diffusing through the probe's internal boundary layer to a perfectly adhering wall surface. The procedure was to calculate the particle diffusivity in air and to determine the deposition rate per unit area, R_o, following Davis (1966): $R_o = D\, C^*/\delta^*$. To do this, the boundary layer thickness δ^* had to be determined as a function of distance down the probe axis. This was accomplished using a combination of the velocity profile determination methods of Langhaar (1942) and Millsaps and Pohlhausen (1953). The application of these methods to the problem of flow in a probe nozzle will be discussed in a future publication (Mulvey and Sheaffer, 1976). Then one could evaluate the deposition rate for various sections of the probe surface.

The magnitude of wall deposition for typical sampling conditions was determined to be at least two orders of magnitude below what was experimentally observed. This seems reasonable in light of the turbulent nature of the flow in the experimental setup. Such turbulence would have caused large angular and velocity deviations, thus enhancing impaction and deposition in the intake nozzle. In view of the errors in theoretical calculations and the nature of the flow durthe experimental phase, it is believed that the wall depositional losses during actual flight sampling would not be as high as those experimentally observed.

5. SYSTEM DESIGN

The sampler intake should be located outside of the aircraft boundary layer in the free stream flow upwind of engine or cabin exhausts to eliminate aircraft contamination. The alignment should be such as to approximate isoaxial flow during sampling flight attitude. An inline intergral probe nozzle-collection device system should be employed to minimize impaction and deposition. The probe should also be heated to

Table 1. Summary of internal deposition studies

Set Number	Nozzle Velocity	Total Amount of Ag Collected	Amount of Ag in Probe	Amount of Ag in Holder	Percent Lost	Percent Lost in Probe
Y1	106.1m/s	1667 ng	415 ng	42 ng	27	91
S1	101.2	1202	183	43	19	81
Q1	67.4	816	107	45	19	70
Q2	61.3	645	89	32	19	74
M2	60.4	561	53	43	17	55
I3	49.5	486	31	59	19	20
J3	47.0	803	57	53	14	52

help minimize deposition and icing. To eliminate the nozzle wall rebound phenomenon and reduce flow distortions the thin wall criteria of Belyaev and Levin (1974) should be used. Their criteria are (1) relative edge thickness $E/d \leq .05$, (2) relative wall thickness $D/d \leq 1.1$, and (3) taper angle $\alpha^* \leq 15°$. Beyond these general considerations a realistic probe design must take into account a broad range of factors. Some of the factors are (1) aerosol spectrum to be sampled, (2) sampling environment, (3) collection device, and (4) economical and technological feasibility.

The size spectrum of aerosols to be sampled is the primary factor controlling the degree of anisokinetic and anisoaxial flow which can be tolerated for a given percent error. Aerosols of sizes less than 0.1 μm (within the feinstaub region) can be collected at relatively large anisokinetic and anisoaxial values but will suffer relatively large internal depositional losses. The coaser particles, within the grabstaub region, are just the opposite and require more attention to be paid to maintaining isokinetic and isoaxial flow conditions. The next three factors, the sampling environment, the type of collection device and the economical and technological feasibility interact in complex modes with each other requiring various compromises to be made. To illuminate this, let us consider a case where cold cloud penetrations to sample for ice nuclei over the central U.S.A. are to be made using membrane filters as a collection device.

Because the aerosol size spectrum is quite broad one should sample isokinetically and isoaxially with a fairly large diameter intake probe. The large diameter intake will also allow de-icing equipment to be istalled on the probe. This would also reduce internal wall deposition. However, the large probe diameter would require a large volume flux of air to keep the probe isokinetic. This might not be feasible in light of the pressure drop required, in order to maintain the flow rate, for a 0.1 μm pore size filter. Also in order to keep the probe heated and free of ice the thin wall criteria may be impossible to meet. Alternately, making the inlet diameter small enough to meet the thin wall criteria and the flow requirements may rule out de-icing equipment and/or raise the construction costs above the desired limits. Thus, for a given sampling project a series of compromises must be made in order to obtain a usuable probe with limited inherent sampling errors.

6. SUMMARY AND IMPLICATIONS

Typical error types usually encountered in aerosol sampling have been outlined and investigated utilizing a combination of experimental, theoretical and semi-emphirical approaches. The results indicate that for quantative measurements of small aerosols such as some types of silver iodide generator effluent and Aitken nuclei, internal deposition can be the primary source of sampling error. When collection of larger particles such as "giant cloud nuclei" and sea salt nuclei are attempted, representative samples may not be obtained if anisokinetic and anisoxail errors are not corrected. Both of the above situations can be encountered when sampling for particles with a broad size such as ice nuclei and cloud condensation nuclei. A realistic approach to probe design as to minimize the errors encountered in sampling broad spectra aerosols, has also been presented.

This represents only an outline of the steps required to obtain representative samples of aerosols from aircraft.

7. LIST OF SYMBOLS

A	aspiration coefficients
C	aerosol concentration as sampled
C_o	aerosol concentration in air
d	nozzle entry diameter
D	outer diameter of the nozzle
D*	particle diffusivity
E	nozzle entry wall thickness
f(p)	empirical function of modified Stokes parameter = $\frac{4r^2\rho U_o}{18\nu D}$
g	acceleration of gravity
r	particle radius
R_o	deposition rate per unit area
Stk	Stokes number = $\frac{V_s U_o}{2rg}$
U	nozzle entry velocity
U_o	free stream velocity
V_s	terminal fall velocity of the particle
α	coefficient of Bodziock's aspiration formula
γ	nozzle entry velocity fluctuation
Δ	acceptable error due to rebound phenomenon
δ*	internal boundary layer thickness
θ	angle of attack of the probe
ρ	particle density

8. ACKNOWLEDGMENTS

We would like to thank Dr. Dennis Garvey and Mr. Cleon Swain for their help in the conduct of the experimental deposition studies. This work was performed under support of the National Science Foundation and RANN through Grants ERT 71-01885-A03 and GI34813. The opinions expressed in this paper do not necessarily represent those of the National Science Foundation and RANN.

9. REFERENCES

Belyaev, S., and L. Levin, 1974: Techniques for collection of representative aerosol samples. Aerosol Science, Vol. 5, 325-338.

Bodzioch, S., 1959: Collection of gas borne dust particles by means of an aspirated sampling nozzle. British Journal of Applied Physics, Vol 5, 325-338.

Davies, C., 1966: Aerosol Science, Acedamic Press, London, Great Britain.

Davies, C., 1968: The entry of aerosols into sampling tubes and heads. British Journal of Applied Physics, Ser. 2., Vol. 1, 912-932.

Dennis R., W. Samples, D. Anderson, and L. Silverman, 1957: Isokinetic sampling probes. Industrial and Engineering Chemistry, Vol 49, No. 2, Feb., 294-302.

Fuchs, N., 1975: Review papers: Sampling of aerosols. Atmospheric Environment, Vol. 9, 697-707.

Grant, L., 1971: The second international workshop on Condensation and ice nuclei. Report on Workshop Goals, Program Instruments, Observations and Preliminary Analysis, 146-147

Hemeon, W., and G. Haines, 1954: The magnitude of errors in stack dust sampling. Air Repair, Vol. 4, No. 3, Nov., 159-164.

Langhaar, H., 1942: Steady flow in the transition length of a straight tube. Journal of Applied Mechanics, Vol. 9, No. 2, June, A-55 - A-58.

Millsaps, K., and K. Polhausen, 1953: Thermal distribution in Jeffery-Hamel flows between nonparallel plane walls. Journal of the Aeronautical Sciences, Vol. 20, March, 187-196.

Mulvey, G., and J. Sheaffer, 1976: In preparation.

Parungo, F., E. Ackerman, and R. Pueschel, 1974: AgI ice nuclei: Physical and chemical properties depending on their generating procedure. Proceedings of the 4th Conference on Weather Modification, Nov., 165-172.

Shaeffer, J., and G. Mulvey, 1976: In preparation.

Stern A., 1968: Air Pollution. Academic Press.

Vitols, V., 1966: Theoretical limits of errors due to anisokinetic sampling of particulate matter. Journal of the Air Pollution Control Association, Vol. 16, No. 2, Feb. 79-84.

Watson, H., 1954: Errors due to anisokinetic sampling of aerosols. American Industrial Hygienic Association Quarterly, March, 15, 21-25.

Wilcox, J., 1956: Isokinetic flow and sampling. Journal of the Air Pollution Control Association, Vol. 5, No. 4, Feb. pp 226 and 245.

7.2.7

IN SITU MEASUREMENT OF ICE CRYSTAL CONCENTRATIONS USING A LASER-TELEVISION-MEMORY SYSTEM

Lyle E. Lilie, Thomas C. Grove, and Dennis M. Garvey

Department of Atmospheric Science
Colorado State University
Fort Collins, Colorado

1. BACKGROUND

The development at CSU of a dynamic cloud chamber operating at pressures lower than ambient brought about a need for an ice crystal detection system which would function without direct contact with the ice crystals in the chamber. In the past, ice crystals in large laboratory chambers such as the CSU Isothermal Chamber, Garvey (1975), have been counted through the use of microscope slides. Ice crystals are allowed to fall on the slides which are removed from the chamber, placed in a cooled microscope, and counted. It was recognized, however, that dynamic chamber operation would present major problems in transferring the slides from the lower pressure environment inside the chamber to the higher pressure laboratory environment. One approach to this problem was taken by Dunsmore and Steele (1974). They used a television camera with a long focal lens focused on a microscope slide located inside the chamber. Since they could not change the slide during the experiment, only low concentrations could be measured. It was decided in conversations with Dr. A. Gagin of the Hebrew University in Jerusalem that an approach utilizing a television camera to directly image free falling crystals would have an advantage over simply remoting the slide technique. The following system was developed to measure ice crystal concentrations during dynamic and isothermal operations of the CSU Controlled Slow Expansion Cloud Chamber (CSECC).

2. MEASUREMENT SYSTEM

The concentration measuring system consists of three major parts; light source, television camera, and video processor. The light source is a 50 milliwatt helium-neon laser, Spectra Physics #125A. The output beam of the laser is expanded and collimated to a 5.0 cm diameter beam, masked to a rectangle 1.0 cm by 5.0 cm and directed at the center of the chamber with the longer dimension oriented vertically. The detector is a modified Sony television camera, model AVC-3400. The camera has been changed from its normal 525 line interlaced frame to a 300 line noninterlaced frame. The vertical period was changed to 51.4 hz instead of the normal 60 hz, and the cadmium sulphide vidicon was replaced with a silicon diode target vidicon. A noninterlaced scan was chosen because an interlaced scan provides two alternate fields which must be matched to produce the entire picture while a noninterlaced scan provides strictly serial output from the image. The camera is fitted with a 50 mm F1.2 lens and is directed at 90° to the incoming laser at a distance of 75 cm from the sample volume. The intersection between the camera's field of view and the laser beam forms a box 5 cm x 5 cm x 1 cm, giving a sample volume of 25 cm^3.

The video processor provides synchronization signals for the camera; vertical and horizontal sweep for the display; and processing of the analog video signal from the camera. The processor defines a threshold for the video signal. If the video output of the camera exceeds this threshold, a digital "one" is registered in the processor for that point in the sample volume. Since it is possible that the image of a single crystal could occupy more than one scan line, there is a possibility that it could be erroneously counted twice. To avoid this, the video processor locates each crystal image in space, or more precisely, its time relationship to the vertical and horizontal synchronization signals, and protects an area of approximately 1 percent of the total volume, centered on the initial image of the crystal. In this blanked area the processor will not accept any further counts. Thus the crystal could move or could occupy more than one scan line and would be counted only once. The video processor also interfaces to a computer tape drive where the number of crystals in each frame as well as status information about the chamber is recorded. The positions of the crystals in the sample volume are not recorded presently, although this is technically feasible and would be useful for studies of particle motion.

3. COMPARISON EXPERIMENTS

3.1 Procedures

Since the standard procedure for determining ice crystal concentrations has been the microscope slide, experiments were performed to compare the performance of the electronic imaging system with the slide technique. A slide holder was mounted at the same height as the electronic sample volume. A cloud generator similar to the one used in the CSU Isothermal Chamber was fitted into the chamber. A sample of silver iodide complex was injected into the chamber at cloud temperatures of -12 C, -16 C, and -20 C to produce crystals of different sizes and habits. Slides were then exposed for two minute intervals and counted through a microscope. The crystals on the slide were photographed immediately after they were counted and the film was analyzed to determine the size and shape of the crystals. During the time the slides were being exposed the ice crystal concentration was measured with the television system. Initially, the ice crystal concentration is very high and decreases with a roughly exponential decay, having a time constant of approximately 300 seconds.

3.2 Results

It was initially found that the ratio between the concentrations measured by the television camera and those measured by the slide system were highly variable with crystal size, habit, and concentration being important factors. Ice crystal concentrations were calculated for the two measurement methods according to (1) and (2).

$$C(\text{slide}) = N_s/(A_v \times t \times w) \quad (1)$$

$$C(\text{elec}) = \overline{N}_e/(v_e \times \varepsilon) \quad (2)$$

where N_S is the number of crystals counted through the microscope, A_V is the view area of the microscope ($2mm^2$), t is the exposure time of the slide, w is the crystal fall velocity (10 cm sec^{-1}), $\overline{N}_e$ is the average number of crystals counted per television frame, v_e is the television sample volume (25 cc), and ε is the efficiency of the camera system. ε is given in (3).

$$\varepsilon = (\overline{N}_e * A_v * t * w)/(N_s * v_e) \quad (3)$$

Table 1 shows the efficiency of the television camera as a function of concentration and temperature. The categories used in the table are obtained from the slide measurements and correspond to low, medium, and high concentrations of crystals in the chamber. The table also shows the sizes of the crystals. We can see that there is a considerable variation in efficiency, ranging from a low of $.53 \times 10^{-3}$ to a high of 8.5×10^{-3}. The following hypothesis is offered to explain this variation of the television camera's performance.

Since the experiments last on the order of one-half hour and the fallout time for crystals is on the order of 30 seconds, nucleation must be proceeding during the entire experiment. In addition, a crystal must have an appreciable fall velocity in order to be counted by the slide technique. We hypothesize that if there is severe competition for the available water vapor, small crystals are generated which are counted by the television camera system but do not fall on the slide, thus causing an apparent increase in the camera's efficiency. A similar effect was also noted by Dunsmore and Steele (1974). Given the available supply of moisture from the cloud generator, the rate at which crystals are lost from the chamber, and sizes typical of crystals that grow at -20 C, a concentration of 2000 $liter^{-1}$ represents the balance between the supply of moisture to the cloud and the loss through crystal fallout. At -16 C a concentration of 400 $liter^{-1}$ represents this balance; while at -12 C the balance occurs at 10,000 $liter^{-1}$. The efficiencies are given in Table 2, according to concentrations above and below the balance of moisture. The efficiency of the camera, at one temperature, remains nearly constant up to the balance point and then increases above that point. The total variation is only 4 to 1 between the lowest and the highest efficiency for cases where the supply is greater than the loss. Our hypothesis is strengthened by the fact that the sizes of the crystals remain relatively constant up to the supply-equals-loss point but drop above that point.

Table 3 shows the frequencies with which various crystal habits observed on the microscope slides. At -12 C and -20 C the crystals are primarily hexagonal plates while at -16 C they are almost exclusively regular dendrites. The data for both -12 C and -16 C show the crystals having a monohabit, while at -20 C the relatively large fraction of dendritic crystals indicate that parts of the chamber volume were ~2 C warmer than the monitored temperature. An examination of the chamber revealed that a port between the inner vessel and outer shell had inadvertently been left open. This was corrected before the experiments at warmer temperatures.

4. PROGNOSIS

The separation of the combined effects of size and habit on camera efficiency were not specifically addressed in this series of experiments. In particular no attempt was made to correct the fall velocity (w) for variations due to size and shape. Still, while the experiments do show that the camera has a greater sensitivity for the larger dendritic crystals

Table 1

Camera Efficiency vs. Concentration

Temperature and Concentration C	L^{-1}	Camera Efficiency $X10^3$	Efficiency Std. Dev. $X10^3$	Average Crystal Size um	Size Std. Dev. um	Number of Cases
-12	100-500	.53	.18	67	9	6
	500-2500	.69	.19	62	6	12
	2500-12,500	1.2	.61	59	5	9
-16	100-500	2.6	1.7	224	42	23
	500-2500	4.6	2.4	195	53	41
	2500-12,500	8.5	4.0	136	38	8
-20	100-500	.67	.35	166	123	15
	500-2500	.41	.15	110	29	24
	2500-12,500	.97	.52	75	19	39

Table 2
Camera efficiency vs. water supply and loss

Temperature and Concentration C	L^{-1}	Camera Efficiency $X10^3$	Efficiency Std. Dev. $X10^3$	Average Crystal Size um	Size Std. Dev. um	Number of Cases
-12	sup > 2X Loss	.71	.44	65	9	30
	sup > Loss	.89	.72	64	9	38
	sup < Loss	2.1	---	52	---	2
-16	sup > 2X Loss	2.1	1.3	225	49	12
	sup > Loss	2.3	1.6	226	43	19
	sup < Loss	4.8	2.9	191	54	62
-20	sup > 2X Loss	.57	.29	139	97	28
	sup > Loss	.52	.27	135	83	37
	sup < Loss	.9	.5	76	19	47

Table 3
Fractions of crystals of different habits for experiments at three temperatures

Temp (C)	Hex Plates	Dendrites	Double Plates	Columns
-12	93%	0%	5%	2%
-16	3%	96%	1%	0%
-20	72%	27%	1%	0%

grown at -16 C than for the smaller hexagonal plates which occur at -12 C and -20 C, the variation in camera sensitivity is small enough so that it is useful for certain kinds of experiments. A monitor for the output of the laser source has been added since those experiments were performed. This allows us to standardize the source intensity thus reducing the variability in the camera's efficiency. With this improvement the television system has been used successfully in recent months to investigate the relative nucleating abilities of nuclei injected at cloud base and at the -10 C isotherm. Attempts are being made to further quantify the size-habit dependence so that a temperature-efficiency curve can be determined. Until now no corrections have been applied to measurements obtained by this system. We are further investigating the use of signature analysis on the output video signal. Presently, only a simple thresholding device is used to analyze a crystal's image; however, advanced techniques, such as depolarization analysis, Sassen (1976), could be applied to differentiate between the signatures of crystals and droplets and even among the crystals of different habits. This would allow us to raise the sensitivity of the system and improve the efficiency of the camera.

5. ACKNOWLEDGMENTS

Thanks are due to Randy Horn, Cleon Swain, and Pat Fiegen of the Cloud Simulation and Aerosol Laboratory at Colorado State University for their help in performing these experiments.

6. REFERENCES

Dunsmore, H. and R. L. Steele, 1974: An investigation of sequences dependent effects in seeding simulated cumulus clouds. Preprints Fourth Conference on Weather Modification, Fort Lauderdale, Florida, 183-189.

Garvey, D. M., 1975: Testing of cloud seeding materials at the cloud simulation and aerosol laboratory, 1971-1973. J. Applied Meteor., 14, 883-890.

Sassen, K., 1976: Ice crystal habit discrimination with the optical backscatter depolarization technique. Paper submitted for publication.

THE NOAA AIRCRAFT OBSERVATION SYSTEM

Byron B. Phillips

Weather Modification Program Office, ERL
NOAA, Boulder, Colorado 80302

1. INTRODUCTION

The needs of meteorological, oceanographic, and air-sea interaction and/or boundary layer research are plainly dependent on aircraft observation and measurement. Over land, present technology can provide very powerful remote sensing instrumentations in form of equipment and equipment systems such as microwave and acoustic radars, optical lidar arrays, dual and three-unit Doppler radars, laser and microwave equipments and methodologies for determining vertical temperature, humidity, wind, and particulate loading distributions, etc. The Doppler techniques provide for the study of the kinematics of storm and storm environments and of turbulence and mixing interactions over a wide range of atmospheric scale of motions. Other multifrequency remote sensing methods are developed which are capable of delineating hail vs rain precipitation areas and of quantitative evaluation of precipitation amounts. Together with conventional surface-mounted measurements such as obtainable from precipitation networks, these presently developed remote sensors are being exploited to yield new and important knowledges of atmospheric processes.

Powerful as these ground based systems are, they are not sufficient. The in-situ measurements obtained from and by aircraft are not merely supportive, but rather are a necessary additive to the overall meteorological measurement capability which, together with the ground systems, can and will provide for progress in weather forecasting and weather control. In storms, for example, aircraft in-situ measurements are needed for the cloud and hydrometeor concentration and size distribution, the crystal habit, the ice-water mixture properties, total water content, for obtaining bulk and individual hydrometeor samples for chemical analysis, for dynamical and structural information of cloud boundary and cloud interior regions, for electrification information, for determining cloud and precipitation processes, for extending the measurement capability in both space and time (beyond the observational limits of the surface based sensors), etc. Such examples are seen to represent far more than mere "calibration" observations such as are required for verifying surface remote sensing data. Equally valid statements of requirement and utilization can be made for other research areas such as boundary-layer studies, transport studies, etc.

Over oceanic areas, the necessity of measurements from an instrumented aircraft is even more clearly evident. Here, in the absence of the ground based sensor systems, the aircraft is a stand-alone system which must be capable of providing the gamut of required measurements for atmospheric and oceanographic research. In comparison, by virtue of both the extent and the nature of the processes, the oceanic areas are of equal and greater importance than the land areas, yet a paucity of research measurements have been obtained over the oceans for past decades. For both meteorologic and oceanographic research, the long range instrumented aircraft offers great potential and programs in these areas should be sharply increased in the future. Examples of such programs include investigations of ITCZ dynamics and kinematics, tropical storms, hurricanes, horizontal and vertical mass and water substance transport at all latitudes, extra-tropical storm analysis, etc. For oceanographic and air-sea interactive processes, the aircraft can more economically (than by ship launch) obtain near synoptic data over large ocean expanses through use of AXBT, SDT, sondes, gust probes, side looking aircraft radar, and other developed systems. Little use of aircraft has been made by oceanographic researchers in the past.

The history of aircraft instrumentation for atmospheric or oceanographic research is comparatively recent and limited in extent. Primitive systems were used in the middle 1950's. Since the early 1960's, NOAA and its predecessor agencies, ESSA and USWB, has maintained a fleet of aircraft for hurricane and severe storm research. Relatively outstanding efforts have resulted at a few universities (usually involving a single aircraft), for example, at University of Chicago, of Washington, of Wyoming, and in conjunction with the Researach Aircraft Facility of NCAR. Progress in cloud physics instrumentation has been generally slow but has accelerated somewhat in recent years. The measurement of cloud microphysical properties and assessment of cloud processes from an aircraft moving through the cloud at 150 to 250 knots represents one of the most challenging of all physical measurements! The transfer of laboratory technologies to the aircraft platform has been slow. With the advent of the minicomputer, new on-board data handling systems for aircraft have occurred within the past five years. Little effort has been made to provide for good expendible, droppable sensor packages until very recently. Quantitative aircraft meteorological radar utilizing existing (but recent) ground system digital data processing is non-existent. The utilization of modern inertial navigation equipment for meteorological purposes (horizontal and vertical winds, gusts) has been pioneered at NCAR and more recently by Kaman Aerospace under Air Force contract.

Recognizing the requirements for more capable aircraft instrumented for state-of-the-art measurements and data processing, NOAA in 1973 initiated a program for modernization of their research aircraft fleet. The program will provide by mid-1977 a fleet of four four-engined turboprop aircraft composed of two Lockheed WP-3D (current Navy derivative of the Electra aircraft), a Lockheed C130B Hercules, and a second C130B obtained on bailment from Air Force. The two WP-3D have been purchased configured to atmospheric and oceanographic research needs. The first of these was delivered to NOAA in May 1975, the second in January 1976. The instrumentation and data subsystems are being developed for installation to provide for a versatile, integrated Research Aircraft Measurement System (RAMS). The first WP-3D RAMS with partial instrumentation and the NOAA C130B aircraft have been scheduled for participation in NOAA's STORMFURY (Hurricane Modification) Program during the present summer. The following describes the overall research aircraft systems and subsystems which should provide for a major utilization within the national research efforts throughout the next decade. Major emphasis are given to the configuration and instrumentation of the newer WP-3D aircraft systems but C130B features are compared in an effort to present to the reader a better overview of the NOAA total aircraft research capability.

2. AIRCRAFT

The WP-3D and C130B are four engine turboprop aircraft of similar flight and performance characteristics. The C130B is a cargo configured, high wing aircraft capable of operation with minimum runway requirements. Equipped with a rear opening lower fuselage on-off load ramp, the C130B is extremely flexible as to scientific payload. In contrast, the WP-3D is a passenger configured, low wing aircraft with a single entrance door and limited scientific loading (floor loading and total payload) capability. With equal scientific payload of 12,000 lbs or less, maximum flight altitudes are in the range of 28,000 to 35,000 ft for both aircraft depending on fuel load. Advantages of the WP-3D aircraft are increased flight endurance and range, provisions for lower fuselage and tail radomes, wing hard points interior and outboard of the engine nacelles for instrumentation installation (improved sampling exposure), better cabin environmental control for electronic cooling and crew comfort, greater engine generator and APU power capability, and provisions for a gust probe boom for vertical and horizontal turbulent flux measurements.

3. INSTRUMENTATION SUBSYSTEMS

3.1 Navigation Subsystem

Aboard research aircraft the navigational equipments serve two essential purposes. They provide for the normal function of aircraft navigation and position fixing. More importantly to the research mission, they provide the ground speed and ground track information basic to the evaluation of flight level winds and basic to atmospheric motion fields that may be remotely sensed from the aircraft platform. For such measurements of atmospheric and/or oceanographic parameters the aircraft velocity error contributes a primary error component to the total measurement error. Analysis shows, for example, that CEP errors of 1 m/sec or less are needed for wind measurements to be used for convergence studies over a broad scale of atmospheric motions. To accomplish this accuracy smaller ground speed errors are required from the navigational system.

All NOAA aircraft are equipped with integrated, computer linked, inertial and Omega navigation equipment. The Omega navigational equipment (ONE) operates by means of the world wide network of VLF Omega transmitters. On the WP-3D, Omega, Loran C, and an on-board Doppler navigational systems are used to update dual inertial navigation units (INU) to give both long term (5 to 12 hour) and short term (<2 hour) total system accuracy in both position (<1 nm) and ground velocity (<1 m/s CEP) anywhere on the globe. The method of INE updating is switch selectable so that, for example, the errors of the Doppler navigational equipment under hurricane "high-sea" conditions are defeated from contributing to the total system error.

3.2 Data Acquisition and Display Subsystem

For data recording, on-board data processing and data display, a state-of-art data system has been engineered for installation on the WP-3D. Digital and analog inputs are formatted and recorded on magnetic tape by a primary computer which also generates a fixed format display for distribution through the aircraft and also passes processed data to a magnetic disk recorder. Sampling rates, formats, processing methods are flexible within wide ranges. A second computer accesses data from the disk and provides, through keyboard control, for on-board data presentation by TV monitors of graphics in x-y coordinates, listings, path plots, wind vector plots, etc. at all scientific consoles. Prior data can be recalled for comparison with present or current data. The associated video distribution system can access any TV-raster scan source such as the radar or a forward scanning TV for presentation at all consoles. The primary and secondary computers are switch interchangeable; parallel analog and digital inputs and back-up tape recorders provide for a redundant data handling capability with no single point failure path through the data recording process. An impact printer, graphical hard copier and multichannel chart recorders provide on-board outputs for scientist useage.

A similar data system with less flexibility and more limited display capability is installed on the two C130B aircraft. These systems were designed under Air Force contract as part of the Airborne Weather Reconnaissance System (AWRS).

3.3 Cloud Physics Instrumentation

A comprehensive grouping of meteorological and cloud physics instrumentation is provided. Where possible, redundant instrumentation is installed where, however, a dissimilar secondary instrument is used which utilizes either another measurement principle, time constant, etc. For example, air temperature is measured by a conventional Rosemount resistance thermometer of time constant 0.1 second or greater, and by a remote sensing CO_2-band IR-radiometer of a few millisecond response time. The latter permits the measurement of in-cloud temperatures (wet bulb temps since primary source is the cloud droplets). In common with research aircraft elsewhere, instrumentation groupings are used where no single instrument exists capable of a given measurement requirement. Thus the Johnson-Williams meter, NOAA designed nimbiometer, evaporative Lyman-alpha total water content meter, Particle Measuring System's cloud and precipitation spectrometer probes, and foil impact sampler all are used to construct a best possible data set for evaluation of water and ice content. An upward looking microwave radiometer (21.5 GHz) is being developed jointly with scientists of NOAA's Wave Propagation Laboratory for the measurement of the integrated water content above the aircraft. (This measurement is particularly important to hurricane and severe storm modification concepts.) Formvar ice crystal replicators are being installed which, together with existing laboratory technologies, will permit an analysis of the chemistry of nuclei and the role of artificially introduced seeding nuclei (i.e., nucleation or scavenging) in modification experiments. Throughout, emphasis is and will be placed on instrumentation sampling (exposure).

3.4 Radar

Quantitative meteorological radar with digital data processing and recording has not been previously available on research aircraft. Radar systems scheduled for fall 1976 installation on the WP-3D and the NOAA C130B aircraft are designed to transfer existing ground conventional radar technology to the aircraft platforms. The WP-3D installation provides for a three radar system including a forward scanning C-band nose conical beam radar, a 360° horizontally scanning C-band lower fuselage radar, and a 360° vertically scanning X-band tail mounted radar. Radar R/T characteristics are given in Table 1. The radar system is equipped with its own data system consisting of digital video integrator processor, dual magnetic tape recorders, dual scan converters (for changing from rho, theta to x, y coordinates for TV raster scan on board monitoring), and back-up video recording.

The NOAA C130B aircraft will have only a nose radar (± 110° scan) and digital recording system of characteristics similar to the WP-3D nose radar. A five foot antenna planned for C130 installation will give a smaller 2.7° conical beam width.

3.4.1 Doppler Radar

Initial plans for WP-3D tail and nose Doppler radar modes were abandoned because of high initial development costs and related schedule and performance risks. Several radome and antenna design characteristics (such as size and stabilization) have been retained with the aim of a later two step Doppler radar program to include (1) initial prototype Doppler radar flight test, and (2) conversion of existing conventional radars to incorporate Doppler mode operation. Present planning is to accomplish the first step in spring 1977 by means of a test installation of an operational 3 cm Doppler radar R/T unit connected to the existing tail antenna on the WP-3D aircraft.

3.5 Boundary Layer, Turbulent Flux Instrumentation

Each of the WP-3D aircraft are equipped with a gust probe boom extending forward immediately starboard of the nose radome. Scientists within the Weather Modification Program Office are equipping the boom with strain-gauge alpha and beta vane sensors, high response thermistors, vertical and horizontal accelerometers and microwave refractometers for boundary layer air and water flux measurements. The boom assembly is removable for non-gust probe missions.

3.6 Expendable Sensors: Dropsonde, AXBT, SDT Systems

3.6.1 Omega Dropsonde

Prototype "dropwindsonde" systems have been developed and operated during GATE. The sonde released from the aircraft carries, in addition to pressure, temperature, and humidity sensors, a 13.6 kHz Omega Navigation VLF receiver and VHF transmitter. Omega data received by the sonde are retransmitted via VHF link to the sonde releasing aircraft. A receiver, data system on the aircraft decodes and demodulates the sonde position and PTH data and derives the vertical

Table 1

WP-3D Radar Specifications

	Xmtr Freq.	Beam Pattern	Beam Size	Peak Power	Pulse Duration	PRF
Nose	5.280 GHz	Conical	3.5°	70 kW	3.0 μsec	400 sec^{-1}
Lower Fuselage	5.370 GHz	Fan	1° x 4.1°	70 kW	6.0 μsec	200 sec^{-1}
Tail	9.315 GHz	Elliptical	1.4° x 1.9°	60 kW	0.5 μsec	1600 sec^{-1}

profile of wind (derived from successive sonde positions) and the PTH. Currently two developments are underway. Second generation Omega Dropsonde receiver-processors are being developed under NOAA contract; NCAR and NOAA are updating and improving the sonde itself.

3.6.2 AXBT, SDT

Existing AXBT sensors are satisfactory for use and aircraft release. Presently no Salinity, Density, Temperature sensor is developed suitable for aircraft release. Development of such a sensor package is currently being considered because it appears that large economic and scientific benefits are probable.

3.6.3 Aircraft Launch Systems

WP-3D launch systems for expendable sensors are being designed for fall or winter installation. System definition will be known at the time of the Conference.

3.7 Seeding Subsystems

An internally mounted seeding "gun" and pyrotechnic cartridge are designed and tested for utilization on the WP-3D and C130B aircraft. This system provides for magazine loading and auto-firing of a small pyrotechnic from within the aircraft. Firing rates are variable up to two per second (50 to 80 meter horizontal spacing at normal flight speed). The pyrotechnic can be for general utilization but is designed specifically for the STORMFURY Modification Experiment. Test data will be available by the date of the Conference.

3.8 Oceanographic Subsystem

Several efforts are in the planning stages and may be initiated in response to active programs. At least one C130B and one WP-3D will be modified to fly a laser waveheight profilometer. AXBT capability will exist for each aircraft type by mid 1977 in time for utilization in that summer's hurricane modification experiments. SDT development is being explored. Side looking aircraft radar (SLAR) for wave study is planned probably for the C130B aircraft. Modification designs for mounting SLAR to that aircraft and flight tests have been accomplished. A downward looking scanning IR radiometer is purchased and can be used for study of oil spills, etc.

3.9 Photo Subsystem

Each NOAA aircraft is being equipped with nose, right and left looking, and downward looking 16 mm cameras capable of time lapse andcine-mode operation.

4. SUMMARY AND SCHEDULE

The above aircraft observation systems are scheduled for completion by mid summer 1977. It is obvious that a continuing support must be maintained thereafter, first to insure proper operation and calibration of the equipment described and secondly to continue development and improvement of required sensor systems. Together, these RAMS aircraft are expected to serve for the next decade and longer as primary components of the national atmospheric and oceanographic research facility. The related scientific community is urged to plan for, contribute toward, and promote utilization of these facilities for coordinated and single research programs in weather modification, environmental monitoring (both atmosphere and ocean), severe storms, wave and storm surge research, water mass and heat transport processes over oceanic areas from tropics to pole, etc.

7.3.2

LIGHTNING CHARGE CENTER LOCATIONS RELATIVE TO PRECIPITATION IN A THUNDERSTORM

Paul Krehbiel, Marx Brook, Roy McCrory, and David Tarbox

New Mexico Institute of Mining and Technology
Socorro, New Mexico

1. INTRODUCTION

The means by which a thunderstorm becomes electrified, and the extent to which electrification affects the microphysical processes of precipitation formation, is not completely understood and is the subject of some controversy. It has long been recognized, for example, that precipitation and lightning often accompany each other in convective storms, but the cause and effect relationship is not established.

In this paper, we present some interesting initial results that relate the location of lightning charge centers to the radar-measured reflectivity structure of the storm. It is hoped that studies of this type, coupled with other measurements of the charge structure and storm dynamics, will help to resolve some of the questions concerning thunderstorm electrification.

2. MEASUREMENTS

In the present study, measurements of the electrostatic field change caused by lightning flashes were used to locate the centers of charge effectively neutralized by individual strokes of a discharge to ground. The measurements were obtained from a network of eight ground-based stations distributed over a flat area 10 x 17 km in extent. The charge centers were located by comparing the field change values observed for individual ground strokes with the field generated by a spherically symmetric charge, and by varying the position and magnitude of the charge until a best fit was obtained (see Jacobson and Krider, 1976). It was found that the field change values were reasonably well-fitted by the monopole model, and that the centers of charge could typically be located within several hundred meters or less in space.

Radar observations of the clouds were made using a pulsed, vertically-scanning radar system of 3 cm wavelength located near the center of the network. The pulse length of the radar was 2 μsec and the antenna beamwidth was 1.5°, so that at 10 km range the size of a resolution volume was $\leq$ 300 m on a side. The transmitted power was 40 kwatts peak. Backscattered radiation from the cloud was received in a logarithmic amplifier to extend the dynamic range of the data, and the returns were recorded by photographing a standard RHI display of intensity vs. elevation angle. By stepping the antenna in azimuth between elevation scans, the full hemisphere overhead was surveyed once each eight minutes.

3. RESULTS

The accompanying figures show charge center results superimposed upon contoured representations of the radar return for two multiple-stroke lightning flashes to ground. The circles denote the charge locations for each of the strokes, and indicate the size of a spherical volume which would have contained the charge at a uniform density of 20 coul/km^3.

The radar data was contoured from the original film by Dr. R.E. Orville, using a false color video densitometer (see for example Orville, 1974). The colors are reproduced here as shades of gray separated by white borders. Each contour represents equal increments of film density, or, because of the logarithmic receiver response, roughly equal "db" increments in received power. Actual calibration of density vs. received power is not known, but it is estimated that the contour intervals are approximately 10 db apart. The density contours differ from contours of equal reflectivity because they are not compensated for 1/R^2 loss or attenuation. The returns thus tend to decrease monotonically from the radar, which is located in the white dot at the lower center of the picture. The range ring is 5 nautical miles (9.26 km) in radius and the overlaid scale is in kilometer divisions.

The lightning discharges shown were the 9th and 17th flashes of the storm and occurred about 4 minutes apart in time, 6 minutes after the first flash of the storm. At the time of the data, heavy rain was falling at the radar site, which received two inches of precipitation during the approximate one hour lifetime of the storm. By happenstance, the radar cross-sections were obtained about one minute after each discharge in the approximate plane of the charge centers, and are oriented at right angles to each other in azimuth.

The results for flash 17 (Figure 2) will be discussed first. Charge centers for successive strokes of this flash begin at the upper left and are displaced downward and from left to right (west to east) with increasing stroke order. Viewed from above, the charge centers lie along a circular arc that begins 0.7 km in front of the picture, passes through the picture to a depth of 1.0 km behind it, and ends slightly in front of the picture. The first stroke volume contained 20 coulombs of charge, while the fifth stroke volume contained 2.6 coulombs. The fourth stroke produced a continuing current down the channel, and two cumulative charge center results are shown for it. Data and results for this flash are presented in greater detail in a previous report (Krehbiel et al. 1974).

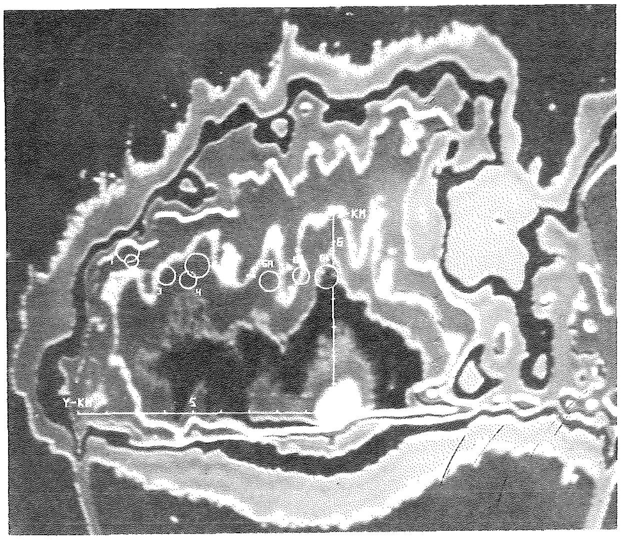

Figure 1. Charge center locations relative to radar precipitation echo for individual ground strokes of Flash 9. Total charge = 30 coulombs.

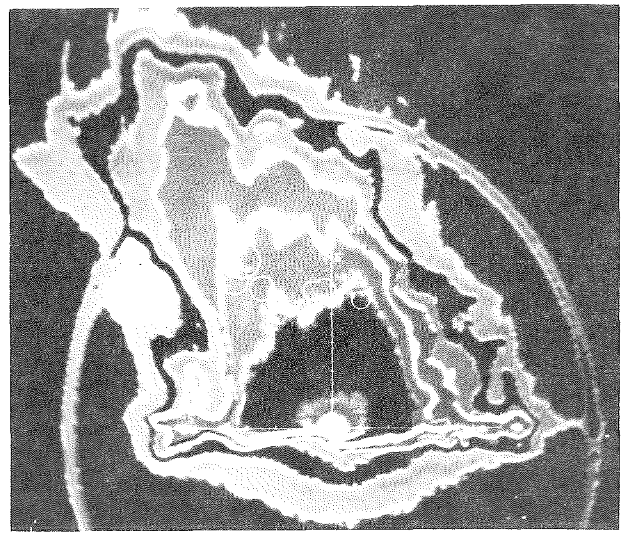

Figure 2. Charge locations for Flash 17. Overlaid scale is in kilometer divisions. Total charge = 43 coulombs.

The charge volumes lie within the horizontal extent of the higher reflectivity region of the cloud, between 4.5 and 6.0 km above terrain. At these elevations, the environmental temperature ranged from -9°C to -17°C. (The 0°C isotherm was at 3.2 km and cloud base at approximately 2.0 to 2.5 km above terrain.) While the radar data shows significant vertical development of the cloud, this is only slightly reflected in the charge center locations.

Flash 9 (Figure 1) produced six strokes to ground, the last of which sustained a long (220 msec) continuing current down the channel. The stroke order proceeds from left to right (north to south), with the last three results representing incremental charge values and locations during the first half of the continuing current. The charge centers lie 0.7 km behind the picture for stroke 1, in the plane of the picture for strokes 2,3,4, and 0.7 km in front for stroke 5. The continuing current charges lie from 1.0 to 1.5 km in front of the picture, and undoubtedly progress further to the right during the last half of the current.

The radar data of Figure 1 shows a number of precipitation cells or shafts, seen at mid-cloud level as upward-extending "fingers". As before, the charge centers are distributed horizontally throughout the higher reflectivity region of the storm, between 4.5 and 6.0 km above terrain. In spanning several precipitation cells, however, there is a striking tendency for the charge volumes to lie selectively in the precipitation. This observation is less certain for those charges that do not lie in the plane of the picture.

4. DISCUSSION

The above results provide a direct indication of the relationship between lightning and precipitation in a thunderstorm, and support the generally held view that the two are closely ralated. The results also emphasize the large horizontal extent of the lightning charge within the storm. Since the lightning charge was induced by negative charge within the cloud, it is reasonable to assume that the negative charge was horizontally distributed as well, although not necessarily coincident with it.

In order to evaluate the implications of such results in terms of charge separation mechanisms and electrical-precipitation interactions, a more detailed and comprehensive study of the time history of the storm is required. Thus, while it is tempting to speculate further on possible implications, we feel that it would be improper at this time.

5. ACKNOWLEDGEMENTS

We would like to express our thanks to Dr. R.E. Orville for the quantitative contour analysis of the radar data, upon which the substance of this paper is based. This work was supported by the National Science Foundation under Grants GA 32591 and DES72-01371 and by the Office of Naval Research under Contract N00014-75-C-0167.

6. REFERENCES

Jacobson, E. A., and E. P. Krider, 1976: Electric field changes produced by Florida lightning. J. Atmos. Sci., 33, 103-117.

Krehbiel, P., M. Brook and R. McCrory, 1974: Lightning ground stroke charge location from multistation electrostatic field change measurements. Proc. Fifth Intern. Conf. Atmospheric Electricity, Garmisch-Partenkirchen, Germany, 1974.

Orville, R. E., J. H. Helsdon, Jr. and W. H. Evans, 1974: Quantitative analysis of a lightning return stroke for diameter and luminosity changes as a function of space and time. J. Geophys. Res., 79, 4059-4067.

RADAR AND RELATED HYDROMETEOR OBSERVATIONS INSIDE A MULTICELL HAILSTORM

D. J. Musil, C. Knight,[1] W. R. Sand,[2]
A. S. Dennis, and I. Paluch[1]

Institute of Atmospheric Sciences
South Dakota School of Mines and Technology
Rapid City, South Dakota 57701

1. INTRODUCTION

An armored T-28 aircraft (Sand and Schleusener, 1974) has routinely penetrated active hailstorms since 1972 to investigate their internal structure. During the 1975 field season the T-28 system was tested with several new instruments in order to assure a reliable platform for future penetration work with the National Hail Research Experiment (NHRE). The requirement for new equipment evolved in an effort to answer some of the current questions about hailstorms such as: origin of hailstone embryos, details of storm microphysics, and particle size distributions.

There were a total of 48 penetrations made on 9 days during the 1975 field season. The aircraft observations made on these days were supported by accurate aircraft tracking, detailed 10-cm radar data, and single Doppler radar data. This paper reports a case study of a hailstorm on 21 July 1975, relying on the data from four T-28 penetrations, the radar data, and a hail collection at the ground.

2. METEOROLOGICAL SITUATION

Due to the abbreviated nature of the 1975 field season, local soundings were not available; however, the 12Z Denver sounding on 21 July showed a moderate amount of instability and suggested cloud tops greater than about 11 km MSL. A local area surface chart analyzed on the morning of 21 July prior to storm formation was characterized by dew points in excess of 10C corresponding to low-level moisture of about 8 g kg^{-1}, light easterly winds at the surface, and a suggestion of low-level mesoscale convergence, the combination of which appear to be necessary ingredients for the formation of hailstorms in northeast Colorado.

The average cloud level winds were computed to be 256/19 m sec^{-1}. Cloud base observations could not be routinely made during the field season, so they had to be estimated based on the Denver sounding and by observations by the pilot early in the T-28 flight. Cloud base was estimated to be about 4.4 km MSL.

3. RADAR HISTORY

The storm on 21 July first formed about 30 km south-southwest of Grover and then showed a general movement to the southeast due to the formation of new cells on that side. The storm was multicellular in nature with individual cells showing little movement until later in their life cycle when they began to line up with the cloud level winds.

Table 1 shows the characteristics of the cells that were identified from the 10-cm radar data gathered at Grover on 21 July. The geographic location of each cell at the time of its first echo (FE) is shown in Fig. 1, which gives a picture of the general motion of the storm. No attempt is made to show individual cell movements because many tend to overlap if the entire track is shown. New cells formed in the southeast quadrant of the cloud complex associated with this storm. Those cells having quite long lifetimes (Cells 1, 2, 6, 7, and 8) tended to form in a more restricted area on the southeast side of a more mature cell, which happened to be in existence at the time of formation of the new cell.

The storm can be classed as multicellular, but after about 1630 MDT, new cells became difficult to identify because the storm became more organized and new growth tended to appear as protrusions, appearing anywhere from east through south through southwest of the mature cell present at the time. Because of this problem, FE heights could not be identified for Cells 5 and 7.

4. PENETRATION HISTORY

Four penetrations were made on 21 July near an altitude of about 6 km MSL. The flight tracks of the T-28 for Penetrations 3 and 4, superimposed on a slant range PPI presentation nearest the flight level of the T-28, are shown in Figs. 2 and 3, respectively. Also identified are the cells in existence during those penetrations (see Table 1). Penetrations 1 and 2 are

[1]National Center for Atmospheric Research, National Hail Research Experiment, Boulder, Colorado.

[2]Department of Natural Resources, University of Wyoming, Laramie, Wyoming.

TABLE 1: Radar Summary

Cell	Time of First Echo (MDT)	End of Cell (MDT)	Duration (min)	Height of First Echo (km MSL)	MEH (km MSL)	Remarks
1	1551	1626	35	7.5	13.2	DSPTD
1A	1601	1613	12	8.8	11.8	Merged with 1
2	1606	1654	48	8.3	13.2	DSPTD
2A	1611	1626	15	8.3	11.6	Merged with 4
3	1611	1627	16	7.2	11.8	Merged with 4
4	1617	1644	27	8.3	12.5	Merged with 2
5	~1627	1651	24	NA	11.5	Merged with 6
6	1640	1720	40	~6.7	13.8	DSPTD
7	~1630	1731	61	NA	14.3	Merged with 8
8	1703	1802	59	7.5	13.7	DSPTD

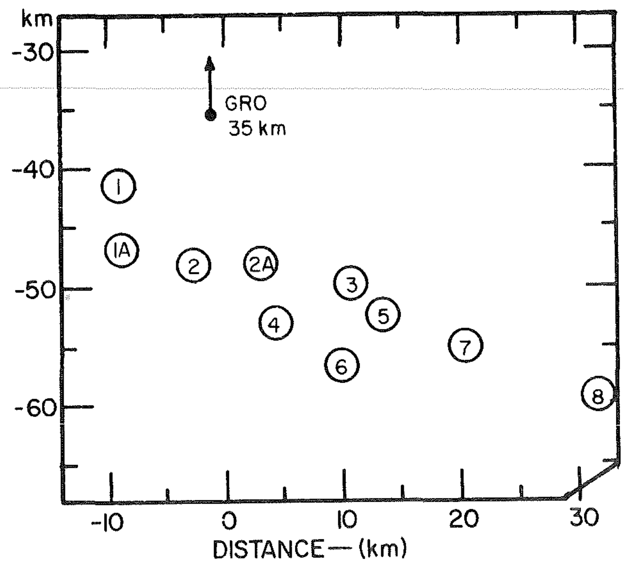

Fig. 1. Location of first echoes with respect to Grover on 21 July 1975.

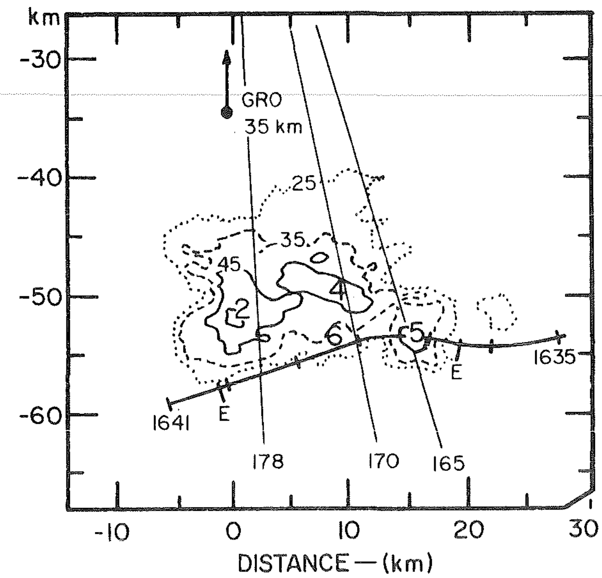

Fig. 2. Slant range PPI presentation for Penetration 3 near 6 km MSL on 21 July 1975. Selected contours are labeled in dBz. Dark line shows the path of the T-28, tick marks represent 1-min time intervals, and the E's along the path represent entry and exit for the penetration. The lines labeled 165, 170, and 178 are radials along which the RHI's of Fig. 6 are constructed. The numbers within the echo are cell numbers corresponding to those in Table 1.

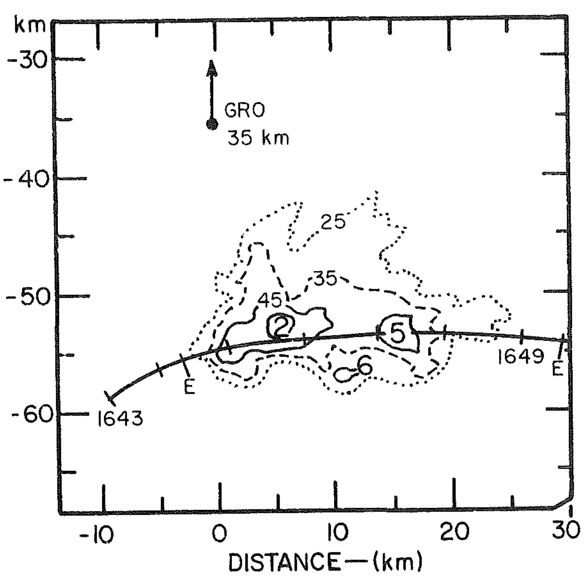

Fig. 3. Same as Fig. 2 except for Penetration 4.

not shown in this paper as subsequent discussion will concentrate on Penetrations 3 and 4. Observations of vertical velocity, Johnson-Williams liquid water concentration and temperature corresponding to Penetrations 3 and 4 are shown in Figs. 4 and 5. Cell 5 is of significant importance because it was penetrated twice, approximately 10 min apart.

5. DYNAMICS OF THE STORM

Mean Doppler velocities in the storm were recorded from the Grover 10-cm radar for all locations in which the reflectivity exceeded about 30 dBz. The location of the storm roughly south of Grover, the fact that a relatively uniform feature of the storm was a 15 to 30 km long east-west wall

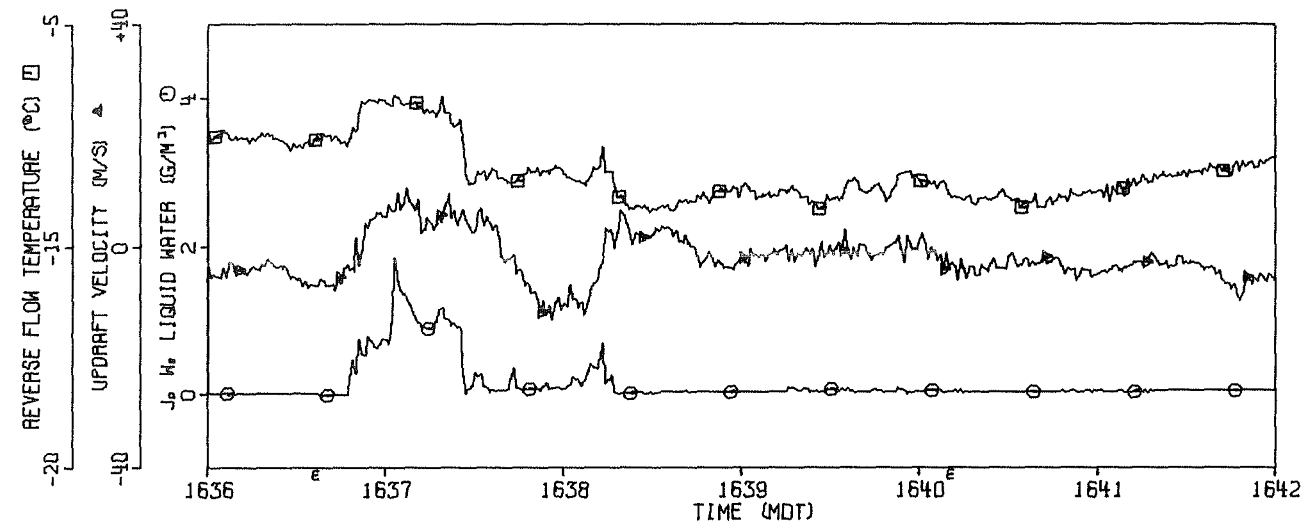

Fig. 4. T-28 FLIGHT 125E 21 JULY 1975 PEN 3

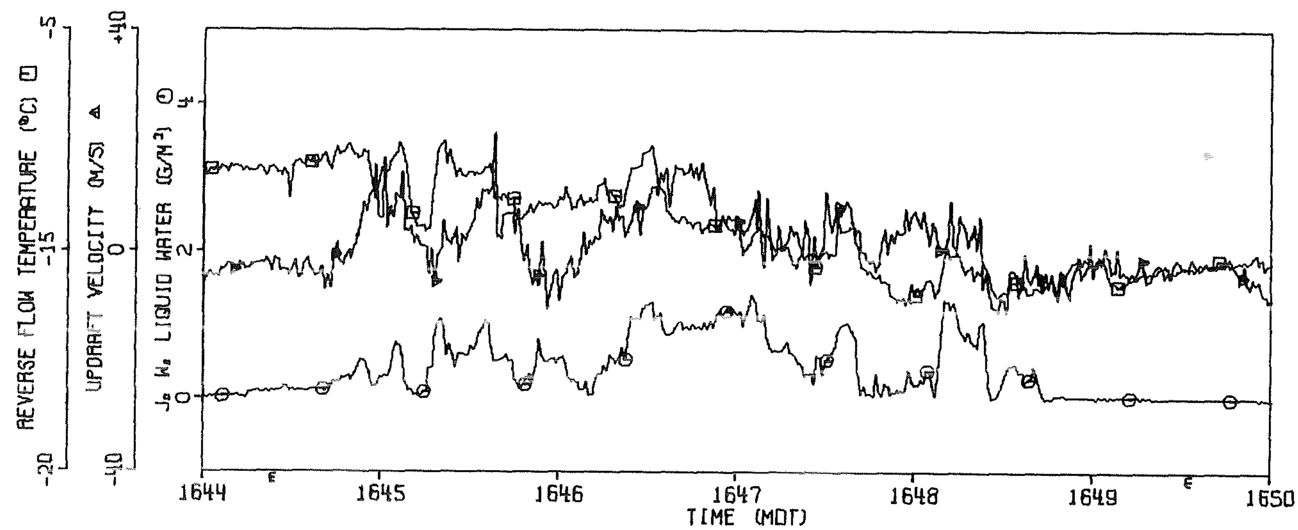

Fig. 5. T-28 FLIGHT 125E 21 JULY 1975 PEN 4

of sharp reflectivity gradient on its south side, and the expected inflow direction from the southeast or south, all combine to make interpretation of the single Doppler velocities relatively straightforward. Three radial Doppler and reflectivity RHI's (radials indicated in Fig. 2) through the storm all during Penetration 3 are shown in Fig. 6. The general velocity pattern with motion from the north at low levels and in the northern part of the echo, motion from the south entering the echo at between about 5 and 8 km MSL and dominating in the upper central part of the storm, and a fringe of northerly motion along the north side above 8 km but not always well marked, was present throughout the 90 minutes of radar coverage. The qualitative flow pattern is shown in Fig. 7 and is justified by the vertical velocities measured by the T-28, which are shown in Fig. 6 by the arrows. We reemphasize that this is a two-dimensional interpretation of a very consistent, persistent, single Doppler velocity pattern, justified by the factors given above and by the agreement of the interpreted flow field with direct measurements of vertical velocity. There is probably a substantial component of the inflow from the east, but this does not invalidate Fig. 7 in principle.

The selected RHI's in Fig. 6 illustrate one strong correlation encountered in the penetrations; the active parts of this storm, those with the strongest vertical velocities both up and down, are within the radar echo. At least this is true along the penetration track at the flight level of the T-28. Penetration 2 was outside the echo entirely, 1 to 5 km south of the 20 dBz contours, and encountered no significant up- or downdrafts. In the other penetrations, the updrafts and downdrafts had substantial reflectivity, particularly in Penetration 3, where the T-28 showed 10 m sec^{-1} updraft in 50 dBz reflectivity.

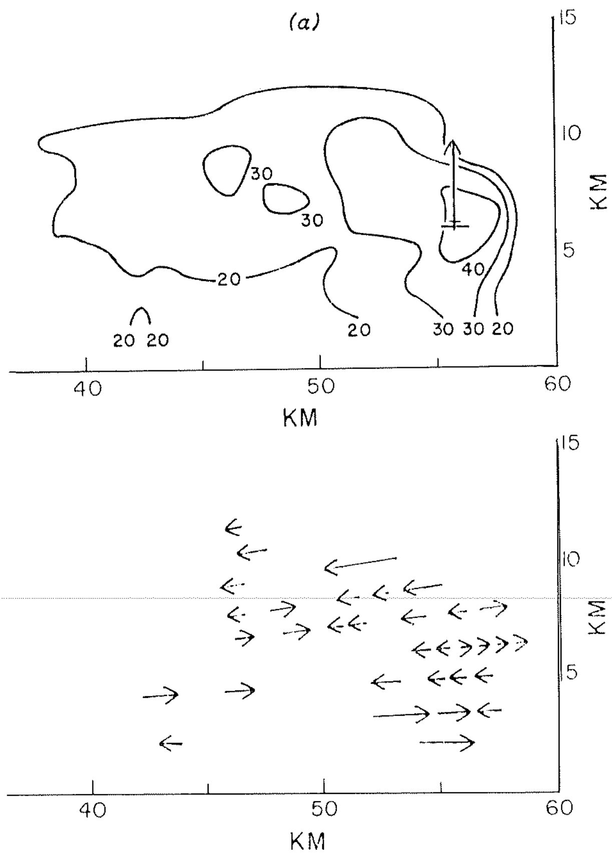

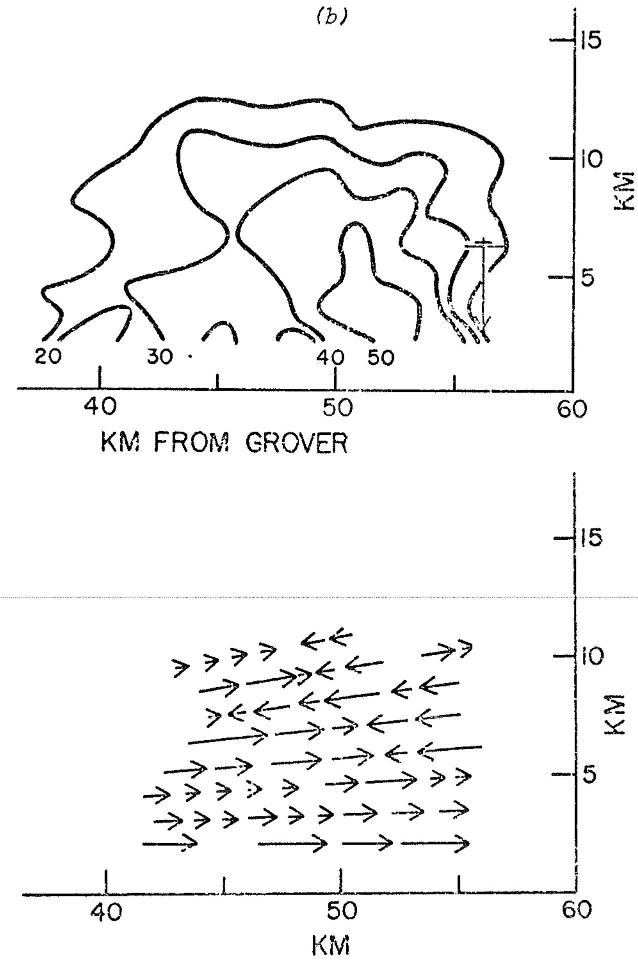

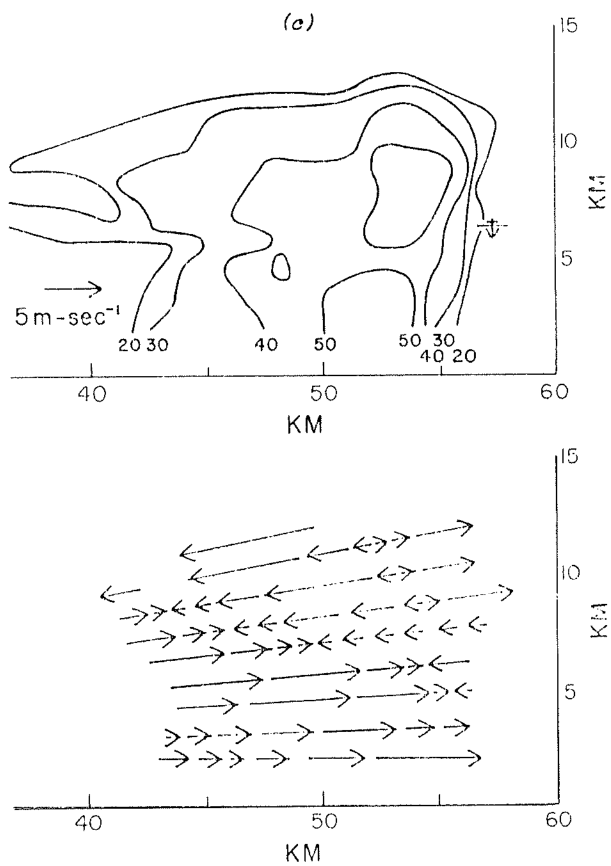

Fig. 6. RHI presentations (upper) and single Doppler velocity patterns (lower) along radials shown in Fig. 2. Figures 6a-c correspond to radials 165, 170, and 178, respectively. The vertical velocity measured by the T-28 is shown on each figure. The key for the scalar value for all velocities is indicated in Fig. 6c. Reflectivity factors are given in dBz.

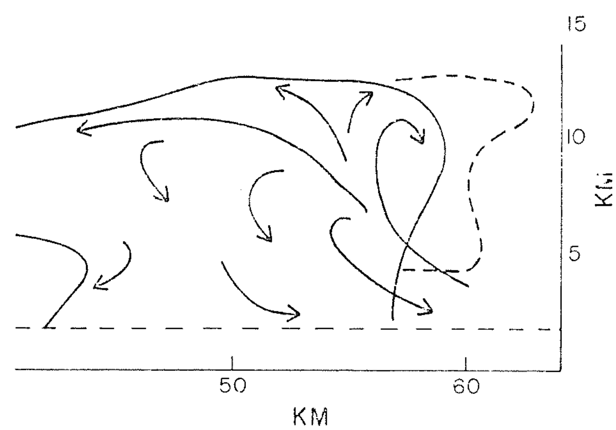

Fig. 7. Schematic of deduced airflow from single Doppler velocity patterns. The dashed line indicates best estimate of cloud outline.

Echo overhangs along the south side of the storm were sometimes updrafts and sometimes downdrafts. The two were not distinguishable from single radar scans, but were by means of the echo time history. The updrafts were accompanied by reflectivity increase with time; the downdrafts, generally, were not.

6. MICROPHYSICS

The microphysical instruments aboard the T-28 included a foil impactor, a Johnson-Williams (JW) liquid water content meter, a hail spectrometer (Smith et al., 1976; in these Proceedings), a PMS forward scattering spectrometer probe (FSSP) for measuring droplets to 30 μm diameter, and a PMS two-dimensional imaging probe, which shows the sizes of particles down to 32 μm and shapes of particles above some 200 μm diameter.

The major purpose of the 1975 flights was to test these instruments in thunderstorm environments. Some problems were encountered, but the following general results appear to be trustworthy: 1) In the updrafts, the cloud droplet concentration varies between about 500 and 1500 cm^{-3} with an upper count of 2000. Very few droplets with diameters > 20 μm were recorded; 2) Liquid water content from the FSSP and the JW ranged up to about two-thirds adiabatic within the updrafts. An adiabatic value of 2.2 g m^{-3} was computed at flight altitude using +2°C as cloud base temperature. The actual values in the cloud could still be adiabatic since questions concerning instrument accuracy still exist; 3) Presence of supercooled water drops above cloud droplet size could not be proved or disproved with certainty with this instrument combination. A few foil imprints and a few two-dimensional images could have been liquid drops (Knight et al., 1976; in these Proceedings); 4) By far, the majority of the particles sensed on the foil or the two-dimensional probe were clearly ice; 5) Much of the ice shown on the two-dimensional probe was mixed snow, sometimes clearly hexagonal; 6) A comparison of data from the foil impactor with data from the two-dimensional probe in the 0.25 to 0.75 mm size range shows particle concentrations up to 50 times higher on the two-dimensional probe for the 250 μm particles, decreasing to 20 times greater for the 750 μm particles. A tentative explanation is that many of the particles in this size range are snow that is so lightly rimed that it does not imprint the foil; 7) Ice particle concentrations on the two-dimensional probe were highly variable, but ranged up to a few hundred per liter; 8) Radar reflectivities calculated from the foil impactor data and hail spectrometer data each compared well with measured radar reflectivities along the T-28 track.

Of particular interest here is the observation of millimetric, rimed snow crystals (Fig. 8). The crystals, mostly stellars, were recognizable during portions of the flight when the T-28 was to the southeast of the radar echo in low vertical velocities and within some updrafts; notably, Penetration 3 (16:37:30 - 16:37:40 MDT in Fig. 4) in updrafts of 5 to 10 m sec^{-1} at a temperature of about -11°C, where they could only be recirculating upwards.

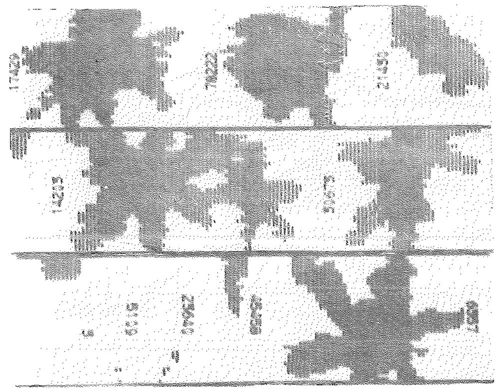

Fig. 8. Examples of rimed snow crystals observed by 2-D Knollenberg imaging probe during Penetration 3 at about 1637 MDT.

7. HAIL COLLECTION

One of the two hail chase vehicles available collected hailstones from this storm. Hail fell at 20.8 km east, 58.4 km south of the radar from 17:13-17:16 and 17:20-17:22 MDT and collections from each hailfall were made. The time was 20 - 30 minutes after the last T-28 penetration and the collections were about 3 km north of the edge of the precipitation wall determined by radar, apparently from Cell 7. The collection corresponded very well in space and time with a local reflectivity maximum of 60 to 65 dBz (calculated for ice) that extended from the ground to 11 km MSL.

The first burst of hail was very sparse with a few stones up to 1-cm diameter. The stones exhibited alternate clear and bubble layers and a uniform, large, crystal size. The second burst contained much more hail, but still with a maximum size of about 1 cm. These stones were mostly bubbly and many exhibited a transition from large to small crystals. Embryos of all 45 stones sectioned appeared to be graupel (Fig. 9) with the exception of 2, which had possible frozen drop embryos. The crystal size interpretation (Pitter and Pruppacher, 1973; Rye and Macklin, 1975) is that the first burst of hail grew entirely below the -15 to -20°C level, while the second grew while ascending through that level.

8. SYNTHESIS

Our view of the mechanics of hail and precipitation formation in this storm should be clear already from the descriptive material. The configuration shown in Fig. 7 is relatively steady, though with local, detailed intensification and fallout of regions of precipitation. The updraft velocities are locally quite strong up to 20 m sec^{-1} and more, but the updrafts become filled with precipitation quite soon by rimed snow crystals forming in eddies within the cloud on its south side and falling back into the updraft where they grow into graupel and small hail. This overloads the updraft, and fallout from the cloud follows.

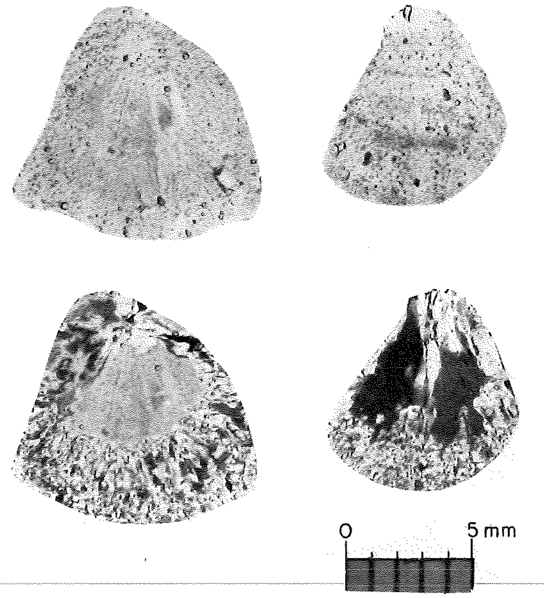

Fig. 9. Sections of two samples of hailstones collected on 21 July 1975. Polarized sections show transition from large to small crystals. Large crystals indicate growth temperatures warmer than -15C.

There was a notable lack of liquid particles larger than cloud droplet sizes in all of the penetrations made on 21 July. This is not unusual when one considers that a Bigg (1953) process would freeze any reasonable concentration of raindrops in about 2 minutes at temperatures found at penetration levels. It is not likely that rain freezing to hail played a significant part in the hail growth in this storm, anyway, because the vast majority of the stones collected at the ground had graupel centers. This means that the ice particles encountered at penetration altitudes (and above) must have been growing by accretion of cloud droplets, which were present in concentrations of 1 - 2 g m^{-3} in the updrafts associated with Penetrations 3 and 4. Estimates have been made, assuming dry growth, that show the largest hailstones encountered in Cell 5 during Penetration 3 (about 1.5 cm) could have grown to diameters in excess of 2 cm in about 10 minutes, which is in agreement with observations made in the same cell during Penetration 4.

Using measured assemblages of ice particles and cloud droplets, echo growth rates of 2 - 3 dBz min^{-1} are calculated in agreement with observation. Using the same assemblages, and averaging over 1/2 km distances of flight path, time constants for depleting the cloud water by accretion are at least 3 - 4 minutes. Depletion rates may be faster in narrow regions, but the statistics of the concentration measurement in narrower regions are not good enough to justify calculation. The 3 to 4 minute depletion time constant agrees qualitatively with the horizontal distance of the echo maximum from the south echo boundary using the measured horizontal Doppler velocities.

Acknowledgments. This research was performed as part of the National Hail Research Experiment, managed by the National Center for Atmospheric Research and sponsored by the Weather Modification Program, Research Applications Directorate, National Science Foundation.

The authors also wish to express their appreciation to Nancy Knight and Linda Chapel for collection of the hailstones in the field, to Robert Stone for preparation of the RHI's, and to the entire Grover crew without whose efforts this study would not have been possible.

REFERENCES

Bigg, E. K., 1953: The supercooling of water. Proc. Phys. Soc. B, 66, 668-694.

Knight, C., W. R. Sand, W. W. Grotewald, and N. C. Knight, 1976: Interpretation and calibration of foil impactor impressions of water and ice particles. Int'l. Cloud Phys. Conf., (this volume).

Pitter, R. L., and H. R. Pruppacher, 1973: A wind tunnel investigation of freezing of small water drops falling at terminal velocity in air. Quart. J. Roy. Meteor. Soc., 99, 540-550.

Rye, P. J., and W. C. Macklin, 1975: Crystal size in accreted ice. Quart. J. Roy. Meteor. Soc., 101, 207-215.

Sand, W. R., and R. A. Schleusener, 1974: Development of an armored T-28 aircraft for probing hailstorms. Bull. Amer. Meteor. Soc., 85, 1115-1122.

Smith, P. L., Jr., D. J. Musil, S. F. Weber, J. F. Spahn, G. N. Johnson, and W. R. Sand, 1976: Raindrop and hailstone size distributions inside hailstorms. Int'l. Cloud Phys. Conf., (this volume).

INFRARED AIRBORNE IMAGERY OF ARCTIC STRATUS DEVELOPMENT AND DISSIPATION

P. M. Kuhn and L. P. Stearns

Atmospheric Physics and Chemistry Laboratory
NOAA - Boulder, Colorado

1. INTRODUCTION

An infrared line-scanning imager, airborne on a jet aircraft, provides the remote sensing capability for observing large scale physics of stratus cloud development, cloud top temperature contouring, mechanical turbulence in cell formation, heights, radiation effects and morphology. The basis for the research is an evaluation of the possibilities for cloud modification techniques. Color enhanced imagery affords a striking analysis of the vertical temperature contours, cellular nature and time history of Beaufort sea stratus. These systems form downwind from shore ice shear zones, ice leads in the open sea ice and polynyas over a -12C to -20C ice surface.

Cloud brightness temperatures converted to physical temperatures were related to cloud parameters. The IR imagery was false color enhanced by amplitude-slicing techniques to highlight the cloud structure. The physical temperature of cloud tops is obtained by "calibrating" the atmosphere during ascent and decent.

NASA's Convair 990 Jet Laboratory supporting the research efforts carried an IR line scanning mapper during the 1975 experiments. Flight operations over the ice and clouds were conducted at elevations ranging from 300 m to 11.5 km. Due to frequent (50% of the time) interspersion of cirriform clouds between flight level and the surface, the 11.5 km altitude did not yield as good IR imagery as did the 3.3 km and 300 m altitudes. However, uniform cirrus coverage allowed good imagery from 10 km. The 3.3 km altitude with its wide scan track, 6.6 km furnished excellent false color enhanced imagery with a spatial, elemental resolution of approximately 2.0 m. The adjustment of the brightness temperature of the low clouds to obtain the physical temperature is approximately +1.5C at 3.3 km and +4.0C at 11.5 km in the 840-1237 cm^{-1} window channel employed.

2. INFRARED MAPPING SYSTEM

The infrared mapper is a passive, airborne imaging system employing an LN cooled Hg-Cd-Te detector (Texas Instruments, RS-310-C) that scans the interface below, along, and out to 45^{o} to either side of nadir of the flight track. In so doing, it produces a continuous image of the surface beneath.

True angle rectification is always maintained by gyro roll-stabilization. In-flight calibration is achieved without sacrifice of lateral imagery coverage by a "blackbody" dual temperature monitored sliding door aperture (Fig. 1). The system was installed in the engineering and electronics hold area of the NASA Convair 990 jet, immediately to the rear of the nose wheel well. A small boundary layer fence, visible in the illustration, eliminated any resonance effects in the cavity. The complete scanner system was sealed to the jet hull via a pressure bulkhead.

Optical mechanical imaging systems collect electromagnetic energy at wavelengths from the ultraviolet to the far infrared. A passive system as employed in this research senses the long wavelength thermal energy emitted from an air-surface interface such as a cloud, terrain, ice or the sea. The imager scans an area below and to either side of the aircraft track. Fig. 1 shows a typical scanner sweep path and the instantaneous field of view of the scanner, and illustrates the relationship of the scanning system to the ground. Θ is the sweep angle of 45^{o}; ln is the altitude and D is the line segment distance of the instantaneous sweep width. The cooled detectors of the two channel system which we employ are mercury-cadmium-telluride with a minimum temperature resolution of 0.15K and an overall speed of response of 500 m sec. Figure 2 illustrates the installation on the NASA CV-990.

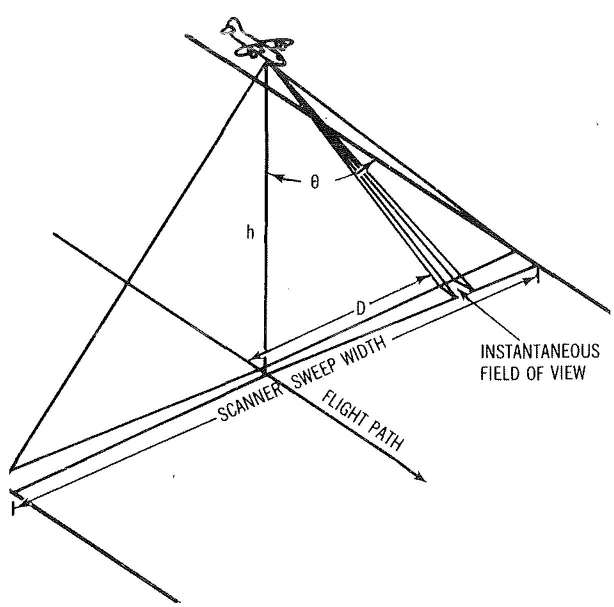

Figure 1. Scanner sweep path illustrating instantaneous field of view, sweep width and flight path.

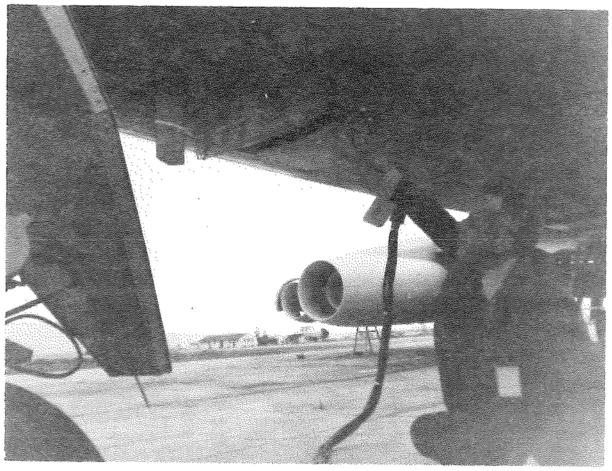

Figure 2. Installation of IR imager in electronics compartment of NASA Convair 990 showing boundary layer fence, sliding door just aft of DME antenna.

3. COMPUTATION OF NEAR SURFACE WATER VAPOR PRESSURE

Laevaster and Harding's (1974) modification of the Dalton type formula for the computation of sea minus air vapor pressure is given as follows:

$$\frac{d(\Delta e)}{dt} = \backslash V.\nabla T_w - \frac{de_a}{dt}, \qquad (1)$$

Where e is vapor pressure in mb; t is time in hours; $\backslash V.\nabla T_w$ is the rate of change of sea surface temperature along the sea as in a polynya; e_a is the vapor pressure in the air at 8m from the sea surface. Laevaster and Harding (op cit) develop the work of Boyum (1962) incorporating their expression for the change of vapor pressure over water into (1) which, after integration, gives

$$\Delta e = (e_w - e_a) = \Delta e_o \exp^{-.5t} \qquad (2)$$

$$+ (.8 + 2.0\, V_r \frac{\partial T_w}{\partial r})(1.0 - \exp^{-.5t})$$

Where e_w is the vapor pressure in mb over water; Δe_o is $e_w - e_a$ at the initial computation period at time $t = 0$, t_o, or at the upwind edge of a sea ice lead, the focus of our research, V_r is the wind speed over the range, r, and T_w is the water temperature. In the Arctic leads

$$V_r \frac{\partial T_w}{\partial r} = 0. \text{ downwind.}$$

The evaluation of Δe in (2) immediately results in the inference of e_a and thus to the critical atmospheric water pressure for cloud formation. As an example, we observed the following initial conditions and computed the vapor pressure in mb of the air traversing an open lead as a function of time:

T_{air} (over ice) Observed -15C

e_a (saturation vap. pressure over ice) .83 mb at rel. hum. = .50

$e_w - e_a = \Delta e_o$(at time t = 0)= 4.7 mb

Δe(at time t = 0.2 hrs)= 4.3 mb

Δe(at time t = 0.5 hrs)= 3.8 mb

From these results and observing from the imager no change in the water temperature along the extended open lead surrounded by ice, we infer the following vapor pressure in the air

t = 0	e_a = .83 mb
t = 0.2 hr	e_a = 1.23 mb
t = 0.5 hr	e_a = 1.70 mb
t = 0.75 hr	e_a = 2.00 mb

Thus in 45 minutes of travel over an open lead, the atmosphere would be saturated at 2.00 mb and fog and stratus will form over water and at 1.67 mb vapor pressure over the ice at end of a lead. Additional examples and illustrations of the imagery over leads extending for 24 km evidence the formation of clouds downstream in the winds from the lead. Dissipation of the stratus is a reverse function of the water to lower atmosphere vapor pressure gradients. However, one should note that we do not employ the gradient approach. The color enhanced IR imagery clearly shows the clouds forming downstream of the leads. Dissipation occurs some 25 to 35 km downstream.

4. LOW CLOUD STRUCTURE

Our airborne observations of the bases of downstream (from leads in the ice) stratus or stratus cumulus clouds in the Arctic north of the north coast between 72^o and 78^o north latitude over the Beaufort Sea ice ranged from 0.15 km to 0.30 km. The tops on occasion reached 2.0 km. The imagery shows top temperature varying from -5.0 to -10.0C indicating some internal convection. Several illustrations employing the areal IR imagery show the clouds forming downstream from the lead with low bases due to the very cold air overlying the water. As the air temperature in the lower layers modifies downstream along the lead, the base tends to lift (Laevaster and Harding, 1974). Herman (1975) has discussed the thermodynamics of the ice-air and water-air interfaces in the Arctic. He states, based on observations and calculations, that water evaporates from the surface of a lead at a very rapid rate since the saturation vapor pressure of the water is so much greater than that of the air. Condensation occurs rapidly in the cold air upstream in the lead. Fog and/or low-based stratus forms and the base lifts as the cold surface air layers are warmed downstream along the lead.

Figure 3 shows the increase in vapor pressure downstream along a lead with a 10 knot wind condensation over water occurs at a saturation vapor pressure of 2.0 mb and over ice at 1.67 mb. Thus the Amot-Mosby (1944) method of computing near-surface water vapor pressure changes with time can be employed to illustrate the formation and dissipation of Arctic Stratus assuming sufficient condensation nuclei are present.

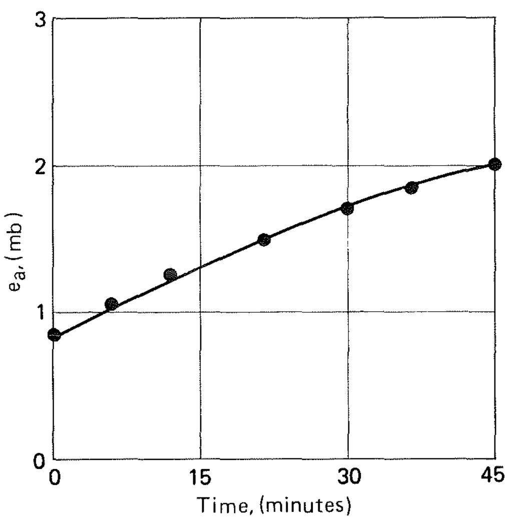

Figure 3. Vapor pressure increase downstream over sea ice lead with time.
C = 0.4 K = 0.5 Δe = .83 mb

REFERENCES

Amot, A., 1944: On the temperature difference between the air and sea surface and its applicability in the practical weather analysis. Met. Ann., 1, 19, 488-527.

Boyum, G., 1962: A study of evaporation and heat exchange between the sea surface and the atmosphere. Geofys. Pub., 22, 7, 1-15.

Herman, G., 1975: Radiative-diffusive models of the Arctic boundary layer. Mass. Inst. of Tech., Scientific Rept # 3, COO-2195-21, 170 pp.

Laevaster, T. and J. M. Harding, 1974: Numerical analysis and forecasting of surface-air temperature and water vapor pressure, J. Geophys. Res., 79, 4478-4480.

7.3.5

PROGRESS IN PRECIPITATION GROWTH MEASUREMENTS

Robert M. Cunningham

Air Force Geophysics Laboratory
Hanscom Air Force Base, Bedford, MA 01731

1. INTRODUCTION

Precipitation growth studies involving measurement and modeling have concentrated largely on the convective storm. Limited quantitative studies have been made on cyclonic storms with large precipitation shields, most have explored the mesostructure of frontal storms. An attempt was made some time ago by the author, Cunningham (1952), to compute from limited observations the precipitation growth in various regions of a cyclonic storm. This study obtained the surprising result that much of the water that reached the ground was added to the falling hydrometeors in the lower levels below the frontal surfaces. Recent advances which have permitted more extensive particulate measurements, make it possible to pursue growth studies in a more realistic fashion.

Many studies of all types of storms have been made with radar. However, the difficulty of conversion of the radar reflectivity factor to the particulate population details, especially in the case of snow and ice crystal clouds, has not permitted quantitative growth calculations.

This paper discusses an analysis procedure whereby radar data and particulate measurements from aircraft can be combined to form a basis for computation of precipitation growth.

There is a long history of development of the techniques which enable one to convert the radar signal from rain near the ground to precipitation rate over an area at the ground. Working out a similar procedure in the snow and and ice crystal regions requires knowledge of the distribution of particle size - in particular the distribution of the equivalent melted diameters. With the development of automatic sizing and counting sensors it is now possible to gather sufficient particle statistics to try to determine, in a similar manner as is done on the ground, relationships between the precipitation type, radar reflectivity and parameters of the particle distribution. There are some important differences between the airborne and ground situations. For one, there is as yet no satisfactory "flying rain gauge" available. The simple check of comparing the integral parameter (mass) of the distribution to the total water collected is not as yet available.

The two difficult parts of this analysis are then: a) a measurement difficulty, that is an inadequate check of the integrated parameters of the measured distribution and b) an operational difficulty, i.e., not being able to sample with one or more aircraft in the exact time and place that one wishes. One wishes usually to follow from one or more radar presentations the growth of precipitation along a recognizable pattern in the echo, such as a precipitation streamer. An example is given of the application of this method illustrating the type of results that can be obtained and the limitations encountered using this method.

2. ANALYSIS OF PARTICLE SIZE SPECTRA

The particle data to be discussed in this paper are derived from optical array devices manufactured by Particle Measuring Systems, Inc. (PMS) and described by Knollenberg (1970, 1972, 1976). Particle shadow size along one dimension is quantized into 15 channels nominally ranging in the "cloud" probe from 20 μm to 300 μm and in the "precipitation" probe from 300 μm to 4.5 mm. In the case of all but the largest raindrops the conversion from shadow dimension (in this case the maximum dimension) to mass is straightforward and sufficiently accurate as the particles are assumed spherical with density of one. For ice and snow particles both shape and density can vary considerably, and the probe recording of a one dimension size does not necessarily correspond to the maximum dimension. Because the probe is exposed so that the laser beam is vertical, particles which are largely two dimensional and falling with the larger dimension horizontally, will be recorded at close to their maximum dimension. Many of the problems of interpretation of the probe response to non-spherical particles have recently been investigated and reported on by Knollenberg (1976). The empirical relationships formed have been smoothed and used here. Conversion of the recorded sizes, adjusted by these relationships, to distribution of mass and reflectivity factor requires knowledge of relationships between the above dimension and the "melted diameter." A number of investigations have developed empirical relations between particle maximum diameter and mass (or melted diameter) see for instance some recent contributions, Locatelli and Hobbs (1974), Heymsfield and Knollenberg (1972), Knollenberg (1976).

A selection of the above reported relations are being used in this study. A fairly large error in determining mass (m) or radar reflectivity factor (Z) can result from incorrectly identifying particle type.

Fortunately, both the problem of sensor response to irregular shapes and the conversion of size to melted diameter are involved in a similar way in deriving M and Z from the distribution. We have utilized a suggestion of Plank (1976) to minimize the effect of these inaccuracies. If one uses the ratio of M to $\sqrt{Z}$ one obtains a parameter much less sensitive to the above problems. This ratio, based on aircraft measurements, is used as a parameter to relate to simultaneous radar measurements from the ground. We use this ratio as a parameter of the particle distribution. The relation we obtain between it and the simultaneously measured radar reflectivity factor (Z_R) remains reasonably constant for the altitude of measurement during a period within the storm where no major change in storm character has occurred.

The above would be applied to the problem of radar pattern interpretation in a similar fashion as the usual R-Z (R, rainrate) or M-Z relation. Instead of using an aircraft derived M (M_A) related to a radar derived Z_R, which, as we have explained above, retains the many inaccuracies involved in obtaining M_A, we use the ratio $M_A/\sqrt{Z_A}$ related to Z_R. In the next section, the procedure used to derive M from a measured Z_R will be described for a time or place not measured by the aircraft.

3. PARTICLE DISTRIBUTION ANALYSIS

Aircraft measurements of the particle count per sensor channel are summed every four seconds. This time interval corresponds roughly to the length of time required to fly through one sample volume used in the ground radar analysis procedure. A sample run with the aircraft at any one altitude is limited to approximately five minutes. A sample with the "precip" probe is about .4 m^3 in volume for the 4 second sample and about 30 m^3 for the total five minutes. Calculations based on Joss and Waldvogel (1969) suggest that the larger sample is of reasonable size but the 4 second sample is very poor. To compensate for this poor sample size the 75 samples were combined. They were combined by normalizing the distribution in a manner suggested by Sekhon and Srivastava (1970). The effects on this non-dimensional distribution of various real changes in water content within the five minute samples are minimized in this process, yet allowing one to derive a more statistically valid estimate of the upper tail of the distribution. A more complex procedure has recently been developed by Joss and Gori (1976) whereby distribution shape changes that were correlated with water content could also be accounted for.

The combination of the 4 second samples used for this paper is accomplished by converting the distribution measured each 4 seconds into the above non-dimensional form. Where Y = Log $(N\rho_w D_0^4/M)$ and $X = D/D_0$ where N = number of particles per cubic meter per mm bandwidth, ρ_w = density of water in mg/mm^3, D_0 is the volume median drop size and M is the water content in mg/m^3. Average values of 10^Y for some 22 intervals between D/D_0 of 0 to 4 are computed. The average values obtained in the upper end of the distribution are usually derived from a number of 4 second samples of zero count and a few with single counts. A D/D_0 value which represents a reasonable instrumental maximum ratio is determined by picking a D/D_0 value with not more than 1/2 of the input sample in the zero class. This value of D/D_0 is then used to represent, when multiplied by D_0, a reasonable maximum size D_x sampled by the instrument. This size also represents the maximum size contributing appreciably to M_A and Z_A in the ratio $M_A/\sqrt{Z_A}$.

4. DERIVATION OF DISTRIBUTION AND M

With the plots of $M_A/\sqrt{Z_A}$ vs Z_R and the normalized distribution, one can derive a distribution and an M_c (distribution integrated to D/D_0 value of 4, i.e. effectively infinity) for any reasonable input value of Z_R. This calculation involves double iteration on the normalized distribution, and its M and Z integral parameters. It involves adjusting D_0 and Y until (1): M (cumulative) at D_x is equal to $(M_A/\sqrt{Z_A})\sqrt{Z_x}$ where Z_x is the value of Z (cumulative) at D_x and until (2): Z (cumulative) at $D/D_0 = 4$ is equal to Z_R. With aircraft identification of particle type, measurements of particulate distribution and simultaneous values of radar determined reflectivity factor one can, with the above procedures, derive particulate distribution from radar data alone for a time and place other than at the aircraft sampling time. For altitudes other than aircraft sampling altitudes, the $M_A/\sqrt{Z_A}$ ratio and distribution function could be derived by interpolations.

5. APPLICATION TO CASE OF 9 JAN 75

An active trough line with a developing coastal low passed just north of the sampling area off Wallops Island, VA late on the 8th of Jan. A deep warm frontal precipitation system was probed at a number of altitudes by an AFGL/ASD C-130 equipped with a number of hydrometeor sensors. Results from the two airborne PMS optical array probes and radar measurements from the AFGL/APL/NASA SPANDAR radar will be discussed here to illustrate the procedures outlined above.

Coordinated runs with the radar were made at four altitudes all in the snow above the bright band. Surface rain rates and raindrop distribution data (Joss disdrometer) were available from a point three miles east of the radar. One of the better results from the correlation runs is illustrated in Fig. 1. Here the computed radar Z_A is compared every 4 seconds with the measured radar value Z_R. The similarity in detail of these two records is quite good when one remembers that the aircraft sample is approximately 30 m^3 while the radar sample is 4 x 10^6 m^3. The agreement indicates that, at least in this case, a thin line sample through a large apparently well mixed volume can be representa-

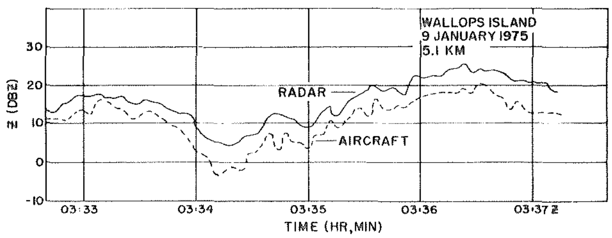

Figure 1. Comparison of calculated Z from aircraft measurements with measured Z by the SPANDAR radar.

tive. Fig. 2 shows the corresponding relation between the ratio of $M_A/\sqrt{Z_A}$ and Z_R. The best fit line is used to extrapolate this relation to values of Z_R used in the final analysis steps.

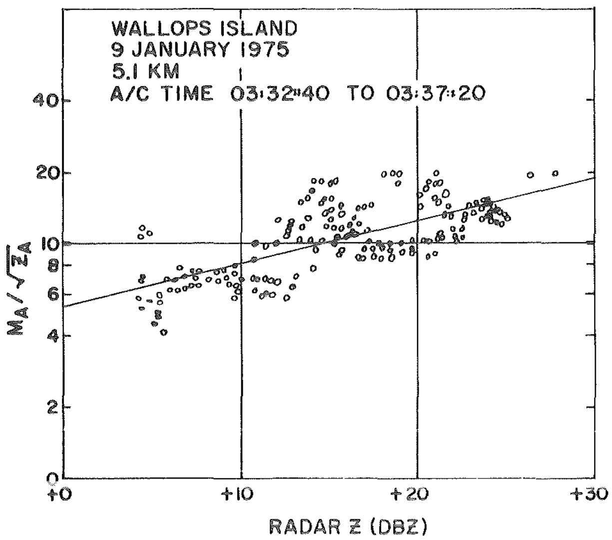

Figure 2. Plot of ratio $M_A/\sqrt{Z_A}$ calculated for each 4 second period of aircraft measurement against simultaneous measurement of Z by the SPANDAR radar.

The distribution scatter diagram is shown in Fig. 3. The wide scatter at values of D/D_0 between .7 and 1.1 is caused by problems related to the poor sampling volume of the upper channels of the "cloud" probe and quantizing errors in the first channel of the "precip" probe. Fig. 4 shows the relationships found on all four passes between $M_A/\sqrt{Z_R}$. Thick lines indicate the range of measured values. Also shown are some nominal relations of $M/\sqrt{Z}$ vs Z derived from data of Heymsfield (1975) for bullet rosette ice crystals (IC), Ohtake and Henmi (1970) for snow aggregates (LS) and Joss, et al (1968) for widespread rain (R).

An RHI scan taken upwind within an hour before the flight measurements was chosen for study. Fig. 5 is a tracing from an original color contoured RHI picture. The Z values (in DBZ) indicated are derived from a calibration of the radar using several techniques including comparison with ground rainrate and disdrometer devices. The values of Z in the bright band region are omitted as not meaningful. Two lines were drawn through what appears to be a precipitation streamer. Values of Z were read along this

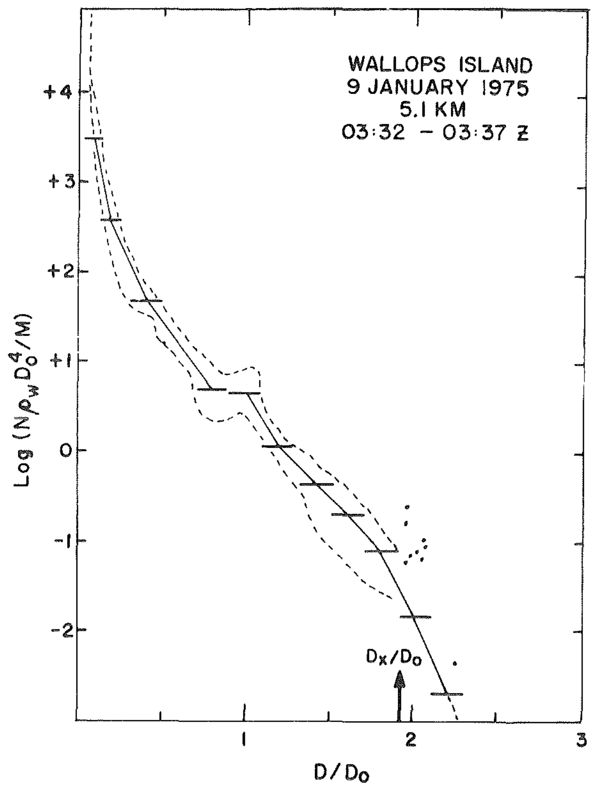

Figure 3. Non-dimensional plot of particle distribution. Solid line joins average values in 11 size ratio intervals. Dashed line encloses approximately 68% of the individual 4 second points. Individual values are plotted beyond the D_X/D_0 value.

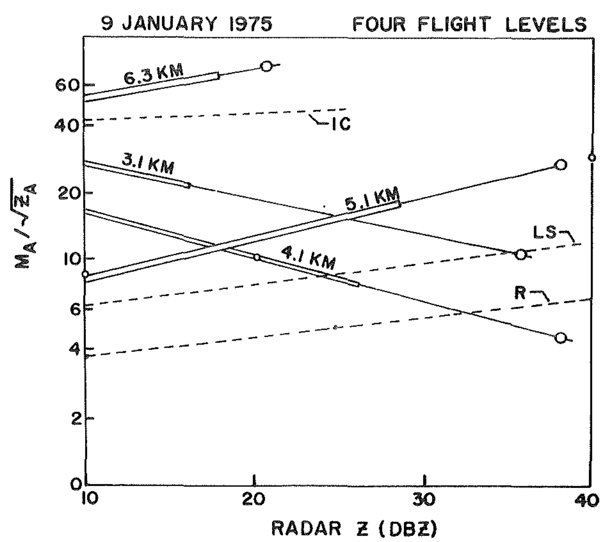

Figure 4. Best fit lines for the four flight altitudes. Data limited to the portion shown as double lines. Circles indicate points used in computations given in Tables 2 and 3.

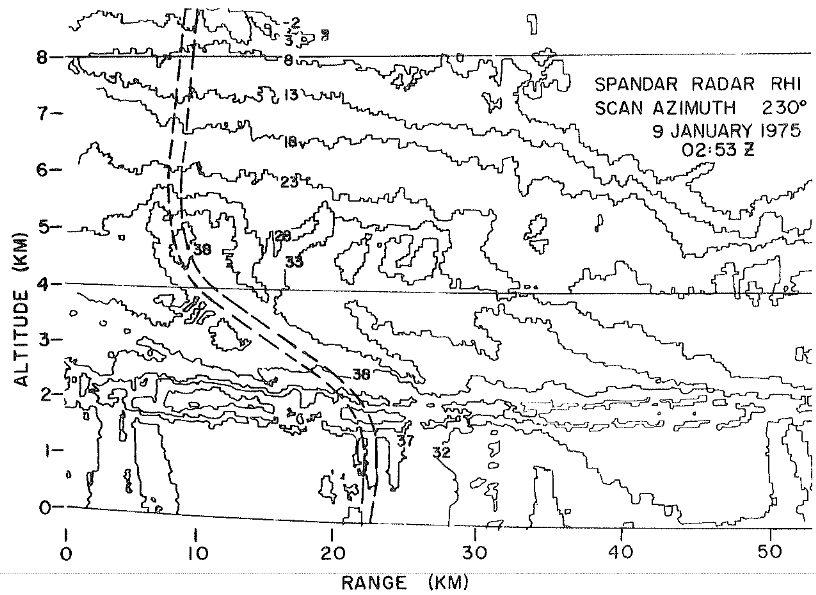

Figure 5. Tracing of contoured RHI from SPANDAR radar. Contours labeled in DBZ. Precipitation streamer is indicated by the double dashed line.

line at flight altitudes, at 8.2 km and the surface. The procedures outlined above were followed except that for the 8.2 km level the relations found for 6.3 km were used. For the surface data, disdrometer data (averaged over 2 minutes) were chosen that indicated a Z value close to that recorded at the bottom of the streamer.

The type of ice crystal and snow for the chosen altitudes was obtained from supplementary visual observations.

The conversion from maximum crystal size to melted diameter for the range of sizes involved in this study is shown in Table 1.

TABLE 1

Melt Diam	Crystal Type, Maximum Diam or Lengths mm		
mm	B-R	SS	LS
.04	.06	.053	--
.4	.9	1.0	1.0
1.0	2.3	3.9	2.8
2.4	--	--	7.8

B-R, bullet-rosettes; SS, single crystals and aggregates of a few crystals; LS, aggregates of many crystals.

The growth of the precipitation particle by sublimation and by aggregation is illustrated by the size distribution changes shown in Table 2.

TABLE 2

Number of particles per cubic meter

ht km	Total*	Total above melted size indicated			
		>.04 mm	>.4 mm	>1 mm	>2.4 mm
8.2	8.1×10^5	5×10^4	155	0	0
6.3	6.0×10^5	1.3×10^5	6.7×10^3	0	0
5.1	2.5×10^5	2.2×10^5	8.1×10^3	856	1
4.4	1.8×10^4	1.8×10^4	708	74	8
3.1	3.8×10^4	3.2×10^4	1.3×10^3	348	3
0	---	---	115	36	5

*The lower size limit increases slightly from high to low levels.

The water content values along the streamer as well as the drop distribution are calculated. Fall velocities from papers by Heymsfield (1972) and Locatelli and Hobbs (1974) have been used to compute the precipitation rate from the calculated particle distributions. The fall velocities have been adjusted for altitude using the relation $V = V_R \left(\frac{P_R}{P}\right)^{1/3}$. Where V_R is the fall velocity in the referenced publication measured at a pressure (P_R). P is the pressure at the height of this study.

The slope of the precipitation streamer was calculated from the rawinsonde winds and the snowfall velocity values used above. This calculated slope was compared with the pattern shown on Figure 5. The computed slope was less than the pictured slope, fall velocities some 50% greater than used here would result in similar slopes.

TABLE 3

Ht km	Temp ^{o}C	Particle Type	Z DBZ	M $Mg/_{M}3$	D_0 mm	R mm/hr
8.2	-37	B-R	8	130	.3	.43
6.3	-21	SS	21	570	.5	1.4
5.1	-13	SS→LS	38	2030	.9	3.9
4.4	- 9	LS	38	350	1.9	1.4
3.1	- 2	LS	36	640	1.2	2.5
0	+ 8	R	36	130	2.3	3.1

The large liquid water content computed for the 5.1 km level is possible; it is at the level where the precipitation streamer starts and may reflect a storage area due to convection. The low value below at 4.1 km, however, is highly suspect. Note that the large extrapolation shown on Fig. 4 results in a very low value of $M_A/\sqrt{Z_A}$.

The precipitation rate changes from 8.2 km to the surface suggest that a major source of the total water that reaches the ground is supplied at high levels in contrast to the results found in the case studies in 1952.

6. COMMENTS AND SUGGESTIONS

The 1975 case chosen was the first one for which data were available in the form required. There are some obvious lessons to be learned from this study. Some of these are: 1) Extrapolation of the $M_A/\sqrt{Z_A}$ vs Z_R relation, at least to the extent needed in this case, should not be repeated. 2) The time interval between the aircraft-radar sampling and the use of the relations should be shorter than tried here. (Additional sampling flights have been made during this last winter to determine the stability with time of the above relation.) 3) Methods should be developed for preserving changes in the drop spectrum shape if and when these changes are correlated with water content. 4) To avoid variations within a precipitation streamer at one instant of time either high values should be followed down the streamer or, probably a more realistic method would be to average Z values among a number of similar streamers. 5) Measurements of fall velocities obtainable from doppler radar would add a very useful dimension to this type of study.

REFERENCES

Cunningham, R. M. (1952) Distribution and growth of hydrometeors around a deep cyclone, MIT Weather Research Report No. 18.

Heymsfield, A. J. and Knollenberg, R. G. (1972) Properties of cirrus generating cells, J. Atmos. Sci., 29:1358-1366.

Heymsfield, A. J. (1972) Ice crystal terminal velocities, J. Atmos. Sci., 29:1348-1357.

Heymsfield, A. J. (1973) The cirrus uncinus generating cell and the evolution of cirriform clouds, Ph.D. Thesis, The University of Chicago.

Joss, J., Thams, J. C., and Waldvogel, A. (1968) The variation of raindrop size distributions at Locarno, Proc. Internatl. Conf. on Cloud Physics, Toronto, Amer. Meteorol. Soc., Boston, p. 369.

Joss, J. and Gori, E. G. (1976) The parameterization of raindrop size distribution, (submitted to the Journal of Applied Meteorology).

Joss, J. and Waldvogel, A. (1969) Raindrop size distribution and sampling size errors, J. Atmos. Sci., 26:566-569.

Knollenberg, R. G. (1970) The optical array: An alternative to scattering or extinction for airborne particle size determination. J. Appl. Meteor. 9:86-103.

Knollenberg, R. G. (1972) Measurements of the growth of the ice budget in a persisting contrail, J. Atmos. Sci., 29: 1367-1374.

Knollenberg, R. G. (1975) The response to optical array spectrometers to ice and snow AFCRL-TR-75-0494 Air Force Cambridge Research Laboratories.

Locatelli, J. D. and Hobbs, P. V. (1974) Fall speeds and masses of solid precipitation particles, J. Geo. Res., 79:2185-2197.

Ohtake, T. and Henmi, T. (1970) Radar reflectivity of aggregated snowflakes, preprints of papers presented at the 14th Radar Meteorology Conf., Tucson, Arizona, 17-20 November 1970, pp. 209-211.

Plank, V. G. (1976) Hydrometeor data and analytical-theoretical investigations pertaining to the SAMS rain erosion flights of the 1972-73 season at Wallops Island, Virginia. Air Force Geophysics Laboratory Technical Report (to be published).

Sekhon, R. S. and Srivastava, R. C. (1970) Snow size spectra and radar reflectivity, J. Atmos. Sci. 27:299-307.

7.3.6

CLOUD DROPLET DISTRIBUTION IN HIGH ELEVATION CONTINENTAL CUMULI

Daniel W. Breed and Lewis O. Grant
Department of Atmospheric Science
Colorado State University
Fort Collins, Colorado

and

James E. Dye
National Center for Atmospheric Research[1]
Boulder, Colorado

1. INTRODUCTION

The South Park Area Cumulus Experiment (SPACE) was initiated during the summer of 1973 to systematically study the cumulus clouds that form over the Mosquito Range west of South Park in Colorado using radar, terrestrial photogrammetry, instrumented aircraft, a surface mesonet, and other monitoring devices (see Danielson and Grant, 1974). From July 7 to August 8, 1975, measurements of cloud droplet distribution and liquid water content were made by three different aircraft using a variety of sampling devices. Data taken by the NOAA-NCAR sailplane, supplemented by data taken by the University of Wyoming's Queen Air and the Colorado State University's Aerocommander, are the basis of this analysis. The sailplane, operating out of the Lake County Airport near Leadville, made measurements during the entire period while the Queen Air operated during the first week of the period and the Aerocommander operated during the last week of the period. The clouds sampled were generally growing cumulus congestus with bases near or above the freezing level (∿ 4500 m MSL). A representative description of these mountain cumuli in terms of a cloud droplet spectrum, its variation in space and time, and a liquid water structure has been constructed from the data. This description is in turn being related to precipitation processes and possible mixing processes taking place in the clouds, and is being used as an aid in verifying the parameterized cumulus models being developed and tested for the SPACE area.

2. AIRCRAFT INSTRUMENTATION

The Explorer is a Schweitzer 2-32 sailplane owned by NOAA but instrumented and operated by NCAR. It is a unique cloud physics research aircraft in that it samples clouds in a semi-Lagrangian manner, spiralling up in the updraft regions of the clouds. The data obtained every 0.5 sec is telemetered to a ground station where they are recorded on magnetic tape for computer processing. A complete description of the Explorer's instruments and sampling procedure has been presented by Sartor (1972), Abbott et al. (1972), Cannon et al. (1974), and others. The following descriptions serve only as a brief summary of the capabilities of the Explorer instruments pertinent to this study.

An electrostatic disdrometer is mounted on the Explorer on a nose boom 75 cm long. Number concentrations $cm^{-3}\ \mu m^{-1}$ are recorded in 9 data channels with a minimum detectable cloud droplet size of 8 μm in diameter. The first six channels have diameter intervals of 3 μm, the next two have intervals of 6 μm, the ninth channel records droplets > 38 μm diameter, and a tenth channel gives the total number concentration cm^{-3} for the 0.5 sec sampling period. Liquid water content is obtained through integration of the disdrometer derived spectrum.

The operation and sampling restrictions of the Johnson-Williams (J-W)[2] hot wire liquid water content meter have been well documented in the literature (Owens, 1957; Spyers-Duran, 1968; Knollenberg, 1972). Reliable measurements can be obtained if proper adjustments are made for the particular situation and environment the J-W will be used in. Because the telemetry system of the Explorer cannot handle the negative voltages which may arise from zero drift errors, the J-W's baseline was set at a value > 0 soon after take-off. This adjusted zero ranged from 0.2 to 1.5 $gm\ m^{-3}$ but was usually close to 0.6 $gm\ m^{-3}$. The greatest source of error when using the processed data is the subjective determination of this baseline value which could be estimated to ± 0.05 $gm\ m^{-3}$.

The CSU cloud physics aircraft is an Aerocommander equipped during SPACE to measure cloud liquid water content and droplet spectra as well as state parameters. A cloud droplet slide gun sampler on loan from the University of Wyoming measured cloud droplet spectra at a rate of 1 slide per cloud penetration. The details of its design and operation are given in an unpublished report by Auer (1969) to the Bureau of Reclamation. Peak J-W values at the time of the slide exposures were logged by a flight observer. A

---

1 The National Center for Atmopsheric Research is sponsored by the National Science Foundation.

2 Johnson-Williams, Inc., 2300 Leghorn Ave., Mountain View, California.

continuous record of the J-W values was not obtained due to a software problem with the airborne mini-computer. Although this problem limited any direct comparison of the J-W and the slide gun sampler, the two instruments gave reliable measurements during SPACE.

The University of Wyoming's Queen Air made measurements of the cloud droplet spectrum using the cloud droplet slide gun sampler mentioned and an Axially Scattering Spectrometer Probe (ASSP) designed and developed by Dr. R.G. Knollenberg (1976). Because testing of the ASSP is still in progress, any comparisons presented between these two instruments are contingent on future developments. For this study, the emphasis has been on the analyzed slides.

3. SAMPLING PROCEDURES

The 13 clouds sampled by the Explorer and analyzed in this study were generally cumulus congestus which were not precipitating at the time of the Explorer's release from the towplane although a few developed precipitation while the penetration was in progress. Sampling for these particular analyses was usually restricted to the lowest 1000 m of the cloud due to the inability of the variable and discontinuous updrafts to sustain the Explorer's operations in the upper levels of the clouds. Cloud depths were usually greater than 1500 m. July 9, when the Explorer was released near the top of a large cumulus congestus, is the only day the Explorer sampled the upper portions of a cloud. Pilot observations were used to determine the position of the Explorer in relation to the visible extent of the cloud (i.e., near the edge), and to determine regions of turbulence and/or graupel encounters.

The Aerocommander penetrated three clouds of about the same size and stage of development making 3-5 passes in steps of decreasing altitude, and penetrated two others 3 times at a constant altitude. The penetrations were about 3 minutes apart, and the slide samples were usually taken within the first 10 seconds of penetration (∿ 800 m). The clouds penetrated on August 7 and 8 were the same as sampled by the Explorer with the penetrations usually commencing as the Explorer exited the cloud.

Measurements were made on July 7 and 9 by Wyoming's Queen Air. The majority of the penetrations were through isolated cumulus congestus and through tops and turrets of larger cloud agglomerations. Observer comments are used to correlate the slide samples with the characteristics of the cloud (i.e., turbulence, updraft, precipitation encounters).

4. RESULTS

Although natural variability in individual clouds as well as among different clouds is quite high, it can be kept to a minimum if the sample is restricted to a single class of clouds in the same stage of development. To aid in the comparison of measurements in different clouds, the sample has been normalized to some extent by stratifying the data into intervals above cloud base, since cloud parameters at the same cloud level for an average updraft are of about the same age and have had the same interactions. The diversity of the data taken during SPACE restricts any fine scale interpretations of the comparisons between instruments, but the capability of determining the general features of the cloud droplet spectrum and liquid water content is still there. These features are important in understanding the development of cumulus congestus into large cumulonimbus and cumulonimbus sytems in the South Park area.

4.1 Droplet Concentration and Size Spectrum

The soot-coated slide samples gave the most detailed information about the droplet spectra and total concentration, but were restricted by their sampling volume. Twenty-one slides were averaged to obtain a total droplet concentration of 553 cm^{-3} (range 72 to 930 cm^{-3}) with a mean diameter of 7.5 μm (range 5.3 to 9.9 μm) and a mean coefficient of dispersion of 0.225 (range, 0.085 to 0.360). Only 2 of the slides had total concentrations < 300 cm^{-3}, one of 72 cm^{-3} and one of 109 cm^{-3}, and both of these were exposed near the edges of the clouds. Sixteen of these slides were exposed in the lowest 1000 m of cloud depth. They were grouped into 100 m intervals above observed cloud base, and their averages are plotted as solid lines in Figs. 1-10. The plots in Figs. 5 and 10 are the result of just one slide sample. The spectrum near cloud base (Figs. 1 and 2) is very narrow with an approximate modal diameter of 6 μm. The spectrum stays very narrow throughout the first 1000 m of cloud depth with a gradual shift of the modal diameter to about 9 μm at 900-1000 m above cloud base. Assuming a constant updraft of 3 m sec^{-1}, any broadening of the spectrum with height can be accounted for by condensational growth in supersaturations of < 0.1%, except in the 300-400 m interval. For broadening of the spectrum in that interval, supersaturations of 0.4% would have been necessary to account for the largest droplets. This seems unlikely considering the high droplet concentrations and the short growth period. The droplet spectrum at 300-400 m is dominated by slide samples taken in the last two penetrations of one cloud. The lack of droplets in upper intervals as large or larger than those in the 300-400 m interval suggests that aging of the cloud and its corresponding variabilities complicated the steady-state growth approximations that were made. From such a small number of slides, a growth process of these larger cloud droplets cannot be clearly defined.

The disdrometer data were also averaged over 100 m intervals above cloud base and are plotted as histograms in Figs. 1-10, beginning at the lower limit of 8 μm. This data, within its resolution limits, also shows a narrow spectrum with a slight but steady increase of concentrations in channel 2 (11-14 μm diameter) and channel 3 (14-17 μm diameter). No droplets were detected in channels 5-9 (> 20 μm). There is fair agreement between the slide averaged spectra and the disdrometer averaged spectra with the disdrometer concentrations becoming a little higher as the diameter increases, probably a result of its larger sampling volume.

Values of the disdrometer total concentrations ranged from 0-600 cm^{-3} while the average concentration was around 100 cm^{-3}. The average number of droplets > 8 μm from the slides was

FIGURE 1. 0-100 m

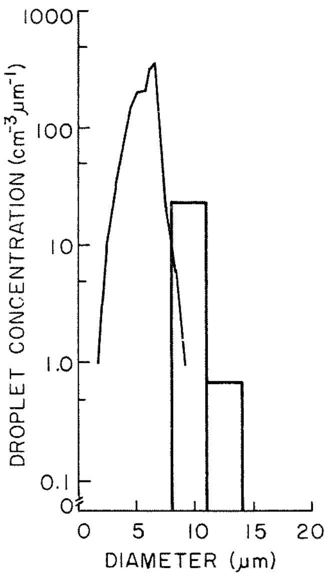

FIGURE 2. 100-200 m

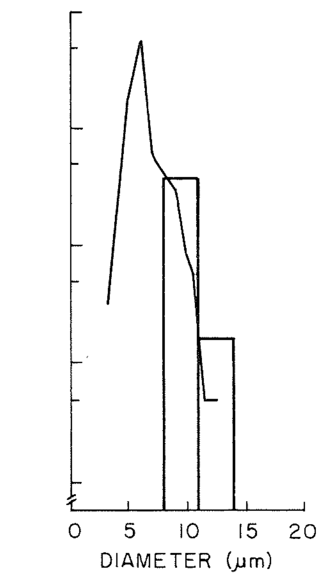

FIGURE 3. 200-300 m

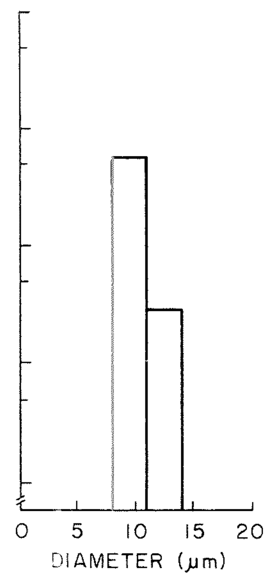

FIGURE 4. 300-400 m

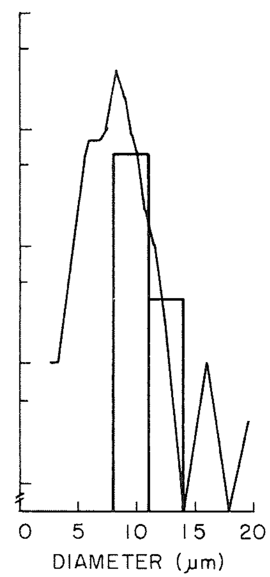

FIGURE 5. 400-500 m

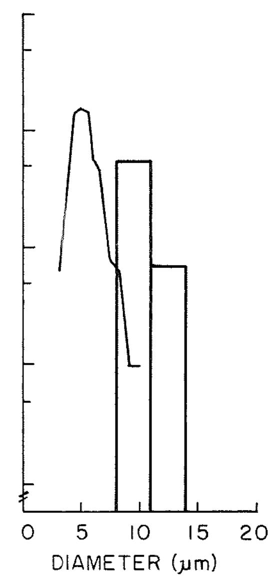

FIGURE 6. 500-600 m

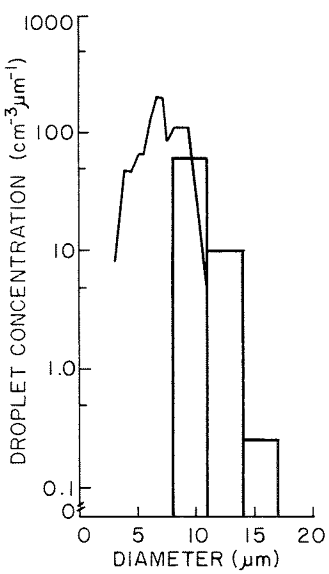

FIGURE 7. 600-700 m

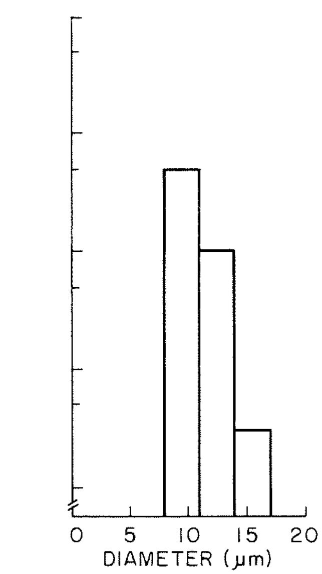

FIGURE 8. 700-800 m

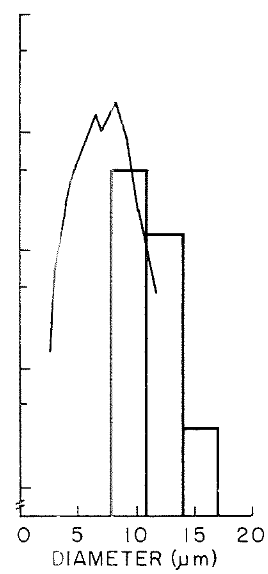

FIGURE 9. 800-900 m

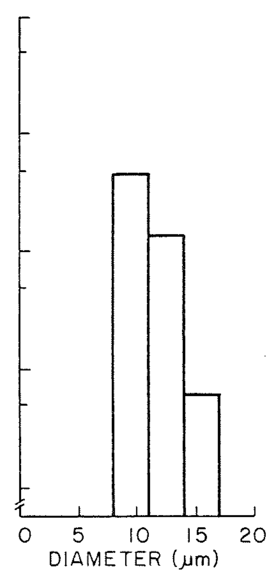

FIGURE 10. 900-1000 m

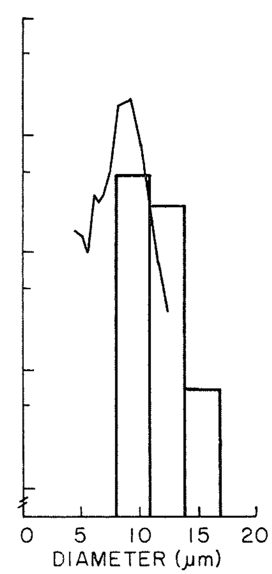

208 cm^{-3} (range, 6 to 560 cm^{-3}). On August 7 in the same cloud, the two slides exposed from the Aerocommander measured concentrations (d > 8 μm) of 65 cm^{-3} at 6310 m MSL (near the edge of the cloud) and 560 cm^{-3} at 5550 m MSL. The Exporer's disdrometer concentrations peaked at 240 cm^{-3} (5790 m MSL) but averaged about 100 cm^{-3}. Near cloud base on August 8, the slide samples measured low concentrations in the d > 8 μm range (6, 10, 32 cm^{-3}) while the average for the disdrometer was 22.6 cm^{-3}. In general, the agreement of total concentrations between the two instruments is reasonable, although the variability in sampling procedures restricts detailed quantitative comparisons.

Table 1 shows the comparison of the slide samples taken by the Queen Air to the ASSP. The data indicate that the ASSP measured a flatter, broader spectrum than the slides. On most penetrations, the ASSP consistently gave counts in the 30 μm diameter range. This may be due in part to a more accelerated growth of droplets in the upper levels of the clouds where the Queen Air made its penetrations, or it may be due to a calibration error in the ASSP. The agreement in total concentrations of the ASSP and the slides is reasonable.

TABLE 1. Sooted slides compared to the ASSP

Date		Total Conc.	Mean Dia.	Max. Dia.	LWC
July 7	slide 18	687 cm^{-3}	8.4 μm	12.4 μm	.216 gm m^{-3}
	ASSP	559	9.7	24	.405
	slide 19	72	7.4	11.8	.015
	ASSP	104	7.1	18	.028
July 9	slide 9	487	9.7	17.1	.234
	ASSP	64	8.3	22	.027
	slide 11	565	9.3	13.0	.236
	ASSP	209	8.1	22	.085
	slide 12	461	9.9	16.2	.233
	ASSP	352	9.5	22	.234

In summary, the growing cumulus congestus clouds of this sample are characterized by a narrow droplet spectrum with high total concentrations for all instruments, the cloud droplet gun, the disdrometer, and the ASSP. The maximum droplet diameter is less than 20 μm except possibly in the upper regions of the clouds. This colloidal stability is consistent among the various days and with other observations reported in Colorado (Auer, 1967 and Cannon et al., 1974).

4.2 Liquid Water Content

The Johnson-Williams on the Explorer was carefully mounted to minimize any of the known sampling problems (i.e., wetting of the reference wire, aircraft boundary layer effects, etc.). Within the limitations of the instrument and instrument mounting, reliable, continuous measurements were made during SPACE. An average J-W value in the steady-state region of the sampled updrafts was about 0.4 gm m^{-3} with maximums generally near 1 gm m^{-3}. The cloud sampled on July 9 was an exceptional one with an average LWC of 1.2 gm m^{-3} and a maximum of 3.6 gm m^{-3}. Although continuous measurements from the J-W on the Aerocommander were not recorded, the average values from the observational notes was 0.25 gm m^{-3}, ranging from 0.10 to 0.57 gm m^{-3}. There is reasonable agreement between the two J-W instruments.

Simultaneous measurements of the J-W and the disdrometer allowed good comparisons to be made between these instruments. Figure 11 is a one minute time plot of some processed Explorer data obtained on August 7. At the top is the vertical velocity in m sec^{-1}, in the center is liquid water content (LWC) from the J-W (solid line) and the integrated disdrometer spectrum (dashed line) in gm m^{-3}, and in the lowest portion of the plot is the disdrometer total concentration cm^{-3} (T) and channel concentrations cm^{-3} μm^{-1} (1, 2, etc.). The J-W baseline zero was 0.50 gm m^{-3} on August 7, and the adjusted LWC is indicated on the left ordinate. The variability of the J-W trace is highly correlated with the disdrometer data, especially when the LWC drops off rapidly. Almost all of the processed data show as good a correlation as in Fig. 11. However, magnitude differences between the two instruments are substantial. On August 7, the J-W was consistently higher than the disdrometer derived LWC by about 0.4 gm m^{-3}. Other days show the same consistent discrepancy, ranging from 0.3 to 0.8 gm m^{-3}. The exceptional case of July 9 at one point reached a difference of 3 gm m^{-3}.

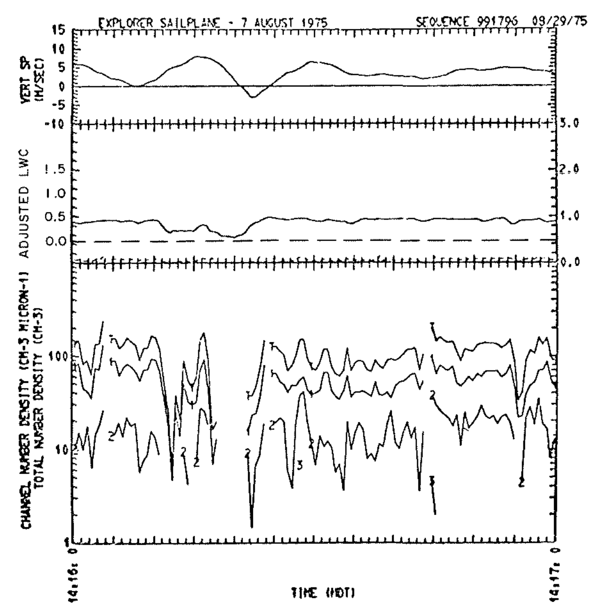

Fig. 11. One minute time plot of processed data taken on August 7, 1975 by the Explorer.

Droplets below the 8 μm cut-off for the disdrometer can account for part of the discrepancy between instruments. Table 2 shows the percentage of total LWC that is contributed by droplets ≤ 8 μm, and compares the total LWC derived from the disdrometer, the total LWC derived from the slides, and the LWC contribution of droplets ≤ 8 μm from the slides as averaged in intervals above cloud base (from Figs. 1-10). A large majority of the liquid water content, derived from the slide spectra in the lowest 1000 m of cloud depth, is contributed by droplets with d ≤ 8 μm.

TABLE 2. Total LWC from the disdrometer (d > 8 μm), total LWC from the slides, LWC for d ≤ 8 μm from the slides and percentage of total LWC in droplets ≤ 8 μm. [Parentheses indicate results based on only one slide.]

Ht. interval above cloud base	Disdro. Total LWC	Slide Total LWC	LWC for droplets ≤ 8 μm	Percentage of total LWC in droplets ≤ 8 μm
0- 100 m	.011 gm m^{-3}	.148 gm m^{-3}	.148 gm m^{-3}	100%
100- 200	.017	.185	.165	89
300- 400	.030	.287	.155	54
400- 500	.031	(.053)	(.052)	(98)
500- 600	.035	.221	.152	69
700- 800	.036	.197	.136	69
900-1000	.045	(.302)	(.100)	(33)

Based on the liquid water content from the slides, the disdrometer, with a threshold of droplets > 8 μm could be expected to detect only about 1/4 to 1/3 of the liquid water in these clouds. After taking this into account it appears that the disdrometer derived LWC values are about 0.5 of those observed with the J-W instrument. Although the comparison is restricted by the uncertainties of the baseline zero and the contribution of droplets ≤ 8 μm, it is in agreement with comparisons made in Abbott et al. (1972) and findings reported by Dye (1976). Dye has suggested a systematic instrument error in the disdrometer that could account for its consistently low derived LWC even above the 8 μm cut-off. The tendency of the disdrometer to partition larger droplets into smaller droplet channels decreases the integrated LWC while the spectra would still compare satisfactorily with slide spectra when droplet diameters are less than 20 μm.

Comparison of the J-W to sooted slides on the Aerocommander is limited by the small number of observations. J-W values from observational notes are available for 10 slide exposures, and the J-W gave 10-90% higher values than the slide derived LWC. The average value from these 10 slides was about 0.15 gm m^{-3}, while the average of all the slides (in Table 2) is about 0.20 gm m^{-3}. This is slightly lower than the J-W averages (∿ .25 gm m^{-3}) and higher than the disdrometer averages (0.10 gm m^{-3} or less).

The ASSP derived LWC's show fair agreement with the slide derived LWC's taken on the Queen Air, considering the small number of cases (see Table 1). However, when concentrations were similar, the ASSP had larger values than the slides due to its tendency to measure a broader spectrum. This observation is tentative pending results of more strictly controlled comparisons presently being done at the University of Wyoming.

While the comparisons between the different instruments are rather crude in their susceptibility to large fluctuations in the differing clouds and cloud volumes, the results generally agree with those in Abbott et al. (1972) and Dye (1976). They show that the J-W values are consistently and substantially higher than the disdrometer derived liquid water contents and slightly higher than the slide derived liquid water contents, while the slides are higher than the disdrometer. The typical J-W values of the cumulus congestus sampled are 0.25-0.50 gm m^{-3}. Although these values are somewhat lower than previous measurements in similar clouds, they are quite reasonable, considering the height and temperature of cloud base in the SPACE area.

4.3 Liquid Water Content Compared to Adiabatic Liquid Water Content (Q/Q_a)

Because the Explorer sampled continuously in an active portion of the clouds and in a semi-Lagrangian manner, its measurements should be observationally more consistent than previous investigations in evaluating adiabatic models of cumulus clouds. Bulk entrainment in these models is usually parameterized as $\frac{1}{M}\frac{dM}{dz} = \frac{b}{R}$, where M is cloud mass, z is vertical direction, R is the updraft radius, and b is the entrainment coefficient. The entrainment coefficient is usually chosen to verify observed cloud top heights in a given region for certain clouds. On the cumulus congestus scale, $0.16 \leq b \leq 0.22$ is the quoted range for predicting cloud top height. Warner (1970) criticized the adiabatic model approach by concluding that it cannot simultaneously predict cloud top height and the liquid water content profile. The entrainment parameterization was insufficient in limiting the model derived liquid water contents to observed liquid water contents and at the same time sustaining enough buoyancy to grow the clouds to their observed heights. Q/Q_a has been one method used to normalize different samples of clouds, assuming that similar mixing processes are diluting the adiabatic LWC to the observed LWC. For this reason, it is often used as a measure of entrainment or mixing. This ratio has been plotted in Figure 12 for 7 clouds in which the Explorer exceeded a height of 500 m above cloud base. Q is averaged over 50 m intervals, and Q_a is computed using the pilot observed cloud base (± 40 m), the cloud base temperature derived from the 1200 MDT sounding in South Park, and the mean height of a given interval above cloud base. The Q/Q_a profile of Warner's (1955) observations is used for comparison (the dark line).

The values in South Park are much higher than those found by other researchers, with averages between 0.5 and 0.8. There is a tendency for the profile to be constant or increasing with height, while the sharp drop at the top of the different traces is due to a dilution of the mean Q. This dilution is caused by the loss of the updraft or by exiting the cloud, both of which would average in lower values of Q. The lone upper profile is from a cloud sampled on July 9. The fluctuations in this case can be attributed to the variable encounters with an updraft as the Explorer flew through the cloud, rather than continuously sampling it in one sustaining updraft.

Possible errors in computing Q and Q_a are the estimatation of the baseline zero for the J-W and observer estimation of the cloud base height. To test the sensitivity of the ratio to these errors, the baseline zero was decreased by the error limit of 0.05 gm m^{-3} and the cloud base was increased 40 m to obtain an upper limit on the

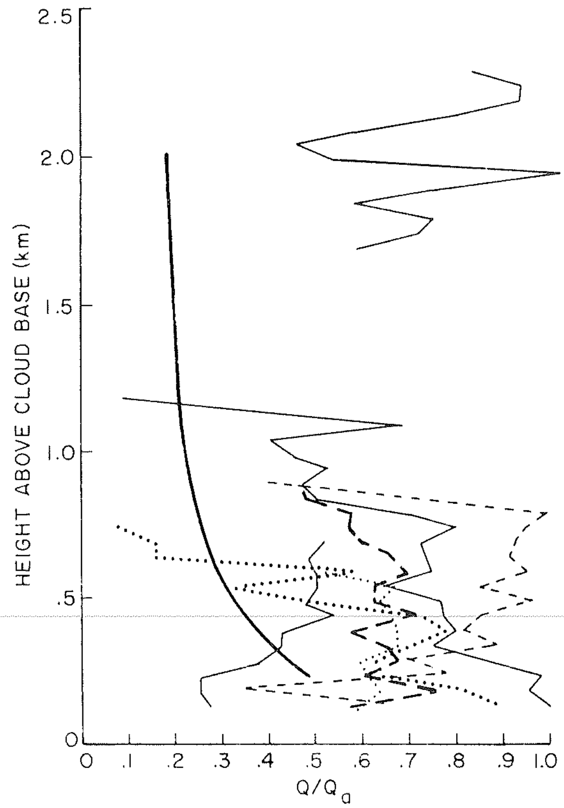

Fig. 12. The ratio of the mean LWC in 50 m intervals above cloud base to the adiabatic value.

ratio. The values were subsequently changed in the opposite direction to obtain a lower limit on the ratio. The lowest 300 m experienced the most variability due to the large relative change of Q and small relative change of Q_a. At 300 m above cloud base, the maximum error values varied from the plotted values by 30%, decreasing to 15% in the upper portion of the flights. Another possible error exists in determining cloud base temperature. The sounding temperature differed from the Explorer's measured temperature at cloud base by 2°C or less, which would change Q_a very little at the temperature and pressure of the cloud bases in the SPACE area. Instrument error in the J-W would have to have been been severe to cause the discrepancy between the Q/Q_a values. Decreases of 40-100% of the J-W LWC would be needed to achieve Q/Q_a values similar to Warner's, and it is unlikely that the J-W mounted on the Explorer is the source of such errors. All the possible errors and uncertainties cannot account for the differences between Warner's profile and the Explorer profiles.

5. DISCUSSION

Evidence collected by Auer (1967) and Knight et al. (1972) suggests that growth through the ice phase is the dominant precipitation formation mechanism in northeastern Colorado cumuli, and the coalescence mechanism plays no major role. Similar microphysical features of the same types of clouds with bases very near the 0°C isotherm lead to the same conclusions in the South Park area. Data collected by a decelerator on the Explorer (Schreck et al., 1974) were characterized by ice particle collections of rimed crystals, rime fragments, and low-density graupel. Also, photographs from the Explorer's cloud particle camera (Cannon 1974a; Cannon 1974b) revealed mostly graupel and occasionally single crystals as typical cloud particles with d > 100 μm, the resolution limit of the camera with the optics used in 1975. Only three water drops with d > 100 μm were detected in the 11,000 photographs examined (sampling volume approximately 275 ℓ). All three drops were sampled within 2.5 minutes of each other on July 23, which is presently being studied to determine their origin and subsequent role in that particular cloud. The lack of large droplets in the clouds sampled during SPACE, especially on July 9 in the upper portion of a cumulus congestus with an exceptionally high LWC, suggests that the coalescence process is not an efficient mechanism for producing precipitation particles. The ice phase process appears to be the dominant mechanism for precipitation formation in the cumuli of the South Park area.

The results of high Q/Q_a values in the sampled cumuli are supported to some degree by a case study of Danielson (1975). Using photogrammetric techniques to follow the ascent of a cloud parcel through the top of an existing cloud, an updraft radius, vertical velocity, cloud base height, and cloud top height were determined. These parameters were inputted into the Cotton (1972) cumulus cloud model which incorporates cold cloud physics, and the entrainment coefficient b was adjusted to compare model predicted vertical velocity profiles and cloud top heights to the observed values. Considering the maximum of all possible errors, this case necessitated an entrainment coefficient of less than 0.05 for model verification of the observed vertical velocity profile and cloud top height. Another investigation by Danielson et al. (1976) lends additional support to his earlier case study and to the values of Q/Q_a obtained from the Explorer measurements. Although the results are not conclusive, it is evident that models must carefully parameterize the entrainment processes if they are to be used in the SPACE area.

6. CONCLUSIONS

A microphysical description of liquid water in the cumuli in the South Park area can be characterized by: 1) high concentrations of cloud droplets, averaging >500 cm^{-3}; 2) narrow droplet spectra with $\bar{d} \sim 8$ μm and $d_{max} < 20$ μm; 3) relatively low liquid water contents on the cumulus congestus scale, $0.25 < \bar{Q} < 0.5$ gm m^{-3} (except for $\bar{Q} \sim 1.2$ gm m^{-3} on July 9). These characteristics do not favor liquid drop growth process and are in agreement with other measurements made during SPACE that indicate the ice phase mechanism dominates precipitation formation in this area. In addition the Q/Q_a values are much larger and somewhat more constant with height than previous investigations, suggesting a lower entrainment rate in the active regions of cumuli in the South Park area. Continuing analyses of some case studies are expected to add some insight into the reasons for these conclusions.

7. ACKNOWLEDGEMENTS

The authors would like to thank Patti Walsh of the University of Wyoming for analyzing the slide samples taken by the Queen Air. One of us (DWB) was partially supported by a University Corporation for Atmospheric Research graduate student assistantship.

Part of the research performed by the Explorer was supported by the National Hail Research Experiment, managed by the National Center for Atmospheric Research and sponsored by the Weather Modification Program, Research Applications Directorate, National Science Foundation. Additional support was provided by National Science Foundation grants ERT 71-01885 and DES 75-17313, and by the State of Colorado.

8. REFERENCES

Abbott, C.E., J.E. Dye and J.D. Sartor, 1972: An electrostatic cloud droplet probe. J. Appl. Meteor., 11, 1092-1100.

Auer, A.H., Jr., 1967: A cumulus cloud design for continental airmass regimes. J. Rech. Atmos., 3, 91-100.

Auer, A.H., Jr., 1969: A cloud droplet sampler. An Information Supplement Prepared for the Office of Atmospheric Water Research, U.S. Bureau of Reclamation, 18 pp.

Cannon, T.W., 1974a: A camera for photography of atmospheric particles from aircraft. Rev. Sci. Instrum., 45, 1448-1455.

Cannon, T.W., 1974b: Cloud and precipitation element studies using an airborne particle camera. Preprints Conf. on Cloud Physics, Tucson, Ariz., Amer. Meteor. Soc., 292-295.

Cannon, T.W., J.E. Dye and V. Toutenhoofd, 1974: The mechanism of precipitation formation in northeastern Colorado cumulus. II. Sailplane measurements. J. Atmos. Sci., 31, 2148-2151.

Cotton, W.R., 1972: Numerical simulation of precipitation development in supercooled cumuli: Part II. Mon. Wea. Rev., 100, 764-784.

Cotton, W.R., 1975: On parameterization of turbulent transport in cumulus clouds. J. Atmos. Sci., 32, 548-564.

Danielson, K.S. and L.O. Grant, 1974: Description and parameterization of continental mountain cumuli. Preprints Conf. on Cloud Physics, Tucson, Ariz., Amer. Meteor. Soc., 342-347.

Danielson, K.S., 1975: Continental mountain cumulus clouds. Master's Thesis, Colo. State Univ., Ft. Collins, Colo., 172 pp.

Danielson, K.S., L.O. Grant and A.J. Schanot, 1976: Description of mixing processes in initial cumulus. Preprints Intern. Cloud Physics Conf., Boulder, Colo., U.S.A.

Dye, J.E., 1976: Comparisons of the electrostatic disdrometer with impactor slides. Submitted to J. Appl. Meteor.

Knight, C.A., N.C. Knight, J.E. Dye and V. Toutenhoofd, 1974: The mechanism of precipitation formation in northeastern Colorado cumulus. I. Observations of the precipitation itself. J. Atmos. Sci., 31, 2142-2147.

Knollenberg, R.G., 1972: Comparative liquid water content measurements of conventional instruments with an optical array spectrometer. J. Appl. Met., 11, 501-508.

Knollenberg, R.G., 1976: Three new instruments for cloud physics measurements: the 2-D spectrometer, the Axially Scattering spectrometer, and the Active Scattering spectrometer. Preprints Intern. Cloud Physics Conf., Boulder, Colo., U.S.A.

Owens, G.V., 1957: Wind tunnel calibration of three instruments designed for measurement of the liquid water content of clouds. Tech. Note No. 10, Cloud Physics Laboratory, The University of Chicago, 15 pp.

Sartor, J.D., 1972: Clouds and precipitation. Physics Today, 25, No. 10, 32-38.

Schreck, R.I., V. Toutenhoofd and C.A. Knight, 1974: A simple airborne, ice particle collector. J. Appl. Meteor., 13, 949-950.

Spyers-Duran, P.A., 1968: Comparative measurements of cloud liquid water using heated wire and cloud replicating devices. Proc. Intern. Conf. on Cloud Physics, Toronto, Canada, 154-158.

Warner, J., 1955: The water content of cumuloform cloud. Tellus, 7, 449-457.

Warner, J., 1970: On steady-state one-dimensional models of cumulus convection. J. Atmos. Sci., 27, 1035-1040.

7.3.7

FORECASTING AND VERIFYING HYDROMETEOR SPECTRA

Arnold A. Barnes Jr. and Vernon G. Plank

Air Force Geophysics Laboratory
Hanscom AFB, Massachusetts 01731

1. INTRODUCTION

Air Force Geophysics Laboratory, AFGL (formerly AFCRL) has been supporting Air Force testing of high speed aerospace vehicles by measuring the hydrometeor environment encountered by test vehicles (Barnes et al, 1974b; Metcalf et al, 1975a, b, c, d, e; Plank, 1974a, b, c). Specifically we have provided values of liquid (or ice) water content (LWC or IWC) and crystal habit along the trajectories of test vehicles and recently have been tasked to provide particle size spectra as well.

The purpose of this paper is to describe the procedures and techniques which have been developed to forecast and measure the water contents, M in gm/m^3, crystal habits and the size spectra. These procedures have evolved over the years as there have been advances in cloud physics and radar instrumentation and changes in the test requirements. Support has been provided at Wallops Island, Virginia for the past six years and at Kwajalein in the Marshall Islands (Barnes, et al, 1974a) for the last three years. Procedures used at Kwajalein were taken from our experience at Wallops Island but had to be modified to incorporate the available instrumentation and different test objectives. In each of the following sections we first describe the procedures used at Wallops Island and follow up with differences at Kwajalein.

2. LONG RANGE FORECASTING

Almost all of the missions are carried out in moderate to heavy weather. In order to adequately forecast and sample the hydrometeors, only large scale, homogeneous storms are chosen. Because of this requirement, the Wallops Island season is limited to the winter storms from November through April. During the rest of the year the storms are convective in character, inhomogeneous and extremely difficult to characterize. Climatologically, the best months for "weather" testing at Kwajalein are October and November when easterly waves in the intertropical convergence zone are present. Convective clouds are avoided because (1) the rapid changes of the convective cells in time significantly degrades the applicability of radar and aircraft sampling and (2) both the M values and the size spectra change rapidly over small distances. Our experience in the field has shown that we have to wait a month or so to get the required heavy weather missions accomplished, and for this reason we now deploy into the field and rotate teams every three or four weeks.

3. MEDIUM RANGE FORECASTS

Forecast from three days to twelve hours before the experiment are provided by NWS forecasters at Wallops Island and by Kentron Weather Service at Kwajalein. Standard synoptic, rawinsonde and weather satellite data are utilized. From E-12 hours to E-4 hours the local forecasters refine the forecasts. The local WSR-57 weather radars become more useful as the weather moves into the experimental area. Data from the synchronous satellite provided every 30 minutes are extremely valuable at Wallops. We have found the satellite data at Kwajalein to be so important for forecasting that we attempt to schedule the experiments a few hours after a weather satellite is scheduled to pass overhead.

Specific M and size spectra forecasts are not provided at this time. Only recommendations to continue the countdown, hold the count or scrub are provided by the AFGL Field Director to the Test Director prior to E-4 hours.

4. SHORT RANGE FORECASTS

This covers the period from approximately E-4 hours to E-0, start time of the experiment. It is at this point that the AFGL Field Director becomes the prime forecaster with the local forecasters backing him up.

All of the above mentioned instrumentation is utilized. Special rawinsondes are released and the temperature soundings are used to provide initial determination of crystal habit as a function of height. This information is then combined with quantative weather radar data to provide vertical profiles of liquid (ice) water content, M.

Approximately two hours before the experiment, aircraft sample the clouds to provide in-situ crystal habit, particle size spectra and M. Radar and aircraft M values are checked for correspondence and are incorporated along with the usual short range forecasts to provide forecast M values versus height.

At Wallops Island, data from a 10 cm radar are fed into an integrator (Glover, 1972) to provide values of dBZ which are displayed on a Color Display (Jagodnik, et al, 1975). The data are also processed by a mini computer using the crystal habit versus height information to produce real-time estimates of M versus height. Surface rainfall and drop size distributions are also available in real time to the Field Director. These instruments are located on land as close to the experimental area as possible.

A 5 cm radar, ALCOR, is used at Kwajalein along with an AFGL integrator and Color Displays. Forecast profiles of M vs height are worked up by hand rather than by a computer for two reasons; firstly, ALCOR is not continuously available to make weather scans and, secondly, the last forecast is made approximately one hour before the experiment and consequently relies more heavily on conventional short range forecasting. (At Wallops Island the last forecast is approximately two minutes before the experiment).

All three aircraft have PMS 1-D and 2-D equipment to measure particle sizes and shapes, replicators to capture hydrometeors, temperature, humidity and altitude measurements, time lapse cameras and snow sticks. Computers on the Lear and the C-130E provide real-time M values from the PMS 1-D equipment. Each of the C-130s has two foil samplers (Church et al, 1975). Experimental devices have been installed to measure M values directly. The Lear has a Total Water Content Indicator being developed by MRI using a cyclone-separator principal. On the C-130E a Lyman Alpha device is used to measure the difference in water vapor between air mechanically stripped of hydrometeors and air with the hydrometeors vaporized. This equipment is being developed by Aerospace Corporation. The Raindrop Spectrometer on the C-130A utilizes the scattering of light from the liquid hydrometeors to obtain values of M.

5. FINAL DETERMINATION OF M AND HYDROMETEOR SPECTRA

In order to obtain M and size spectra along the experimental flight paths, the radars are used to obtain weather data along the flight trajectories within minutes of the experiment. The radar data are presented in units of dBZ and must be converted to M and size spectra. In order to make these conversions, aircraft measurements of size spectra and M are taken during correlation runs with the radar. At Wallops Island the radar tracks the airplane and the radar datum gate is located at a range slightly closer to the radar but far enough away from the radar returns coming from the aircraft so that the weather returns are not contaminated by the aircraft returns. This is referred to as the "link-mode". At Kwajalein the "link offset mode" is utilized (Barnes et al, 1974b). The aircraft beacon is tracked by one radar, an MPS-36. Using this track, an offset track is computed which places the ALCOR datum gates a given distance, normally 3 km, in front of the airplane. This must be done to remove the airplane from the side lobes of ALCOR which exist in range as well as in angle due to the CHIRP pulses used (Metcalf et al, 1975f).

The correlation runs are scheduled to be completed within two hours of the experiment. In order to accomplish these runs in the minimum amount of time and as close to the experiment in time as possible, we normally use two aircraft so that a correlation run can be made with one aircraft while the other aircraft is being maneuvered into position for the next correlation run. The C-130E usually covers the altitudes between 28000 ft (8.5 Km) and 300 ft (100 m) while the Lear 36 operates from 45000 ft (14 km) or the top of the storm down as low as required. The C-130A has a ceiling of 32000 ft (10 Km) and is used as a backup for either of the other two aircraft.

6. EXAMPLE

Figure 1 depicts the final values of M versus altitude for an experiment performed at Wallops Island on 16 March 1974. The storm top was just over 40,000 ft as determined by the vertically pointing radar. The C-130A and two aircraft instrumented by MRI, a Citation and a Navajo, made a total of twenty sampling passes at fifteen different levels between 10.7 and 0.2 km. Single ice crystals were found above 8.1 km; predominantly columns above 10 km and bullet rosettes below. The ice to snow transition zone was noted by both the Citation and the C-130A. In the snow region the intensity and aggregation increased as the aircraft descended towards the melting zone. Three passes were made within the melting zone starting with wet snow at the top and changing to all rain at the lower edge of the melting zone.

Figure 1 was derived from the radar reflectivity values, Z, obtained from the JAFNA monopulse radar. In the ice crystal region the equation $M = .038Z^{.529}$ was used to convert from Z to M (Heymsfield, 1973). The ice to snow transition zone is almost always discernible by the cloud physicist. We have also found that the Z-M relationship changes significantly in this zone. In the snow region the aggregation increased as the melting zone was approached, and the aircraft sampling found that the intensity of the snow increased as the melting zone was approached.

In the past we have divided this region into an upper "small snow" region and a lower "large snow" region as is shown in Figure 2. Our experience has shown that it is very difficult to delineate the large snow to small snow transition zone and the data indicate a gradual change of the Z-M relationship from the top to the bottom. For this experiment we derived an equation of the form:

$$M = K_m Z^{E_m} \text{ where } K_m = .00495 + .009545 \frac{(H-H_1)}{(H_2-H_1)}$$

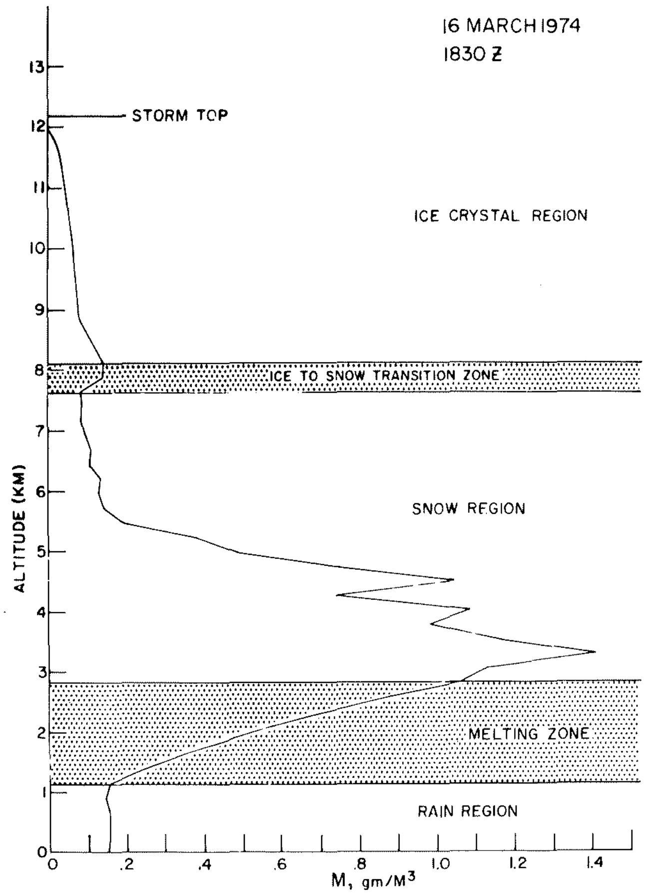

Fig. 1. Liquid and ice water content values as a function of height for experiment conducted at Wallops Island, Virginia assuming a gradual transition from small snow to large snow from the top to the bottom of the snow region.

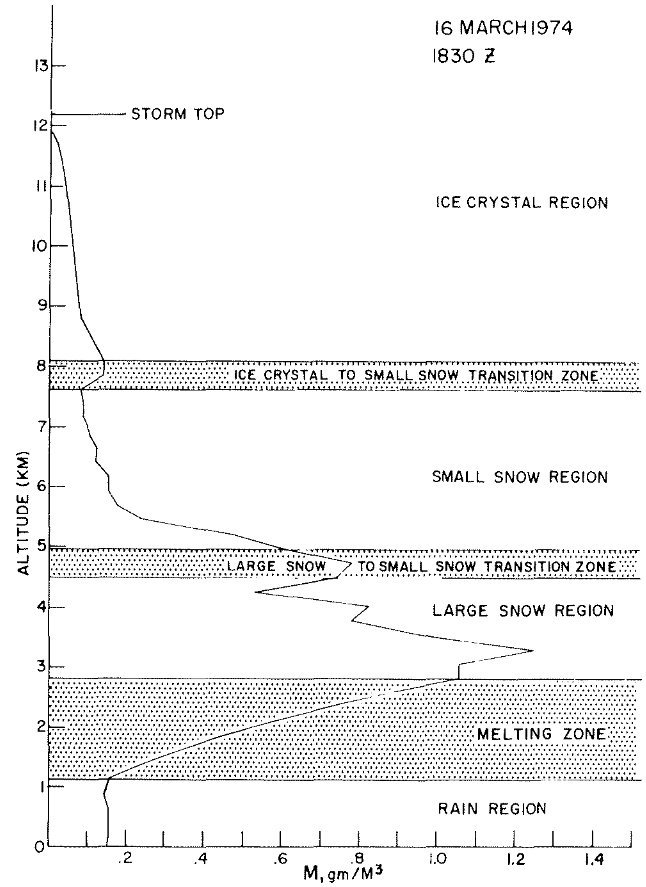

Fig. 2. Liquid and ice water content values as a function of height for the same experiment as shown in Figure 1. In this analysis the snow region was taken to consist of an upper small snow region, a narrow zone for the transition from small to large snow and a lower large snow region.

$$E_m = .596-.058 \frac{(H-H_1)}{(H_2-H_1)}, \quad H_1 = \text{height at}$$

bottom of snow region, H_2 = height at top of snow region and $H_1 \leq H \leq H_2$ was the height of interest. This equation was used in the construction of Figure 1.

As mentioned above, Figure 1 was based on the radar data. The melting zone is taken to be the bright band as seen by the radar because, at the present time, we do not know how to relate radar returns in the bright band to the desired M values. M values in the melting zone are derived from calculated precipitation rates just above and just below the melting zone and the assumption that the precipitation rate varies uniformly from the top to the bottom.

Z-M relations are obtained by two different methods in the rain region. For one method aircraft M values and radar Z values are obtained on correlation passes as is done above the melting zone. The second method is to use the radar data, the tipping bucket data and the drop size distribution from the Joss distrometers and a size/fall-speed relation to obtain a Z-M relationship.

The structure seen in Figure 1 indicates that this was a fairly homogeneous storm, and this was verified by other radar and aircraft data. The steady state assumption used to bridge across the melting zone obviously did not apply in the lower half of the snow region. The maximum at 3.5 and 8 km are attributed to storage and are considered to be real.

7. HYDROMETEOR SIZE SPECTRA

Size spectra from past experiments were obtained in real-time in a very crude form from observations of the snow stick made by the onboard cloud physicist. Post flight spectra were obtained by laborous analyses of foil data (Church, et al, 1975). The PMS equipment has recently allowed us to obtain quantitative size spectra data in real-time. These data are provided to the Field Director so that they may be incorporated into his short range forecasts.

Since the aircraft spectral information is not taken along the experimental trajectory at the time of the experiment, we use the Z and M values at a particular level and modified the slope of the spectral distribution to give consistent Z and M values. These modified size distributions are calculated for all regions except the melting zone. In the melting zone, the distribution at the bottom of the snow region is used with the assumptions that the smallest particles melt first as they fall through the melting zone. The size distribution at the top of the rain region is used as a boundary condition with the assumption that the melting layer may be treated as being in a steady state.

8. SUMMARY

Forecasts and measurements of ice water content, hydrometeor size spectra and crystal habit have and are being provided by AFGL for Air Force test. Climatology, synoptic, rawinsonde and satellite data are used for forecasts in excess of four hours. Shorter range forecasts and verifications rely on real-time measurements taken by instrumented aircraft, including two C-130s and Lear 36, and on advanced weather radar display techniques.

REFERENCES

Barnes, A. A., L. D. Nelson, and J. I. Metcalf, 1974a: Weather documentation at Kwajalein missile range. 6th Conf. Aerosp. and Aeronaut., Amer. Meteor. Soc., 66-69. AFCRL-TR-74-0430, Air Force Cambridge Research Laboratories, Hanscom AFB, Mass.

Barnes, A. A., J. I. Metcalf, and L. D. Nelson, 1974b: Aircraft and radar weather data analysis for PVM-5. AFCRL-TR-74-0627, Air Force Cambridge Research Laboratories, Hanscom AFB, Mass.

Church, J. F., K. K. Pocs, and A. A. Spatola, 1975: The continuous aluminum foil hydrometeor sampler; design, operation, data analysis procedures, and operating instructions. AFCRL-TR-75-0370, Air Force Cambridge Research Laboratories, Hanscom AFB, Mass.

Glover, K. M., 1972: A precision digital video integrator. 15th Radar Meteor. Conf., Amer. Meteor. Soc., 193-198.

Heymsfield, A. J., 1973. The cirrus uncinus generating cell and the evolution of cirriform clouds, Ph.D. Thesis, The University of Chicago.

Jagodnik, A. J., L. R. Novick, K. M. Glover, 1975: A weather radar scan converter/ color display. 16th Radar Meteor. Conf., Amer. Meteor. Soc., 14-20.

Metcalf, J. I., A. A. Barnes, and M. J. Kraus, 1975a: Final report of PVM-4 and PVM-3 weather documentation. AFCRL-TR-75-0097, Air Force Cambridge Research Laboratories, Hanscom AFB, Mass.

Metcalf, J. I., A. A. Barnes, and M. J. Kraus, 1975b: Final report of STM-8W weather documentation. AFCRL-TR-75-0207, Air Force Cambridge Research Laboratories, Hanscom AFB, Mass.

Metcalf, J. I., A. A. Barnes, and M. J. Kraus, 1975c: Final report of PVM-5 weather documentation. AFCRL-TR-0302, Air Force Cambridge Research Laboratories, Hanscom AFB, Mass.

Metcalf, J. I., M. J. Kraus, and A. A. Barnes, 1975d: Final report of OT-45, PVM-8, and RVTO weather documentation. AFCRL-TR-75-0388, Air Force Cambridge Research Laboratories, Hanscom AFB, Mass.

Metcalf, J. I., M. J. Kraus, and A. A. Barnes, 1975e: Final report of PVM-6 and PVM-7 weather documentation. AFCRL-TR-75-0481, Air Force Cambridge Research Laboratories, Hanscom AFB, Mass.

Metcalf, J. I., A. A. Barnes, and L. D. Nelson, 1975f: Water content and reflectivity measurement by "CHIRP" radar. 16th Radar Meteor. Conf., Amer. Meteor. Soc., 492-495.

Plank, V. G., 1974a: A summary of the radar equations and measurement techniques used in the SAMS rain erosion program at Wallops Island, Virginia. AFCRL-TR-74-0053, Air Force Cambridge Research Laboratories, Hanscom AFB, Mass.

Plank, V. G., 1974b: Hydrometeor parameters determined from the radar data of the SAMS rain erosion program. AFCRL-TR-74-0249, Air Force Cambridge Research Laboratories, Hanscom AFB, Mass.

Plank, V. G., 1974c: Liquid-water-content and hydrometeor size-distribution information for the SAMS missile flights of the 1971-72 season at Wallops Island, Virginia. AFCRL-TR-74-0296, Air Force Cambridge Research Laboratories, Hanscom AFB, Mass.

7.3.8

THE MEASUREMENT OF AIR MOTION IN AND NEAR CLOUDS

P. B. Wagner and J. W. Telford

Desert Research Institute
University of Nevada System
Reno, Nevada

1. INTRODUCTION

Measurement of air motion from aircraft has well recognized advantages in atmospheric studies. When combined with simultaneous temperature and moisture measurements, accurate velocity measurements yield heat and moisture fluxes. These parameters, obtained in detail possible in aircraft experiments, are important for description of turbulent mixing in the development and decay of cloud forms.

This paper deals in somewhat preliminary form with a set of airborne measurements on small cumuli. Data were obtained with the Desert Research Institute research system and NCAR sensors aboard the NCAR Buffalo aircraft. This system with its inertial navigation platform reference has been described previously in detail (Telford and Wagner, 1974) (Telford, Vaziri and Wagner, 1976).

2. FLIGHT PROFILE

Figure 1 shows a ground track of an entire flight originating from Barksdale, Louisiana, proceeding southwesterly over Texas and then returning to Barksdale. This flight contains two soundings to 2000 m and several cumulus cloud encounters. One sounding was near Barksdale early in the flight, and the second was made at the southern extreme of the flight just prior to returning north.

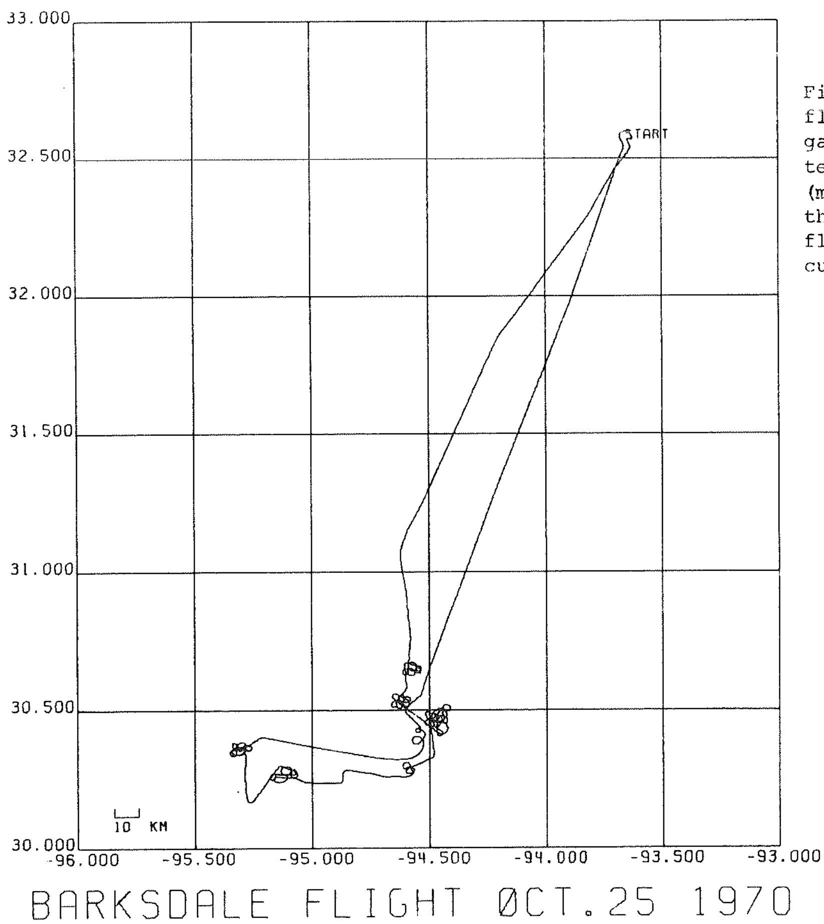

Fig. 1. Aircraft ground track of flight for cumulus cloud investigation. The flight departs and terminates in Barksdale, Louisiana (marked START). Small loops in the southwestern portion of the flight are a spiral sounding and cumuli encounters.

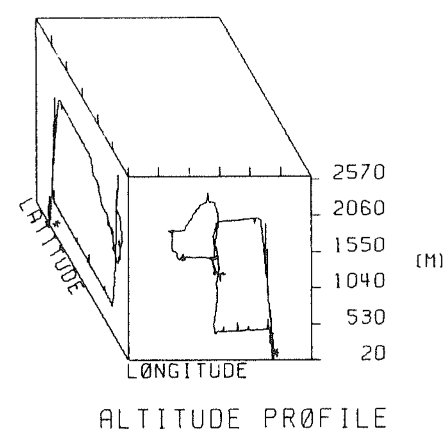

Figures 2 and 3 show vertical profiles of winds and temperatures. The two profiles taken at extremes of the ground track and about 3 hours apart show quite similar low level winds of 5 to 8 m/s with north to northwesterly headings. In both soundings winds shifted towards northeasterly or easterly headings above several hundred meters altitude.

The cumulus clouds encountered were carefully observed by encircling flight and level penetration at approximately mid-cloud height. The procedure of close encirclement (with cloud at wing-tip) and cloud penetration followed by a repeated path in the opposite direction was designed to minimize effects of instrumental bias as well as track the visual cloud outline with time. Figure 4 shows the ground track of the second cloud investigated. (Here the track of the second encirclement is displaced northward 0.5^{o} in the plot for clarity.) The mean wind of 6.2 m s^{-1} and 44^{o} direction has been subtracted and the coordinate system has been given a drift velocity of 6.8 m s^{-1} and 19^{o} so the cloud outline stays in the same place.

In Figure 4 the track proceeds from the point marked START to the first complete encirclement CCW followed by a procedural 270^{o} turn in clear air and penetration of the cloud on a 107^{o} heading. This first penetration was followed by another clear air turn of 270^{o} and a second cloud encirclement in the CCW direction. Finally, after a last procedural turn in clear air, a second cloud penetration was made on a 292^{o} heading, essentially the reverse of the first penetration.

3. DISCUSSION

From comparison of the two cloud encirclements it appeared that the visual cloud boundary shifted relative to its embedding air in the northwesterly direction in the interval between the two maneuvers. This is essentially cross-wind and is nearly the same as the direction of flight penetration. The data for the motion of this and two other clouds is listed in Table 1. It appears that the clouds were generally moving in northerly direction of about 13^{o} on average. However in co-ordinates moving with the mean wind, the clouds moved northwesterly at the average of about 3 m s^{-1} at 50^{o} to the west. The cloud motion relative to the ground corresponds very closely with the magnitude and direction of the wind below cloud base as seen in Figures 2 and 3 noted on table 1. The wind profiles measured during the soundings at the higher levels vary somewhat from those measured in passing near the clouds and may reflect influences on the wind from the cloud field as a whole.

Figures 5 and 6 are plots of vapor mixing ratio, potential temperature and the three wind components measured in the two cloud penetrations shown in Figure 4. Vapor mixing ratio in these figures serves only as an indicator of cloud entry. Unfortunately, the humidity instrument was somewhat erratic and recovered slowly from apparent wetting. Potential temperature serves to mark cloud entry and exit reasonably well. In each case an apparent updraft was

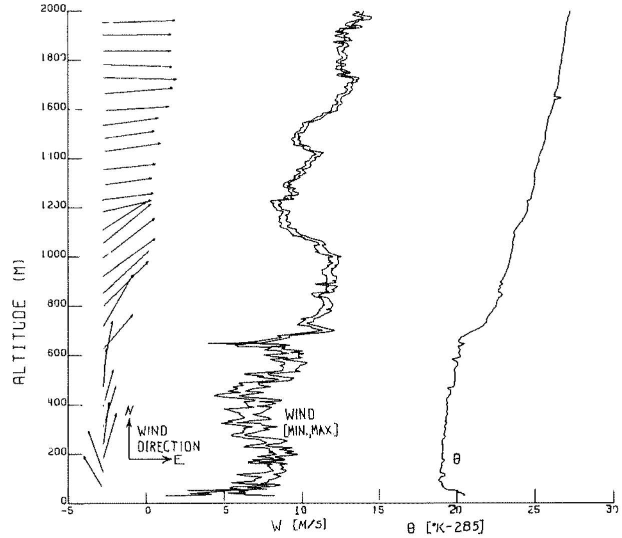

Fig. 2. Sounding to 2000 m near Barksdale early in the flight showing wind velocity and potential temperature.

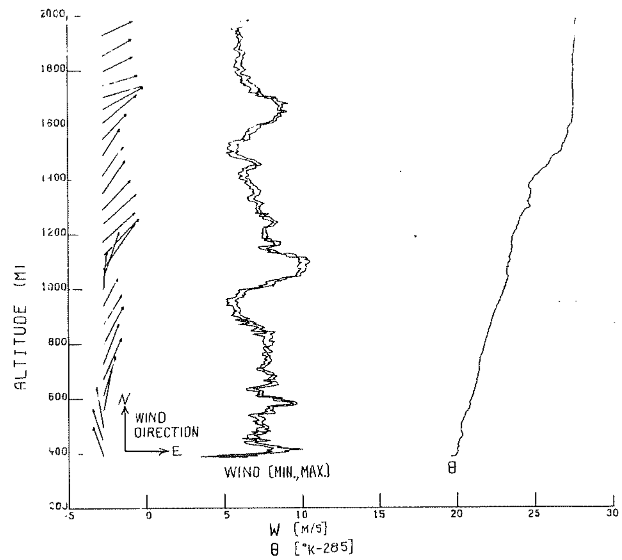

Fig. 3. Second sounding near the southern extreme of the flight 2 hours and 47 minutes after the sounding in Figure 2.

TABLE 1. Wind velocities, cloud drifts relative to the ground and cloud drifts relative to the surrounding air.

Cloud No.	Embedding Wind	Cloud Drift Relative to the Ground	Cloud Drift in Surrounding Air
1	6.7m s^{-1},50^{o}	7.5m s^{-1},10^{o}	4.9m s^{-1},52^{o}
2	6.2m s^{-1},44^{o}	6.8m s^{-1},19^{o}	2.9m s^{-1},48^{o}
3	9.0m s^{-1},20^{o}	7.5m s^{-1},10^{o}	2.1m s^{-1},59^{o}

	Air Motion in Soundings: Low Level	Air Motion in Soundings: Cloud Level
Start of Flight	7.5m s^{-1},10-20^{o}	11m s^{-1},60-90^{o}
End of Flight	7.5m s^{-1},10-20^{o}	7.5m s^{-1},30-60^{o}

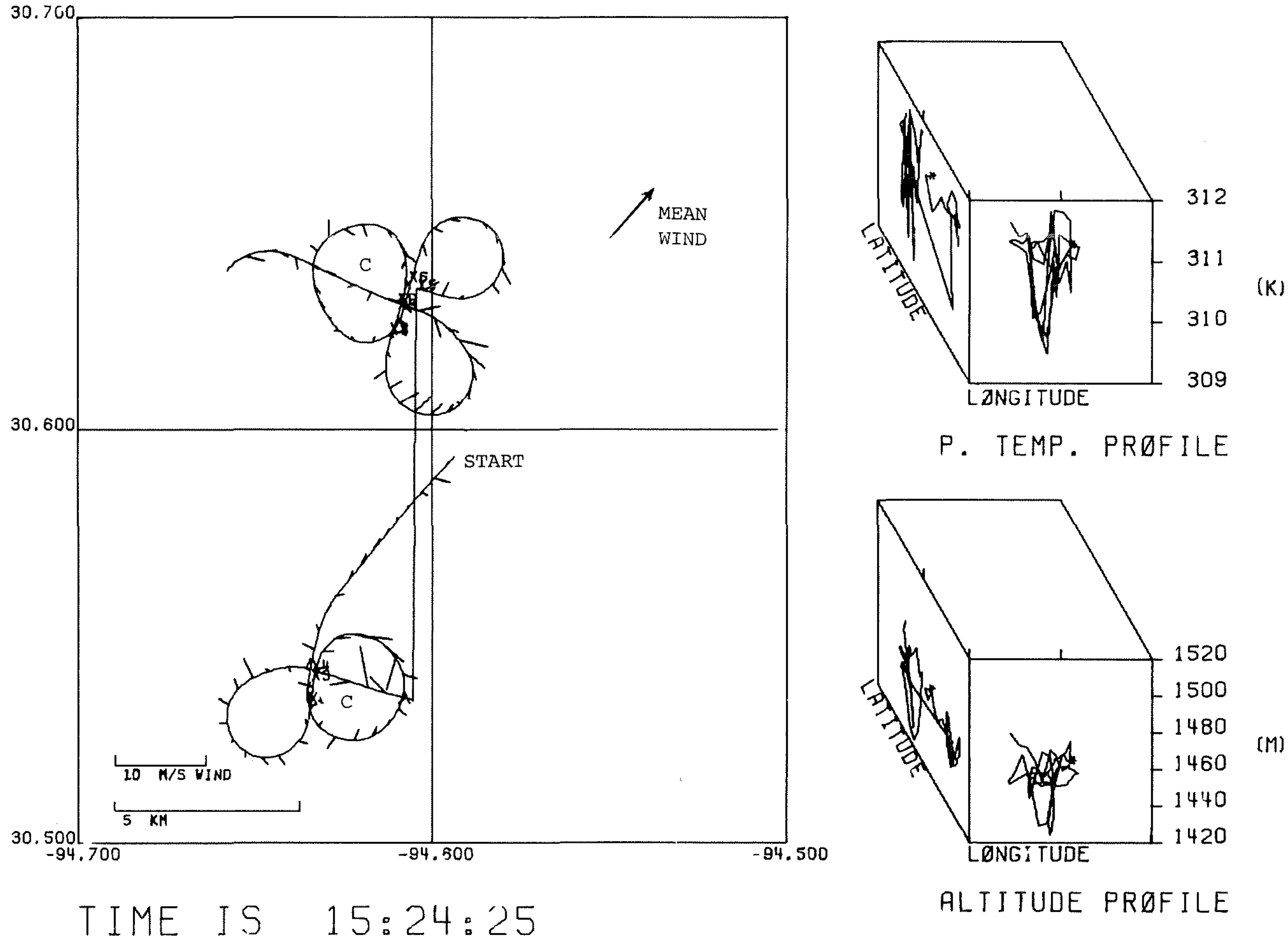

Fig. 4. Aircraft track of cumulus cloud encounter. The cloud (marked C) was encircled twice and penetrated twice. The second pass is displaced one grid section for clarity and the cloud coordinates have been given a drift velocity of $6.8 \mathrm{m\ s^{-1}}$ at 19° to maintain the plotted cloud position approximately stationary. A mean wind of $6.2 \mathrm{m\ s^{-1}}$ at 44° has been subtracted from the winds shown, and horizontal air motion relative to this mean wind is indicated by vectors originating from the aircraft track.

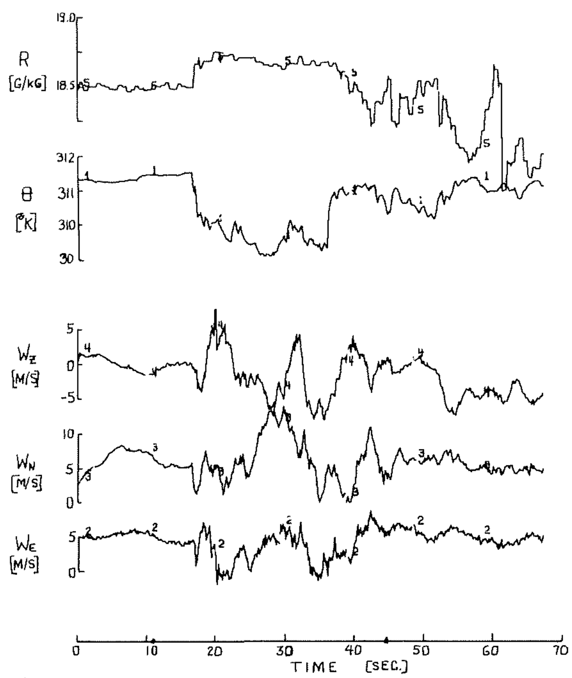

Fig. 5. Vapor mixing ratio, potential temperature and wind components are plotted along the aircraft track penetrating the cloud on a 107° heading.

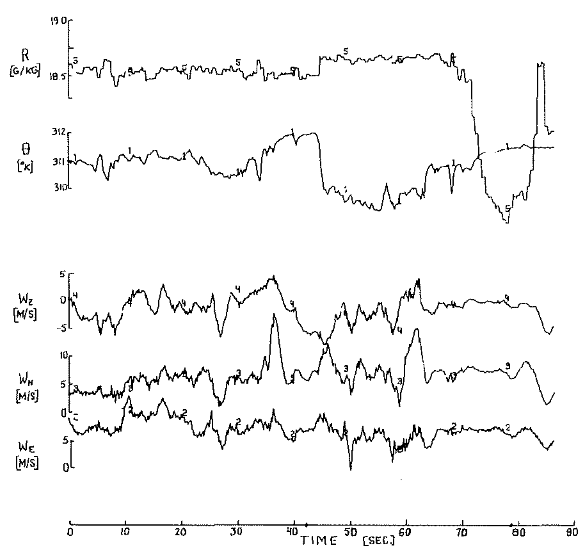

Fig. 6. Same as Figure 5 for second cloud penetration (on a 292° heading).

encountered on the northwestern side of the cloud with generally turbulent or descending air elsewhere along the track inside the cloud. Once again this same behavior was evident in data reduced for the other clouds of the flight.

Outside the cloud marked turbulence existed on decaying side for some distance outside the cloud while air adjacent the developing side was quite smooth. This too was observed in data for other clouds of the flight and is consistent with the direction of apparent growth. Turbulent mixing associated with cloud decay appears to remain in the region of evaporation for a period at least comparable to the dwell time or persistance of a visible parcel of cloud itself, i.e. for at least a cloud diameter "behind" the moving cloud.

4. CONCLUSION

The visible clouds investigated on this flight generally appeared to be moving cross wind relative to the adjacent air at a speed of several meters per second in a northwesterly direction. The measured vertical velocity tended to be positive inside the northwestern edge of the clouds, and turbulence outside the cloud was consistently on the opposite side of the cloud.

The motion of clouds relative to the air at the same level has been observed before. Malkus (1949) described this behavior, and the authors (1974) previously reported similar observations in some detail. For these data, as in the latter case, the moving cloud outlines correlated with the winds at the surface measured before and after the cloud encounters. In these data we have measured the air motion near the clouds, and the outlines are moving relative to this air without appreciably disturbing it. Thus these data strengthen an earlier conclusion that growth and decay of small cumuli remains linked with air movement at the heat and moisture source which is from the surface airflow beneath. The cloud outlines tend to move at or near the velocity of the underlying airflow. The conclusion remains that cumulus cloud evolution may be determined by initial upward motion of a succession of moist, condensing air parcels followed by a dwell time and then decay. The decay may be the result of mixing with dry overlying air, parcel descent or probably both. Horizontal flow in or out of the clouds observed was not marked and generally less than the $1 m\ s^{-1}$ accuracy of wind measurement determined for this flight. These data show disturbed air is left where the cloud has decayed whereas the growing side is surrounded by smooth air.

5. REFERENCES

Malkus, J.S., 1949: Effects of Wind Shear on Some Aspects of Convection. Trans. Amer. Geophys. Union, 30, 19-25.

Telford, J.W., and P.B. Wagner, 1974: The Measurement of Horizontal Air Motion Near Clouds from Aircraft. J. Atmos. Sci., 31, 2066-2080.

Telford, J.W., A. Vaziri and P.B. Wagner, 1976: Aircraft Observations in the Planetary Boundary Layer Under Stable Conditions. Accepted for publication, Boundary-Layer Meteor.

6. ACKNOWLEDGMENTS

This work was undertaken with the assistance of a grant from the Atmospheric Sciences Section of the National Science Foundation.

2.1.5

ELEMENTAL COMPOSITION OF ATMOSPHERIC FREEZING NUCLEI

M. Grosch
H.-W. Georgii

Institut für Meteorologie und Geophysik
der Universität Frankfurt/M.

1. INTRODUCTION

Kumai (1951), Aufm Kampe, Weickmann and Kedesdy (1952) examined solid particles found at the centres of natural snow flakes. The majority of those particles consisted of clay.
In 1958 Mason und Maybank examined several specimen of natural mineral dusts and found in the case of clay minerals high efficiencies as ice nuclei. In contrast to that result Paterson (1967) found low efficiencies.

Measurements (Georgii, Kleinjung, 1968) of the ice nucleating ability of natural aerosol particles yielded a positive correlation between the concentration of natural freezing nuclei and the Calcium-concentration of the aerosols. This result points to a mineral continental source of ice nuclei.

A study on the elemental identification of ice nuclei had been started by Parungo and Pueschel (1973).

An extensive analysis of the natural aerosols with regard to the specific component responsible for the ice forming ability has not yet been performed.

2. EXPERIMENTAL

We have carried out measurements of the elemental composition of atmospheric ice forming nuclei and aerosols which were collected simultaneously. This study was done in cooperation with Dr. Gagin, University of Jerusalem, Israel.
For separating the freezing nuclei from the aerosols, membrane filters were developed in the Gagin-chamber (1969) and in the low pressure diffusion chamber (Gravenhorst et al., 1973). The ice crystals were picked up with a supercooled needle and collected in a thin plastic foil for bulk samples which were analysed with neutron activation. Single ice particles were placed on a film for identification in a scanning electron microscope interfaced with an X-ray energy spectrometer.

The bulk samples were irradiated 6 hours with a thermal neutron flux of 7×10^{11} $n/cm^2/s$. The energy spectra were taken with a Ge-Li-detector in a 4 000 channel analyser. With neutron activation 19 elements were measured while with the electron microscope 11 other elements were detected.

For obtaining one sample of ice nuclei for neutron activation analysis the ice nuclei from 100 filters were collected. These filters were exposed one after another. The total exposure time and the flow rate were the same as for one sample of total aerosol. The total air flow was 20 m^3.
The ice nuclei were developed at -18°C and 100 % r.h.

3. DISCUSSION OF EXPERIMENTAL RESULTS

The results show that the ice nuclei contain the same variation of elements as the atmospheric aerosols as a total. The differences are the concentrations of the elements. In tab. 1 the concentrations of elements are listed. The values are mean values of two samples.

Table 1

Concentrations of elements in synchronic samples of aerosols and ice nuclei

Element	ng/m^3 Aerosol	ng/m^3 Ice Nuclei	%
+Ag	7	3.7	53
As	1	.4	40
Au	.12	.05	42
+Ba	17	15	88
Br	122	3.5	3
Cl	620	160	26
Co	7	2.2	31
+Eu	.04	.03	75
+Fe	1300	800	61
+Hf	2	1.8	90
+K	580	300	52

Element	ng/m^3 Aerosol	ng/m^3 Ice Nuclei	%
La	1.4	.11	8
Mn	7.6	2.0	26
Na	440	100	23
Nd	26	2.4	9
+Sb	3.9	3.5	90
+Sc	.64	.51	80
+Sm	.15	.08	53
Sr	7.5	-.-	0

The last row of the table shows the percentage of the mass of an element in the ice nuclei in comparison to the total aerosol.
As the total mass of the measured elements in the ice nuclei is 44 % of that of the total aerosol these elements are indicated which have a higher concentration than 44% in the ice nuclei than in the total aerosol. The indicated elements are enriched in the ice nuclei compared with the total aerosol.

These elements may be responsible for the nucleation ability. At least they indicate the sources of the ice nuclei:

In an extensive study the sources of the elements in the atmospheric aerosols have been worked out. A series of samples of aerosols was collected in different characteristic regions for air quality and analysed with neutron activation. The collection sites were

1) in marine clean air over the North Atlantic on the research ship "Meteor",
2) in continental clean air in the Alpes, Europe in 2 400 m above sea level,
3) in the highly polluted air of Frankfurt, Germany and
4) in the less polluted air of Jerusalem and two remote areas in Germany, on the Mount Kl.Feldberg/Ts. and in Southern Germany.

The comparison of the concentrations of the elements shows that there are three main sources of investigated elements in the atmospheric aerosol: continental, marine and anthropogeneous source. For instance Si, Sc, Ba, La, Ce, Eu, Sm and other rare earth metals are typical continental elements, while Cl and Na are marine and As and Hg are typical anthropogeneous elements.

On this basis the sources of ice nuclei were traced. These elements which have enriched concentrations in the ice nuclei can be separated into three groups:

Table 2

Elements which are enriched in the ice nuclei

1) Ag	anthropogeneous source
2) K, Fe, Sb	mixed sources
3) Eu, Sm, Sc, Ba	continental source

1) The aerosols and ice nuclei which were collected in Jerusalem are highly contaminated with AgI because of cloud seeding. At the other si es the Ag-concentration is one to two orders of magnitude lower.
2) The elements from the second group are not only anthropogeneous, they can have at least two sources. Fe and Sb are of continental and of anthropogeneous origin, while K may have a marine source. The specific component which is of greatest importance for nucleation cannot be derived from the bulk samples, but it is supposed that only the continental component is decisive, because
3) the elements from the third group are exclusively continental.

It is evident that there are no marine elements enriched in the ice nuclei. This is in good agreement with the antiparallel connection between ice nuclei and hygroscopic particles (Metnieks and Georgii, 1958).

The electron microscope analysis shows that in the ice nuclei the most frequent elements are Si, Ca, Al in this sequence, while in aerosols they are Si, S, Al, Fe. These elements - Si, Ca, Al - are contained in almost all ice nuclei, therefore we consider them to be the base elements. They are like the most enriched elements crustal elements. They have high concentration peaks in the ice nuclei while the other elements - the admixtures - have small peaks. The admixtures vary, their quality depends on the sampling region.

In figure 1 a typical spectrum of an ice nucleus is to be seen.

There is one exception between the analysed ice nuclei which is completely organic.

An other series of ice nuclei were developed at -18°C and 102 % r.h., collected for a bulk sample and analysed with neutron-activation. In this sample there was more Au, Hg, but less As, Co and Mn. This indicates that there are some anthropogeneous elements which reduce ice nucleation and some others which promote nucleation.

Figure 1
Energy spectrum of an ice nucleus

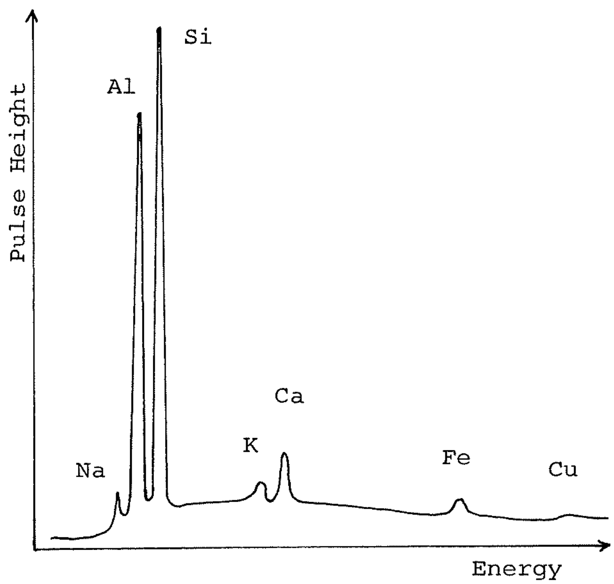

4. CONCLUSION

The base elements and those elements which are enriched in ice nuclei show that the majority of ice nuclei are continental mineral particles with different admixtures of anthropogeneous elements. These admixtures may reduce or promote nucleation.